

# Extraction of Single and Double Differential Cross-Sections on Argon for CC1 $\mu$ 2p0 $\pi$ Event Topologies in the SBND

Emilio Peláez Cisneros

August 19, 2024

## Abstract

The precise measurement of cross-sections for a variety of interactions is critical to the success of upcoming flagship neutrino experiments. Of special interest are neutrino interactions that leave the nucleus in a 2-particle 2-hole state (2p2h). This note will present cross-section measurements for the production of 2p2h states on Argon. Using SBND data collected from the **period** of operation, we select events corresponding to a charged-current  $\nu_\mu$  interaction that left the Argon nucleus in a 2p2h state. These interactions produce a topology with one muon and two protons in the final state (CC1 $\mu$ 2p0 $\pi$ ). This analysis targets both single differential and double differential cross-section measurements for CC1 $\mu$ 2p0 $\pi$  event topologies in a variety of kinematic variables. Comparisons are made to a set of theoretical models that explore different cross-section modeling configurations. Code for this analysis is available on [GitHub](#).

## Contents

<b>1</b>	<b>Introduction and motivation</b>	<b>3</b>
<b>2</b>	<b>Generator analysis</b>	<b>3</b>
2.1	Signal definition	3
2.2	Generators	3
2.3	Variables definition	4
2.4	Pre-FSI events	17
2.5	Double differential plots	20
2.6	Pure MEC events	31
<b>3</b>	<b>SBND analysis</b>	<b>35</b>
3.1	Fiducial volume	35
3.2	Signal definition	35
3.3	Variable plots	38
3.4	Interaction and topology breakdown	41
3.5	Signal efficiency	46
3.6	Migration and response matrices	49
3.7	Systematics	56
3.8	Wiener-SVD unfolding	59
3.9	Closure test	61
3.10	Event rate uncertainties	64
<b>4</b>	<b>Cross-section results</b>	<b>67</b>
4.1	Cross-section uncertainties	70
<b>5</b>	<b>Fake data studies</b>	<b>73</b>
5.1	MEC 2x weight	73
5.2	QE 0.5x and MEC 1.5x weights	78

<b>6 Appendices</b>	<b>83</b>
6.1 Cross section systematics . . . . .	83
6.2 Flux systematics . . . . .	350
6.3 Statistical systematics . . . . .	442
6.4 POT . . . . .	446
6.5 Number of targets . . . . .	450
6.6 Detector . . . . .	454
6.7 Reinteraction . . . . .	458
<b>7 References</b>	<b>462</b>

# 1 Introduction and motivation

2 Since many current and next generation neutrino oscillation experiments will utilize dense nuclear targets,  
3 such as liquid argon (LAr), it is critical to characterize the impact of nuclear effects on neutrino cross-sections.  
4 One area of interest are neutrino events that eject 2 nucleons from the nucleus, leaving it with 2 holes: known  
5 as 2-particle 2-hole states (2p2h). The general picture is that the neutrino has a charged-current interaction  
6 with a neutron in the nucleus, producing a proton with significant momentum; this proton interacts with  
7 another proton, producing the 2p2h state. While the majority of 2p2h states are caused by Meson Exchange  
8 Currents (MEC) [15], some nuclear effects, such as Short-Range Nucleon-Nucleon correlations (SRC) [10],  
9 can also produce these states. In an accelerator-based liquid argon time projection chamber (LArTPC)  
10 experiment, such as SBND, a charged-current (CC) muon neutrino ( $\nu_\mu$ ) interaction that results in a 2p2h  
11 state would have a final state topology of 1 muon, 2 protons, and no charged or neutral pions. While  
12 there are existing measurements of CC1 $\mu$ 2p0 $\pi$  events on argon, the analyses were statistically limited and  
13 no cross-sections were extracted [1, 19]. There was a previous report with single differential cross-section  
14 measurements from the MicroBooNE detector [20], but this document presents the first double differential  
15 cross-section measurements of CC1 $\mu$ 2p0 $\pi$  topologies on argon, using data collected from the period of SBND  
16 operations.

## 17 2 Generator analysis

### 18 2.1 Signal definition

19 We choose charged-current muon neutrino interactions that result in one muon, two protons, no charged pions  
20 with  $P_\pi > 70$  MeV/c, no neutral pions or heavier mesons, and any number of neutrons. These interactions  
21 are denoted as CC1 $\mu$ 2p0 $\pi$ . We require the momentum of the muon and protons to be in the following ranges  
22 (in MeV/c):

$$100 < P_P < 1200 \quad 300 < P_\mu < 1000 \quad (1)$$

### 23 2.2 Generators

24 The following generators are used to create events, which are then discriminated using the signal definition  
25 above: NuWro, GiBUU, NEUT, GENIE G18, GENIE AR23. Information about these generators is  
26 summarized in Table 1.

Name	Generator/Configuration
G18	GENIE v3.0.6 G18_10a_02_11a
AR23	G18 with SuSAv2 MEC model
NuWro	NuWro 19.02.1
NEUT	NEUT v5.4.0
GiBUU	GiBUU 2021

Table 1: Generator and configuration data.

27 The GENIE configurations we used are:

- 28 (i) GENIE G18 [2, 3]: This modern model configuration uses the local Fermi gas (LFG) model [9],  
29 the Nieves CCQE scattering prescription [23], which includes Coulomb corrections for the outgoing  
30 muon [11], and random phase approximation (RPA) corrections [22]. Additionally, it uses the  
31 Nieves MEC model [25], the KuzminLyubushkin-Naumov Berger-Sehgal RES [6, 28, 16], Berger-Sehgal  
32 COH [7] and Bodek-Yang DIS [29] scattering models with the PYTHIA [26] hadronization part, and  
33 the hA2018 FSI model [4].
- 34 (ii) GENIE AR23: Same as the G18 model configuration but using the SuSAv2 MEC model.

35 The alternative event generators are:

- 36 (i) NuWro [12]: Includes the LFG model [9], the Llewellyn Smith model for QE events [18], the Nieves  
37 model for MEC events [24], the AdlerRarita-Schwinger formalism to calculate the  $\Delta$  resonance explicitly [13],  
38 the Berger-Sehgal (BS) COH [7] scattering model, an intranuclear cascade model for FSI [24],  
39 and a coupling to PYTHIA [26] for hadronization.
- 40 (ii) NEUT [14]: Corresponds to the combination of the LFG model [8, 9], the Nieves CCQE scattering  
41 prescription [23], the Nieves MEC model using a lookup table [25], the Berger Sehgal RES [6, 13, 5]  
42 and BS COH [7] scattering models, FSI with medium corrections for pions [2, 3], and PYTHIA [26]  
43 purposes.
- 44 (iii) GiBUU [21]: Uses similar models to GENIE, but they are implemented in a coherent way by solving  
45 the Boltzmann-Uehling-Uhlenbeck transport equation [21]. The modeling includes the LFG model [9],  
46 a standard CCQE expression [17], an empirical MEC model, and a dedicated spin dependent resonance  
47 amplitude calculation following the MAID analysis [21]. The DIS model is from PYTHIA [26]. GiBUU's  
48 FSI treatment propagates the hadrons through the residual nucleus in a nuclear potential consistent  
49 with the initial state.

### 50 2.3 Variables definition

51 Given the momentum vectors for the leading proton  $\vec{p}_L$ , recoil proton  $\vec{p}_R$ , and muon  $\vec{p}_\mu$ , we define several  
52 variables. First, we define the momenta and opening angle of each variable, denoted as  $|\vec{p}|$  and  $\cos(\theta_{\vec{p}})$ , with  
53 the appropriate index for each momentum vector. These variables are plotted in Figure 1.

54 We also define variables relating the multiple momentum vectors. First, the opening angle between the  
55 protons in the lab frame, given by

$$\cos(\theta_{\vec{p}_L, \vec{p}_R}) = \frac{\vec{p}_L \cdot \vec{p}_R}{|\vec{p}_L| |\vec{p}_R|}. \quad (2)$$

56 Then, the opening angle between the total proton momentum ( $\vec{p}_{\text{sum}} = \vec{p}_L + \vec{p}_R$ ) and the muon, given by

$$\cos(\theta_{\vec{p}_\mu, \vec{p}_{\text{sum}}}) = \frac{\vec{p}_\mu \cdot \vec{p}_{\text{sum}}}{|\vec{p}_\mu| |\vec{p}_{\text{sum}}|}. \quad (3)$$

57 The momentum transverse to the direction of the neutrino beam, which we denote  $\delta\vec{P}_T$  and is given by

$$\delta\vec{P}_T = \vec{p}_T^\mu + \vec{p}_T^L + \vec{p}_T^R. \quad (4)$$

58 For the transverse momentum, we will be interested in its magnitude  $|\delta\vec{P}_T|$ . Finally, the angular orientation  
59 of the transverse momentum with respect to the transverse muon is defined as

$$\delta\alpha_T = \cos^{-1} \left( \frac{-\vec{p}_T^\mu \cdot \delta\vec{P}_T}{|\vec{p}_T^\mu| |\delta\vec{P}_T|} \right). \quad (5)$$

60 We plot the differential cross sections of these variables for the given generators in Figure 2. We can also  
61 see the cross section by event type for all variables and all generators in Figures 3 to 12.

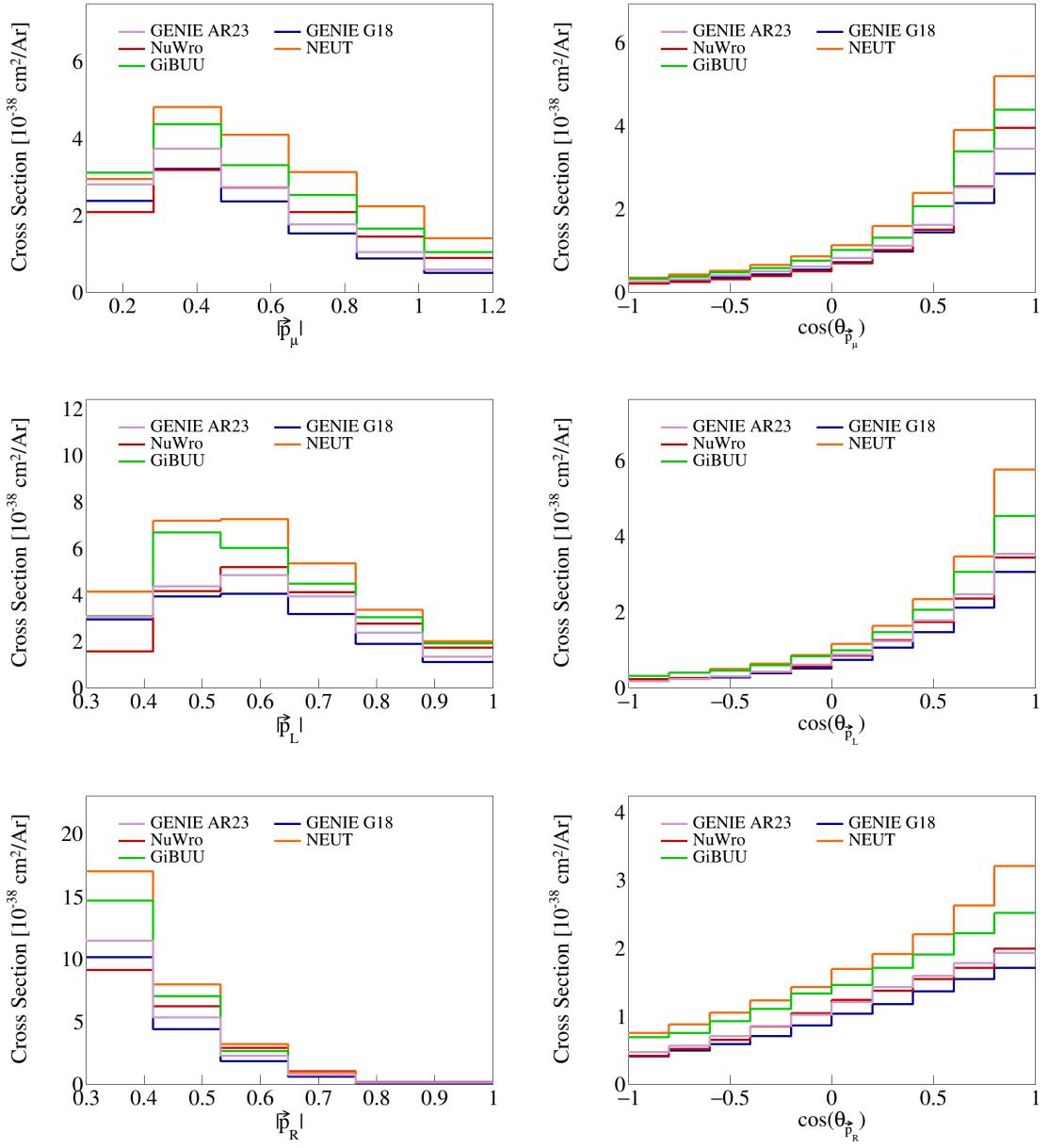


Figure 1: Cross sections for momenta and opening angles of individual particles.

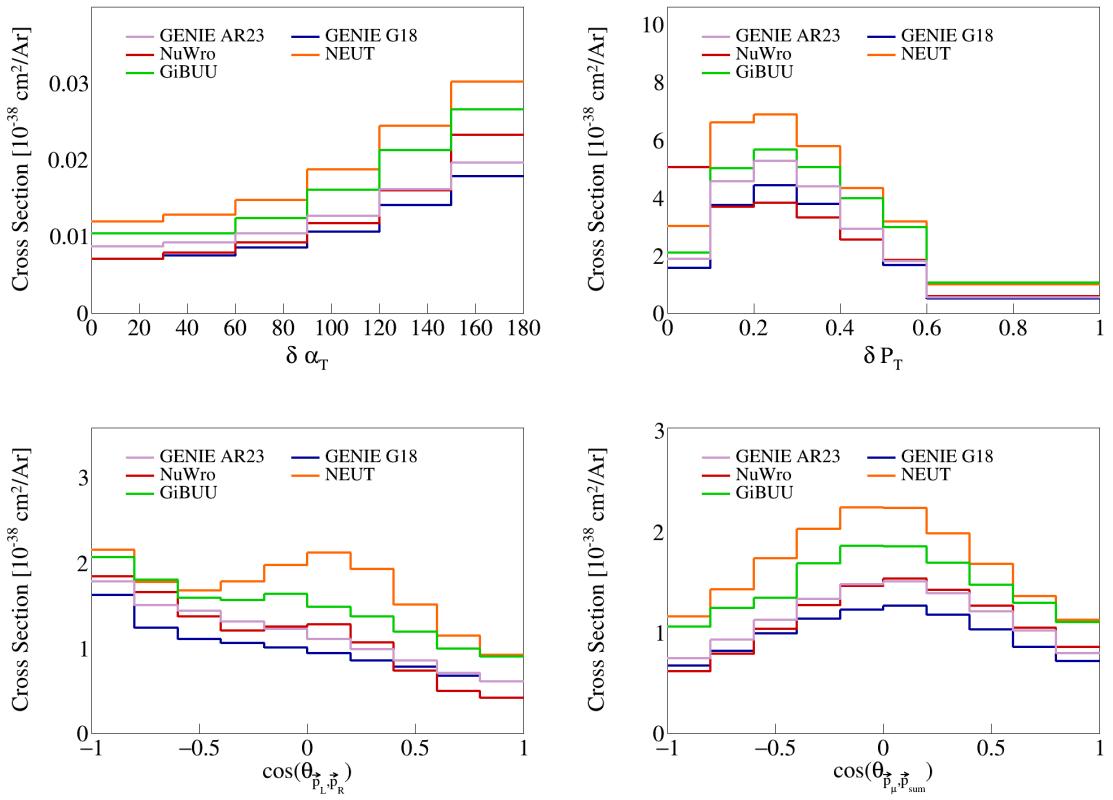


Figure 2: Cross sections for opening angles and transverse momentum.

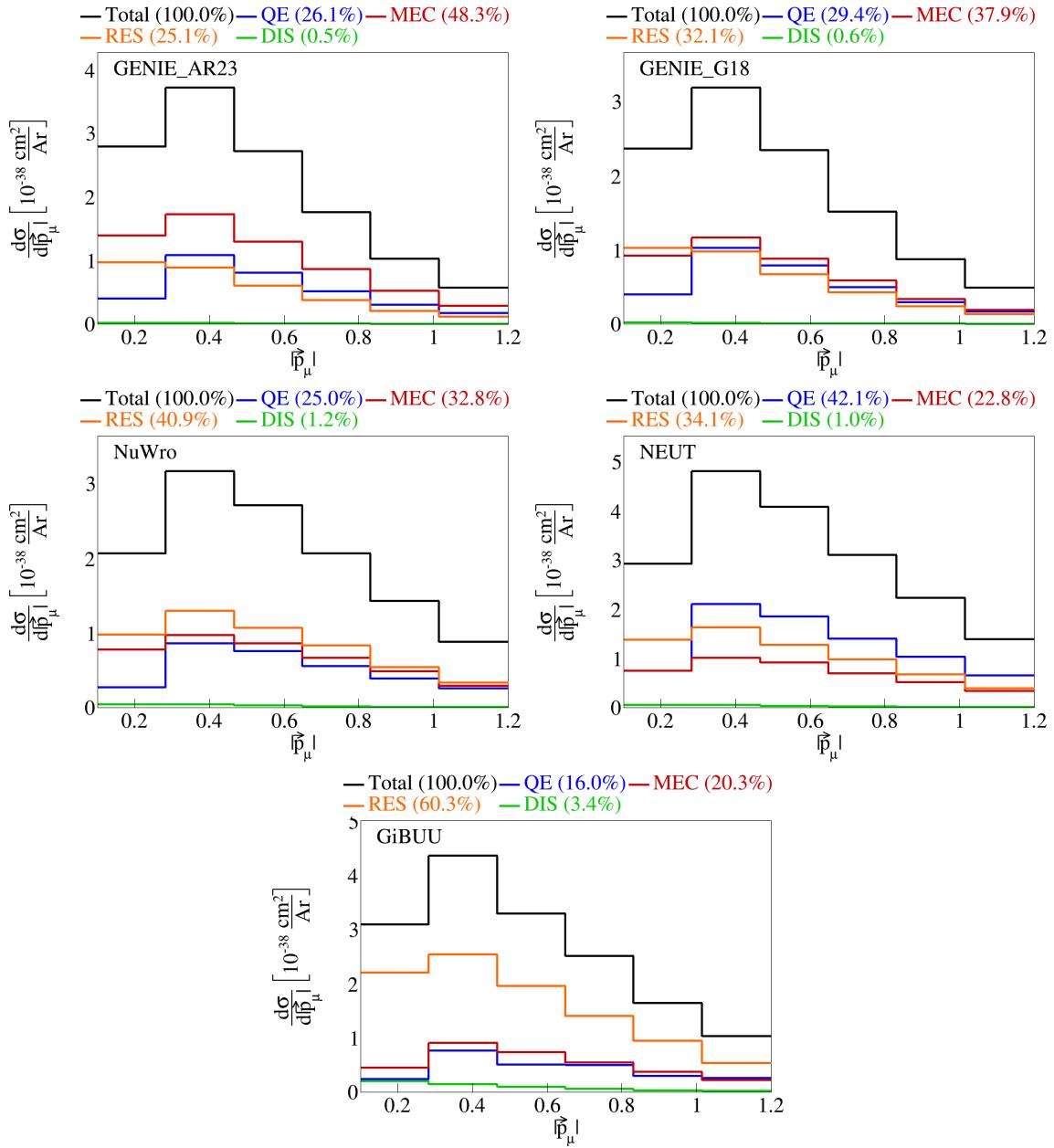


Figure 3: Event interaction breakdown for  $|\vec{p}_\mu|$ .

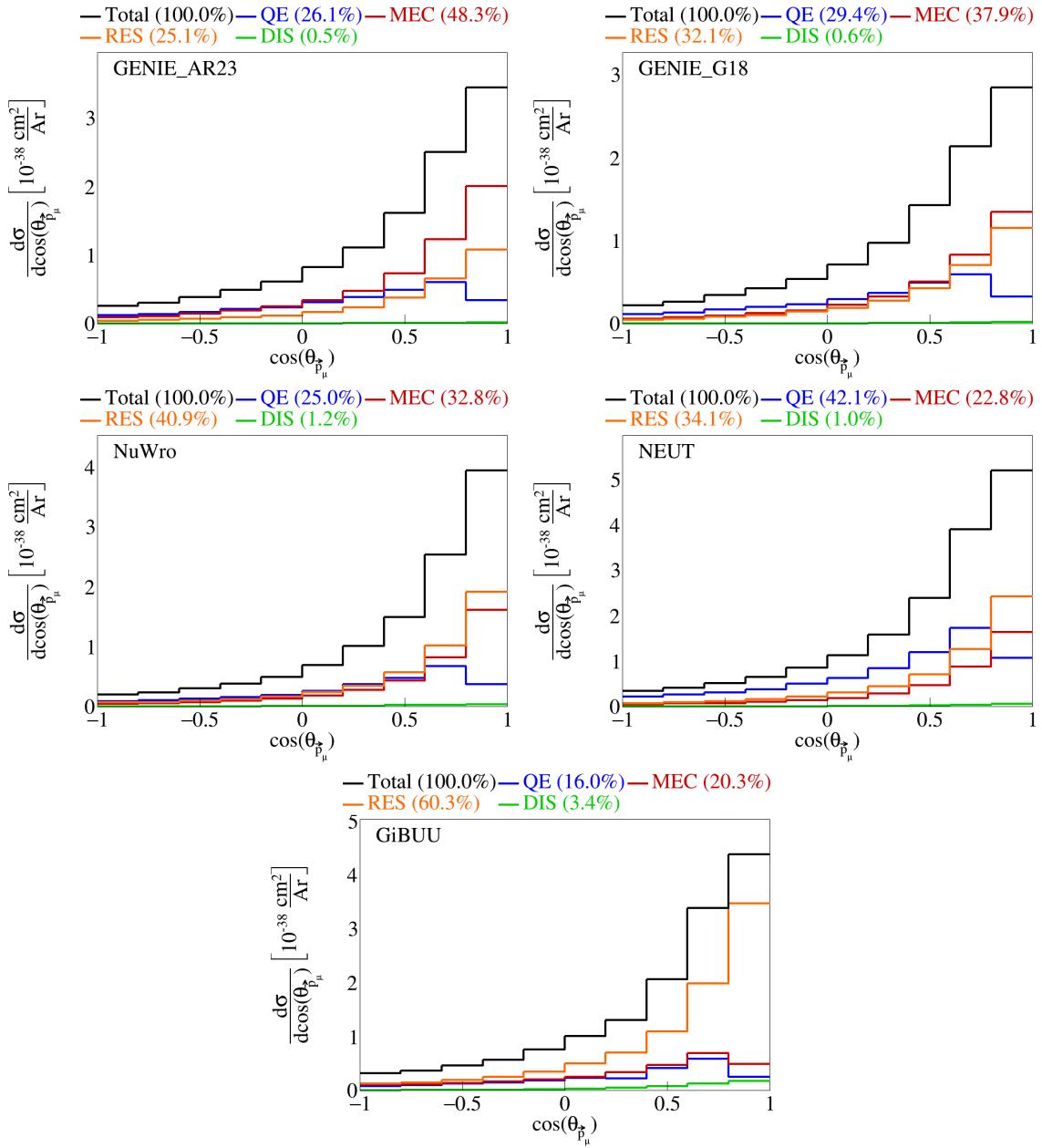


Figure 4: Event interaction breakdown for  $\cos(\theta_{\vec{p}_\mu})$ .

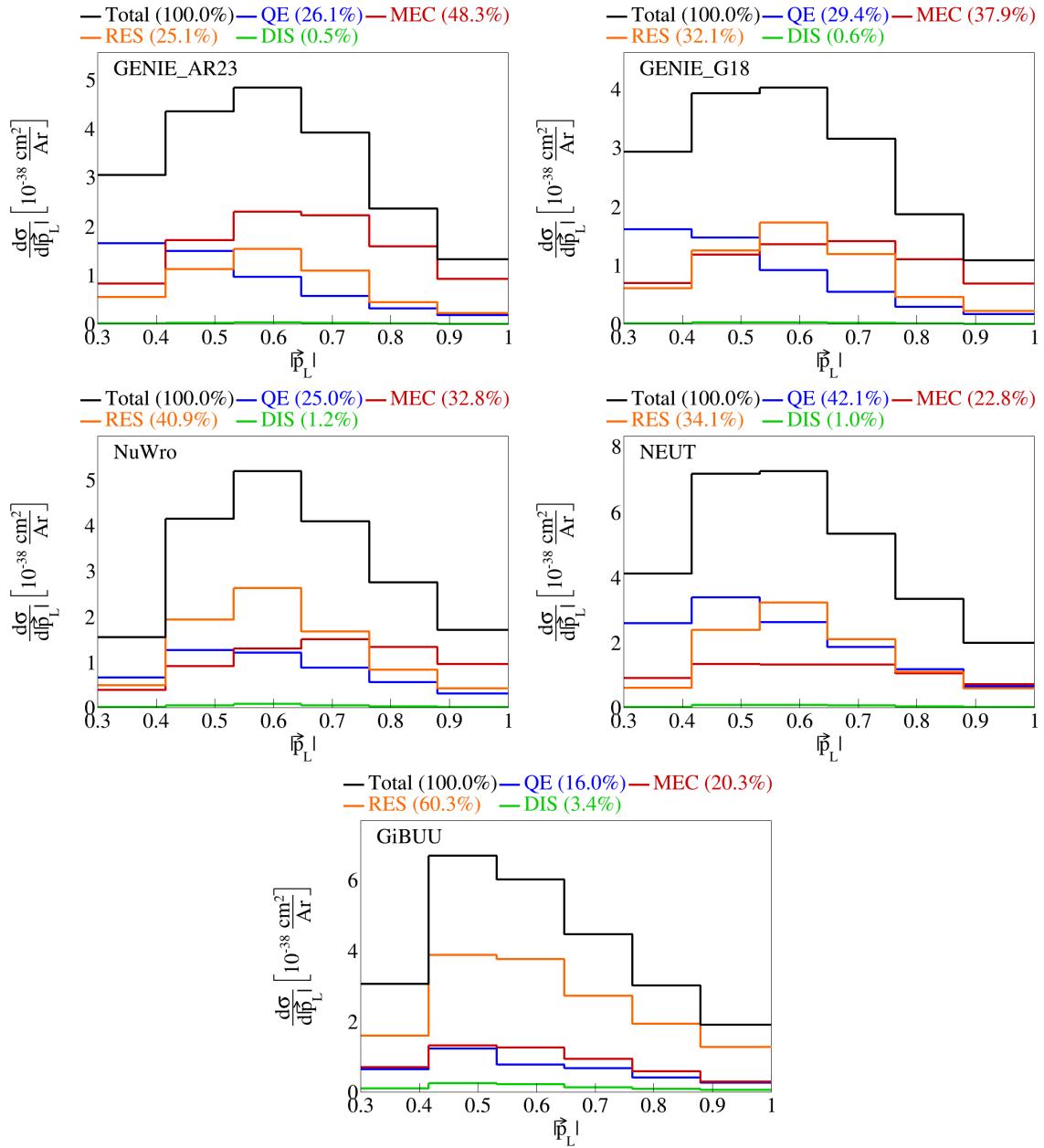


Figure 5: Event interaction breakdown for  $|\vec{p}_L|$ .

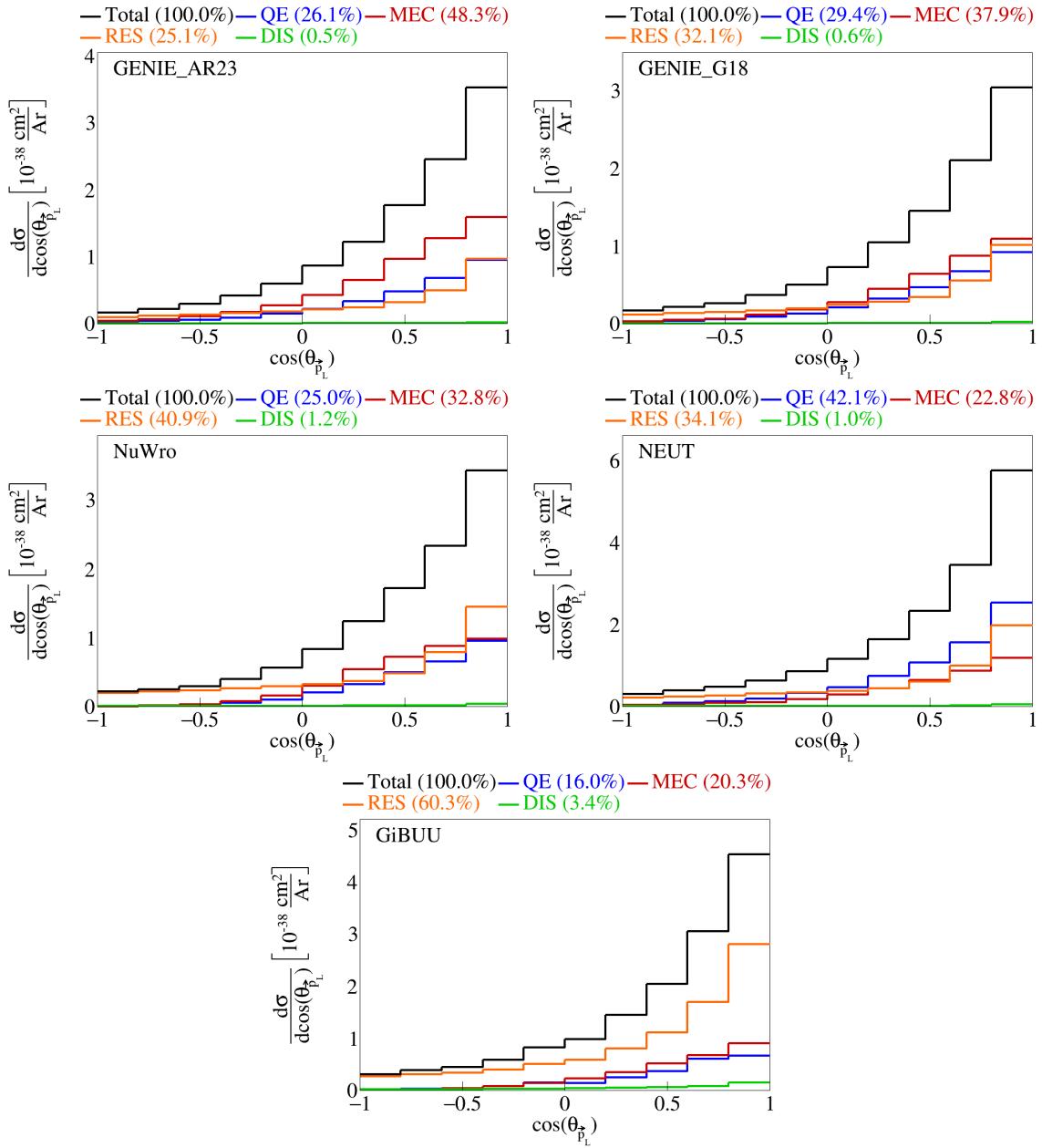


Figure 6: Event interaction breakdown for  $\cos(\theta_{\vec{p}_L})$ .

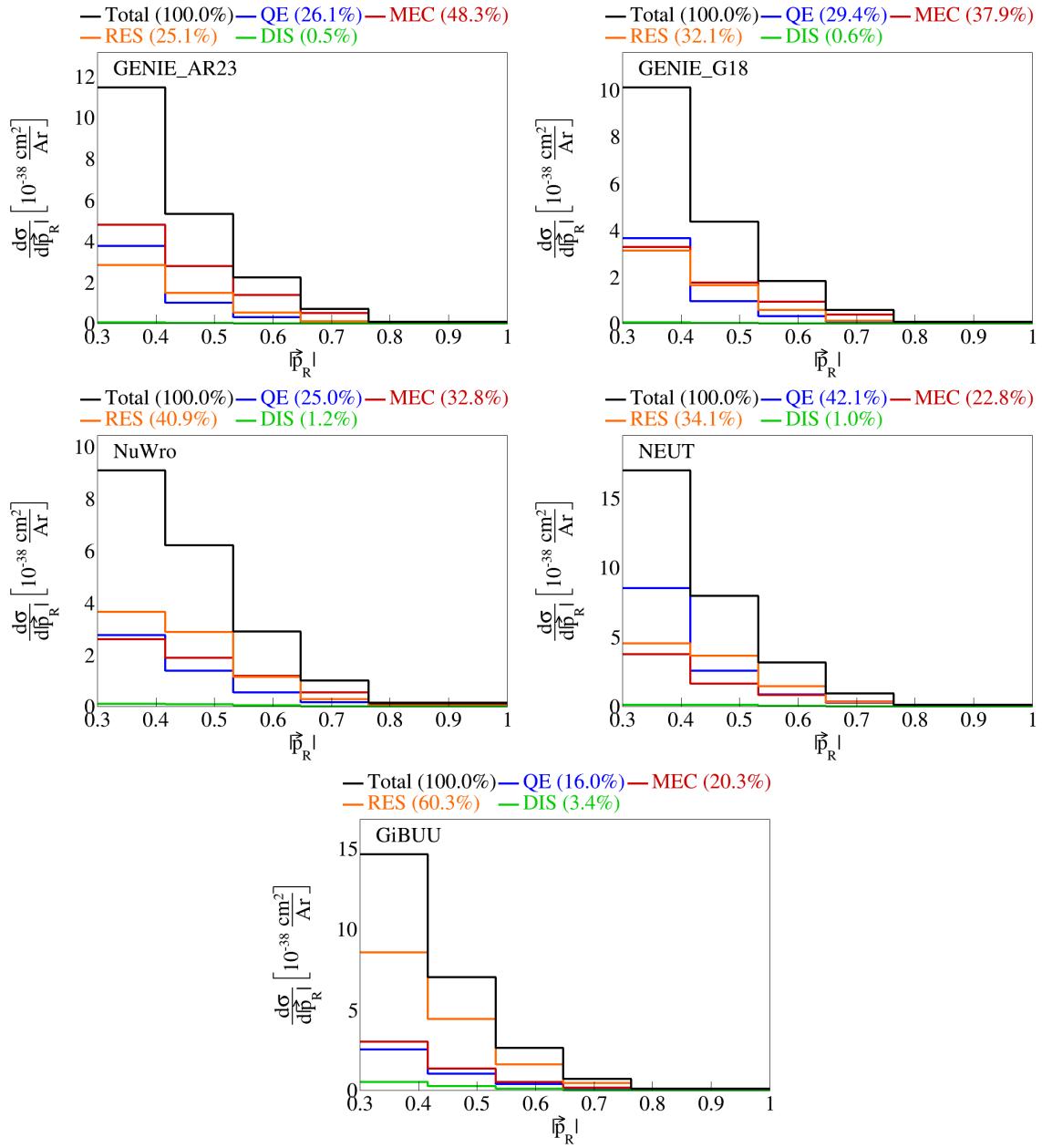


Figure 7: Event interaction breakdown for  $|\vec{p}_R|$ .

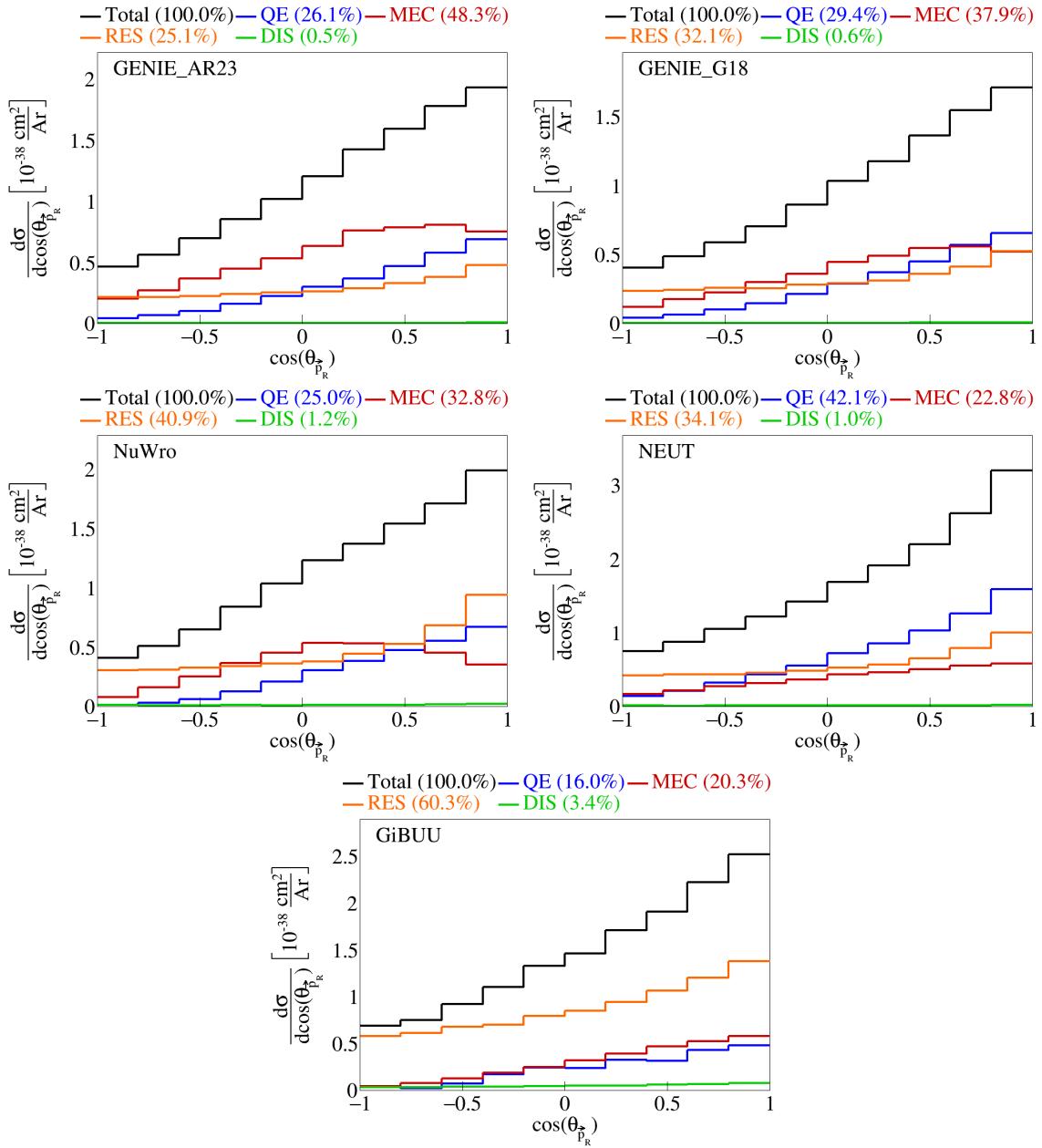


Figure 8: Event interaction breakdown for  $\cos(\theta_{\vec{p}_R})$ .

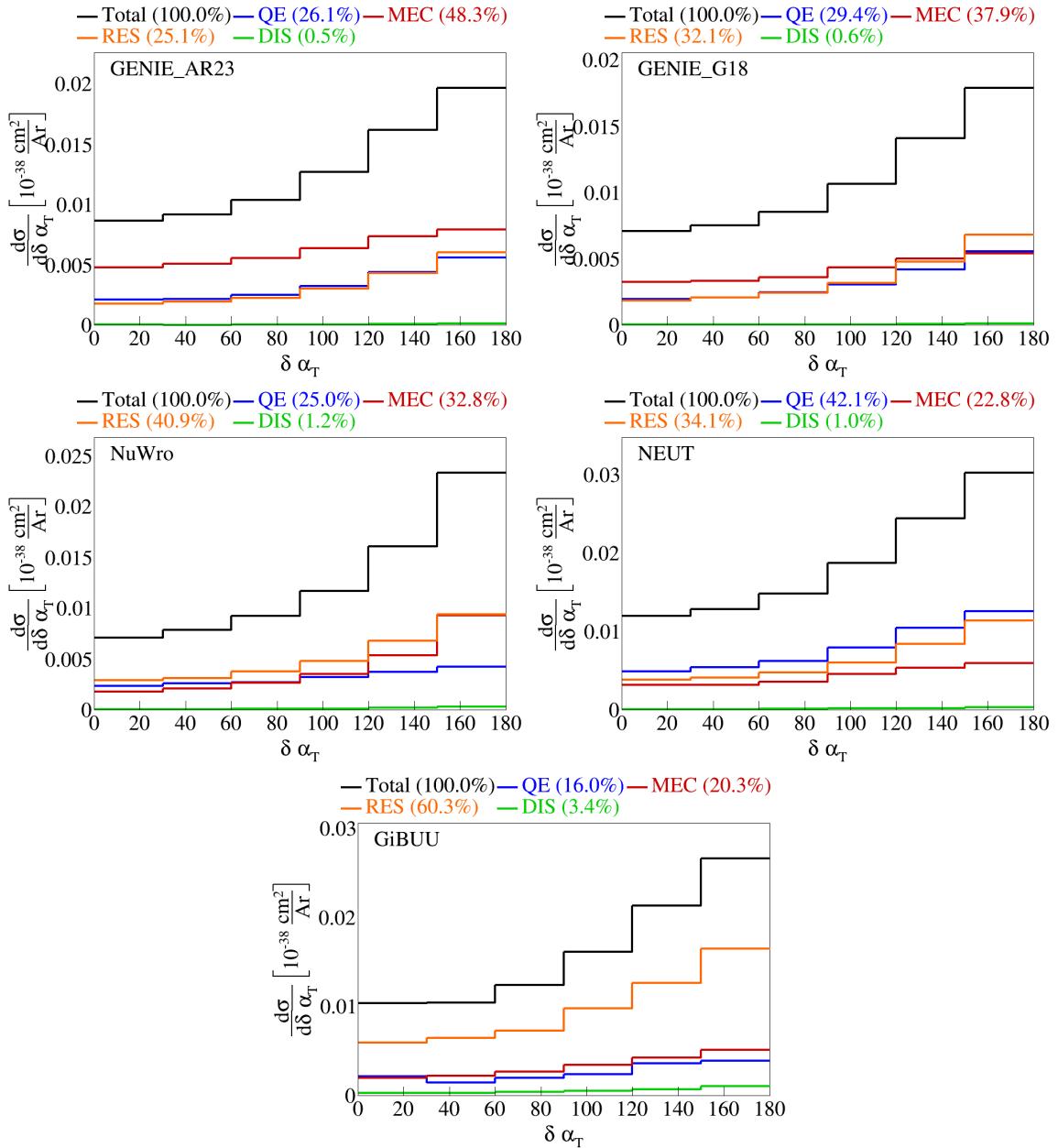


Figure 9: Event interaction breakdown for  $\delta\alpha_T$ .

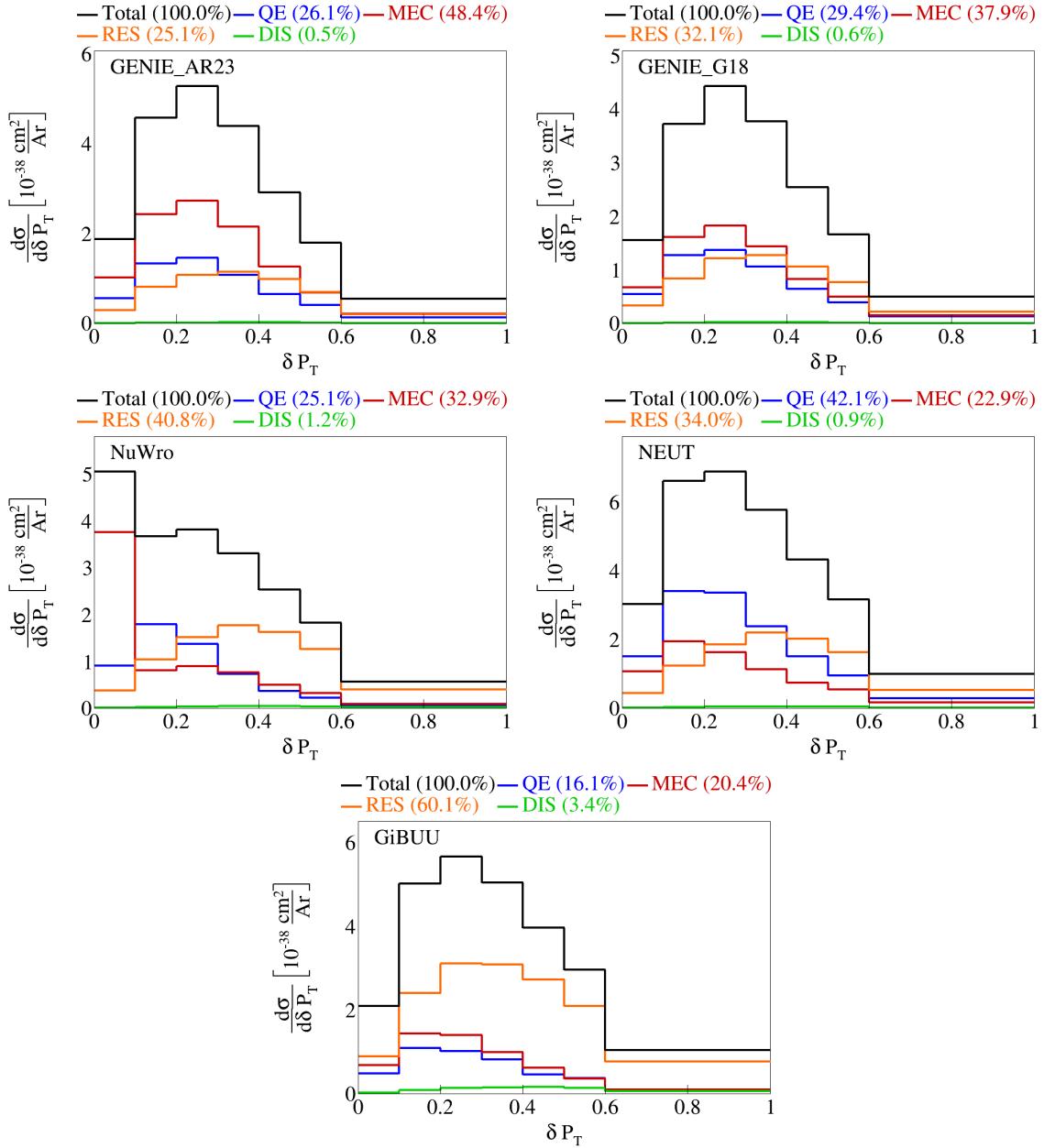


Figure 10: Event interaction breakdown for  $|\delta \vec{P}_T|$ .

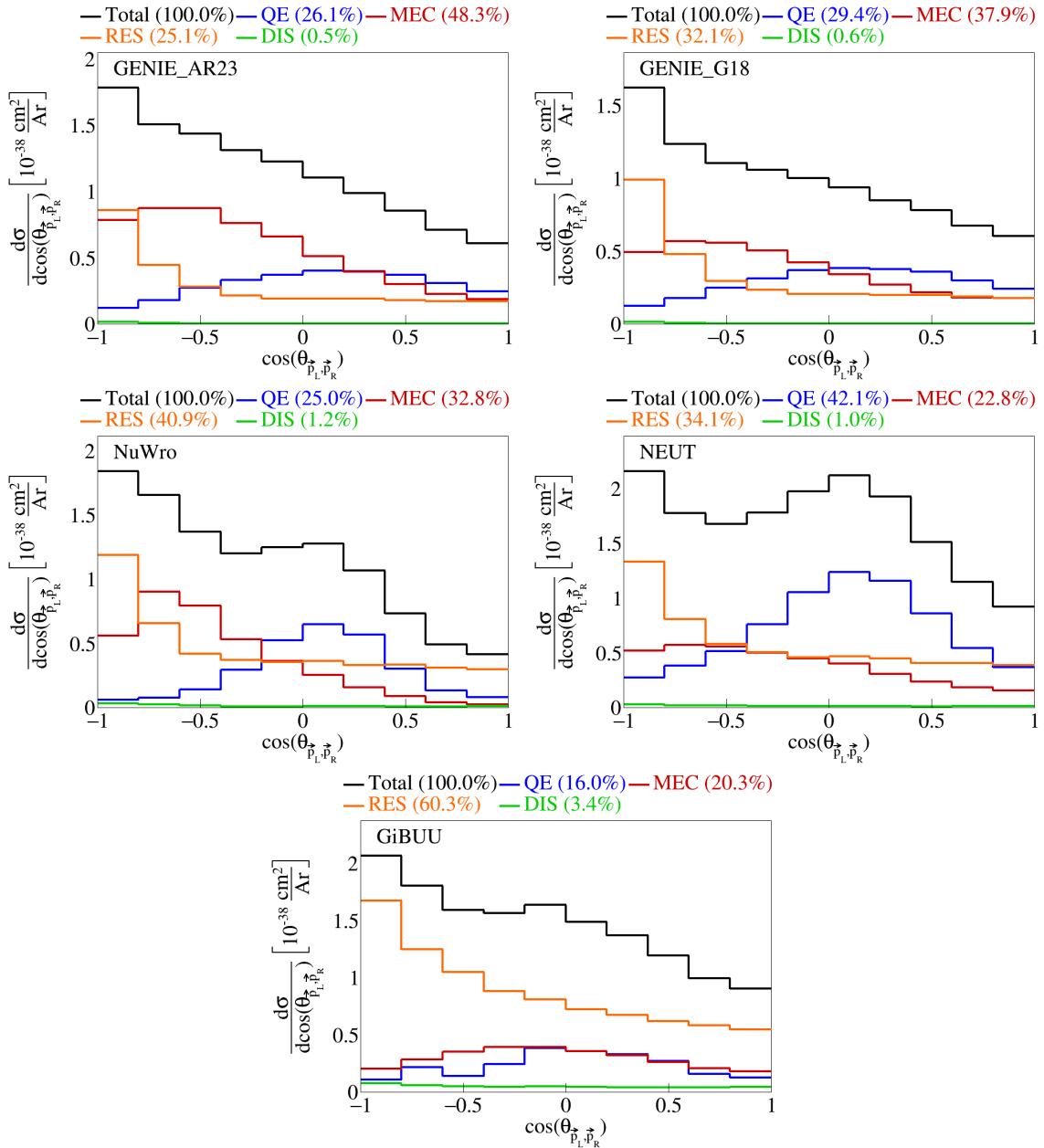


Figure 11: Event interaction breakdown for  $\cos(\theta_{\vec{p}_L, \vec{p}_R})$ .

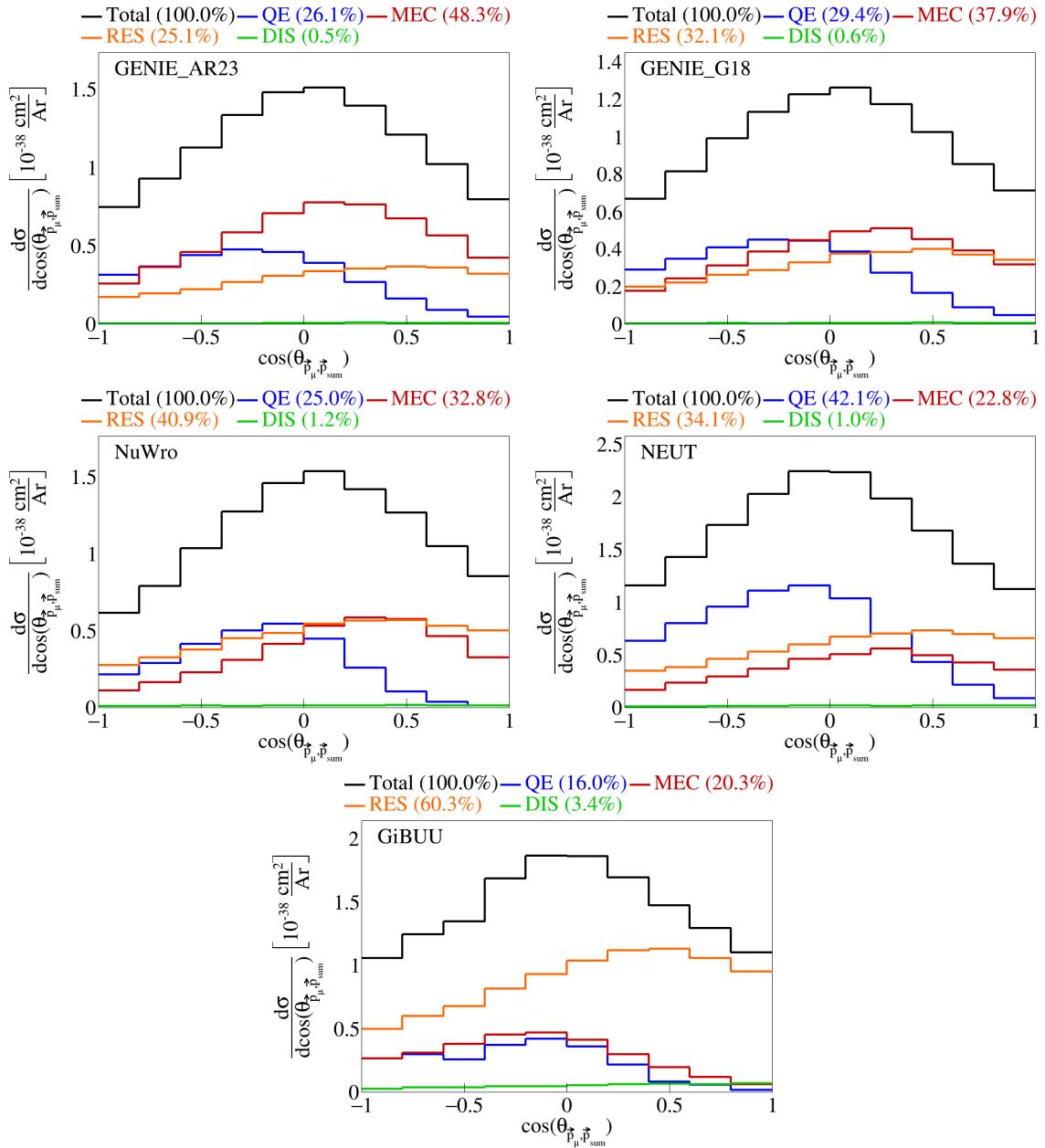


Figure 12: Event interaction breakdown for  $\cos(\theta_{\vec{p}_\mu, \vec{p}_{\text{sum}}})$ .

62 **2.4 Pre-FSI events**

63 To investigate why the percentage of MEC events for some generators is low, we performed event selection  
64 before any final state interactions took place and plotted the interaction breakdown. For both GENIE tunes,  
65 NEUT, and NuWro, we got 100% MEC events pre-FSI. For GiBUU, only 4.1% MEC versus 76.2% RES and  
66 16% DIS events pre-FSI. The interaction breakdown for  $|\vec{p}_\mu|$  for all the generators are shown in Figure 13.  
67 Since GiBUU is the outlier, we checked the specific interaction mode for the resonance events. We got that  
68 10 has 39.3%, 11 has 34.7%, 12 has 0.0136%, 13 has 26 %, and 27, 22, and 23 all have zero percent of the  
69 resonance events.

70 We also checked the event interaction breakdown for GiBUU samples generated without final state  
71 interactions, in which we found that 100% of the events are MEC, shown in Figure 14. Note that the  
72 difference between these two GiBUU samples is that in the former, the samples were generated with final  
73 state interactions, and then we look at the state before the final state interactions reportedly took place,  
74 and in the latter the event generation was done without any final state interactions.

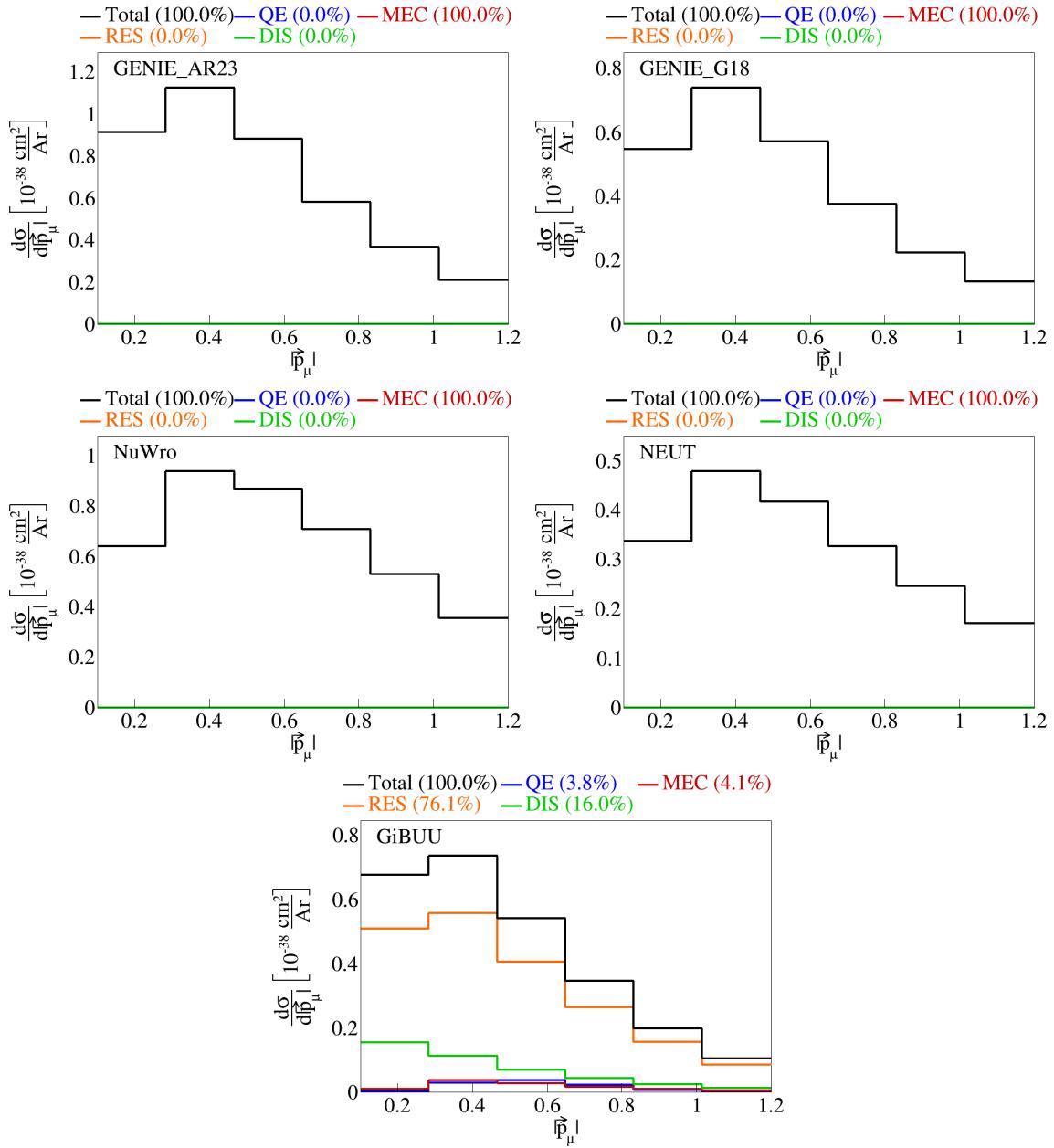


Figure 13: Event interaction breakdown of  $|\vec{p}_\mu|$  before final state interactions.

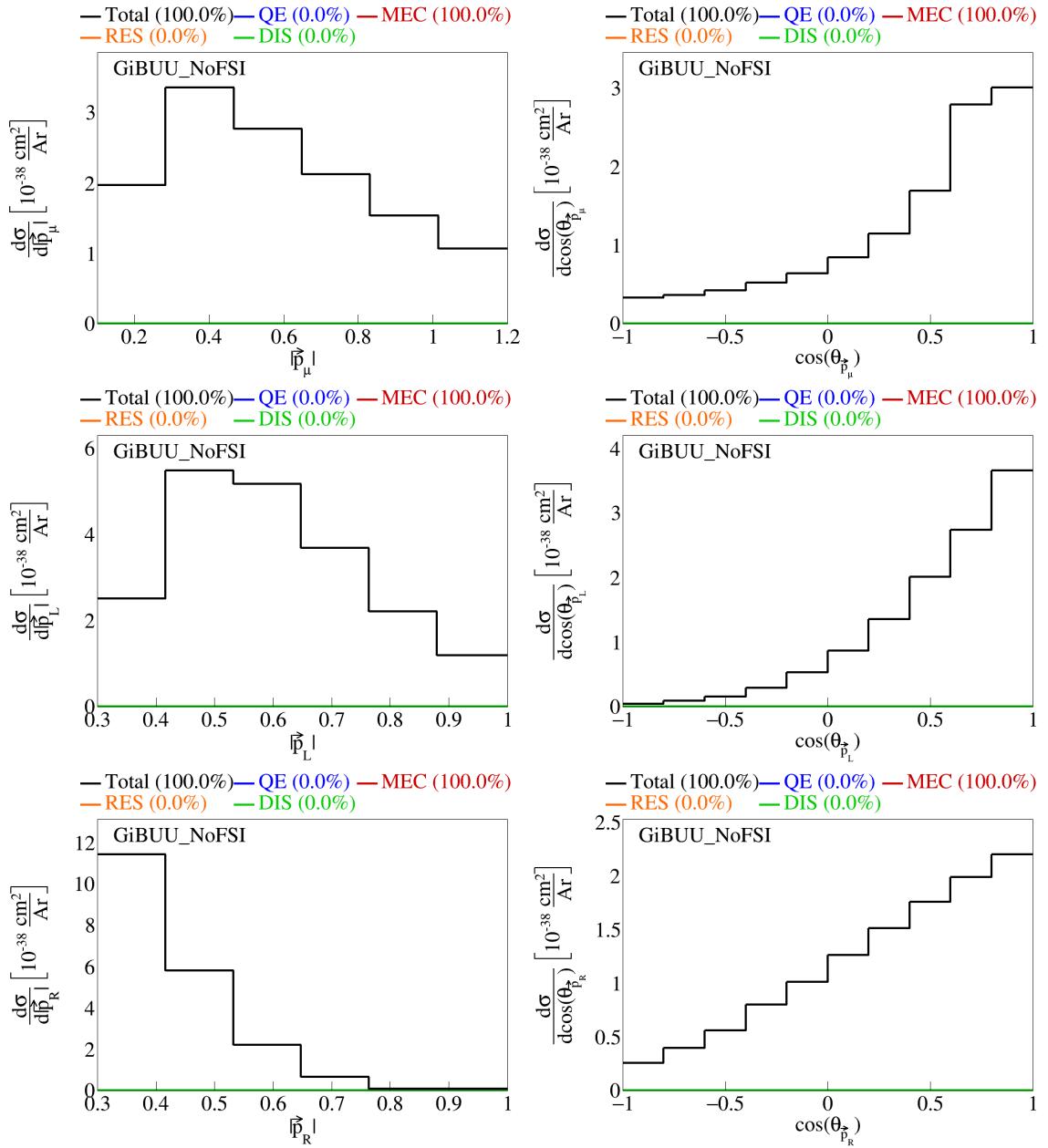


Figure 14: Event interaction breakdown for final events from GiBUU events with no FSI.

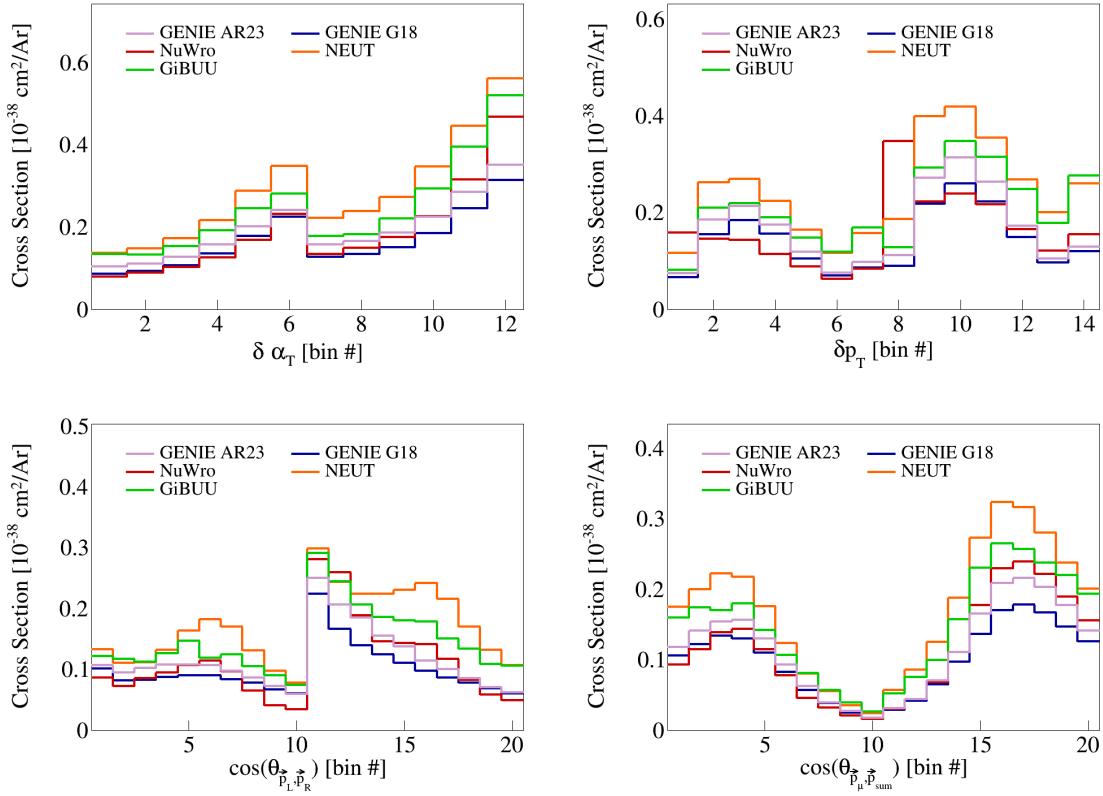


Figure 15: Double differential serial plots, all in  $\cos(\theta_{\vec{p}_\mu})$ .

## 75 2.5 Double differential plots

76 We define four double differential variables as  $\delta P_T$ ,  $\delta \alpha_T$ ,  $\cos(\theta_{\vec{p}_L, \vec{p}_R})$ , and  $\cos(\theta_{\vec{p}_\mu, \vec{p}_{\text{sum}}})$  in  $\cos(\theta_{\vec{p}_\mu})$ . We have  
 77 two bins for  $\cos(\theta_{\vec{p}_\mu})$ , the first one going from  $-1$  to  $0.5$  and the second from  $0.5$  to  $1$ . Therefore, these are  
 78 irregular bins, with the first covering a larger range than the first. These plots are shown in Figure 15. Note  
 79 that, in these plots, the horizontal axis is defined by bin number of the double differential measurement, not  
 80 the value of the variable. This is because we are representing both variables in a single axis, but we can slice  
 81 the plots to get our usual horizontal axis in two slices of  $\cos(\theta_{\vec{p}_\mu})$ .

82 We slice the double differential plots into two plots each, so that we have the variable of interest in the  
 83 horizontal axis instead of bin numbers, and each slice corresponds to one bin of  $\cos(\theta_{\vec{p}_\mu})$ . These plots are  
 84 shown in Figure 16, and the plots broke down by interaction type are in Figures 17 to 20. In these plots,  
 85 the bins contents have been reweighted appropriately, by dividing the content of each bin in the horizontal axis  
 86 by the width of the bin for the variable in the horizontal axis multiplied by the width of the  $\cos(\theta_{\vec{p}_\mu})$  slice.  
 87 Note that the plots for the  $0.5 < \cos(\theta_{\vec{p}_\mu}) < 1$  slice have more events in general, although they span a  
 88 smaller phase space of  $\cos(\theta_{\vec{p}_\mu})$ , as it can be seen by the scale of the vertical axis. We plot the same double  
 89 differential variables for the events before final state interactions. These are shown in Figure 21, and the  
 90 corresponding interaction breakdown plots are in Figures 22 to 25.

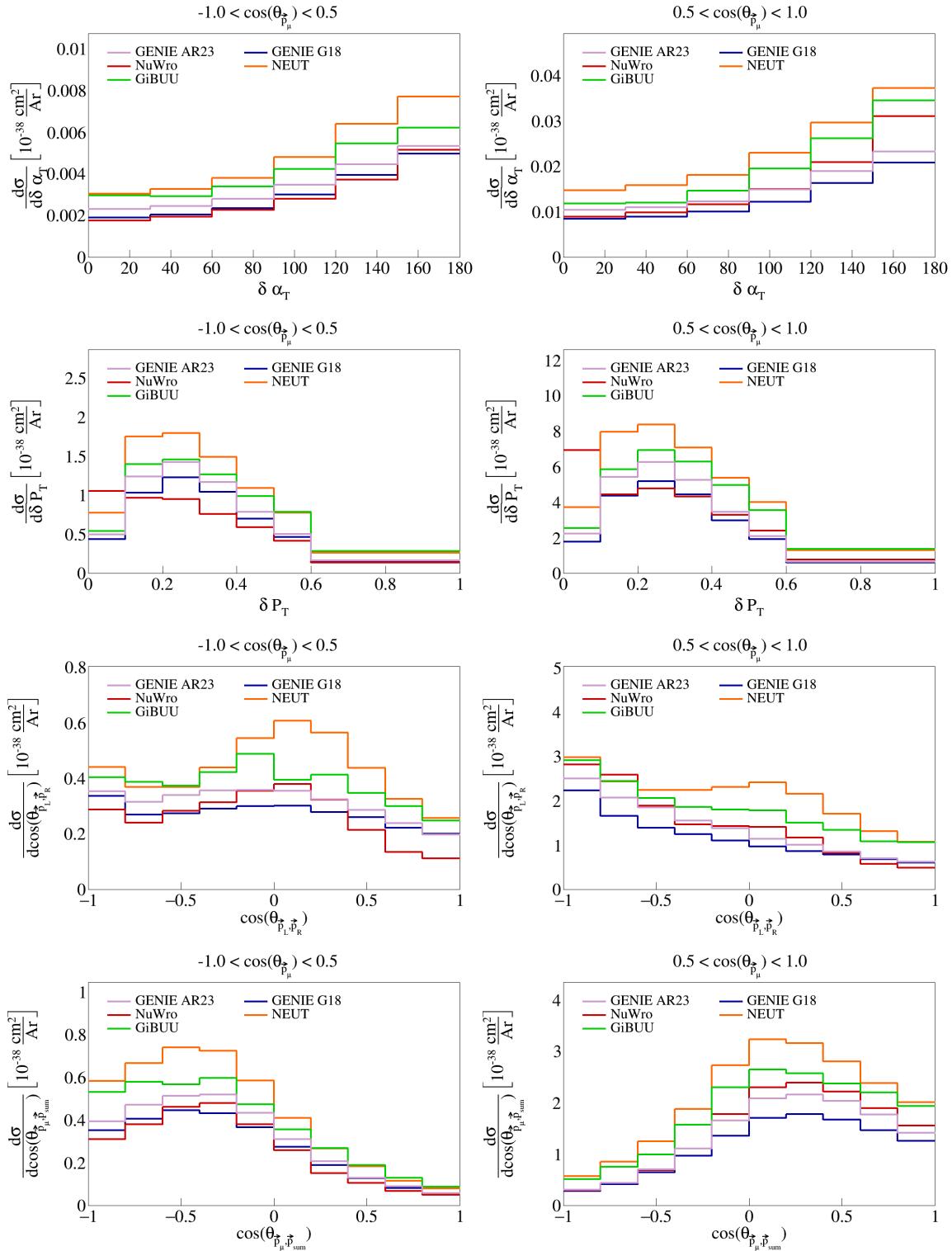


Figure 16: Sliced double differential plots.

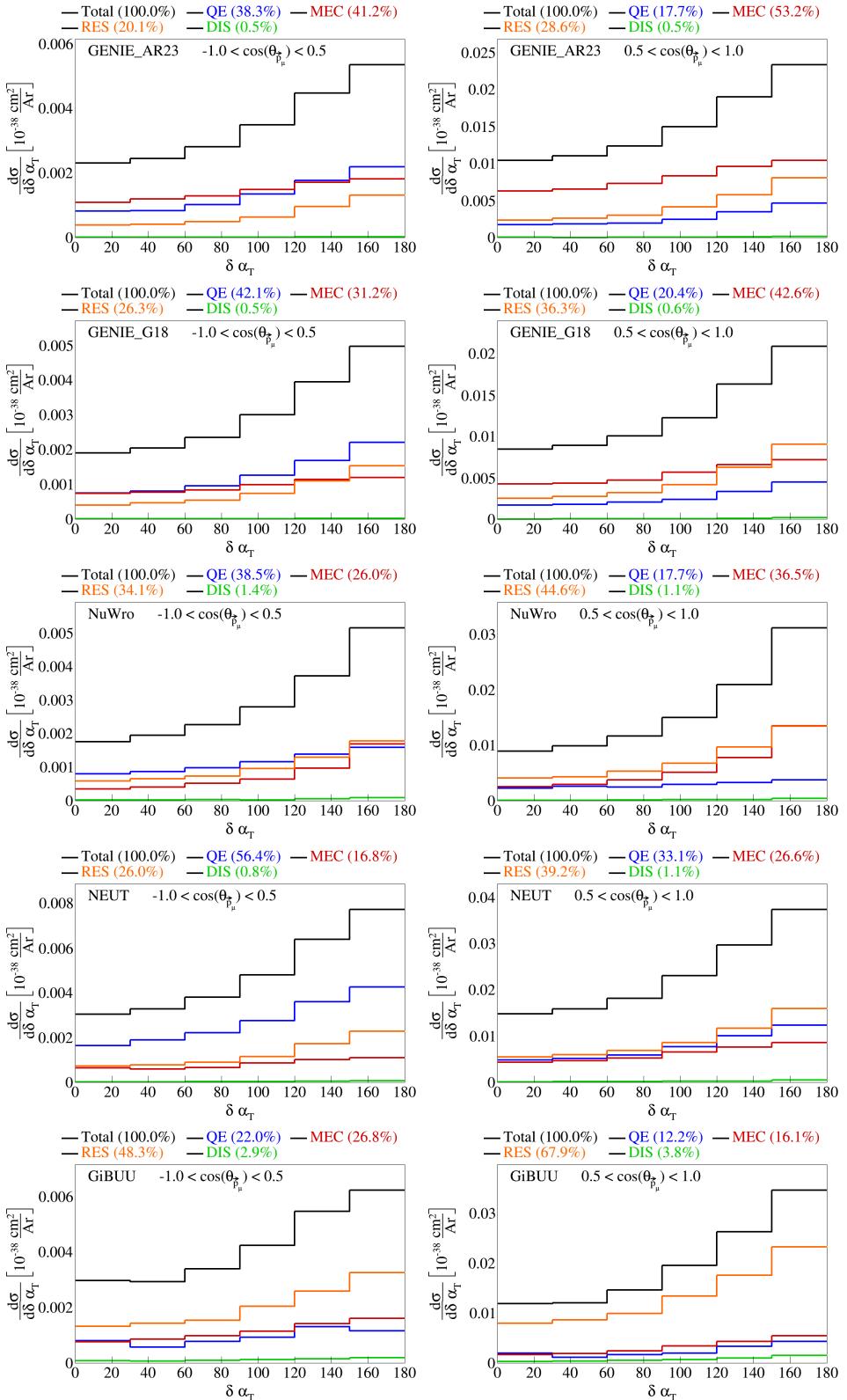


Figure 17: Interaction breakdown for sliced double differential plots for  $\delta\alpha_T$  in  $\cos(\theta_{\vec{p}_\mu})$ .

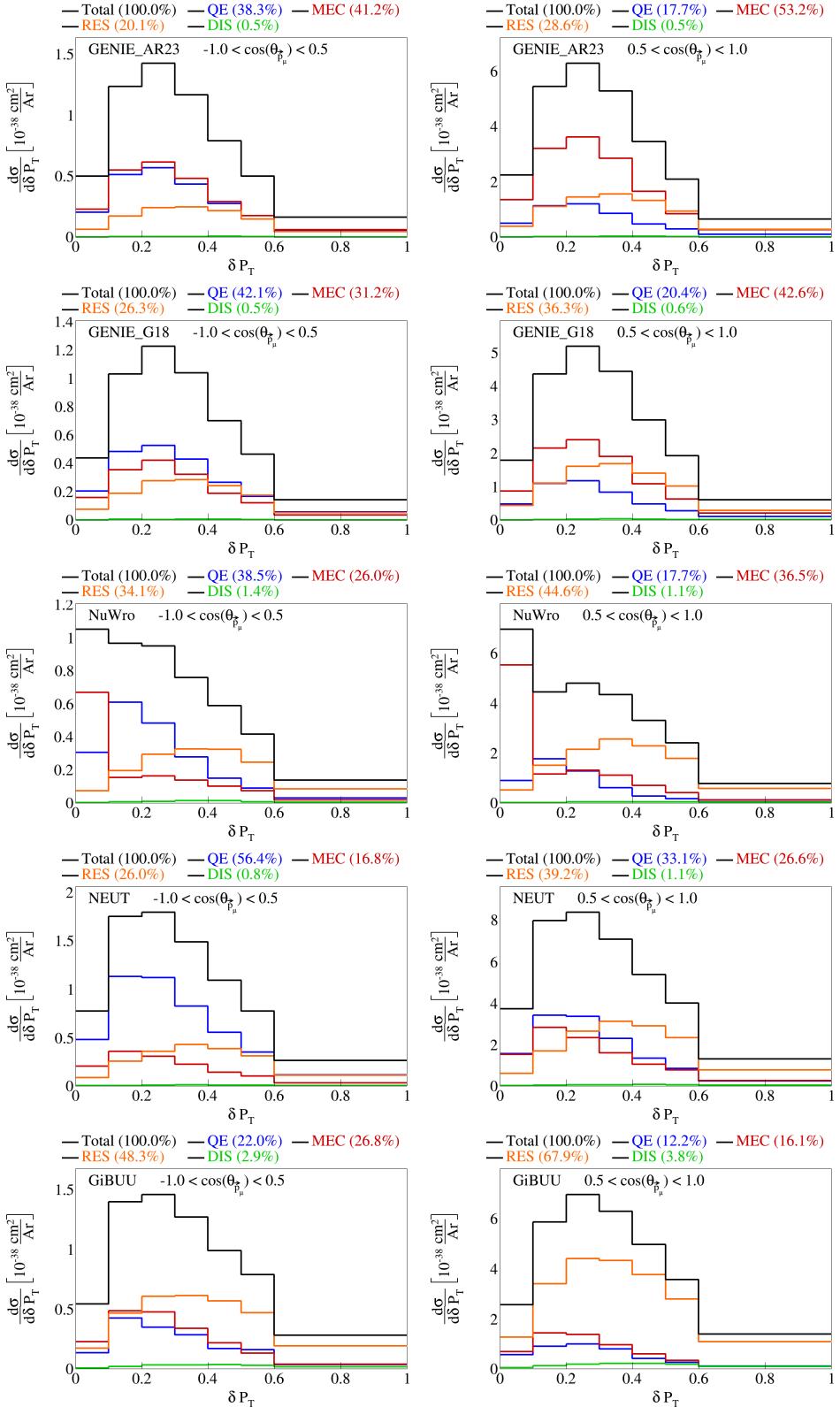


Figure 18: Interaction breakdown for sliced double differential plots for  $|\delta\vec{P}_T|$  in  $\cos(\theta_{\vec{p}_\mu})$ .

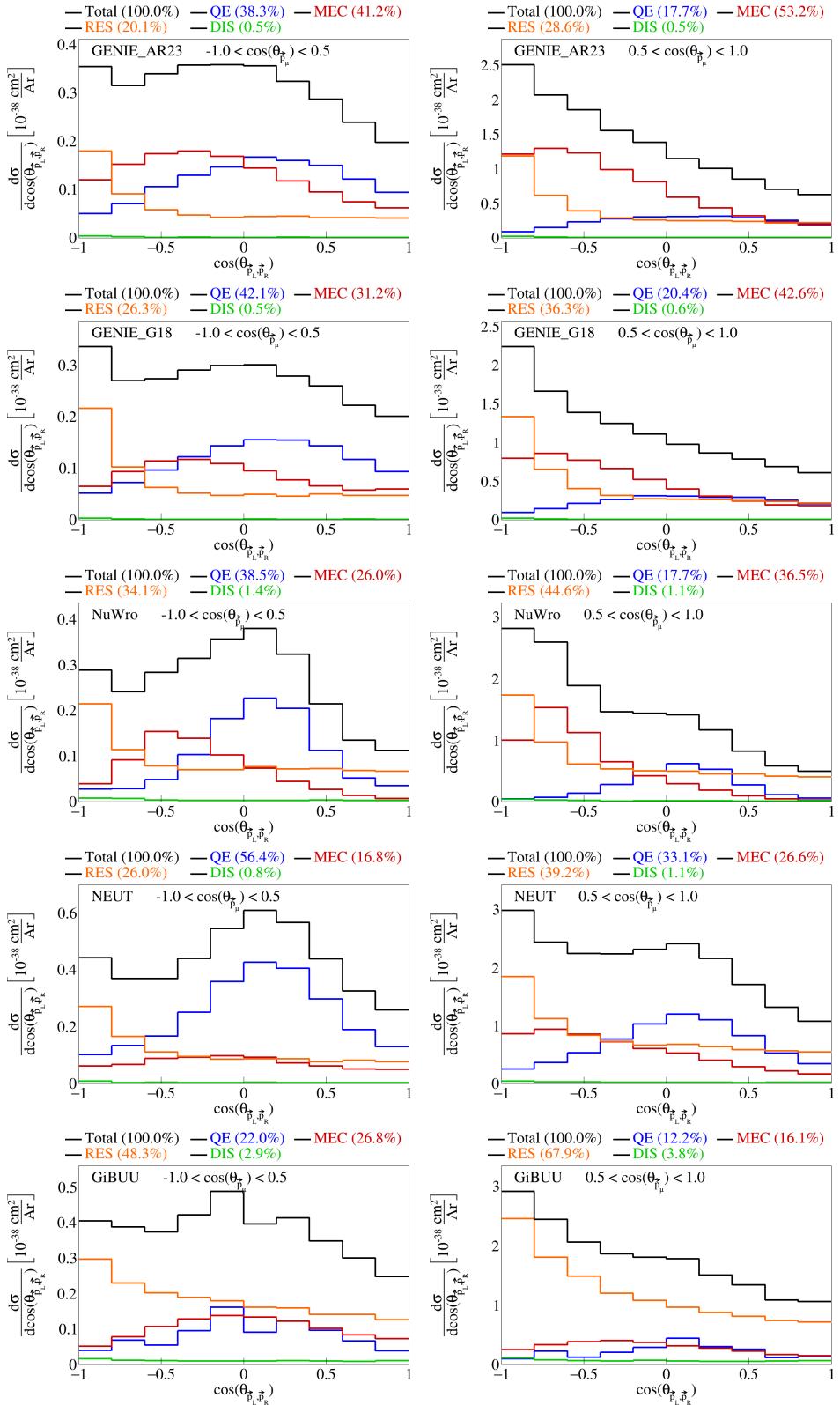


Figure 19: Interaction breakdown for sliced double differential plots for  $\cos(\theta_{\vec{p}_L, \vec{p}_R})$  in  $\cos(\theta_{\vec{p}_\mu})$ .

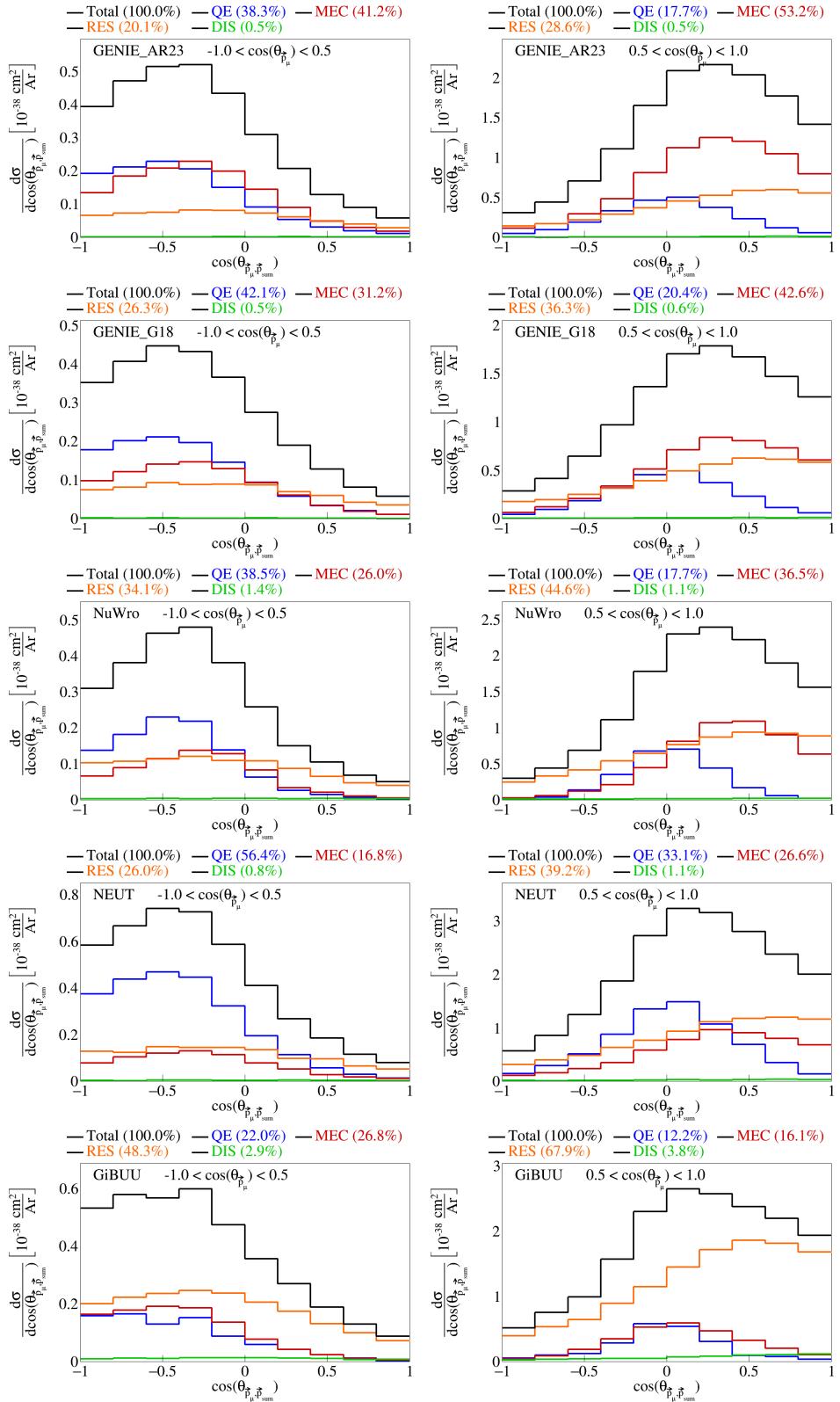


Figure 20: Interaction breakdown for sliced double differential plots for  $\cos(\theta_{\vec{p}_\mu}^* \vec{p}_{\text{sum}}^*)$  in  $\cos(\theta_{\vec{p}_\mu})$ .

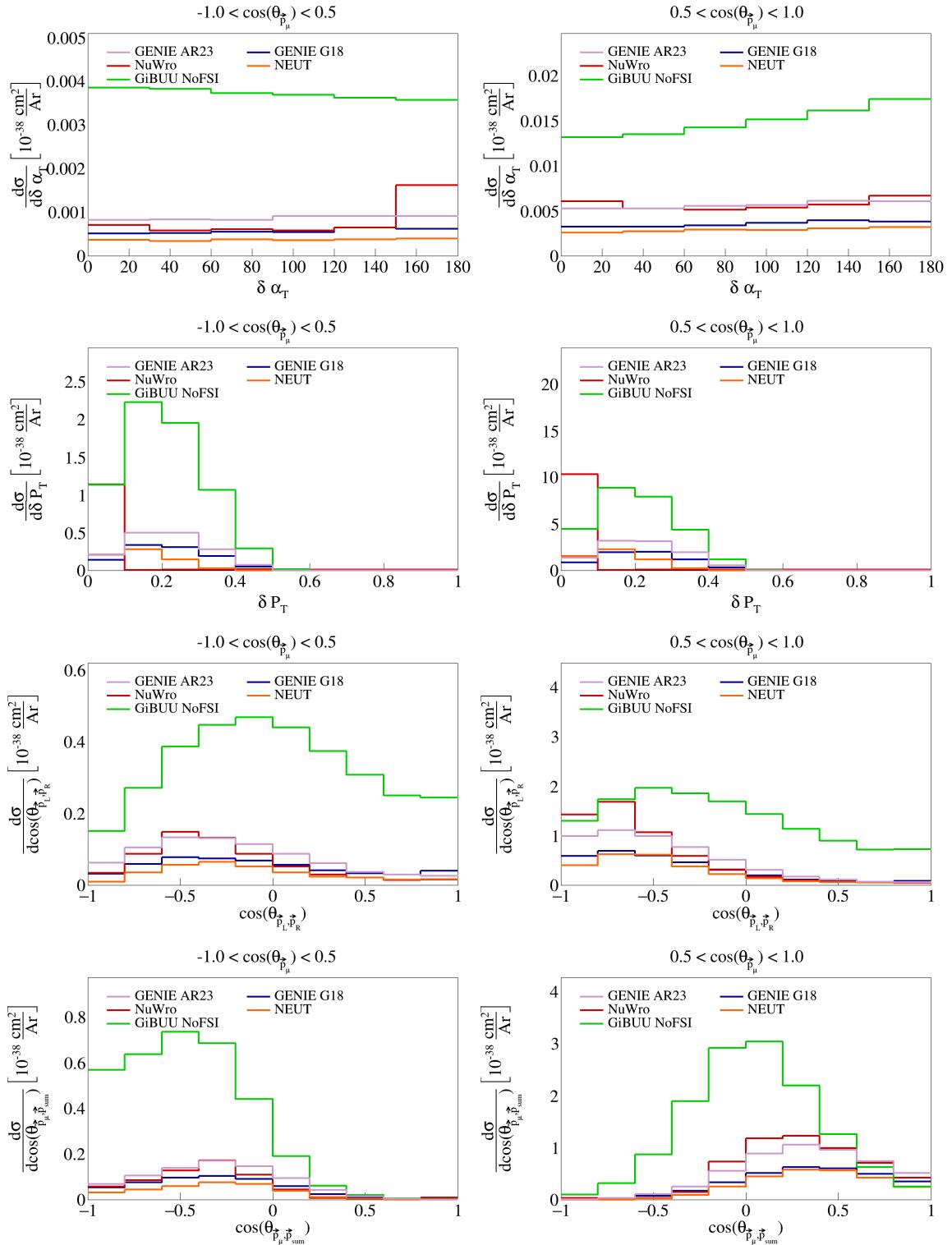


Figure 21: Sliced double differential plots for pre-FSI events.

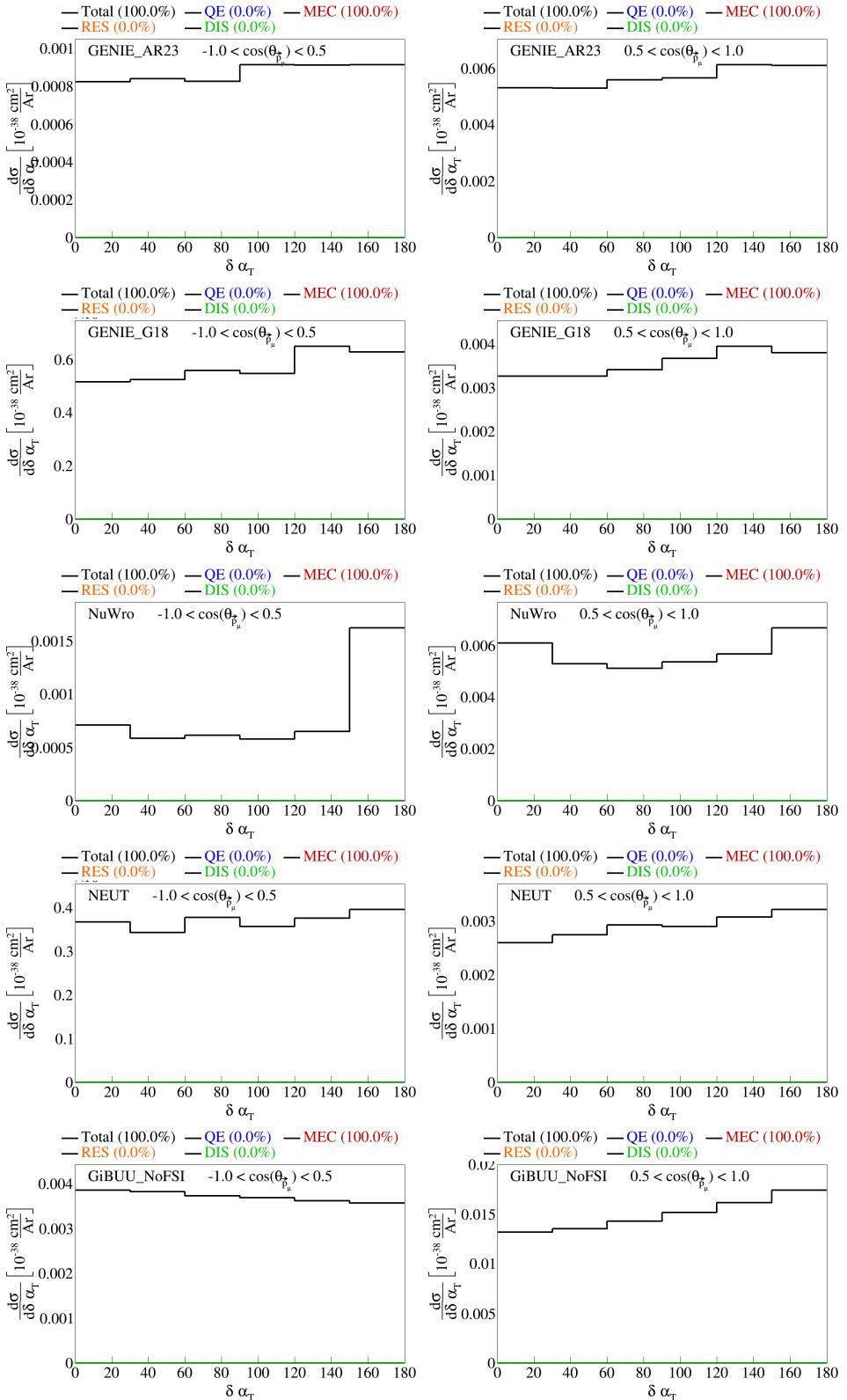


Figure 22: Interaction breakdown for sliced double differential plots for pre-FSI  $\delta\alpha_T$  in  $\cos(\theta_{\bar{p}_\mu})$ .

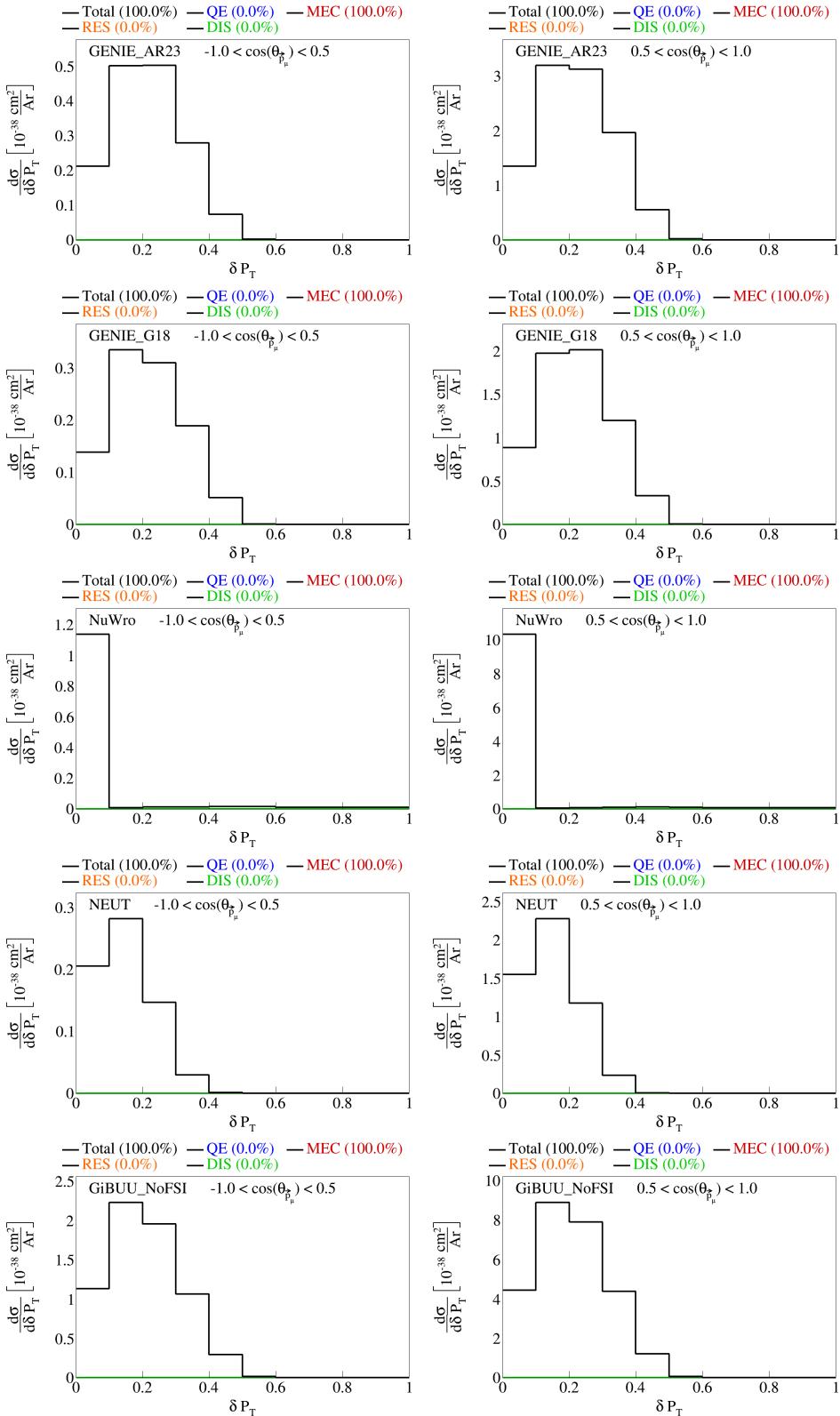


Figure 23: Interaction breakdown for sliced double differential plots for pre-FSI  $|\delta \vec{P}_T|$  in  $\cos(\theta_{\bar{p}_\mu})$ .

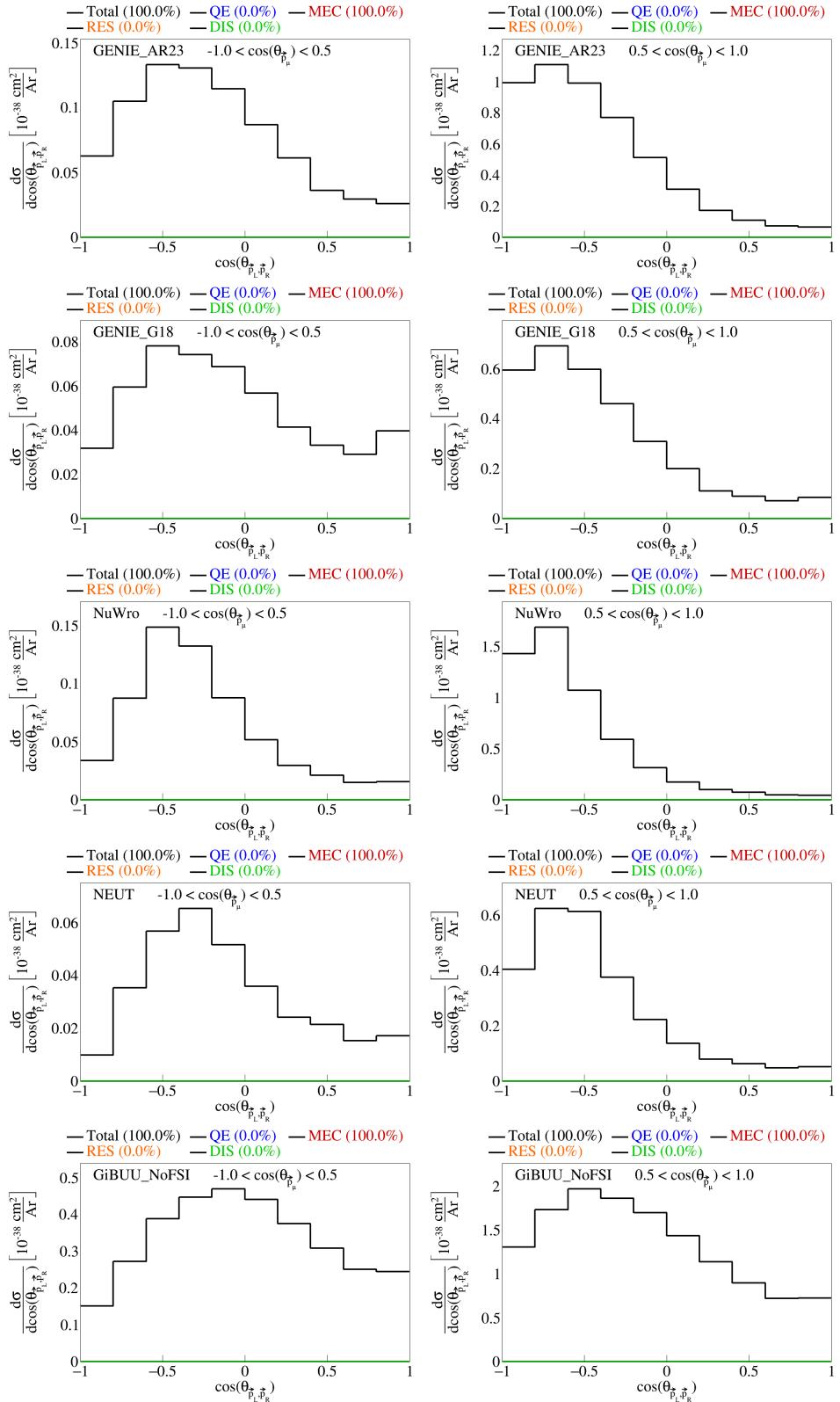


Figure 24: Interaction breakdown for sliced double differential plots for pre-FSI  $\cos(\theta_{\vec{p}_L, \vec{p}_R})$  in  $\cos(\theta_{\vec{p}_\mu})$ .

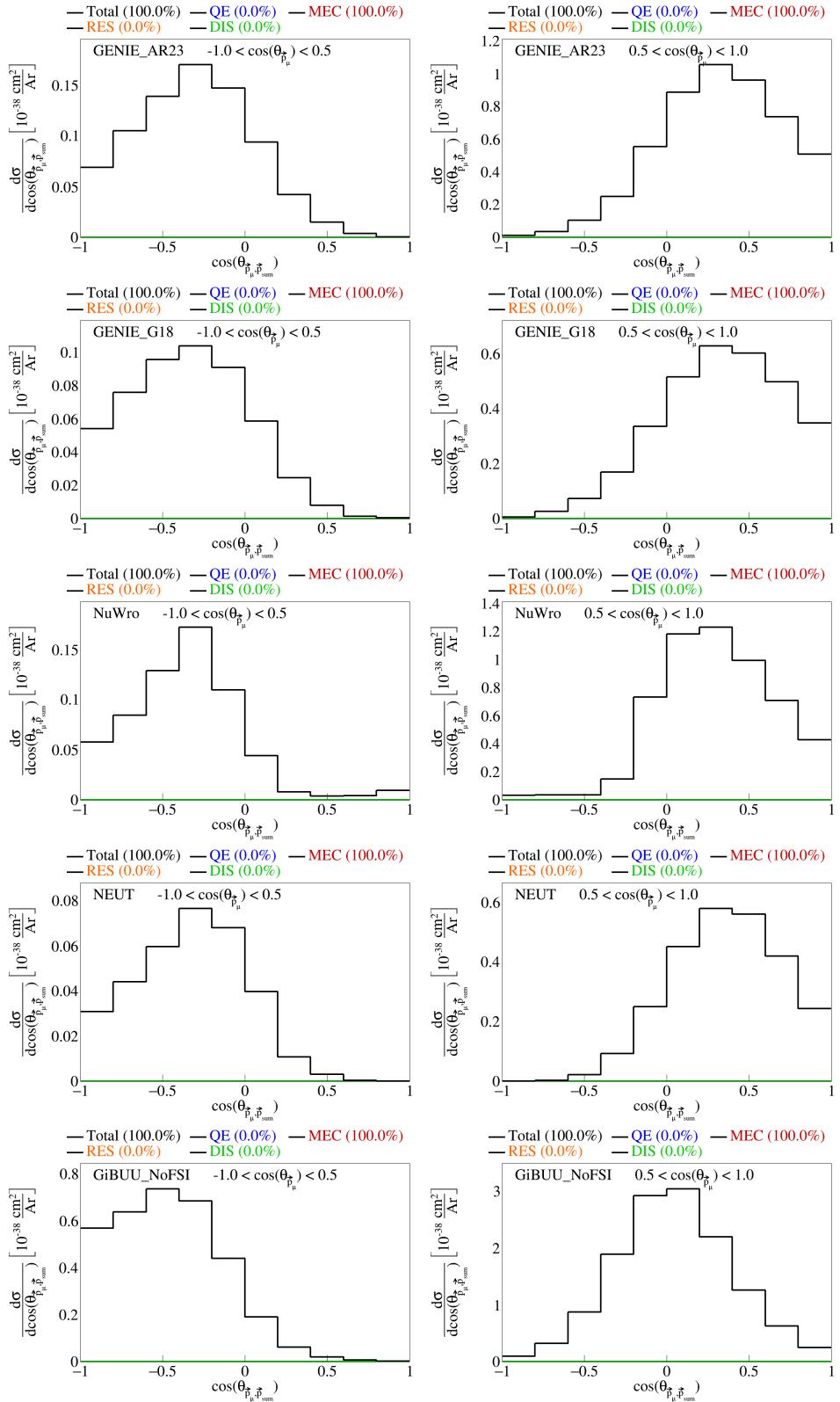


Figure 25: Interaction breakdown for sliced double differential plots for pre-FSI  $\cos(\theta_{\vec{p}_\mu, \vec{p}_{\text{sum}}})$  in  $\cos(\theta_{\vec{p}_\mu})$ .

<sup>91</sup> **2.6 Pure MEC events**

<sup>92</sup> We also generated pure meson exchange current events using different configurations to get the MEC splines.  
<sup>93</sup> These were all generated using different tunes of GENIE:AR23, G18 with Empirical MEC model, and G18  
<sup>94</sup> with Nieves MEC model. The plots for the transverse kinematic variables are shown in Figures 26 and 27.  
<sup>95</sup> The sliced double differential plots are shown in Figure 28.

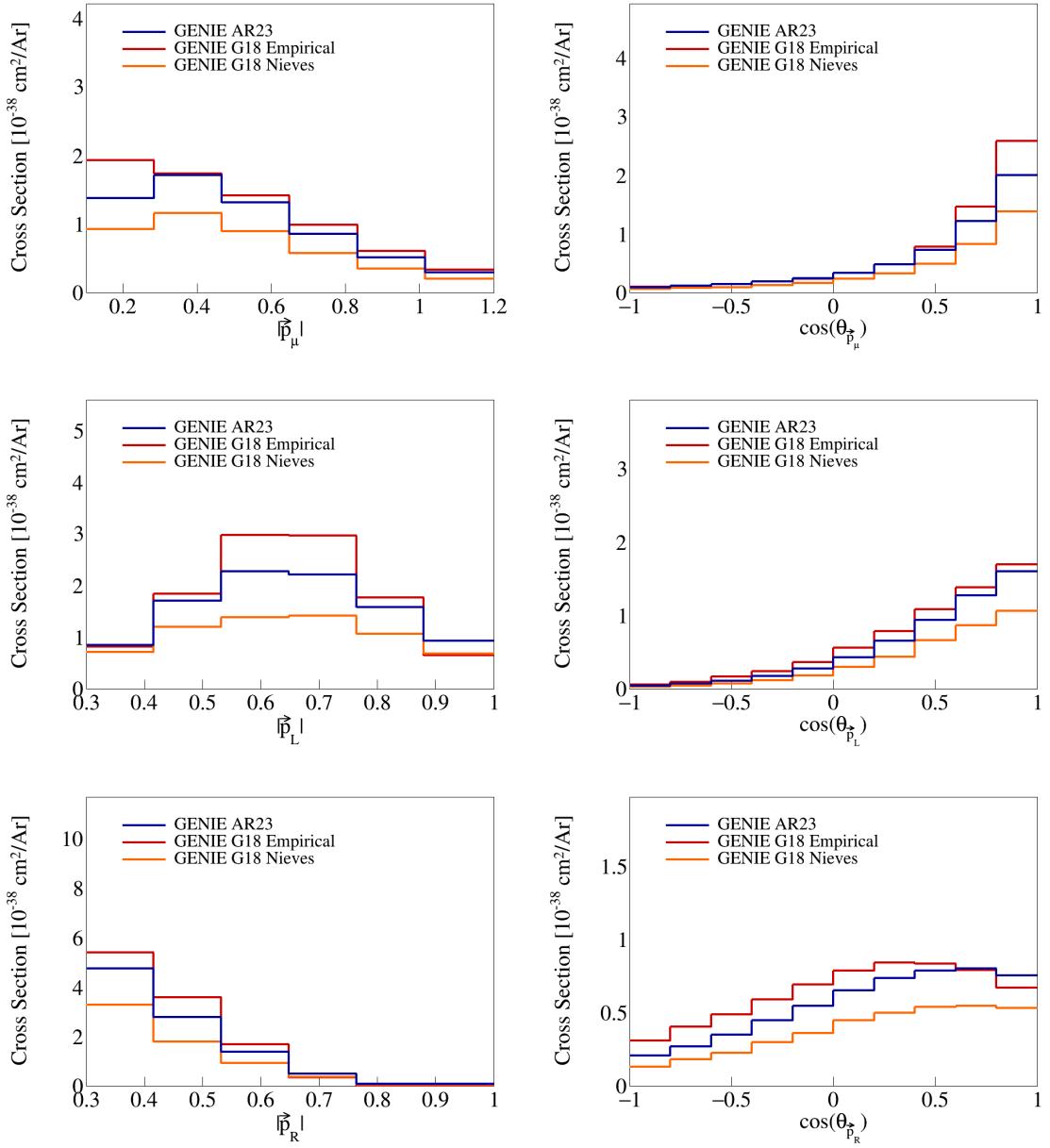


Figure 26: Momenta and opening angles of single particles for pure MEC events.

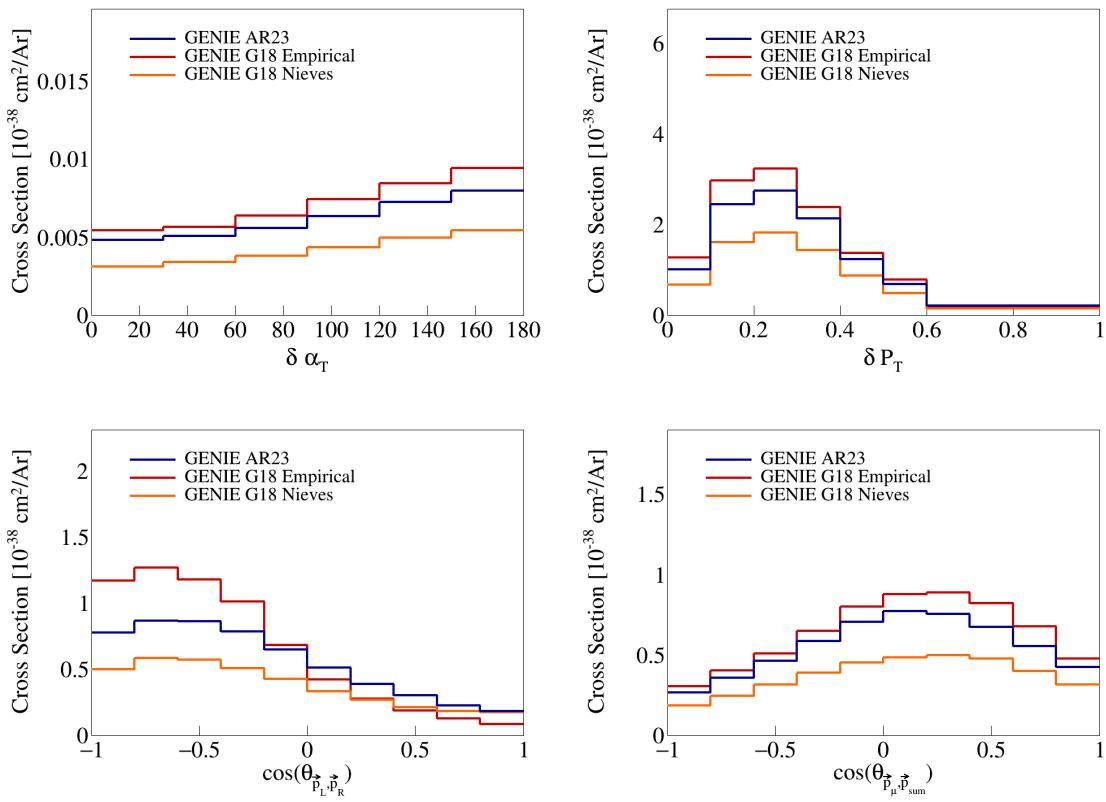


Figure 27: Transverse momentum and opening angles for pure MEC events.

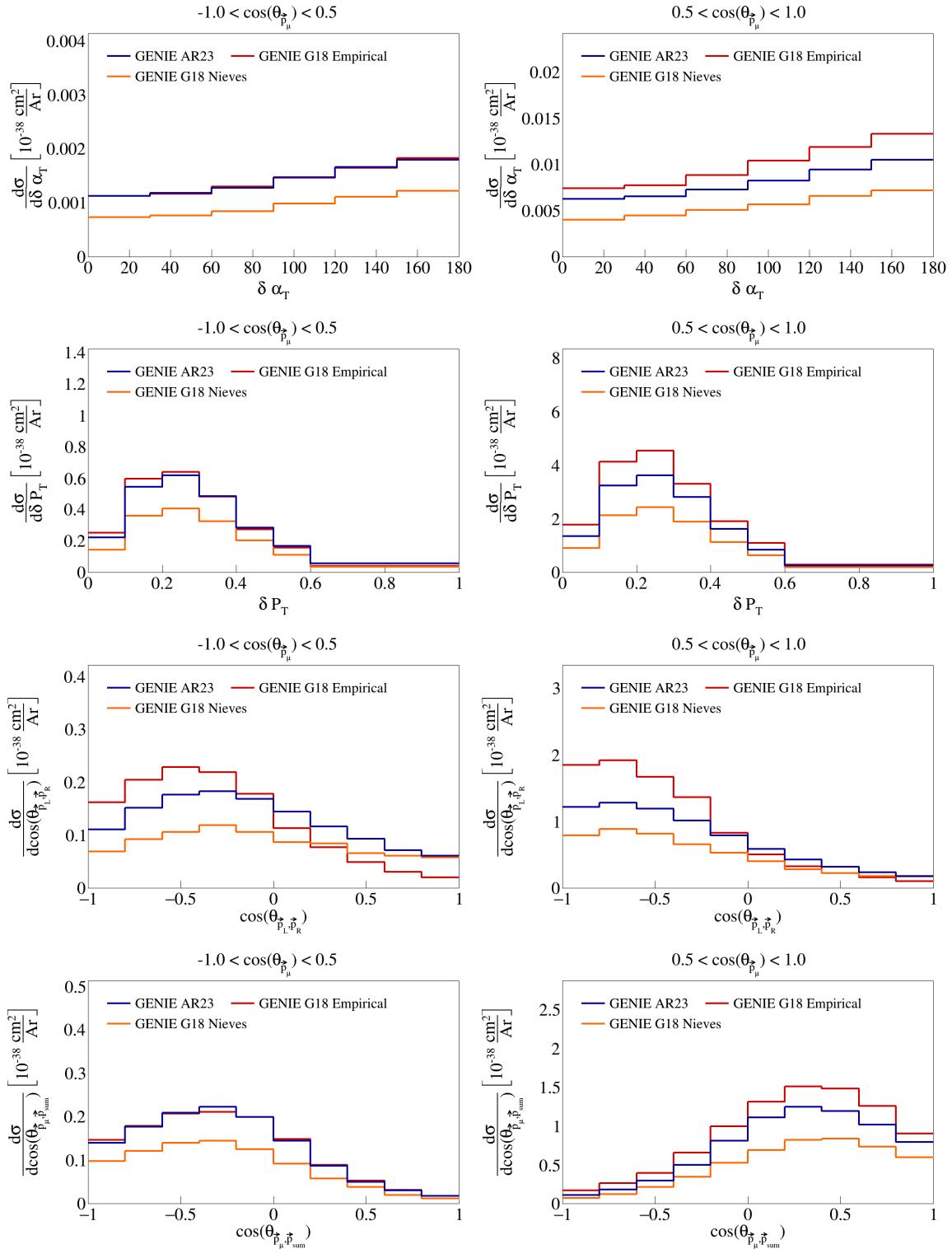


Figure 28: Sliced double differential plots for pure MEC events.

96 **3 SBND analysis**

97 The CAF files used for this analysis are available in the Fermilab gpvms at the path

98 `/pnfs/sbnd/persistent/users/twester/sbnd/v09_78_04/cv/*.flat.caf.root`

99 where the asterisk means that all the files in the directory with the extension `.flat.caf.root` will be used.

100 **3.1 Fiducial volume**

101 To perform the analysis of SBND data, we have to define the fiducial volume of the detector, which represents  
102 a central part of the detector in which we will accept signals, as:

$$5 < |x| < 180 \quad |y| < 180 \quad 10 < z < 450 \quad (6)$$

103 where  $x$ ,  $y$ , and  $z$  are the coordinates in the detector frame, all in centimeters.

104 **3.2 Signal definition**

105 To perform the analysis, we will be using the CAFAna framework. This allows us to perform cuts based  
106 on the reconstructed and Monte Carlo data to discriminate events. To discriminate events based on their  
107 Monte Carlo data and define our true signal, we perform a simple `TruthCut` that checks the following:

- 108 (i) That the neutrino interaction takes place in the fiducial volume.
- 109 (ii) That the neutrino is a muon neutrino.
- 110 (iii) That the interaction is a charged current interaction.
- 111 (iv) That there is only one muon in our allowed momentum range.
- 112 (v) That there are only two protons in our allowed momentum range.
- 113 (vi) That there are no charged/neutral pions in our defined momenta ranges.

114 Using the reconstructed event data, the cut we have to use is not a simple as in the Monte Carlo data  
115 case. We now have to use a `Cut` that looks at different variables of the reconstructed event to determine if  
116 it is a signal event. We perform the following cuts to define our reconstructed signal:

- 117 (i) Cosmic: that the event is not a cosmic event by Pandora's criteria, i.e., requiring `nu_score > 0.4` to  
118 check how neutrino-like the event is, and `fmatch.score < 7` with  $0 < fmatch.time < 1.8$  to check the  
119 event comes from the beam.
- 120 (ii) Vertex in FV: that the reconstructed vertex for the neutrino interaction takes place in the fiducial  
121 volume defined above.
- 122 (iii) One muon: that there is one muon track with  $L_{\text{track}} > 50$  cm, starting point in the fiducial volume,  
123  $\chi^2_\mu < 30$ ,  $\chi^2_p > 60$ , with momentum in our allowed range; if there are multiple candidate tracks, the  
124 one with the longest track length is chosen.
- 125 (iv) Two protons: that there are two proton tracks with  $\chi^2_p < 100$ , full track in the fiducial volume, and  
126 that these have momentum in our allowed range.
- 127 (v) No charged pions: that there are no other reconstructed tracks with momentum in the allowed range  
128 for charged pions inside the fiducial volume.
- 129 (vi) No neutral pions: that there are no reconstructed particles with a positive `trackScore` less than 0.5  
130 indicating a shower, so we don't allow any neutral pions.

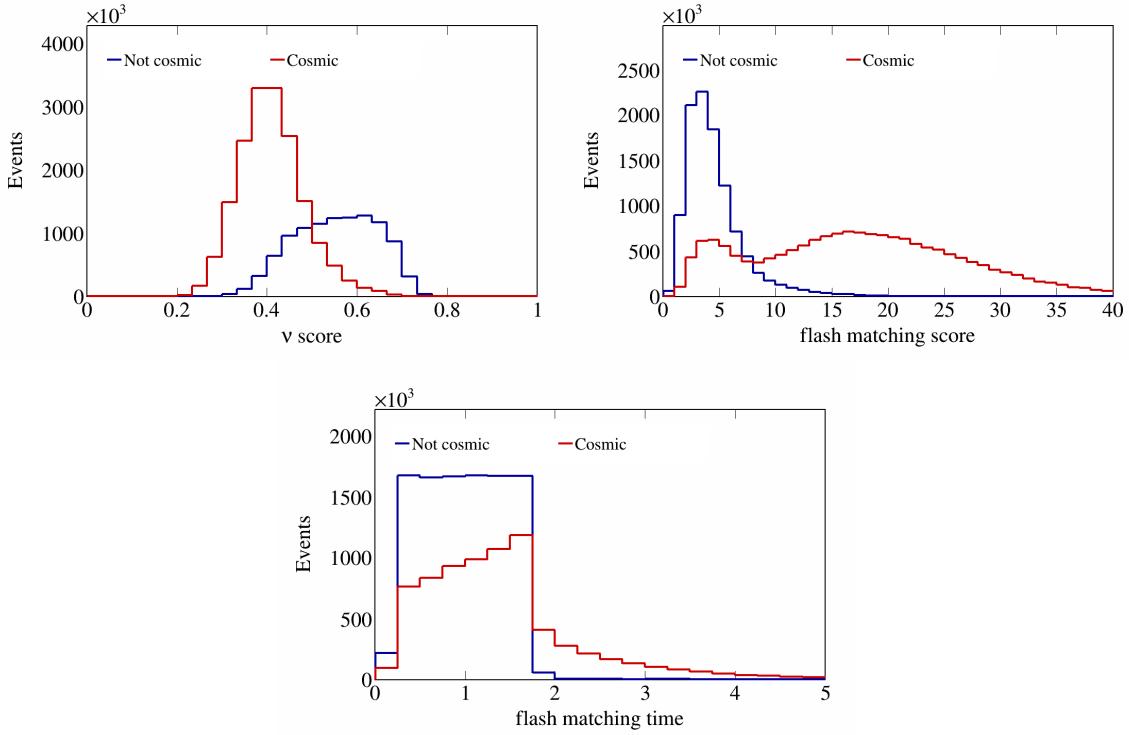


Figure 29: Cosmic cut variables before rejecting cosmic events.

Using these two cuts, we can perform a study of Monte Carlo data. Given the events that pass the reconstructes signal definition, we can look at the background and true signal events. In later sections, we also look at interaction type and topology breakdowns to get a better sense of the composition of our reconstructed signal. To get a better sense of what values the variables chosen to do the cuts take on for each true particle, we plot the flash matching score, time, and  $\nu$  score in Figures 29, and the  $\chi^2$  values for muons and protons in Figure 30.

We use a one-bin histogram to get total counts of generated events, true signal events, all reconstructed events, and efficiency and purity data after each of the cuts described above is applied to the reconstructed events. These results are shown in Table 2. Counts are obtained using ROOT's command `Histo->Integral()` on the histograms generated. Global efficiency is defined as the ratio between events that pass the cut and reconstructed events, signal efficiency as the ratio between true events that pass the cut and all true signal events, and purity as the ratio between true signal events that pass the cut and all events that pass the cut. The numbers reported in this table are POT normalized to  $6.79 \times 10^{20}$ .

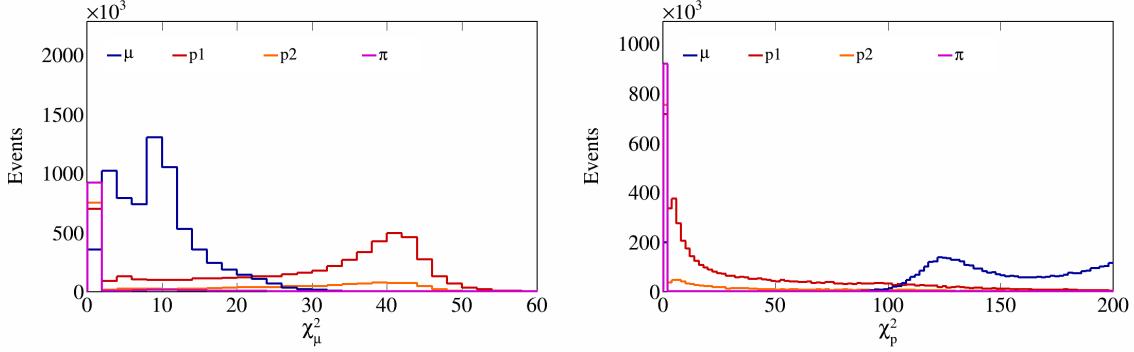


Figure 30: Muon and proton  $\chi^2$  values for all particles.

Cut	Number of events	Global efficiency	Signal efficiency	Purity
All	$1.3938 \cdot 10^7$	-	-	-
True signal events	272161	-	-	-
All reco events	$6.82359 \cdot 10^6$	100%	-	-
Cosmic cut	$5.88624 \cdot 10^6$	86.2632%	89.6205%	4.14377%
Vertex in FV cut	$3.29309 \cdot 10^6$	48.2603%	88.2885%	7.29671%
One muon cut	$2.23536 \cdot 10^6$	32.7593%	70.5202%	8.58603%
Two protons cut	146922	2.15315%	17.517%	32.4488%
No charged pions cut	67852.2	0.994377%	12.6665%	50.8065%
No neutral pions cut	54719.5	0.801917%	11.3094%	56.25%

Table 2: Global efficiency, selection efficiency, and purity for cuts made in signal definition.

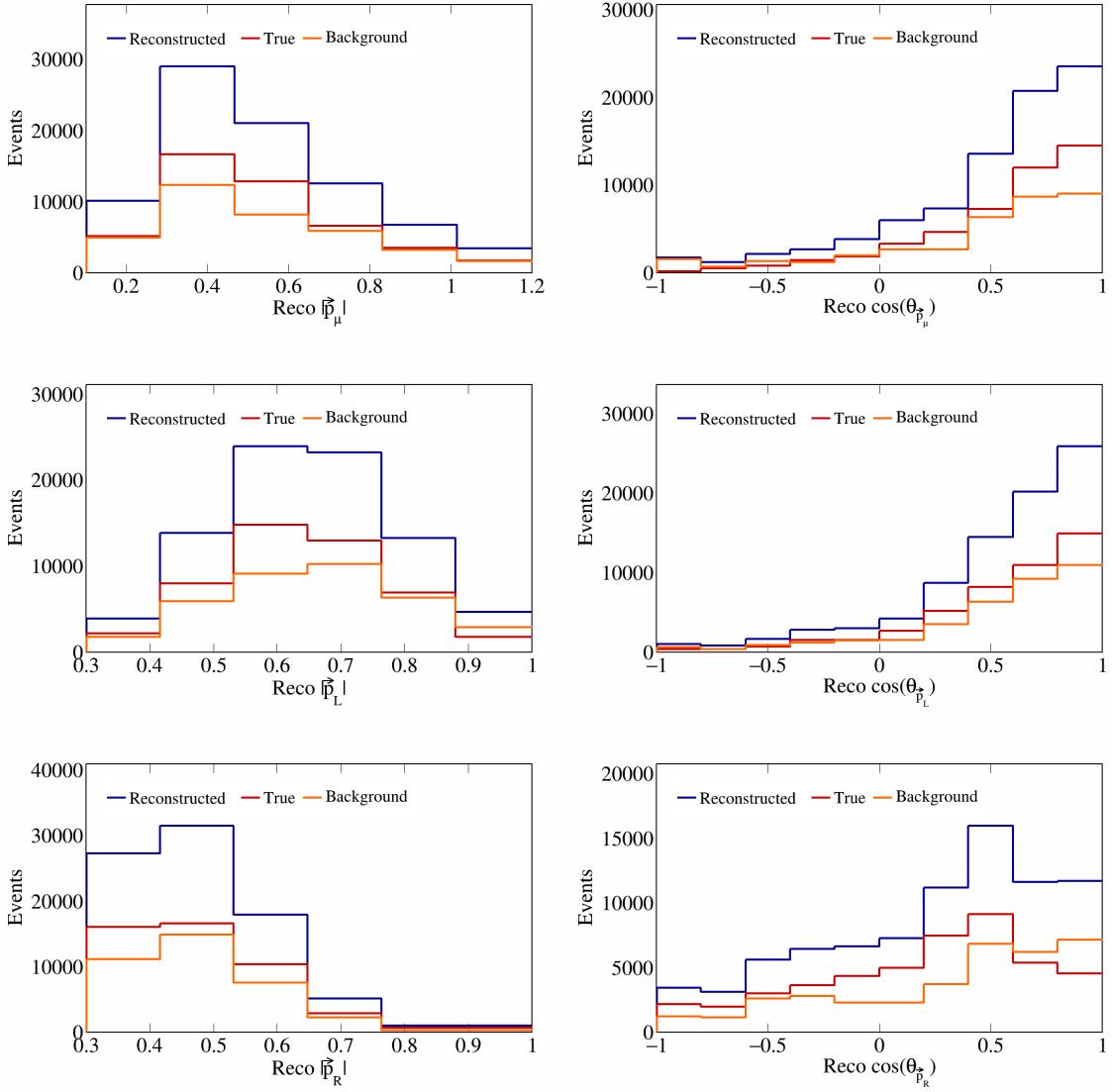


Figure 31: Momenta and opening angles for individual particles for SBND data.

### 3.3 Variable plots

Using all the variable definitions as we did when studying the event generators, and the signal definition based on the cuts described in the previous section, we can generate plots for SBND data. The reconstructed single differential variables corresponding to vector opening angles and magnitudes are shown in Figure 31. In these figures, three lines are shown, corresponding to: all reconstructed (all the reconstructed events that pass our signal definition), signal (reconstructed events that pass signal definition and are true signal events as determined by the TruthCut from our previous section), and background (reconstructed events that pass signal definition but are not true signal events) events. Similarly, the variables relating multiple vectors are shown in Figure 32, and double differential sliced variables are shown in Figure 33.

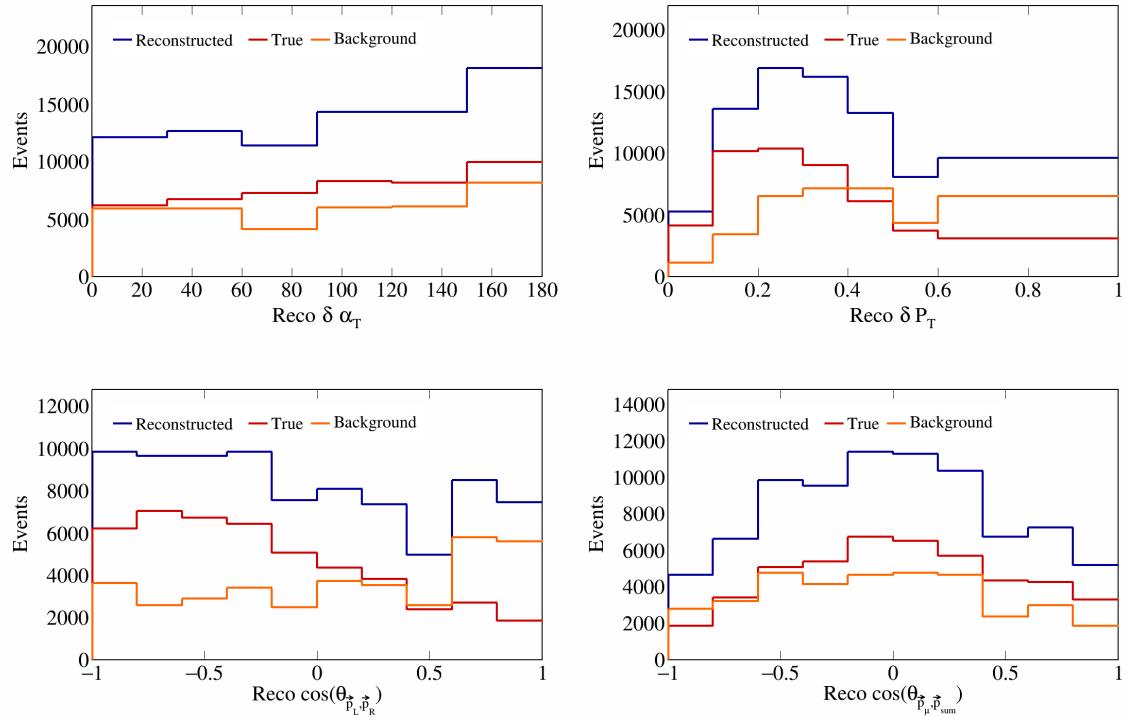


Figure 32: Transverse momentum and opening angles for SBND data.

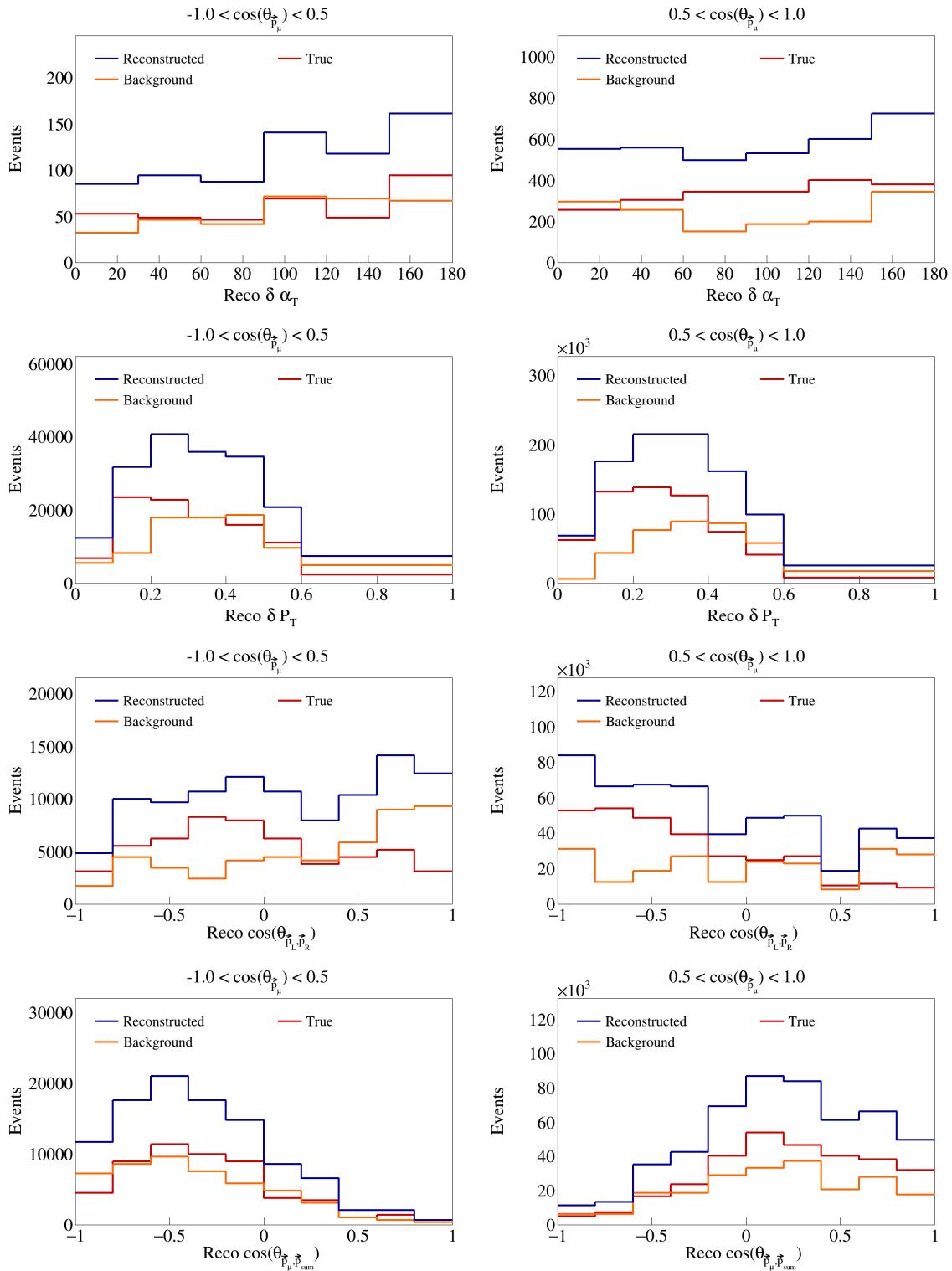


Figure 33: Sliced double differential plots for SBND events.

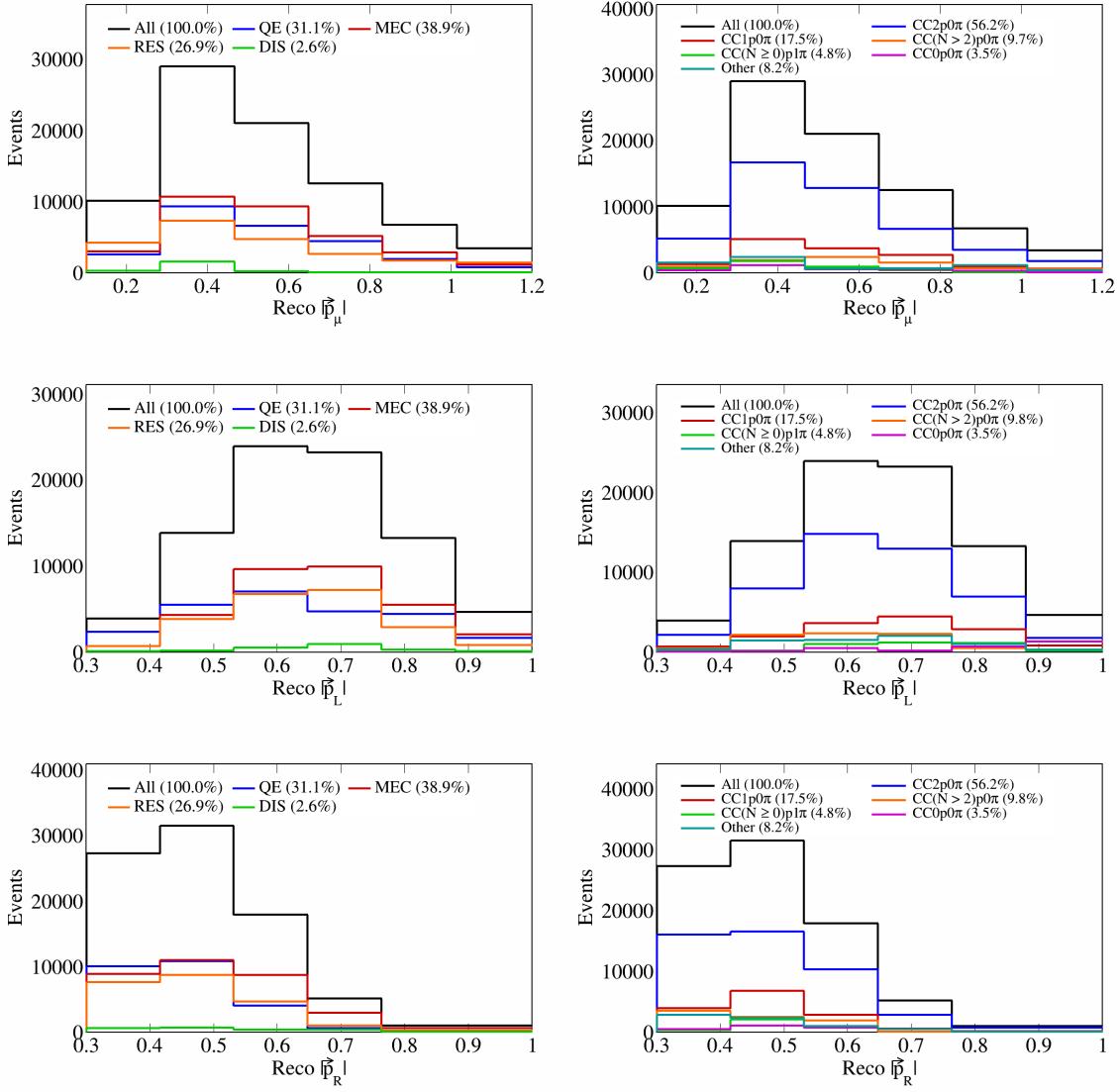


Figure 34: Interaction and topology breakdown for momenta of individual particles.

### 153 3.4 Interaction and topology breakdown

154 We perform an interaction and topology breakdown for the SBND data. For these breakdowns, we look at  
 155 the reconstructed events that pass our signal definitions cuts and see what percentage of these are generated  
 156 from different interaction modes and topologies. This helps us get a better idea of what our background  
 157 signal is composed of. For the interaction breakdown, we look at quasielastic (QE), MEC (meson-exchange  
 158 current), RES (resonance), and DIS (deep inelastic scattering) events. For the topology breakdown, we look  
 159 at the number of protons, pions, and muons in the final state. The topologies we label are CC2p0 $\pi$  (our  
 160 signal definition), CC1p0 $\pi$ , CC(N > 2)p0 $\pi$ , CC(N ≥ 0)p1 $\pi$ , and CC0p0 $\pi$ . Any other event topology is  
 161 labeled as “Other”. These breakdowns are shown in Figures 34 to 38.

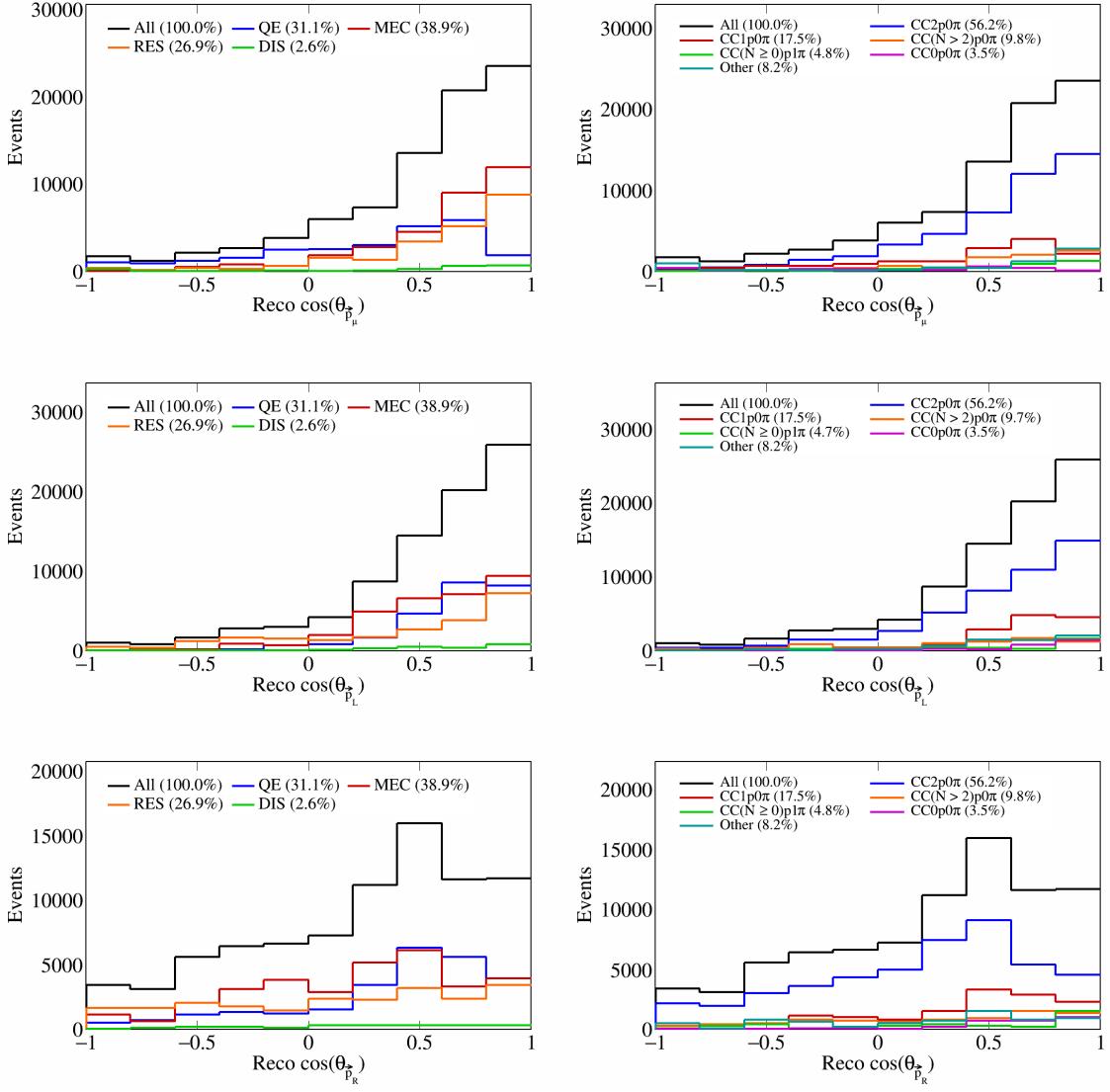


Figure 35: Interaction and topology breakdown for opening angles of individual particles.

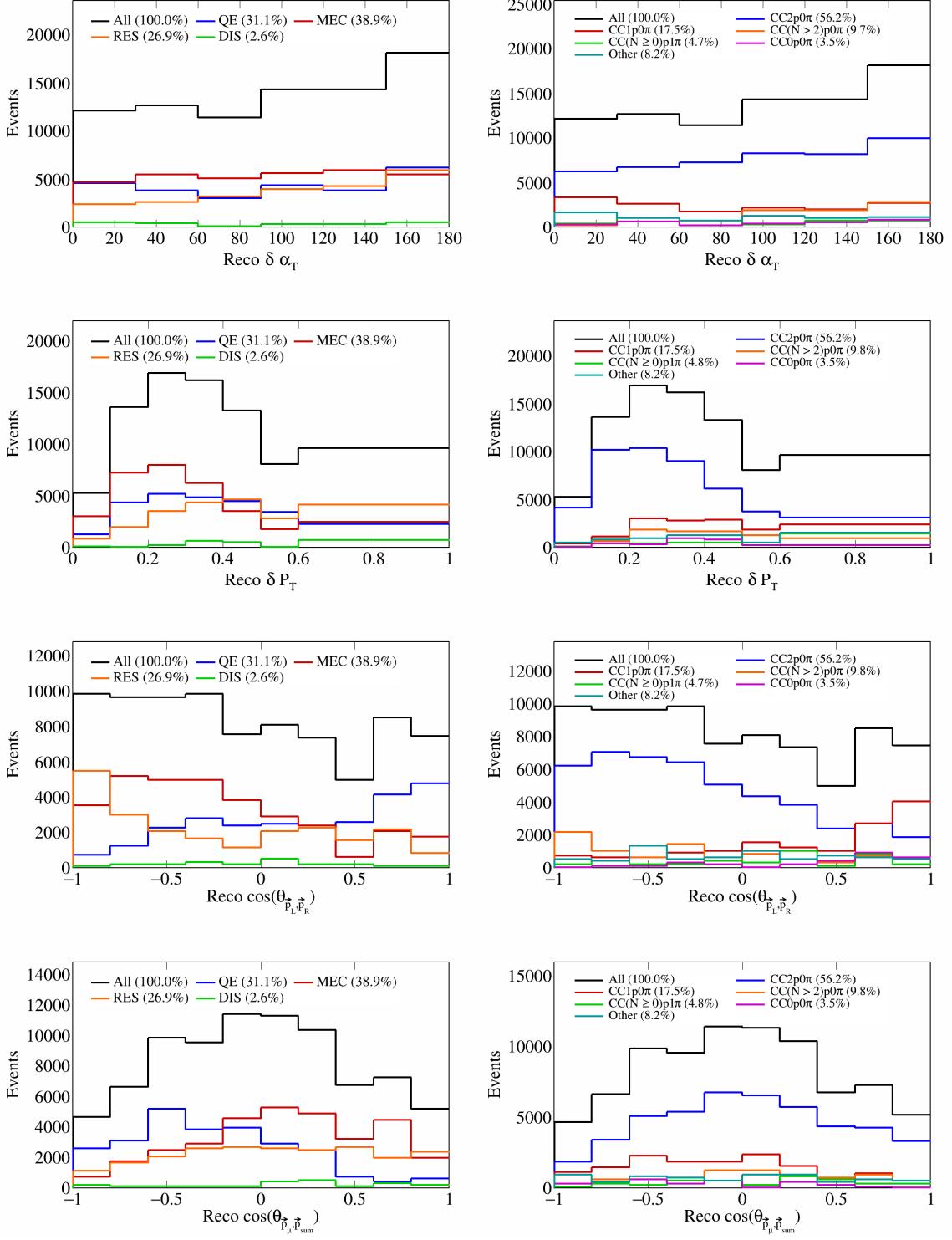


Figure 36: Interaction and topology breakdown for opening angles and transverse variables.

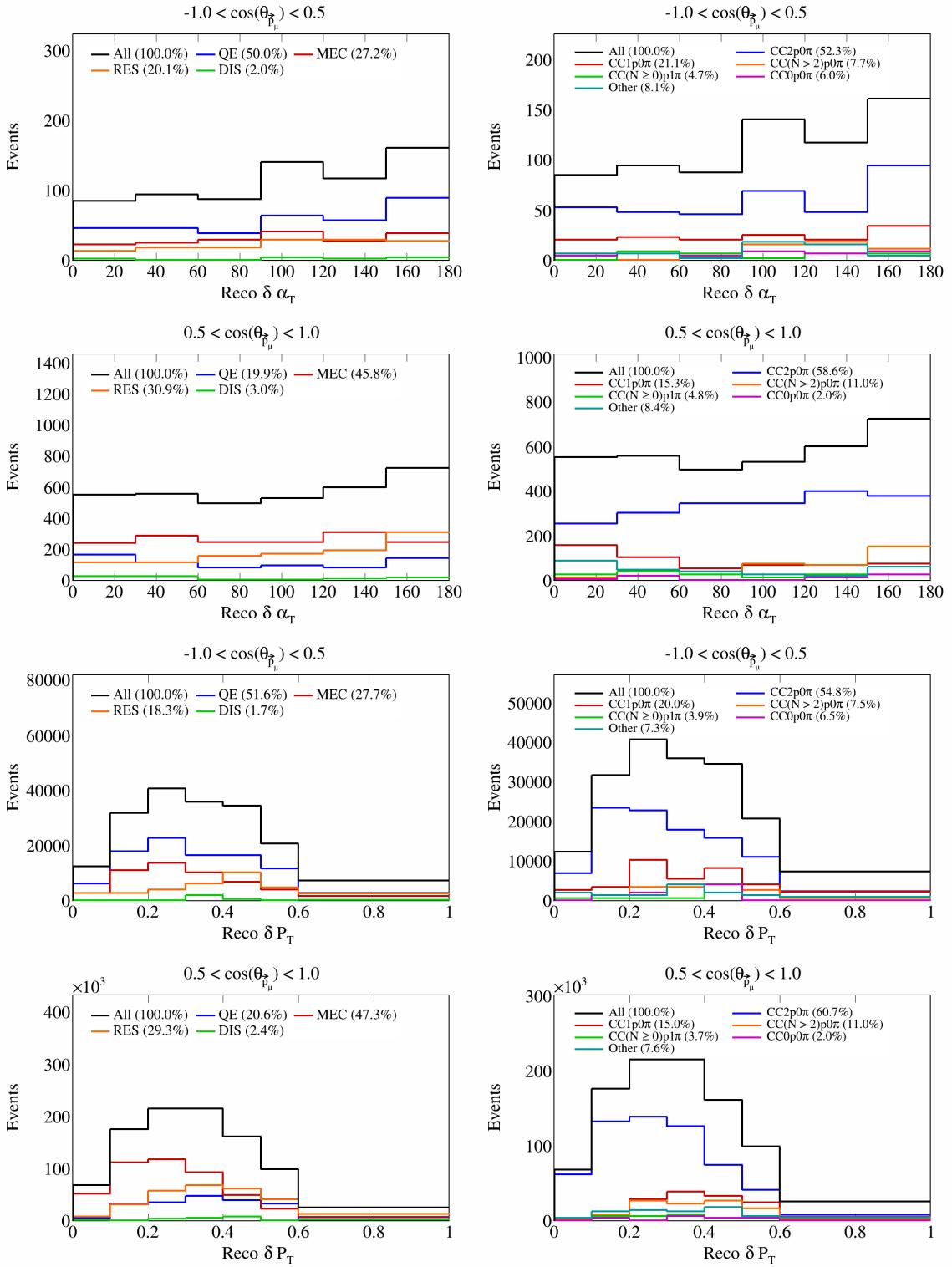


Figure 37: Interaction and topology breakdown for double differential transverse variables.

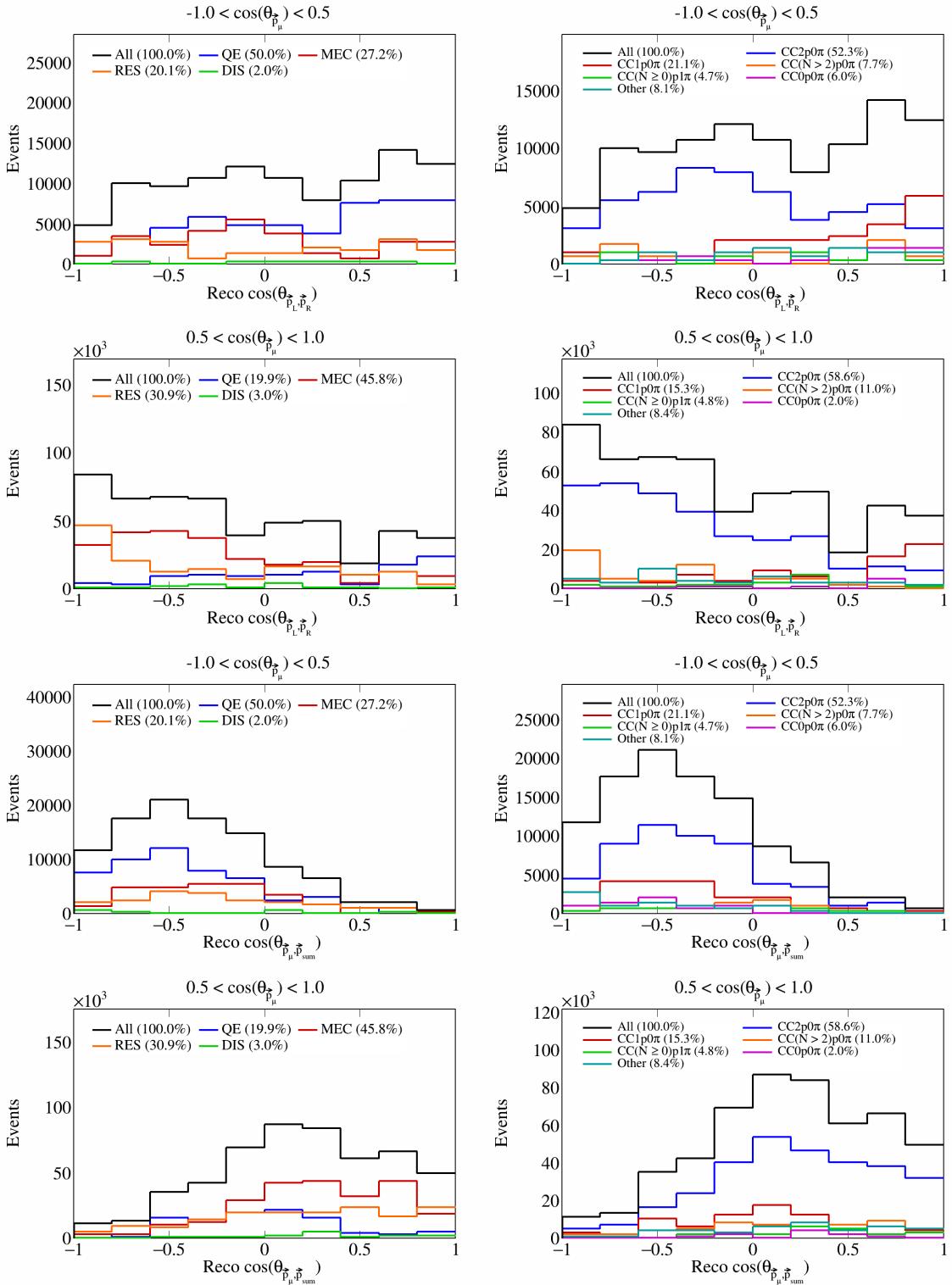


Figure 38: Interaction and topology breakdown for double differential opening angles.

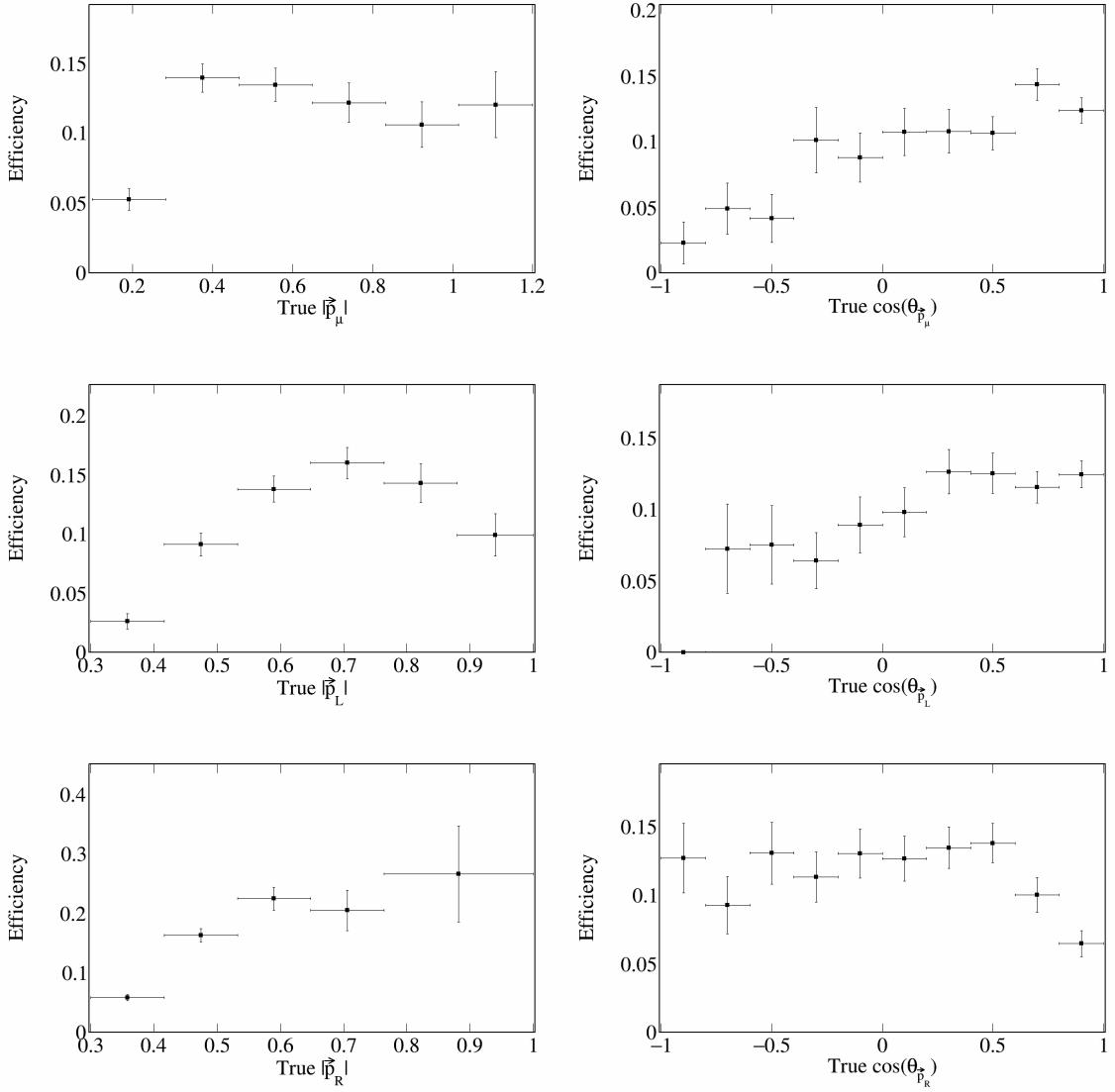


Figure 39: Signal efficiency plots for single differential vector directions and magnitudes.

### 162 3.5 Signal efficiency

163 Using the truth information about reconstructed events, we can also compute signal efficiency on a bin-by-  
 164 bin basis. To be precise, signal definition on a bin  $i$  is defined as the ratio between the number of events  
 165 generated in bin  $i$  and reconstructed in any bin over the number of events generated in bin  $i$ . These plots  
 166 are shown in Figure 39 and Figure 40 for single-differential variables and Figure 41 for double differential  
 167 variables.

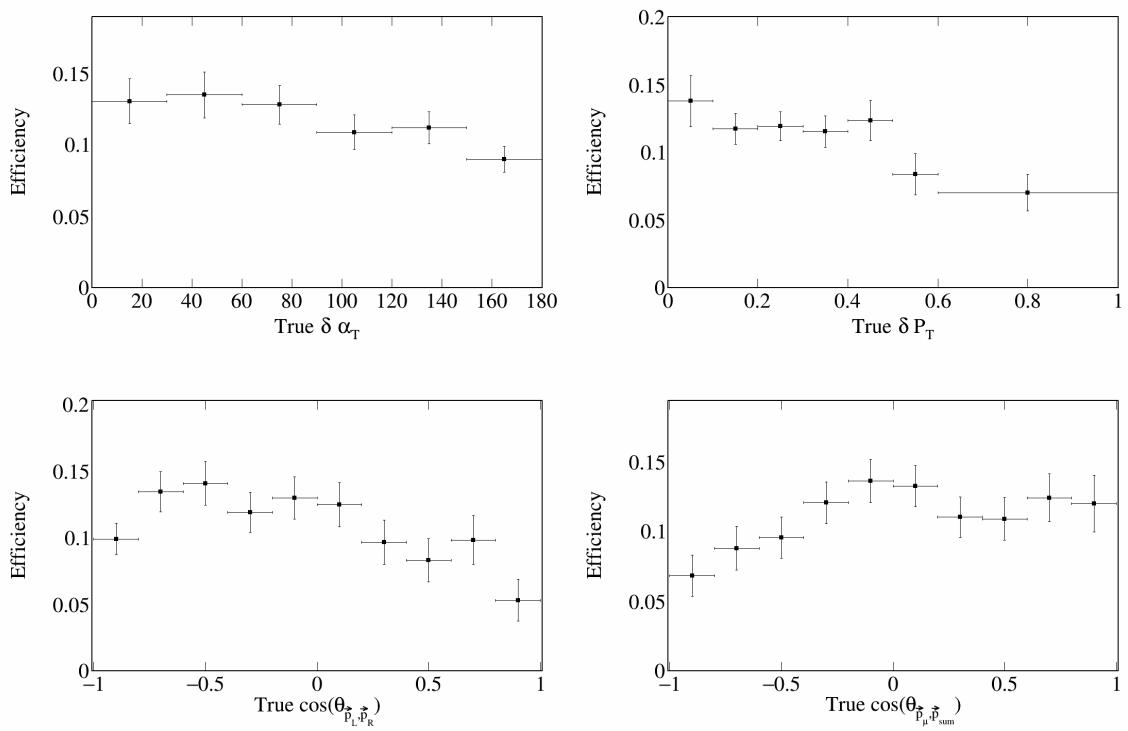


Figure 40: Signal efficiency plots for single differential vector opening angles and transverse momentum.

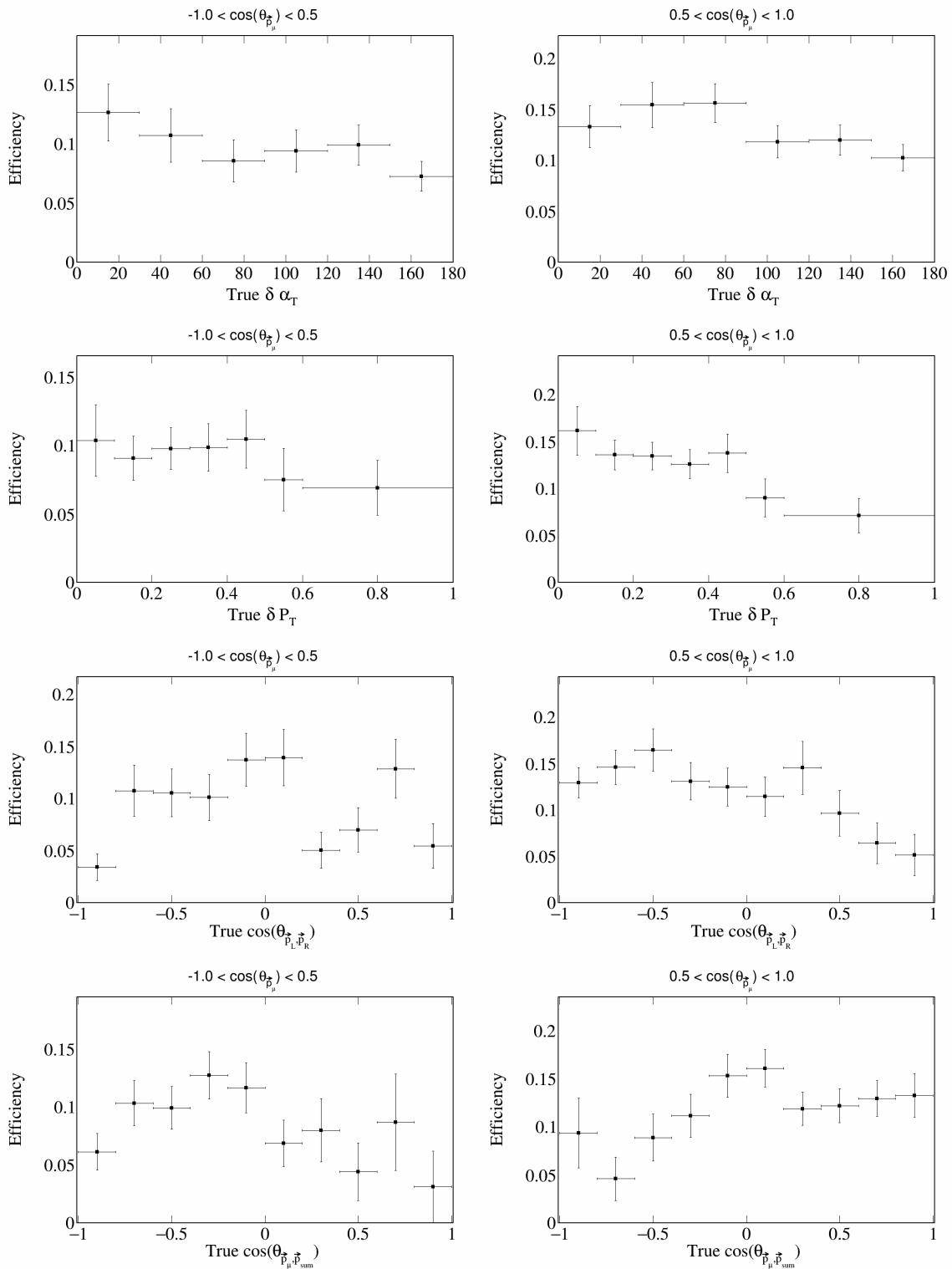


Figure 41: Signal efficiency plots for double differential variables.

168 **3.6 Migration and response matrices**

169 Further, we compute migration matrices which give us a measure of how reliable our reconstructed variables  
170 are. A given column in this matrix represents a bin of the truth variable, i.e., the value with which the  
171 event was generated. Then, each row corresponds to a reconstructed bin of the same variable, and each cell  
172 corresponds to the probability that an event generated with the truth value corresponding to the column gets  
173 reconstructed with the value corresponding to the row. For the migration matrix, we consider true signal  
174 events that were reconstructed and satisfy our signal definition in the denominator. Therefore, the values in  
175 each column must add up to 1. The migration matrices for the single differential variables are presented in  
176 Figure 42 and Figure 43. The migration matrices for the double differential variables (given in terms of the  
177 bin number) are presented in Figure 44.

178 Response matrices are computed in a similar manner, but using the total number of generated events in the  
179 denominator when computing the ratios, i.e., without requiring the events to be successfully reconstructed.  
180 Therefore, for these matrices, the columns of the response matrices do not have to add up to 1. The response  
181 matrices for single differential variables are presented in Figure 45 and Figure 46, and the double differential  
182 response matrices are given in Figure 47. A mathematical definition of the response matrix is given in  
183 Equation (10).

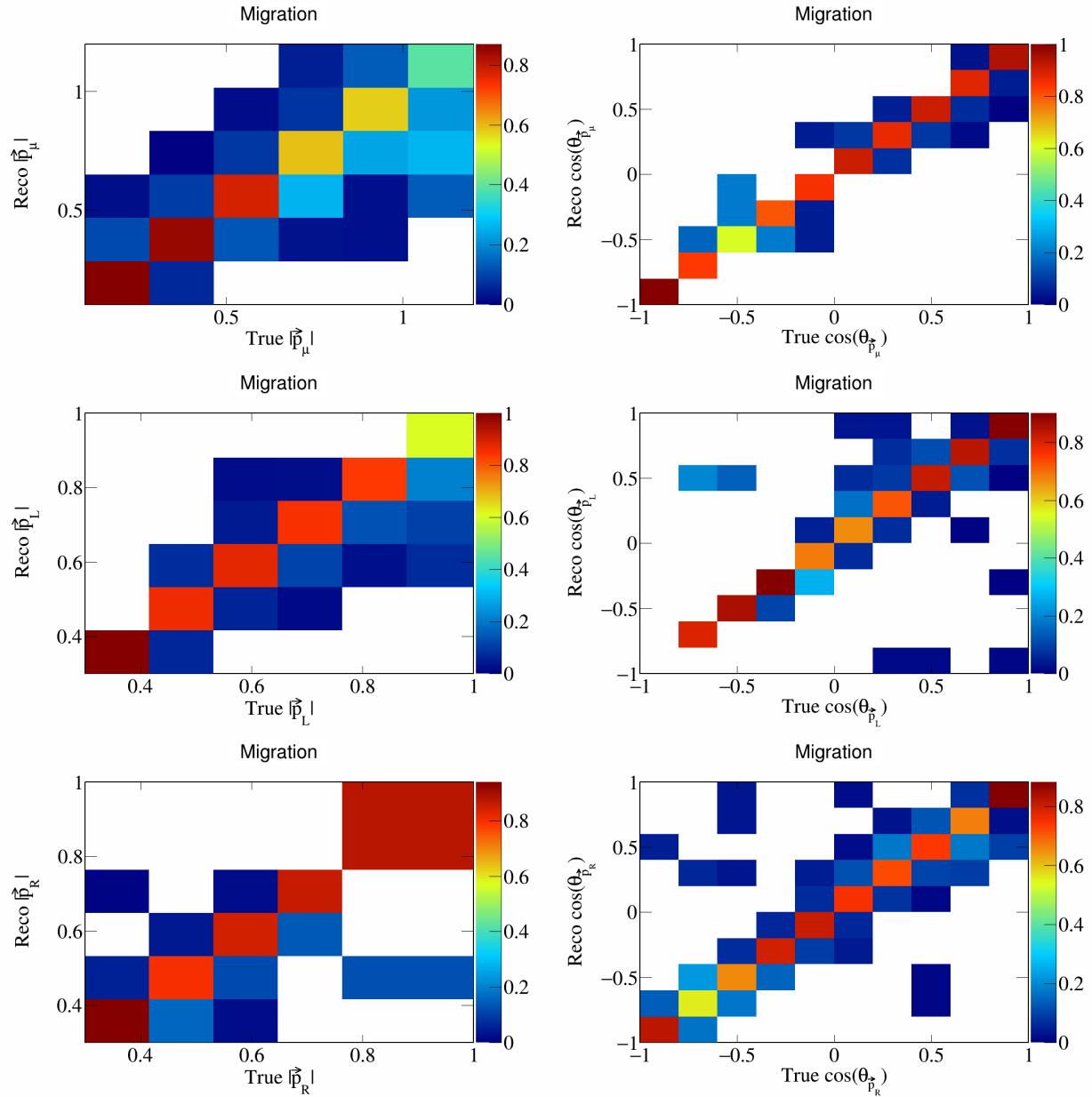


Figure 42: Migration matrices for single differential momenta and opening angles of individual particles.

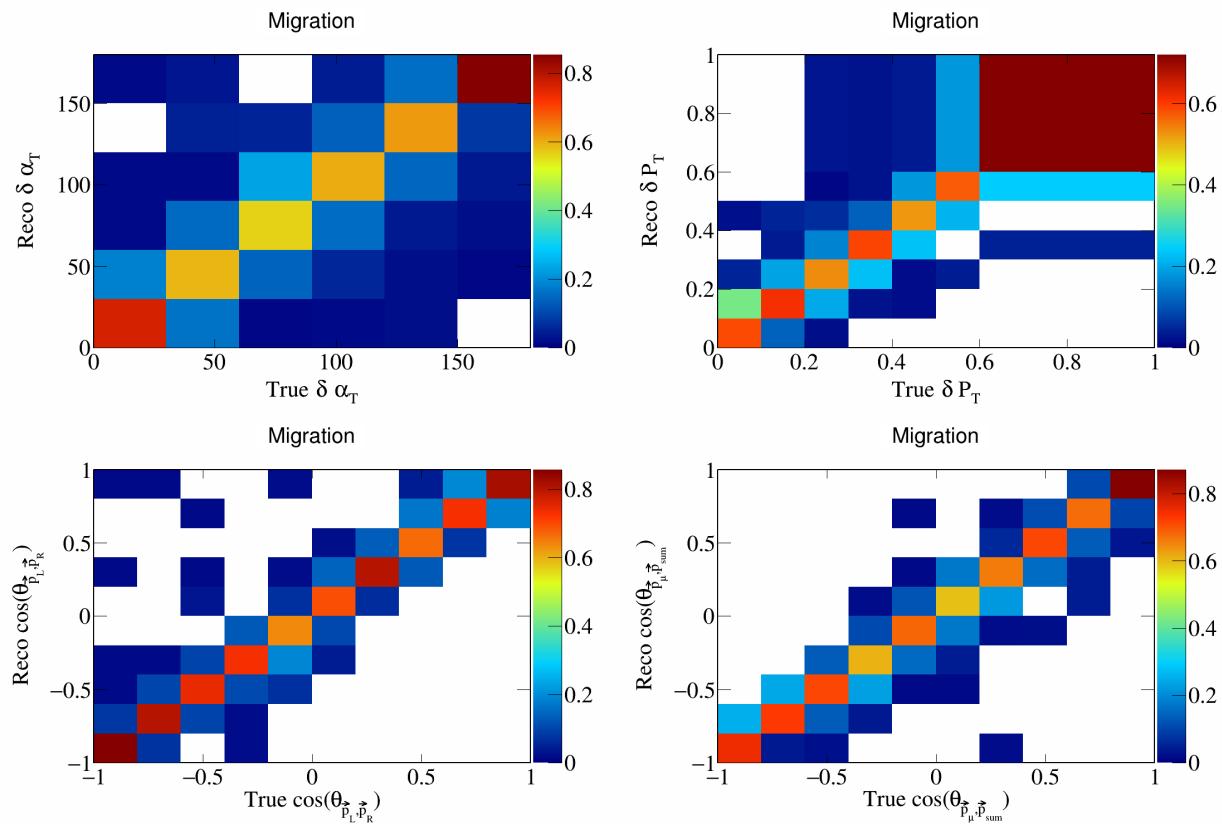


Figure 43: Migration matrices for single differential transverse momentum and opening angles.

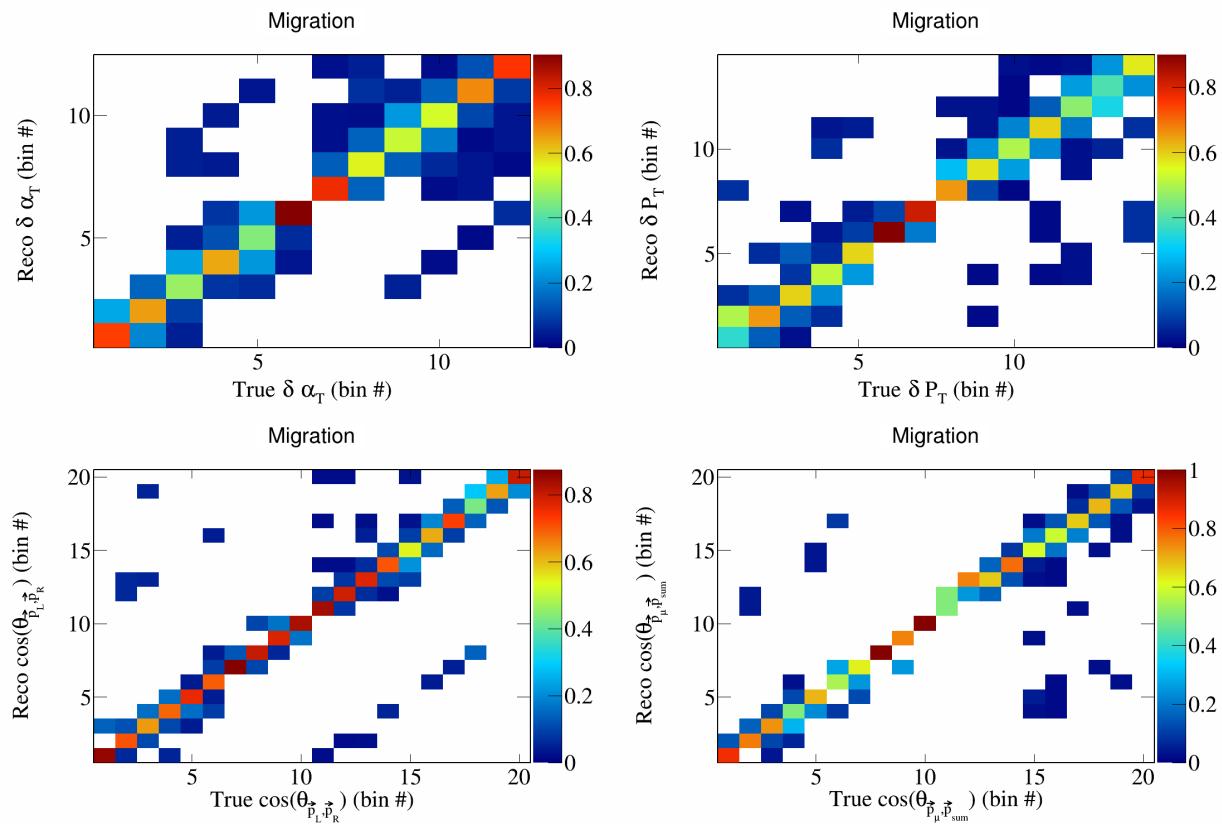


Figure 44: Migration matrices for double differential variables.

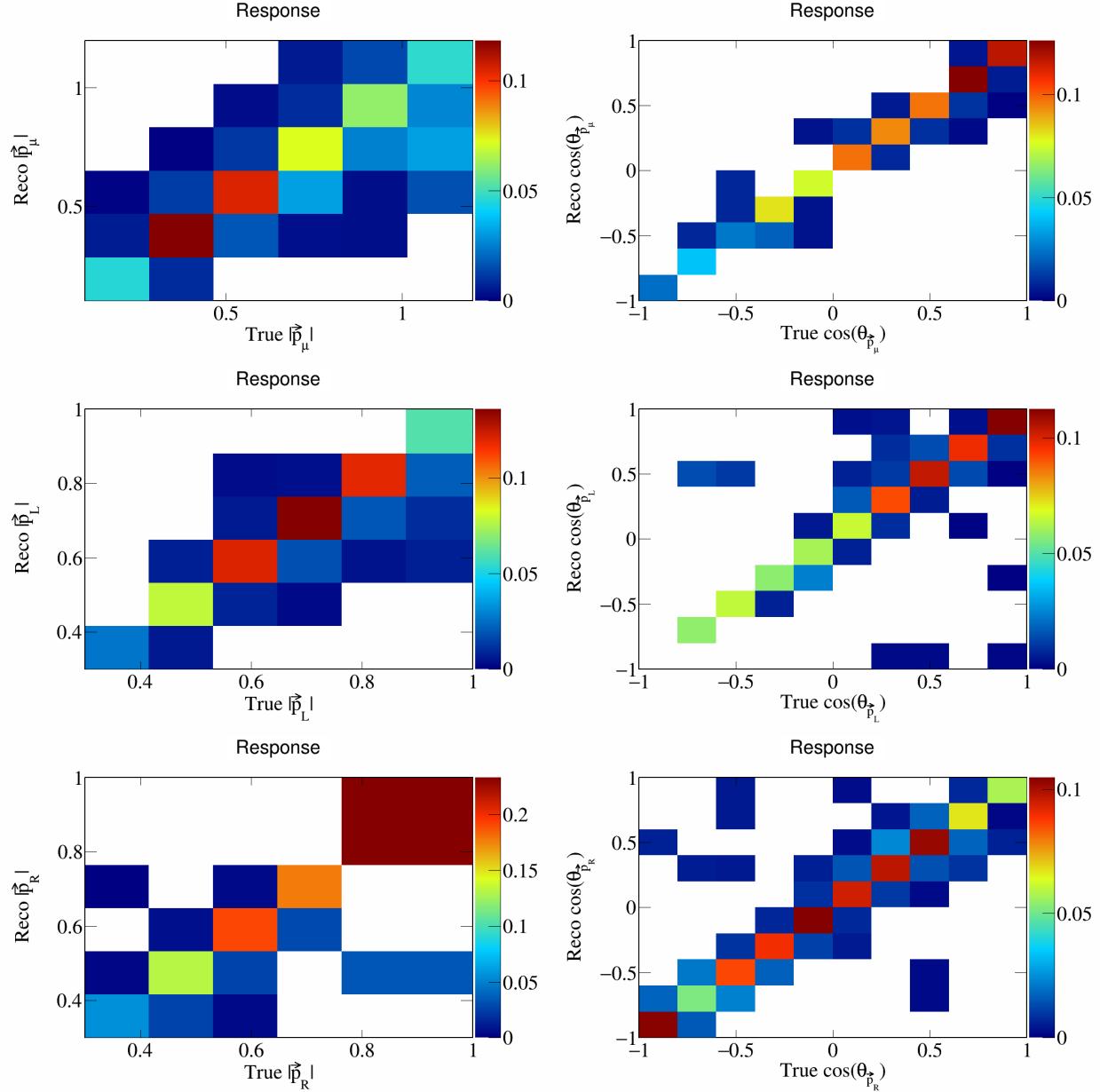


Figure 45: Response matrices for single differential momenta and opening angles of individual particles.

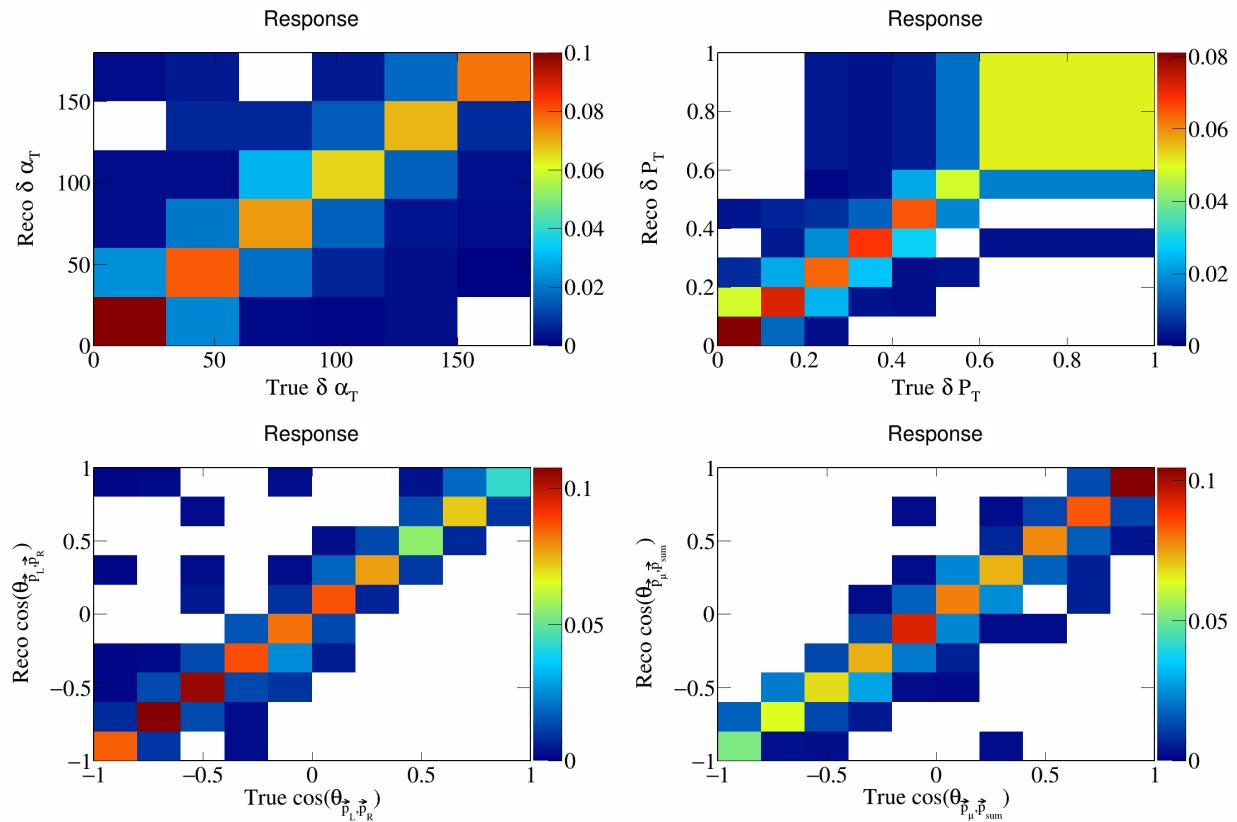


Figure 46: Response matrices for single differential transverse momentum and opening angles.

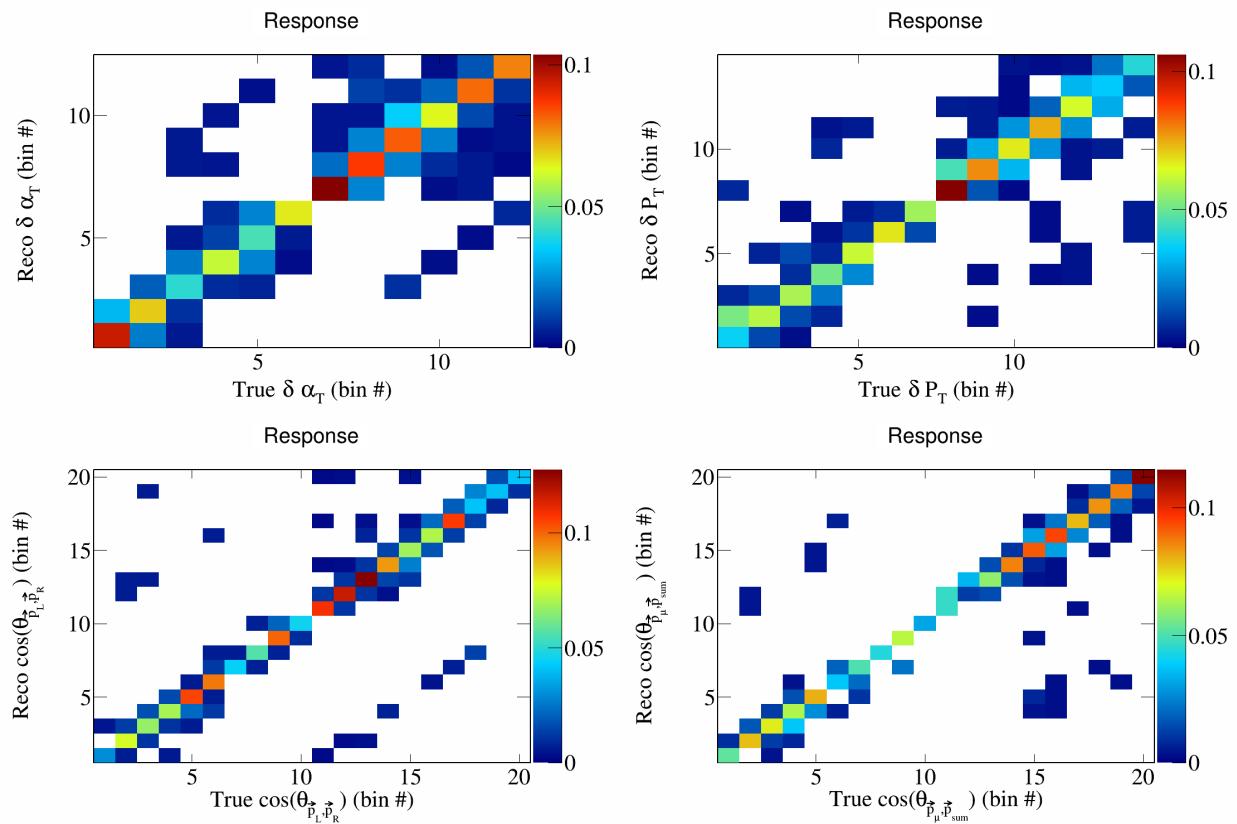


Figure 47: Response matrices for double differential variables.

184 **3.7 Systematics**

185 To include systematic uncertainties in our study, we first consider cross sectional systematics. These are  
 186 variations in the cross section models used to generate the events. They can be of two types: multisigma and  
 187 multisim. For the former, we consider a  $1\sigma$  variation of the affected parameters, and in the latter we consider  
 188 some number of universes, each with a random variation picked from a Gaussian distribution between  $0\sigma$   
 189 and  $1\sigma$ . These weights are already preloaded in the event data file, so we only have to load them into our  
 190 script and use them to compute the relevant quantities. From these variations, we compute the covariance  
 191 matrix as

$$E_{i,j} = \frac{1}{N_{\text{Univ}}} \sum_{s=1}^{N_{\text{Univ}}} (\tilde{\sigma}_i^{\text{Var},s} - \tilde{\sigma}_i^{\text{CV}})(\tilde{\sigma}_j^{\text{Var},s} - \tilde{\sigma}_j^{\text{CV}}) \quad (7)$$

192 where  $\tilde{\sigma}_i^{\text{Var},s}$  represents the variation flux-integrated event rate of the variable in the  $i$ -th bin in the  $s$ -th  
 193 universe, and  $\tilde{\sigma}_i^{\text{CV}}$  is the central value (without any variation) of the flux-integrated event rate in the  $i$ -th  
 194 bin. More formally,

$$\tilde{\sigma}_i = \frac{N^{\text{reco } i}}{\Phi_{\nu}^{\text{CV}} \times N_{\text{targets}}}, \quad (8)$$

195 where  $N^{\text{reco } i}$  is the number of reconstructed events in bin  $i$ ,  $\Phi_{\nu}^{\text{CV}}$  is the central value of the neutrino flux  
 196 (which remains the same for each variation), and  $N_{\text{targets}}$  is the number of target Argon nuclei. Further, we  
 197 have that  $N^{\text{reco } i} = M_{i,j} \times S^{\text{true } j} + B^{\text{reco } i}$ , where  $M_{i,j}$  is the response matrix corresponding to the true bin  $j$   
 198 and reco bin  $i$ ,  $S^{\text{true } j}$  is the number of true signal events in bin  $j$ , and  $B^{\text{reco } i}$  is the number of reconstructed  
 199 background events in bin  $i$ . Therefore, we have that

$$\tilde{\sigma}_i = \frac{M_{i,j}^{\text{univ}} \times S^{\text{true } j \text{ CV}} + B^{\text{reco } i \text{ univ}}}{\Phi_{\nu}^{\text{CV}} \times N_{\text{targets}}}, \quad (9)$$

200 where

$$M_{i,j}^{\text{univ}} = \frac{RS^{\text{true } j, \text{ reco } i \text{ univ}}}{S^{\text{true } j \text{ CV}}}, \quad (10)$$

201 with  $RS^{\text{true } j, \text{ reco } i \text{ univ}}$  being the number of signal events generated in bin  $j$  and reconstructed in bin  $i$ , and  
 202  $S^{\text{true } j}$  being the number of signal events generated in bin  $j$ . For each variation, terms labeled with **univ**  
 203 are modified according to the variation, and terms labeled with **CV** remain the same. When considering the  
 204 cross-section variations, the response matrix is modified via the normalization to the true signal in a given  
 205 universe as

$$M_{i,j}^{\text{univ}} = \frac{RS^{\text{true } j, \text{ reco } i \text{ univ}}}{S^{\text{true } j \text{ univ}}}. \quad (11)$$

206 Then, the fractional covariance matrix is defined as

$$F_{i,j} = \frac{E_{i,j}}{\tilde{\sigma}_i^{\text{CV}} \tilde{\sigma}_j^{\text{CV}}}. \quad (12)$$

207 And the correlation matrix is defined as

$$\rho_{i,j} = \frac{E_{i,j}}{\sqrt{E_{i,i} E_{j,j}}}. \quad (13)$$

208 In the case of a multisigma systematic,  $N_{\text{Univ}} = 1$ , and for a multisim systematic, this number varies but is  
 209 usually 100 or 1000.

210 The plots for all the individual cross sectional systematics are shown in Appendix 6.1. Flux systematics  
 211 are computed in the same way, but each universe varies a flux parameter. The corresponding plots for the  
 212 individual flux systematics are shown in Appendix 6.2. We also consider statistical systematics. This are

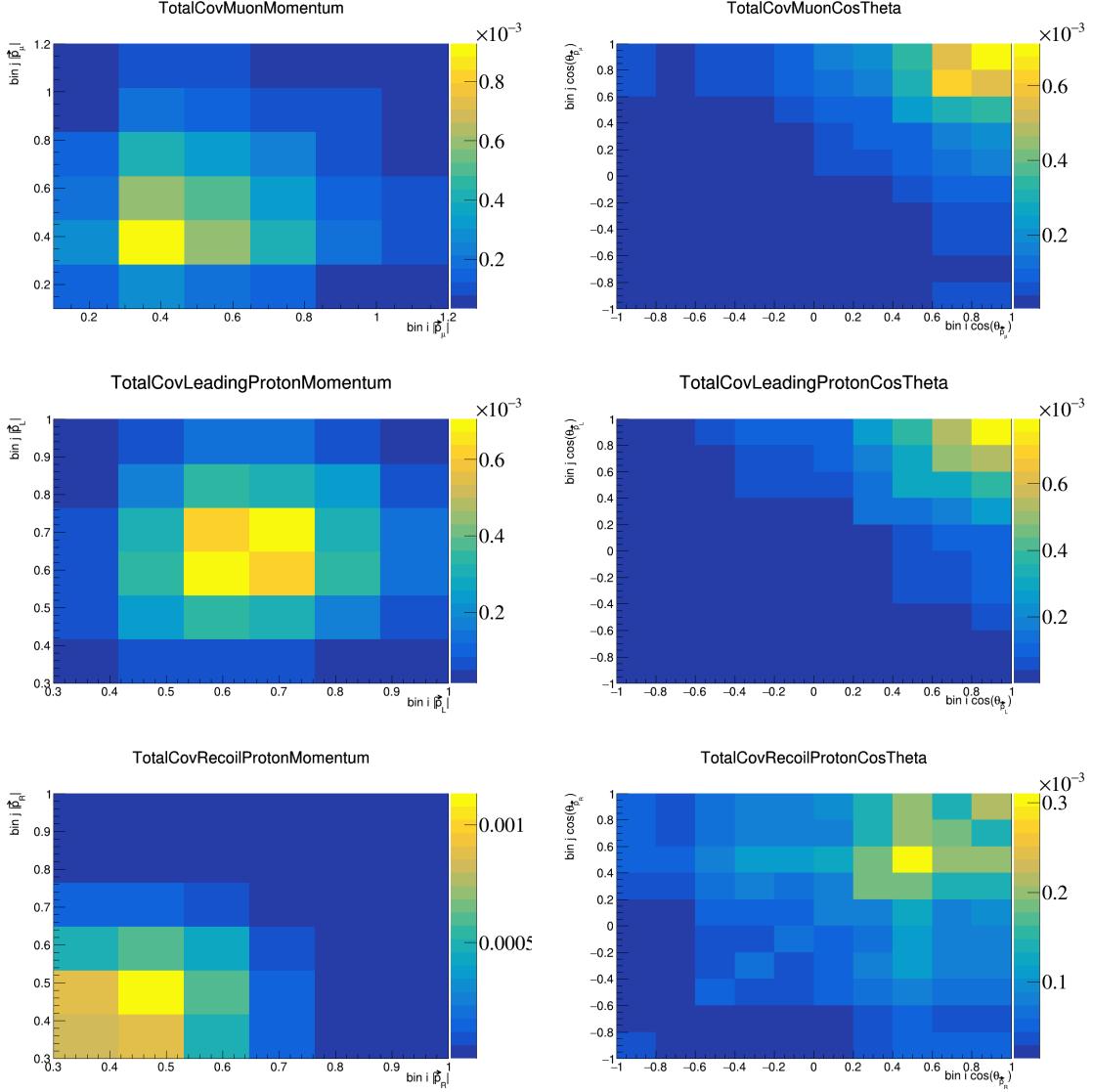


Figure 48: Total covariance matrices for momenta and opening angles of individual particles.

213 straightforward to compute, as the covariance matrix is given by the square root of the number of elements  
 214 in the corresponding bin in the histogram. These statistical covariance matrices are shown in Appendix 6.3.  
 215 For POT systematics, we consider a 2% variation in the number of protons on target and treat it as a  $1\sigma$   
 216 variation. The corresponding plots are shown in Appendix 6.4. For number of target systematics, we likewise  
 217 consider a 1% variation in the number of target nuclei and treat it as a  $1\sigma$  variation. The corresponding  
 218 plots are shown in Appendix 6.5. We consider detector variations of 15% flat for the moment, and these are  
 219 shown in Appendix 6.6. We consider reinteraction systematics as a 2% flat variation, and these are shown  
 220 in Appendix 6.7. The total covariance matrices for each variable are shown in Figures 48 to 50.

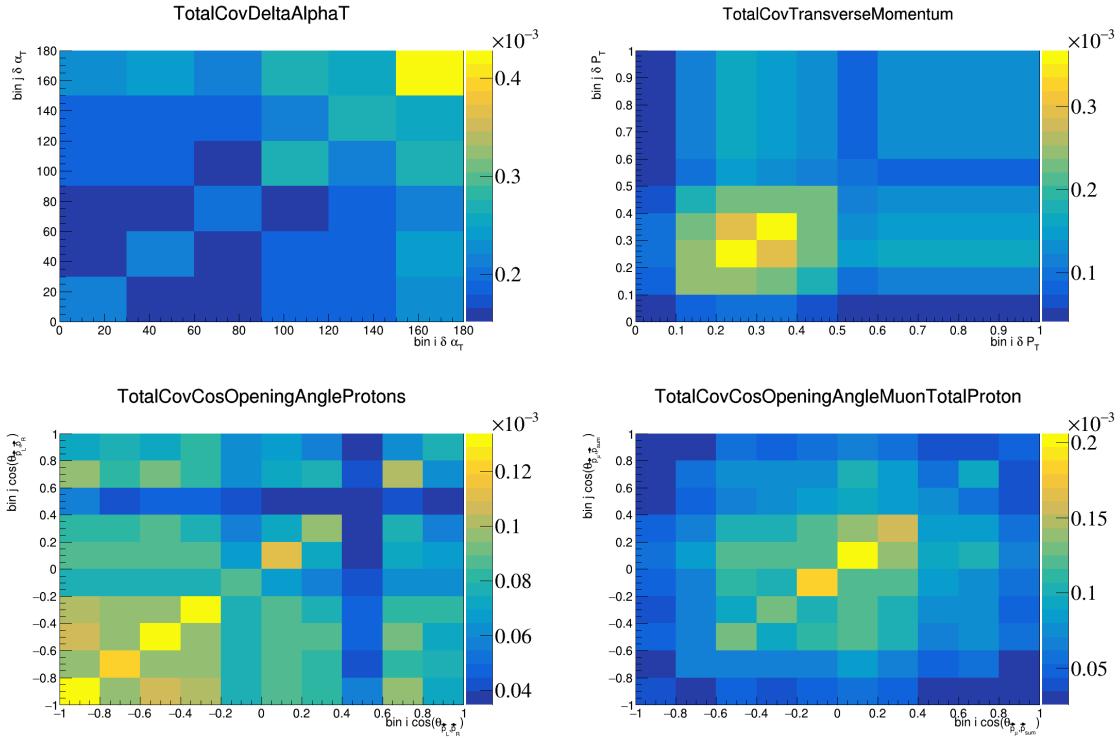


Figure 49: Total covariance matrices for transverse and opening angle variables.

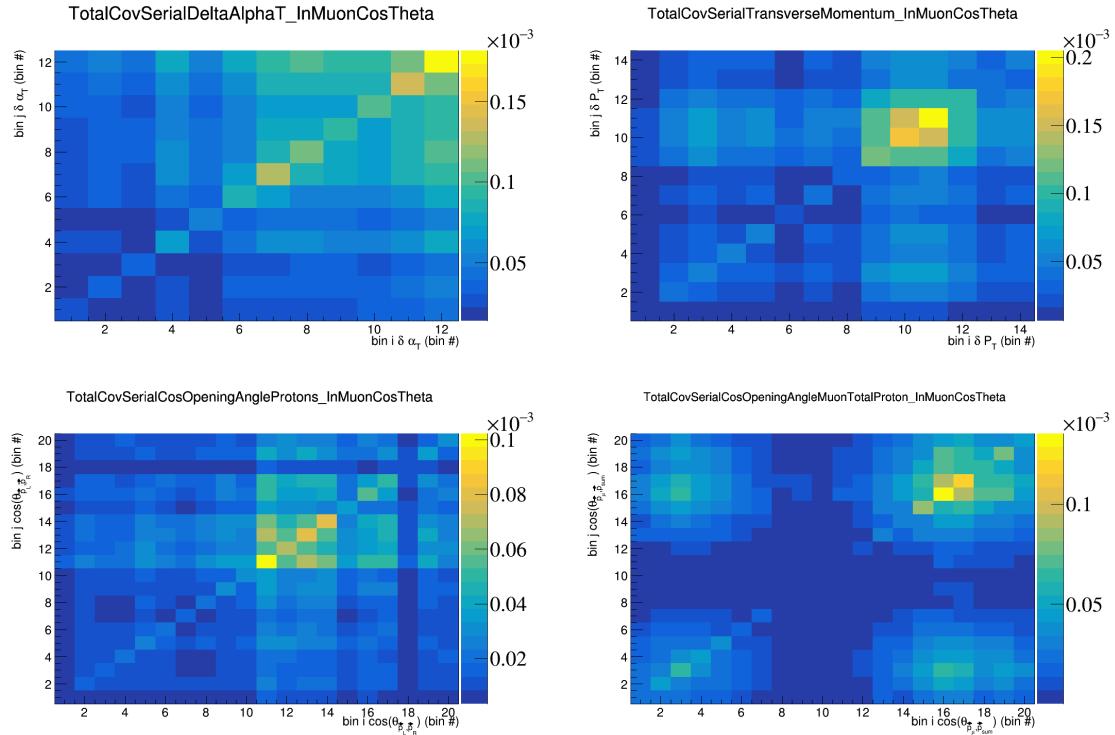


Figure 50: Total covariance matrices for double differential variables.

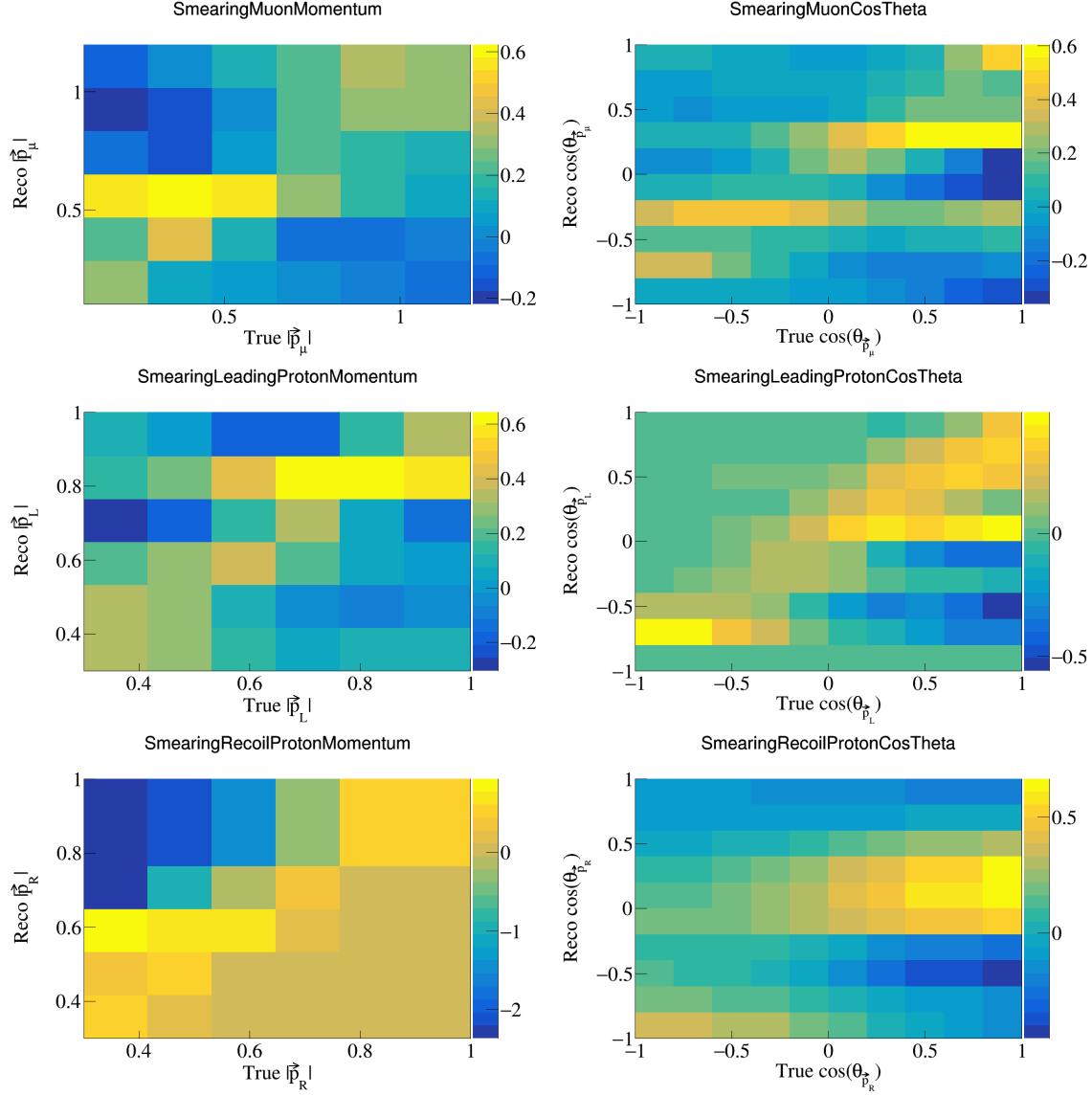


Figure 51: Additional smearing matrices for momenta and opening angles of individual vectors.

### 3.8 Wiener-SVD unfolding

We use the total covariance matrices obtained from all the systematics and shown in the previous section to unfold our data. We perform this unfolding following the Wiener-SVD method [27], which for a given variable takes as input a response matrix, true signal histogram, a reconstructed signal histogram, and the covariance matrix.

The output is the unfolded spectrum, a smearing matrix that can be used to smear true signal histograms, and a covariance rotation matrix to consider uncertainties in the regularized space as opposed to the true space. The additional smearing matrices obtained from the Wiener-SVD unfolding are shown in Figures 51 to 53.

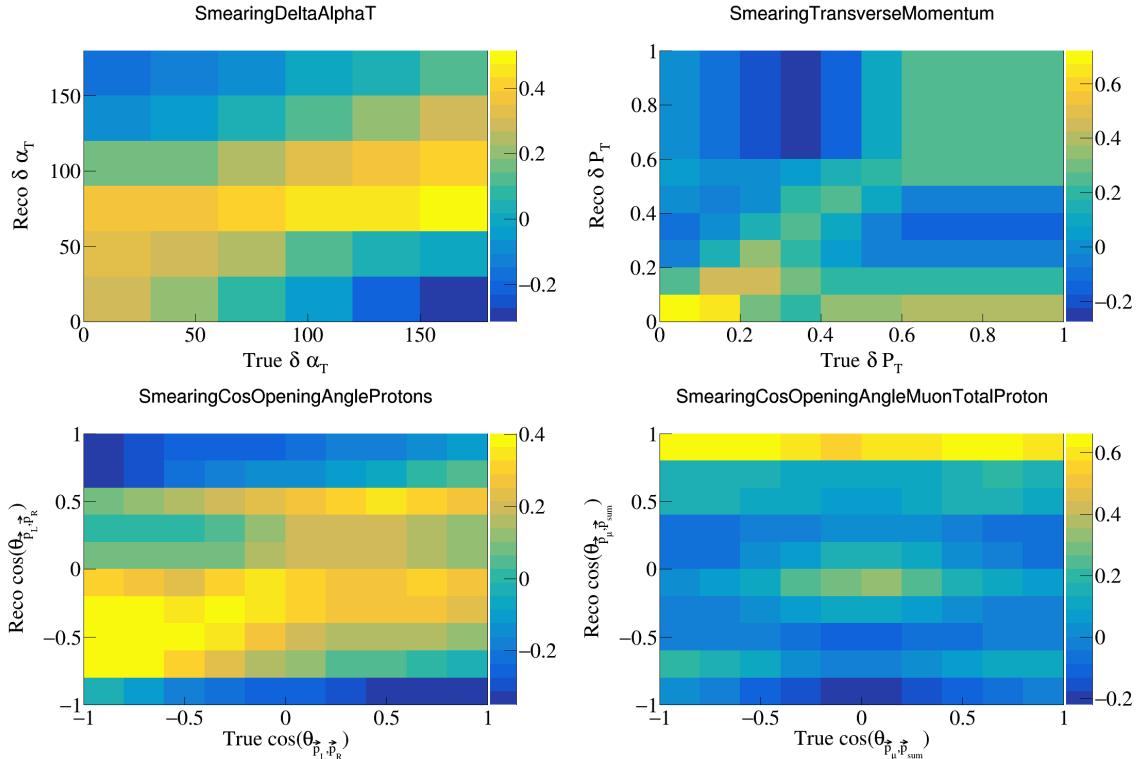


Figure 52: Additional smearing matrices for transverse and opening angle variables.

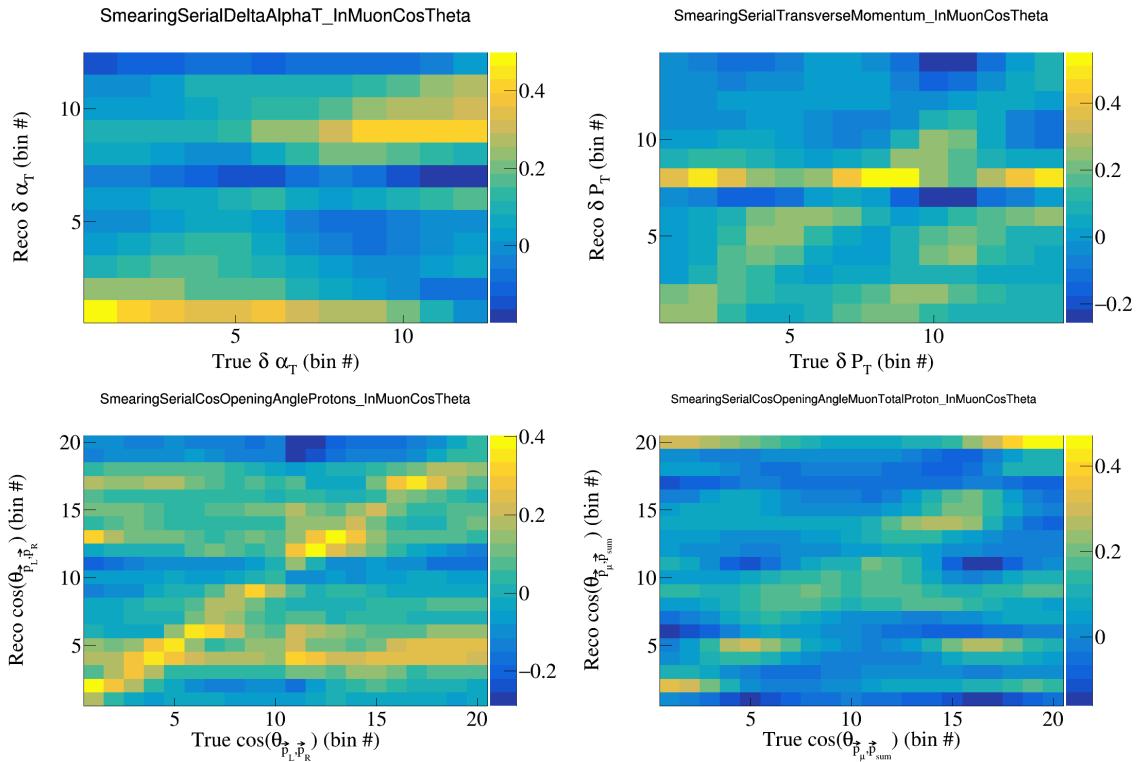


Figure 53: Additional smearing matrices for double differential variables.

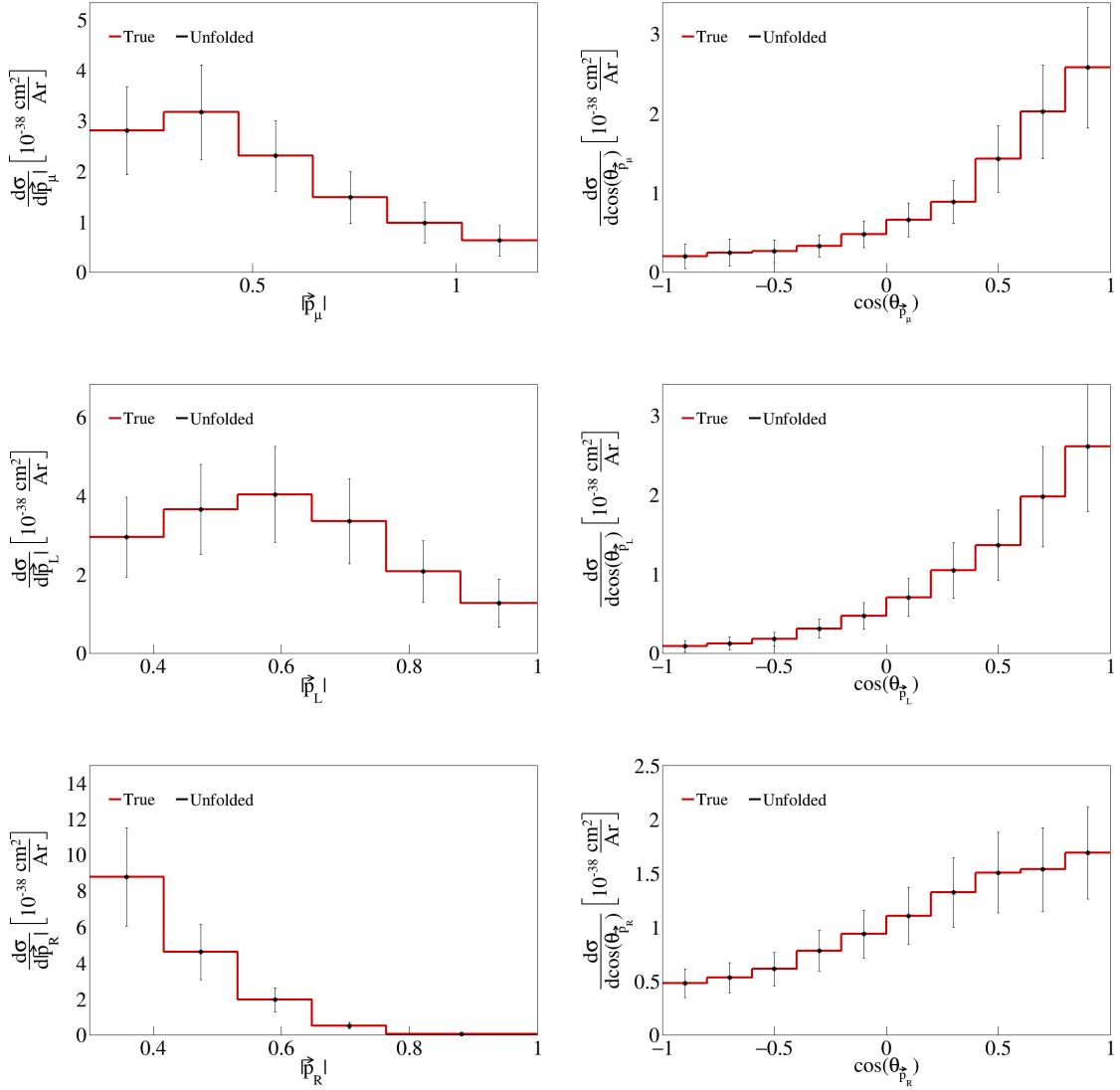


Figure 54: Closure test for momenta and opening angles of individual particles.

### 3.9 Closure test

To ensure that the unfolding techniques implemented work correctly, we use the true signal part of our Monte-Carlo data as our signal, and compare it to the unfolded cross-section obtained from our reconstructed signal to see that they are identical. The plots showing they are identical are in Figures 54 to 56.

The error bands for the unfolded spectra are given by the unfolded total covariance matrices, which are shown in a bin-by-bin basis in the Section 4.1. For the sliced double differential measurements, we make sure to divide by the slice and bin widths to obtain the correct error bands. In the single differential measurements, we only have to divide by the bin width.

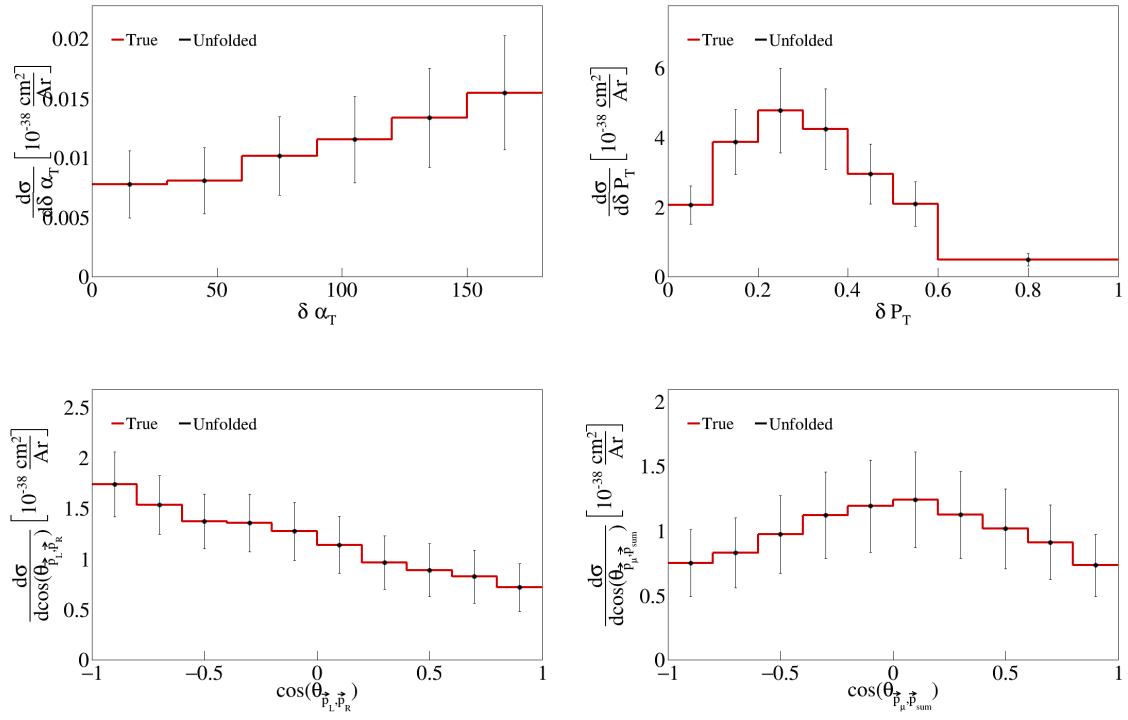


Figure 55: Closure test for transverse and opening angle variables.

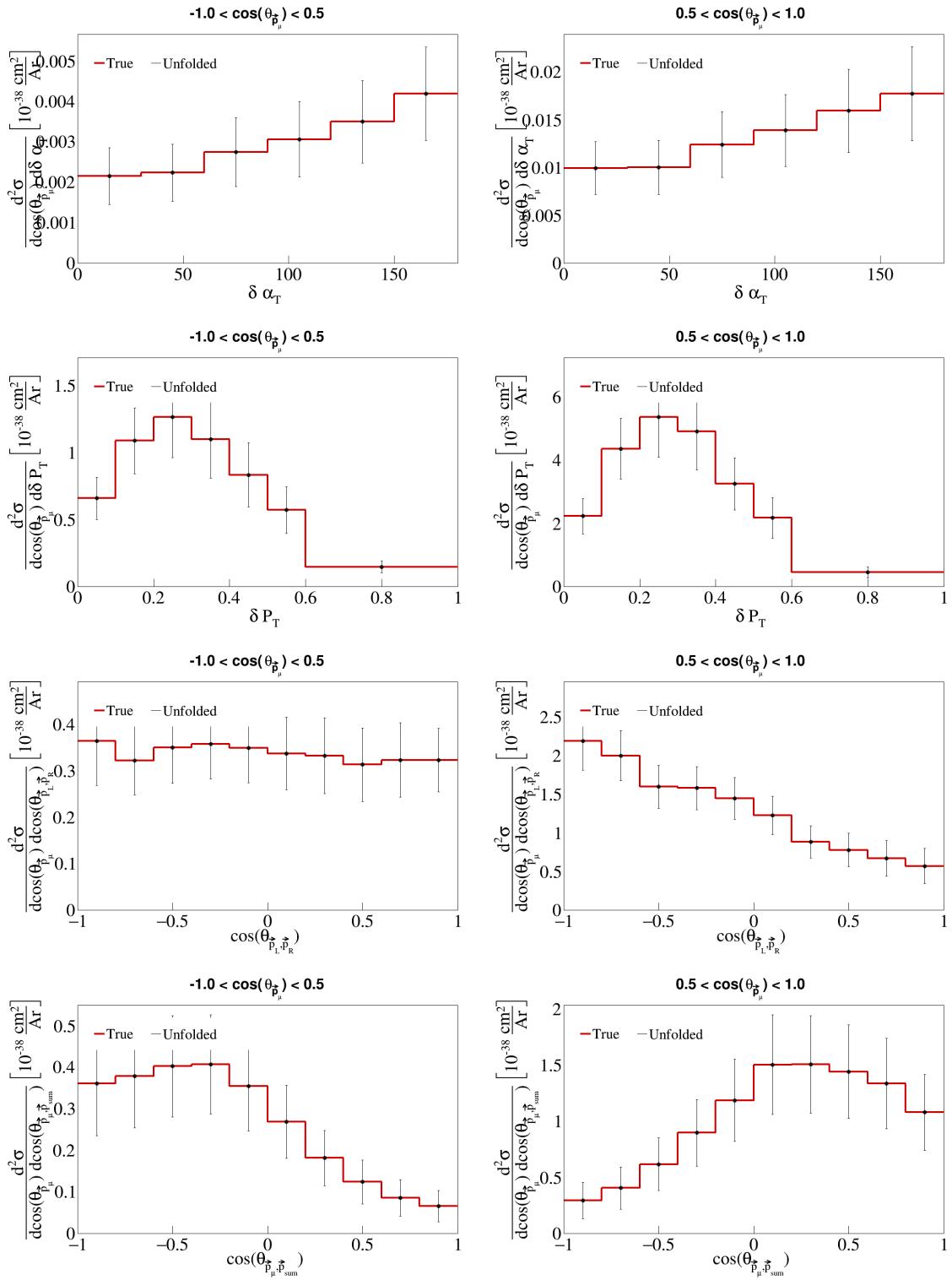


Figure 56: Closure test for double differential plots.

238 **3.10 Event rate uncertainties**

239 Figure 57 shows the single bin uncertainty breakdown using the event rates. We used the square root of  
240 the relevant fractional covariance matrix for each of the outlined sources of uncertainty to obtain the figure.  
241 The bin by bin event rate uncertainties for all our variables are shown in Figures 58 to 60.

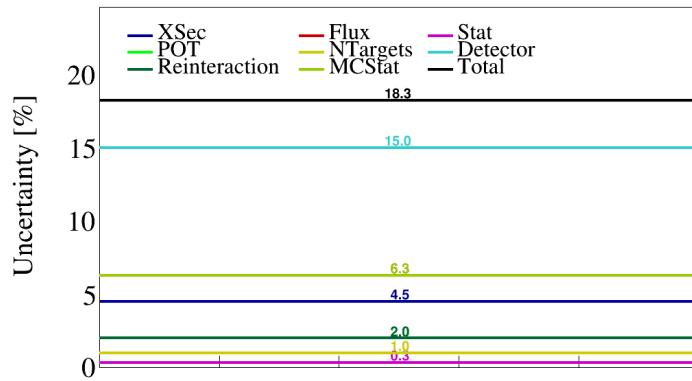


Figure 57: Fractional contribution of the sources of uncertainty using the event rates.

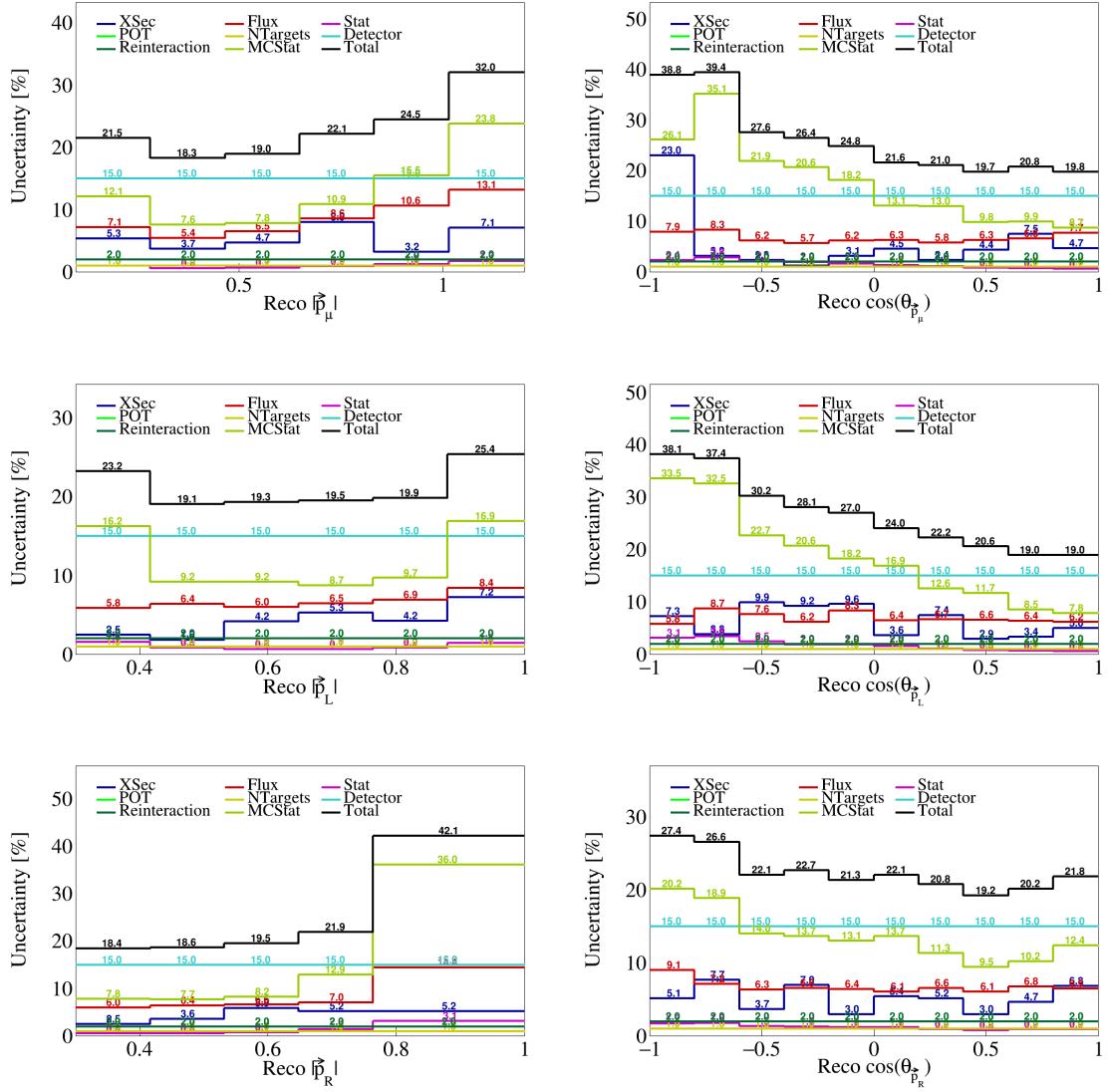


Figure 58: Bin by bin event rate uncertainties for momenta and opening angles of individual particles.

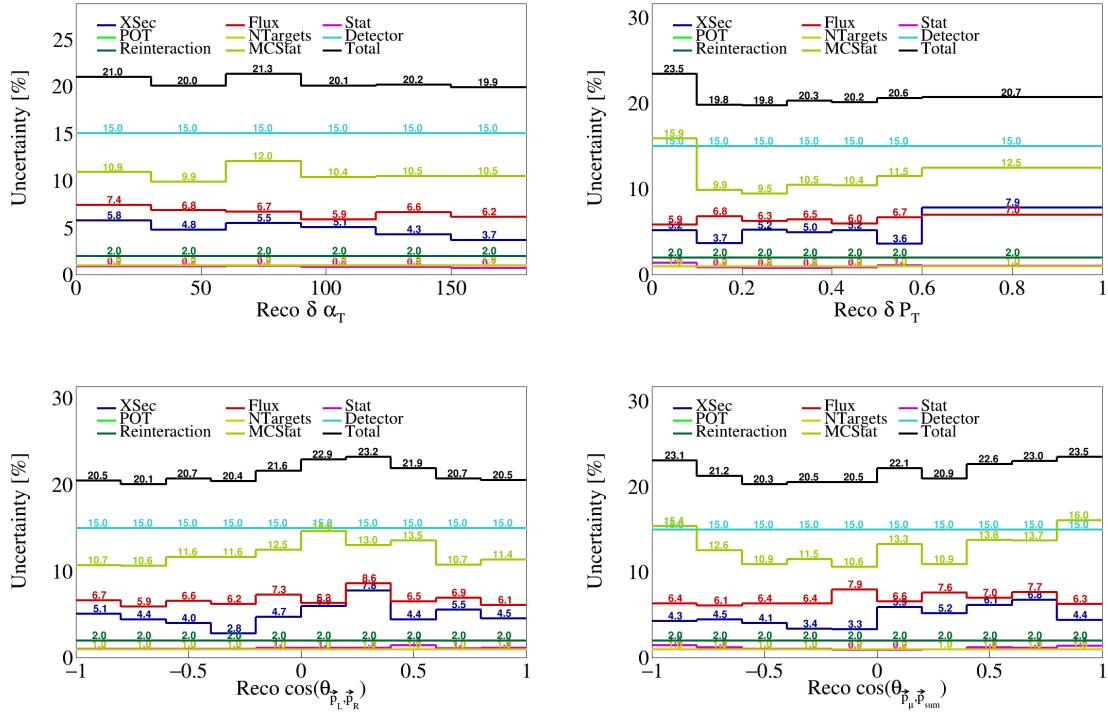


Figure 59: Bin by bin event rate uncertainties for transverse and opening angles variables.

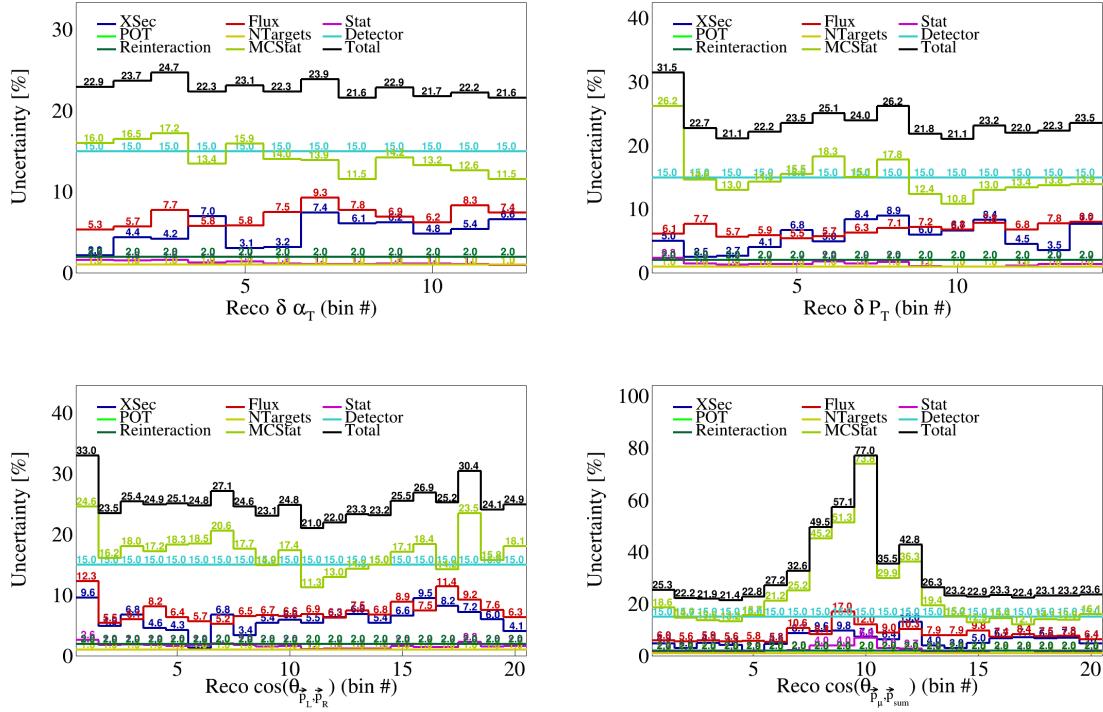


Figure 60: Bin by bin event rate uncertainties for double differential variables.

## 4 Cross-section results

We present the unfolded cross-sections (see note below) using the Wiener-SVD filter, and overlay it with the generators studied in the earlier sections of this document. The generator cross-sections are smeared using the additional smearing matrices, and the uncertainties are obtained using the unfolded total covariance matrix. The unfolded cross-sections are shown in Figures 61 to 63.

*Note: the “results” shown at the moment labeled as data are unfolded cross-sections of Monte-Carlo data, and will be replaced with real data once that is available.*

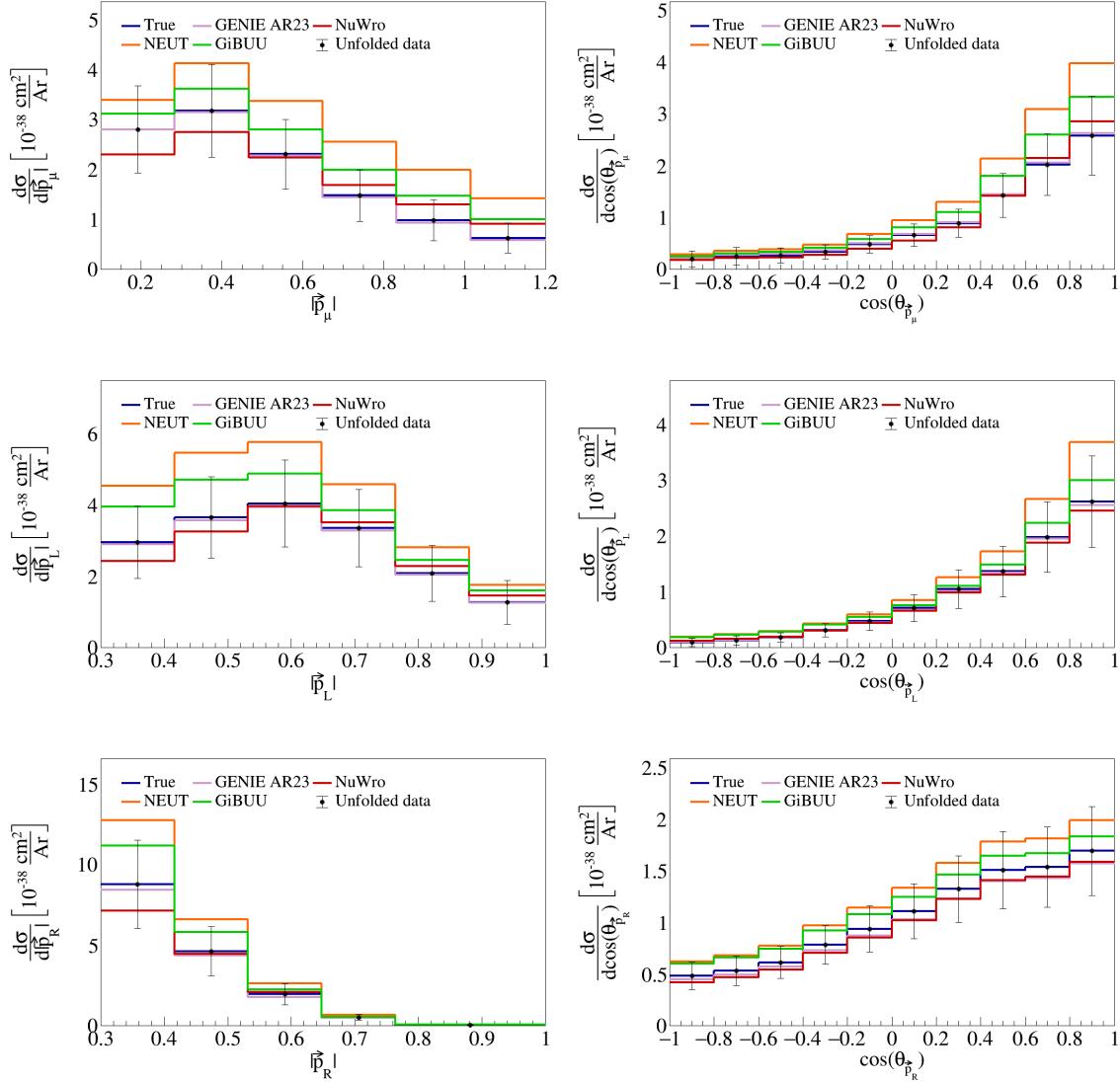


Figure 61: Cross-section results for momenta and opening angles of individual particles.

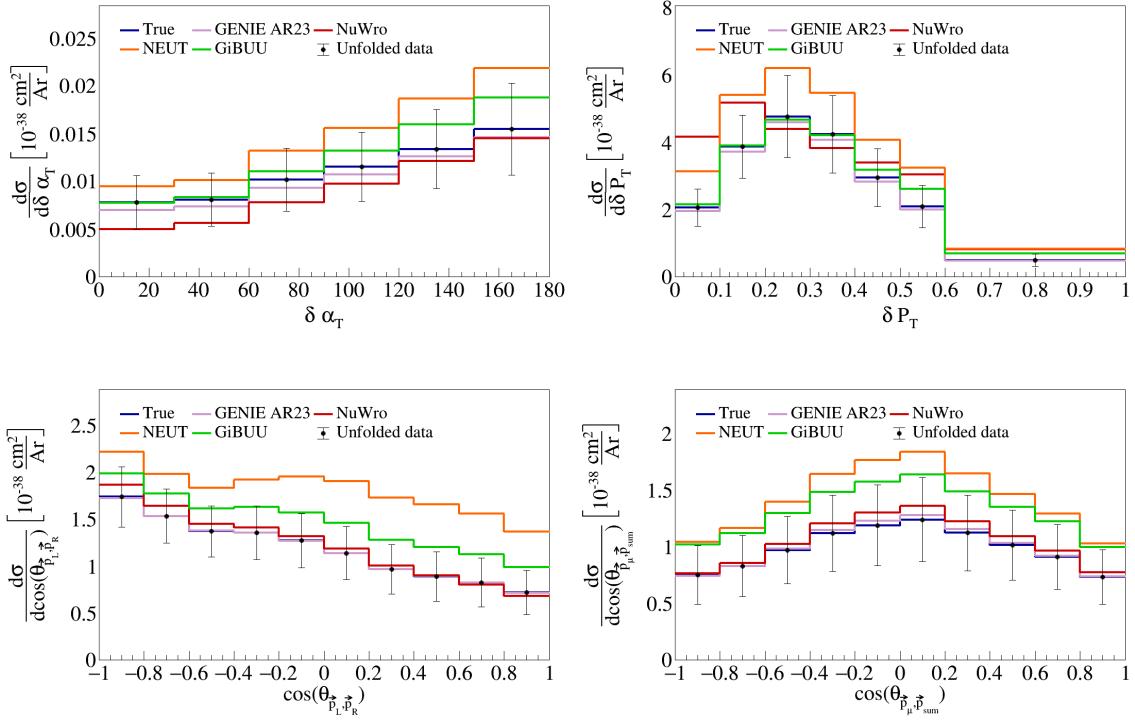


Figure 62: Cross-section results for transverse and opening angle variables.

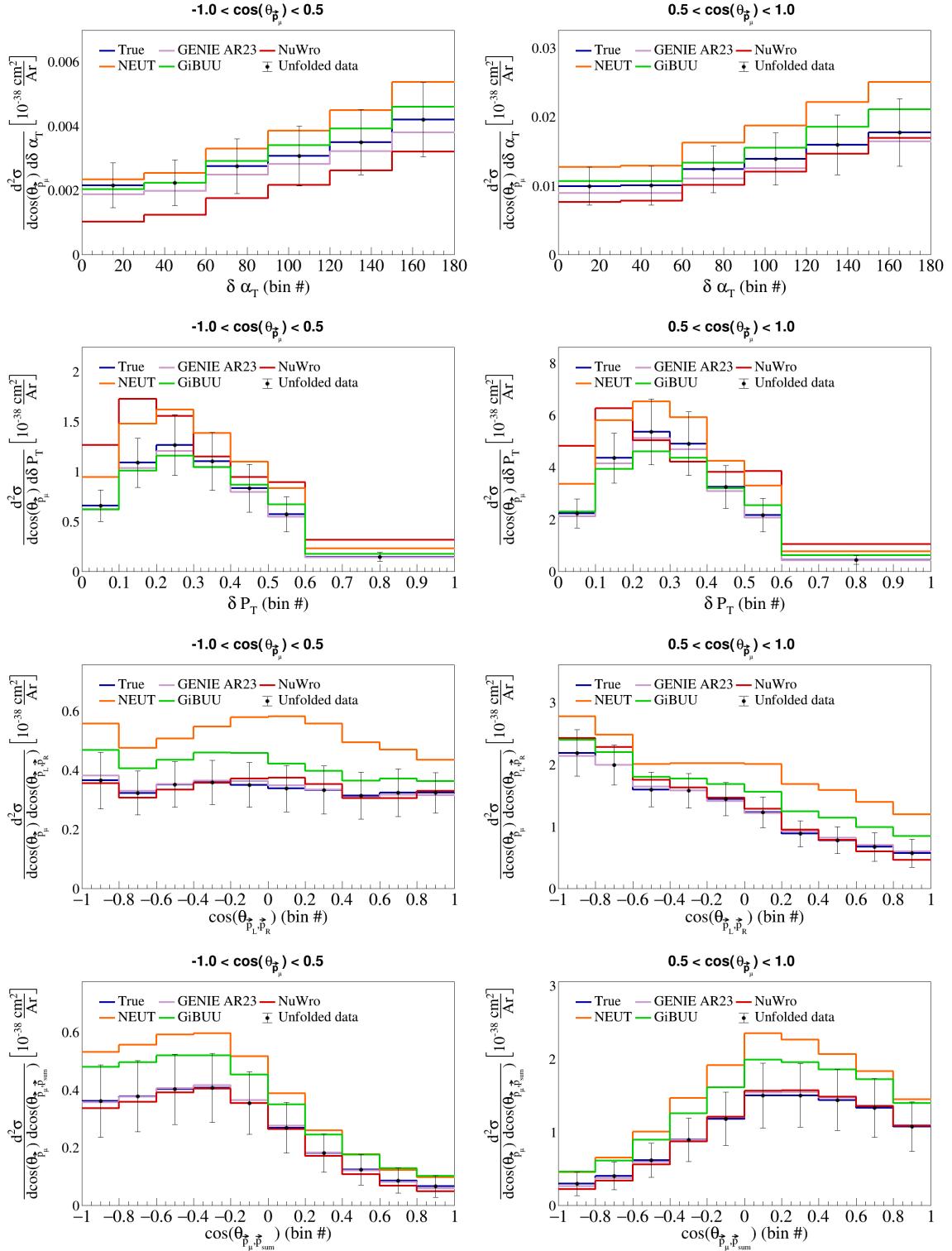


Figure 63: Cross-section results for sliced double differential variables.

<sup>249</sup> **4.1 Cross-section uncertainties**

<sup>250</sup> Figure 64 shows the single bin uncertainty breakdown using the cross sections. We used the unfolded  
<sup>251</sup> covariances obtained with the Wiener-SVD filter for each of the sources of uncertainty. The square root of the  
<sup>252</sup> corresponding fractional covariance matrix is normalized to the CV cross-section value for the uncertainties  
<sup>253</sup> to be obtained. The bin by bin cross section uncertainties for all our variables are shown in Figures 65 to 67.

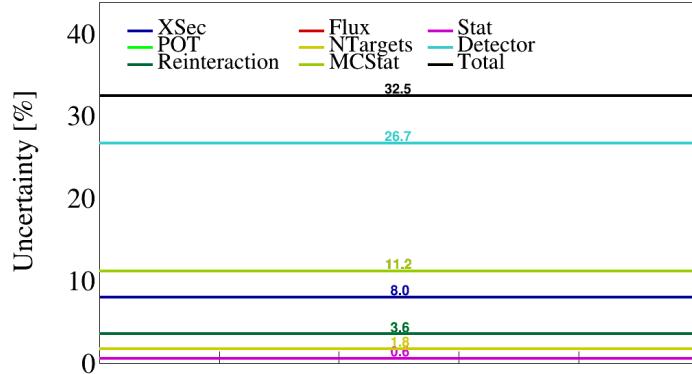


Figure 64: Fractional contribution for the sources of uncertainty using the cross sections.

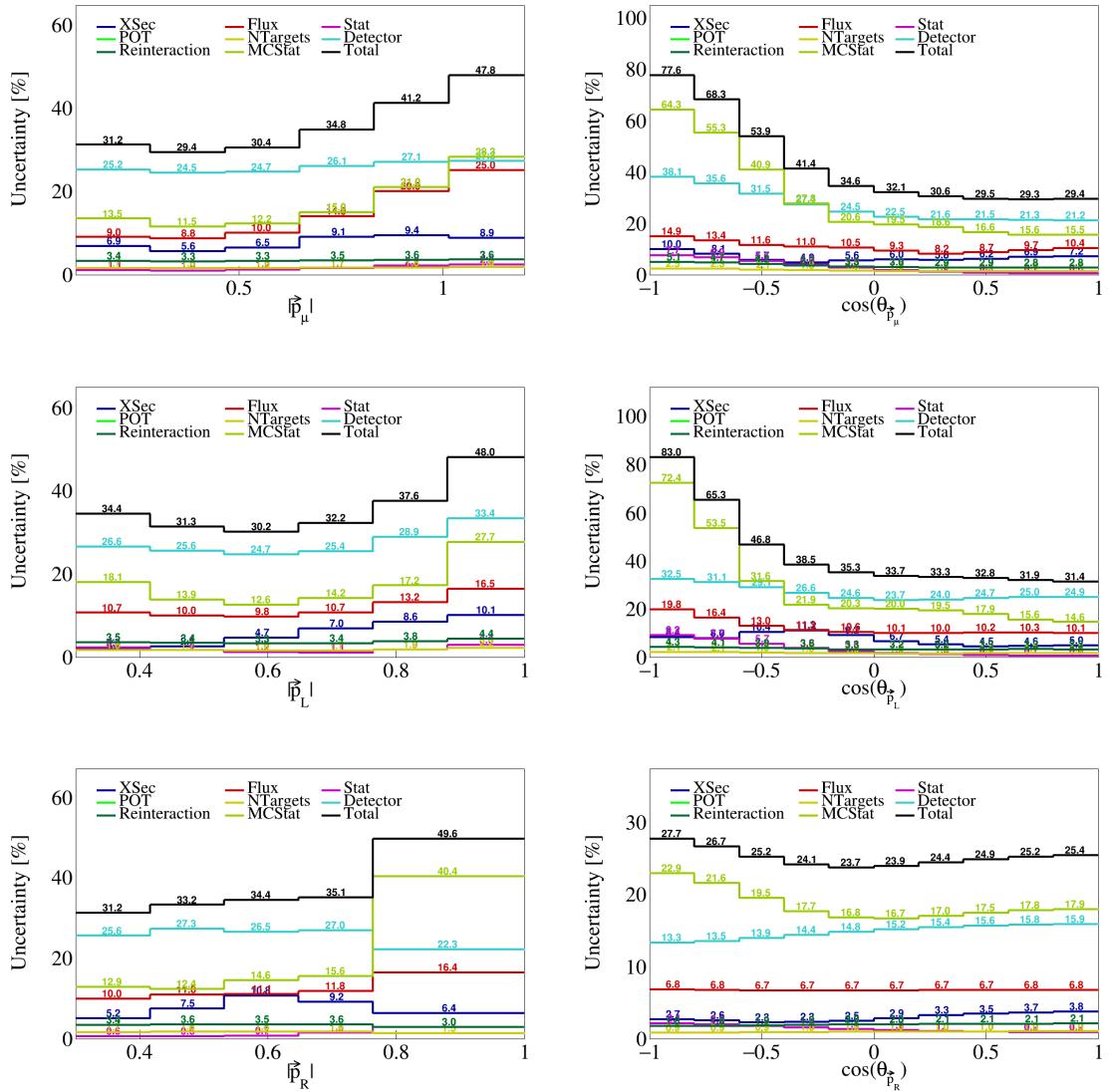


Figure 65: Bin by bin event cross-section uncertainties for momenta and opening angles of individual particles.

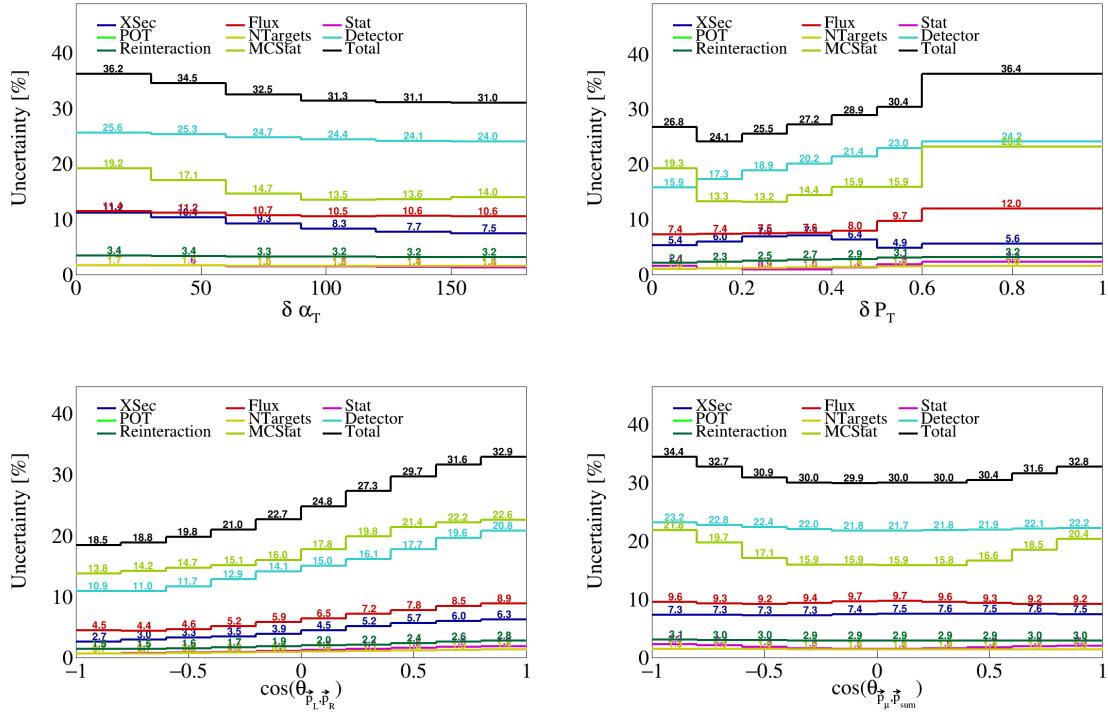


Figure 66: Bin by bin cross-section uncertainties for transverse and opening angles variables.

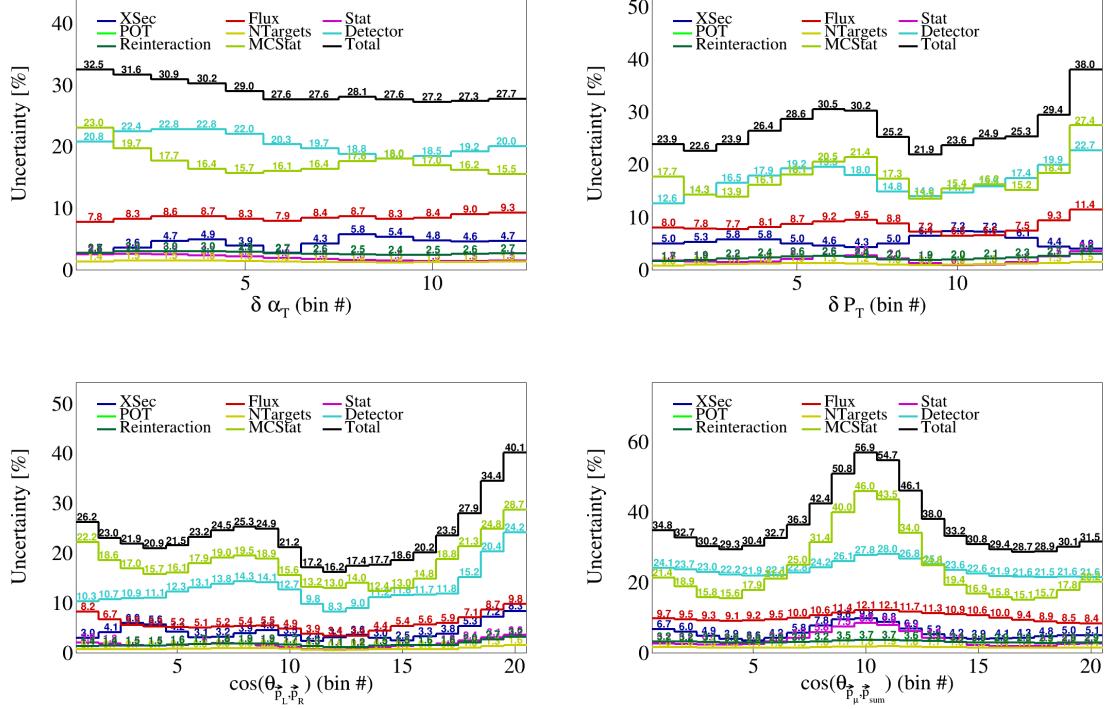


Figure 67: Bin by bin cross-section uncertainties for double differential variables.

254 **5 Fake data studies**

255 To test our unfolding procedure, we generate fake data by increasing the weight of certain events in our  
256 Monte Carlo simulations. We give meson exchange current (MEC) events a weight of 2 in Section 5.1, and  
257 quasi-elastic (QE) events a weight of 0.5 combined with a MEC weight of 1.5 in Section 5.2. We then unfold  
258 these fake data using the nominal Monte-Carlo predictions from the GENIE AR23 generator. Therefore, the  
259 input to the Wiener-SVD unfolding are: the response matrix constructed with the nominal predictions, the  
260 true nominal signal, the reconstructed signal from the fake data (this is the only input that changes), and  
261 the total covariance matrix, which in this case was the statistical covariance matrix for the fake data added  
262 to the MC statistical and cross-section covariance matrices obtained with the nominal predictions.

263 After unfolding the fake data, we compare the unfolded fake data to the smeared fake signal and the  
264 smeared nominal signal, using the additional smearing matrix obtained from the Wiener-SVD unfolding. We  
265 then perform a  $\chi^2$  test to see if the unfolded fake data agrees with the smeared fake signal. Additionally, we  
266 also report the  $p$ - and  $\sigma$ -values for the distributions. We expect to see good agreement between the smeared  
267 fake signal and the unfolded fake data, while the smeared nominal signal should not agree with the unfolded  
268 fake data. In other words, we expect below  $1\sigma$  agreement between the smeared fake signal and unfolded fake  
269 data.

270 **5.1 MEC 2x weight**

271 In this first fake data study, we give MEC events a weight of 2, while keeping all other events with a weight  
272 of 1. We see that we are under  $1\sigma$  agreement between the smeared fake signal and the unfolded fake data  
273 for all our variables, while on or above  $2.9\sigma$  with the smeared nominal signal, as expected. Therefore, we  
274 can conclude that this fake data study was successful. The unfolded fake data along with the two smeared  
275 signals is shown in Figures 68 to 71.

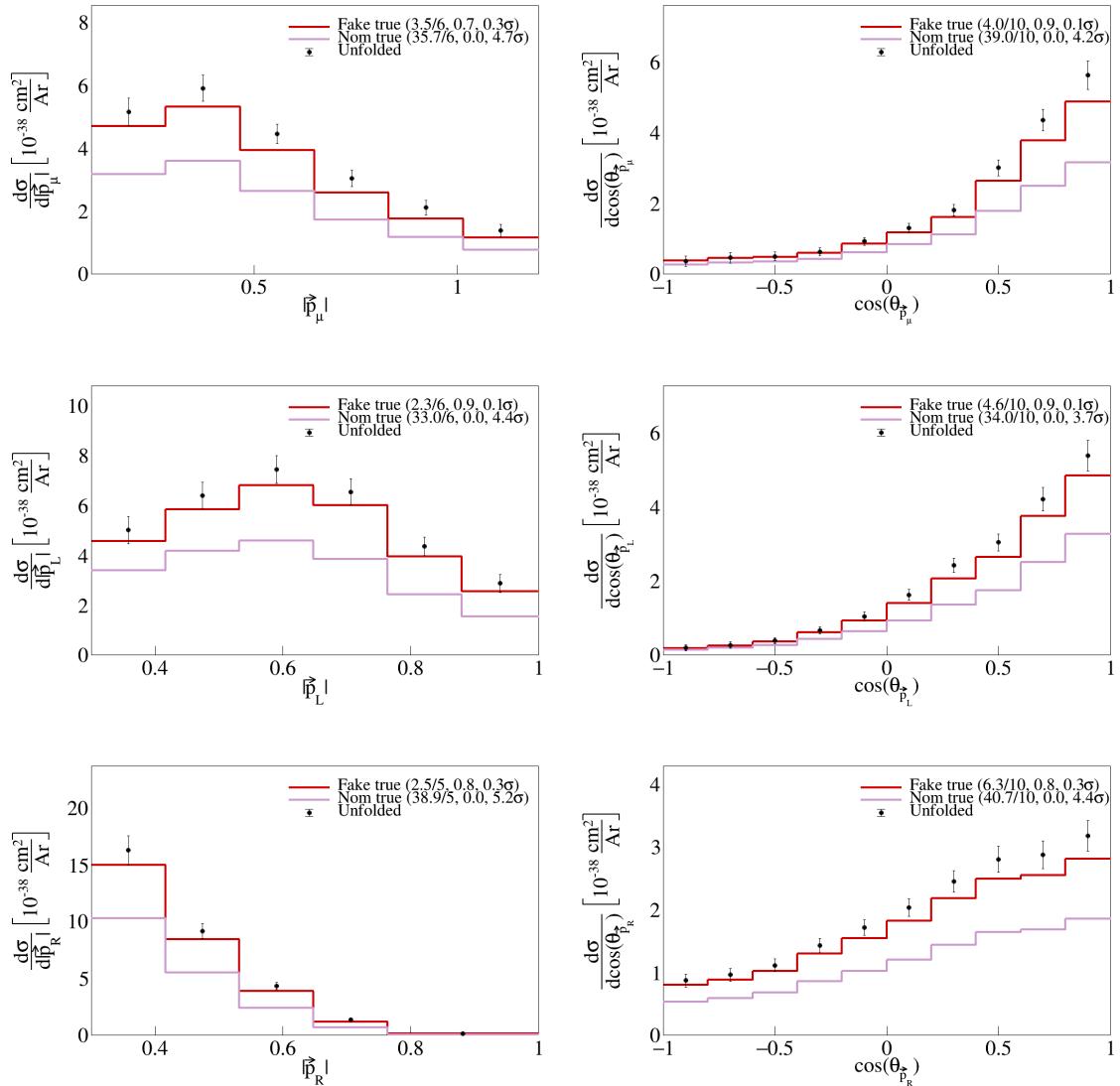


Figure 68: Unfolded 2x MEC fake data showing agreement with smeared fake signal data for single differential vector directions and magnitudes.

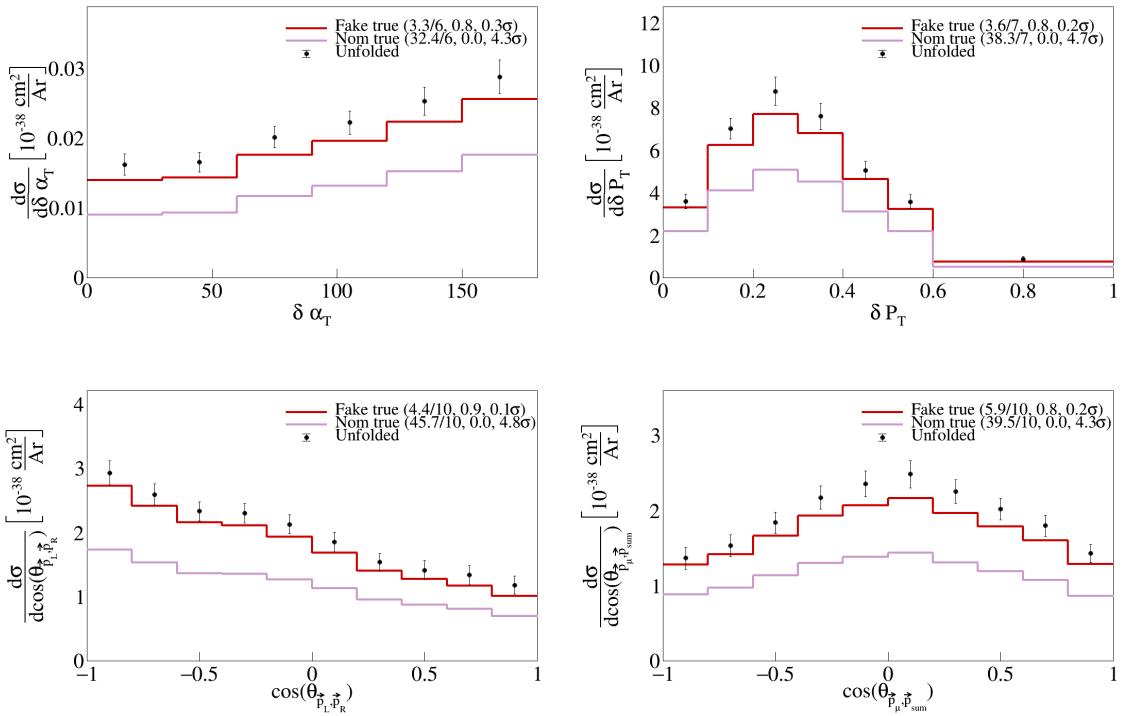


Figure 69: Unfolded 2x MEC fake data showing agreement with smeared fake signal data for single differential vector opening angles and transverse momentum.

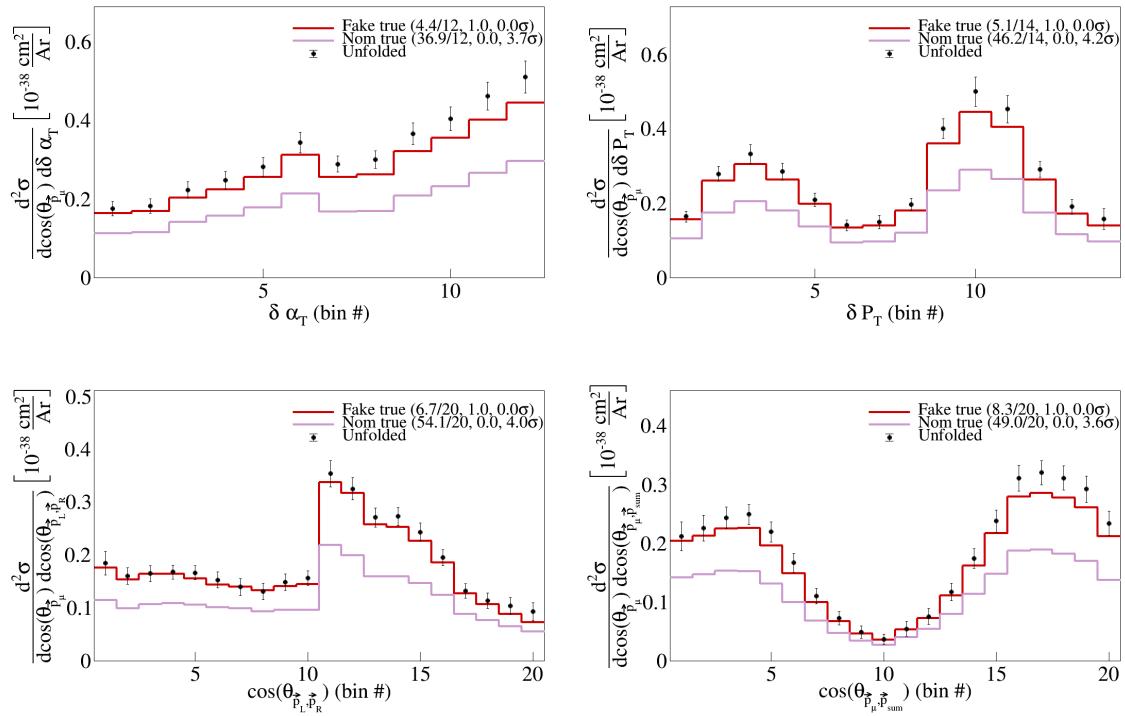


Figure 70: Unfolded 2x MEC fake data showing agreement with smeared fake signal data for serial double differential variables.

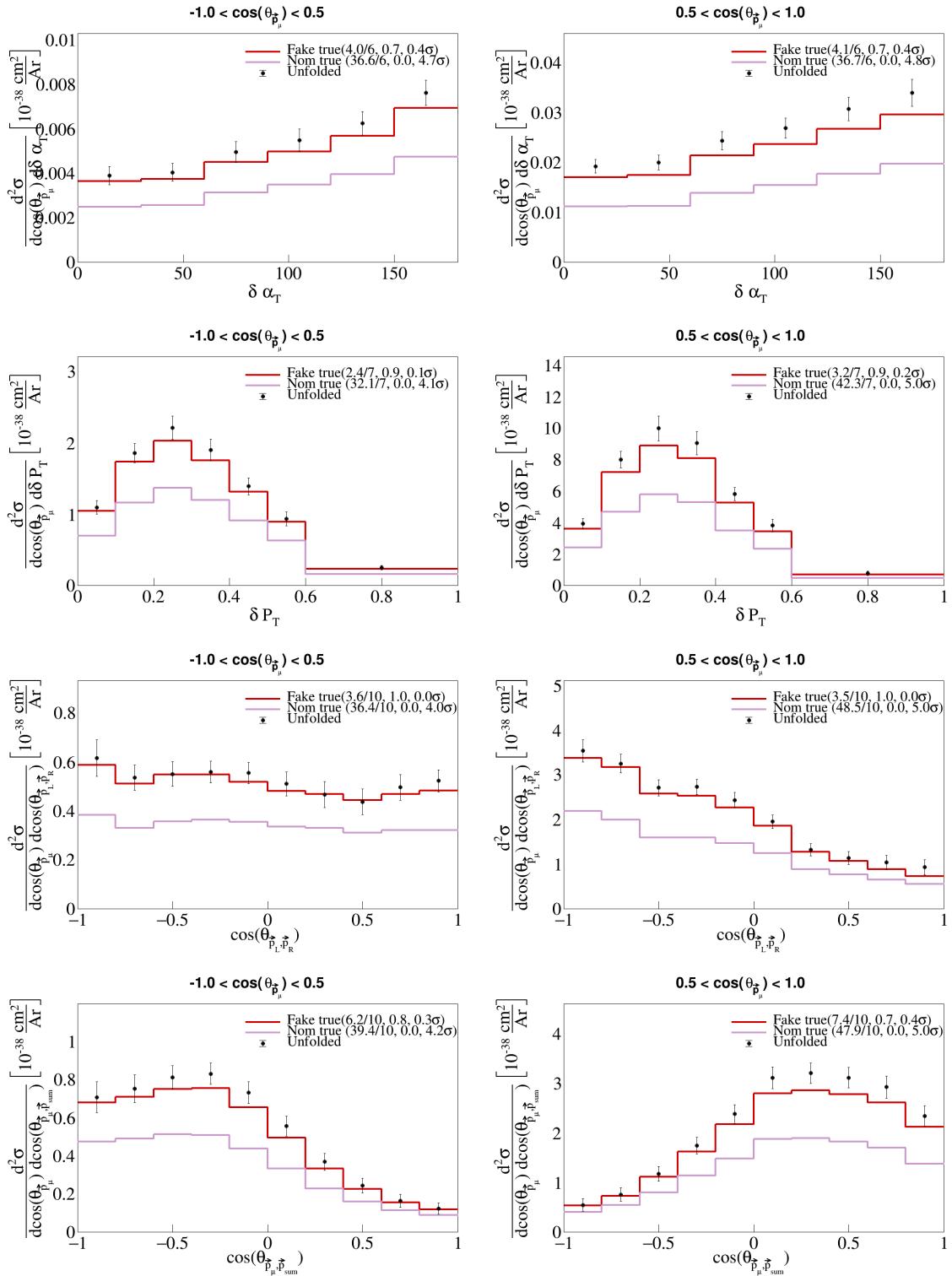


Figure 71: Unfolded 2x MEC fake data showing agreement with smeared fake signal data for sliced double differential variables.

276 **5.2 QE 0.5x and MEC 1.5x weights**

277 For this fake data study we give QE events a weight of 0.5 and MEC events a weight of 1.5, while keeping  
278 all other events with a weight of 1. We see that we are under  $1\sigma$  agreement between the smeared fake signal  
279 and the unfolded fake data for all our variables, but contrary to the first study, we also see agreement with  
280 the smeared nominal signal in many of our variables. The unfolded fake data for this study along with the  
281 two smeared signals is shown in Figures 72 to 75.

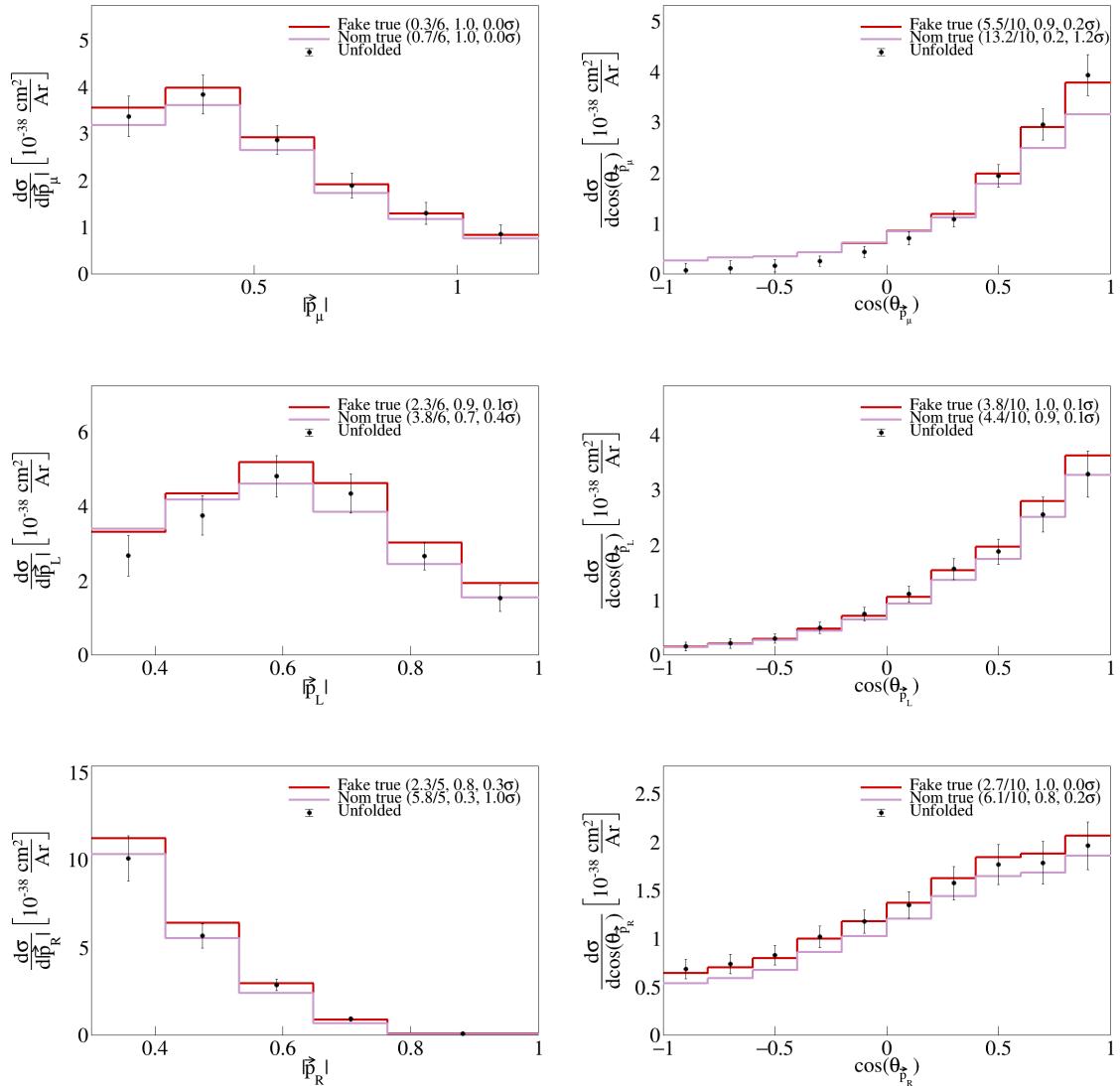


Figure 72: Unfolded combined weights fake data showing agreement with smeared fake signal data for single differential vector directions and magnitudes.

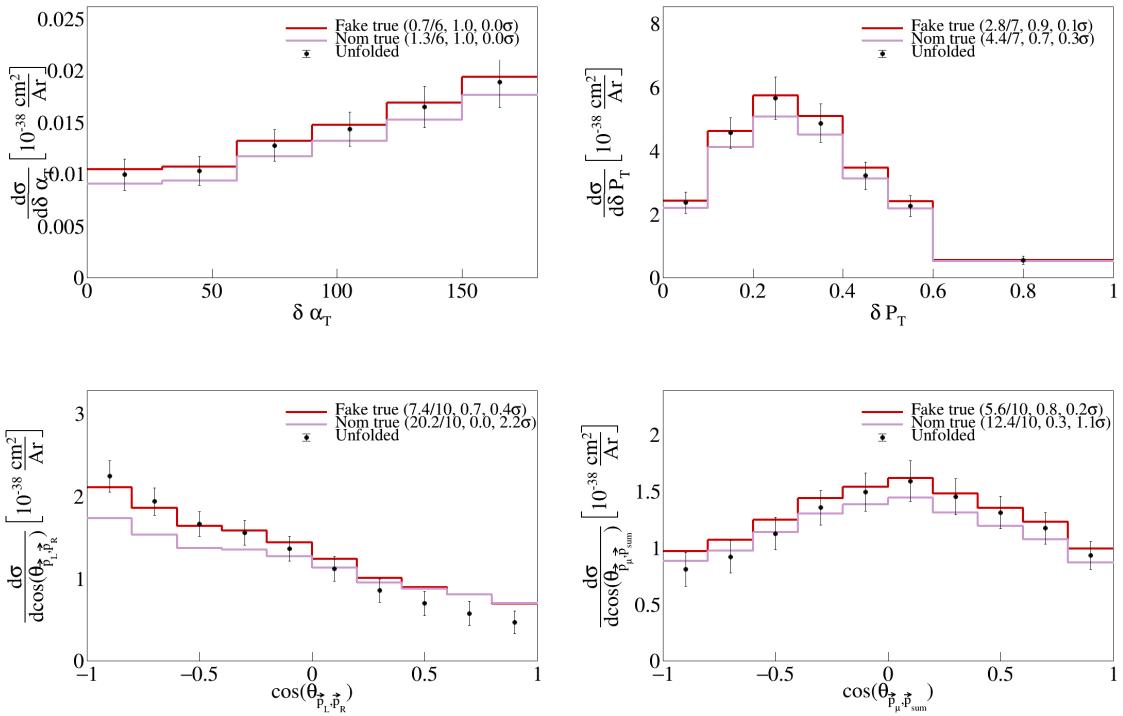


Figure 73: Unfolded combined weights fake data showing agreement with smeared fake signal data for single differential vector opening angles and transverse momentum.

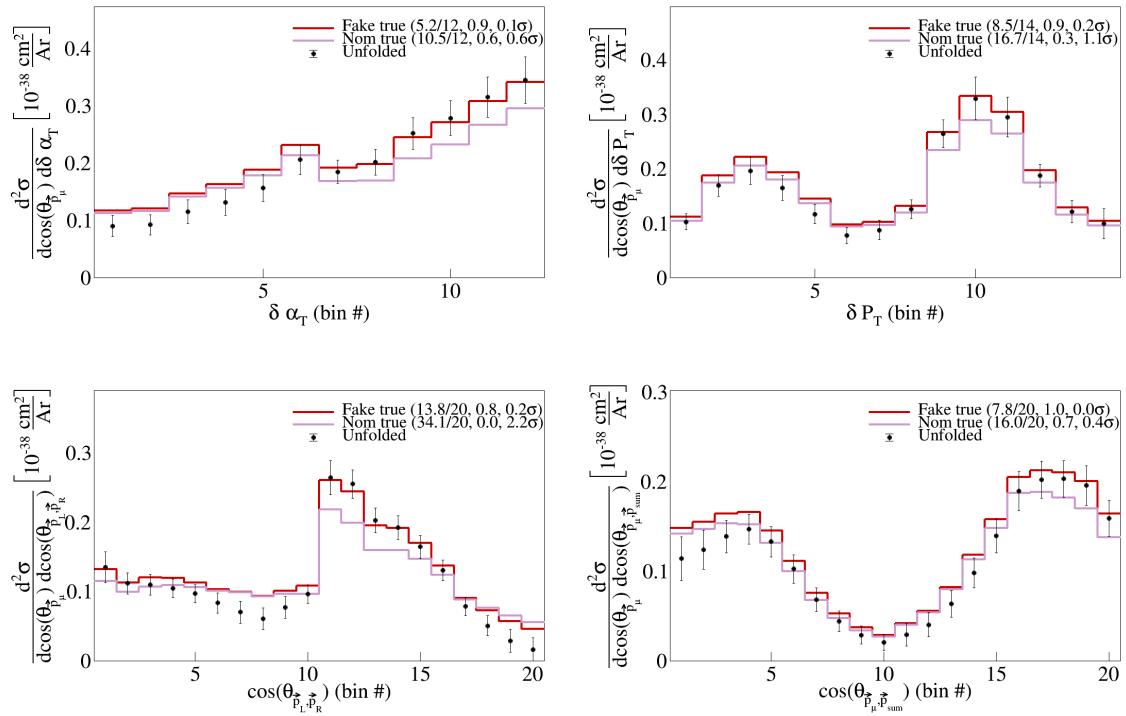


Figure 74: Unfolded combined weights fake data showing agreement with smeared fake signal data for serial double differential variables.

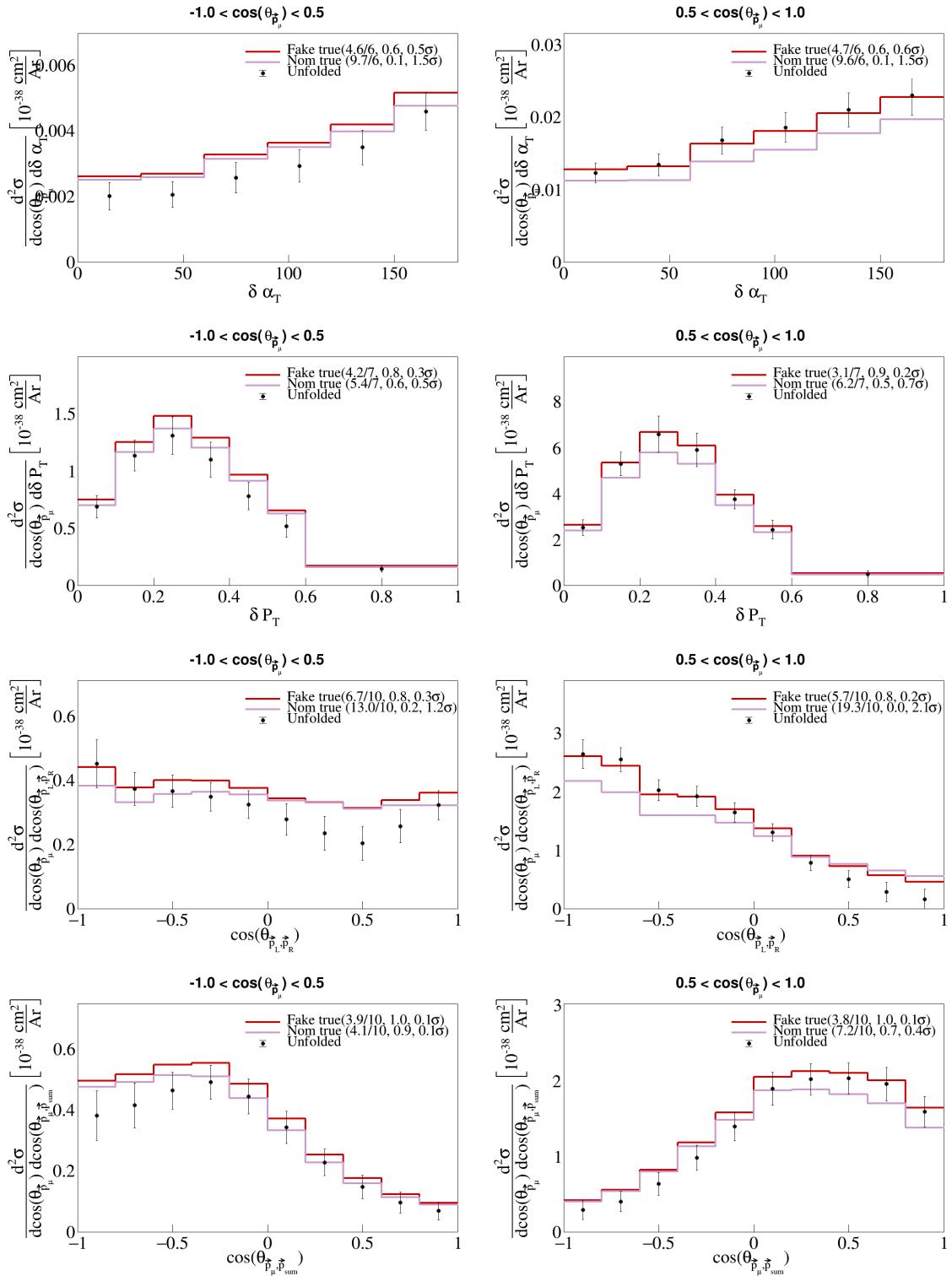


Figure 75: Unfolded combined weights fake data showing agreement with smeared fake signal data for sliced double differential variables.

## 282 6 Appendices

### 283 6.1 Cross section systematics

284 In this appendix, the variations, covariance matrices, fractional covariance matrices, and correlation matrices  
 285 are plotted for all of the cross section systematics and variables.

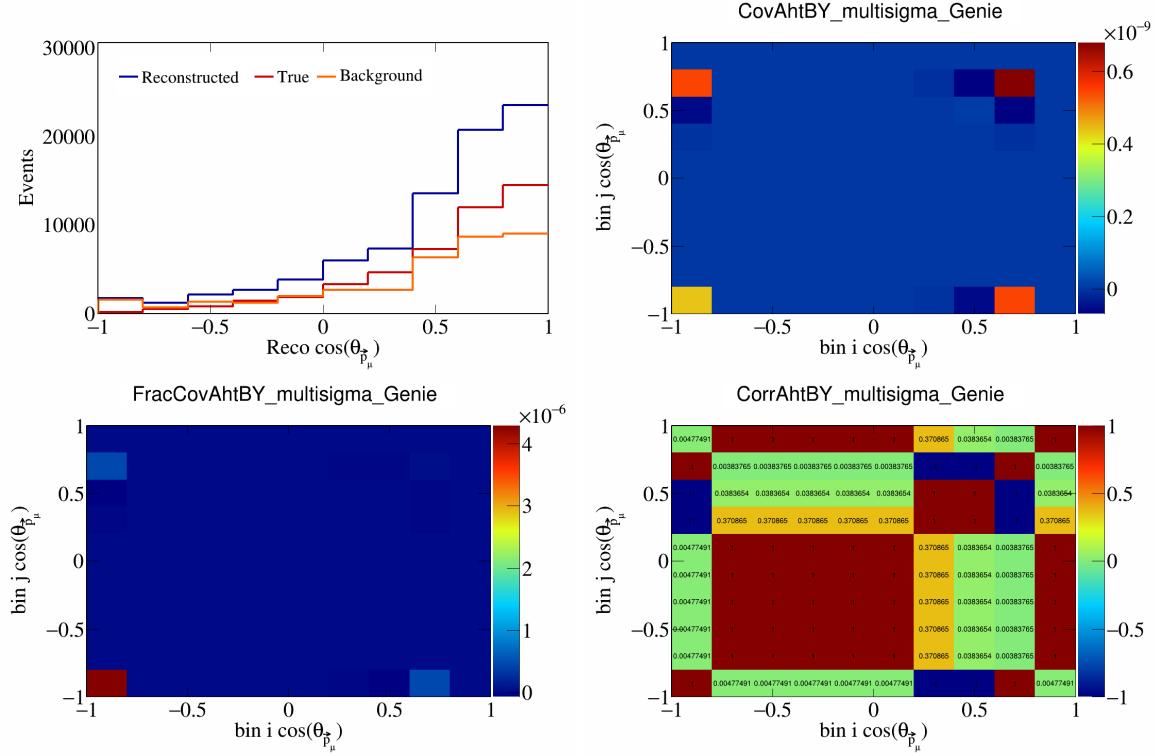


Figure 76: AhtBY variations for  $\cos(\theta_{\vec{p}_\mu})$ .

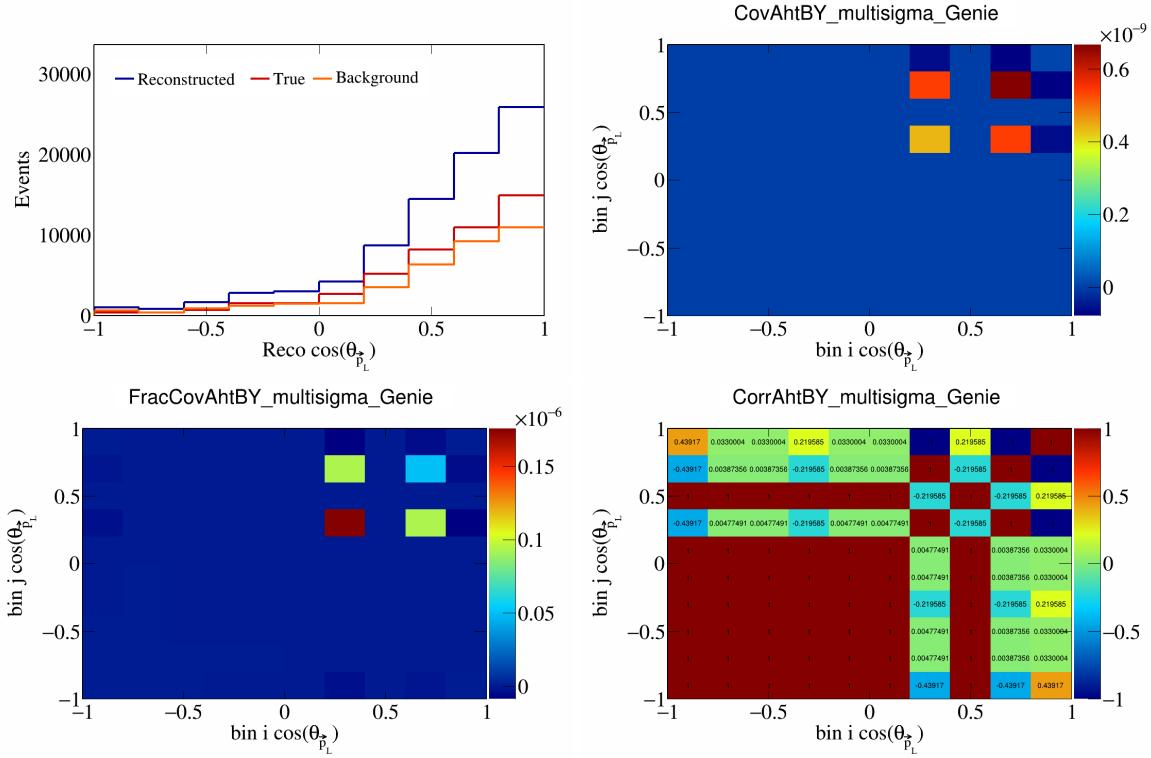


Figure 77: AhtBY variations for  $\cos(\theta_{\vec{p}_L})$ .

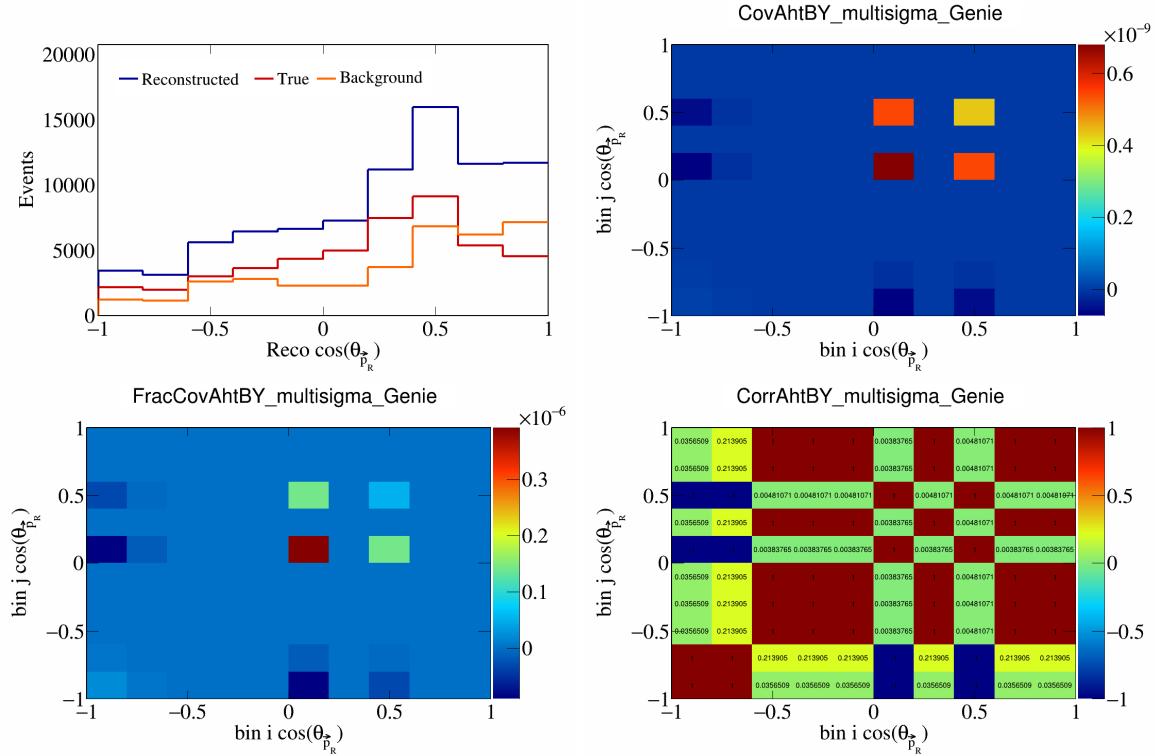


Figure 78: AhtBY variations for  $\cos(\theta_{\vec{p}_R})$ .

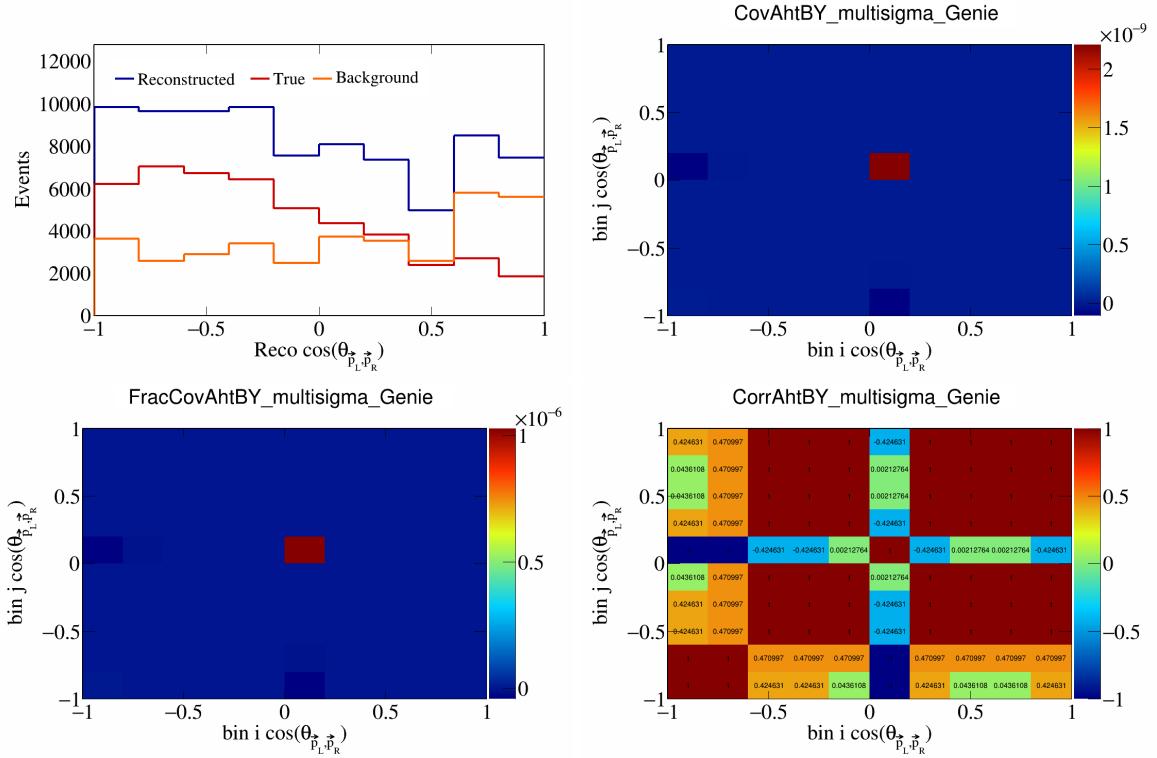


Figure 79: AhtBY variations for  $\cos(\theta_{\vec{p}_L, \vec{p}_R})$ .

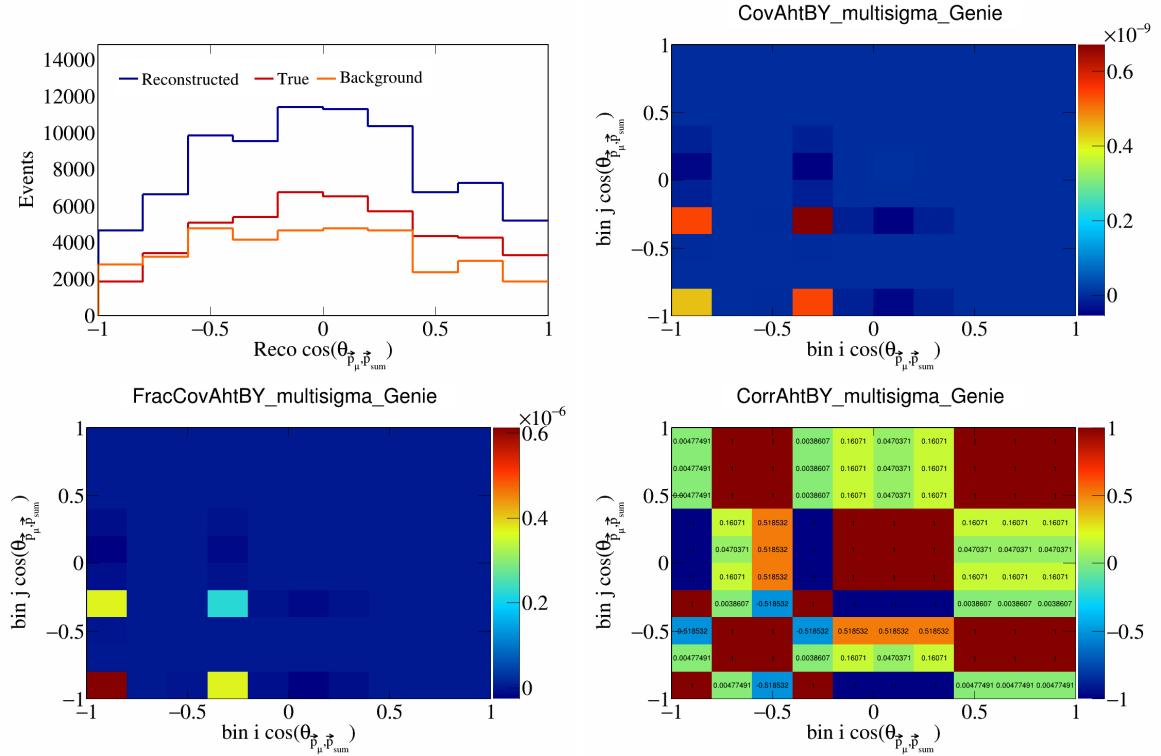


Figure 80: AhtBY variations for  $\cos(\theta_{\vec{p}_\mu, \vec{p}_{\text{sum}}})$ .

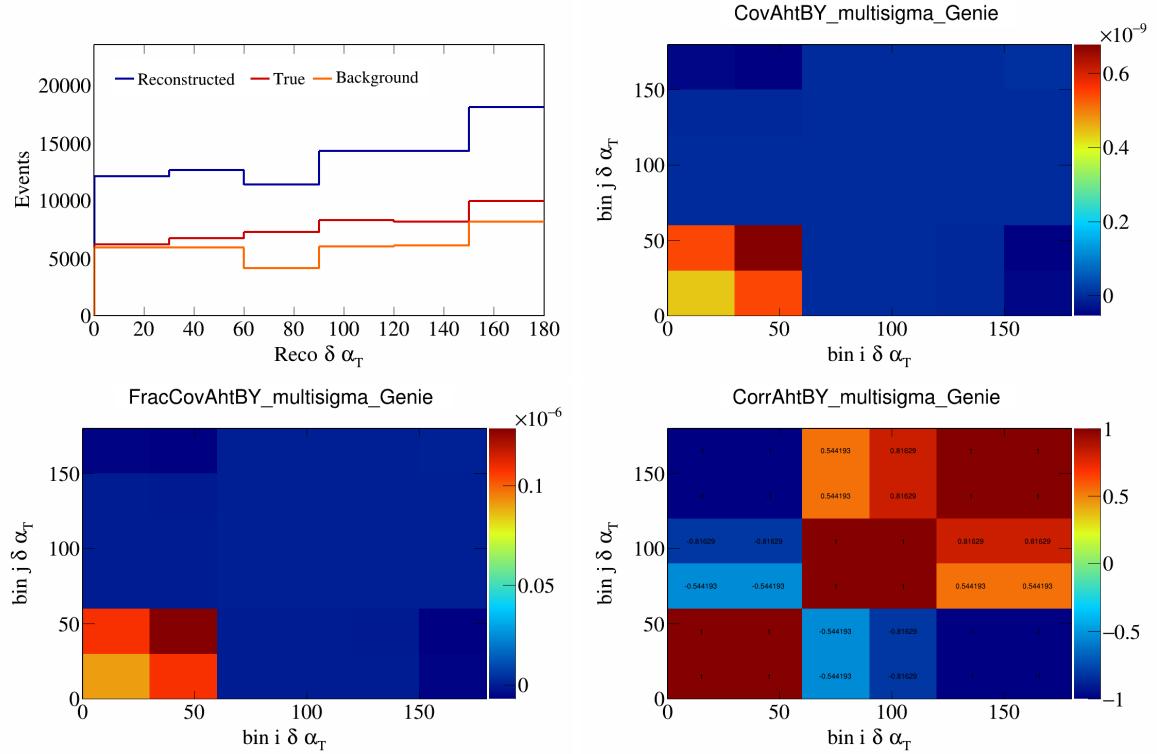


Figure 81: AhtBY variations for  $\delta\alpha_T$ .

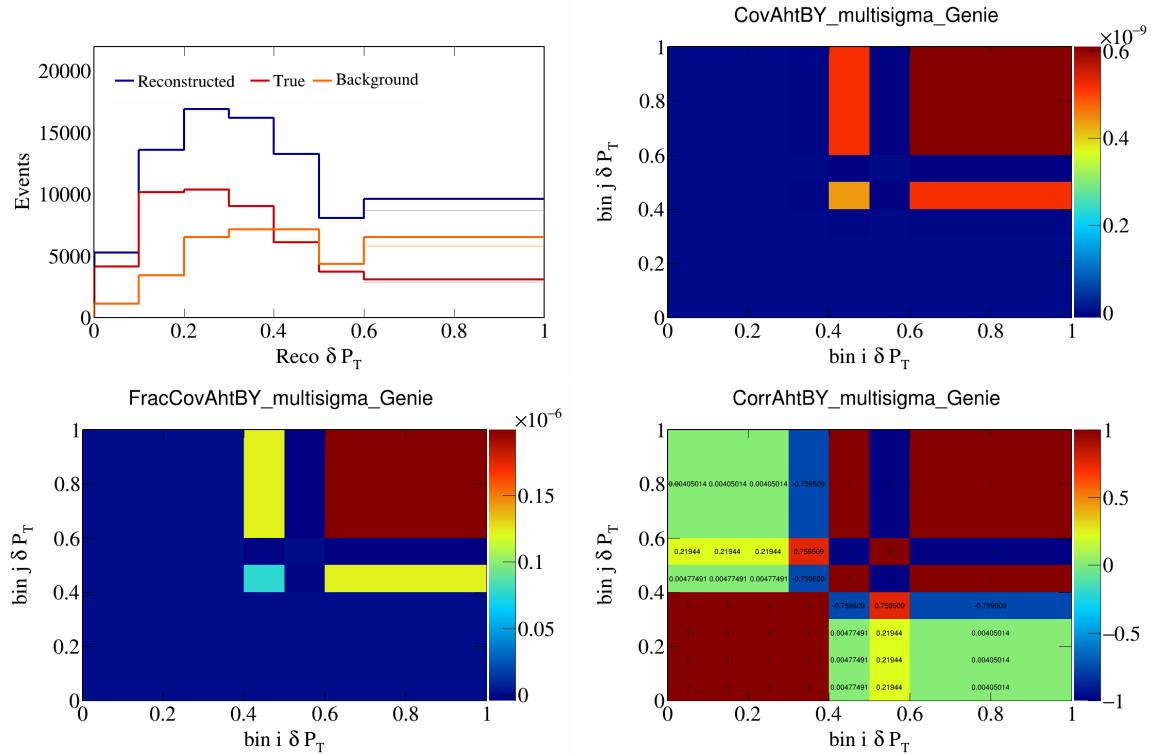


Figure 82: AhtBY variations for  $\delta P_T$ .

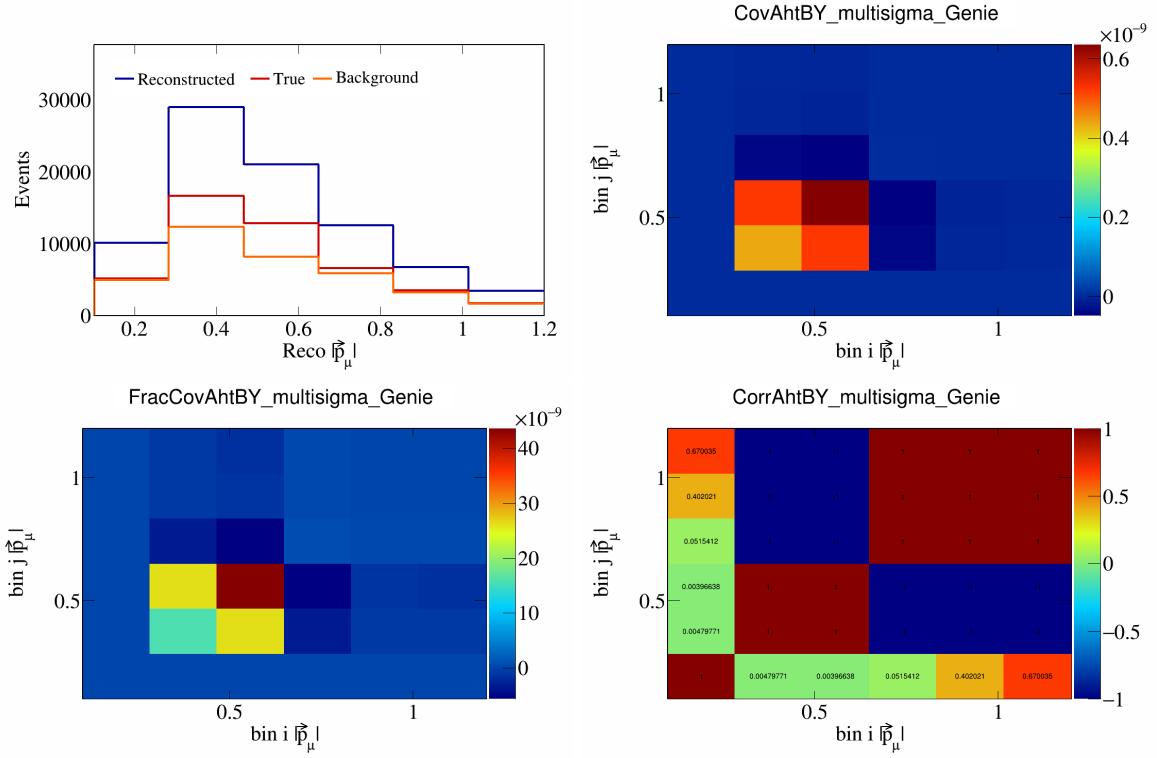


Figure 83: AhtBY variations for  $|\vec{p}_\mu|$ .

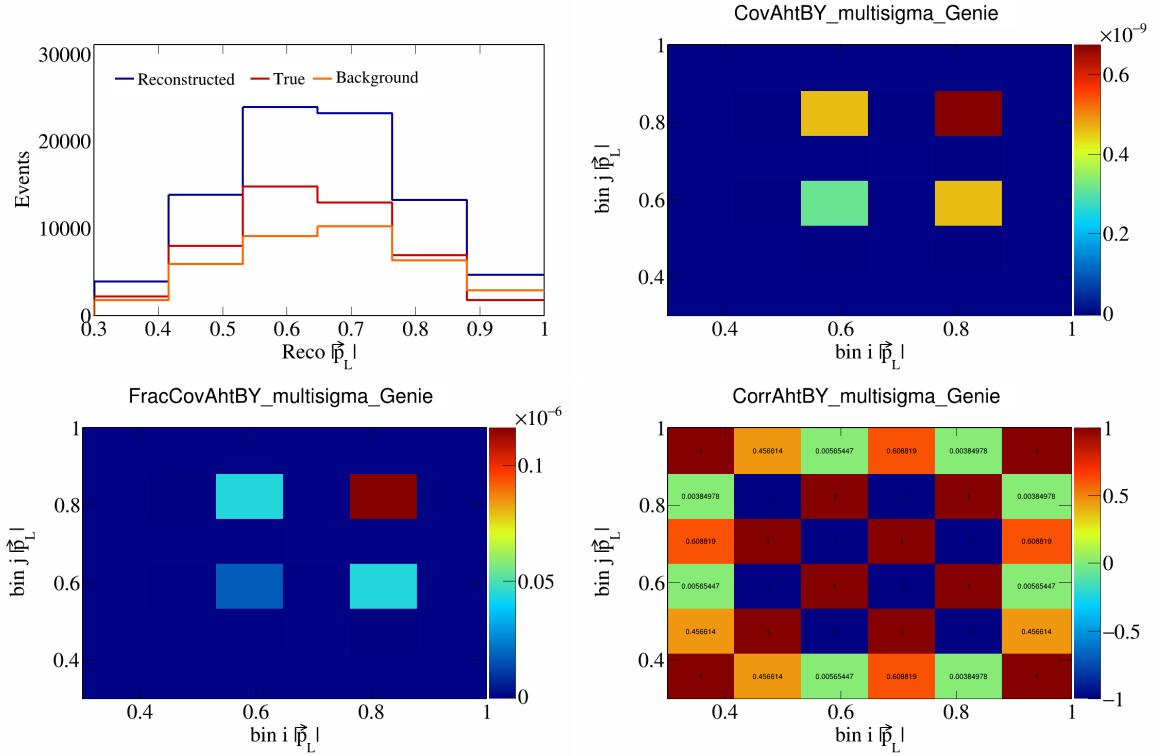


Figure 84: AhtBY variations for  $|\vec{p}_L|$ .

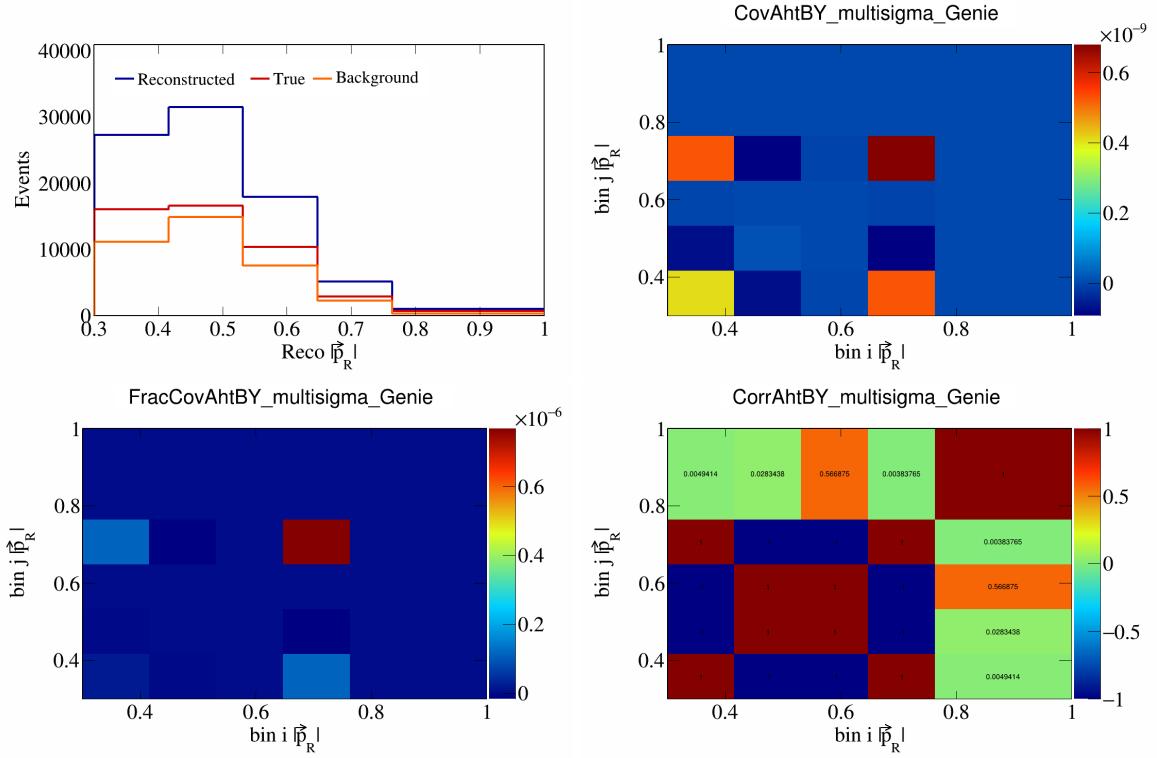


Figure 85: AhtBY variations for  $|\vec{p}_R|$ .

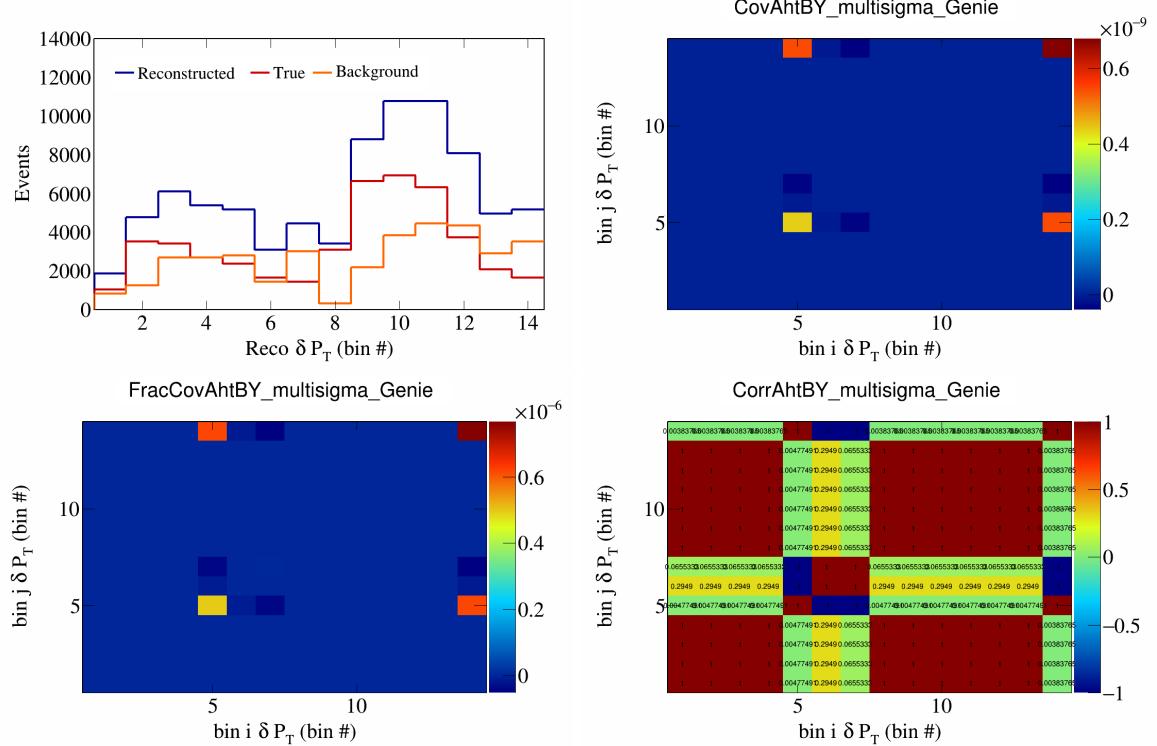


Figure 86: AhtBY variations for  $\delta P_T$  in  $\cos(\theta_{\vec{p}_\mu})$ .

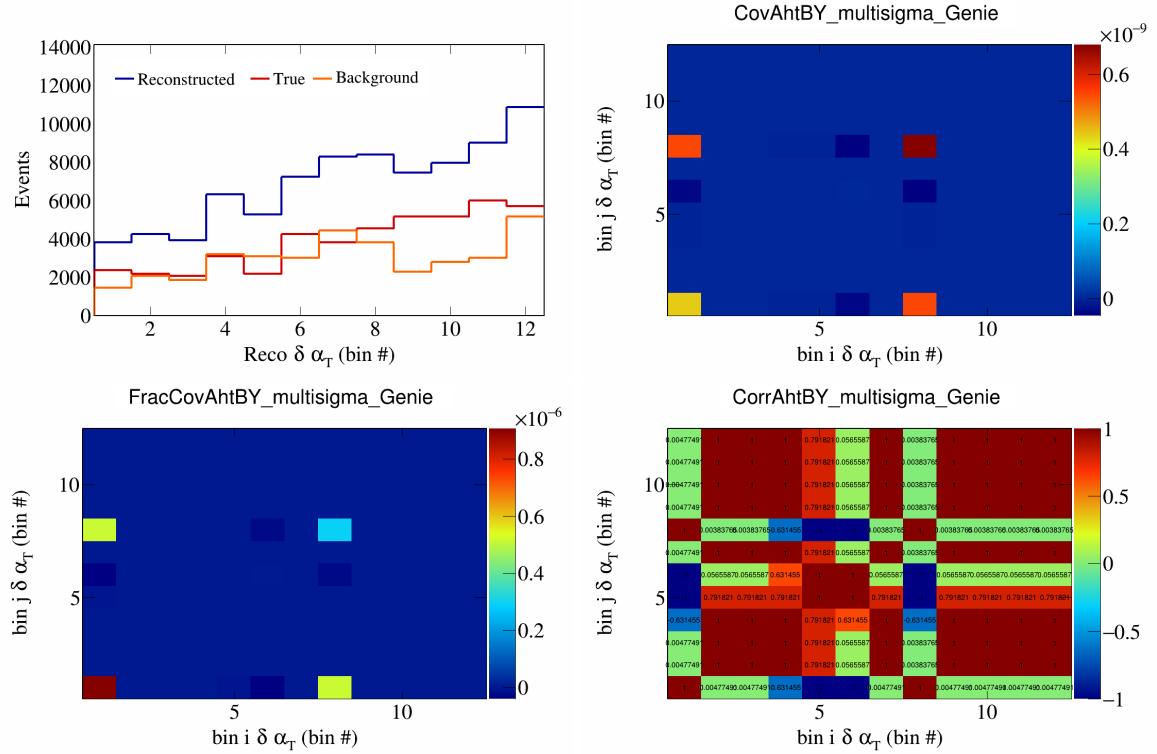


Figure 87: AhtBY variations for  $\delta\alpha_T$  in  $\cos(\theta_{\vec{p}_\mu})$ .

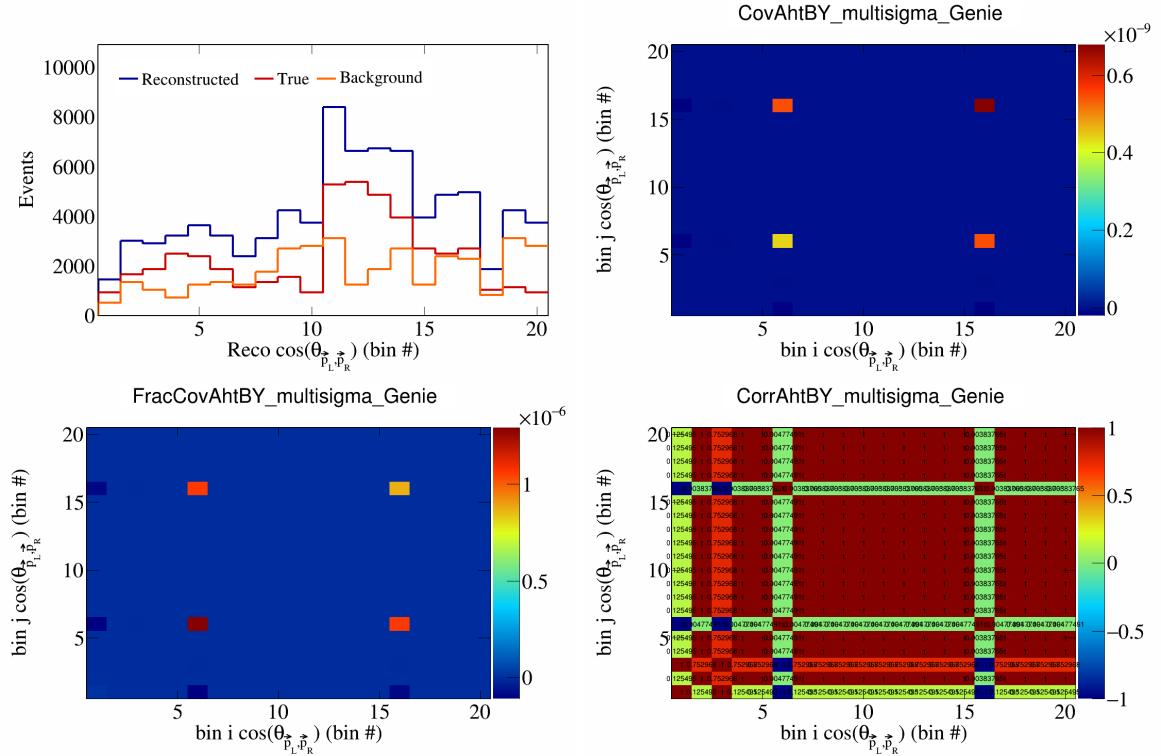


Figure 88: AhtBY variations for  $\cos(\theta_{p_L, p_R})$  in  $\cos(\theta_{\vec{p}_\mu})$ .

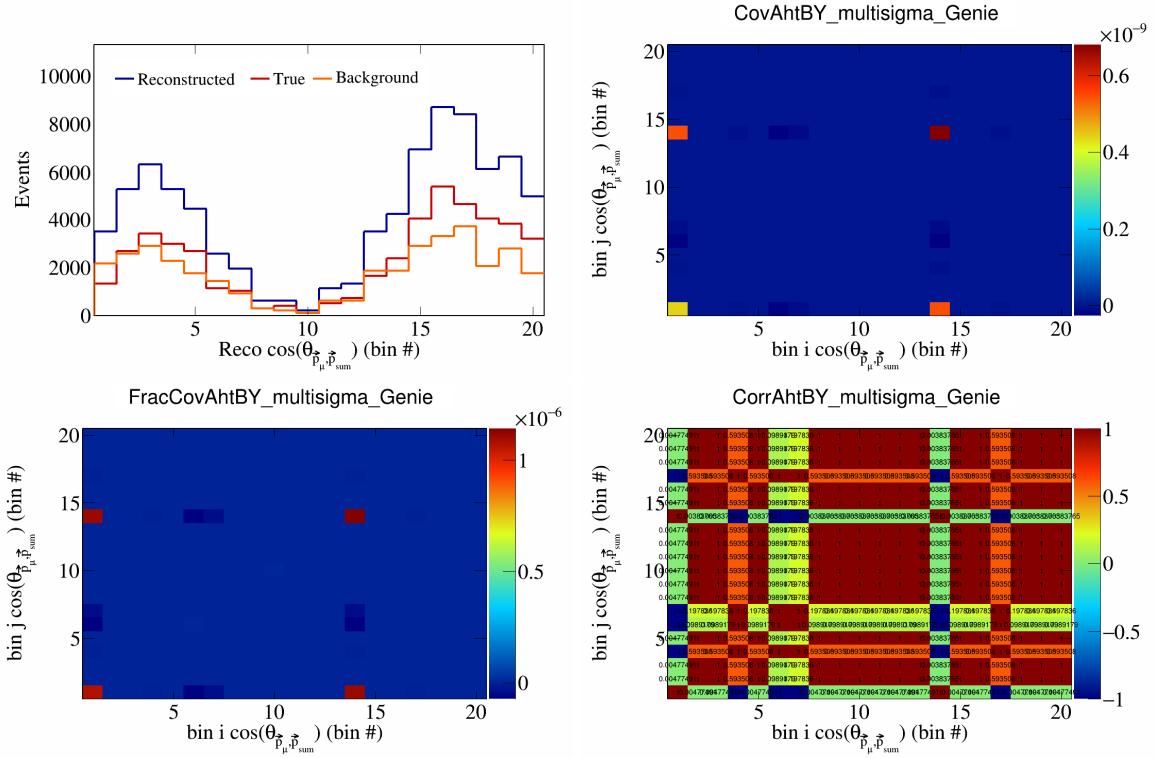


Figure 89: AhtBY variations for  $\cos(\theta_{\vec{p}_\mu, \vec{p}_{\text{sum}}})$  in  $\cos(\theta_{\vec{p}_\mu})$ .

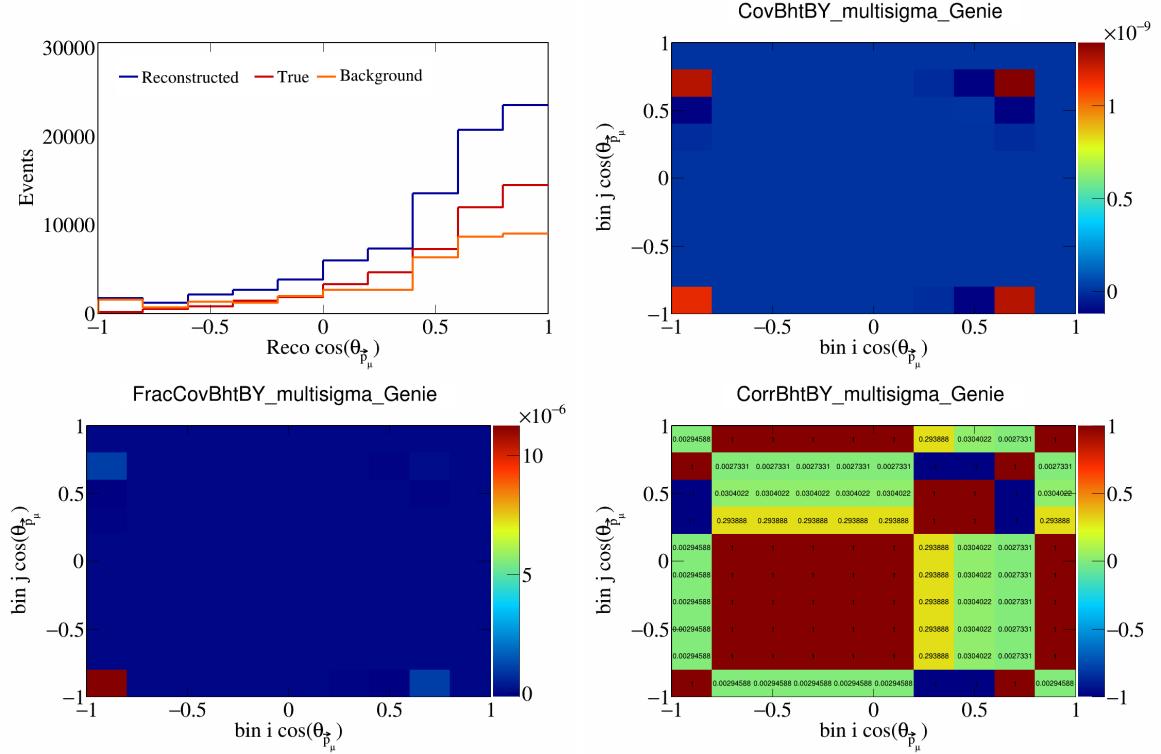


Figure 90: BhtBY variations for  $\cos(\theta_{\vec{p}_\mu})$ .

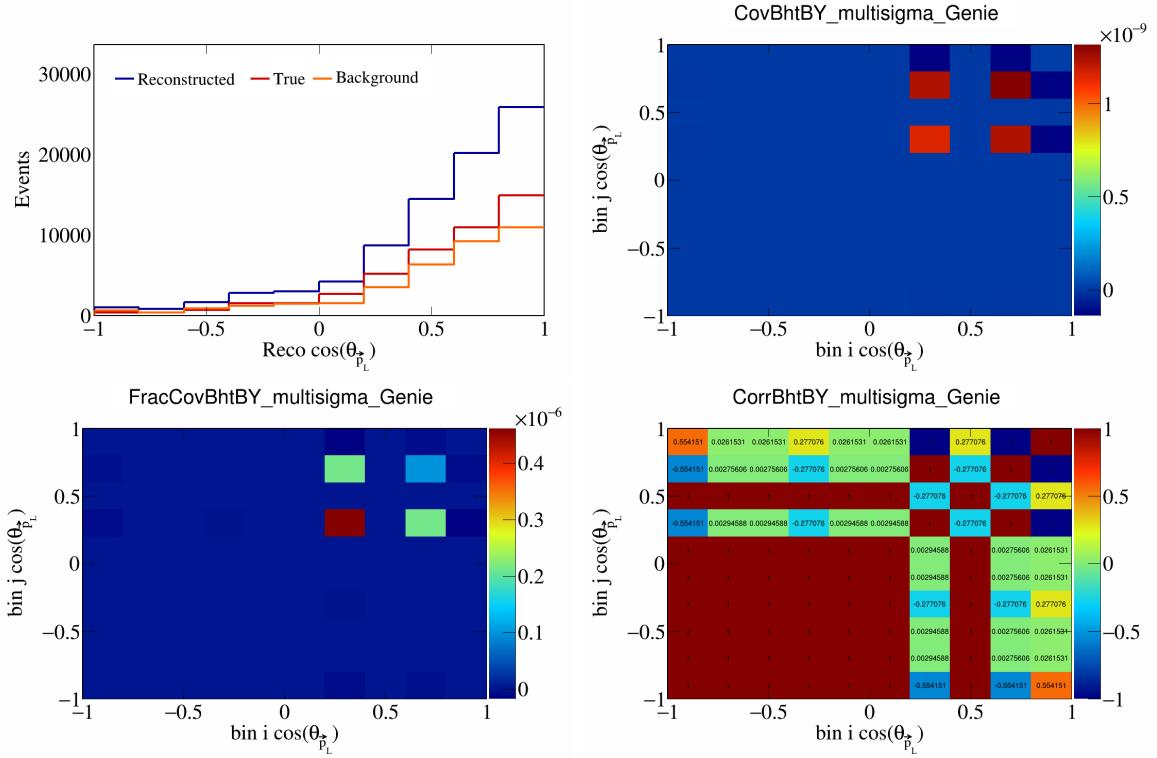


Figure 91: BhtBY variations for  $\cos(\theta_{\vec{p}_L})$ .

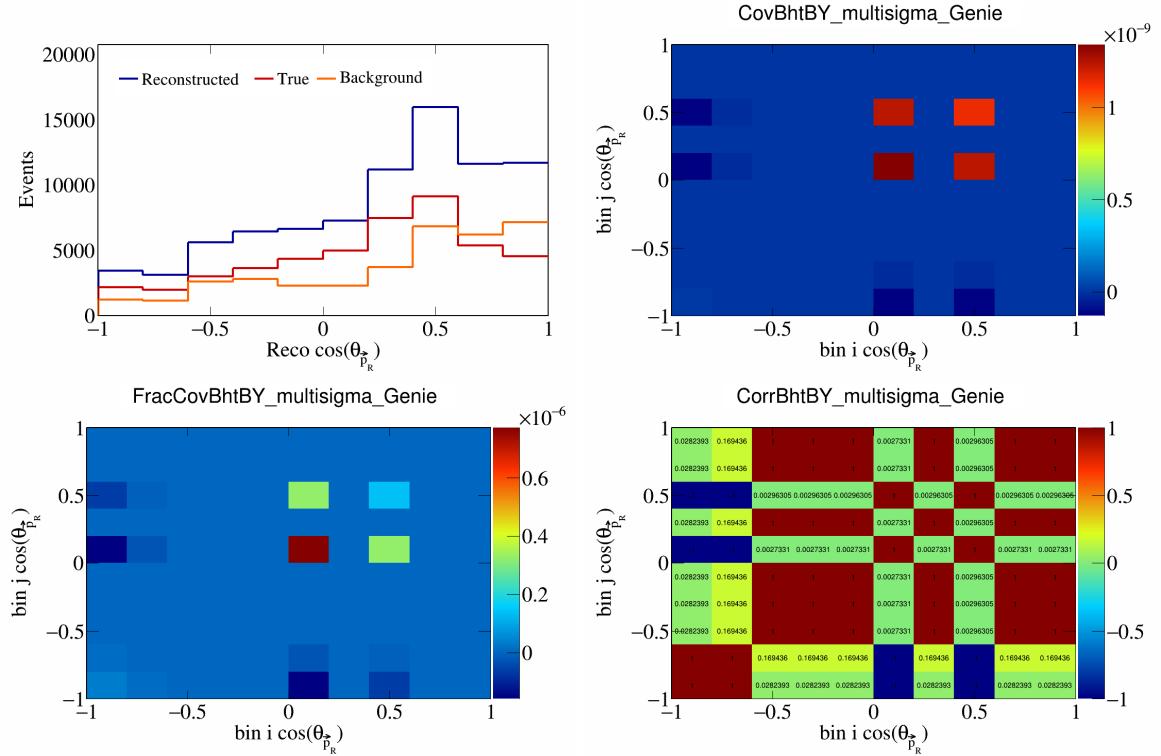


Figure 92: BhtBY variations for  $\cos(\theta_{\vec{p}_R})$ .

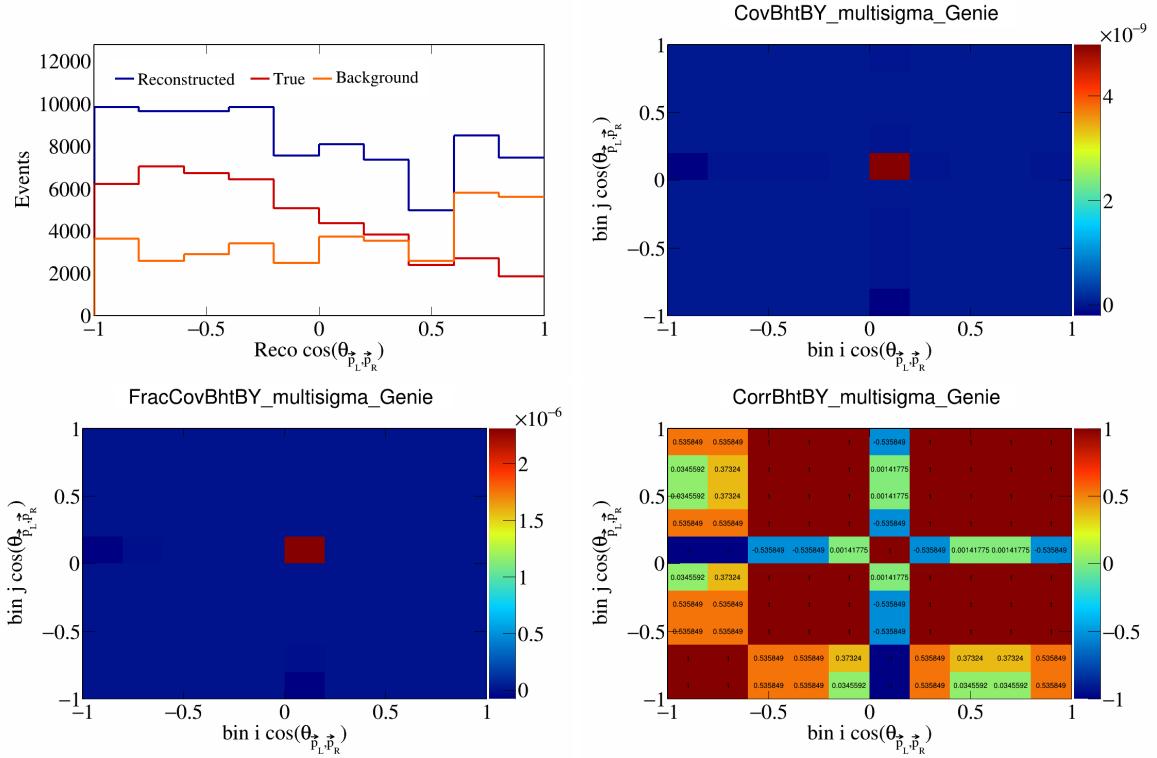


Figure 93: BhtBY variations for  $\cos(\theta_{\vec{p}_L, \vec{p}_R})$ .

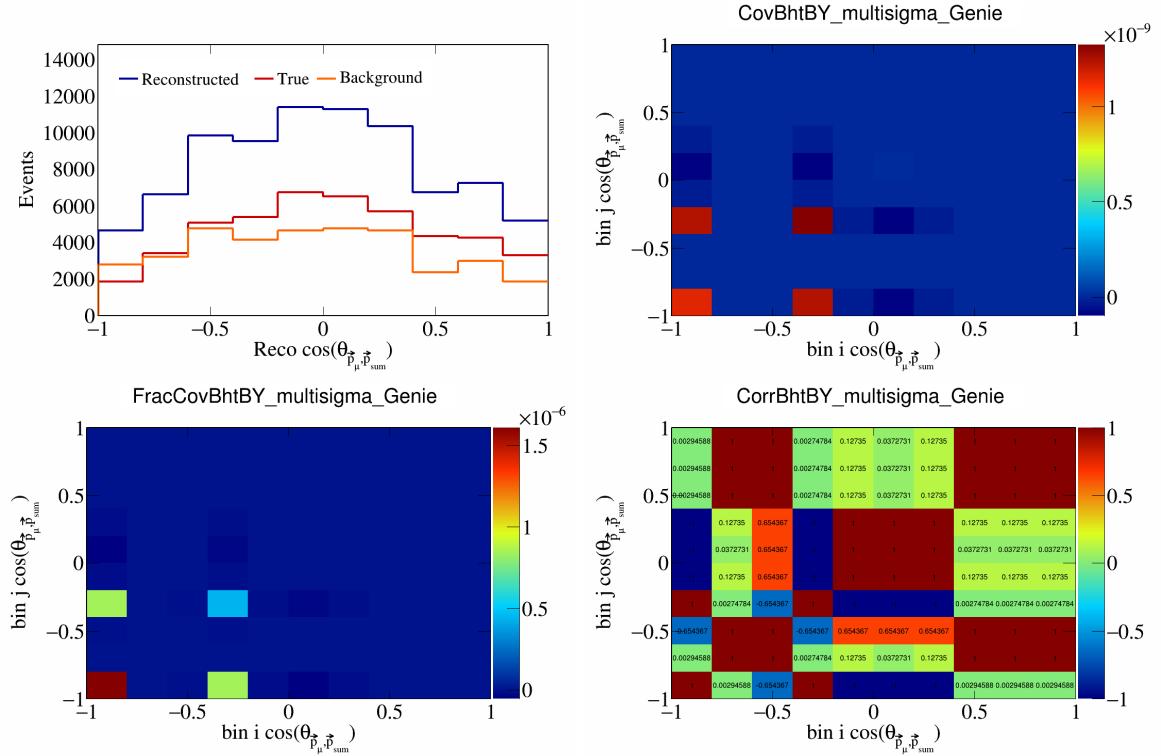


Figure 94: BhtBY variations for  $\cos(\theta_{\vec{p}_\mu, \vec{p}_{\text{sum}}})$ .

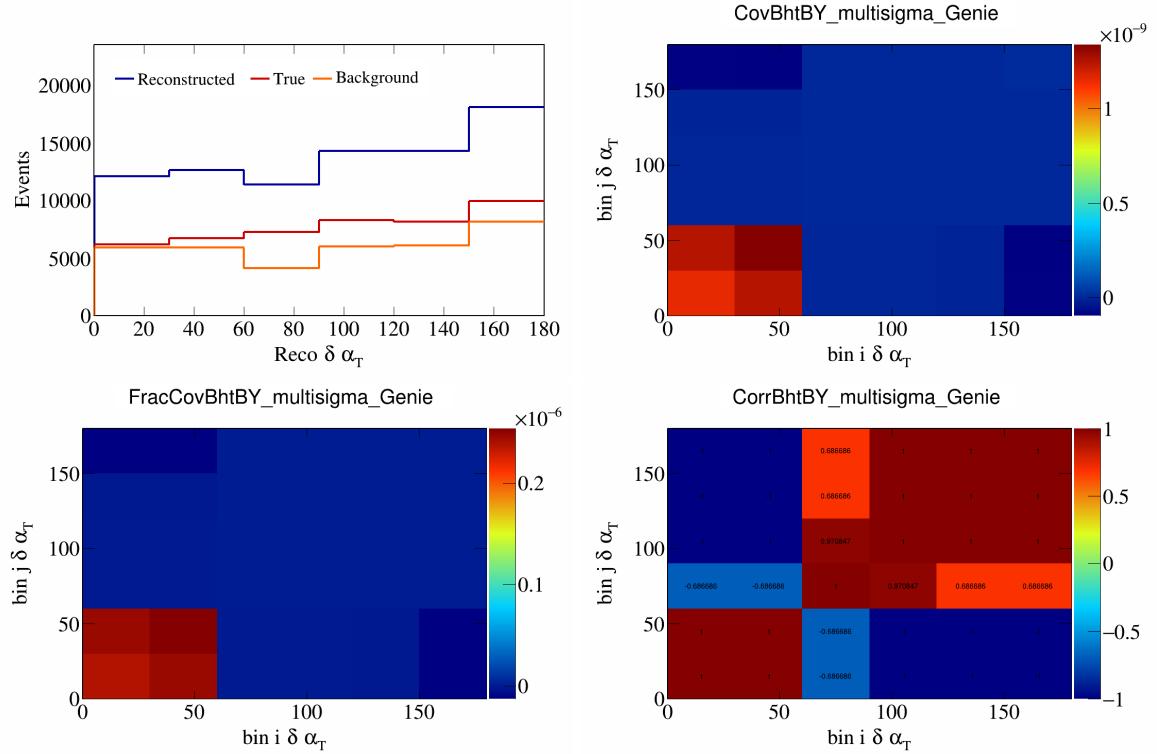


Figure 95: BhtBY variations for  $\delta\alpha_T$ .

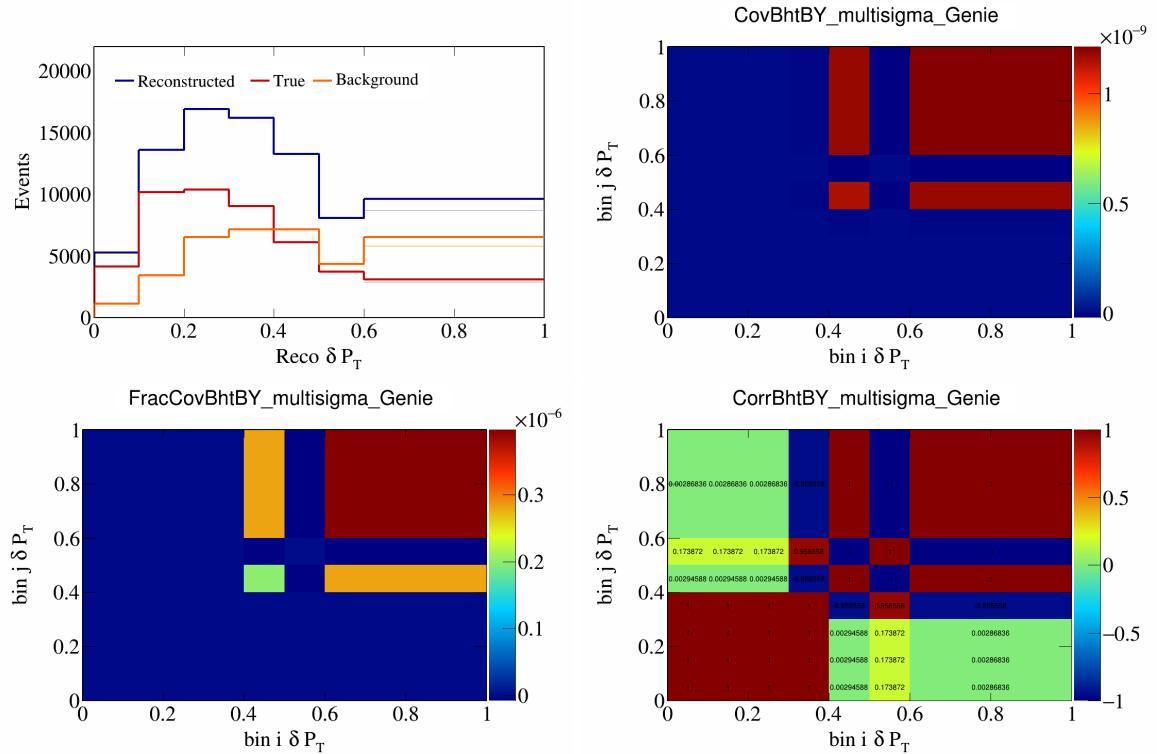


Figure 96: BhtBY variations for  $\delta P_T$ .

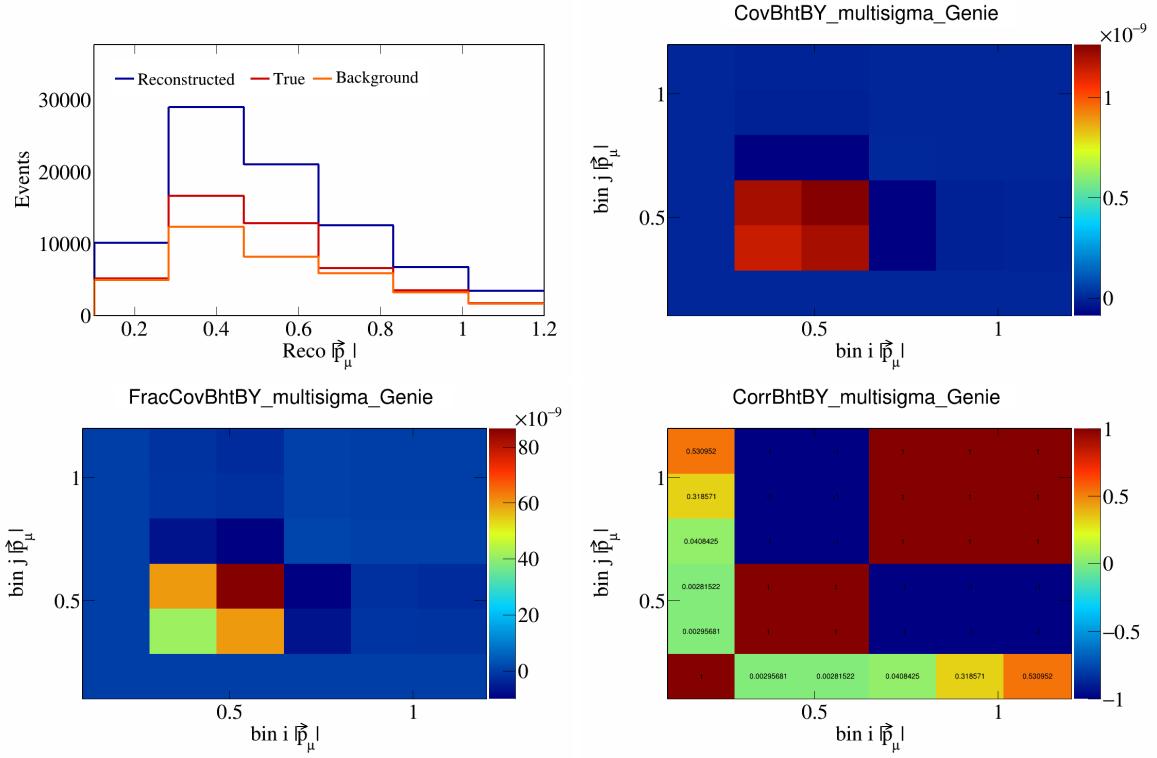


Figure 97: BhtBY variations for  $|\vec{p}_\mu|$ .

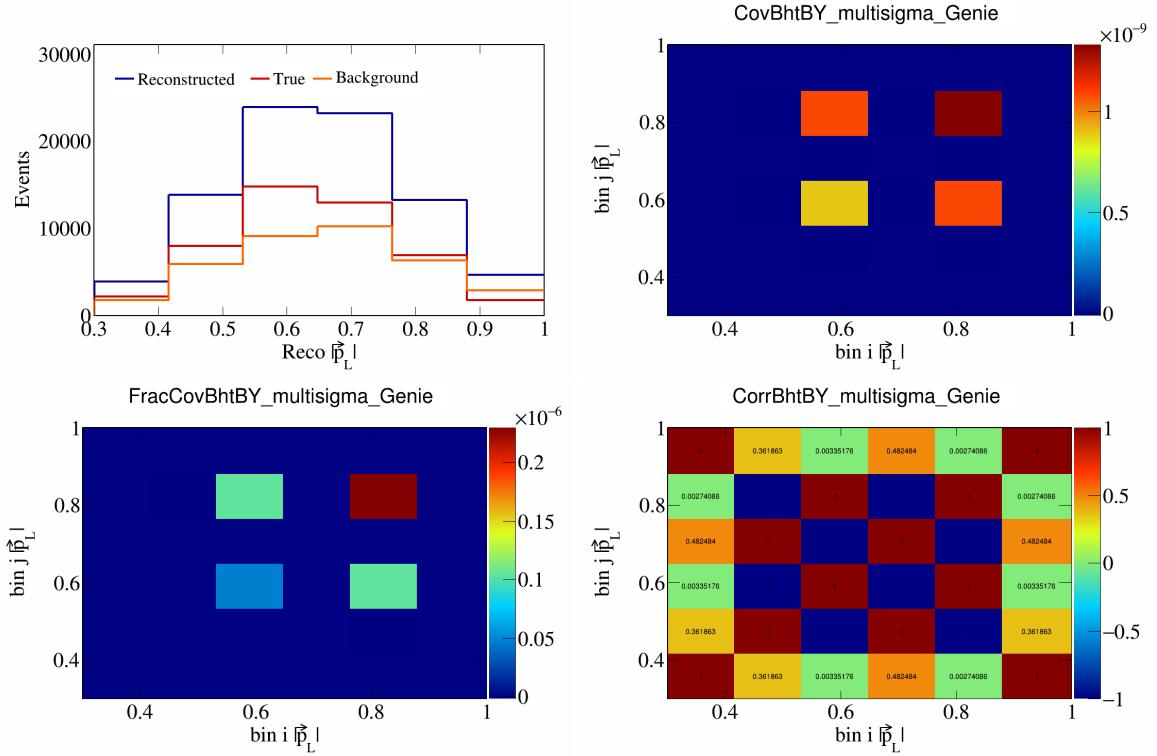


Figure 98: BhtBY variations for  $|\vec{p}_L|$ .

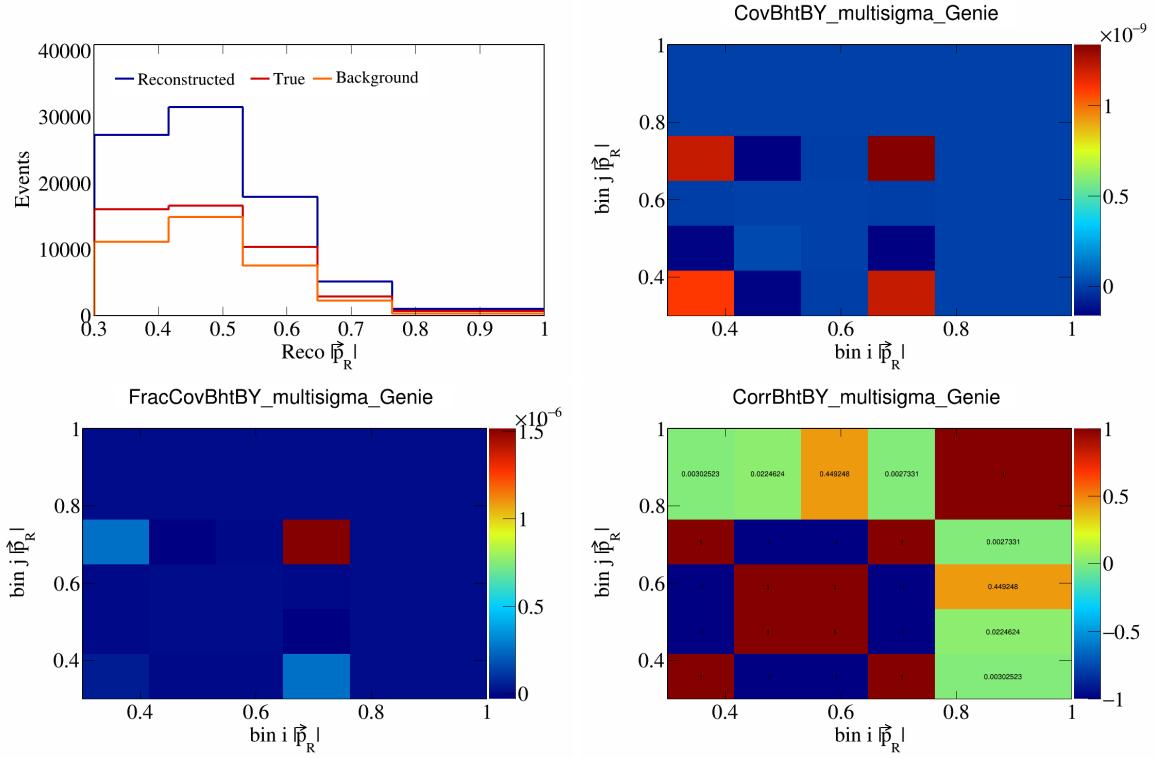


Figure 99: BhtBY variations for  $|\vec{p}_R|$ .

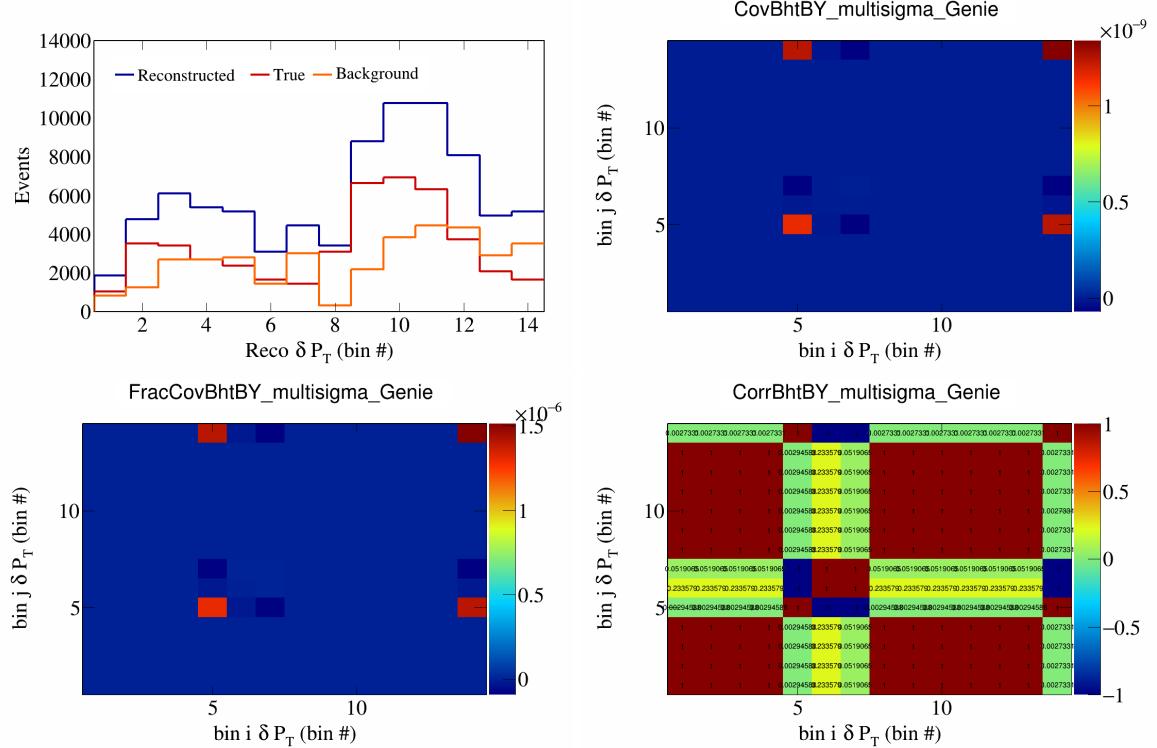


Figure 100: BhtBY variations for  $\delta P_T$  in  $\cos(\theta_{\vec{p}_\mu})$ .

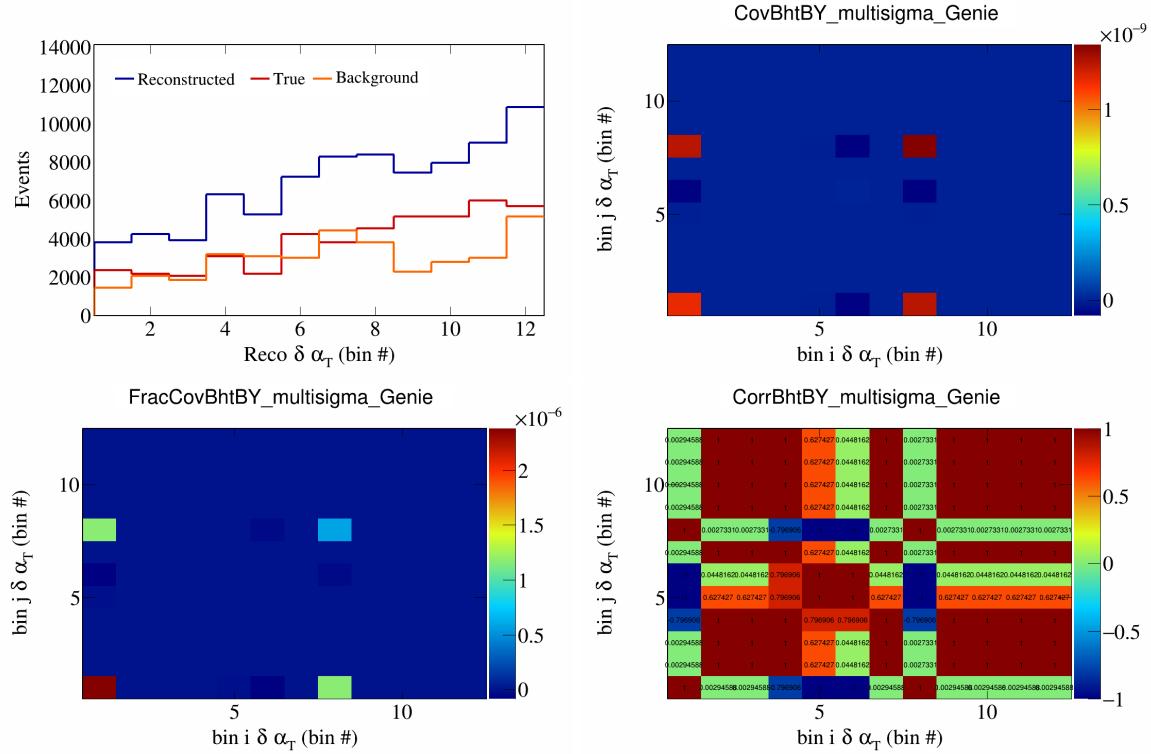


Figure 101: BhtBY variations for  $\delta\alpha_T$  in  $\cos(\theta_{\vec{p}_\mu})$ .

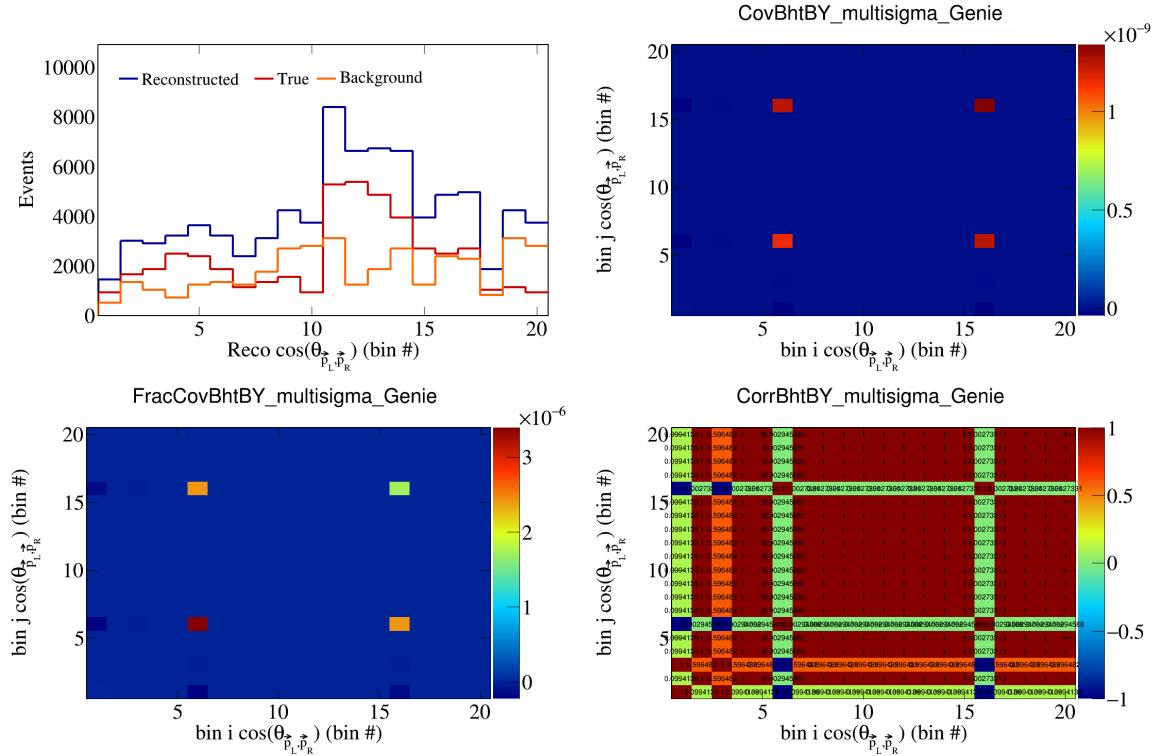


Figure 102: BhtBY variations for  $\cos(\theta_{p_L, p_R})$  in  $\cos(\theta_{\vec{p}_\mu})$ .

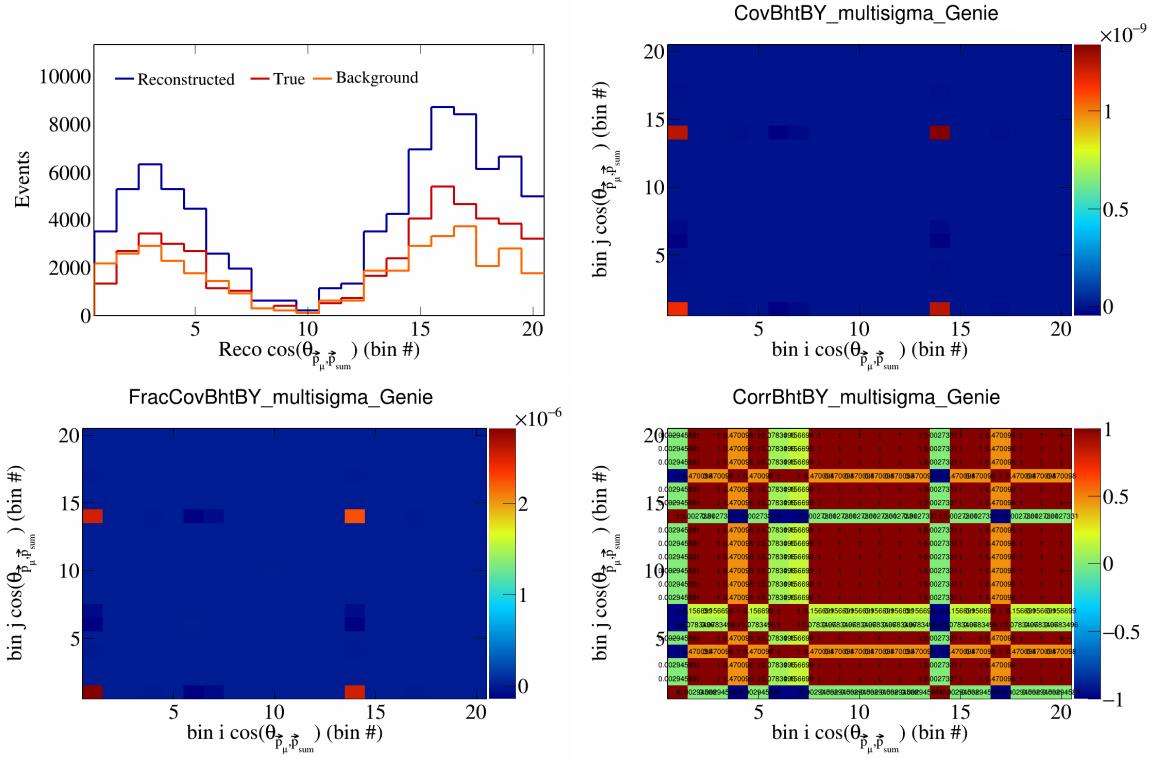


Figure 103: BhtBY variations for  $\cos(\theta_{\vec{p}_\mu, \vec{p}_{\text{sum}}})$  in  $\cos(\theta_{\vec{p}_\mu})$ .

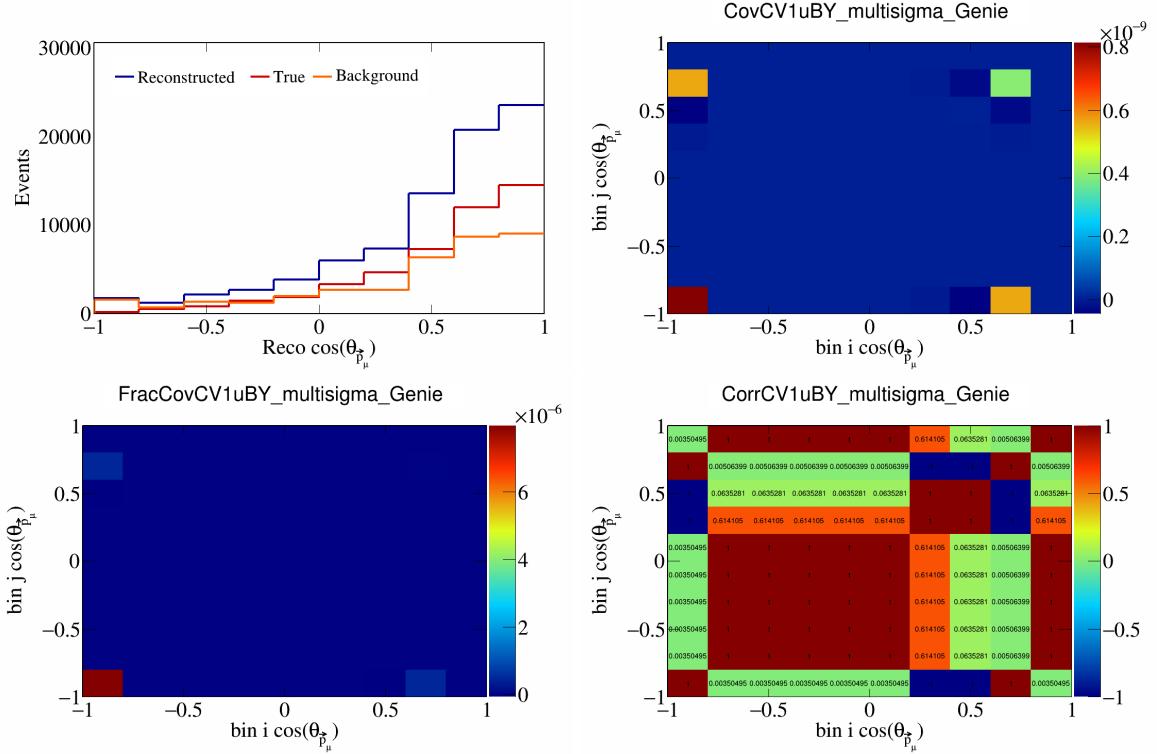


Figure 104: CV1uBY variations for  $\cos(\theta_{\vec{p}_\mu})$ .

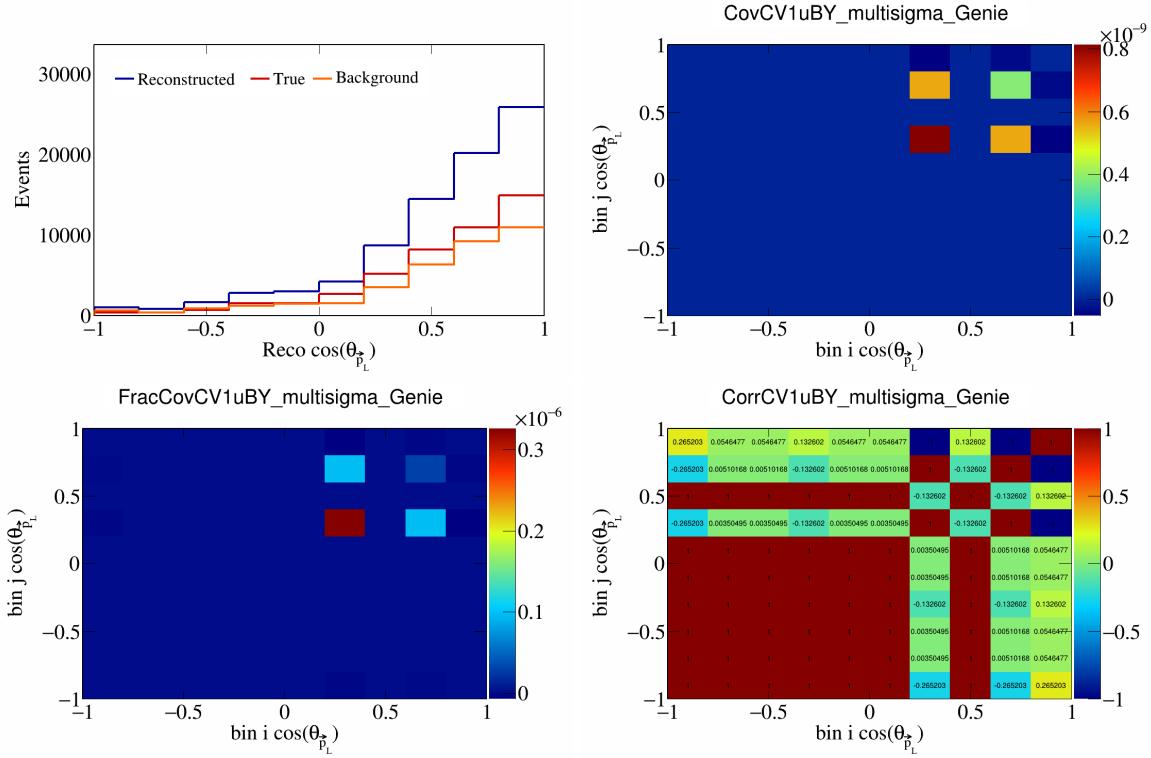


Figure 105: CV1uBY variations for  $\cos(\theta_{\vec{p}_L})$ .

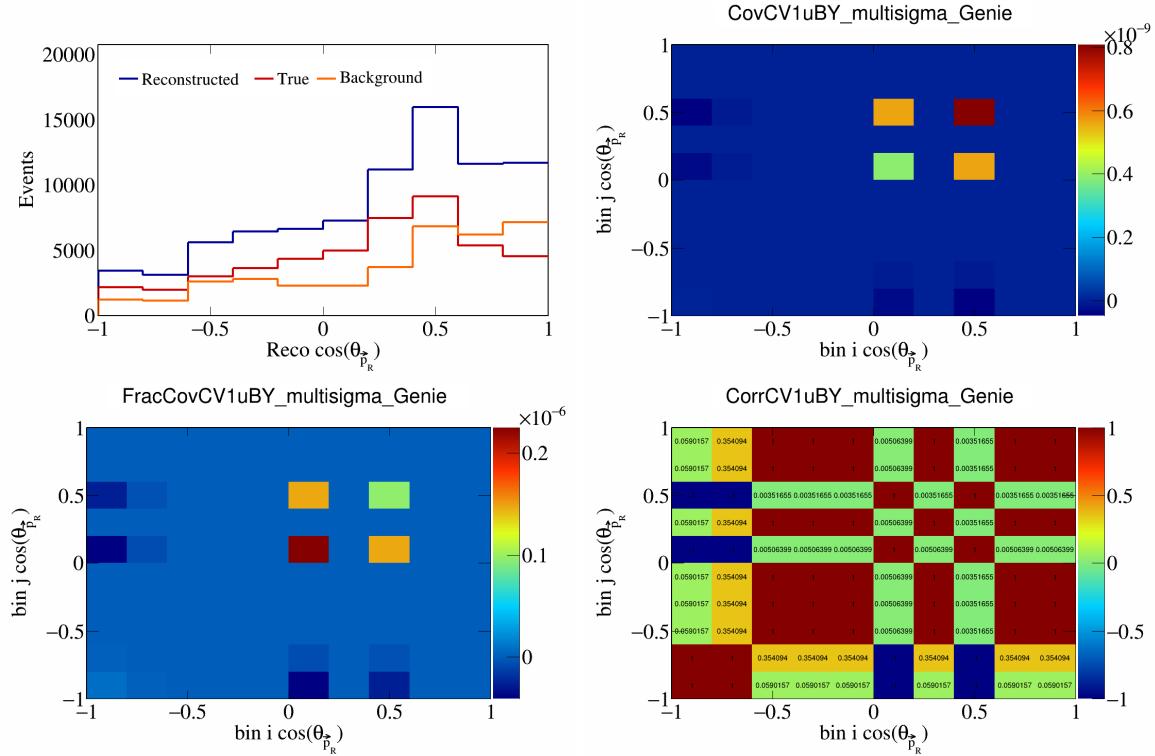


Figure 106: CV1uBY variations for  $\cos(\theta_{\vec{p}_R})$ .

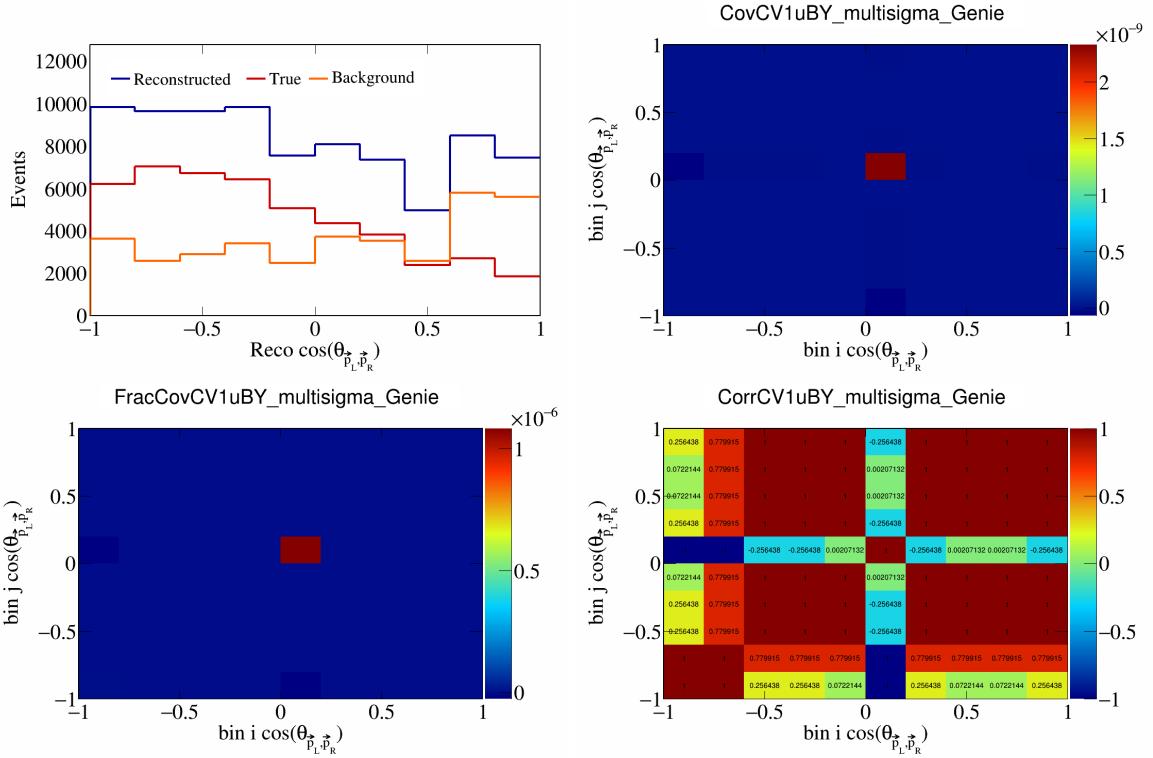


Figure 107: CV1uBY variations for  $\cos(\theta_{\vec{p}_L, \vec{p}_R})$ .

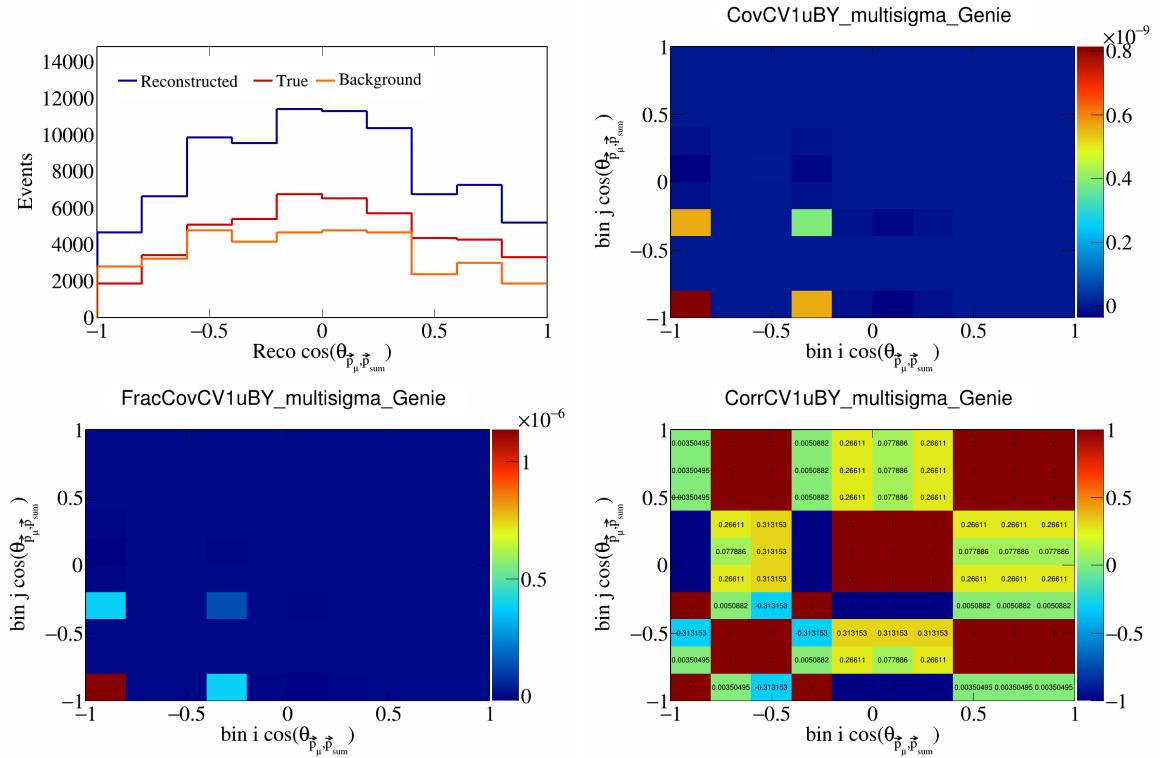


Figure 108: CV1uBY variations for  $\cos(\theta_{\vec{p}_\mu, \vec{p}_{\text{sum}}})$ .

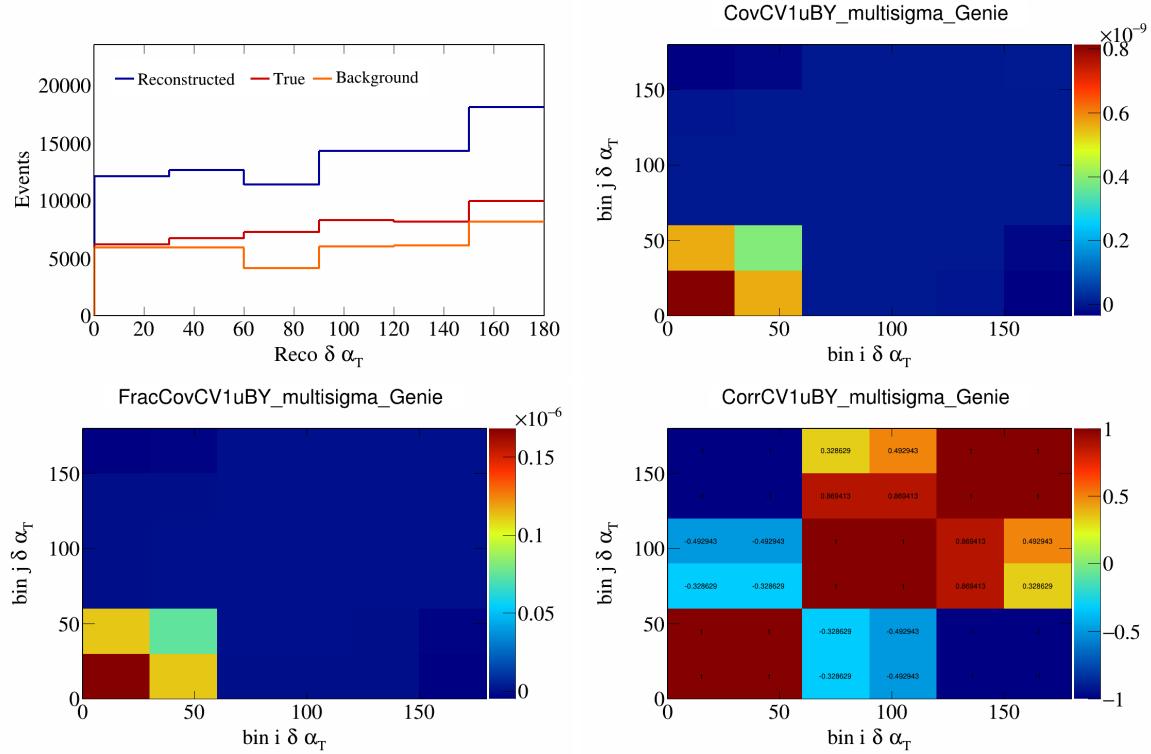


Figure 109: CV1uBY variations for  $\delta \alpha_T$ .

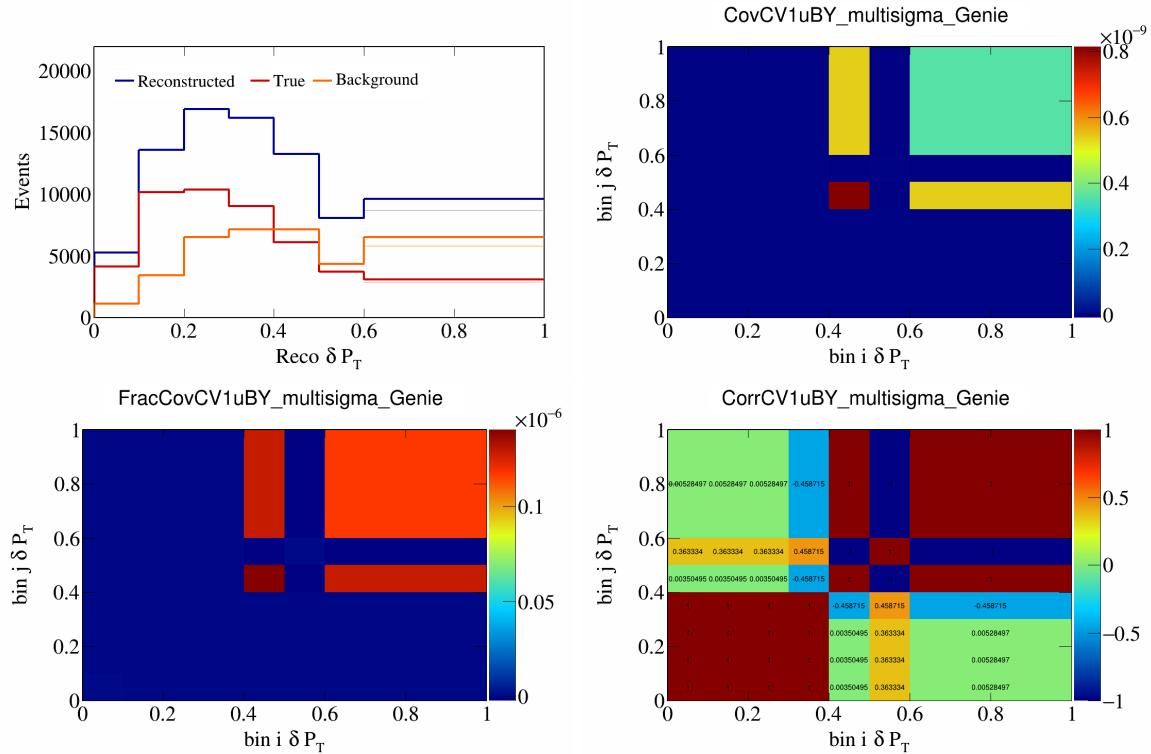


Figure 110: CV1uBY variations for  $\delta P_T$ .

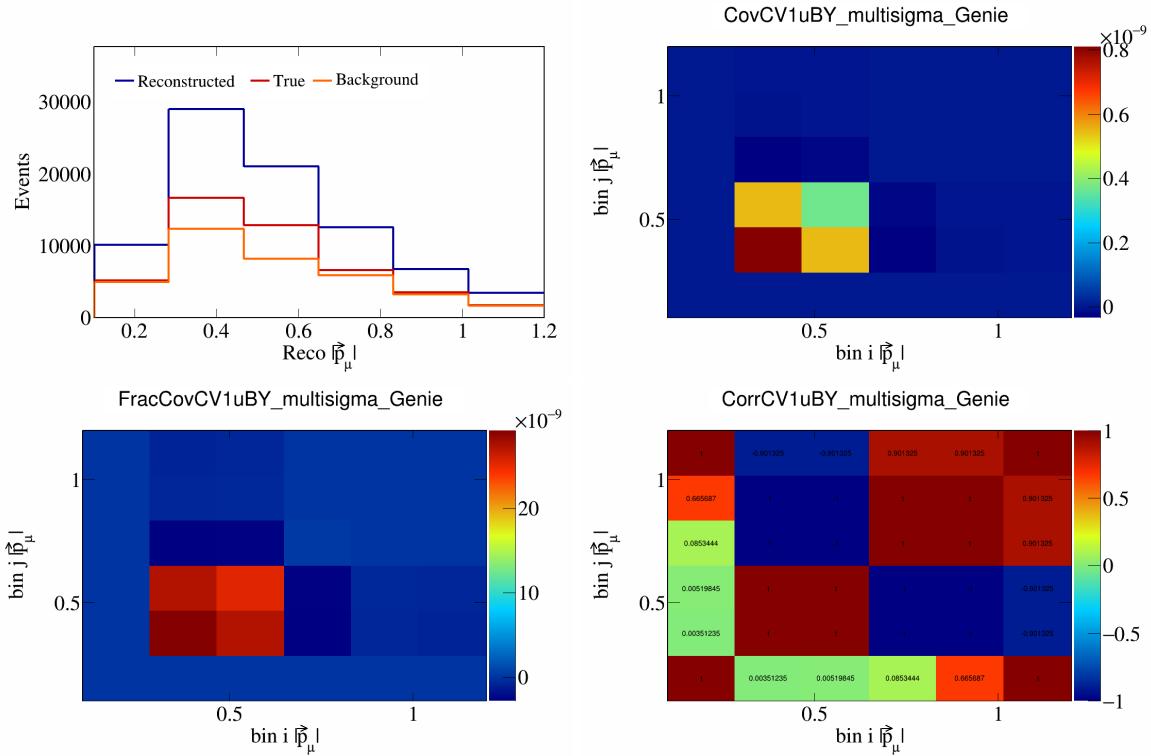


Figure 111: CV1uBY variations for  $|\vec{p}_\mu|$ .

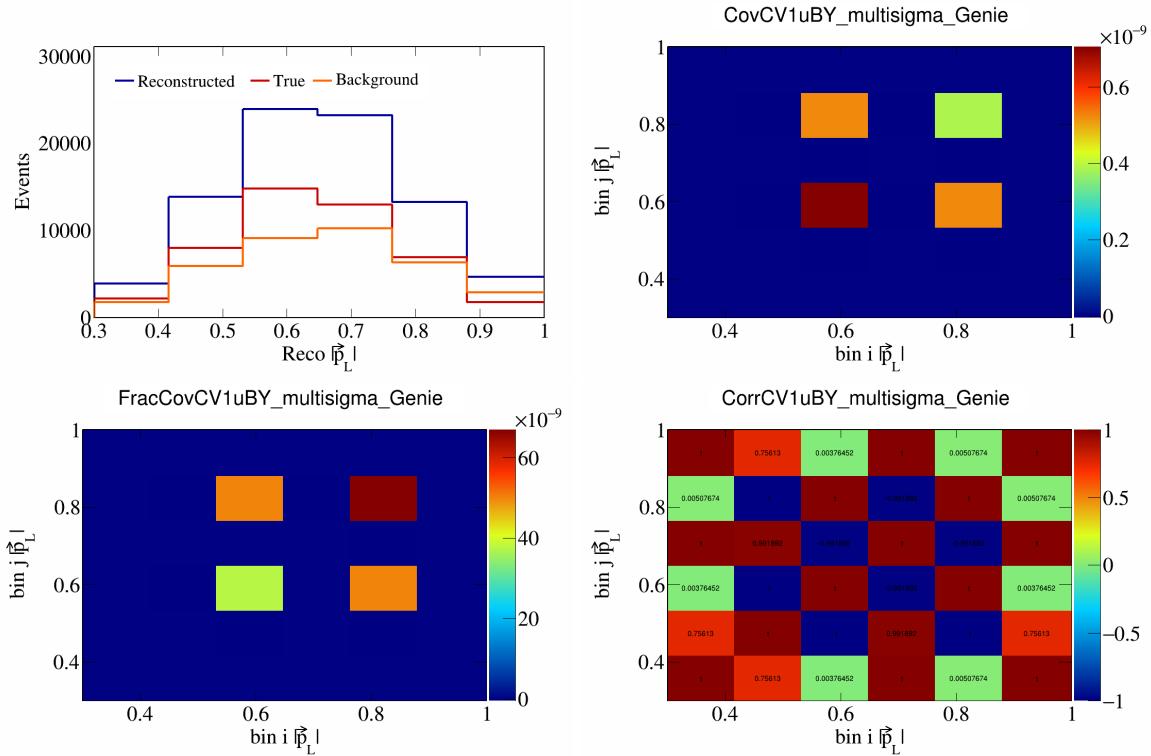


Figure 112: CV1uBY variations for  $|\vec{p}_L|$ .

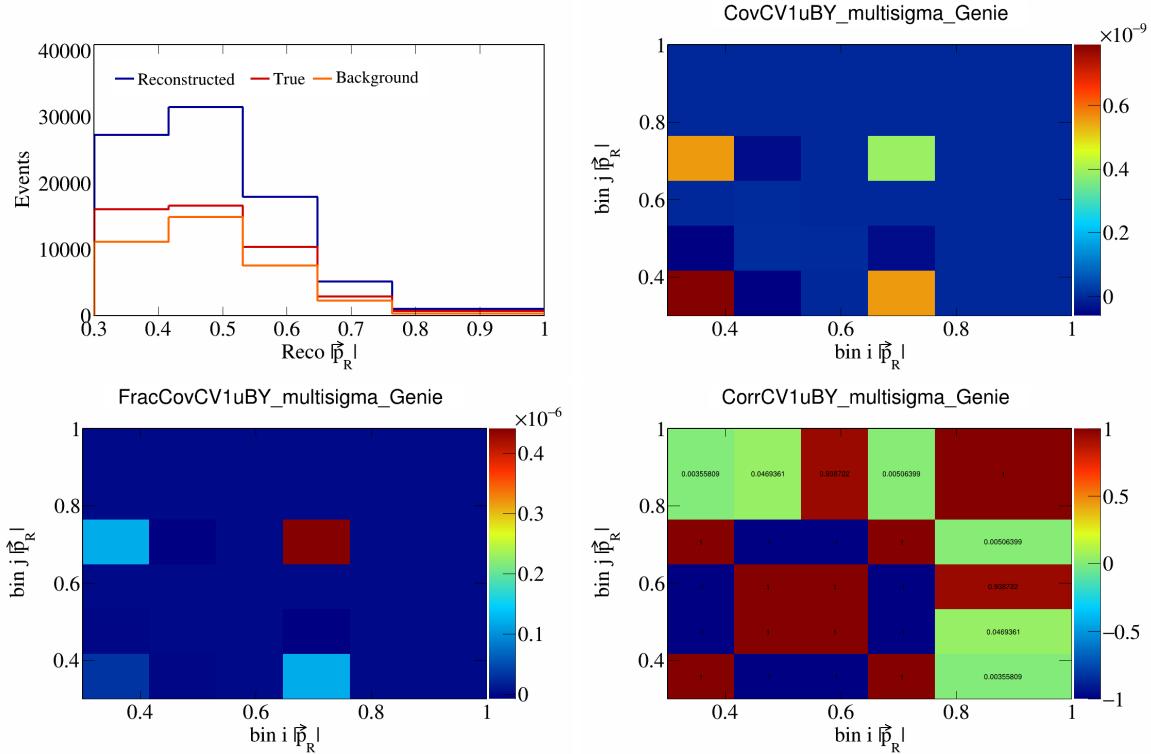


Figure 113: CV1uBY variations for  $|\vec{p}_R|$ .

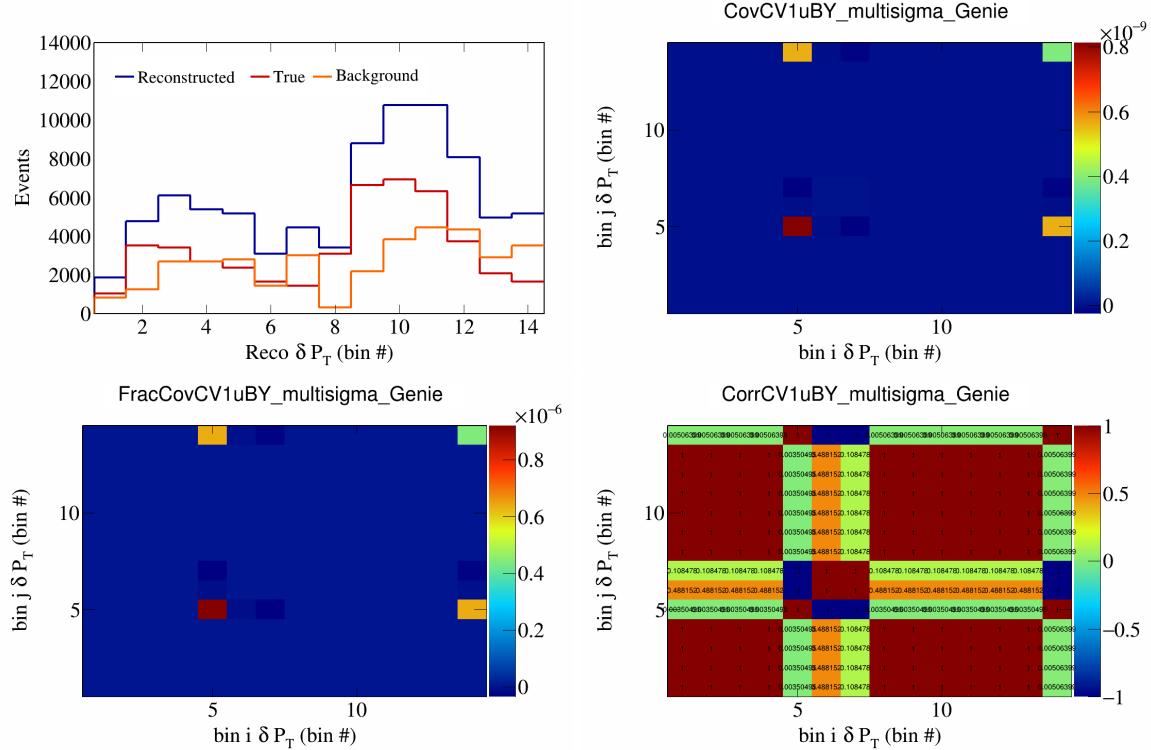


Figure 114: CV1uBY variations for  $\delta P_T$  in  $\cos(\theta_{\vec{p}_\mu})$ .

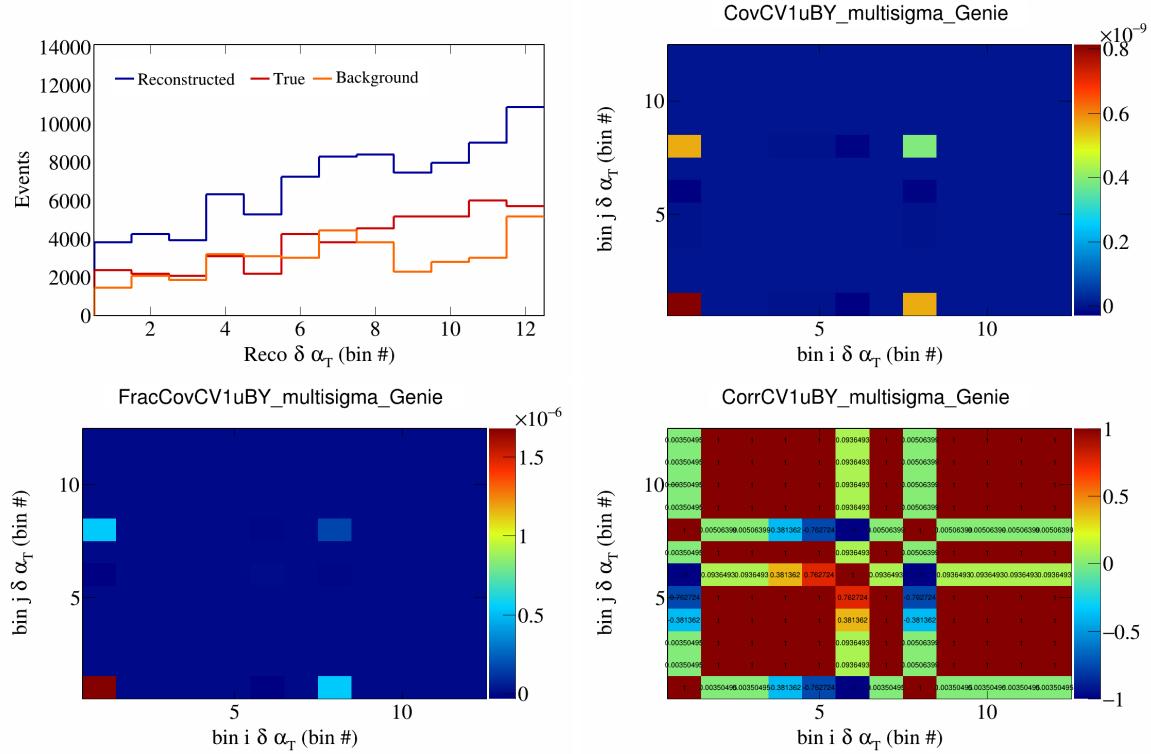


Figure 115: CV1uBY variations for  $\delta\alpha_T$  in  $\cos(\theta_{\vec{p}_\mu})$ .

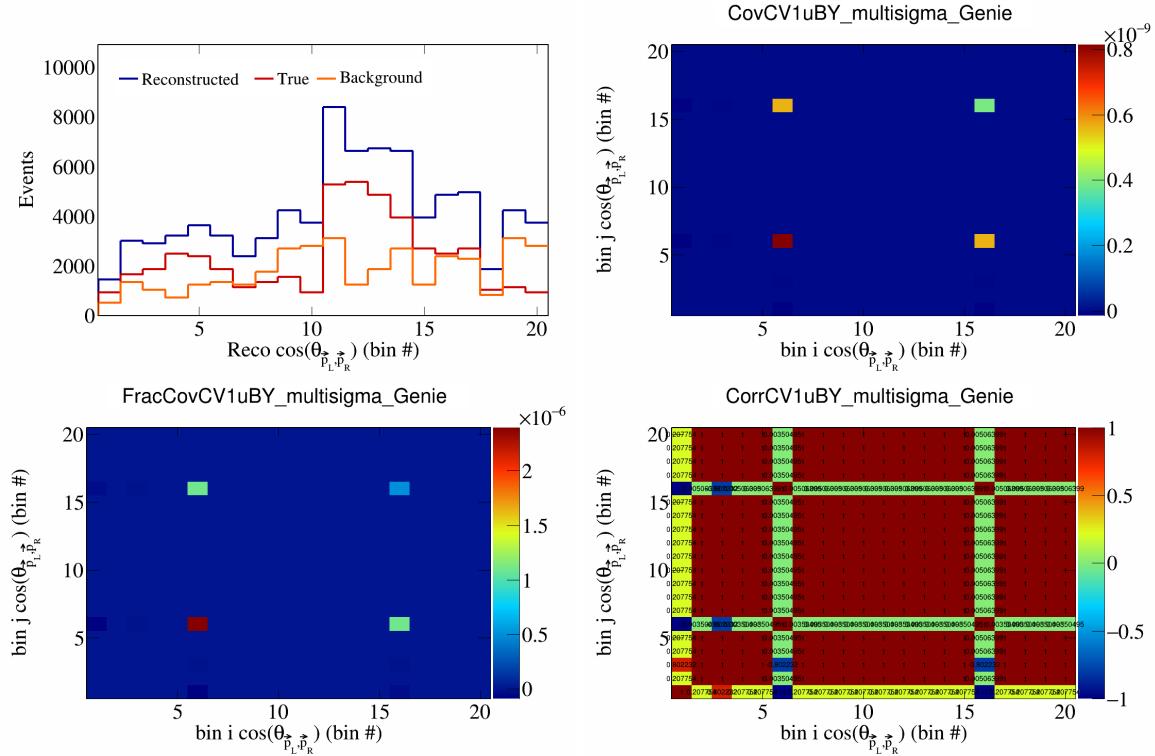


Figure 116: CV1uBY variations for  $\cos(\theta_{\vec{p}_L, \vec{p}_R})$  in  $\cos(\theta_{\vec{p}_\mu})$ .

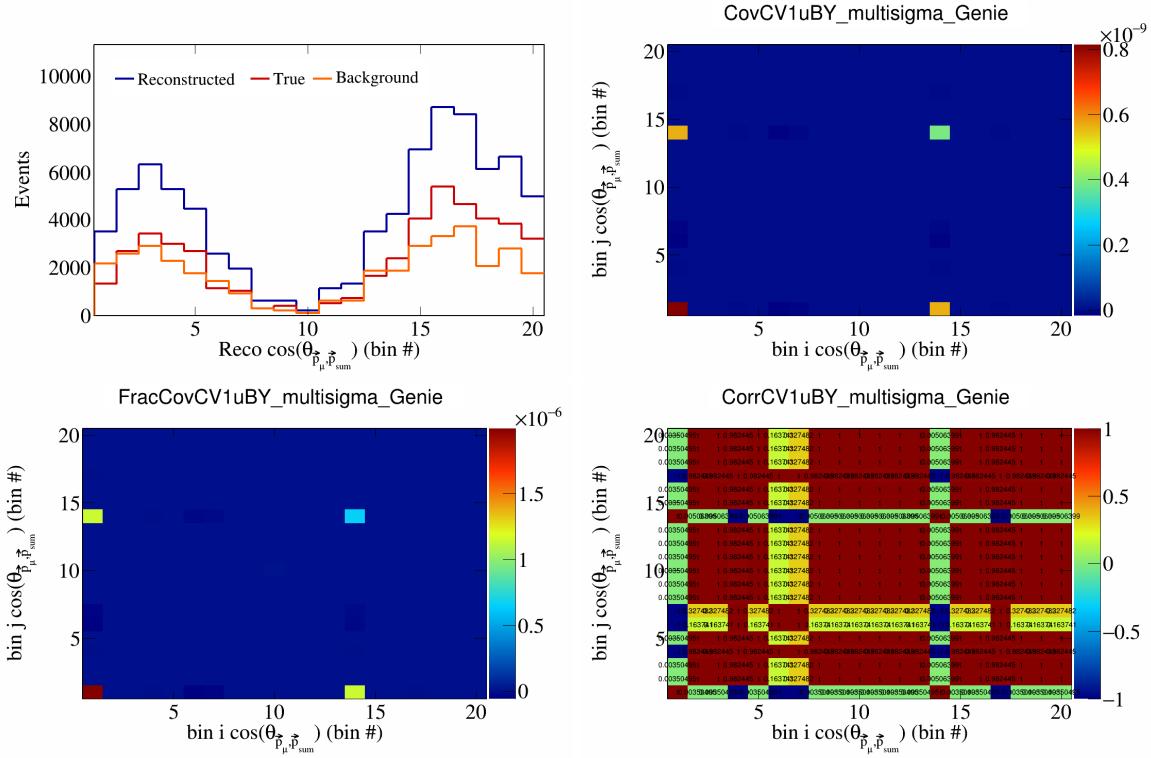


Figure 117: CV1uBY variations for  $\cos(\theta_{\vec{p}_\mu, \vec{p}_{\text{sum}}})$  in  $\cos(\theta_{\vec{p}_\mu})$ .

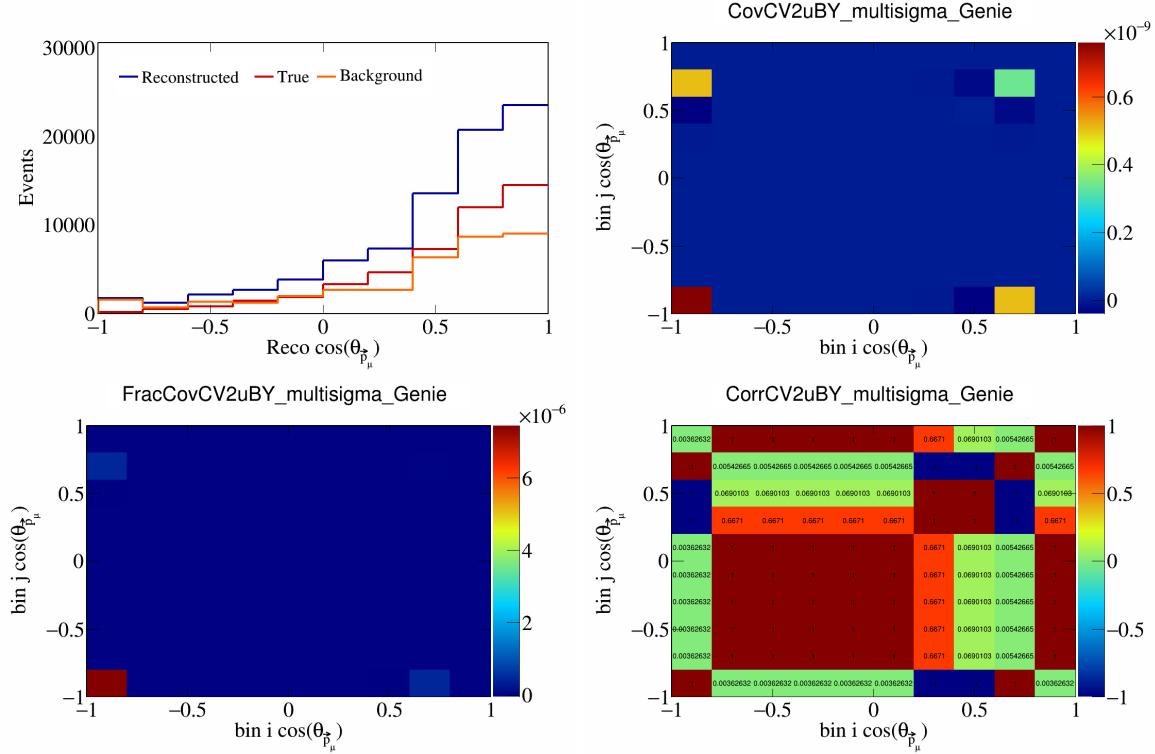


Figure 118: CV2uBY variations for  $\cos(\theta_{\vec{p}_\mu, \vec{p}_{\text{sum}}})$  in  $\cos(\theta_{\vec{p}_\mu})$ .

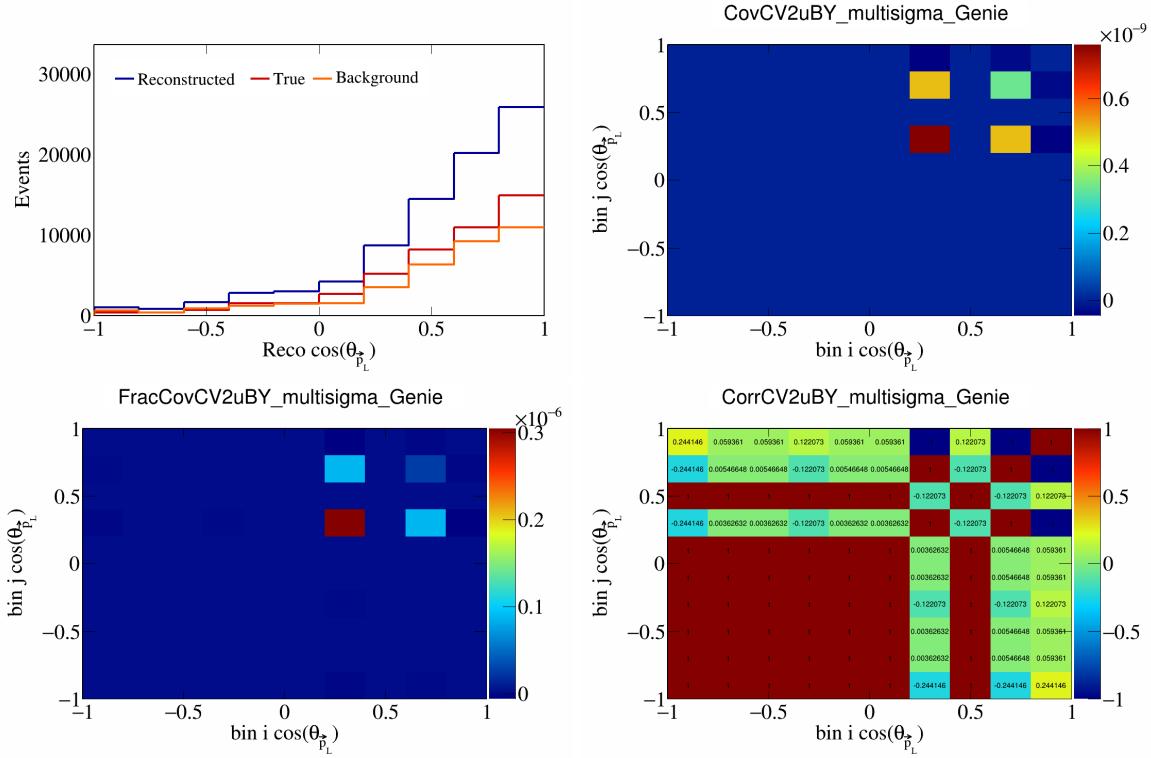


Figure 119: CV2uBY variations for  $\cos(\theta_{\vec{p}_L})$ .

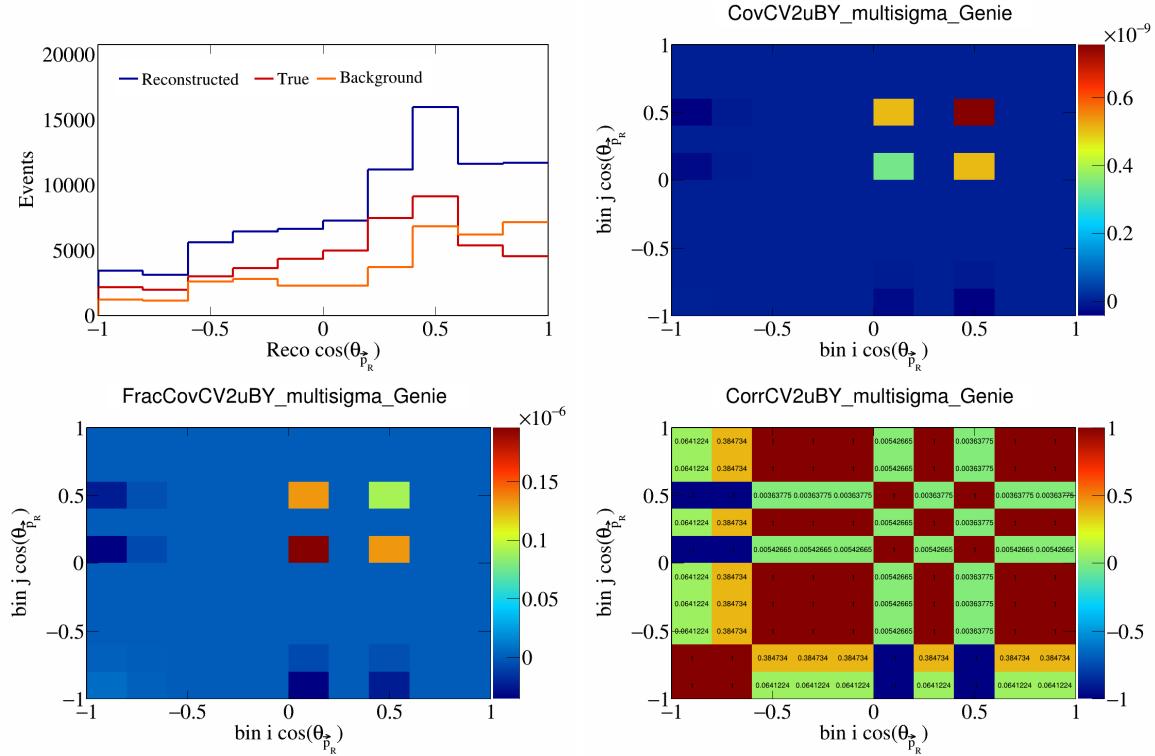


Figure 120: CV2uBY variations for  $\cos(\theta_{\vec{p}_R})$ .

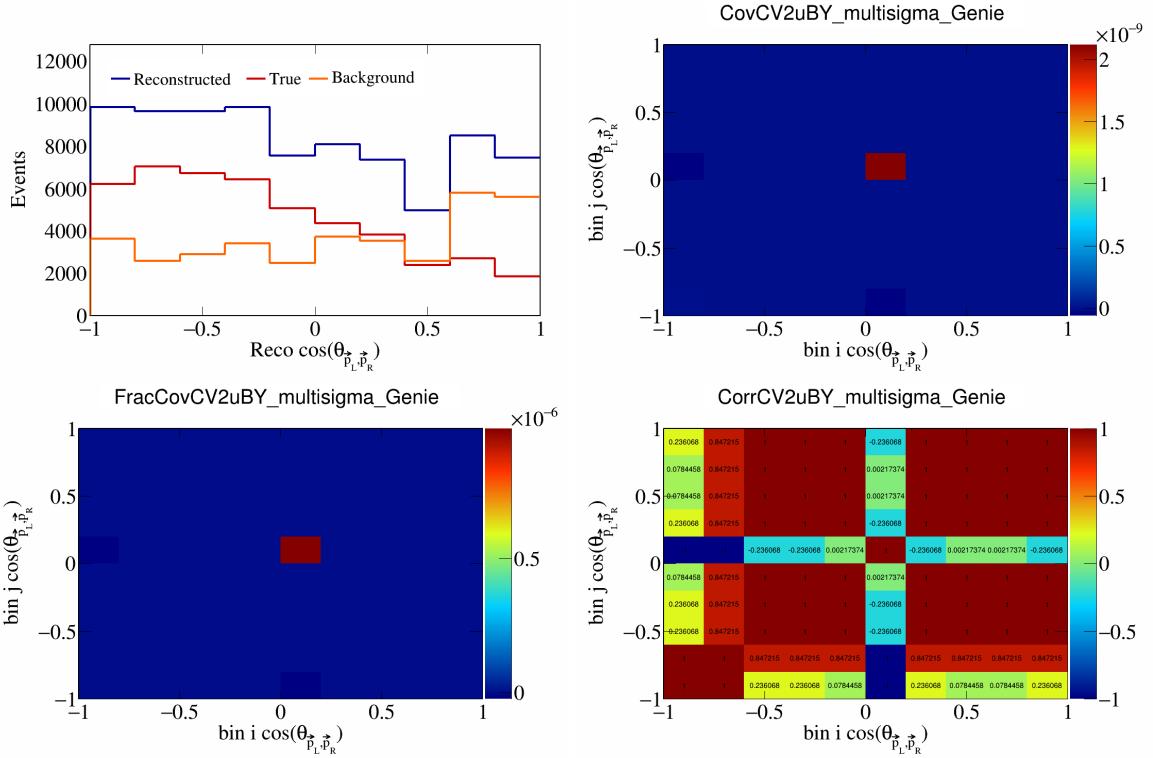


Figure 121: CV2uBY variations for  $\cos(\theta_{\vec{p}_L, \vec{p}_R})$ .

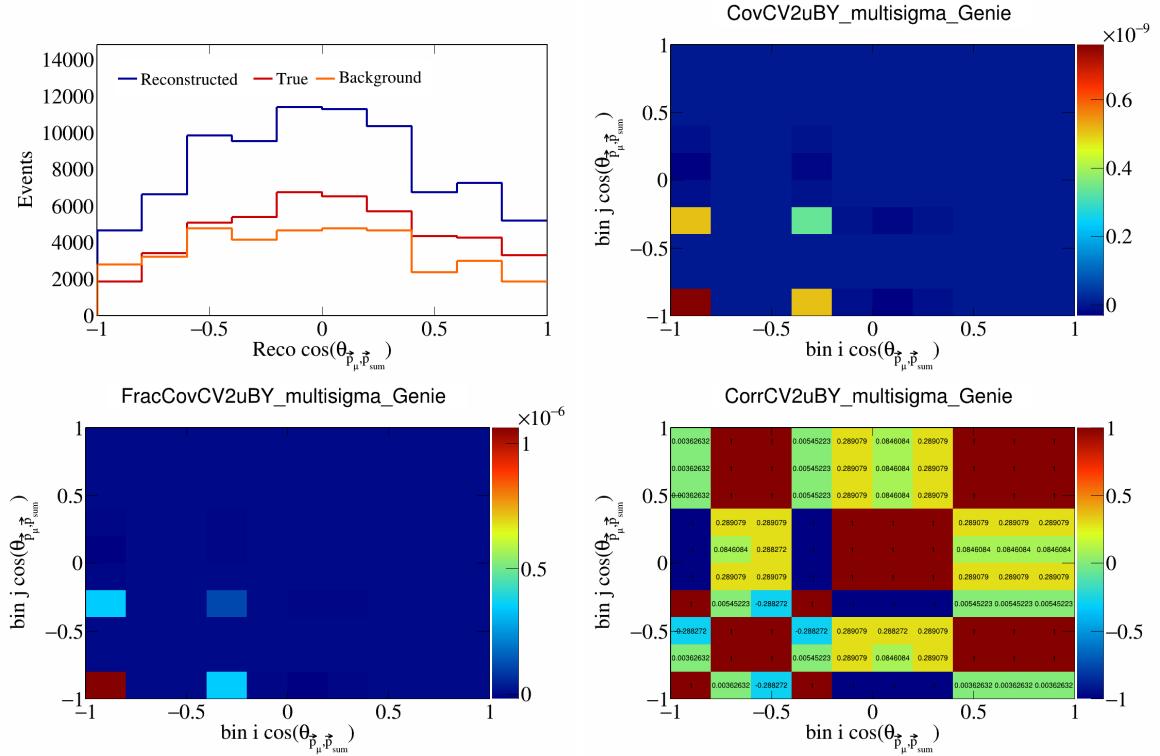


Figure 122: CV2uBY variations for  $\cos(\theta_{\vec{p}_\mu, \vec{p}_{\text{sum}}})$ .

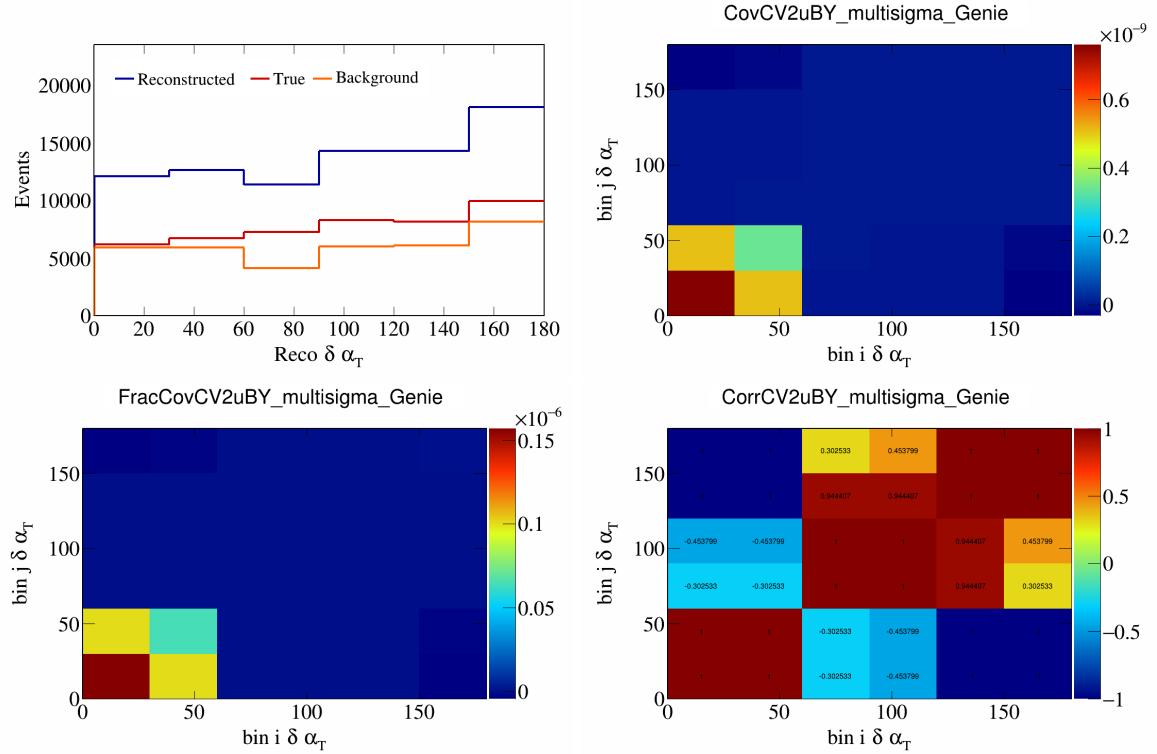


Figure 123: CV2uBY variations for  $\delta\alpha_T$ .

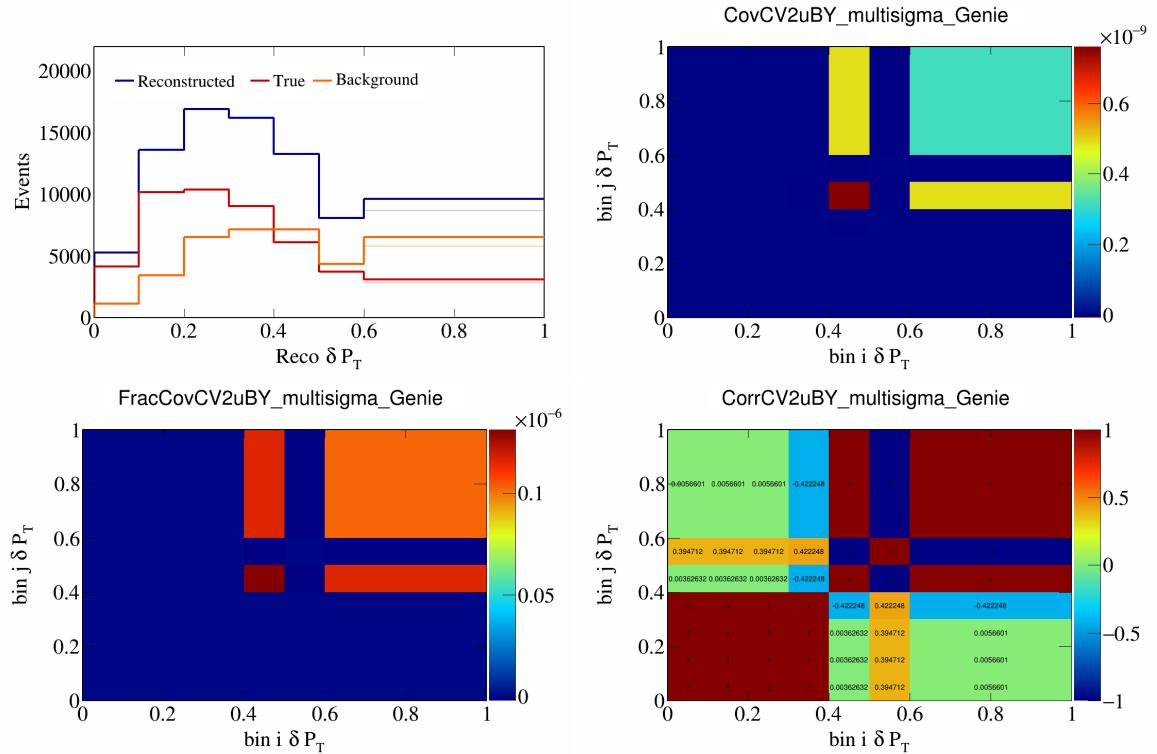


Figure 124: CV2uBY variations for  $\delta P_T$ .

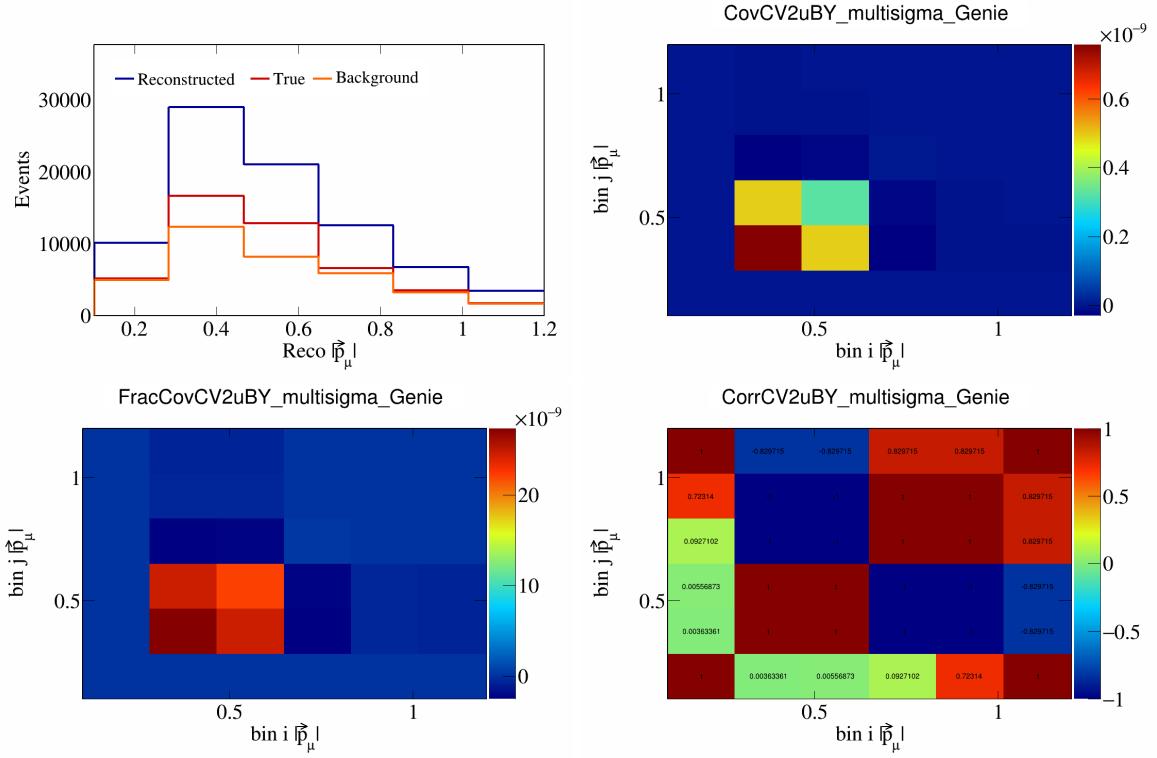


Figure 125: CV2uBY variations for  $|\vec{p}_\mu|$ .

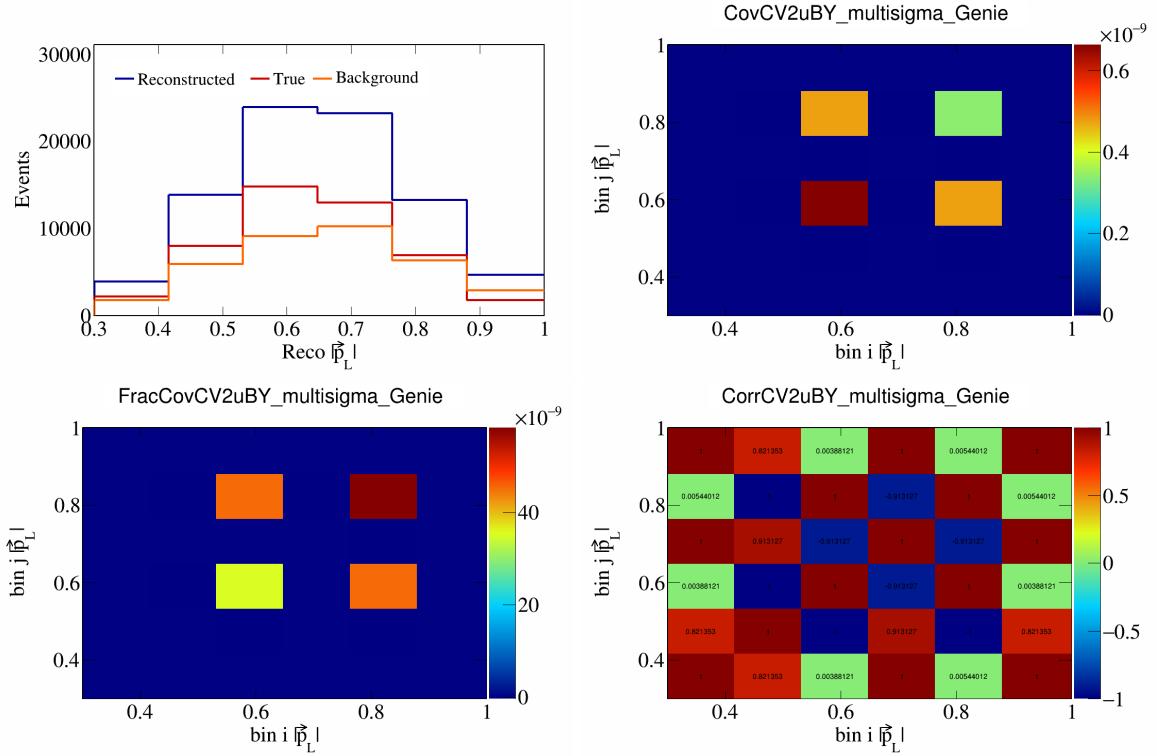


Figure 126: CV2uBY variations for  $|\vec{p}_L|$ .

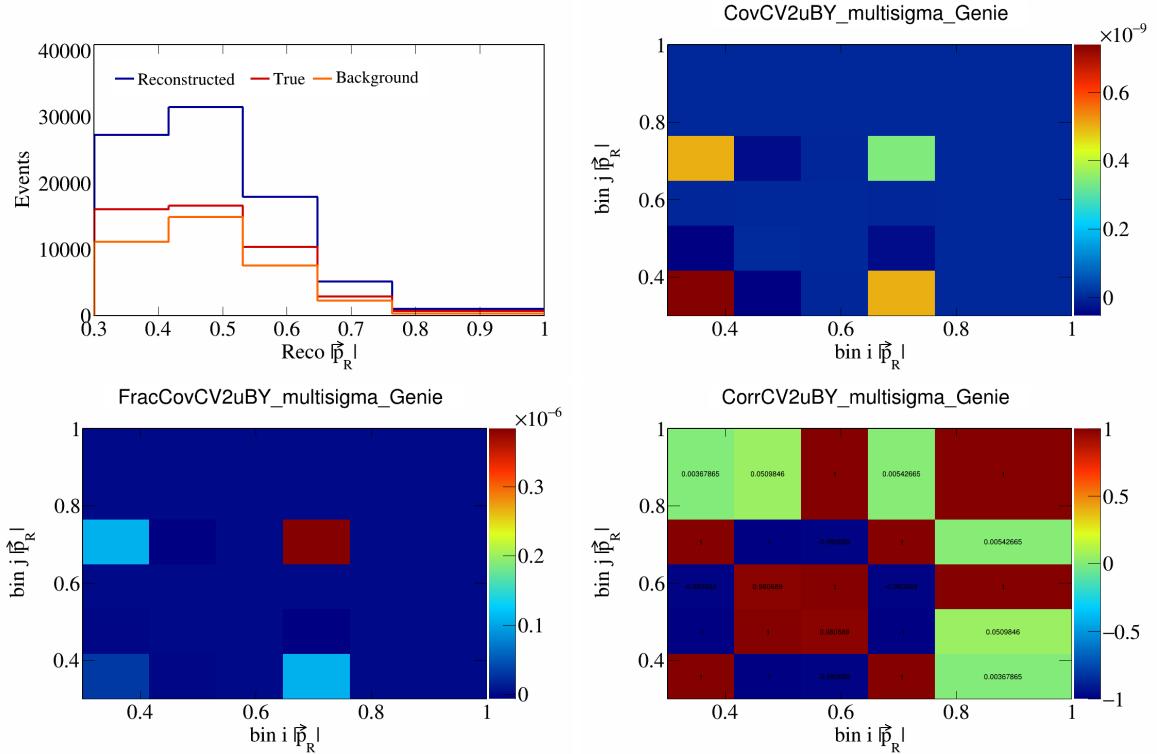


Figure 127: CV2uBY variations for  $|\vec{p}_R|$ .

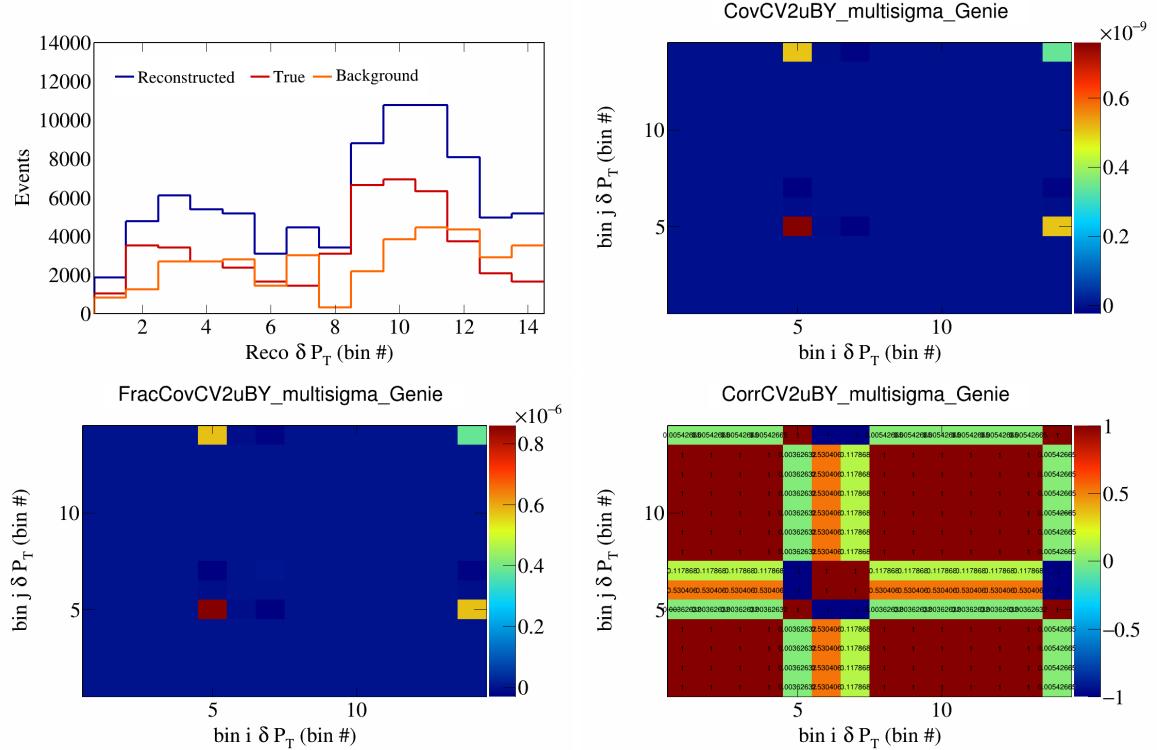


Figure 128: CV2uBY variations for  $\delta P_T$  in  $\cos(\theta_{\vec{p}_\mu})$ .

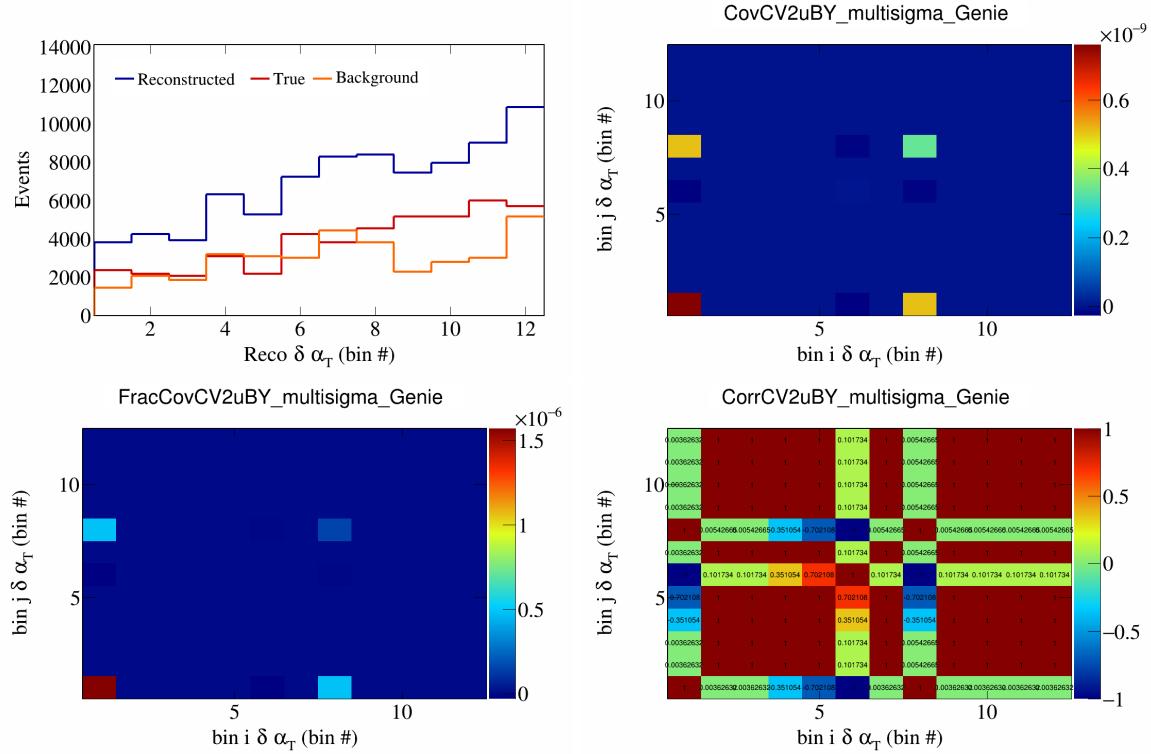


Figure 129: CV2uBY variations for  $\delta\alpha_T$  in  $\cos(\theta_{\vec{p}_\mu})$ .

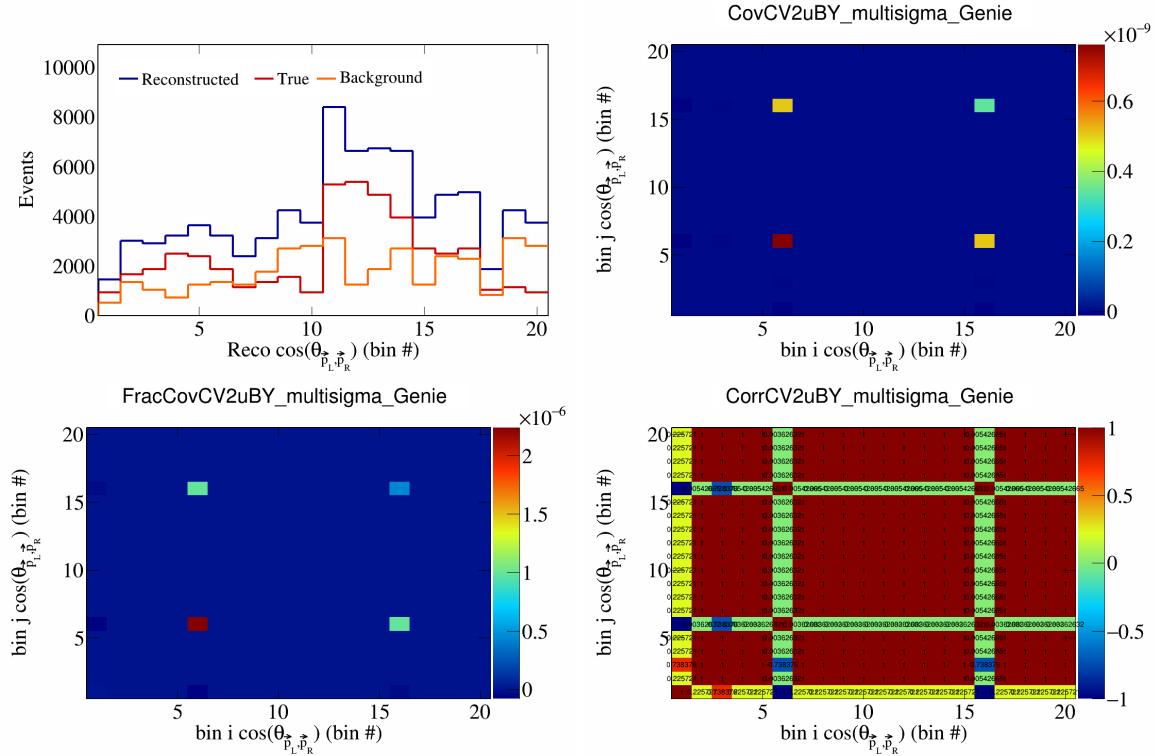


Figure 130: CV2uBY variations for  $\cos(\theta_{\vec{p}_L, \vec{p}_R})$  in  $\cos(\theta_{\vec{p}_\mu})$ .

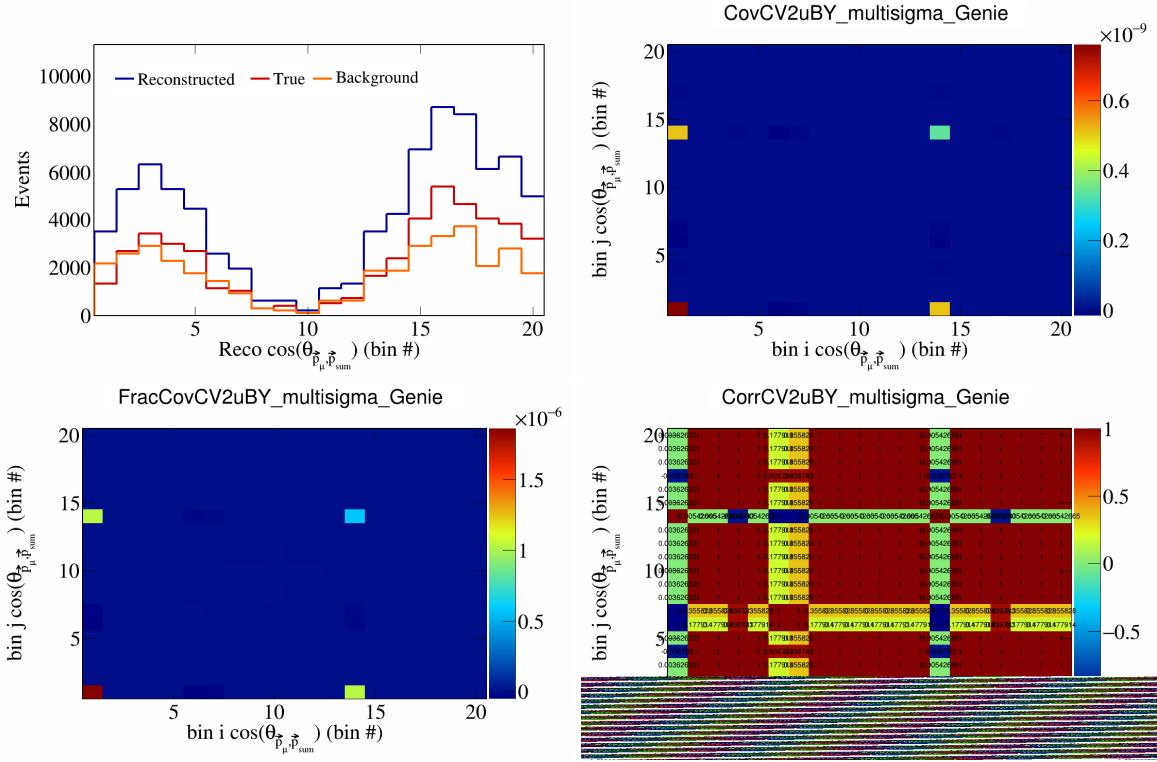


Figure 131: CV2uBY variations for  $\cos(\theta_{\vec{p}_\mu})$  in  $\cos(\theta_{\vec{p}_\mu})$ .

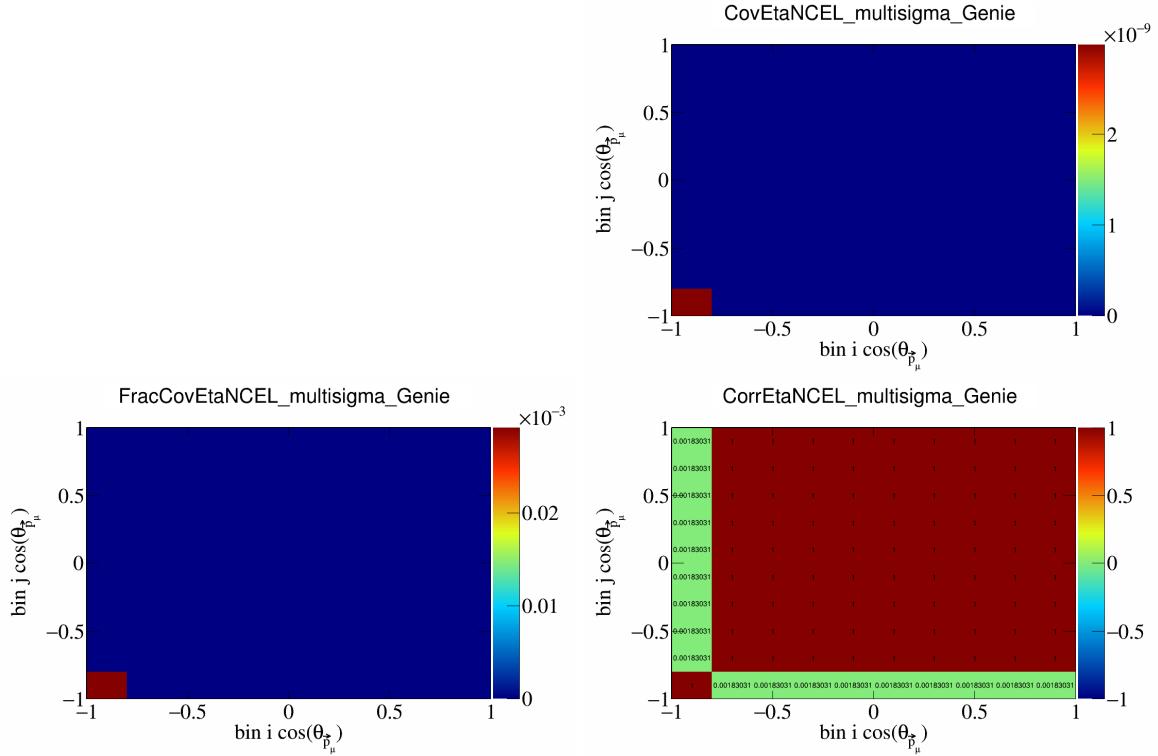


Figure 132: EtaNCEL variations for  $\cos(\theta_{\vec{p}_\mu})$ .

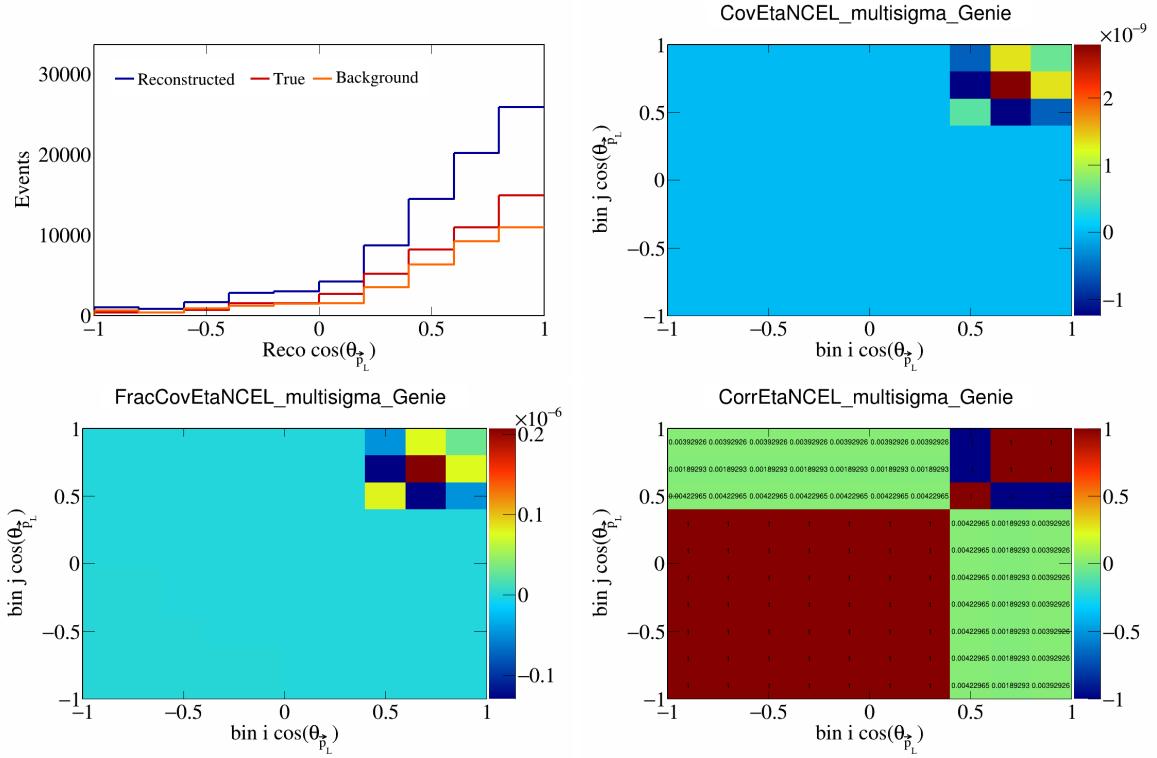


Figure 133: EtaNCEL variations for  $\cos(\theta_{\vec{p}_L})$ .

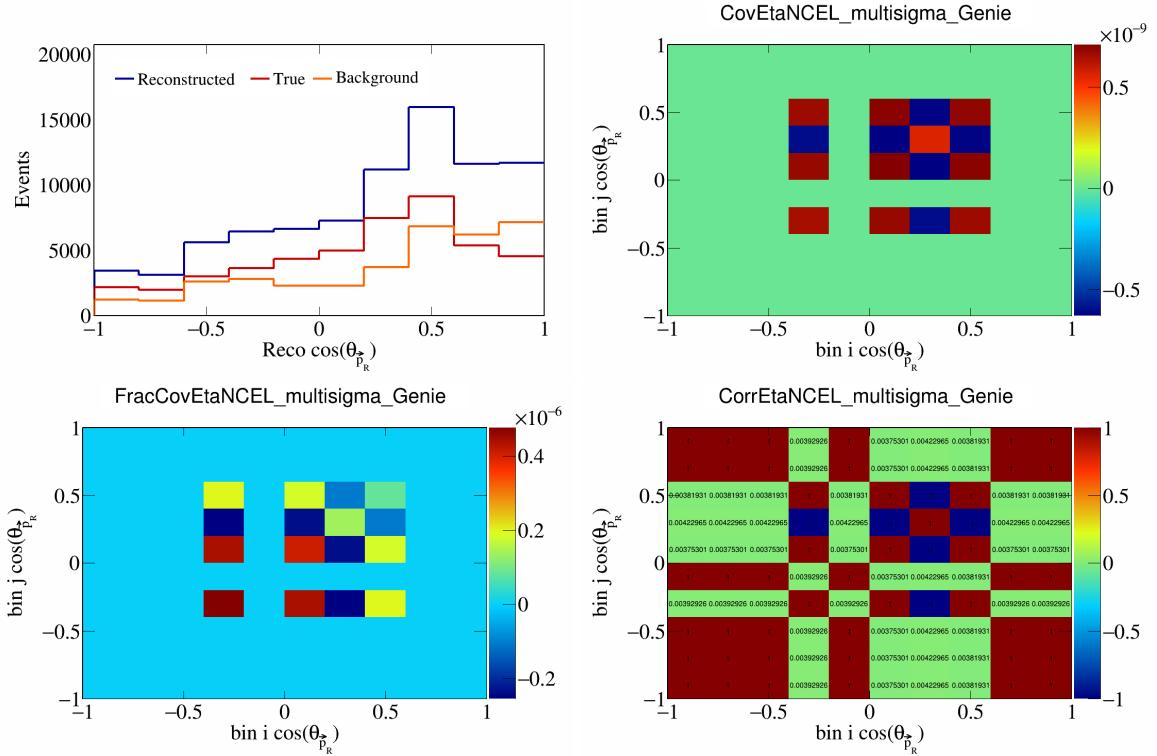


Figure 134: EtaNCEL variations for  $\cos(\theta_{\vec{p}_R})$ .

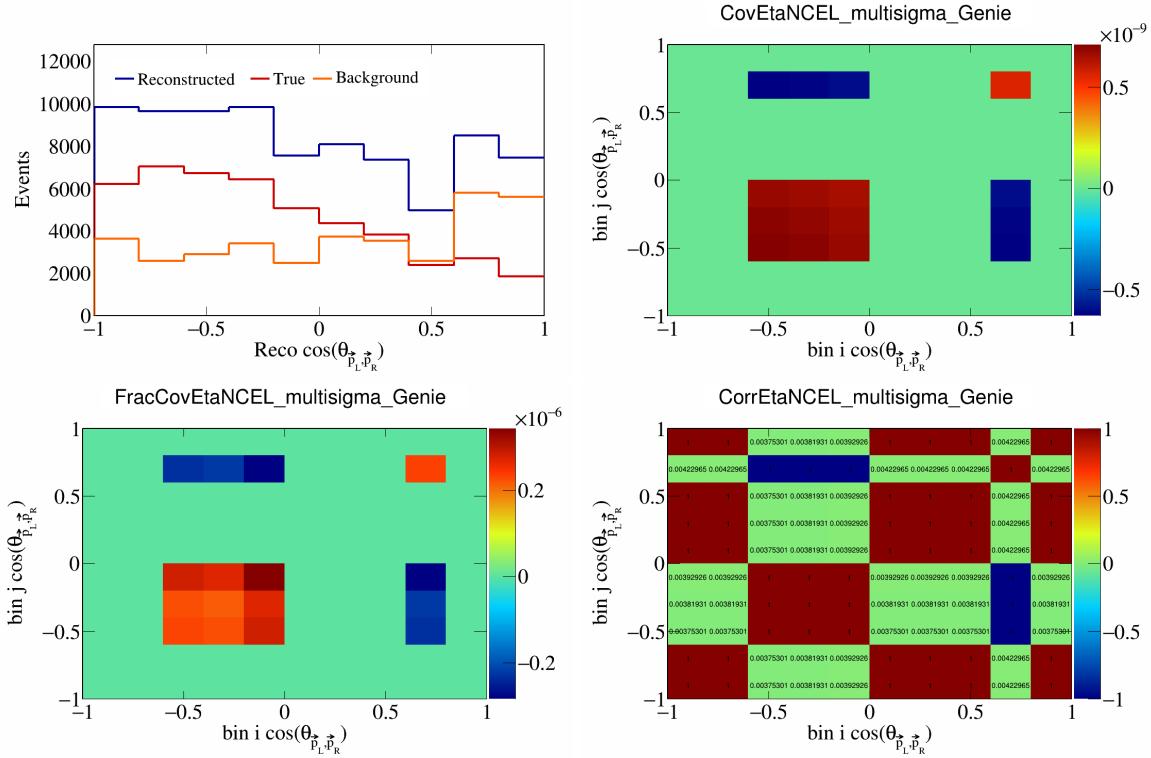


Figure 135: EtaNCEL variations for  $\cos(\theta_{\vec{p}_L, \vec{p}_R})$ .

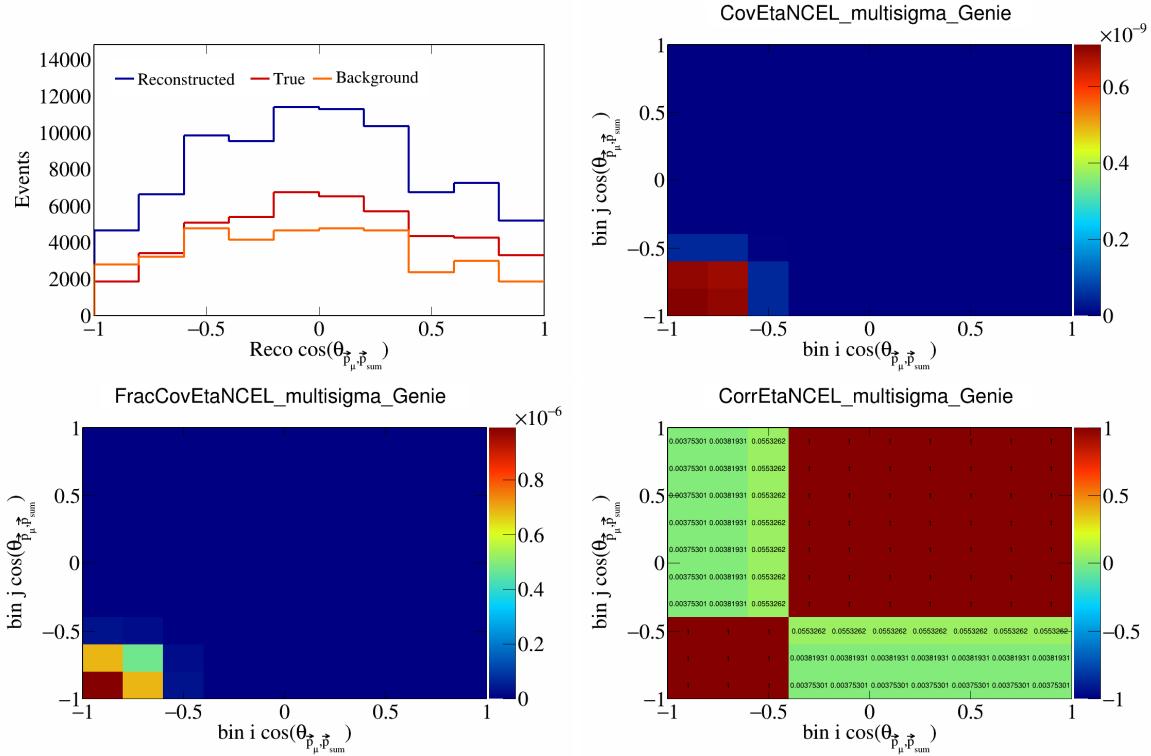


Figure 136: EtaNCEL variations for  $\cos(\theta_{\vec{p}_\mu, \vec{p}_{\text{sum}}})$ .

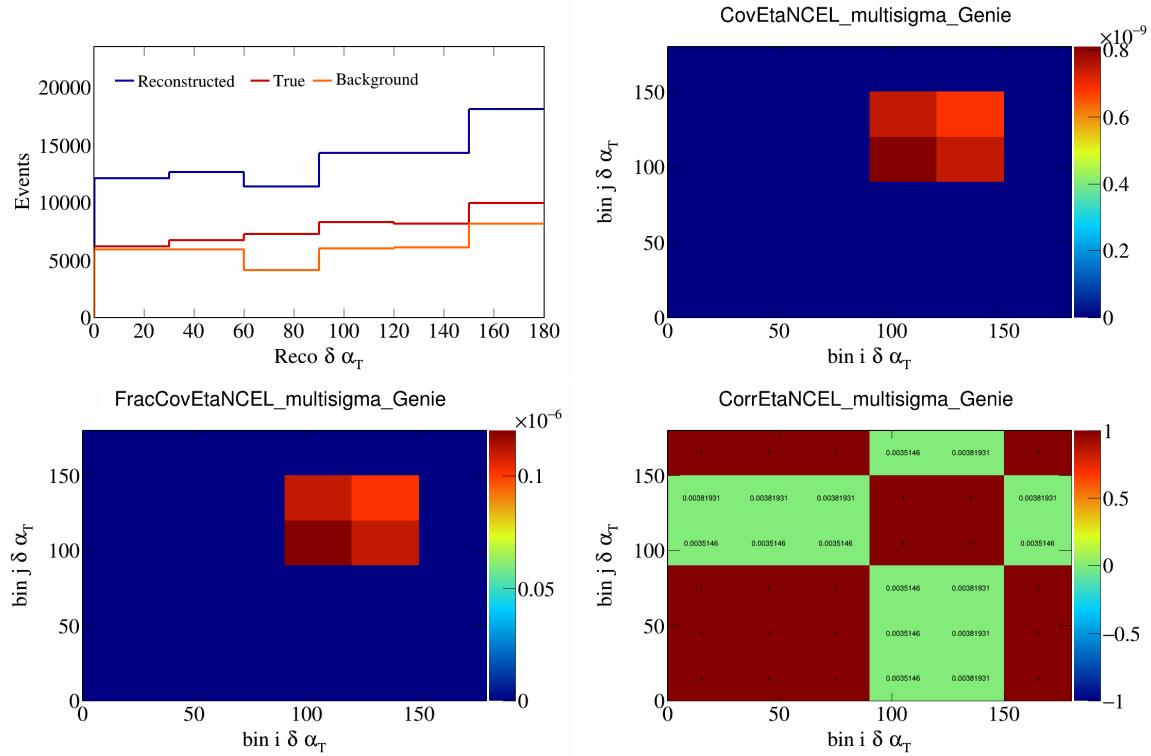


Figure 137: EtaNCEL variations for  $\delta\alpha_T$ .

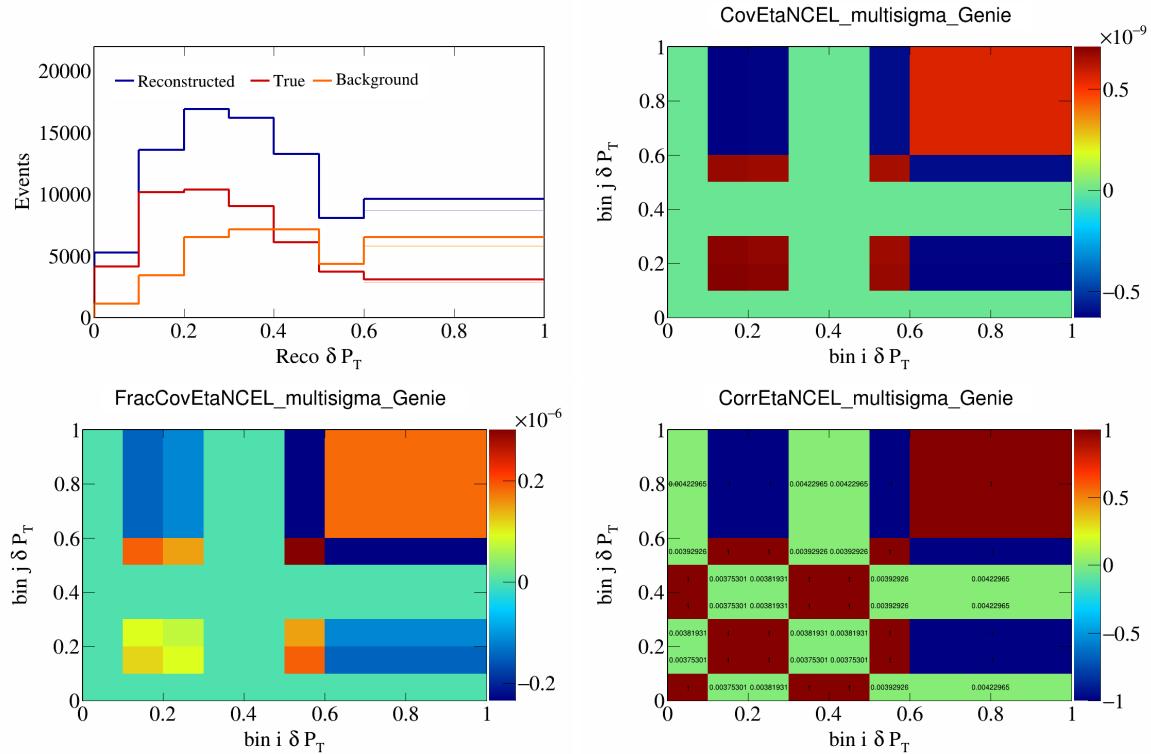


Figure 138: EtaNCEL variations for  $\delta P_T$ .

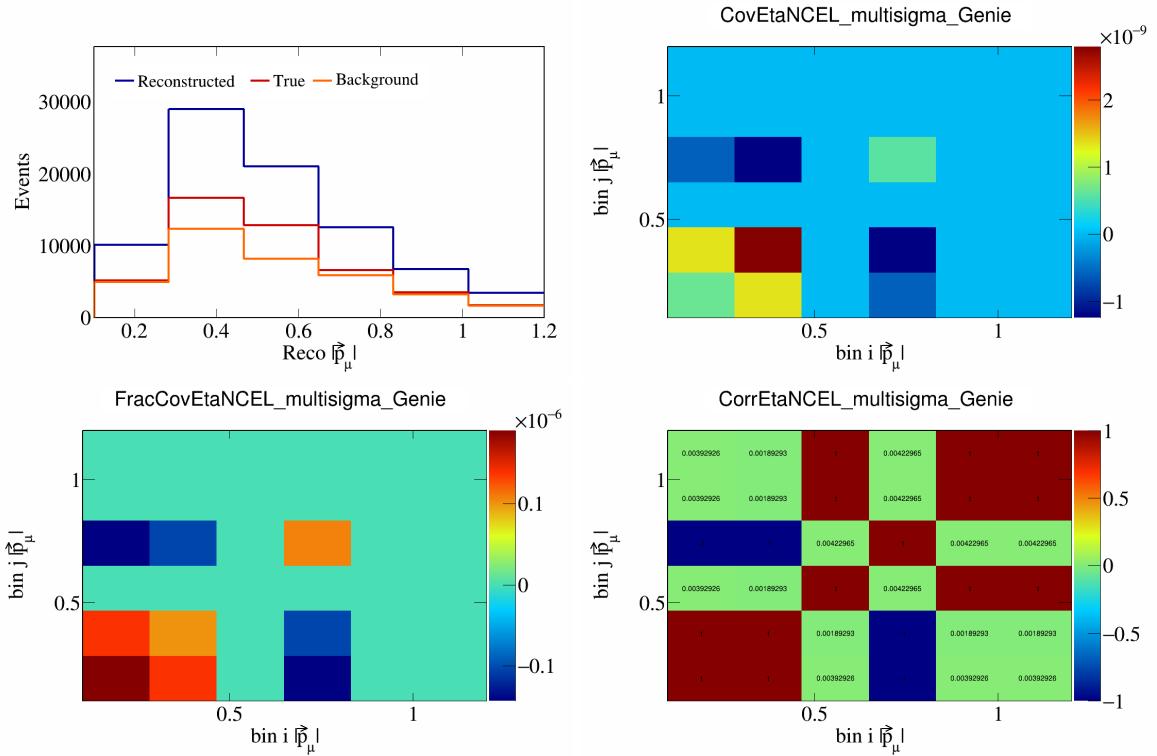


Figure 139: EtaNCEL variations for  $|\vec{p}_\mu|$ .

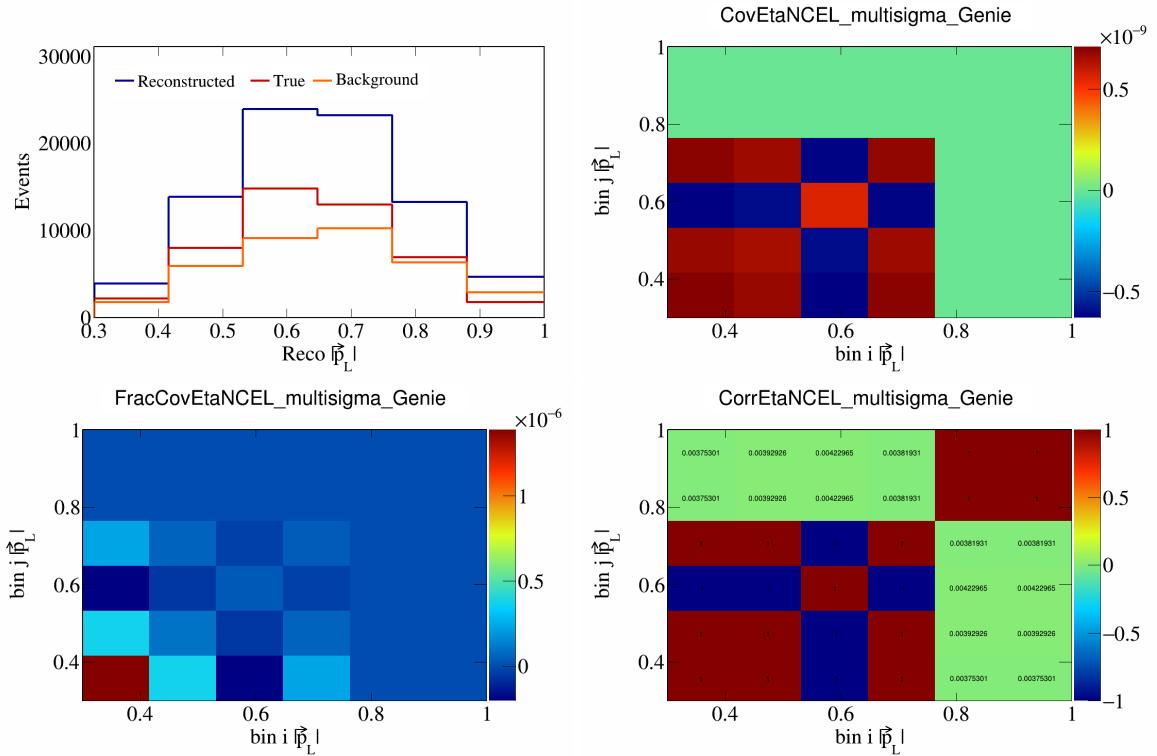


Figure 140: EtaNCEL variations for  $|\vec{p}_L|$ .

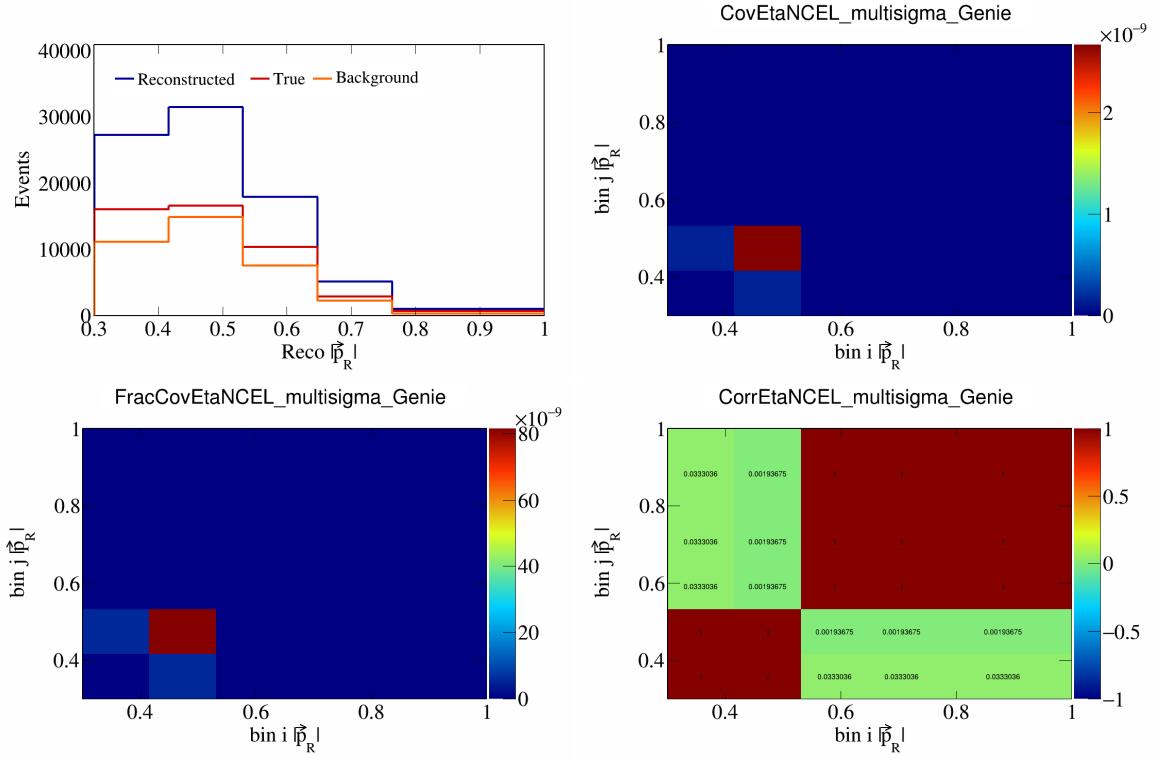


Figure 141: EtaNCEL variations for  $|\vec{p}_R|$ .

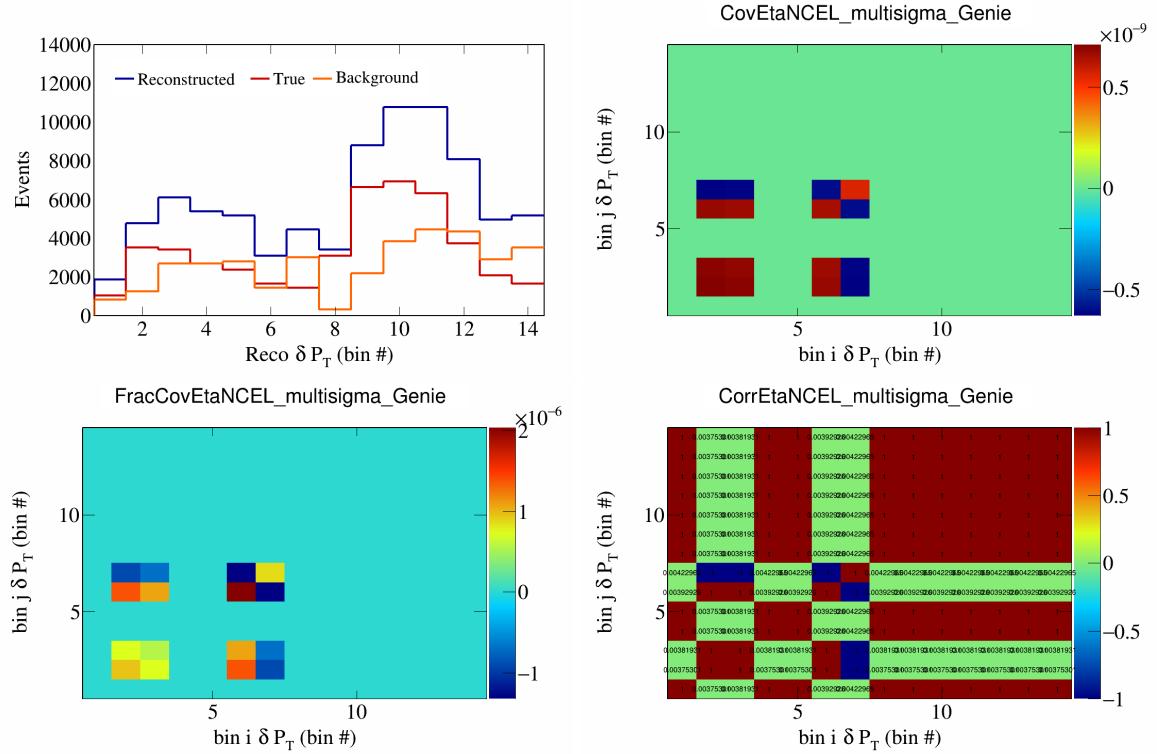


Figure 142: EtaNCEL variations for  $\delta P_T$  in  $\cos(\theta_{\vec{p}_\mu})$ .

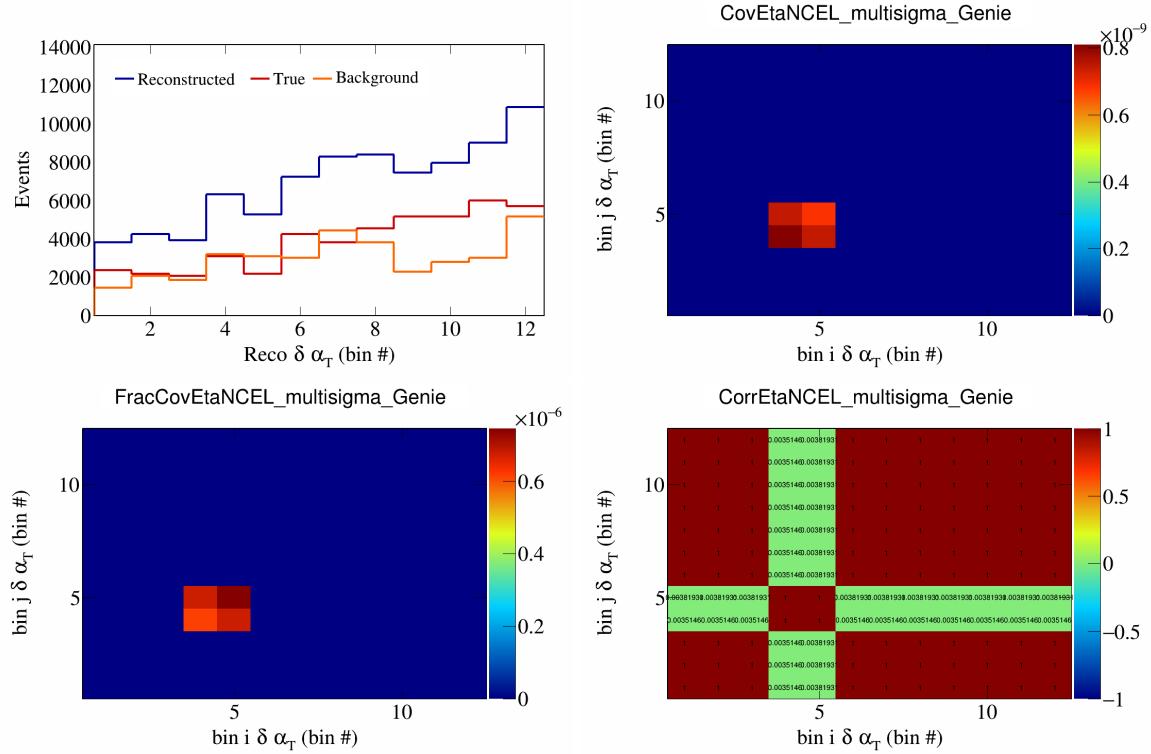


Figure 143: EtaNCEL variations for  $\delta\alpha_T$  in  $\cos(\theta_{\vec{p}_\mu})$ .

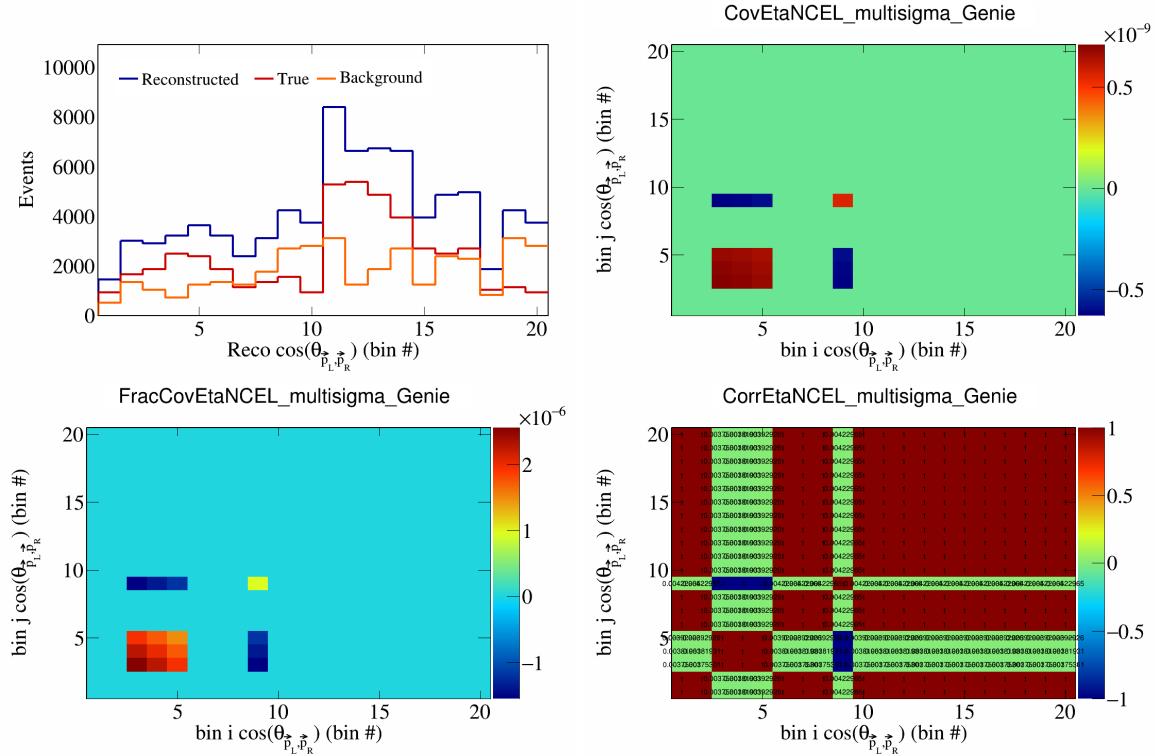


Figure 144: EtaNCEL variations for  $\cos(\theta_{\vec{p}_L, \vec{p}_R})$  in  $\cos(\theta_{\vec{p}_\mu})$ .

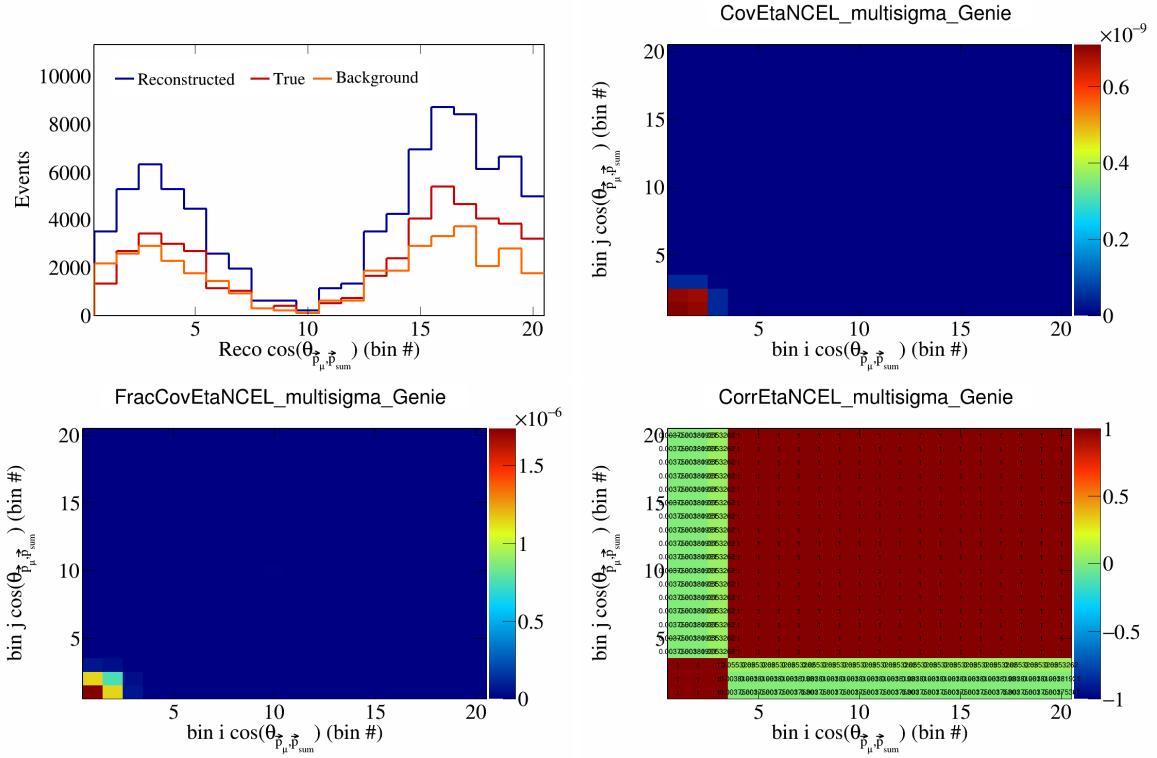


Figure 145: EtaNCEL variations for  $\cos(\theta_{\vec{p}_\mu, \vec{p}_{\text{sum}}})$  in  $\cos(\theta_{\vec{p}_\mu})$ .

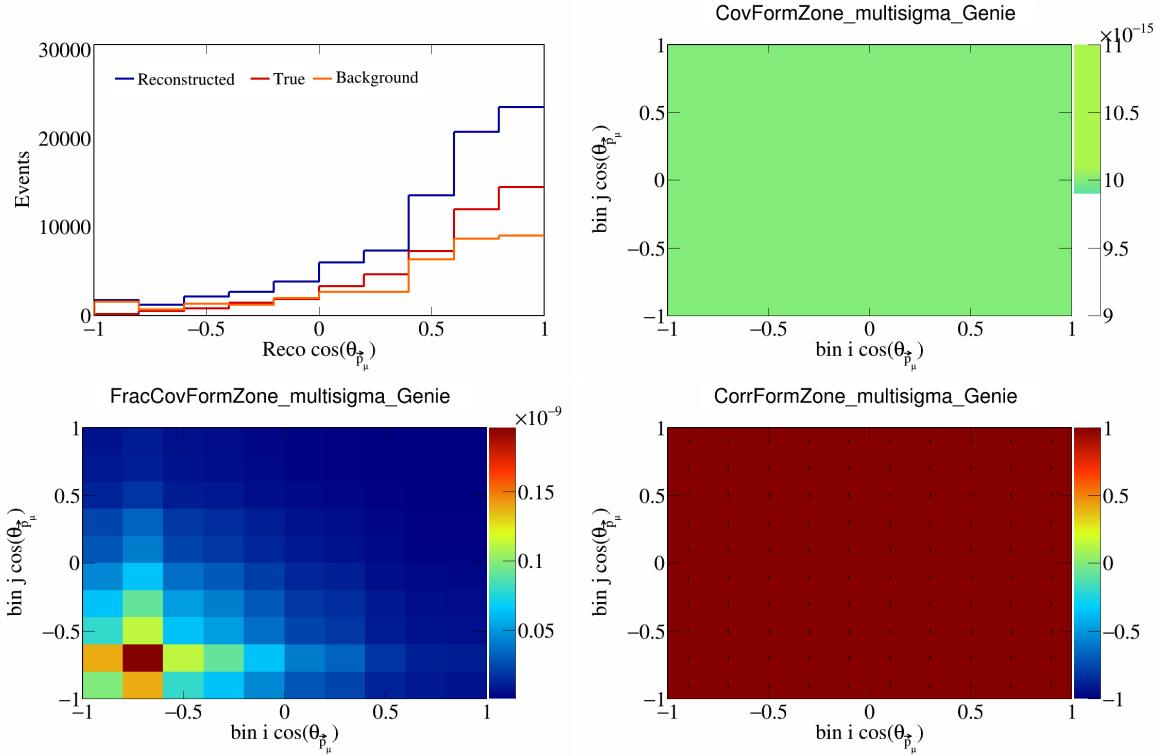


Figure 146: FormZone variations for  $\cos(\theta_{\vec{p}_\mu})$ .

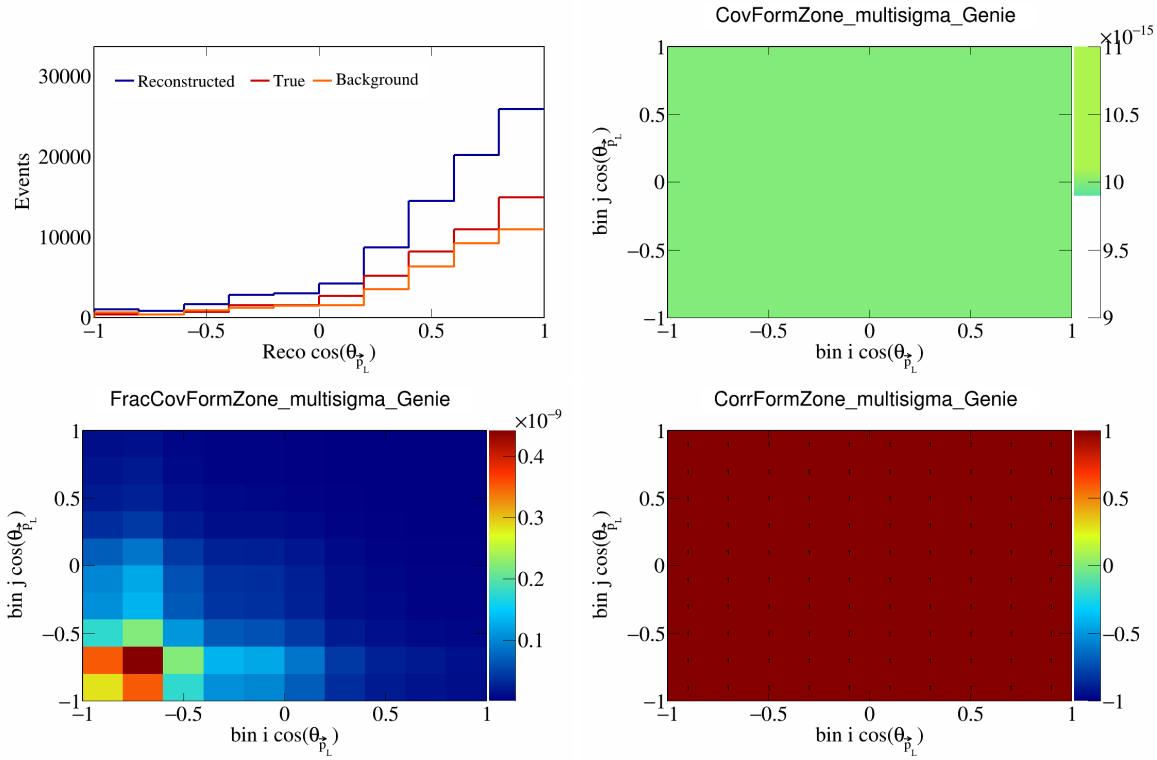


Figure 147: FormZone variations for  $\cos(\theta_{\vec{p}_L})$ .

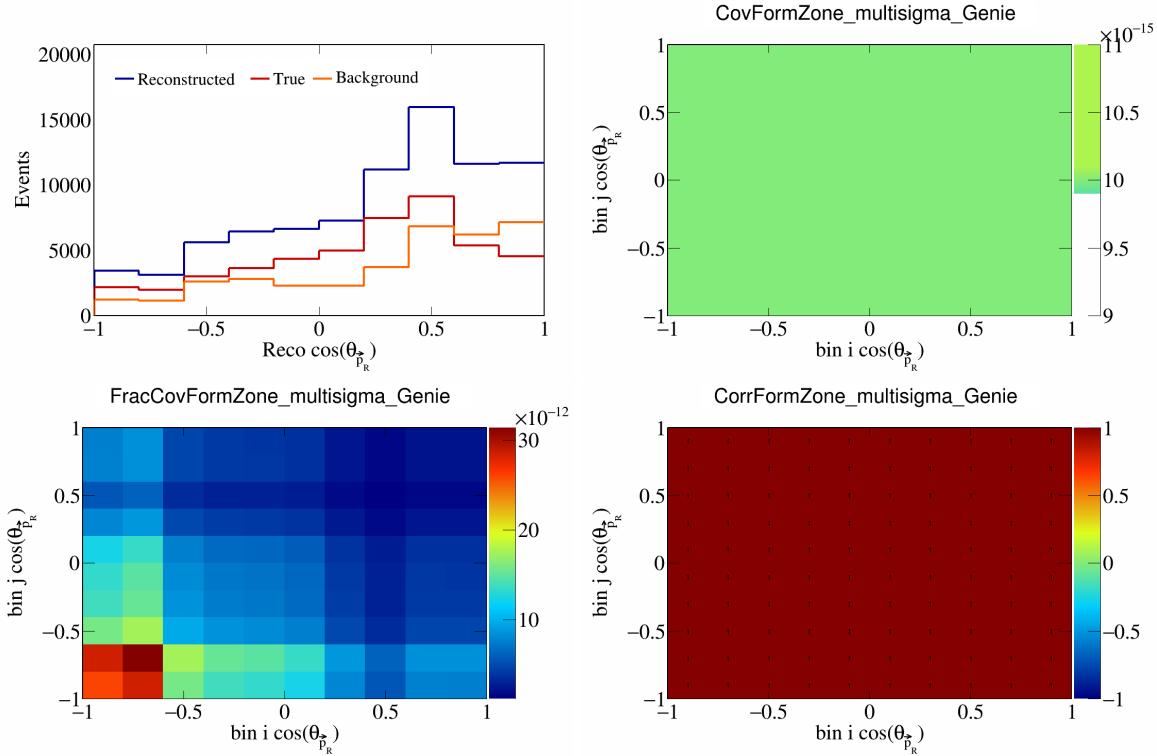


Figure 148: FormZone variations for  $\cos(\theta_{\vec{p}_R})$ .

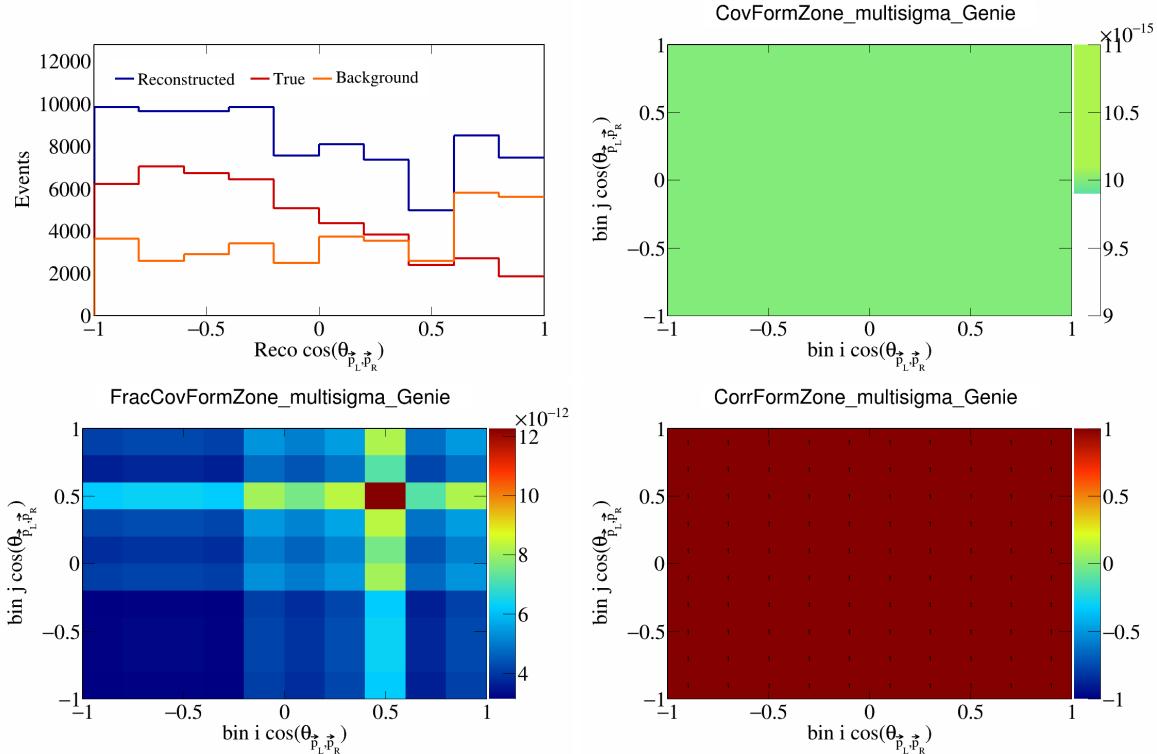


Figure 149: FormZone variations for  $\cos(\theta_{\vec{p}_L, \vec{p}_R})$ .

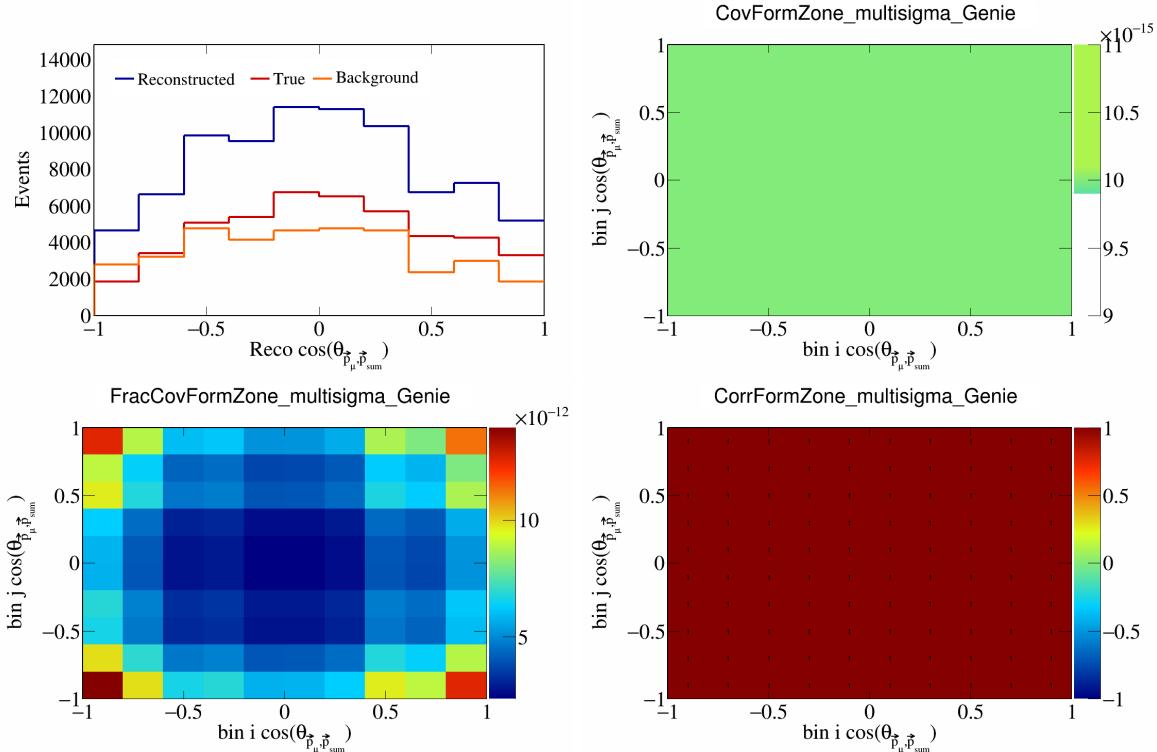


Figure 150: FormZone variations for  $\cos(\theta_{\vec{p}_\mu, \vec{p}_{\text{sum}}})$ .

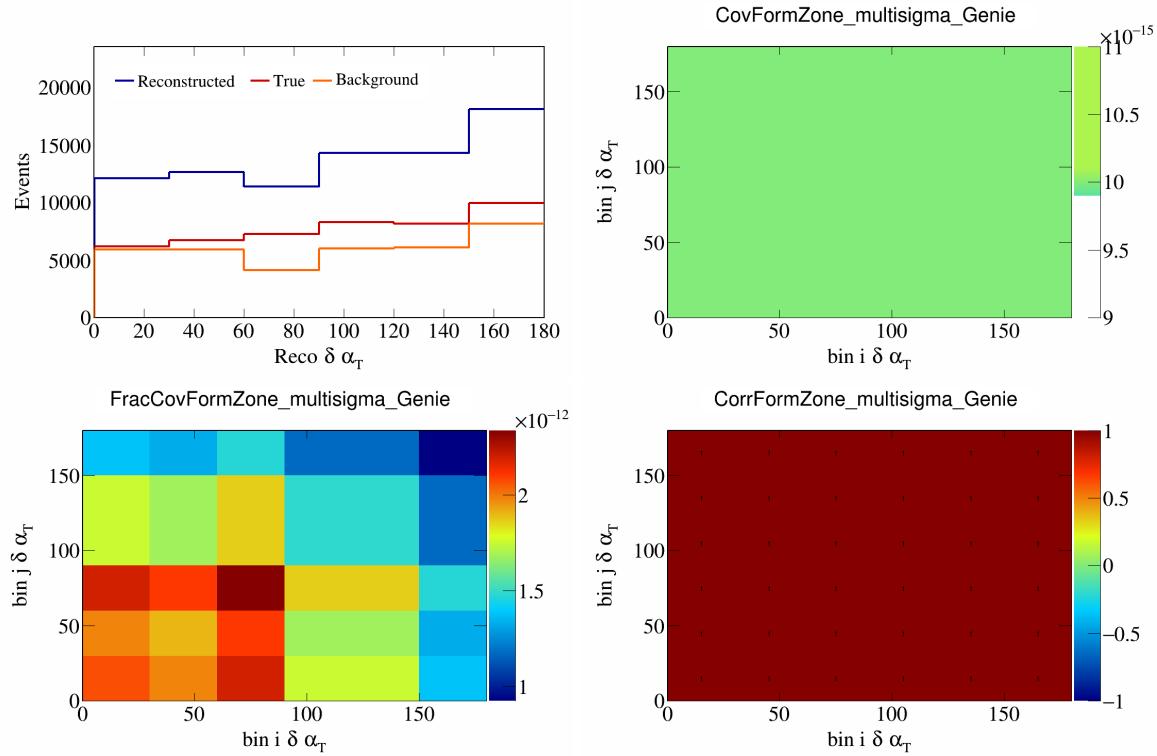


Figure 151: FormZone variations for  $\delta \alpha_T$ .

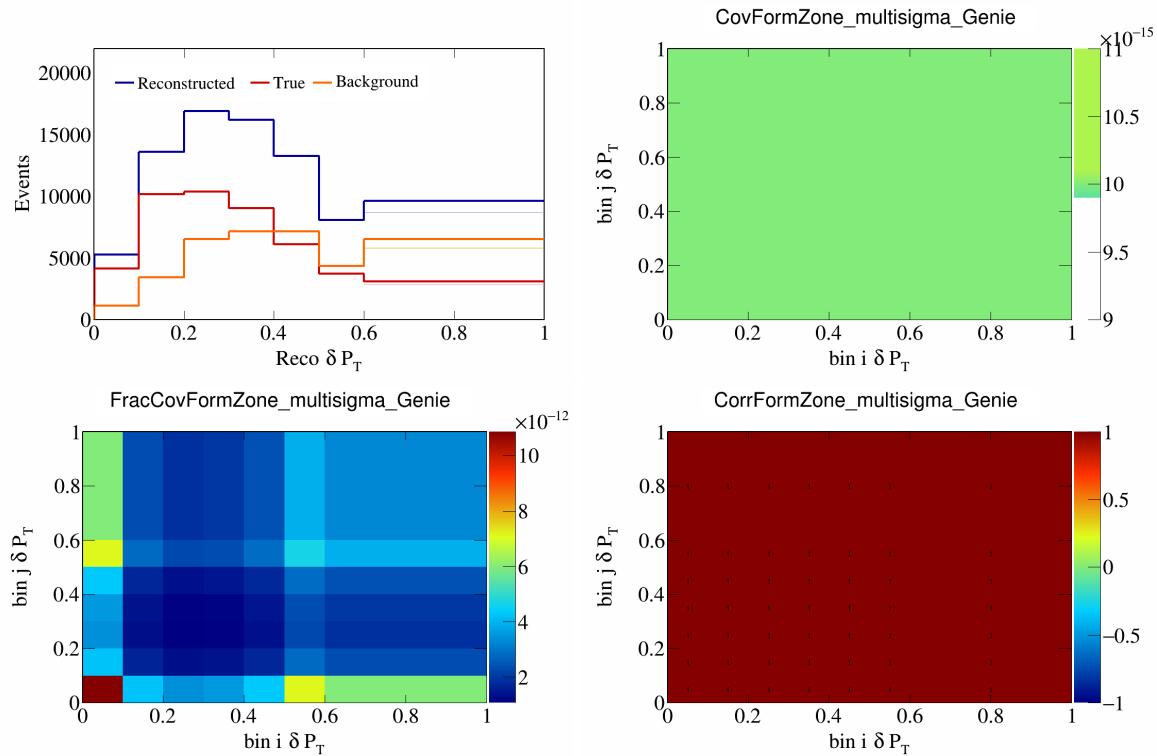


Figure 152: FormZone variations for  $\delta P_T$ .

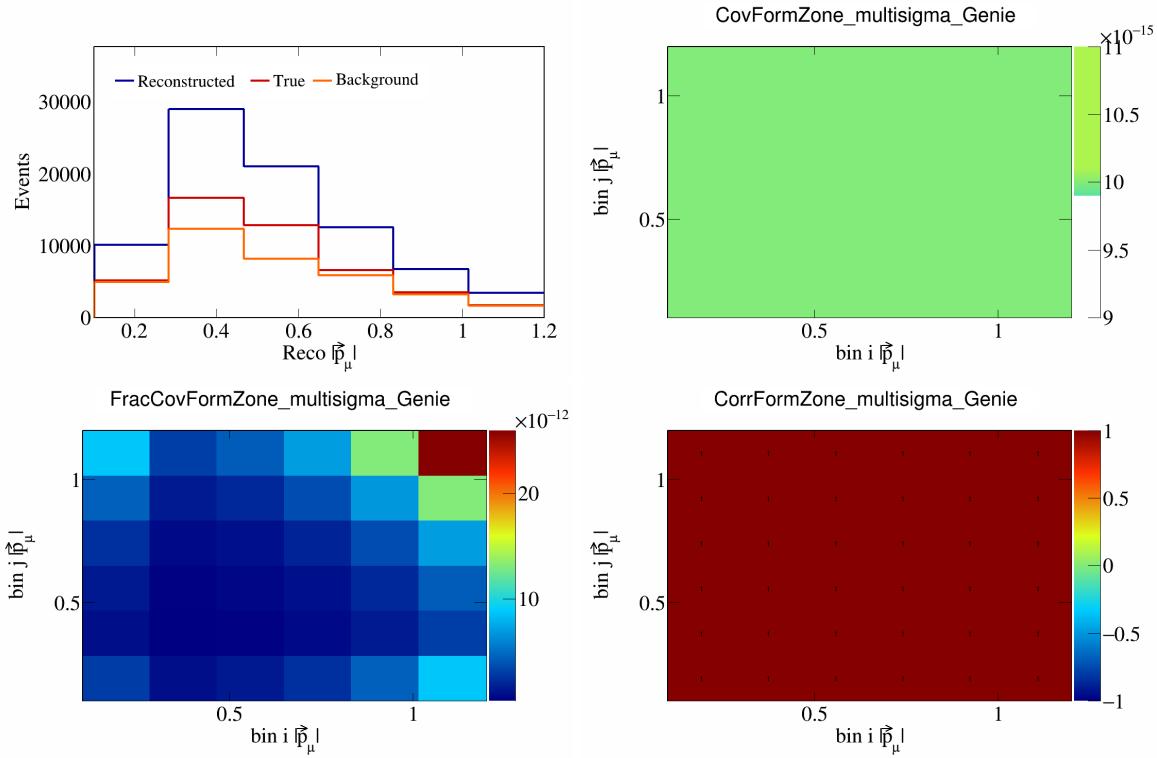


Figure 153: FormZone variations for  $|\vec{p}_\mu|$ .

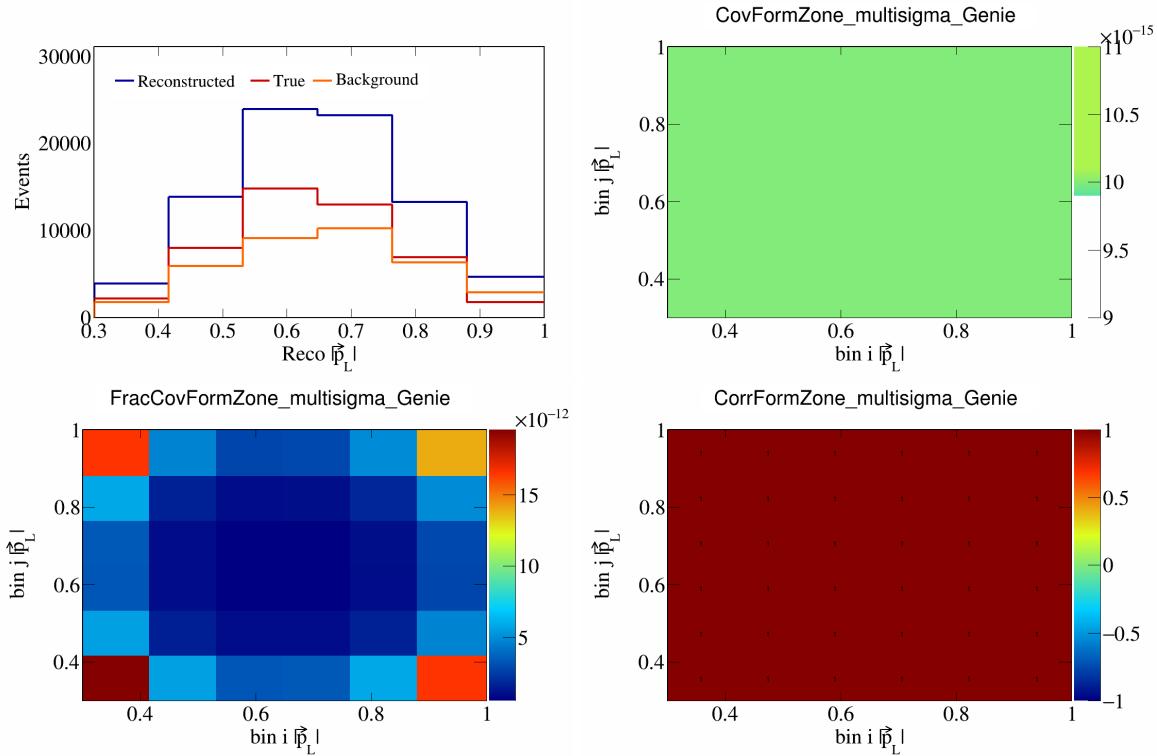


Figure 154: FormZone variations for  $|\vec{p}_L|$ .

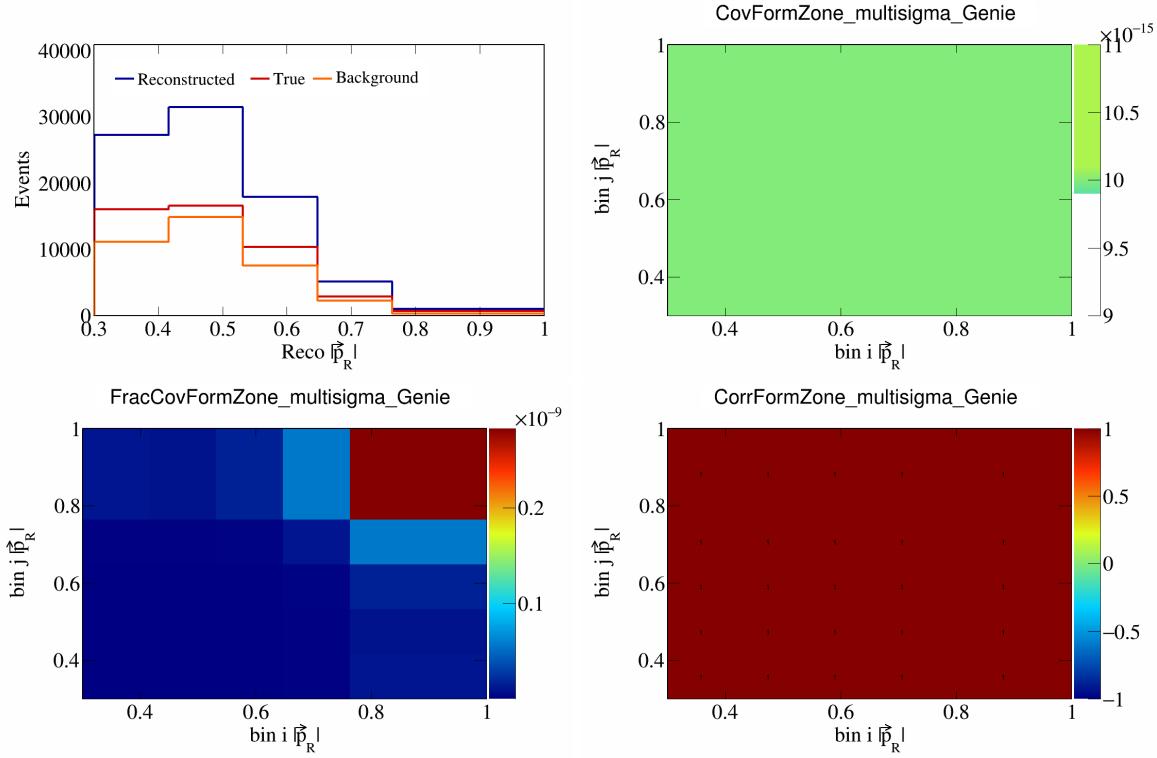


Figure 155: FormZone variations for  $|\vec{p}_R|$ .

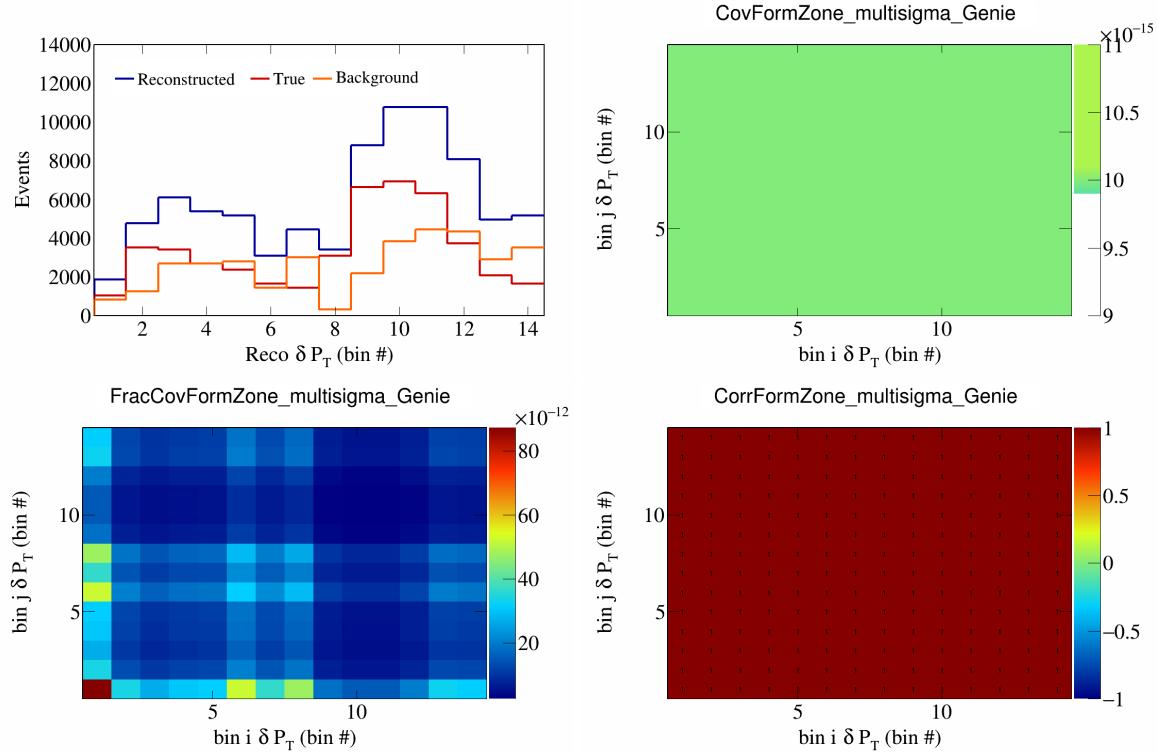


Figure 156: FormZone variations for  $\delta P_T$  in  $\cos(\theta_{\vec{p}_\mu})$ .

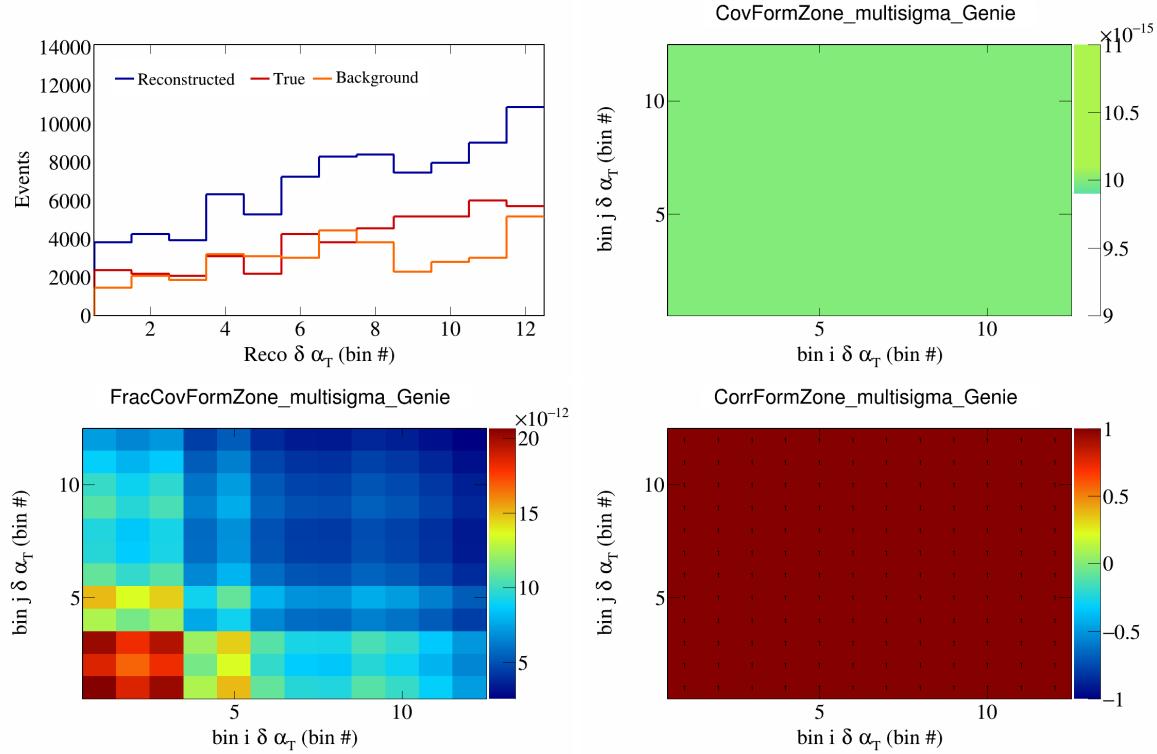


Figure 157: FormZone variations for  $\delta\alpha_T$  in  $\cos(\theta_{\vec{p}_\mu})$ .

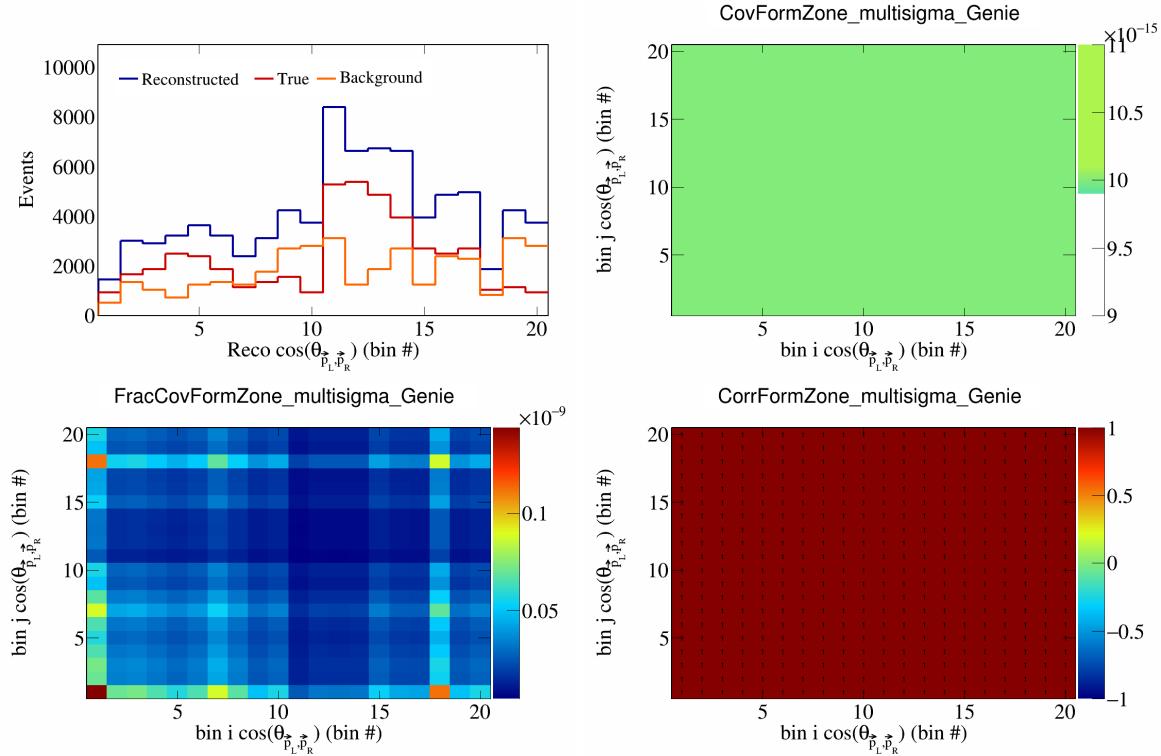


Figure 158: FormZone variations for  $\cos(\theta_{\vec{p}_L, \vec{p}_R})$  in  $\cos(\theta_{\vec{p}_\mu})$ .

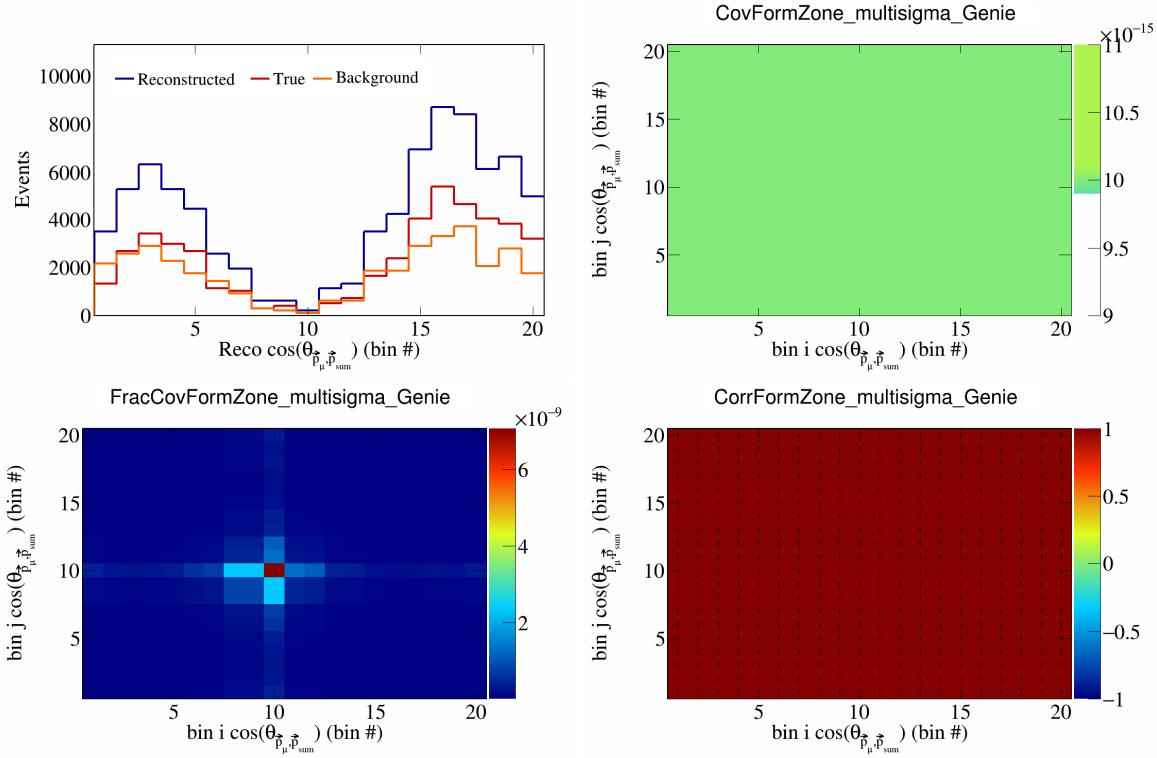


Figure 159: FormZone variations for  $\cos(\theta_{\vec{p}_\mu, \vec{p}_{\text{sum}}})$  in  $\cos(\theta_{\vec{p}_\mu})$ .

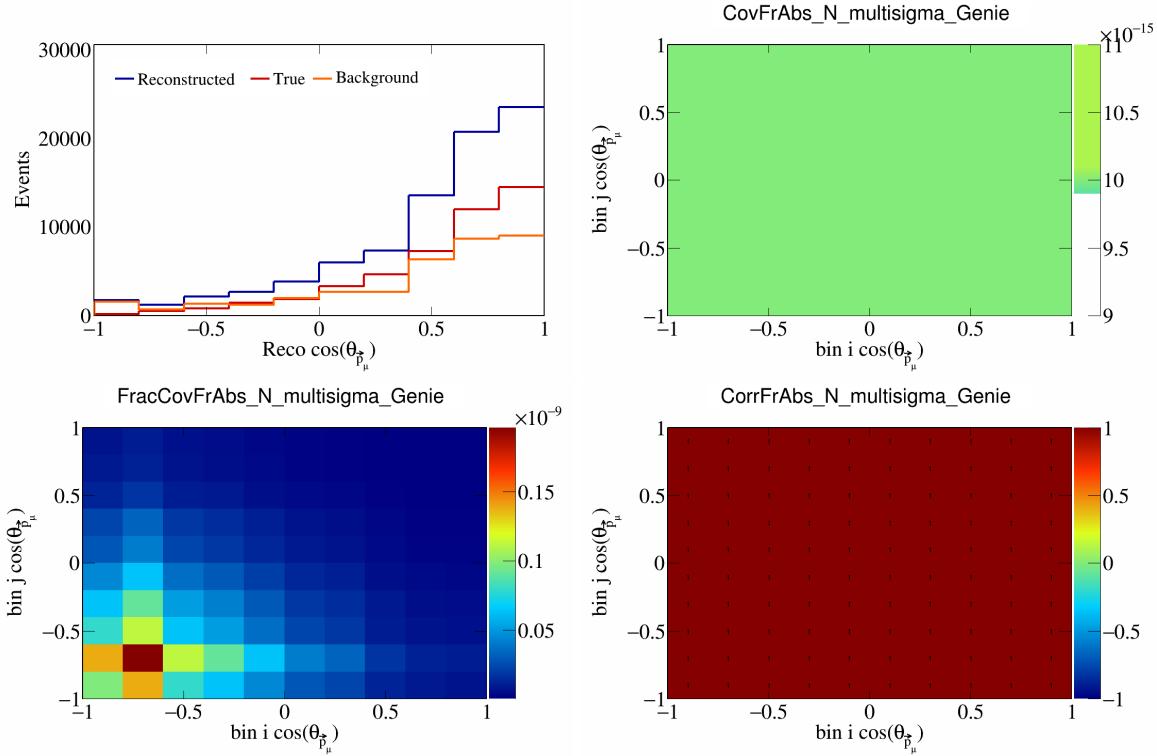


Figure 160: FrAbsN variations for  $\cos(\theta_{\vec{p}_\mu})$ .

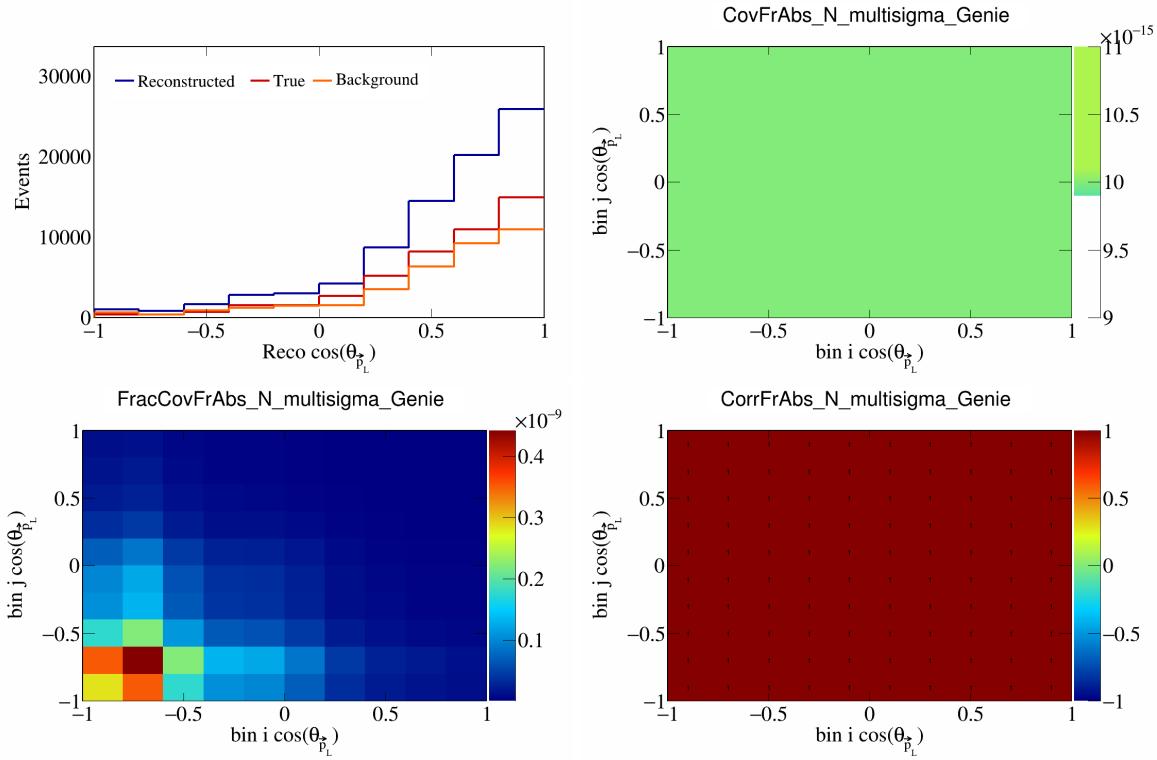


Figure 161: FrAbsN variations for  $\cos(\theta_{\vec{p}_L})$ .

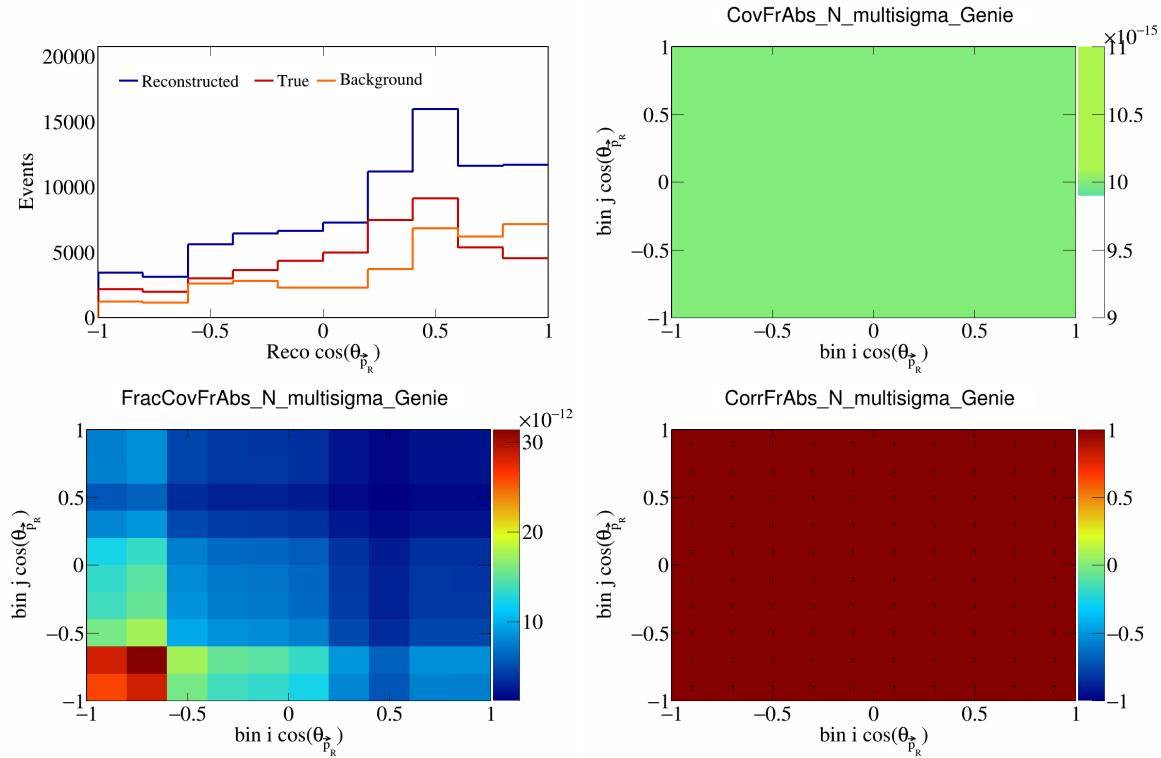


Figure 162: FrAbsN variations for  $\cos(\theta_{\vec{p}_R})$ .

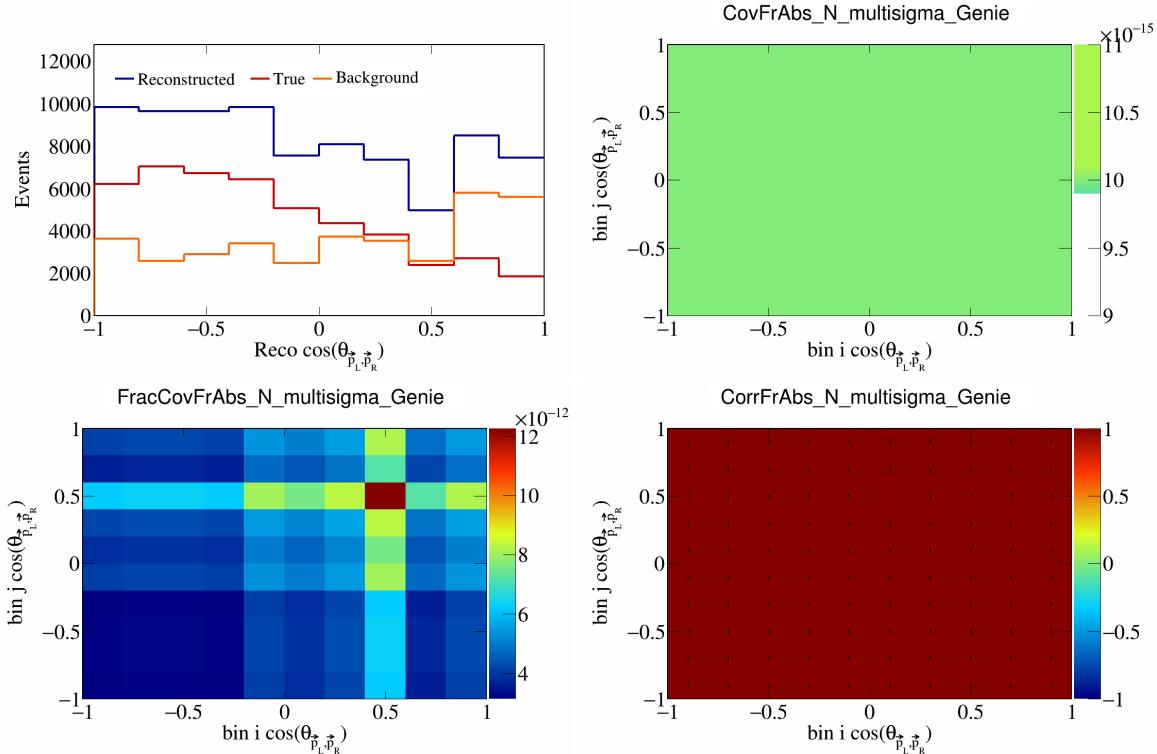


Figure 163: FrAbsN variations for  $\cos(\theta_{\vec{p}_L, \vec{p}_R})$ .

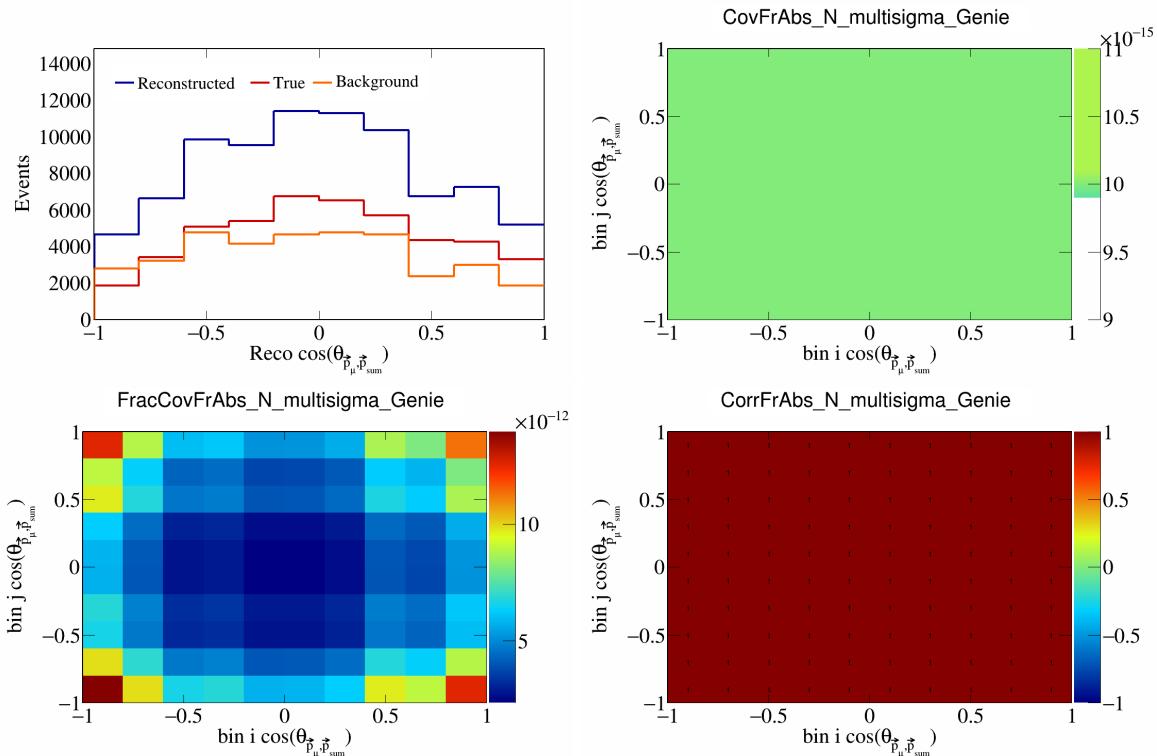


Figure 164: FrAbsN variations for  $\cos(\theta_{\vec{p}_\mu, \vec{p}_{\text{sum}}})$ .

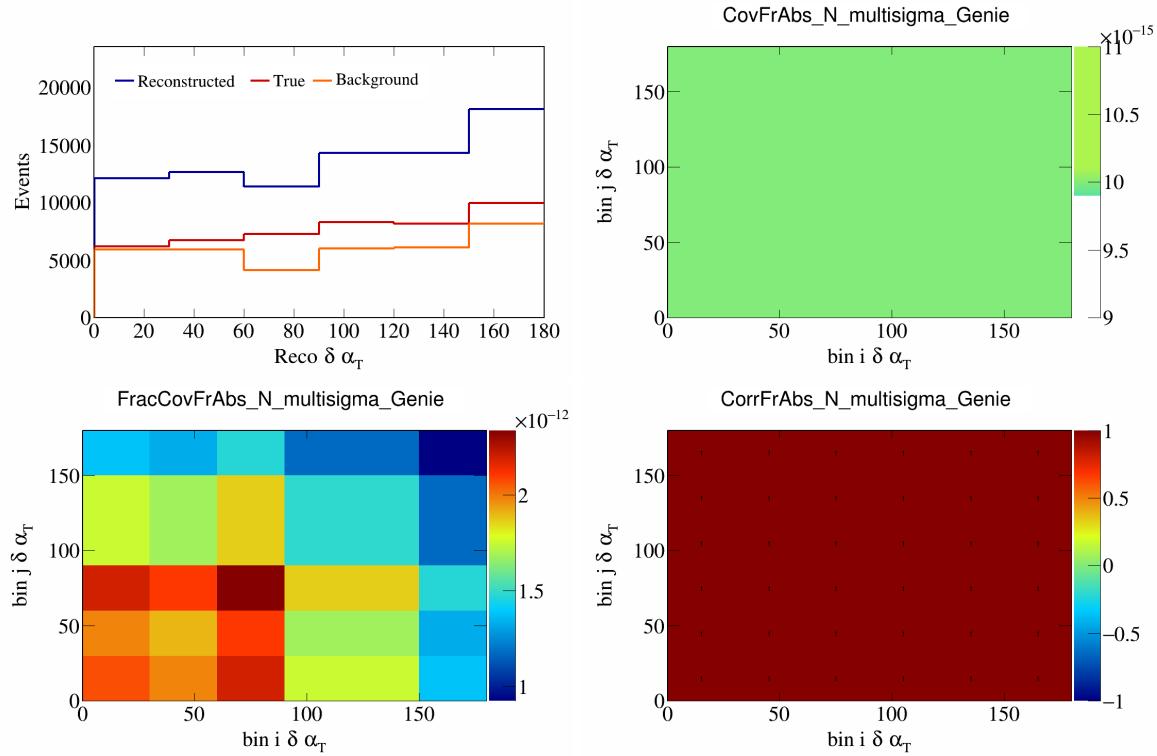


Figure 165: FrAbsN variations for  $\delta\alpha_T$ .

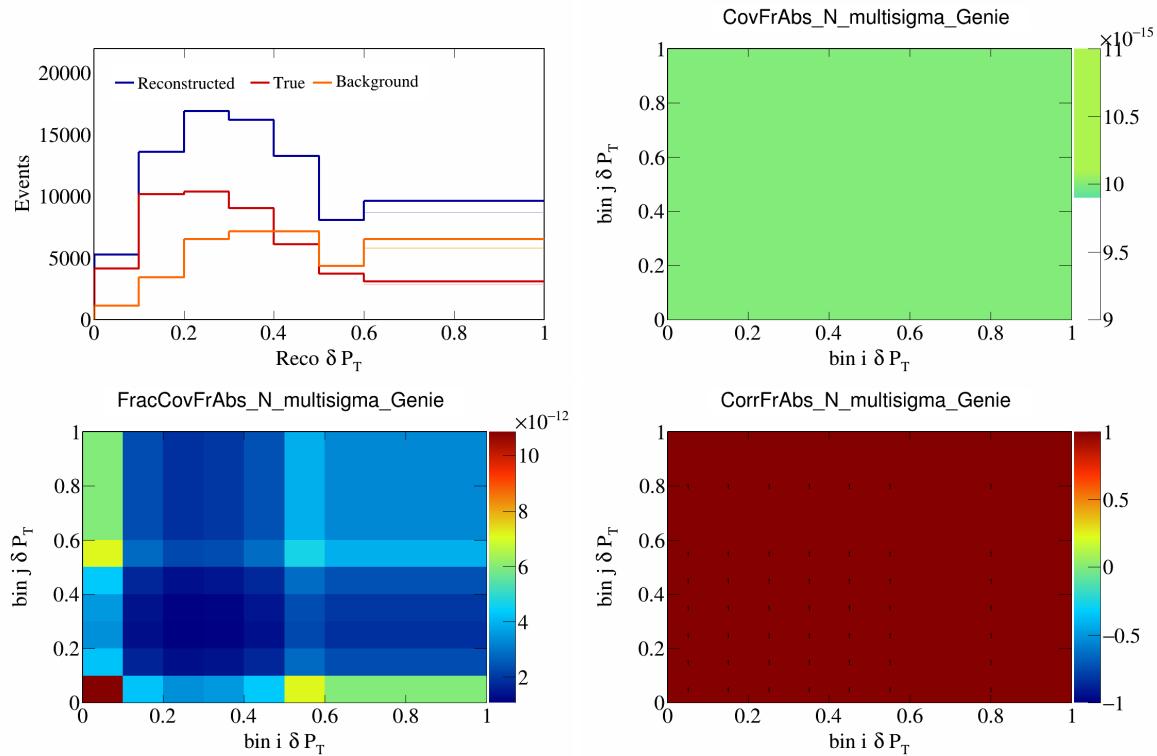


Figure 166: FrAbsN variations for  $\delta P_T$ .

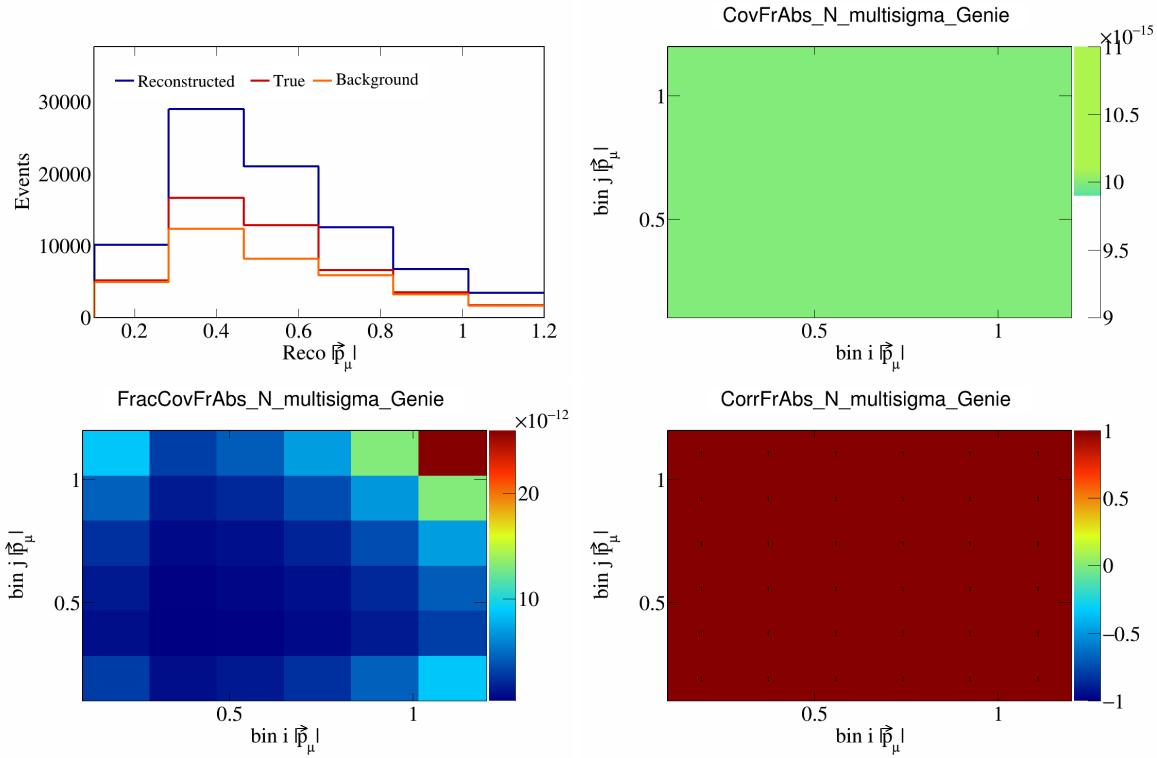


Figure 167: FrAbsN variations for  $|\vec{p}_\mu|$ .

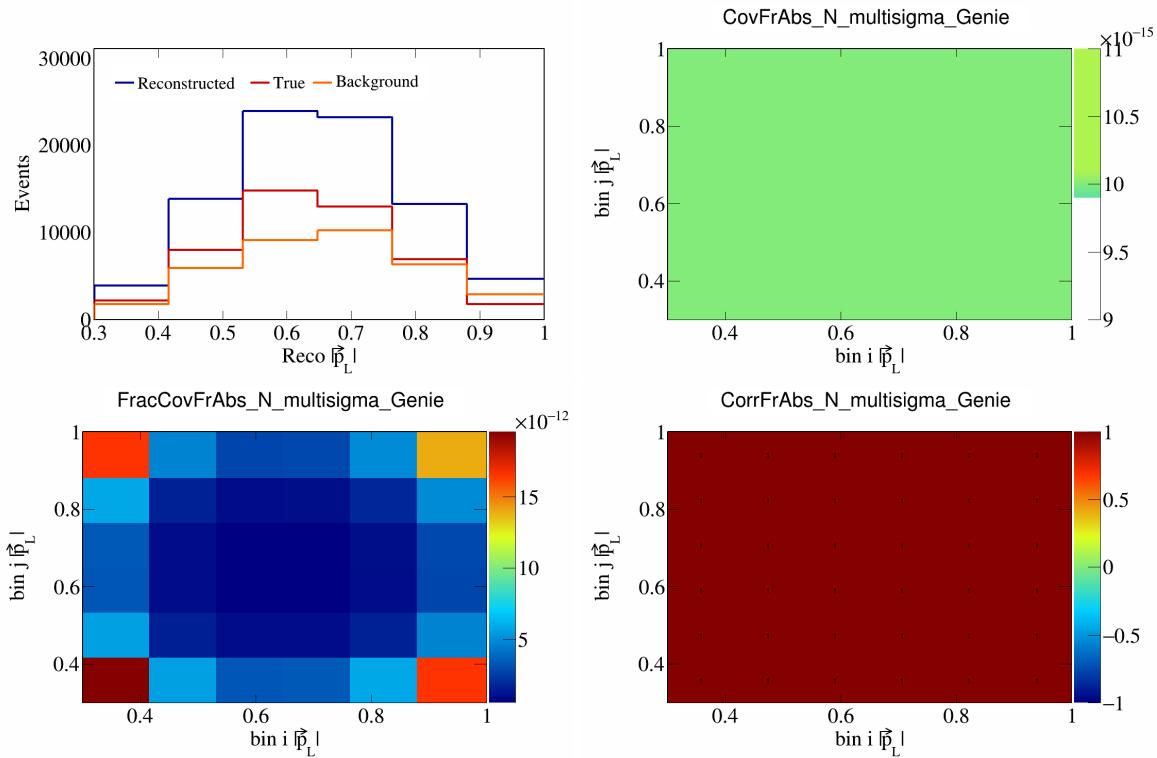


Figure 168: FrAbsN variations for  $|\vec{p}_L|$ .

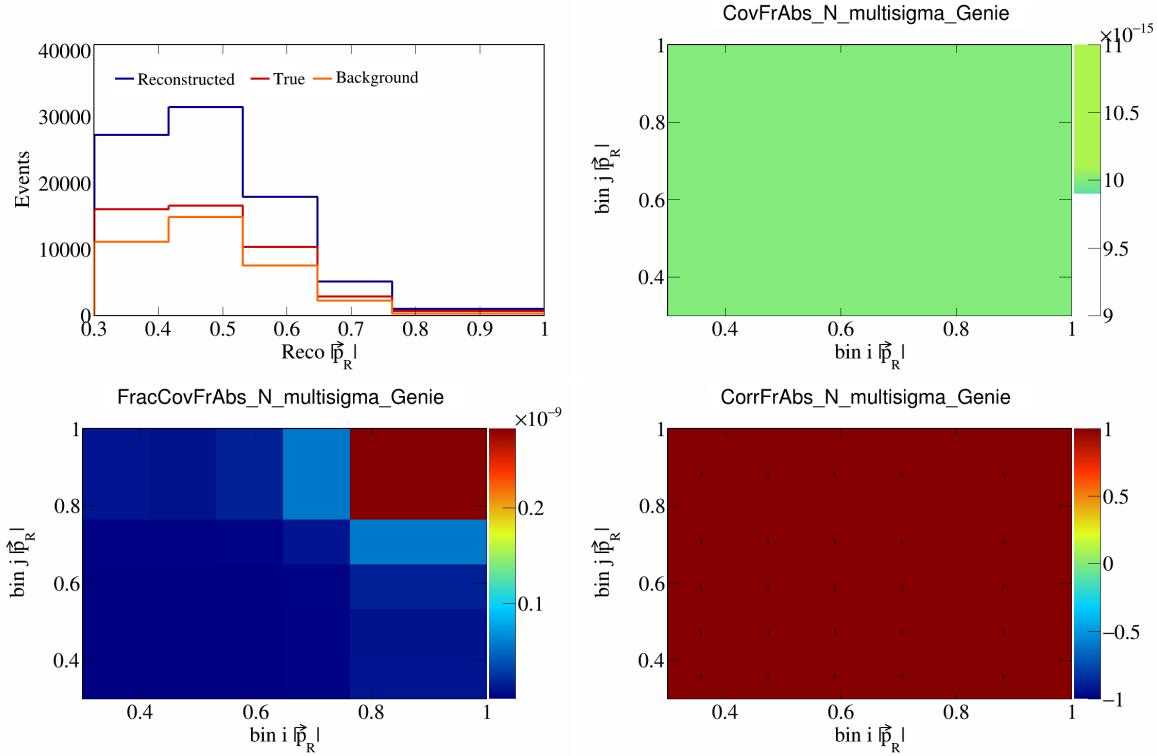


Figure 169: FrAbsN variations for  $|\vec{p}_R|$ .

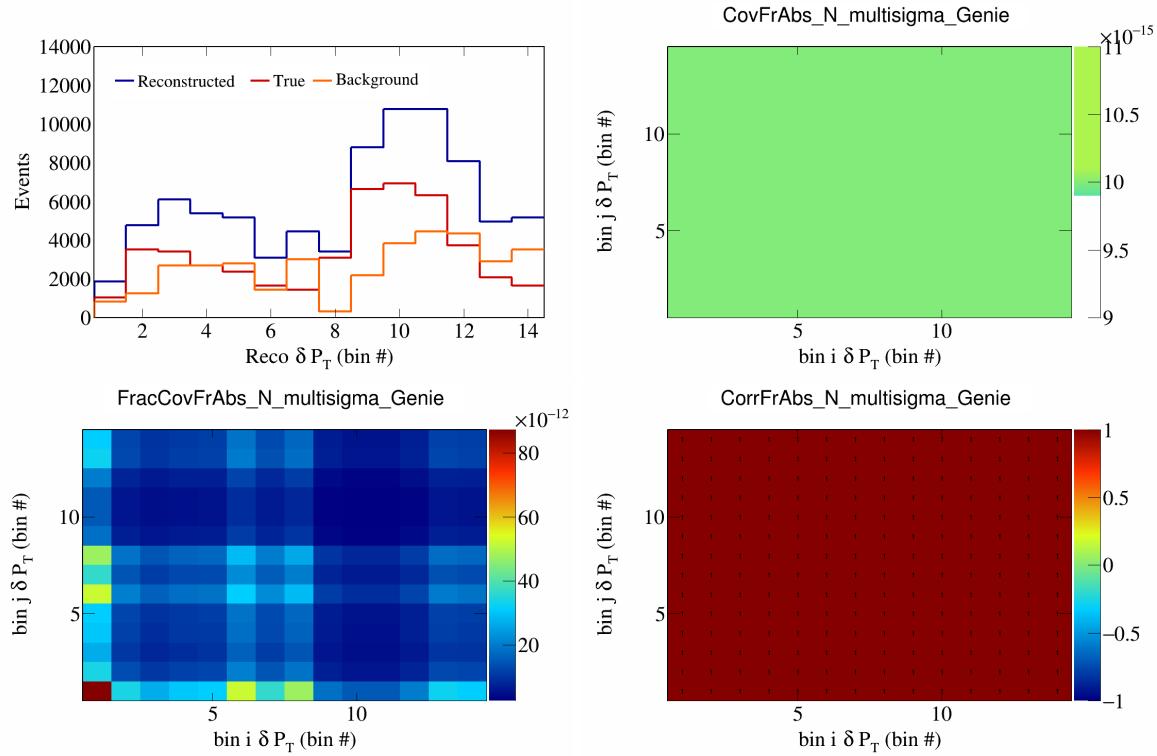


Figure 170: FrAbsN variations for  $\delta P_T$  in  $\cos(\theta_{\vec{p}_\mu})$ .

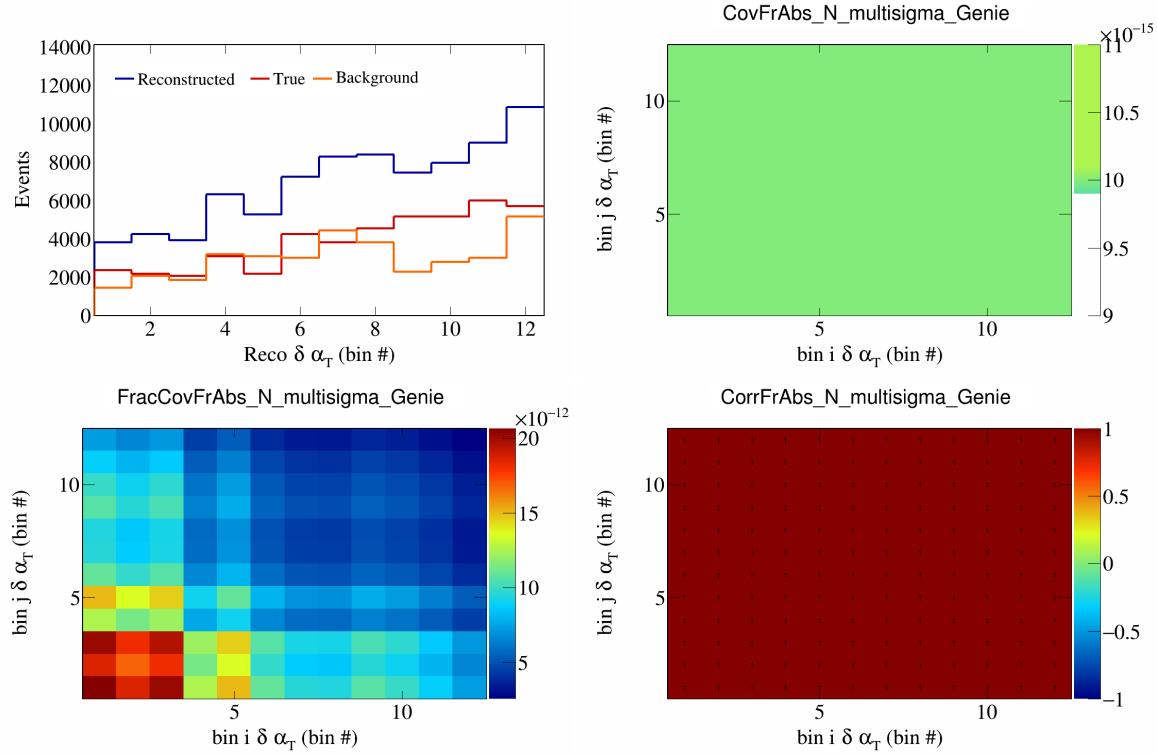


Figure 171: FrAbsN variations for  $\delta\alpha_T$  in  $\cos(\theta_{\vec{p}_\mu})$ .

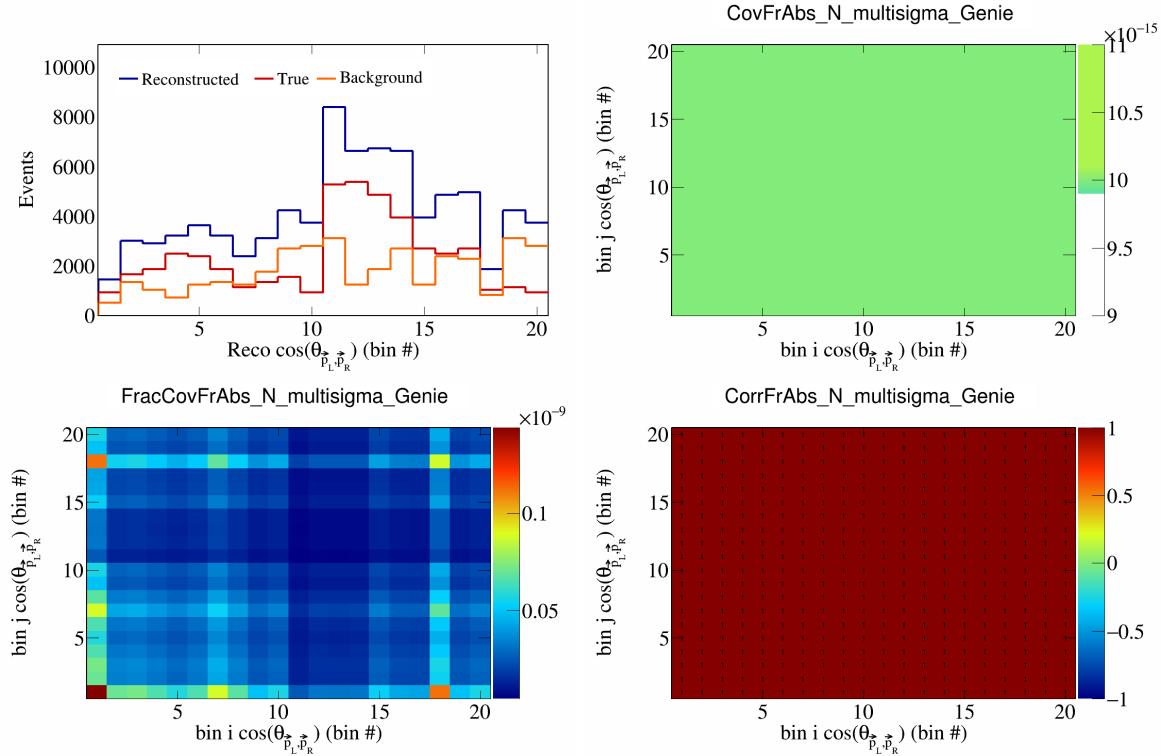


Figure 172: FrAbsN variations for  $\cos(\theta_{\vec{p}_L, \vec{p}_R})$  in  $\cos(\theta_{\vec{p}_\mu})$ .

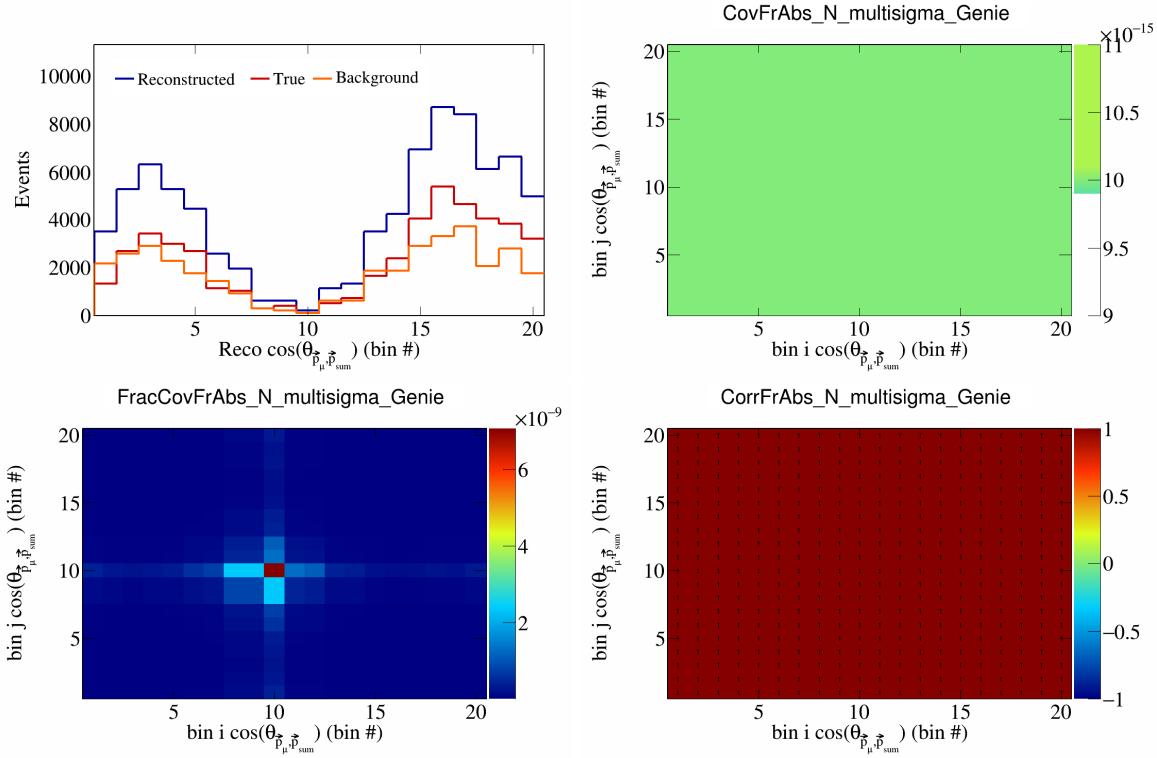


Figure 173: FrAbsN variations for  $\cos(\theta_{\vec{p}_\mu} \cdot \vec{p}_{\text{sum}})$  in  $\cos(\theta_{\vec{p}_\mu})$ .

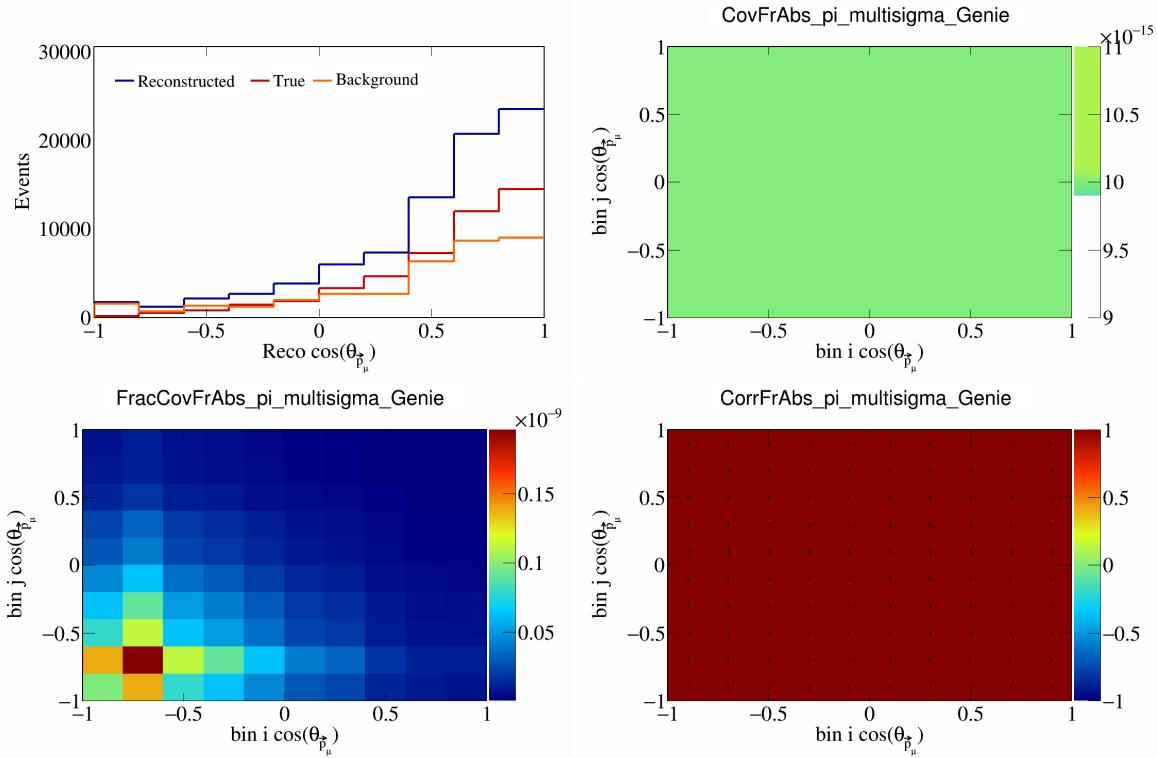


Figure 174: FrAbspi variations for  $\cos(\theta_{\vec{p}_\mu})$ .

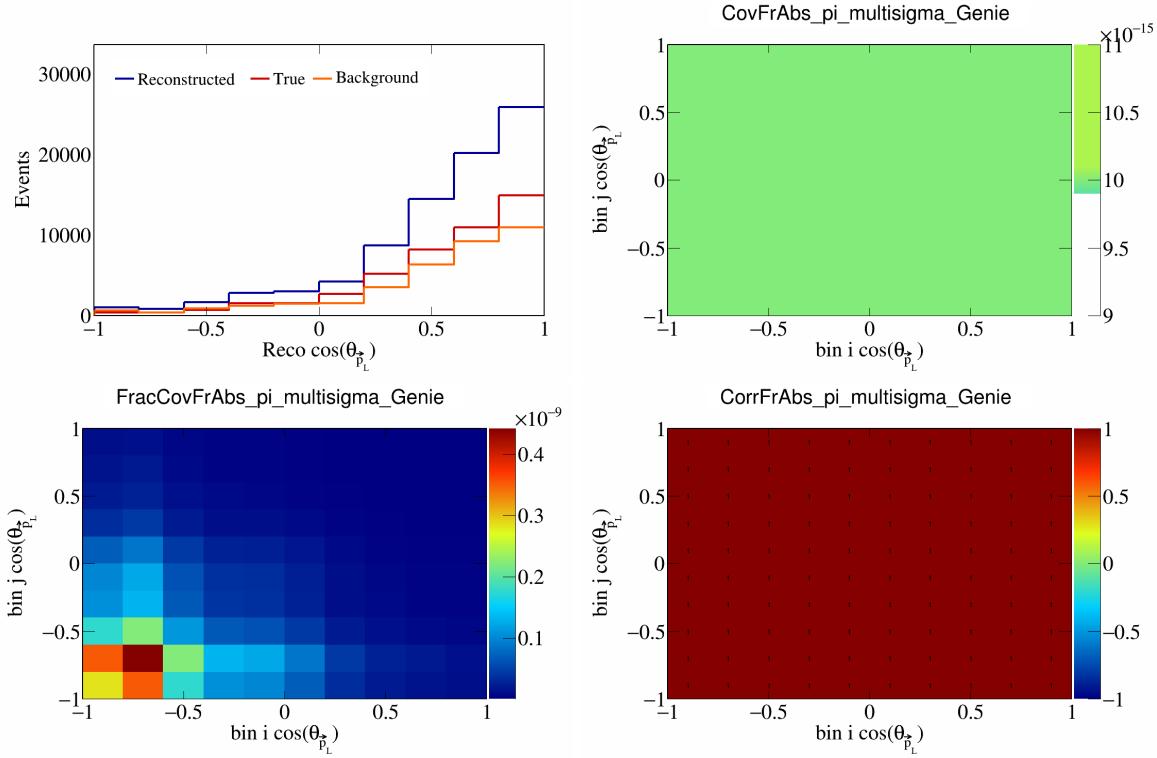


Figure 175: FrAbspi variations for  $\cos(\theta_{\vec{p}_L})$ .

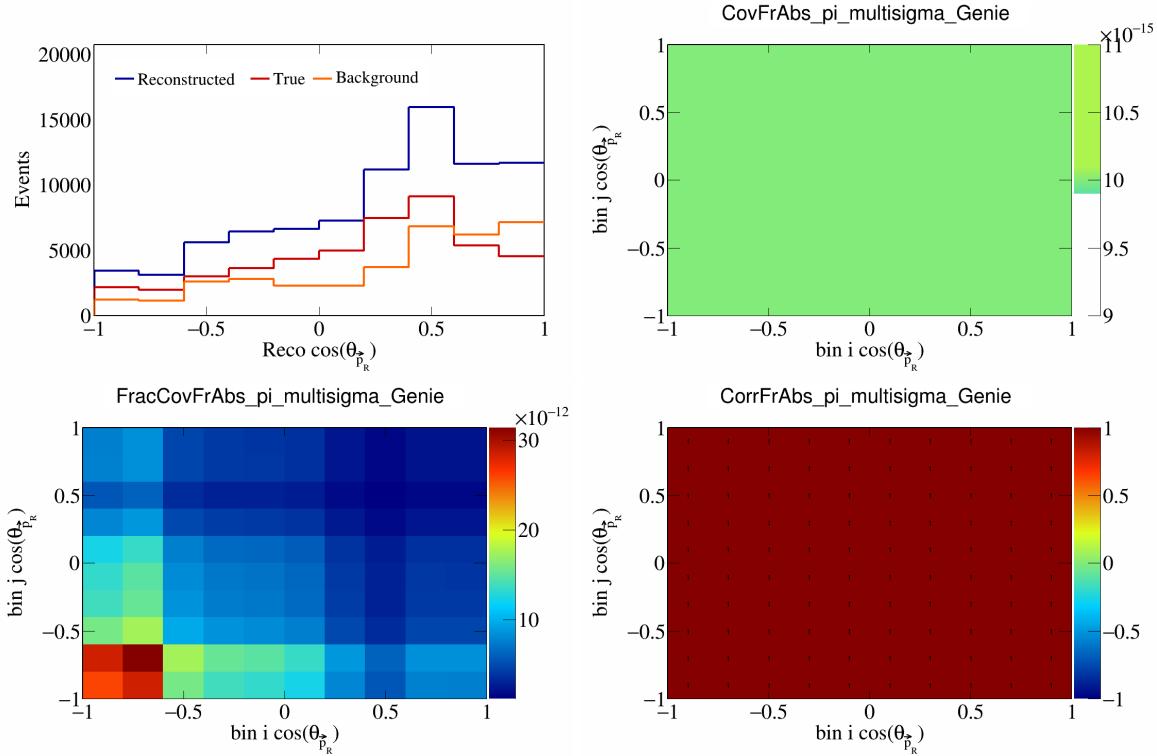


Figure 176: FrAbspi variations for  $\cos(\theta_{\vec{p}_R})$ .

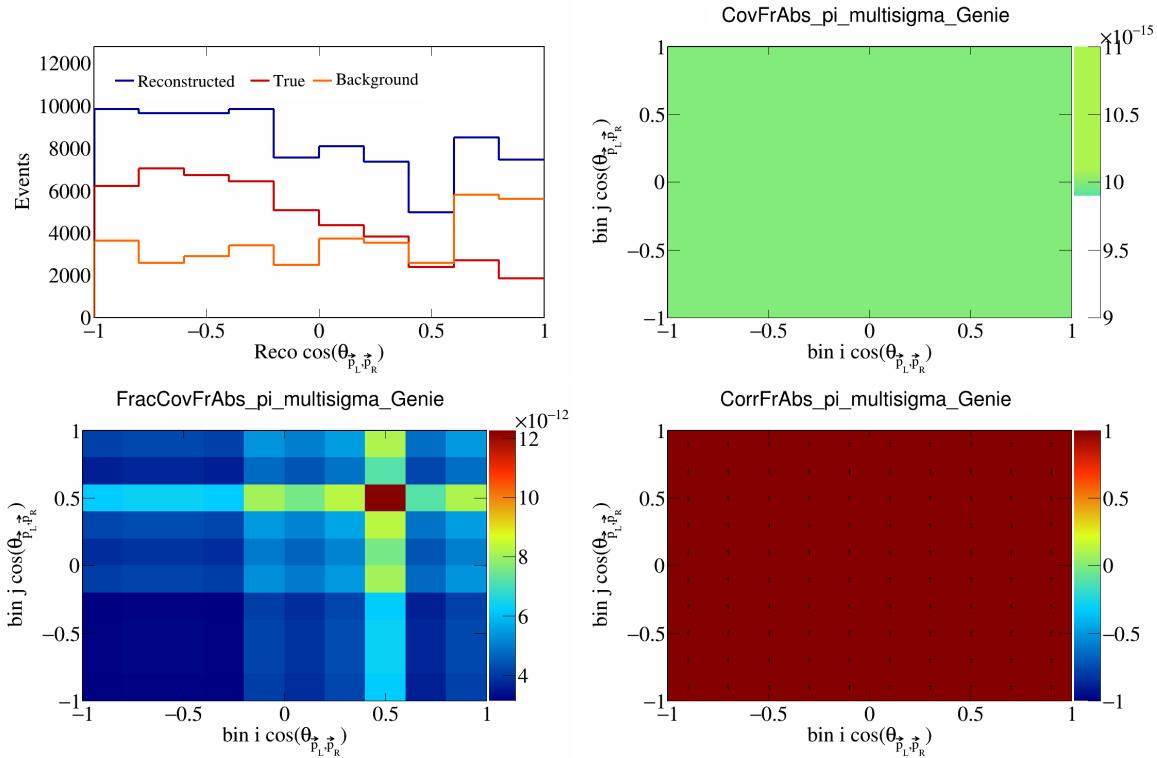


Figure 177: FrAbspi variations for  $\cos(\theta_{\vec{p}_L, \vec{p}_R})$ .

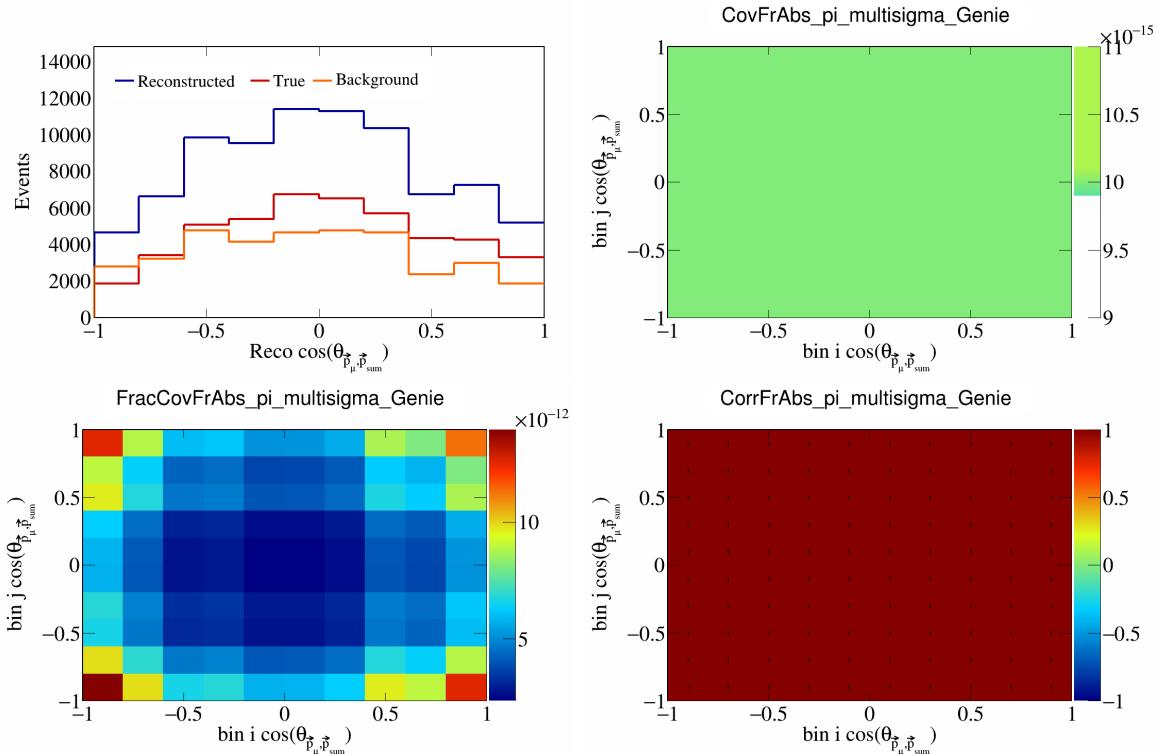


Figure 178: FrAbspi variations for  $\cos(\theta_{\vec{p}_\mu, \vec{p}_{\text{sum}}})$ .

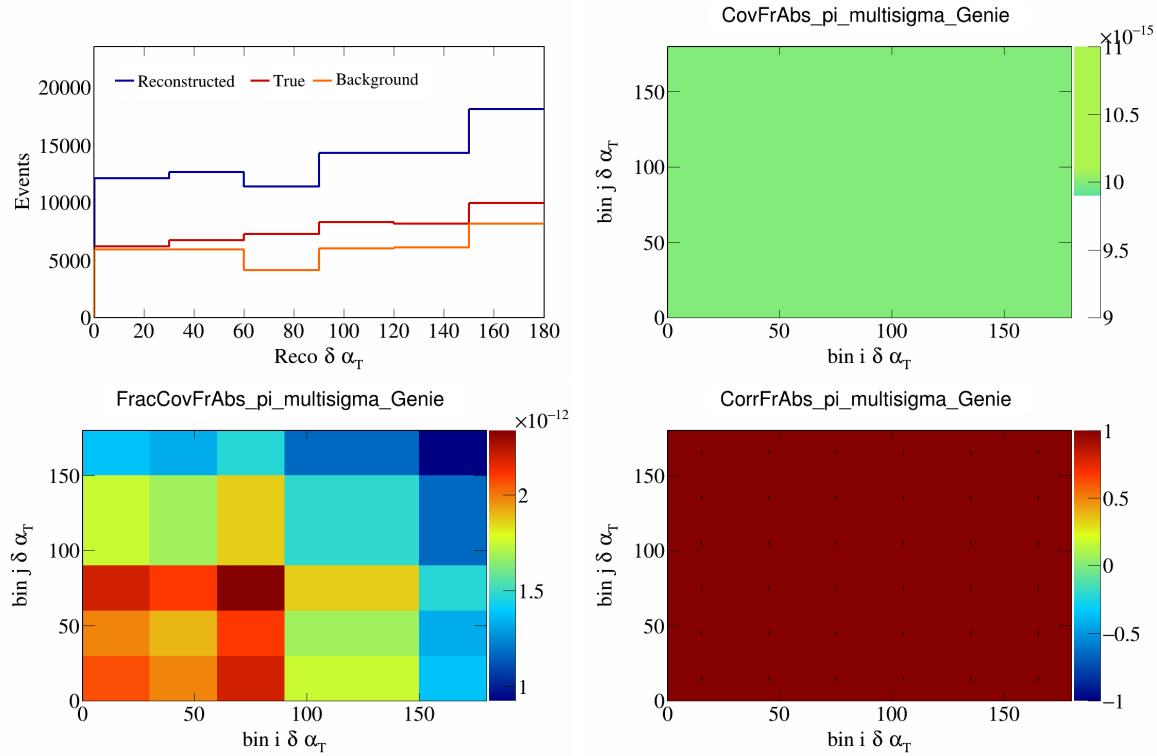


Figure 179: FrAbspi variations for  $\delta \alpha_T$ .

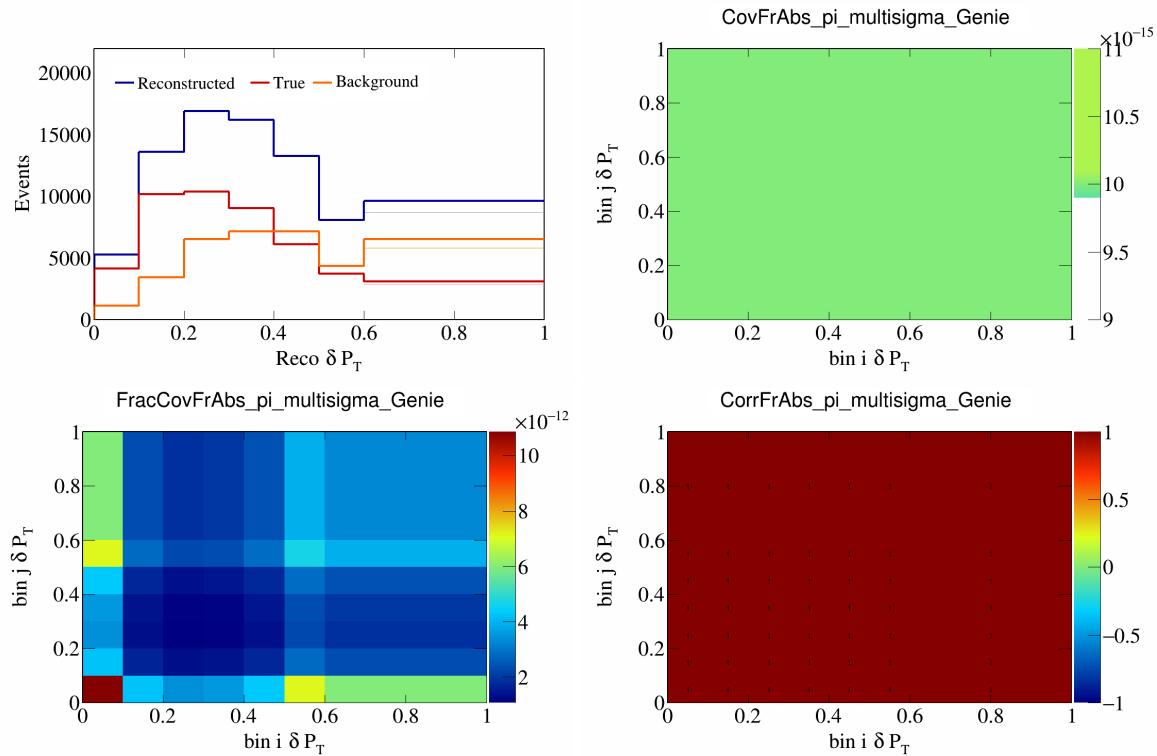


Figure 180: FrAbspi variations for  $\delta P_T$ .

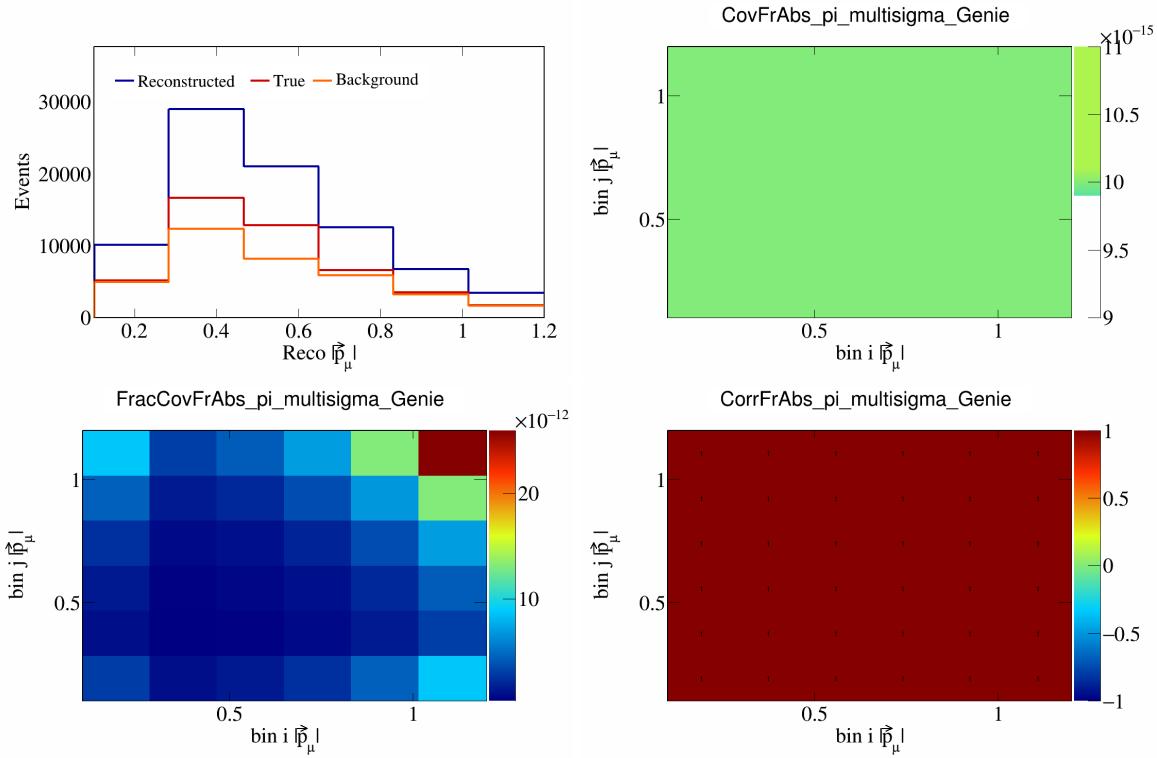


Figure 181: FrAbspi variations for  $|\vec{p}_\mu|$ .

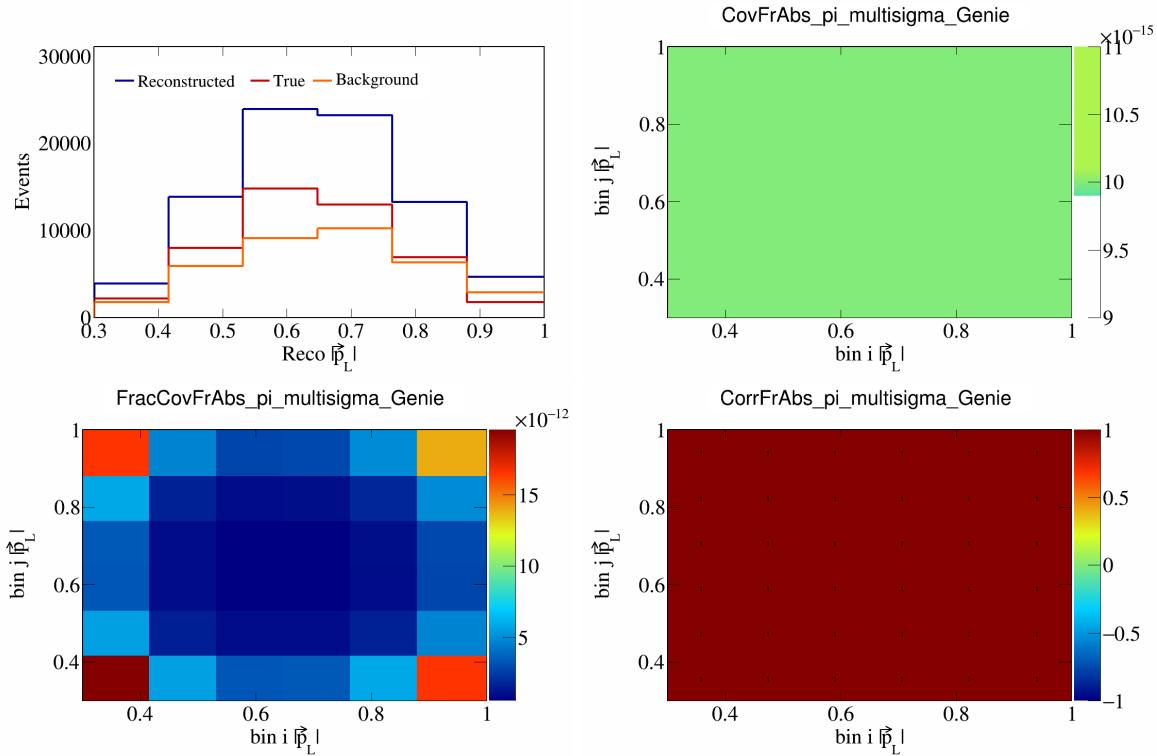


Figure 182: FrAbspi variations for  $|\vec{p}_L|$ .

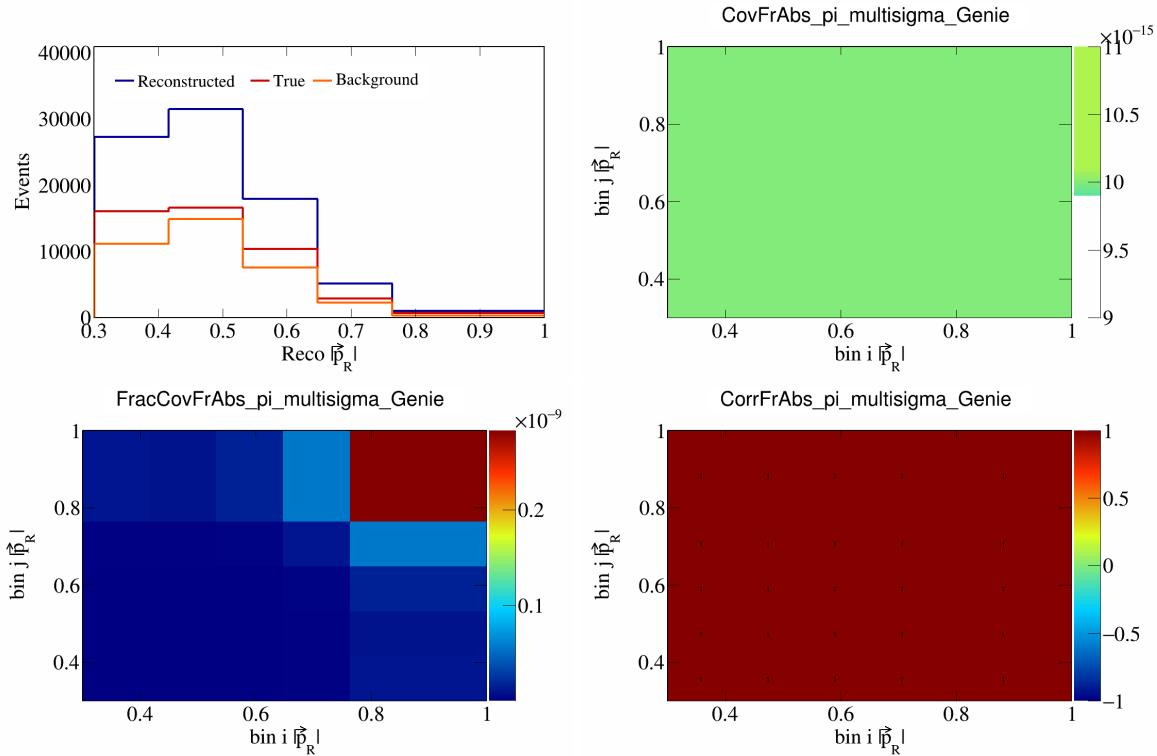


Figure 183: FrAbspi variations for  $|\vec{p}_R|$ .

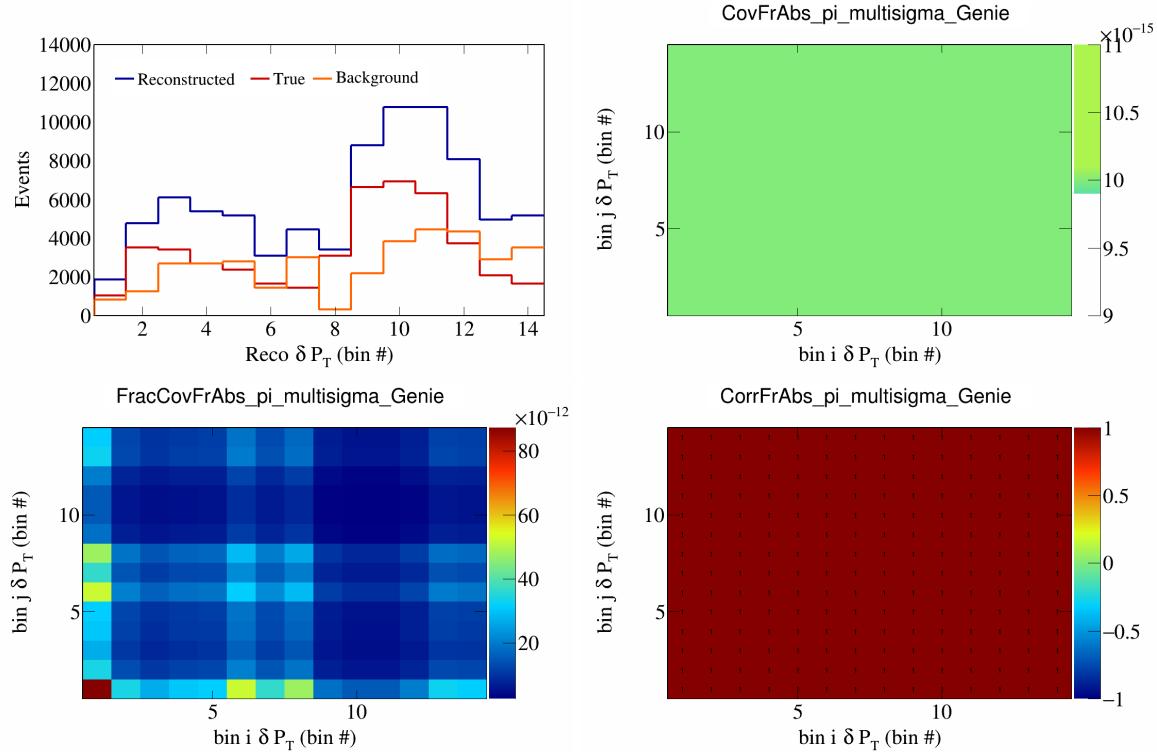


Figure 184: FrAbspi variations for  $\delta P_T$  in  $\cos(\theta_{\vec{p}_\mu})$ .

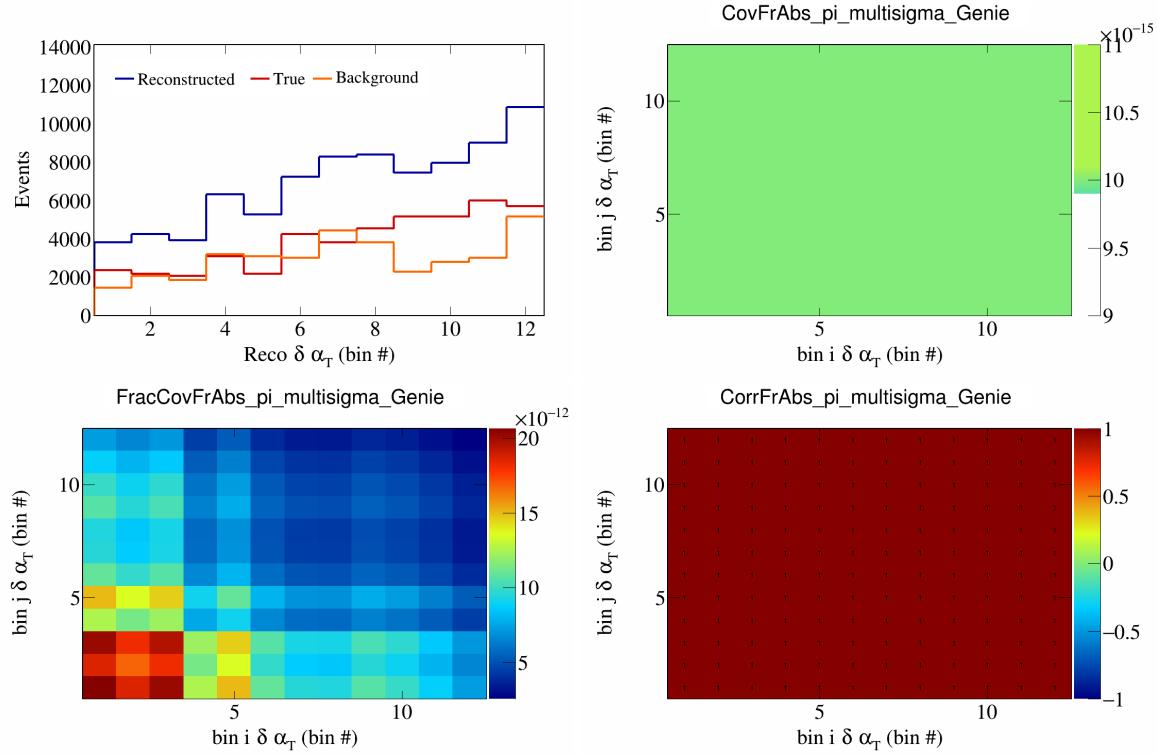


Figure 185: FrAbspi variations for  $\delta\alpha_T$  in  $\cos(\theta_{\vec{p}_\mu})$ .

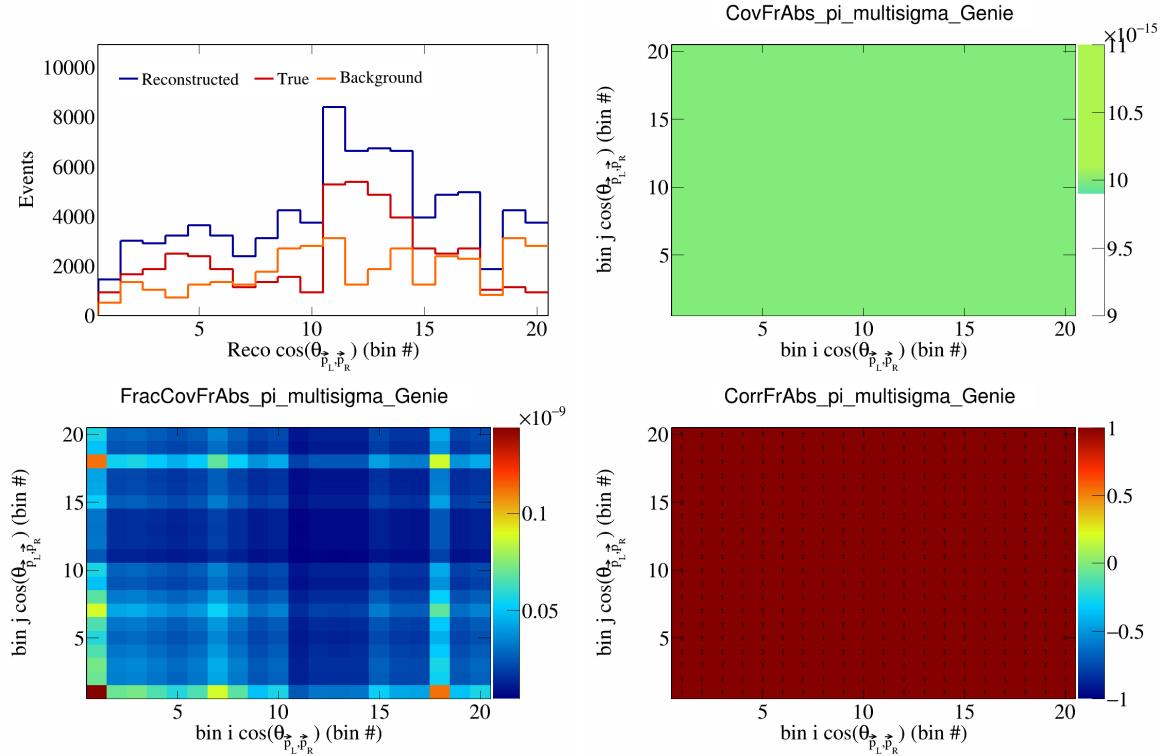


Figure 186: FrAbspi variations for  $\cos(\theta_{\vec{p}_L, \vec{p}_R})$  in  $\cos(\theta_{\vec{p}_\mu})$ .

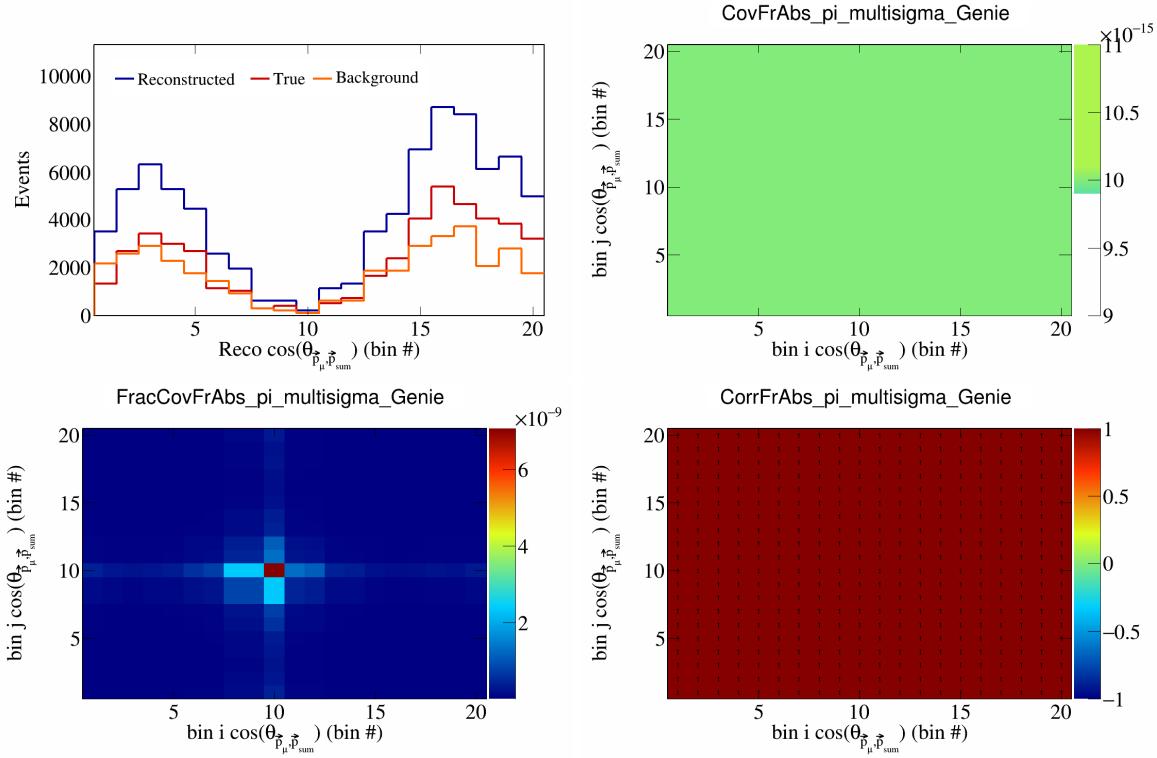


Figure 187: FrAbspi variations for  $\cos(\theta_{\vec{p}_\mu}, \vec{p}_{\text{sum}})$  in  $\cos(\theta_{\vec{p}_\mu})$ .

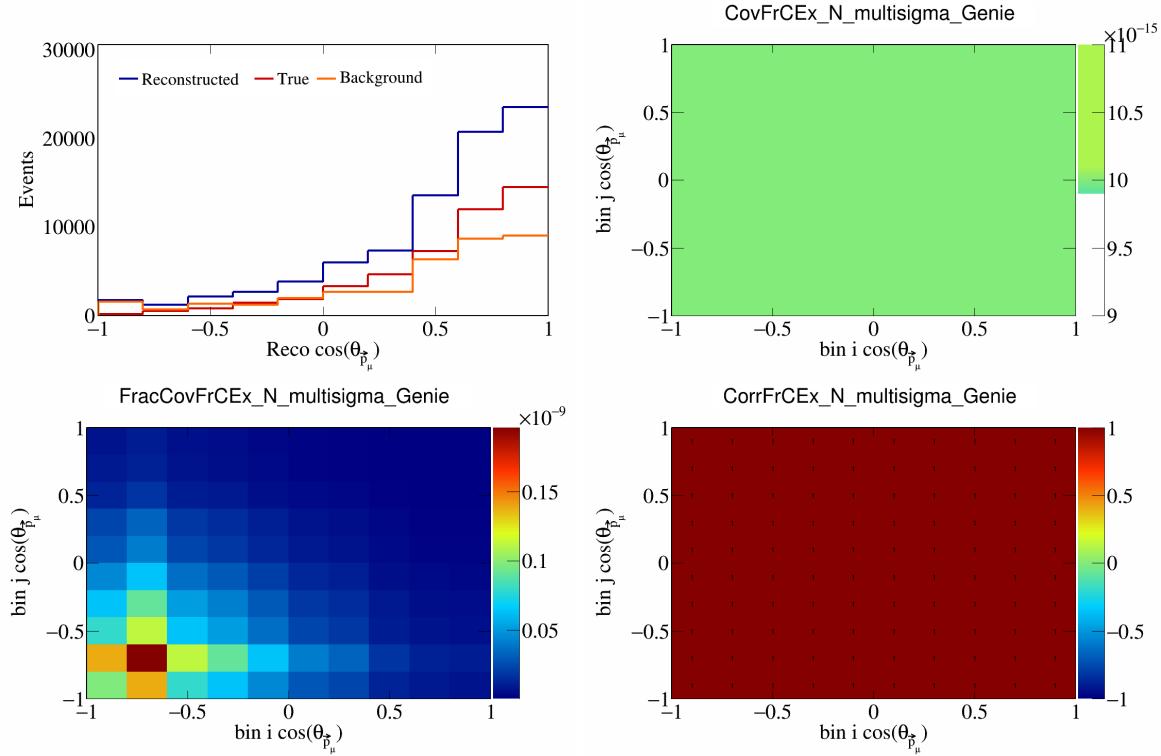


Figure 188: FrCExN variations for  $\cos(\theta_{\vec{p}_\mu})$ .

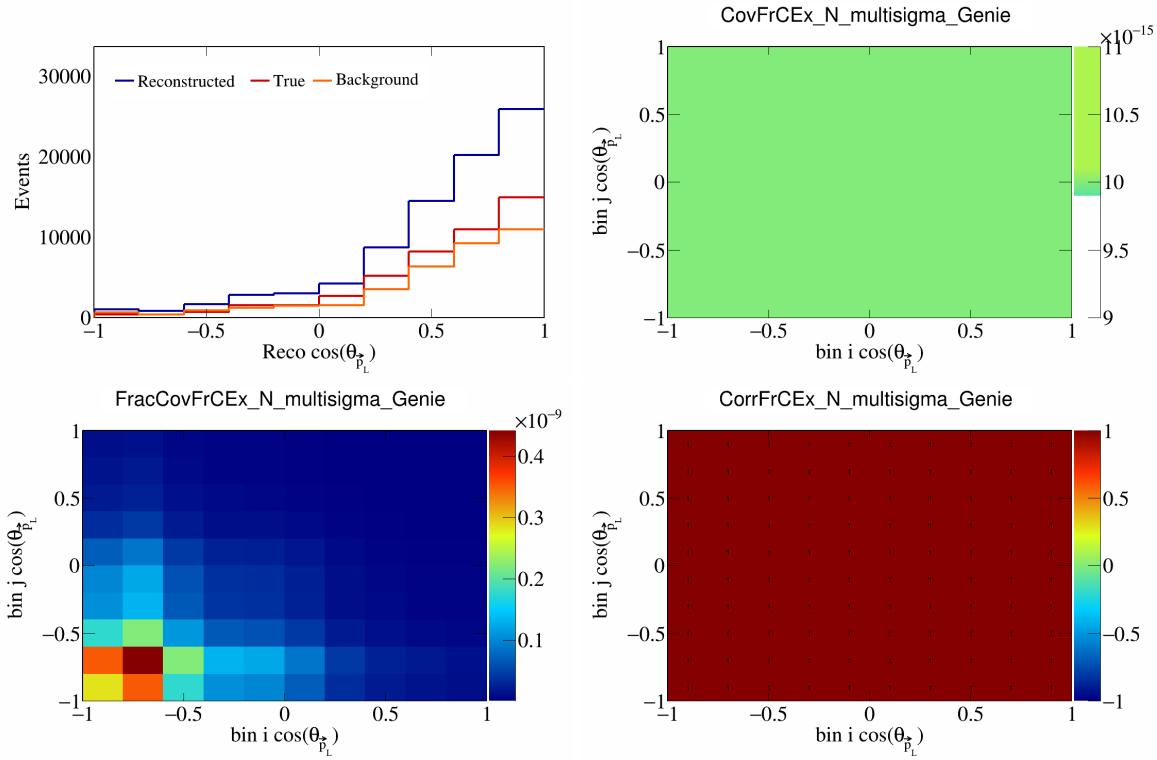


Figure 189: FrCExN variations for  $\cos(\theta_{\vec{p}_L})$ .

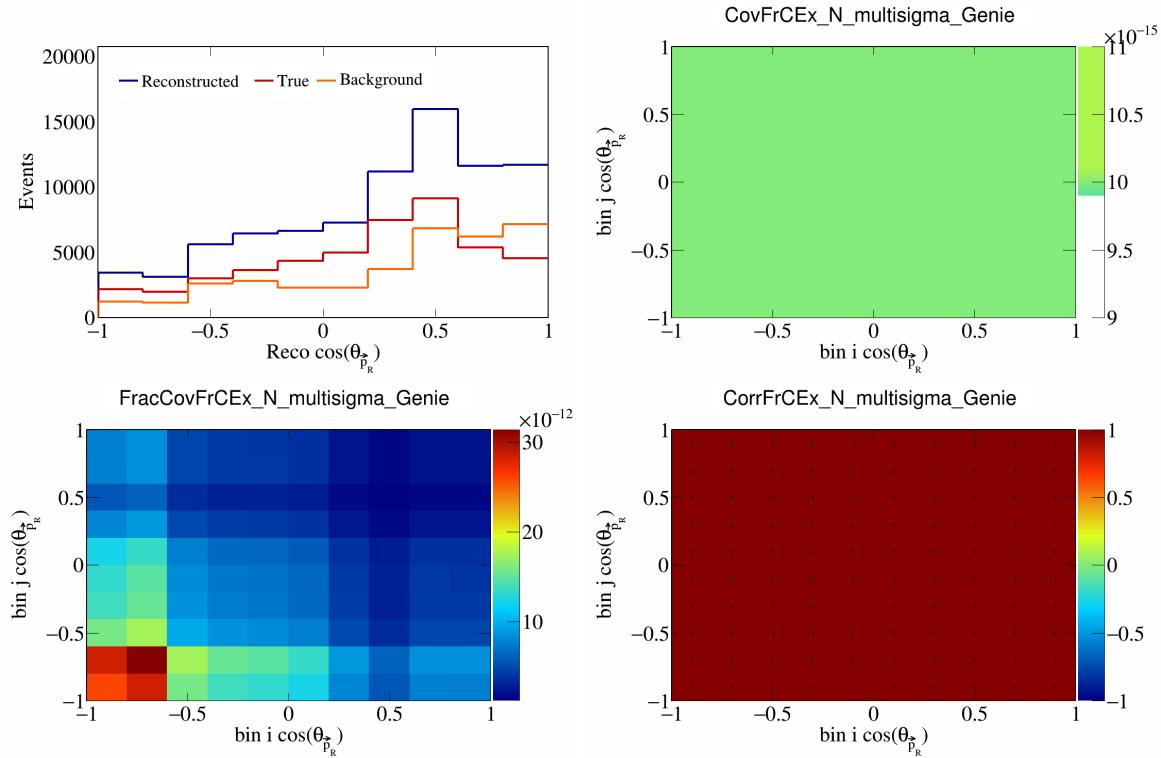


Figure 190: FrCExN variations for  $\cos(\theta_{\vec{p}_R})$ .

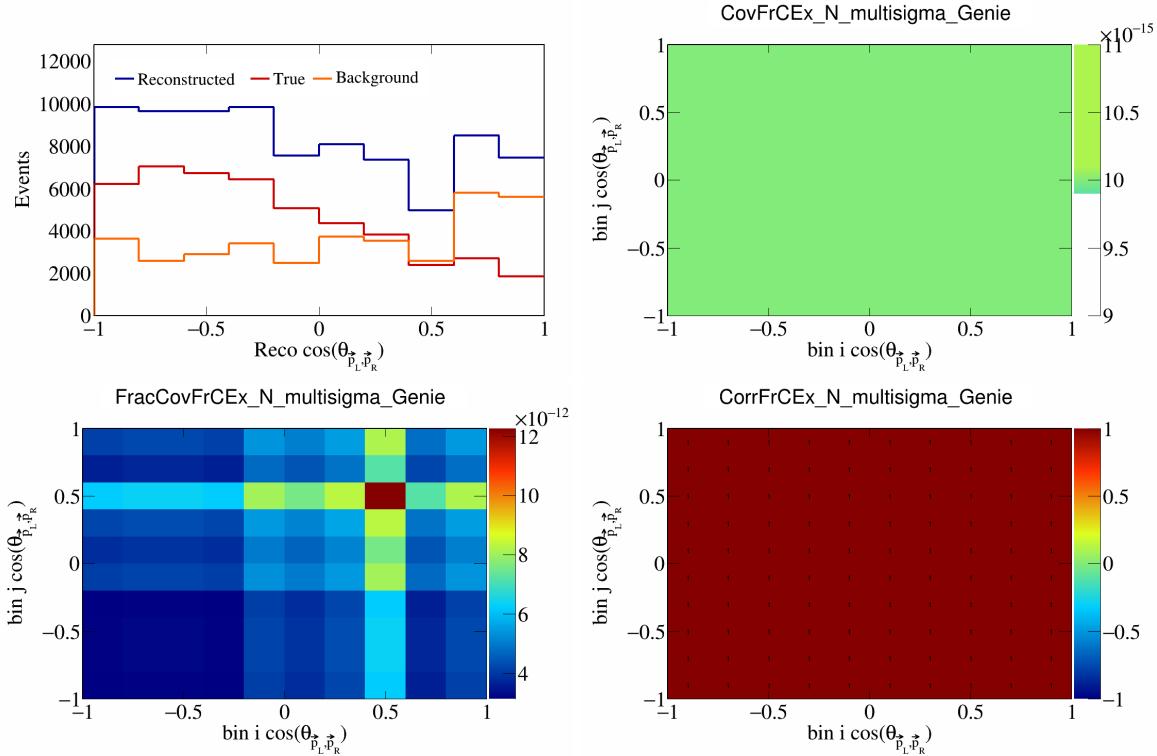


Figure 191: FrCEExN variations for  $\cos(\theta_{\vec{p}_L, \vec{p}_R})$ .

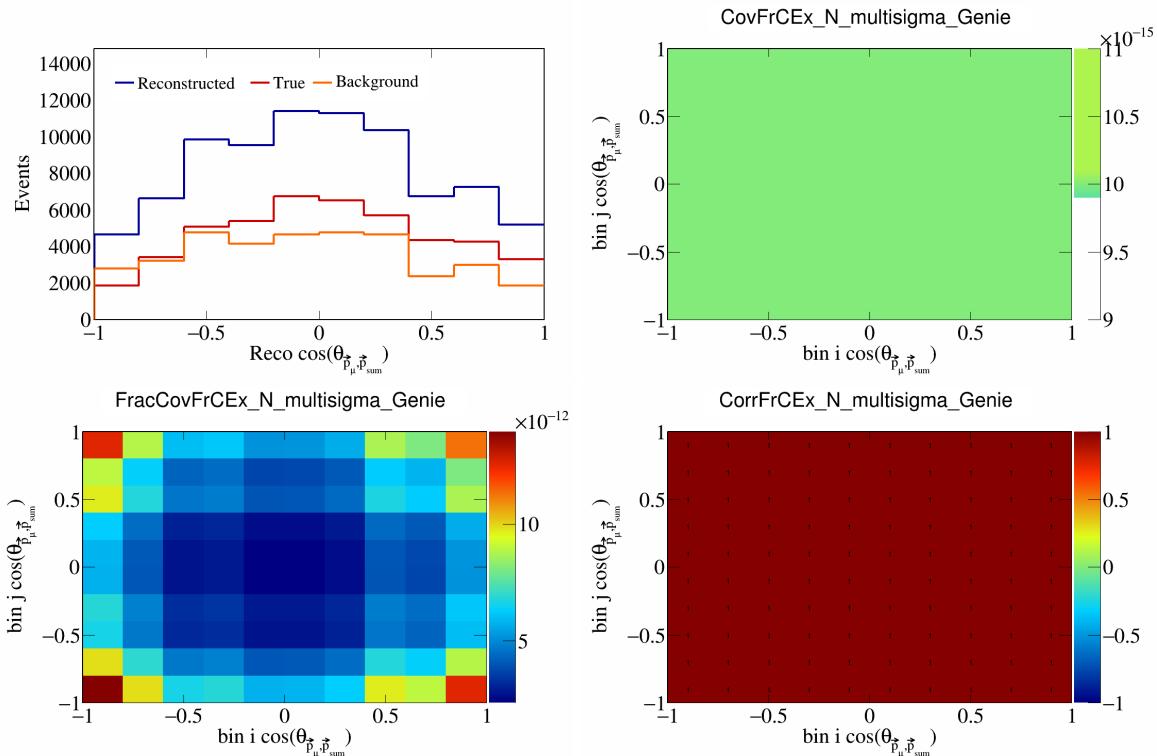


Figure 192: FrCEExN variations for  $\cos(\theta_{\vec{p}_\mu, \vec{p}_{\text{sum}}})$ .

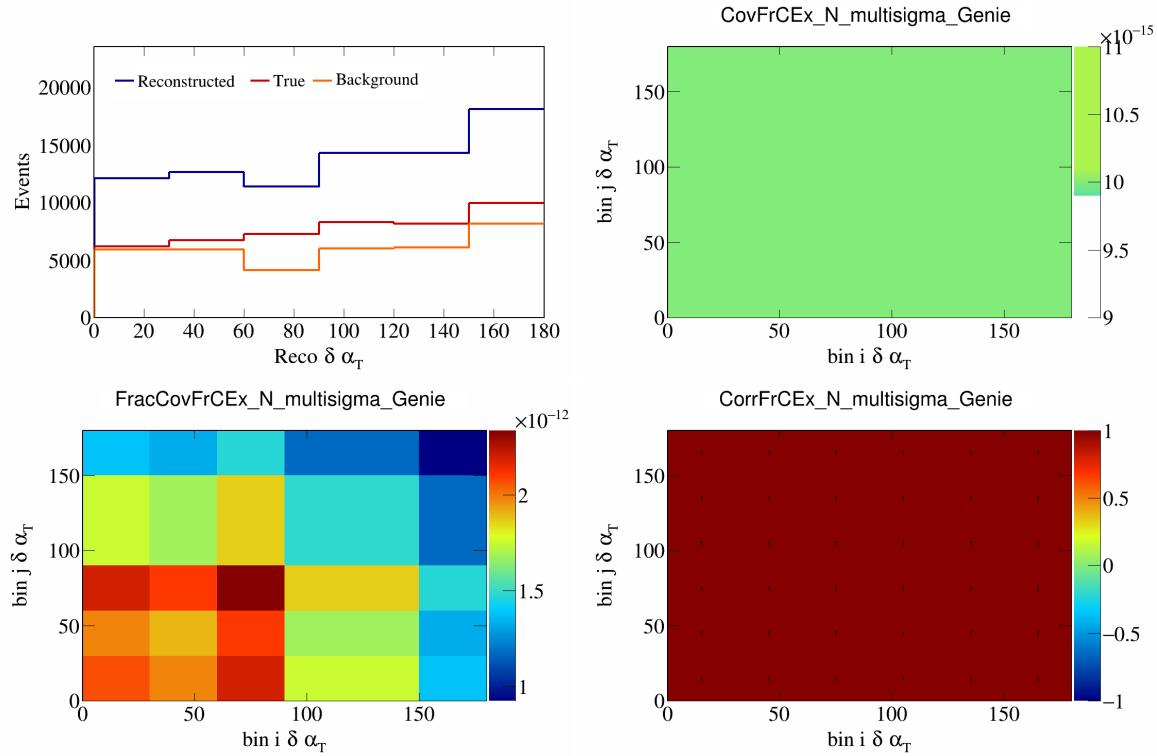


Figure 193: FrCEExN variations for  $\delta\alpha_T$ .

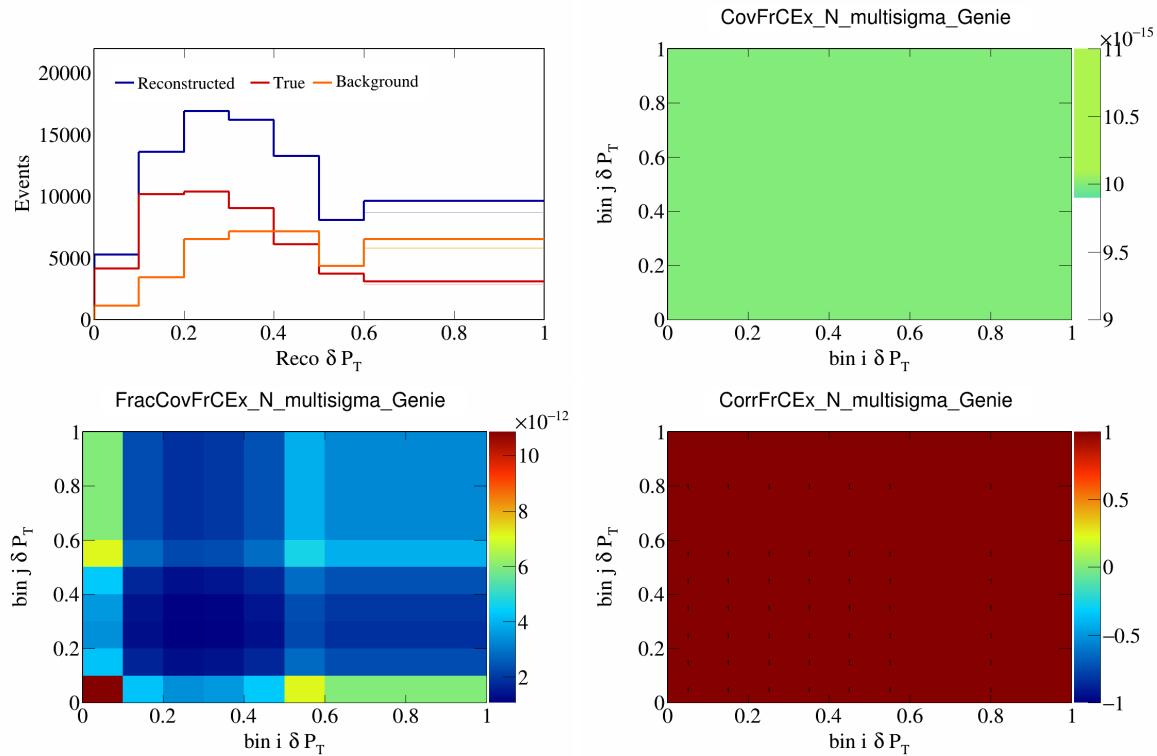


Figure 194: FrCEExN variations for  $\delta P_T$ .

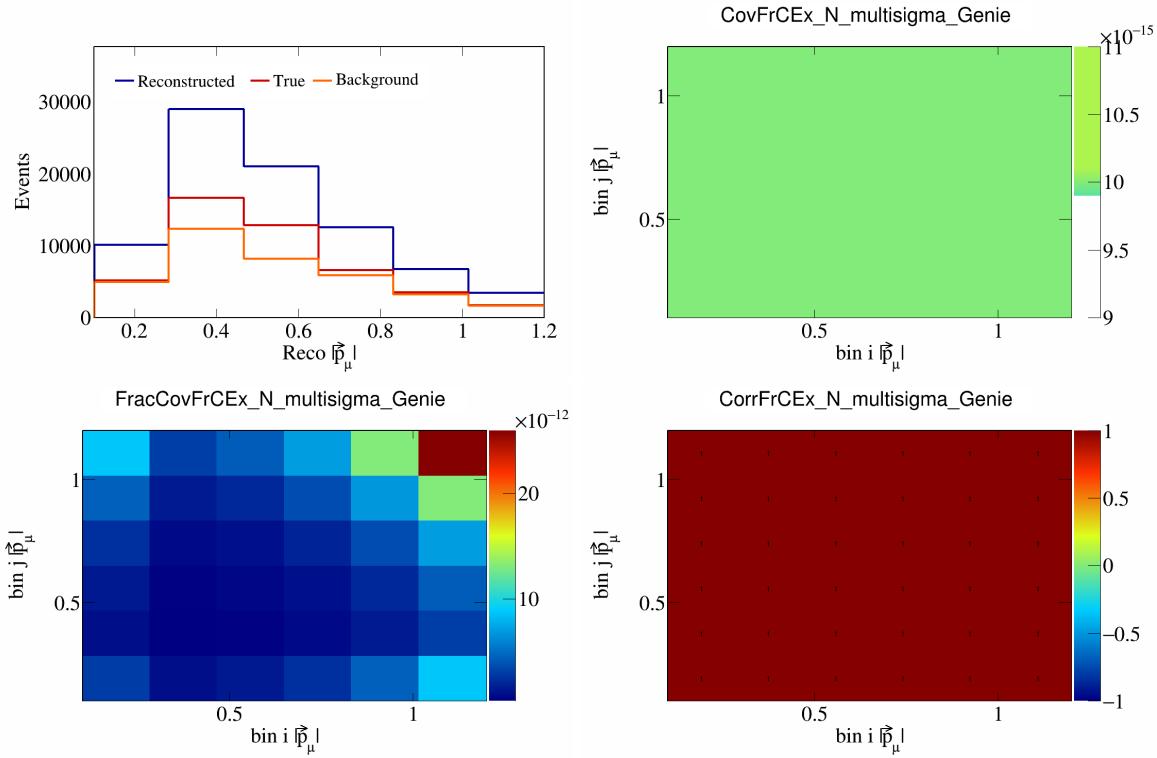


Figure 195: FrCExN variations for  $|\vec{p}_\mu|$ .

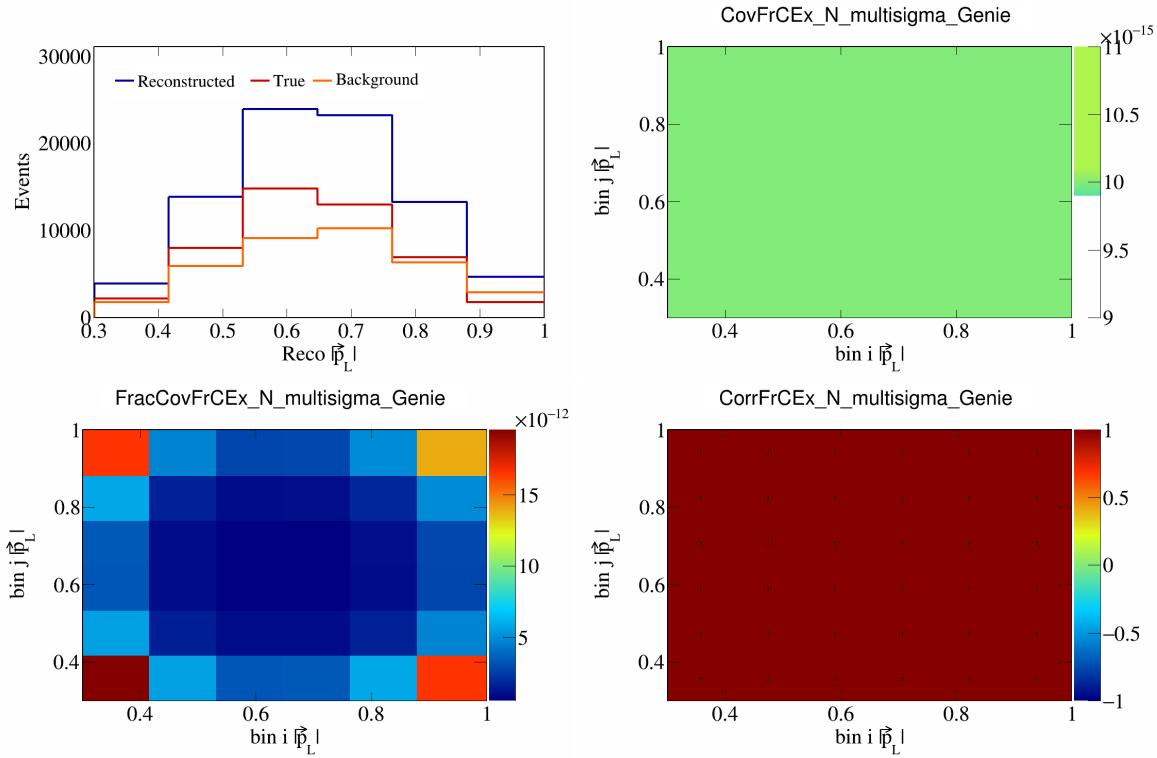


Figure 196: FrCExN variations for  $|\vec{p}_L|$ .

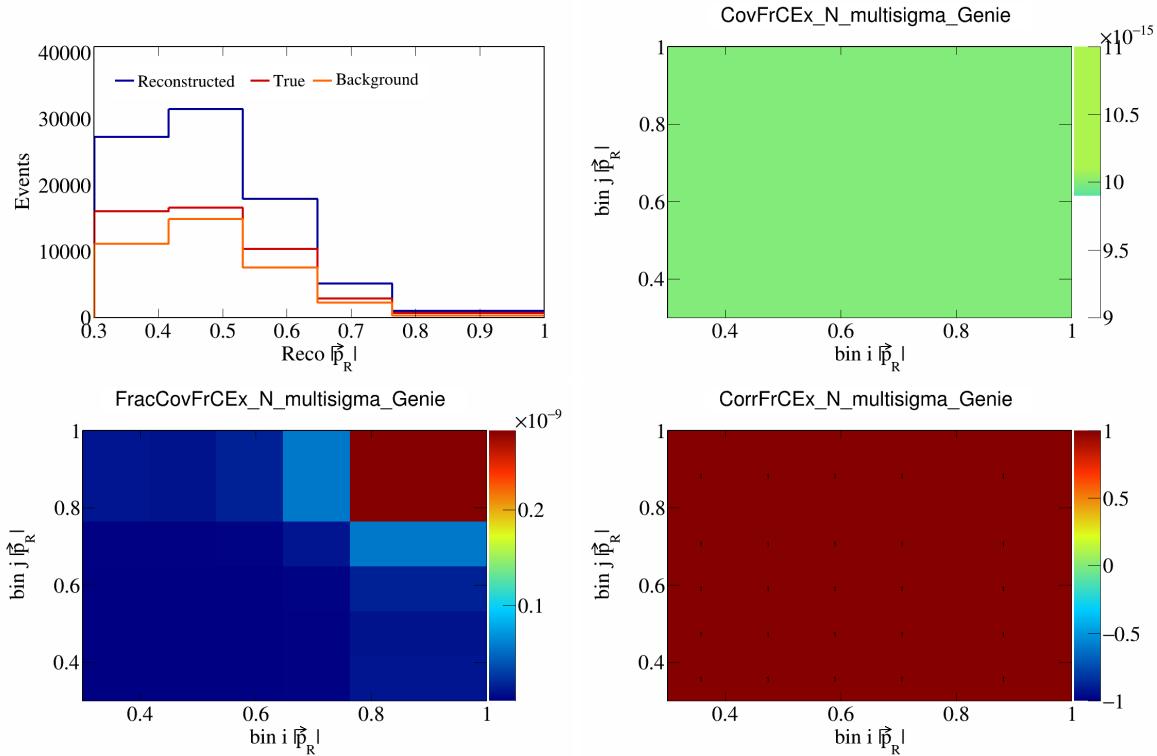


Figure 197: FrCEExN variations for  $|\vec{p}_R|$ .

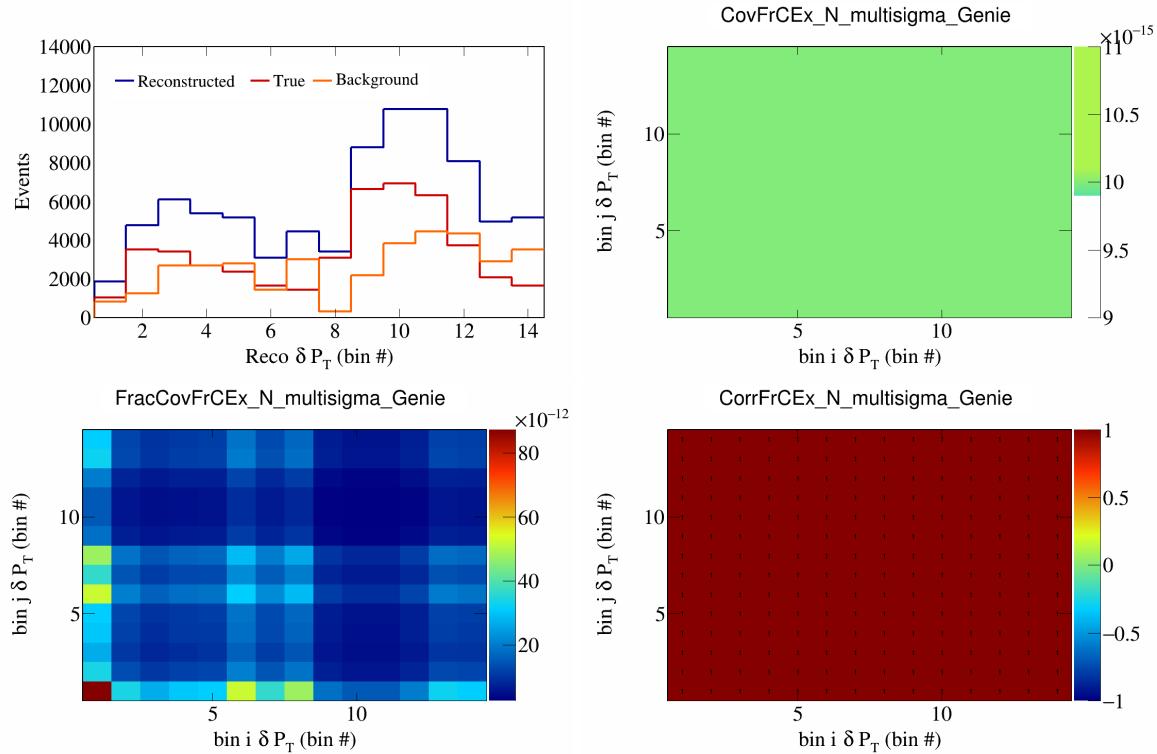


Figure 198: FrCEExN variations for  $\delta P_T$  in  $\cos(\theta_{\vec{p}_\mu})$ .

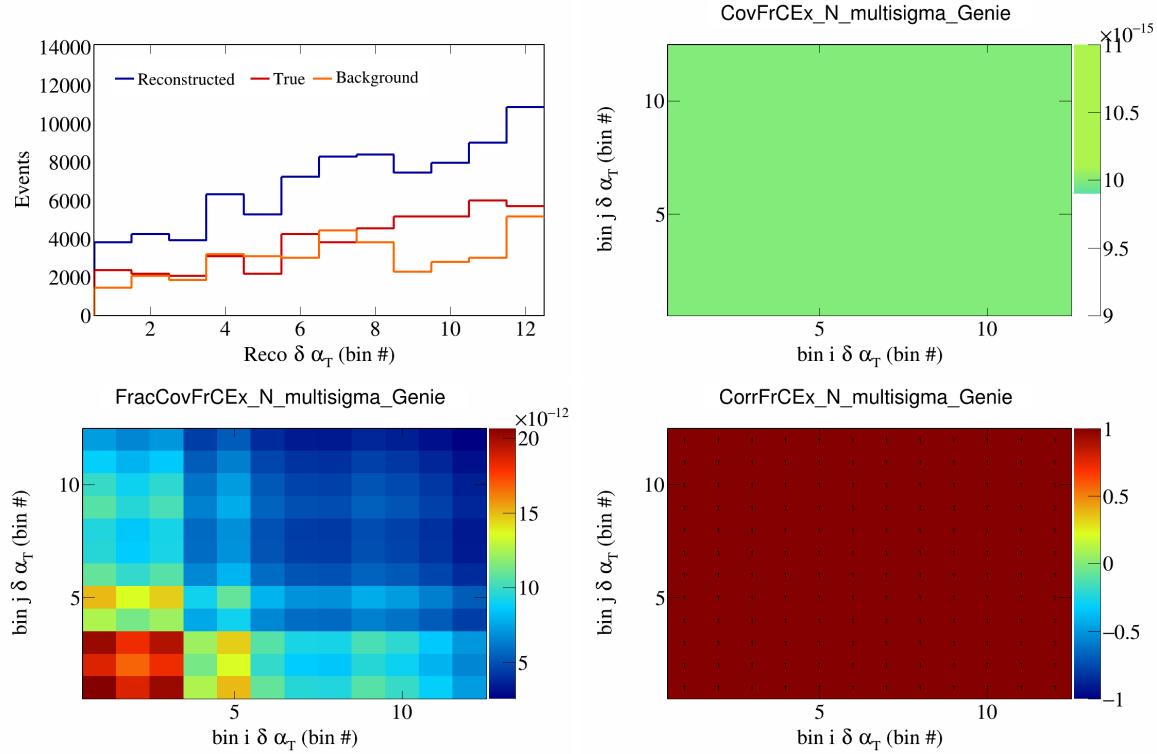


Figure 199: FrCEExN variations for  $\delta\alpha_T$  in  $\cos(\theta_{\vec{p}_\mu})$ .

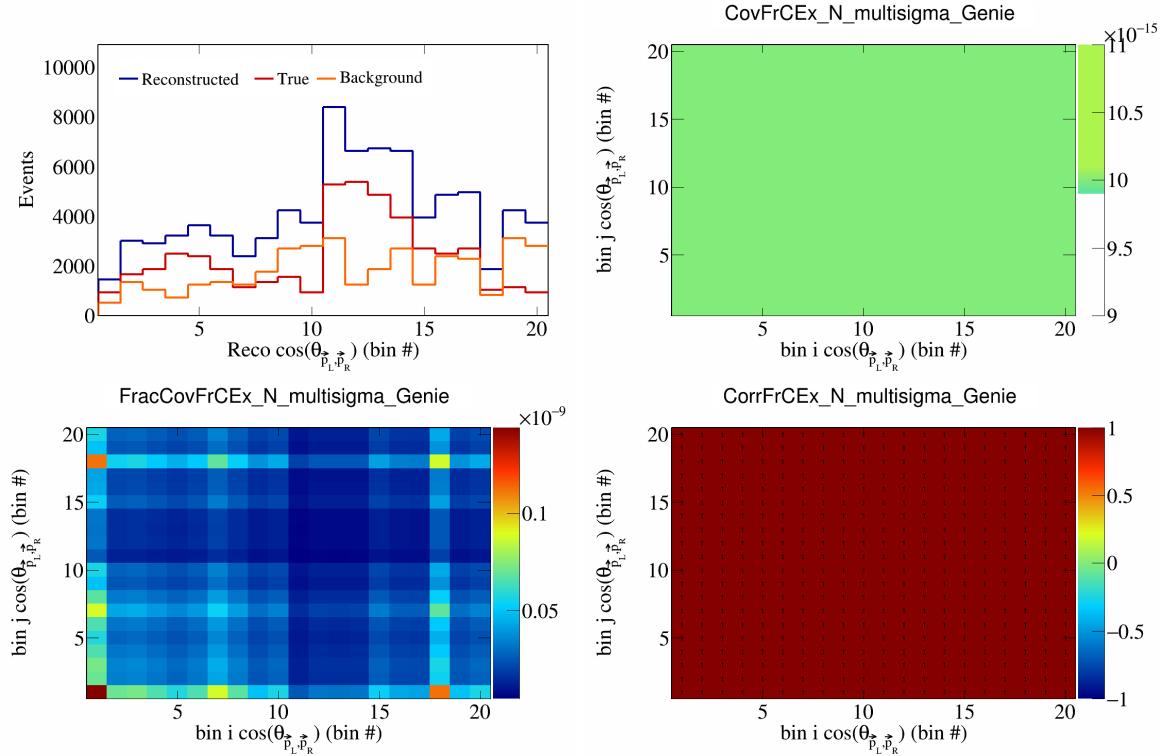


Figure 200: FrCEExN variations for  $\cos(\theta_{\vec{p}_L, \vec{p}_R})$  in  $\cos(\theta_{\vec{p}_\mu})$ .

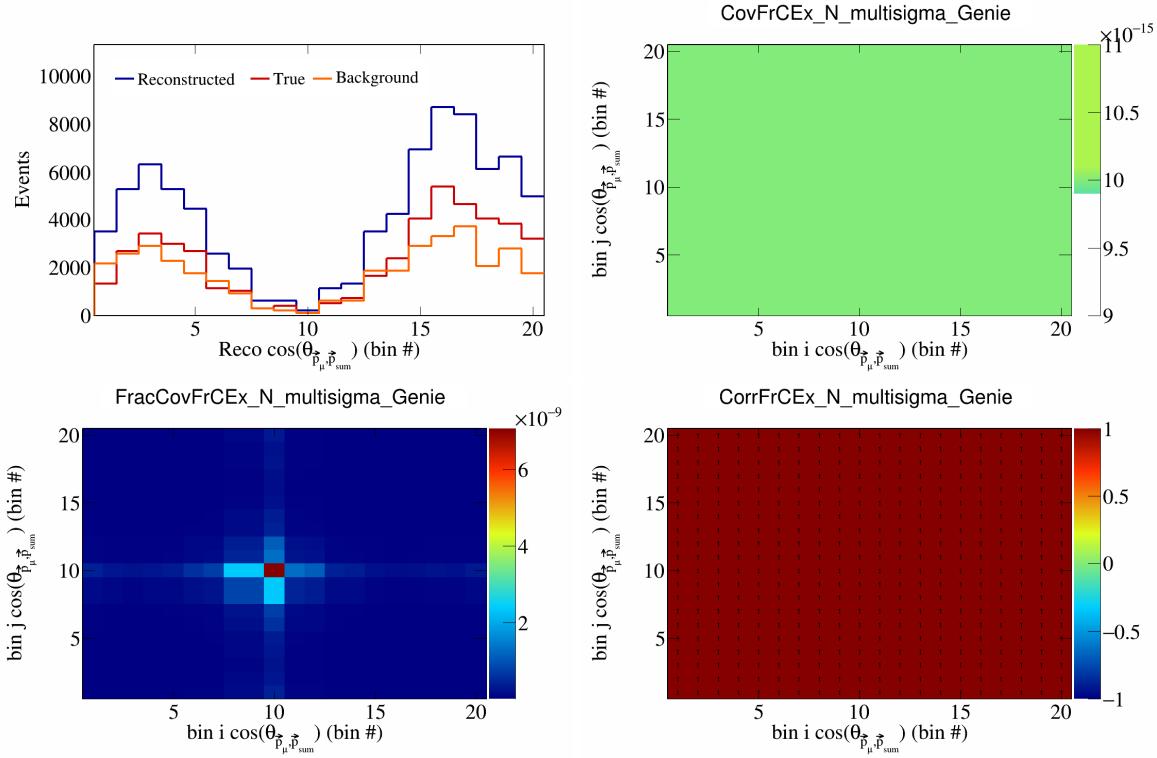


Figure 201: FrCEExN variations for  $\cos(\theta_{\vec{p}_\mu, \vec{p}_{\text{sum}}})$  in  $\cos(\theta_{\vec{p}_\mu})$ .

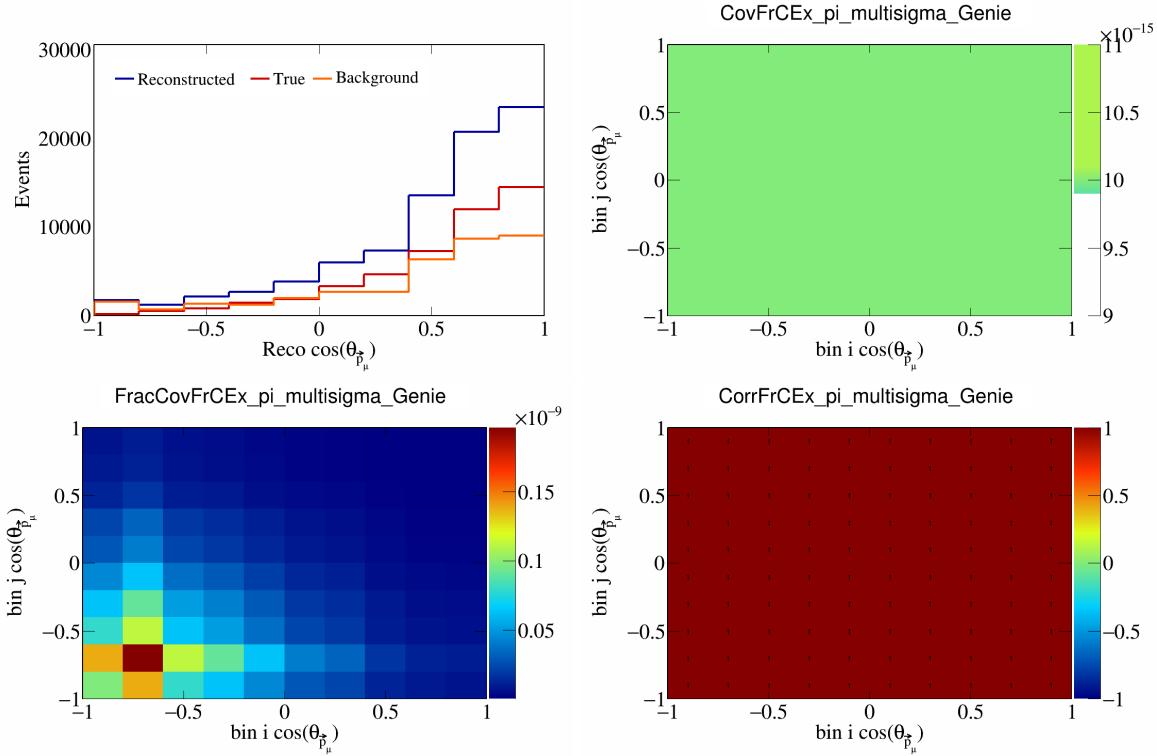


Figure 202: FrCEExpi variations for  $\cos(\theta_{\vec{p}_\mu})$ .

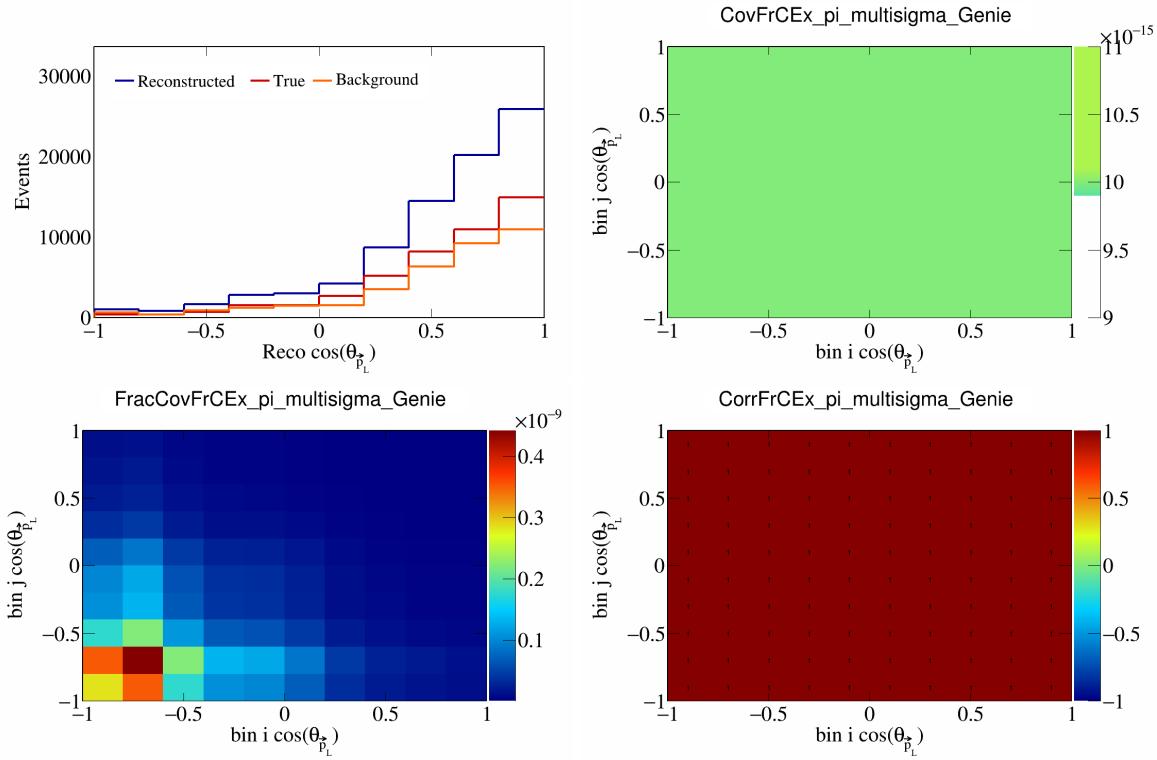


Figure 203: FrCExpi variations for  $\cos(\theta_{\vec{p}_L})$ .

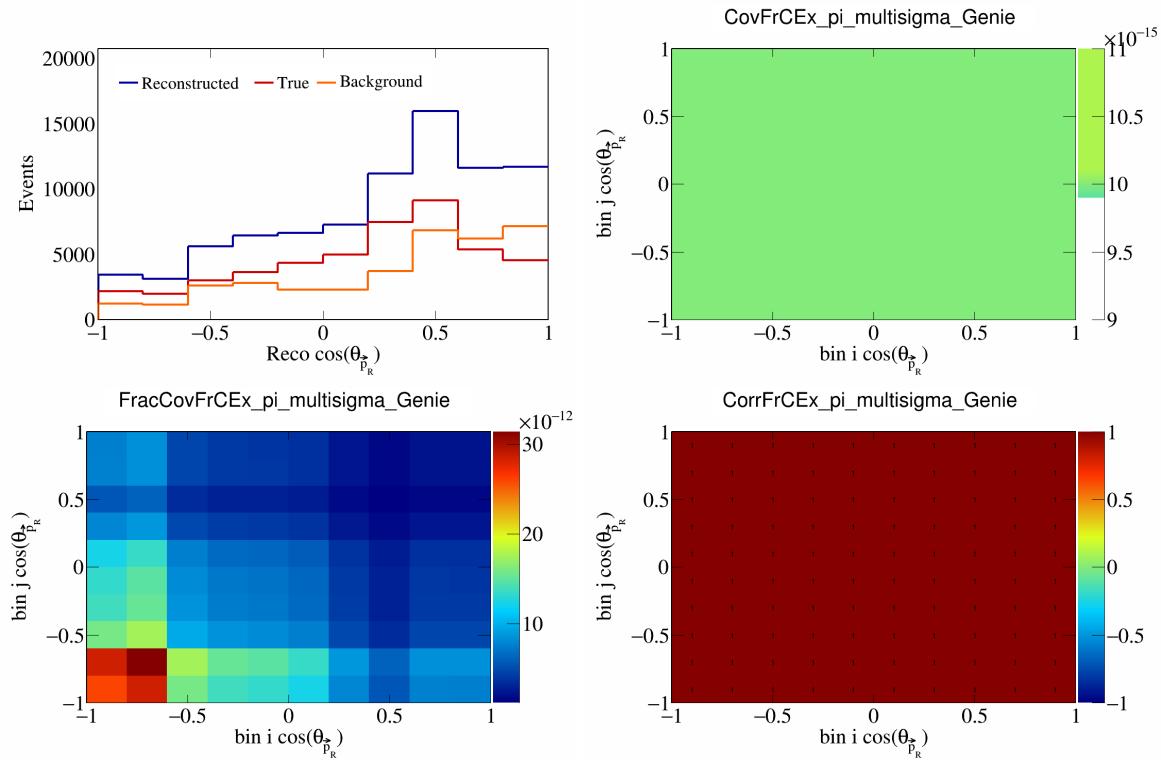


Figure 204: FrCExpi variations for  $\cos(\theta_{\vec{p}_R})$ .

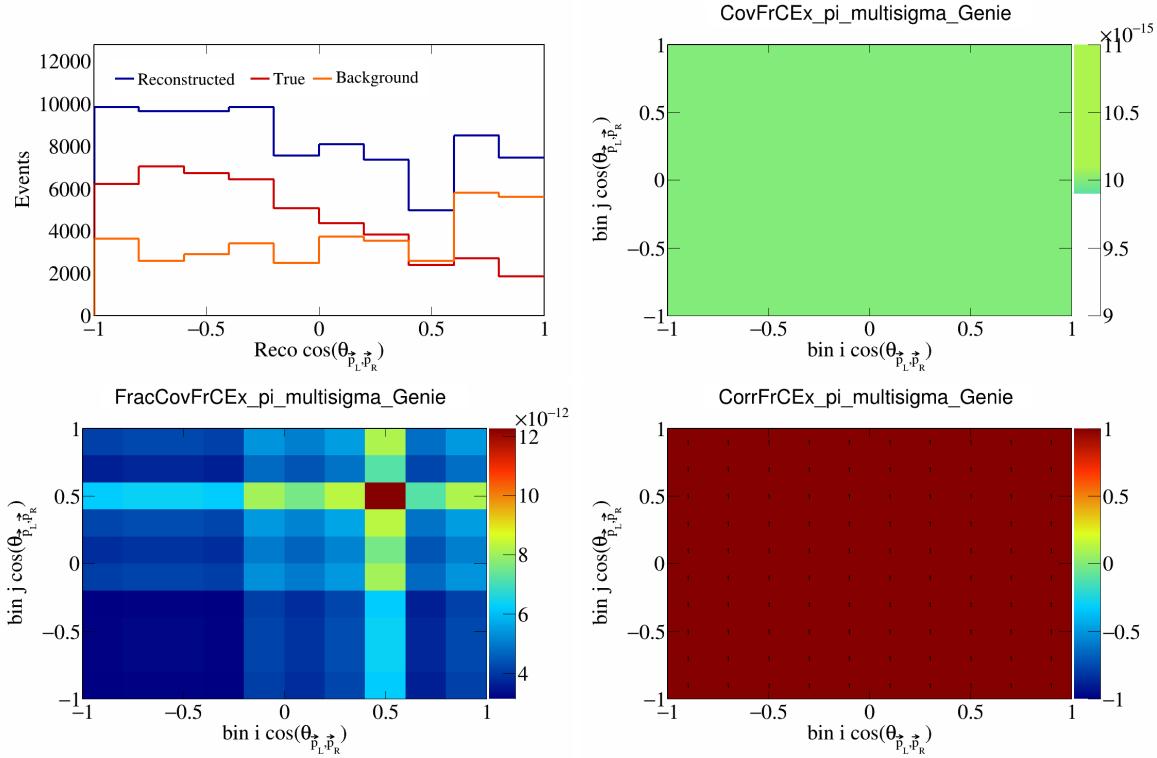


Figure 205: FrCEpi variations for  $\cos(\theta_{\vec{p}_L, \vec{p}_R})$ .

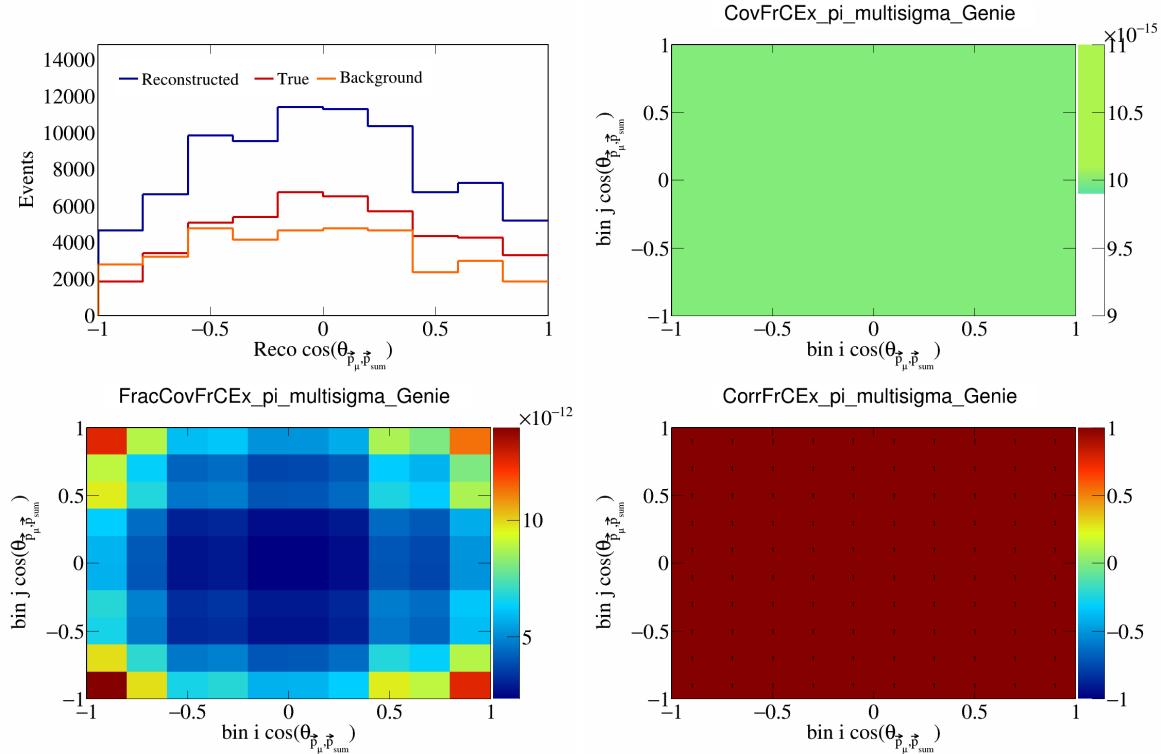


Figure 206: FrCEpi variations for  $\cos(\theta_{\vec{p}_\mu, \vec{p}_{\text{sum}}})$ .

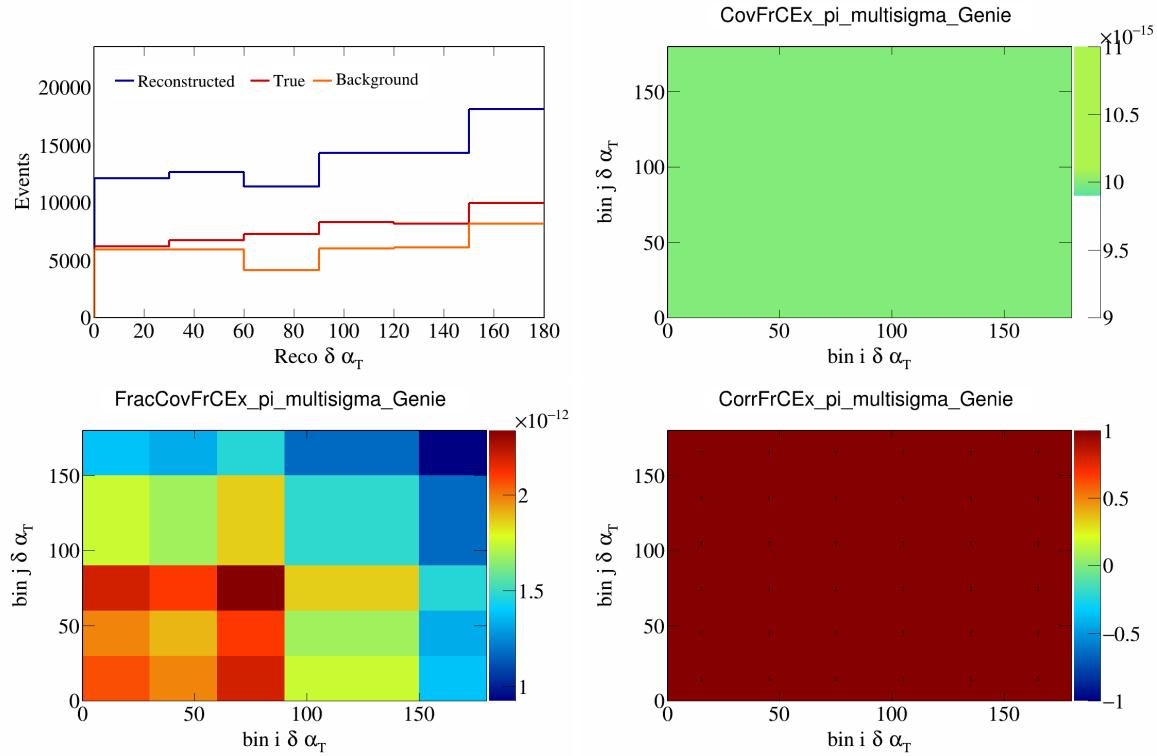


Figure 207: FrCEExpi variations for  $\delta \alpha_T$ .

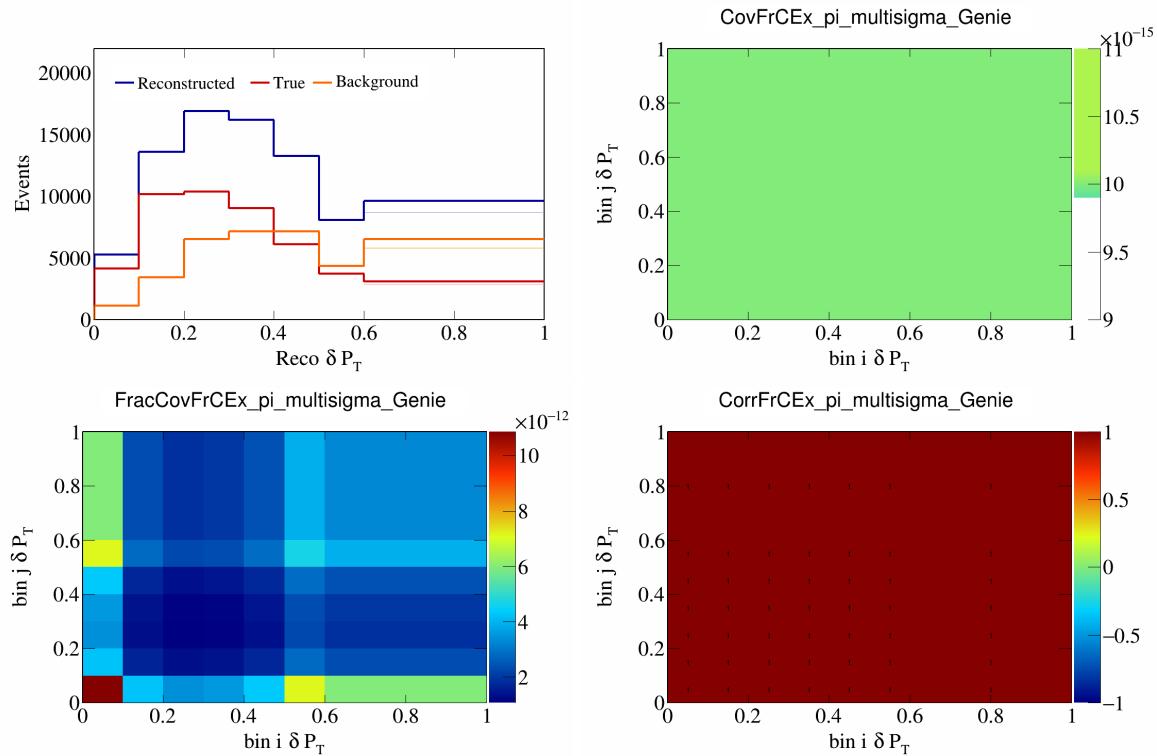


Figure 208: FrCEExpi variations for  $\delta P_T$ .

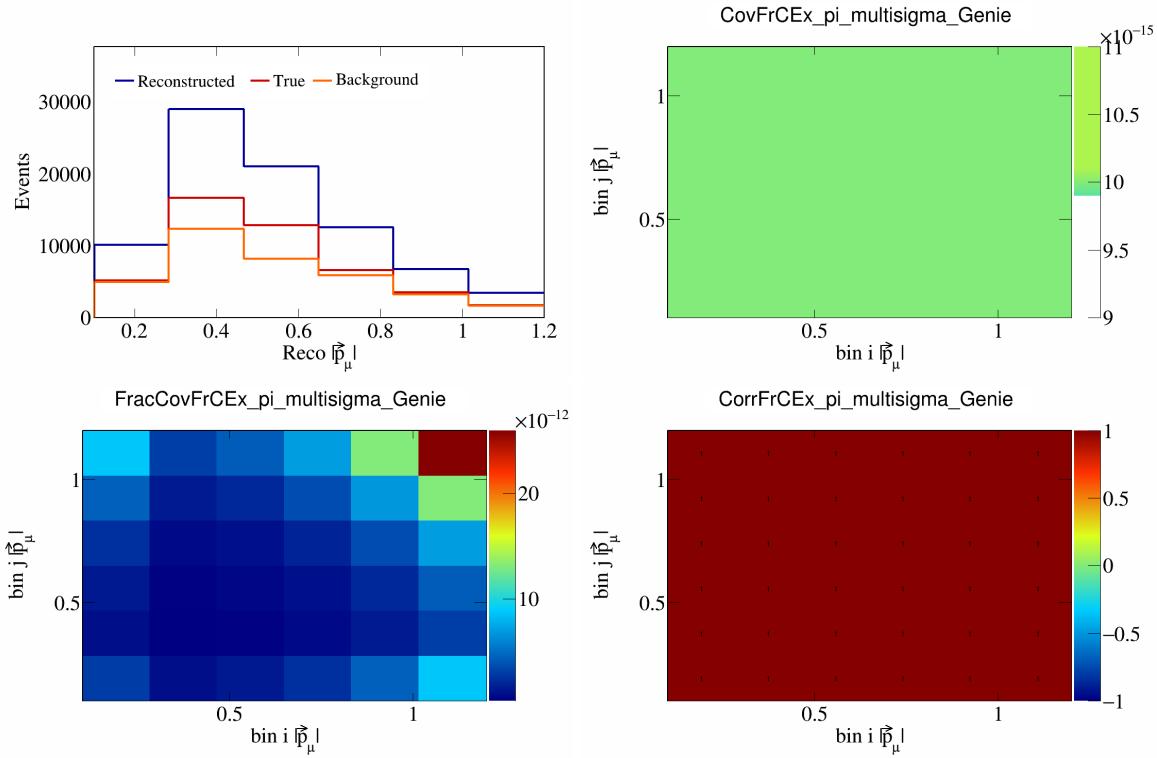


Figure 209: FrCEExpi variations for  $|\vec{p}_\mu|$ .

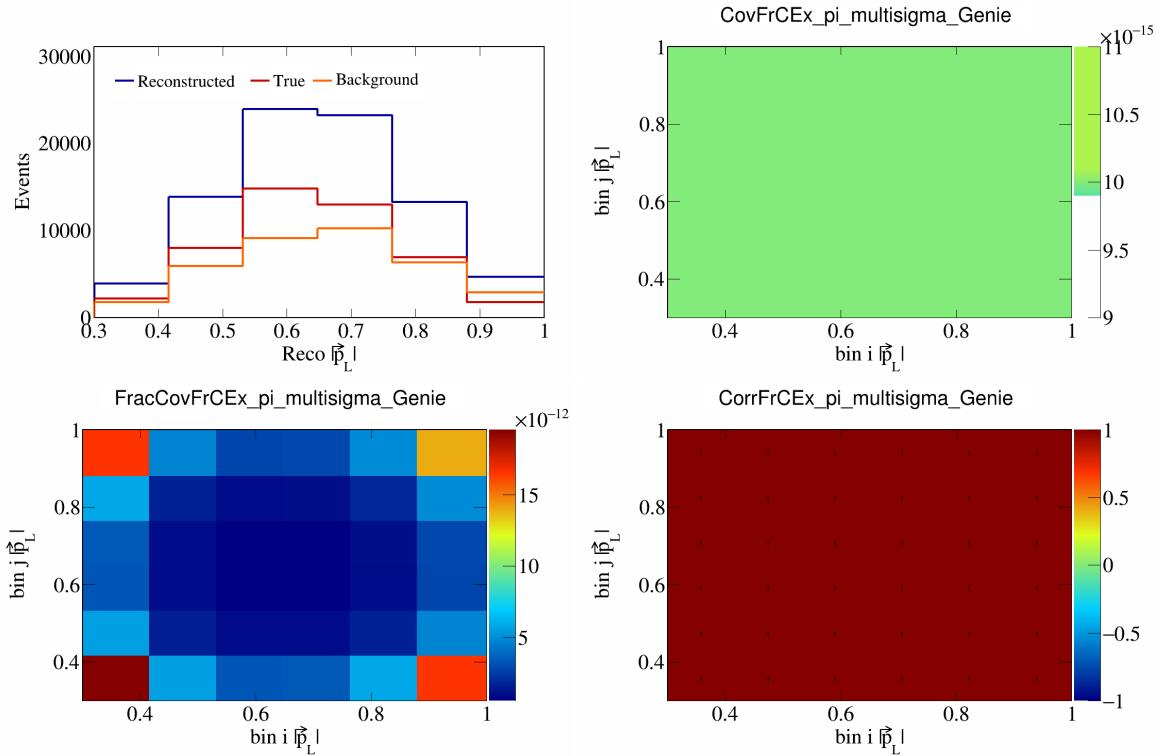


Figure 210: FrCEExpi variations for  $|\vec{p}_L|$ .

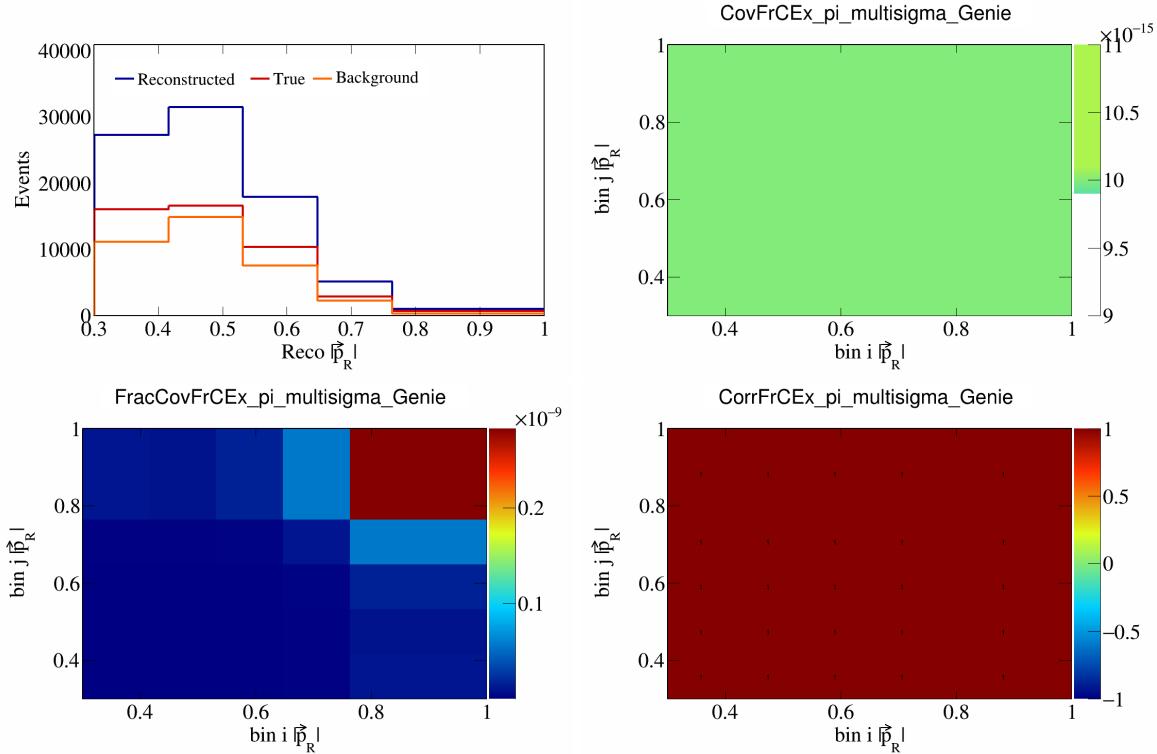


Figure 211: FrCEExpi variations for  $|\vec{p}_R|$ .

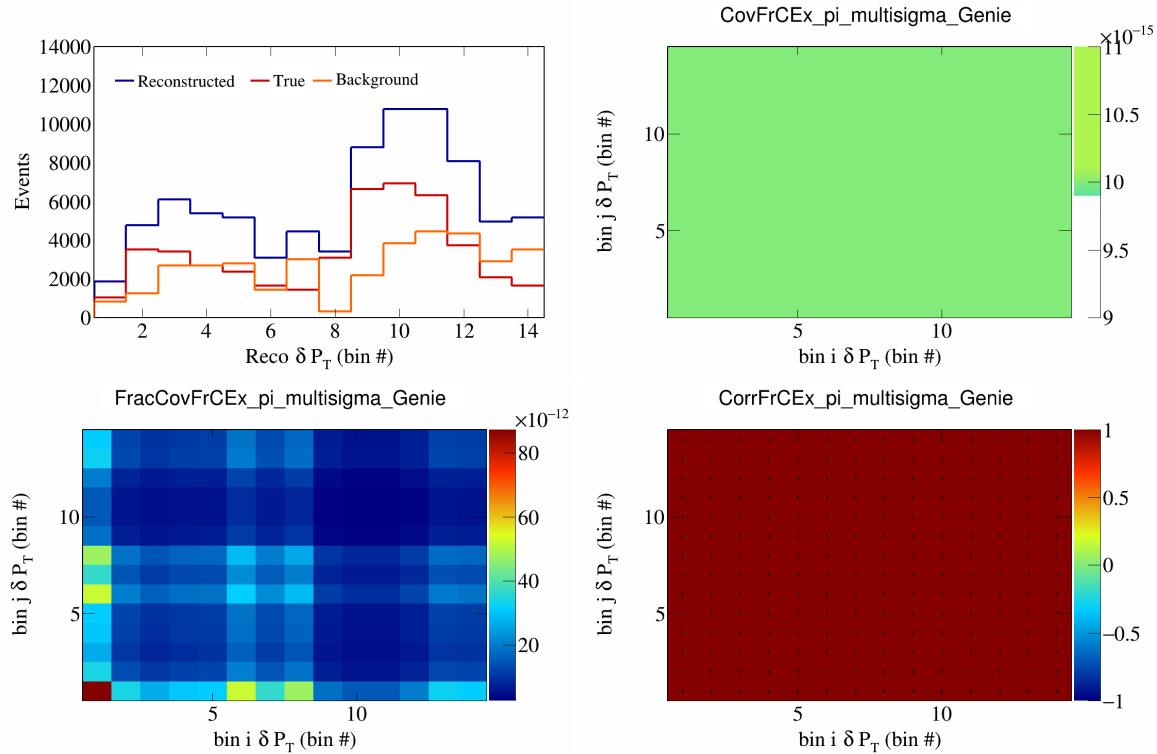


Figure 212: FrCEExpi variations for  $\delta P_T$  in  $\cos(\theta_{\vec{p}_\mu})$ .

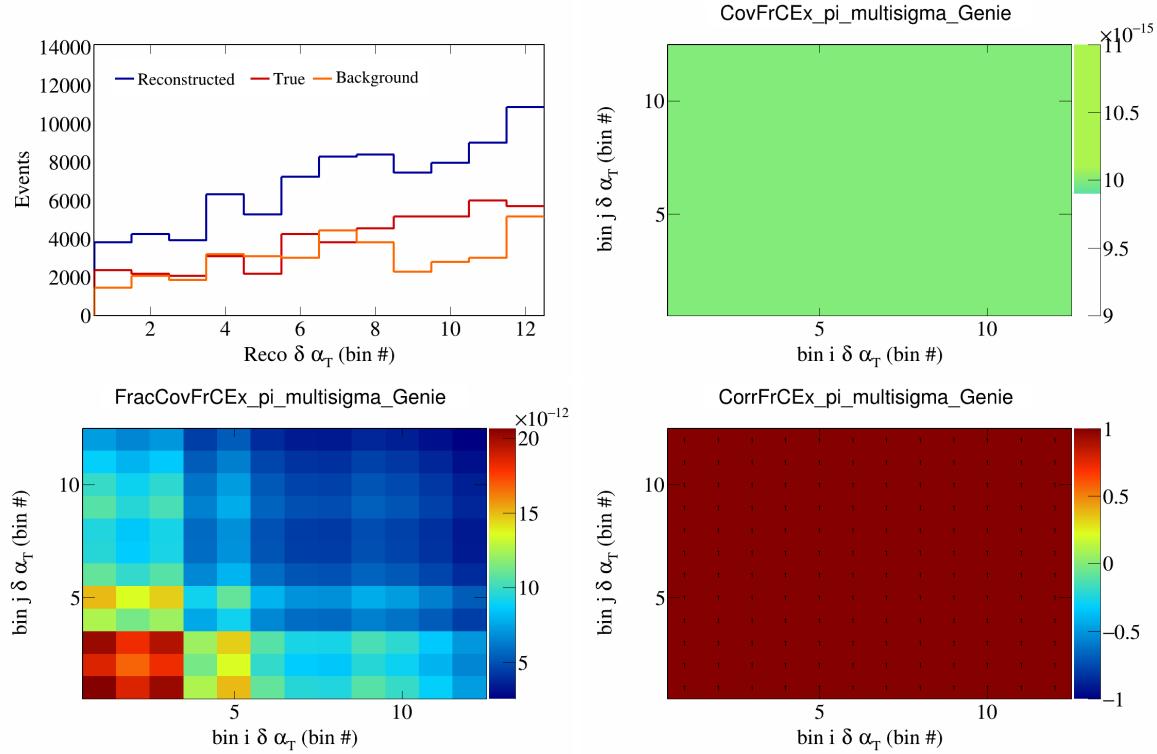


Figure 213: FrCEExpi variations for  $\delta\alpha_T$  in  $\cos(\theta_{\vec{p}_\mu})$ .

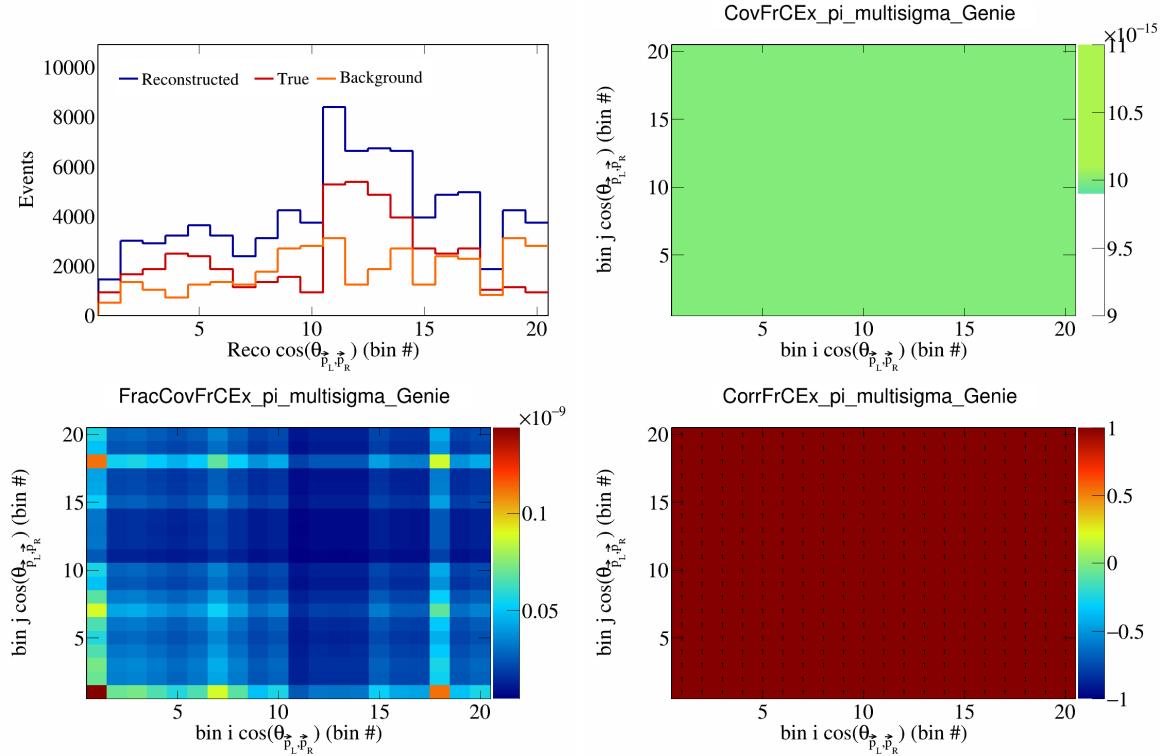


Figure 214: FrCEExpi variations for  $\cos(\theta_{\vec{p}_L, \vec{p}_R})$  in  $\cos(\theta_{\vec{p}_\mu})$ .

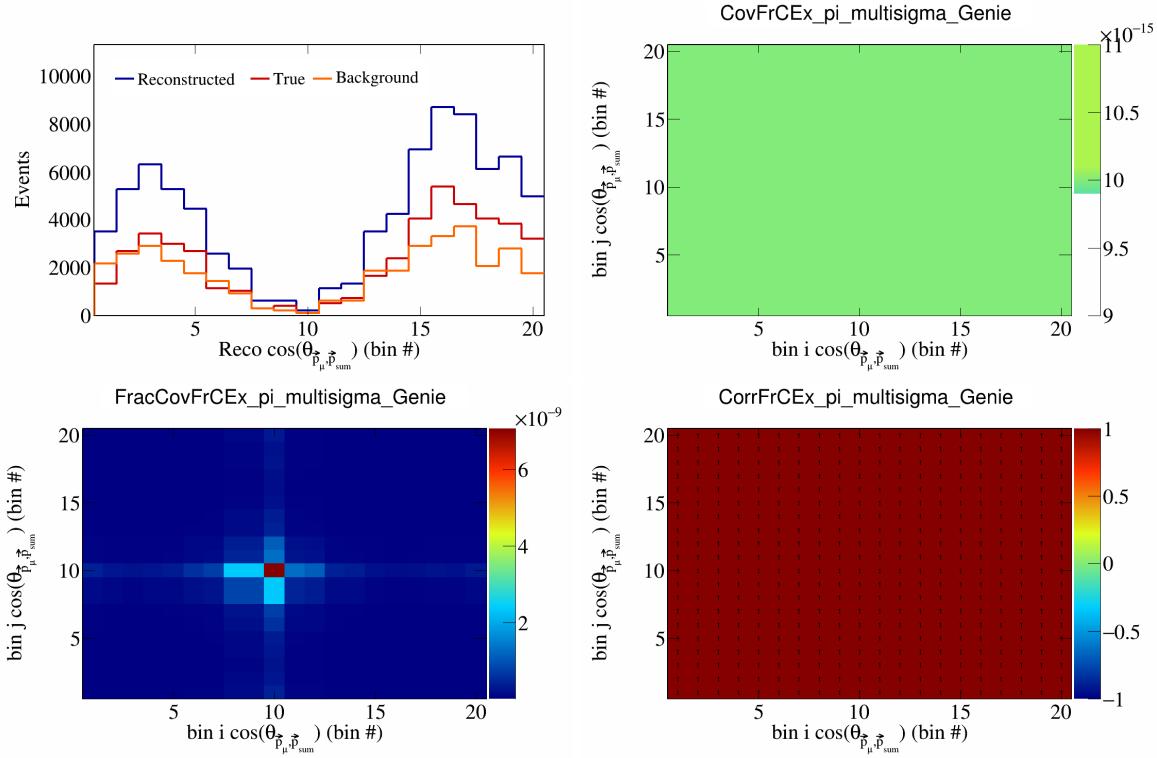


Figure 215: FrCEExpi variations for  $\cos(\theta_{\vec{p}_\mu, \vec{p}_{\text{sum}}})$  in  $\cos(\theta_{\vec{p}_\mu})$ .

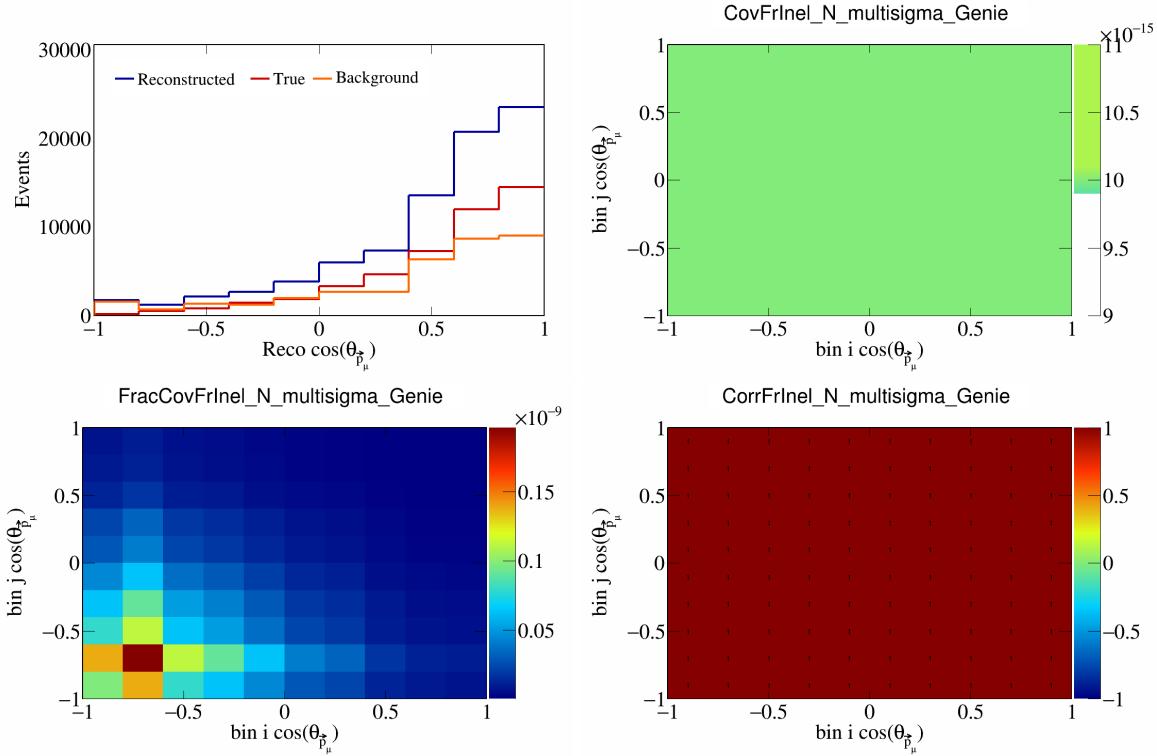


Figure 216: FrInelN variations for  $\cos(\theta_{\vec{p}_\mu})$ .

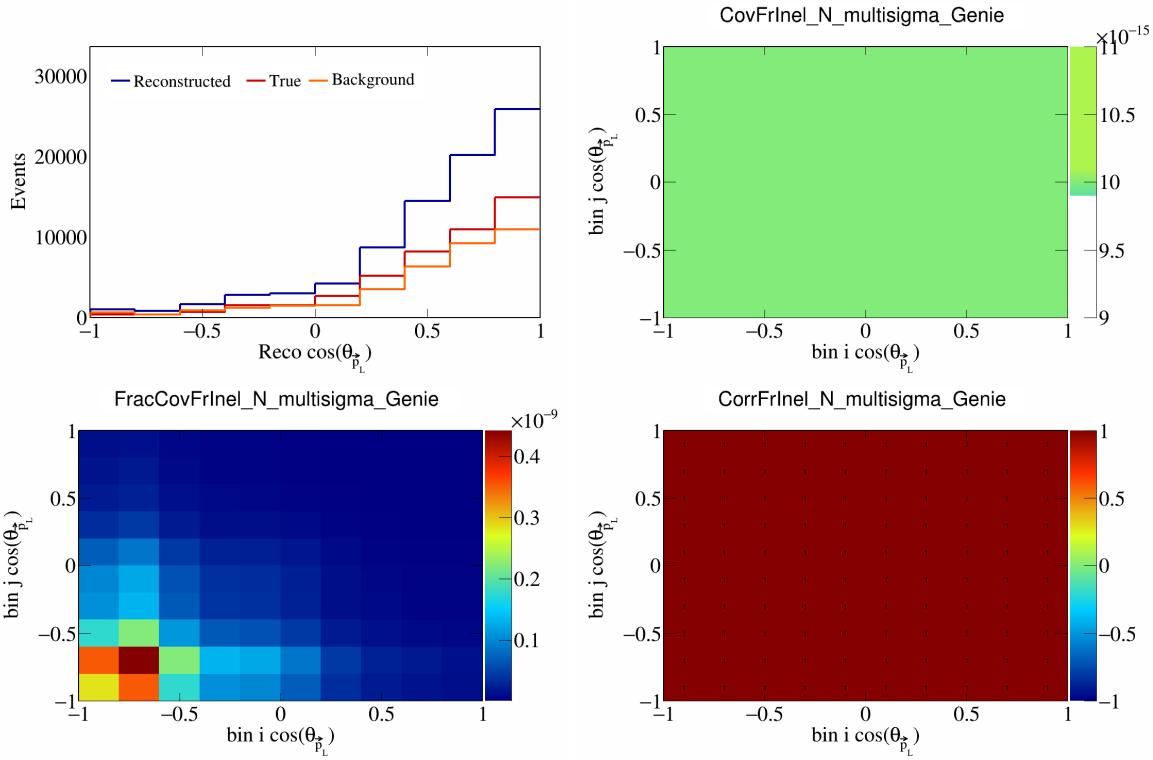


Figure 217: FrInelN variations for  $\cos(\theta_{\vec{p}_L})$ .

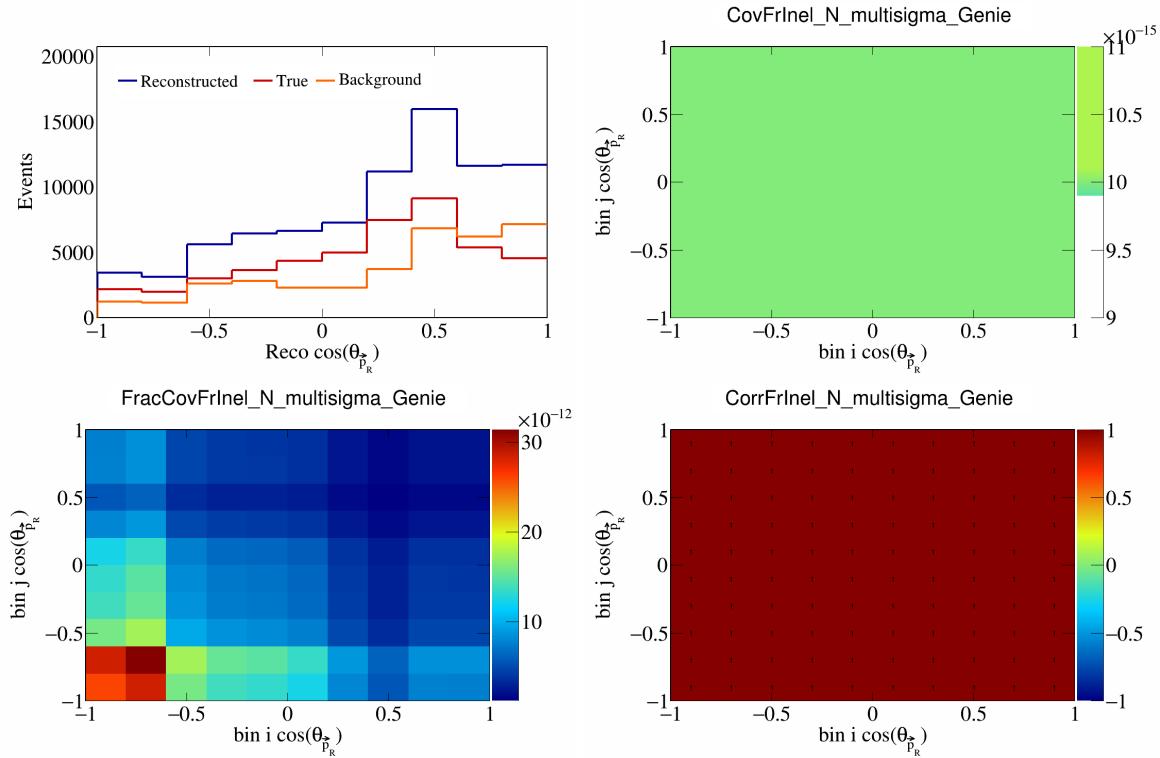


Figure 218: FrInelN variations for  $\cos(\theta_{\vec{p}_R})$ .

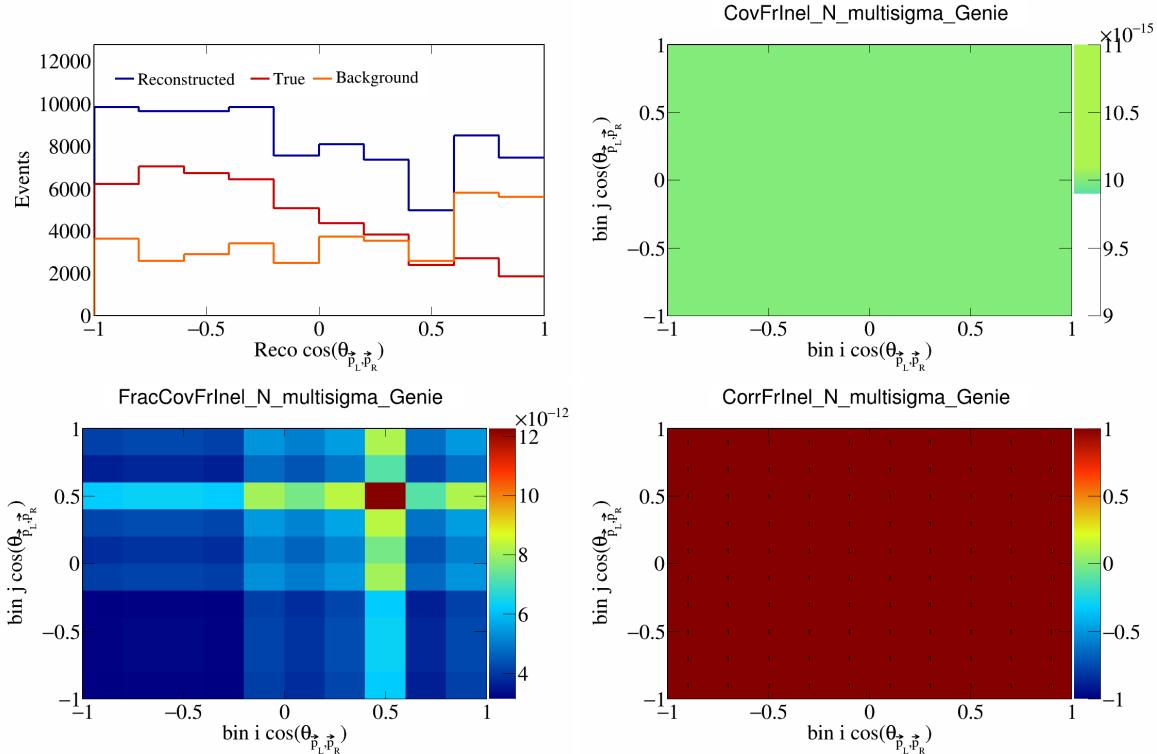


Figure 219: FrInelN variations for  $\cos(\theta_{\vec{p}_L, \vec{p}_R})$ .

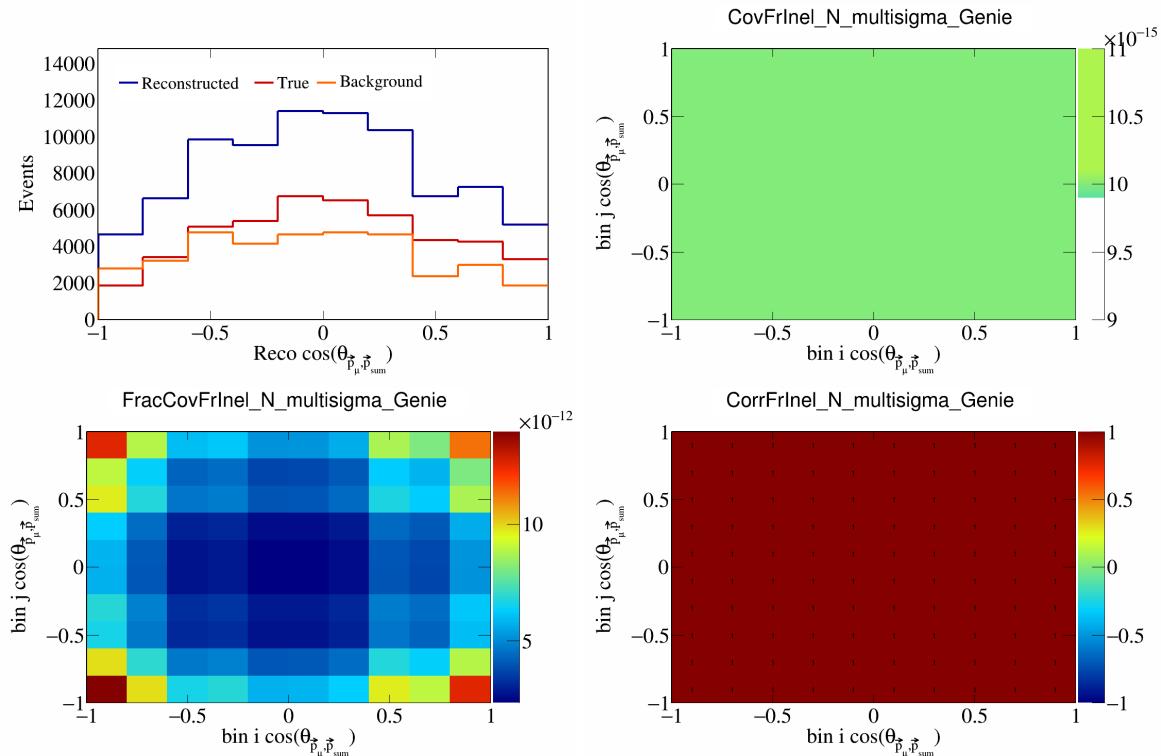


Figure 220: FrInelN variations for  $\cos(\theta_{\vec{p}_\mu, \vec{p}_{\text{sum}}})$ .

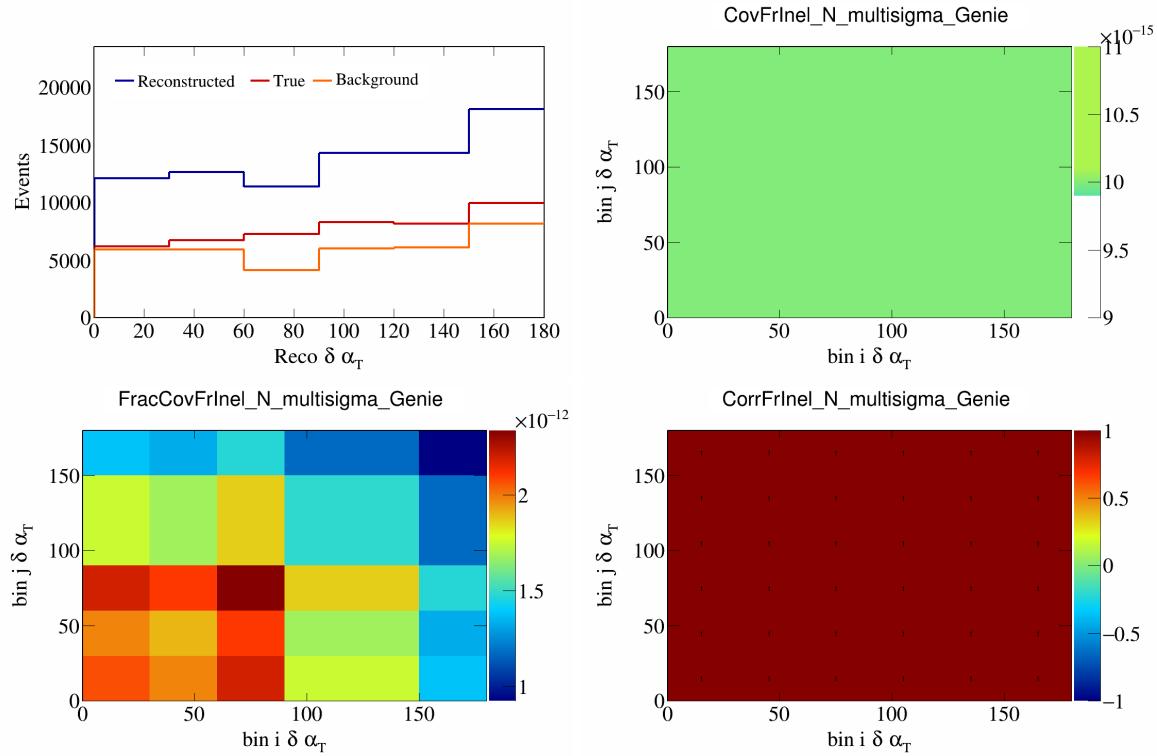


Figure 221: FrInelN variations for  $\delta\alpha_T$ .

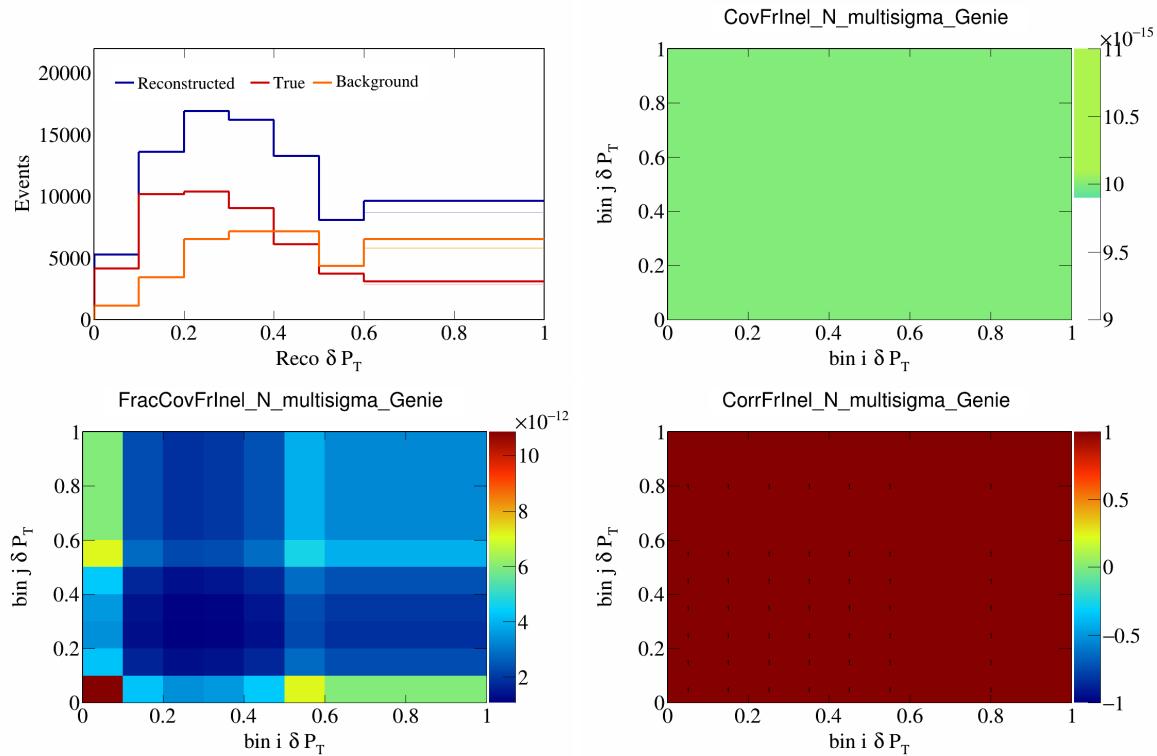


Figure 222: FrInelN variations for  $\delta P_T$ .

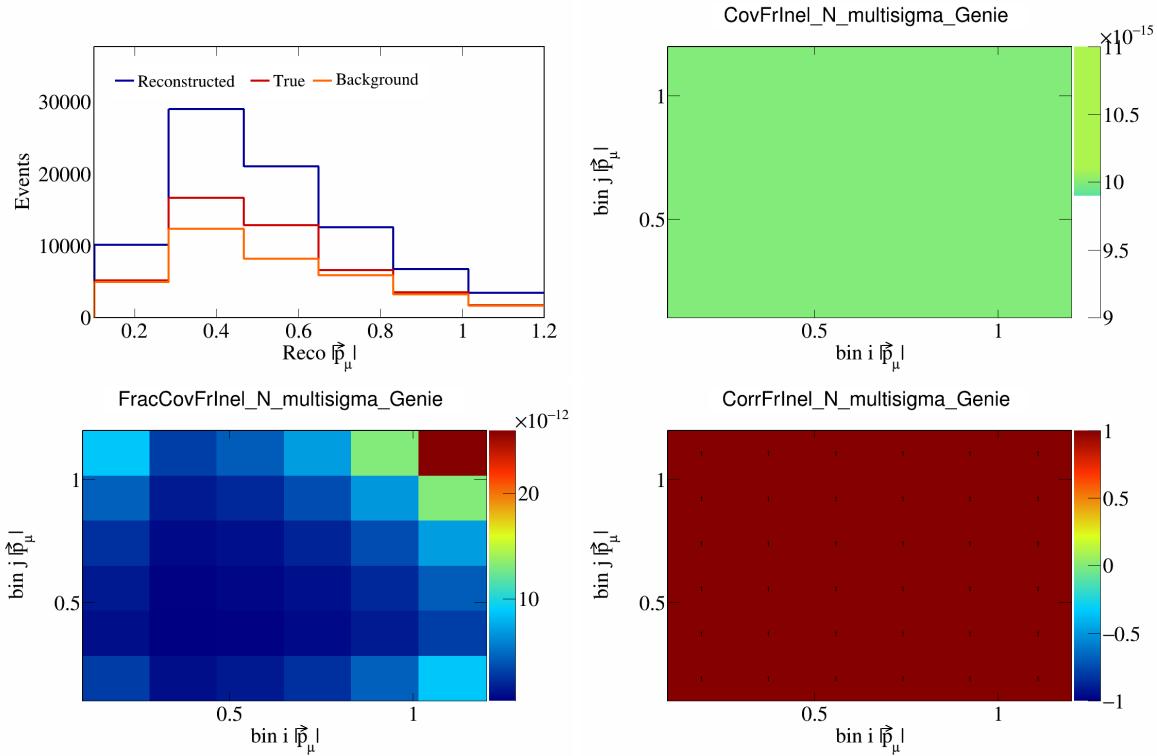


Figure 223: FrInelN variations for  $|\vec{p}_\mu|$ .

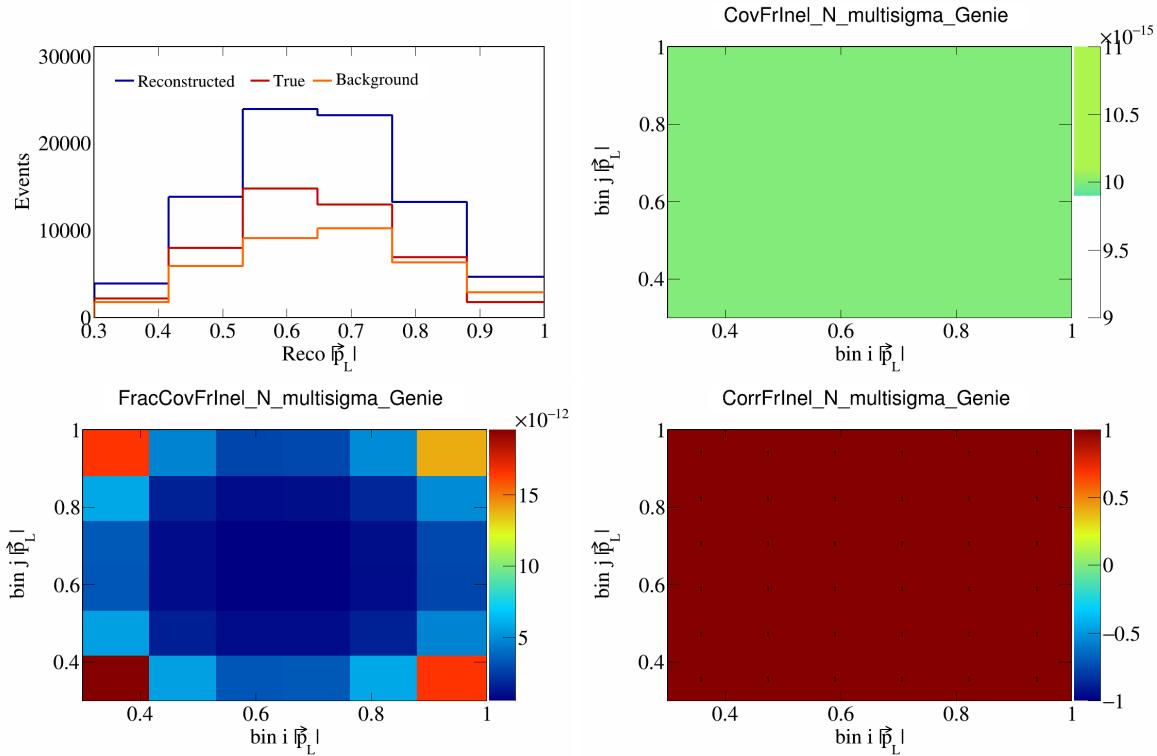


Figure 224: FrInelN variations for  $|\vec{p}_L|$ .

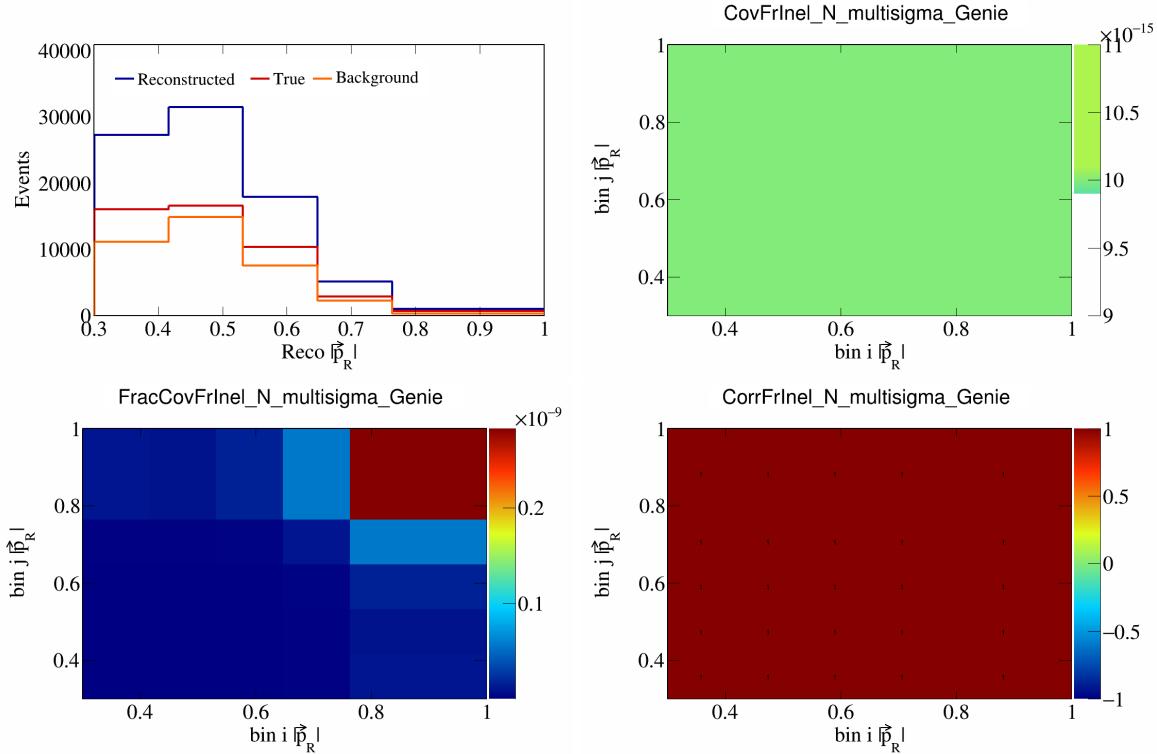


Figure 225: FrInelN variations for  $|\vec{p}_R|$ .

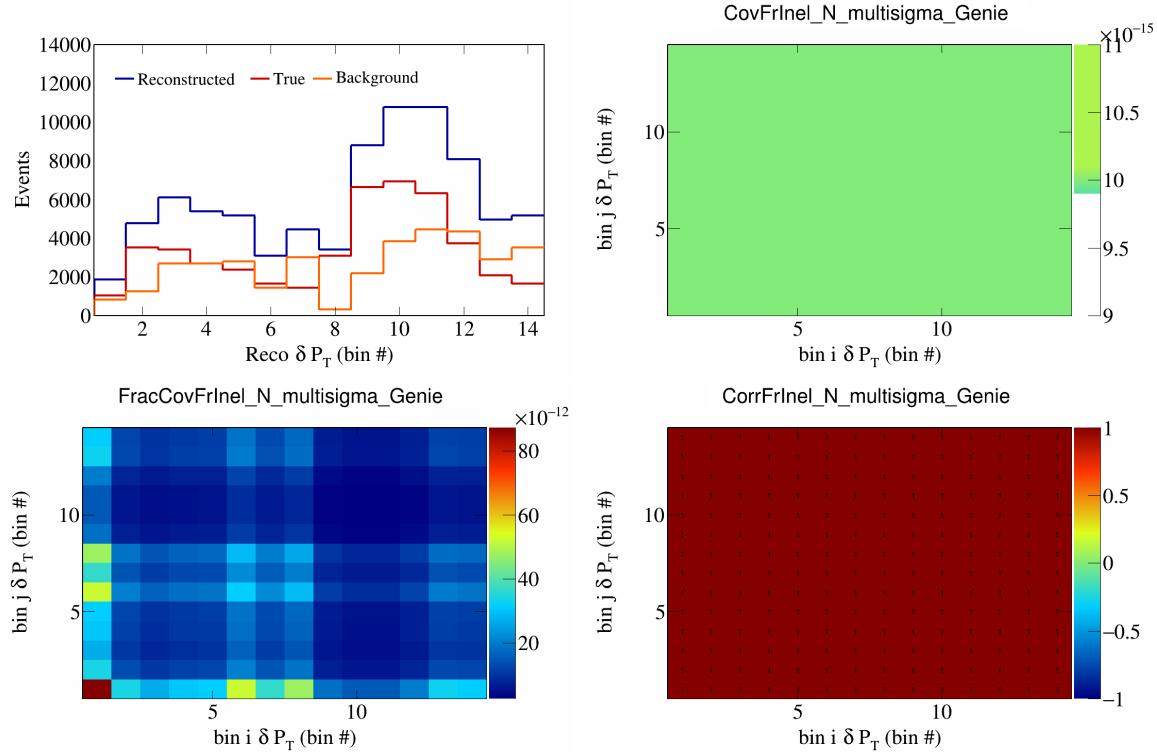


Figure 226: FrInelN variations for  $\delta P_T$  in  $\cos(\theta_{\vec{p}_\mu})$ .

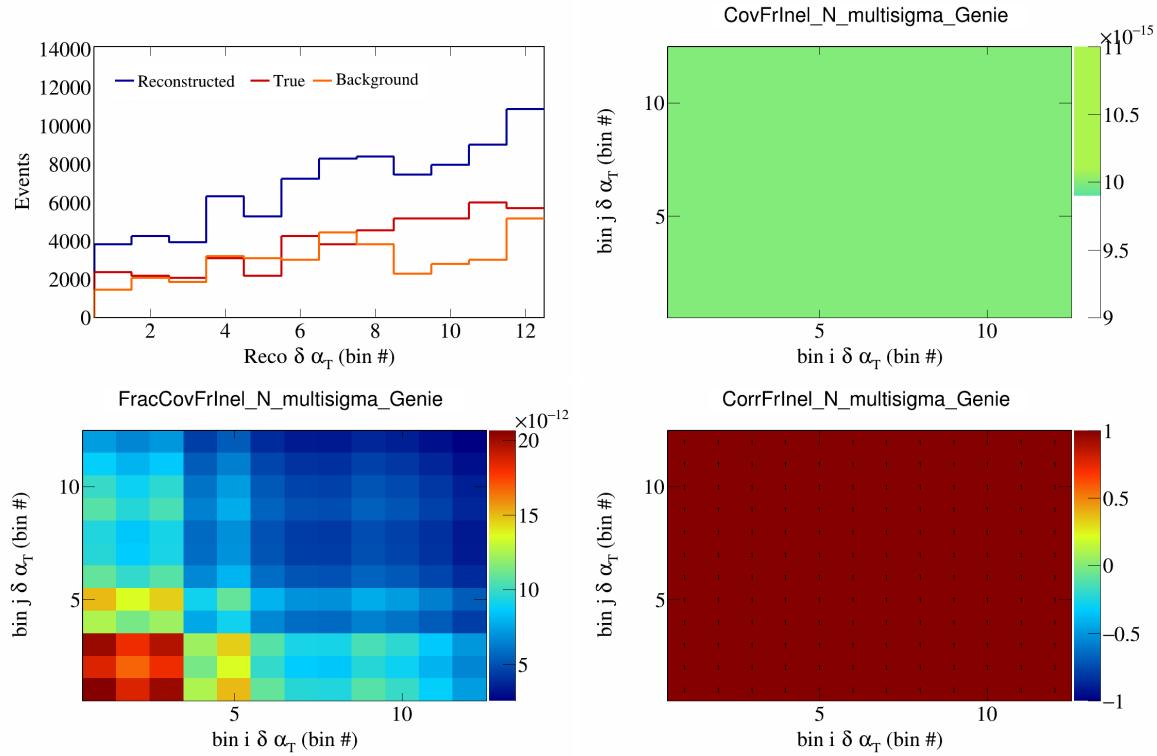


Figure 227: FrInelN variations for  $\delta\alpha_T$  in  $\cos(\theta_{\vec{p}_\mu})$ .

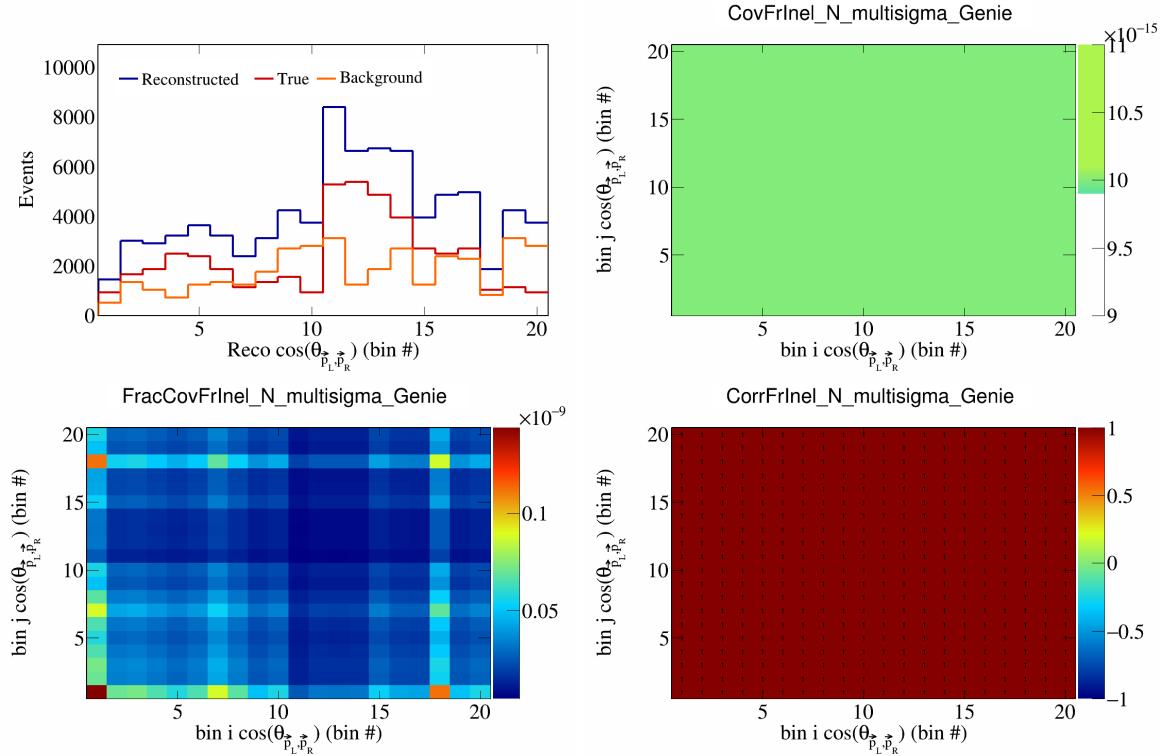


Figure 228: FrInelN variations for  $\cos(\theta_{\vec{p}_L, \vec{p}_R})$  in  $\cos(\theta_{\vec{p}_\mu})$ .

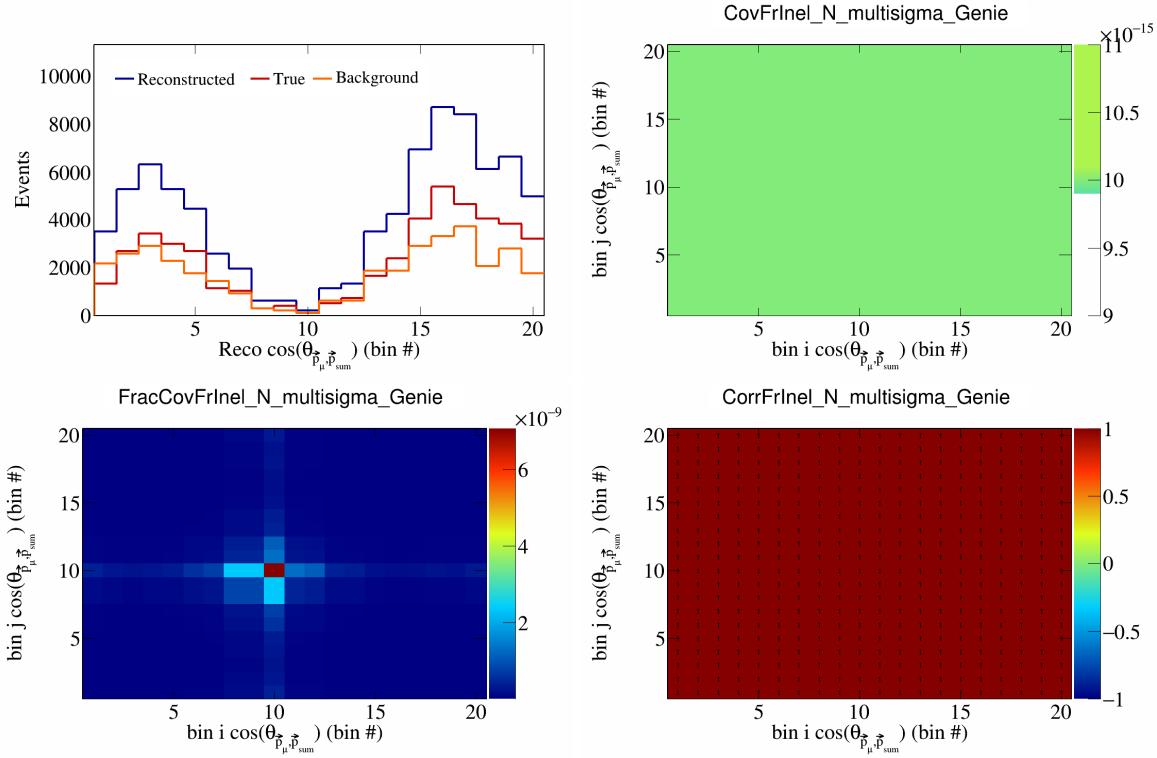


Figure 229: FrInelN variations for  $\cos(\theta_{\vec{p}_\mu}^*, \vec{p}_{\text{sum}})$  in  $\cos(\theta_{\vec{p}_\mu})$ .

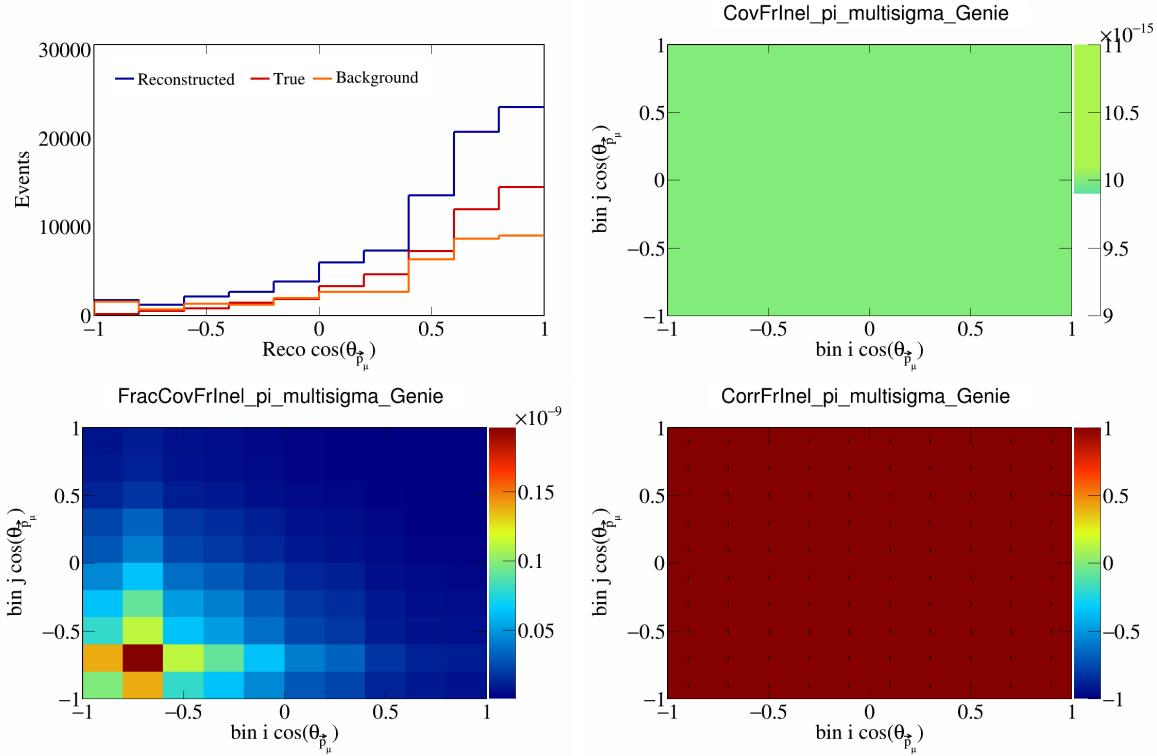


Figure 230: FrInelpi variations for  $\cos(\theta_{\vec{p}_\mu}^*)$ .

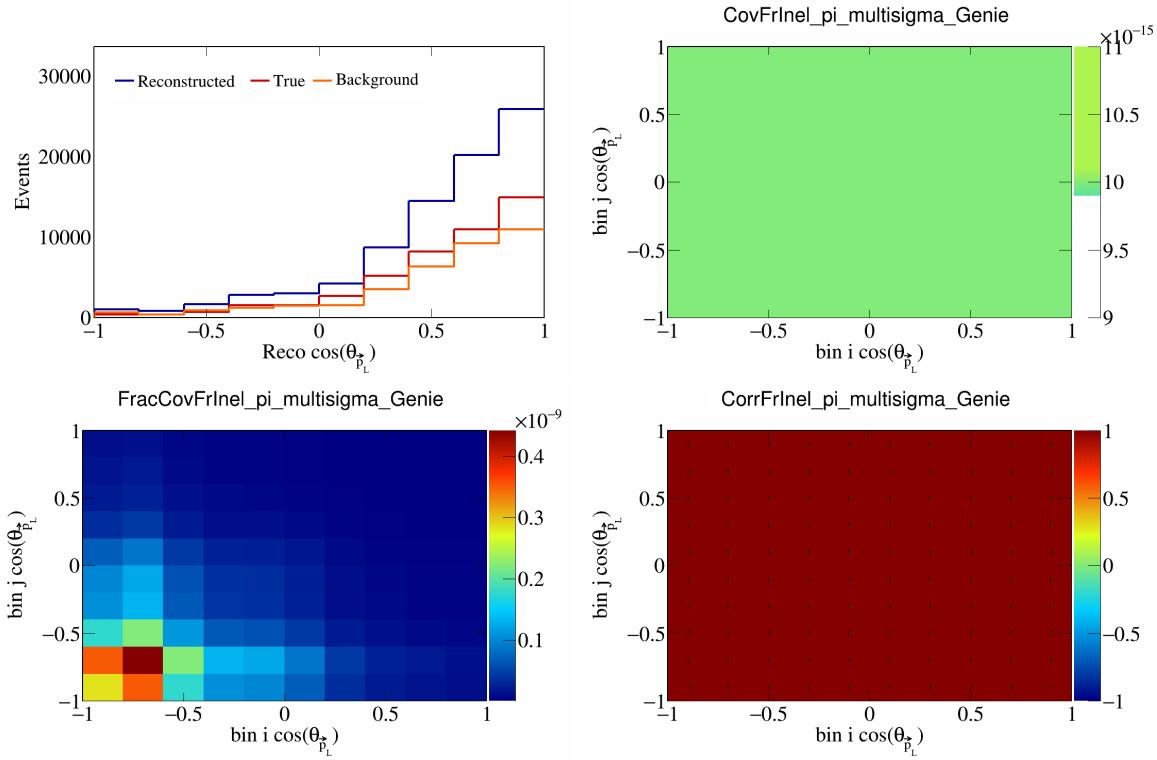


Figure 231: FrInelpi variations for  $\cos(\theta_{\vec{p}_L})$ .

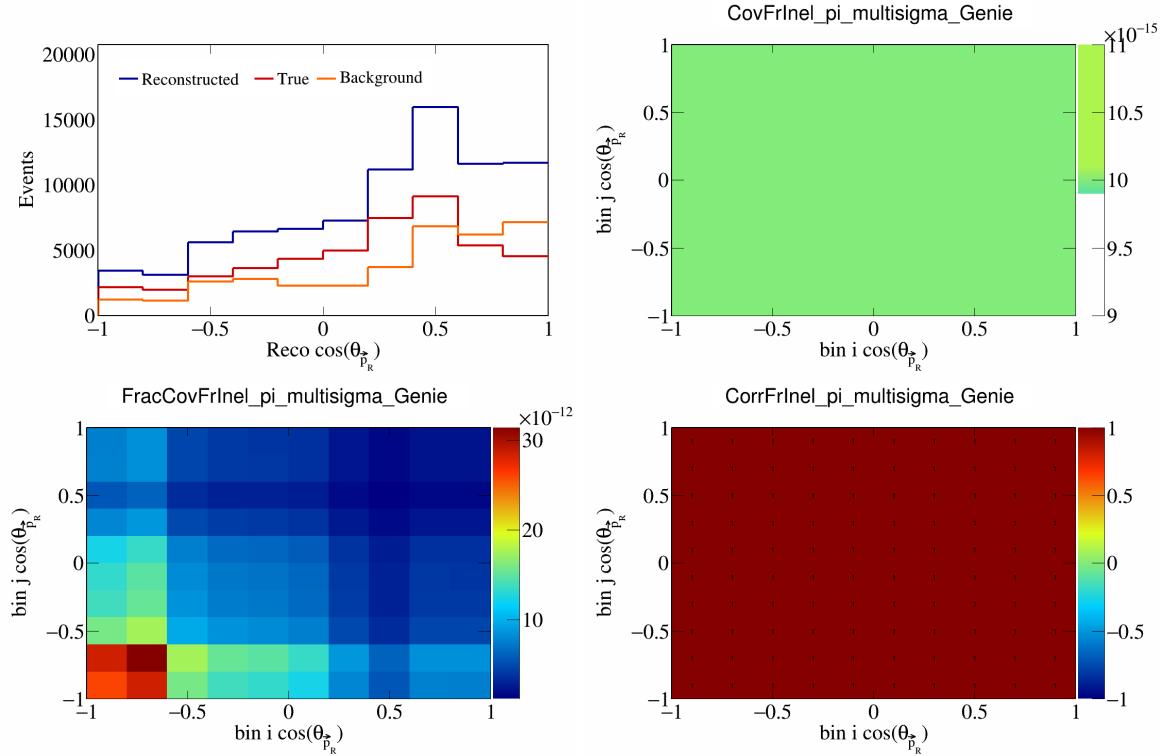


Figure 232: FrInelpi variations for  $\cos(\theta_{\vec{p}_R})$ .

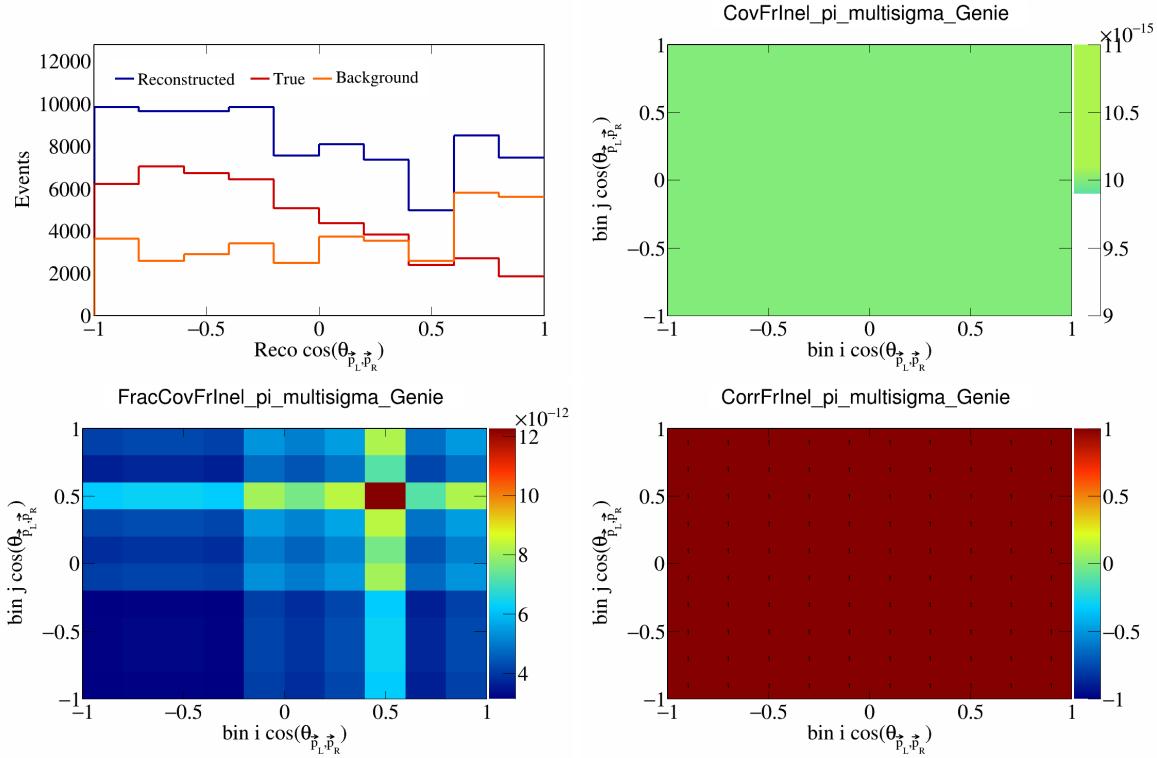


Figure 233: FrInelpi variations for  $\cos(\theta_{\vec{p}_L, \vec{p}_R})$ .

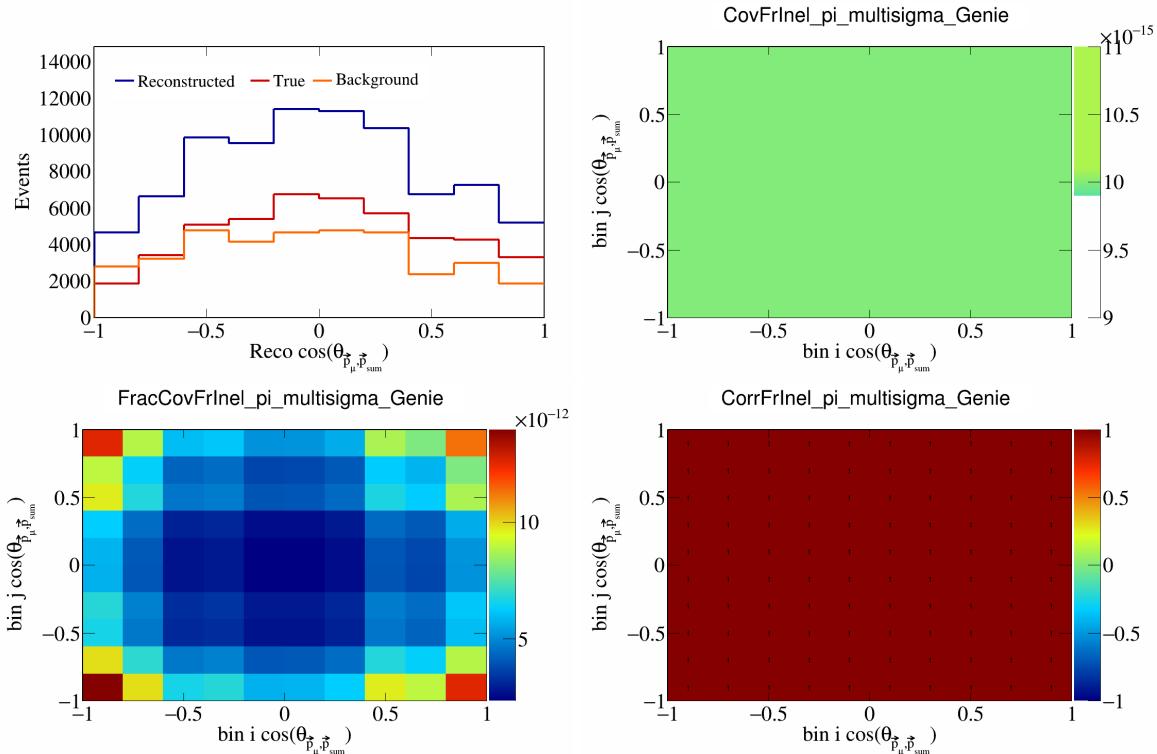


Figure 234: FrInelpi variations for  $\cos(\theta_{\vec{p}_\mu, \vec{p}_{\text{sum}}})$ .

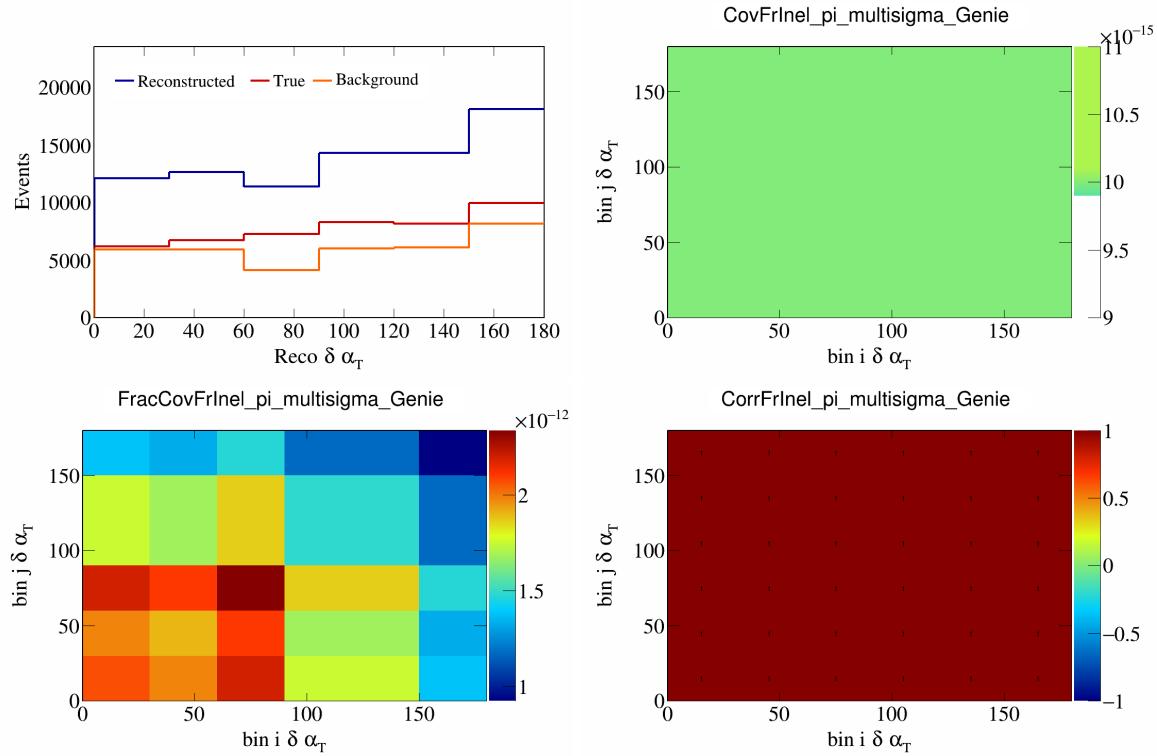


Figure 235: FrInelpi variations for  $\delta \alpha_T$ .

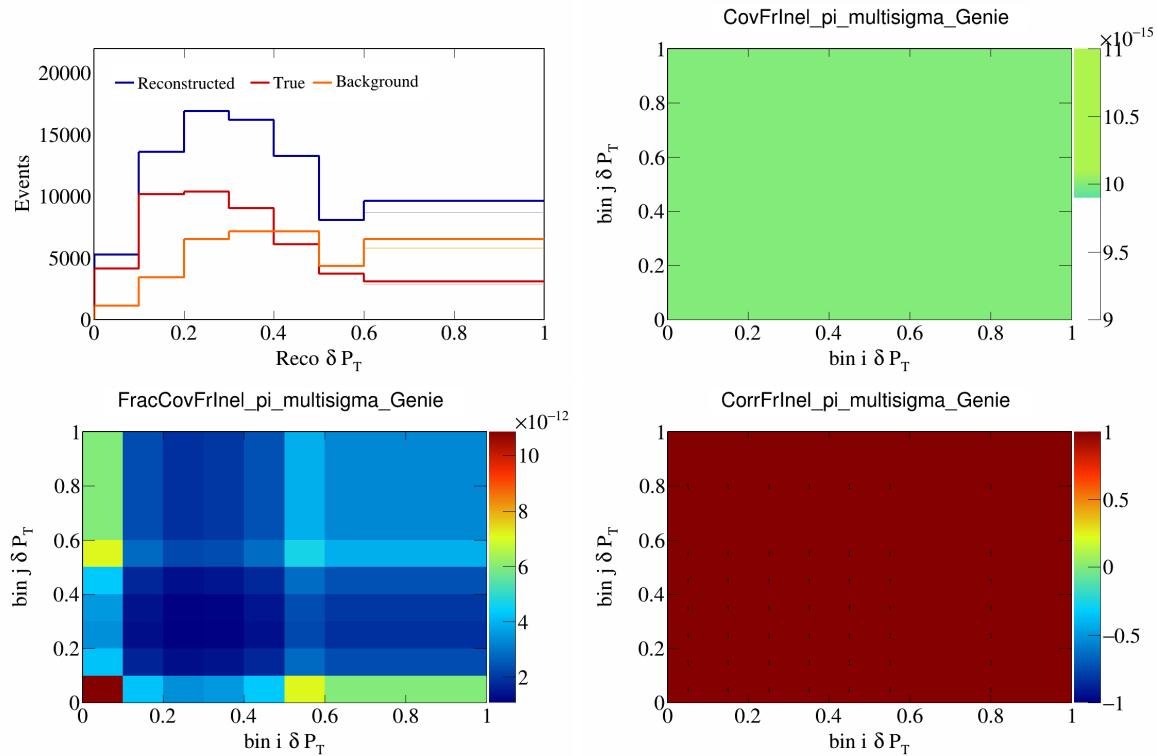


Figure 236: FrInelpi variations for  $\delta P_T$ .

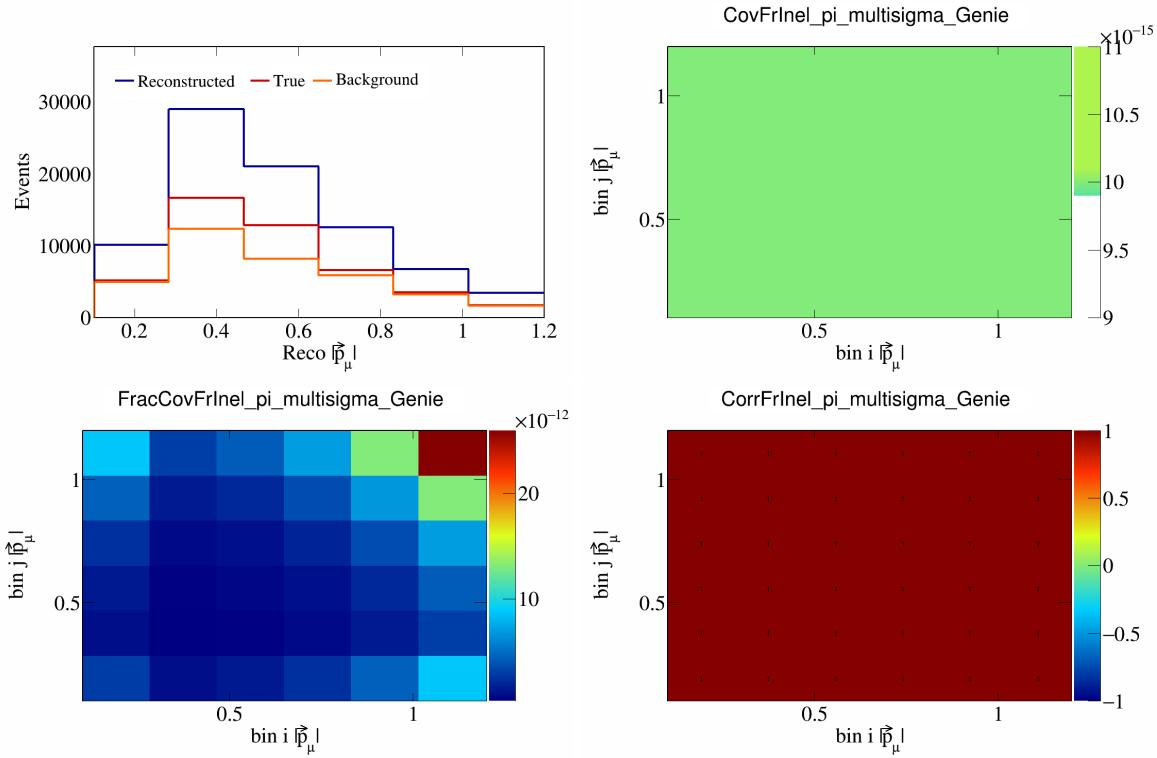


Figure 237: FrInelpi variations for  $|\vec{p}_\mu|$ .

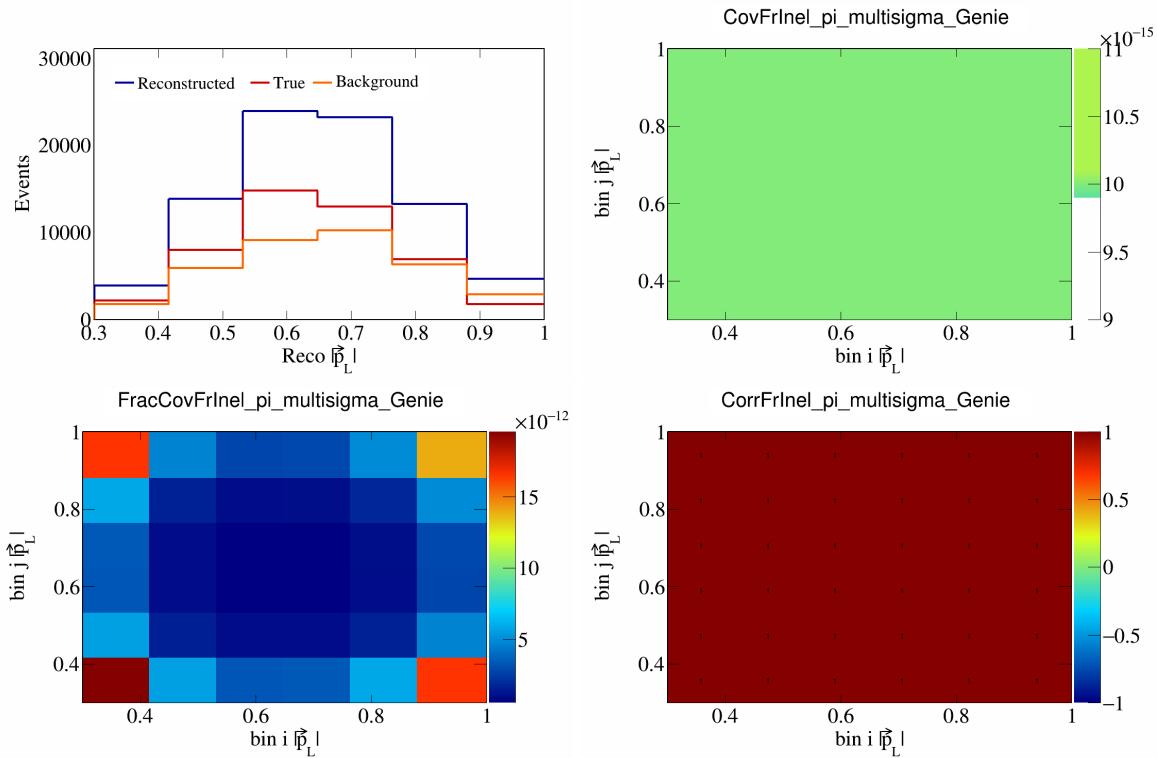


Figure 238: FrInelpi variations for  $|\vec{p}_L|$ .

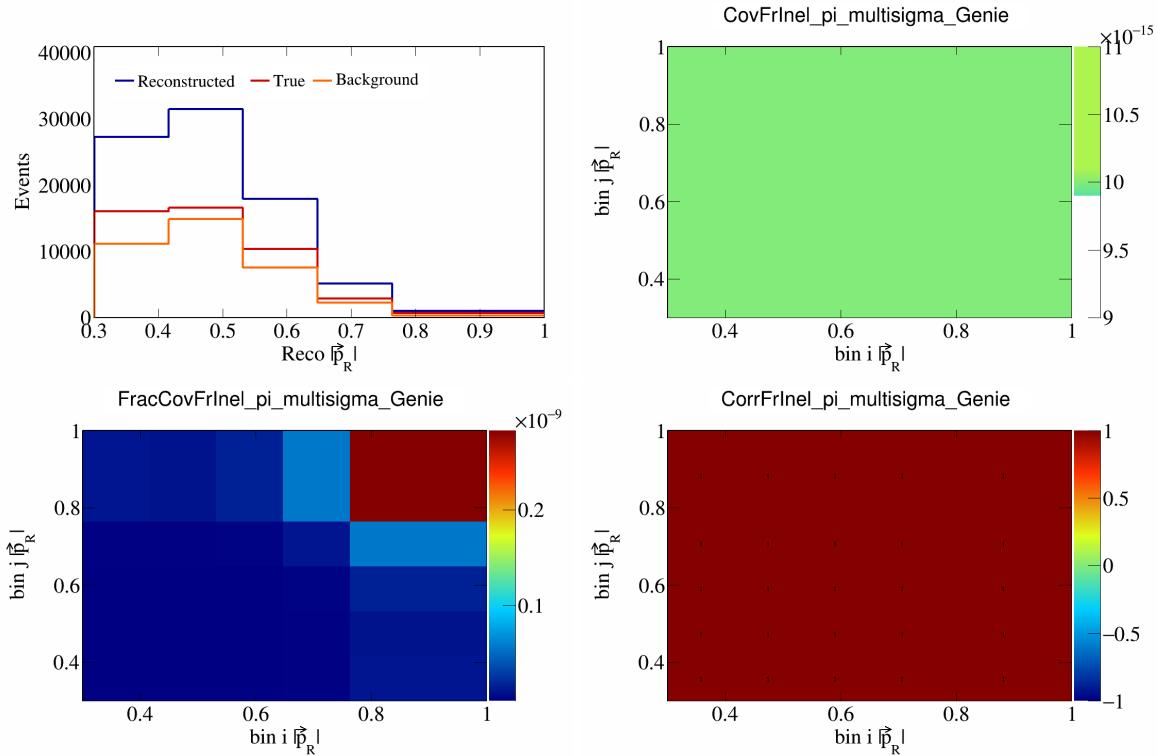


Figure 239: FrInelpi variations for  $|\vec{p}_R|$ .

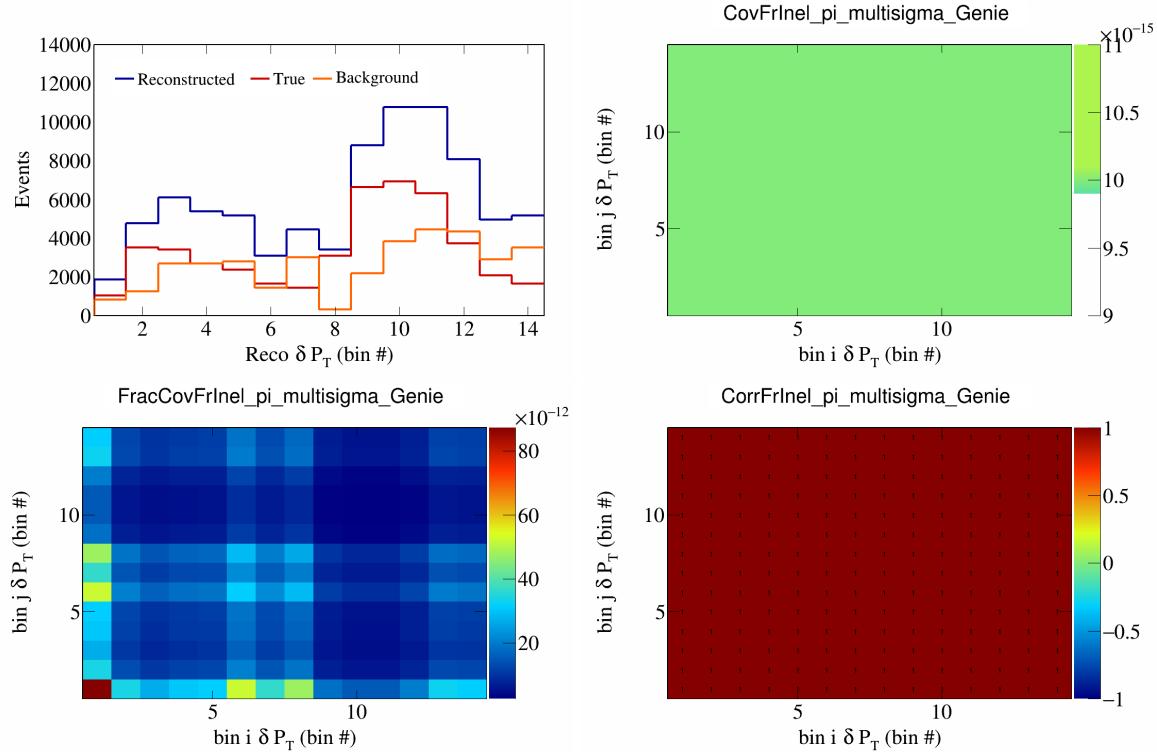


Figure 240: FrInelpi variations for  $\delta P_T$  in  $\cos(\theta_{\vec{p}_\mu})$ .

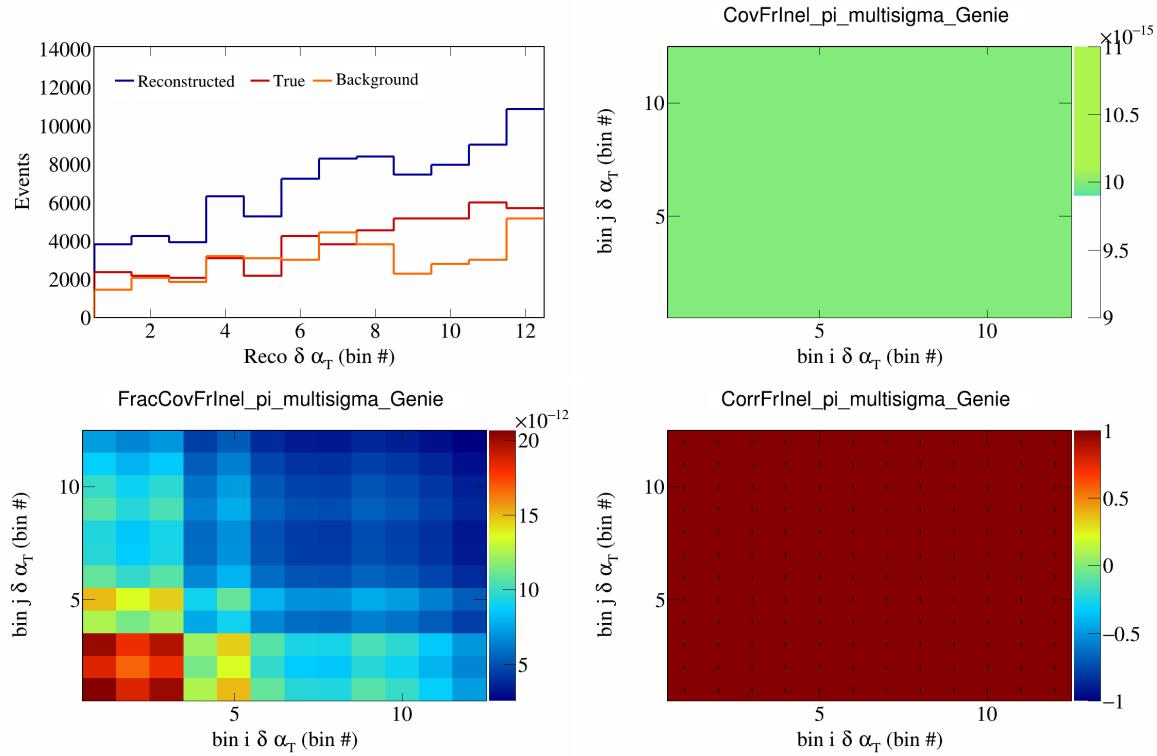


Figure 241: FrInelpi variations for  $\delta\alpha_T$  in  $\cos(\theta_{\vec{p}_\mu})$ .

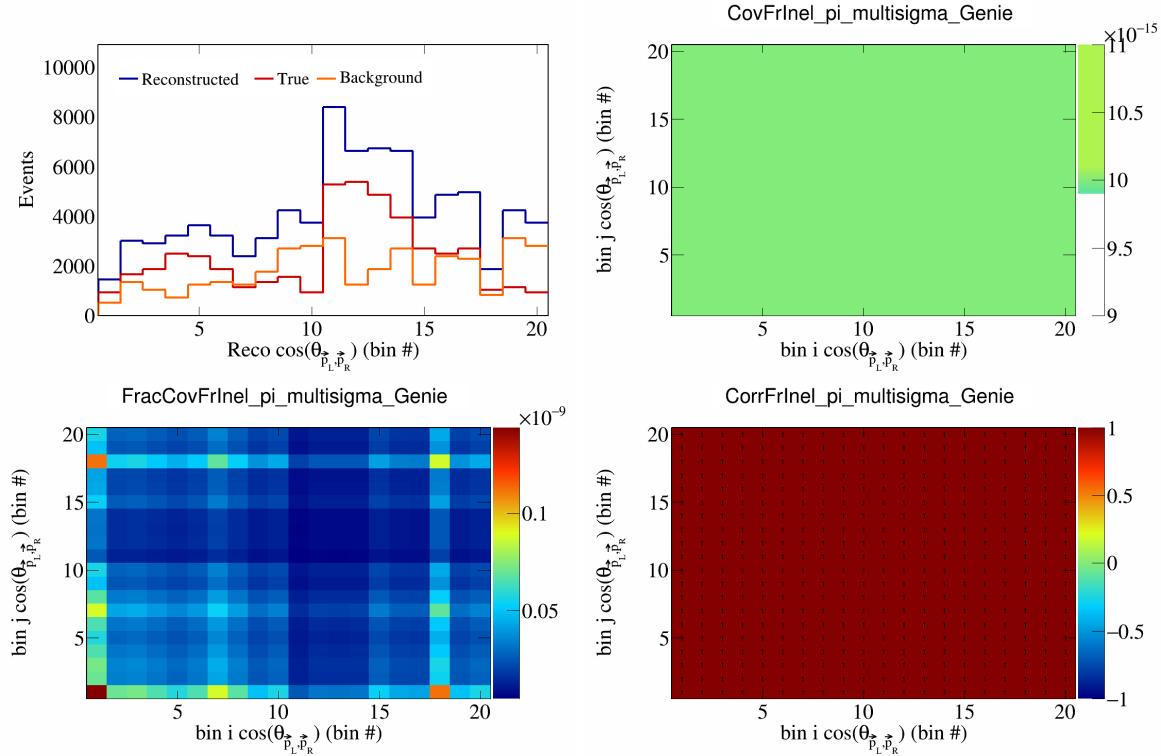


Figure 242: FrInelpi variations for  $\cos(\theta_{\vec{p}_L, \vec{p}_R})$  in  $\cos(\theta_{\vec{p}_\mu})$ .

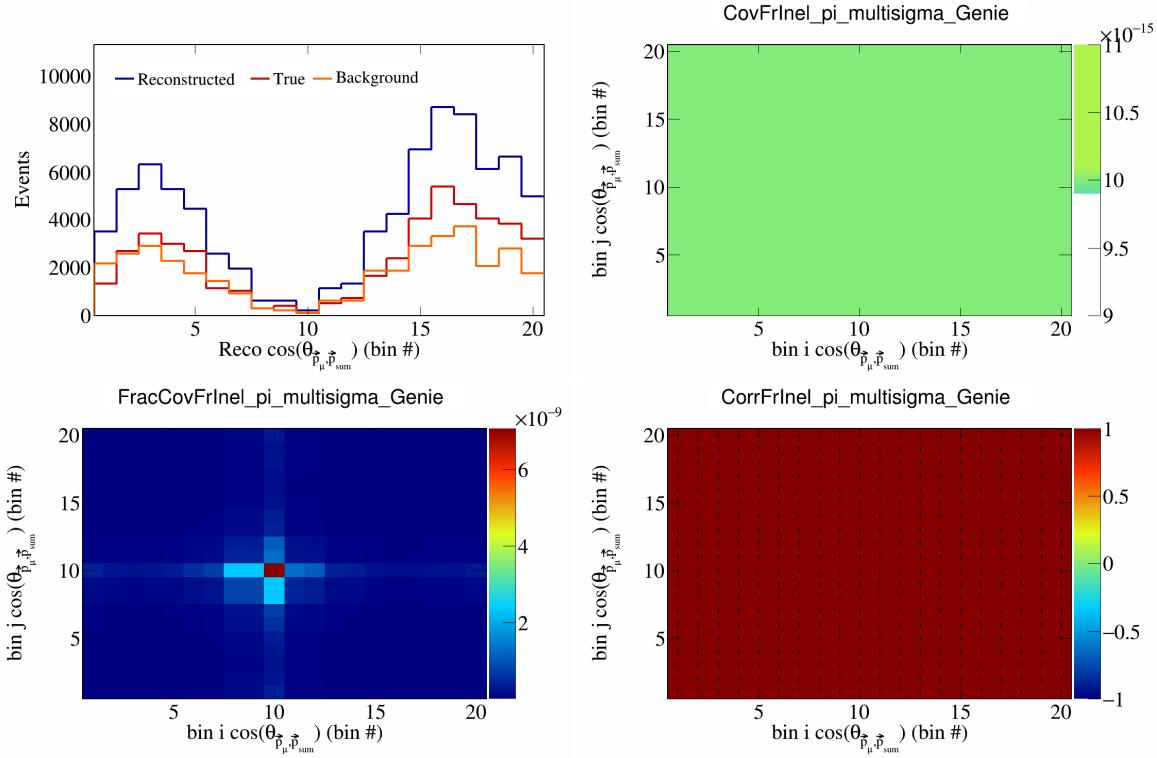


Figure 243: FrInelpi variations for  $\cos(\theta_{\vec{p}_\mu, \vec{p}_{\text{sum}}})$  in  $\cos(\theta_{\vec{p}_\mu})$ .

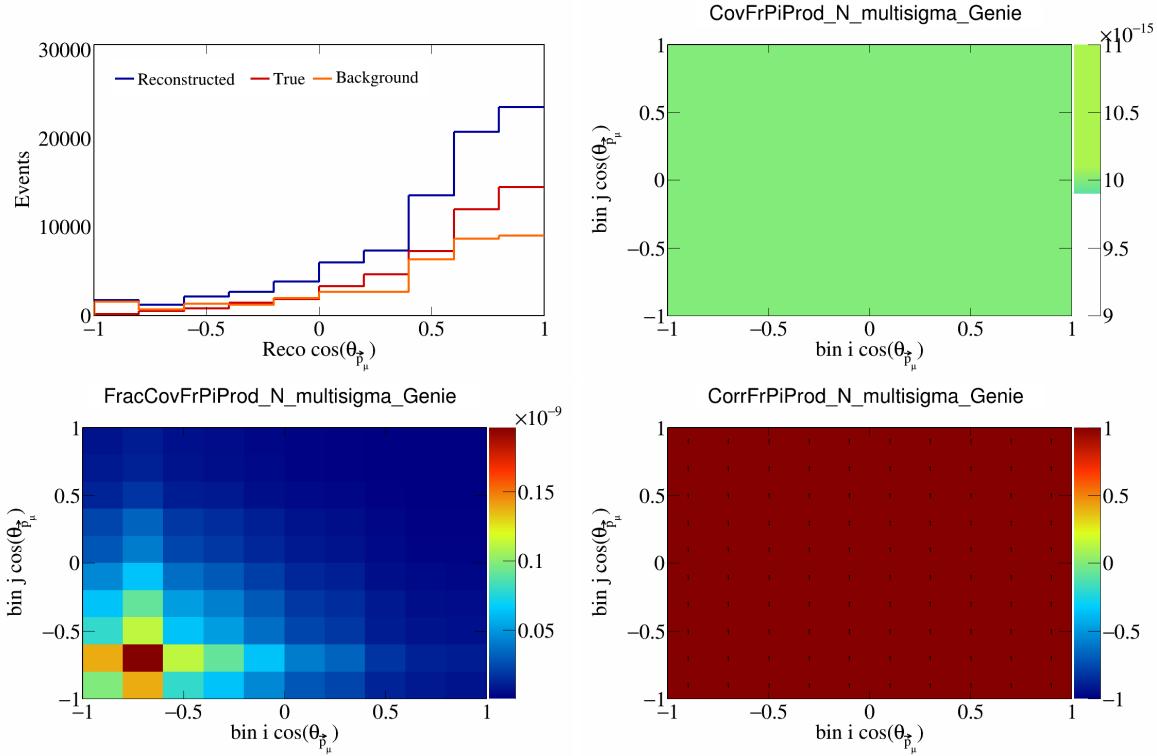


Figure 244: FrPiProdN variations for  $\cos(\theta_{\vec{p}_\mu})$ .

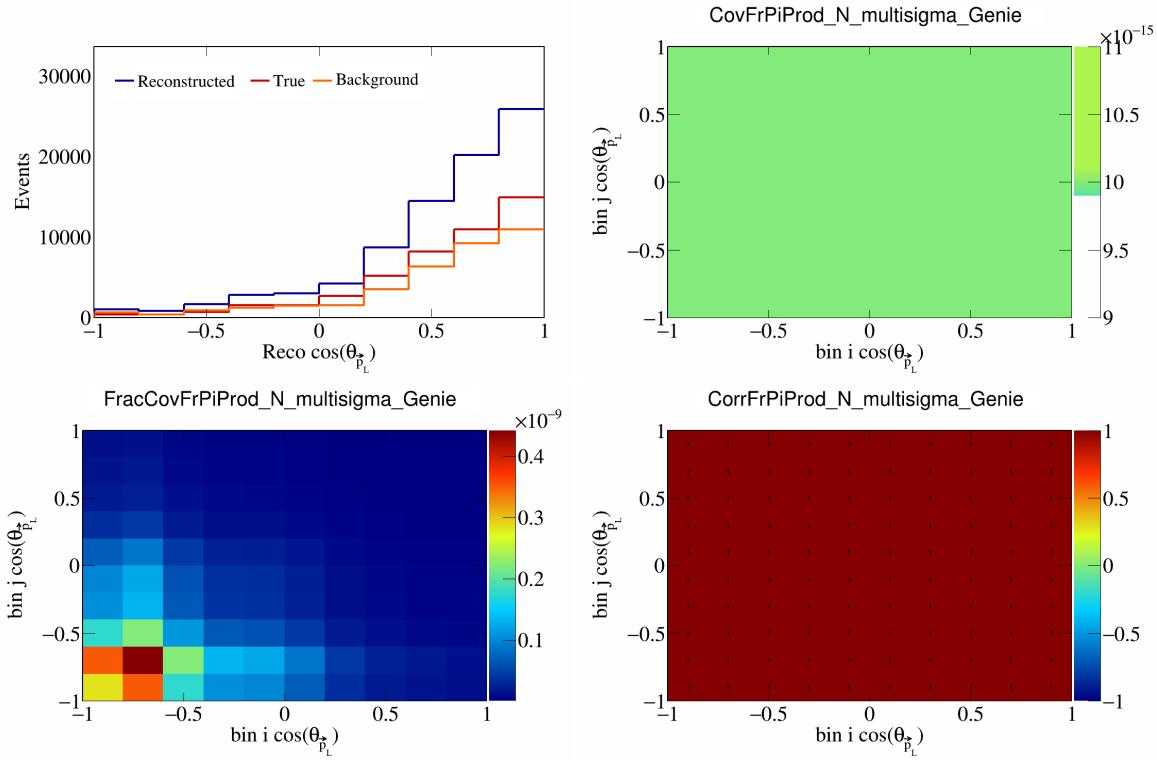


Figure 245: FrPiProdN variations for  $\cos(\theta_{\vec{p}_L})$ .

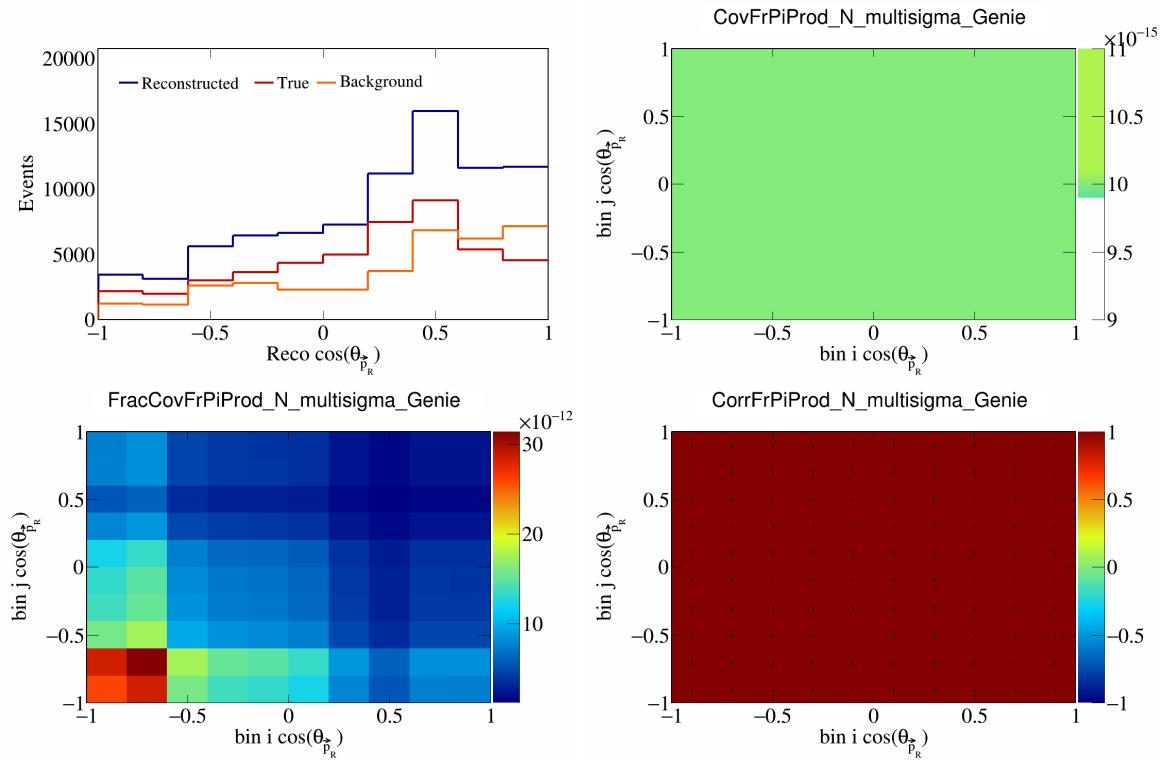


Figure 246: FrPiProdN variations for  $\cos(\theta_{\vec{p}_R})$ .

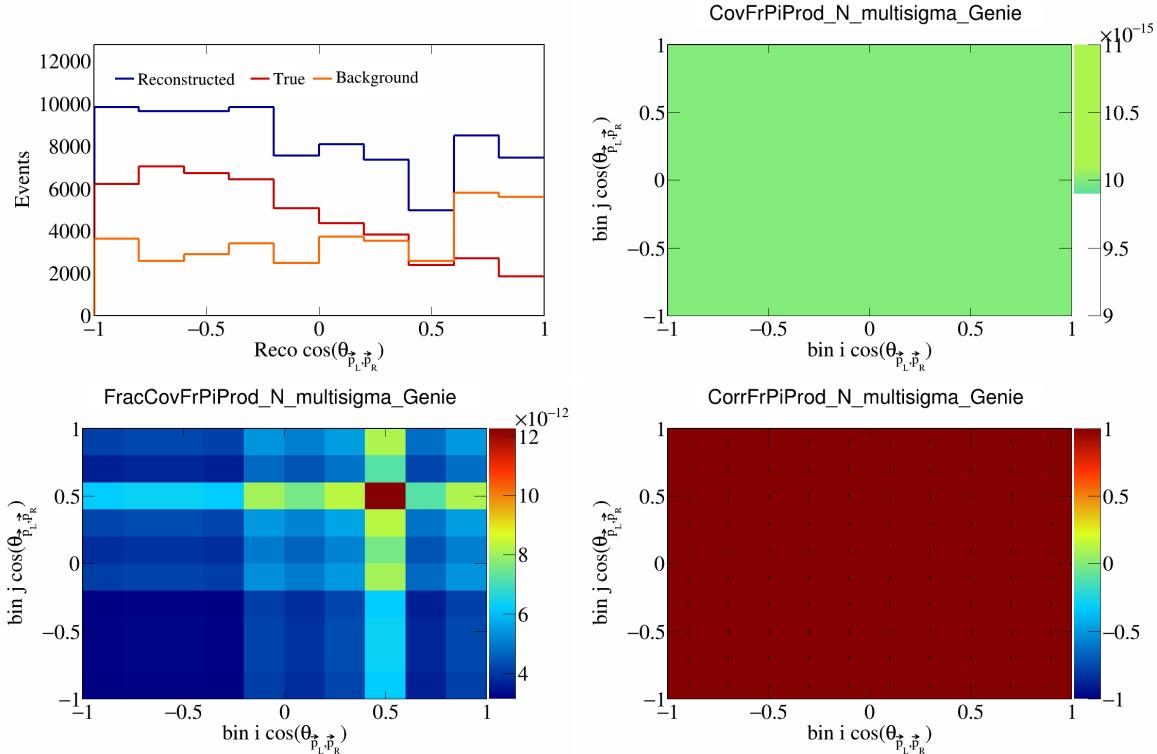


Figure 247: FrPiProdN variations for  $\cos(\theta_{\vec{p}_L, \vec{p}_R})$ .

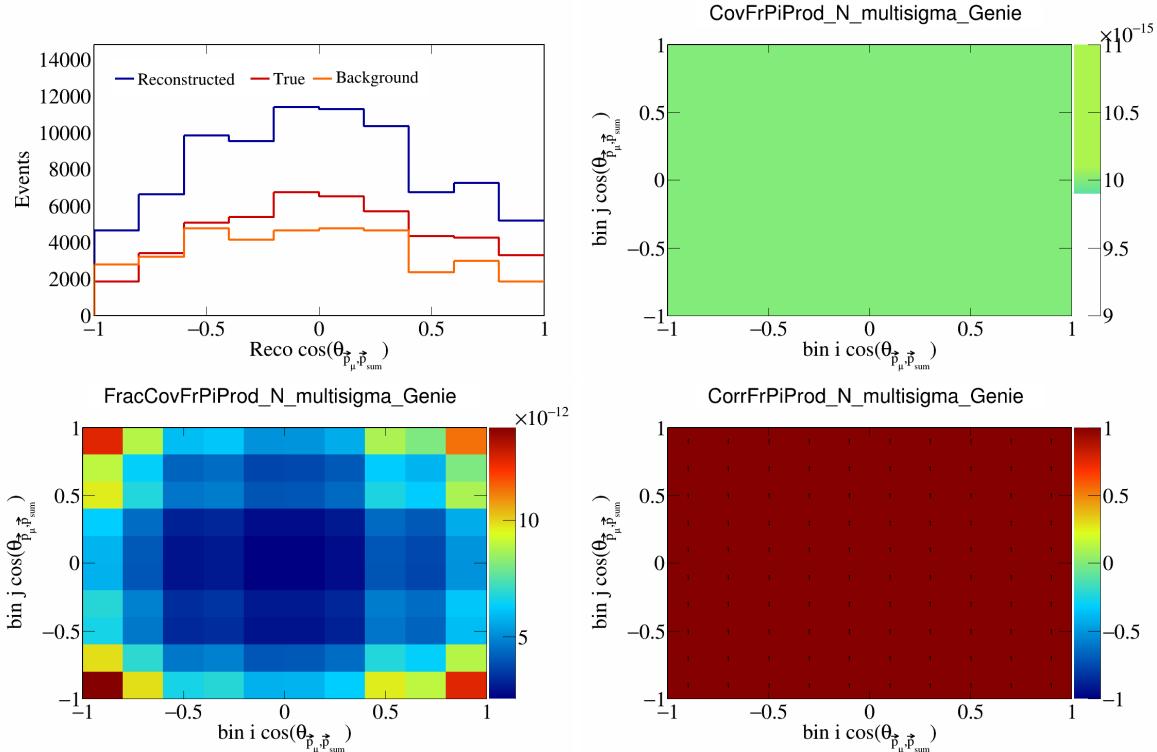


Figure 248: FrPiProdN variations for  $\cos(\theta_{\vec{p}_\mu, \vec{p}_{\text{sum}}})$ .

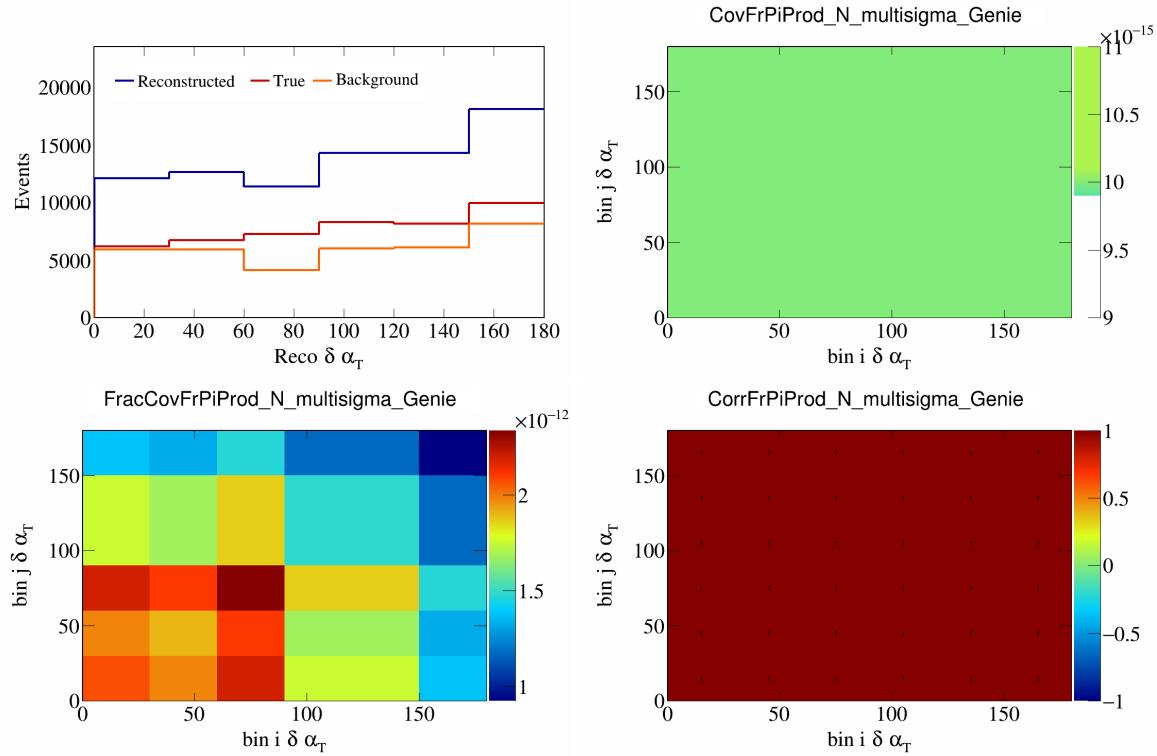


Figure 249: FrPiProdN variations for  $\delta\alpha_T$ .

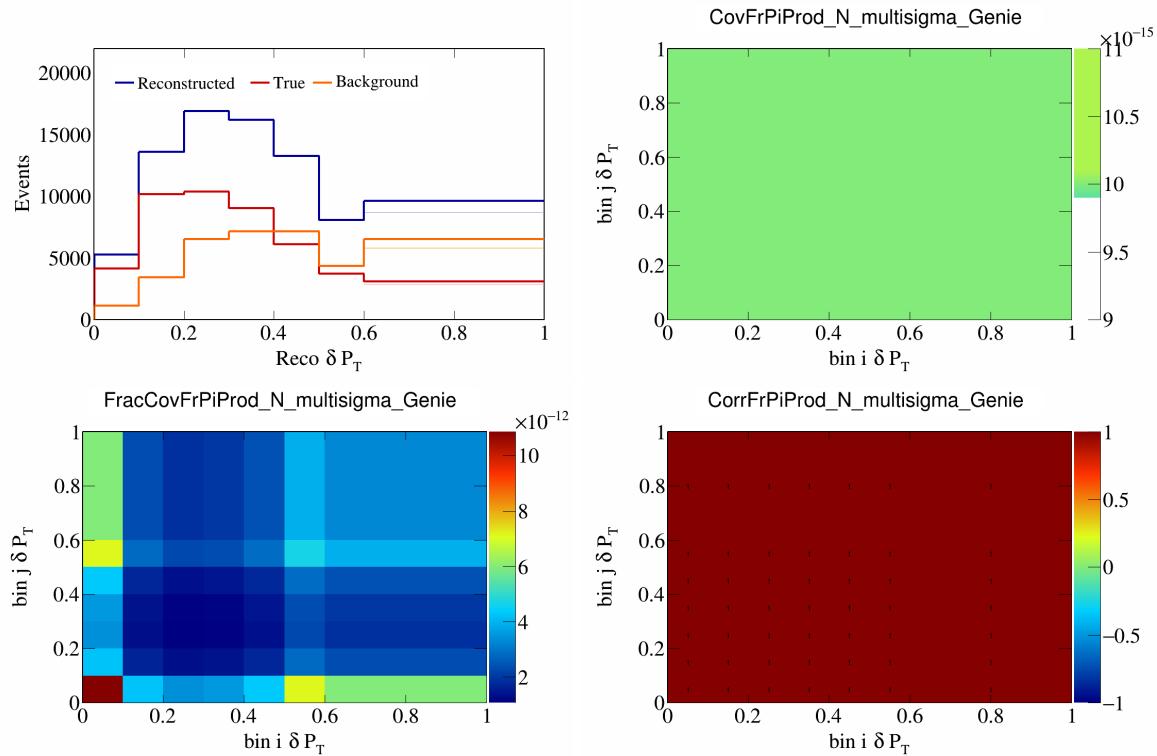


Figure 250: FrPiProdN variations for  $\delta P_T$ .

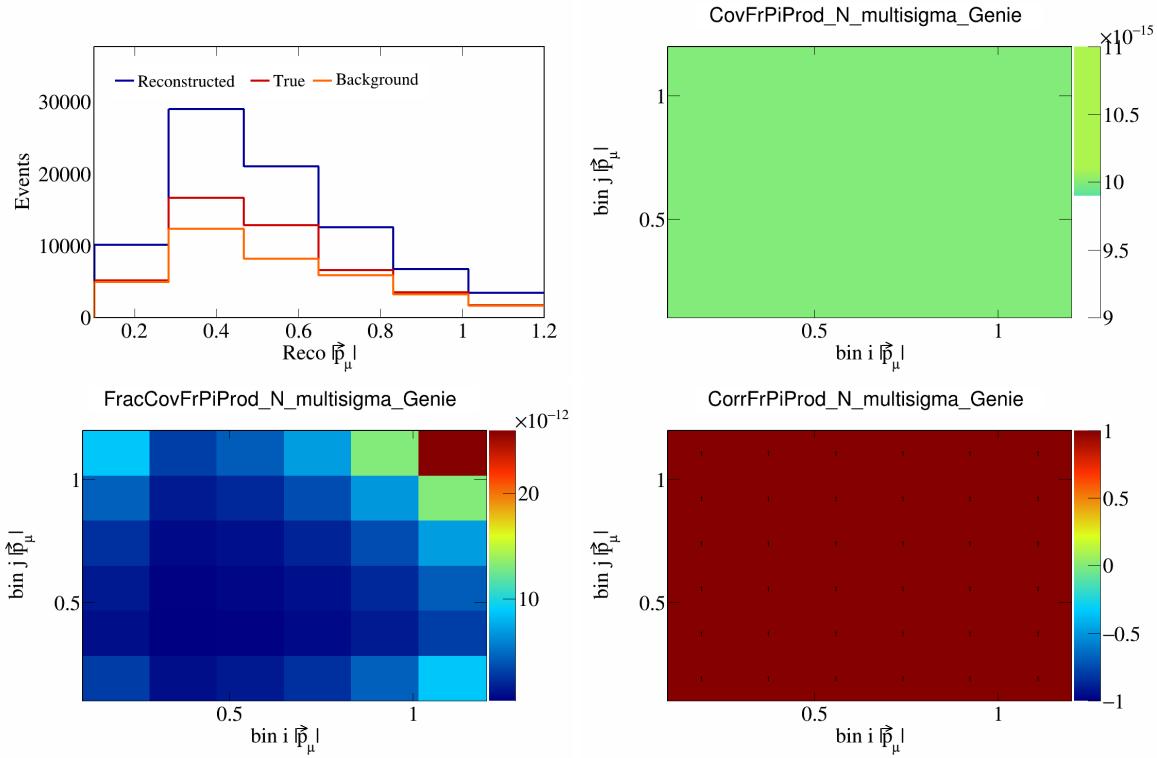


Figure 251: FrPiProdN variations for  $|\vec{p}_\mu|$ .

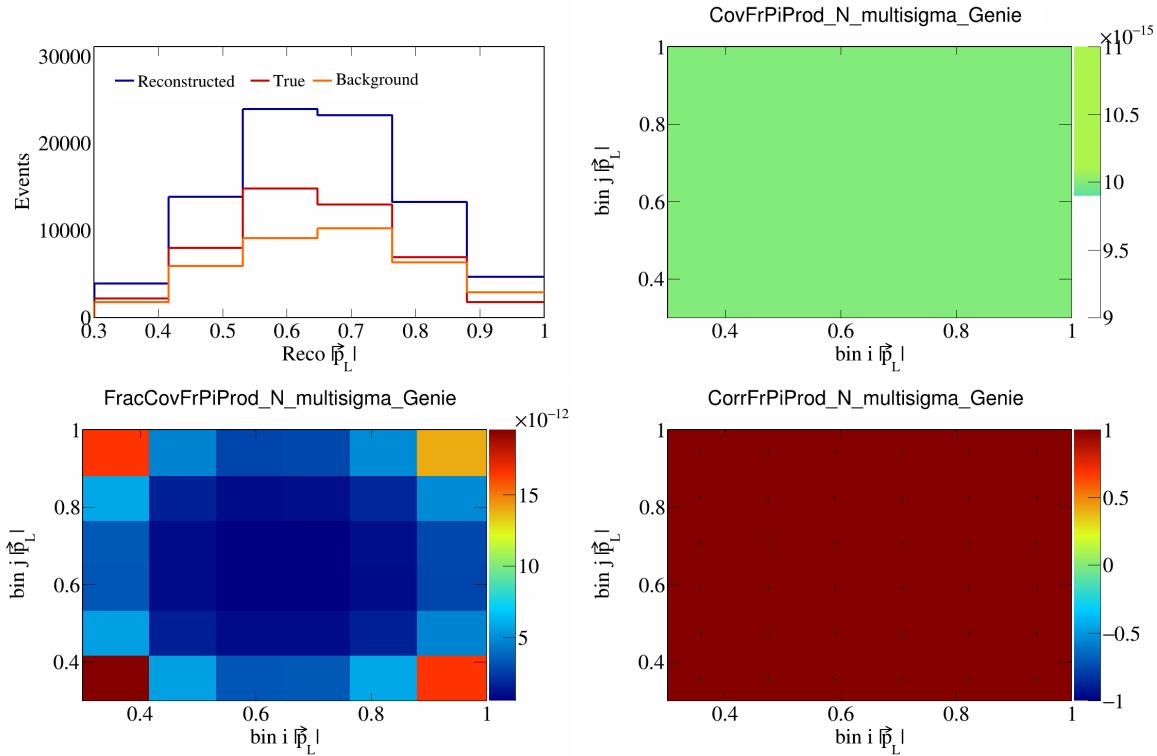


Figure 252: FrPiProdN variations for  $|\vec{p}_L|$ .

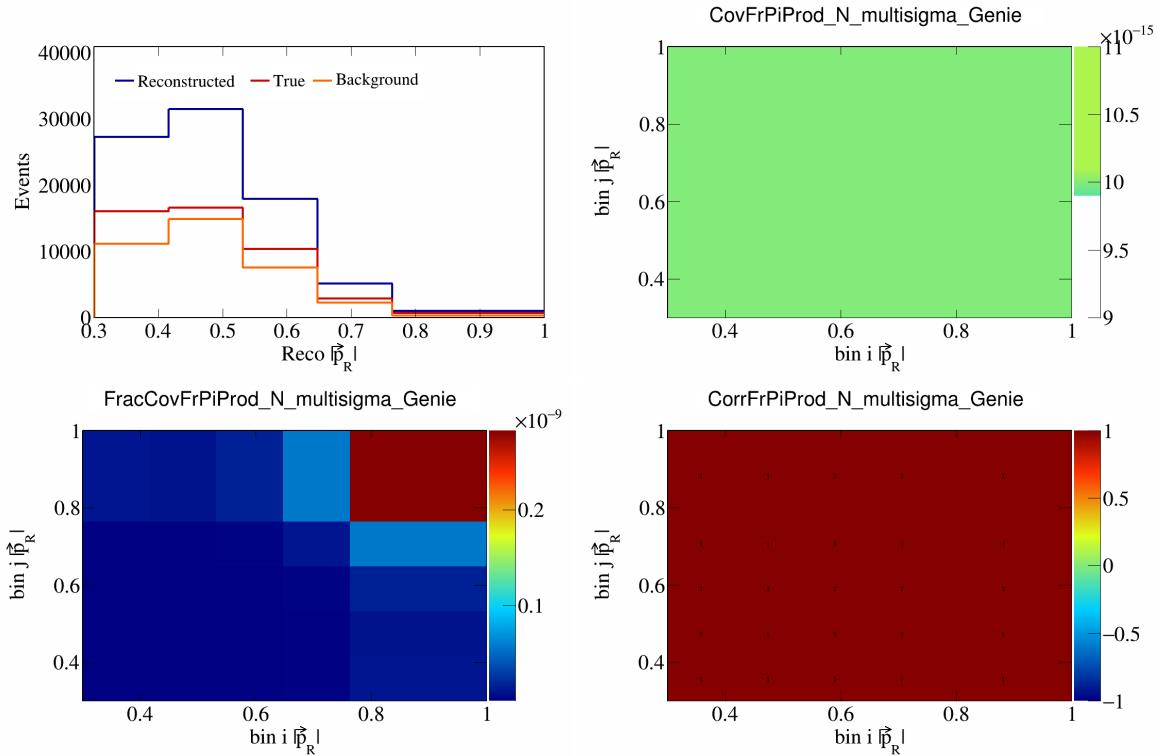


Figure 253: FrPiProdN variations for  $|\vec{p}_R|$ .

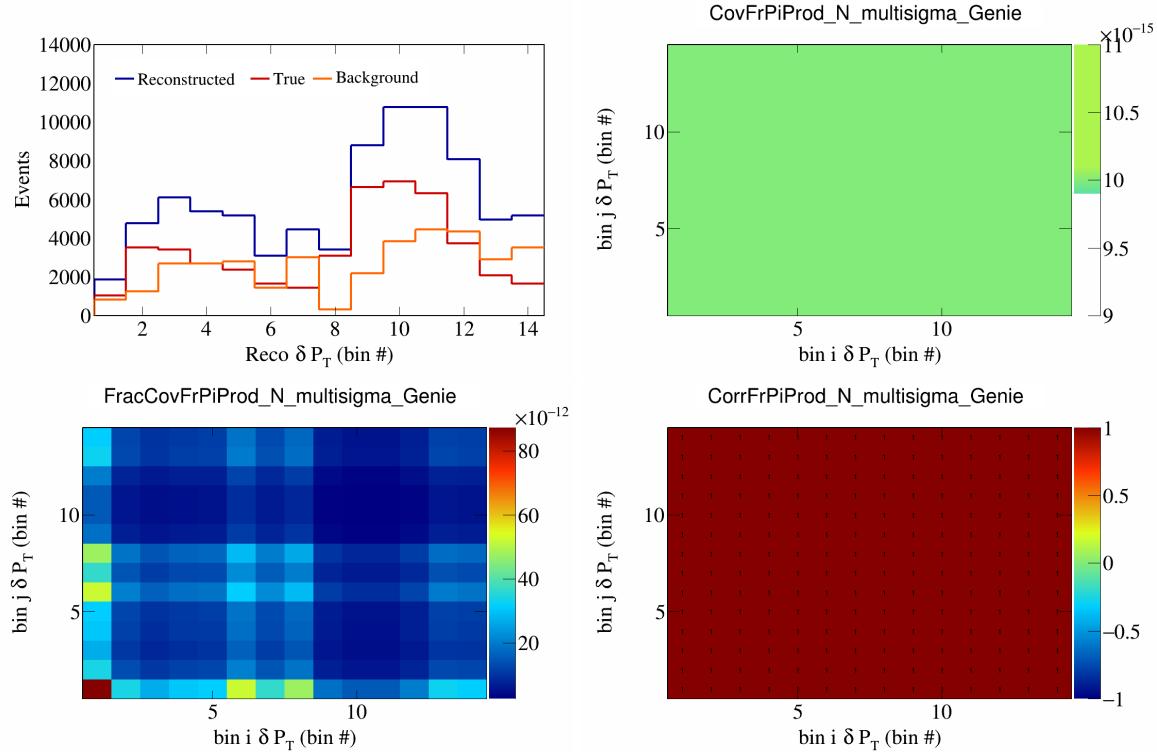


Figure 254: FrPiProdN variations for  $\delta P_T$  in  $\cos(\theta_{\vec{p}_\mu})$ .

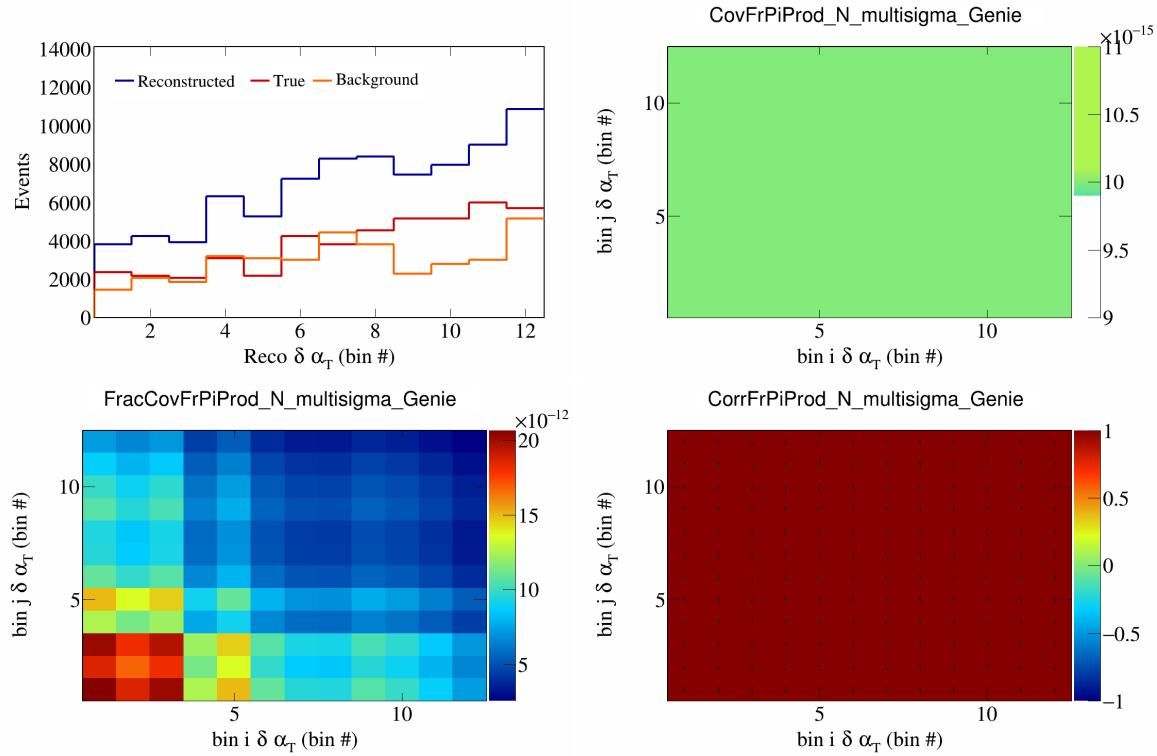


Figure 255: FrPiProdN variations for  $\delta\alpha_T$  in  $\cos(\theta_{\vec{p}_\mu})$ .

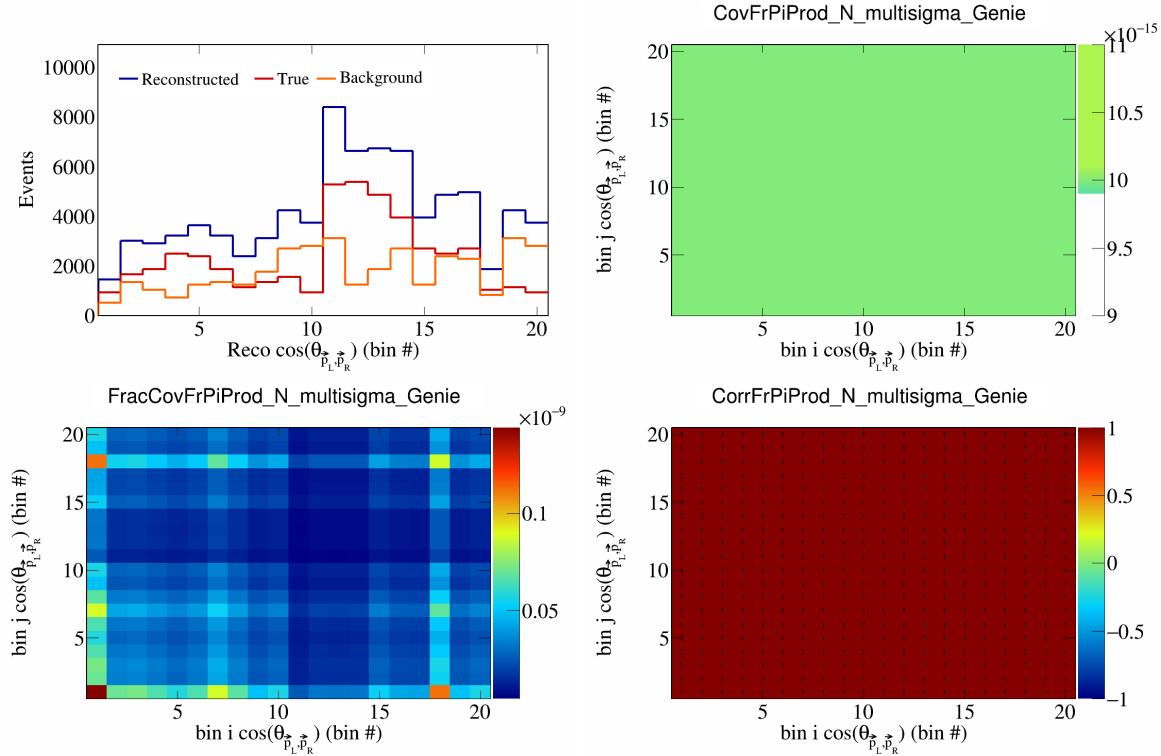


Figure 256: FrPiProdN variations for  $\cos(\theta_{\vec{p}_L, \vec{p}_R})$  in  $\cos(\theta_{\vec{p}_\mu})$ .

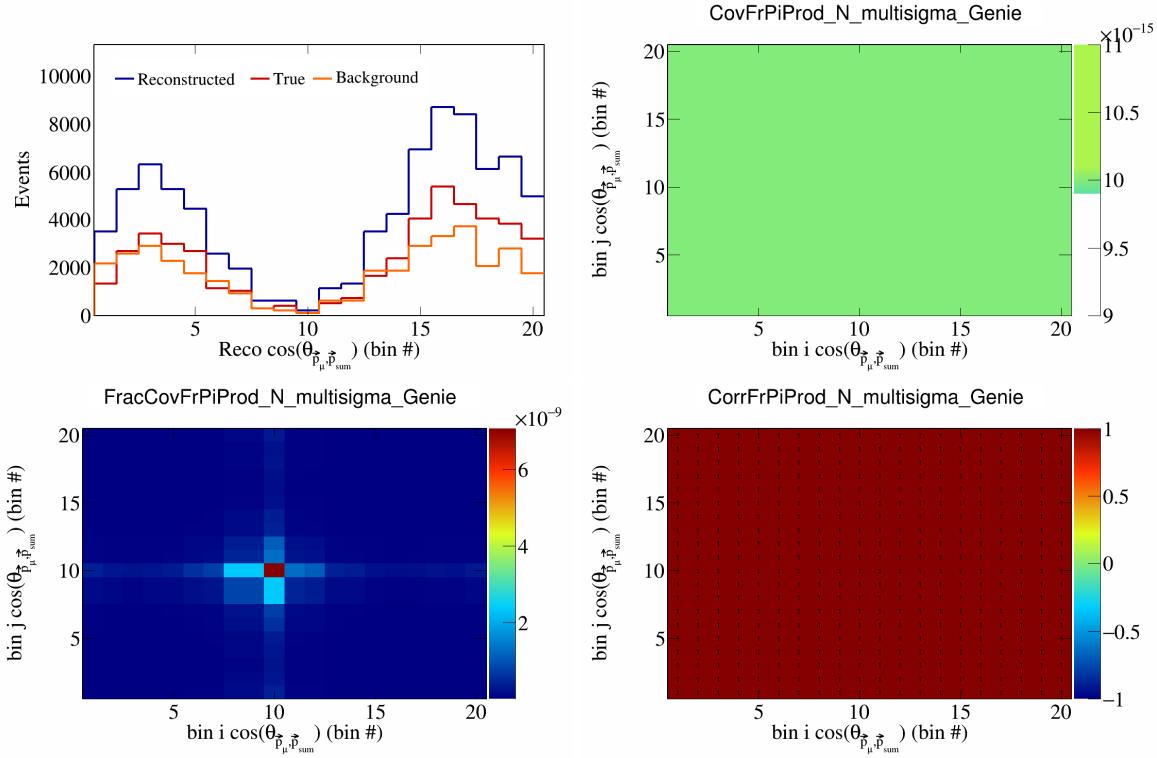


Figure 257: FrPiProdN variations for  $\cos(\theta_{\vec{p}_\mu, \vec{p}_{\text{sum}}})$  in  $\cos(\theta_{\vec{p}_\mu})$ .

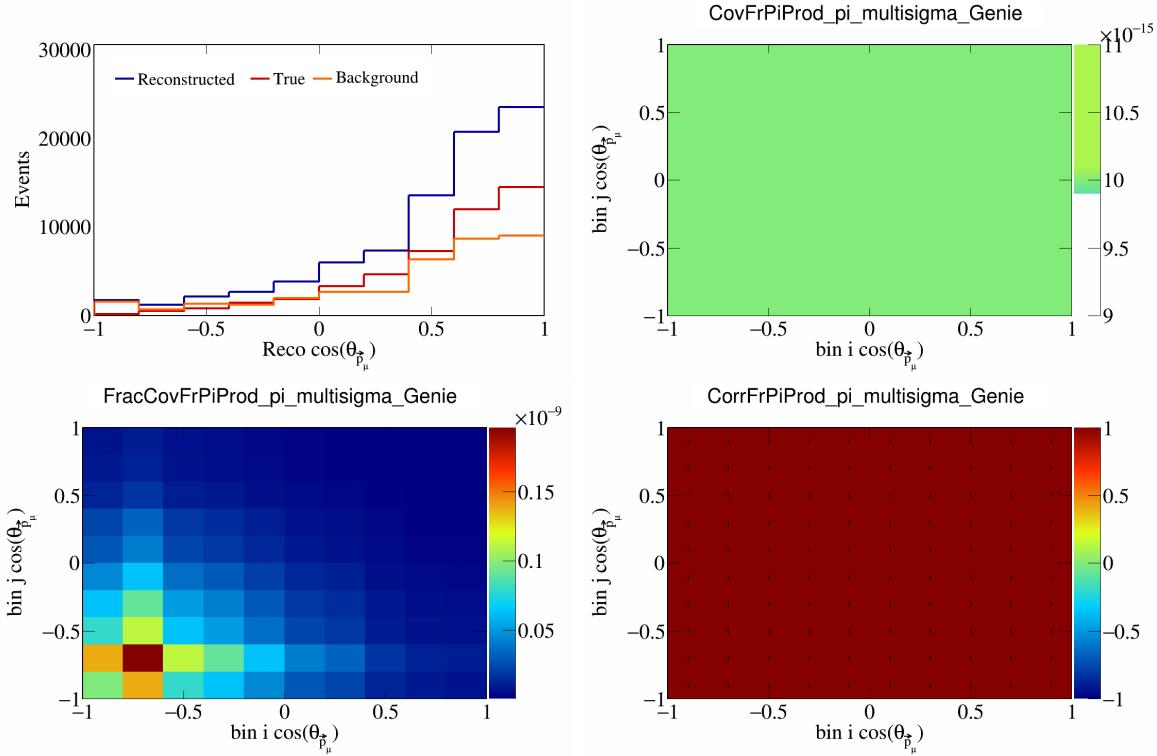


Figure 258: FrPiProdpi variations for  $\cos(\theta_{\vec{p}_\mu, \vec{p}_\pi})$  in  $\cos(\theta_{\vec{p}_\mu})$ .

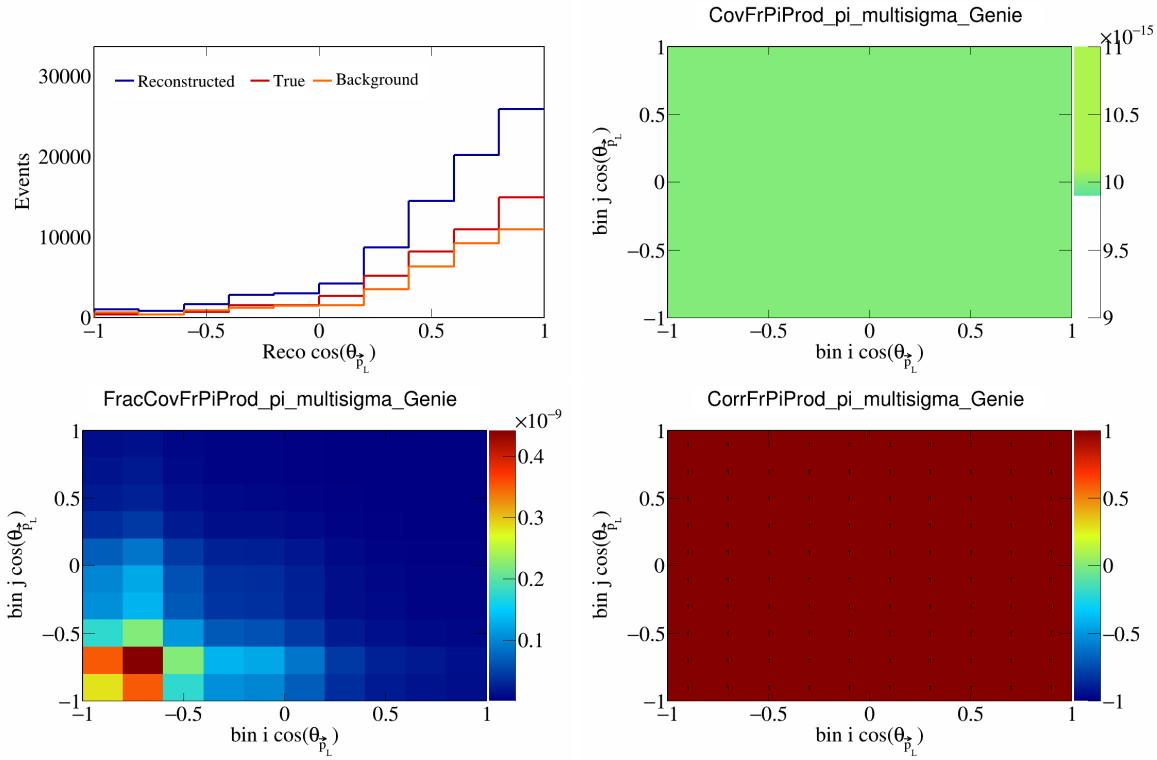


Figure 259: FrPiProdpi variations for  $\cos(\theta_{\vec{p}_L})$ .

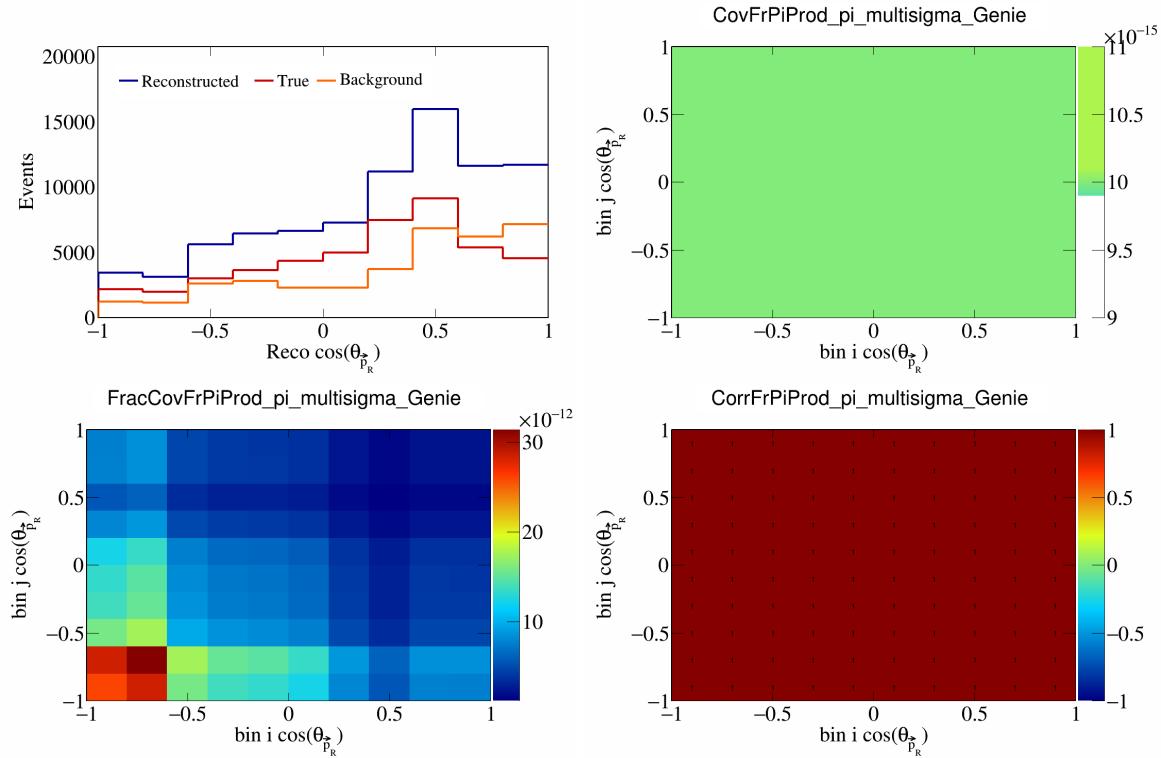


Figure 260: FrPiProdpi variations for  $\cos(\theta_{\vec{p}_R})$ .

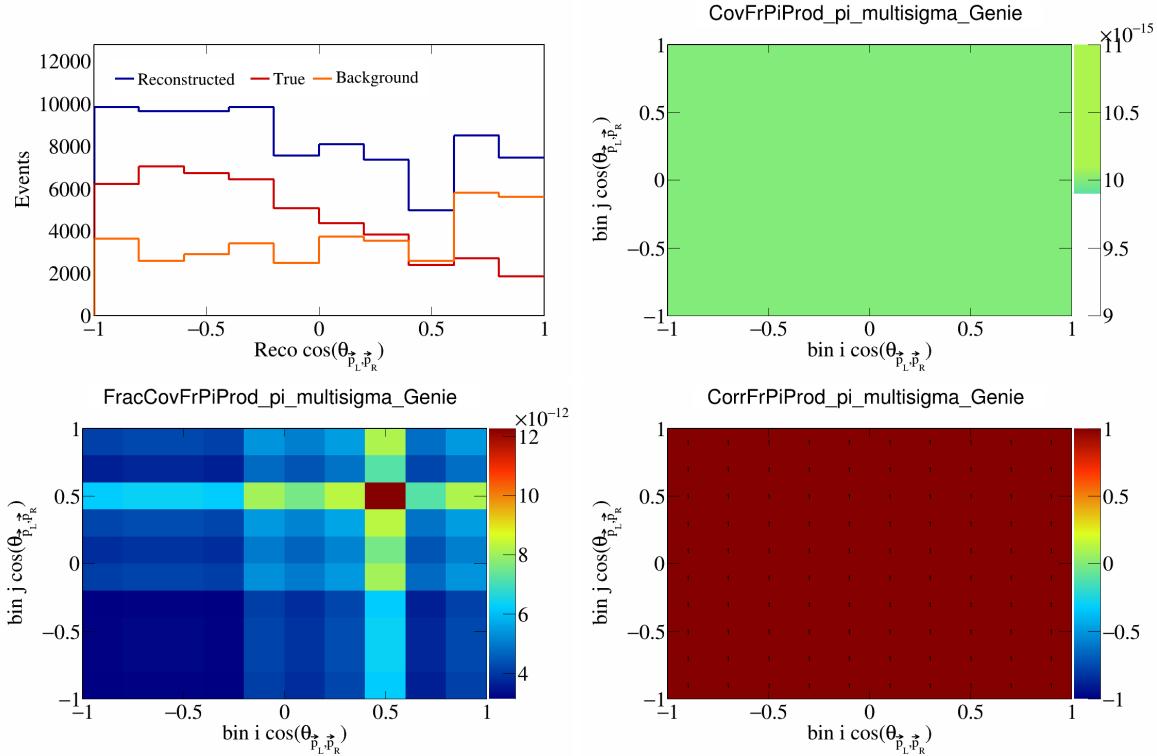


Figure 261: FrPiProdpi variations for  $\cos(\theta_{\vec{p}_L, \vec{p}_R})$ .

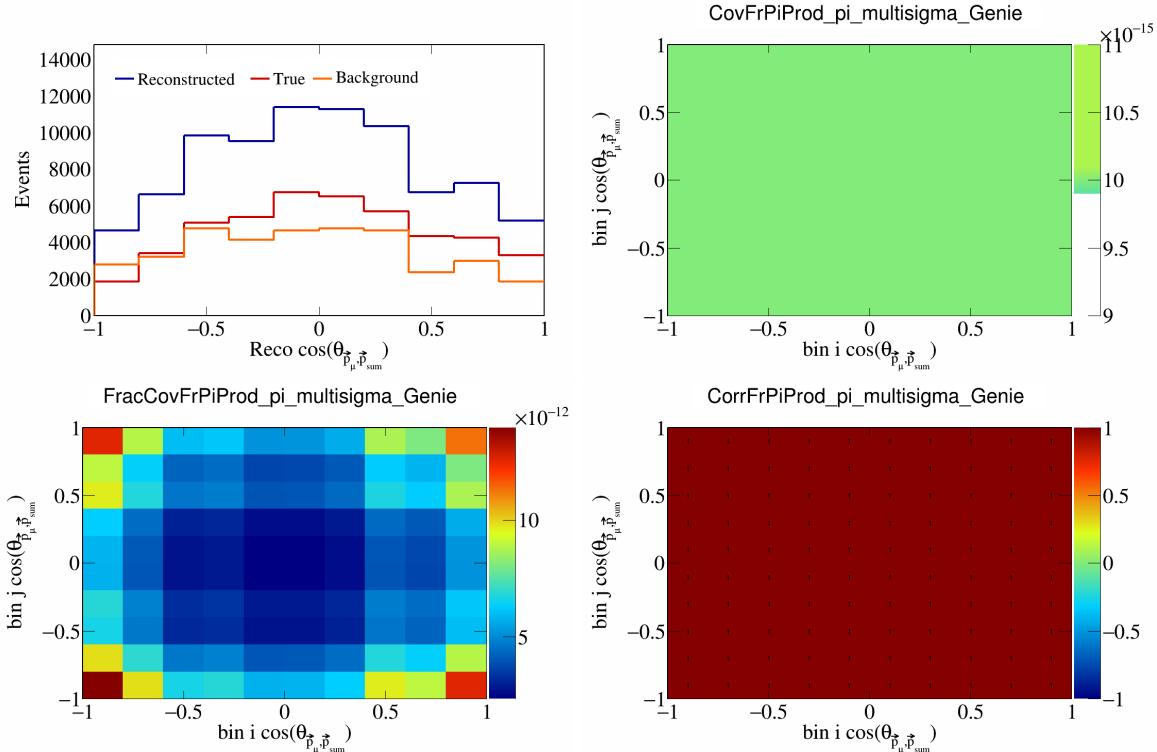


Figure 262: FrPiProdpi variations for  $\cos(\theta_{\vec{p}_\mu, \vec{p}_{\text{sum}}})$ .

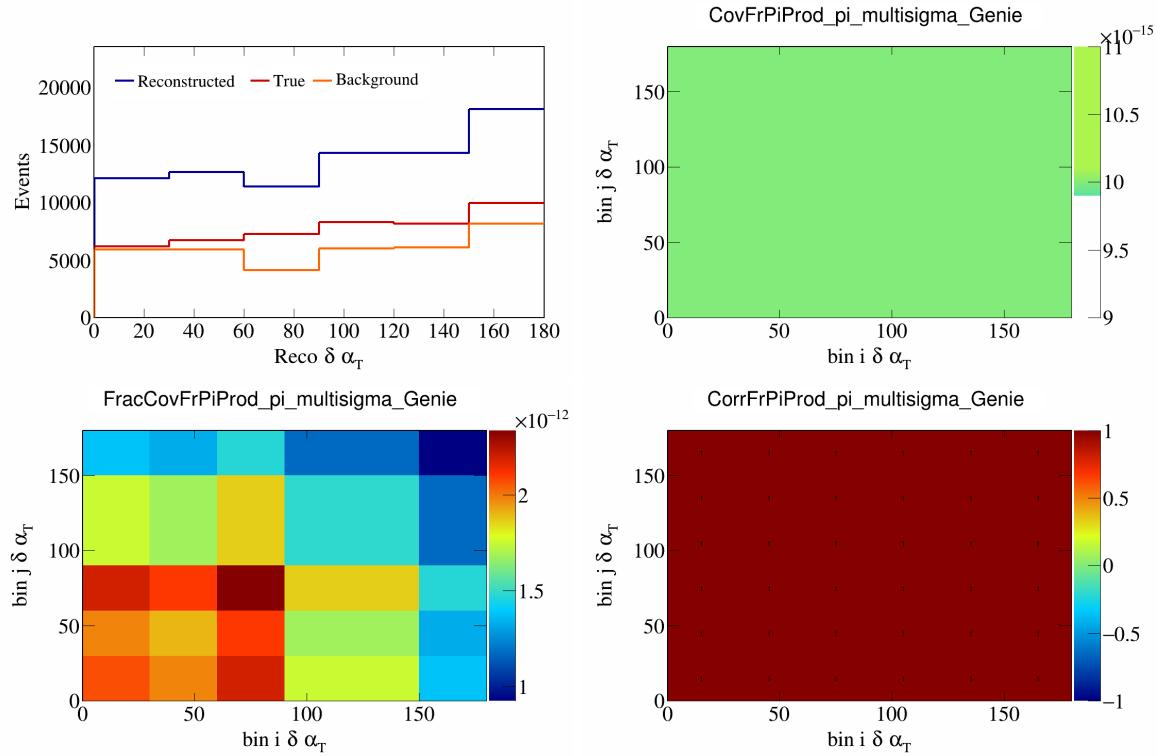


Figure 263: FrPiProdpi variations for  $\delta\alpha_T$ .

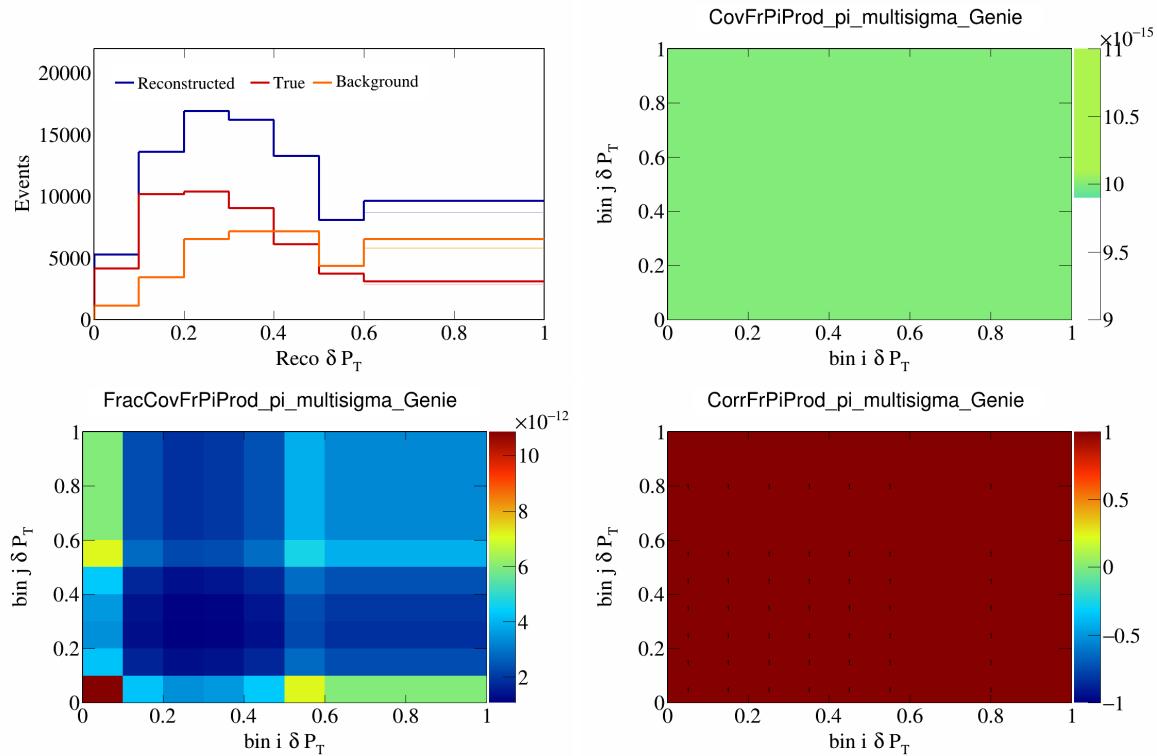


Figure 264: FrPiProdpi variations for  $\delta P_T$ .

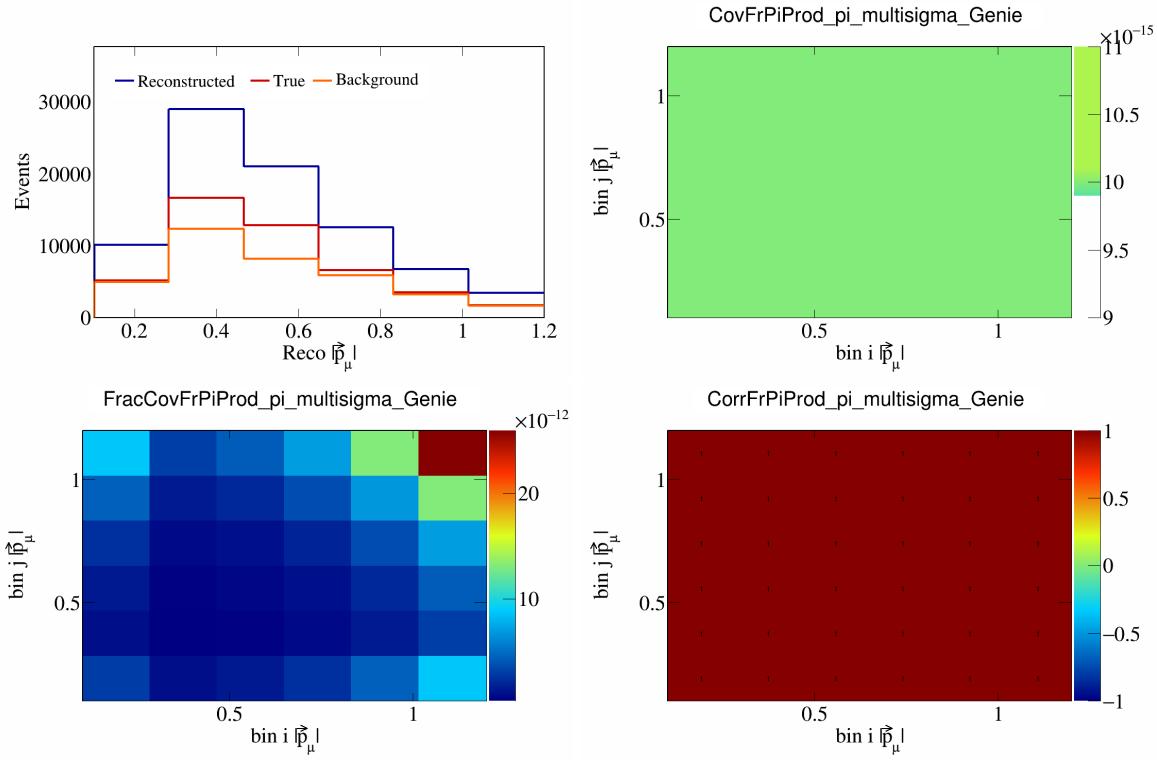


Figure 265: FrPiProdpi variations for  $|\vec{p}_\mu|$ .

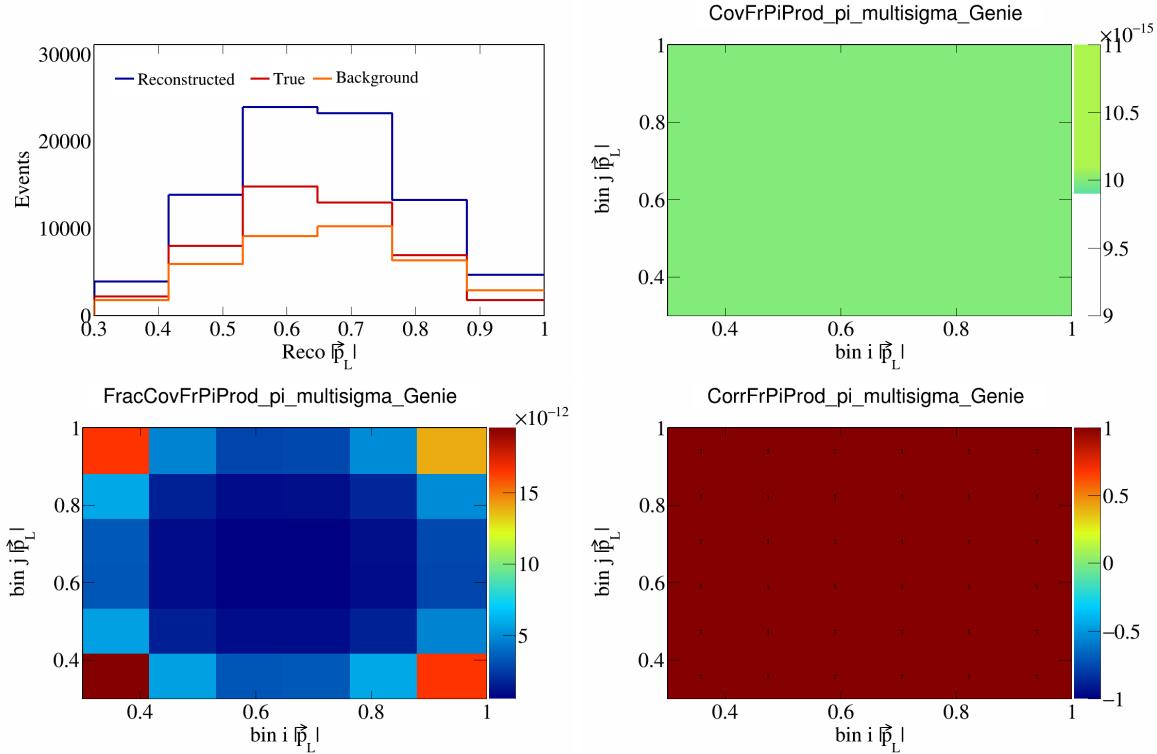


Figure 266: FrPiProdpi variations for  $|\vec{p}_L|$ .

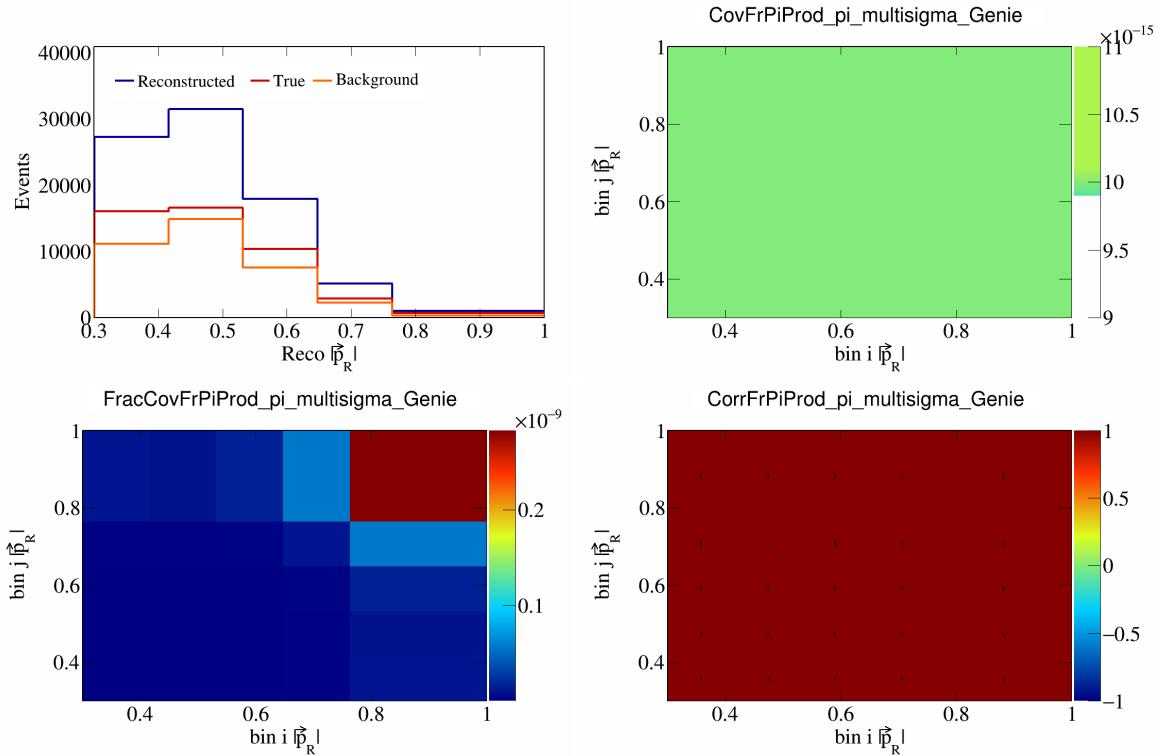


Figure 267: FrPiProdpi variations for  $|\vec{p}_R|$ .

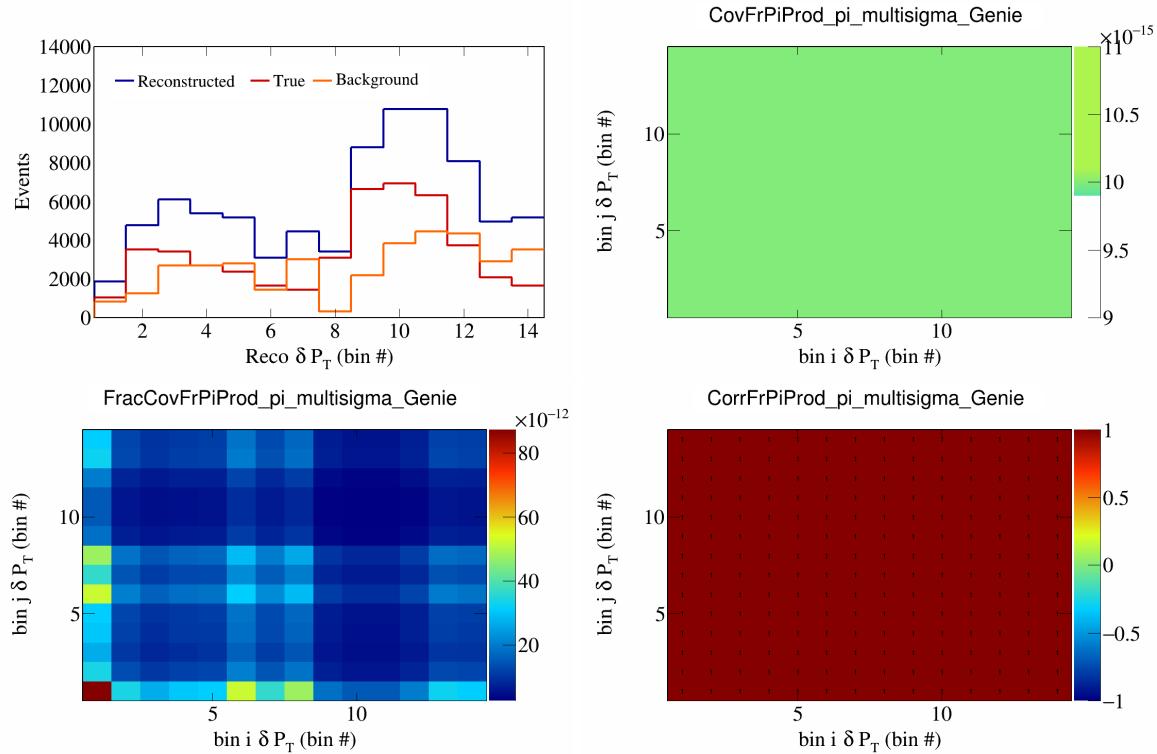


Figure 268: FrPiProdpi variations for  $\delta P_T$  in  $\cos(\theta_{\vec{p}_\mu})$ .

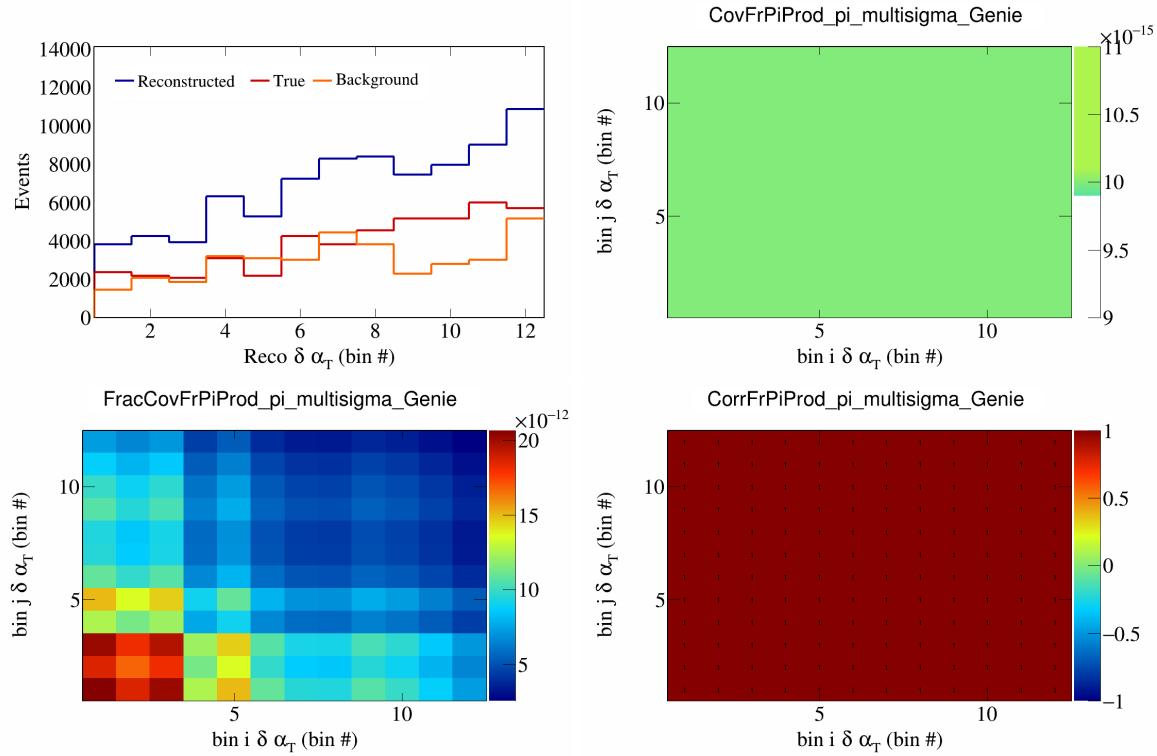


Figure 269: FrPiProdpi variations for  $\delta\alpha_T$  in  $\cos(\theta_{\vec{p}_\mu})$ .

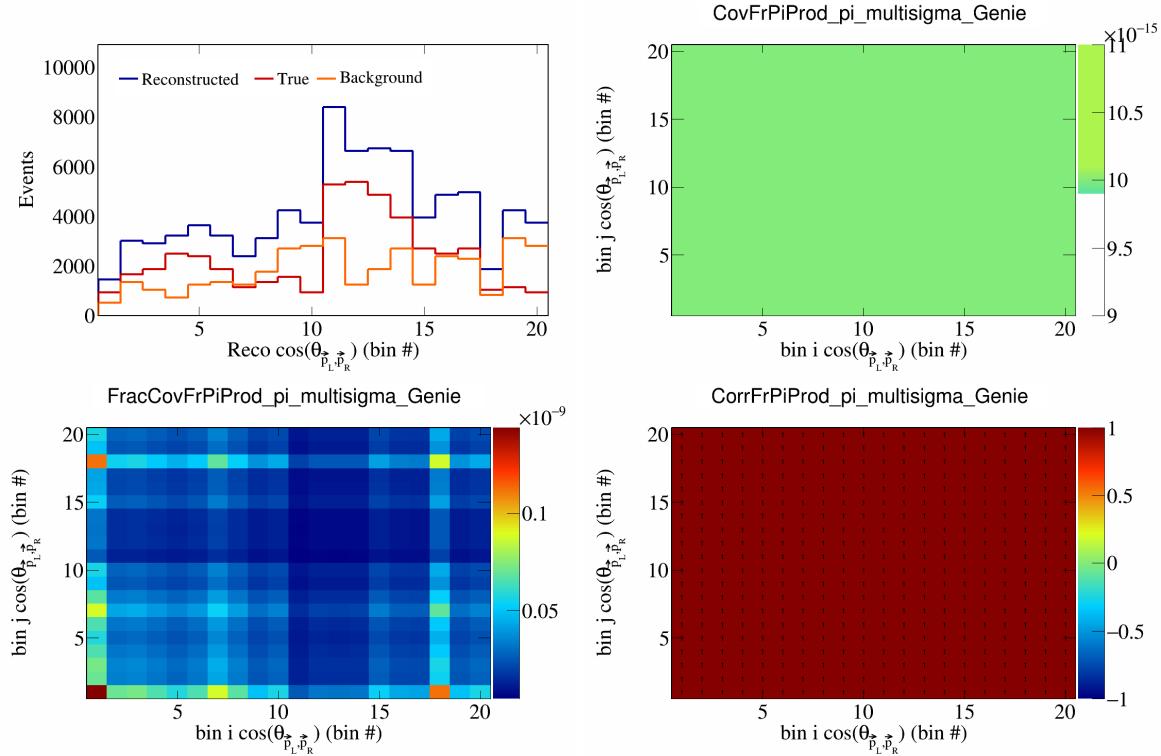


Figure 270: FrPiProdpi variations for  $\cos(\theta_{\vec{p}_L, \vec{p}_R})$  in  $\cos(\theta_{\vec{p}_\mu})$ .

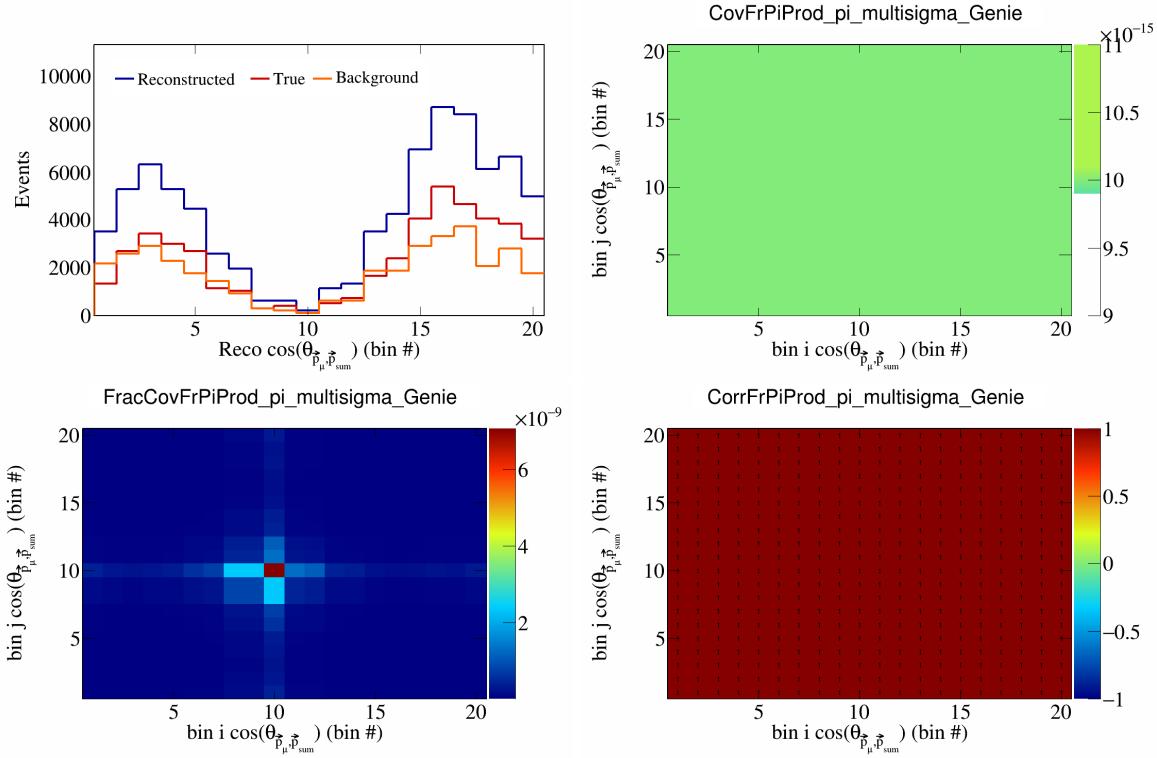


Figure 271: FrPiProdpi variations for  $\cos(\theta_{\vec{p}_\mu, \vec{p}_{\text{sum}}})$  in  $\cos(\theta_{\vec{p}_\mu})$ .

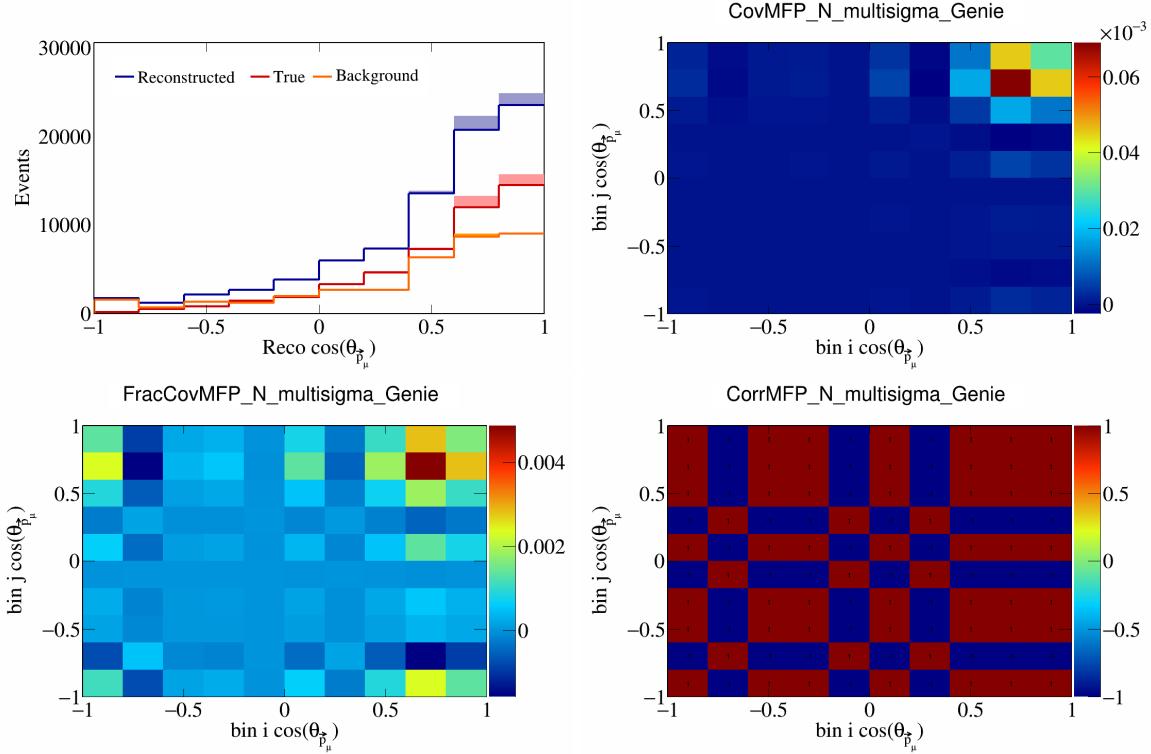


Figure 272: MFPN variations for  $\cos(\theta_{\vec{p}_\mu})$ .

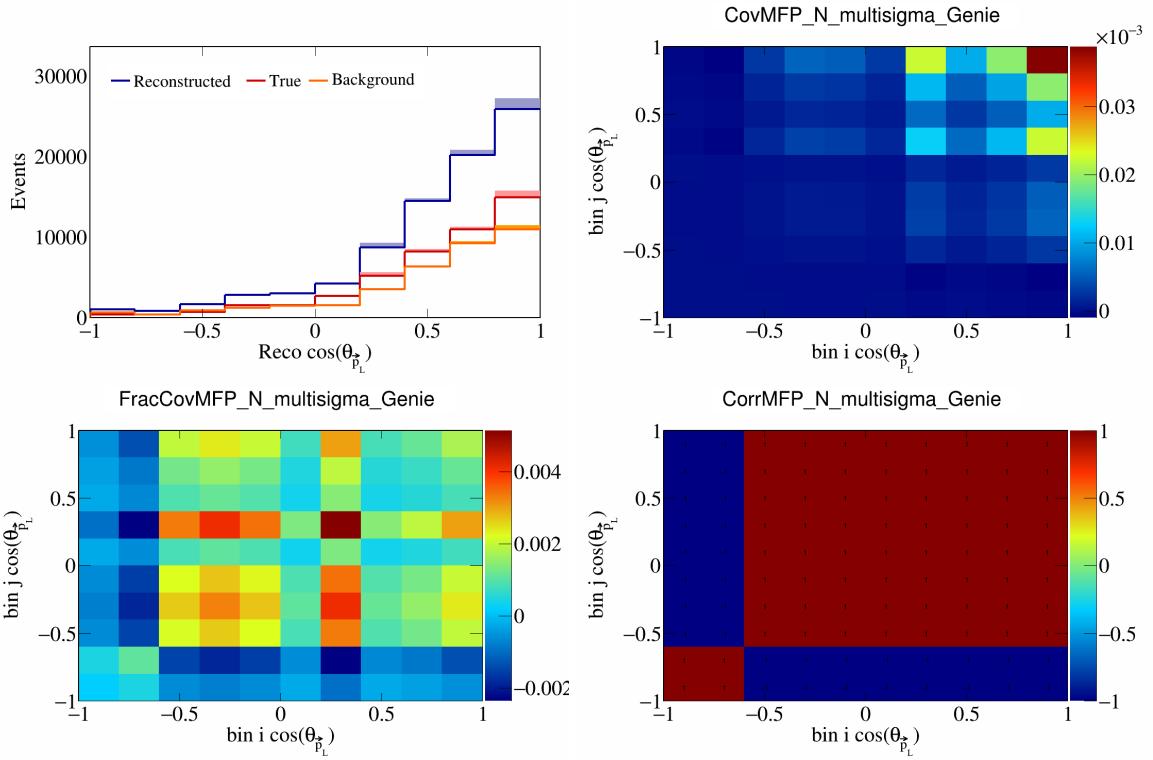


Figure 273: MFPN variations for  $\cos(\theta_{\vec{p}_L})$ .

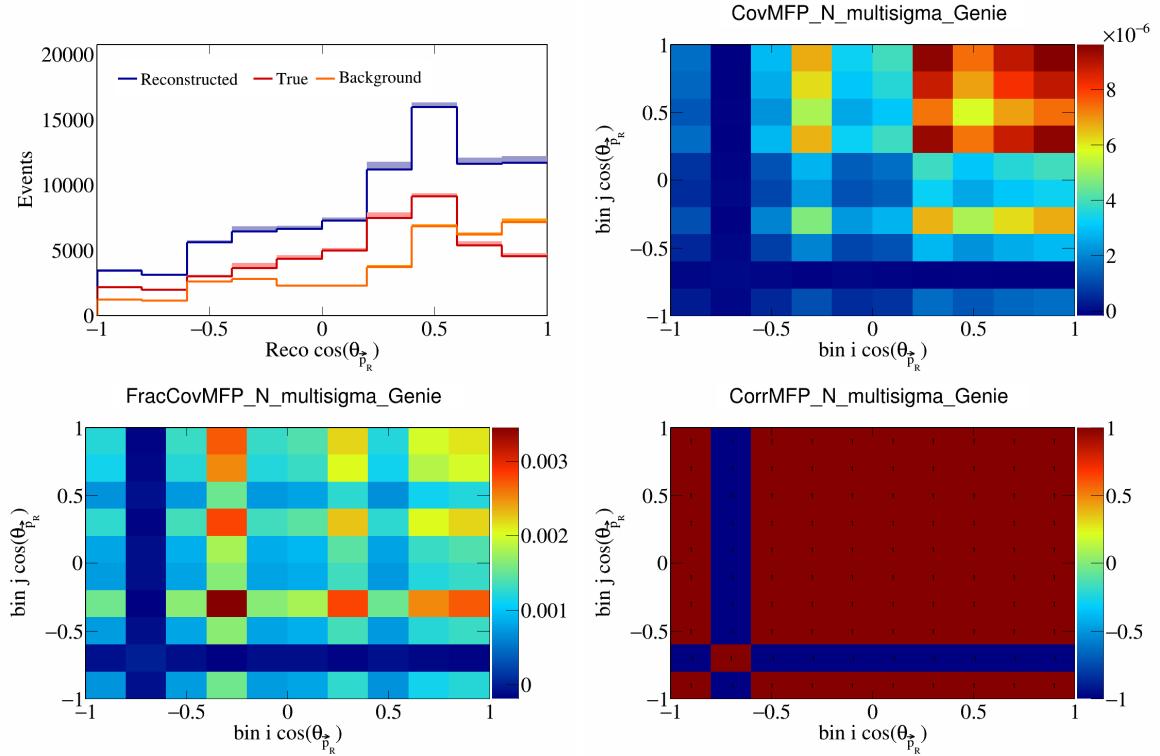


Figure 274: MFPN variations for  $\cos(\theta_{\vec{p}_R})$ .

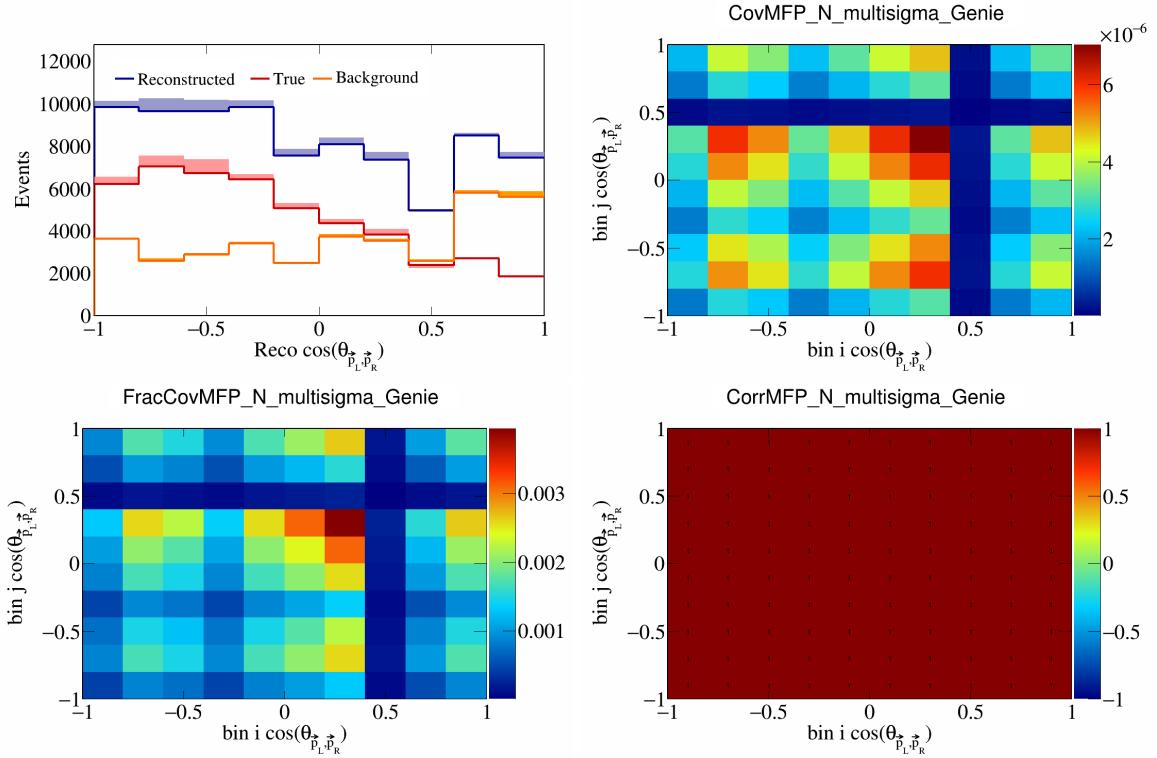


Figure 275: MFPN variations for  $\cos(\theta_{\vec{p}_L, \vec{p}_R})$ .

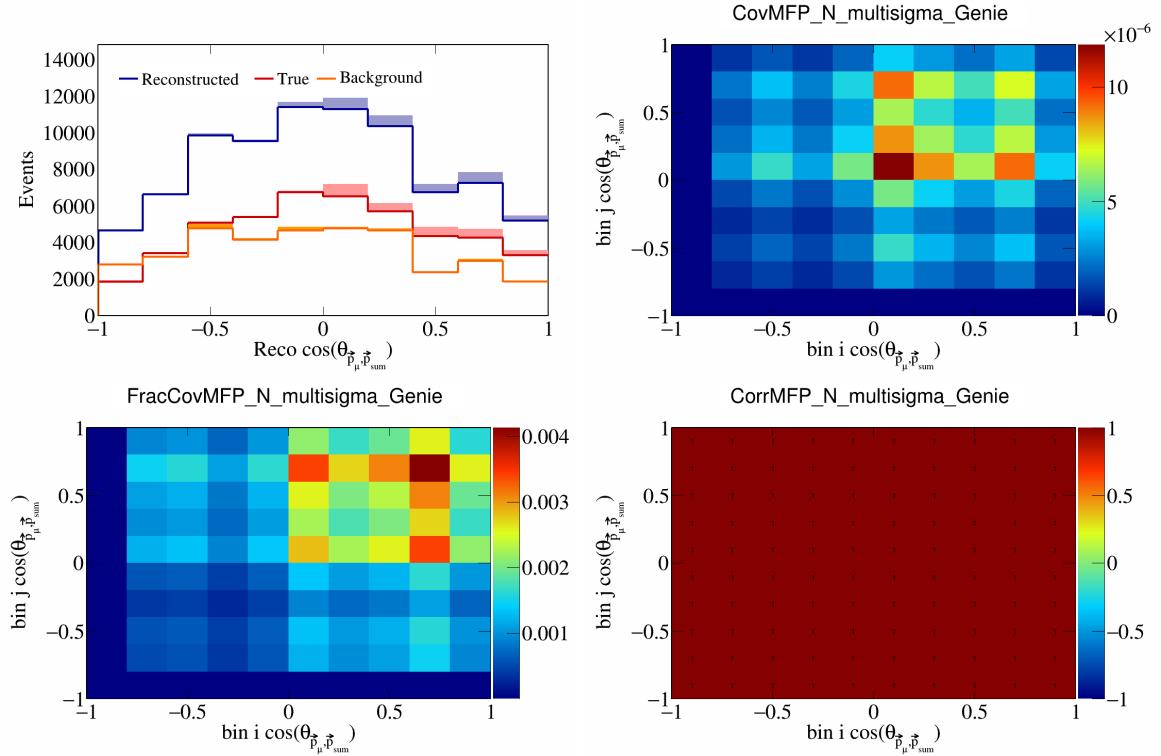


Figure 276: MFPN variations for  $\cos(\theta_{\vec{p}_\mu, \vec{p}_{\text{sum}}})$ .

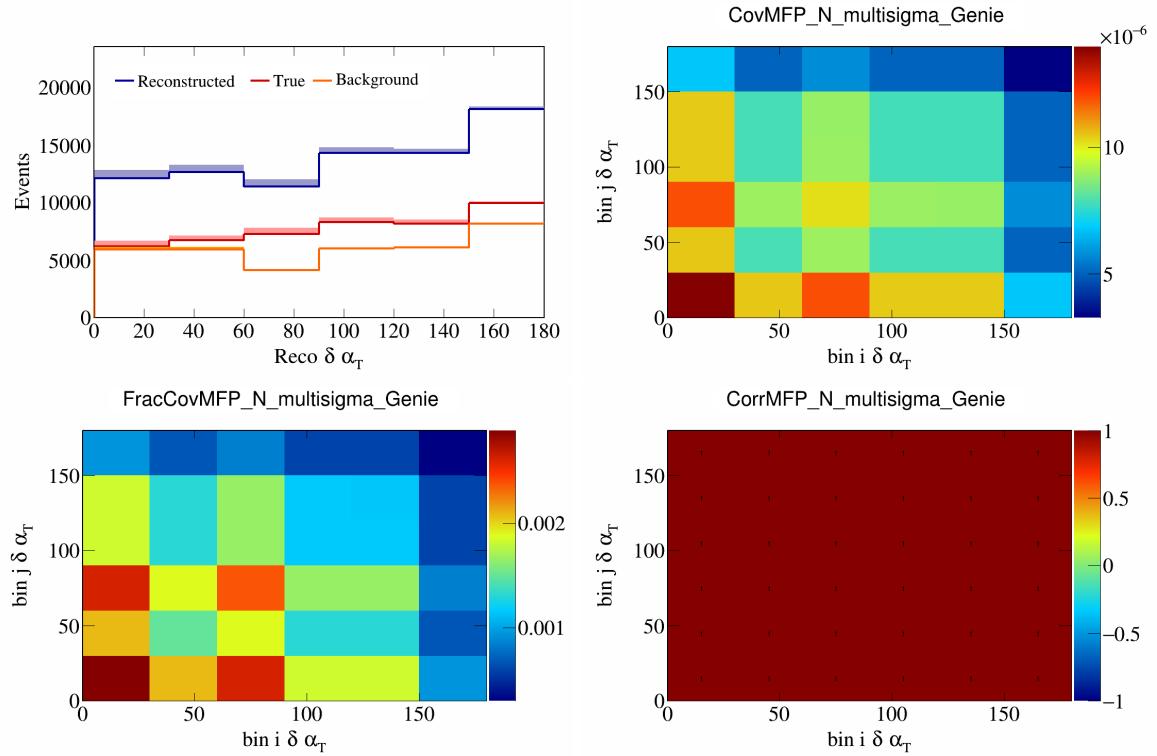


Figure 277: MFPN variations for  $\delta\alpha_T$ .

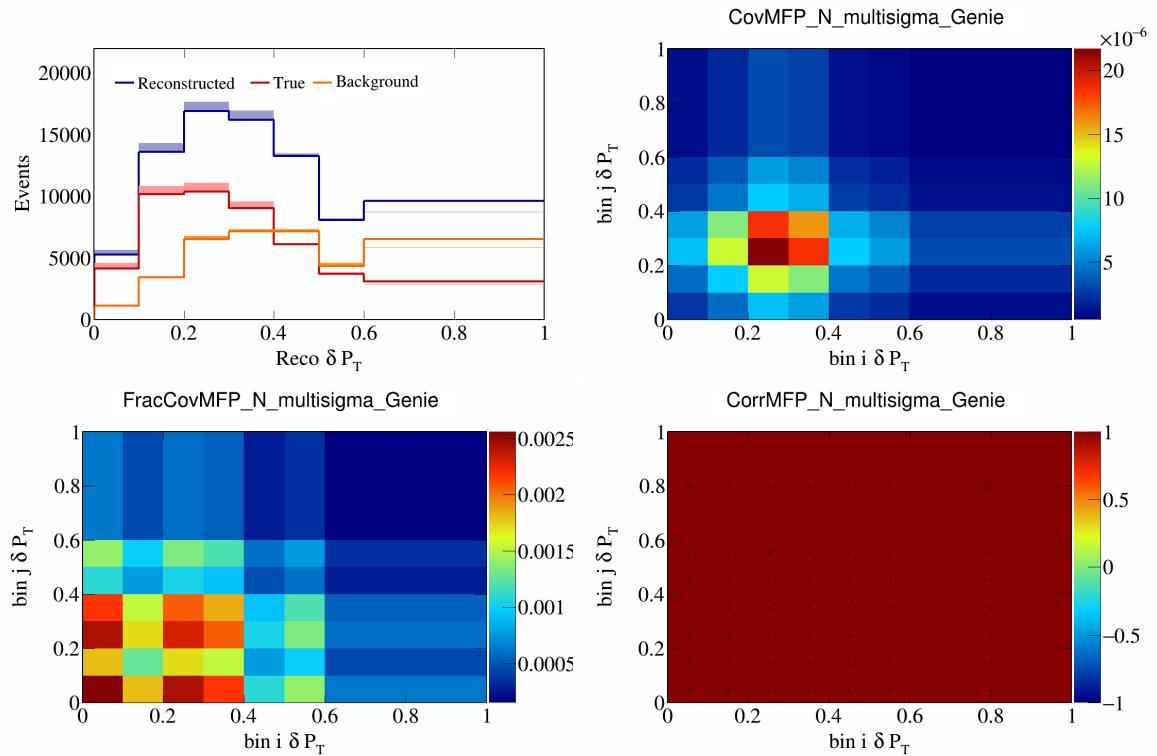


Figure 278: MFPN variations for  $\delta P_T$ .

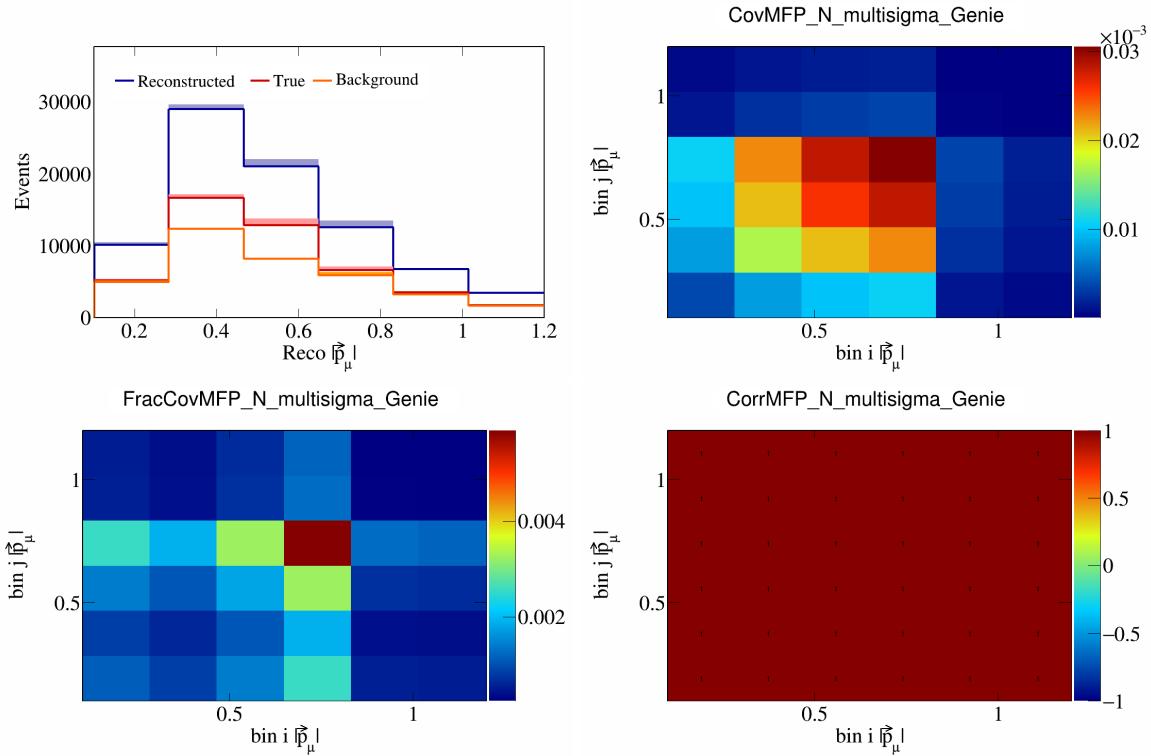


Figure 279: MFPN variations for  $|\vec{p}_\mu|$ .

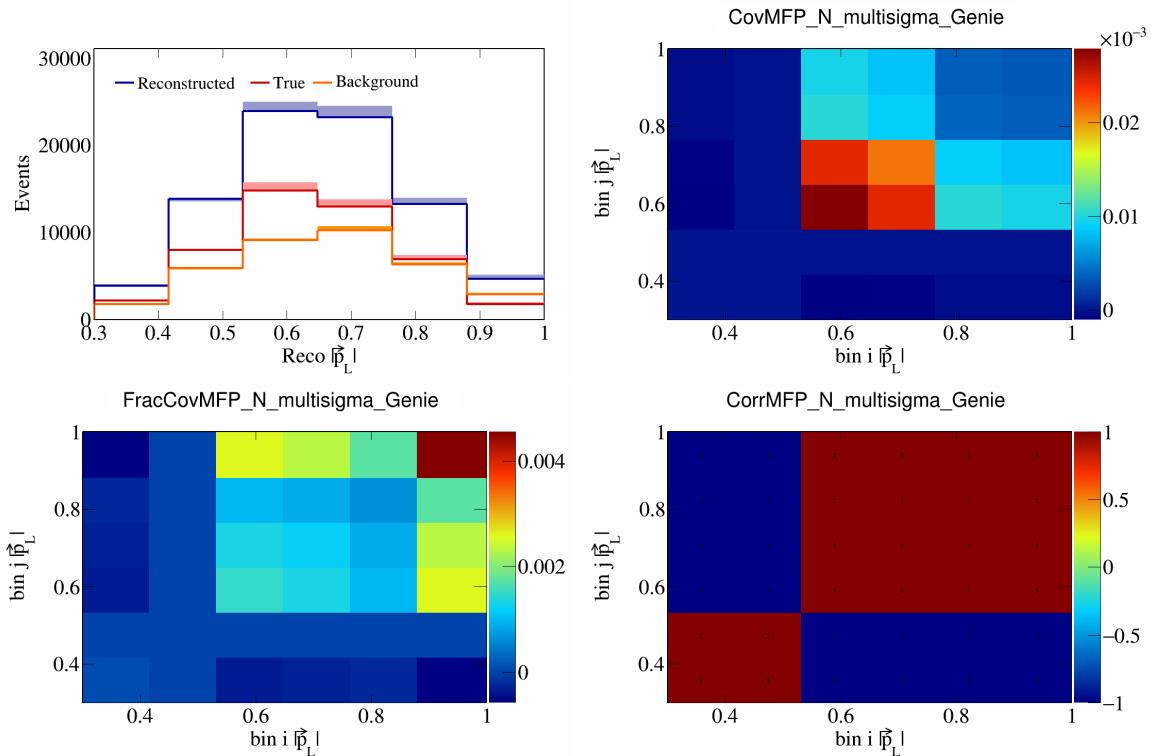


Figure 280: MFPN variations for  $|\vec{p}_L|$ .

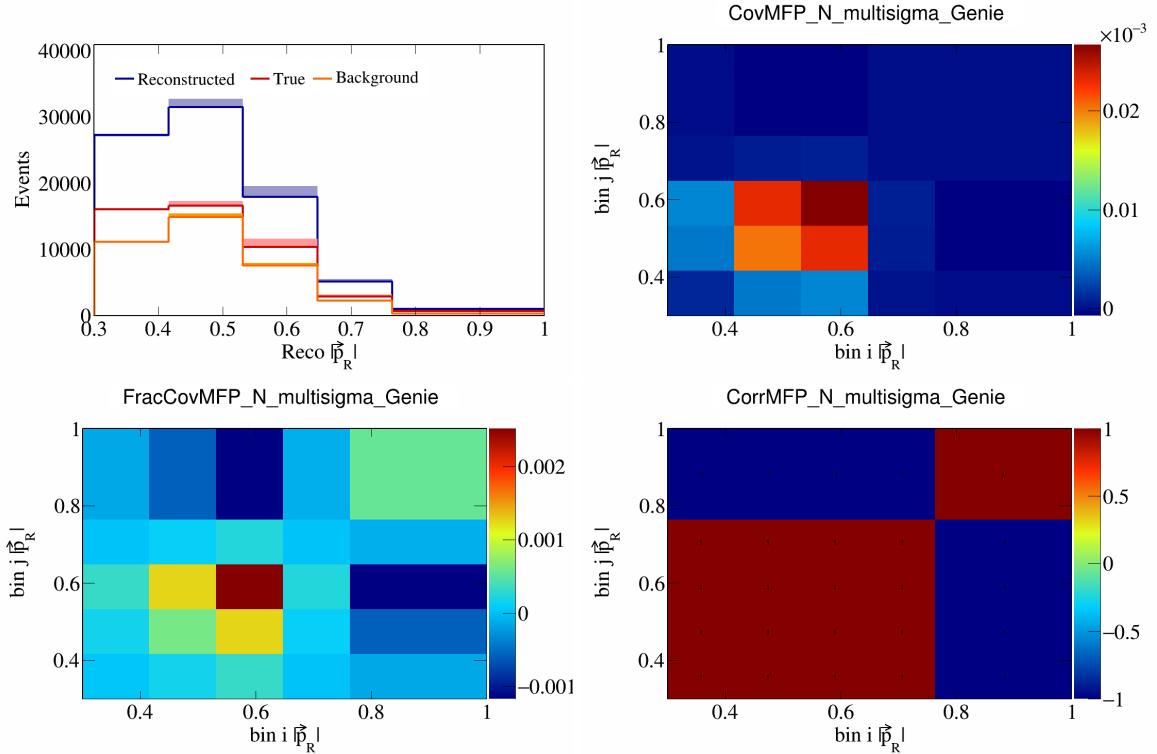


Figure 281: MFPN variations for  $|\vec{p}_R|$ .

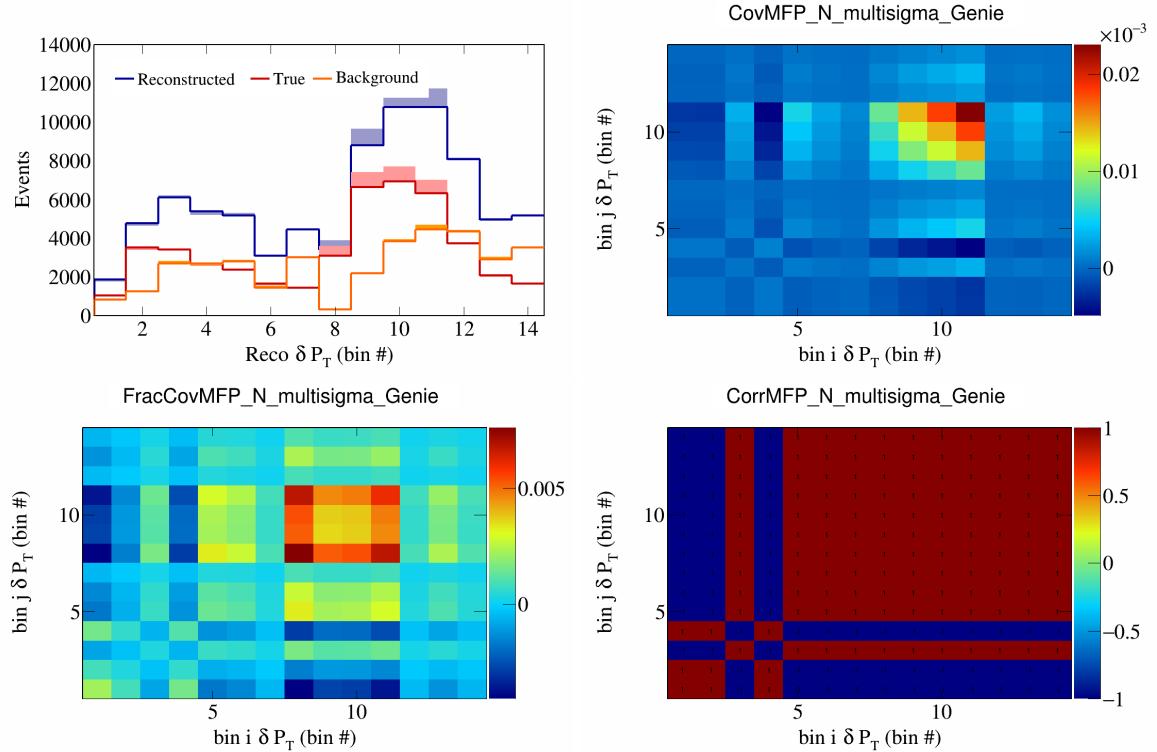


Figure 282: MFPN variations for  $\delta P_T$  in  $\cos(\theta_{\vec{p}_\mu})$ .

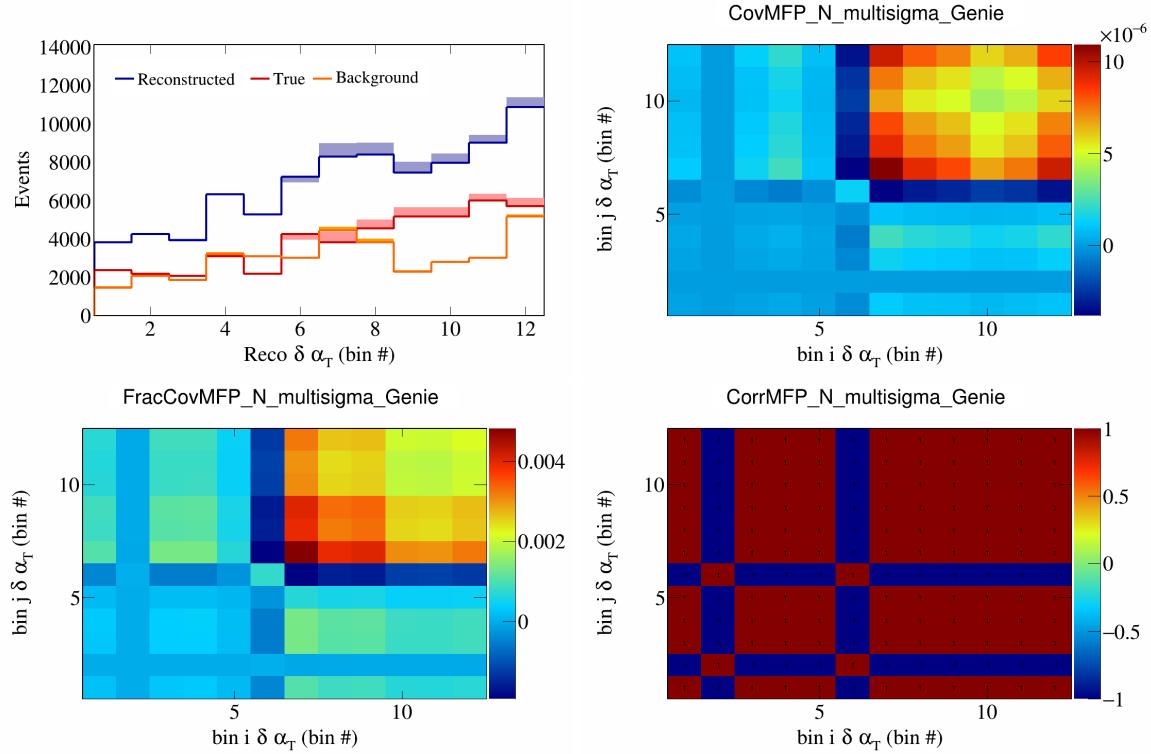


Figure 283: MFPN variations for  $\delta \alpha_T$  in  $\cos(\theta_{\vec{p}_\mu})$ .

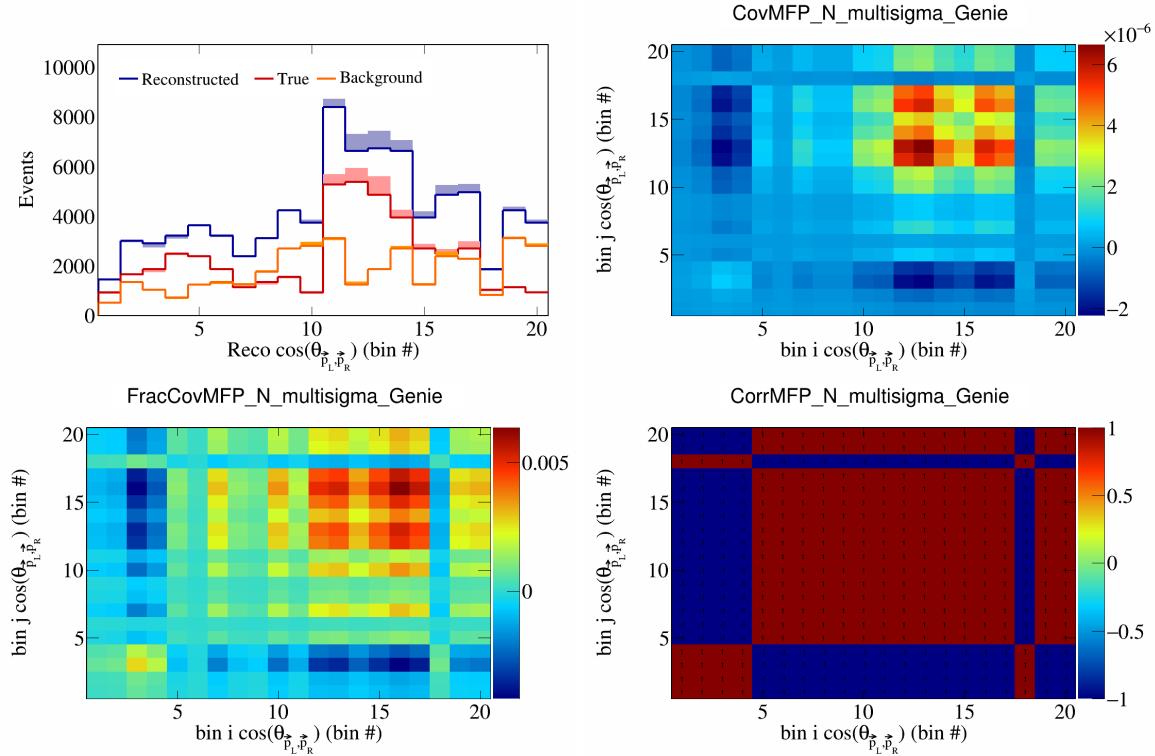


Figure 284: MFPN variations for  $\cos(\theta_{\vec{p}_L, \vec{p}_R})$  in  $\cos(\theta_{\vec{p}_\mu})$ .

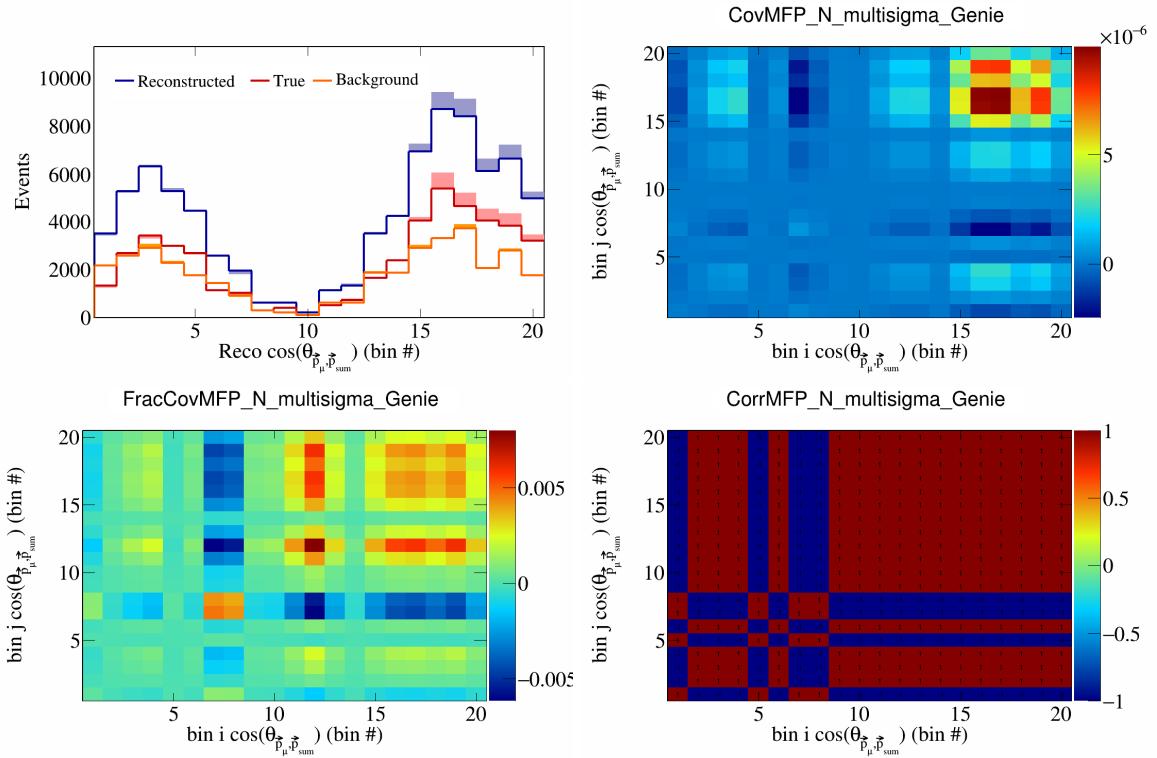


Figure 285: MFPN variations for  $\cos(\theta_{\vec{p}_\mu, \vec{p}_{\text{sum}}})$  in  $\cos(\theta_{\vec{p}_\mu})$ .

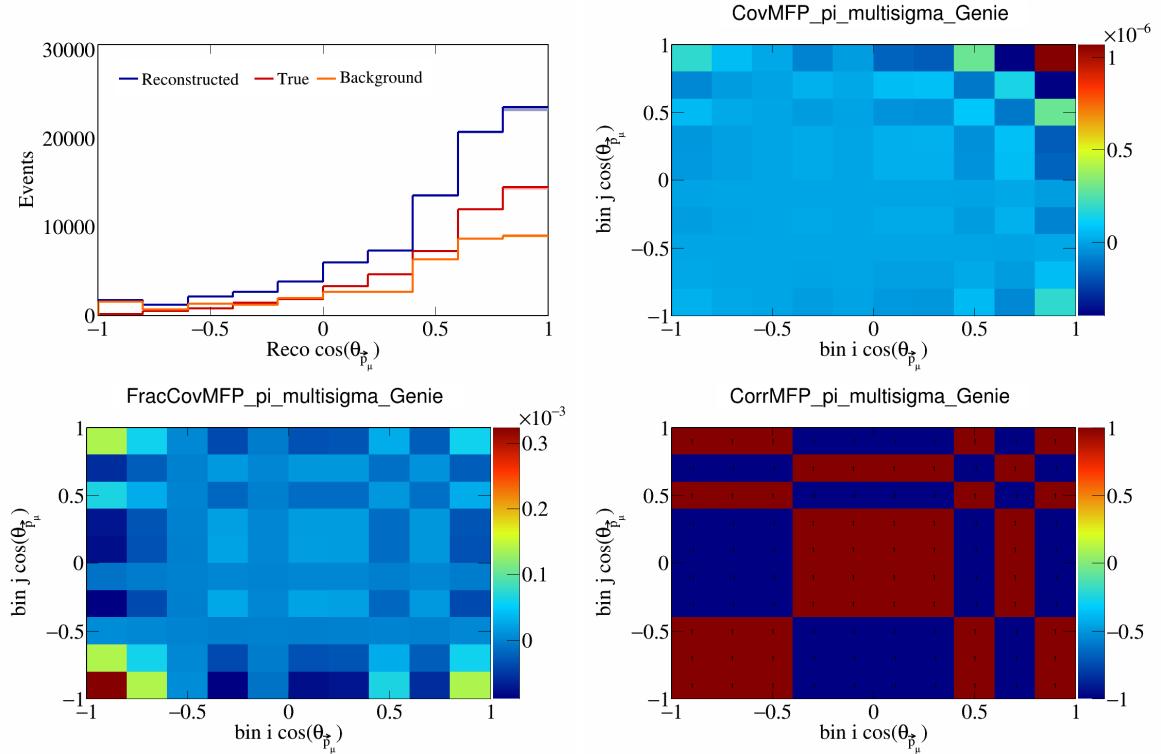


Figure 286: MFPpi variations for  $\cos(\theta_{\vec{p}_\mu})$ .

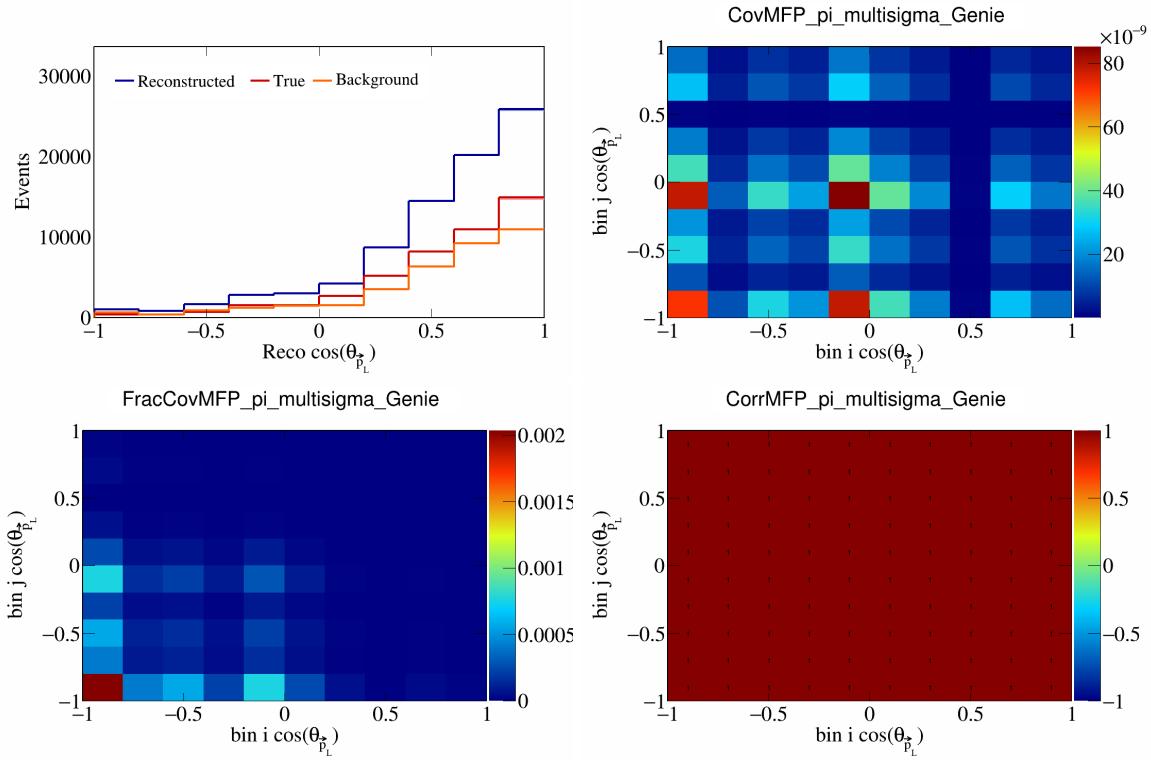


Figure 287: MFPpi variations for  $\cos(\theta_{\vec{p}_L})$ .

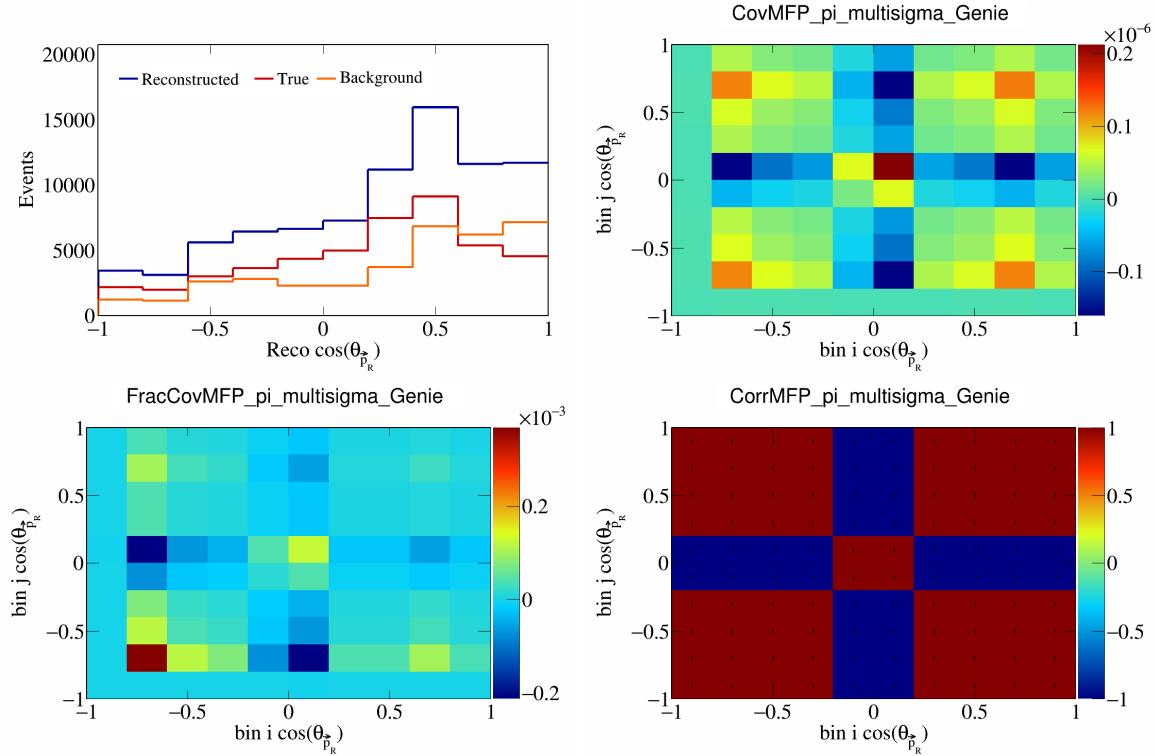


Figure 288: MFPpi variations for  $\cos(\theta_{\vec{p}_R})$ .

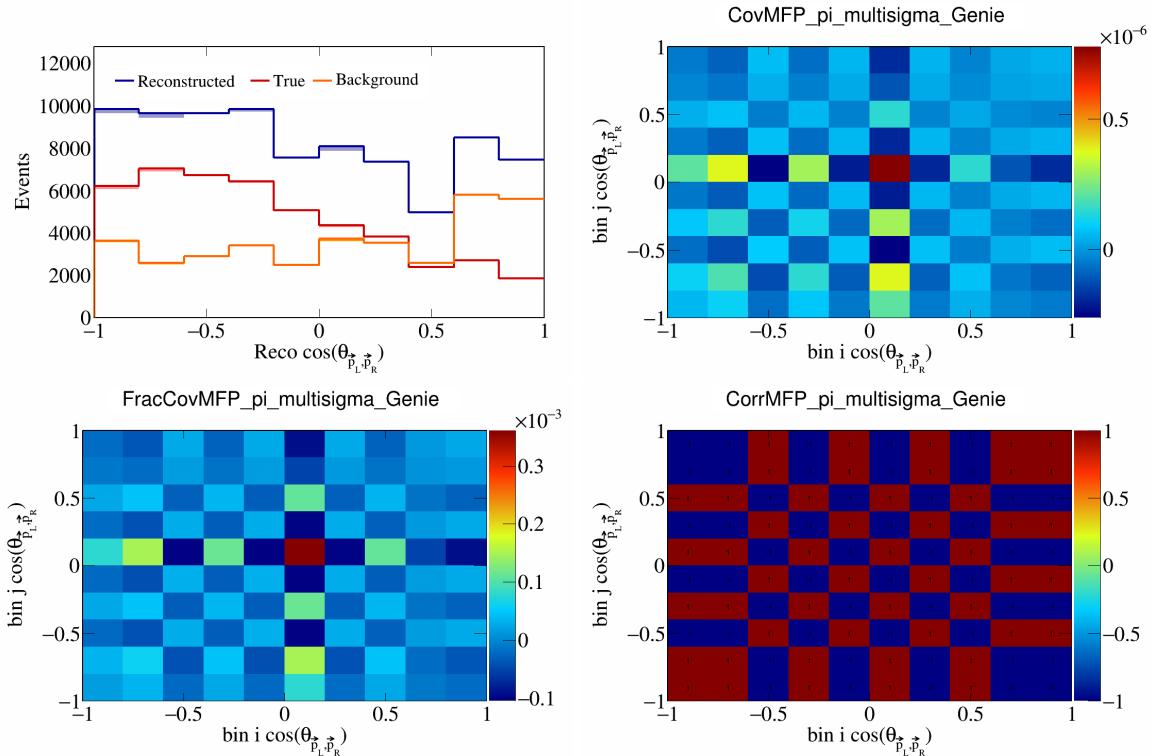


Figure 289: MFPpi variations for  $\cos(\theta_{\vec{p}_L, \vec{p}_R})$ .

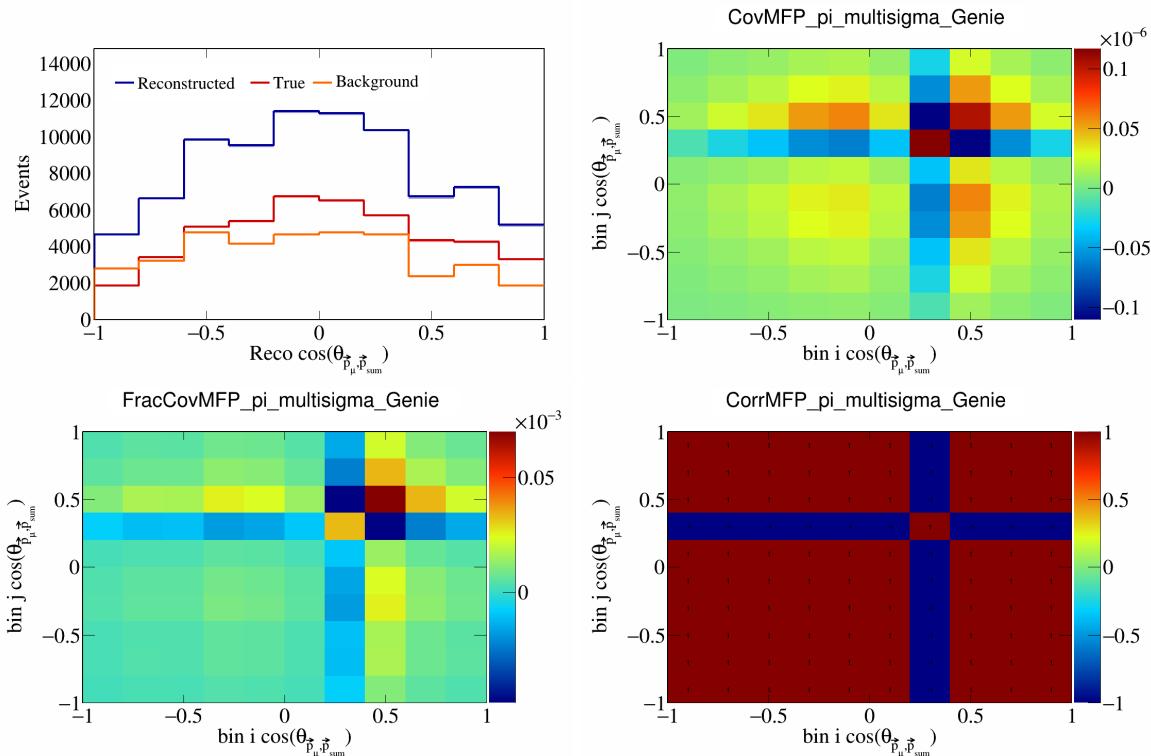


Figure 290: MFPpi variations for  $\cos(\theta_{\vec{p}_\mu, \vec{p}_{\text{sum}}})$ .

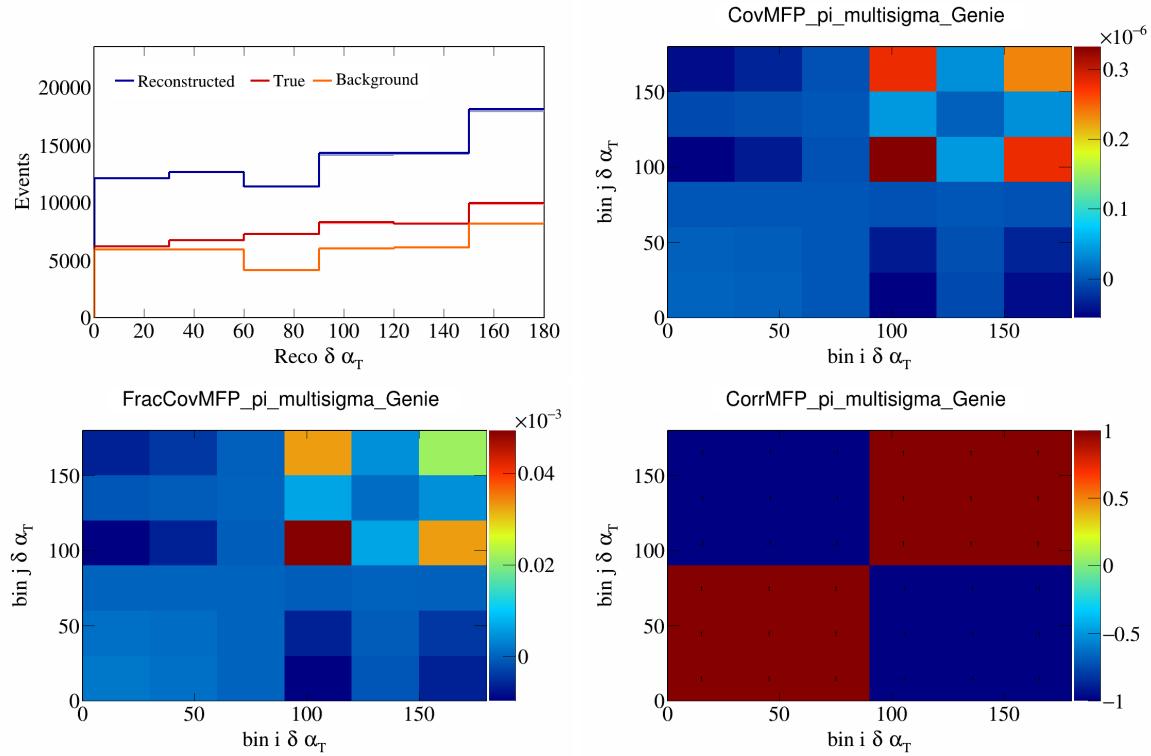


Figure 291: MFPPi variations for  $\delta\alpha_T$ .

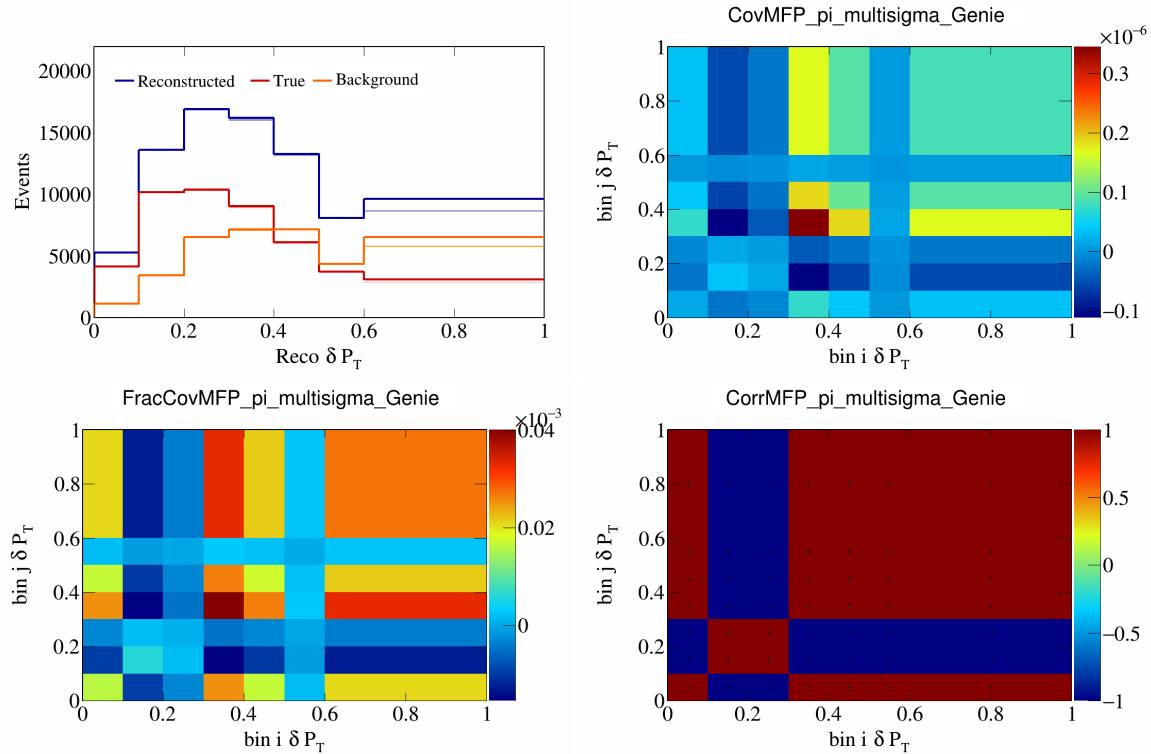


Figure 292: MFPPi variations for  $\delta P_T$ .

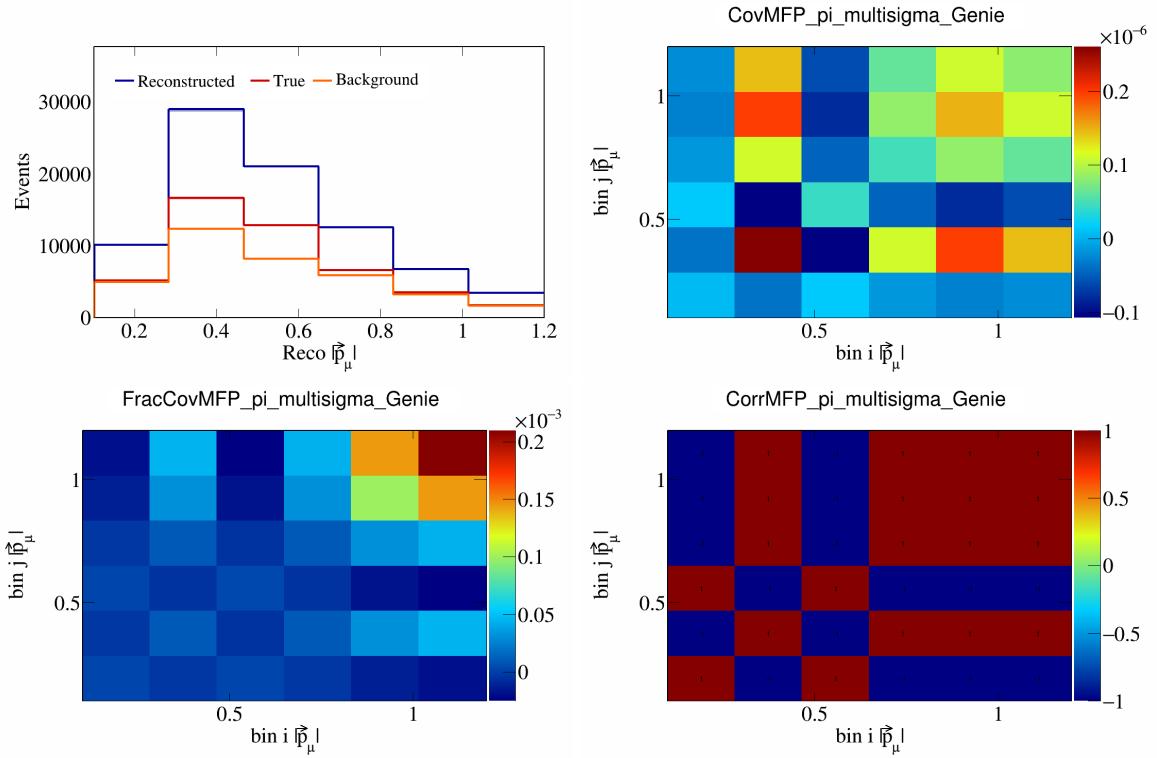


Figure 293: MFPpi variations for  $|\vec{p}_\mu|$ .

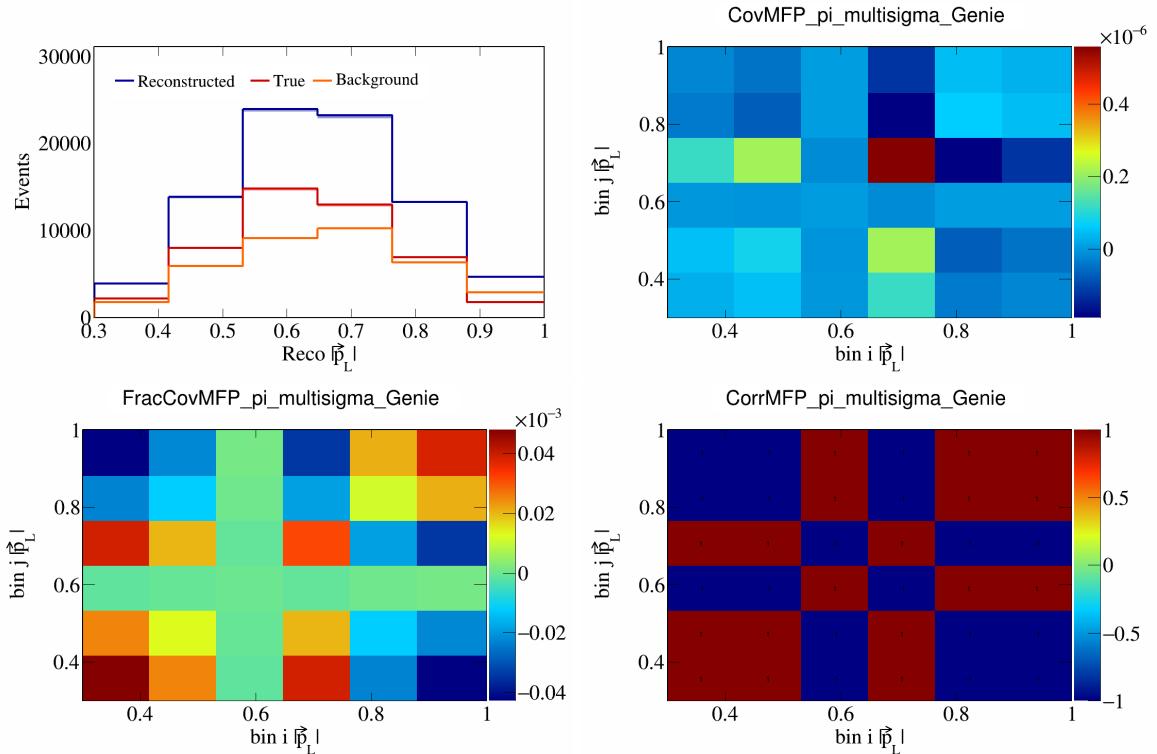


Figure 294: MFPpi variations for  $|\vec{p}_L|$ .

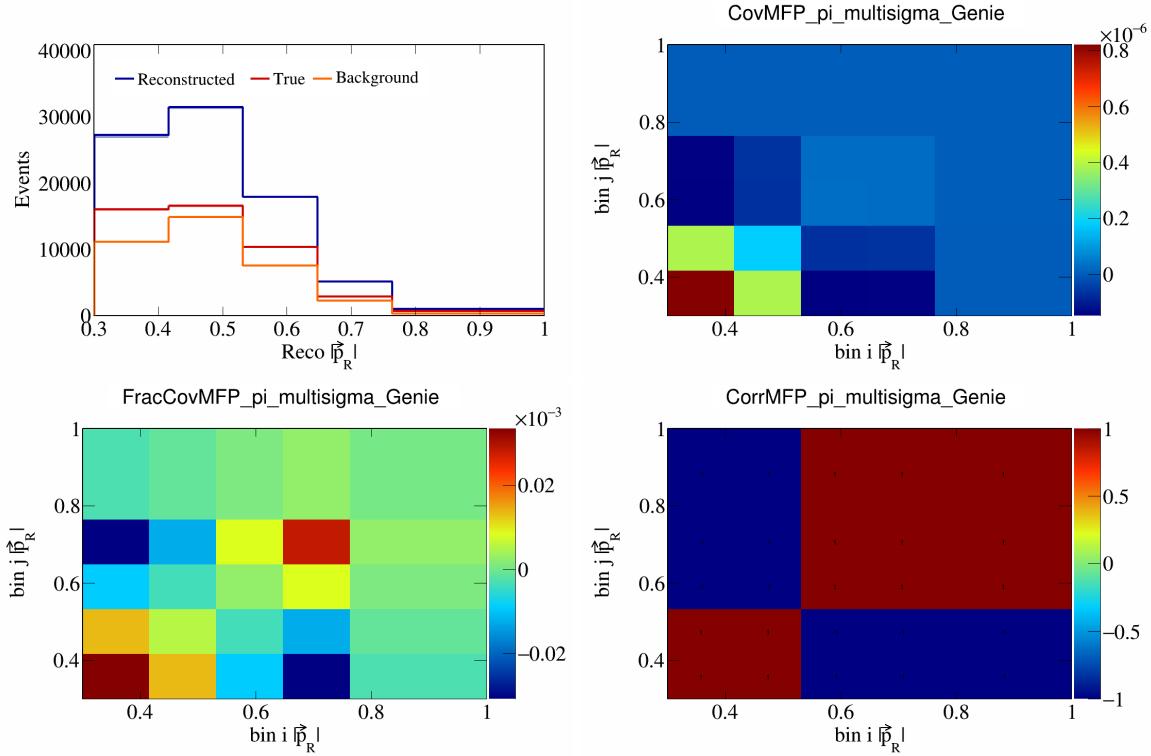


Figure 295: MFPPi variations for  $|\vec{p}_R|$ .

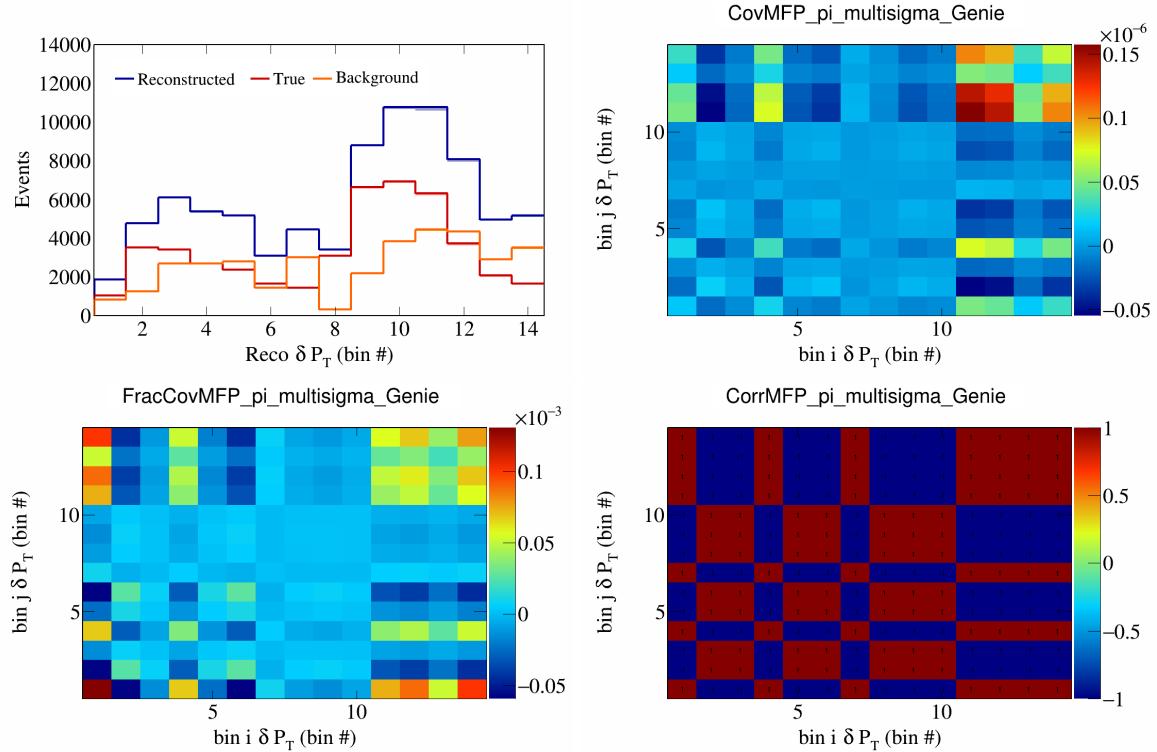


Figure 296: MFPPi variations for  $\delta P_T$  in  $\cos(\theta_{\vec{p}_\mu})$ .

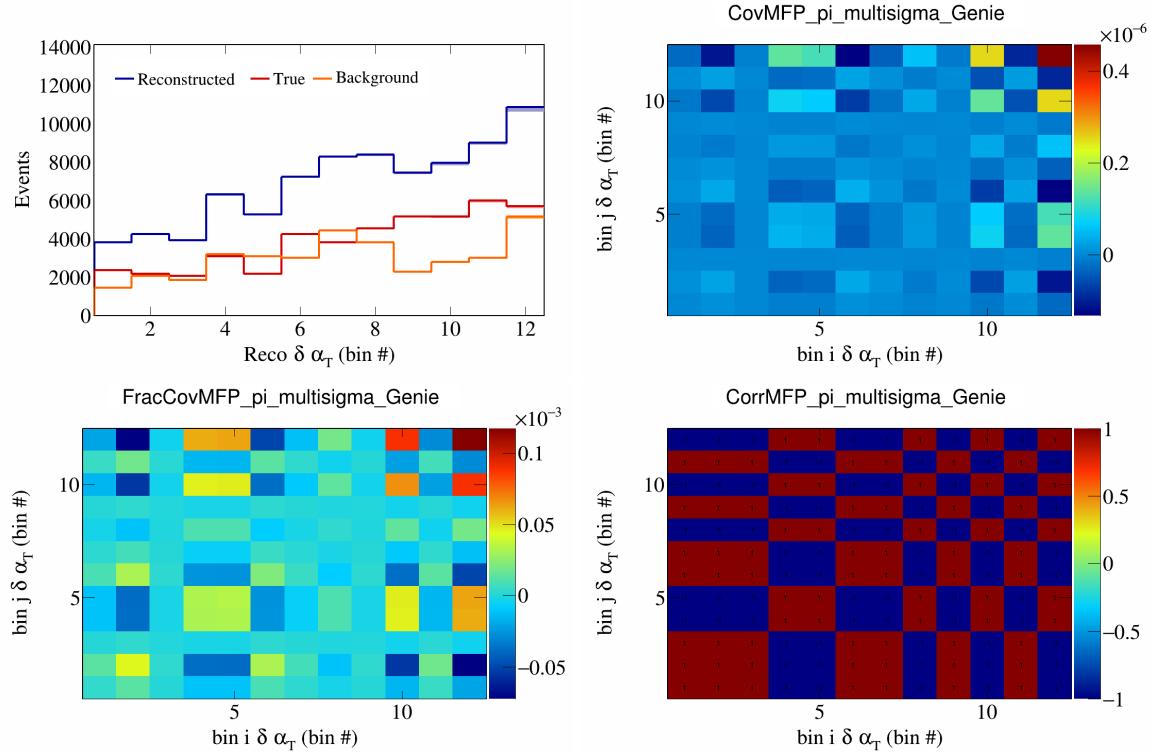


Figure 297: MFPpi variations for  $\delta \alpha_T$  in  $\cos(\theta_{\vec{p}_\mu})$ .

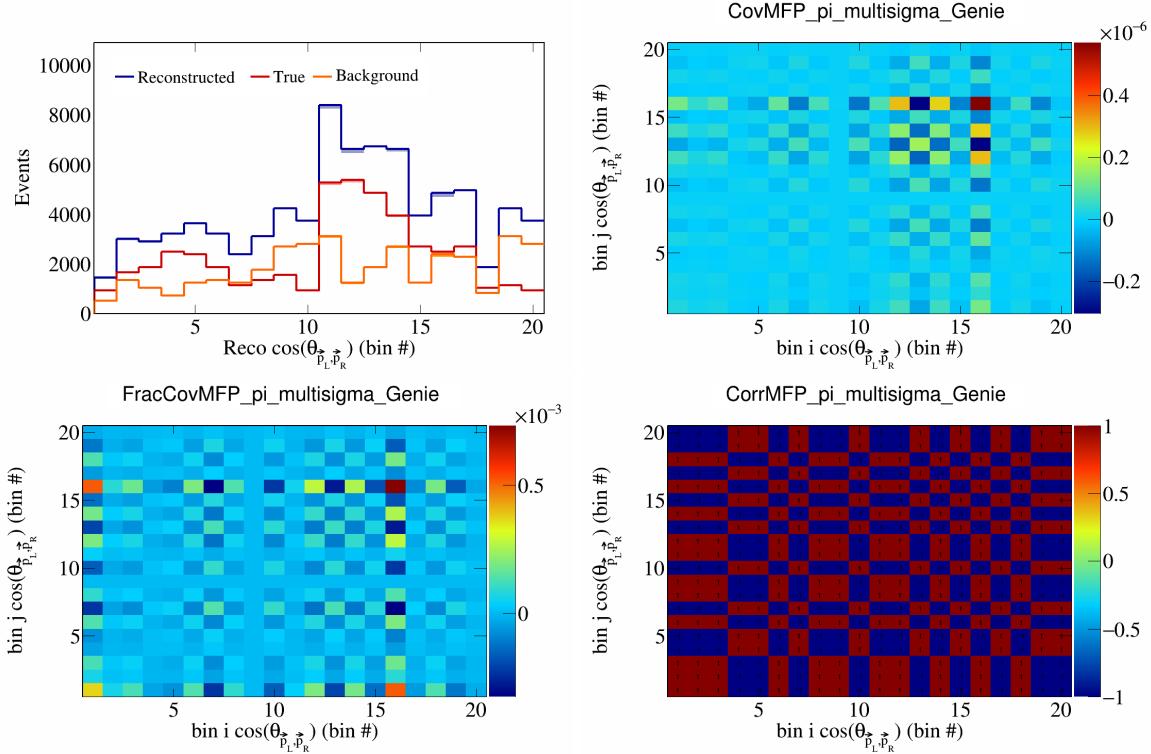


Figure 298: MFPpi variations for  $\cos(\theta_{\vec{p}_L, \vec{p}_R})$  in  $\cos(\theta_{\vec{p}_\mu})$ .

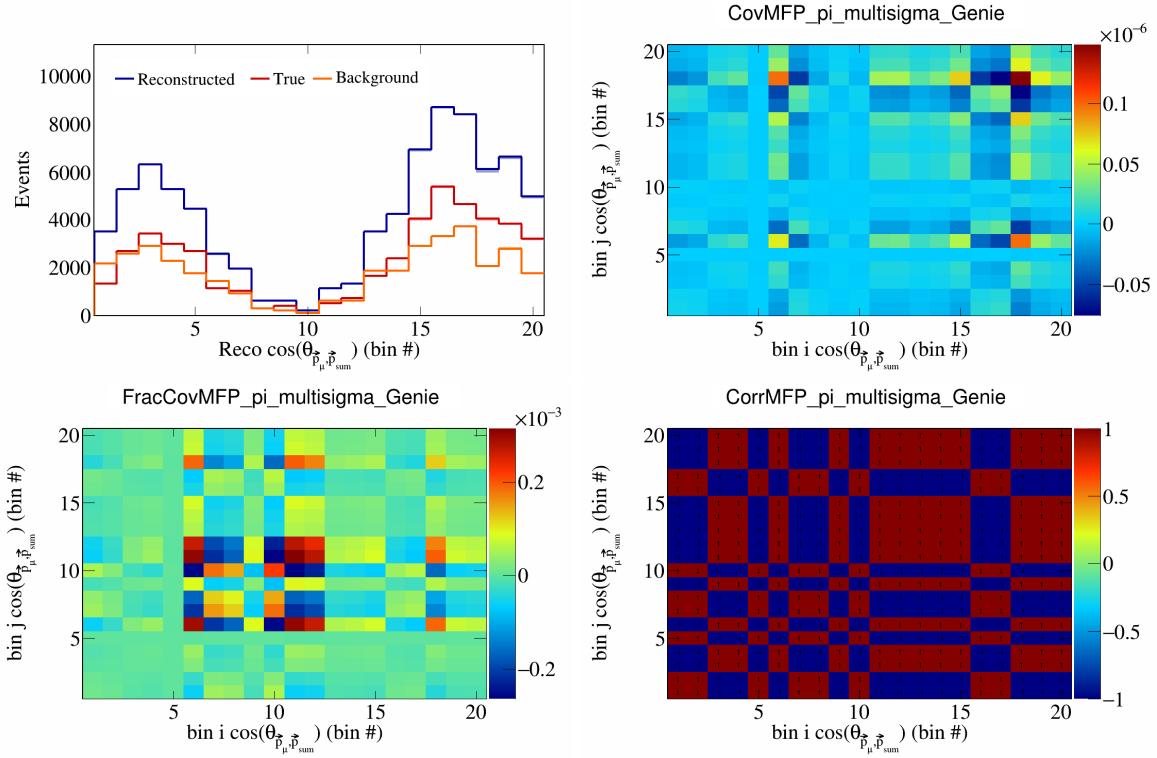


Figure 299: MFPpi variations for  $\cos(\theta_{\vec{p}_\mu, \vec{p}_{\text{sum}}})$  in  $\cos(\theta_{\vec{p}_\mu})$ .

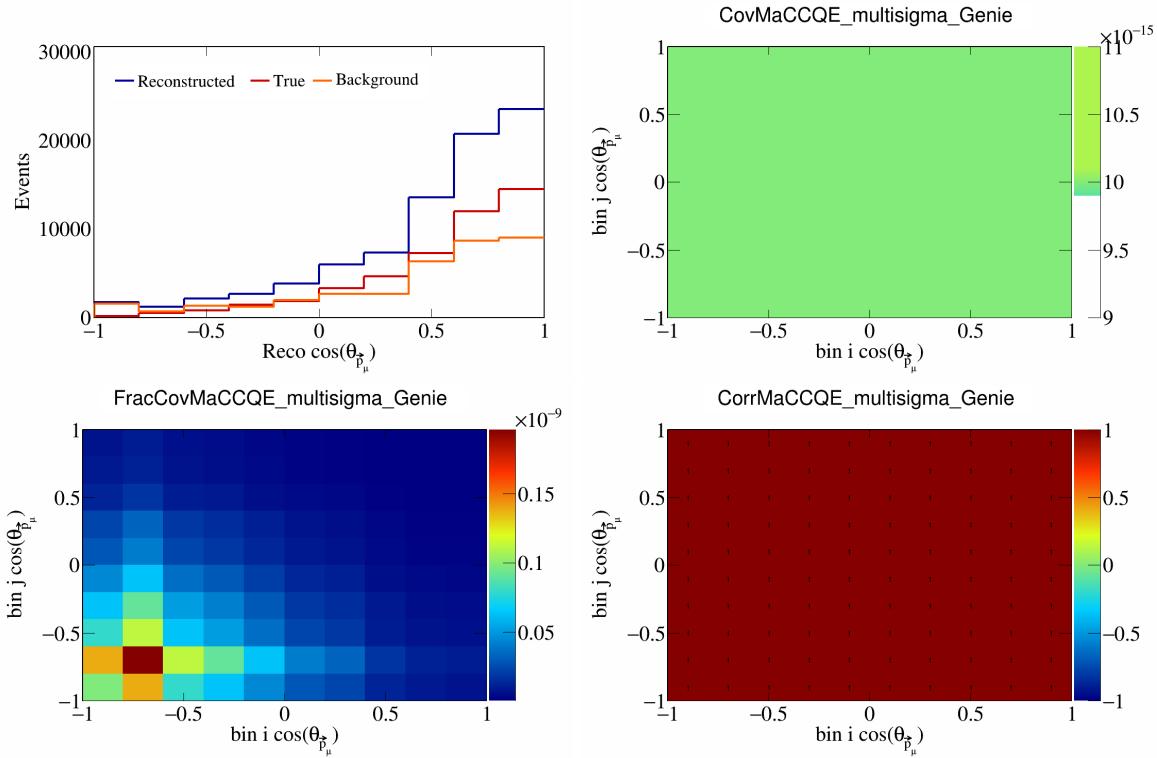


Figure 300: MaCCQE variations for  $\cos(\theta_{\vec{p}_\mu})$ .

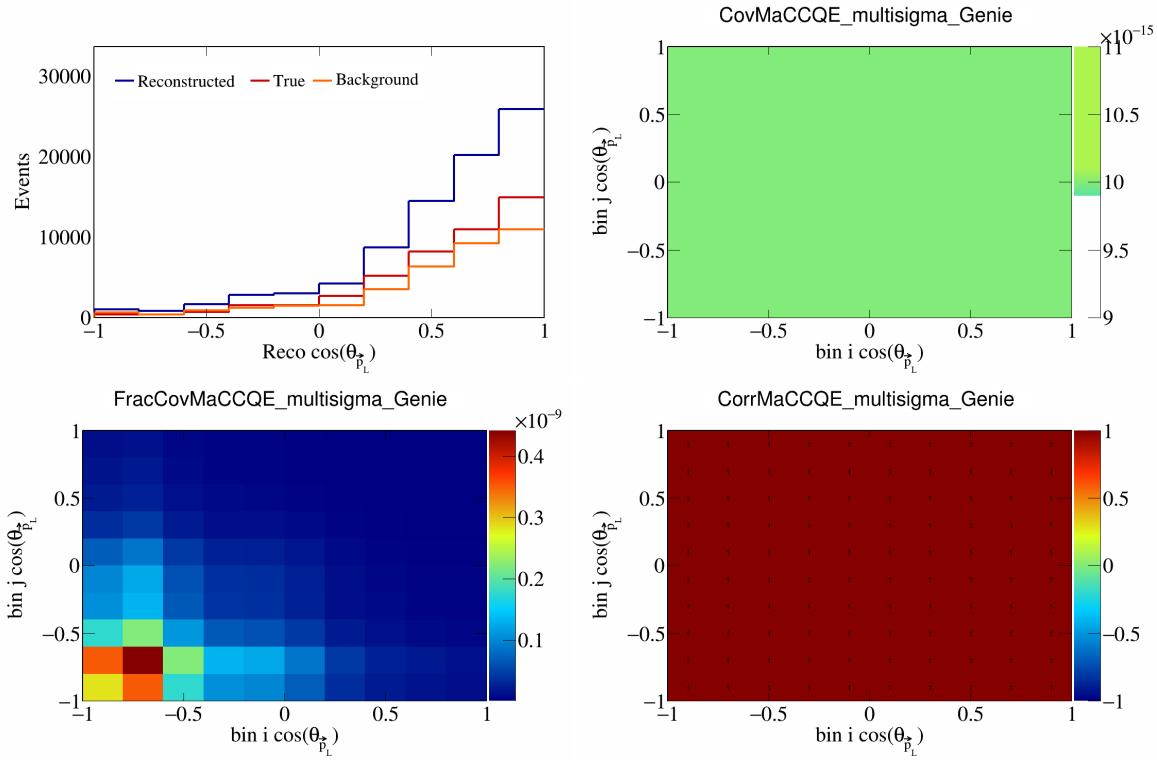


Figure 301: MaCCQE variations for  $\cos(\theta_{\vec{p}_L})$ .

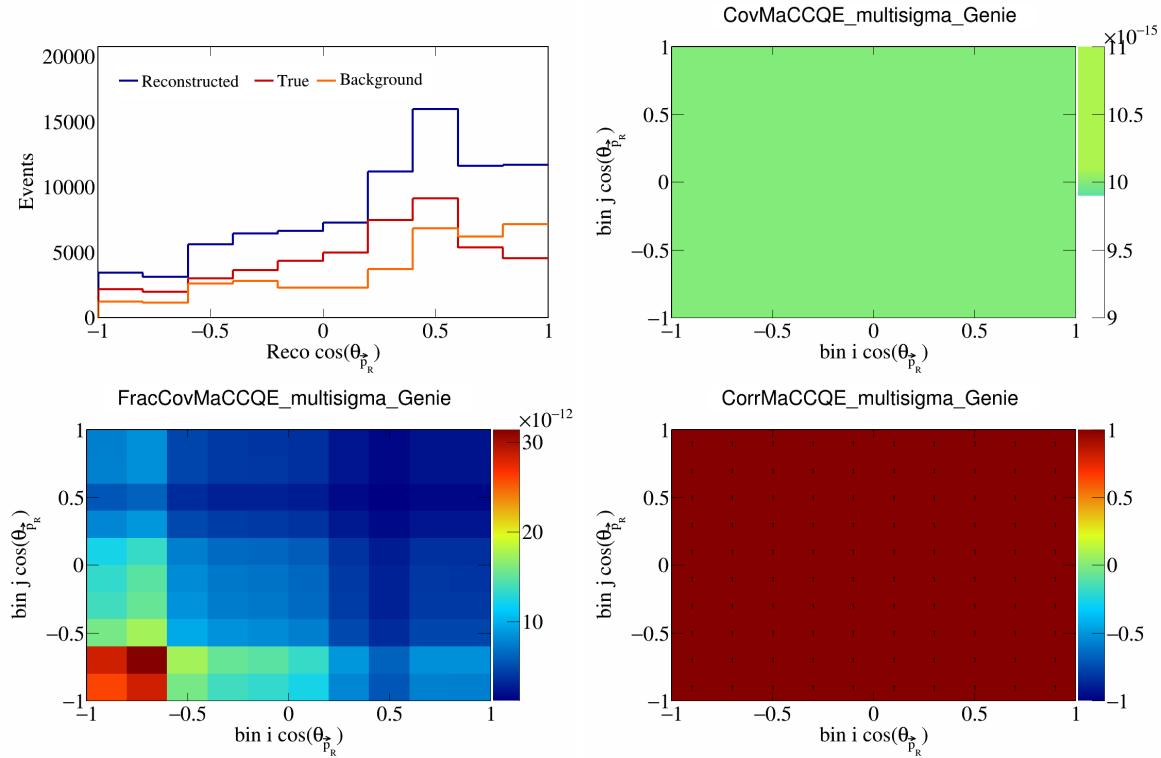


Figure 302: MaCCQE variations for  $\cos(\theta_{\vec{p}_R})$ .

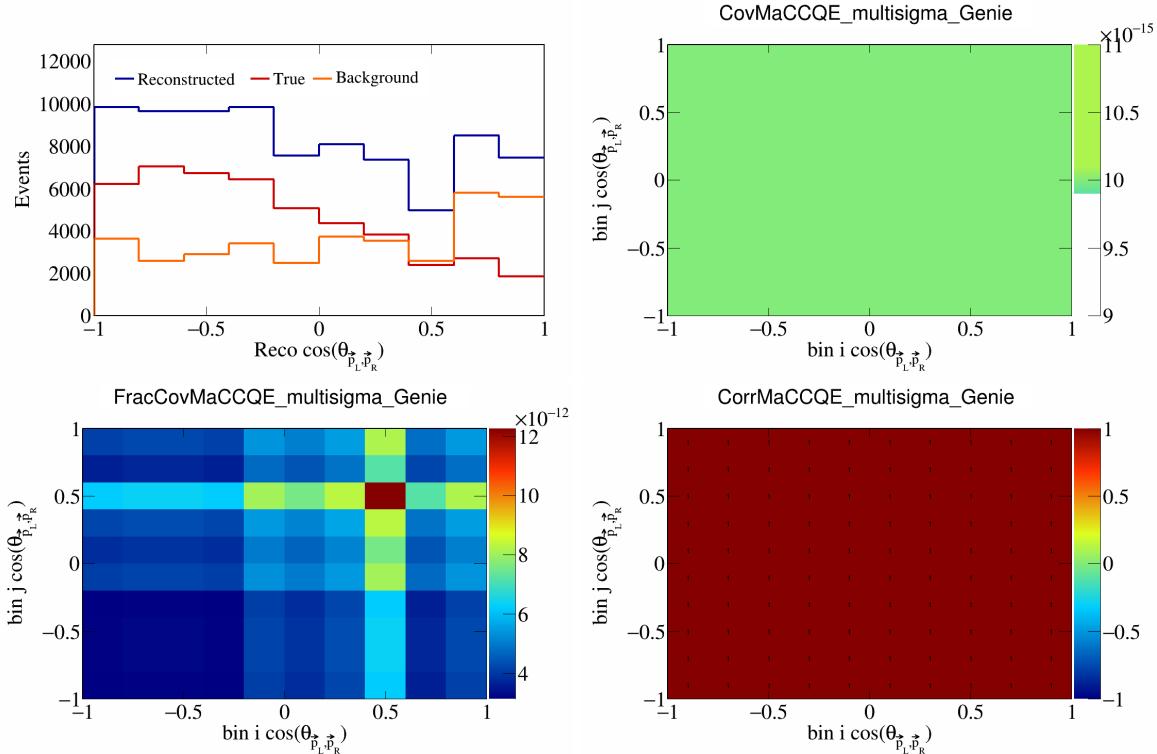


Figure 303: MaCCQE variations for  $\cos(\theta_{\vec{p}_L, \vec{p}_R})$ .

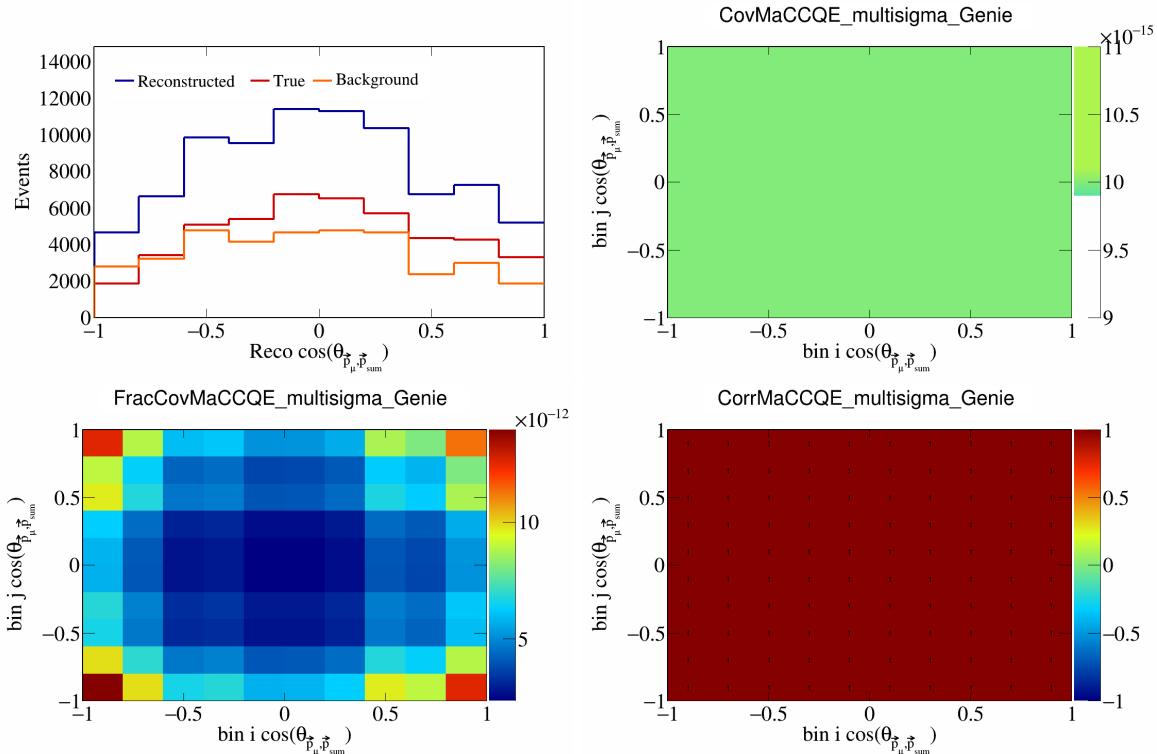


Figure 304: MaCCQE variations for  $\cos(\theta_{\vec{p}_\mu, \vec{p}_{\text{sum}}})$ .

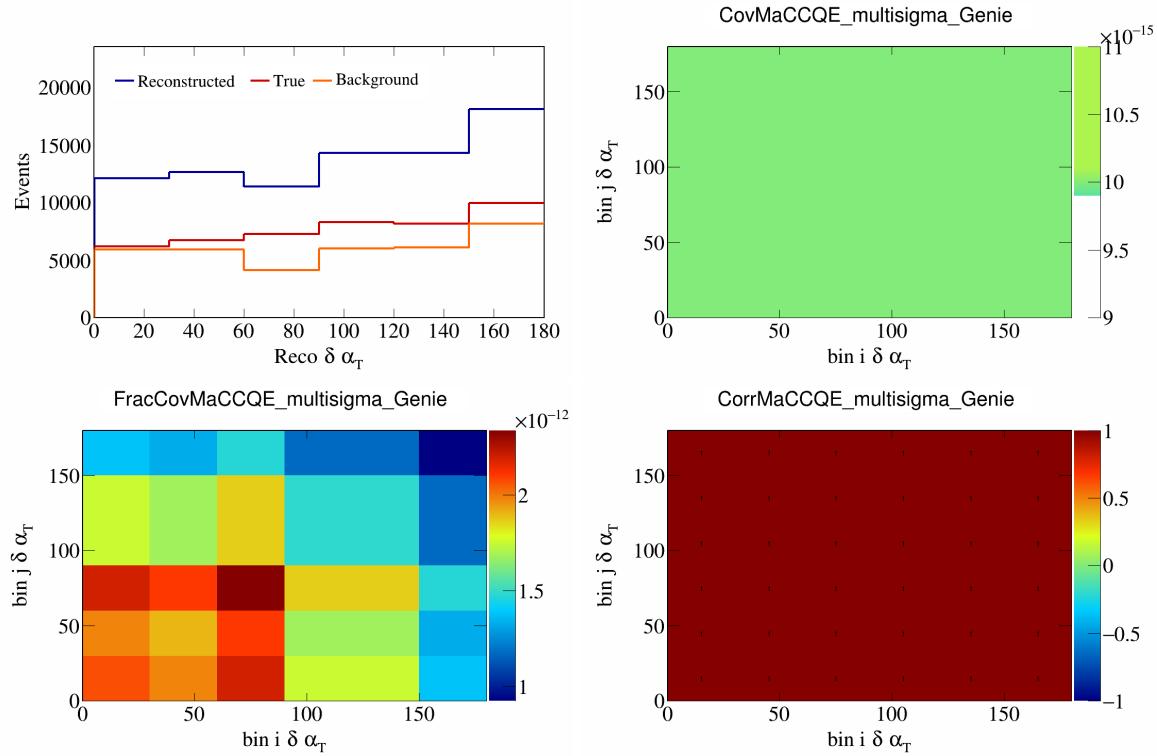


Figure 305: MaCCQE variations for  $\delta \alpha_T$ .

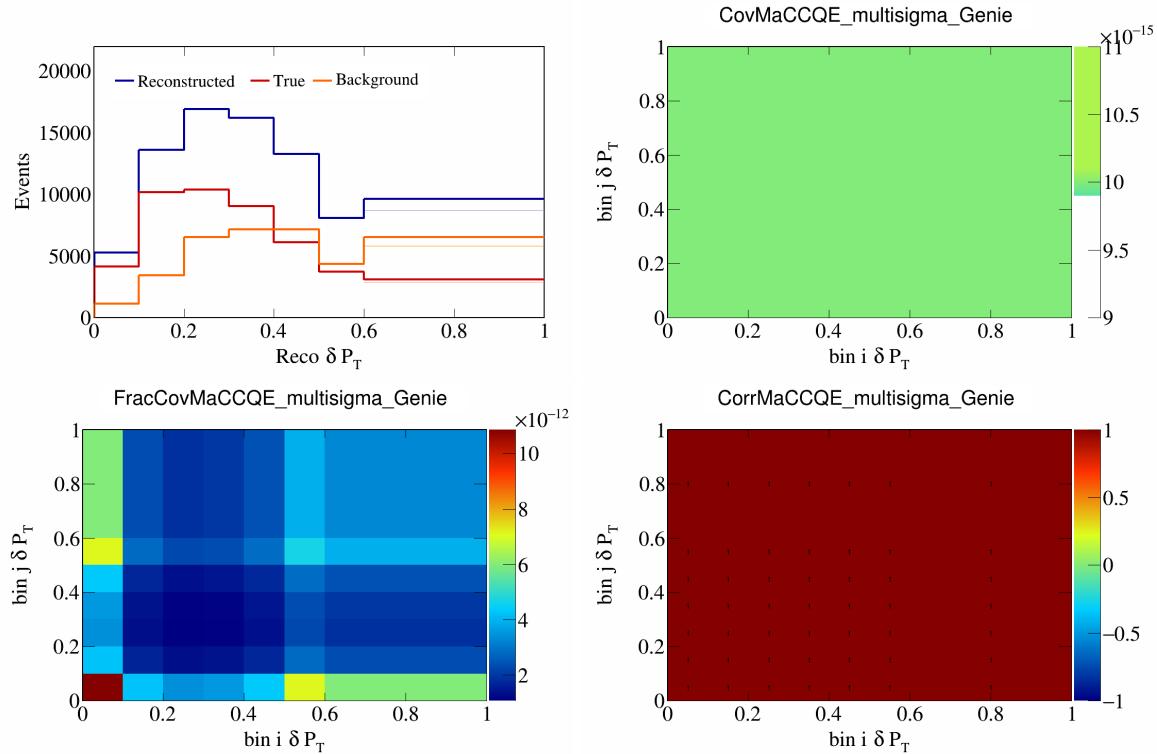


Figure 306: MaCCQE variations for  $\delta P_T$ .

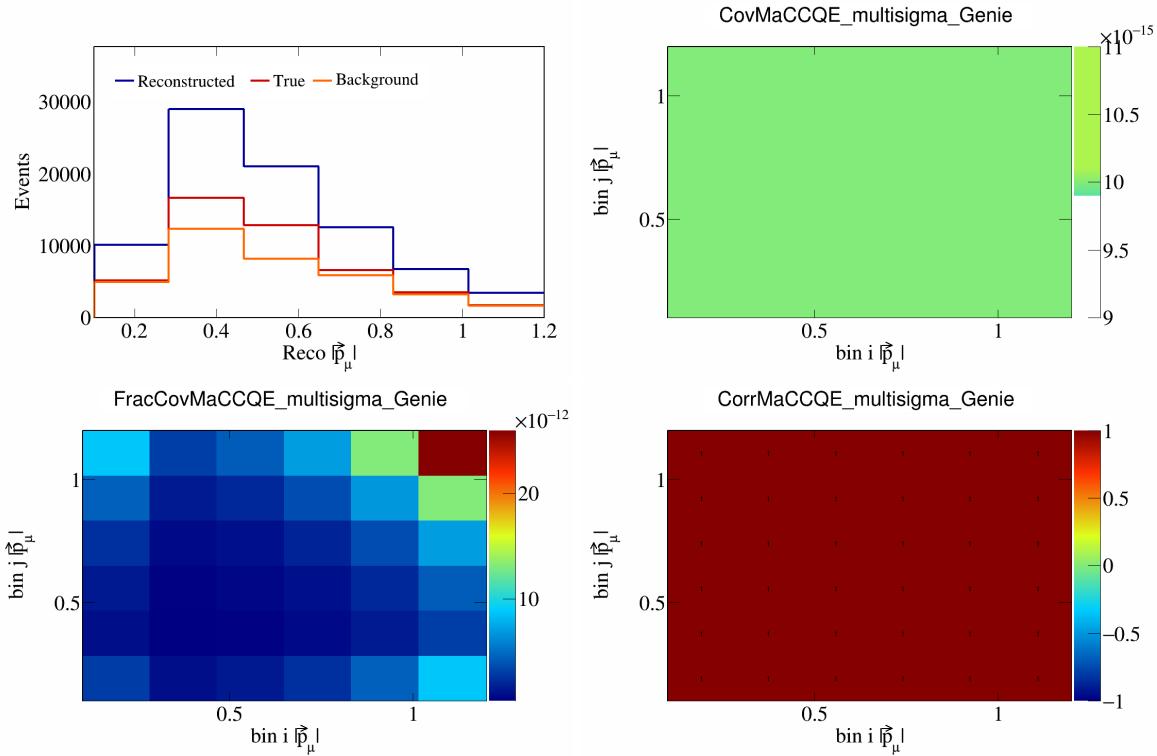


Figure 307: MaCCQE variations for  $|\vec{p}_\mu|$ .

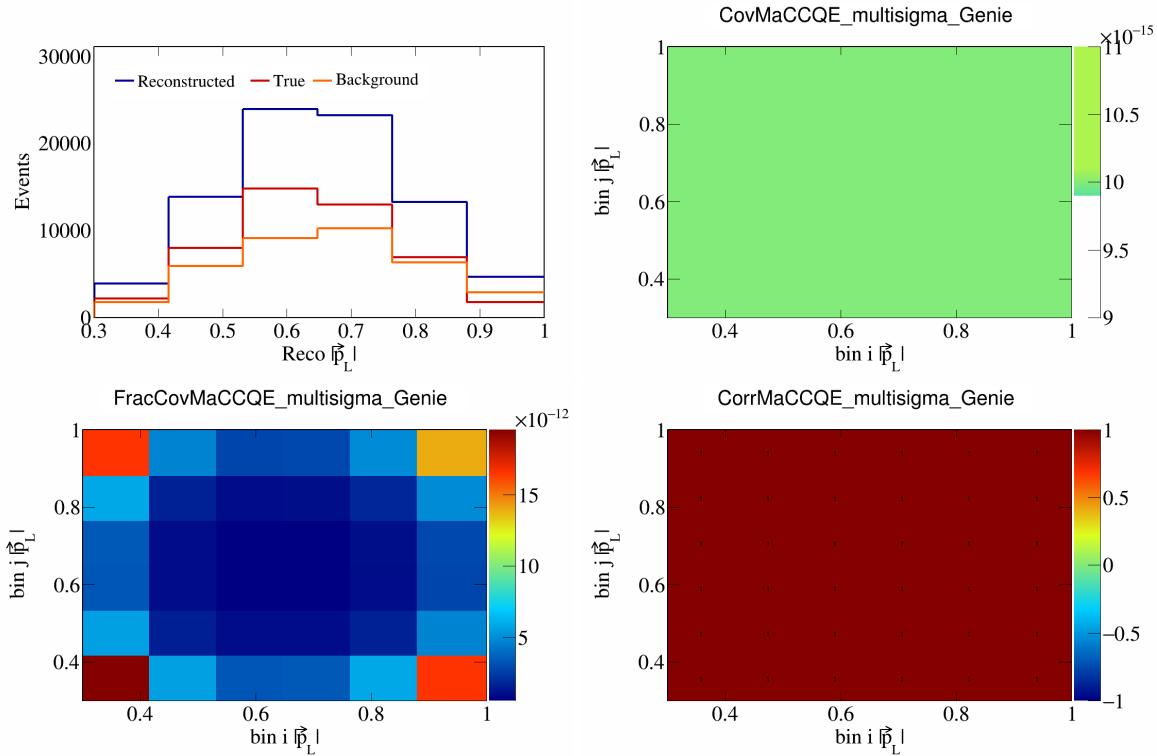


Figure 308: MaCCQE variations for  $|\vec{p}_L|$ .

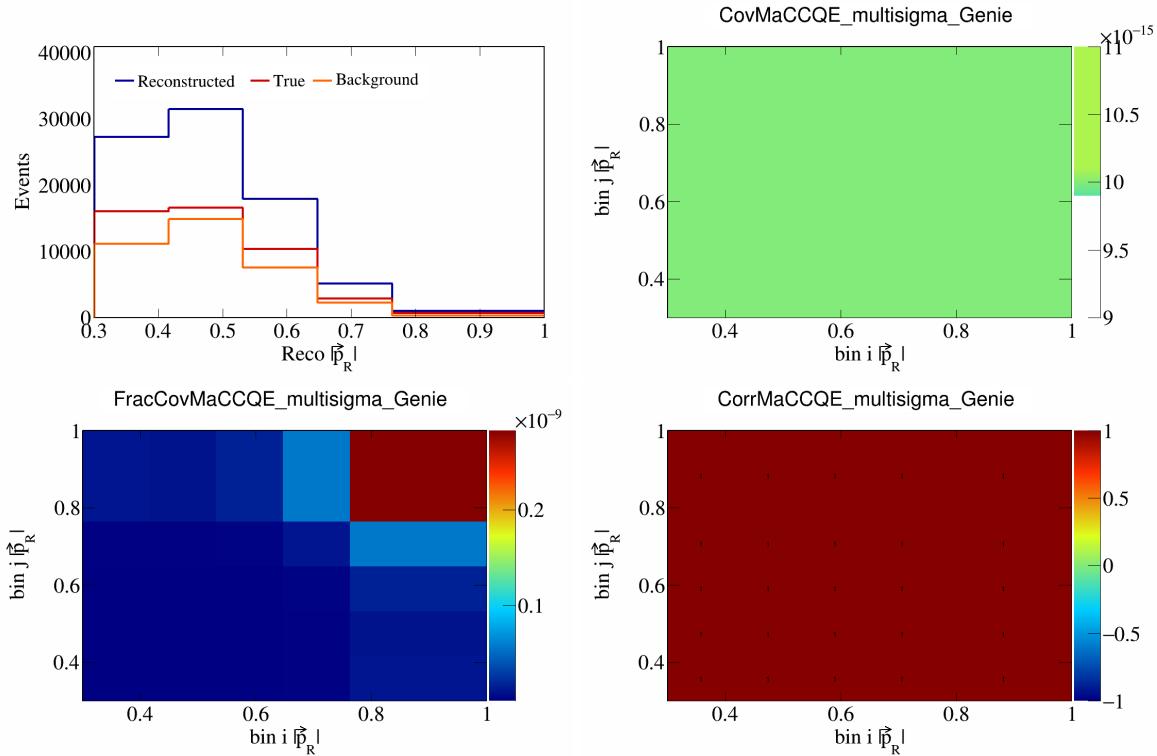


Figure 309: MaCCQE variations for  $|\vec{p}_R|$ .

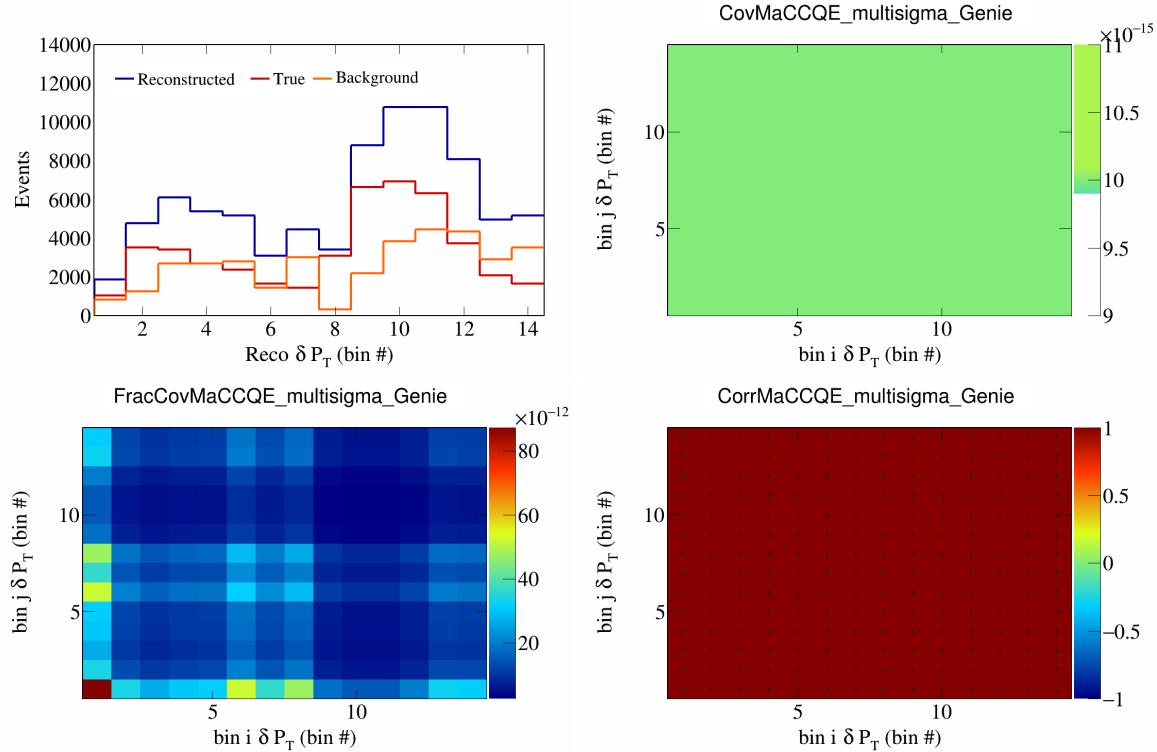


Figure 310: MaCCQE variations for  $\delta P_T$  in  $\cos(\theta_{\vec{p}_\mu})$ .

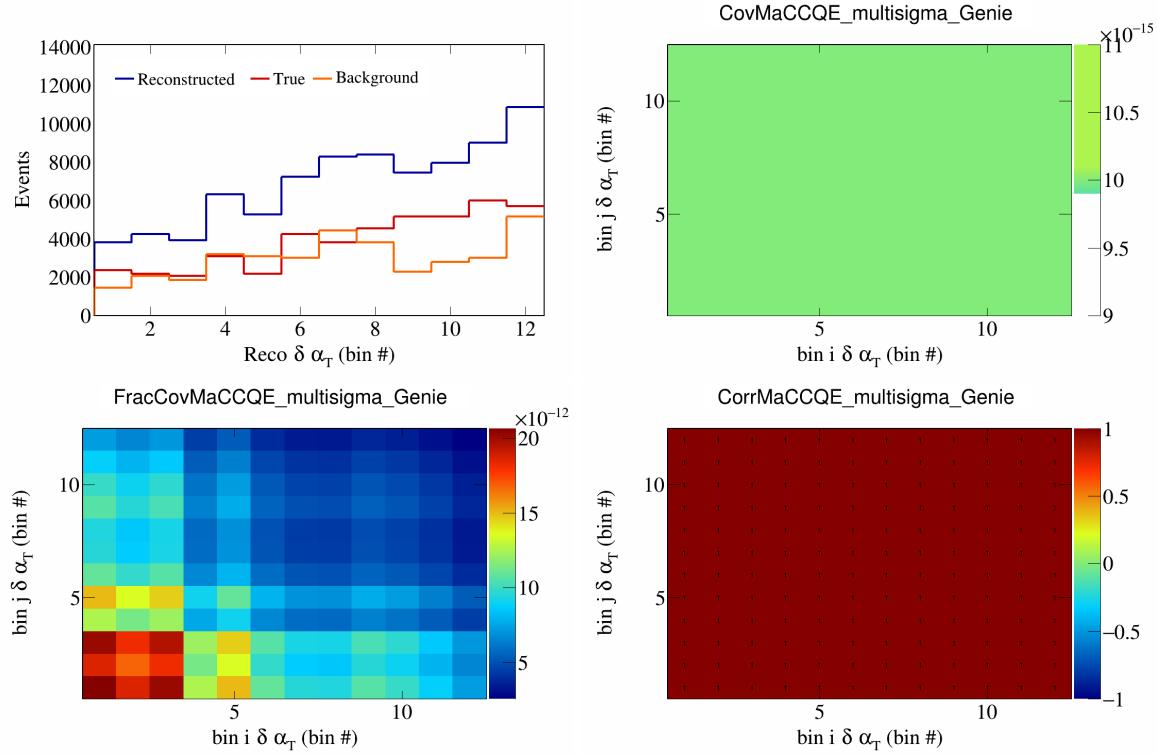


Figure 311: MaCCQE variations for  $\delta\alpha_T$  in  $\cos(\theta_{\vec{p}_\mu})$ .

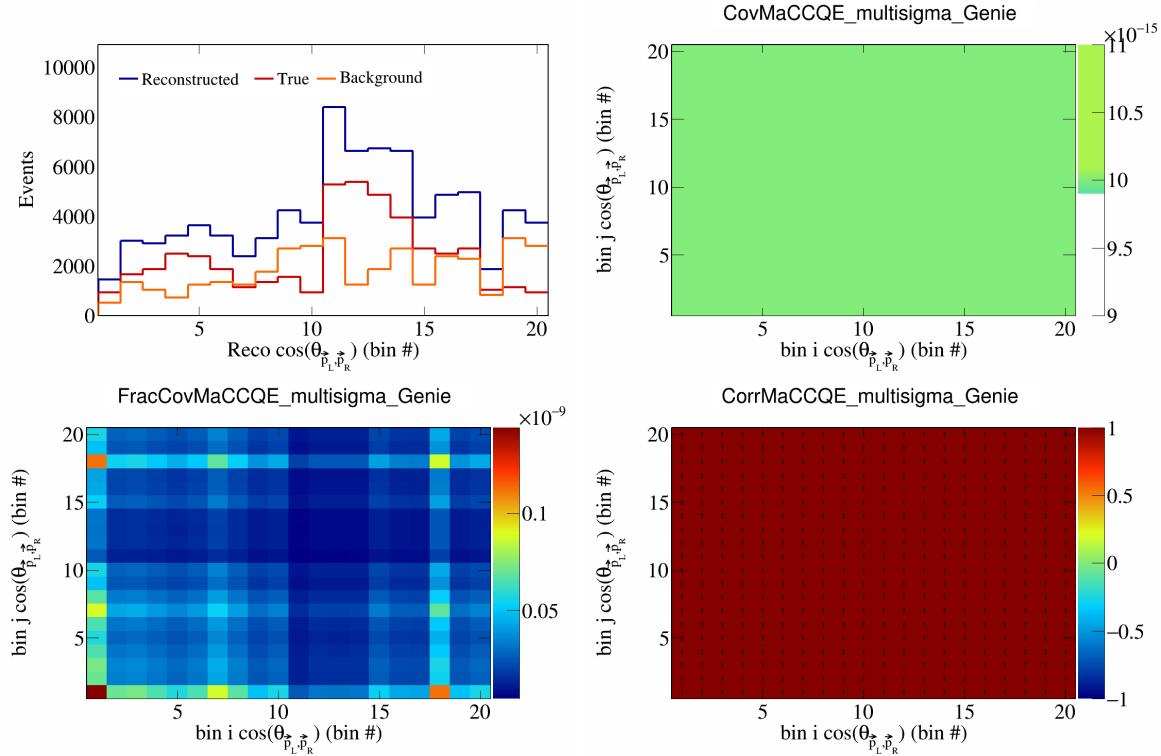


Figure 312: MaCCQE variations for  $\cos(\theta_{\vec{p}_L, \vec{p}_R})$  in  $\cos(\theta_{\vec{p}_\mu})$ .

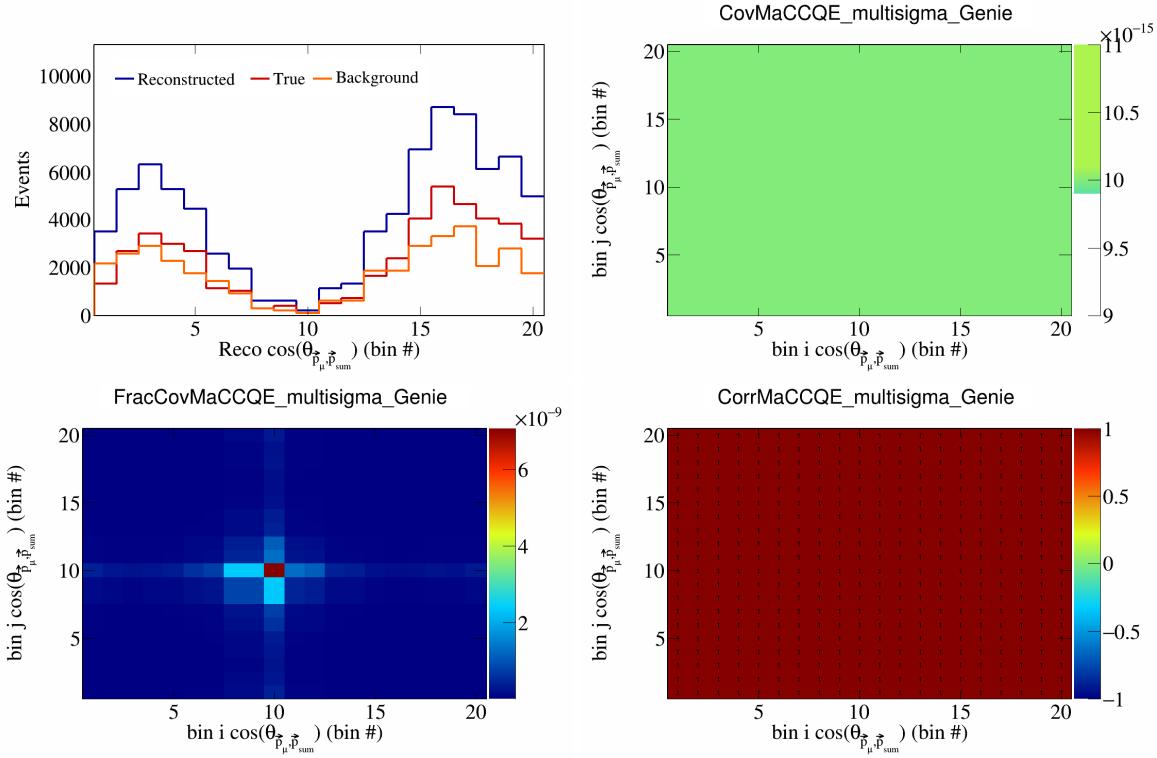


Figure 313: MaCCQE variations for  $\cos(\theta_{\vec{p}_\mu} \cdot \vec{p}_{\text{sum}})$  in  $\cos(\theta_{\vec{p}_\mu})$ .

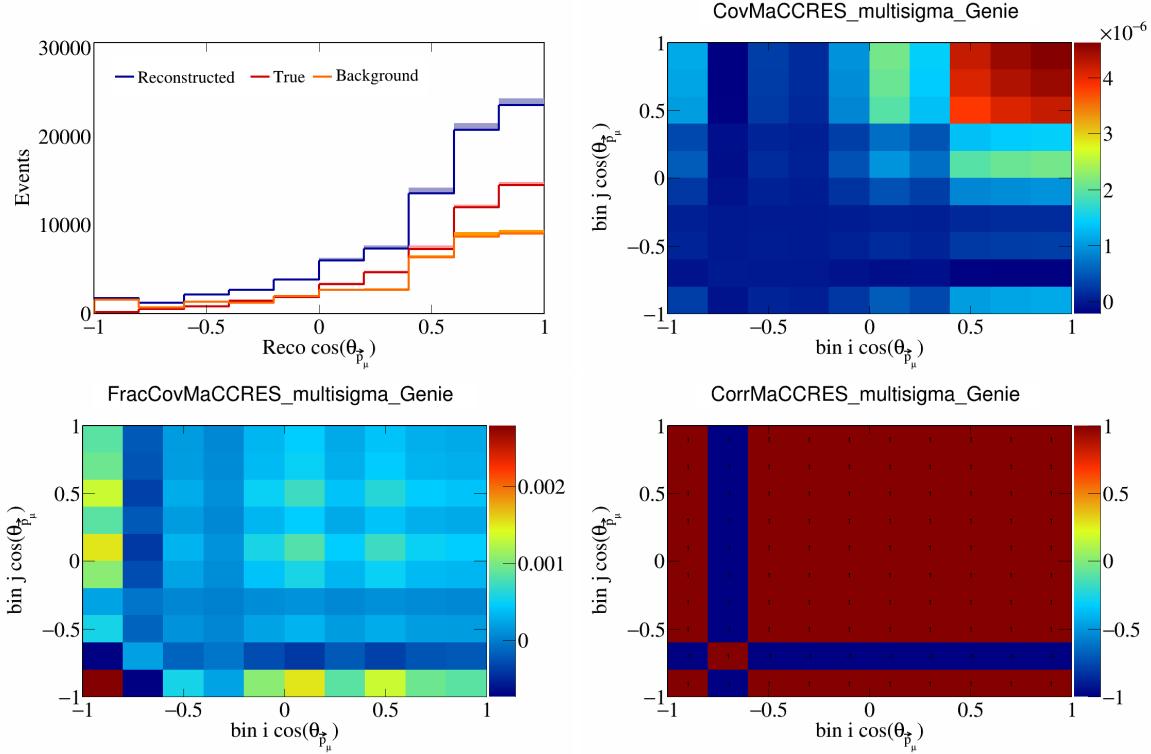


Figure 314: MaCCRES variations for  $\cos(\theta_{\vec{p}_\mu} \cdot \vec{p}_{\text{sum}})$  in  $\cos(\theta_{\vec{p}_\mu})$ .

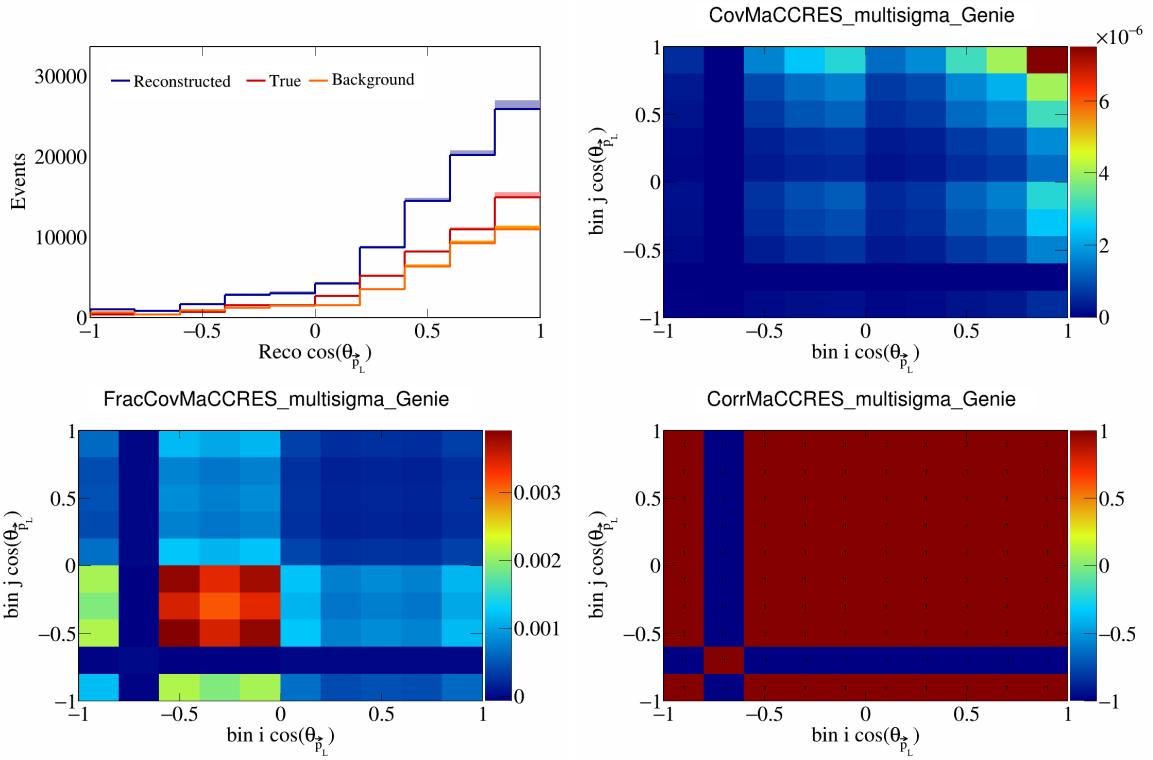


Figure 315: MaCCRES variations for  $\cos(\theta_{\vec{p}_L})$ .

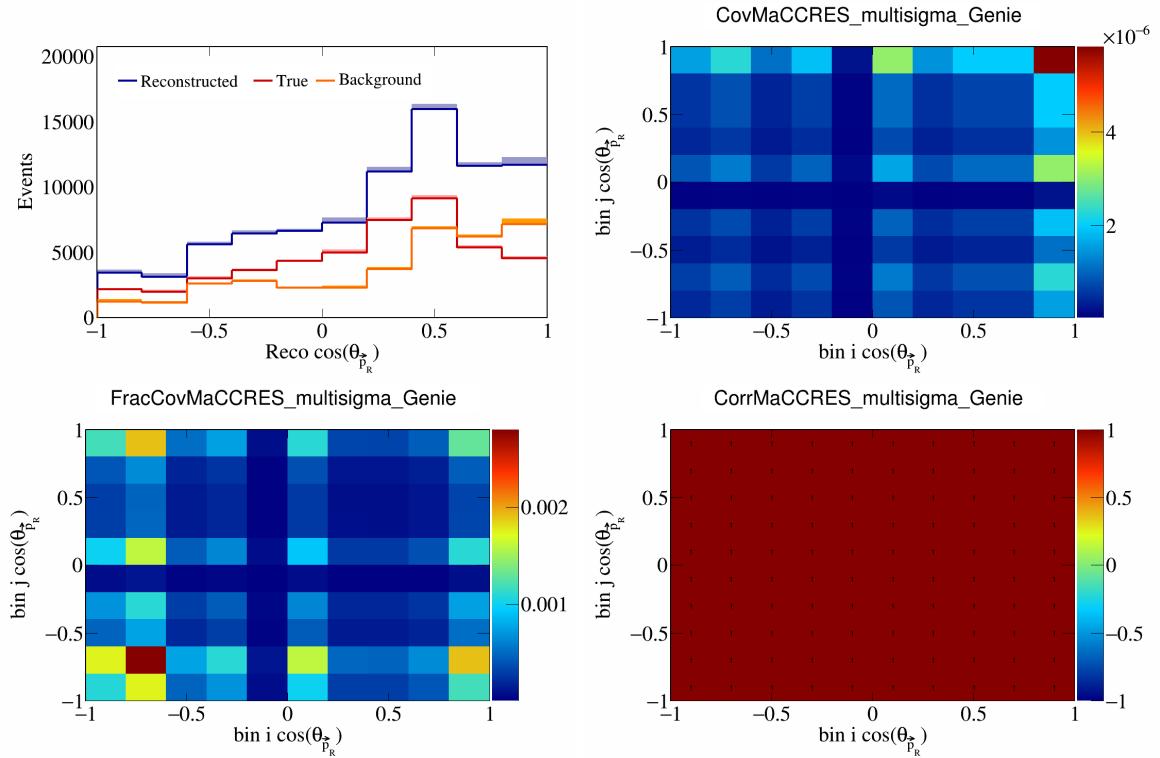


Figure 316: MaCCRES variations for  $\cos(\theta_{\vec{p}_R})$ .

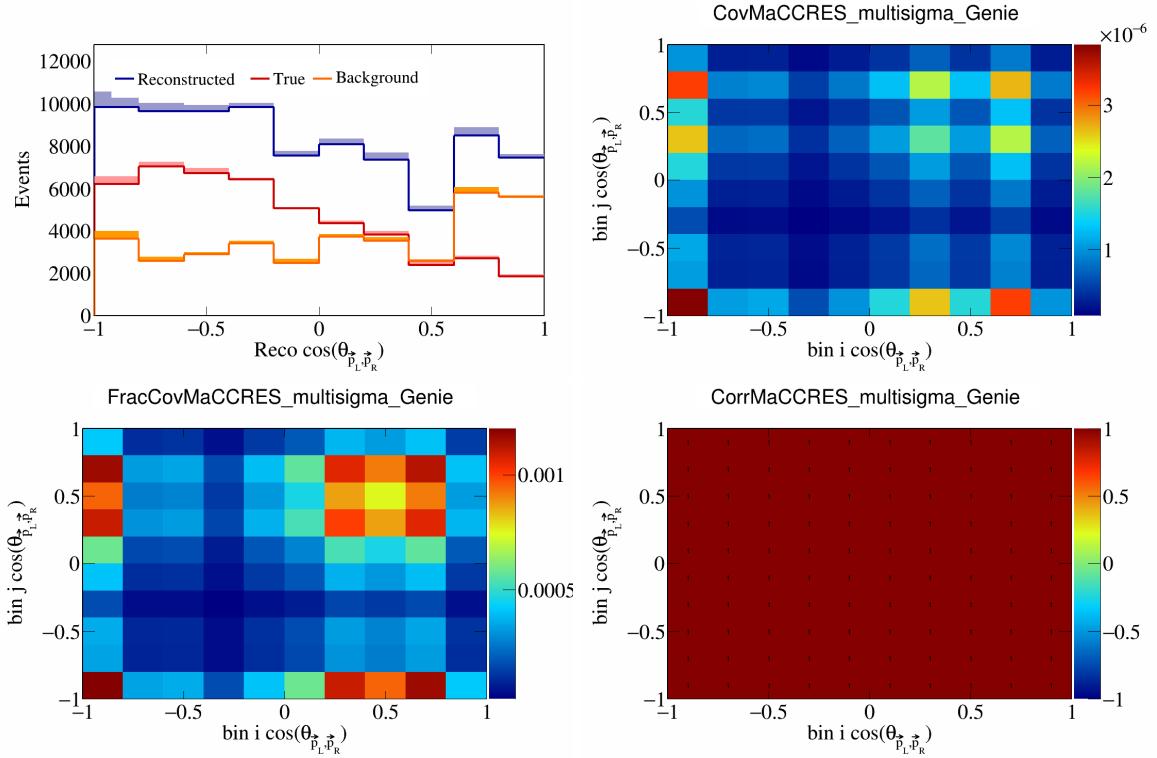


Figure 317: MaCCRES variations for  $\cos(\theta_{\vec{p}_L, \vec{p}_R})$ .

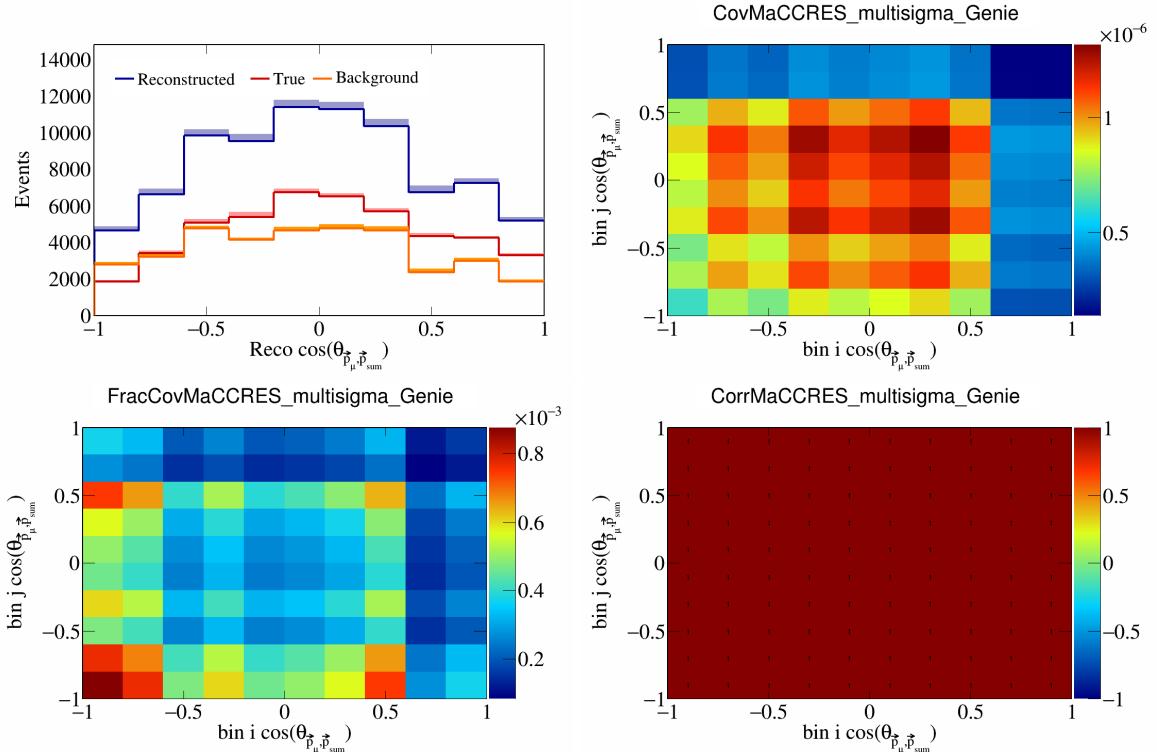


Figure 318: MaCCRES variations for  $\cos(\theta_{\vec{p}_\mu, \vec{p}_{\text{sum}}})$ .

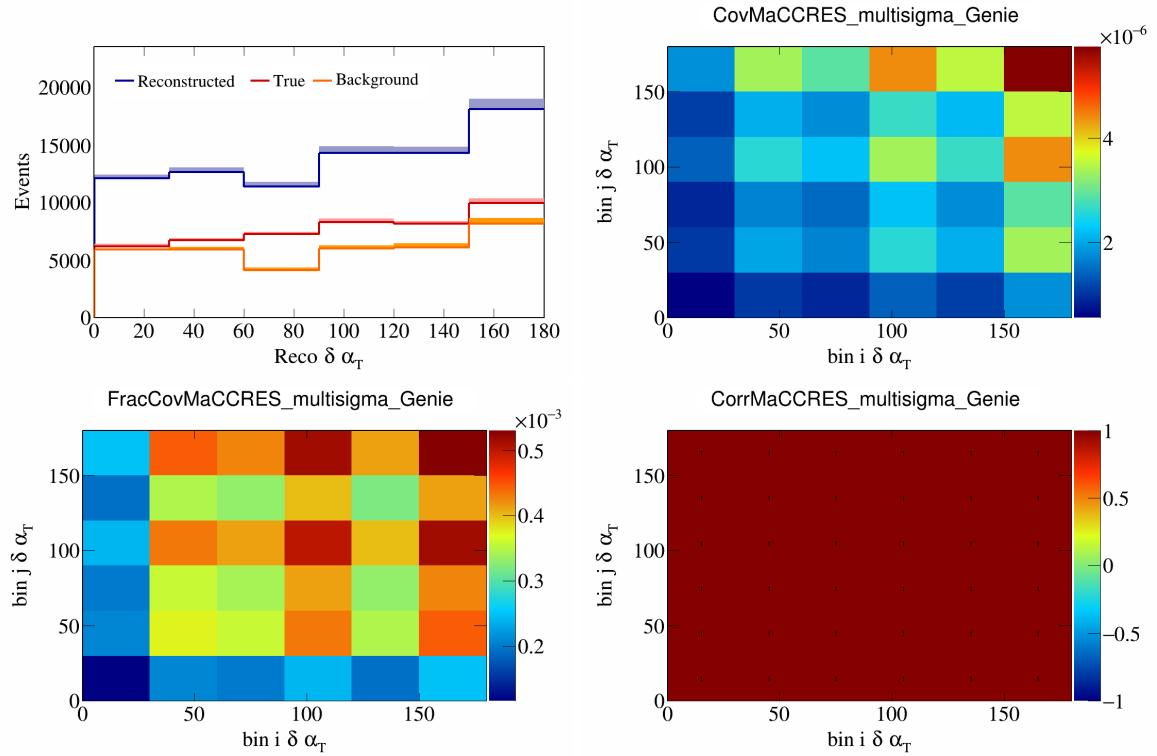


Figure 319: MaCCRES variations for  $\delta\alpha_T$ .

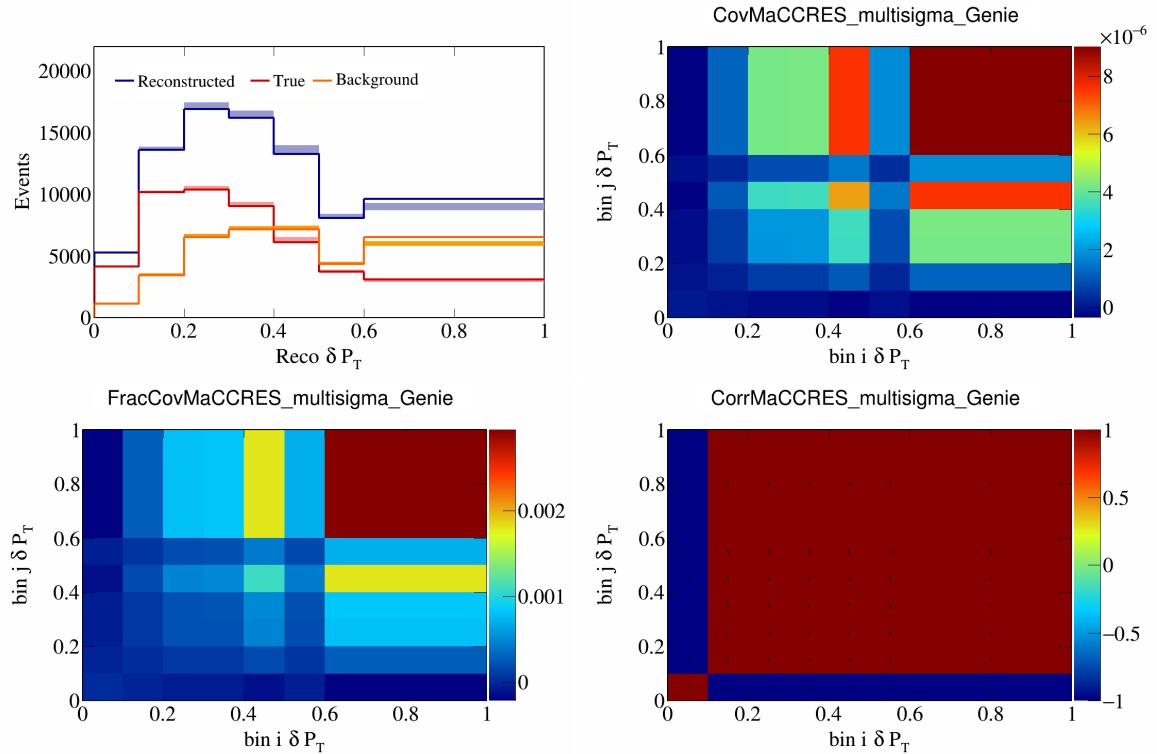


Figure 320: MaCCRES variations for  $\delta P_T$ .

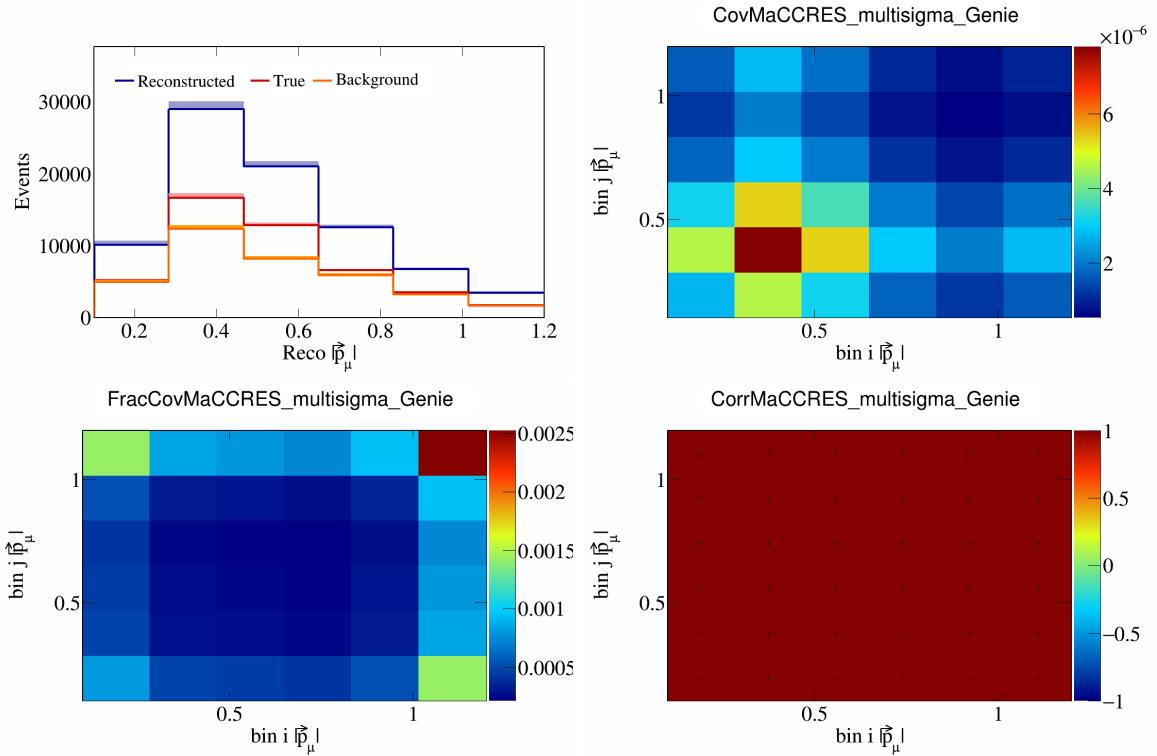


Figure 321: MaCCRES variations for  $|\vec{p}_\mu|$ .

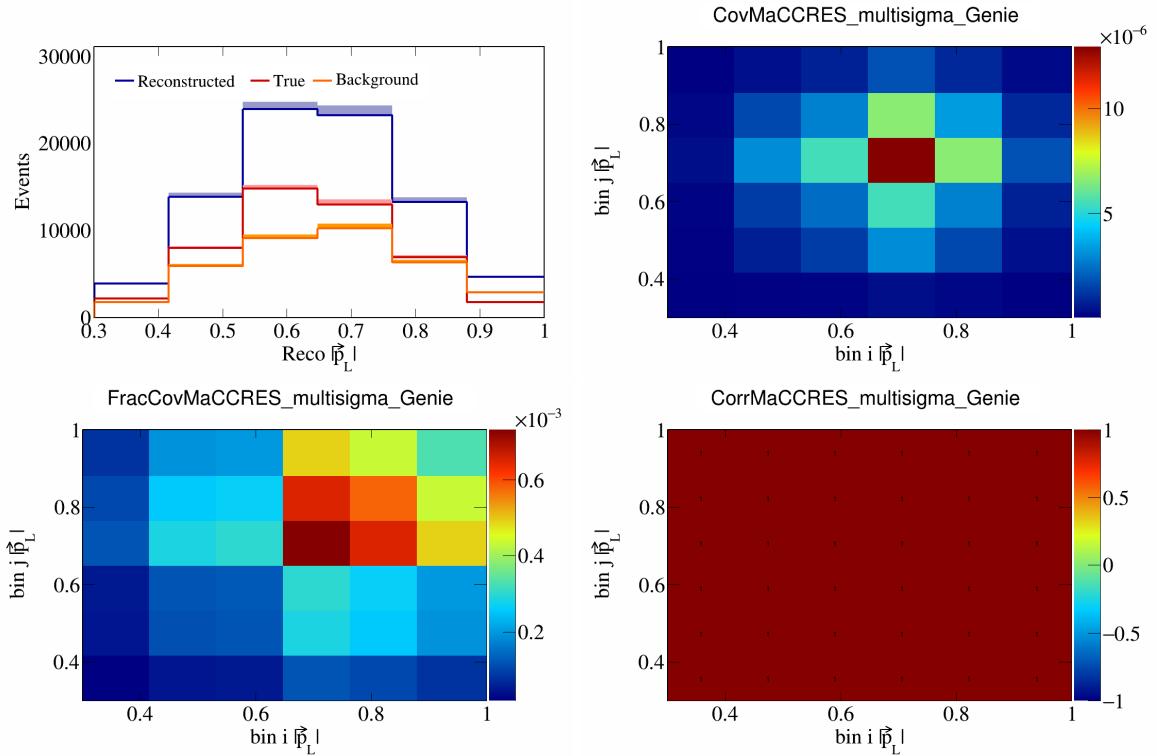


Figure 322: MaCCRES variations for  $|\vec{p}_L|$ .

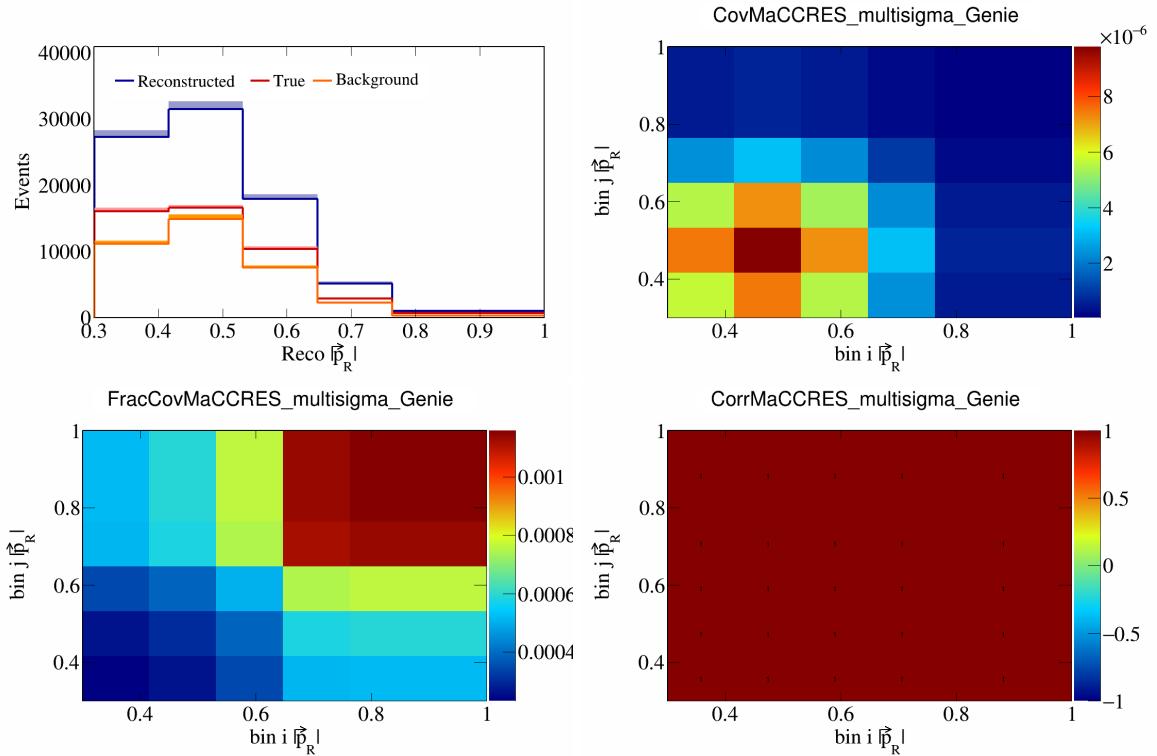


Figure 323: MaCCRES variations for  $|\vec{p}_R|$ .

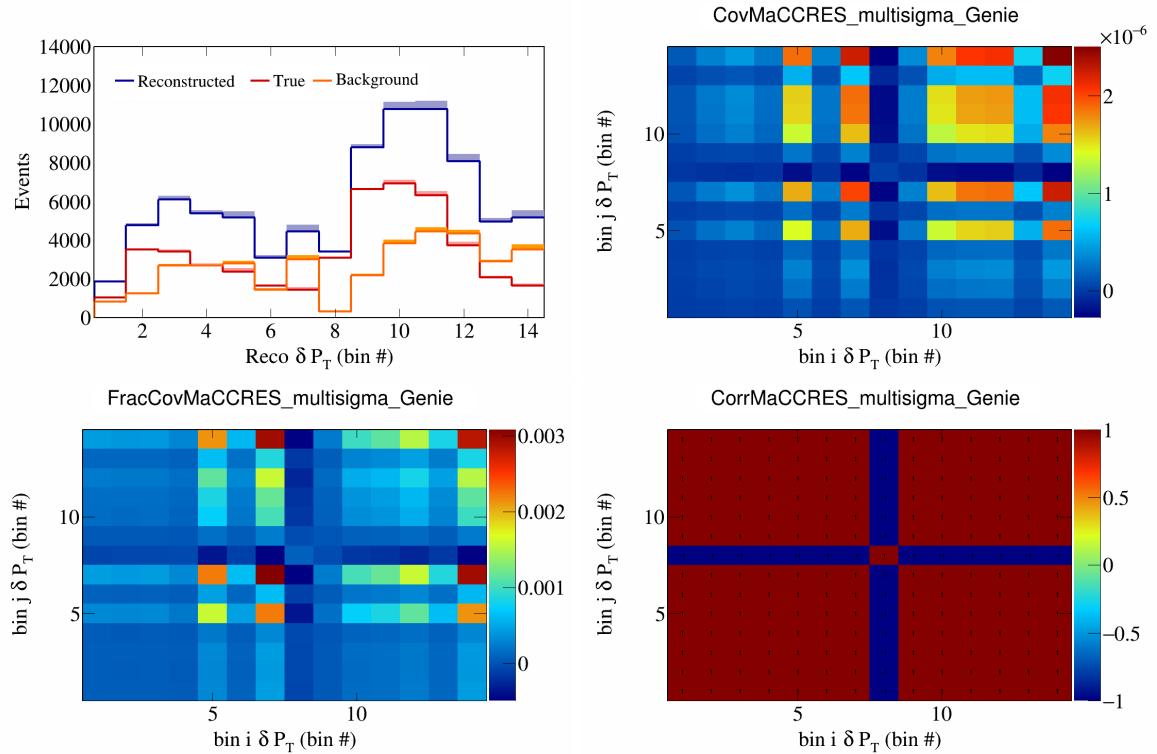


Figure 324: MaCCRES variations for  $\delta P_T$  in  $\cos(\theta_{\vec{p}_\mu})$ .

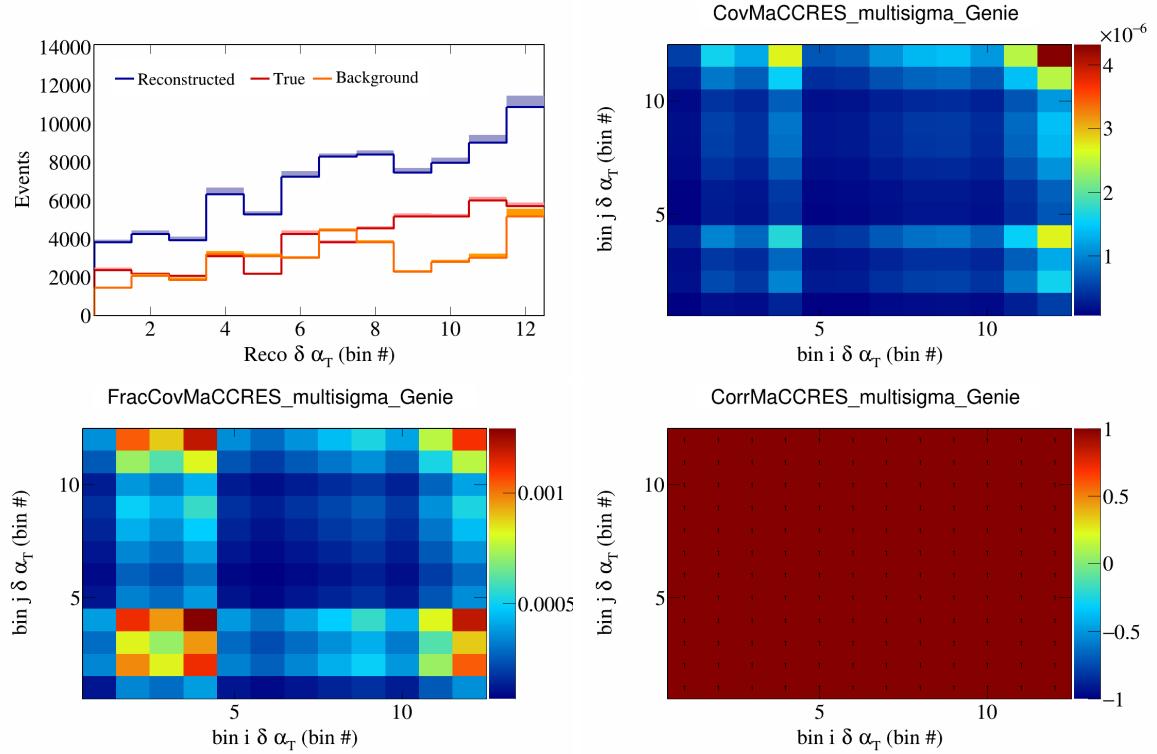


Figure 325: MaCCRES variations for  $\delta\alpha_T$  in  $\cos(\theta_{\vec{p}_\mu})$ .

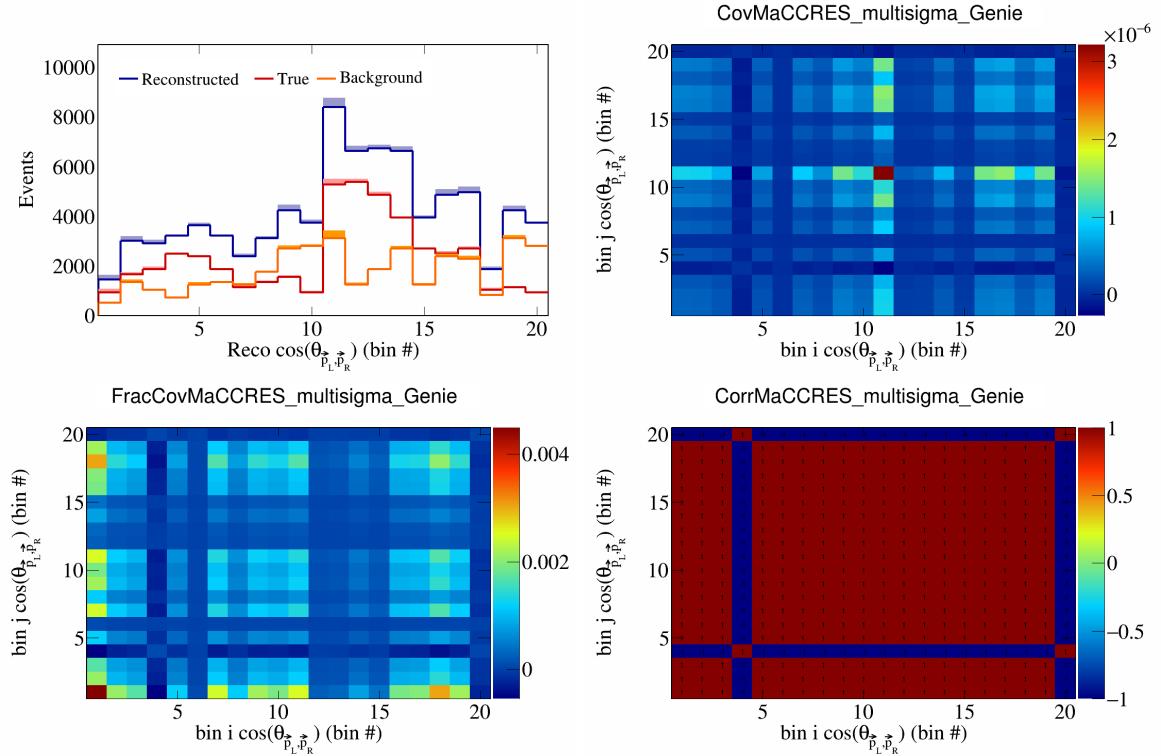


Figure 326: MaCCRES variations for  $\cos(\theta_{\vec{p}_L, \vec{p}_R})$  in  $\cos(\theta_{\vec{p}_\mu})$ .

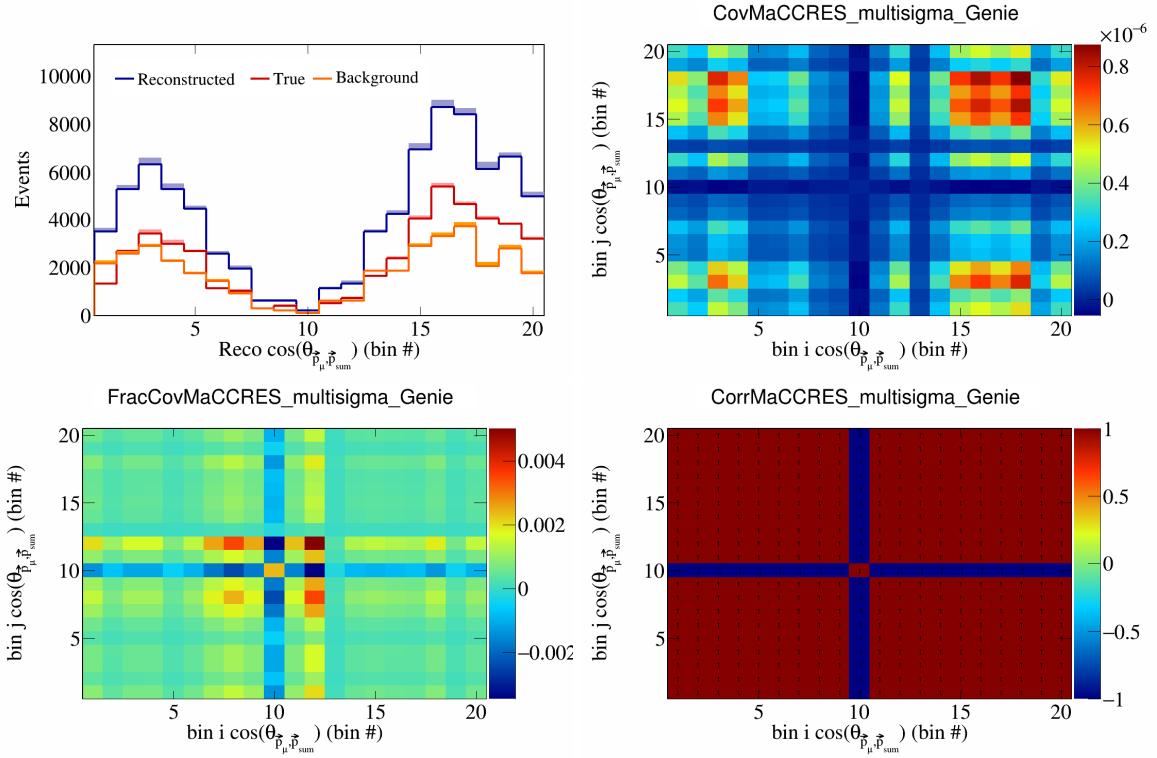


Figure 327: MaCCRES variations for  $\cos(\theta_{\vec{p}_\mu, \vec{p}_{\text{sum}}})$  in  $\cos(\theta_{\vec{p}_\mu})$ .

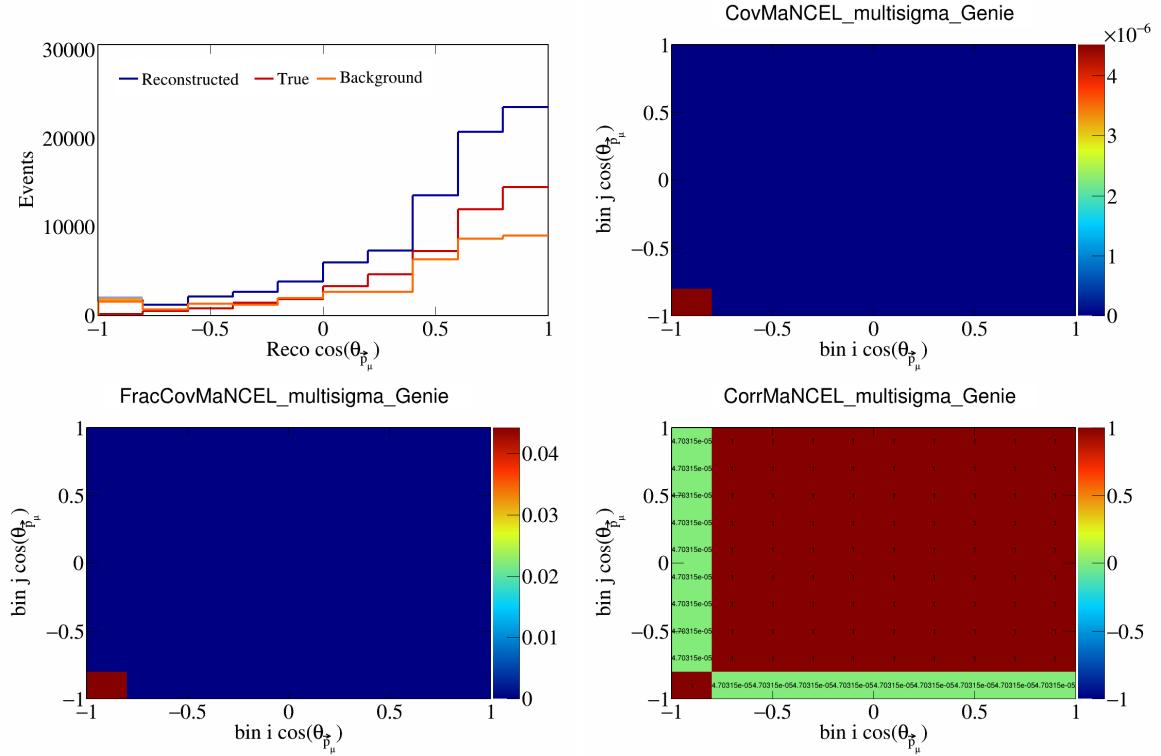


Figure 328: MaNCEL variations for  $\cos(\theta_{\vec{p}_\mu})$ .

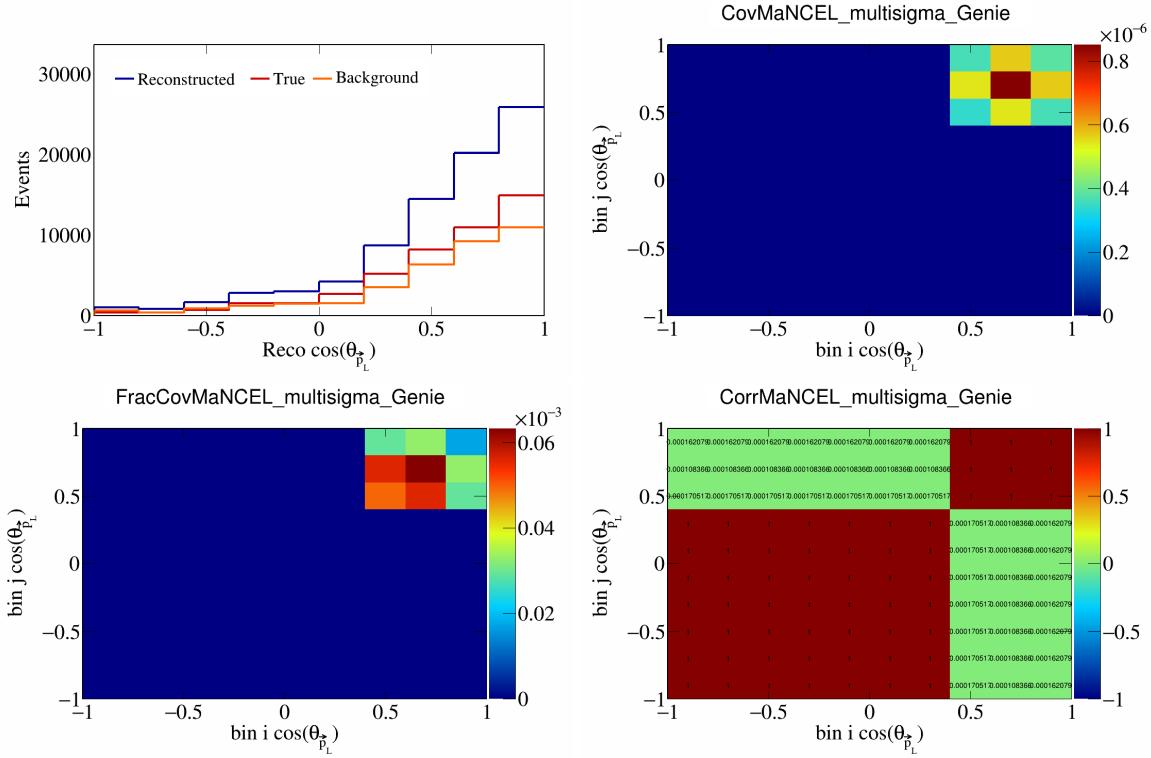


Figure 329: MaNCEL variations for  $\cos(\theta_{\vec{p}_L})$ .

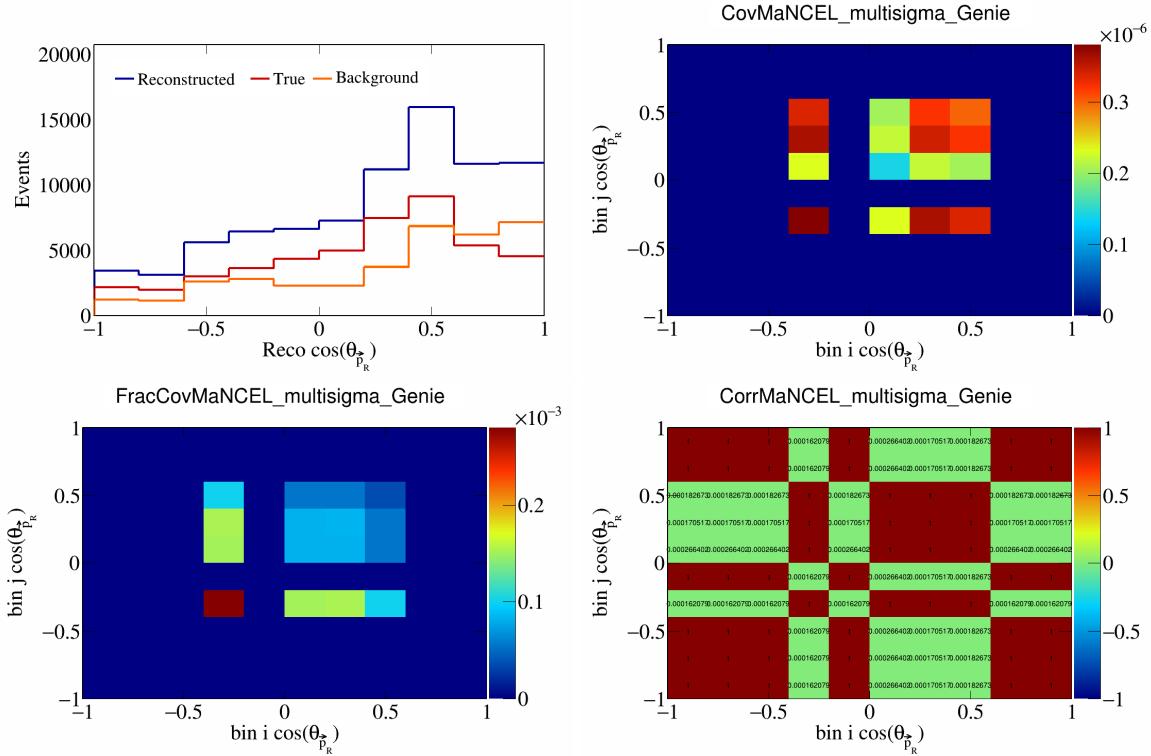


Figure 330: MaNCEL variations for  $\cos(\theta_{\vec{p}_R})$ .

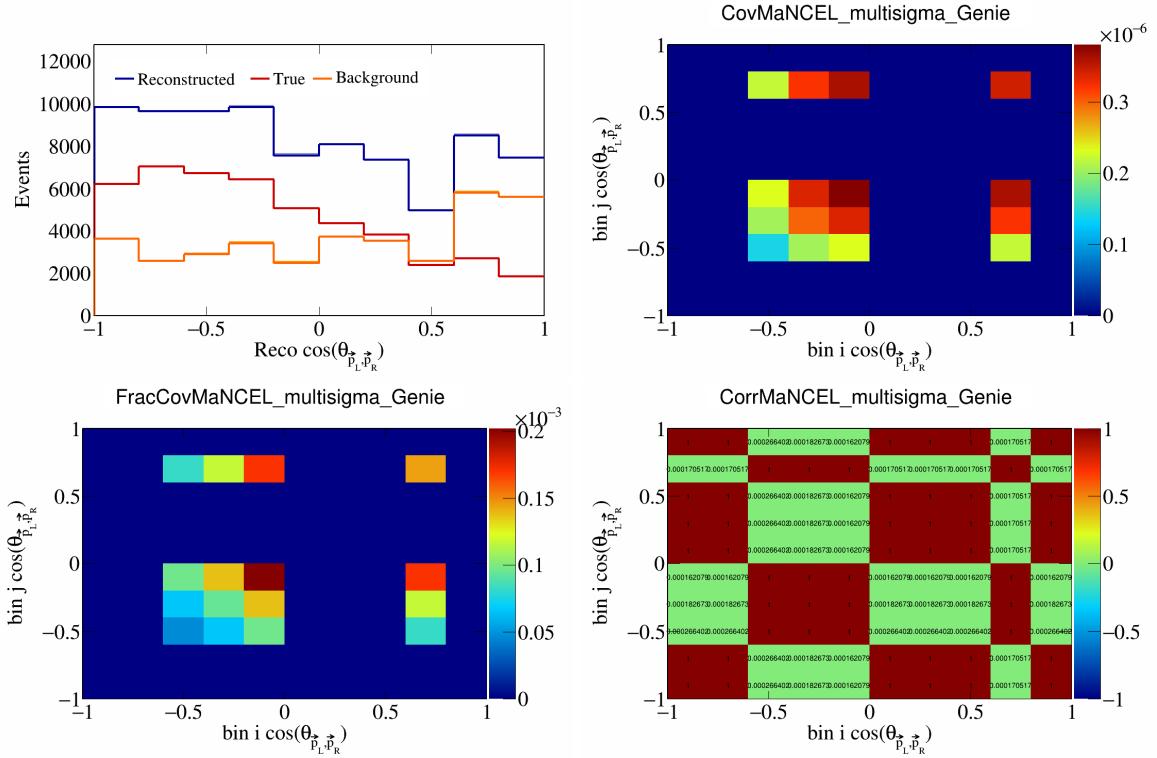


Figure 331: MaNCEL variations for  $\cos(\theta_{\vec{p}_L, \vec{p}_R})$ .

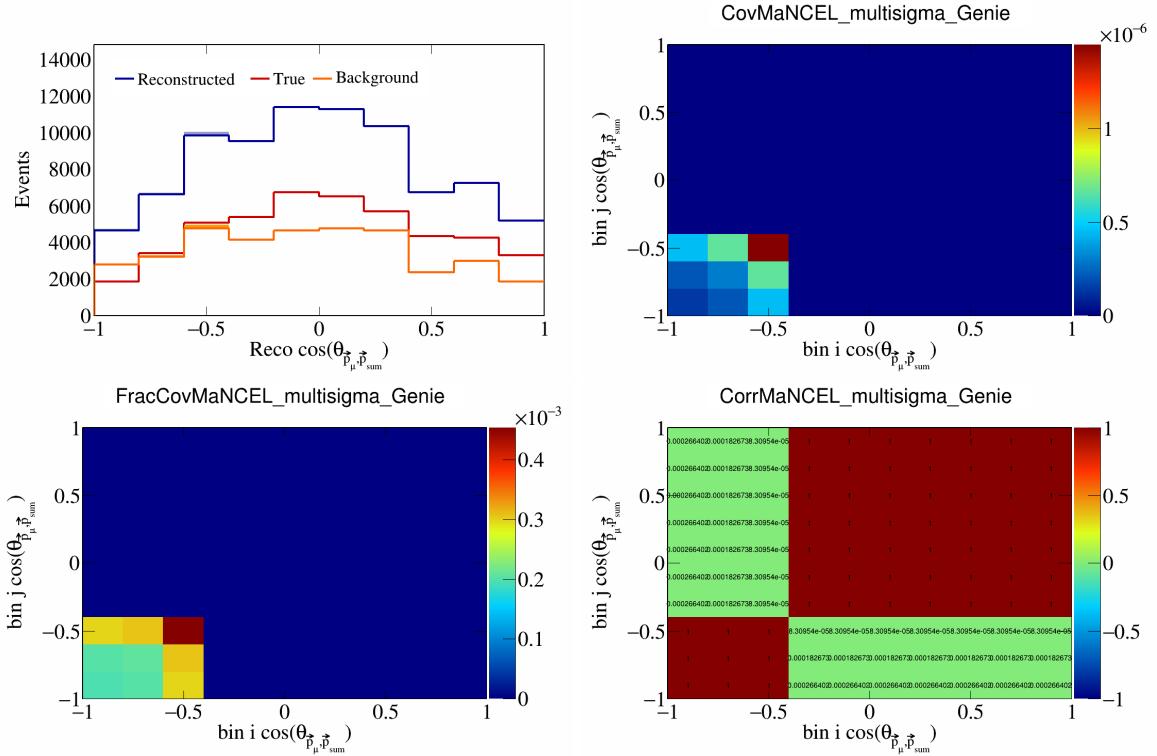


Figure 332: MaNCEL variations for  $\cos(\theta_{\vec{p}_\mu, \vec{p}_{\text{sum}}})$ .

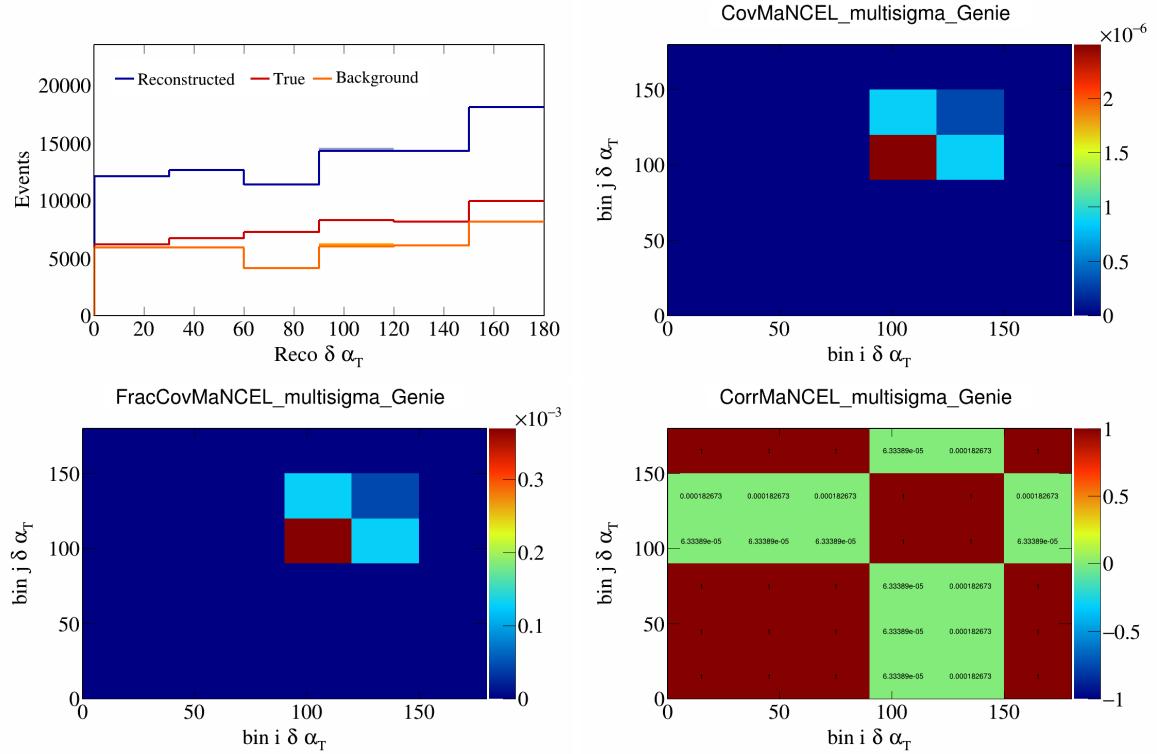


Figure 333: MaNCEL variations for  $\delta\alpha_T$ .

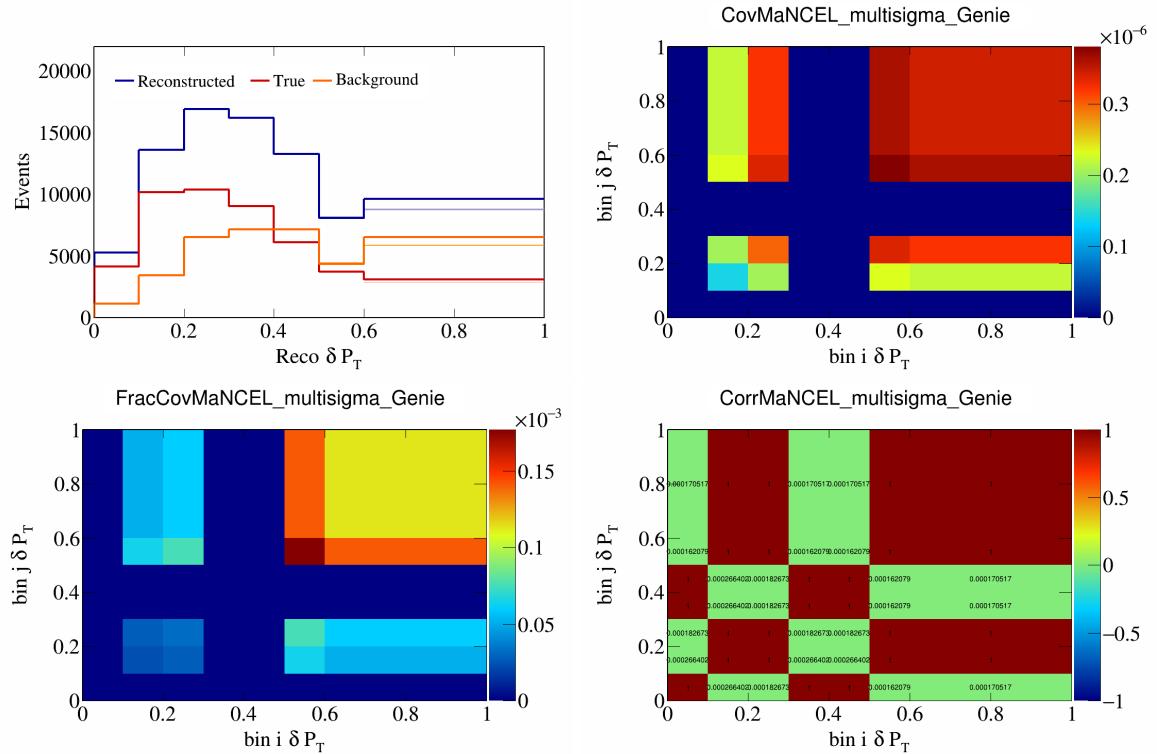


Figure 334: MaNCEL variations for  $\delta P_T$ .

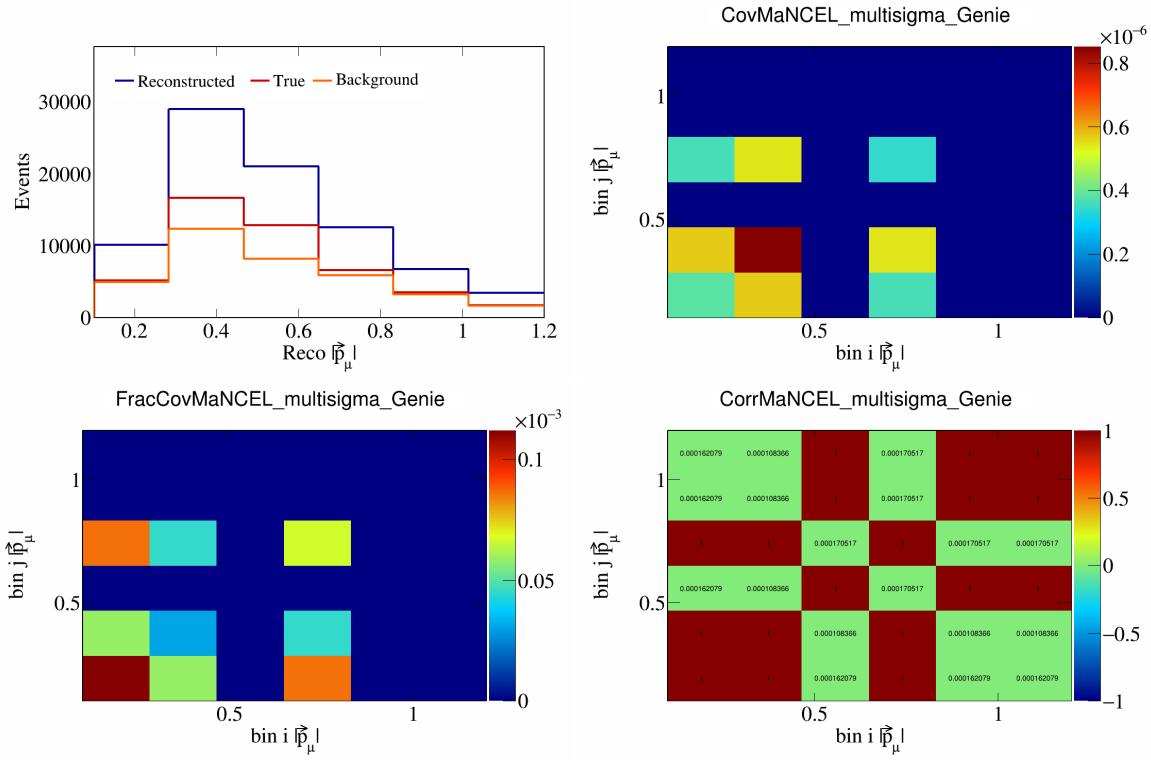


Figure 335: MaNCEL variations for  $|\vec{p}_\mu|$ .

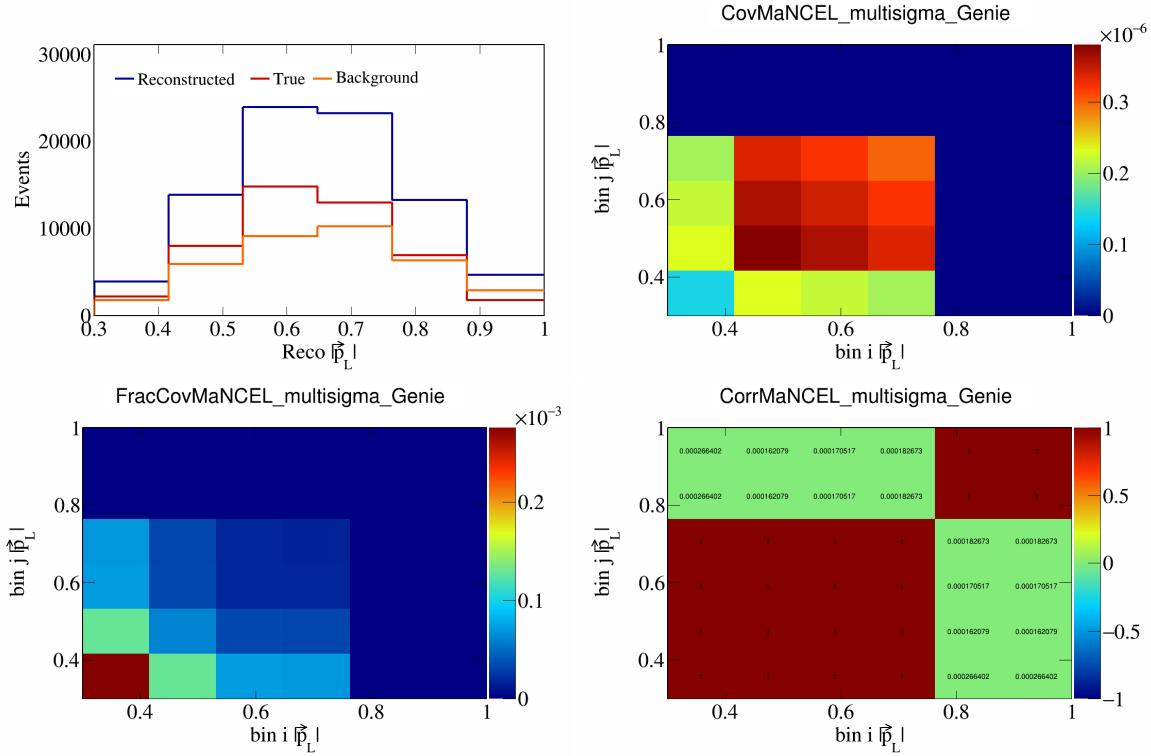


Figure 336: MaNCEL variations for  $|\vec{p}_L|$ .

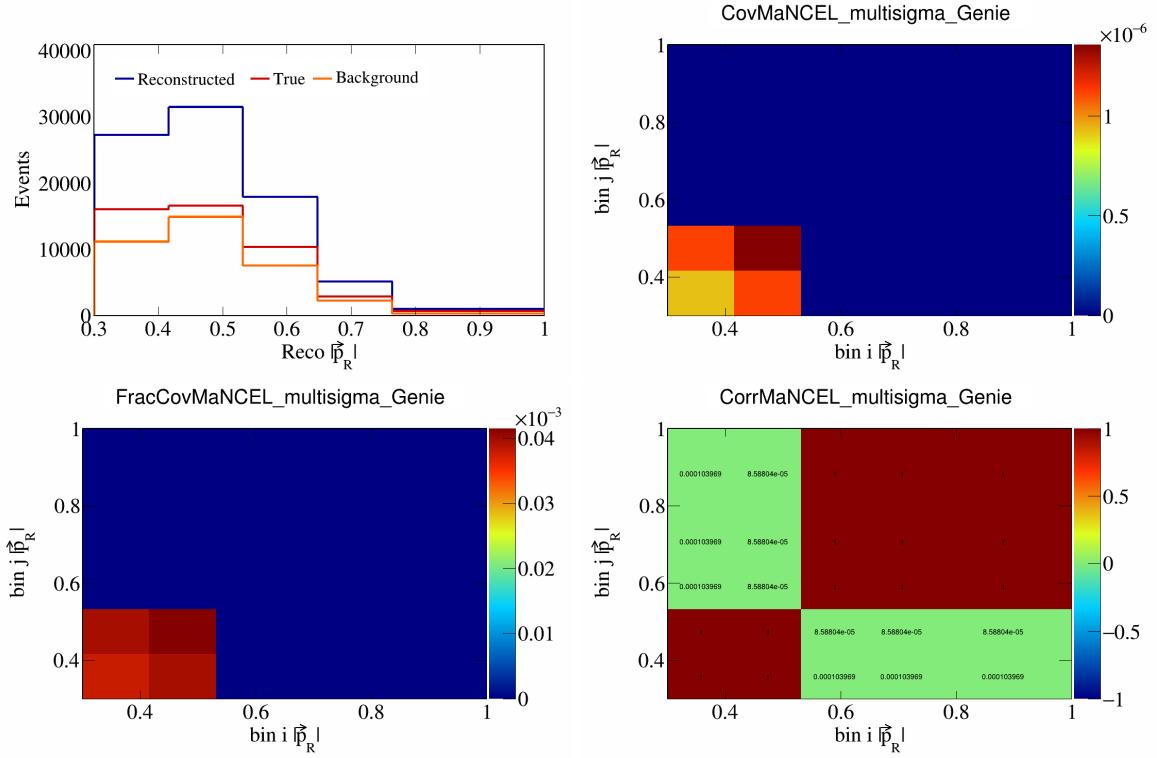


Figure 337: MaNCEL variations for  $|\vec{p}_R|$ .

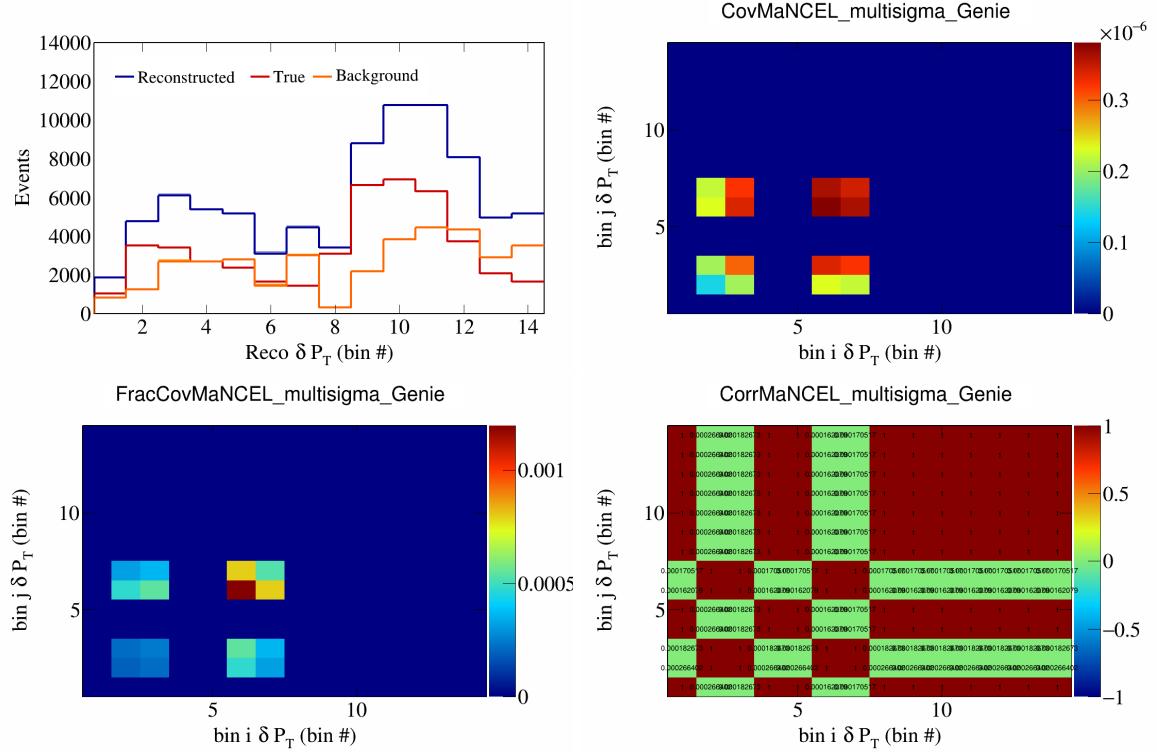


Figure 338: MaNCEL variations for  $\delta P_T$  in  $\cos(\theta_{\vec{p}_\mu})$ .

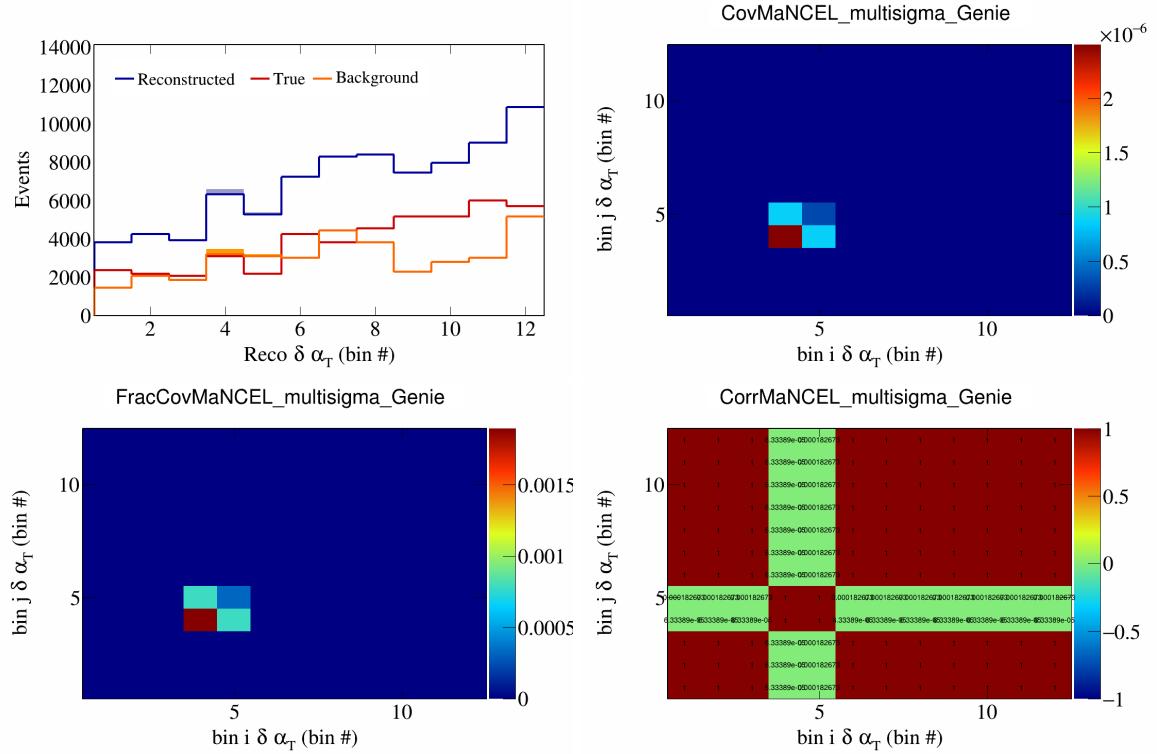


Figure 339: MaNCEL variations for  $\delta\alpha_T$  in  $\cos(\theta_{\vec{p}_\mu})$ .

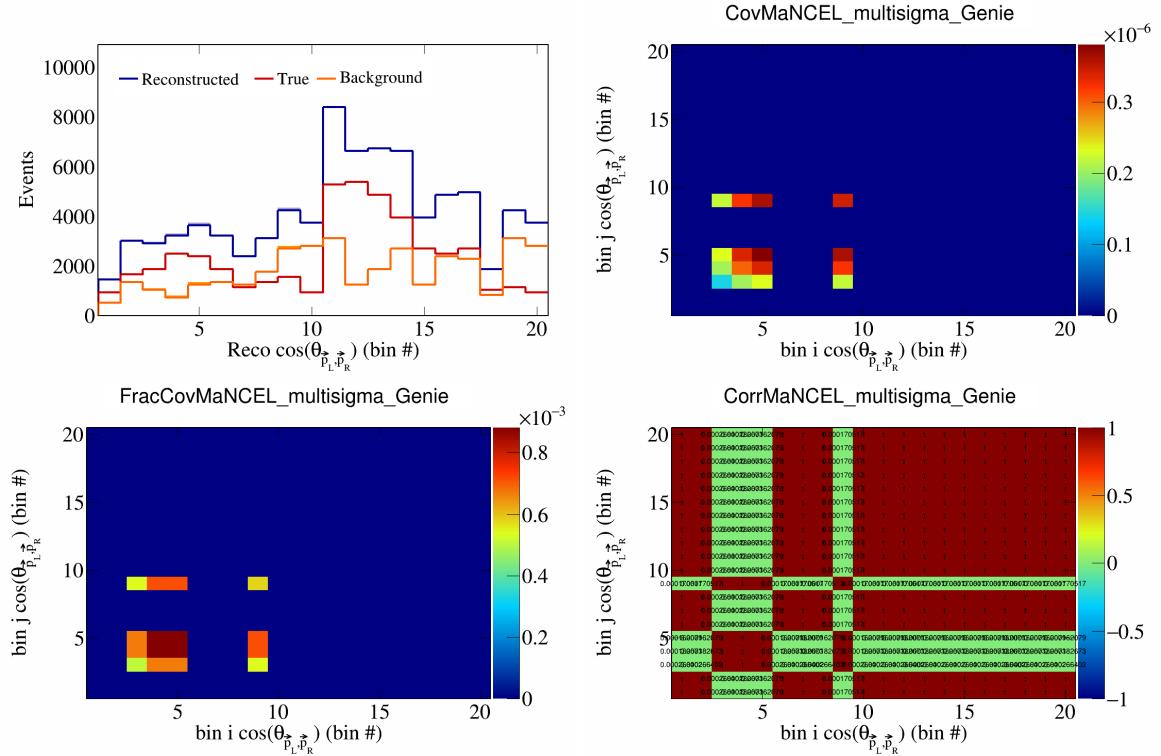


Figure 340: MaNCEL variations for  $\cos(\theta_{\vec{p}_L, \vec{p}_R})$  in  $\cos(\theta_{\vec{p}_\mu})$ .

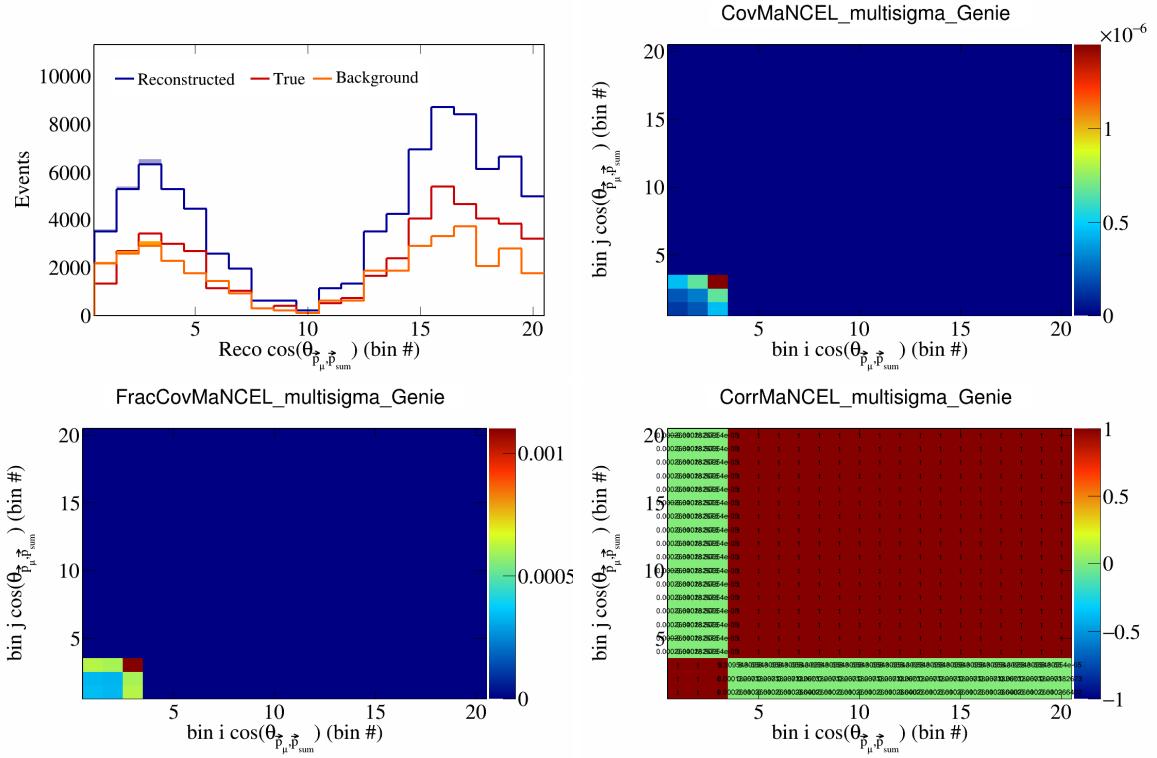


Figure 341: MaNCEL variations for  $\cos(\theta_{\vec{p}_\mu, \vec{p}_{\text{sum}}})$  in  $\cos(\theta_{\vec{p}_\mu})$ .

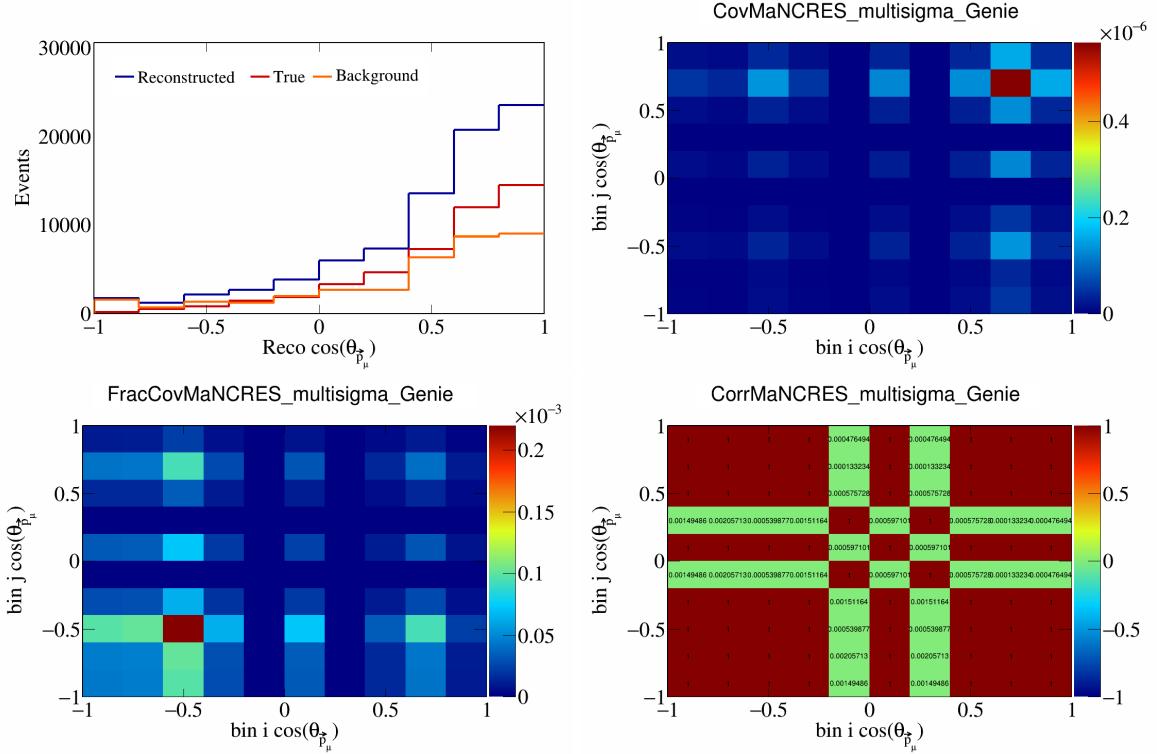


Figure 342: MaNCRES variations for  $\cos(\theta_{\vec{p}_\mu})$ .

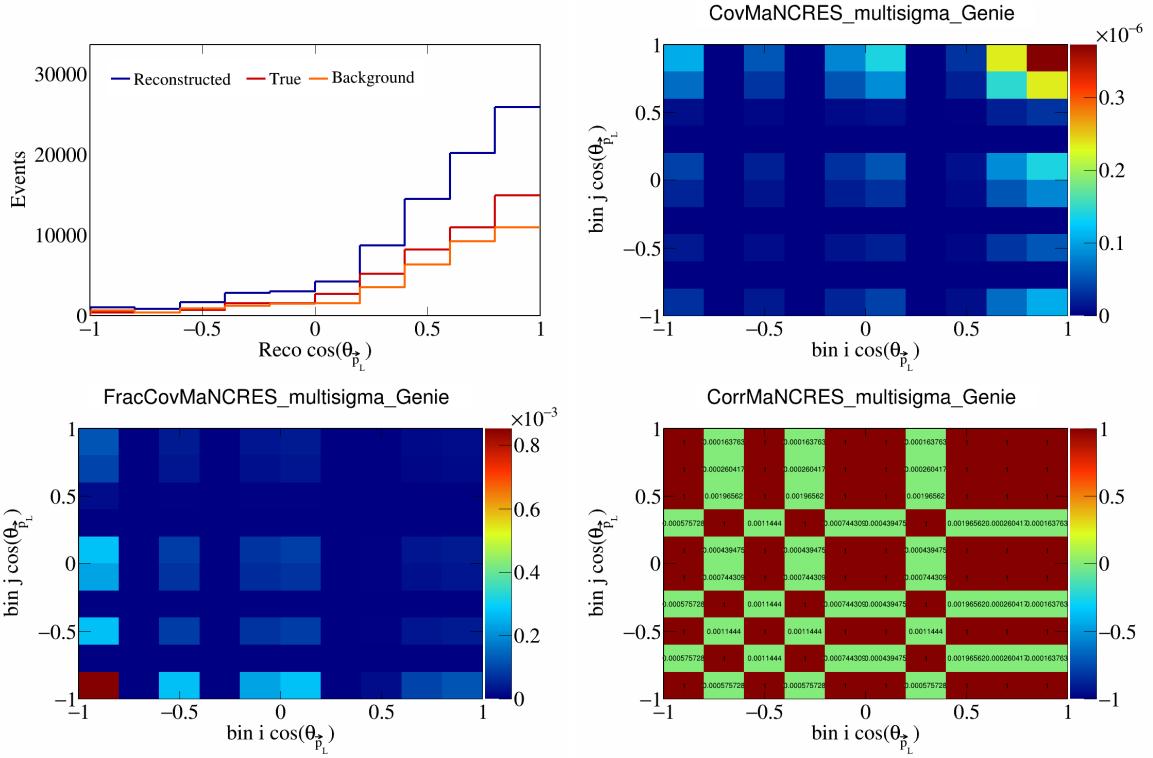


Figure 343: MaNCRES variations for  $\cos(\theta_{\vec{p}_L})$ .

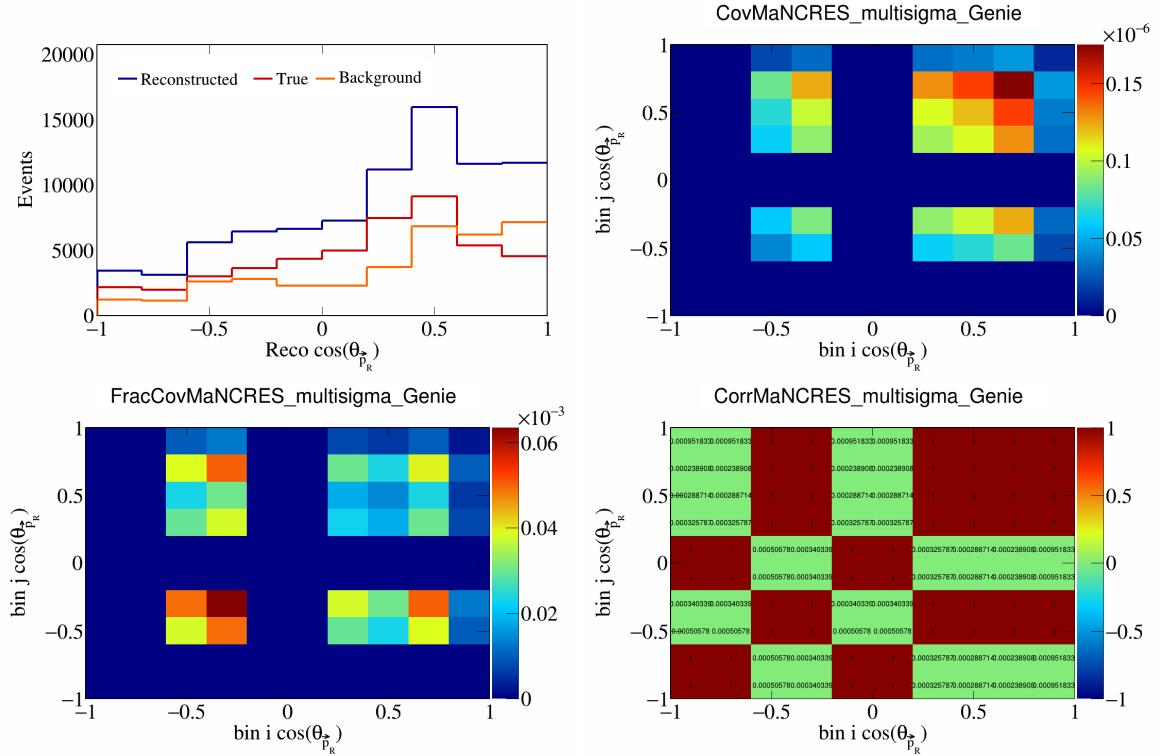


Figure 344: MaNCRES variations for  $\cos(\theta_{\vec{p}_R})$ .

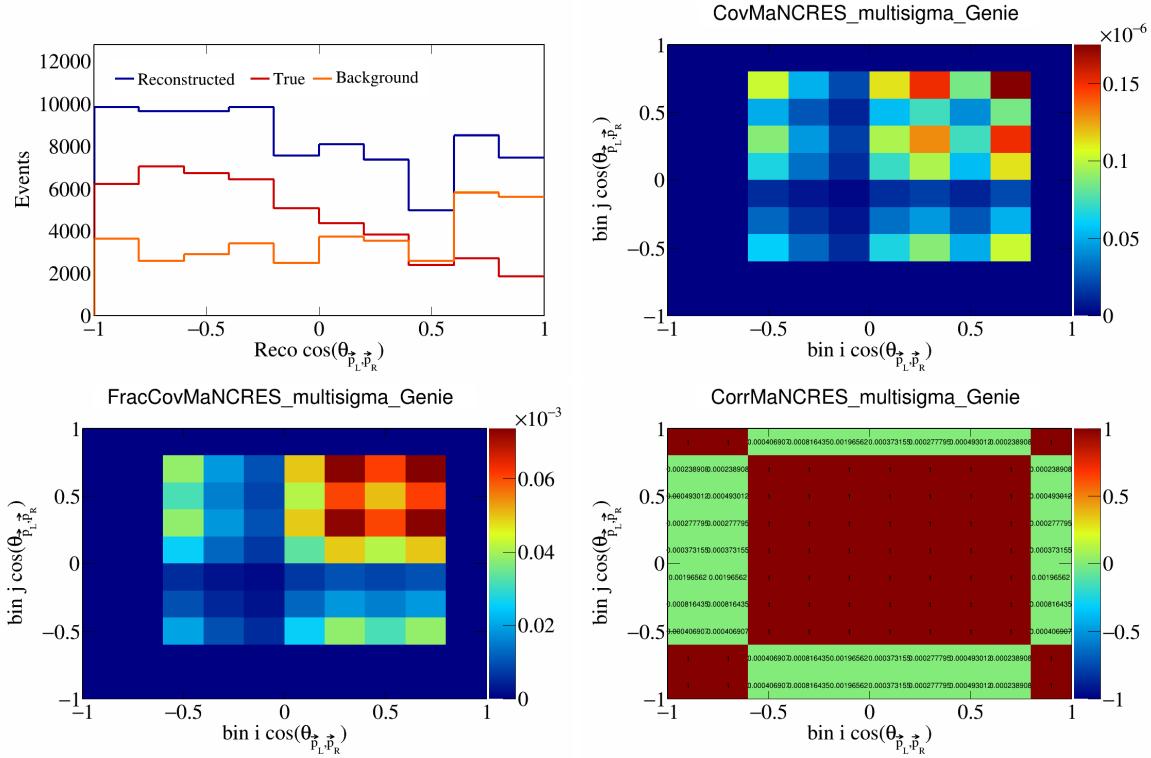


Figure 345: MaNCRES variations for  $\cos(\theta_{\vec{p}_L, \vec{p}_R})$ .

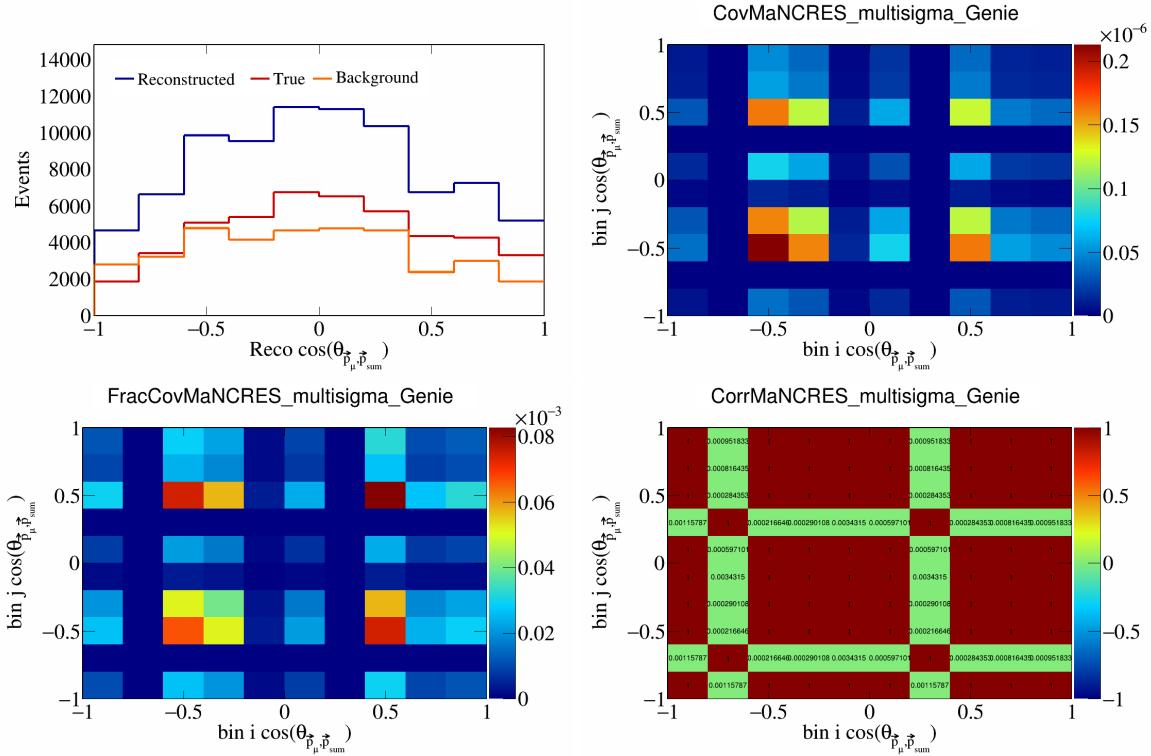


Figure 346: MaNCRES variations for  $\cos(\theta_{\vec{p}_\mu, \vec{p}_{\text{sum}}})$ .

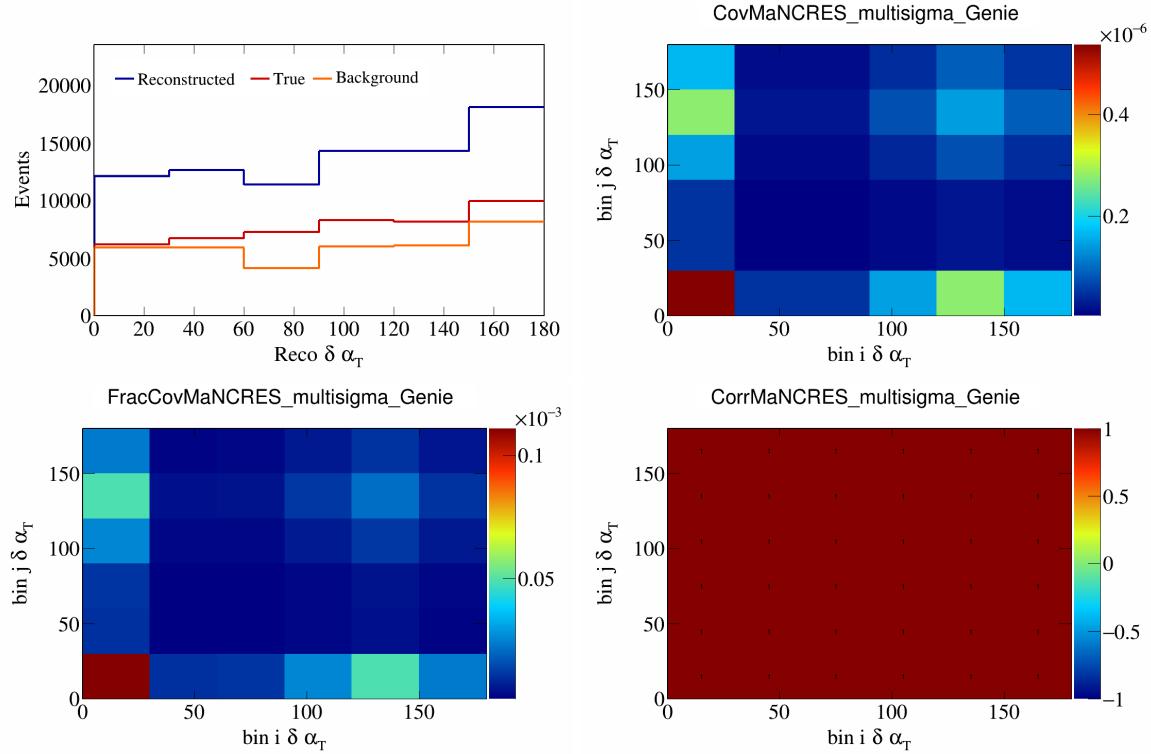


Figure 347: MaNCRES variations for  $\delta\alpha_T$ .

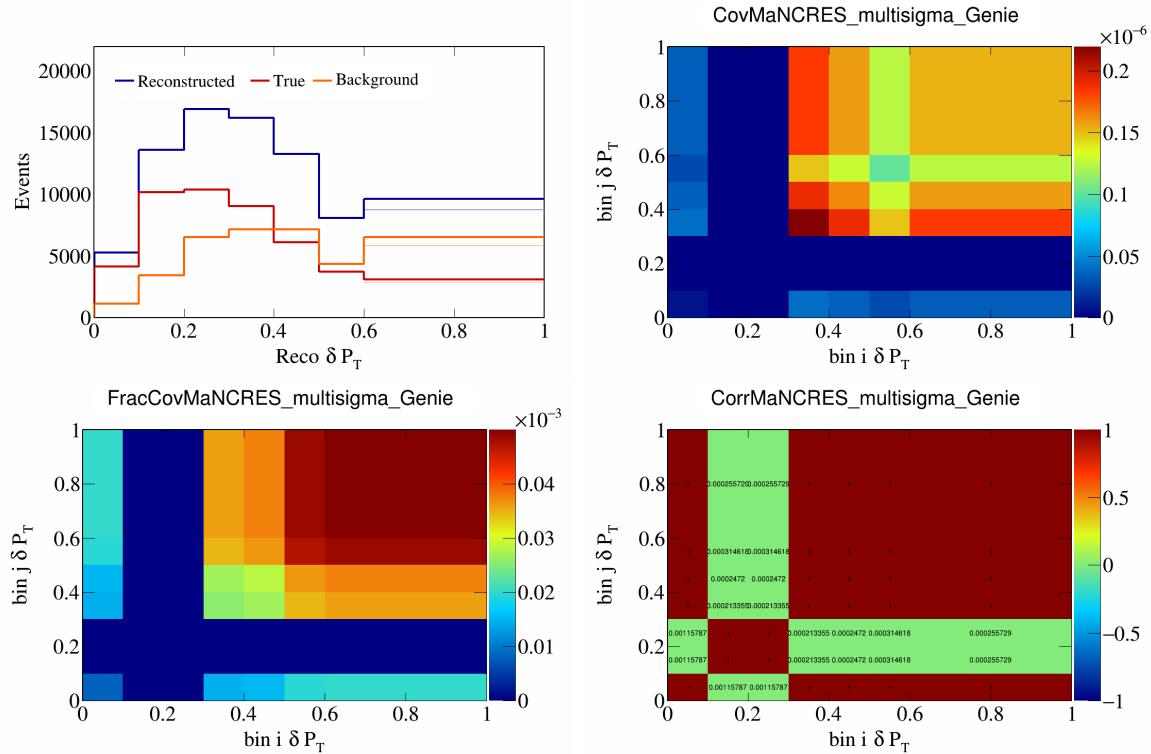


Figure 348: MaNCRES variations for  $\delta P_T$ .

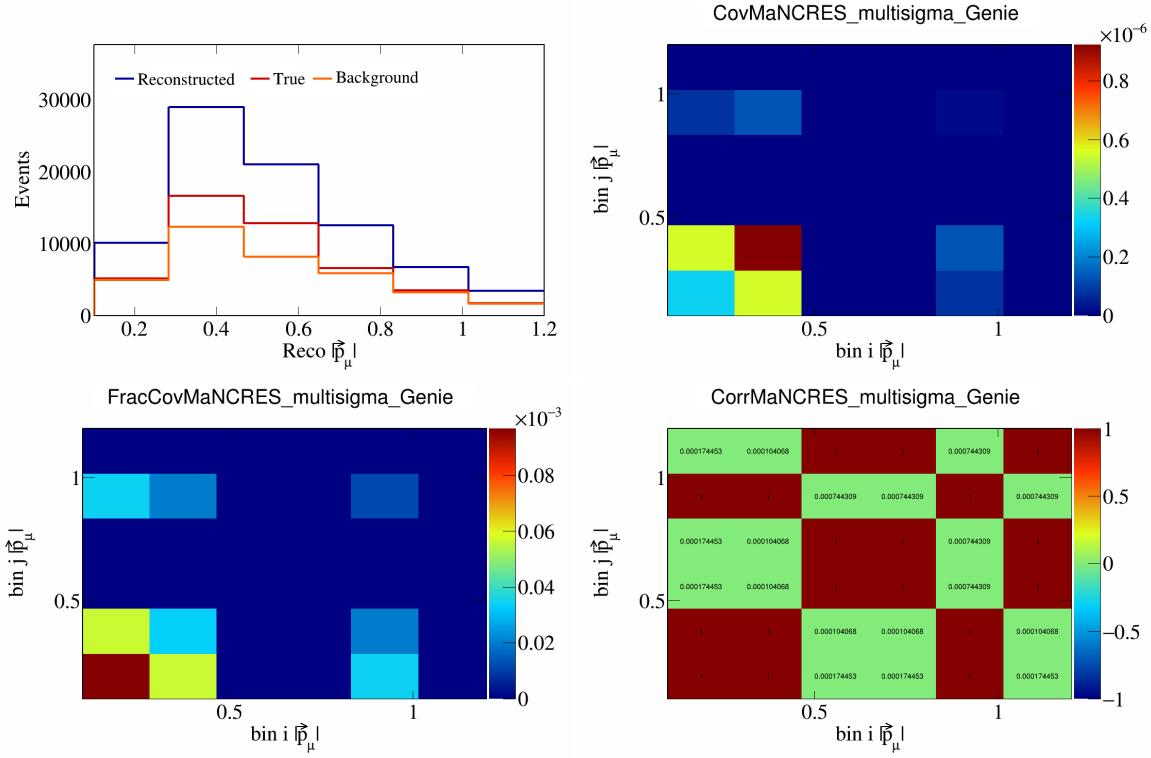


Figure 349: MaNCRES variations for  $|\vec{p}_\mu|$ .

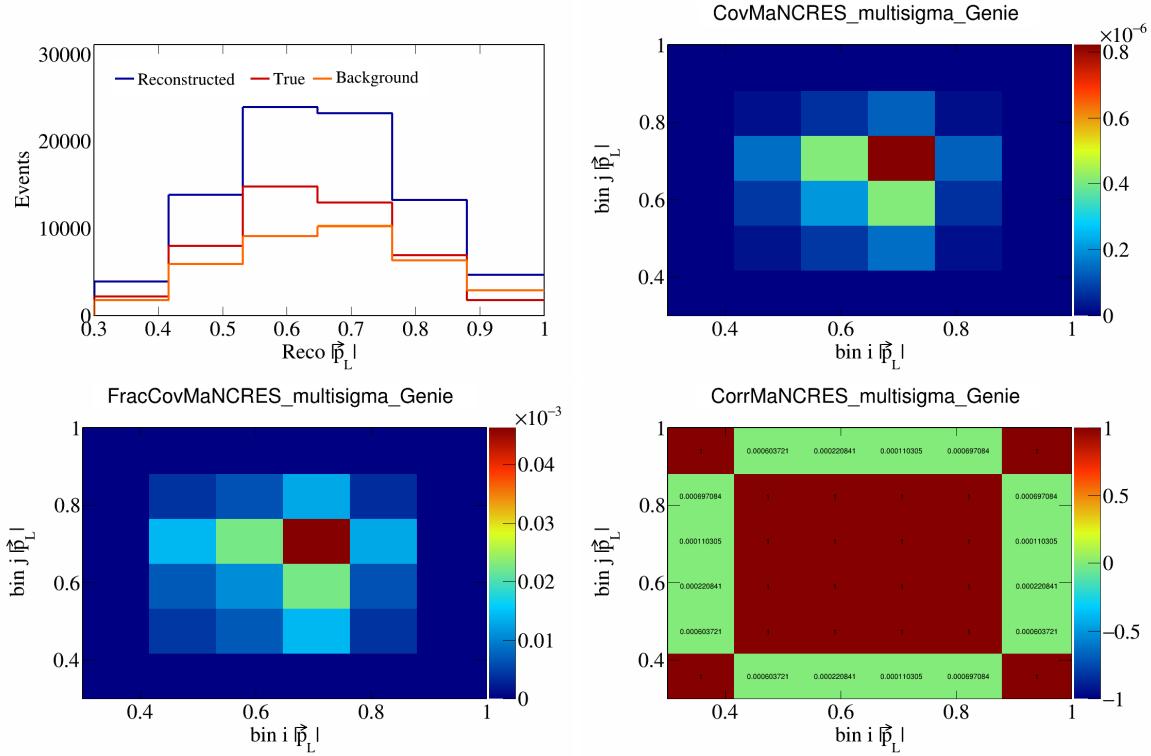


Figure 350: MaNCRES variations for  $|\vec{p}_L|$ .

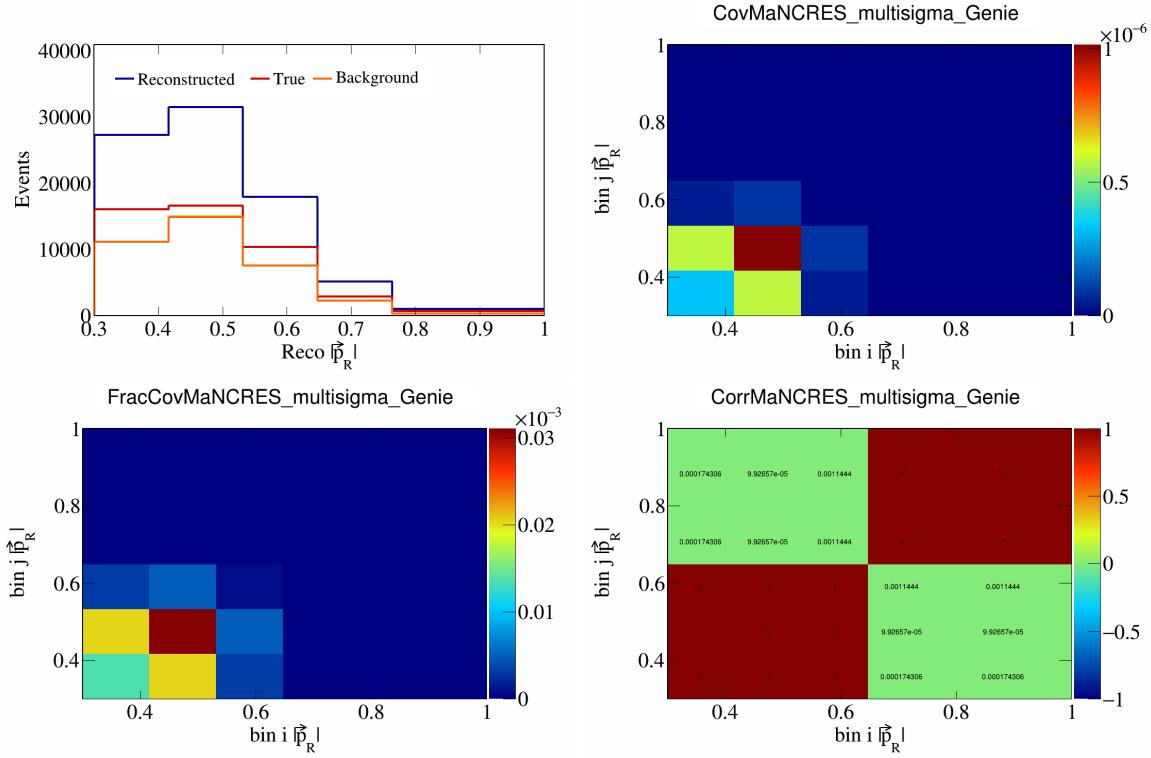


Figure 351: MaNCRES variations for  $|\vec{p}_R|$ .

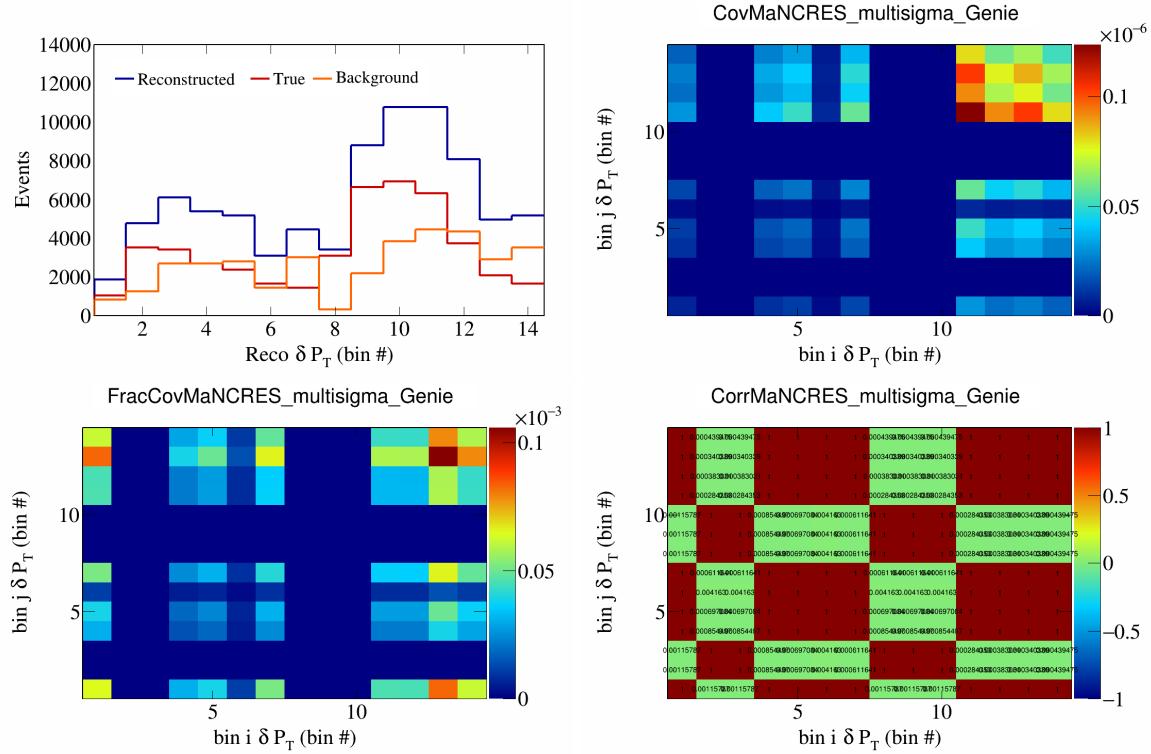


Figure 352: MaNCRES variations for  $\delta P_T$  in  $\cos(\theta_{\vec{p}_\mu})$ .

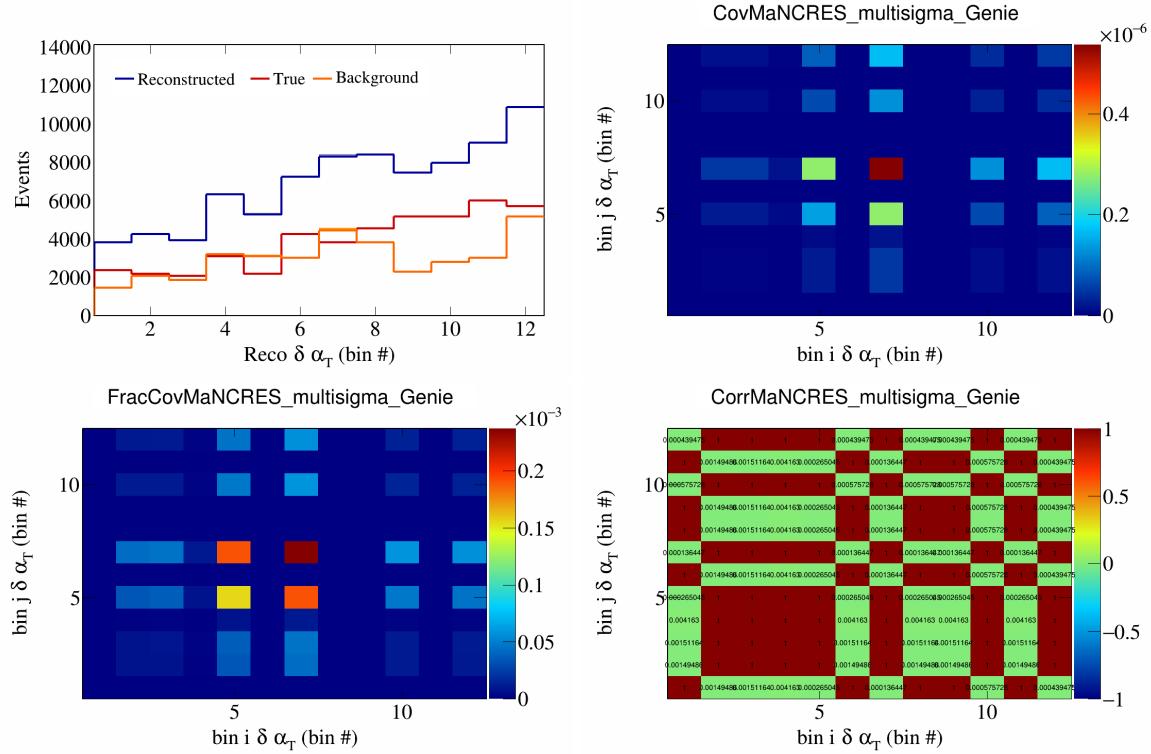


Figure 353: MaNCRES variations for  $\delta\alpha_T$  in  $\cos(\theta_{\vec{p}_\mu})$ .

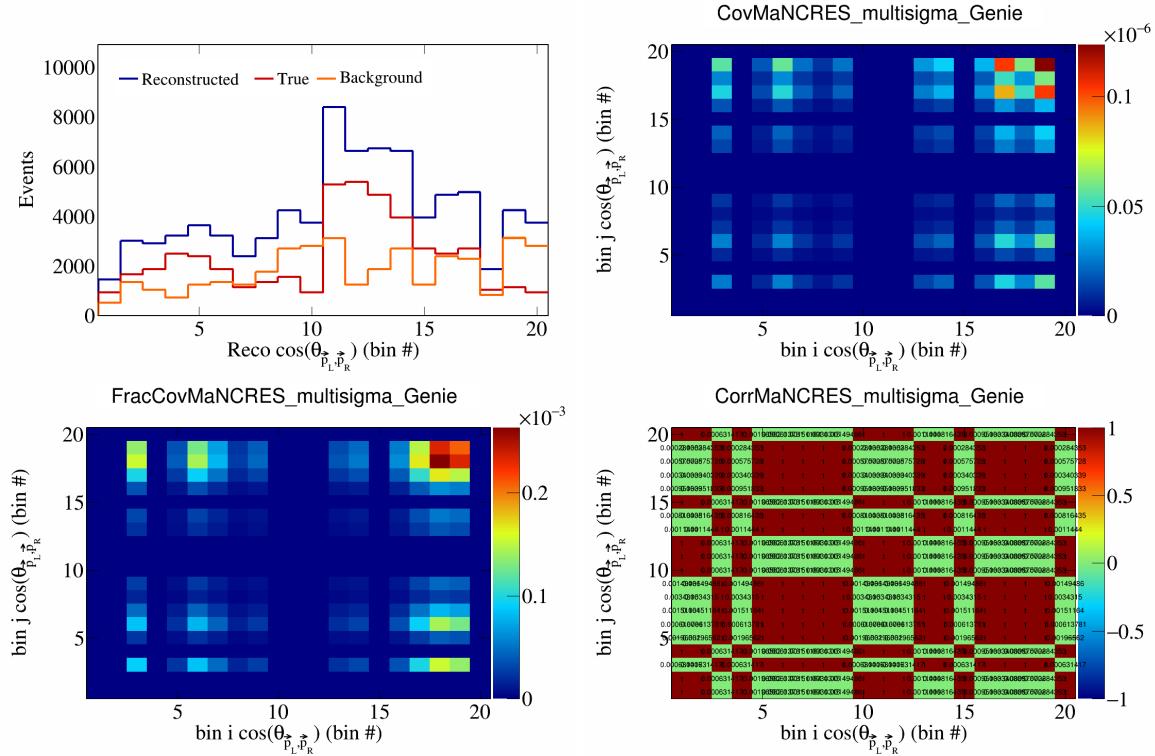


Figure 354: MaNCRES variations for  $\cos(\theta_{\vec{p}_L, \vec{p}_R})$  in  $\cos(\theta_{\vec{p}_\mu})$ .

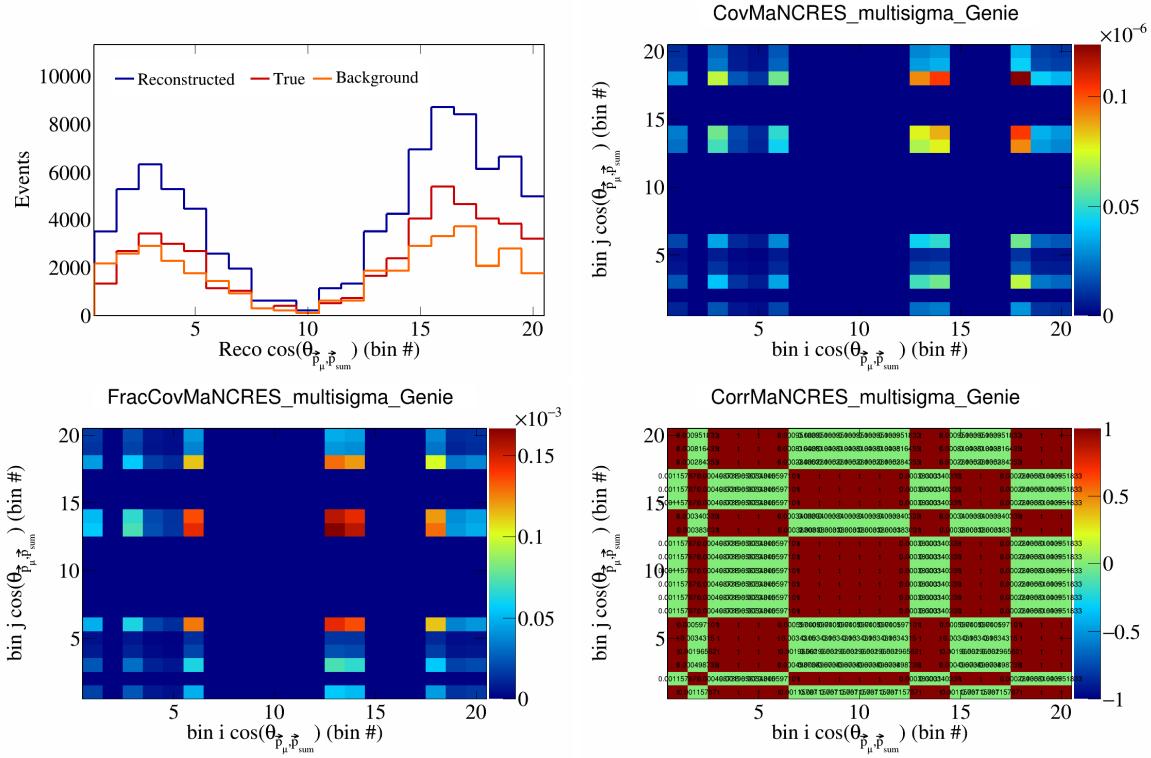


Figure 355: MaNCRES variations for  $\cos(\theta_{\vec{p}_\mu, \vec{p}_{\text{sum}}})$  in  $\cos(\theta_{\vec{p}_\mu})$ .

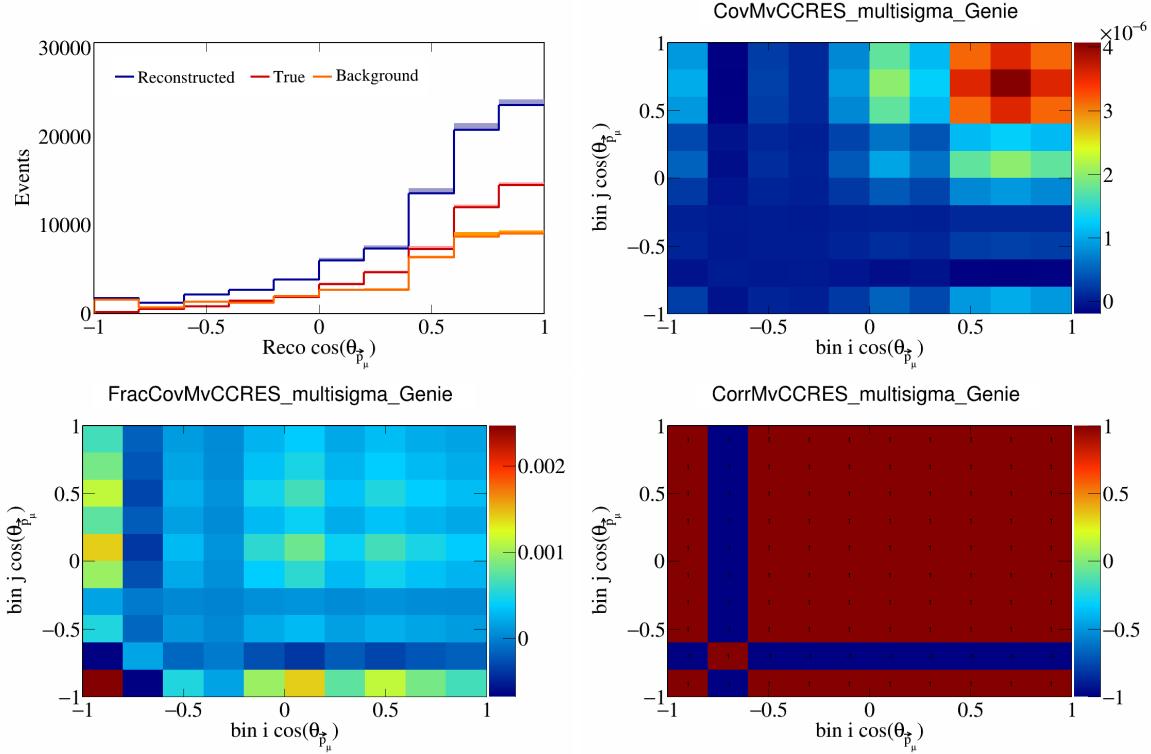


Figure 356: MvCCRES variations for  $\cos(\theta_{\vec{p}_\mu})$ .

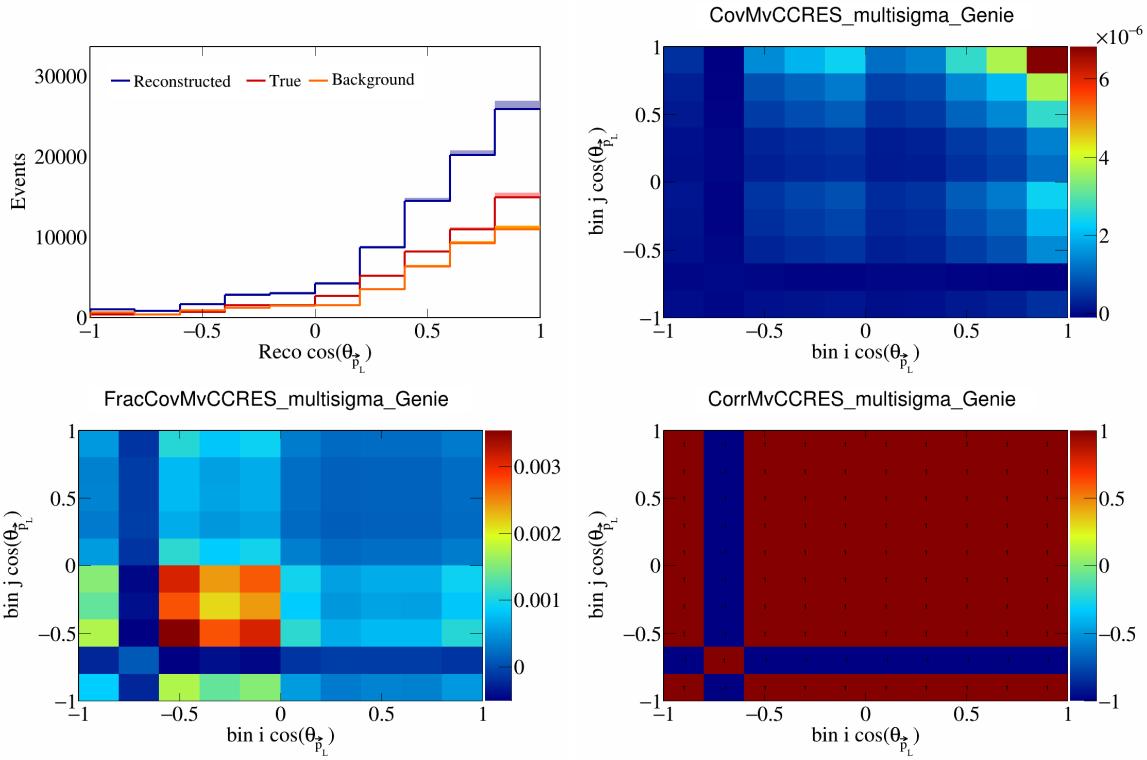


Figure 357: MvCCRES variations for  $\cos(\theta_{\vec{p}_L})$ .

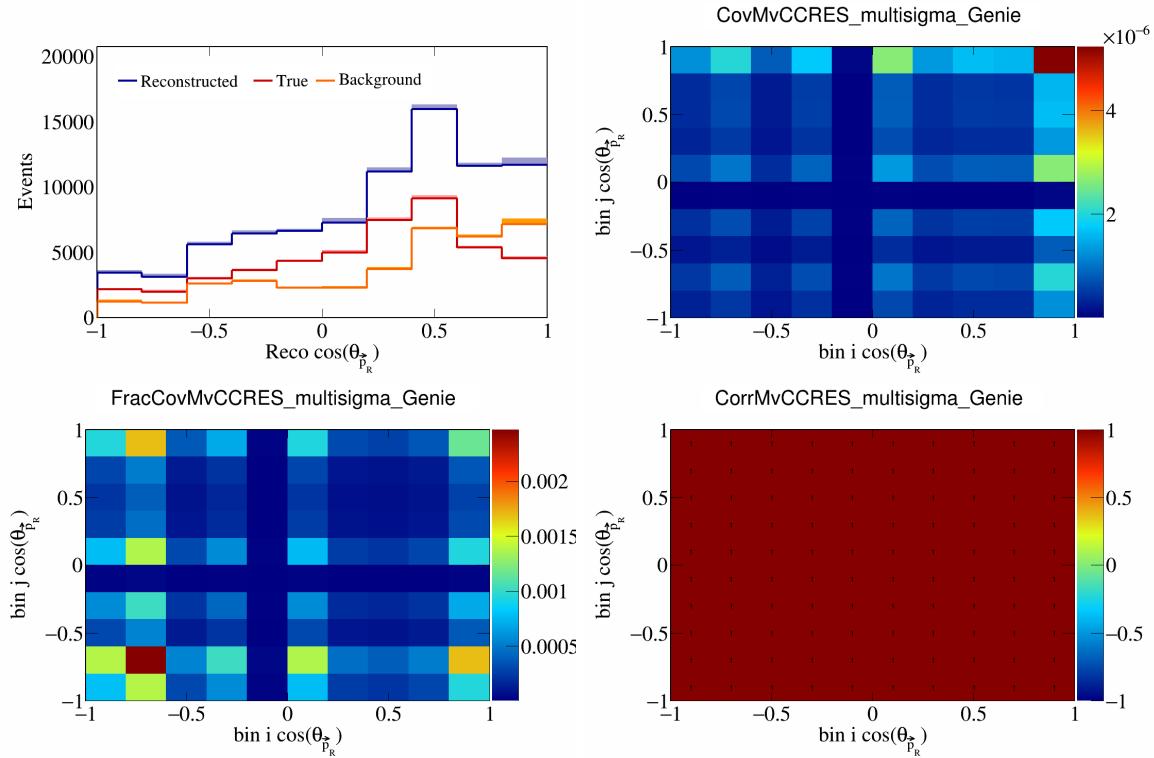


Figure 358: MvCCRES variations for  $\cos(\theta_{\vec{p}_R})$ .

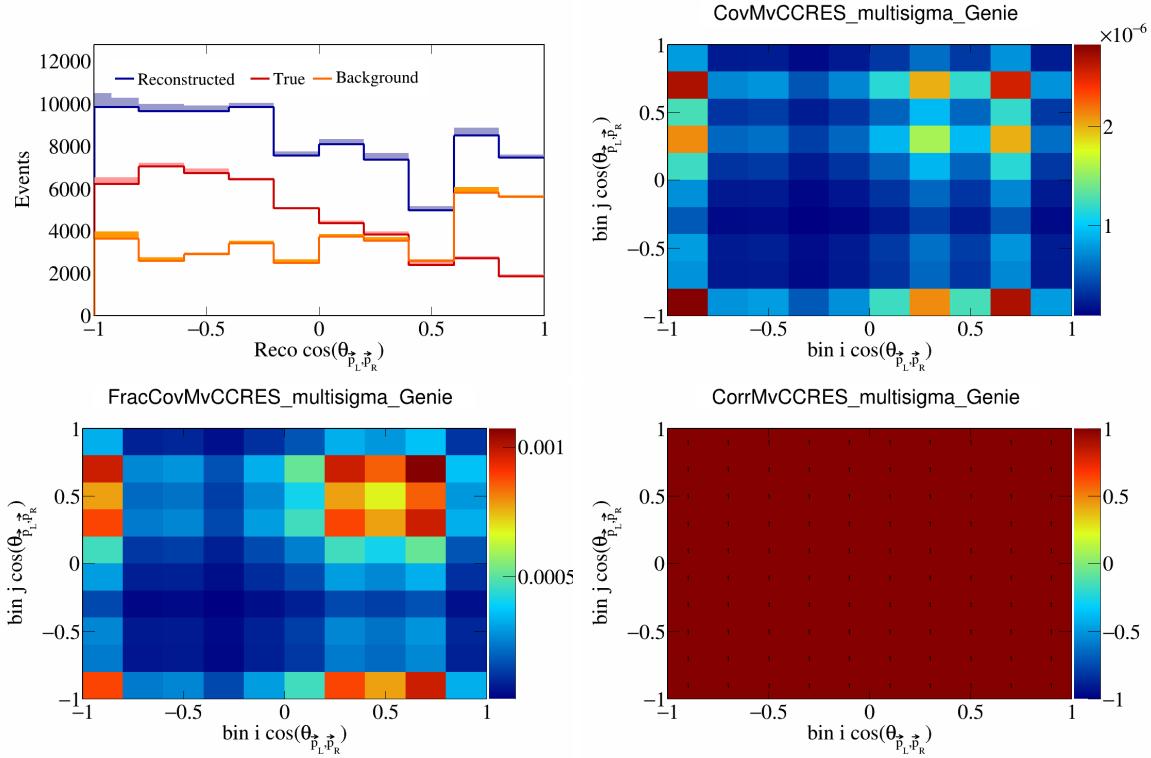


Figure 359: MvCCRES variations for  $\cos(\theta_{\vec{p}_L, \vec{p}_R})$ .

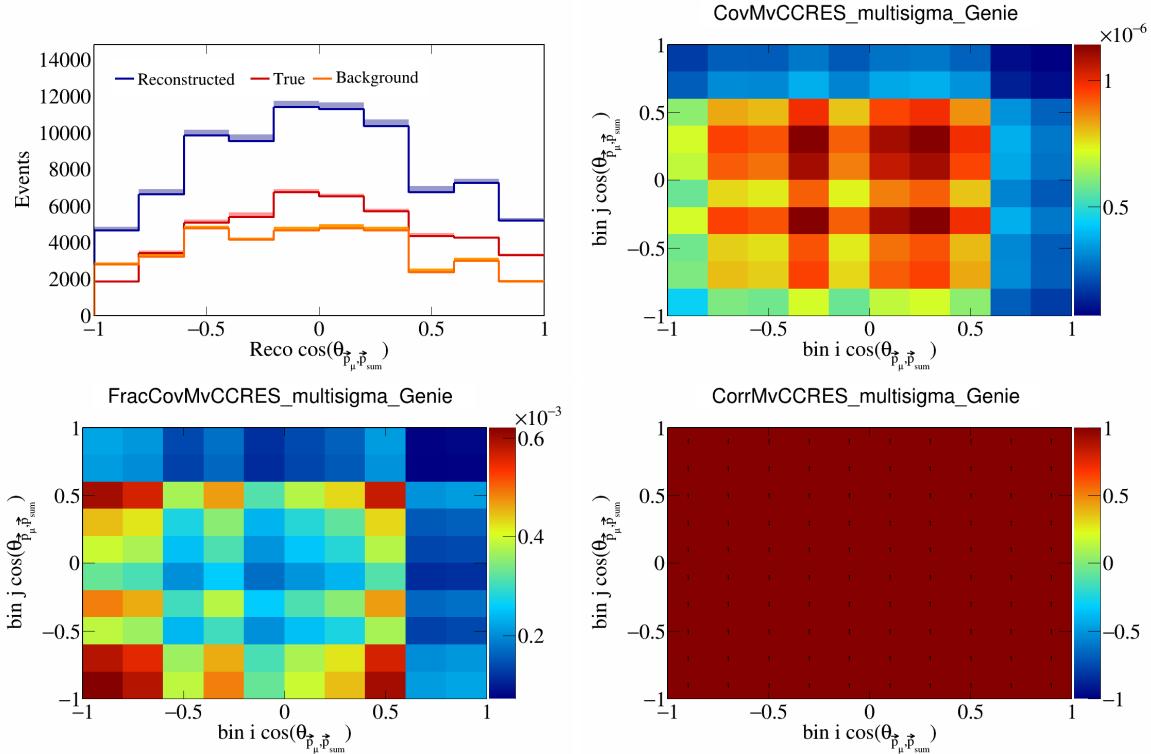


Figure 360: MvCCRES variations for  $\cos(\theta_{\vec{p}_\mu, \vec{p}_{\text{sum}}})$ .

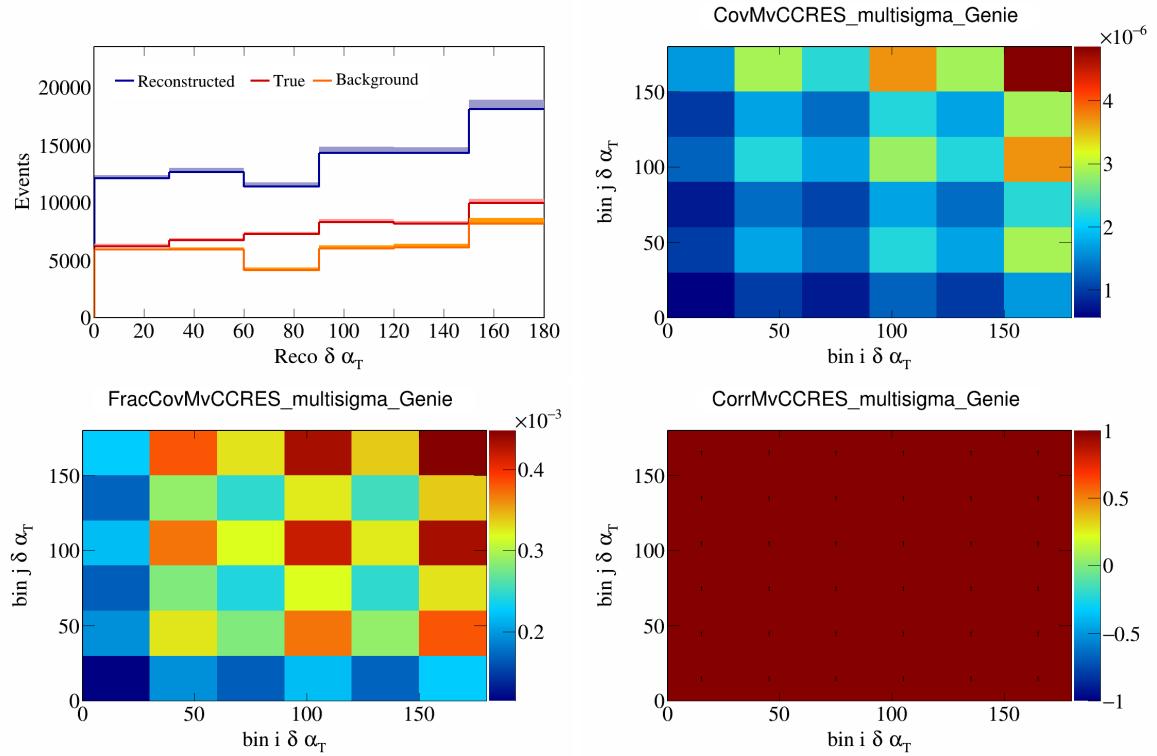


Figure 361: MvCCRES variations for  $\delta\alpha_T$ .

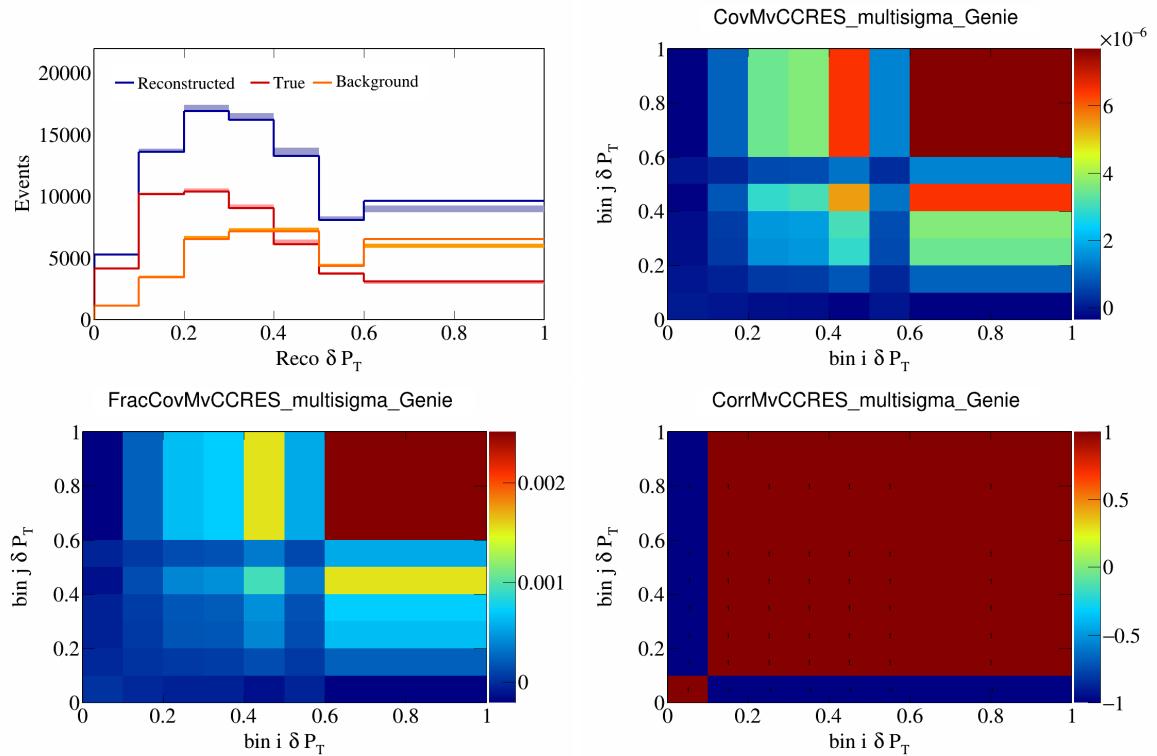


Figure 362: MvCCRES variations for  $\delta P_T$ .

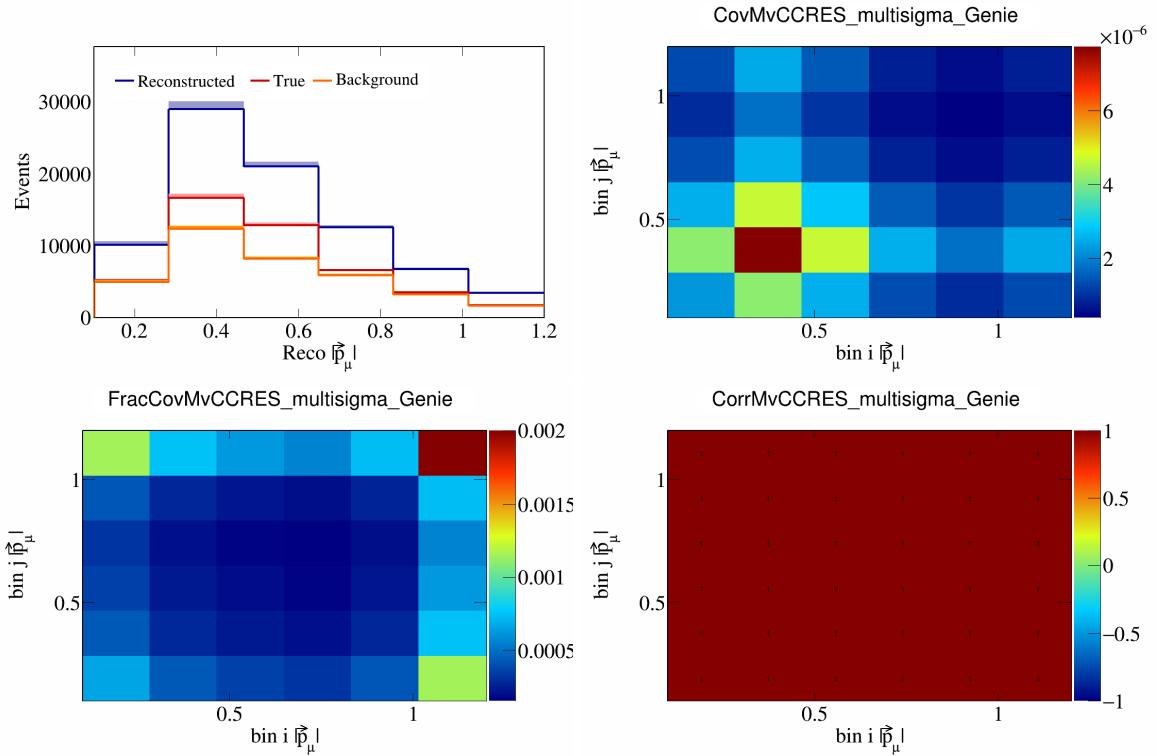


Figure 363: MvCCRES variations for  $|\vec{p}_\mu|$ .

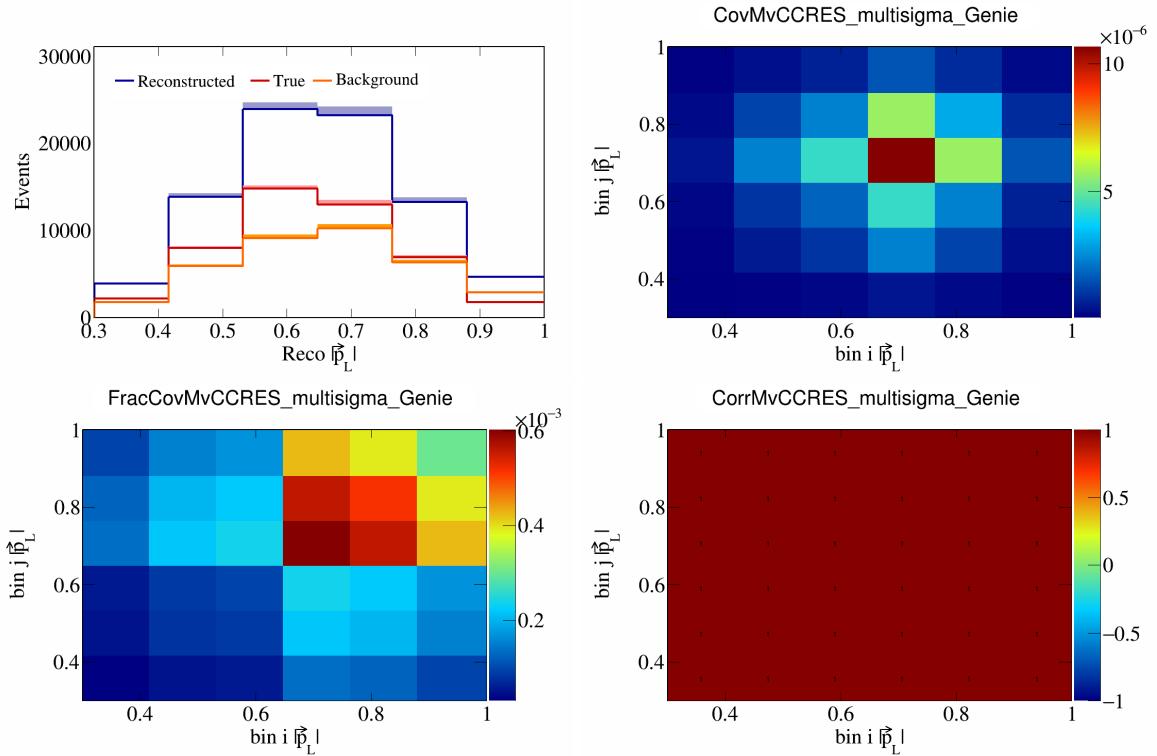


Figure 364: MvCCRES variations for  $|\vec{p}_L|$ .

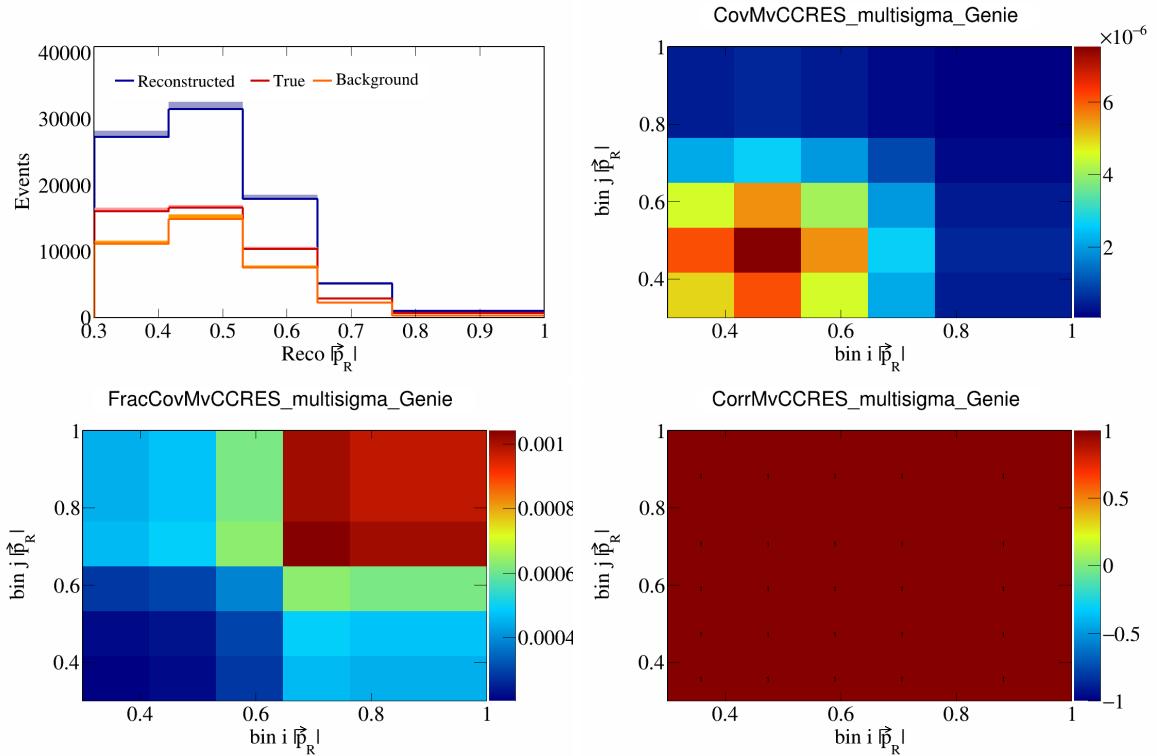


Figure 365: MvCCRES variations for  $|\vec{p}_R|$ .

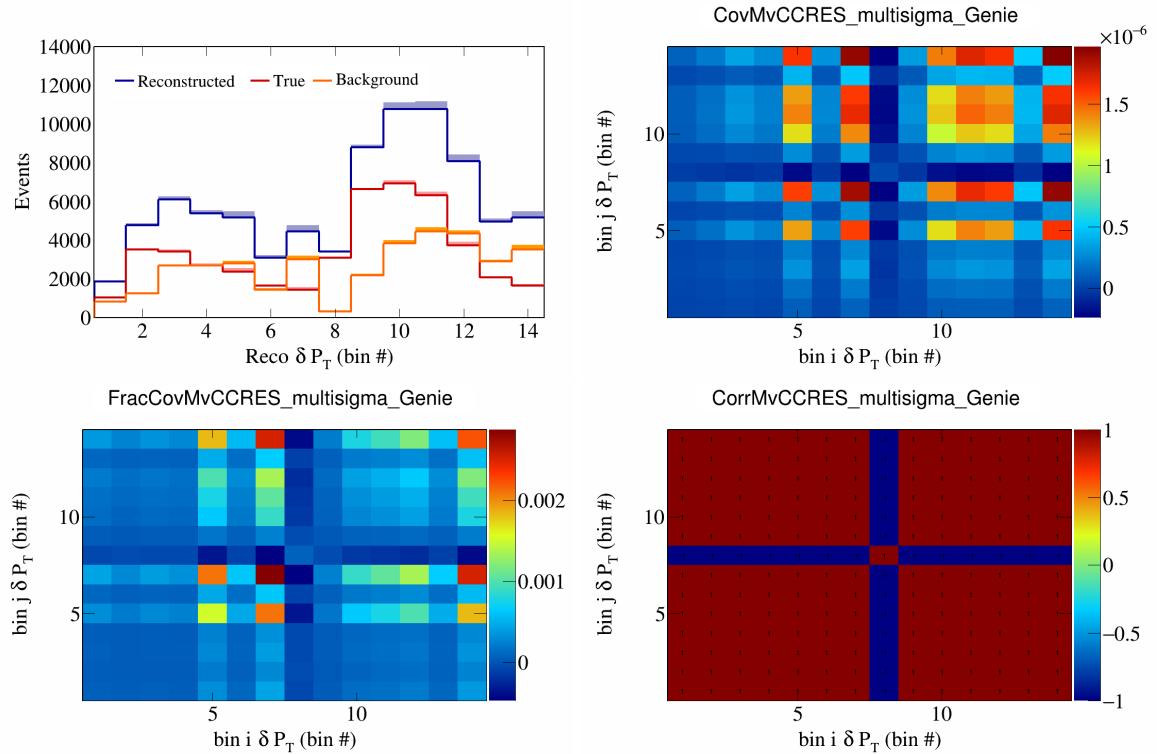


Figure 366: MvCCRES variations for  $\delta P_T$  in  $\cos(\theta_{\vec{p}_\mu})$ .

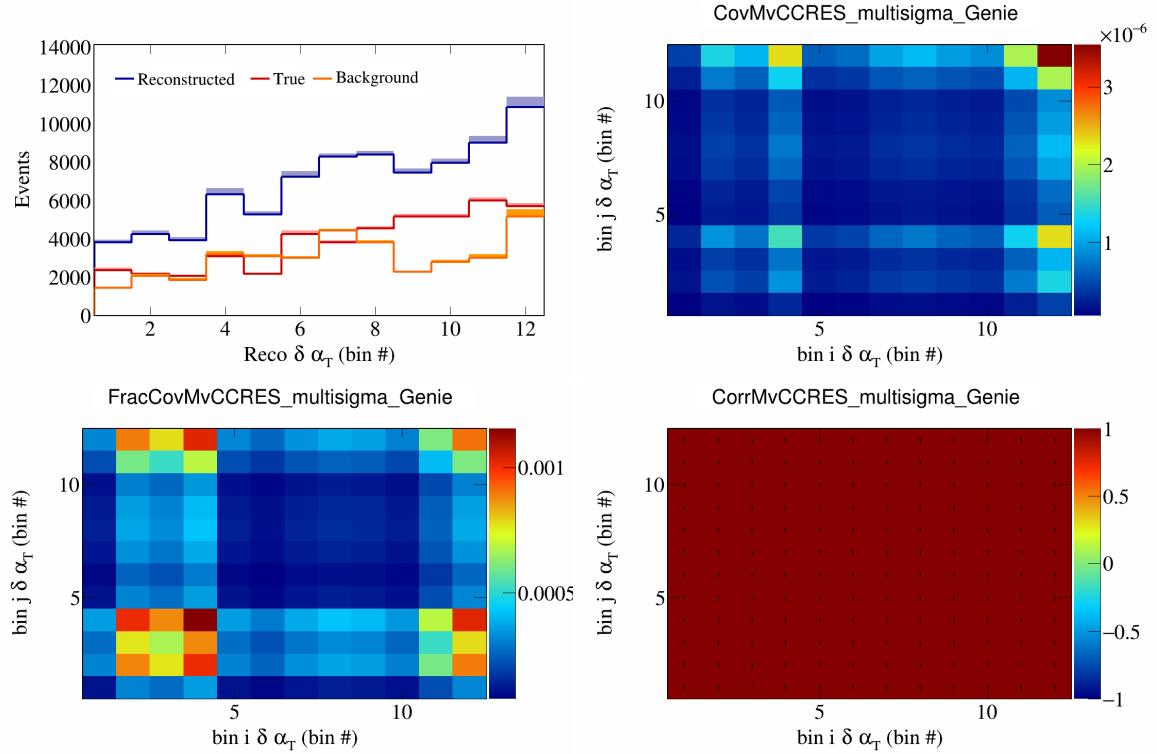


Figure 367: MvCCRES variations for  $\delta\alpha_T$  in  $\cos(\theta_{\vec{p}_\mu})$ .

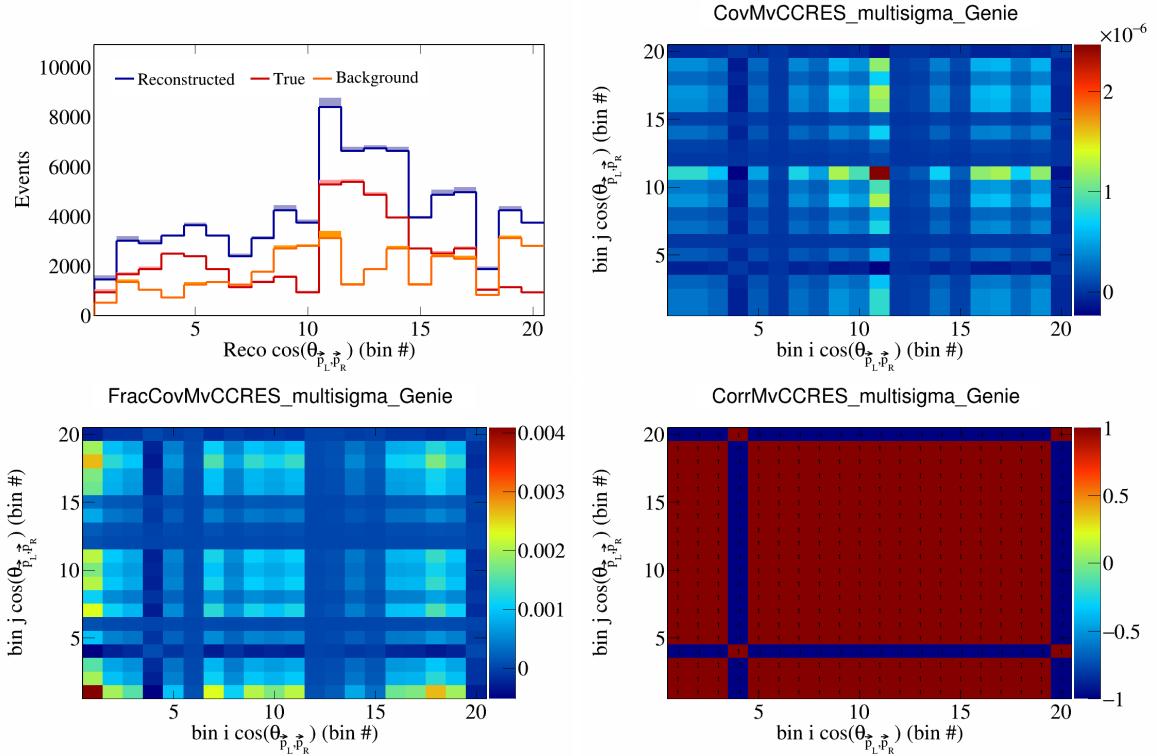


Figure 368: MvCCRES variations for  $\cos(\theta_{\vec{p}_L, \vec{p}_R})$  in  $\cos(\theta_{\vec{p}_\mu})$ .

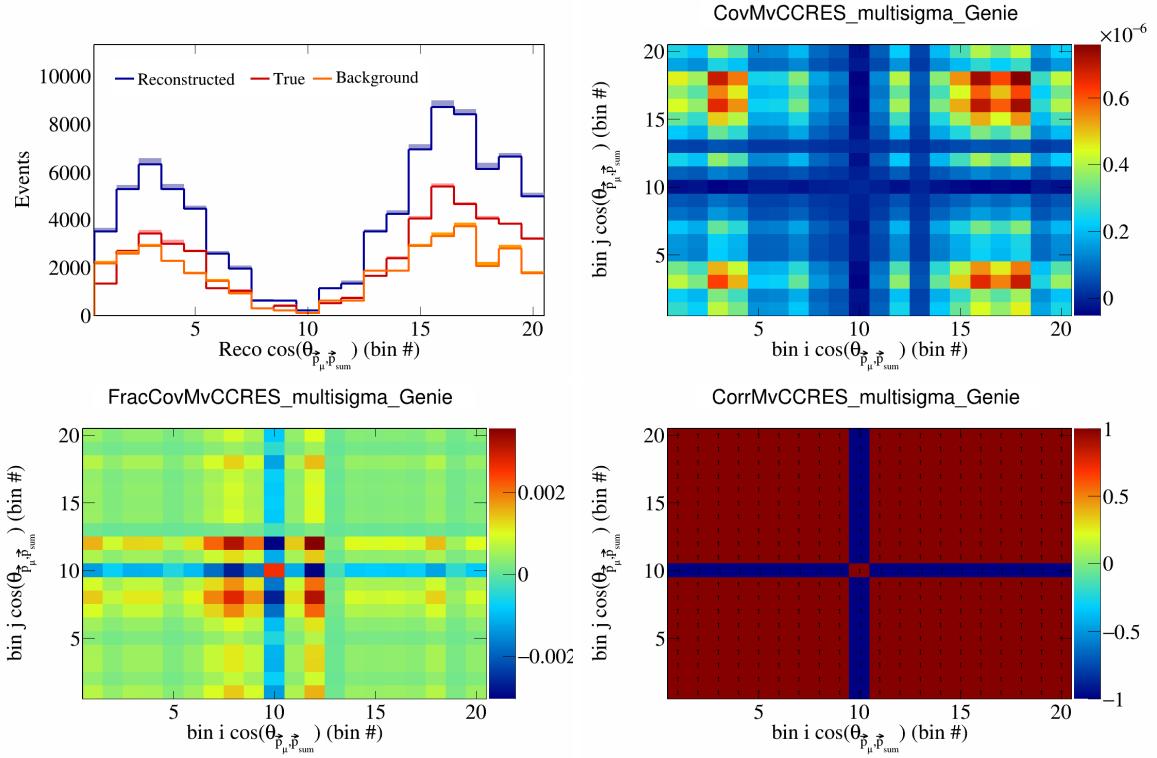


Figure 369: MvCCRES variations for  $\cos(\theta_{\vec{p}_\mu, \vec{p}_{\text{sum}}})$  in  $\cos(\theta_{\vec{p}_\mu})$ .

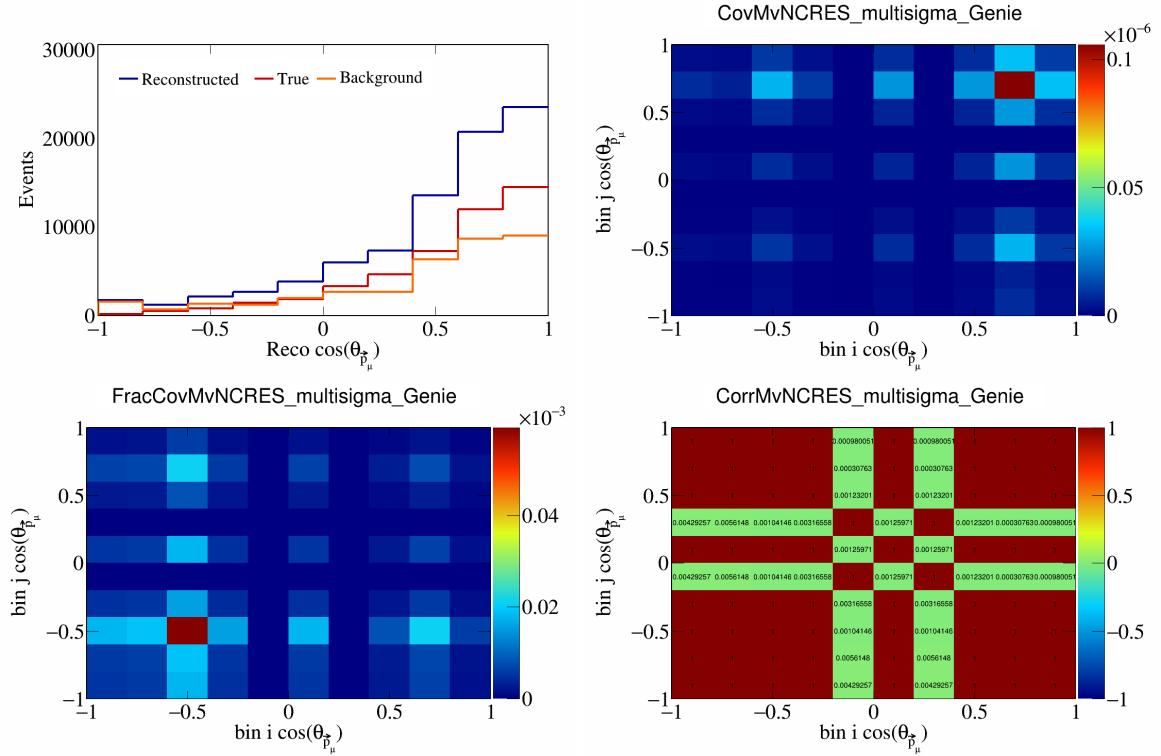


Figure 370: MvNCRES variations for  $\cos(\theta_{\vec{p}_\mu})$ .

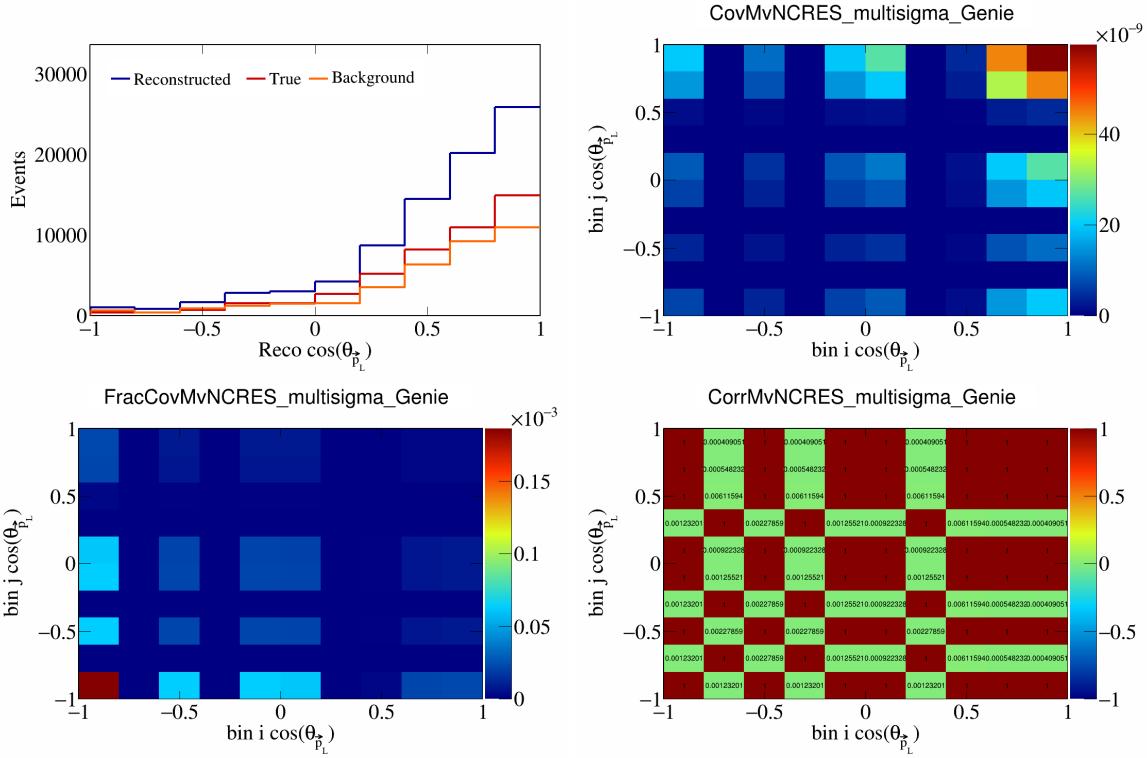


Figure 371: MvNCRES variations for  $\cos(\theta_{\vec{p}_L})$ .

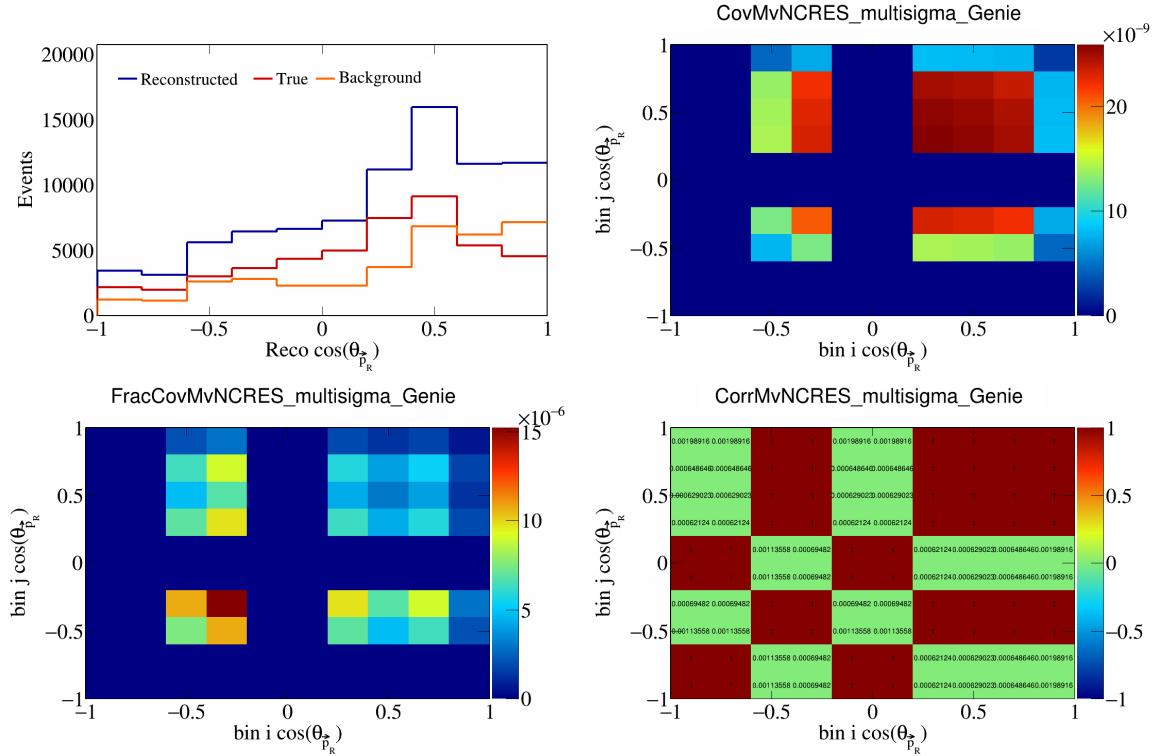


Figure 372: MvNCRES variations for  $\cos(\theta_{\vec{p}_R})$ .

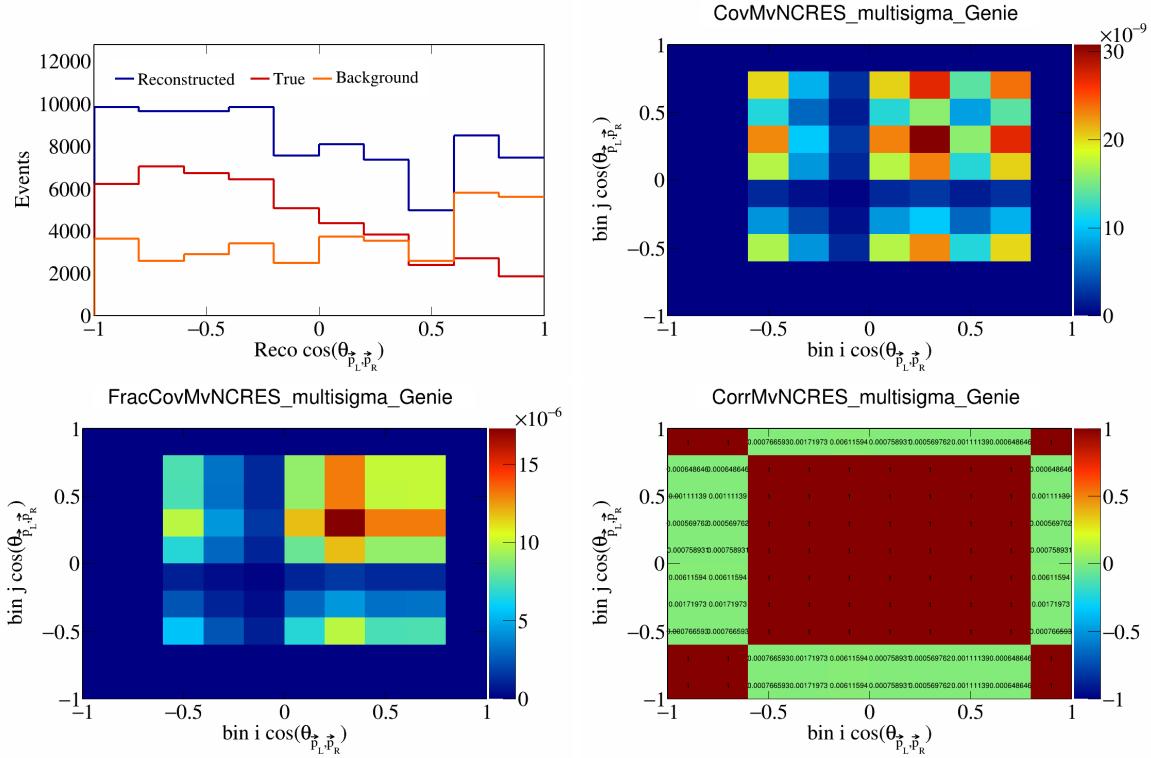


Figure 373: MvNCRES variations for  $\cos(\theta_{\vec{p}_L, \vec{p}_R})$ .

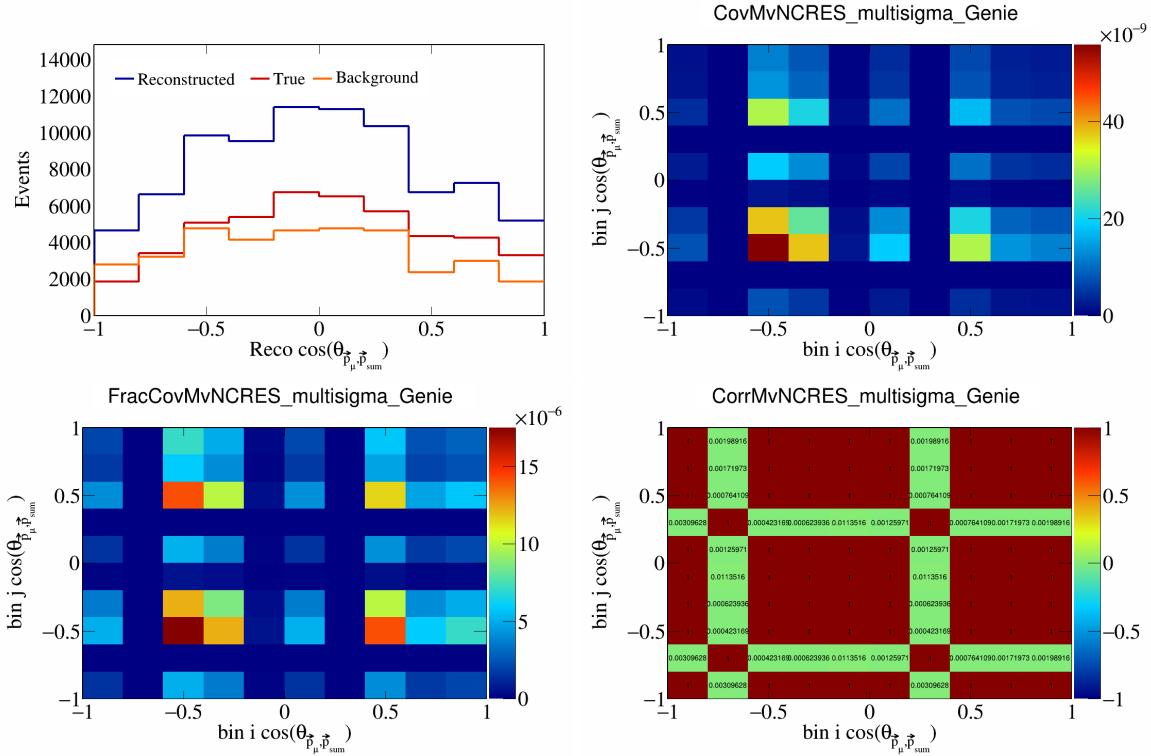


Figure 374: MvNCRES variations for  $\cos(\theta_{\vec{p}_\mu, \vec{p}_{\text{sum}}})$ .

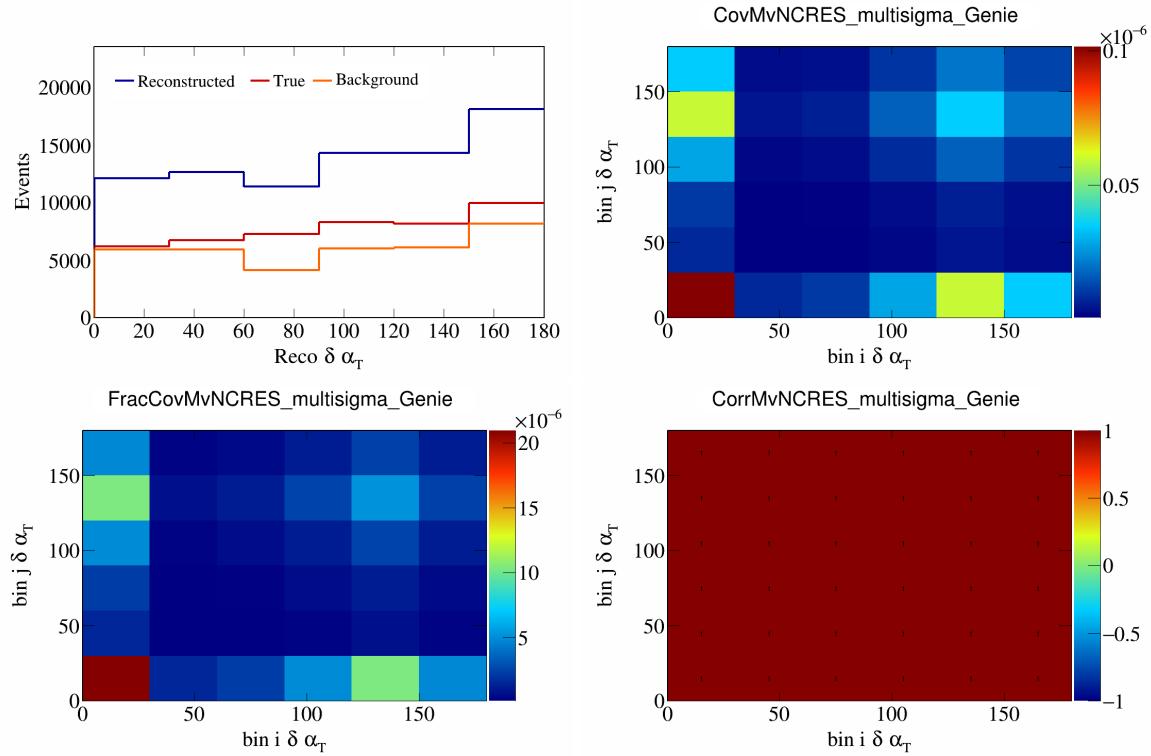


Figure 375: MvNCRES variations for  $\delta\alpha_T$ .

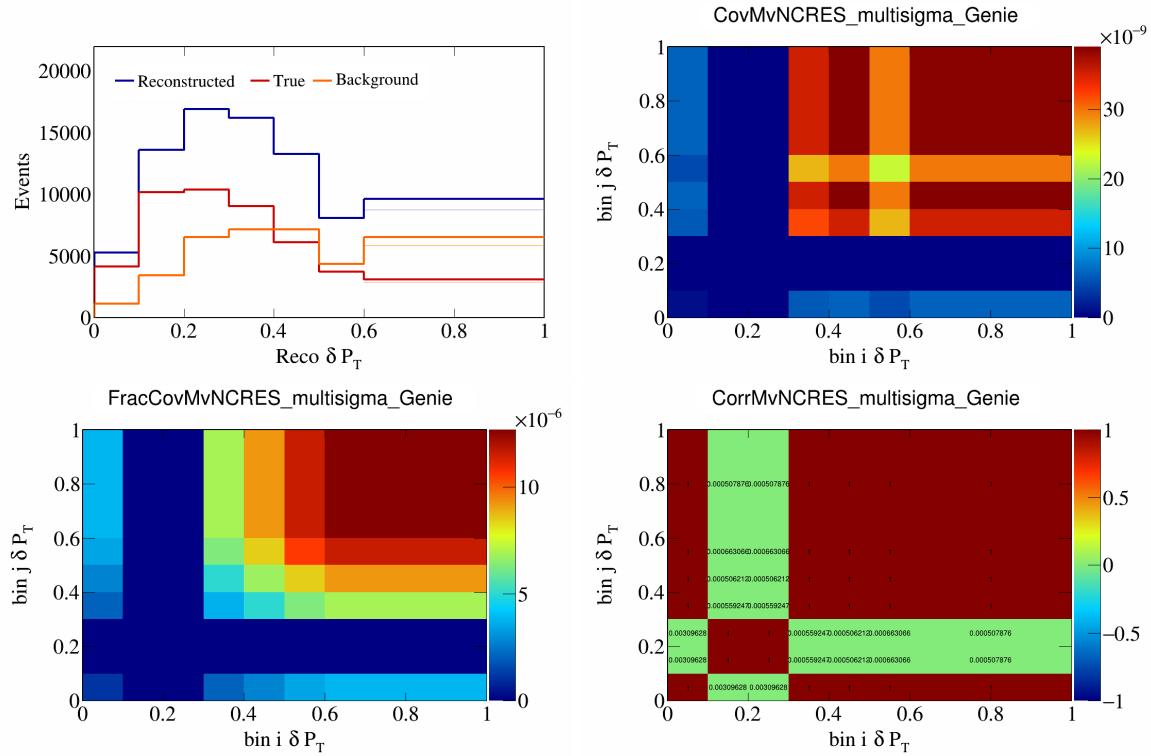


Figure 376: MvNCRES variations for  $\delta P_T$ .

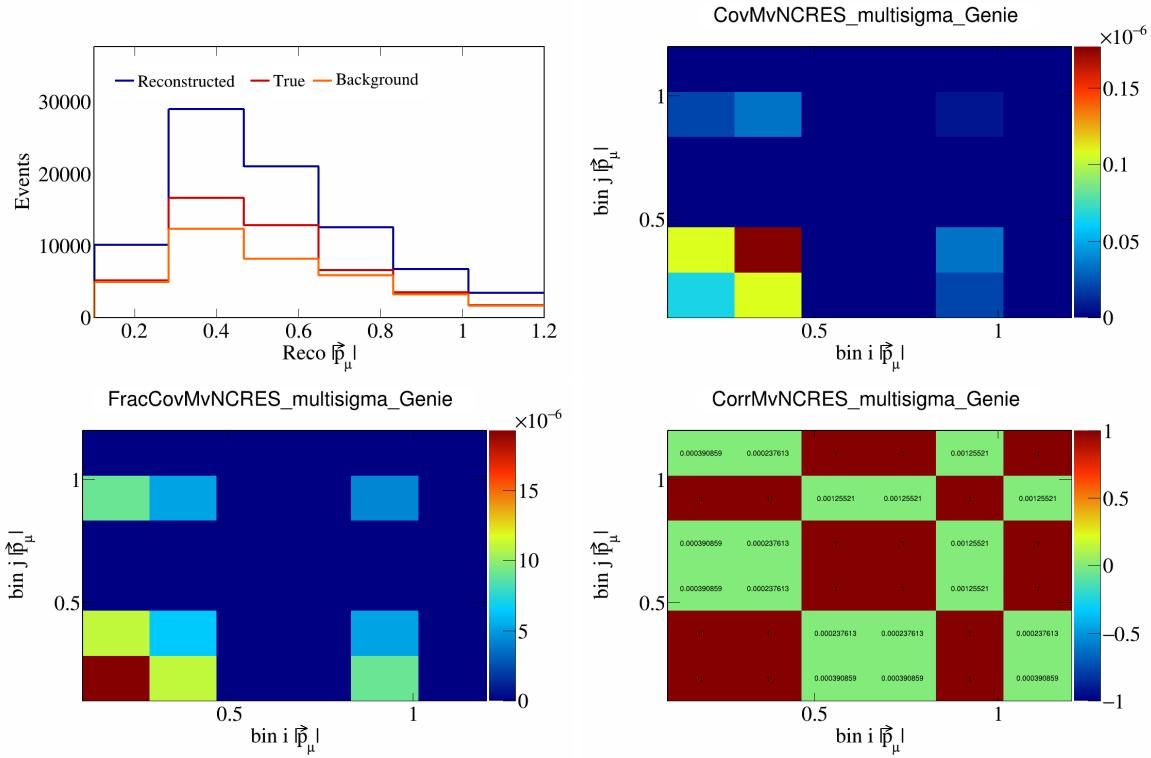


Figure 377: MvNCRES variations for  $|\vec{p}_\mu|$ .

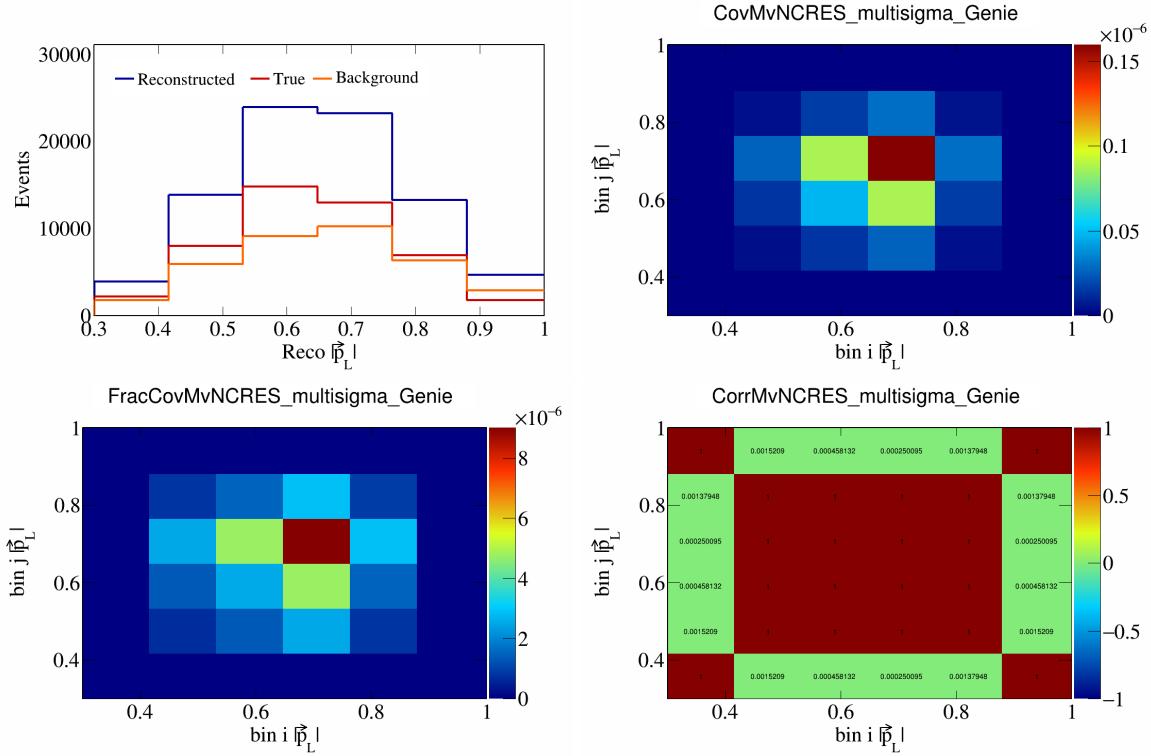


Figure 378: MvNCRES variations for  $|\vec{p}_L|$ .

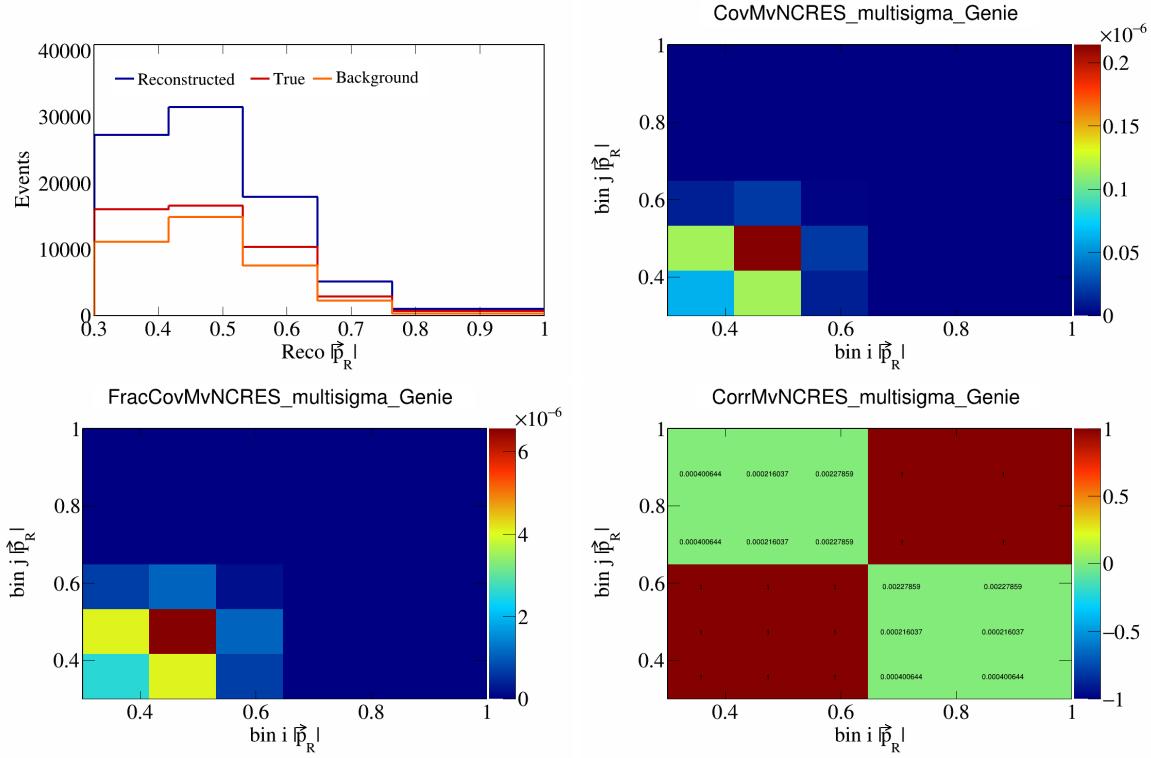


Figure 379: MvNCRES variations for  $|\vec{p}_R|$ .

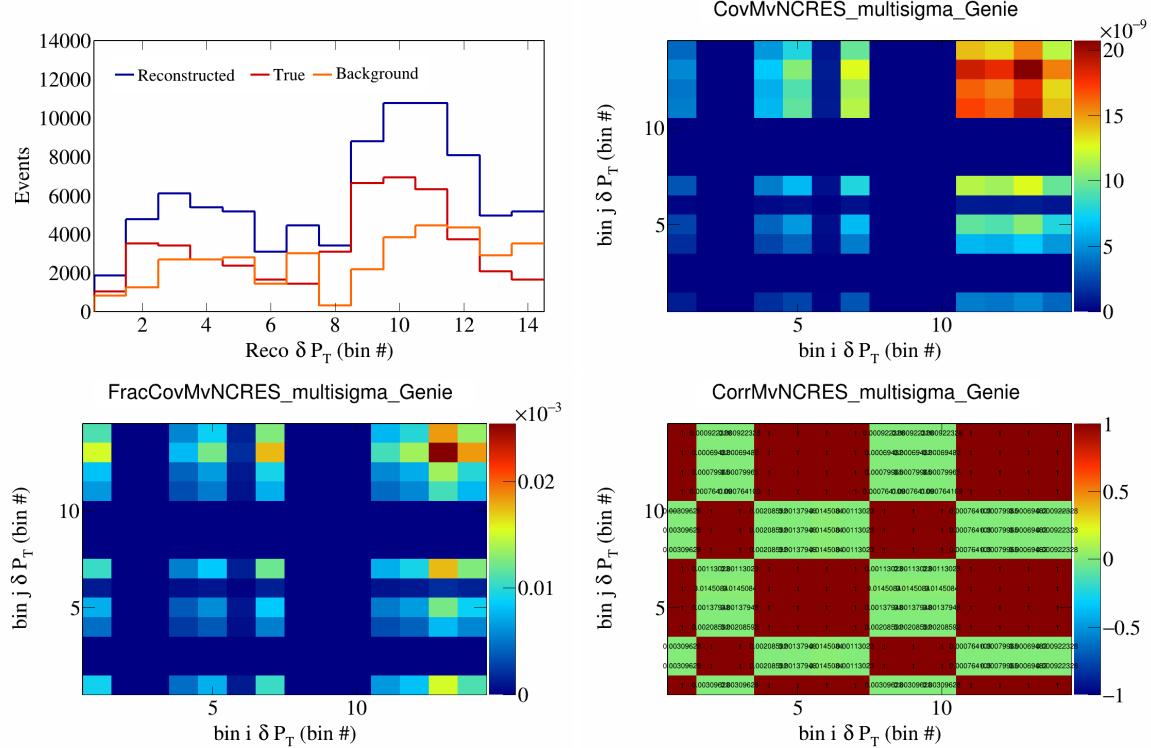


Figure 380: MvNCRES variations for  $\delta P_T$  in  $\cos(\theta_{\vec{p}_\mu})$ .

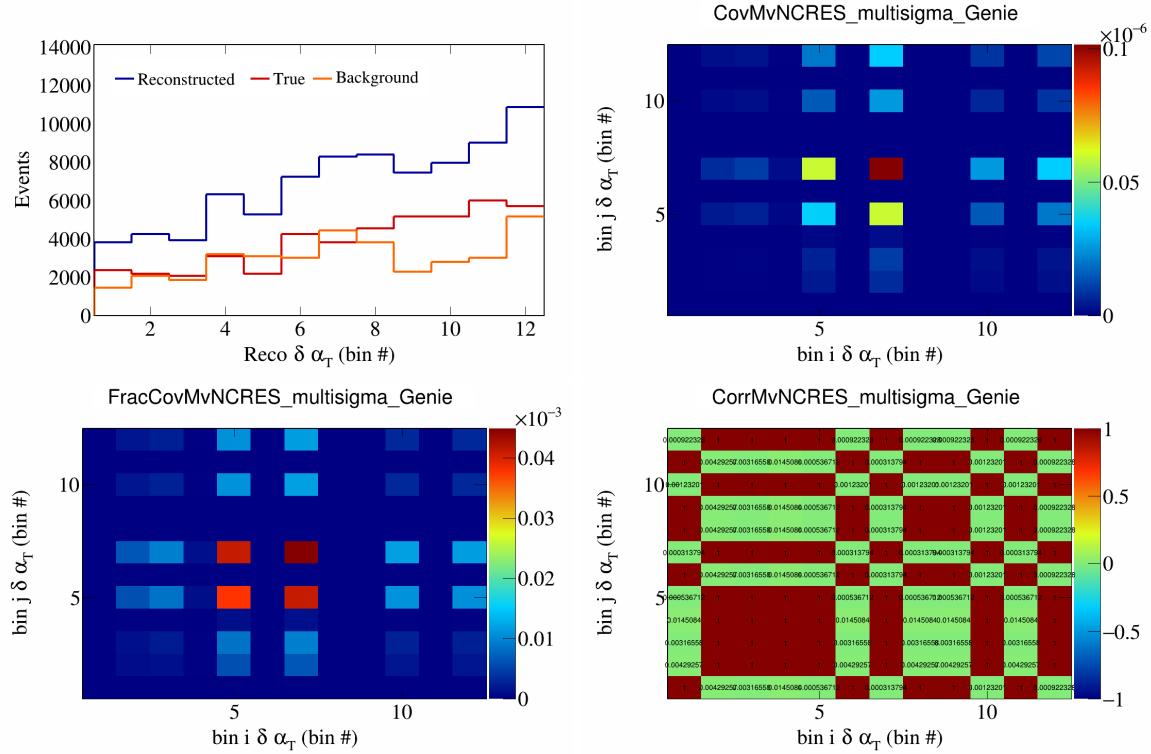


Figure 381: MvNCRES variations for  $\delta\alpha_T$  in  $\cos(\theta_{\vec{p}_\mu})$ .

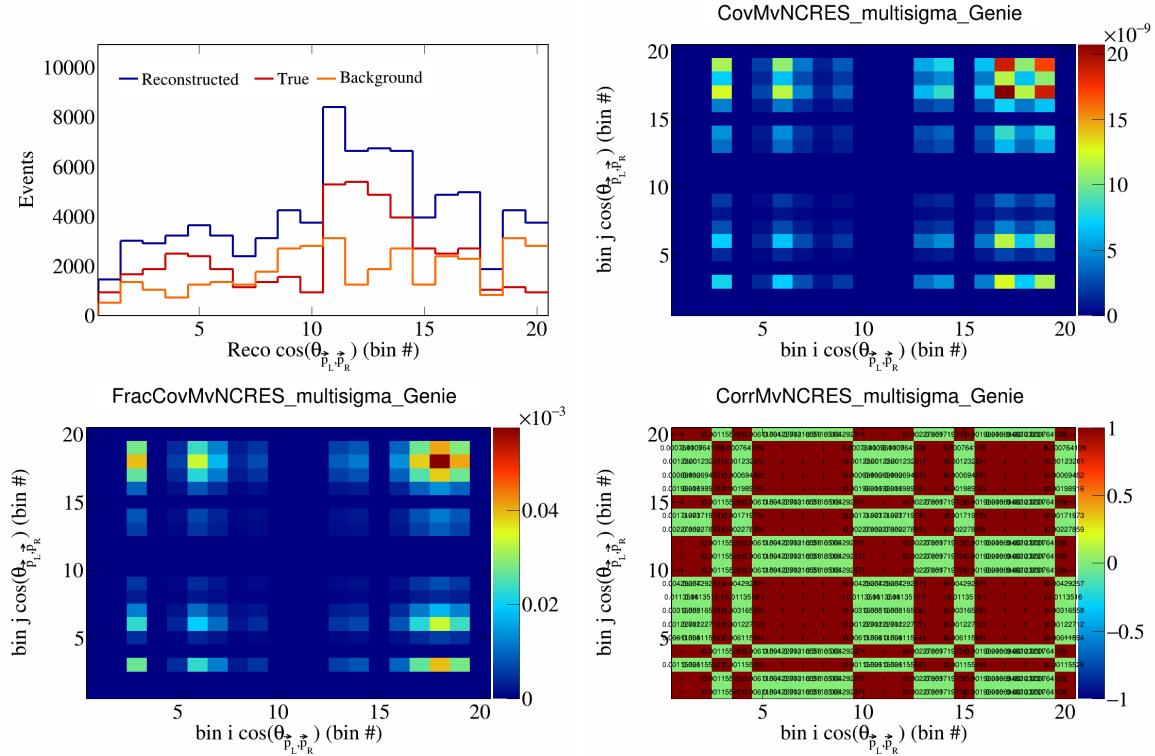


Figure 382: MvNCRES variations for  $\cos(\theta_{\vec{p}_L, \vec{p}_R})$  in  $\cos(\theta_{\vec{p}_\mu})$ .

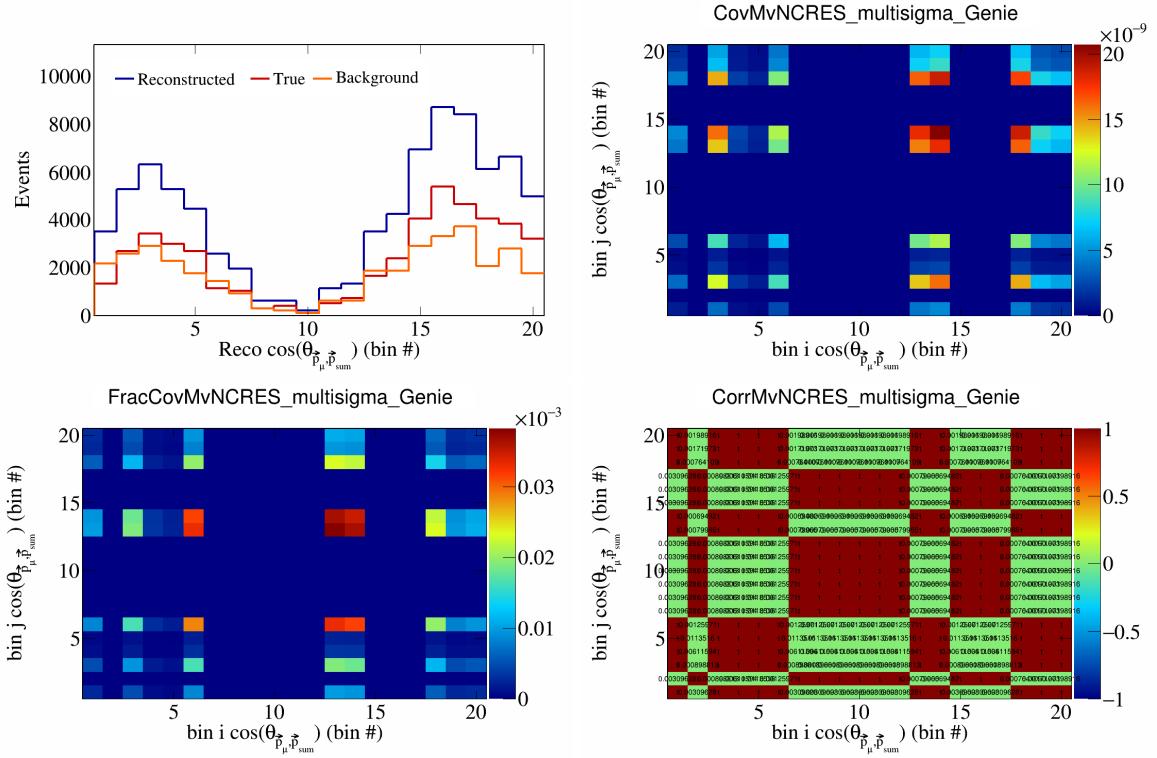


Figure 383: MvNCRES variations for  $\cos(\theta_{\vec{p}_\mu})$  in  $\cos(\theta_{\vec{p}_\mu})$ .

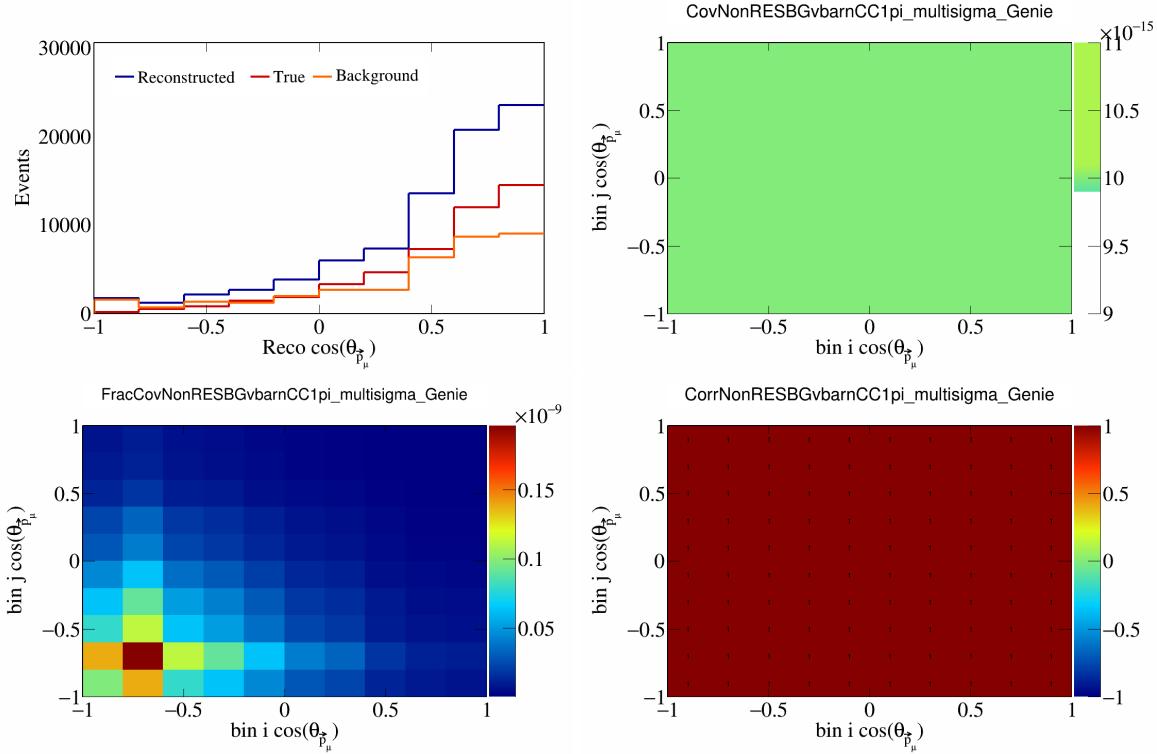


Figure 384: NonRESBGvbarCC1pi variations for  $\cos(\theta_{\vec{p}_\mu})$ .

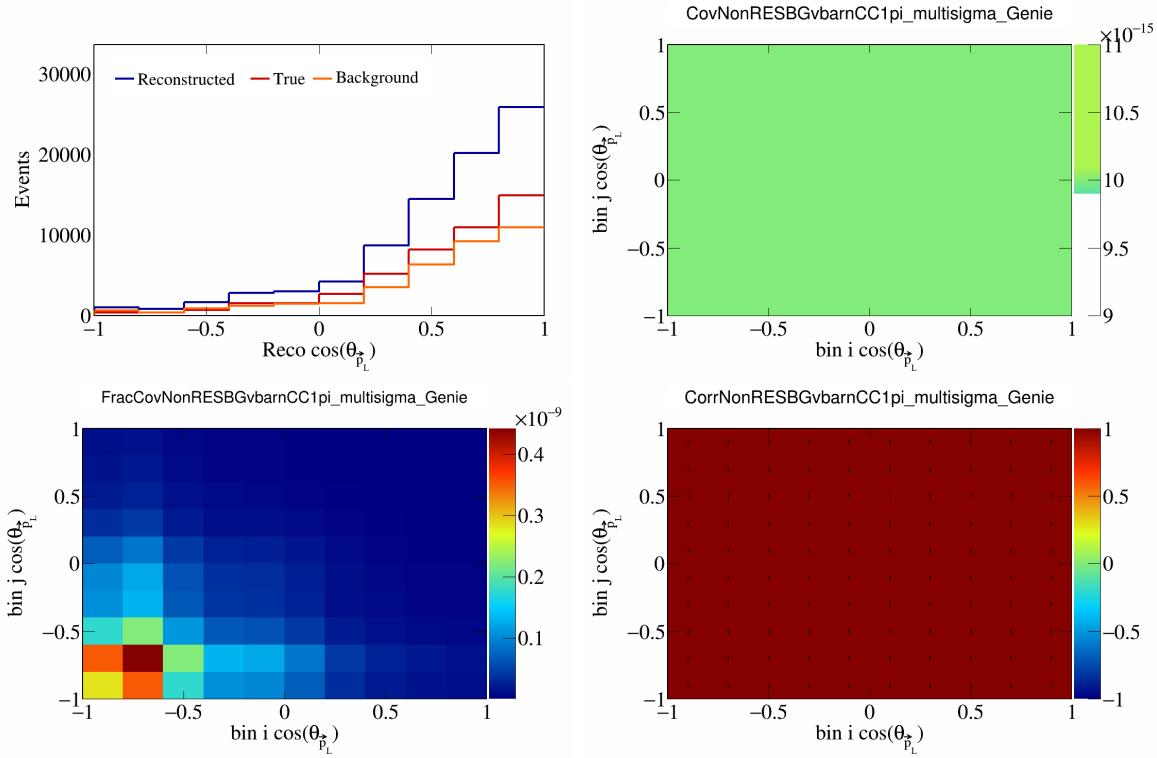


Figure 385: NonRESBGvbarCC1pi variations for  $\cos(\theta_{\vec{p}_L})$ .

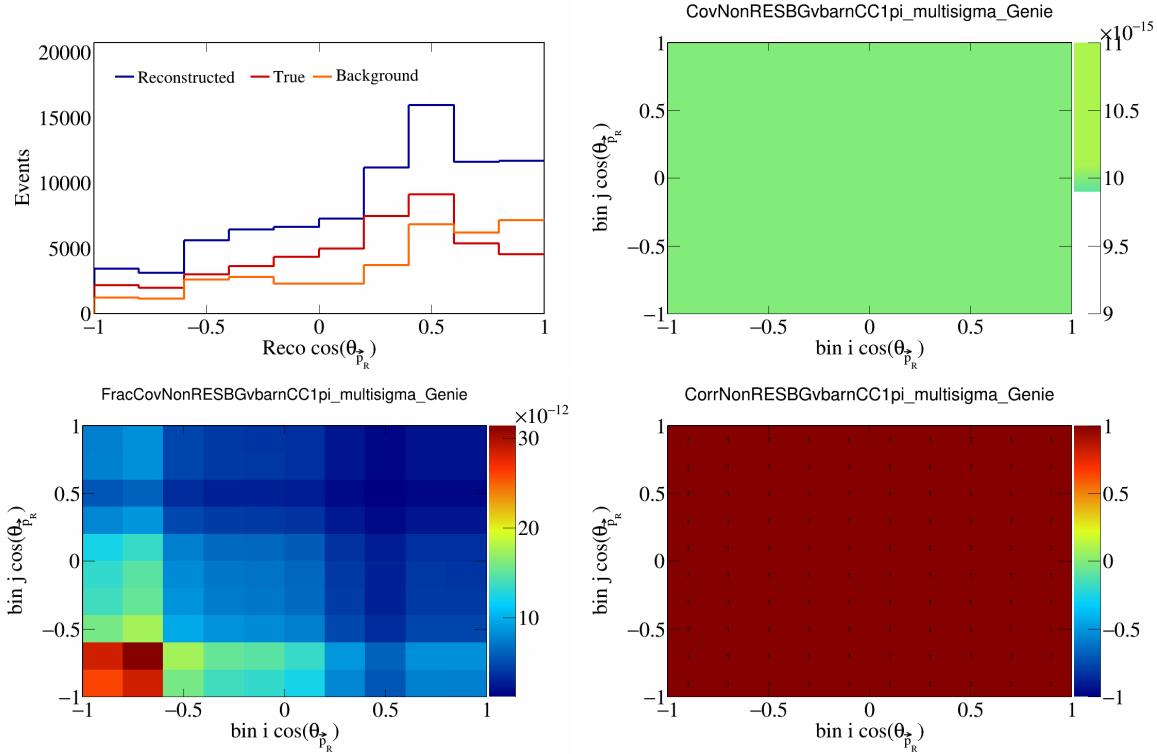


Figure 386: NonRESBGvbarCC1pi variations for  $\cos(\theta_{\vec{p}_R})$ .

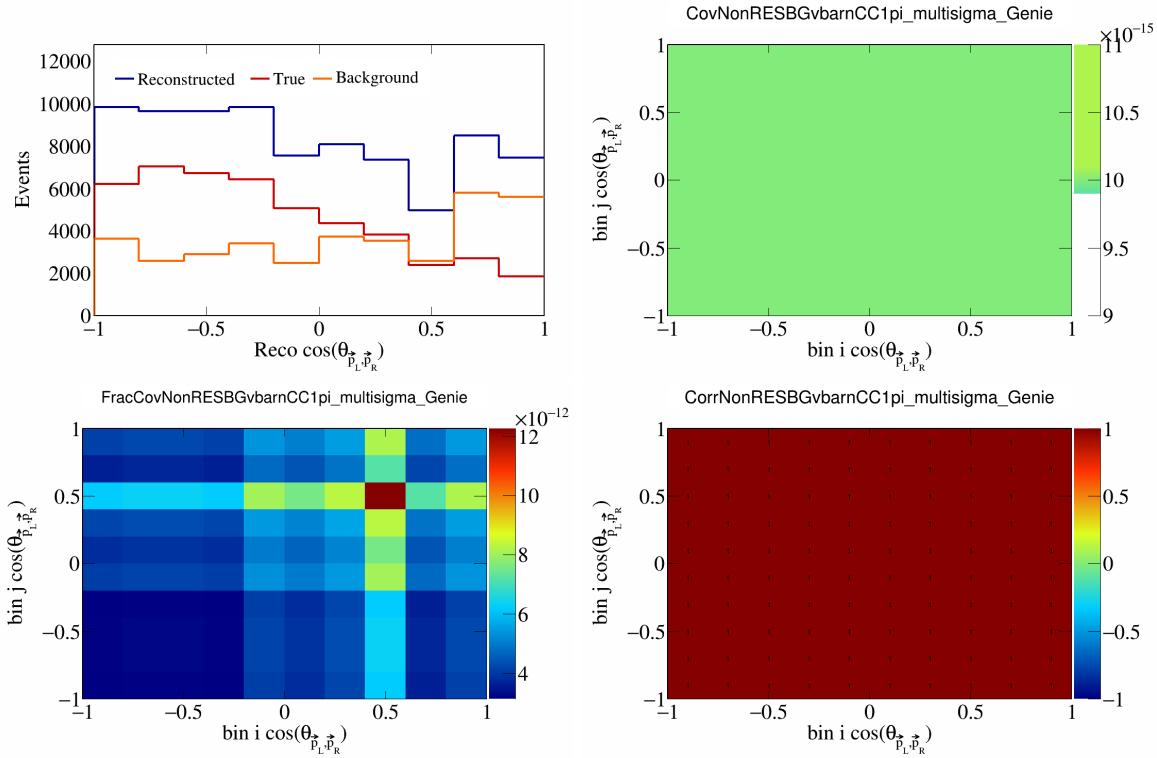


Figure 387: NonRESBGvbarCC1pi variations for  $\cos(\theta_{\vec{p}_L, \vec{p}_R})$ .

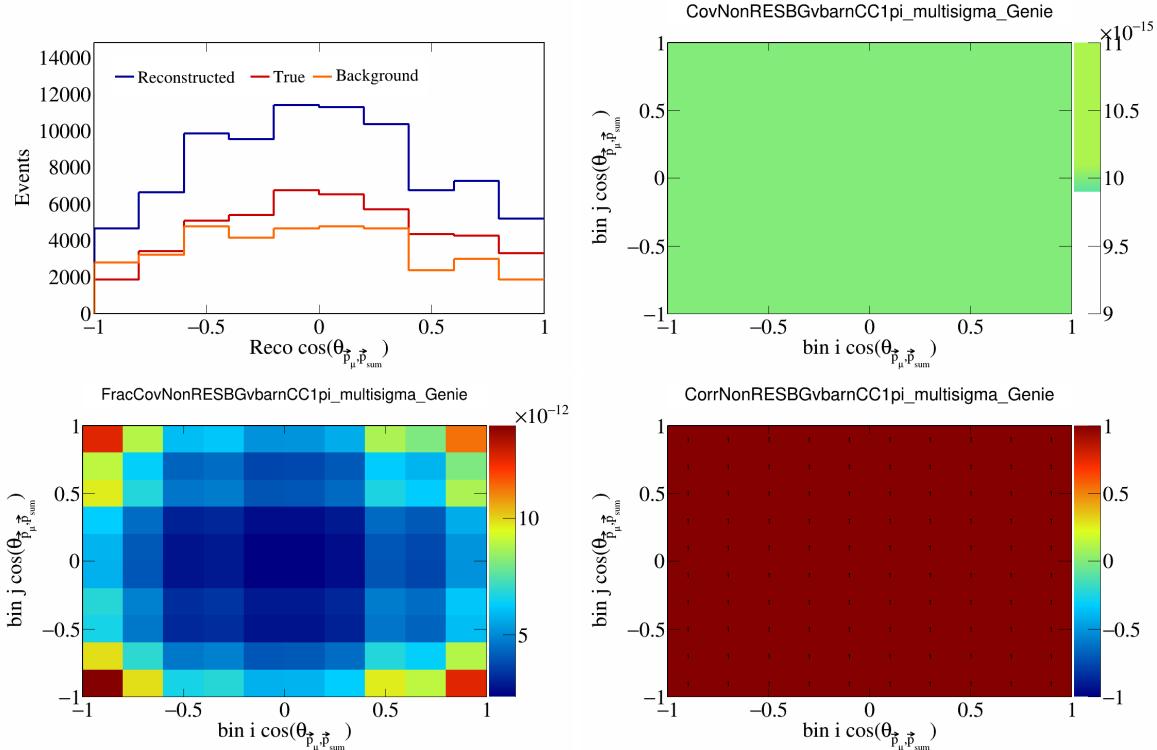


Figure 388: NonRESBGvbarCC1pi variations for  $\cos(\theta_{\vec{p}_\mu, \vec{p}_{\text{sum}}})$ .

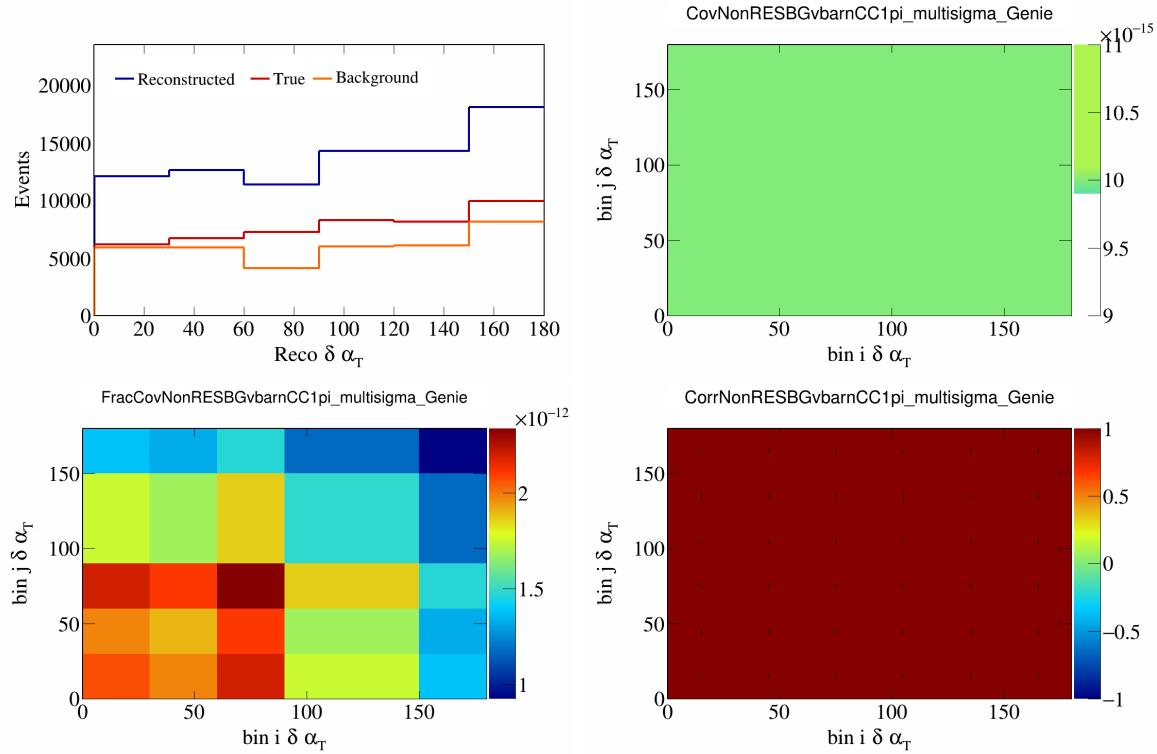


Figure 389: NonRESBGvbarCC1pi variations for  $\delta\alpha_T$ .

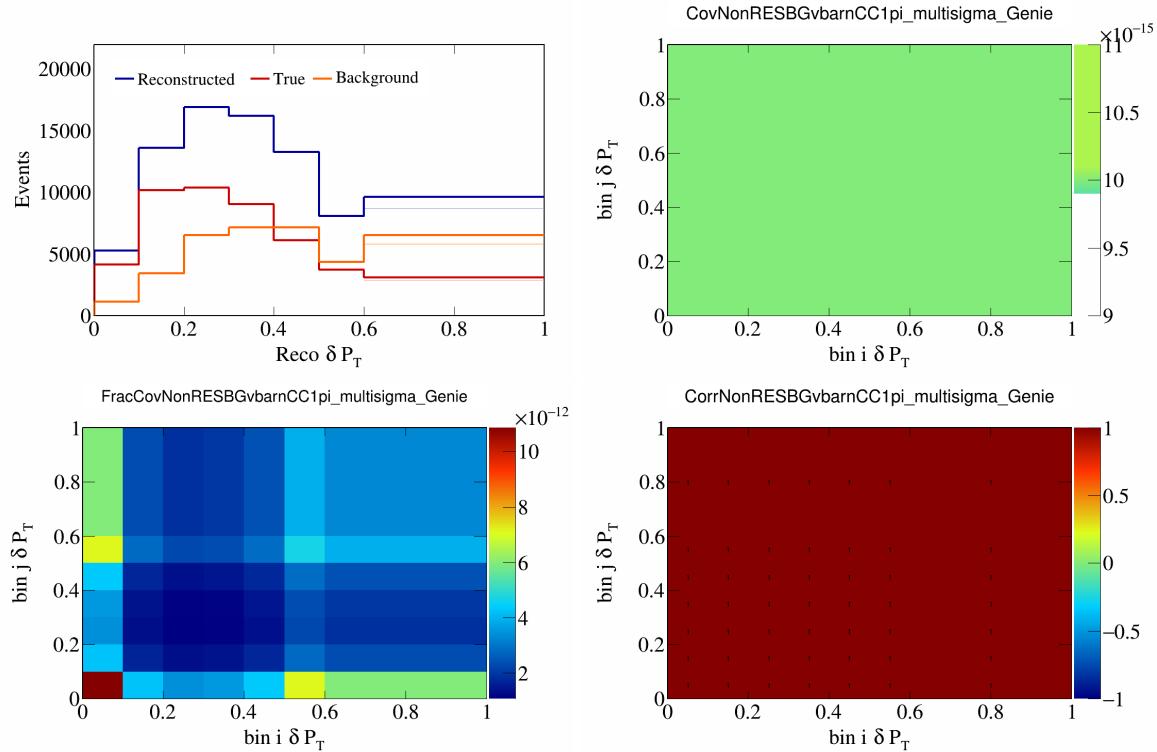


Figure 390: NonRESBGvbarCC1pi variations for  $\delta P_T$ .

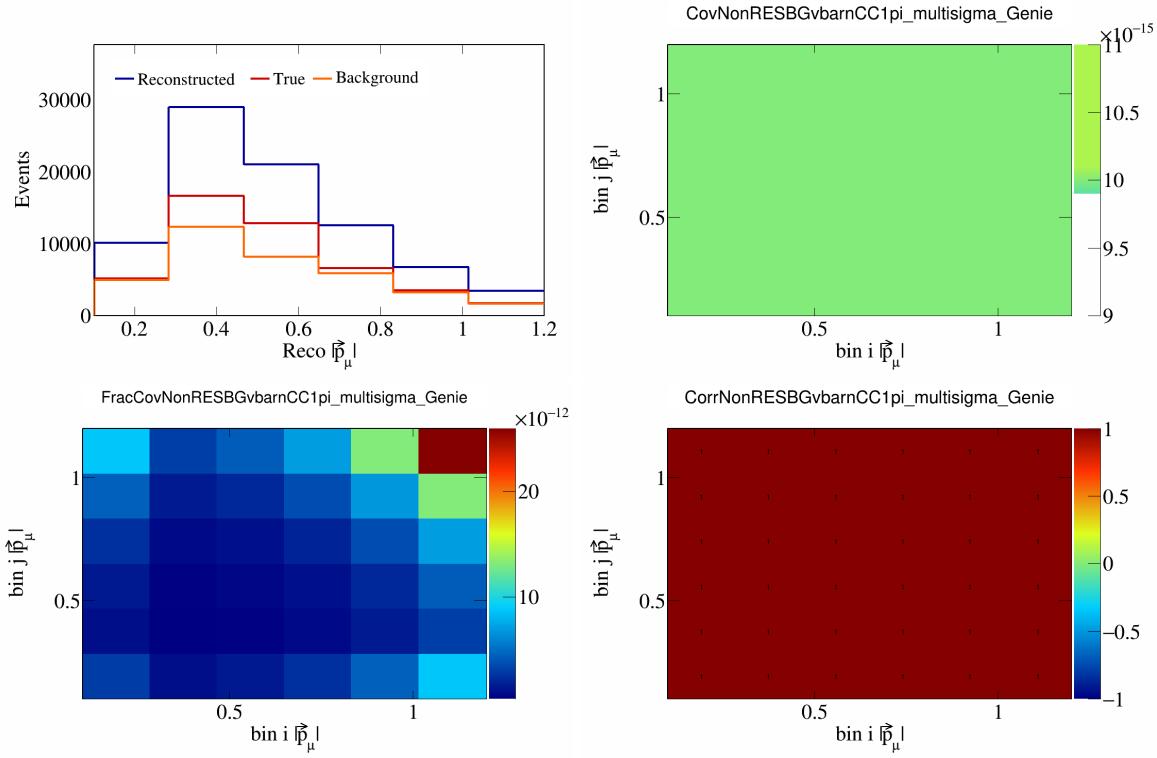


Figure 391: NonRESBGvbarCC1pi variations for  $|\vec{p}_\mu|$ .

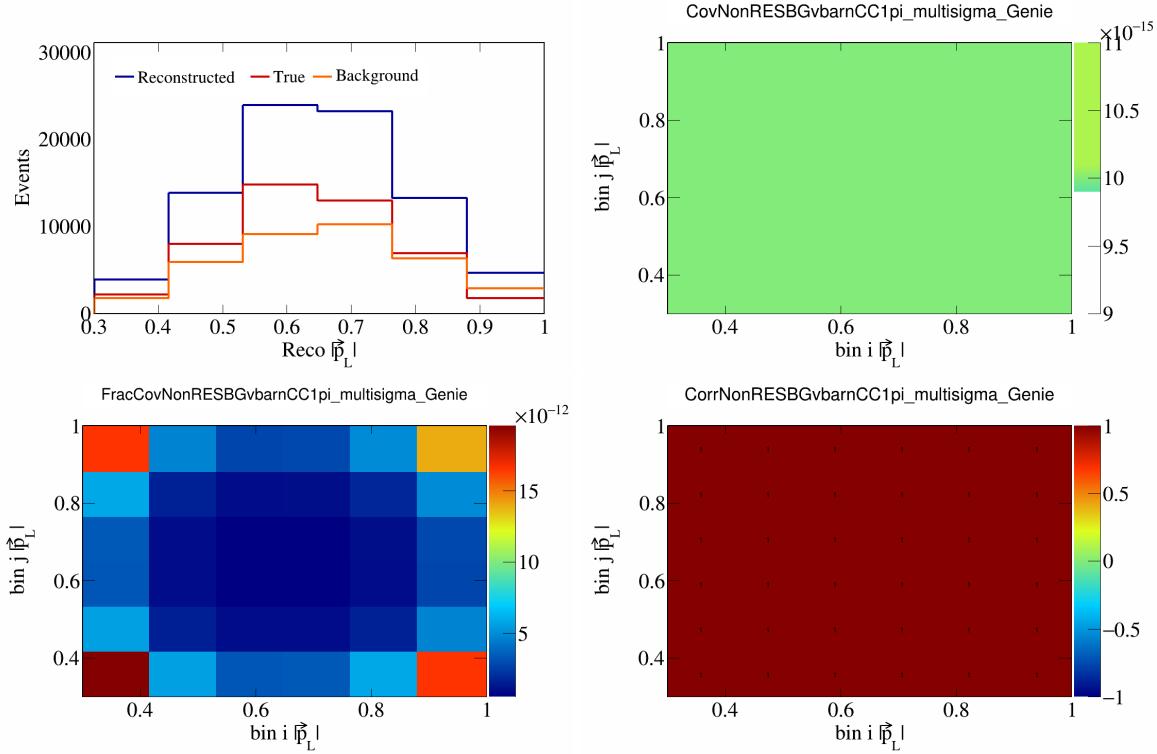


Figure 392: NonRESBGvbarCC1pi variations for  $|\vec{p}_L|$ .

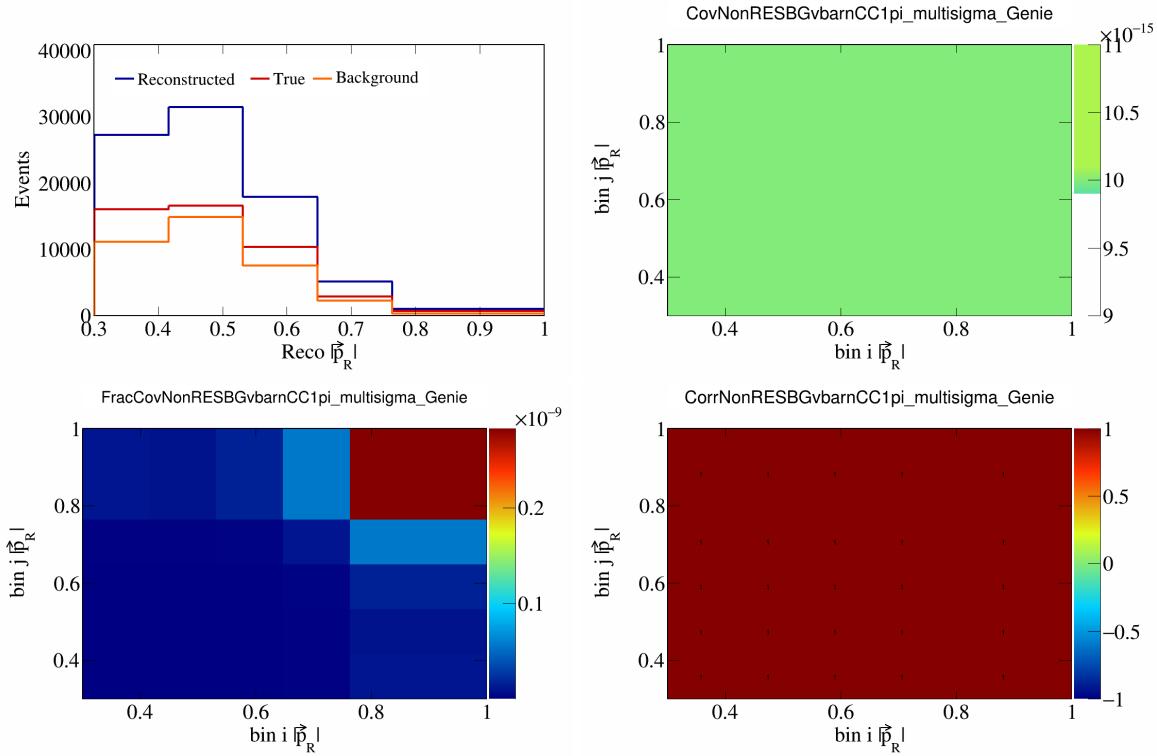


Figure 393: NonRESBGvbarCC1pi variations for  $|\vec{p}_R|$ .

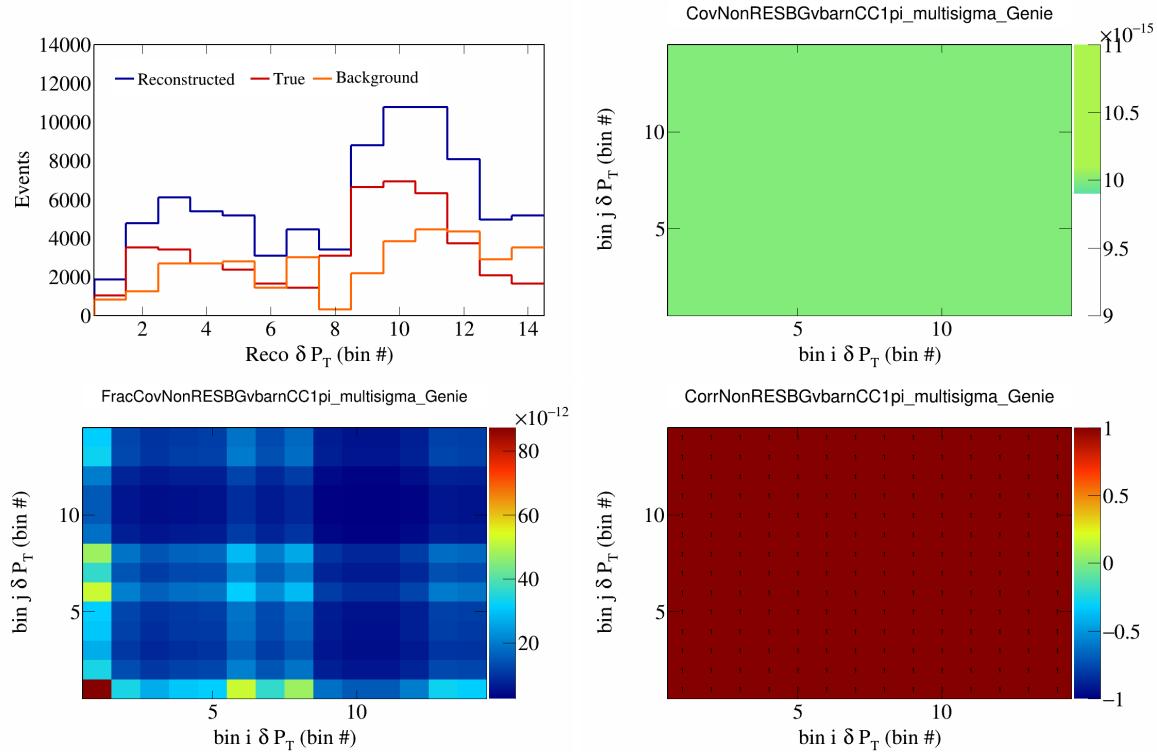


Figure 394: NonRESBGvbarCC1pi variations for  $\delta P_T$  in  $\cos(\theta_{\vec{p}_\mu})$ .

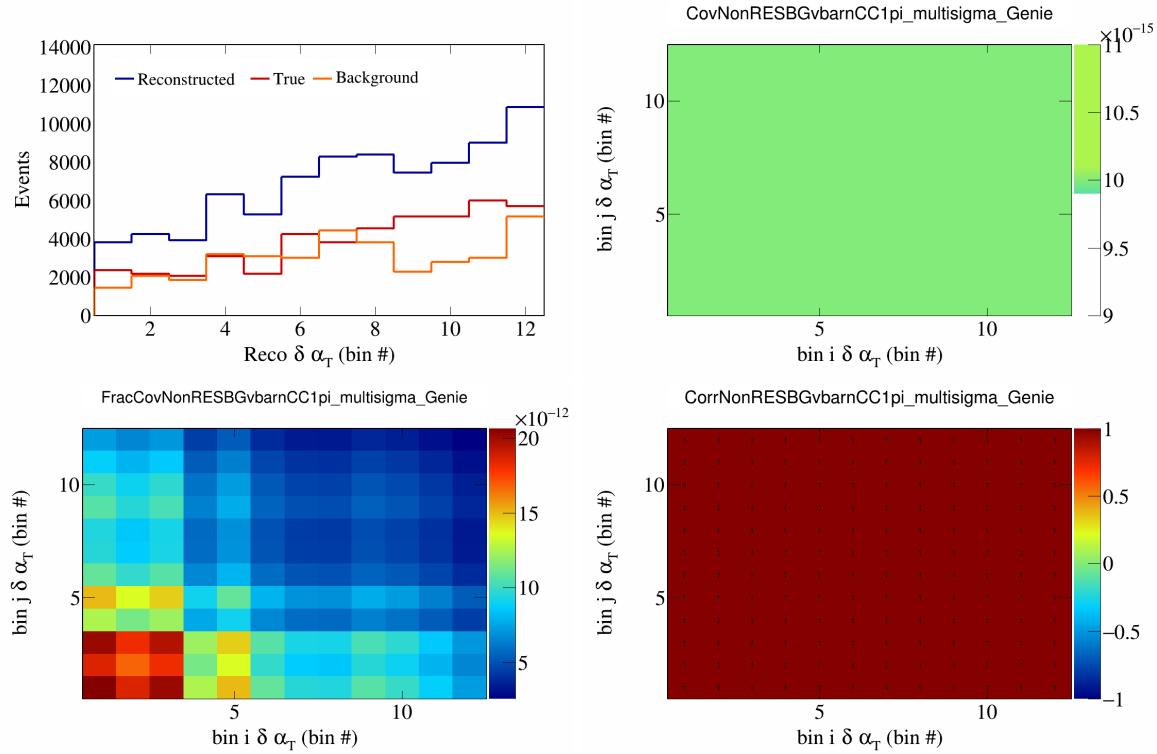


Figure 395: NonRESBGvbarCC1pi variations for  $\delta\alpha_T$  in  $\cos(\theta_{\vec{p}_\mu})$ .

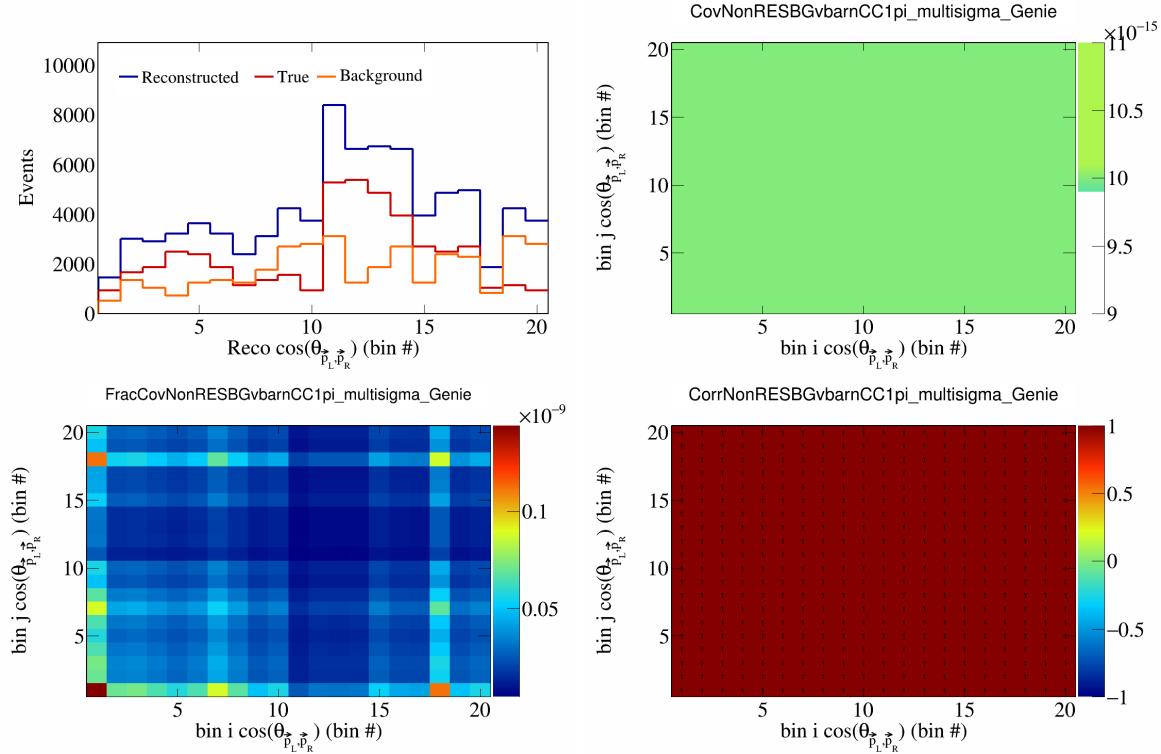


Figure 396: NonRESBGvbarCC1pi variations for  $\cos(\theta_{\vec{p}_L, \vec{p}_R})$  in  $\cos(\theta_{\vec{p}_\mu})$ .

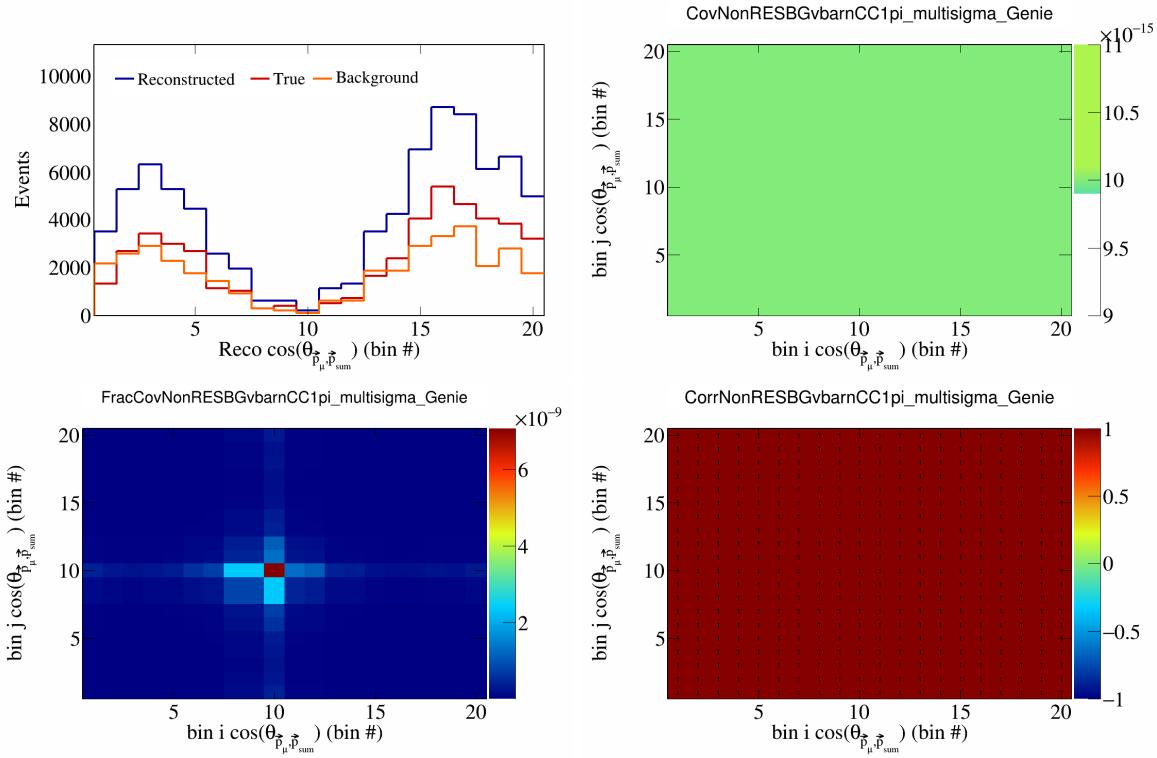


Figure 397: NonRESBGvbarCC1pi variations for  $\cos(\theta_{\vec{p}_\mu})$  in  $\cos(\theta_{\vec{p}_\mu})$ .

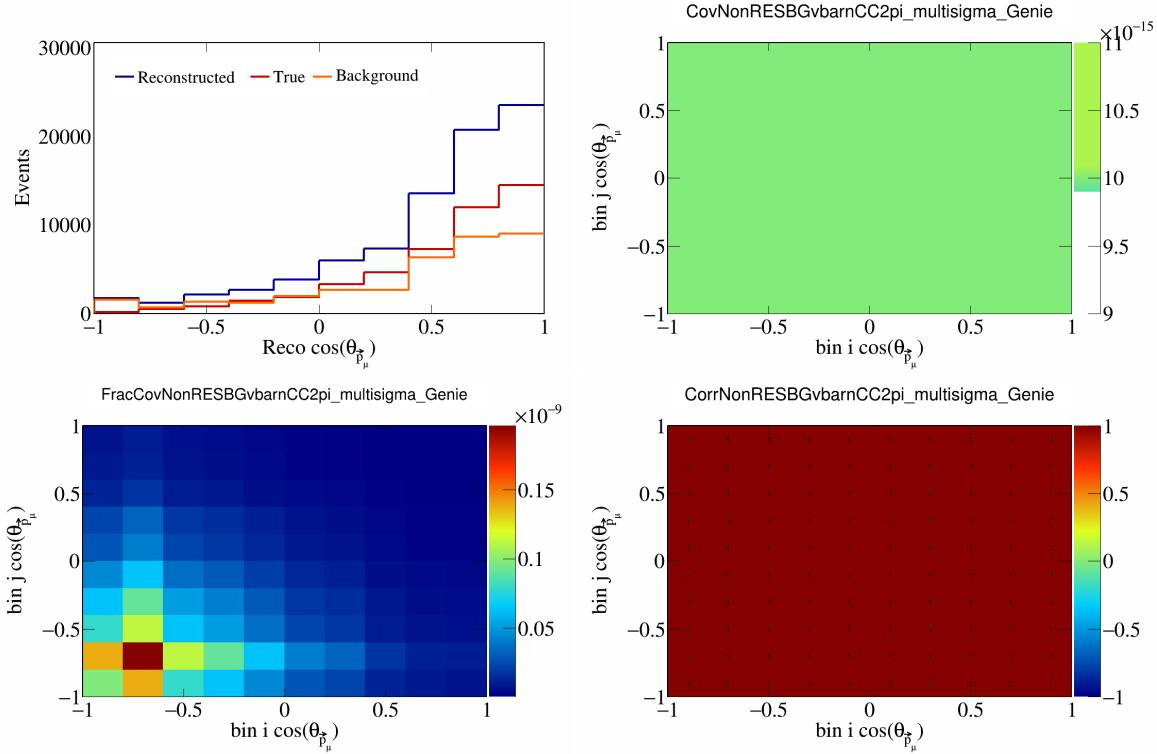


Figure 398: NonRESBGvbarCC2pi variations for  $\cos(\theta_{\vec{p}_\mu})$ .

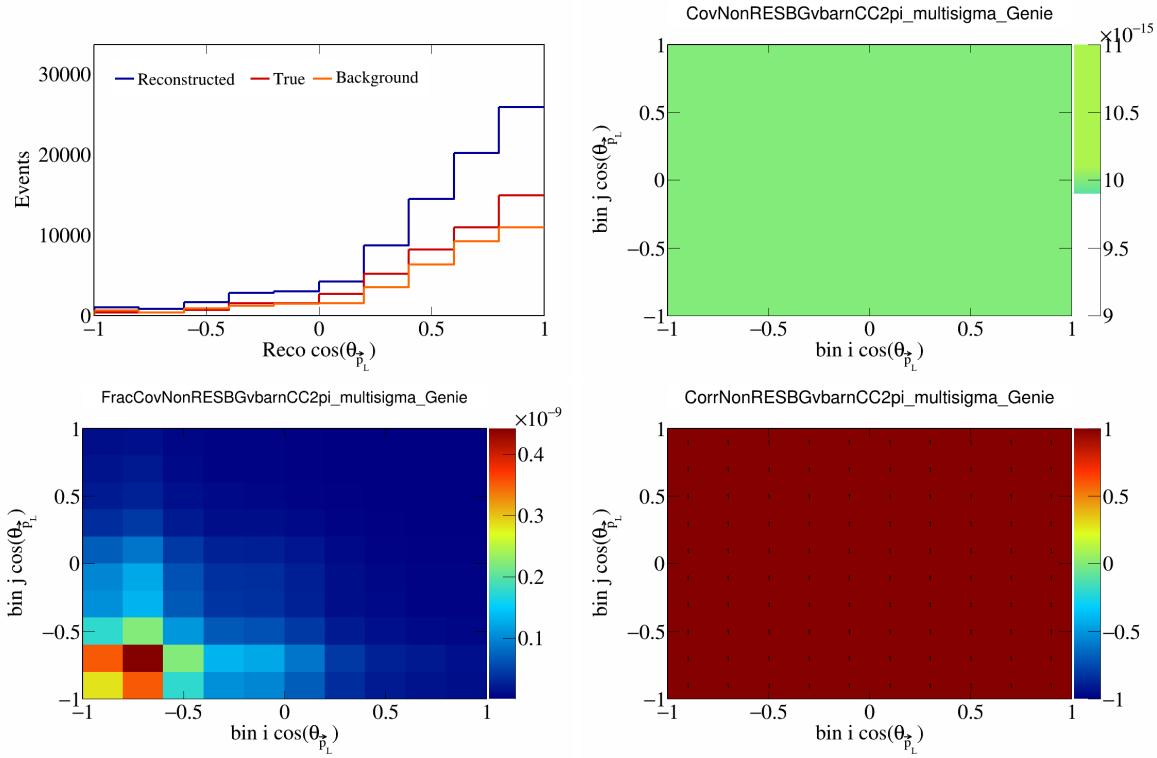


Figure 399: NonRESBGvbarCC2pi variations for  $\cos(\theta_{\vec{F}_L})$ .

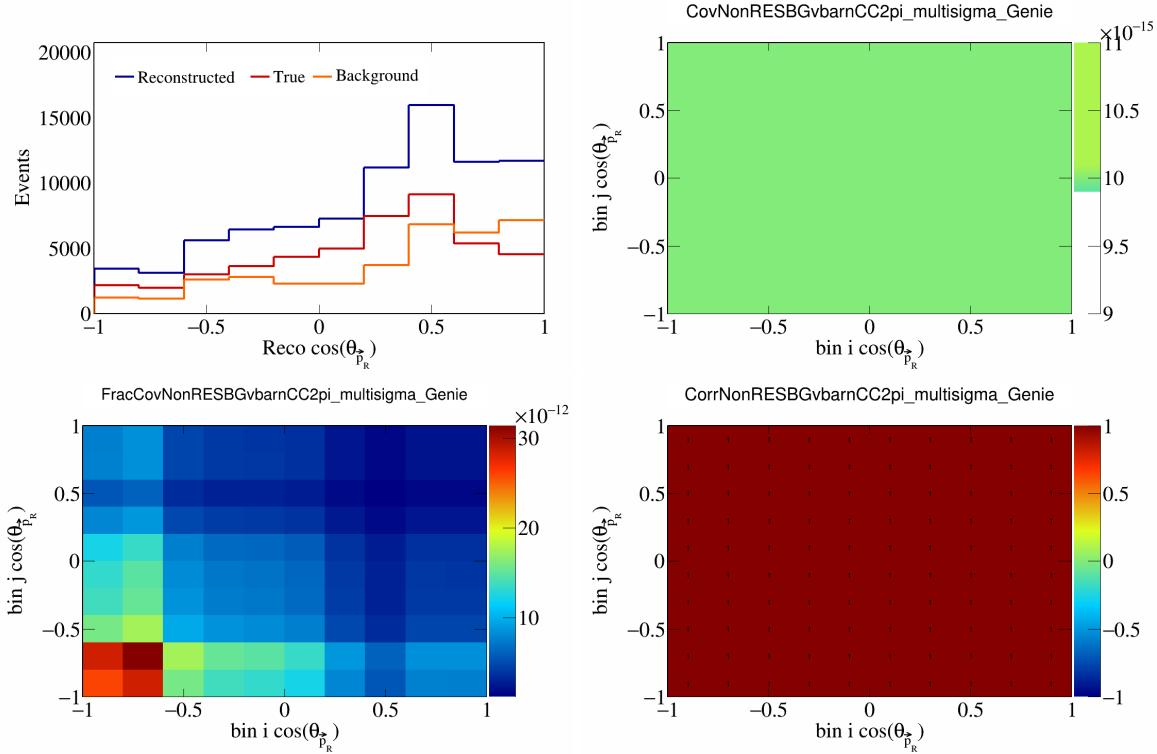


Figure 400: NonRESBGvbarCC2pi variations for  $\cos(\theta_{\vec{F}_R})$ .

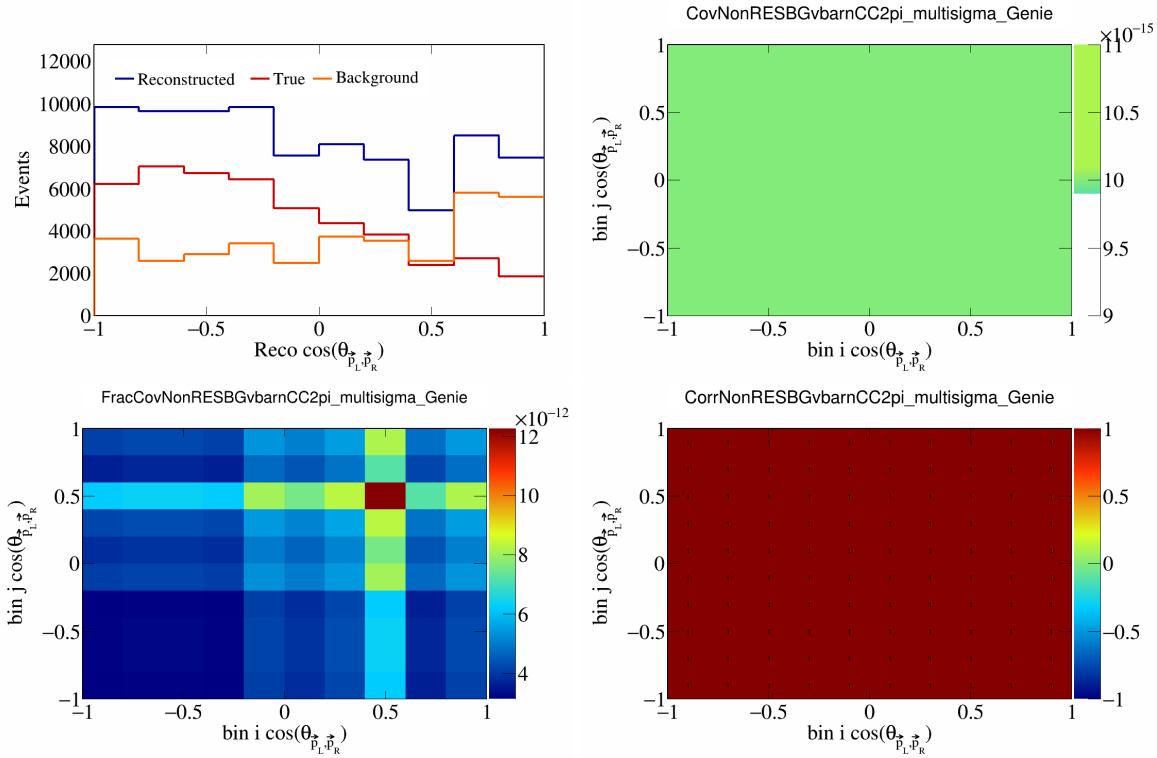


Figure 401: NonRESBGvbarCC2pi variations for  $\cos(\theta_{\vec{p}_L, \vec{p}_R})$ .

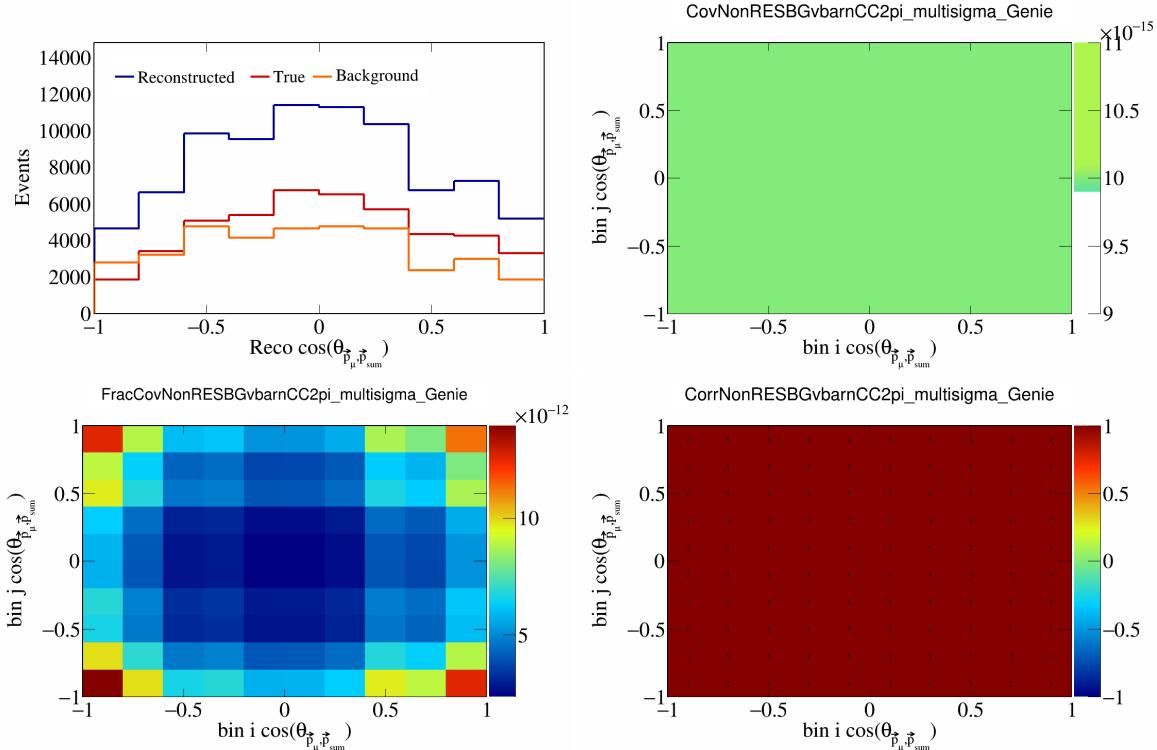


Figure 402: NonRESBGvbarCC2pi variations for  $\cos(\theta_{\vec{p}_\mu, \vec{p}_{\text{sum}}})$ .

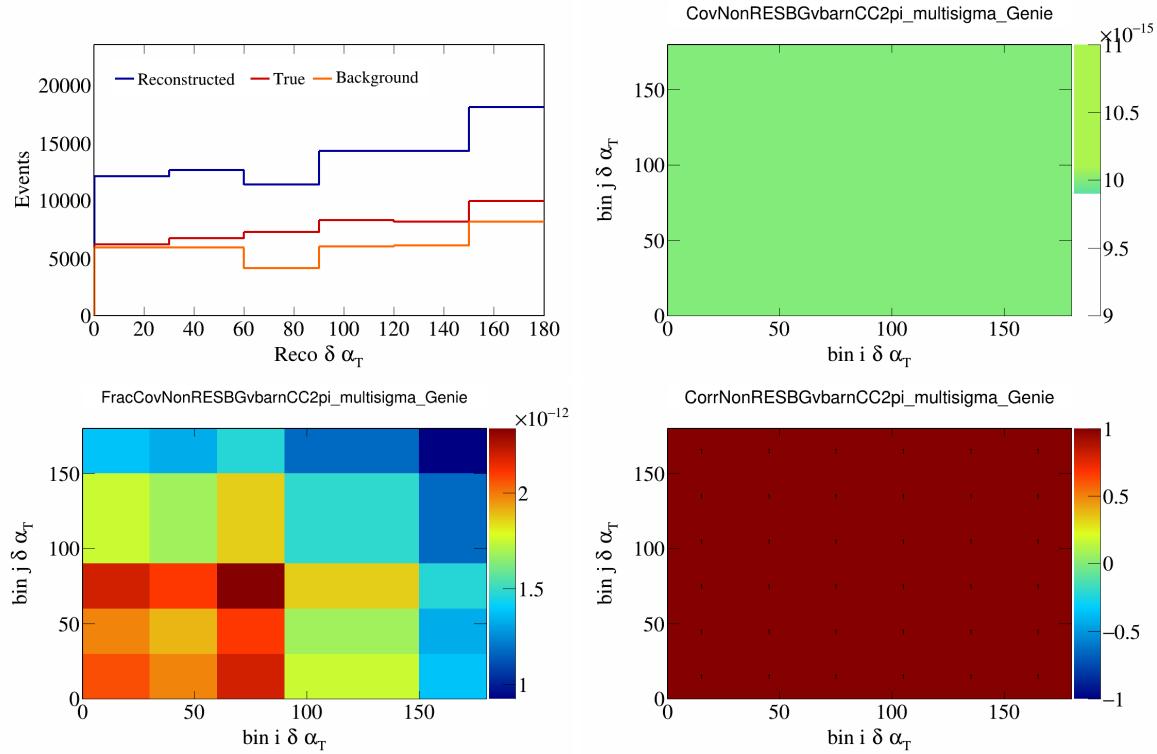


Figure 403: NonRESBGvbarCC2pi variations for  $\delta\alpha_T$ .

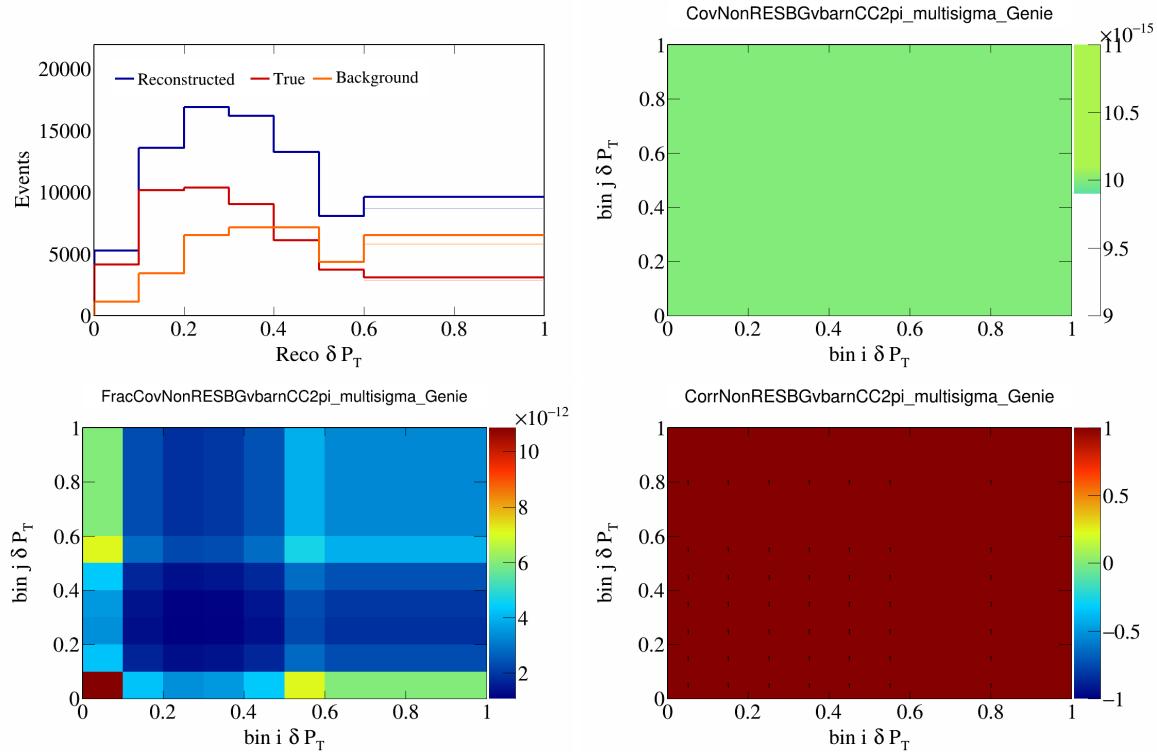


Figure 404: NonRESBGvbarCC2pi variations for  $\delta P_T$ .

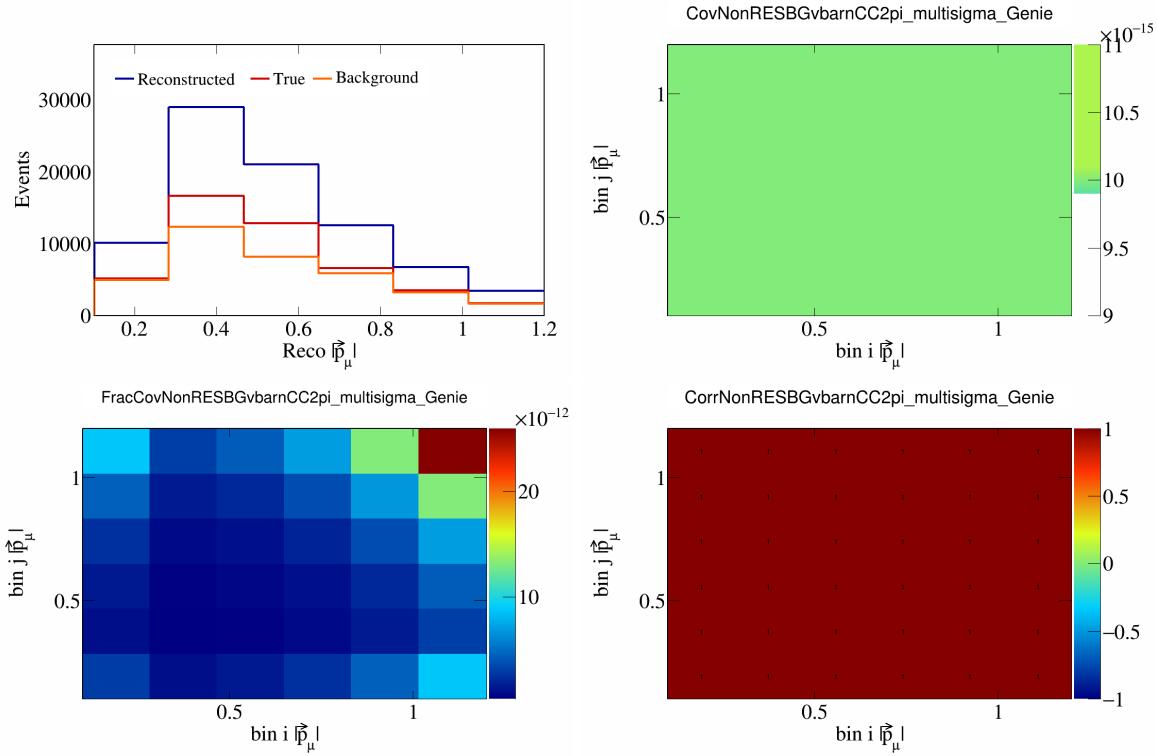


Figure 405: NonRESBGvbarCC2pi variations for  $|\vec{p}_\mu|$ .

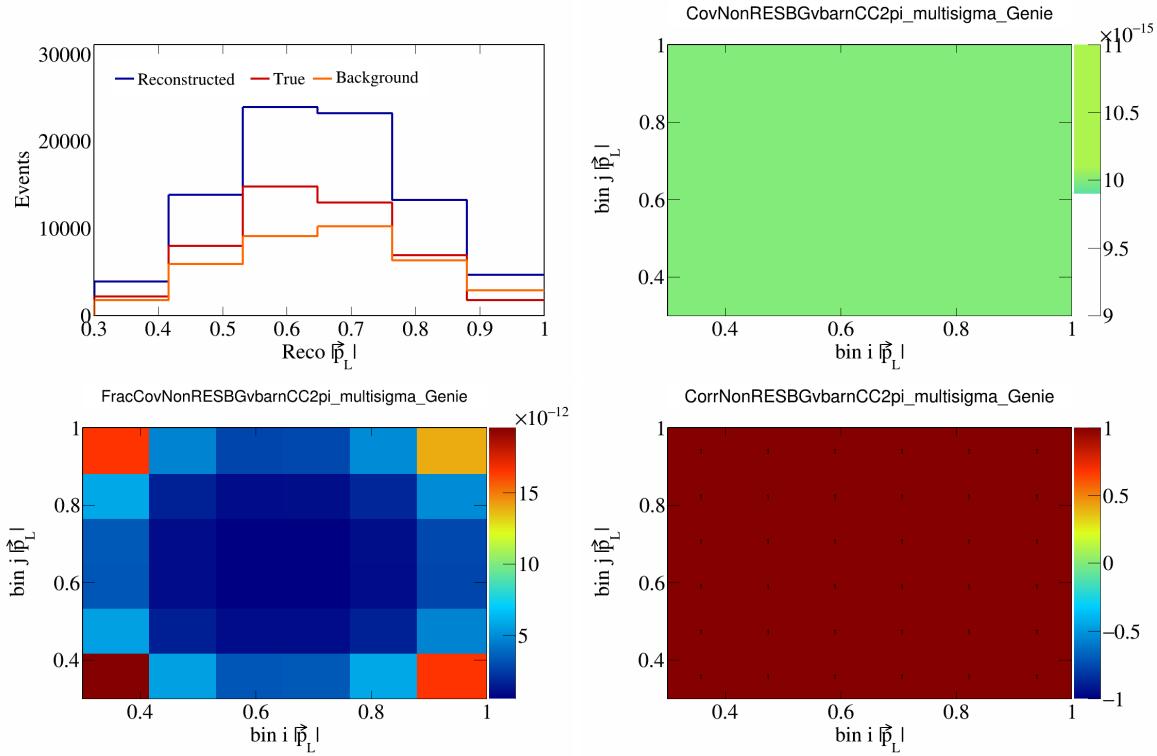


Figure 406: NonRESBGvbarCC2pi variations for  $|\vec{p}_L|$ .

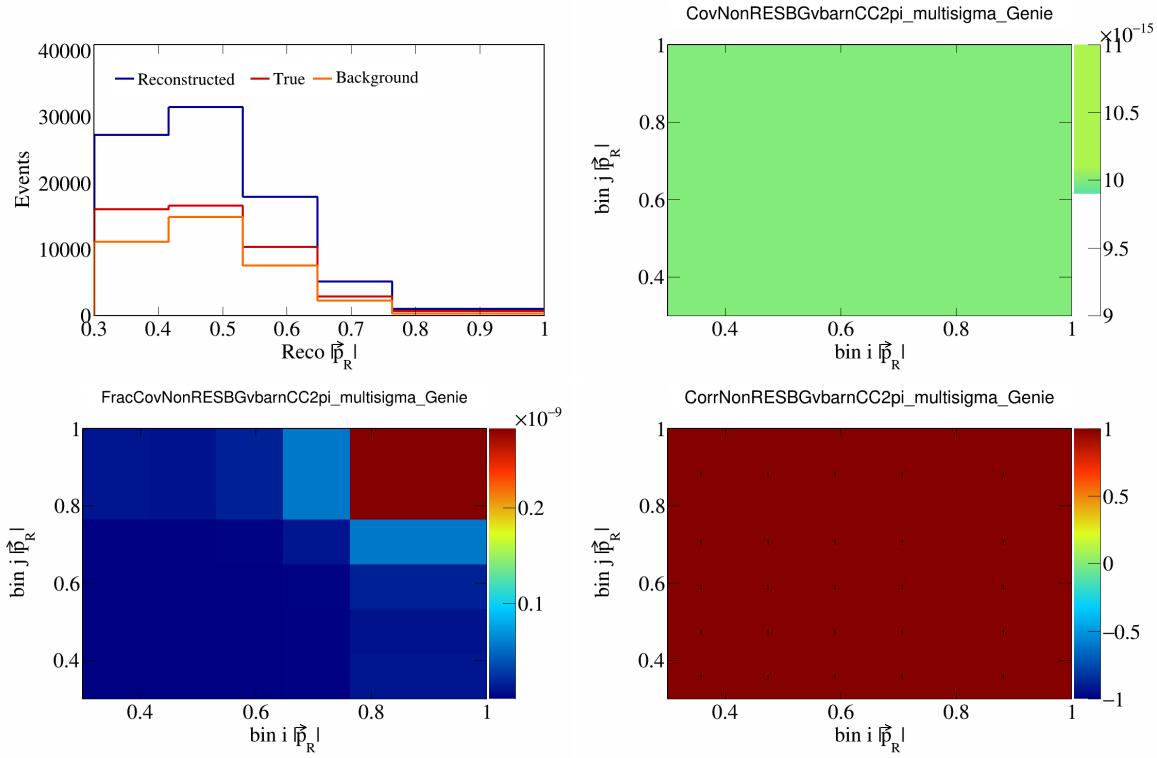


Figure 407: NonRESBGvbarCC2pi variations for  $|\vec{p}_R|$ .

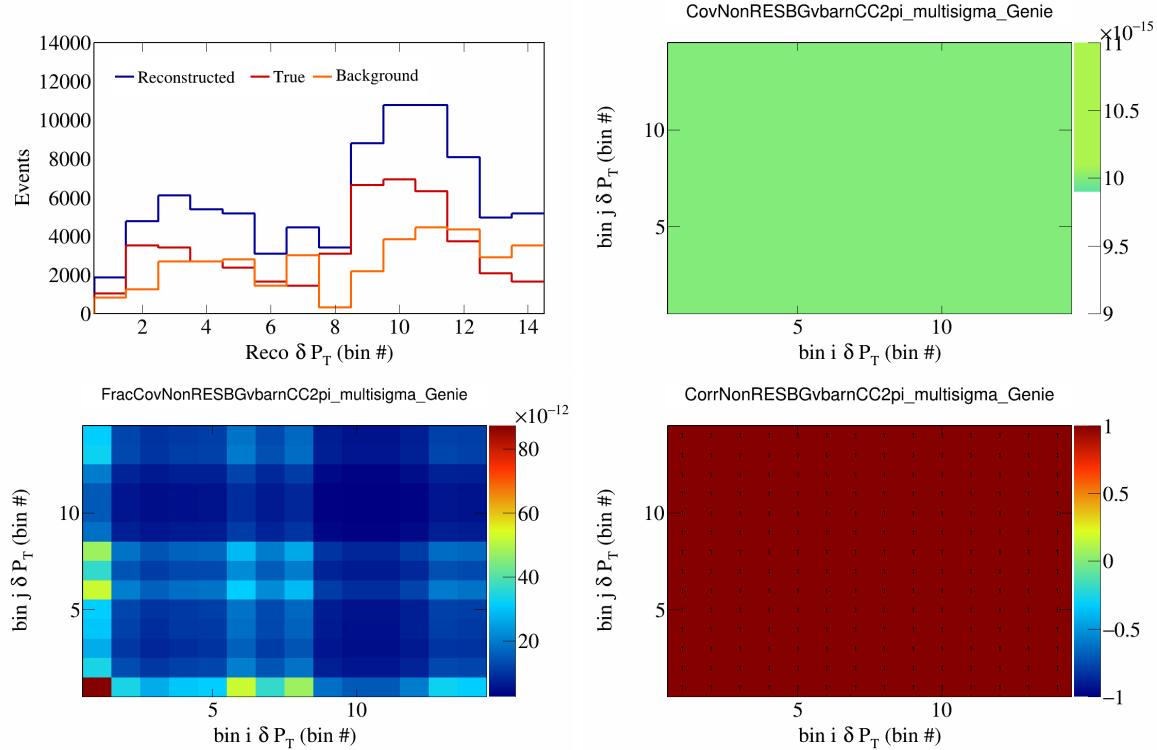


Figure 408: NonRESBGvbarCC2pi variations for  $\delta P_T$  in  $\cos(\theta_{\vec{p}_\mu})$ .

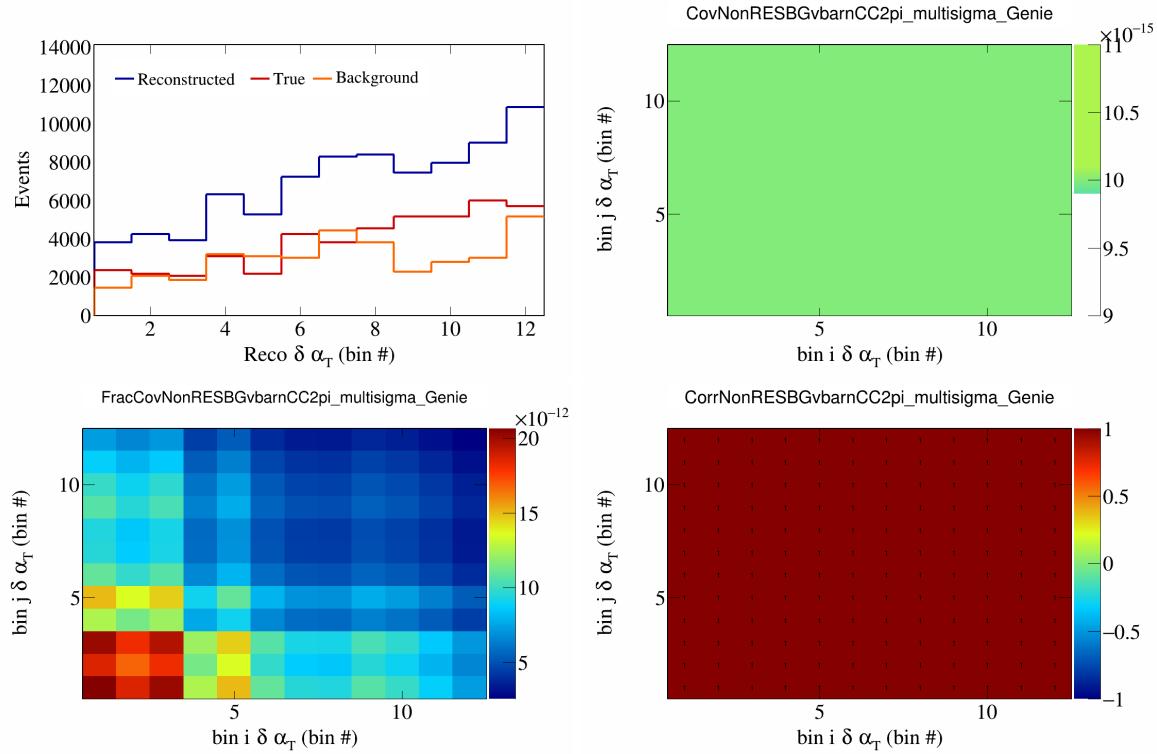


Figure 409: NonRESBGvbarCC2pi variations for  $\delta \alpha_T$  in  $\cos(\theta_{\vec{p}_\mu})$ .

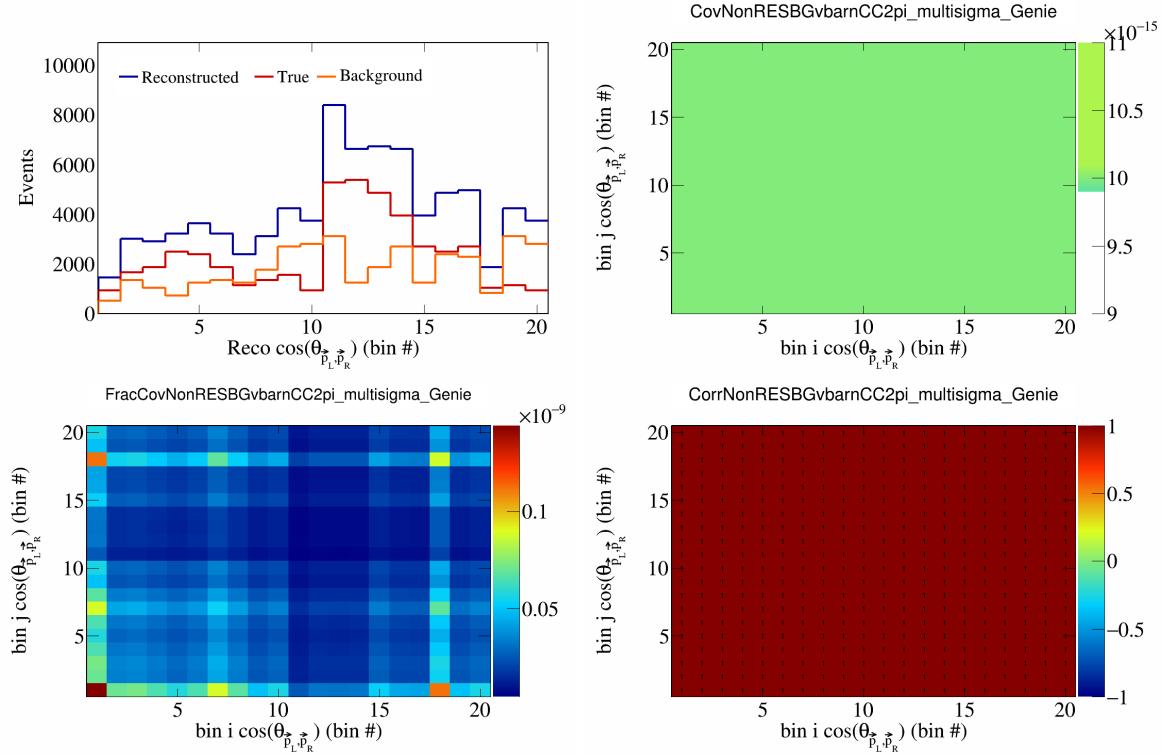


Figure 410: NonRESBGvbarCC2pi variations for  $\cos(\theta_{\vec{p}_L, \vec{p}_R})$  in  $\cos(\theta_{\vec{p}_\mu})$ .

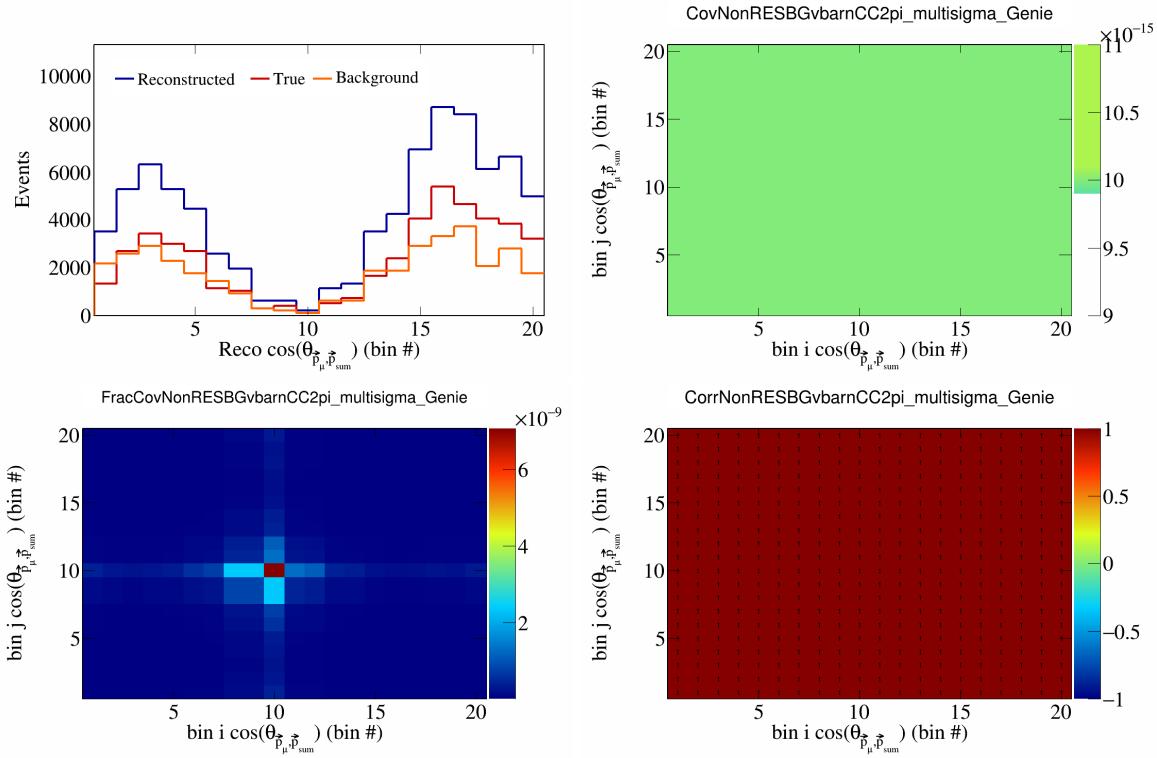


Figure 411: NonRESBGvbarCC2pi variations for  $\cos(\theta_{\vec{p}_\mu})$  in  $\cos(\theta_{\vec{p}_\mu})$ .

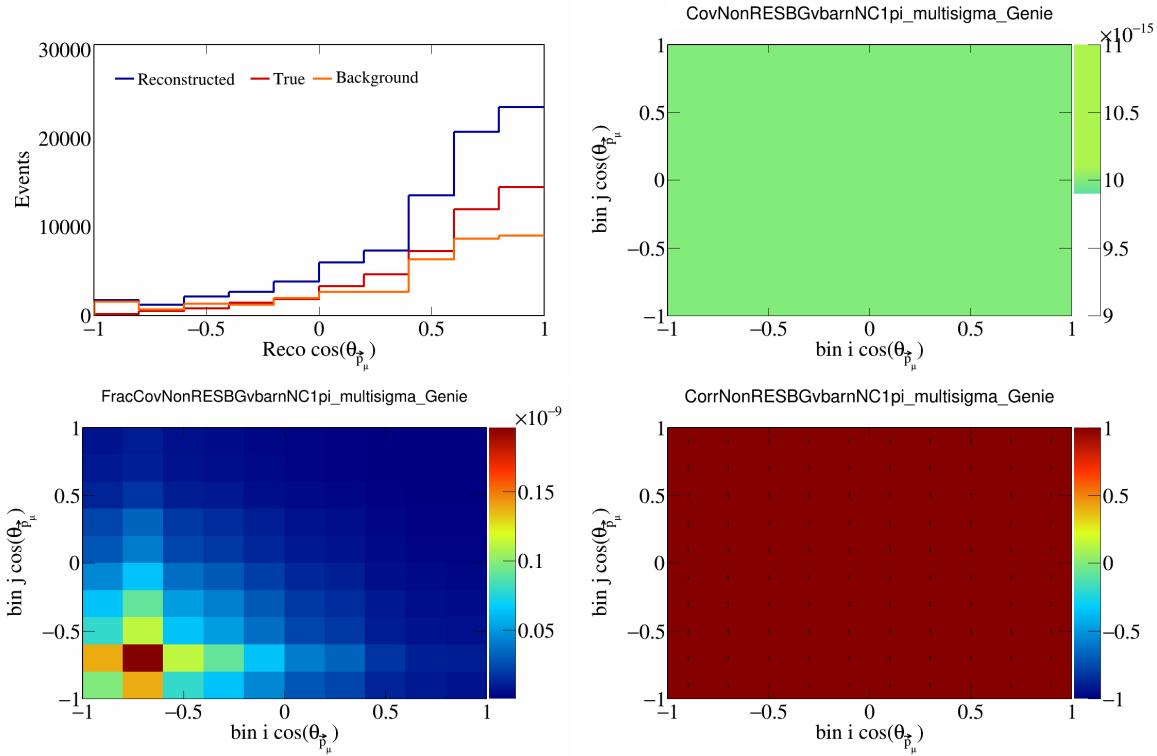


Figure 412: NonRESBGvbarNC1pi variations for  $\cos(\theta_{\vec{p}_\mu})$ .

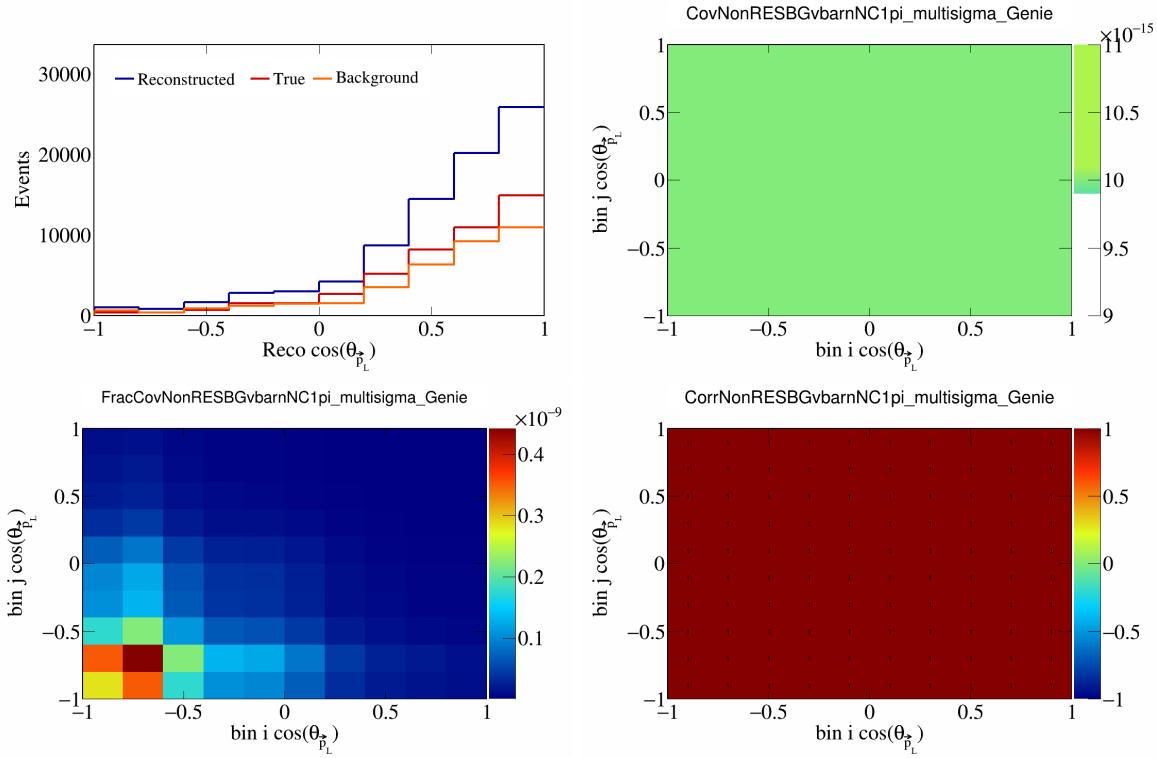


Figure 413: NonRESBGvbarNC1pi variations for  $\cos(\theta_{\vec{p}_L})$ .

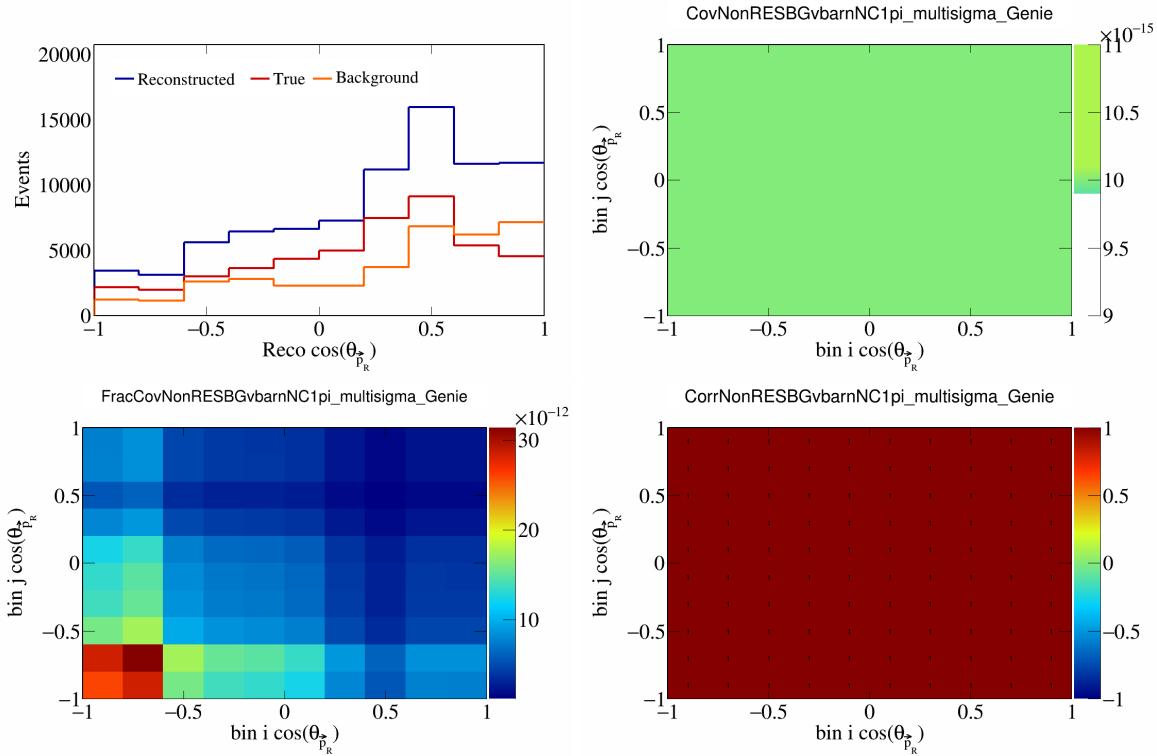


Figure 414: NonRESBGvbarNC1pi variations for  $\cos(\theta_{\vec{p}_R})$ .

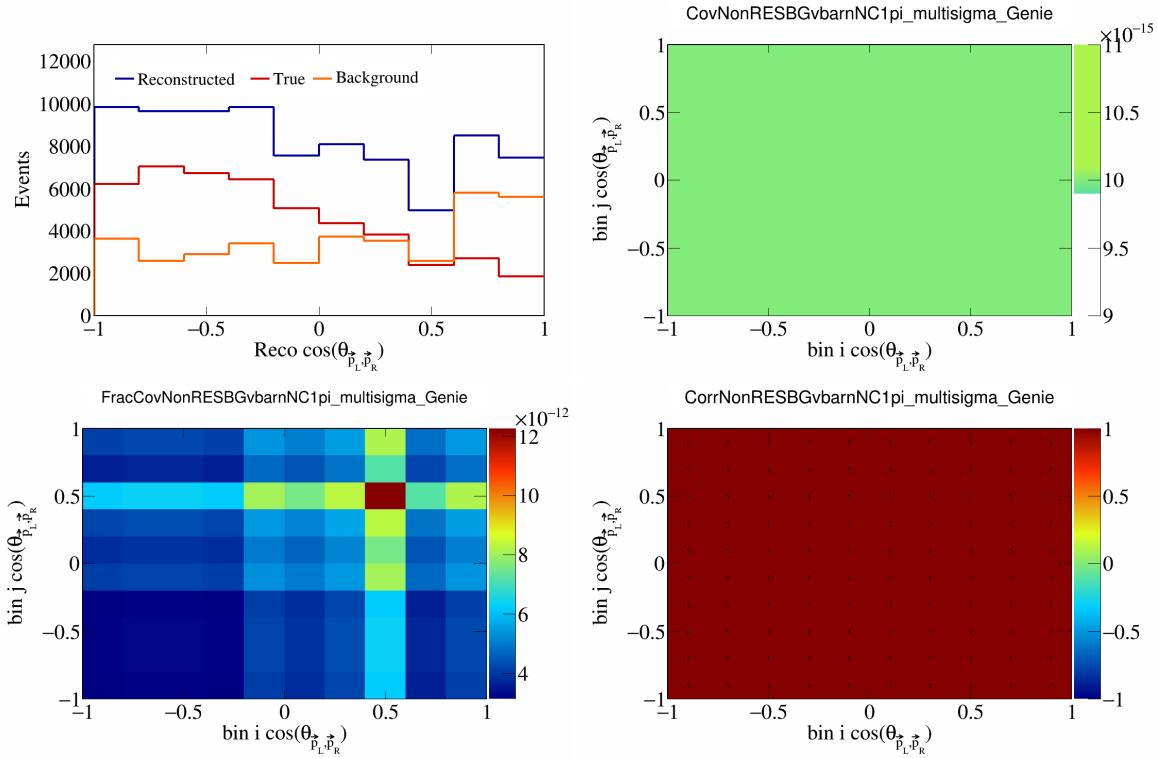


Figure 415: NonRESBGvbarNC1pi variations for  $\cos(\theta_{\vec{p}_L, \vec{p}_R})$ .

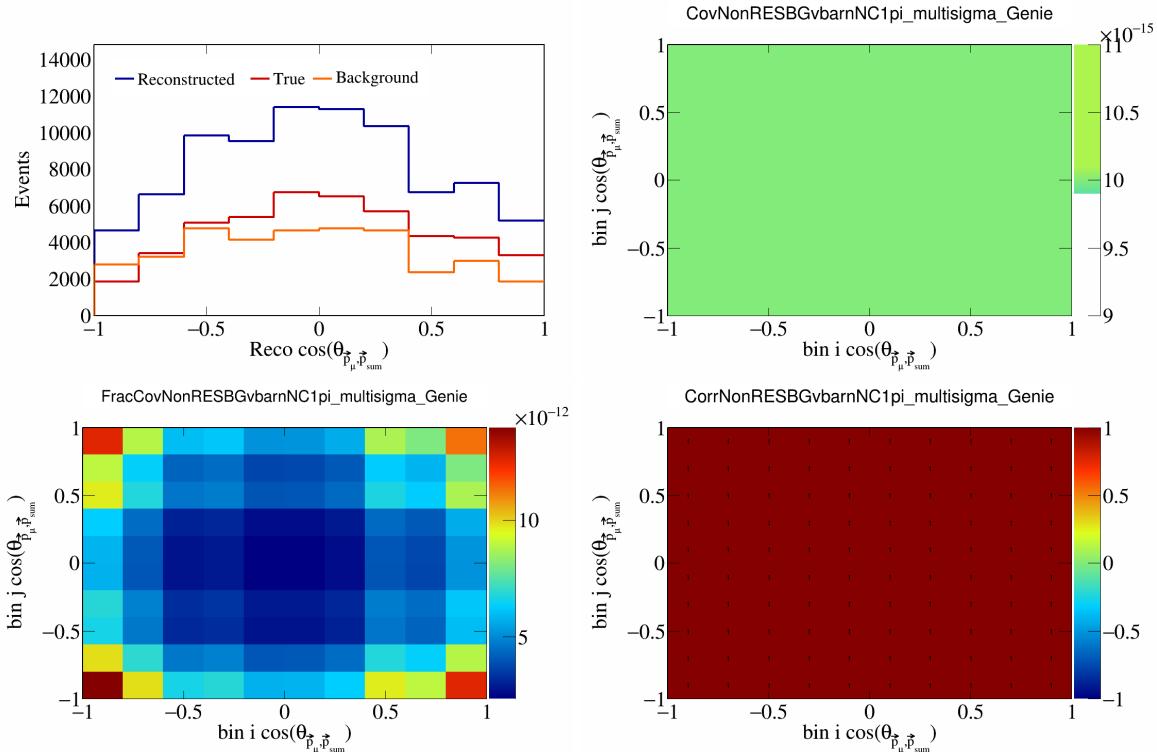


Figure 416: NonRESBGvbarNC1pi variations for  $\cos(\theta_{\vec{p}_\mu, \vec{p}_{\text{sum}}})$ .

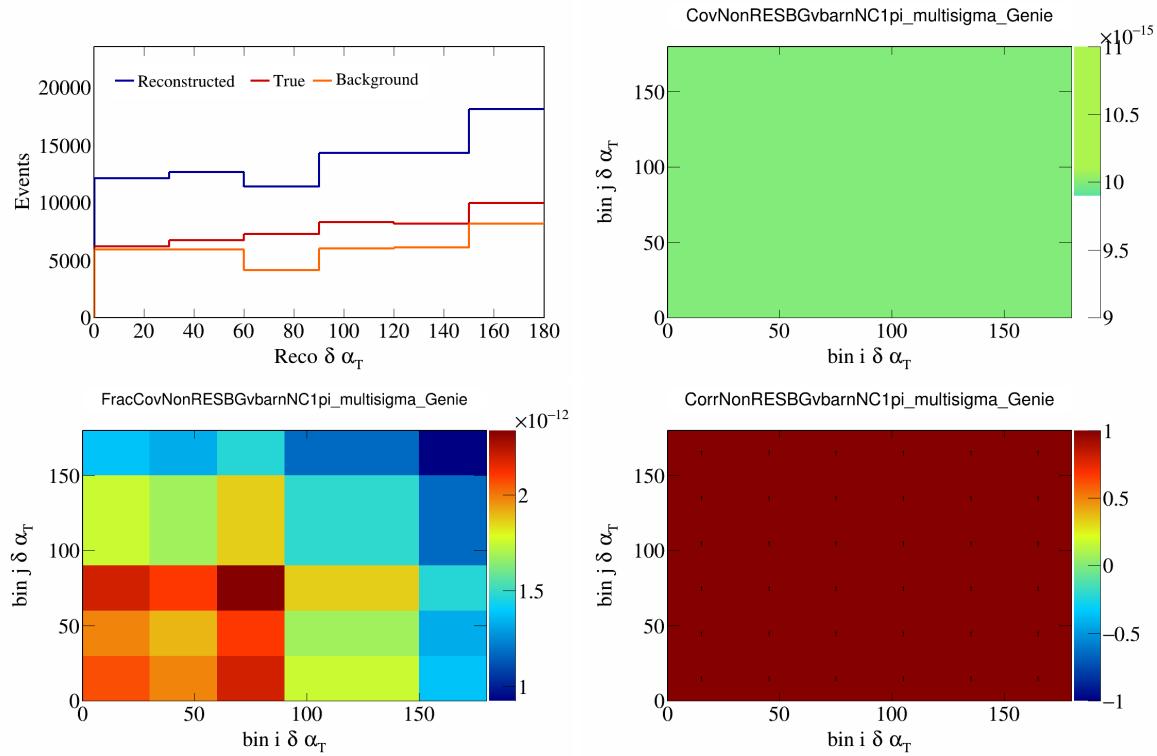


Figure 417: NonRESBGvbarNC1pi variations for  $\delta\alpha_T$ .

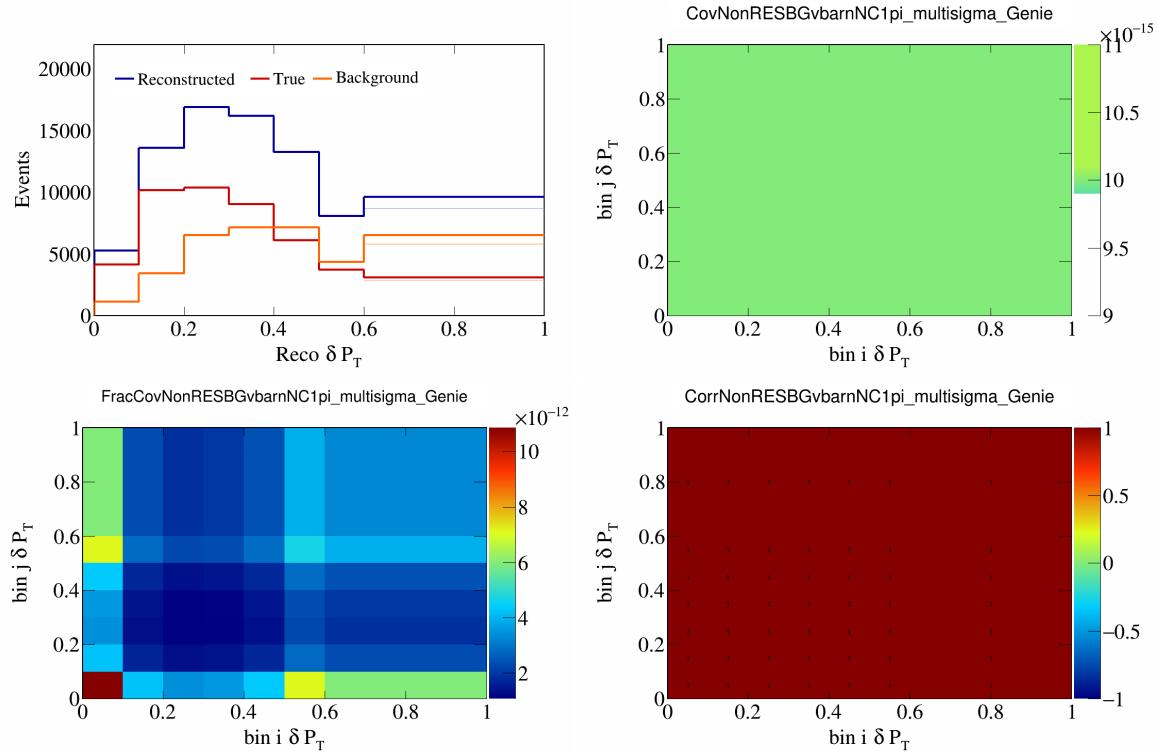


Figure 418: NonRESBGvbarNC1pi variations for  $\delta P_T$ .

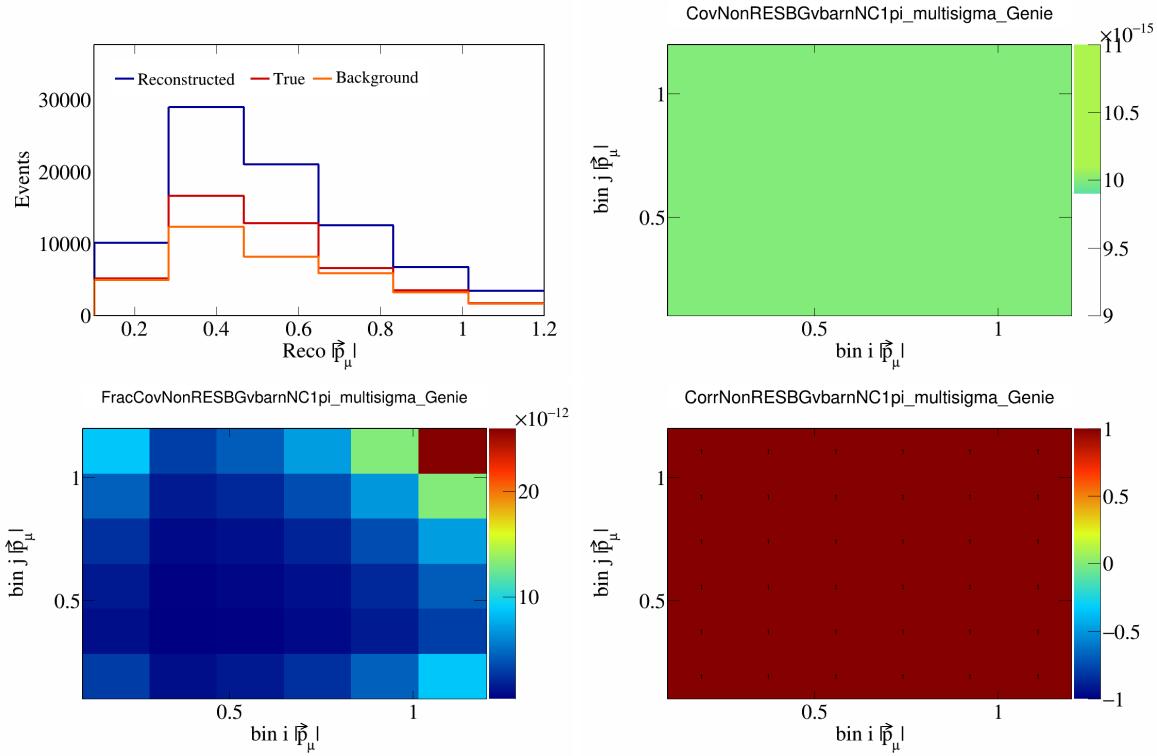


Figure 419: NonRESBGvbarNC1pi variations for  $|\vec{p}_\mu|$ .

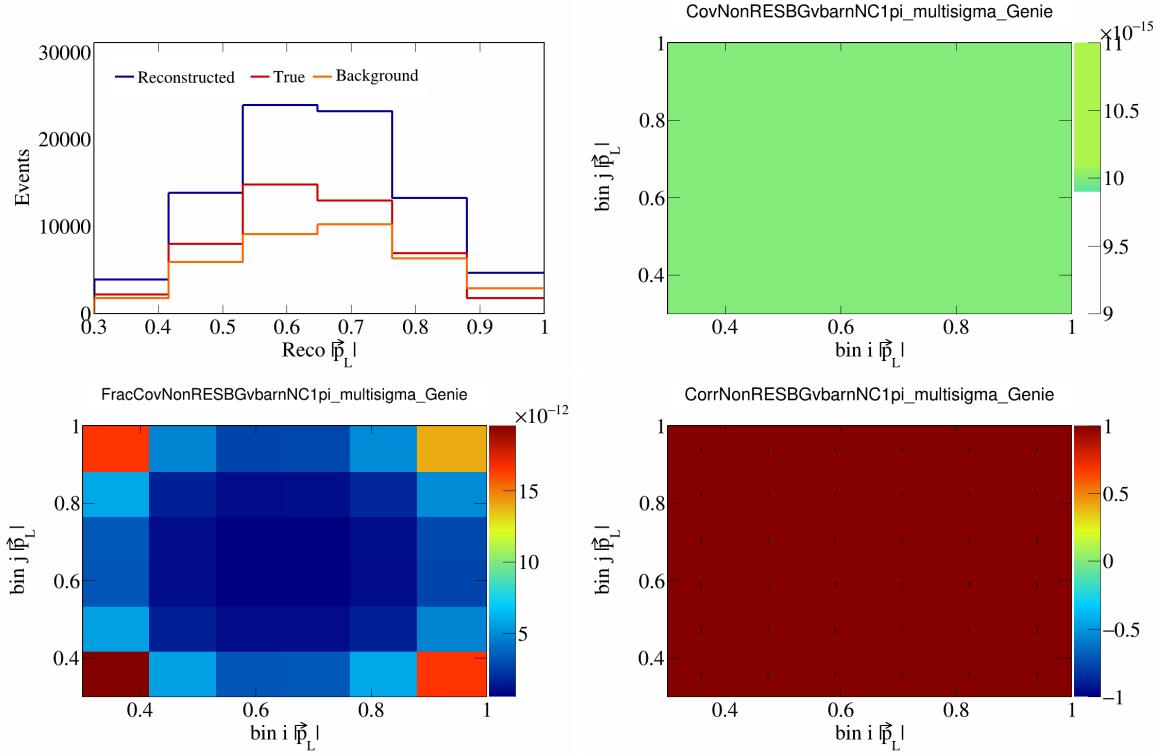


Figure 420: NonRESBGvbarNC1pi variations for  $|\vec{p}_L|$ .

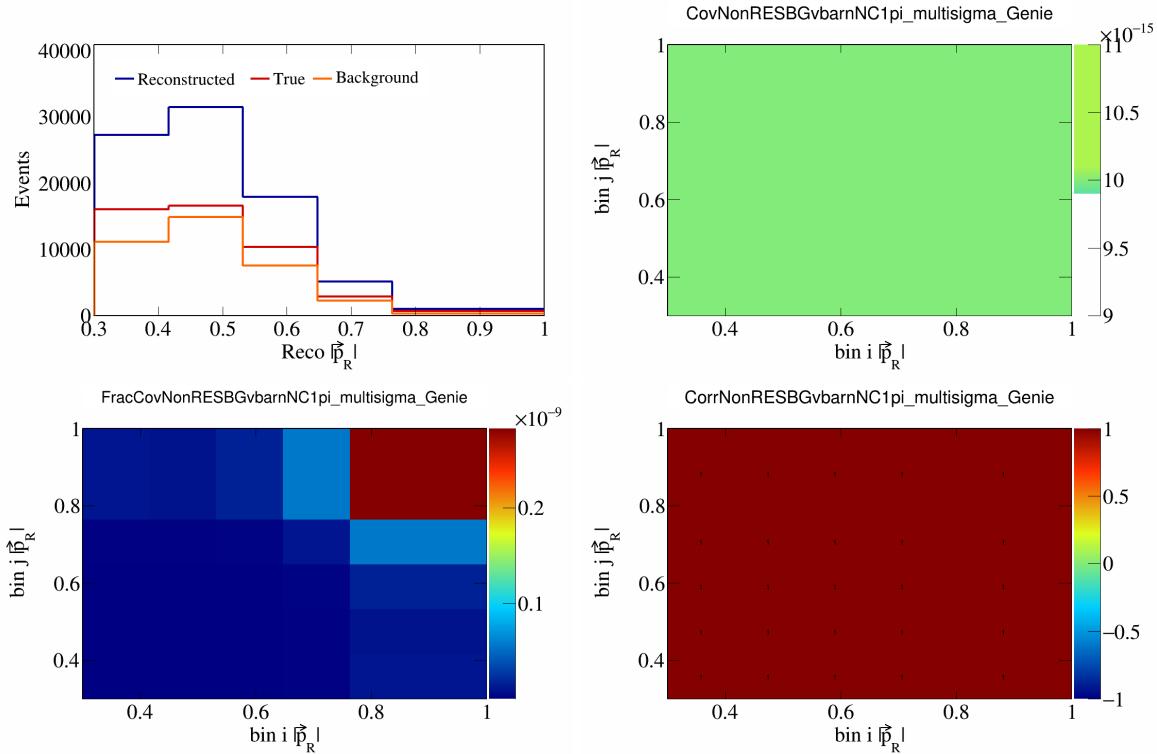


Figure 421: NonRESBGvbarNC1pi variations for  $|\vec{p}_R|$ .

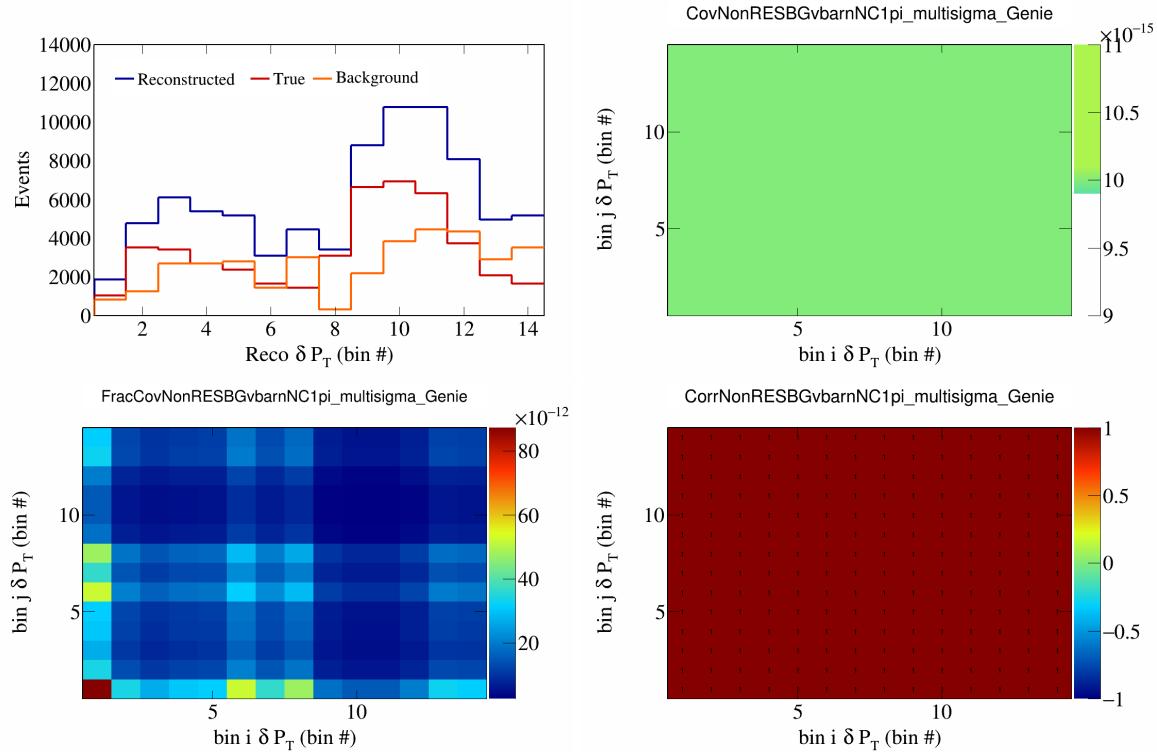


Figure 422: NonRESBGvbarNC1pi variations for  $\delta P_T$  in  $\cos(\theta_{\vec{p}_\mu})$ .

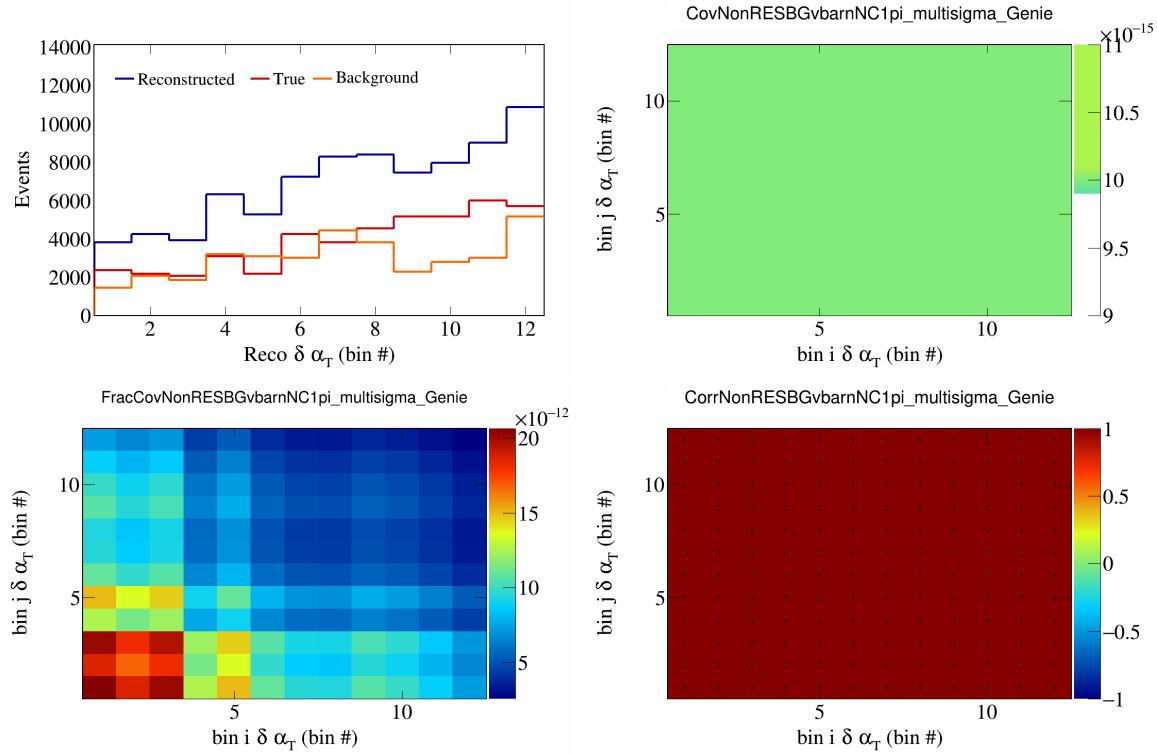


Figure 423: NonRESBGvbarNC1pi variations for  $\delta\alpha_T$  in  $\cos(\theta_{\vec{p}_\mu})$ .

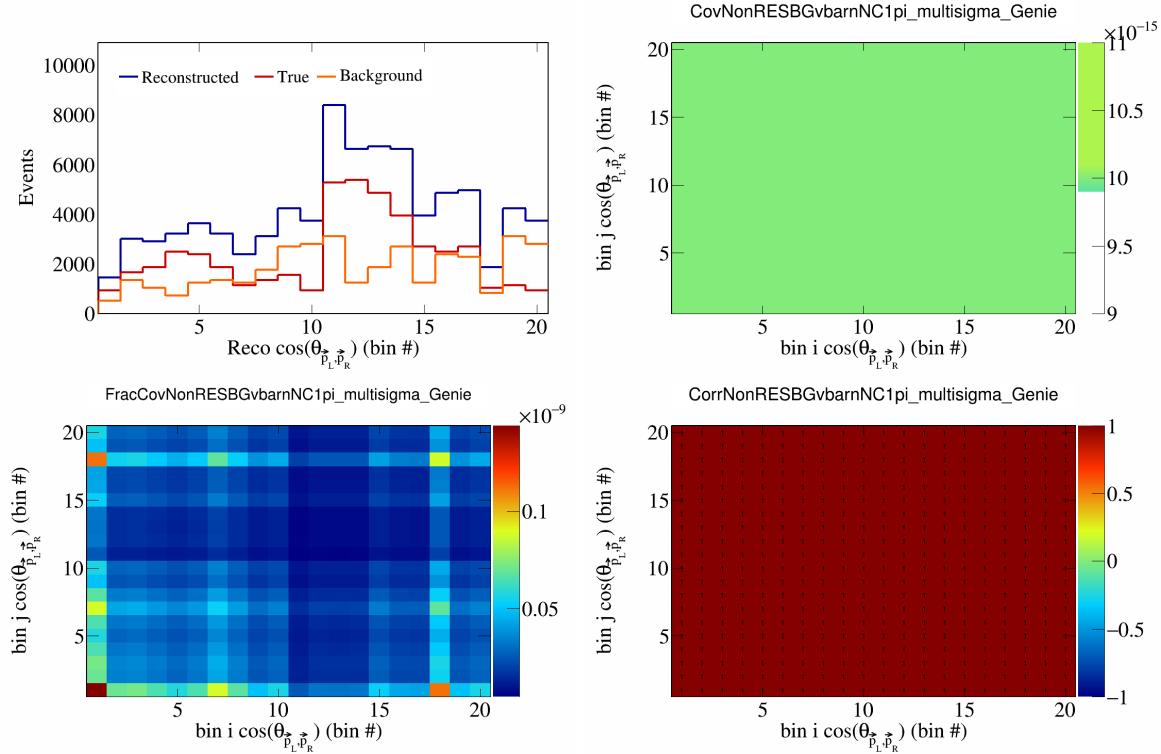


Figure 424: NonRESBGvbarNC1pi variations for  $\cos(\theta_{\vec{p}_L, \vec{p}_R})$  in  $\cos(\theta_{\vec{p}_\mu})$ .

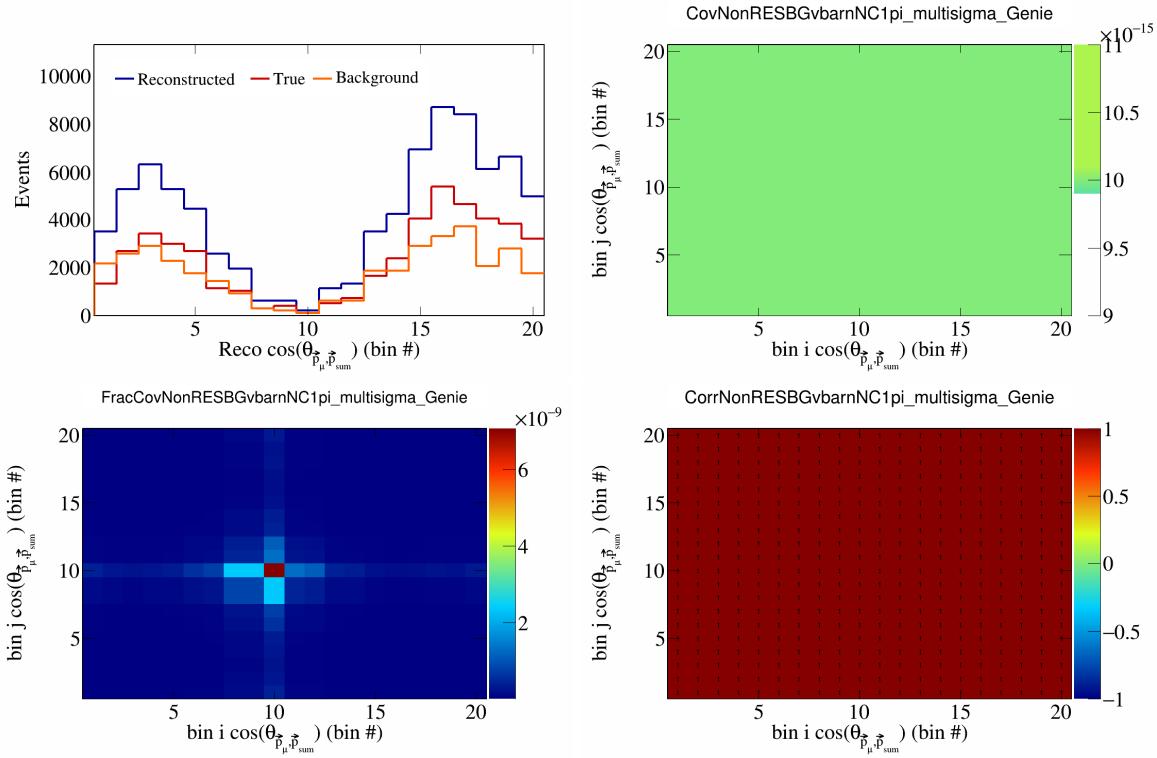


Figure 425: NonRESBGvbarNC1pi variations for  $\cos(\theta_{\vec{p}_\mu})$  in  $\cos(\theta_{\vec{p}_\mu})$ .

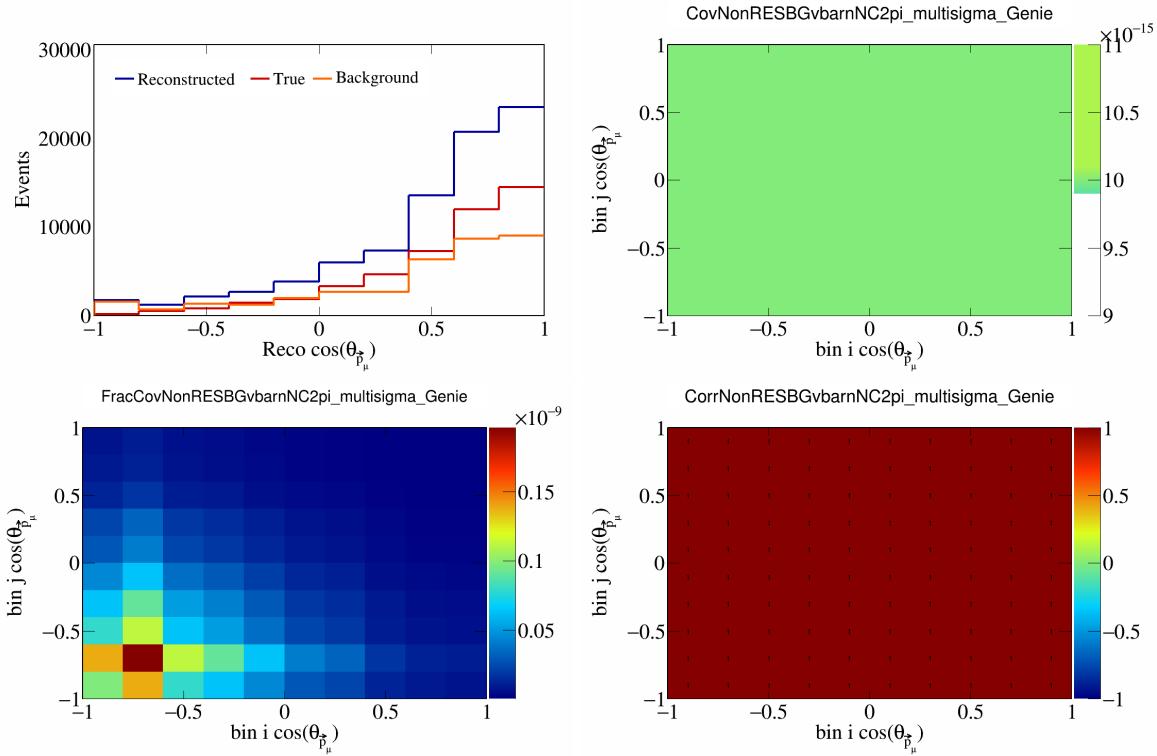


Figure 426: NonRESBGvbarNC2pi variations for  $\cos(\theta_{\vec{p}_\mu})$ .

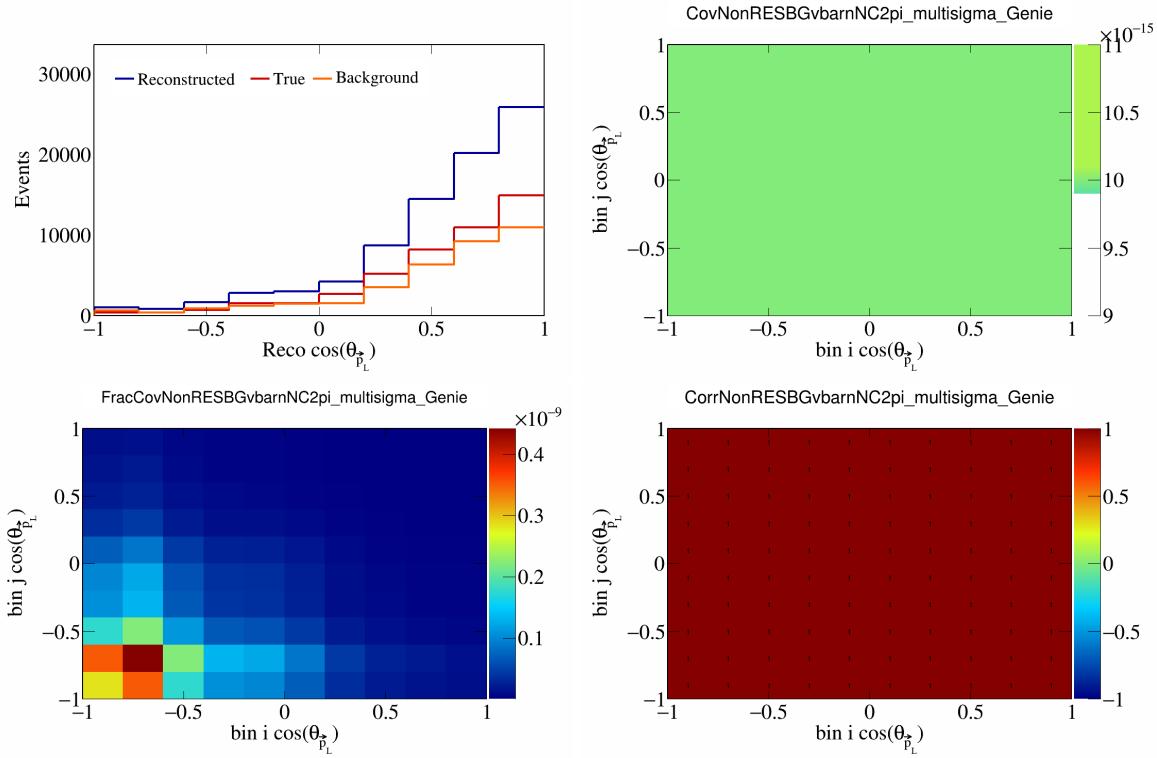


Figure 427: NonRESBGvbarNC2pi variations for  $\cos(\theta_{\vec{p}_L})$ .

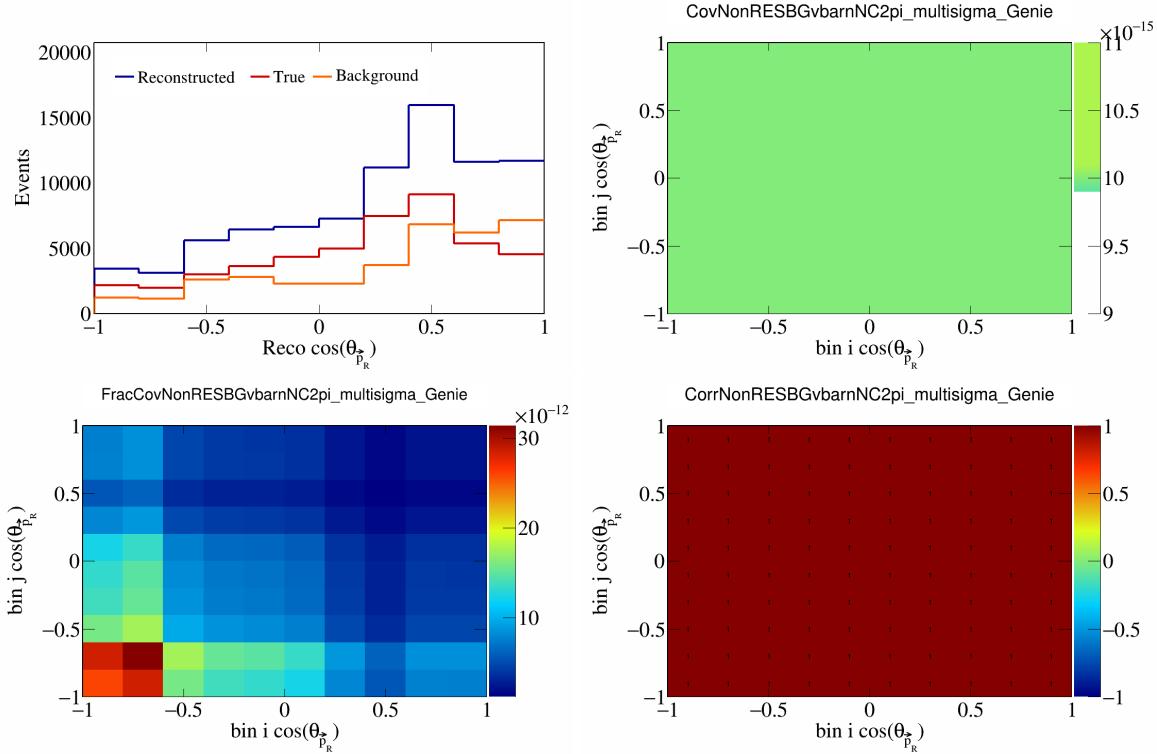


Figure 428: NonRESBGvbarNC2pi variations for  $\cos(\theta_{\vec{p}_R})$ .

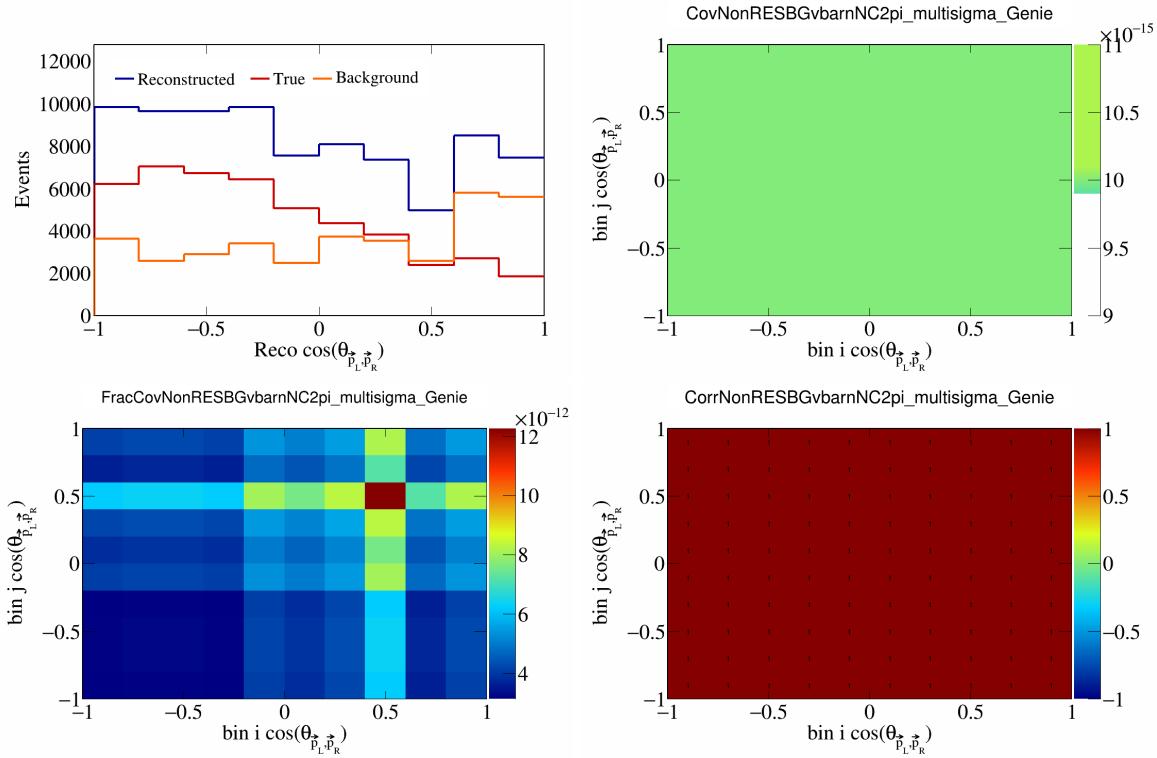


Figure 429: NonRESBGvbarNC2pi variations for  $\cos(\theta_{\vec{p}_L, \vec{p}_R})$ .

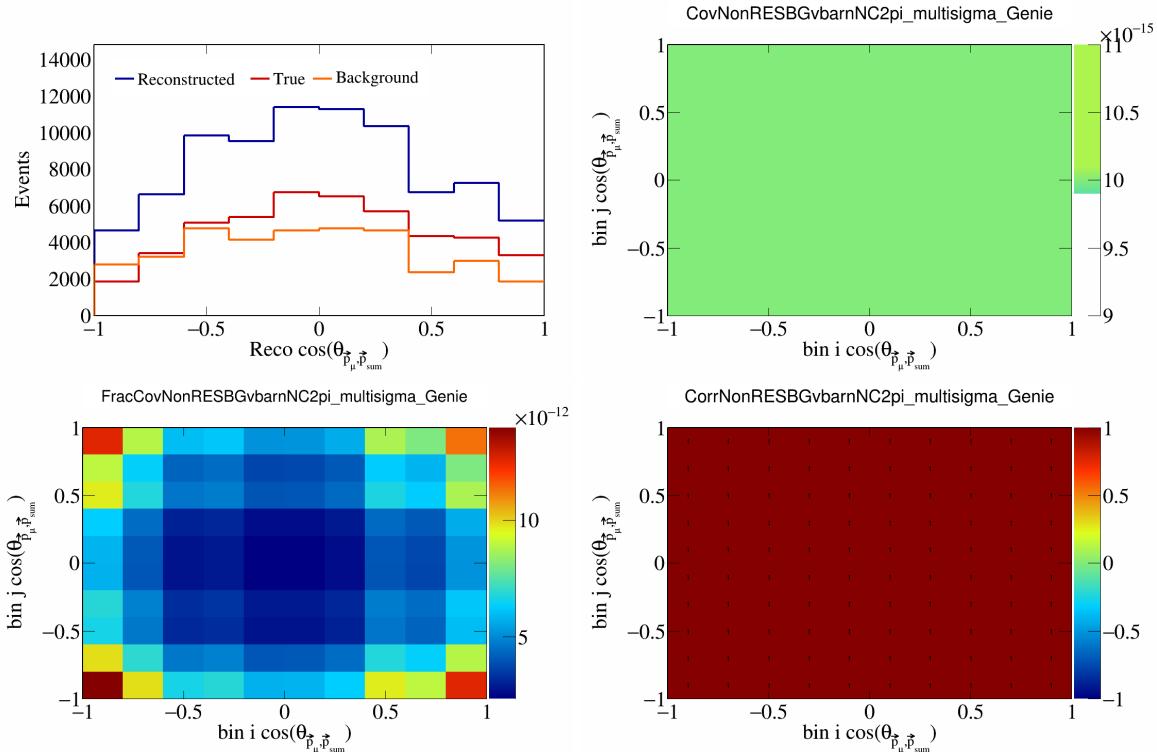


Figure 430: NonRESBGvbarNC2pi variations for  $\cos(\theta_{\vec{p}_\mu, \vec{p}_{\text{sum}}})$ .

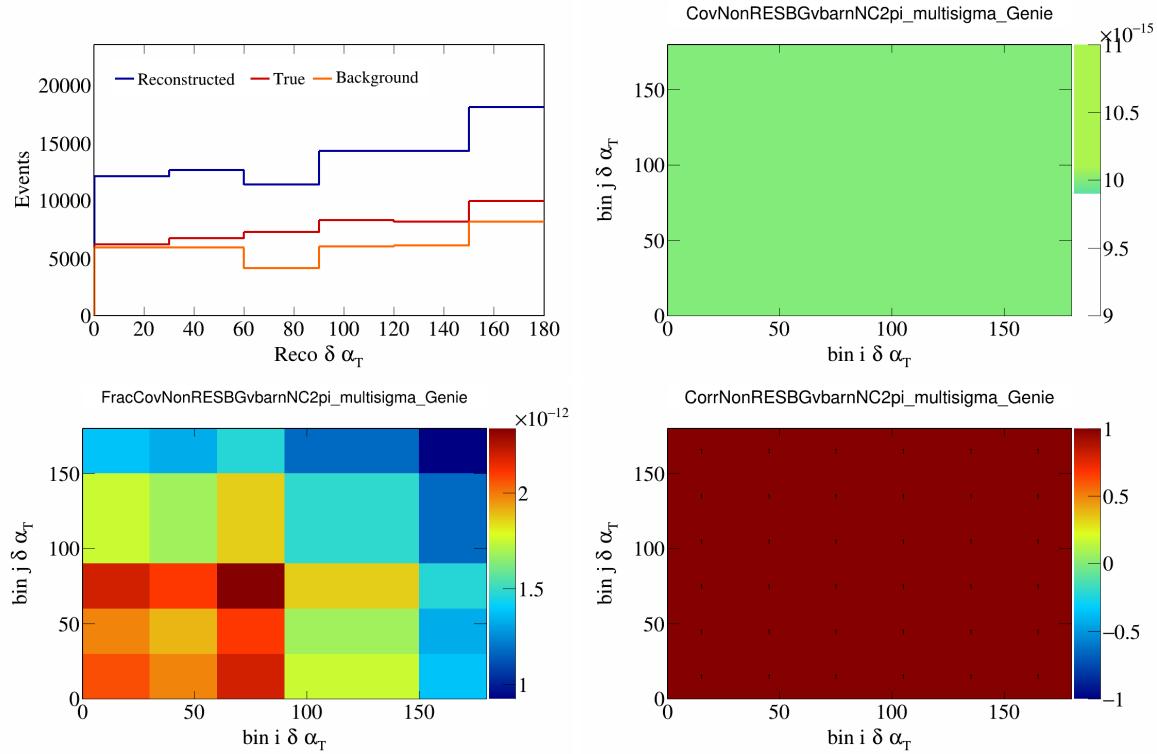


Figure 431: NonRESBGvbarNC2pi variations for  $\delta\alpha_T$ .

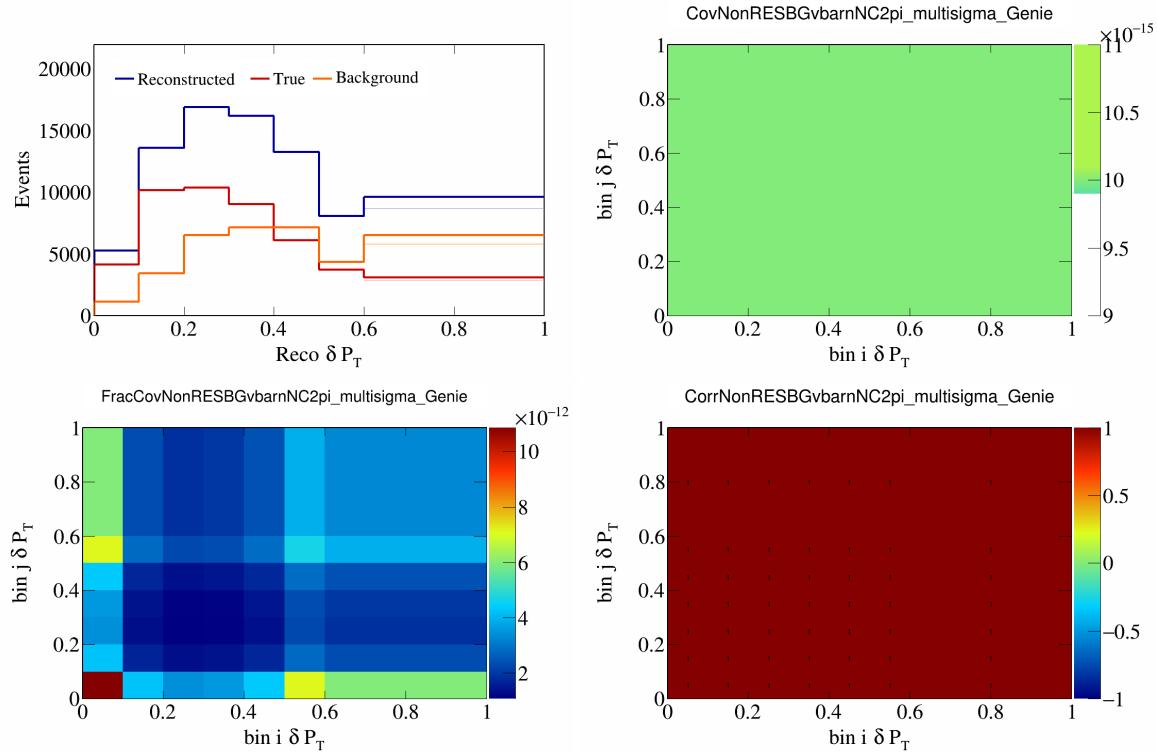


Figure 432: NonRESBGvbarNC2pi variations for  $\delta P_T$ .

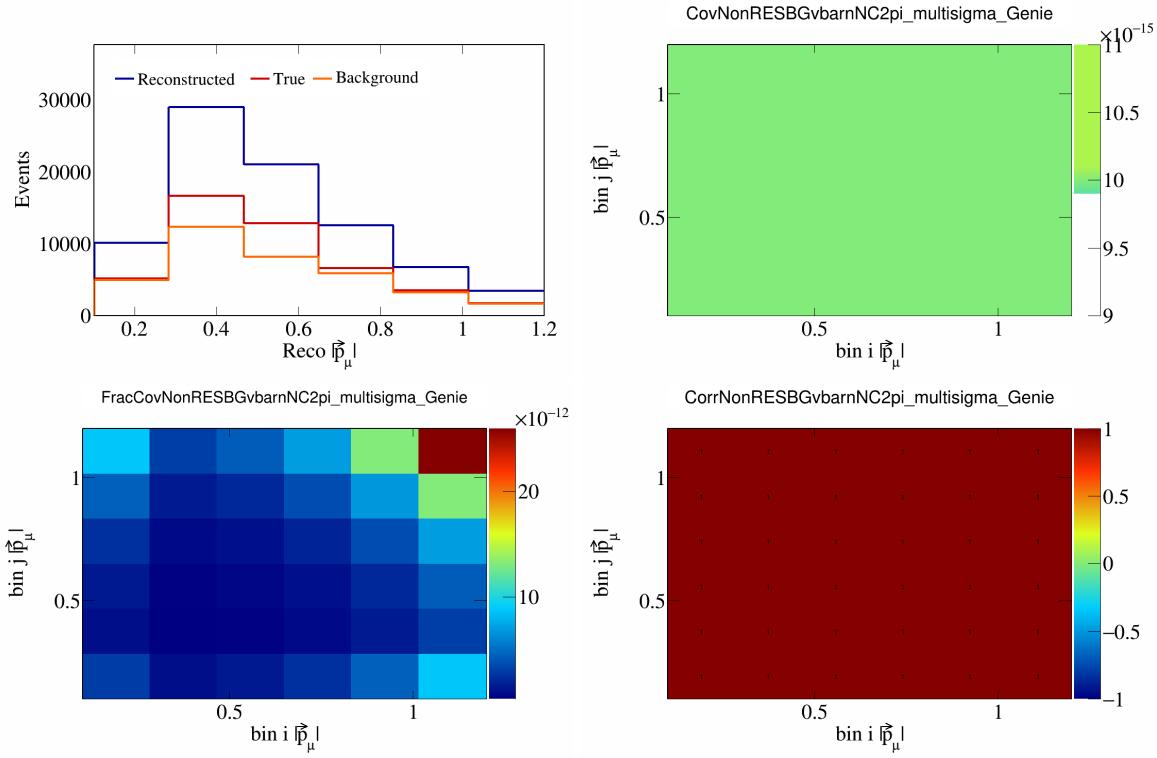


Figure 433: NonRESBGvbarNC2pi variations for  $|\vec{p}_\mu|$ .

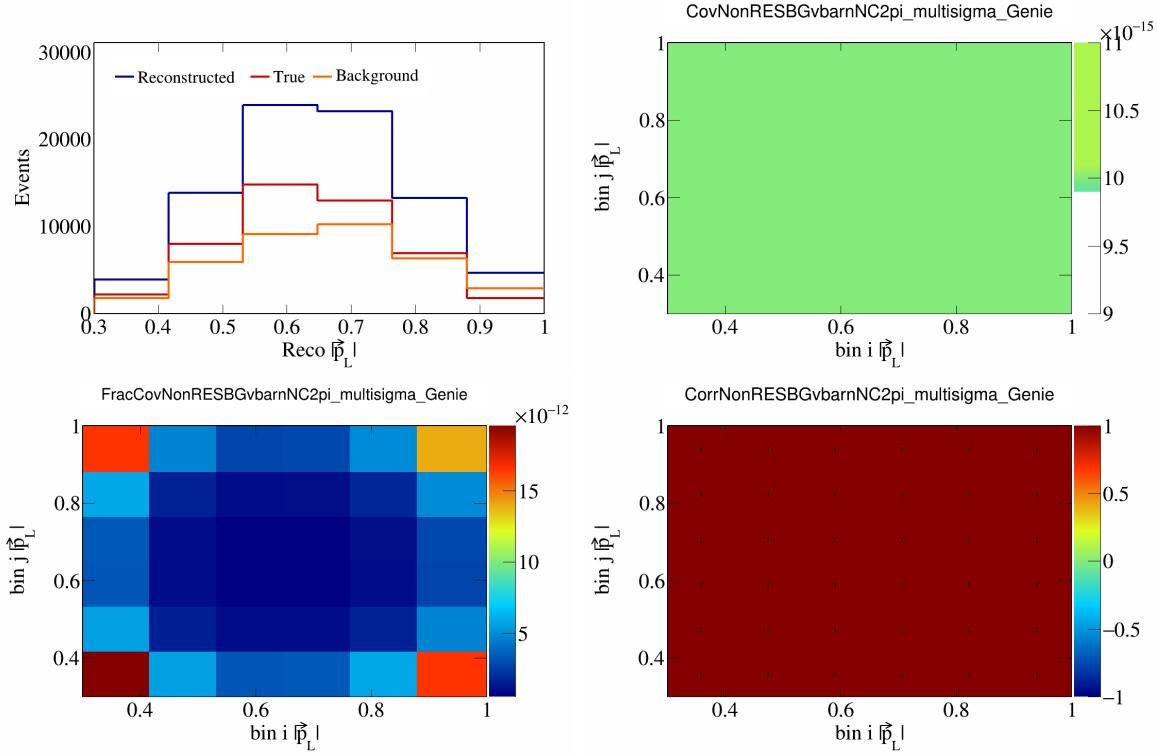


Figure 434: NonRESBGvbarNC2pi variations for  $|\vec{p}_L|$ .

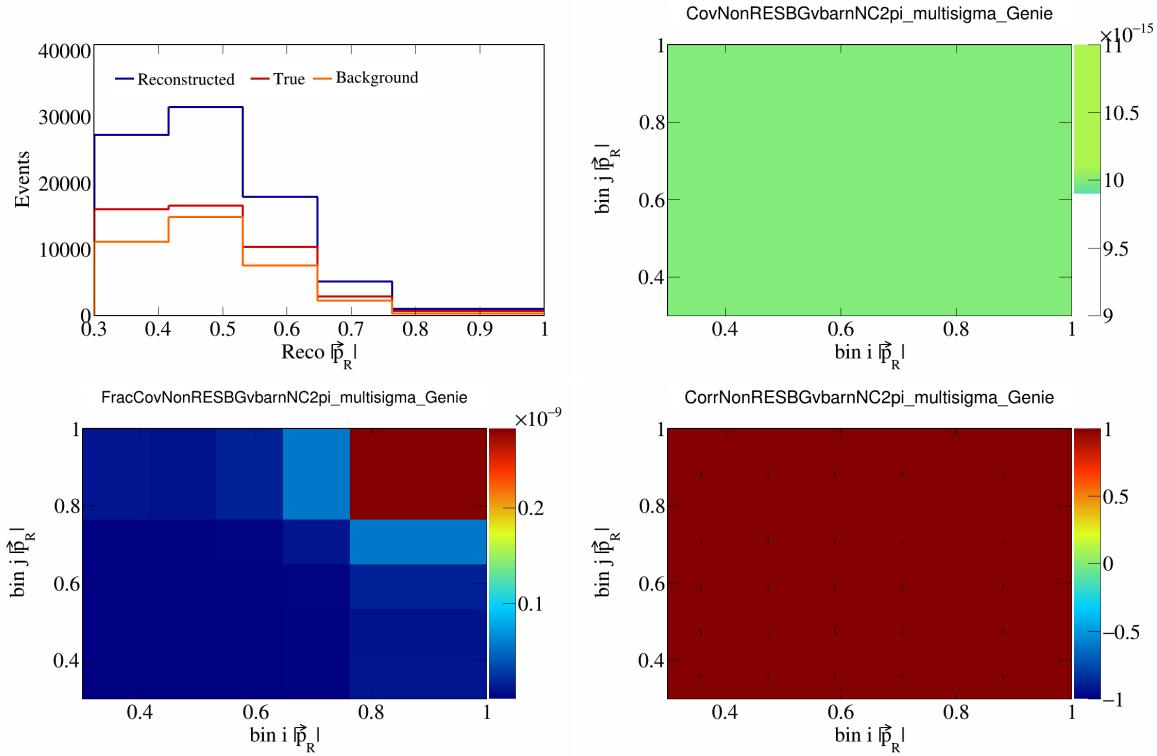


Figure 435: NonRESBGvbarNC2pi variations for  $|\vec{p}_R|$ .

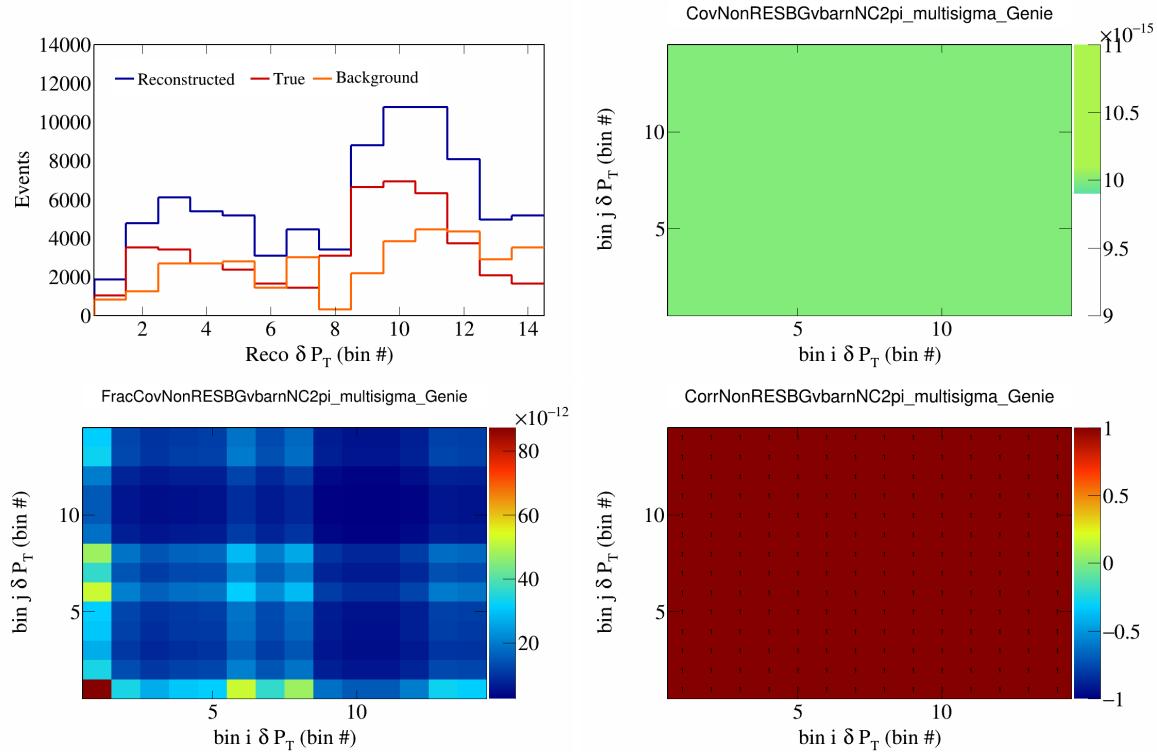


Figure 436: NonRESBGvbarNC2pi variations for  $\delta P_T$  in  $\cos(\theta_{\vec{p}_\mu})$ .

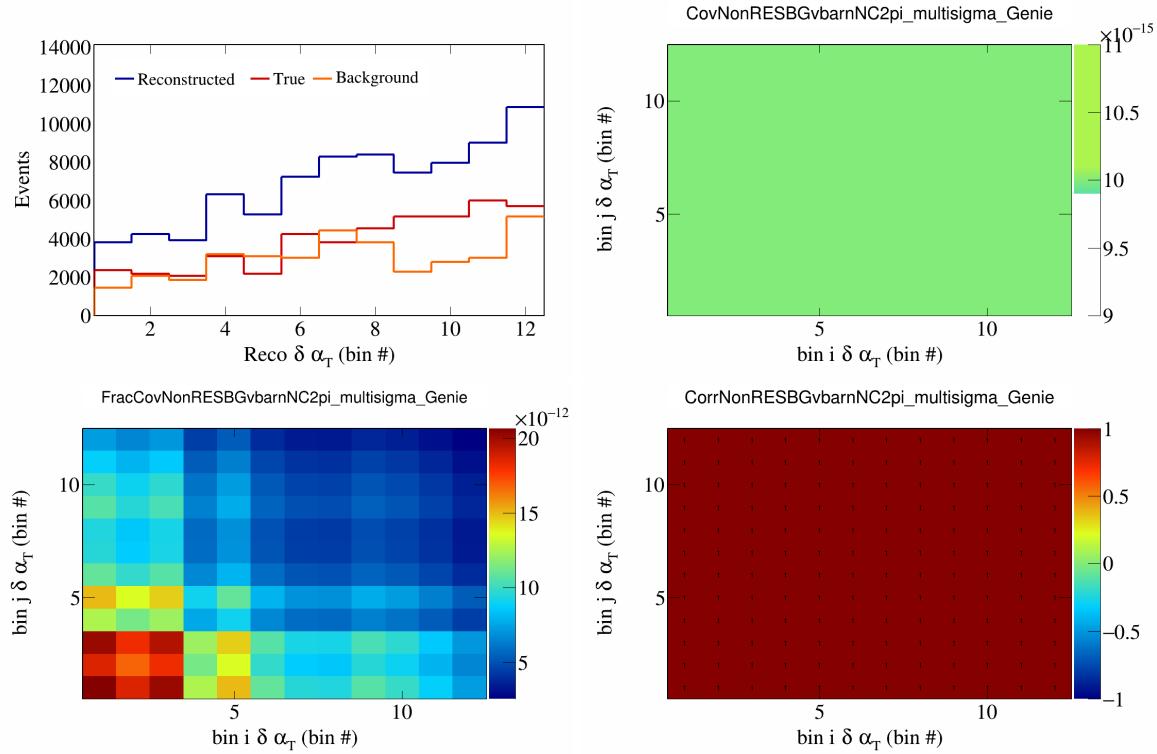


Figure 437: NonRESBGvbarNC2pi variations for  $\delta\alpha_T$  in  $\cos(\theta_{\vec{p}_\mu})$ .

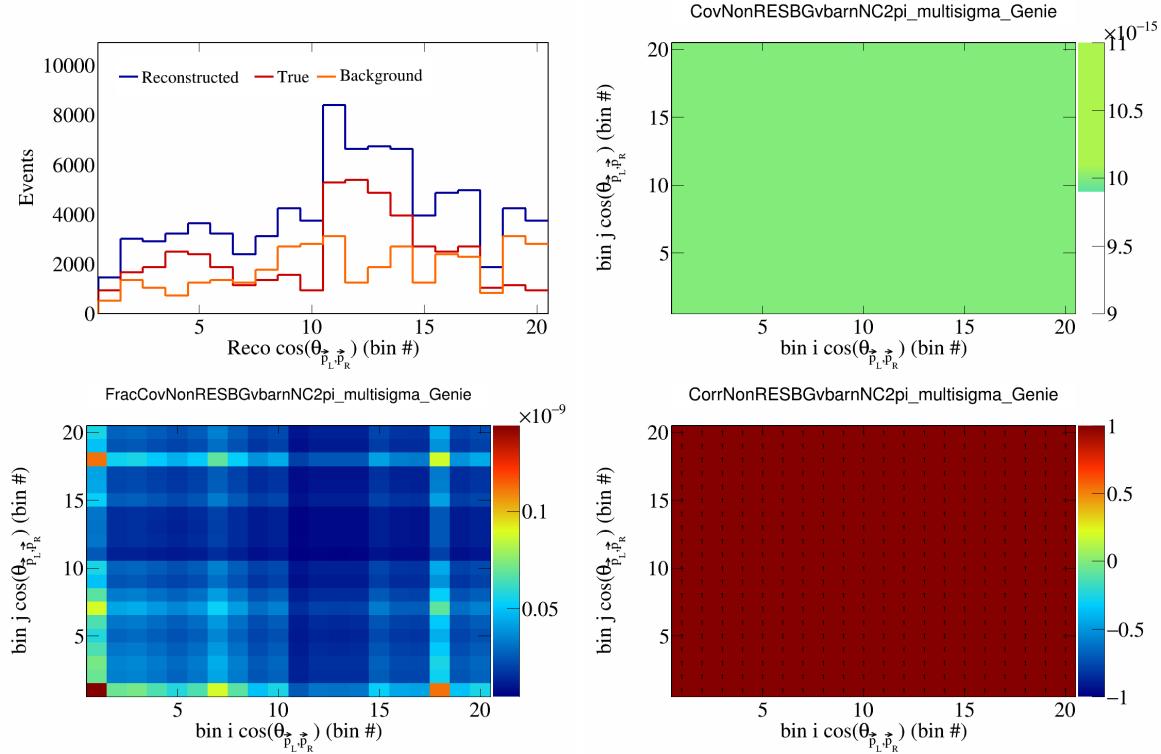


Figure 438: NonRESBGvbarNC2pi variations for  $\cos(\theta_{\vec{p}_L, \vec{p}_R})$  in  $\cos(\theta_{\vec{p}_\mu})$ .

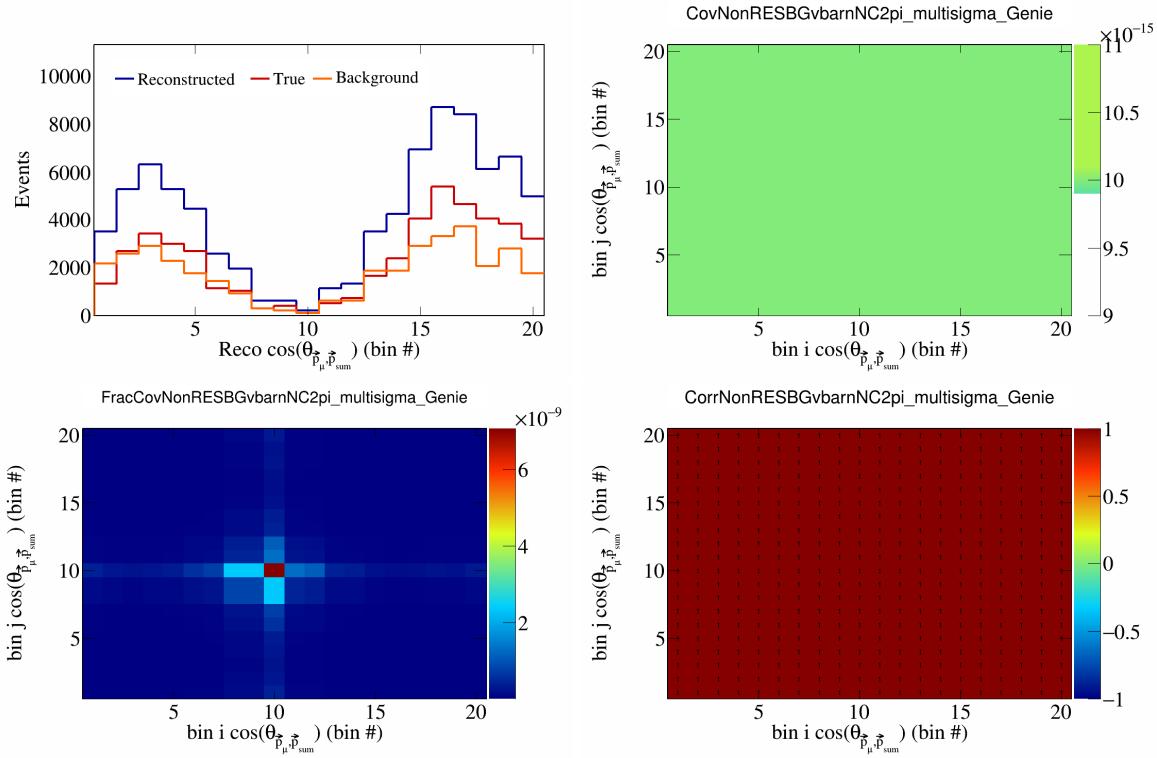


Figure 439: NonRESBGvbarNC2pi variations for  $\cos(\theta_{\vec{p}_\mu, \vec{p}_{\text{sum}}})$  in  $\cos(\theta_{\vec{p}_\mu})$ .

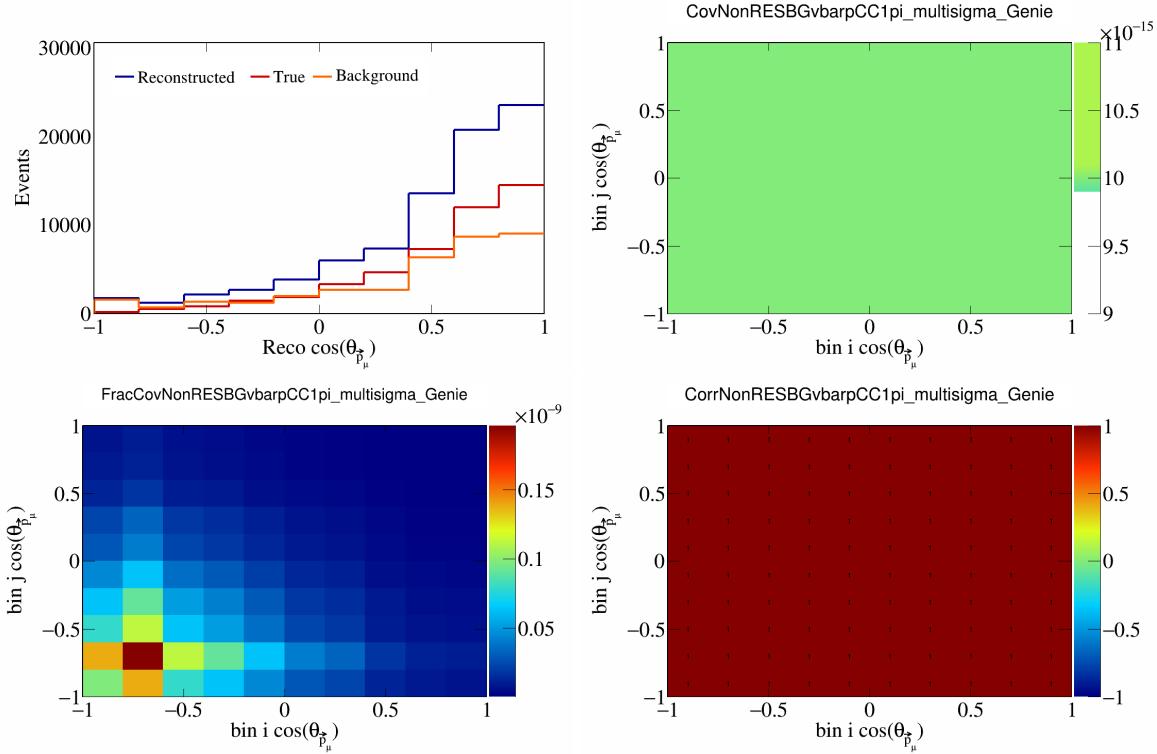


Figure 440: NonRESBGvbarCC1pi variations for  $\cos(\theta_{\vec{p}_\mu})$ .

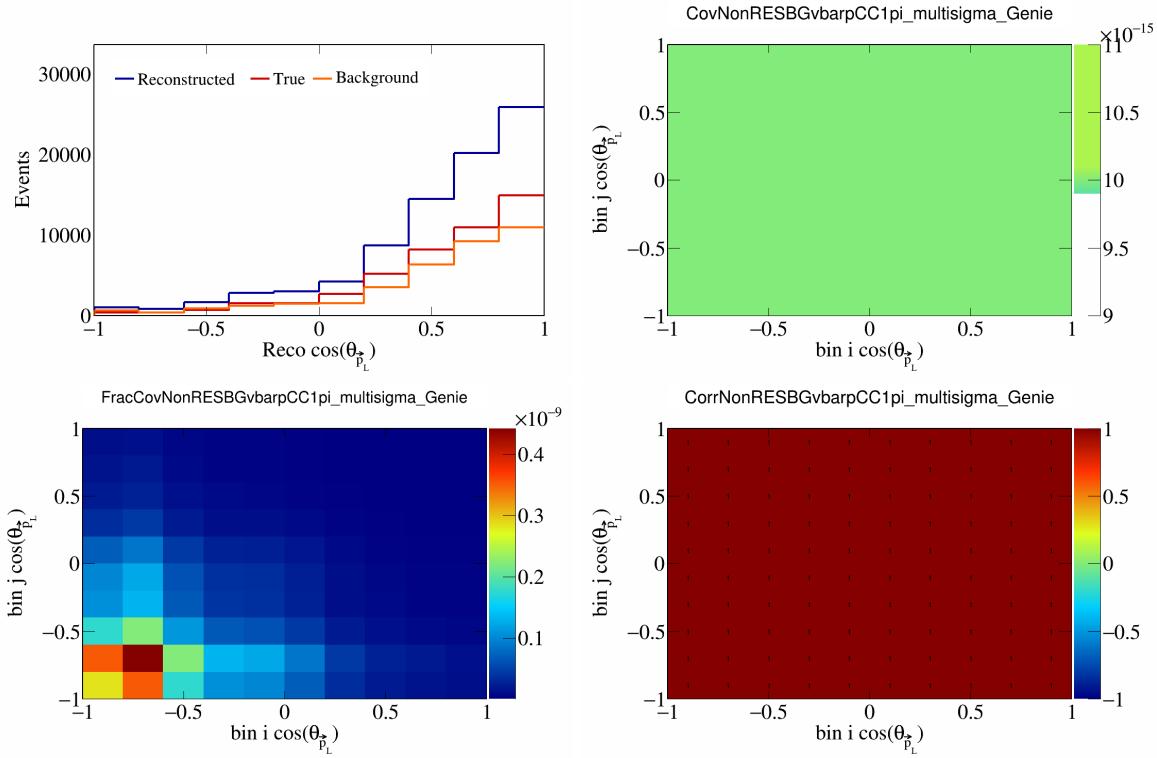


Figure 441: NonRESBGvbarpCC1pi variations for  $\cos(\theta_{\vec{p}_L})$ .

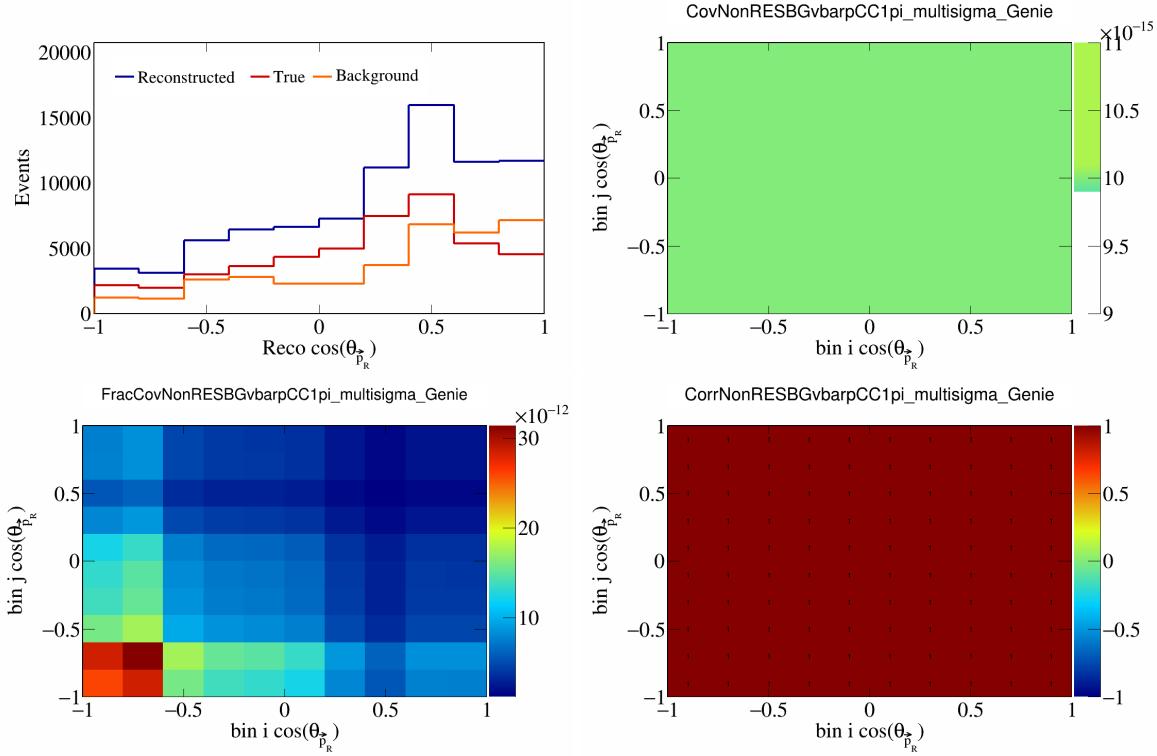


Figure 442: NonRESBGvbarpCC1pi variations for  $\cos(\theta_{\vec{p}_R})$ .

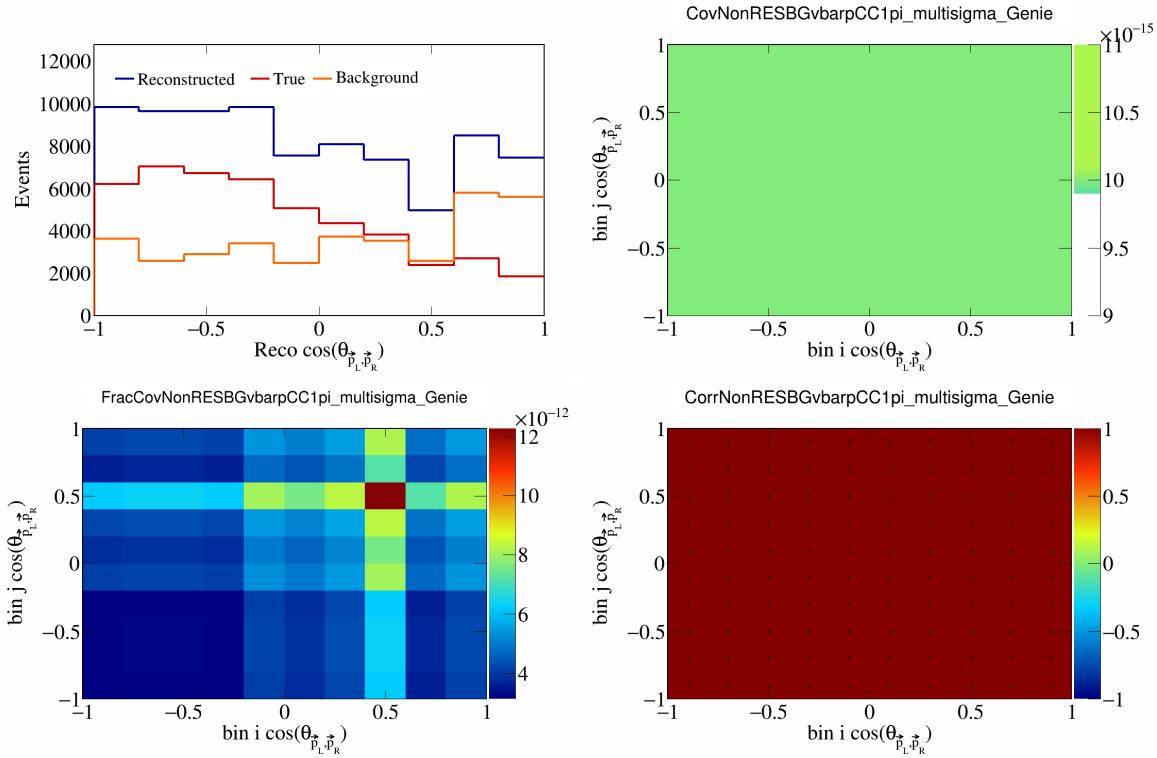


Figure 443: NonRESBGvbarpCC1pi variations for  $\cos(\theta_{\vec{p}_L, \vec{p}_R})$ .

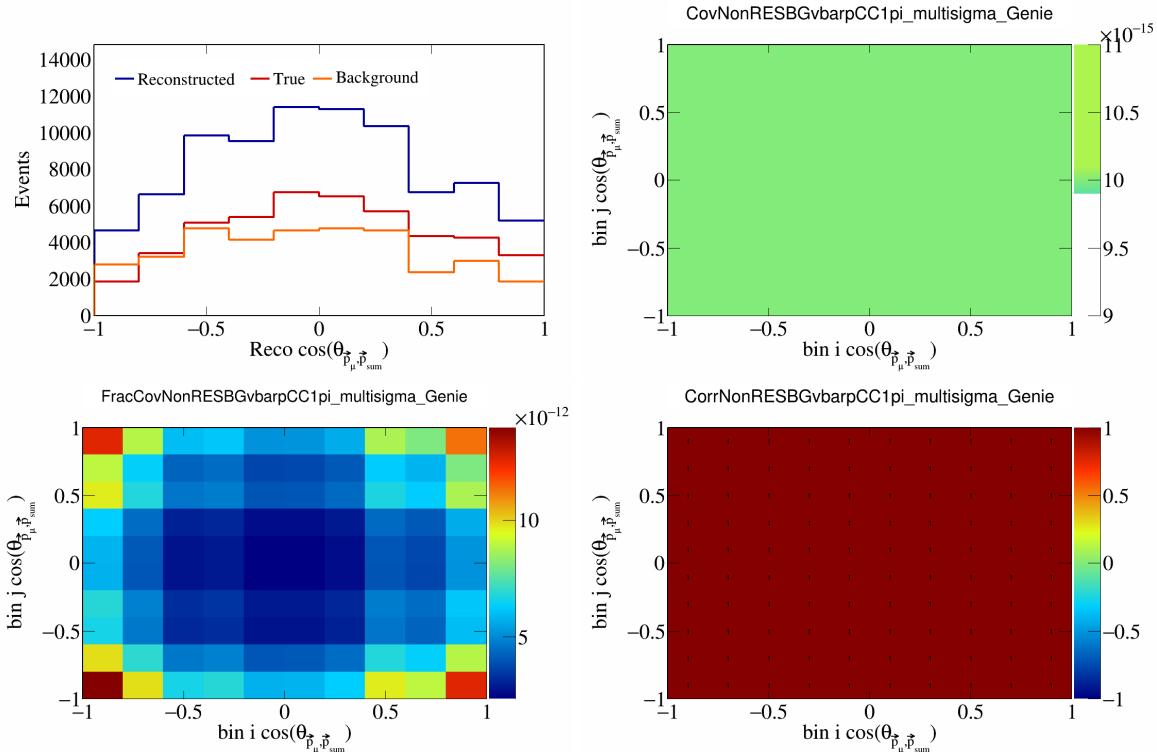


Figure 444: NonRESBGvbarpCC1pi variations for  $\cos(\theta_{\vec{p}_\mu, \vec{p}_{\text{sum}}})$ .

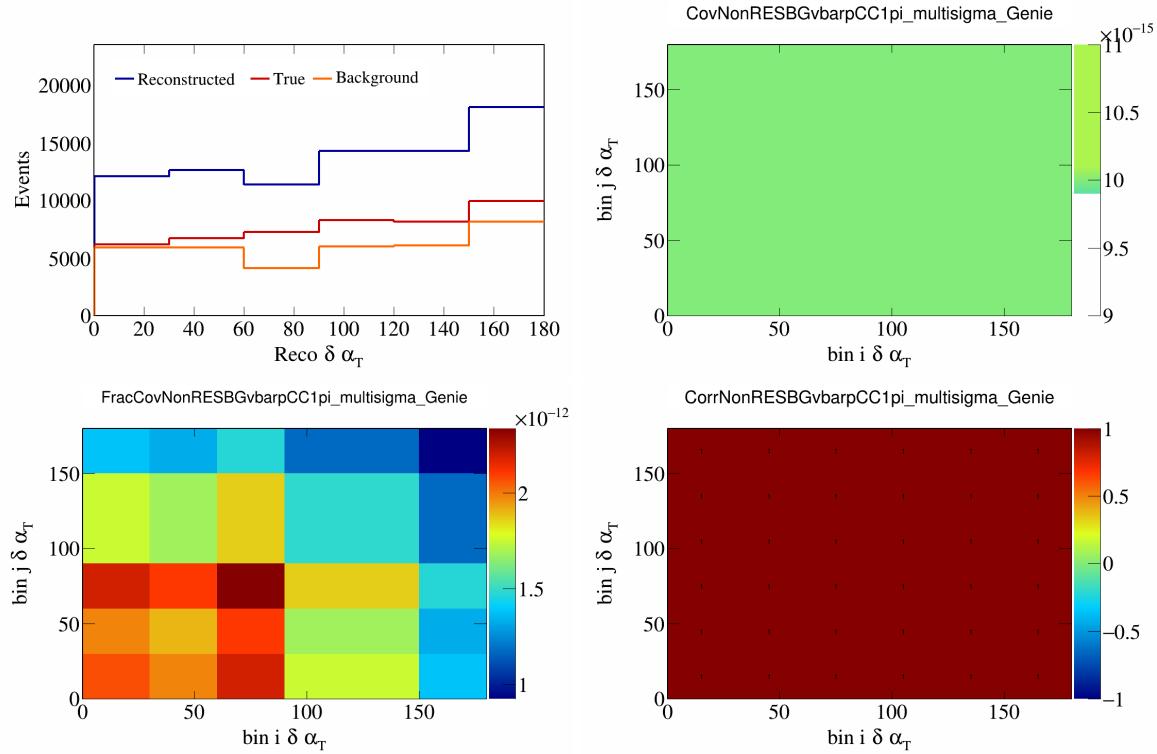


Figure 445: NonRESBGvbarpCC1pi variations for  $\delta\alpha_T$ .

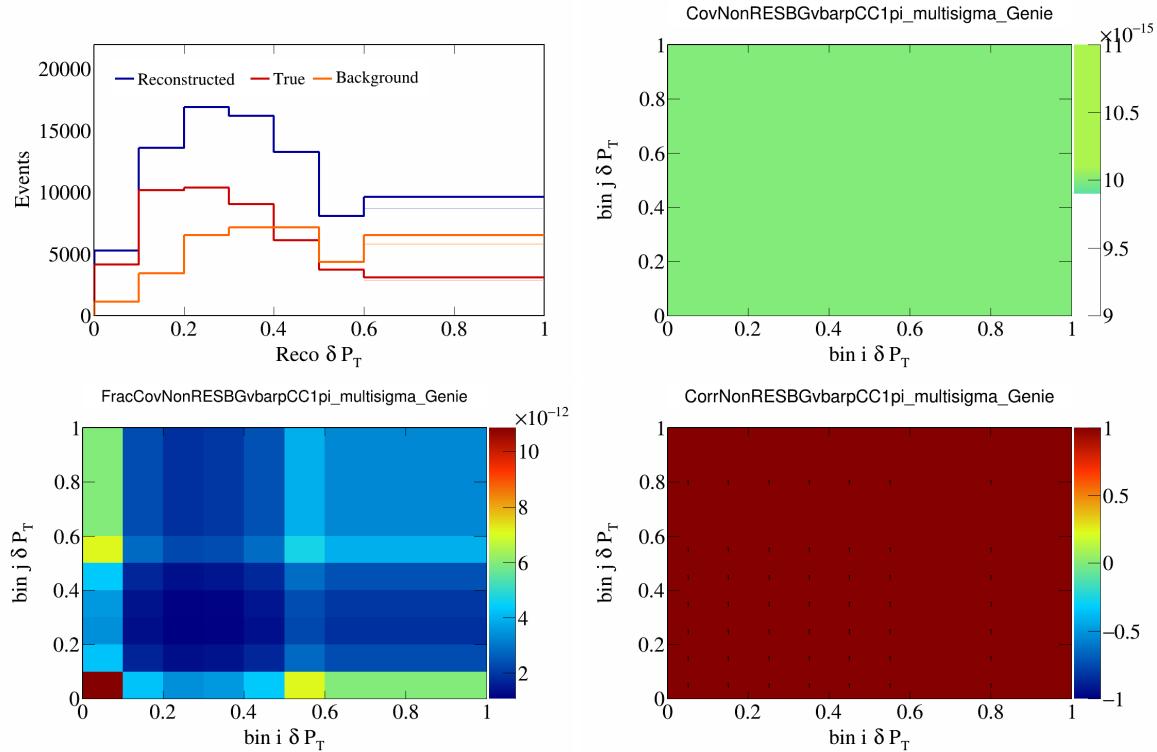


Figure 446: NonRESBGvbarpCC1pi variations for  $\delta P_T$ .

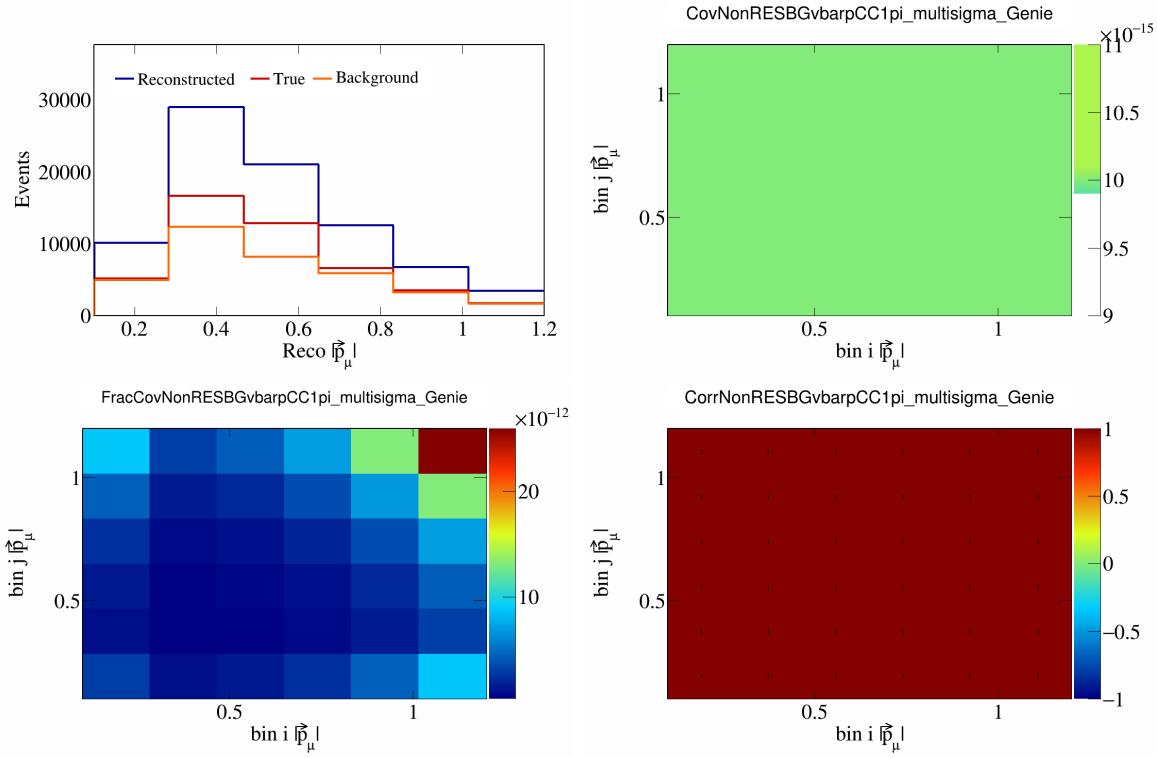


Figure 447: NonRESBGvbarpCC1pi variations for  $|\vec{p}_\mu|$ .

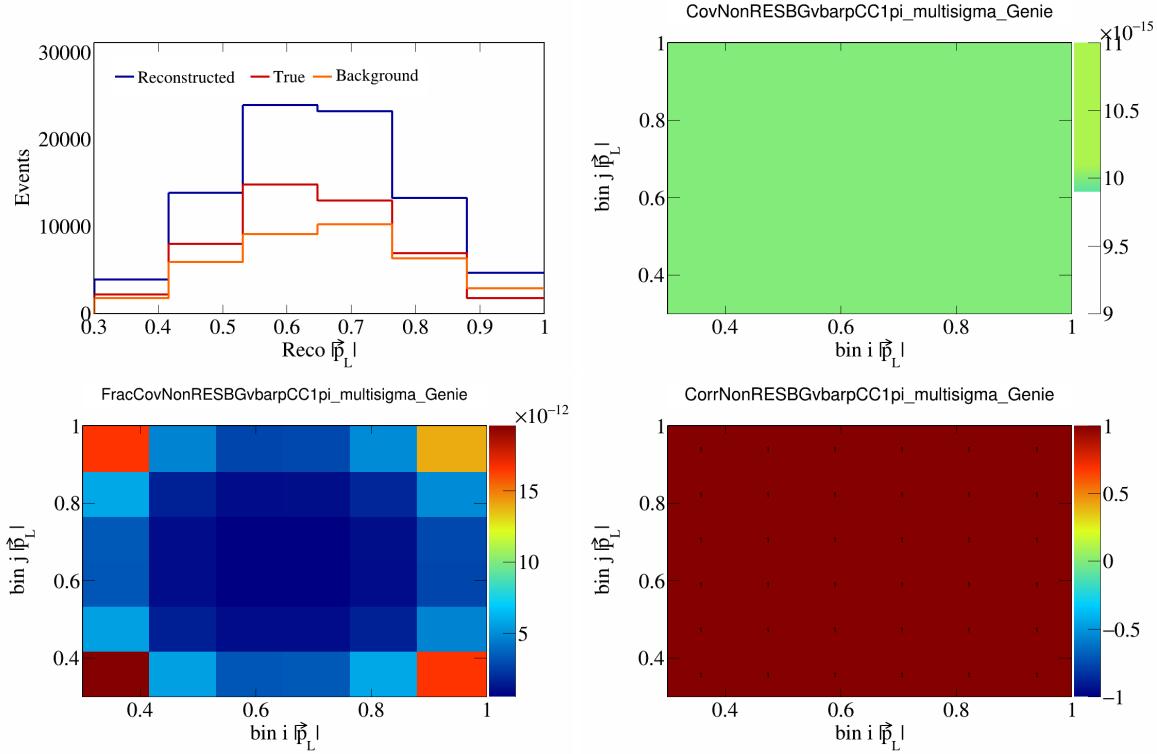


Figure 448: NonRESBGvbarpCC1pi variations for  $|\vec{p}_L|$ .

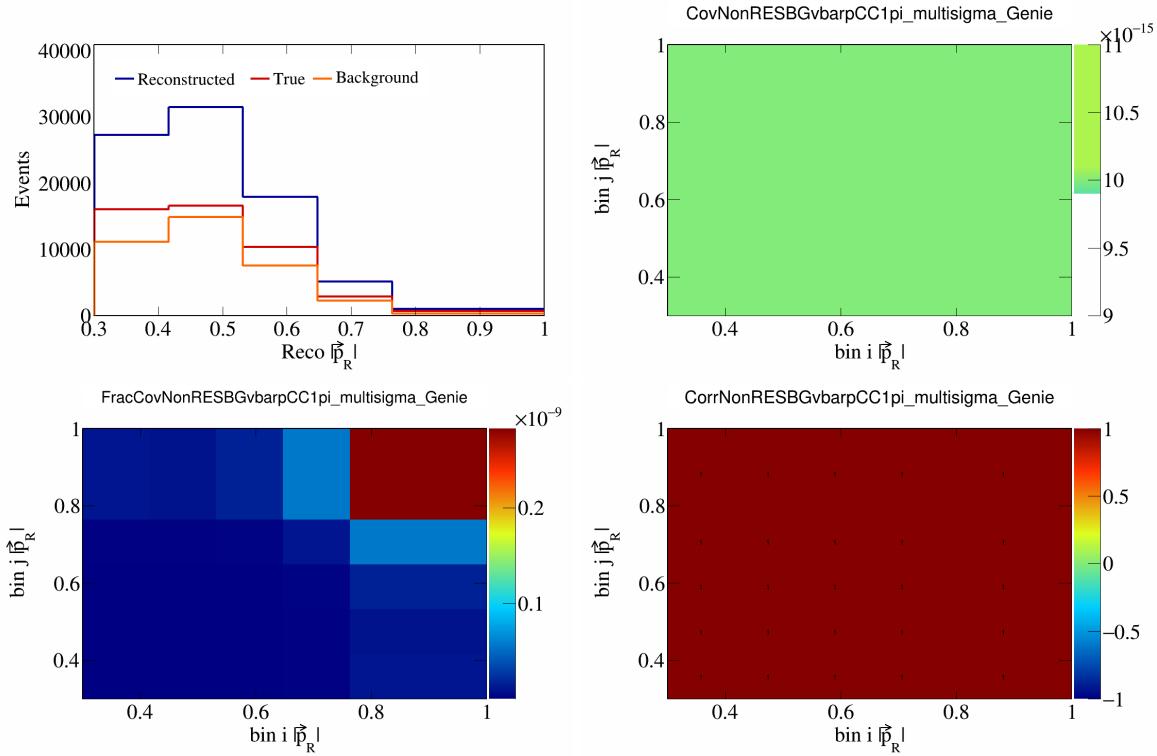


Figure 449: NonRESBGvbarpCC1pi variations for  $|\vec{p}_R|$ .

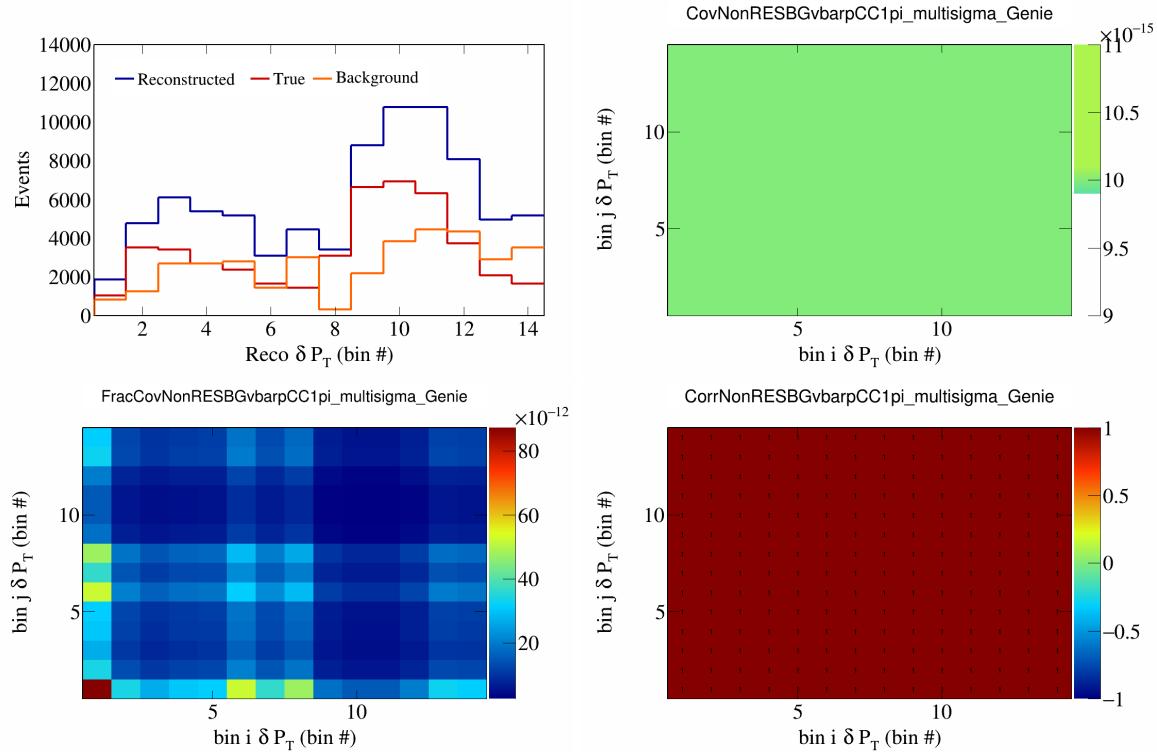


Figure 450: NonRESBGvbarpCC1pi variations for  $\delta P_T$  in  $\cos(\theta_{\vec{p}_\mu})$ .

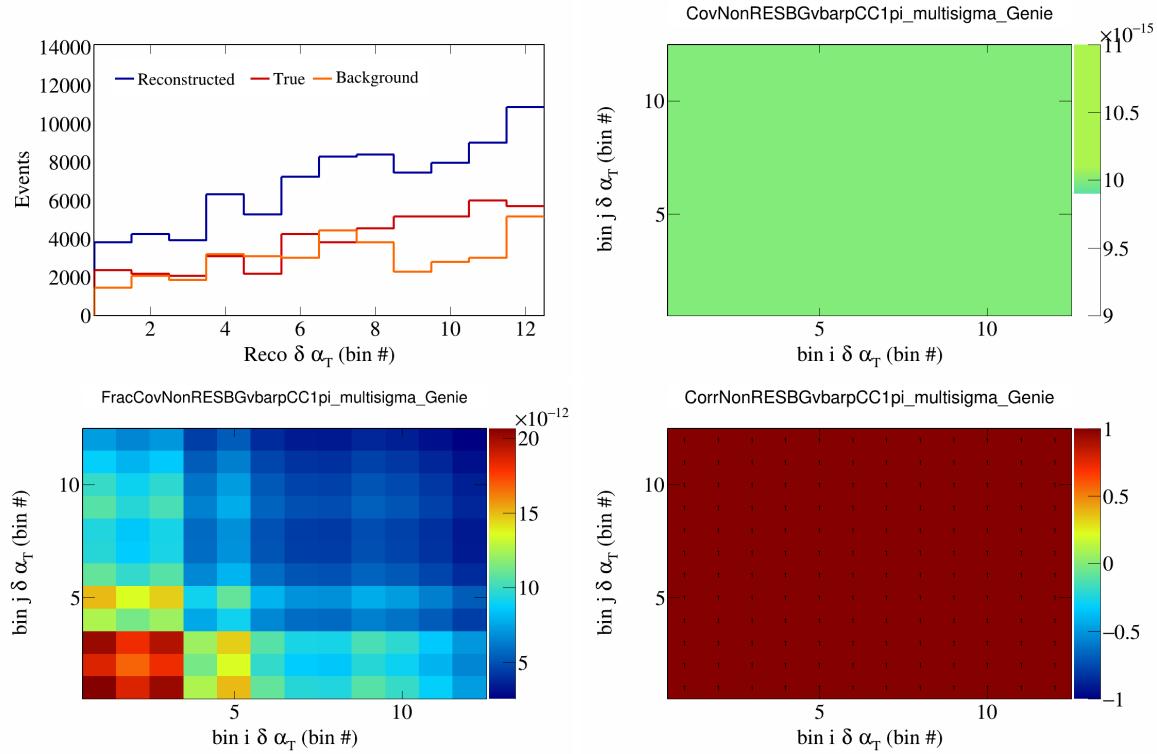


Figure 451: NonRESBGvbarpCC1pi variations for  $\delta\alpha_T$  in  $\cos(\theta_{\vec{p}_\mu})$ .

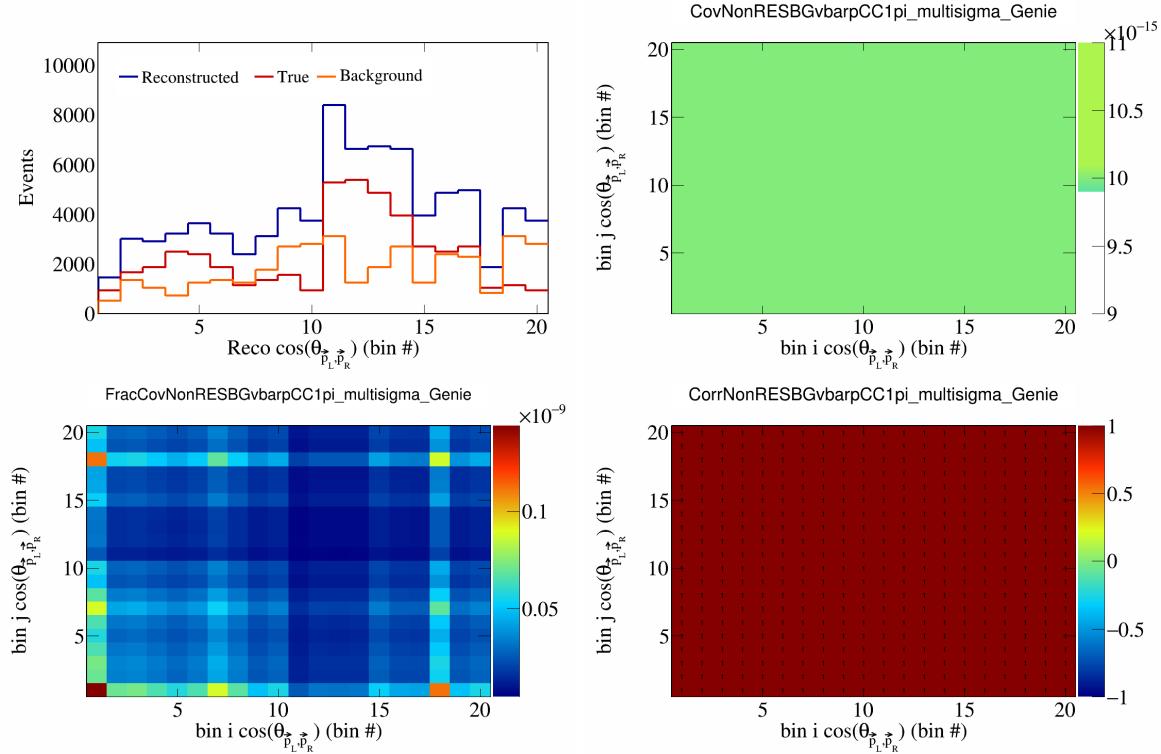


Figure 452: NonRESBGvbarpCC1pi variations for  $\cos(\theta_{\vec{p}_L, \vec{p}_R})$  in  $\cos(\theta_{\vec{p}_\mu})$ .

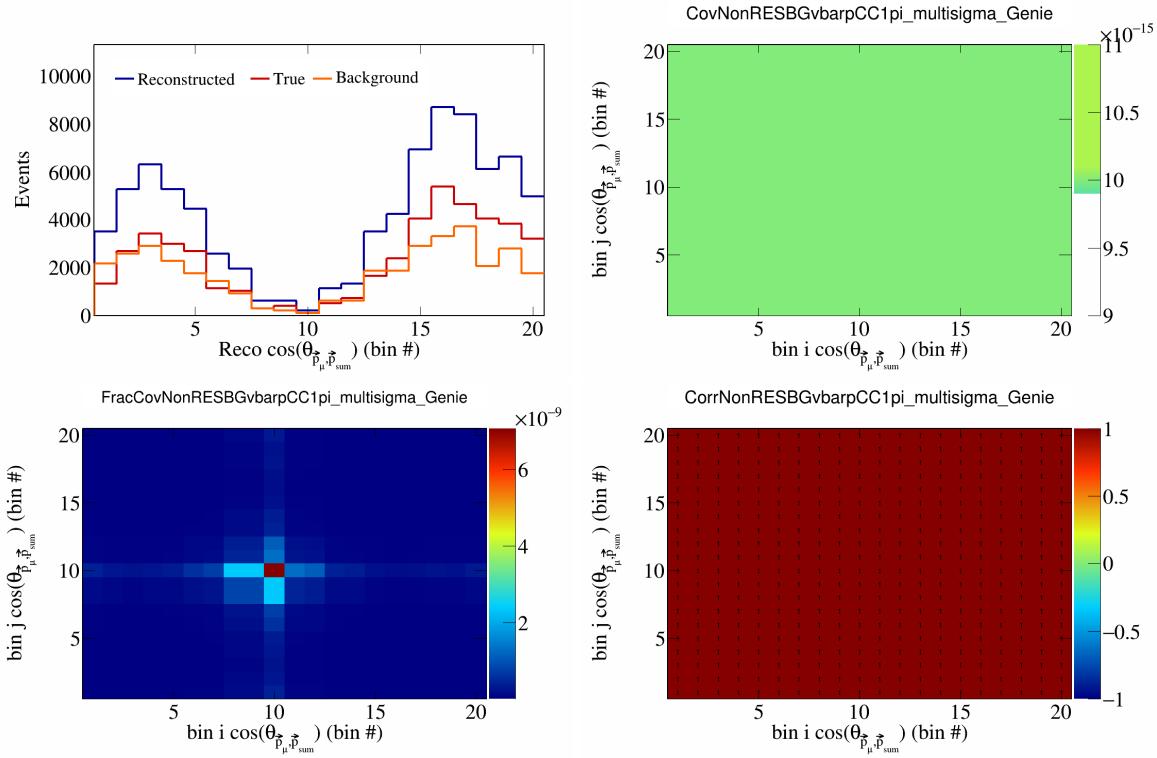


Figure 453: NonRESBGvbarpCC1pi variations for  $\cos(\theta_{\vec{p}_\mu})$  in  $\cos(\theta_{\vec{p}_\mu})$ .

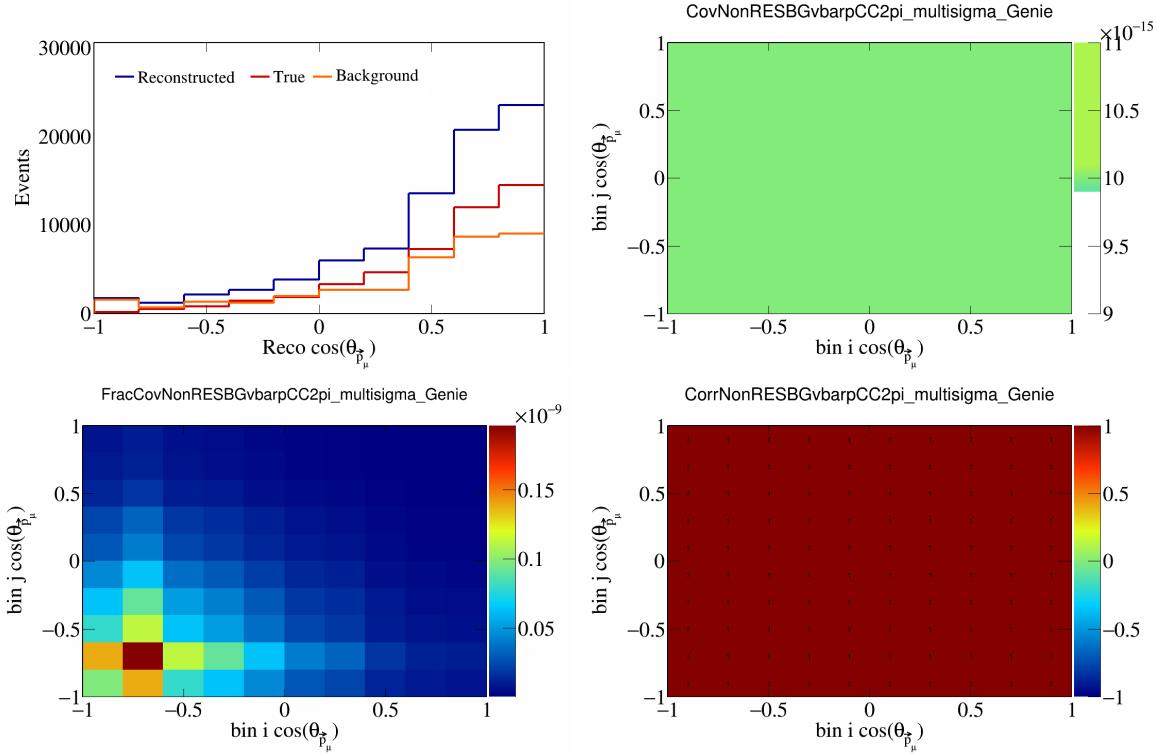


Figure 454: NonRESBGvbarpCC2pi variations for  $\cos(\theta_{\vec{p}_\mu})$ .

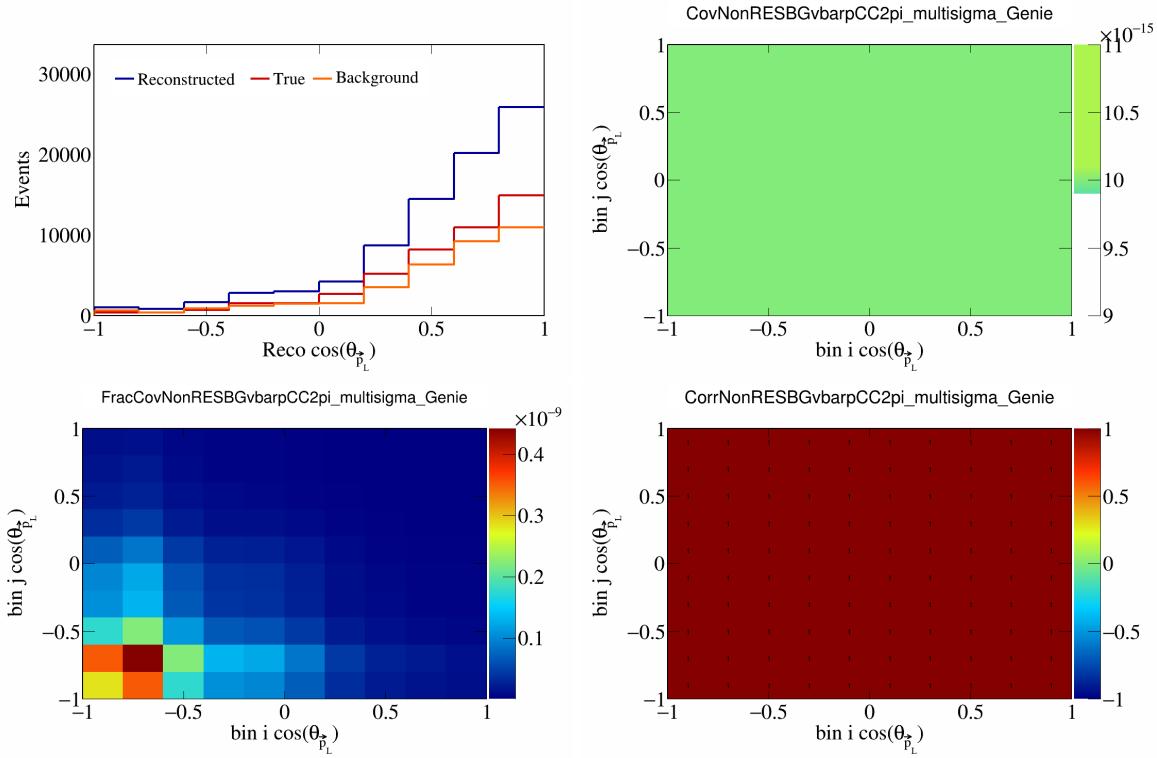


Figure 455: NonRESBGvbarpCC2pi variations for  $\cos(\theta_{\vec{F}_L})$ .

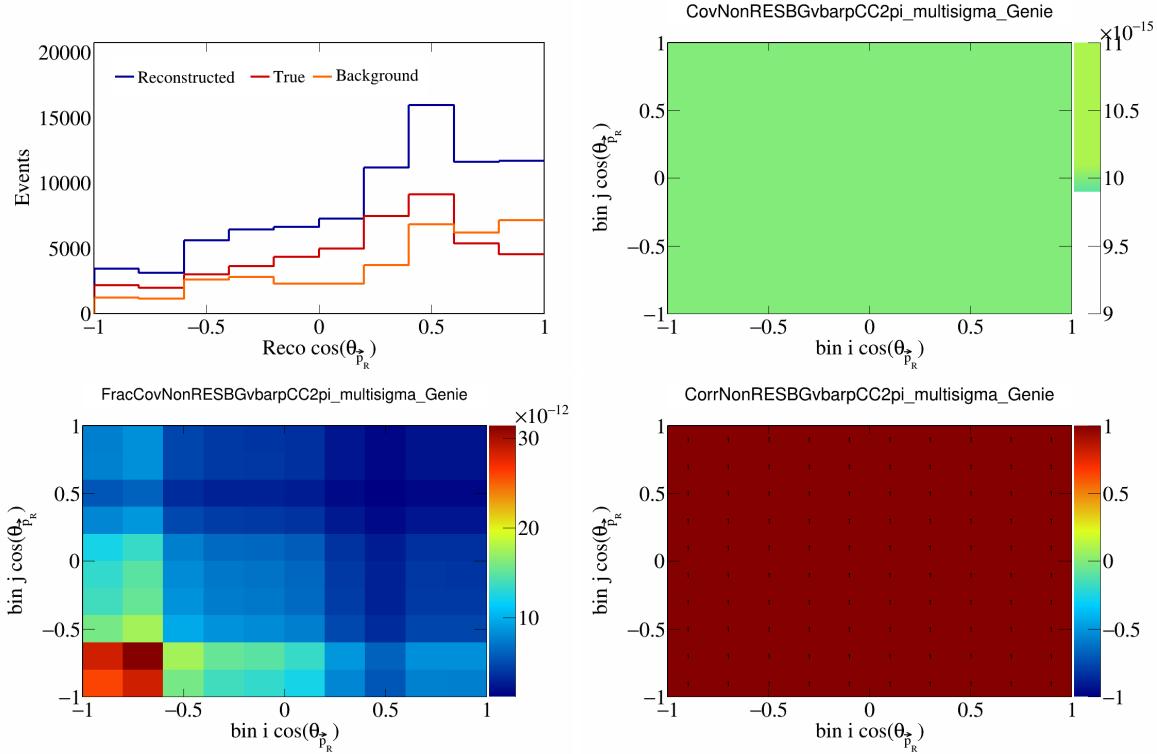


Figure 456: NonRESBGvbarpCC2pi variations for  $\cos(\theta_{\vec{F}_R})$ .

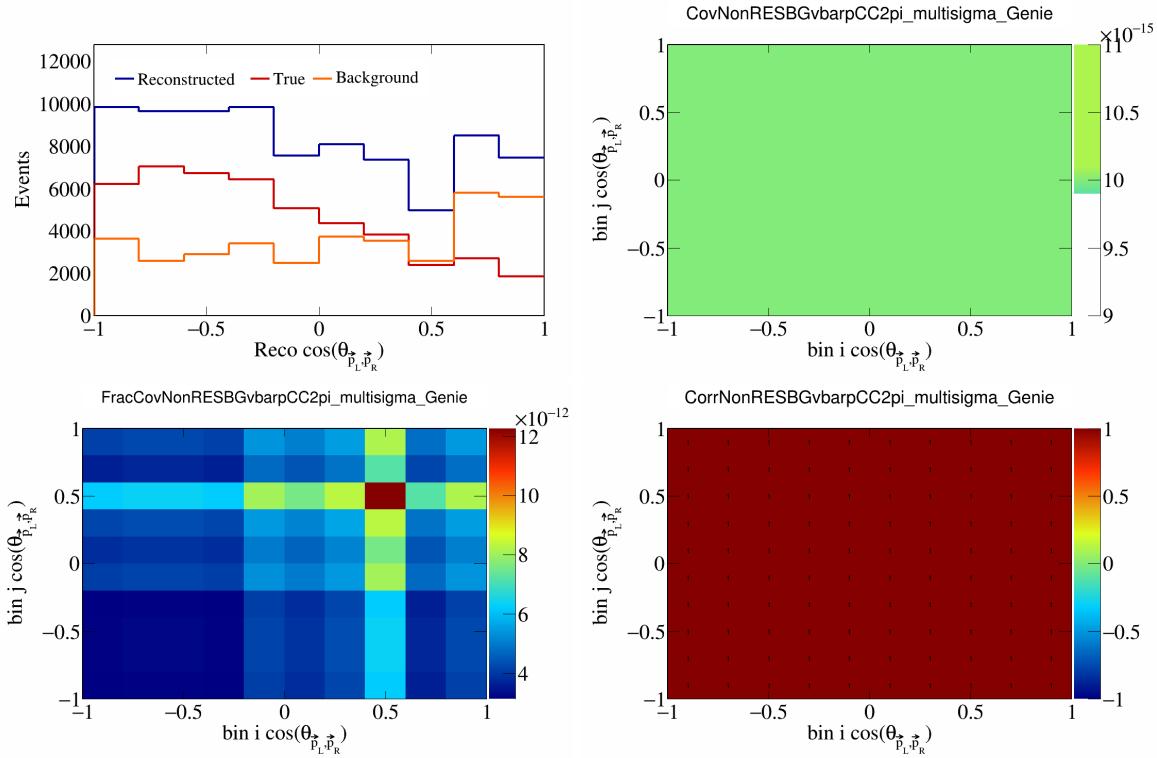


Figure 457: NonRESBGvbarpCC2pi variations for  $\cos(\theta_{\vec{p}_L, \vec{p}_R})$ .

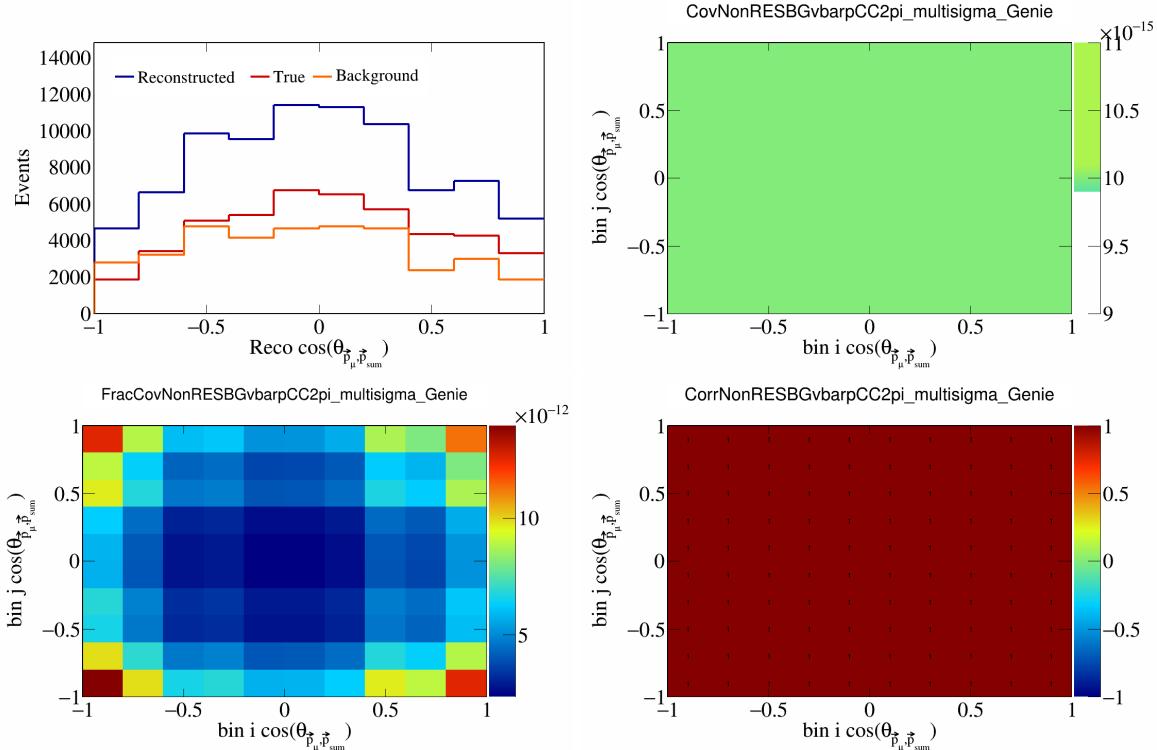


Figure 458: NonRESBGvbarpCC2pi variations for  $\cos(\theta_{\vec{p}_\mu, \vec{p}_{\text{sum}}})$ .

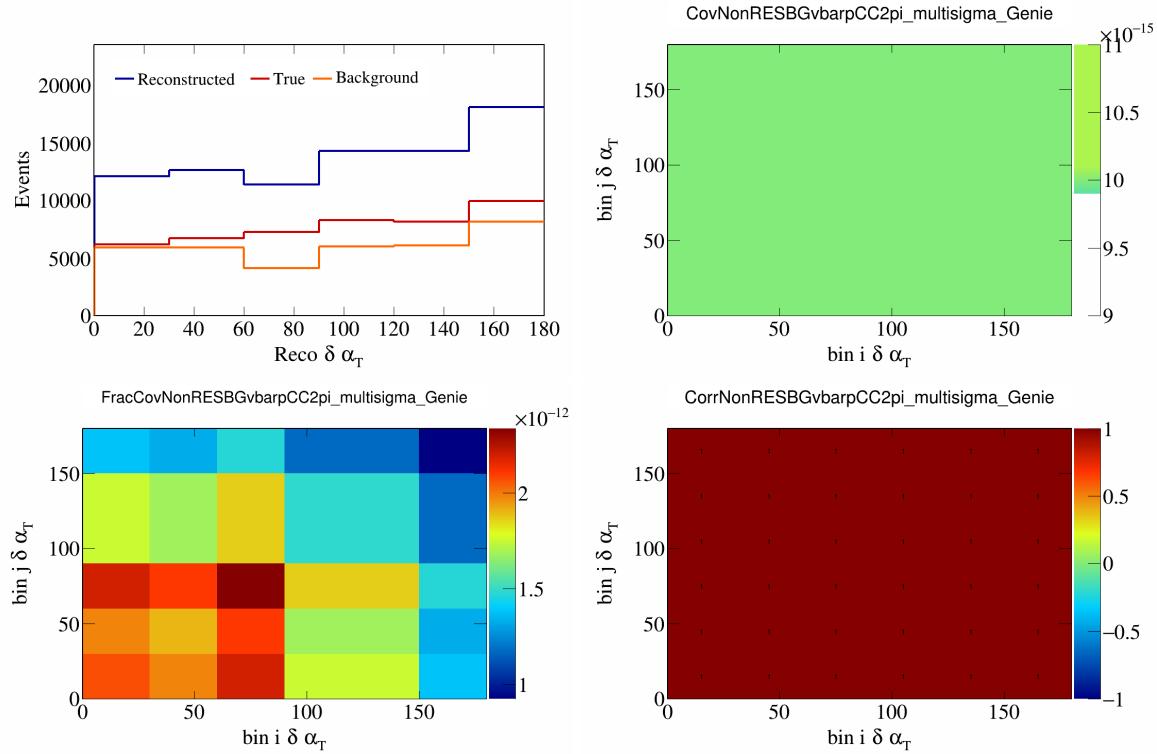


Figure 459: NonRESBGvbarpCC2pi variations for  $\delta \alpha_T$ .

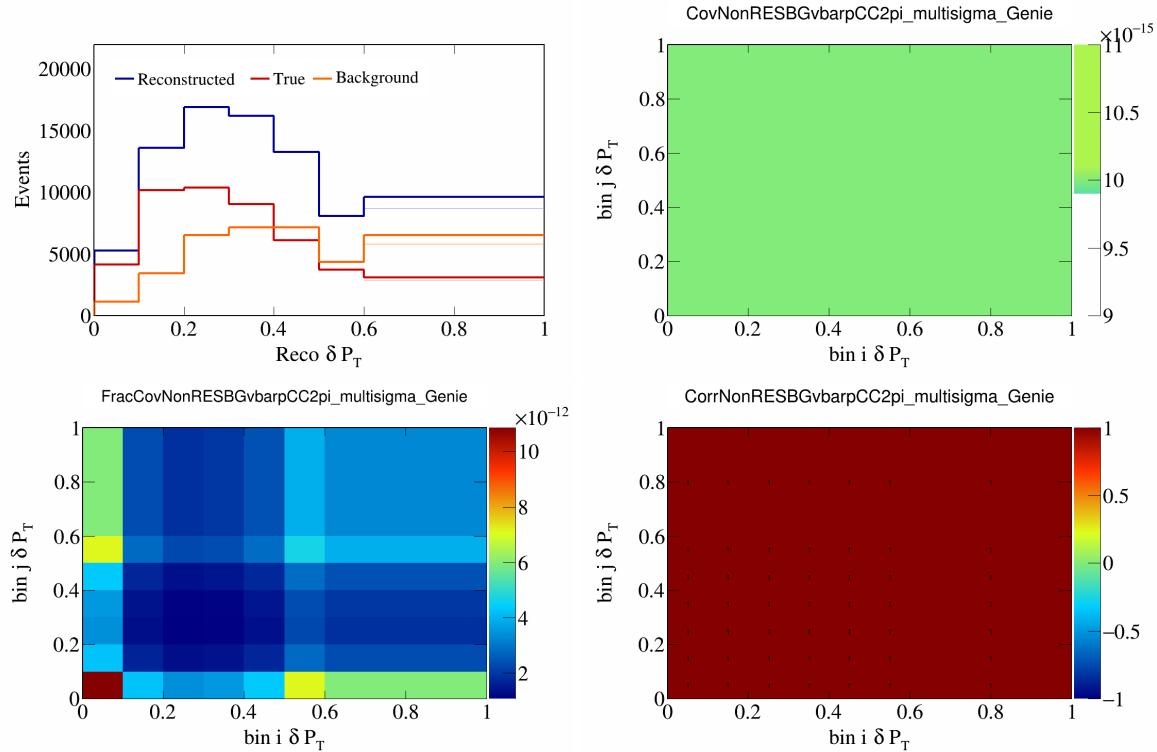


Figure 460: NonRESBGvbarpCC2pi variations for  $\delta P_T$ .

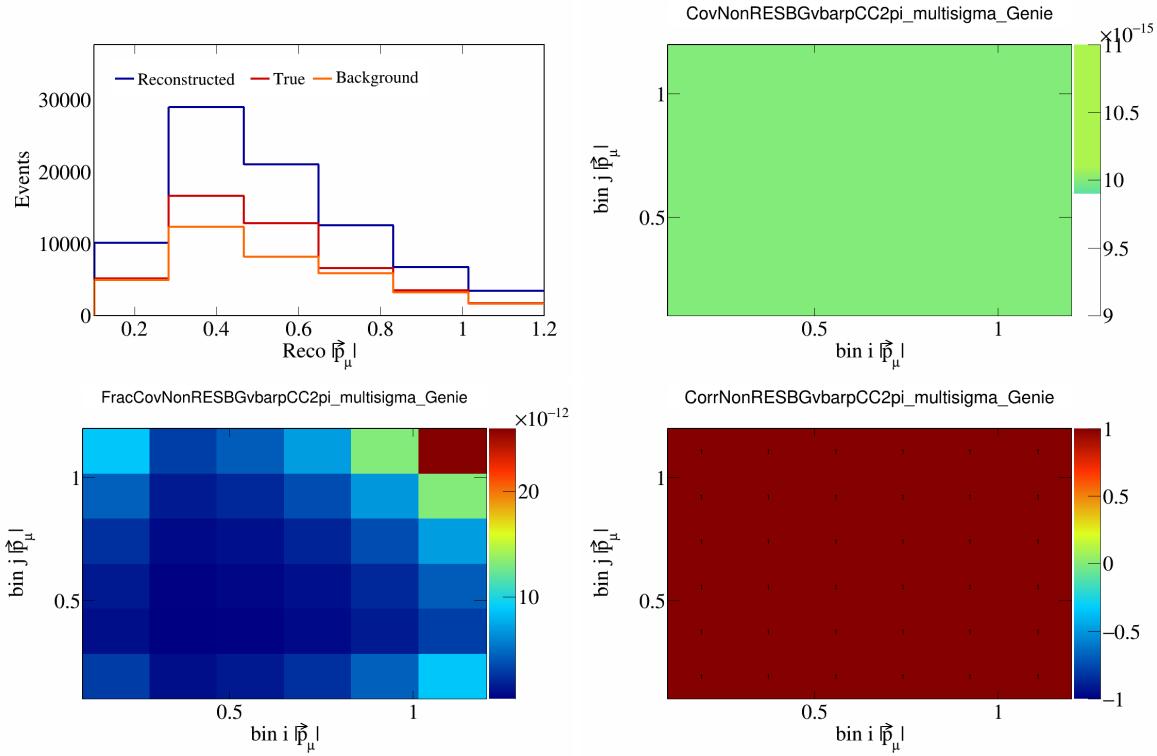


Figure 461: NonRESBGvbarpCC2pi variations for  $|\vec{p}_\mu|$ .

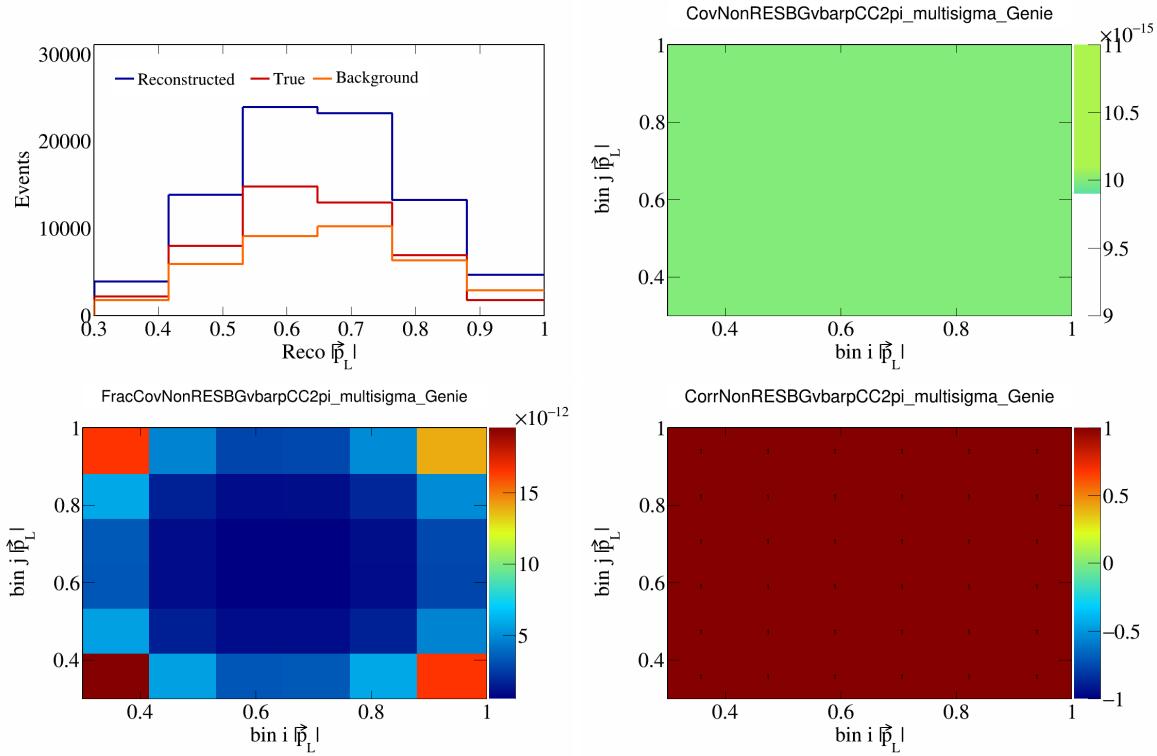


Figure 462: NonRESBGvbarpCC2pi variations for  $|\vec{p}_L|$ .

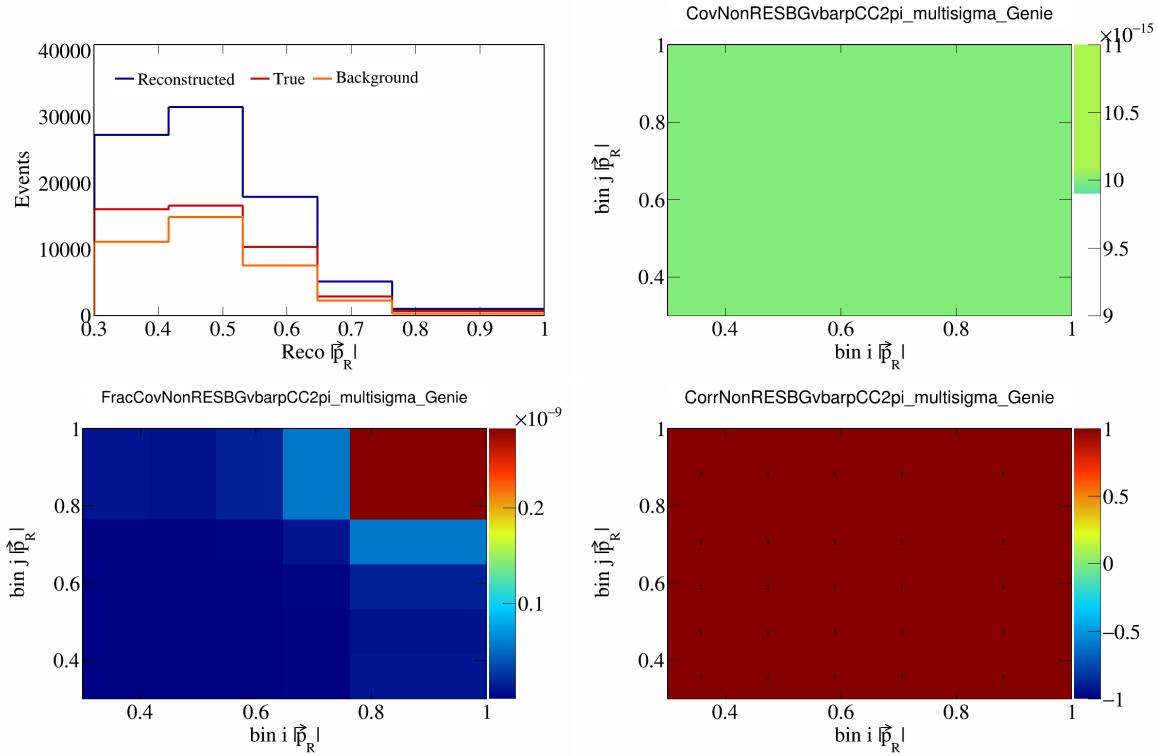


Figure 463: NonRESBGvbarpCC2pi variations for  $|\vec{p}_R|$ .

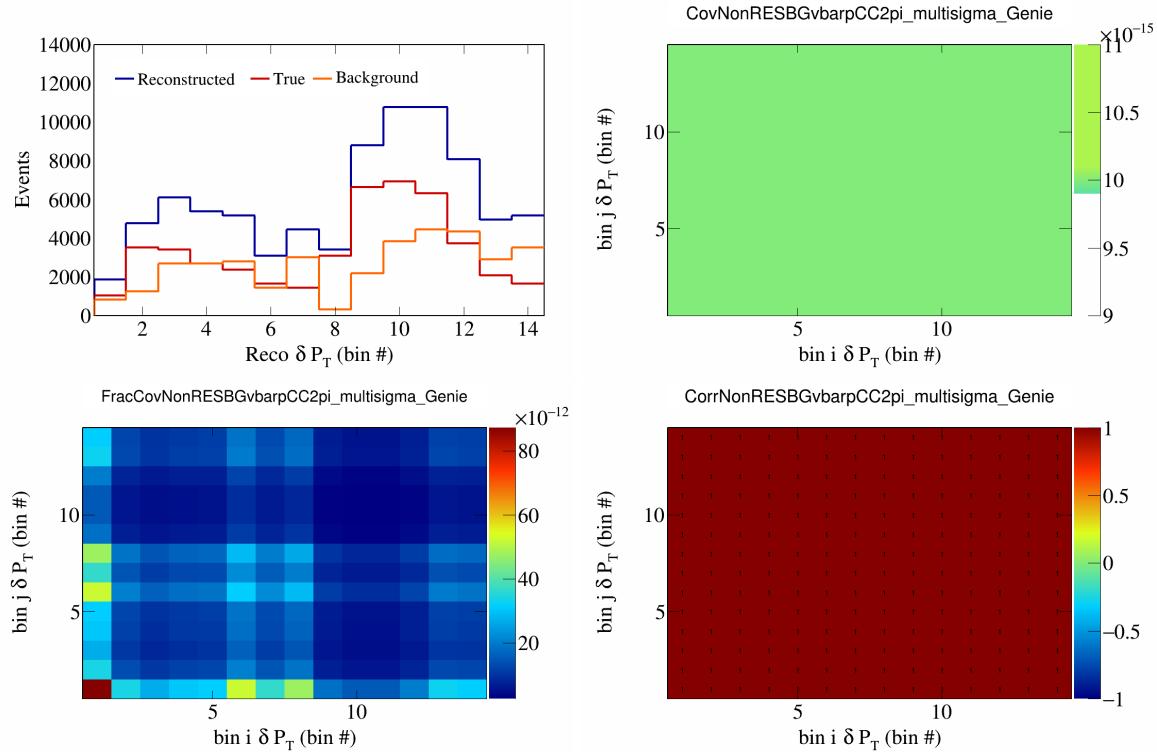


Figure 464: NonRESBGvbarpCC2pi variations for  $\delta P_T$  in  $\cos(\theta_{\vec{p}_\mu})$ .

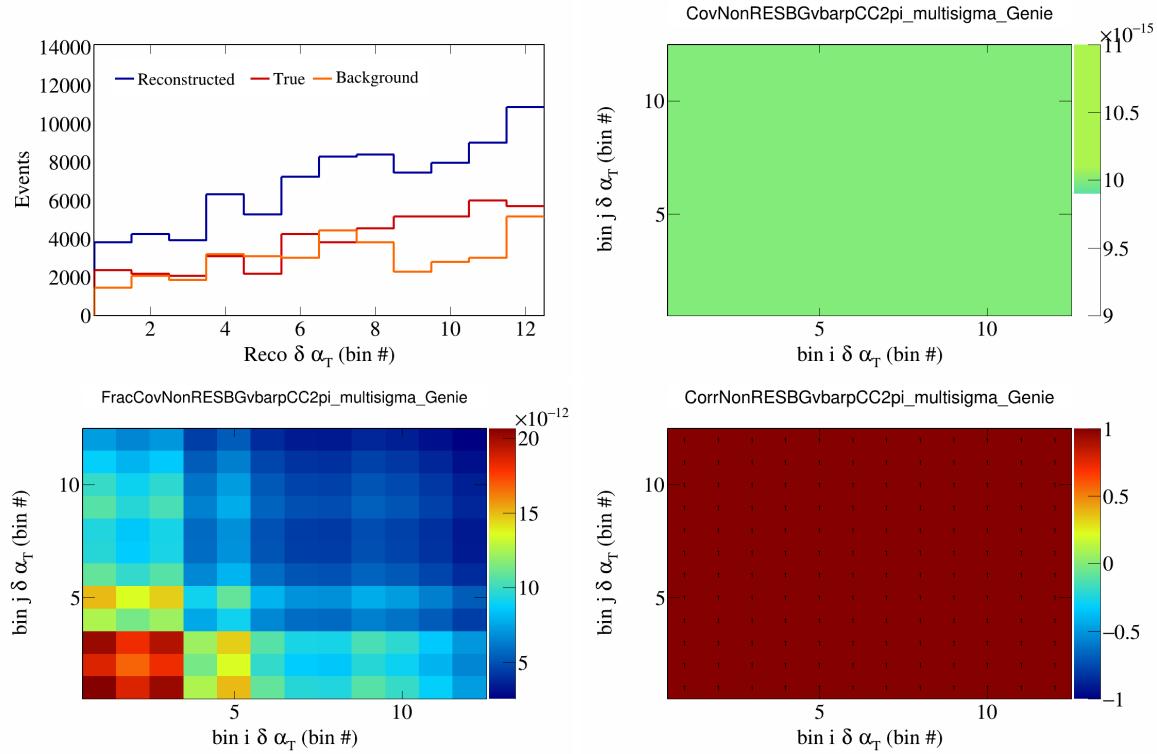


Figure 465: NonRESBGvbarpCC2pi variations for  $\delta\alpha_T$  in  $\cos(\theta_{\vec{p}_\mu})$ .

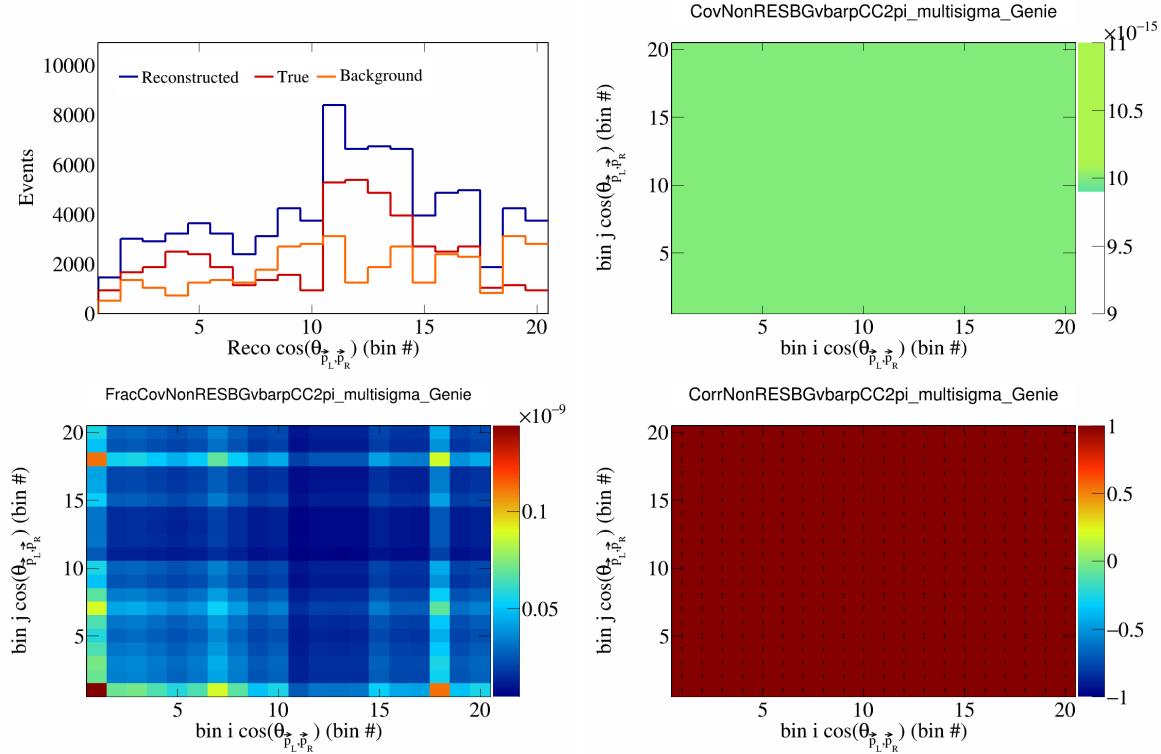


Figure 466: NonRESBGvbarpCC2pi variations for  $\cos(\theta_{\vec{p}_L, \vec{p}_R})$  in  $\cos(\theta_{\vec{p}_\mu})$ .

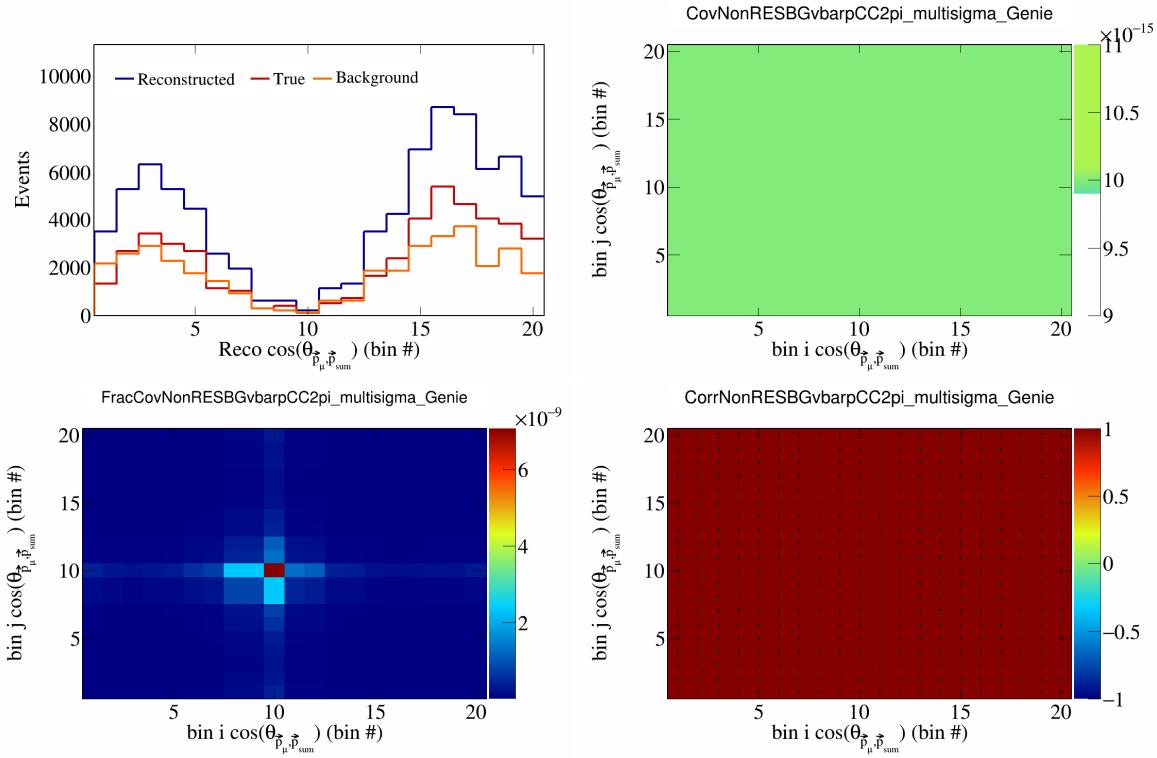


Figure 467: NonRESBGvbarpCC2pi variations for  $\cos(\theta_{\vec{p}_\mu, \vec{p}_{\text{sum}}})$  in  $\cos(\theta_{\vec{p}_\mu})$ .

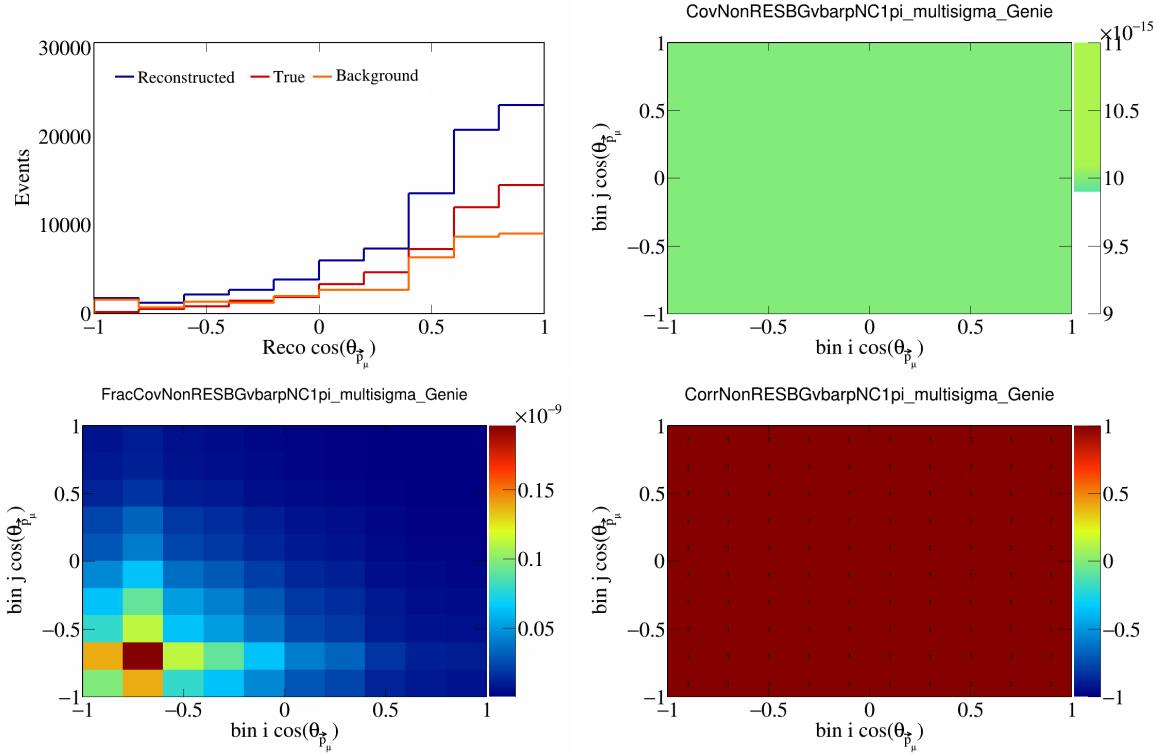


Figure 468: NonRESBGvbarpNC1pi variations for  $\cos(\theta_{\vec{p}_\mu})$ .

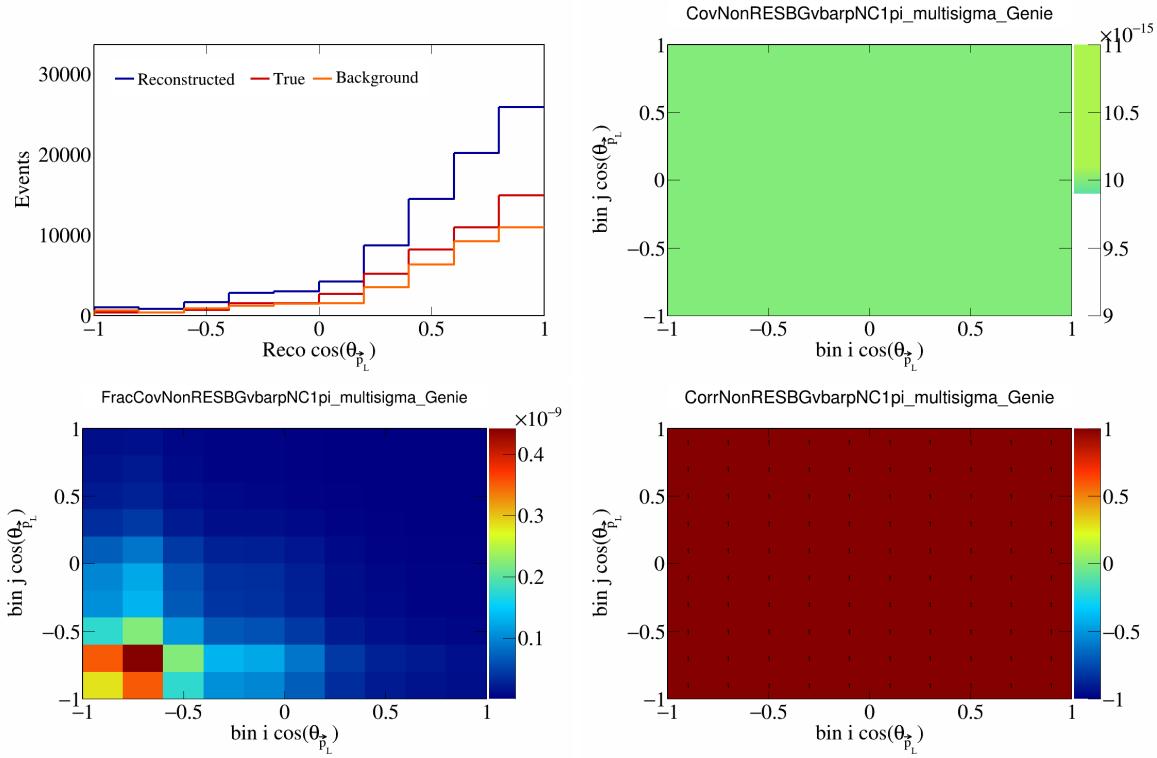


Figure 469: NonRESBGvbarpNC1pi variations for  $\cos(\theta_{\vec{p}_L})$ .

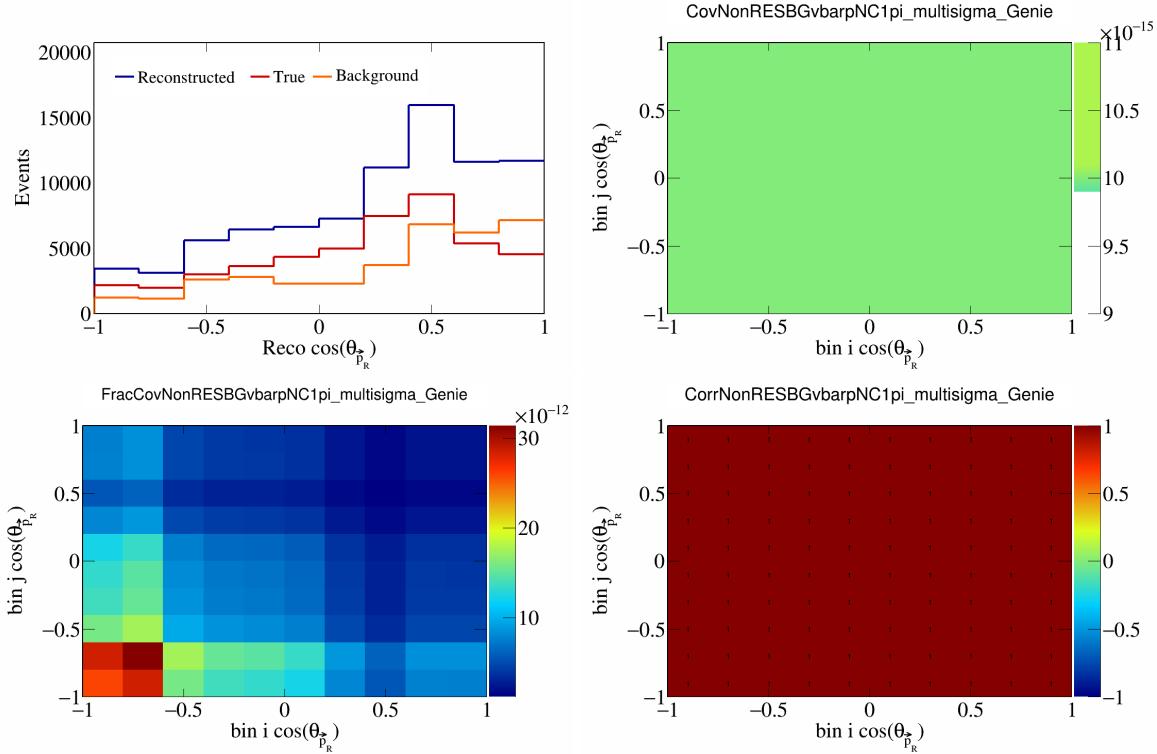


Figure 470: NonRESBGvbarpNC1pi variations for  $\cos(\theta_{\vec{p}_R})$ .

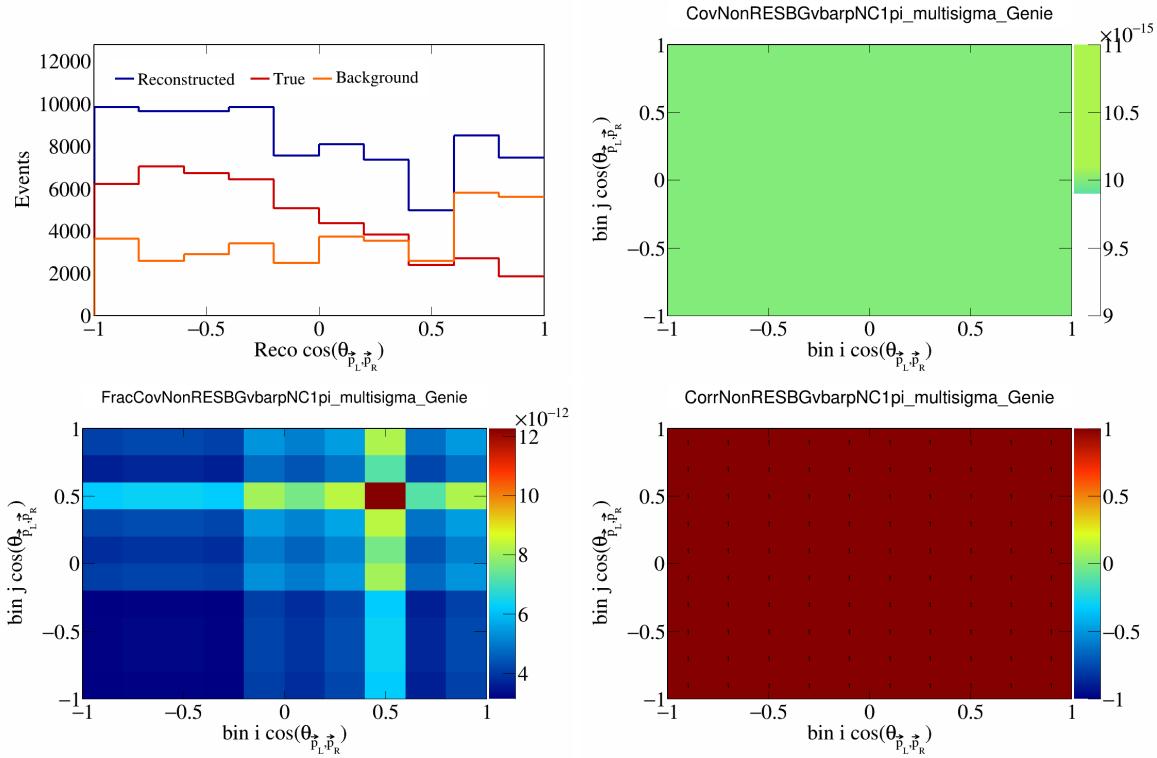


Figure 471: NonRESBGvbarpNC1pi variations for  $\cos(\theta_{\vec{p}_L, \vec{p}_R})$ .

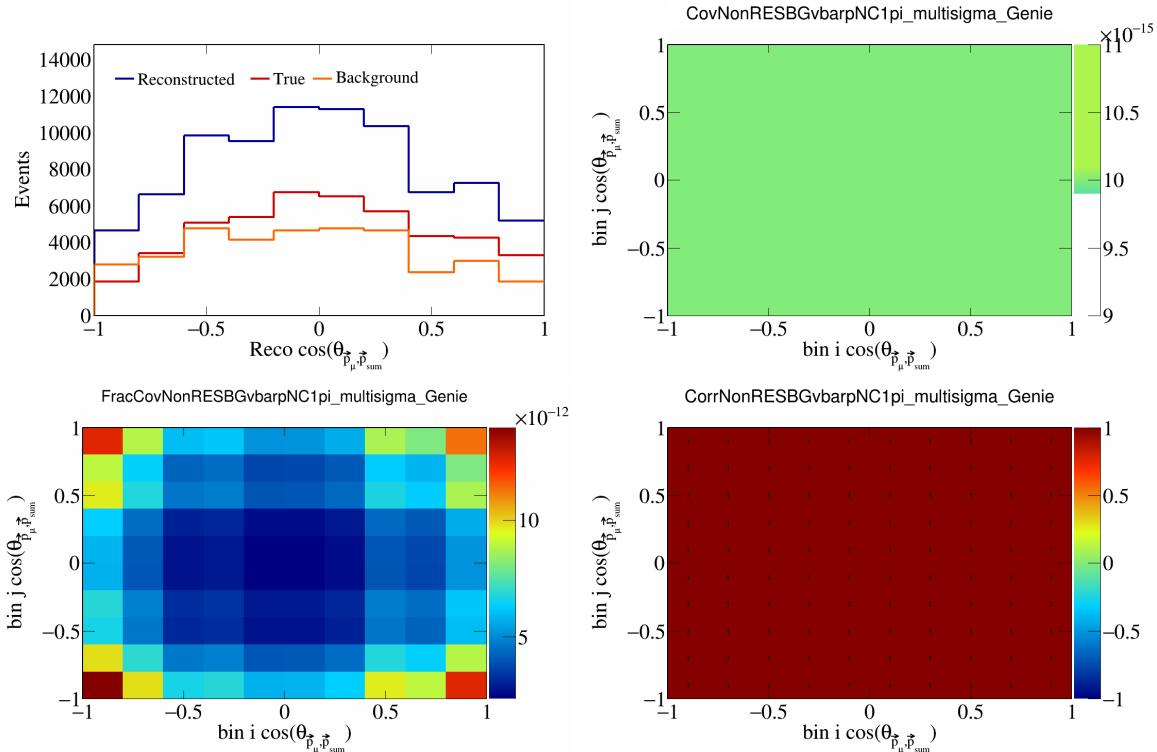


Figure 472: NonRESBGvbarpNC1pi variations for  $\cos(\theta_{\vec{p}_\mu, \vec{p}_{\text{sum}}})$ .

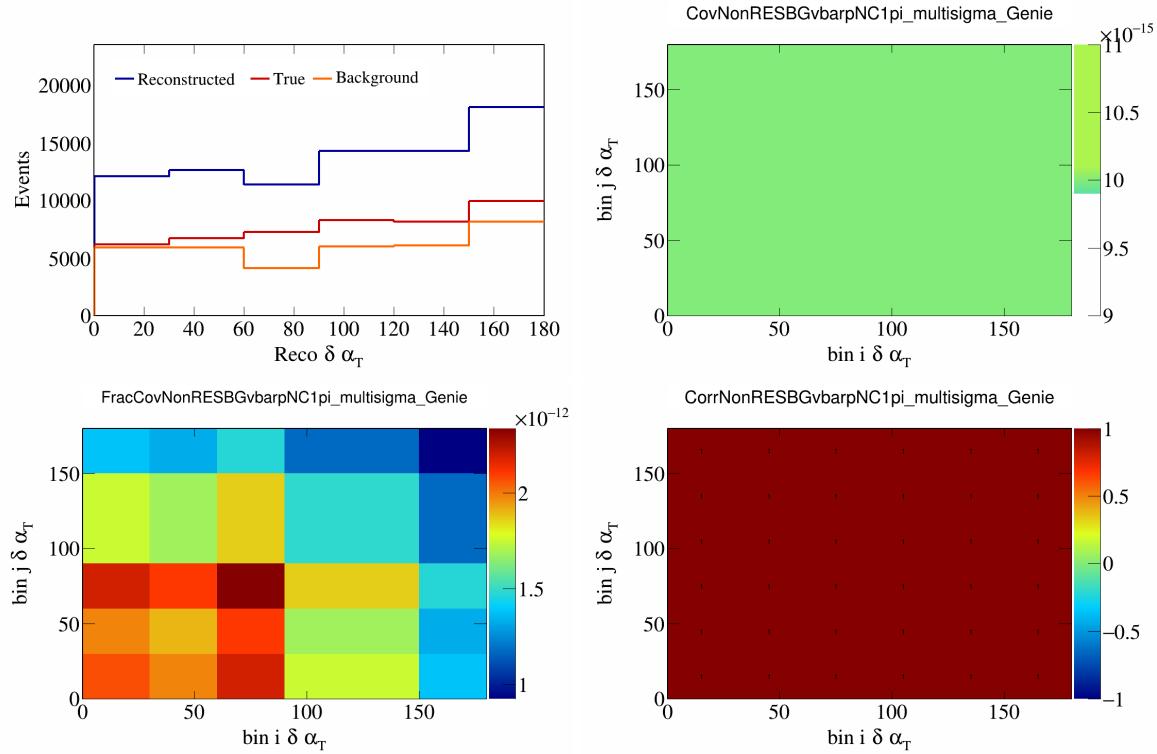


Figure 473: NonRESBGvbarpNC1pi variations for  $\delta\alpha_T$ .

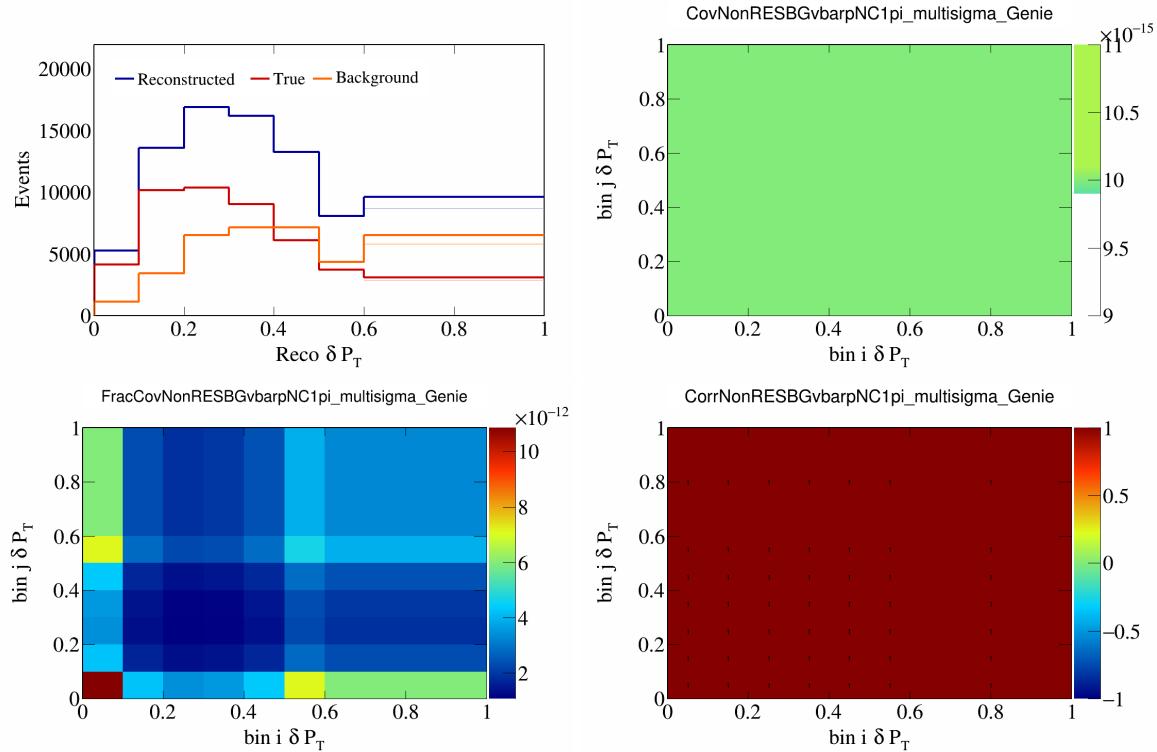


Figure 474: NonRESBGvbarpNC1pi variations for  $\delta P_T$ .

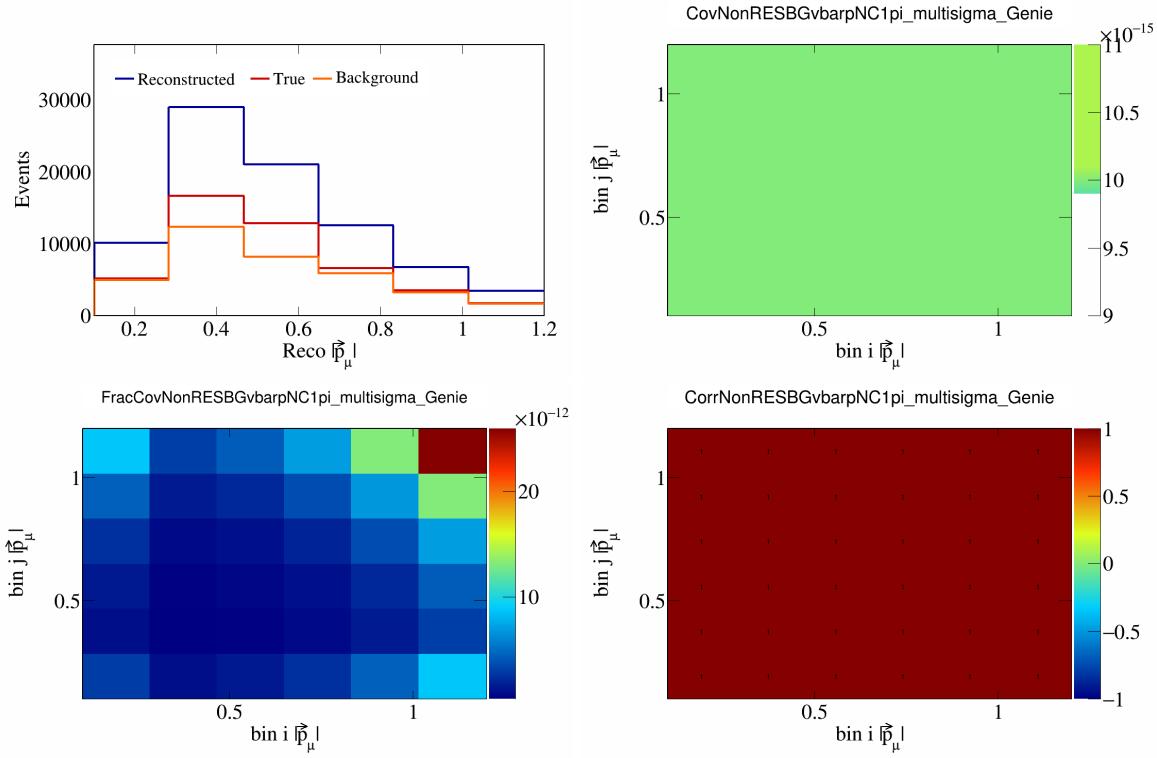


Figure 475: NonRESBGvbarpNC1pi variations for  $|\vec{p}_\mu|$ .

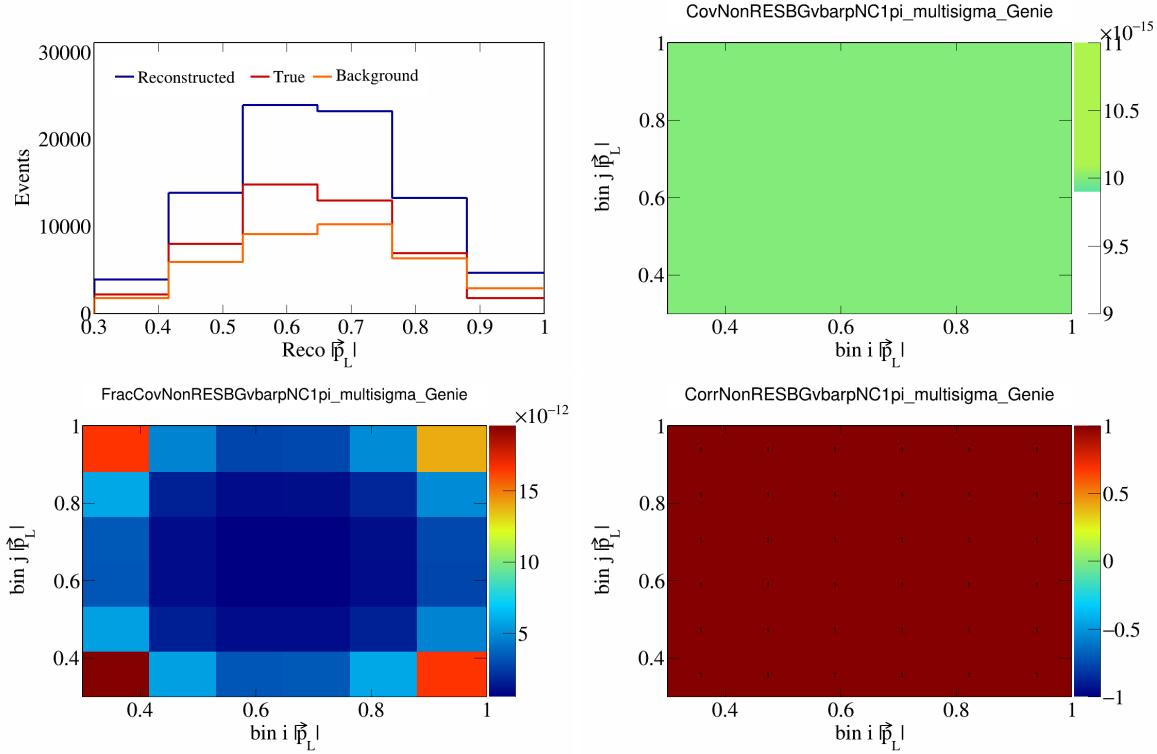


Figure 476: NonRESBGvbarpNC1pi variations for  $|\vec{p}_L|$ .

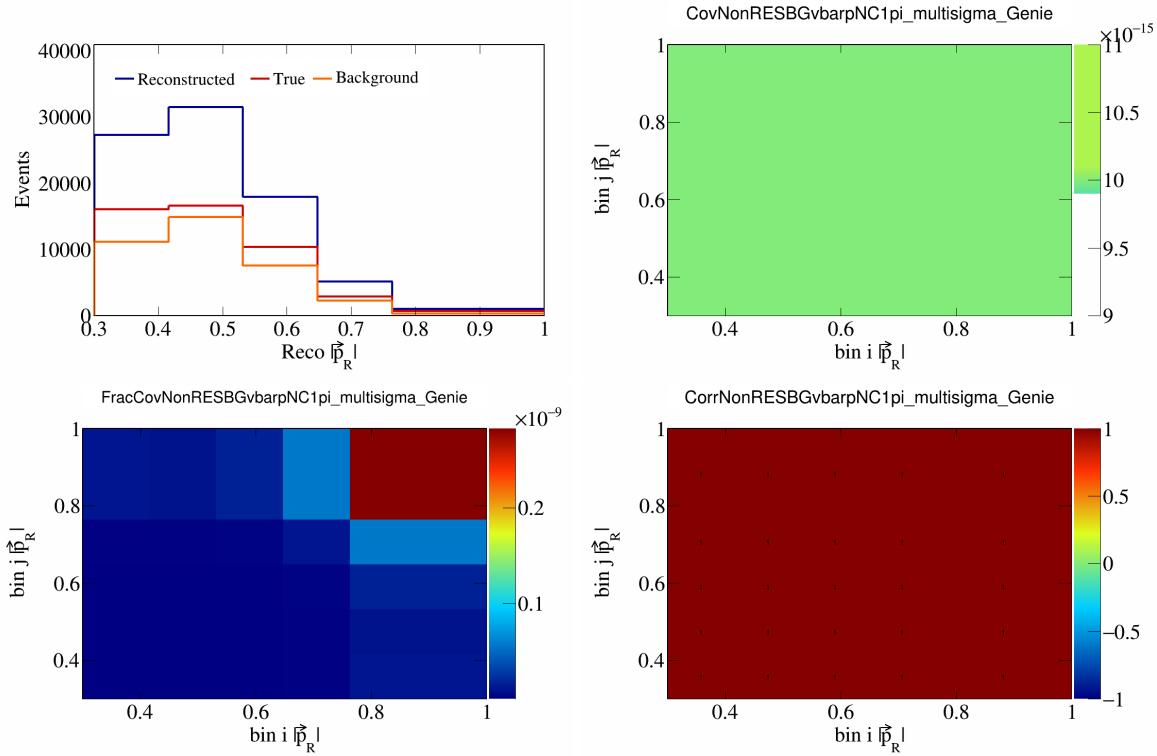


Figure 477: NonRESBGvbarpNC1pi variations for  $|\vec{p}_R|$ .

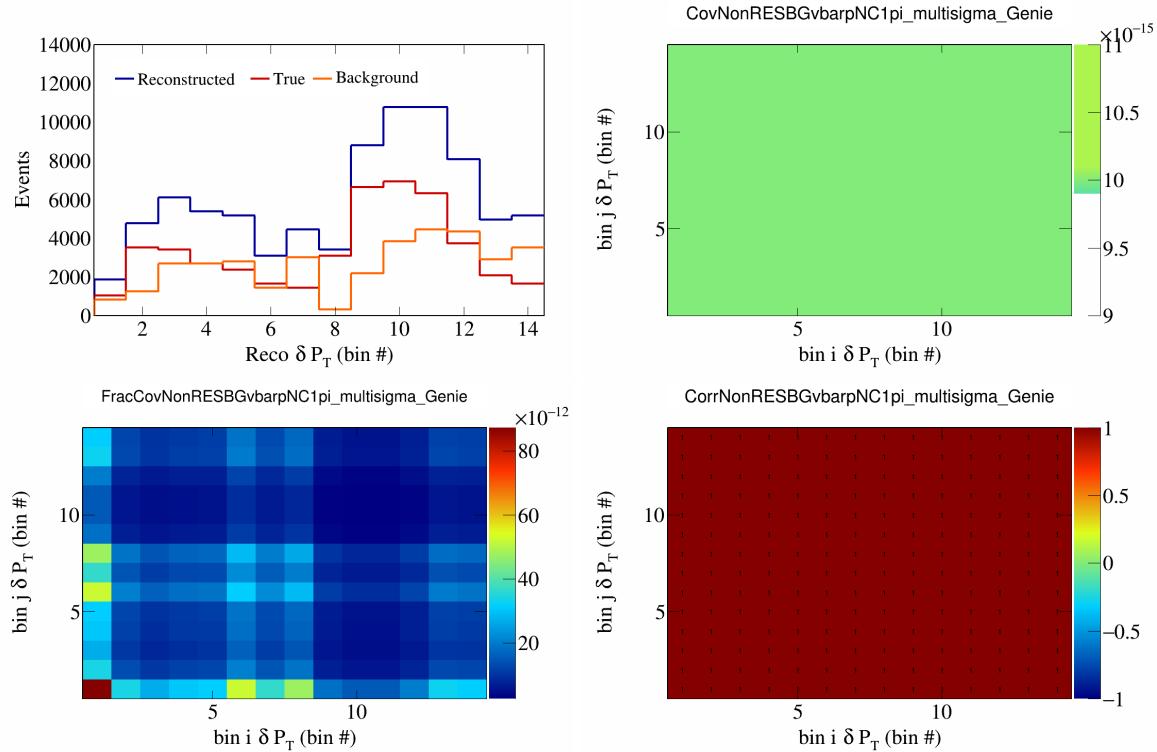


Figure 478: NonRESBGvbarpNC1pi variations for  $\delta P_T$  in  $\cos(\theta_{\vec{p}_\mu})$ .

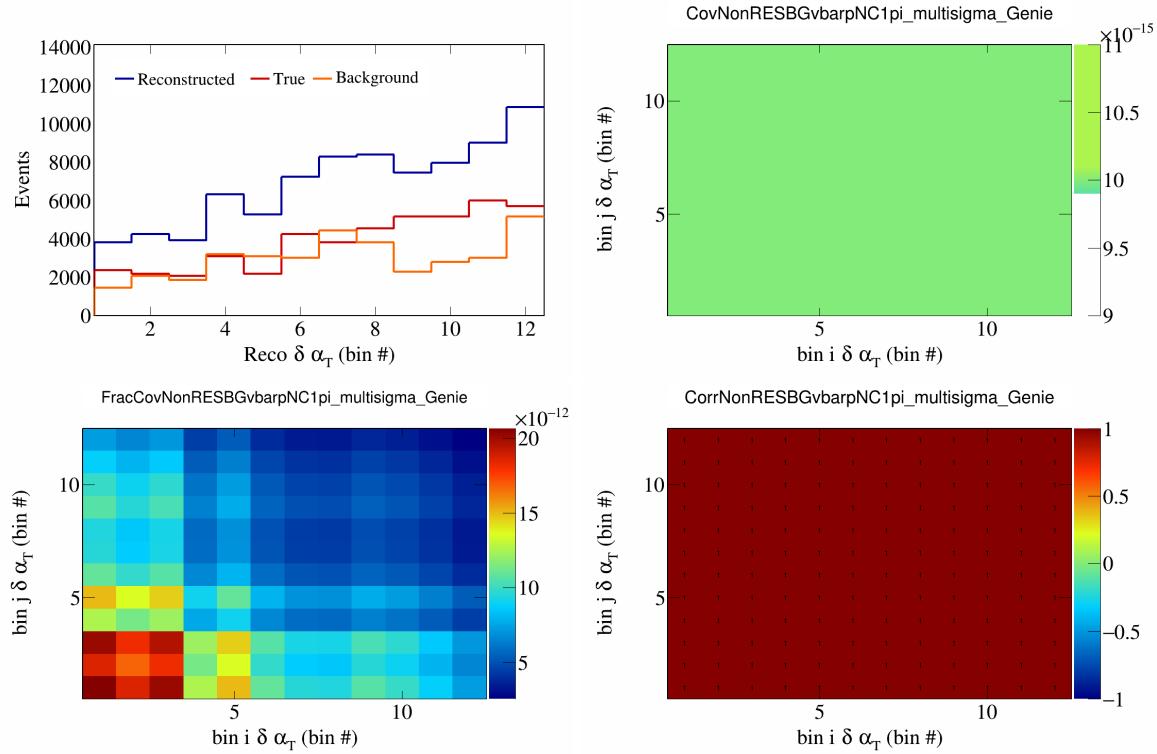


Figure 479: NonRESBGvbarpNC1pi variations for  $\delta\alpha_T$  in  $\cos(\theta_{\vec{p}_\mu})$ .

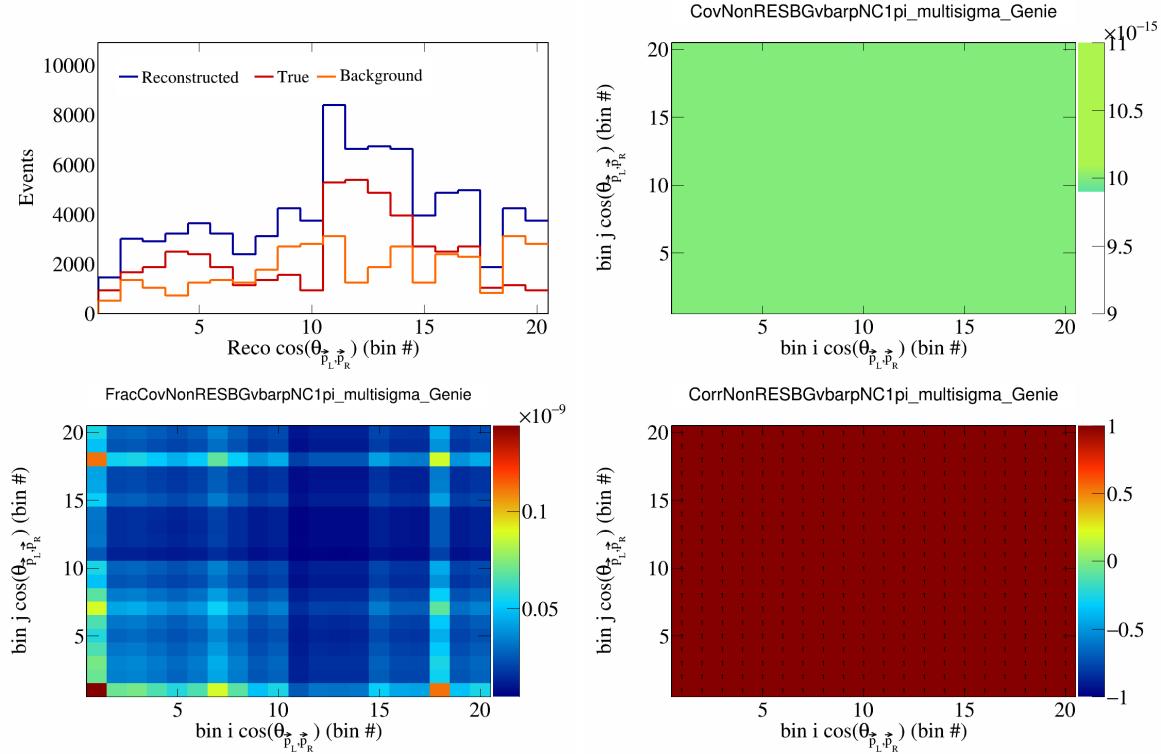


Figure 480: NonRESBGvbarpNC1pi variations for  $\cos(\theta_{\vec{p}_L, \vec{p}_R})$  in  $\cos(\theta_{\vec{p}_\mu})$ .

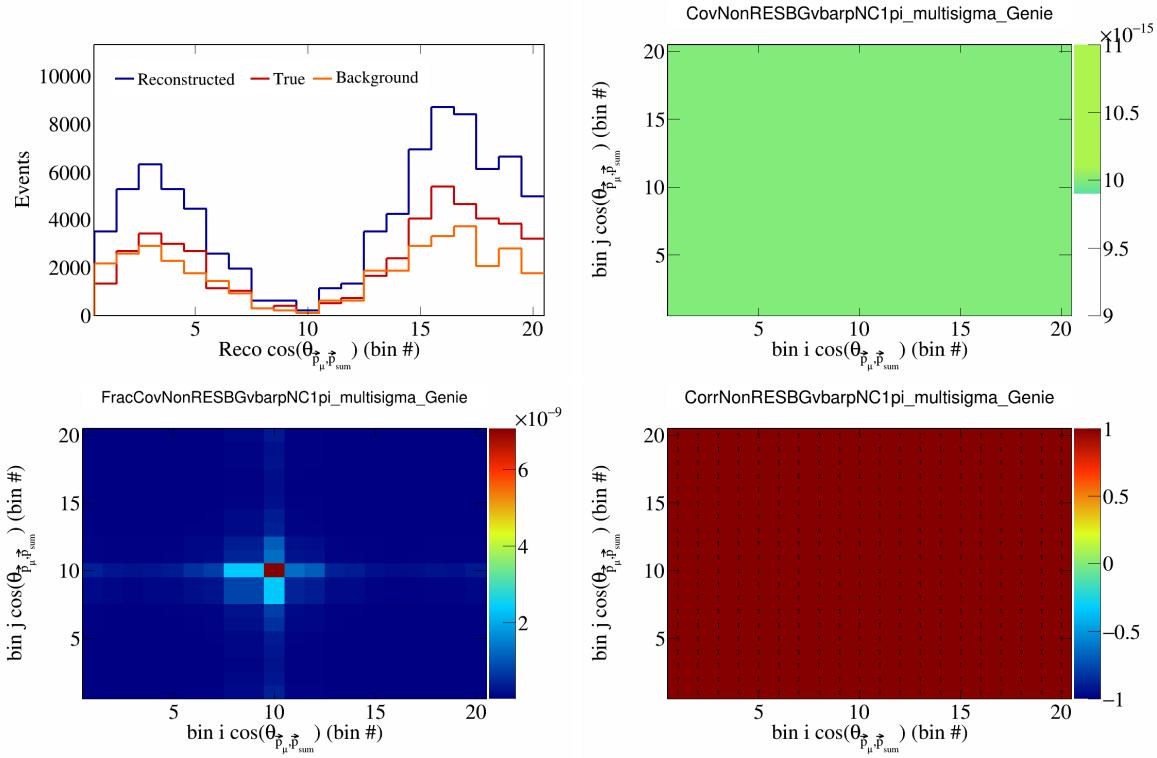


Figure 481: NonRESBGvbarpNC1pi variations for  $\cos(\theta_{\vec{p}_\mu})$  in  $\cos(\theta_{\vec{p}_\mu})$ .

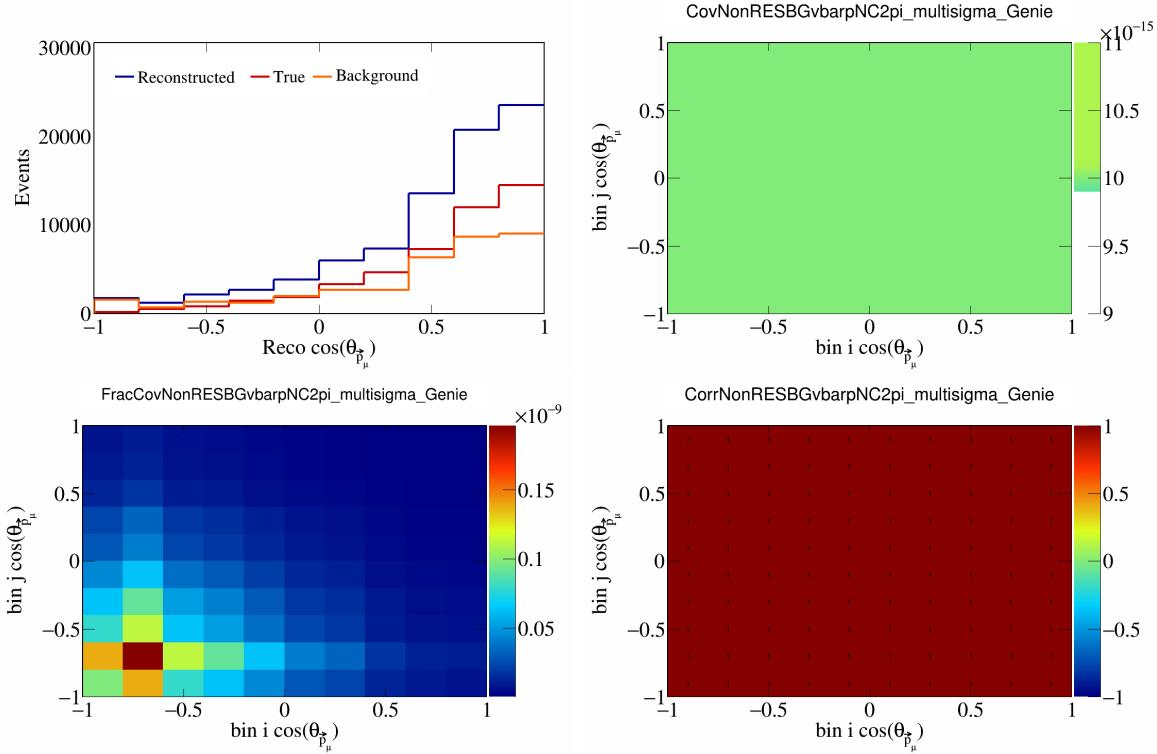


Figure 482: NonRESBGvbarpNC2pi variations for  $\cos(\theta_{\vec{p}_\mu})$ .

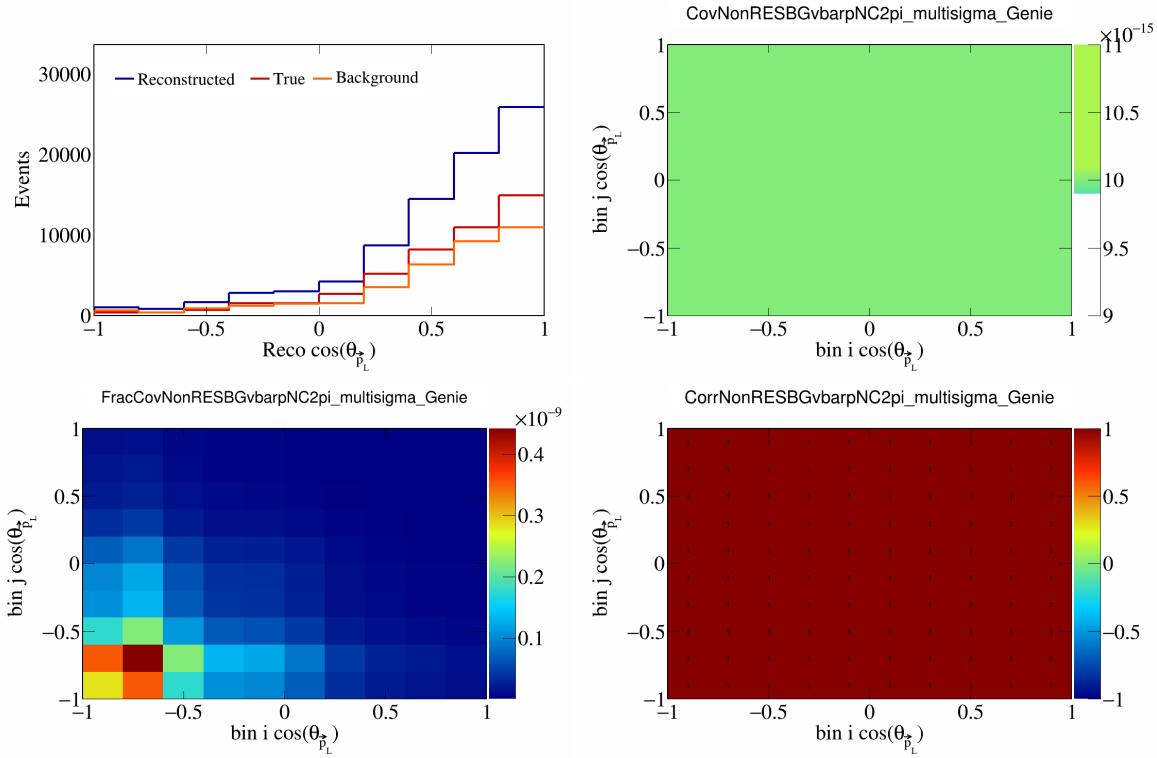


Figure 483: NonRESBGvbarpNC2pi variations for  $\cos(\theta_{\vec{p}_L})$ .

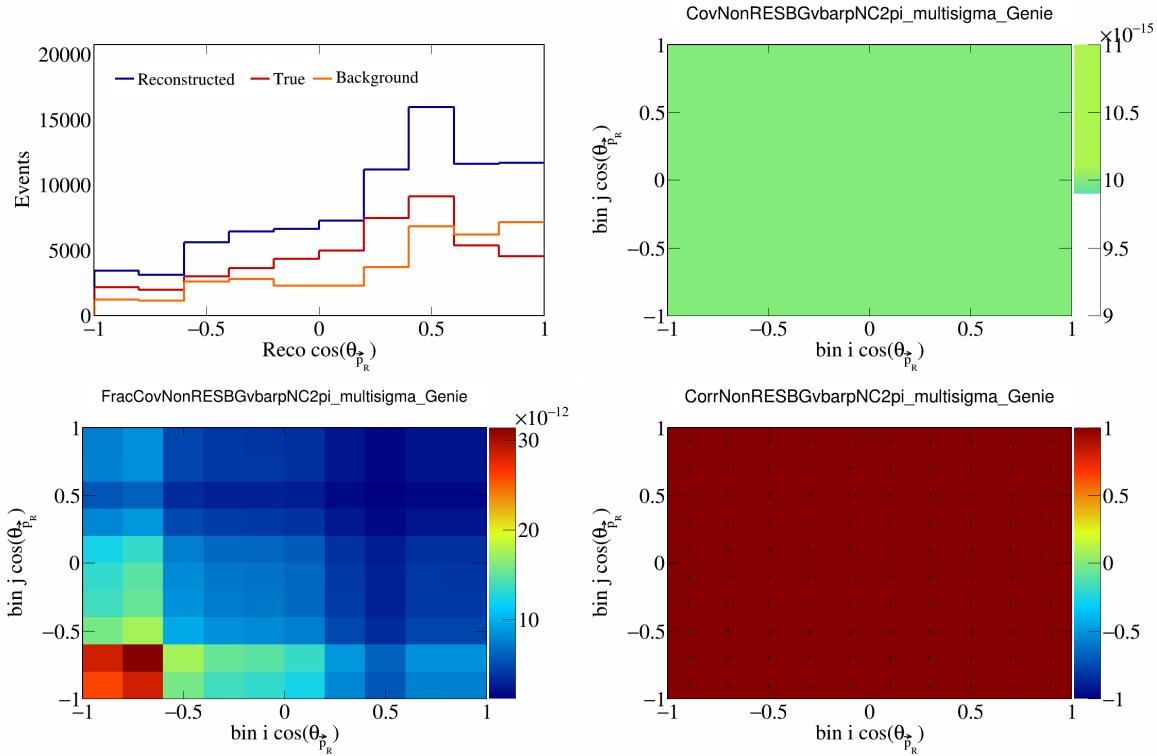


Figure 484: NonRESBGvbarpNC2pi variations for  $\cos(\theta_{\vec{p}_R})$ .

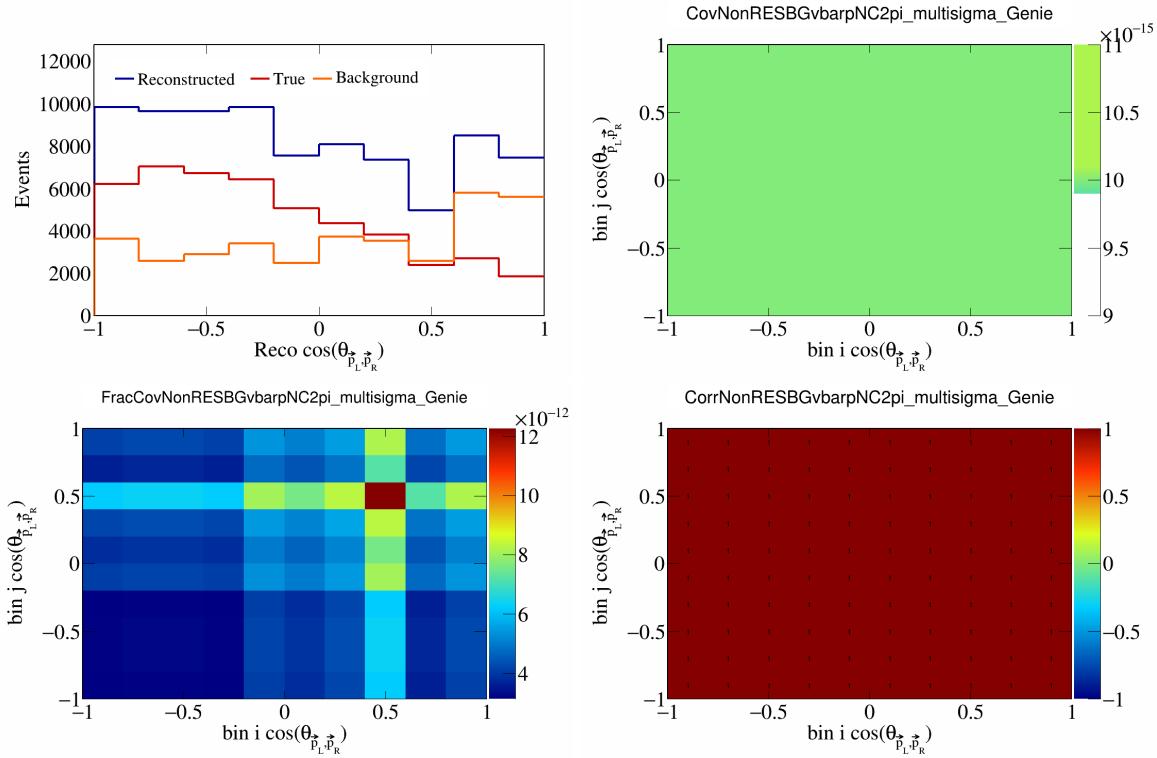


Figure 485: NonRESBGvbarpNC2pi variations for  $\cos(\theta_{\vec{p}_L, \vec{p}_R})$ .

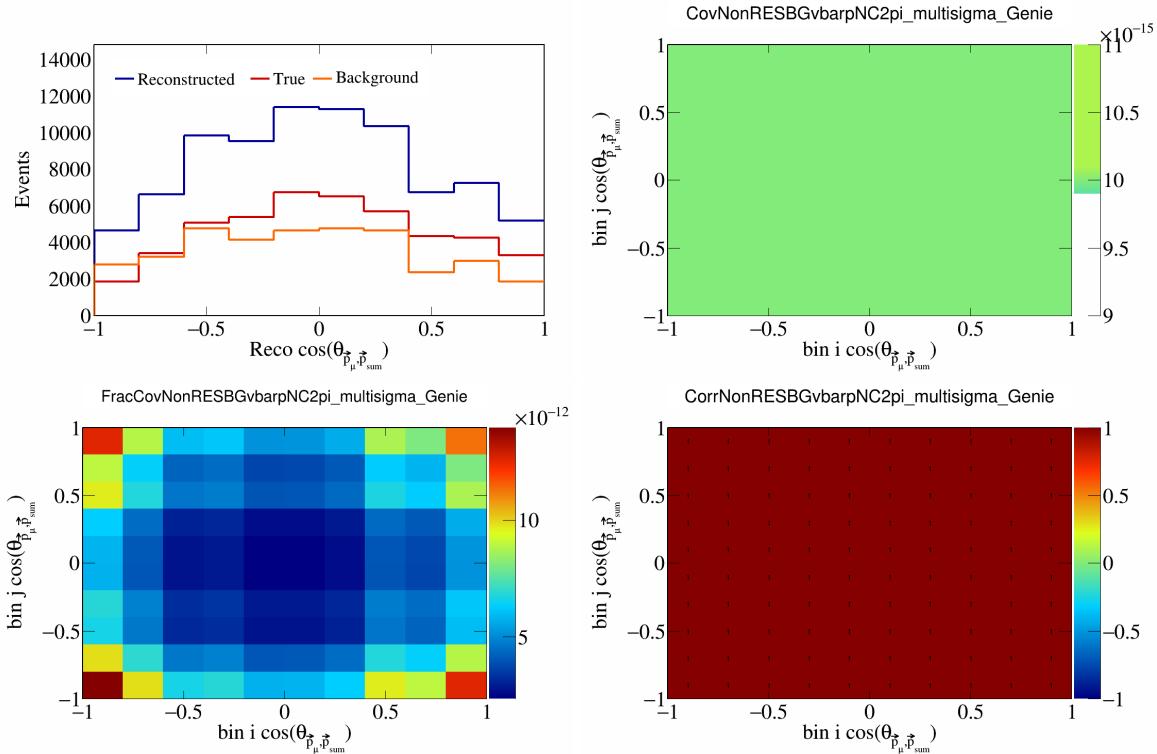


Figure 486: NonRESBGvbarpNC2pi variations for  $\cos(\theta_{\vec{p}_\mu, \vec{p}_{\text{sum}}})$ .

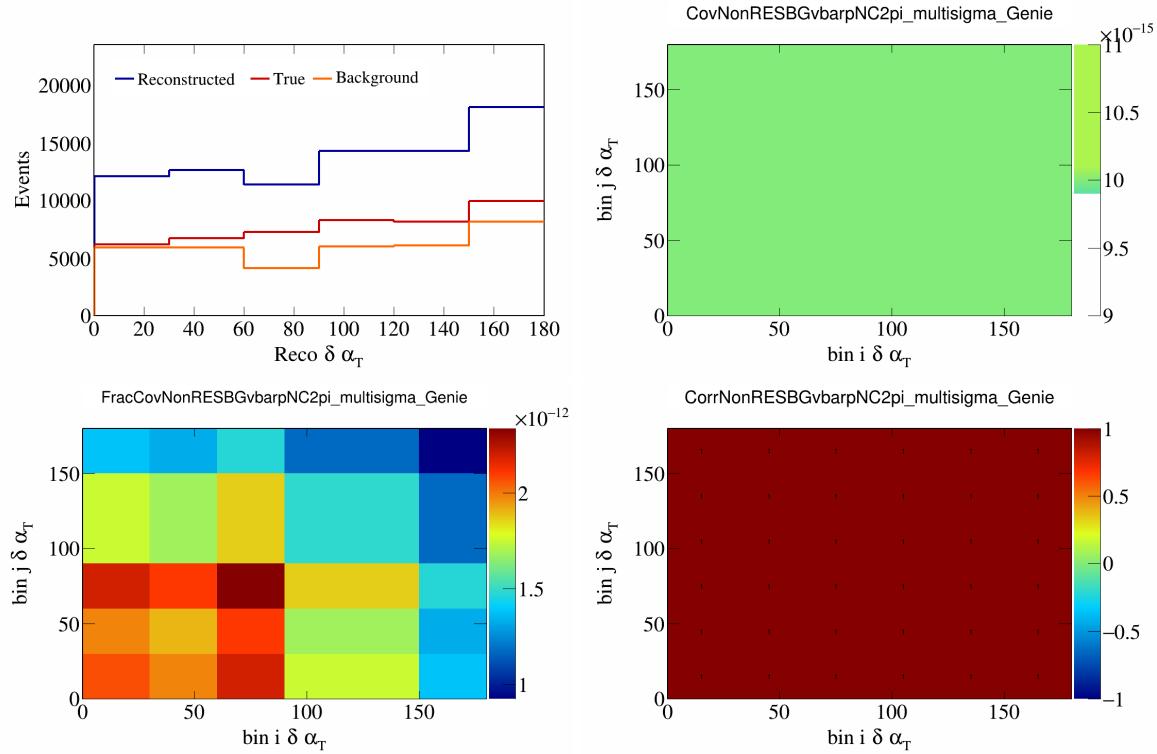


Figure 487: NonRESBGvbarpNC2pi variations for  $\delta\alpha_T$ .

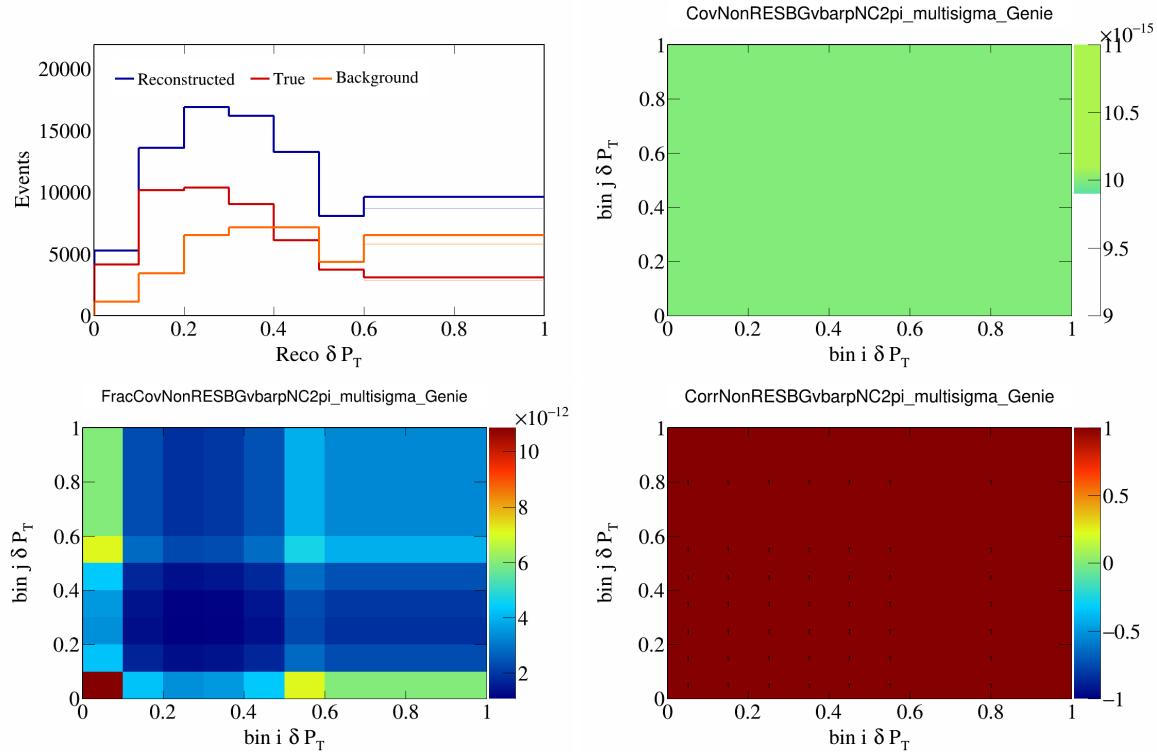


Figure 488: NonRESBGvbarpNC2pi variations for  $\delta P_T$ .

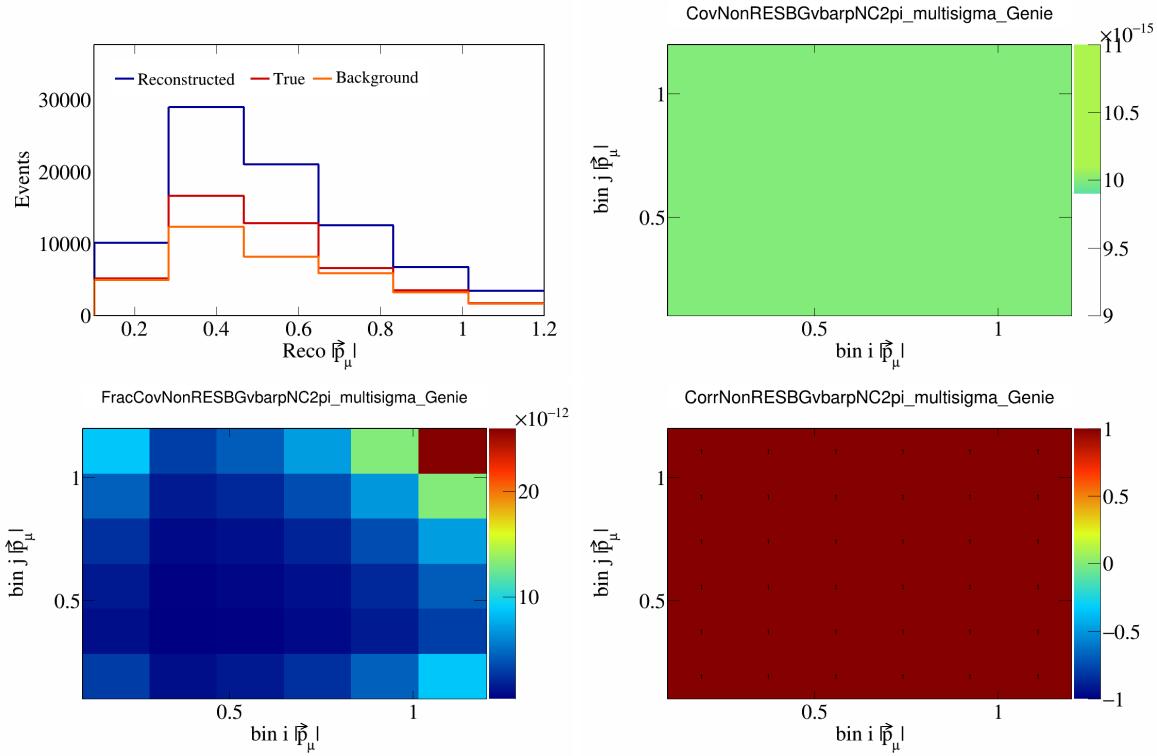


Figure 489: NonRESBGvbarpNC2pi variations for  $|\vec{p}_\mu|$ .

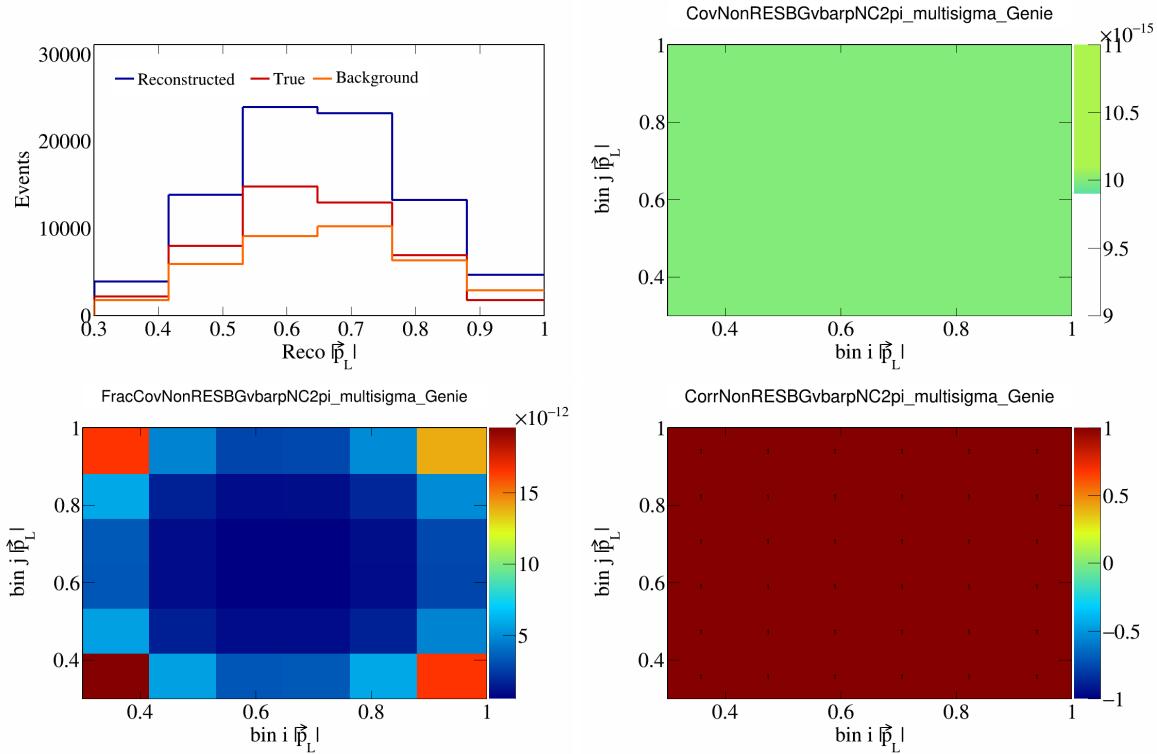


Figure 490: NonRESBGvbarpNC2pi variations for  $|\vec{p}_L|$ .

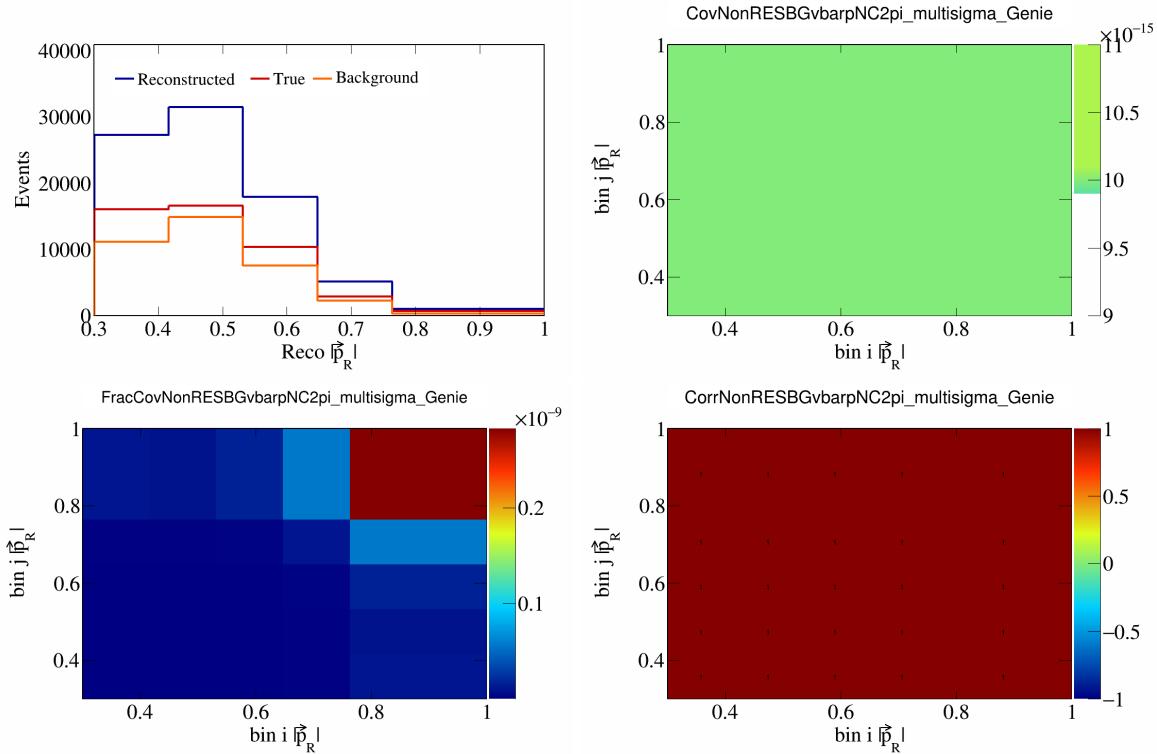


Figure 491: NonRESBGvbarpNC2pi variations for  $|\vec{p}_R|$ .

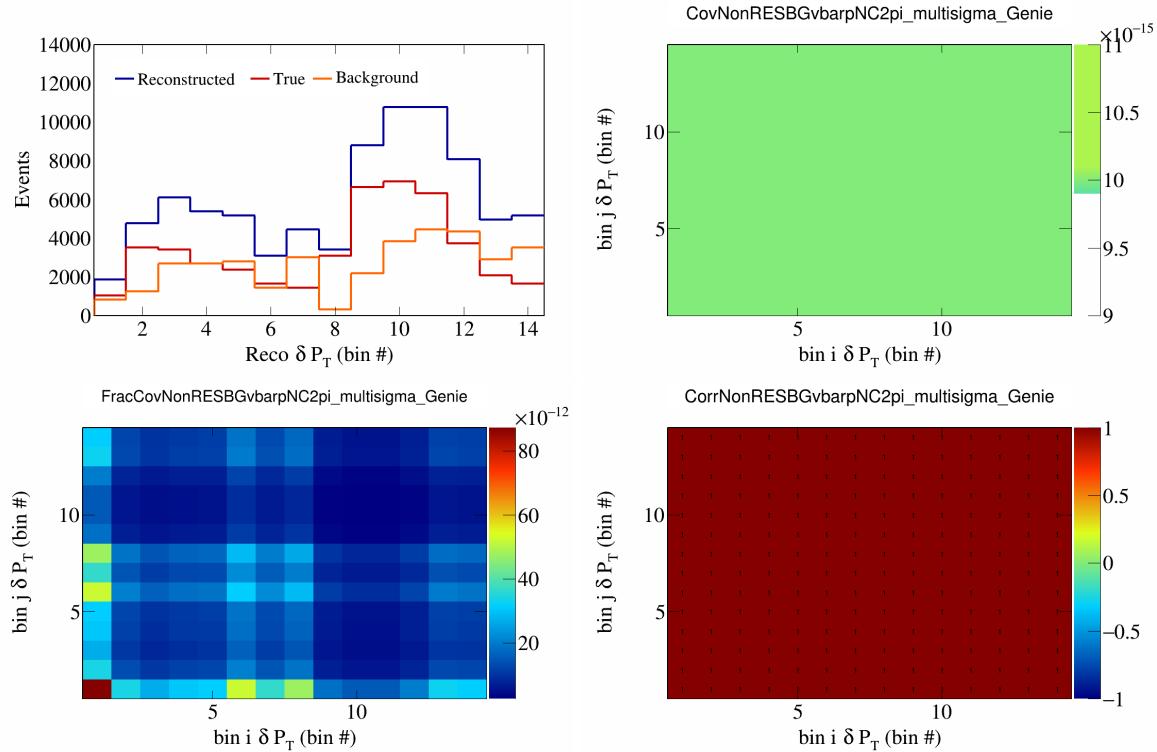


Figure 492: NonRESBGvbarpNC2pi variations for  $\delta P_T$  in  $\cos(\theta_{\vec{p}_\mu})$ .

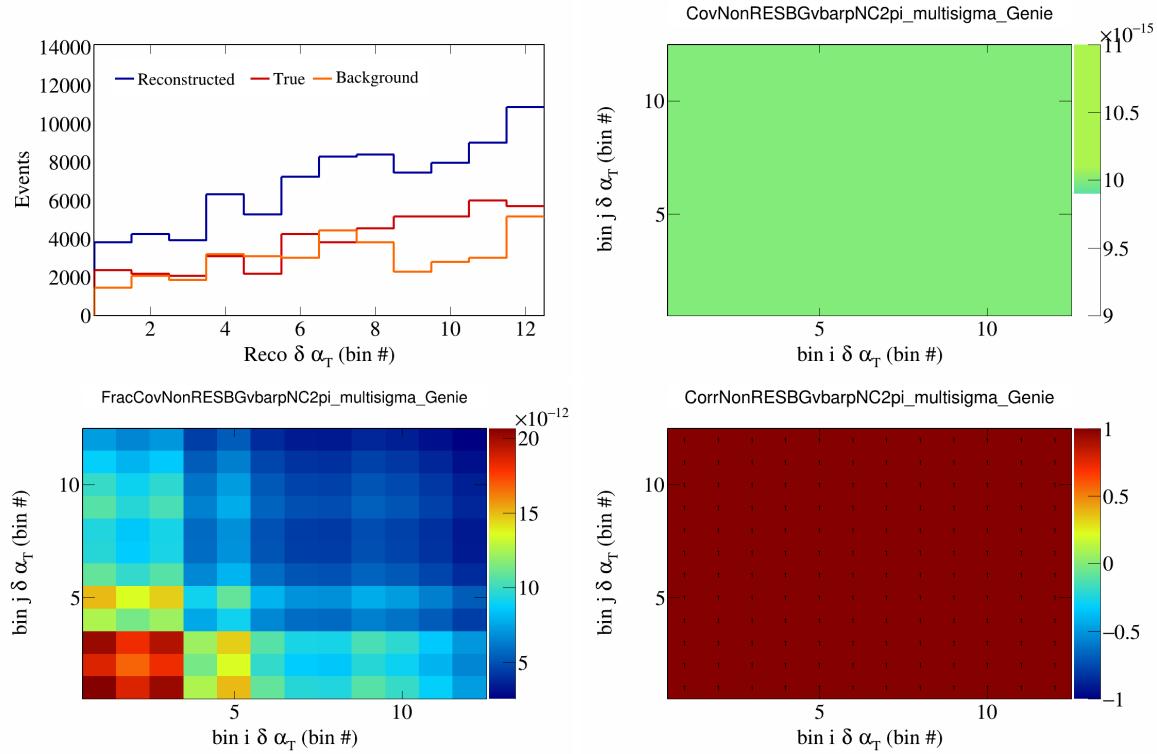


Figure 493: NonRESBGvbarpNC2pi variations for  $\delta\alpha_T$  in  $\cos(\theta_{\vec{p}_\mu})$ .

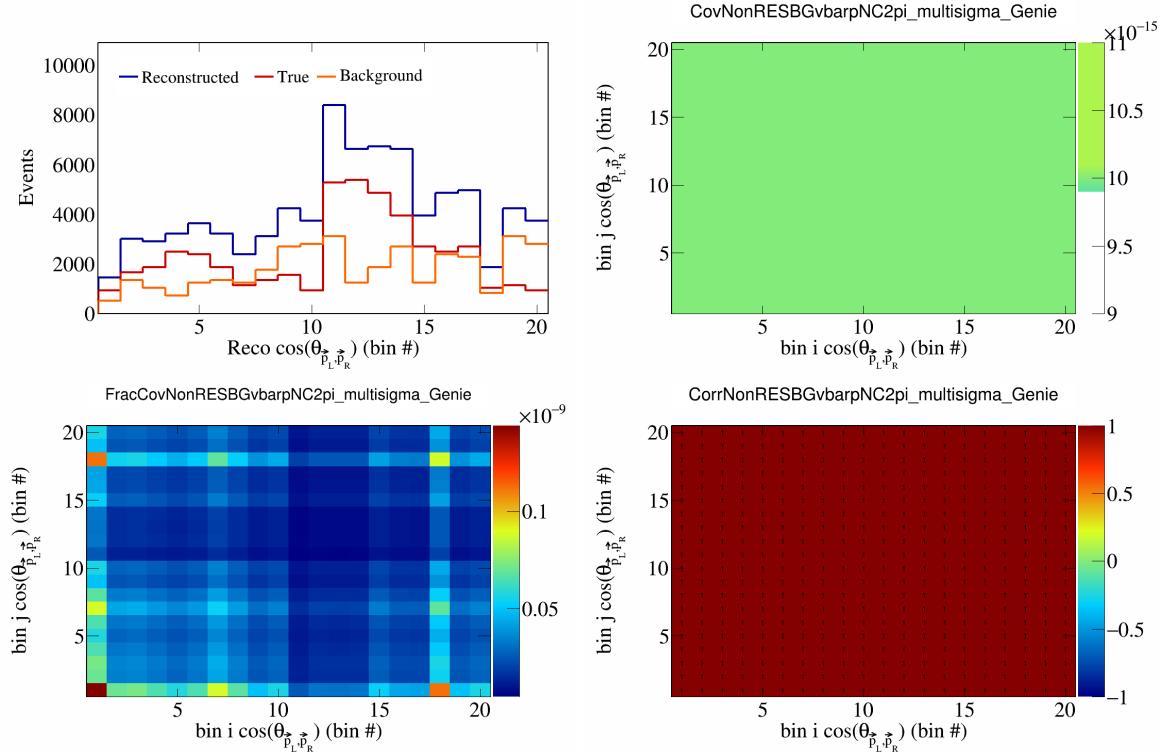


Figure 494: NonRESBGvbarpNC2pi variations for  $\cos(\theta_{\vec{p}_L, \vec{p}_R})$  in  $\cos(\theta_{\vec{p}_\mu})$ .

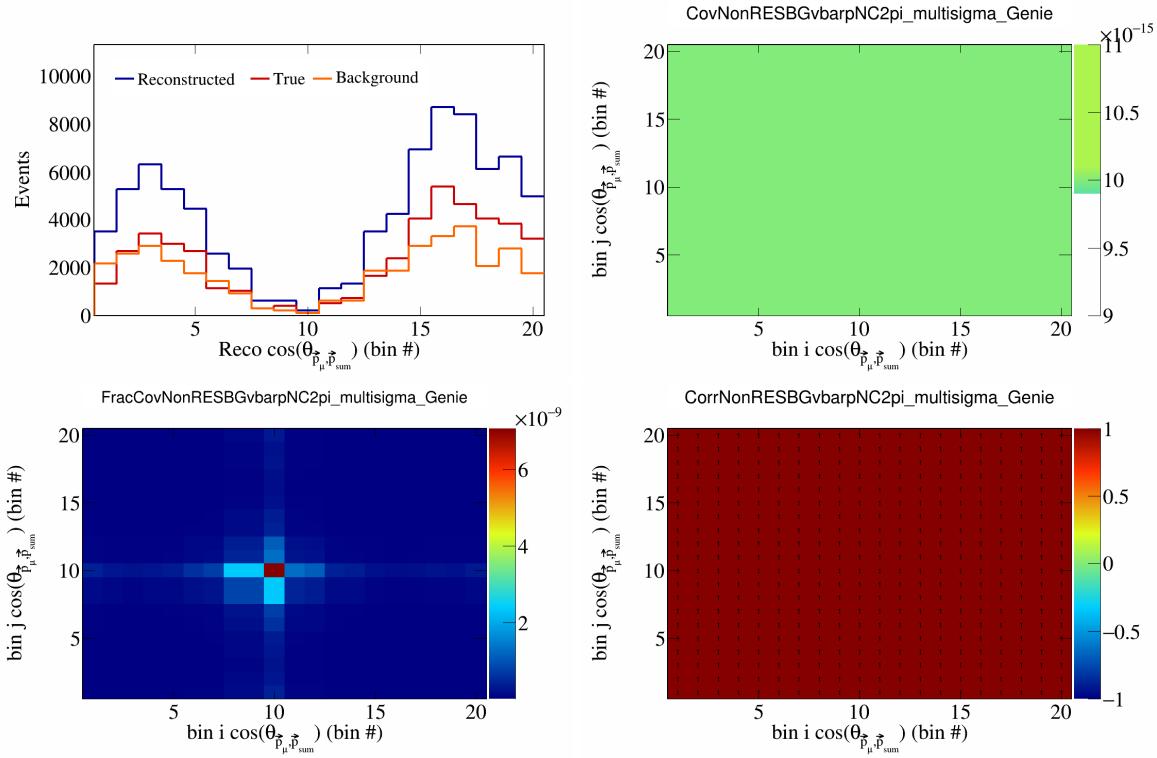


Figure 495: NonRESBGvbarpNC2pi variations for  $\cos(\theta_{\vec{p}_\mu} \cdot \vec{p}_{\text{sum}})$  in  $\cos(\theta_{\vec{p}_\mu})$ .

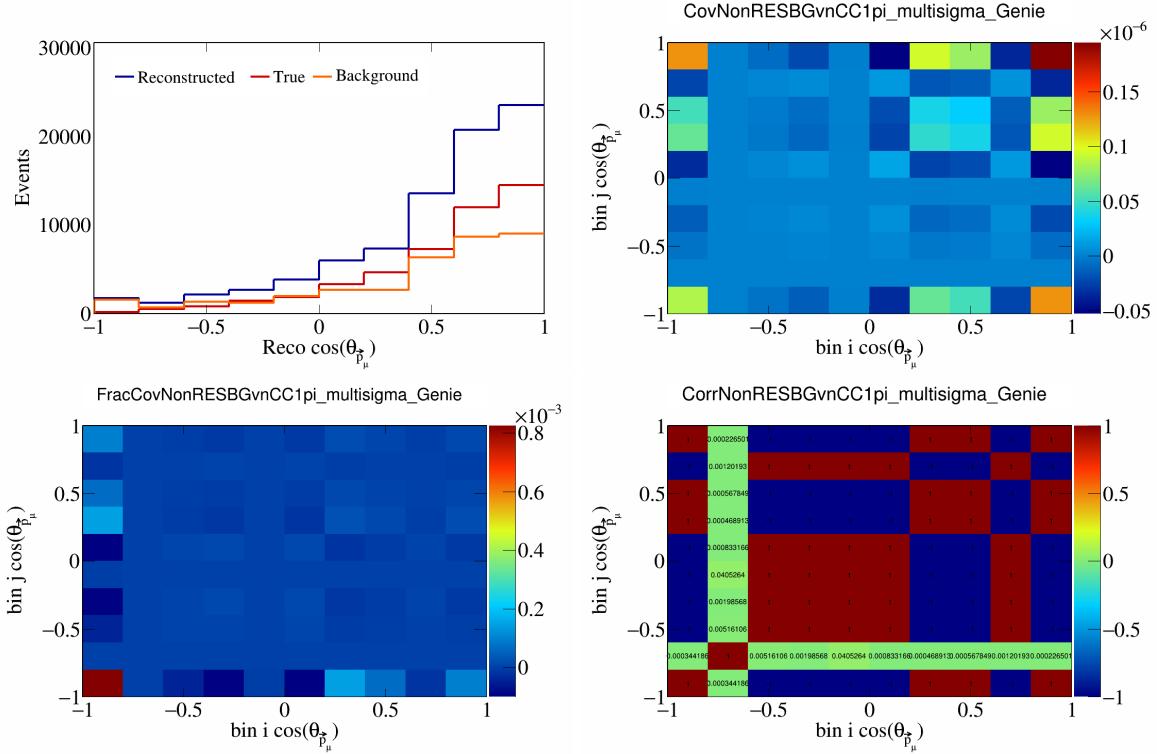


Figure 496: NonRESBGvnCC1pi variations for  $\cos(\theta_{\vec{p}_\mu})$ .

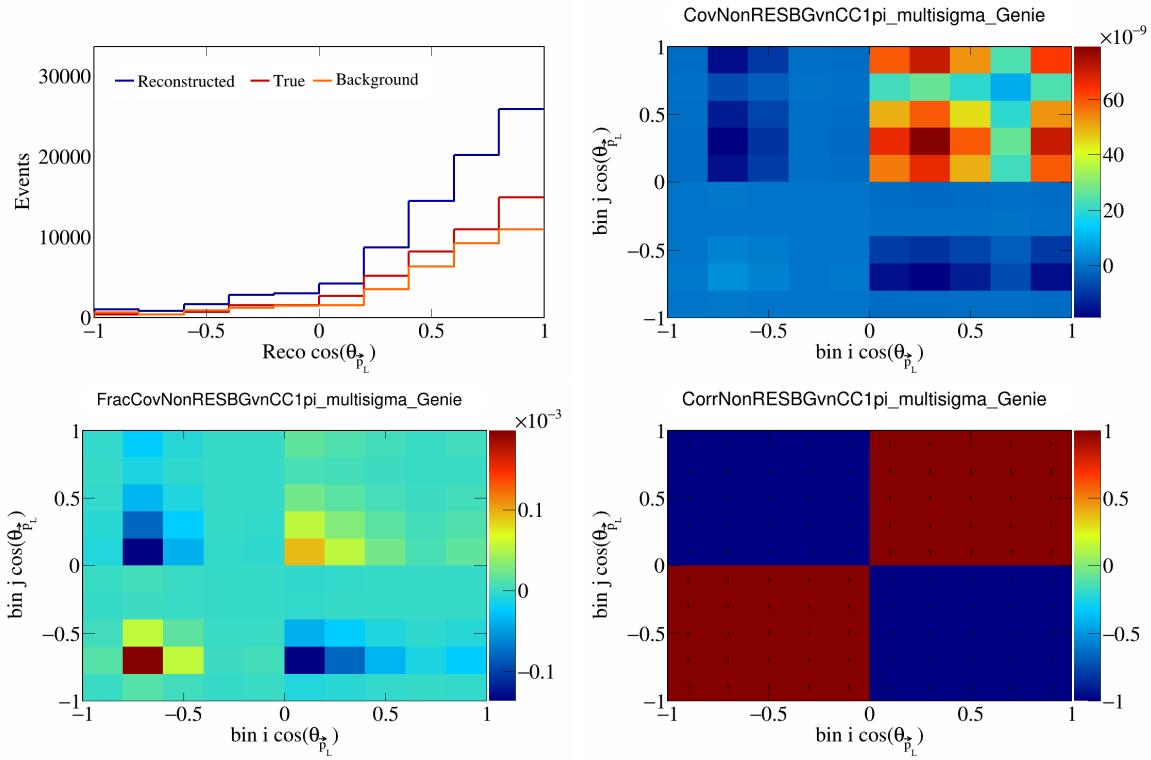


Figure 497: NonRESBGvnCC1pi variations for  $\cos(\theta_{\vec{p}_L})$ .

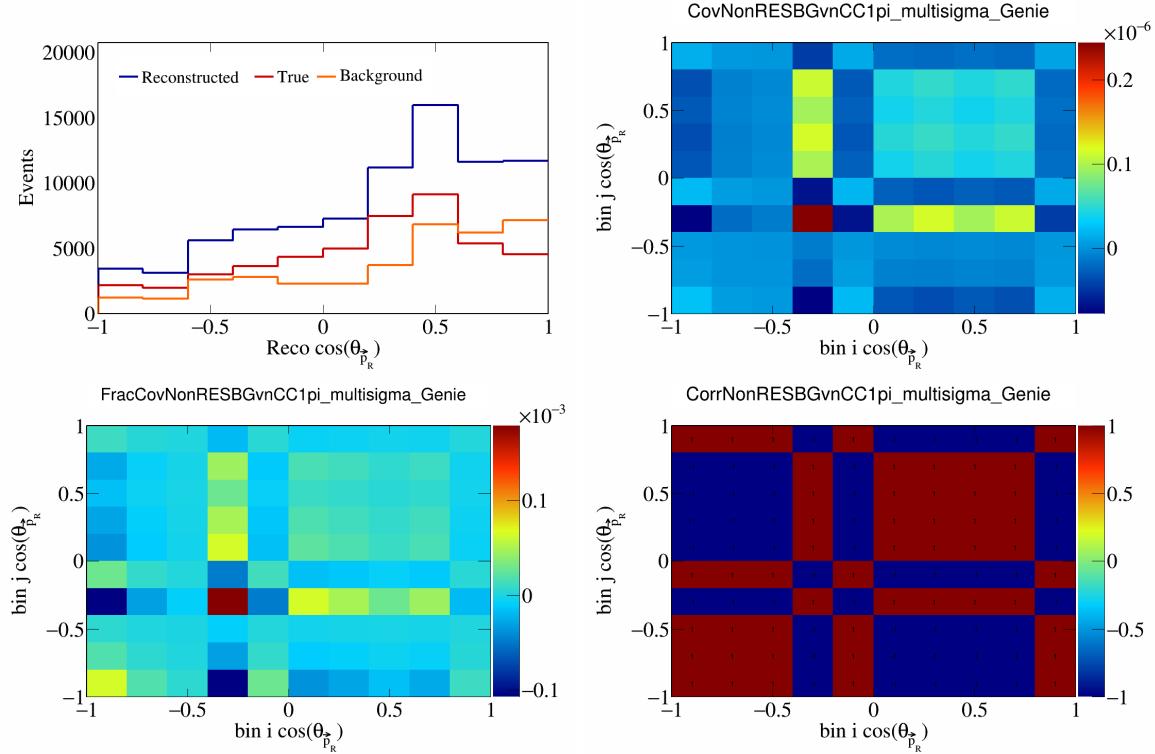


Figure 498: NonRESBGvnCC1pi variations for  $\cos(\theta_{\vec{p}_R})$ .

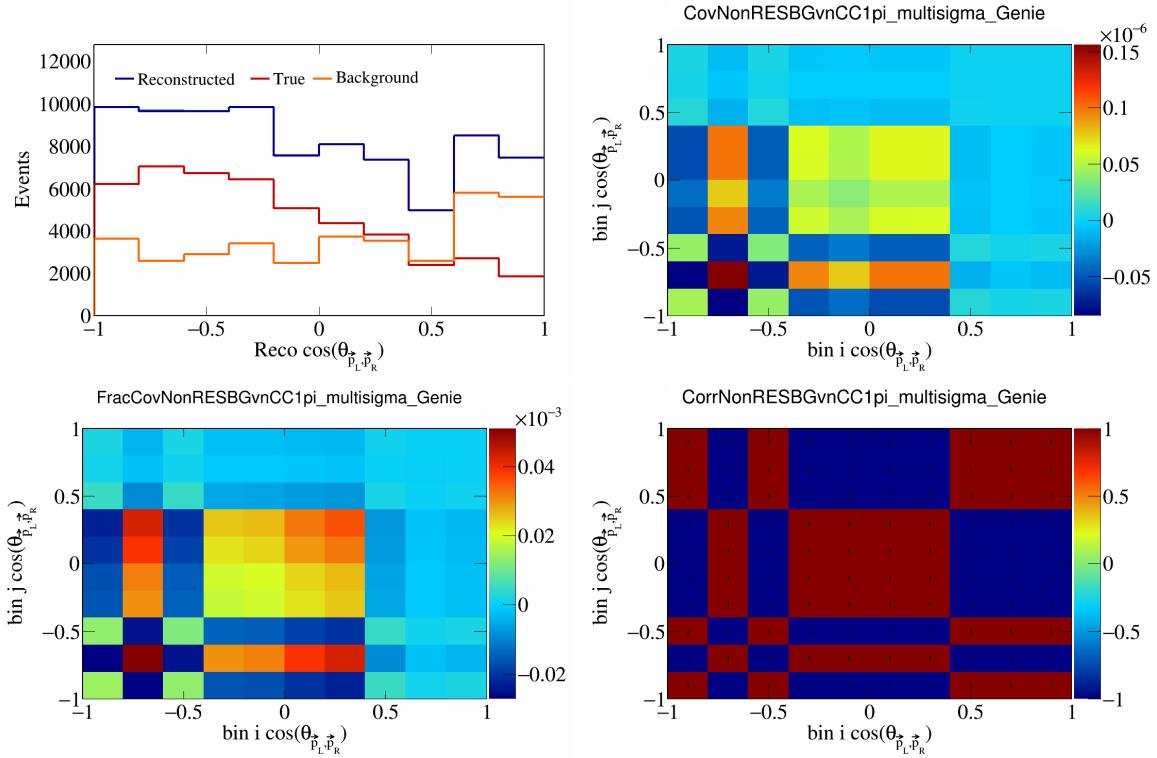


Figure 499: NonRESBGvnCC1pi variations for  $\cos(\theta_{\vec{p}_L, \vec{p}_R})$ .

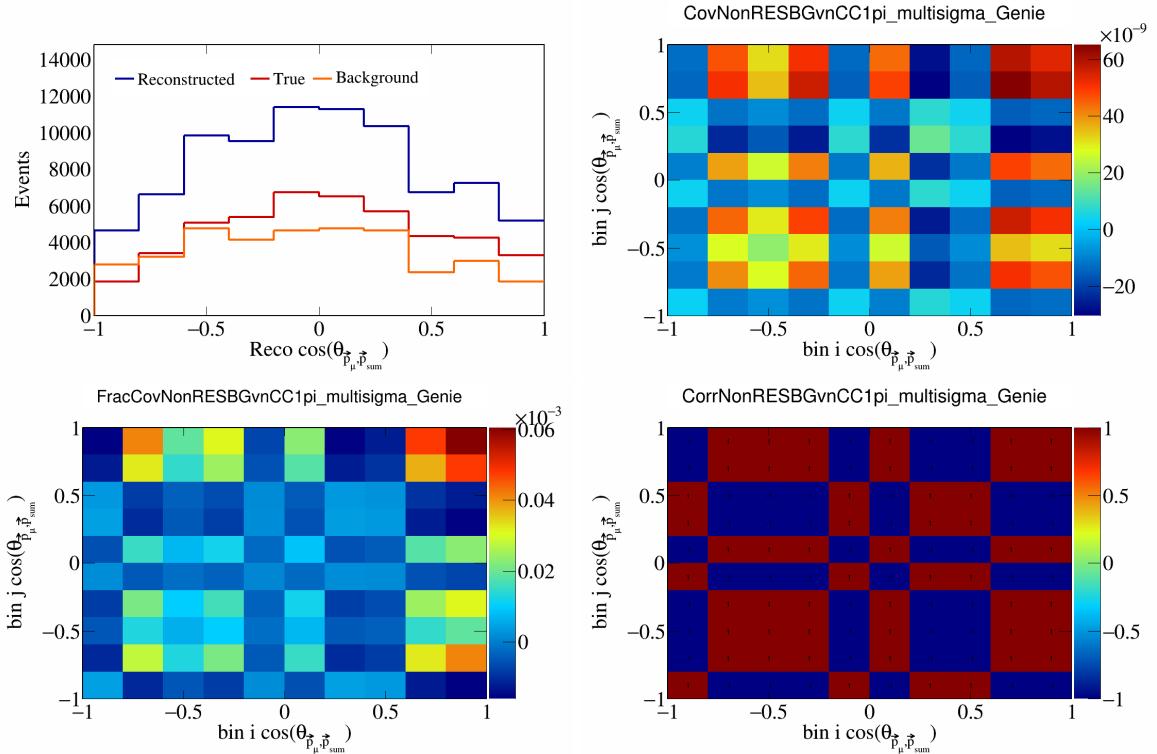


Figure 500: NonRESBGvnCC1pi variations for  $\cos(\theta_{\vec{p}_\mu, \vec{p}_{\text{sum}}})$ .

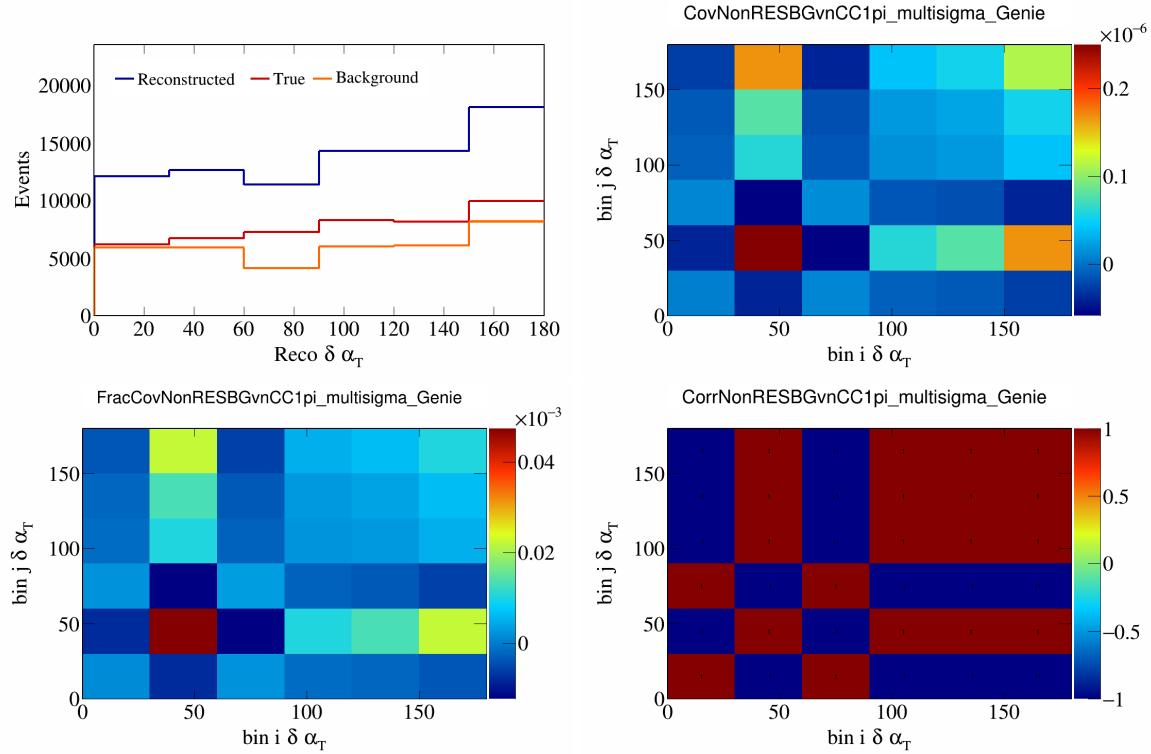


Figure 501: NonRESBGvnCC1pi variations for  $\delta\alpha_T$ .

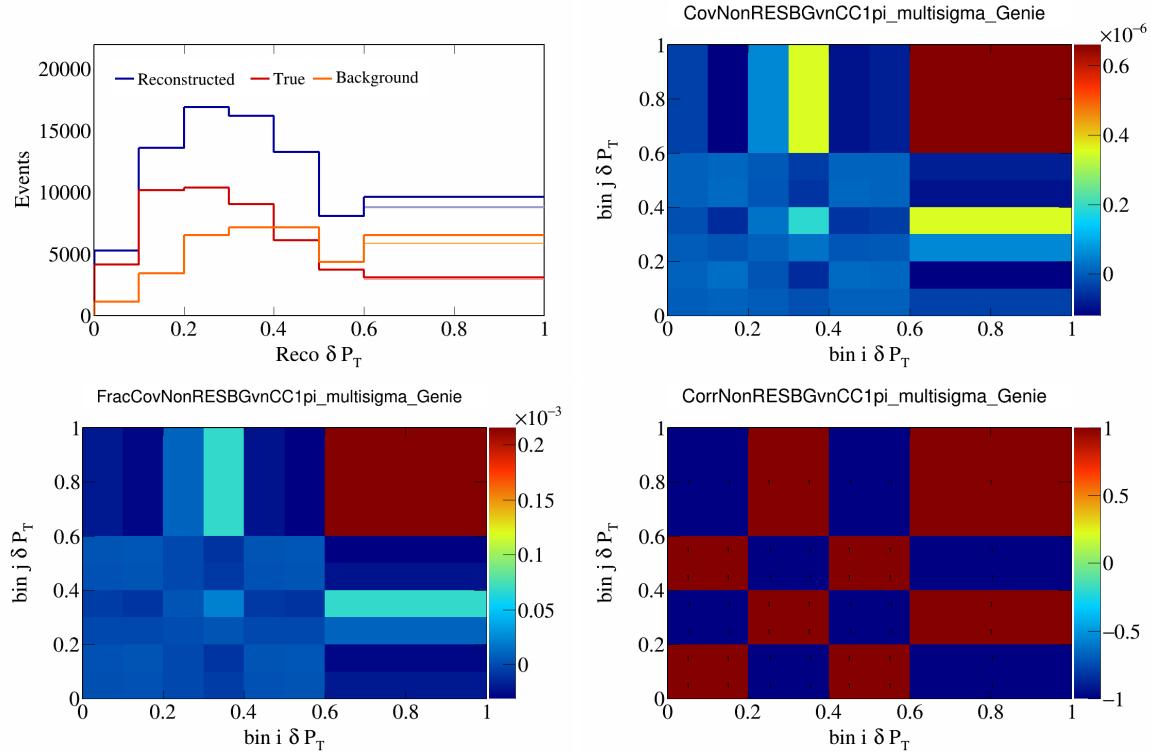


Figure 502: NonRESBGvnCC1pi variations for  $\delta P_T$ .

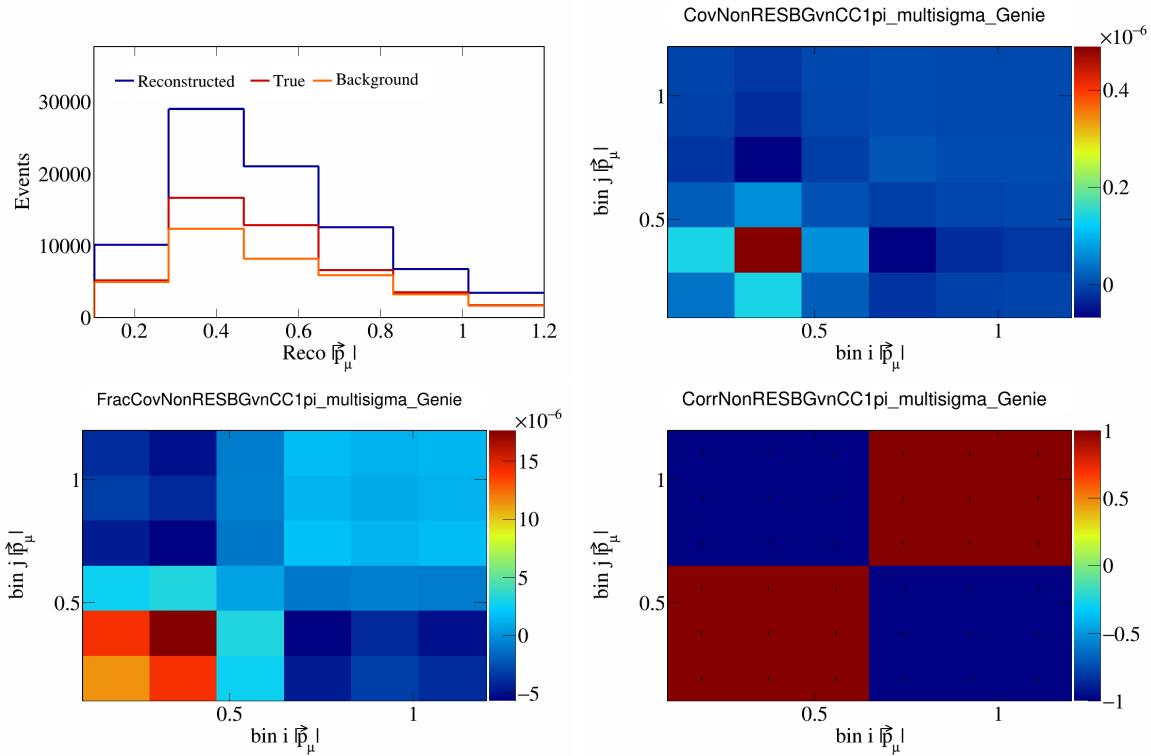


Figure 503: NonRESBGvnCC1pi variations for  $|\vec{p}_\mu|$ .

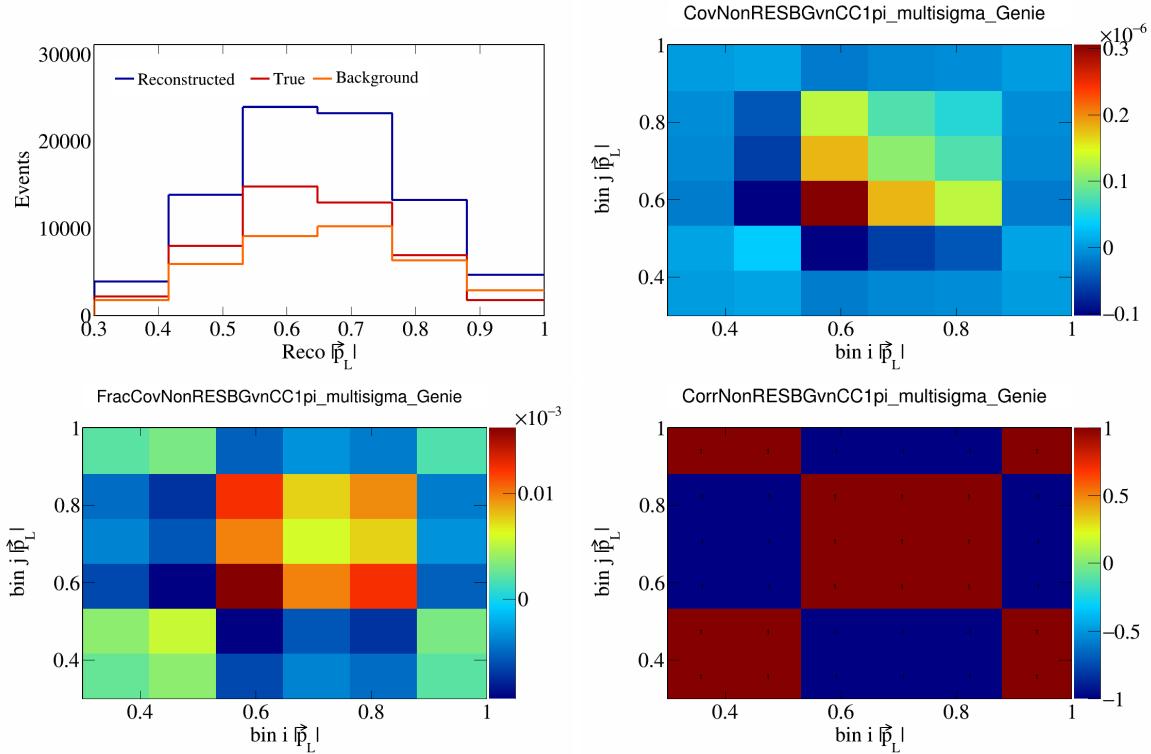


Figure 504: NonRESBGvnCC1pi variations for  $|\vec{p}_L|$ .

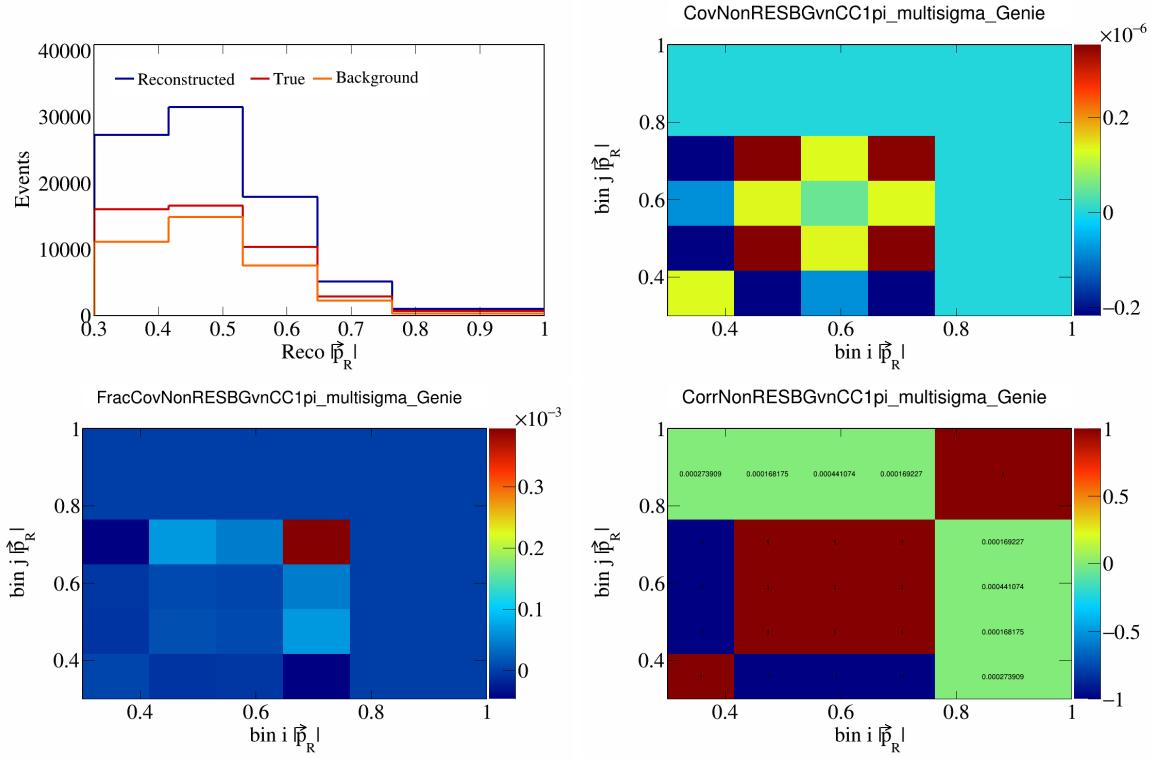


Figure 505: NonRESBGvnCC1pi variations for  $|\vec{p}_R|$ .

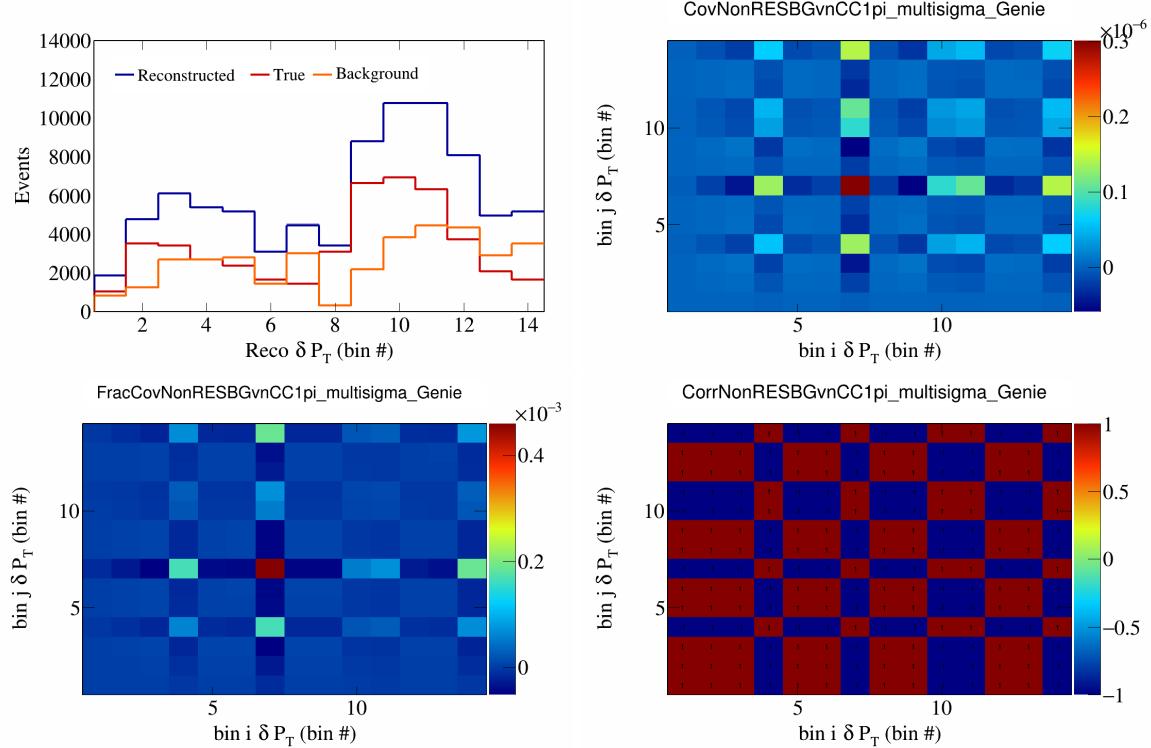


Figure 506: NonRESBGvnCC1pi variations for  $\delta P_T$  in  $\cos(\theta_{\vec{p}_\mu})$ .

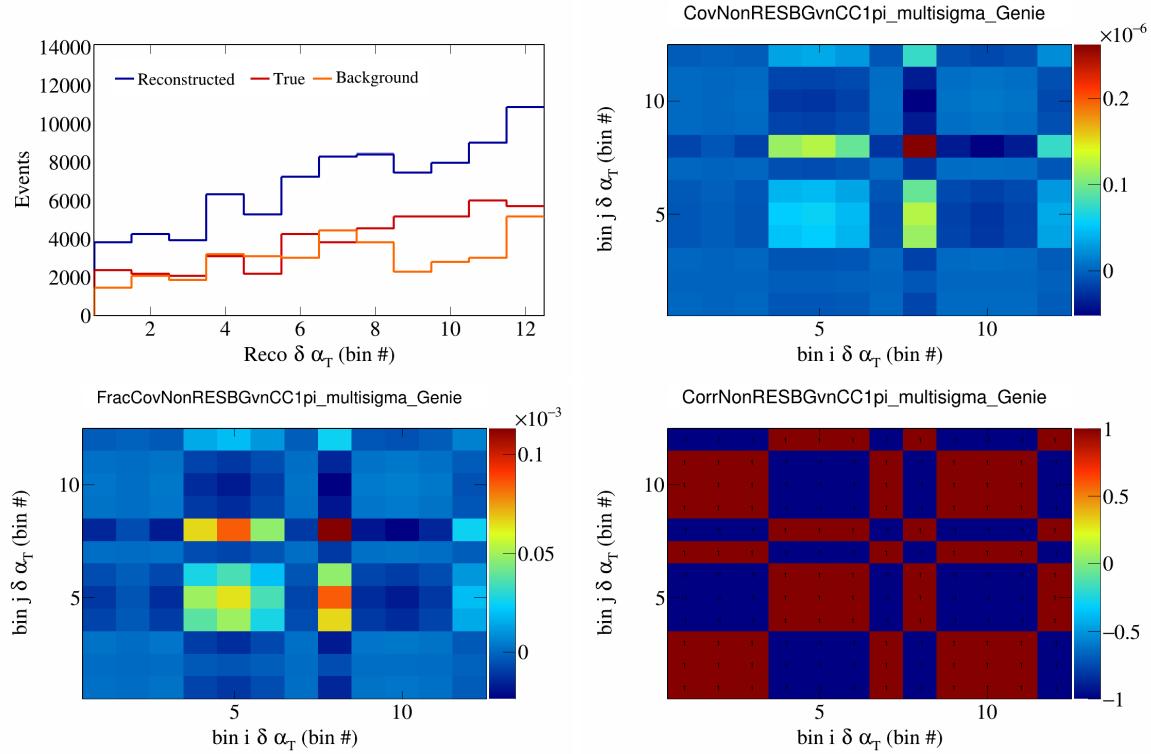


Figure 507: NonRESBGvnCC1pi variations for  $\delta\alpha_T$  in  $\cos(\theta_{\vec{p}_\mu})$ .

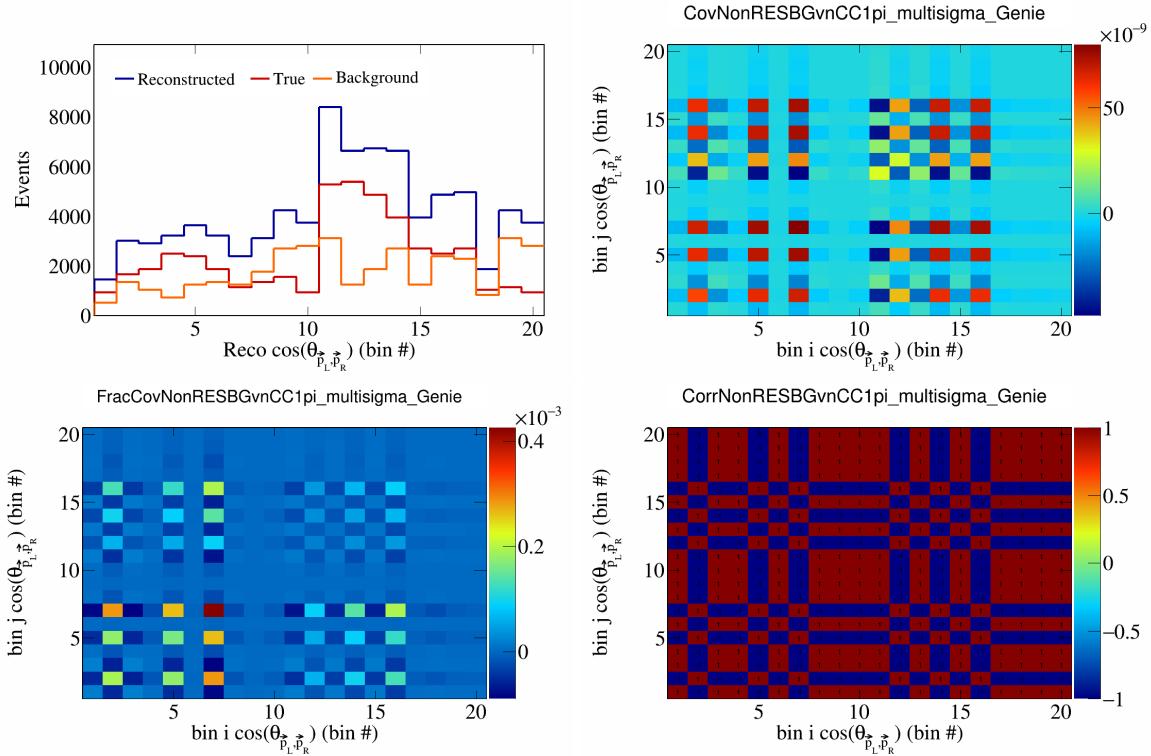


Figure 508: NonRESBGvnCC1pi variations for  $\cos(\theta_{\vec{p}_L, \vec{p}_R})$  in  $\cos(\theta_{\vec{p}_\mu})$ .

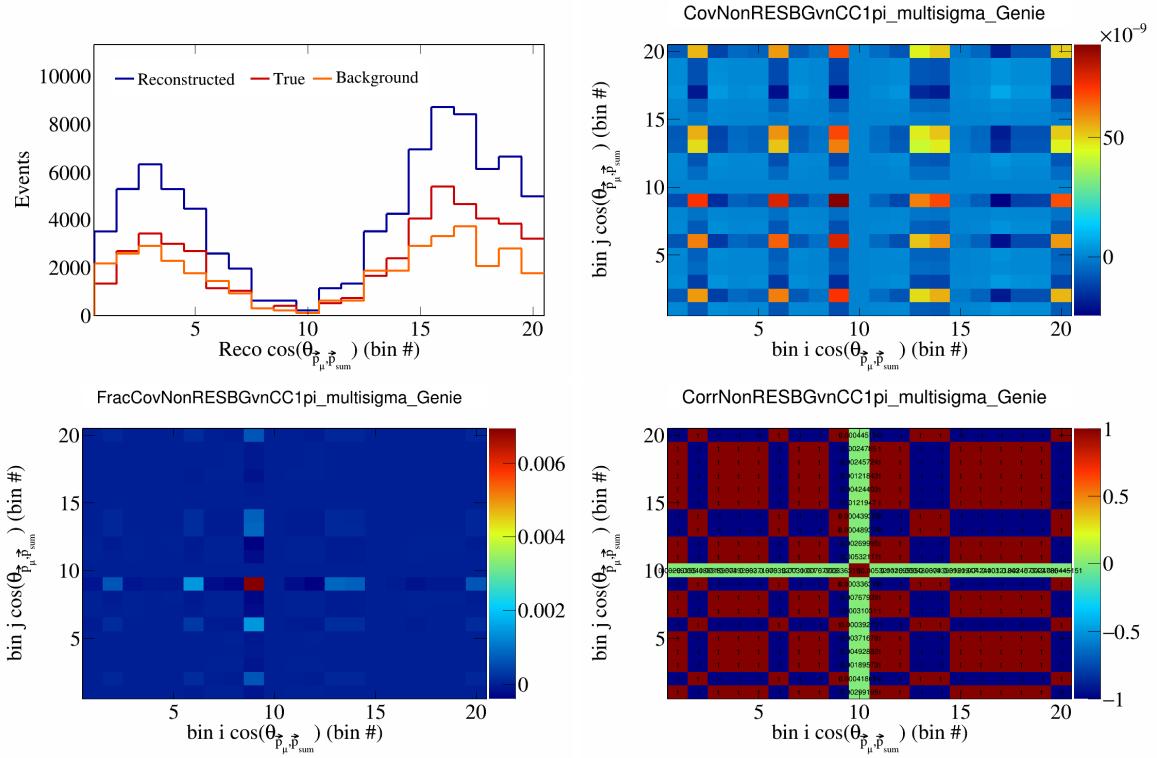


Figure 509: NonRESBGvnCC1pi variations for  $\cos(\theta_{\vec{p}_\mu})$  in  $\cos(\theta_{\vec{p}_\mu})$ .

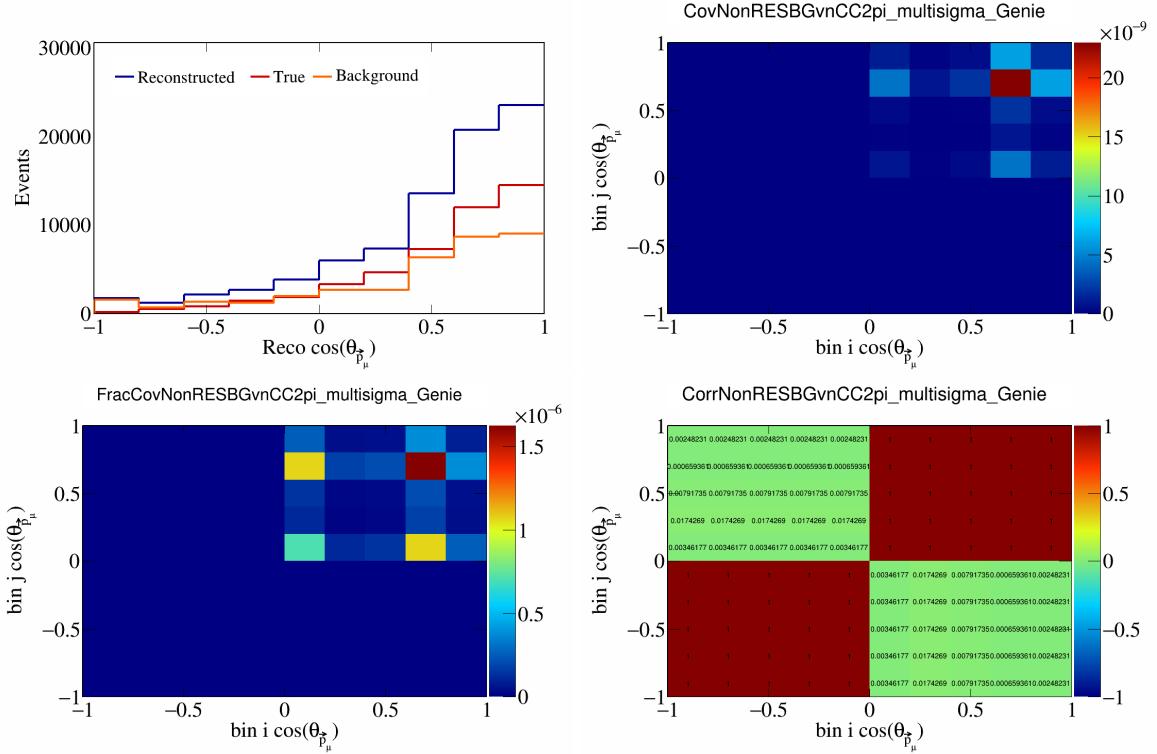


Figure 510: NonRESBGvnCC2pi variations for  $\cos(\theta_{\vec{p}_\mu})$ .

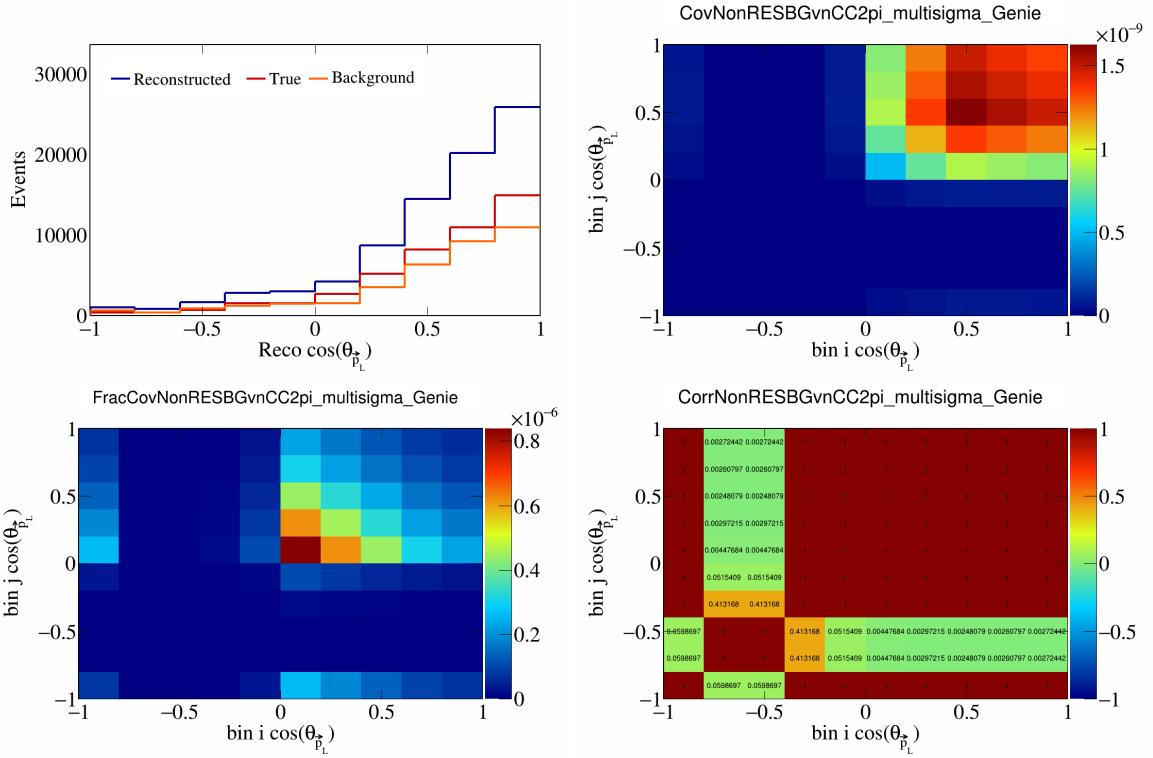


Figure 511: NonRESBGvnCC2pi variations for  $\cos(\theta_{\vec{p}_L})$ .

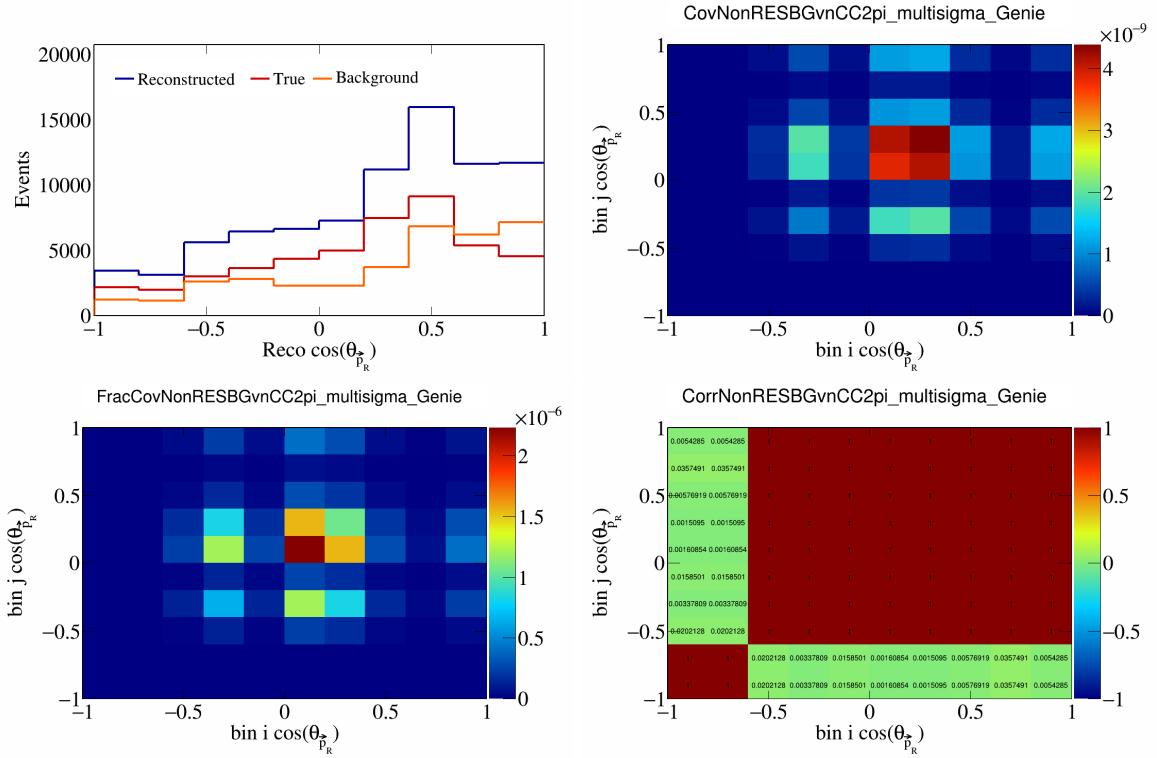


Figure 512: NonRESBGvnCC2pi variations for  $\cos(\theta_{\vec{p}_R})$ .

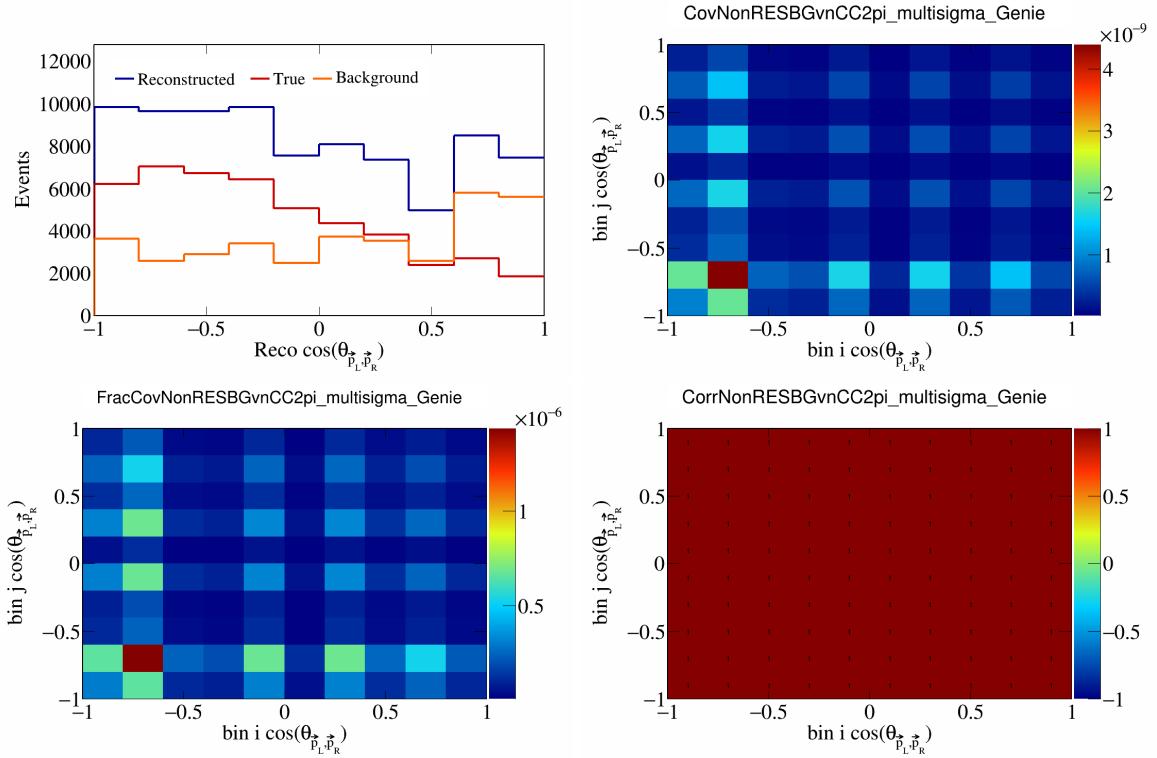


Figure 513: NonRESBGvnCC2pi variations for  $\cos(\theta_{\vec{p}_L, \vec{p}_R})$ .

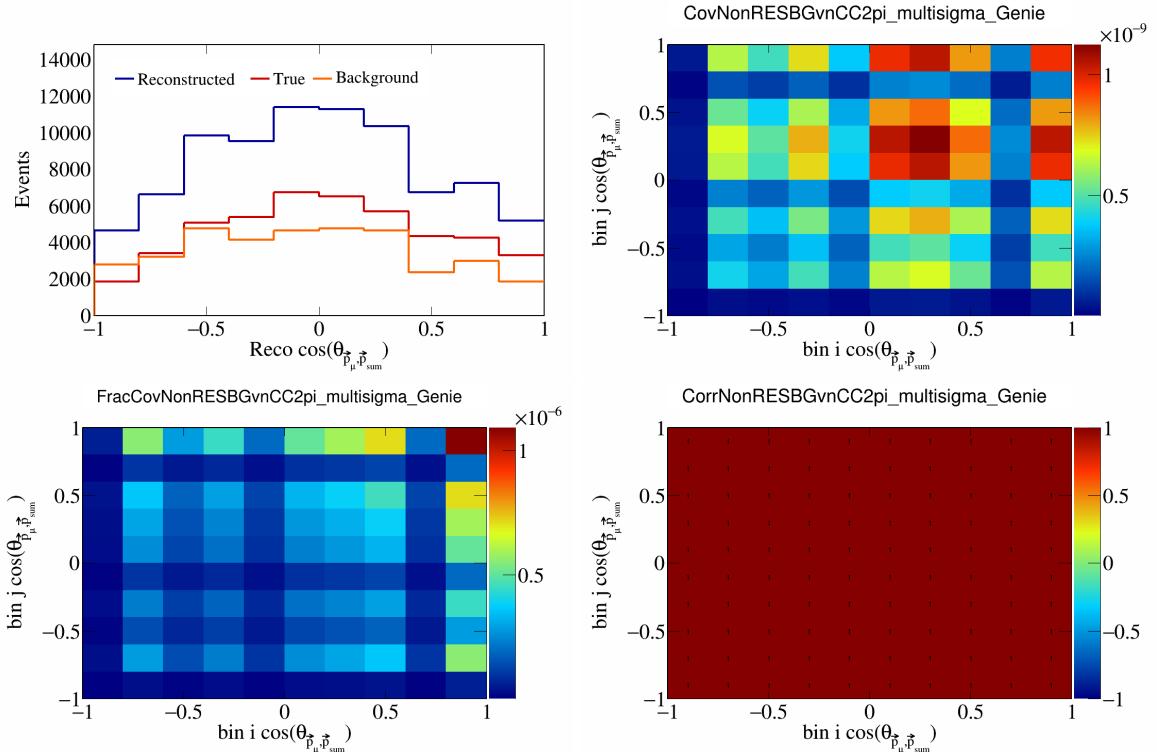


Figure 514: NonRESBGvnCC2pi variations for  $\cos(\theta_{\vec{p}_\mu, \vec{p}_{\text{sum}}})$ .

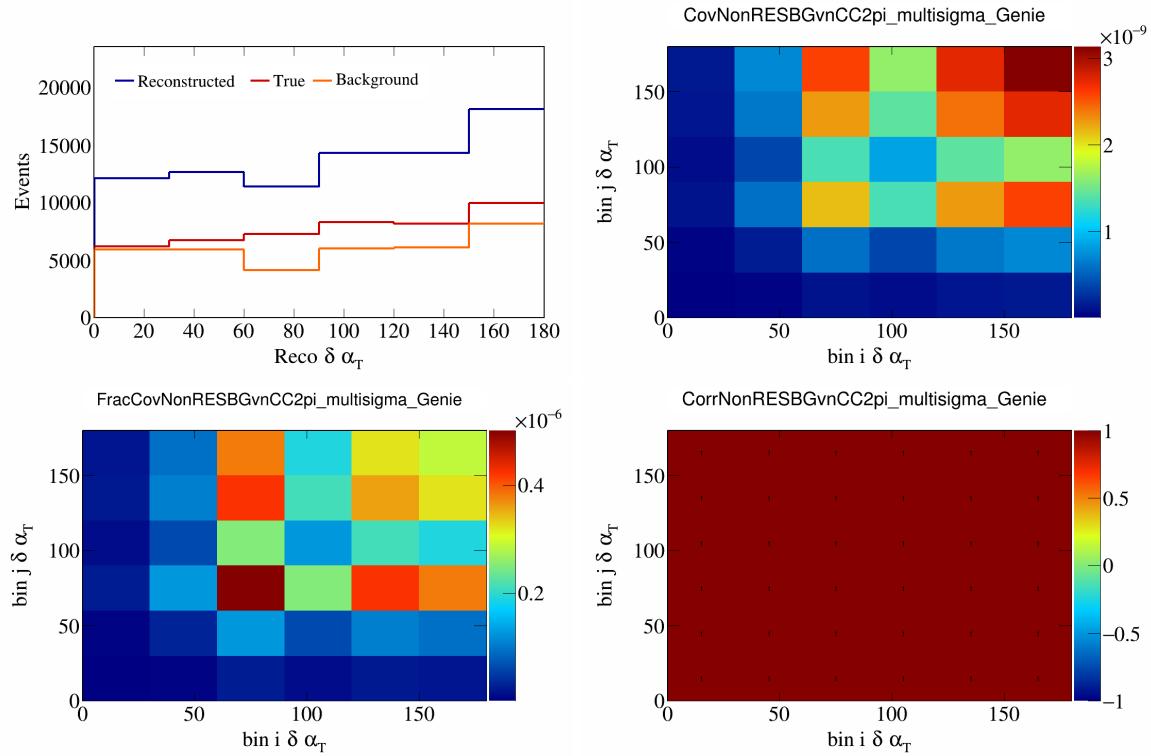


Figure 515: NonRESBGvnCC2pi variations for  $\delta\alpha_T$ .

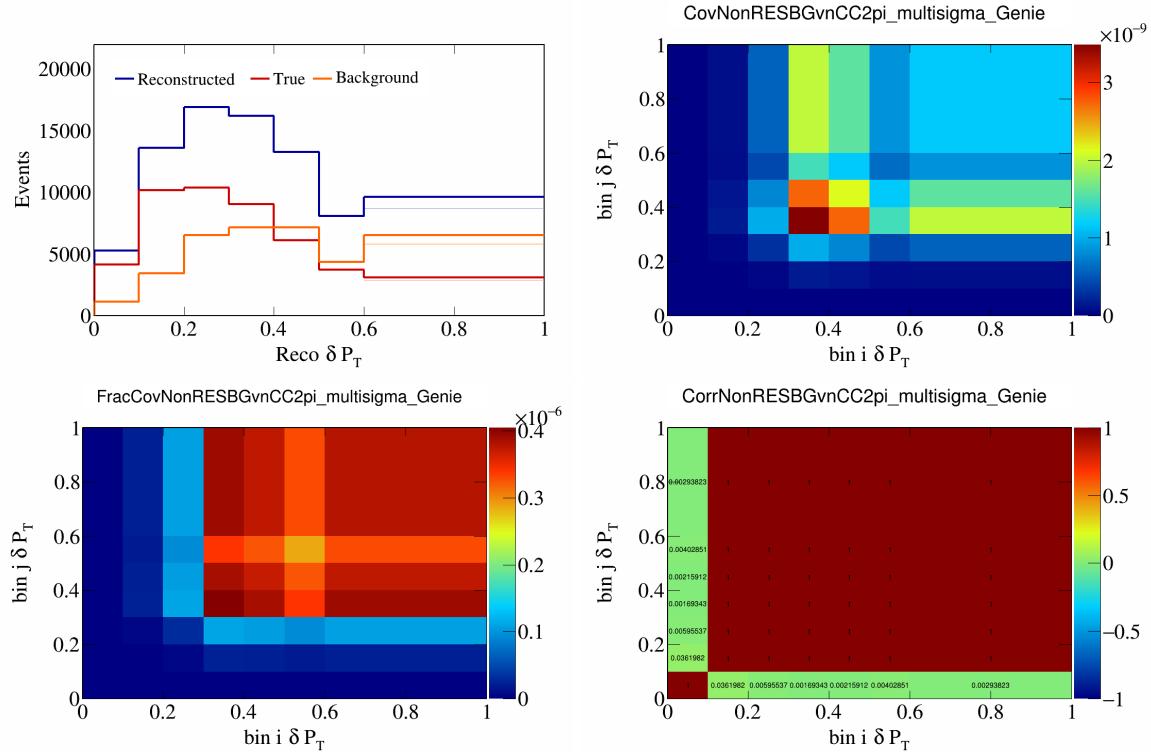


Figure 516: NonRESBGvnCC2pi variations for  $\delta P_T$ .

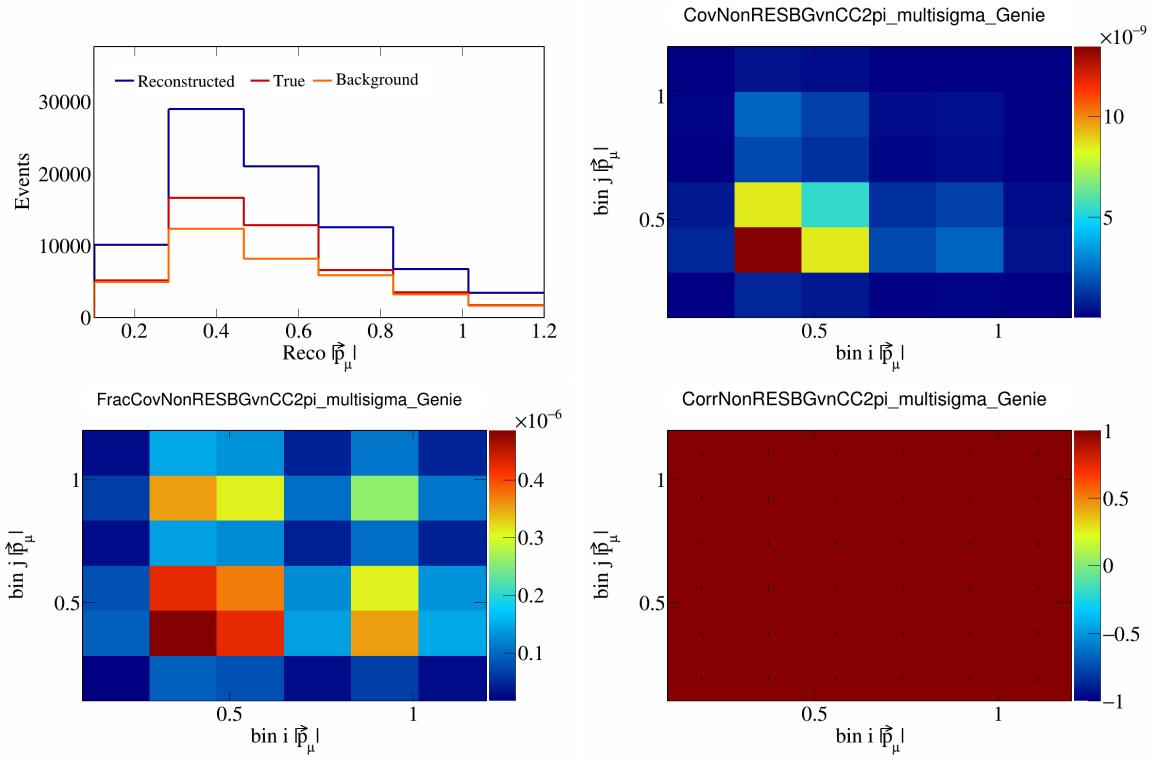


Figure 517: NonRESBGvnCC2pi variations for  $|\vec{p}_\mu|$ .

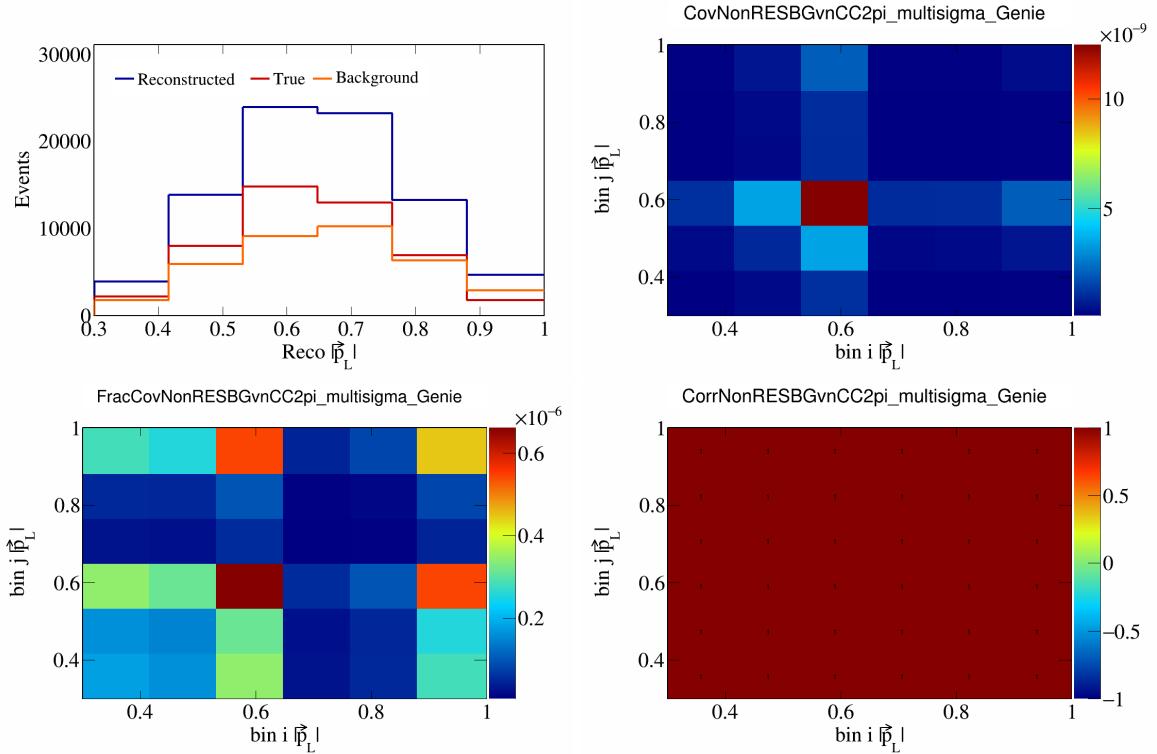


Figure 518: NonRESBGvnCC2pi variations for  $|\vec{p}_L|$ .

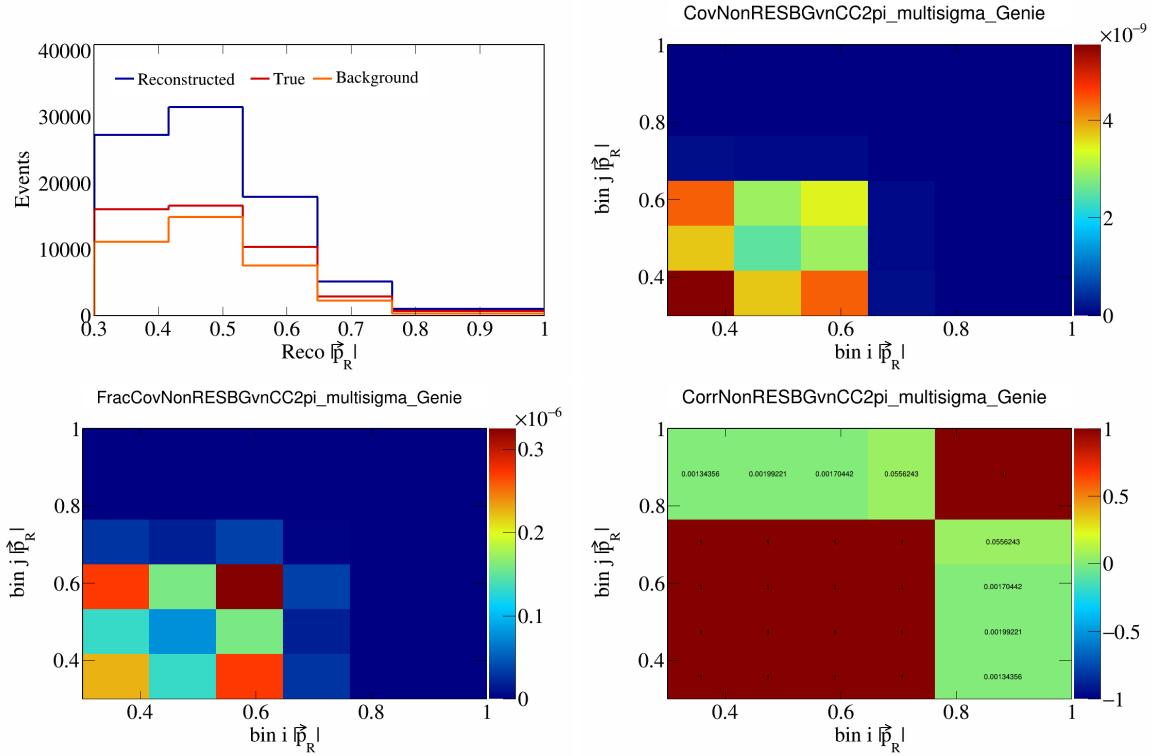


Figure 519: NonRESBGvnCC2pi variations for  $|\vec{p}_R|$ .

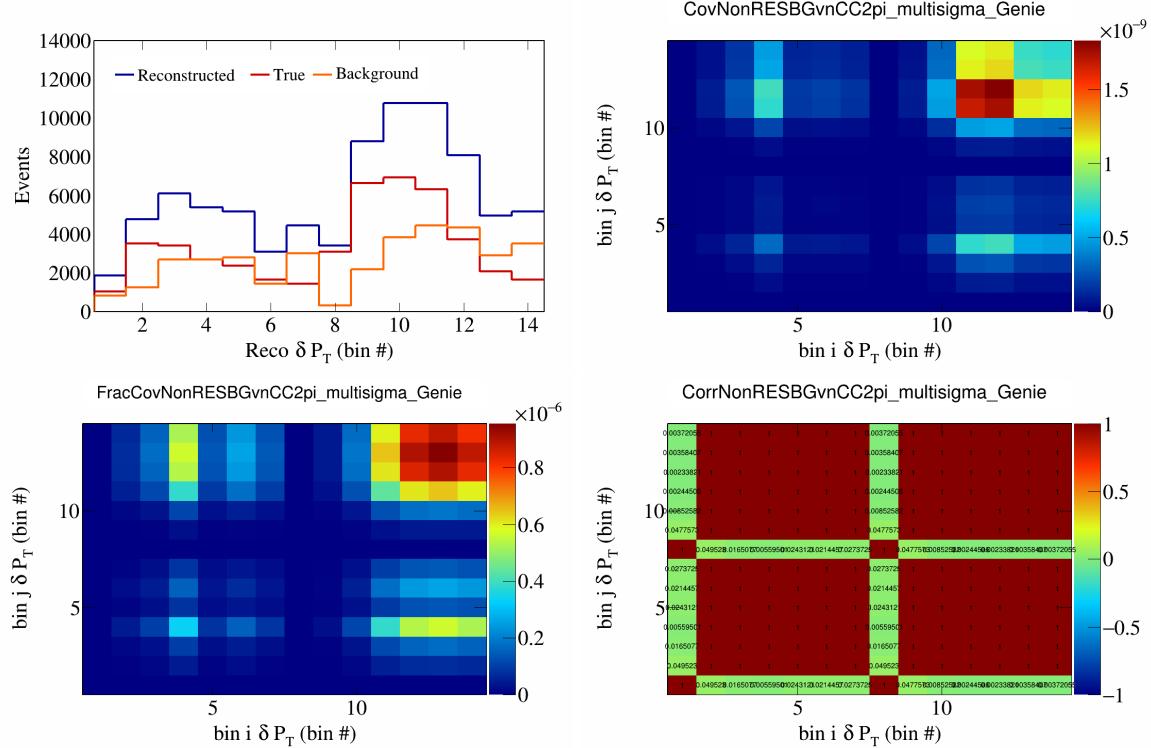


Figure 520: NonRESBGvnCC2pi variations for  $\delta P_T$  in  $\cos(\theta_{\vec{p}_\mu})$ .

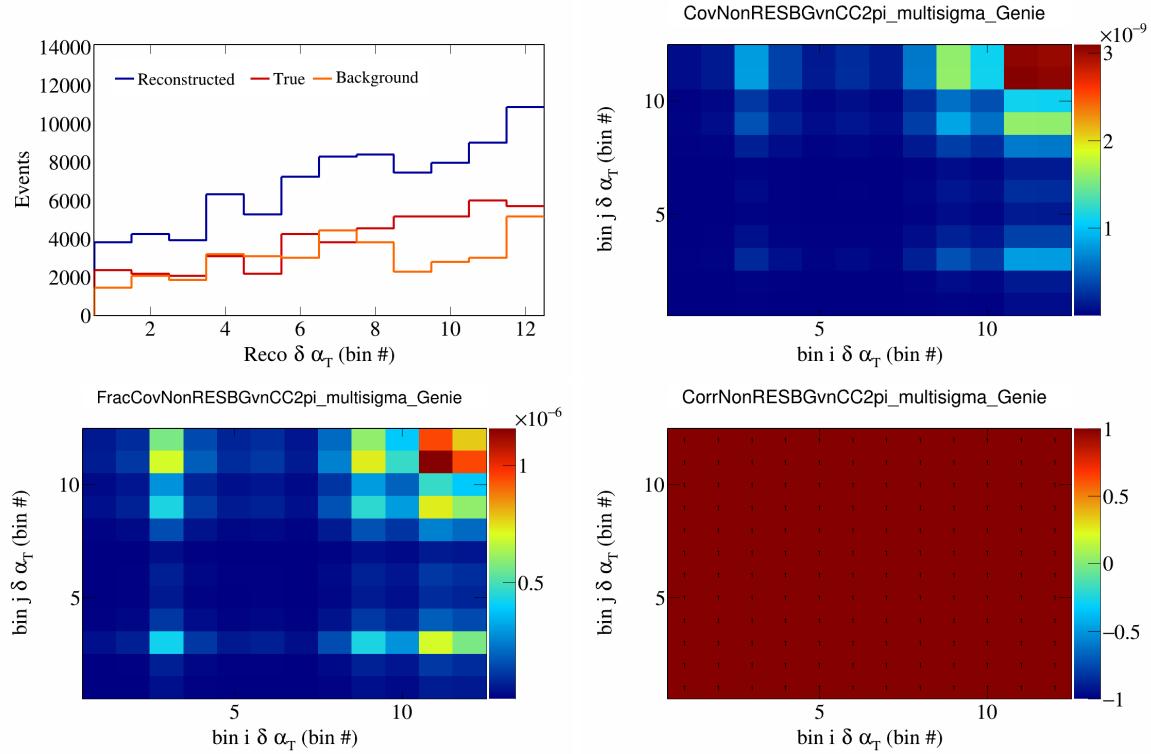


Figure 521: NonRESBGvnCC2pi variations for  $\delta\alpha_T$  in  $\cos(\theta_{\vec{p}_\mu})$ .

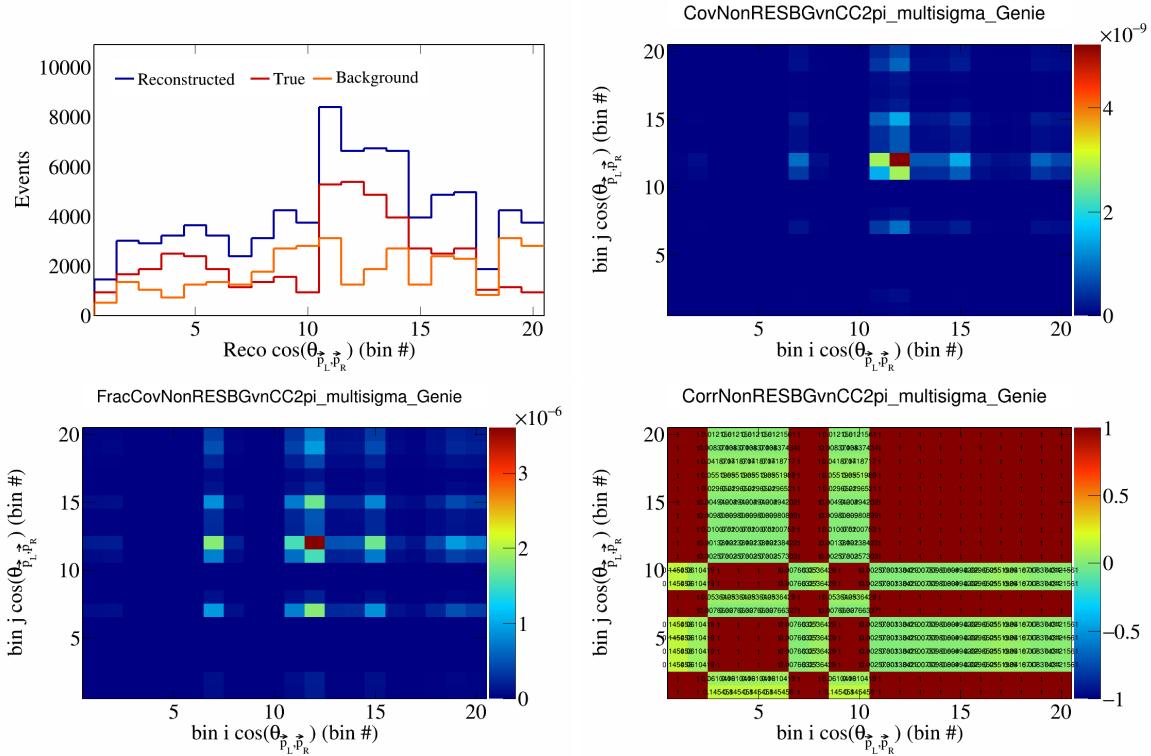


Figure 522: NonRESBGvnCC2pi variations for  $\cos(\theta_{\vec{p}_L, \vec{p}_R})$  in  $\cos(\theta_{\vec{p}_\mu})$ .

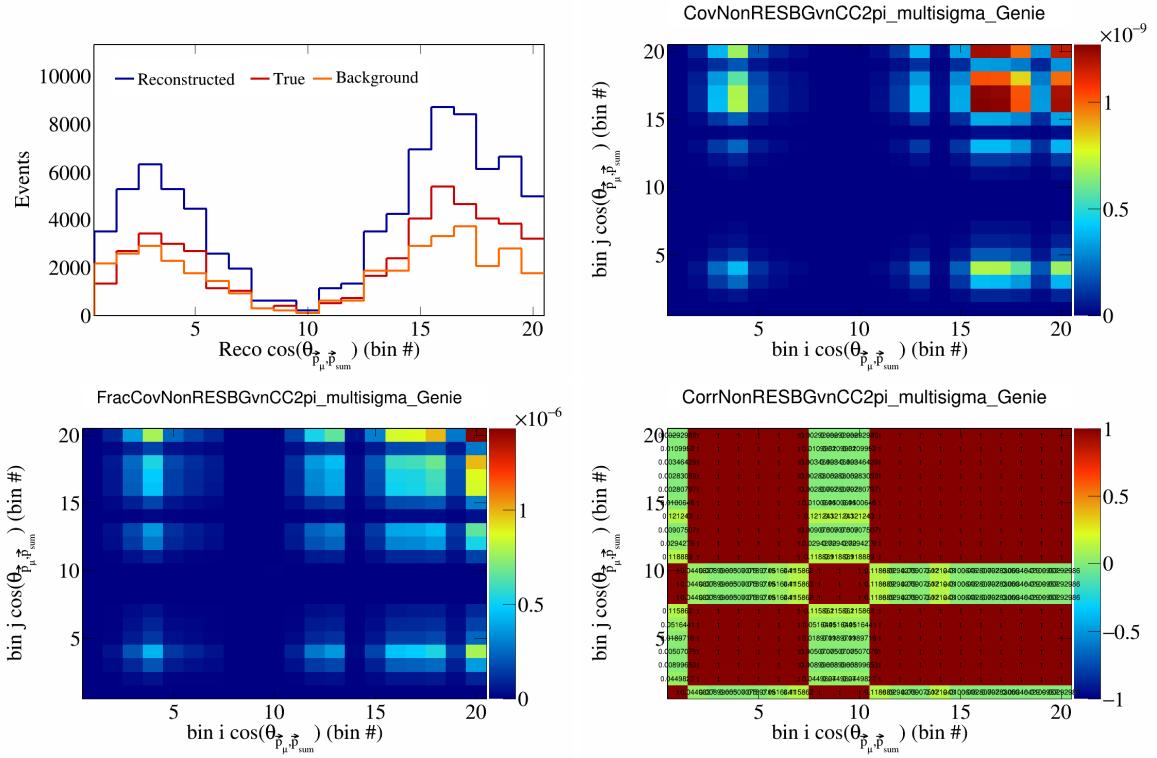


Figure 523: NonRESBGvnCC2pi variations for  $\cos(\theta_{\vec{p}_\mu})$  in  $\cos(\theta_{\vec{p}_\mu})$ .

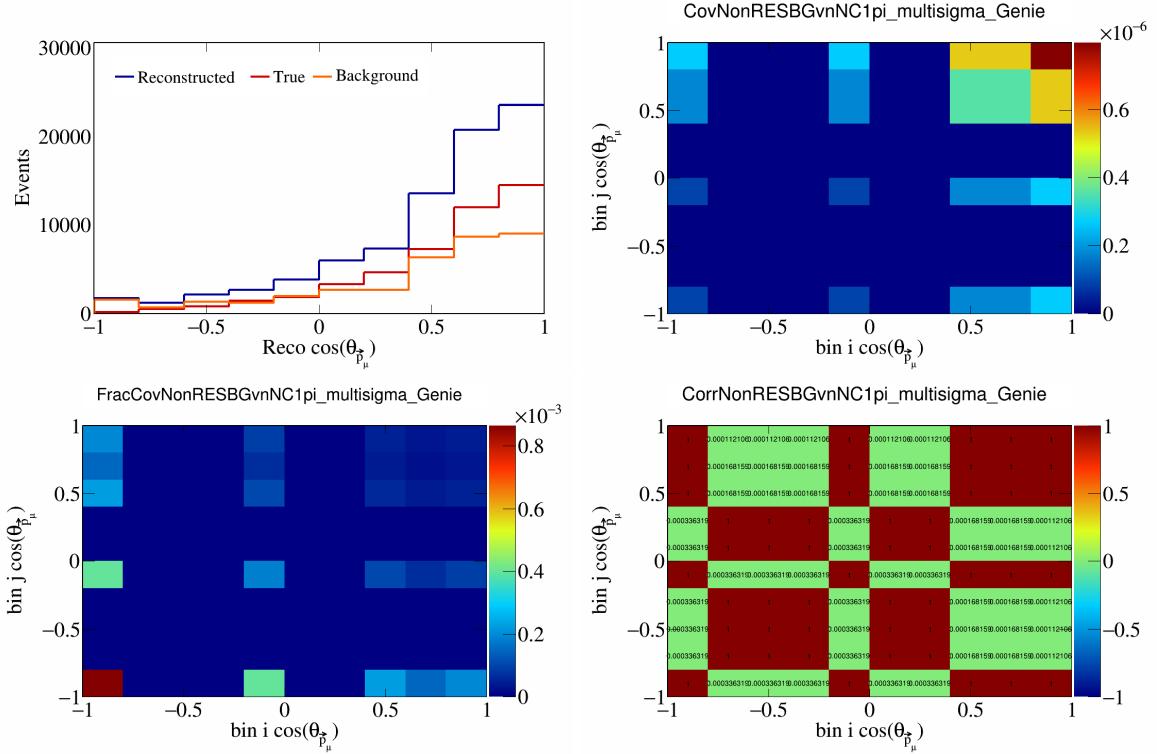


Figure 524: NonRESBGvnNC1pi variations for  $\cos(\theta_{\vec{p}_\mu})$ .

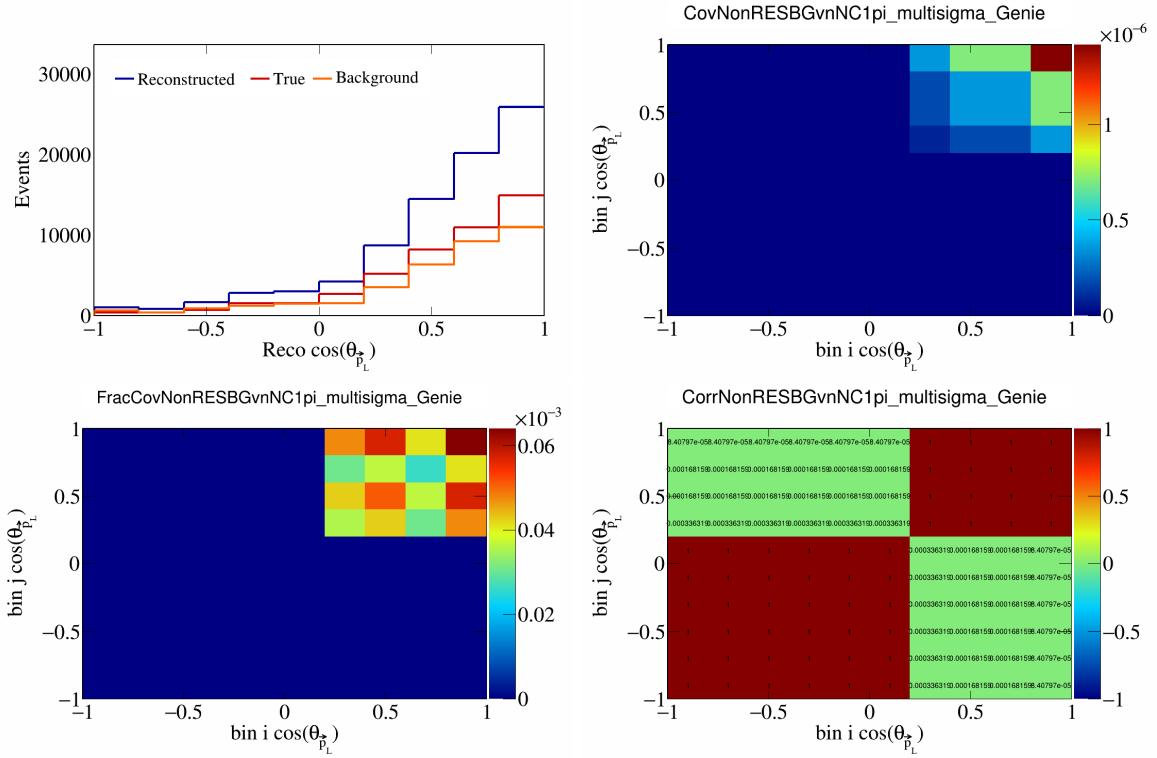


Figure 525: NonRESBGvnNC1pi variations for  $\cos(\theta_{\vec{p}_L})$ .

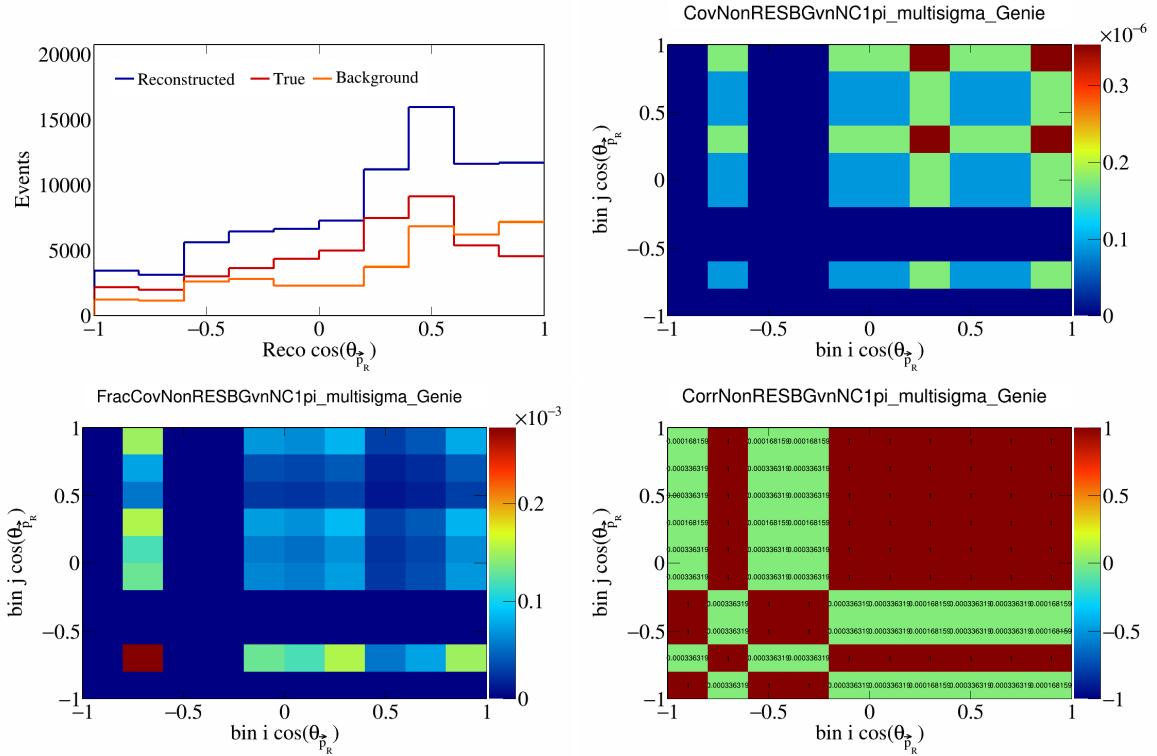


Figure 526: NonRESBGvnNC1pi variations for  $\cos(\theta_{\vec{p}_R})$ .

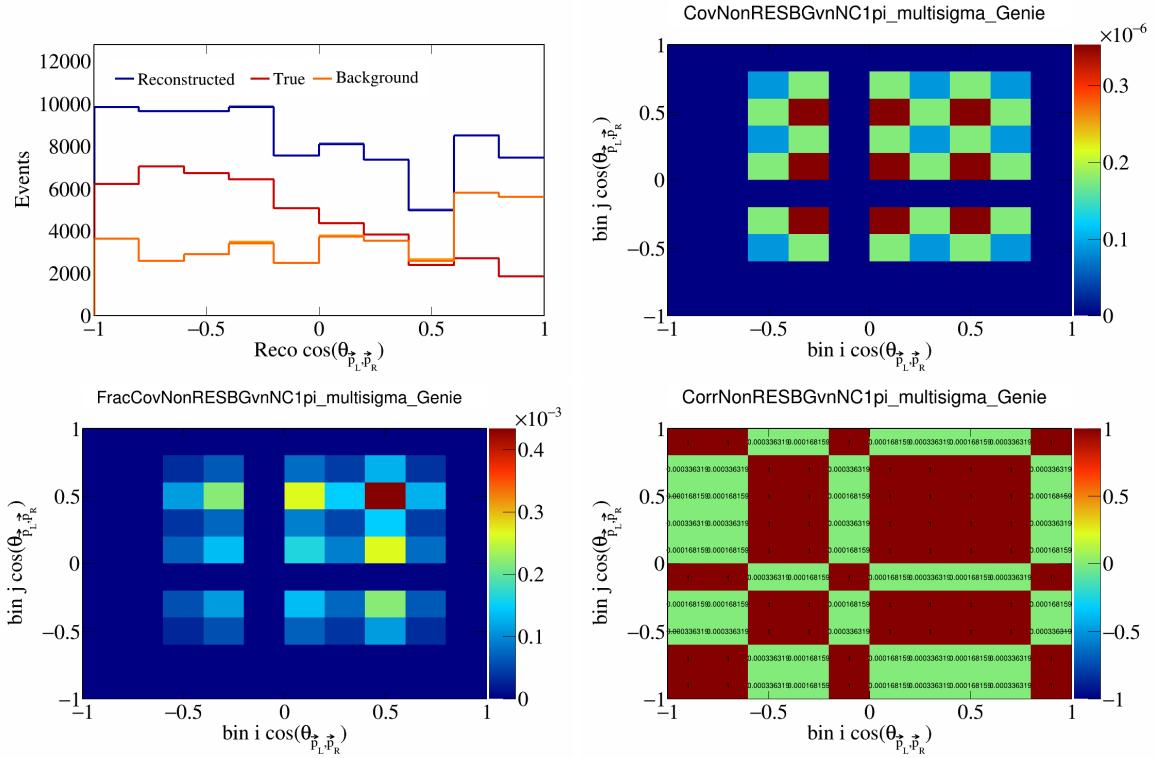


Figure 527: NonRESBGvnNC1pi variations for  $\cos(\theta_{\vec{p}_L, \vec{p}_R})$ .

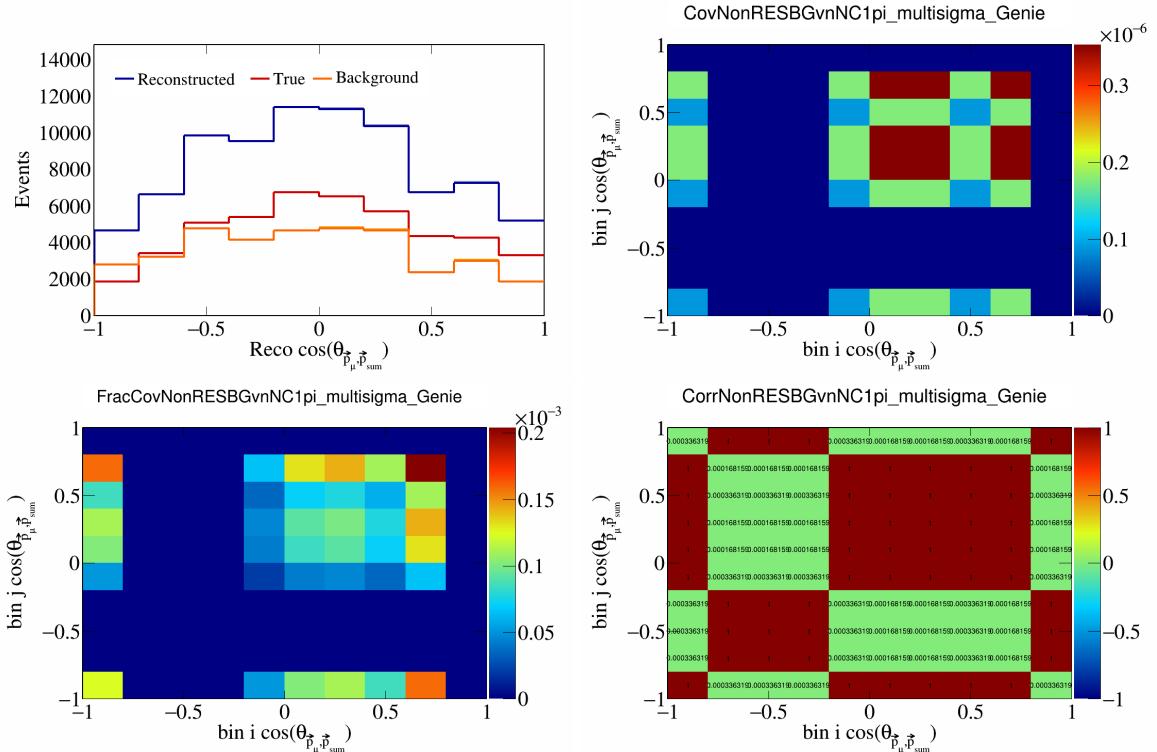


Figure 528: NonRESBGvnNC1pi variations for  $\cos(\theta_{\vec{p}_\mu, \vec{p}_{\text{sum}}})$ .

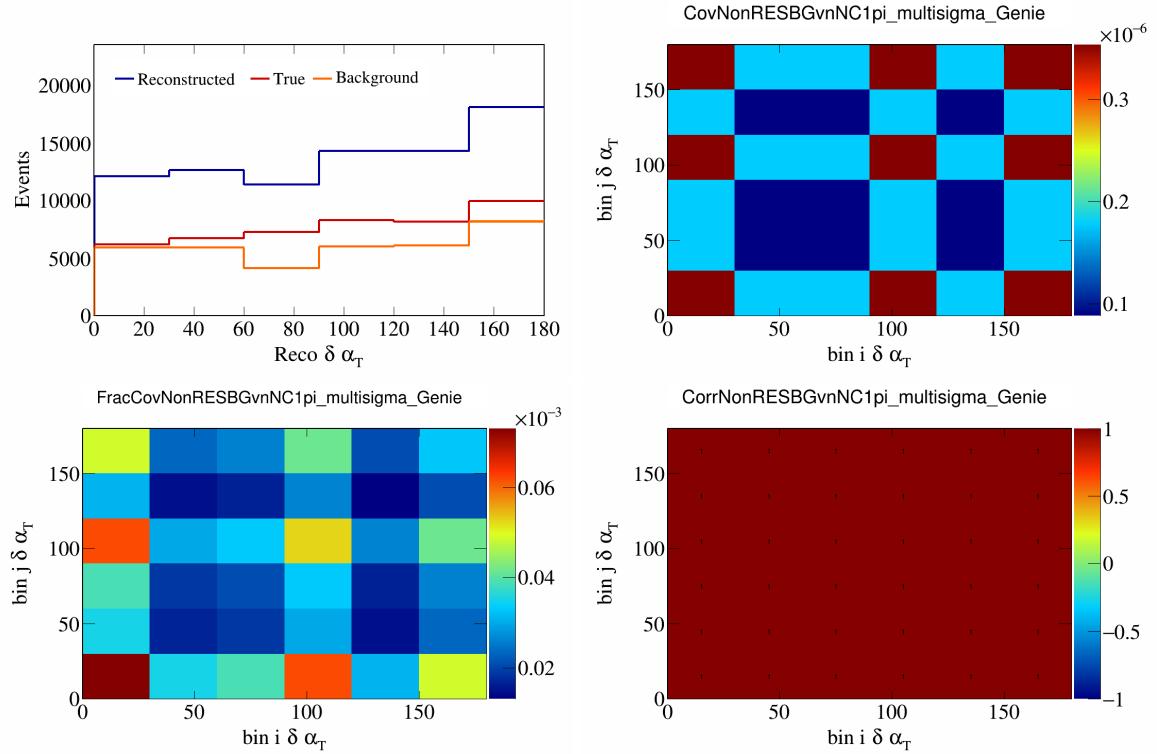


Figure 529: NonRESBGvnNC1pi variations for  $\delta\alpha_T$ .

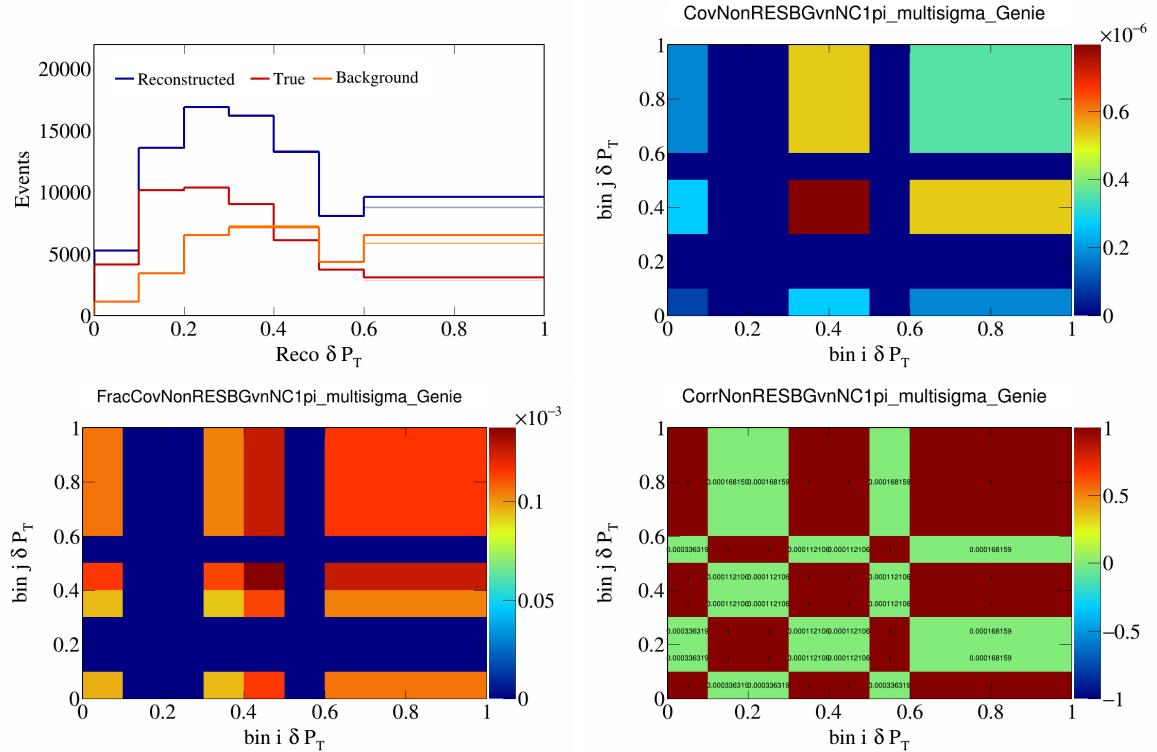


Figure 530: NonRESBGvnNC1pi variations for  $\delta P_T$ .

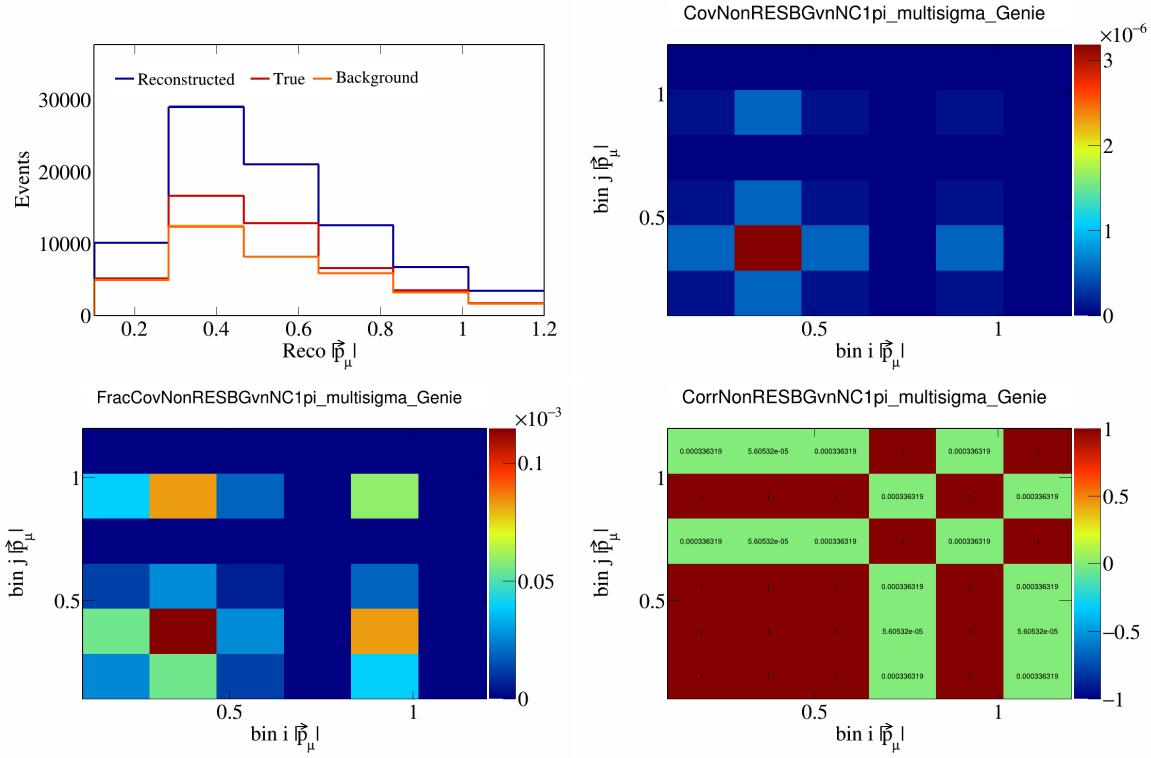


Figure 531: NonRESBGvnNC1pi variations for  $|\vec{p}_\mu|$ .

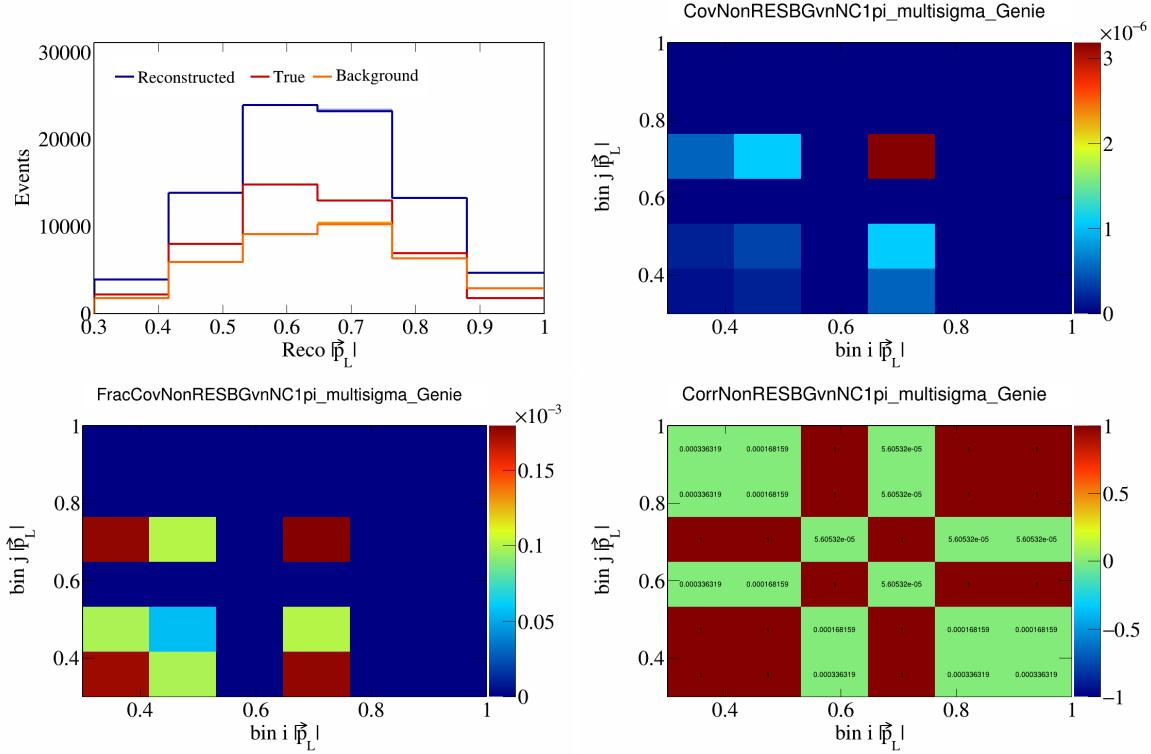


Figure 532: NonRESBGvnNC1pi variations for  $|\vec{p}_L|$ .

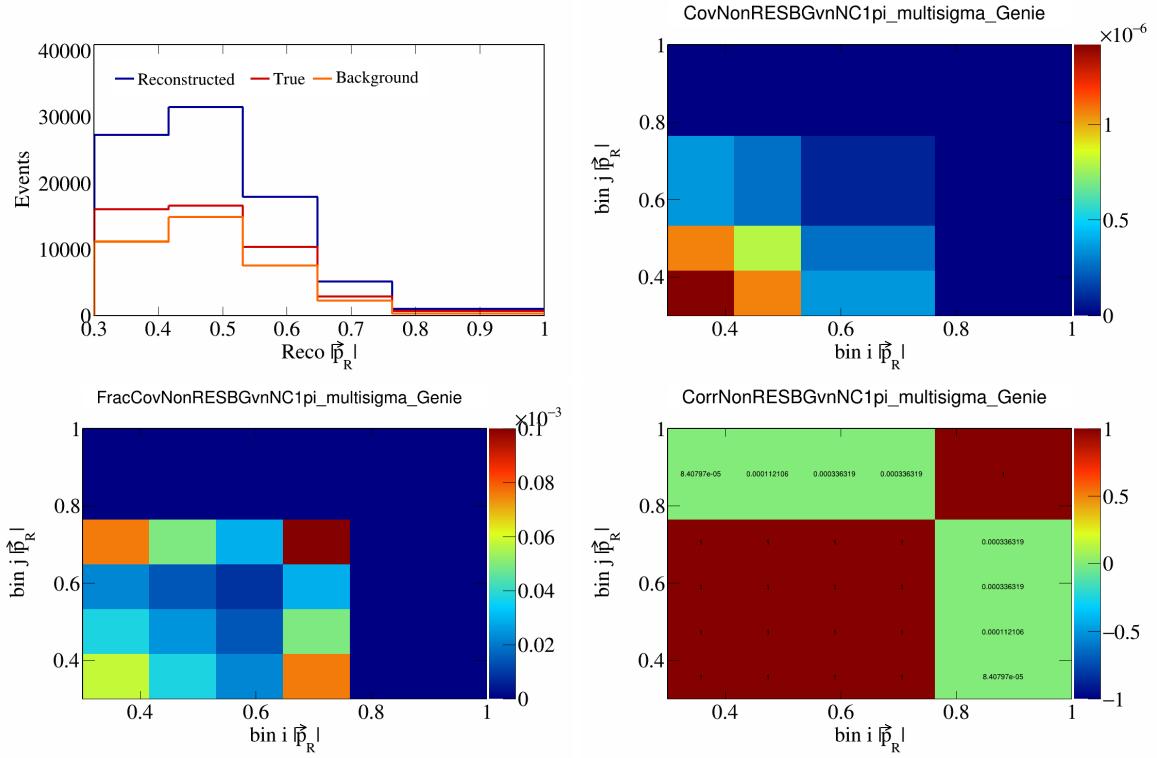


Figure 533: NonRESBGvnNC1pi variations for  $|\vec{p}_R|$ .

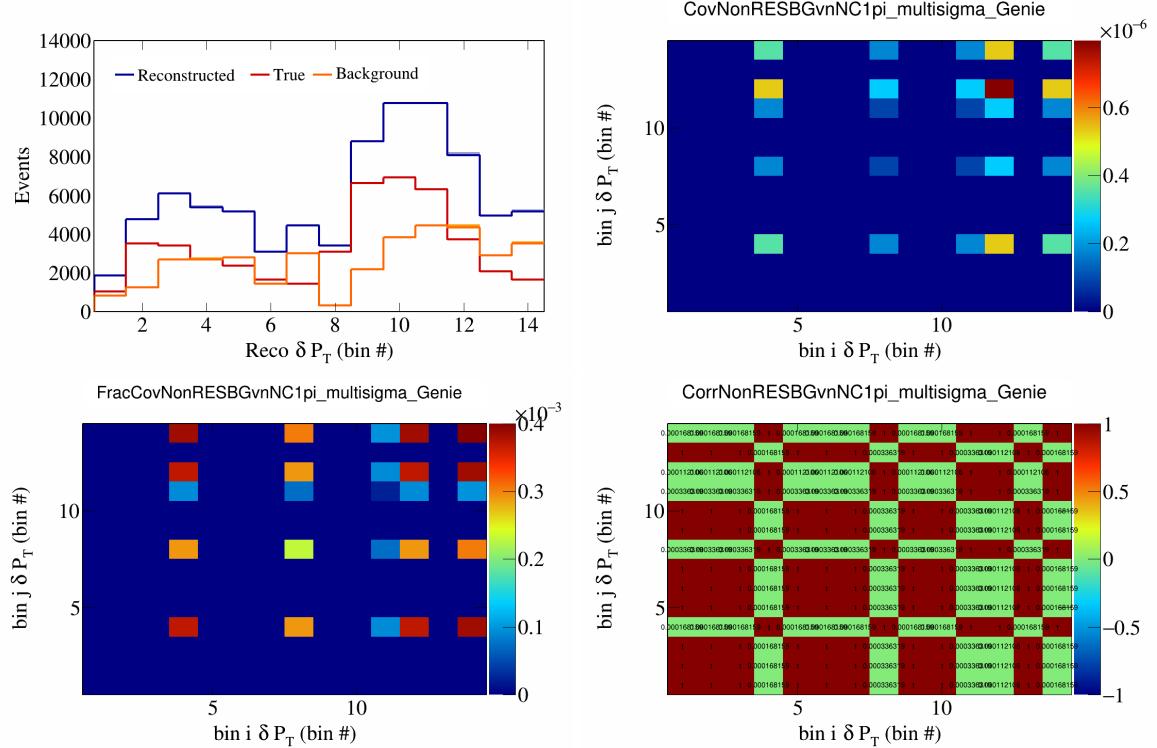


Figure 534: NonRESBGvnNC1pi variations for  $\delta P_T$  in  $\cos(\theta_{\vec{p}_\mu})$ .

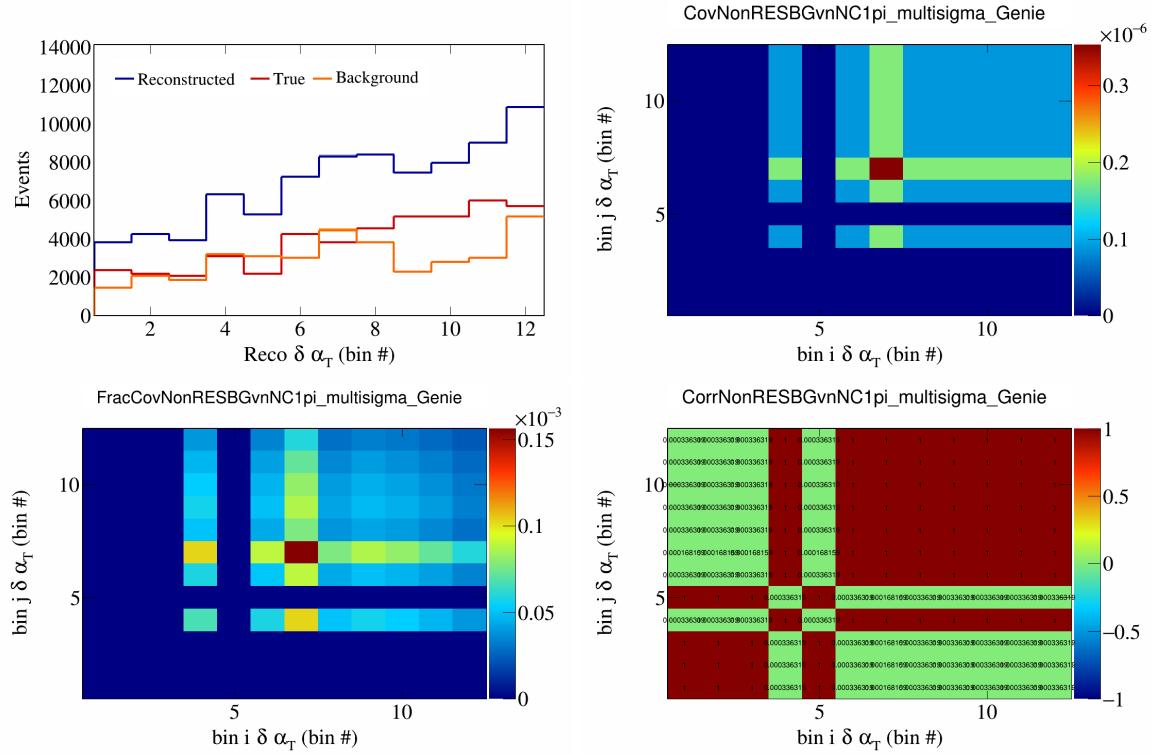


Figure 535: NonRESBGvnNC1pi variations for  $\delta\alpha_T$  in  $\cos(\theta_{\vec{p}_\mu})$ .

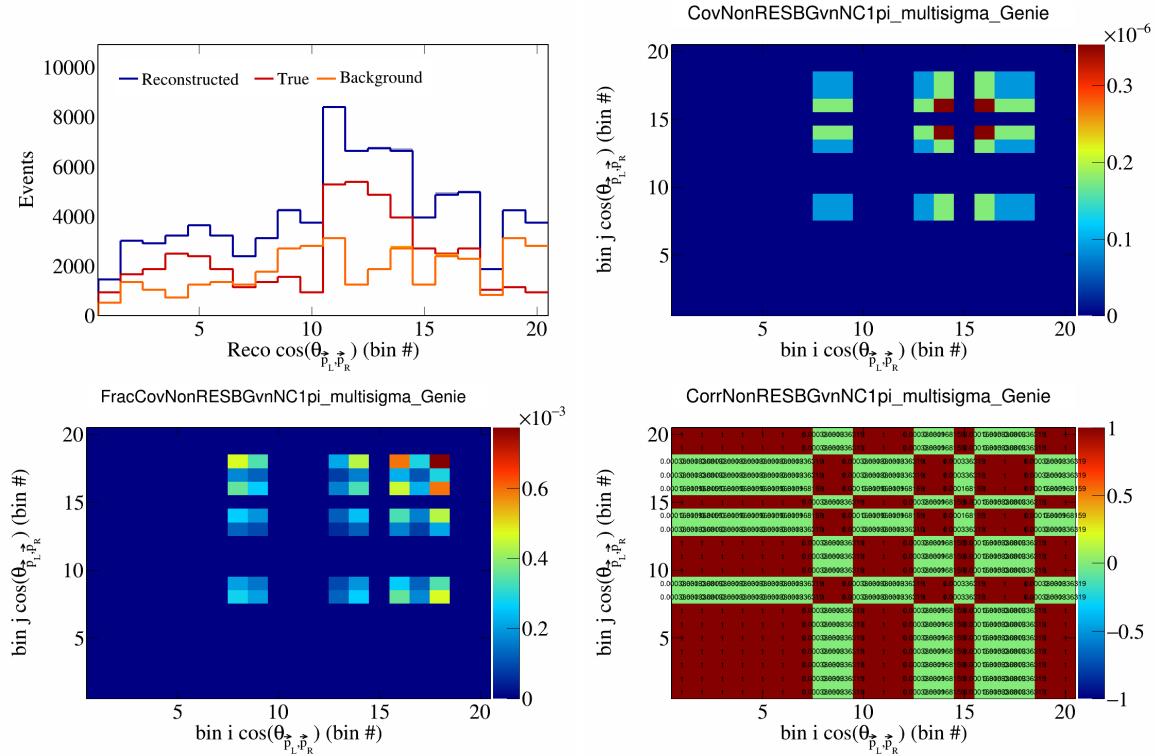


Figure 536: NonRESBGvnNC1pi variations for  $\cos(\theta_{\vec{p}_L, \vec{p}_R})$  in  $\cos(\theta_{\vec{p}_\mu})$ .

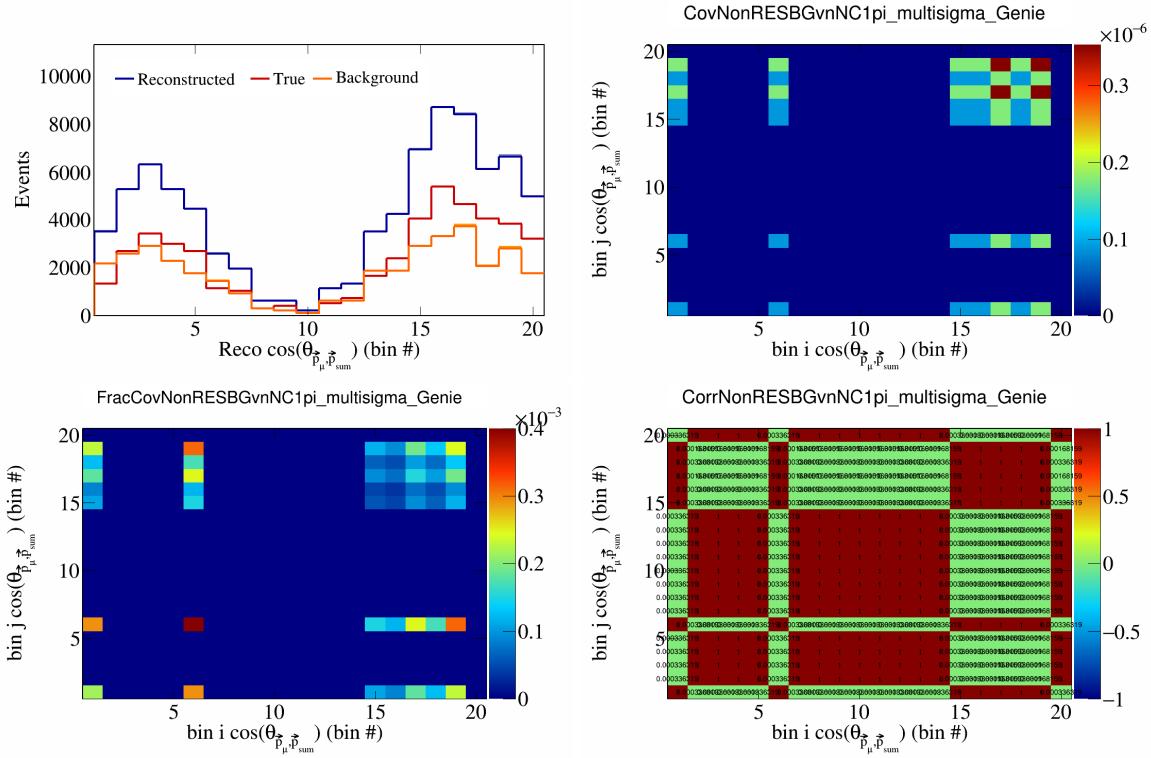


Figure 537: NonRESBGvnNC1pi variations for  $\cos(\theta_{\vec{p}_\mu, \vec{p}_{\text{sum}}})$  in  $\cos(\theta_{\vec{p}_\mu})$ .

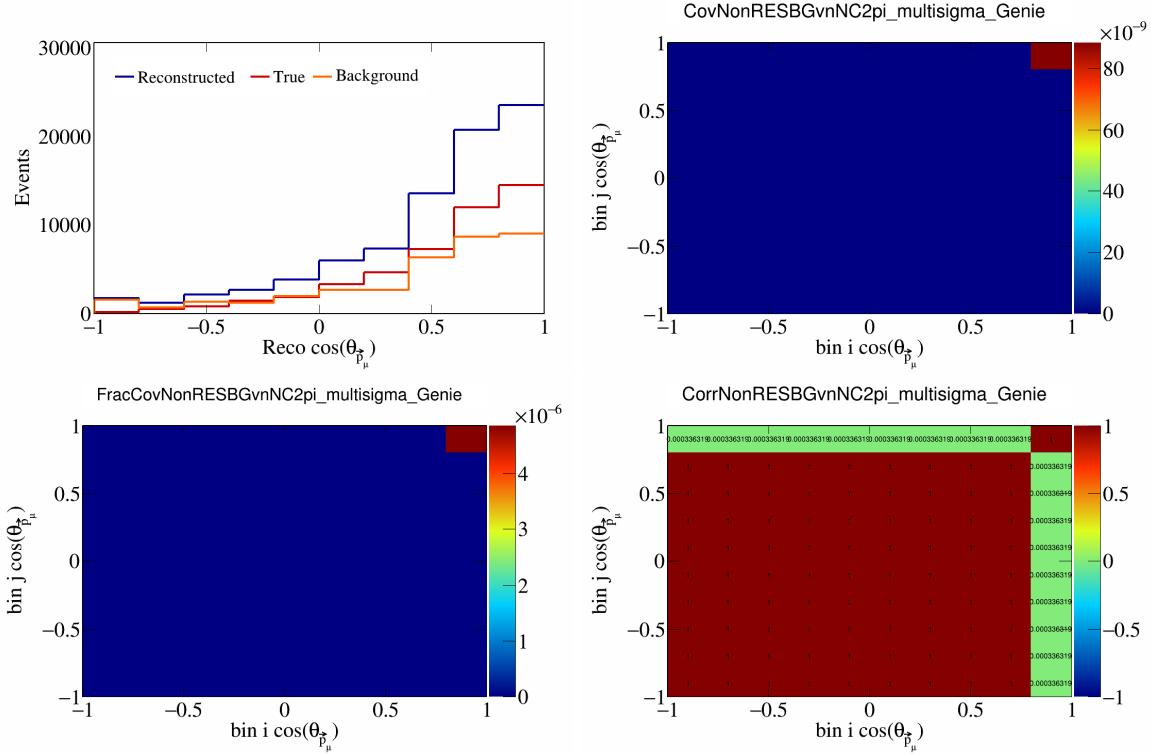


Figure 538: NonRESBGvnNC2pi variations for  $\cos(\theta_{\vec{p}_\mu}^*, \vec{p}_\mu)$ .

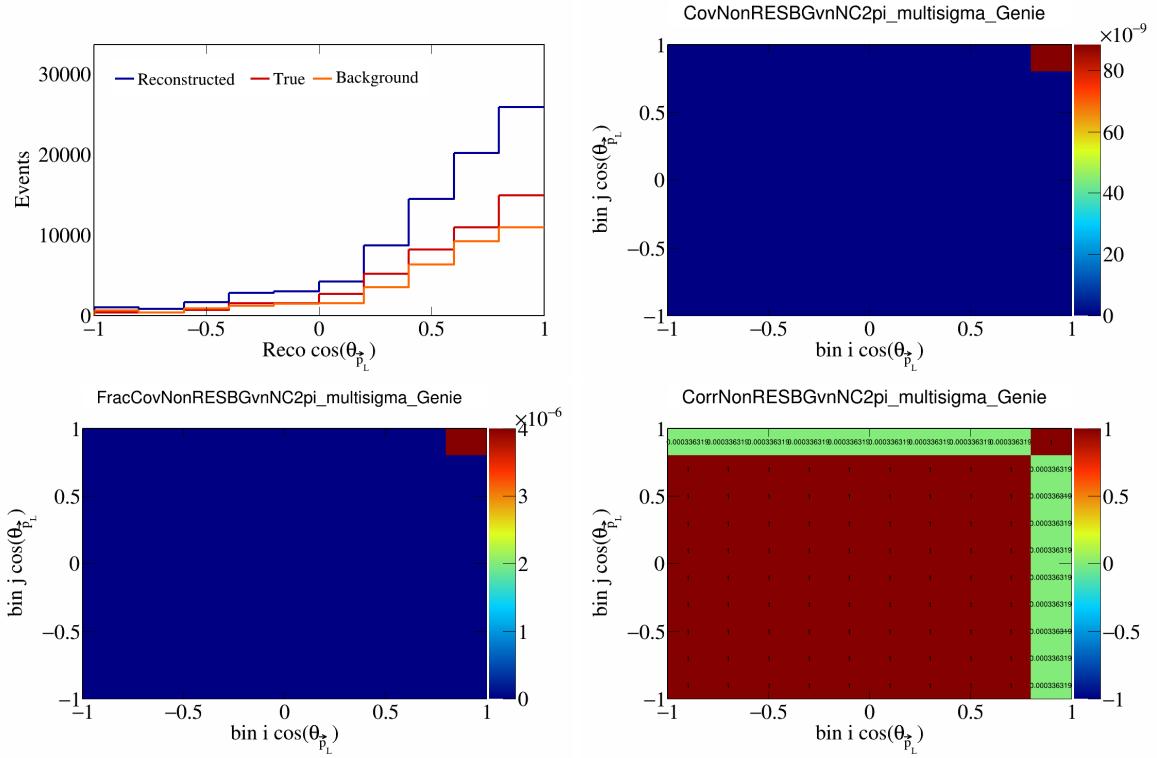


Figure 539: NonRESBGvnNC2pi variations for  $\cos(\theta_{\vec{p}_L})$ .

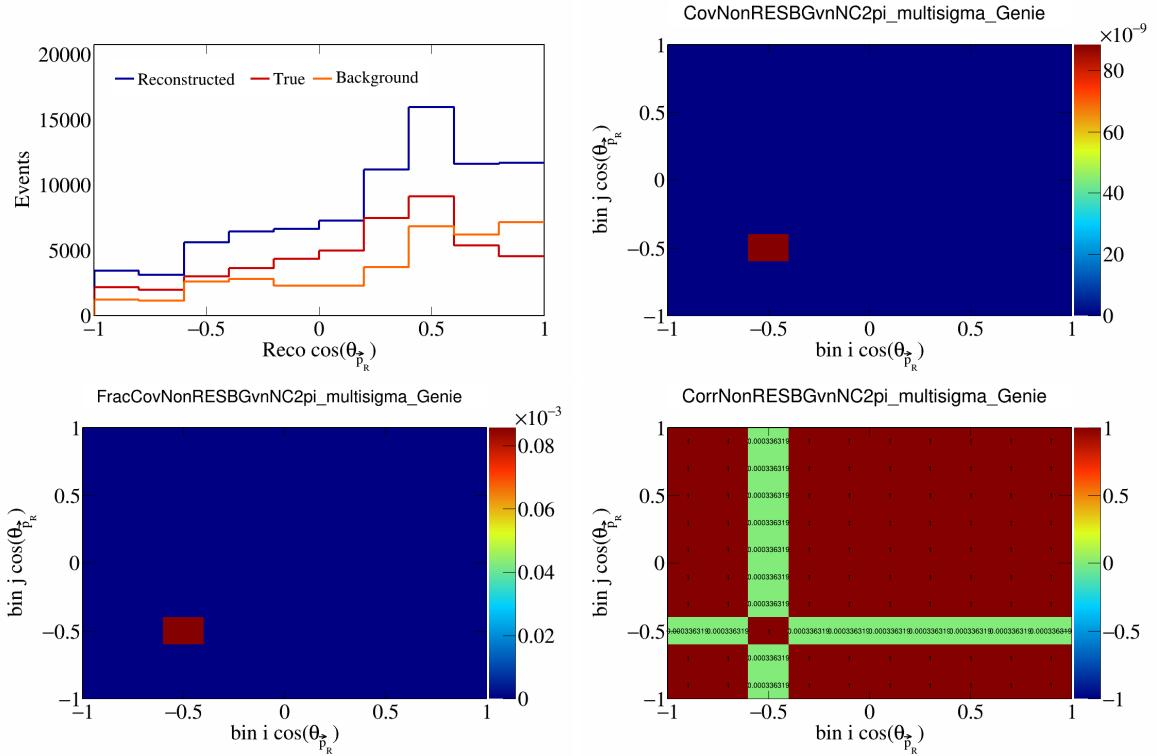


Figure 540: NonRESBGvnNC2pi variations for  $\cos(\theta_{\vec{p}_R})$ .

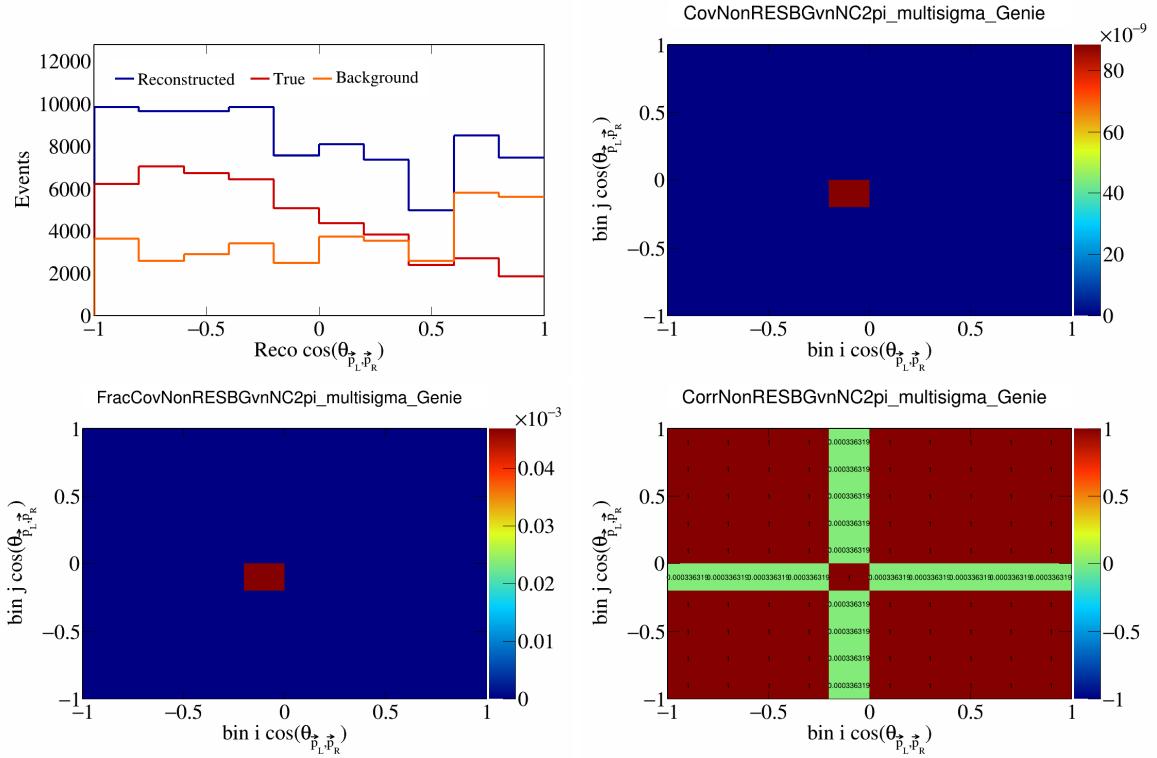


Figure 541: NonRESBGvnNC2pi variations for  $\cos(\theta_{\vec{p}_L, \vec{p}_R})$ .

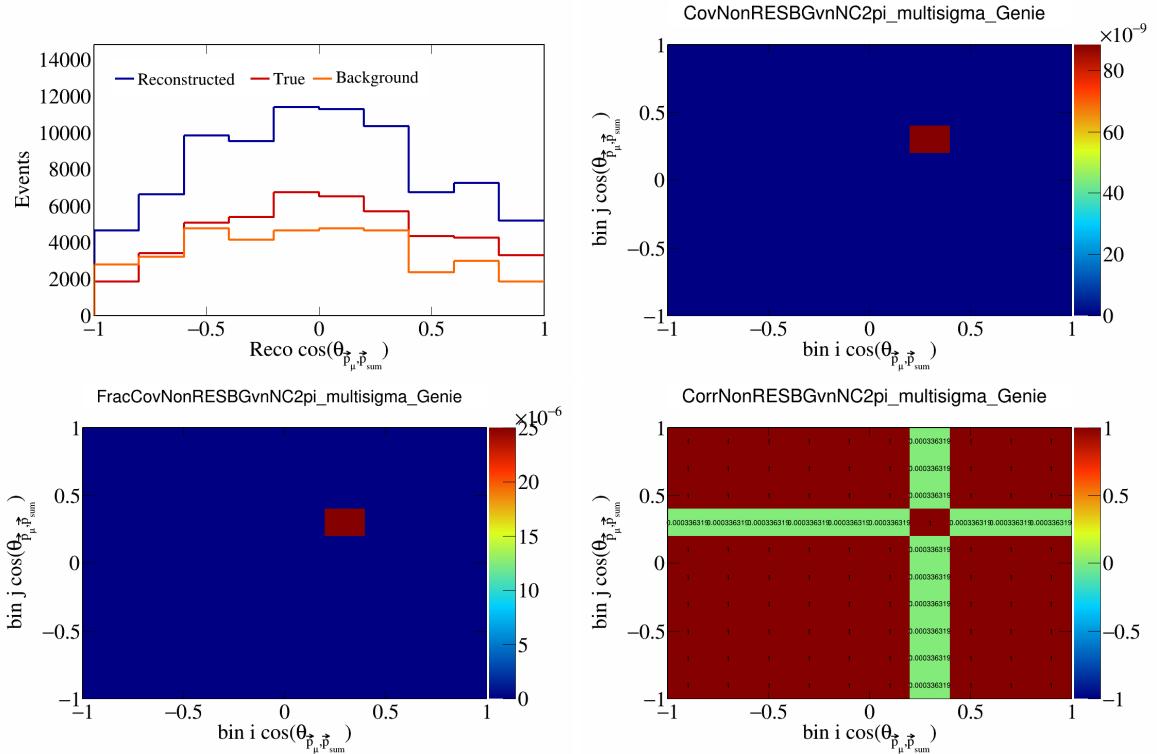


Figure 542: NonRESBGvnNC2pi variations for  $\cos(\theta_{\vec{p}_\mu, \vec{p}_{\text{sum}}})$ .

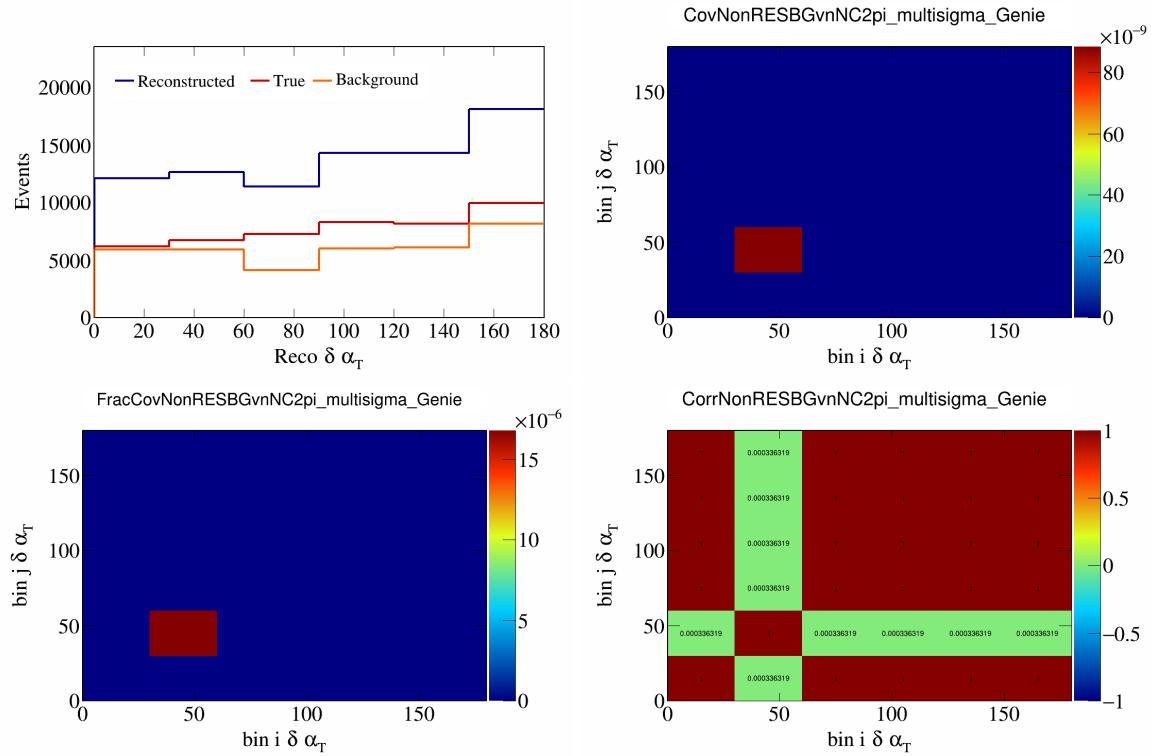


Figure 543: NonRESBGvnNC2pi variations for  $\delta\alpha_T$ .

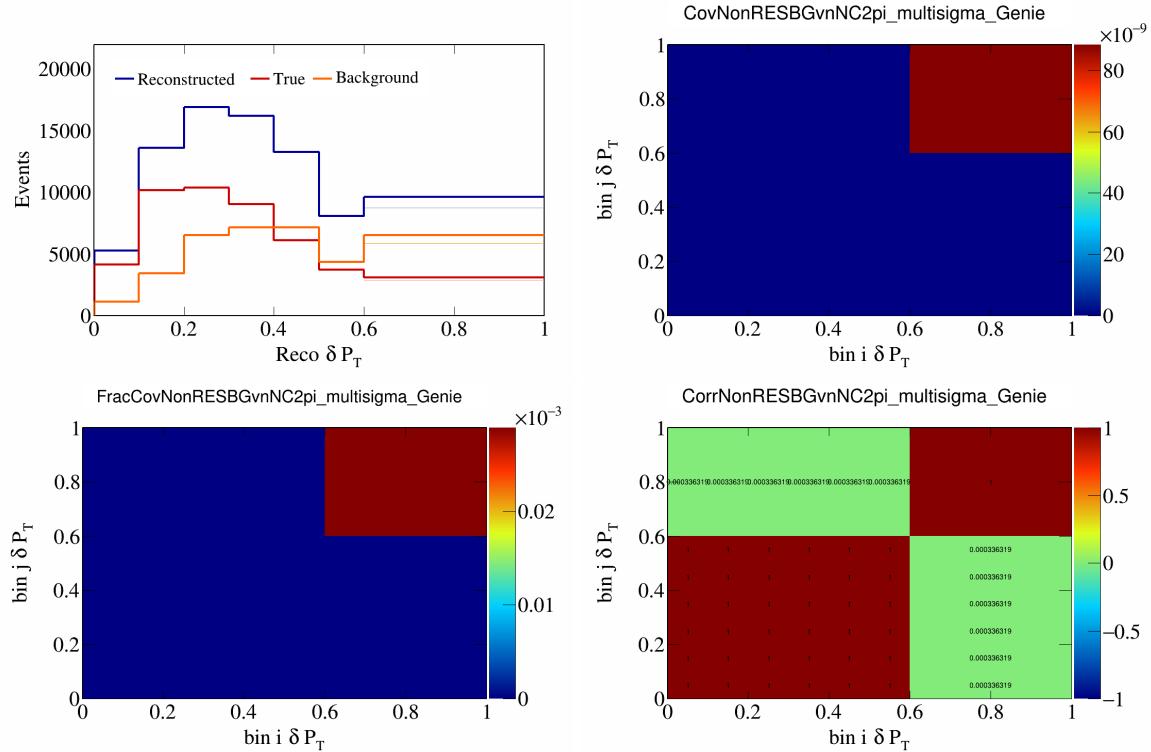


Figure 544: NonRESBGvnNC2pi variations for  $\delta P_T$ .

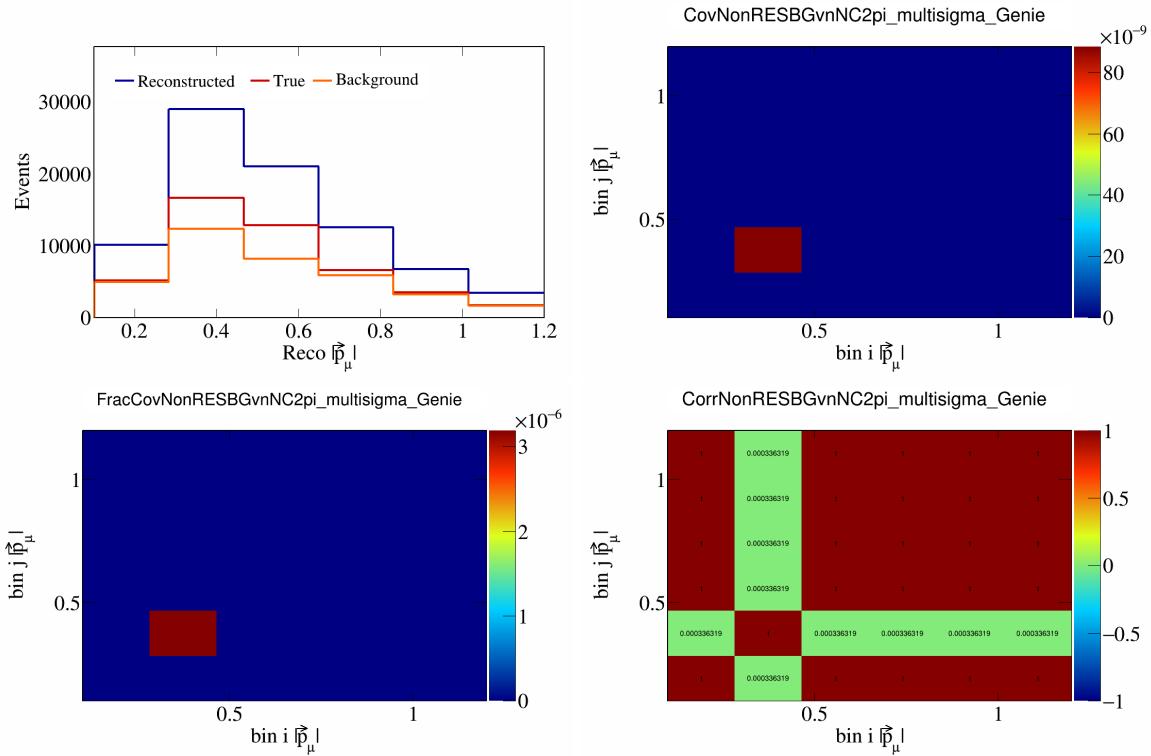


Figure 545: NonRESBGvnNC2pi variations for  $|\vec{p}_\mu|$ .

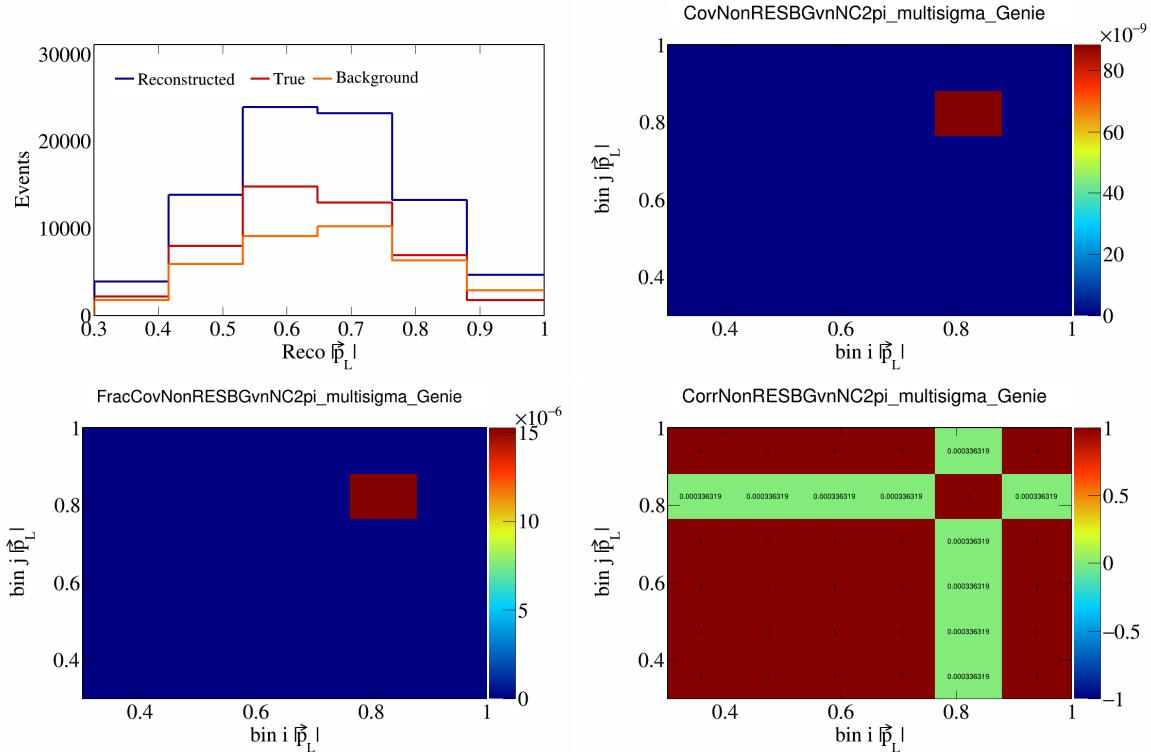


Figure 546: NonRESBGvnNC2pi variations for  $|\vec{p}_L|$ .

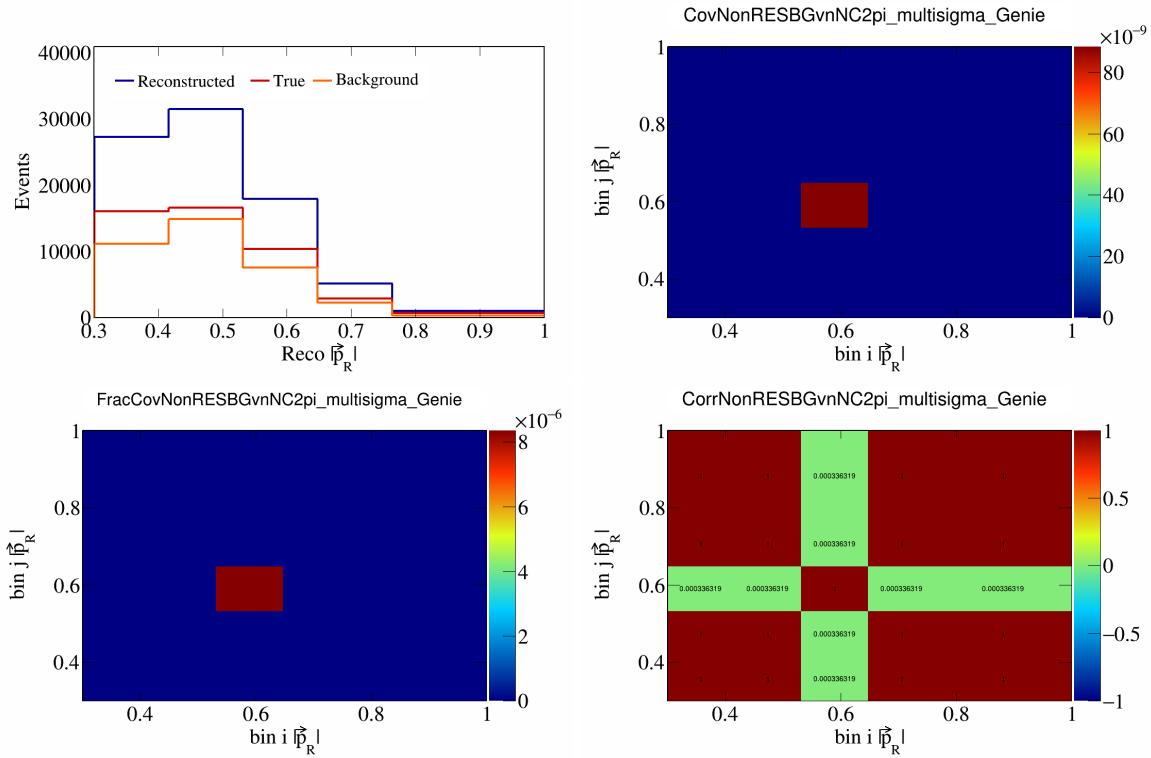


Figure 547: NonRESBGvnNC2pi variations for  $|\vec{p}_R|$ .

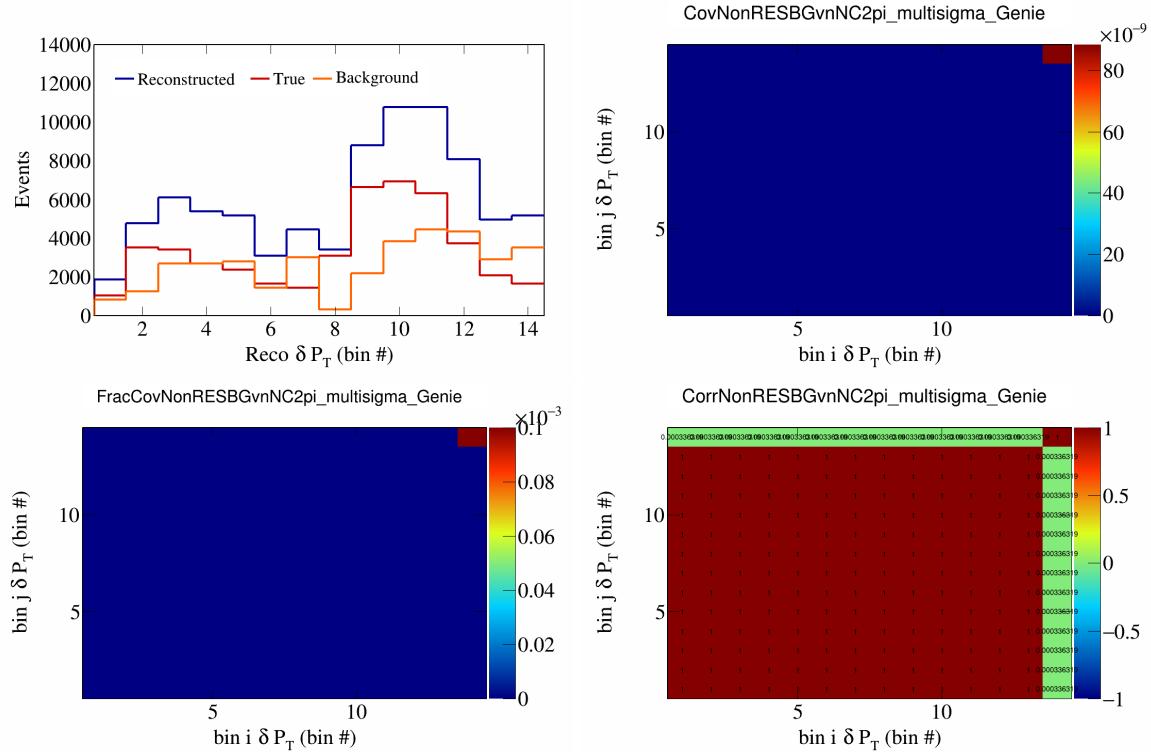


Figure 548: NonRESBGvnNC2pi variations for  $\delta P_T$  in  $\cos(\theta_{\vec{p}_\mu})$ .

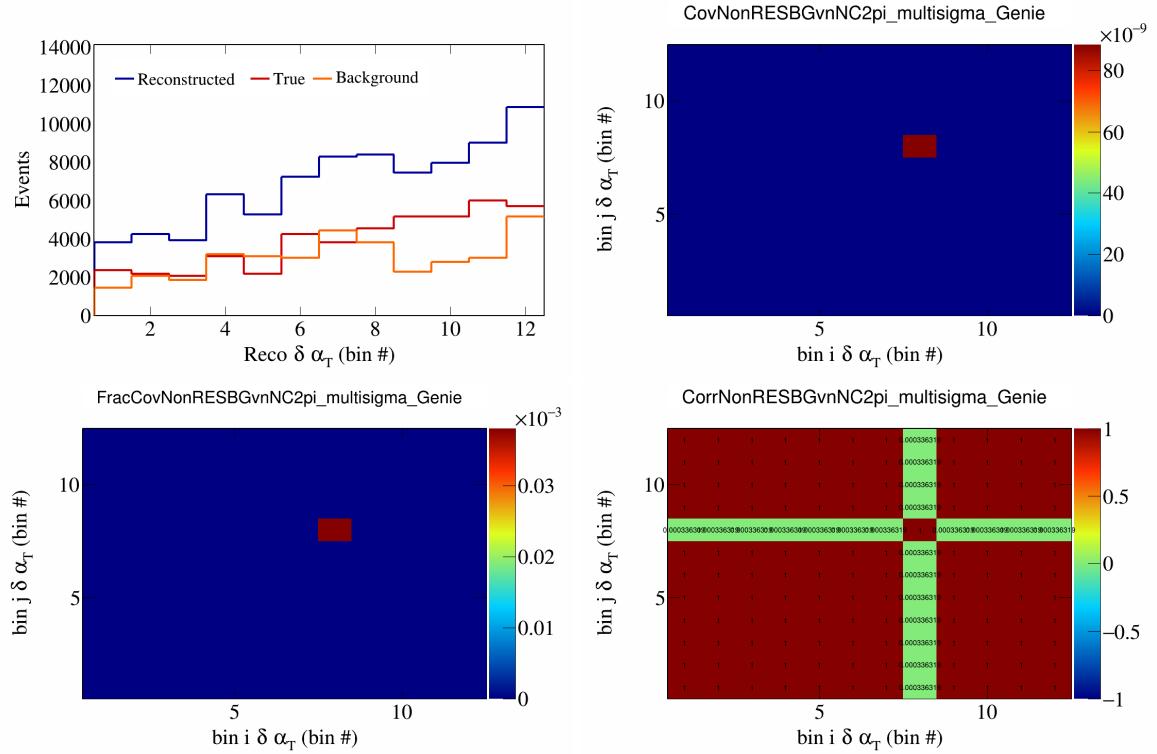


Figure 549: NonRESBGvnNC2pi variations for  $\delta\alpha_T$  in  $\cos(\theta_{\vec{p}_\mu})$ .

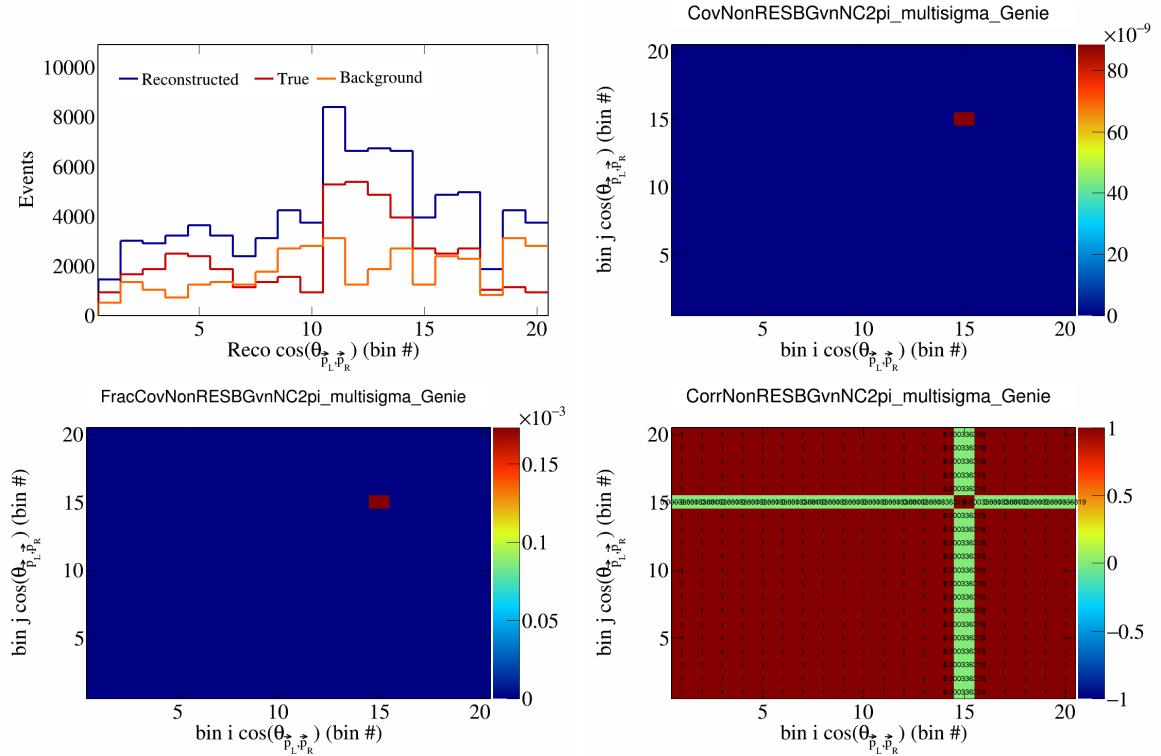


Figure 550: NonRESBGvnNC2pi variations for  $\cos(\theta_{\vec{p}_L, \vec{p}_R})$  in  $\cos(\theta_{\vec{p}_\mu})$ .

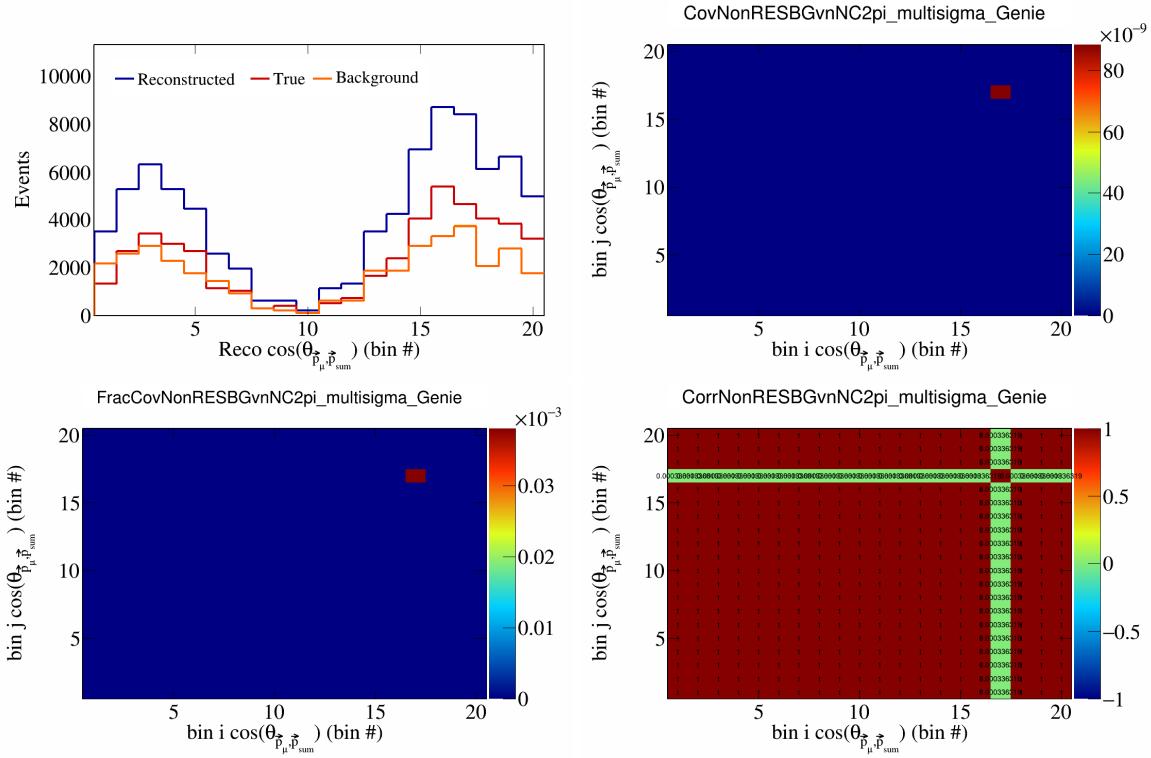


Figure 551: NonRESBGvnNC2pi variations for  $\cos(\theta_{\vec{p}_\mu, \vec{p}_{\text{sum}}})$  in  $\cos(\theta_{\vec{p}_\mu})$ .

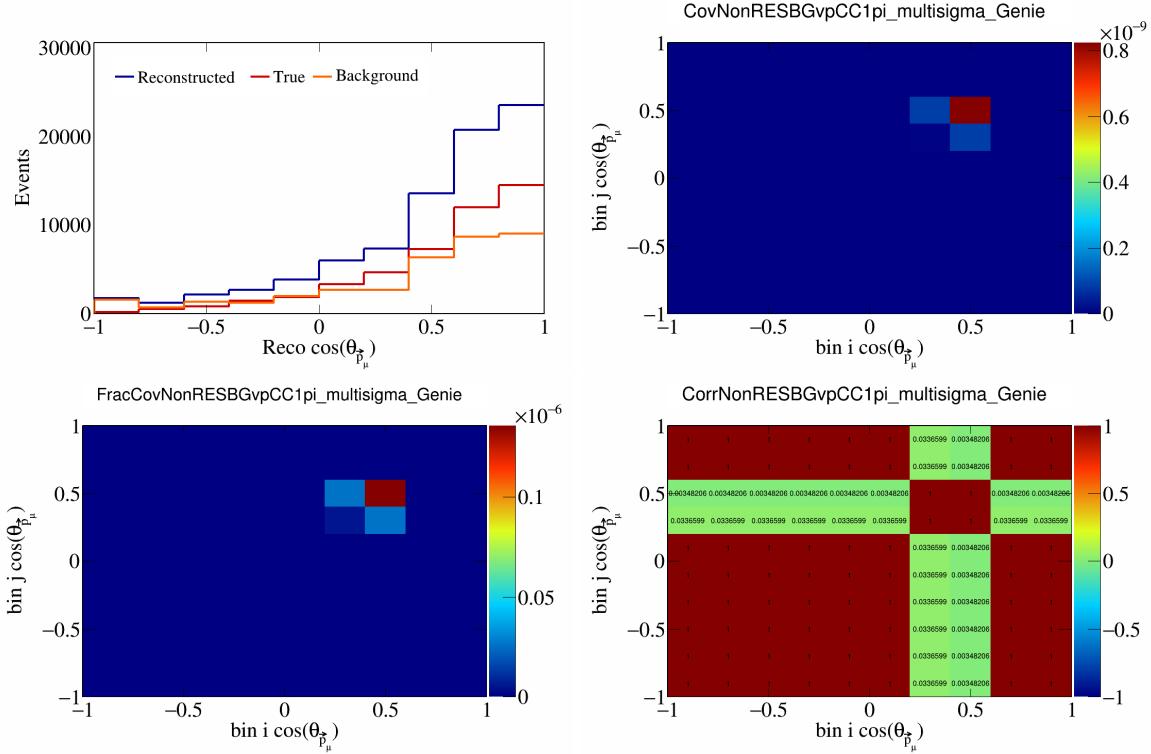


Figure 552: NonRESBGvpCC1pi variations for  $\cos(\theta_{\vec{p}_\mu})$ .

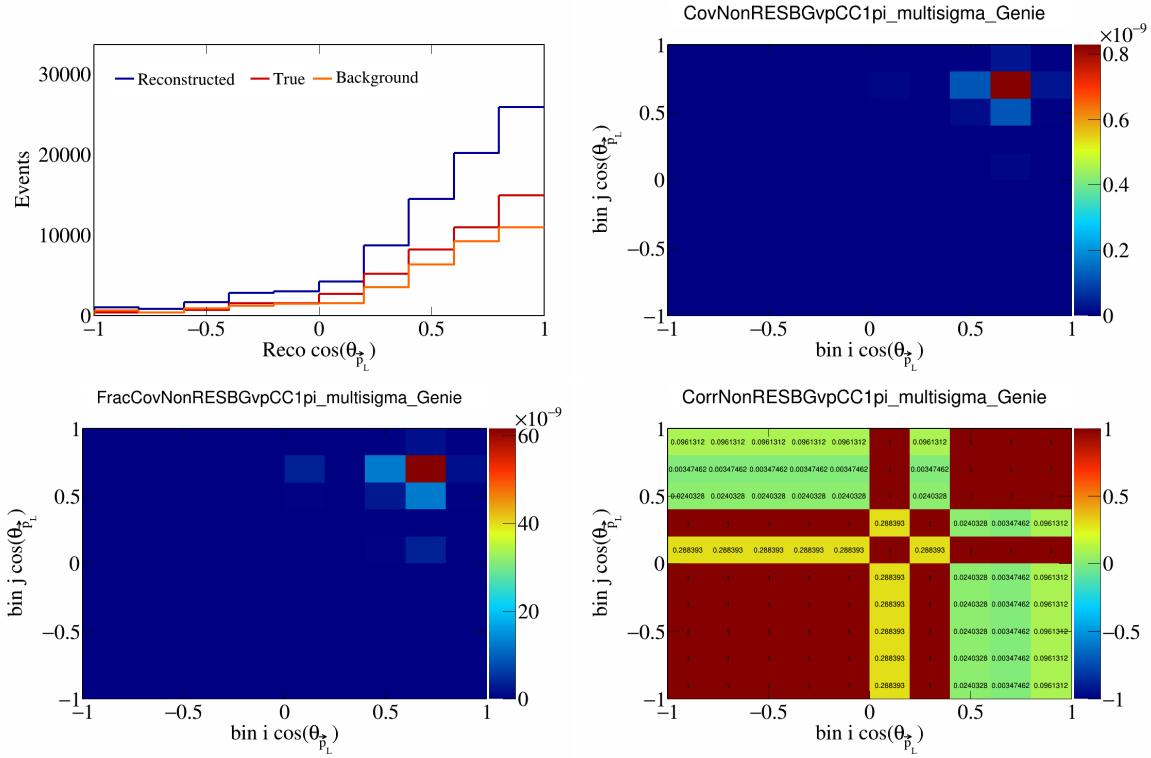


Figure 553: NonRESBGvpCC1pi variations for  $\cos(\theta_{\vec{p}_L})$ .

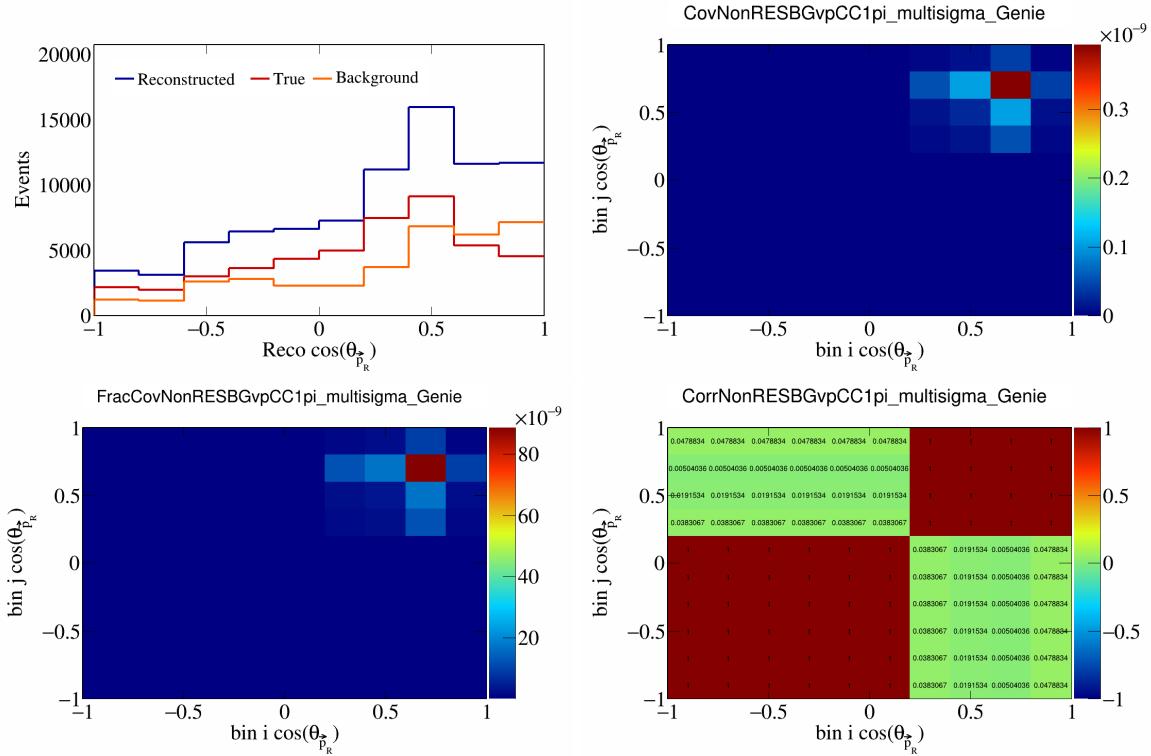


Figure 554: NonRESBGvpCC1pi variations for  $\cos(\theta_{\vec{p}_R})$ .

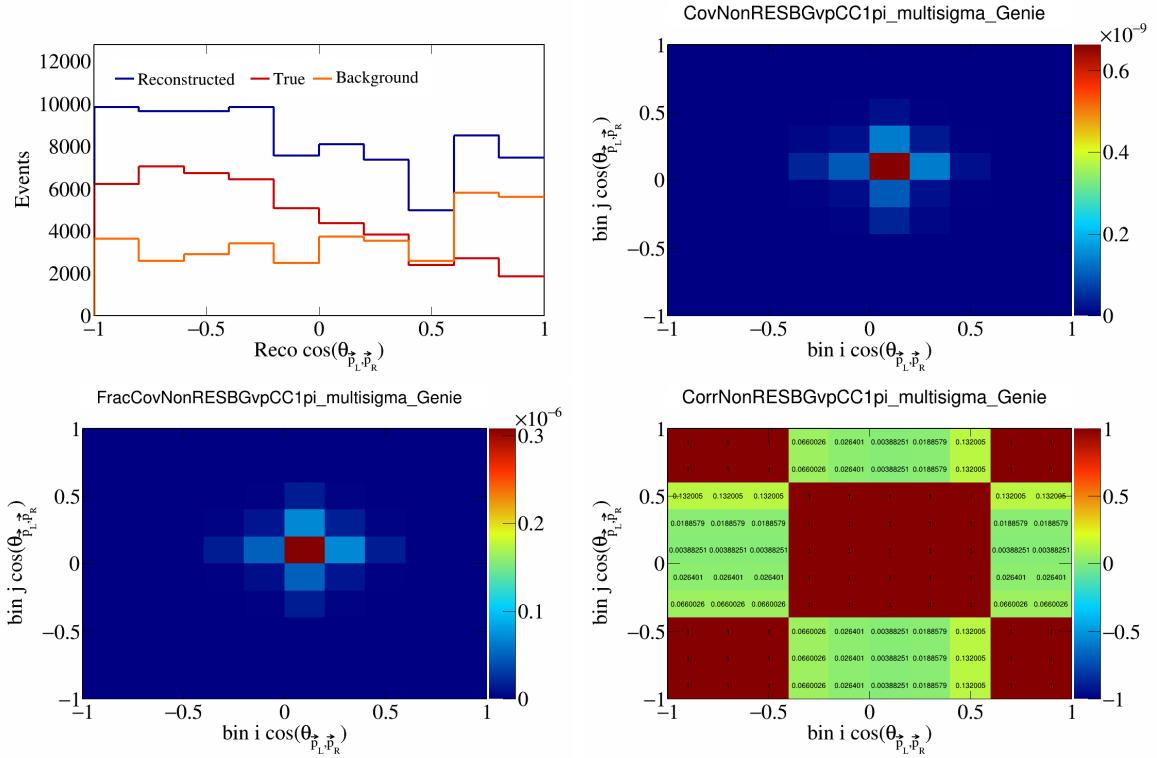


Figure 555: NonRESBGvpCC1pi variations for  $\cos(\theta_{\vec{p}_L, \vec{p}_R})$ .

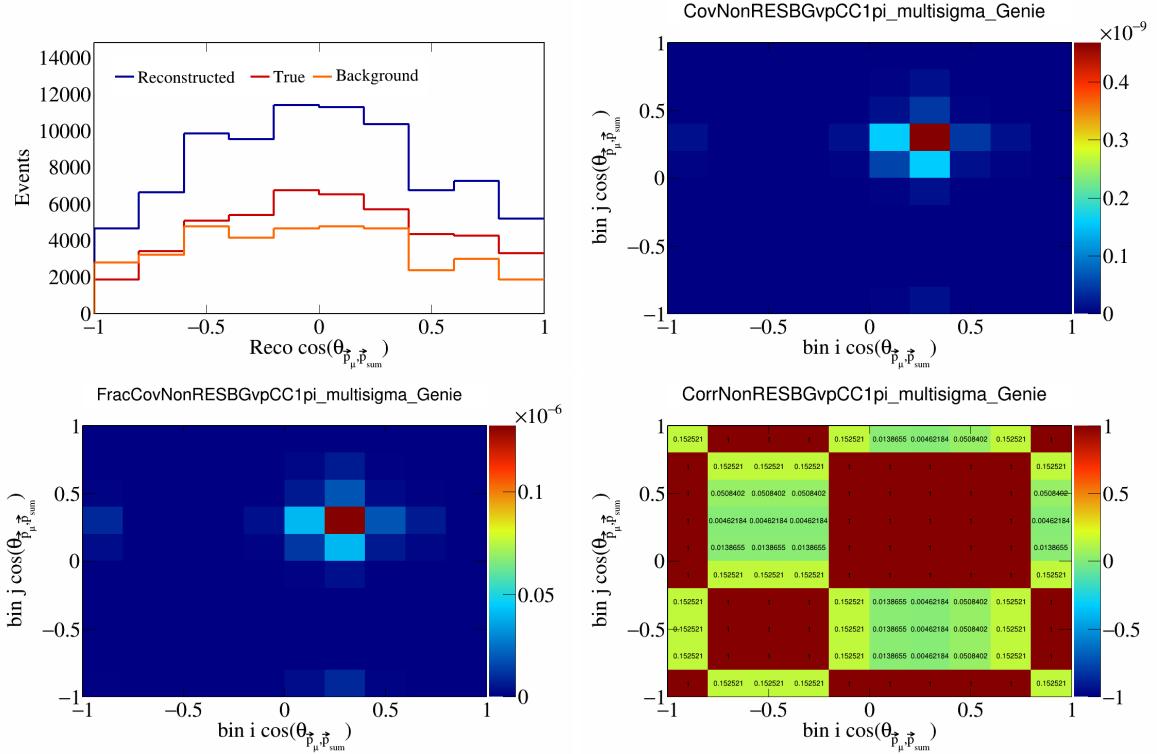


Figure 556: NonRESBGvpCC1pi variations for  $\cos(\theta_{\vec{p}_\mu, \vec{p}_{\text{sum}}})$ .

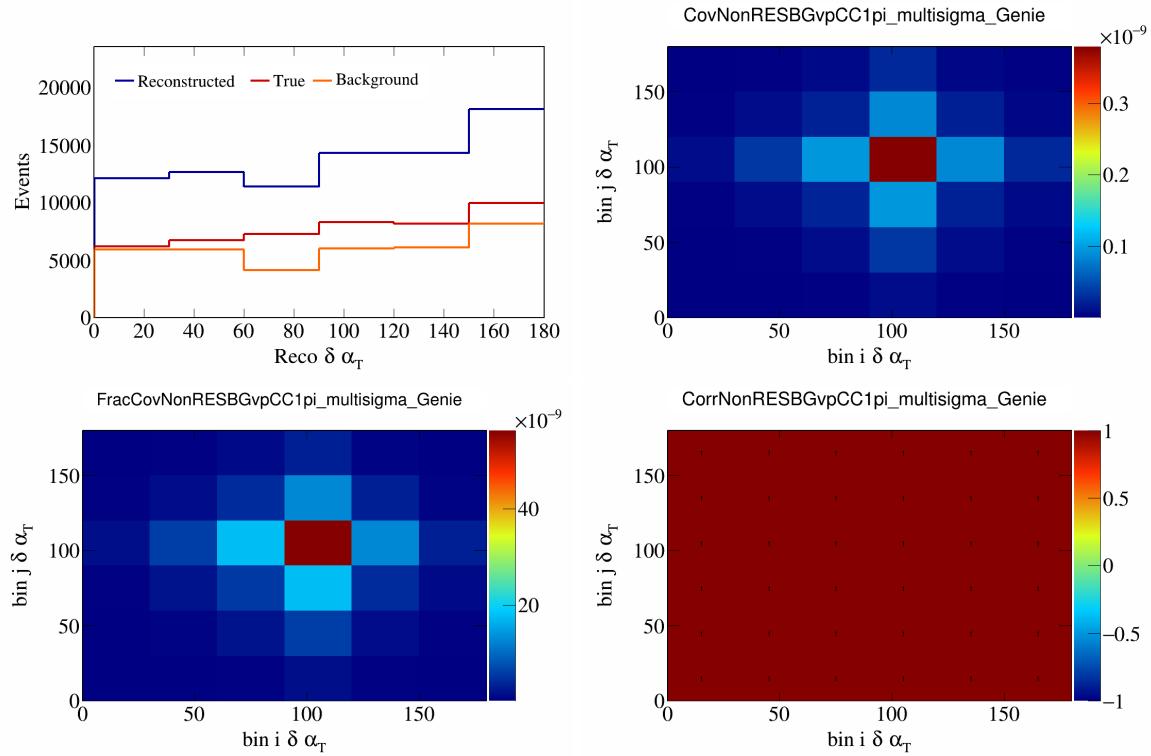


Figure 557: NonRESBGvpCC1pi variations for  $\delta\alpha_T$ .

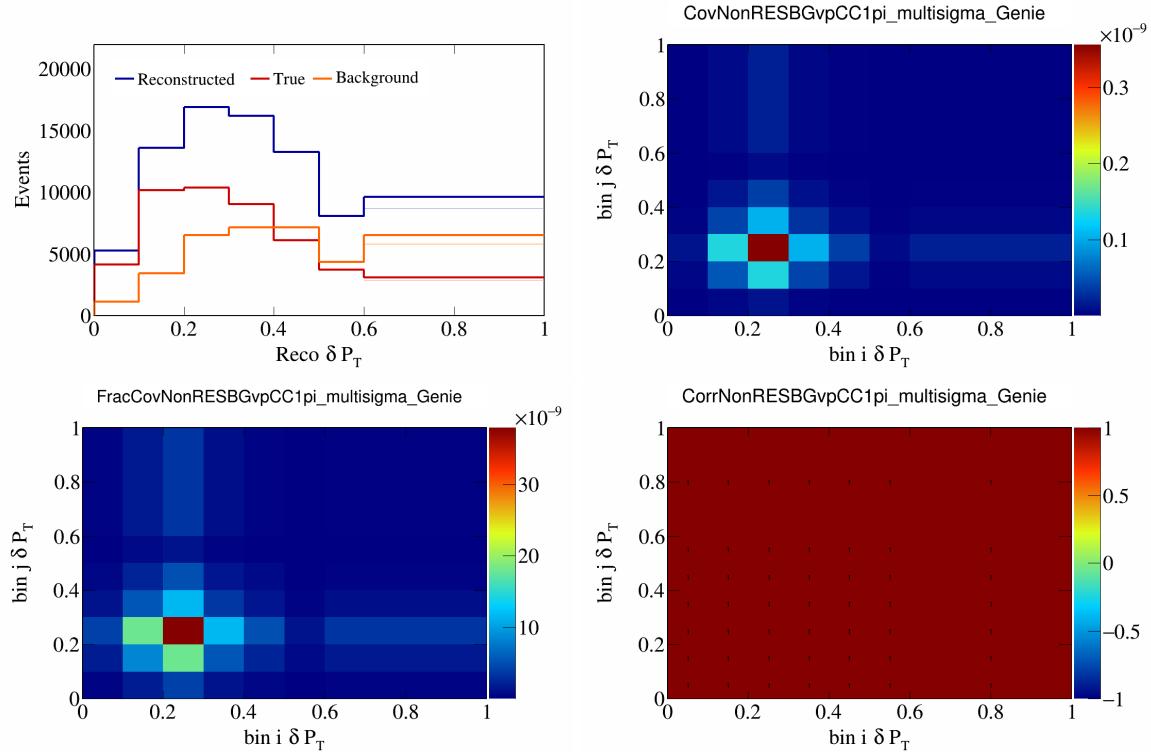


Figure 558: NonRESBGvpCC1pi variations for  $\delta P_T$ .

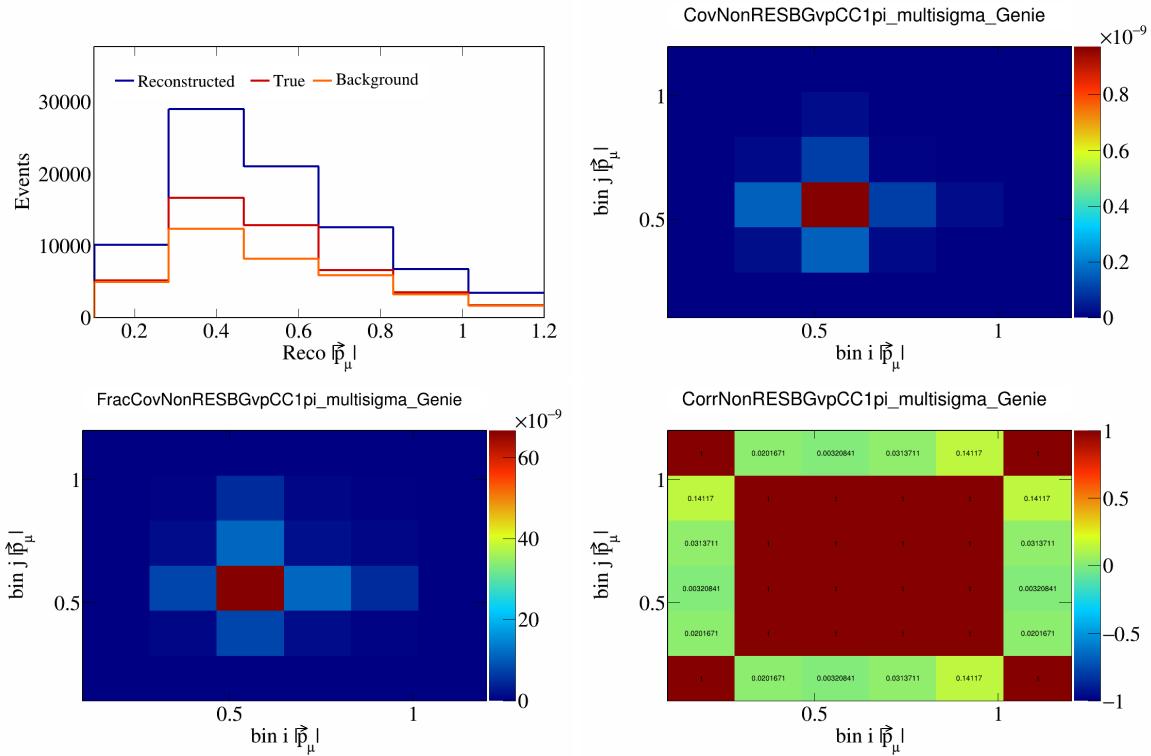


Figure 559: NonRESBGvpCC1pi variations for  $|\vec{p}_\mu|$ .

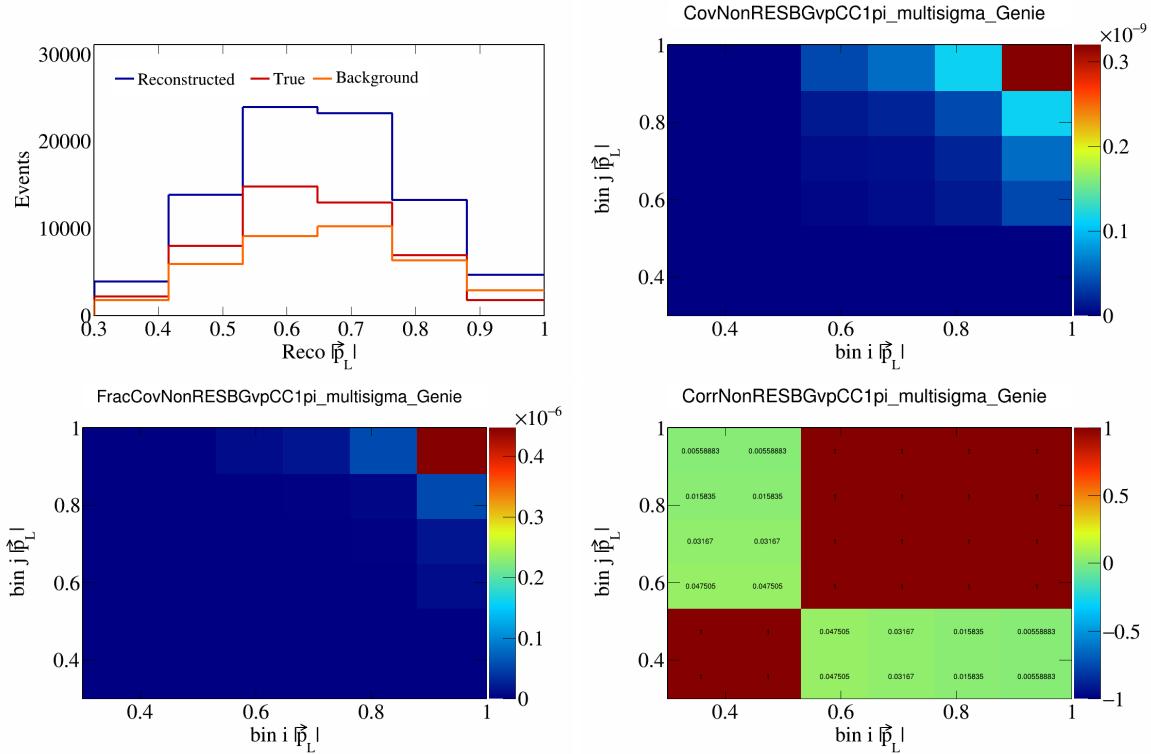


Figure 560: NonRESBGvpCC1pi variations for  $|\vec{p}_L|$ .

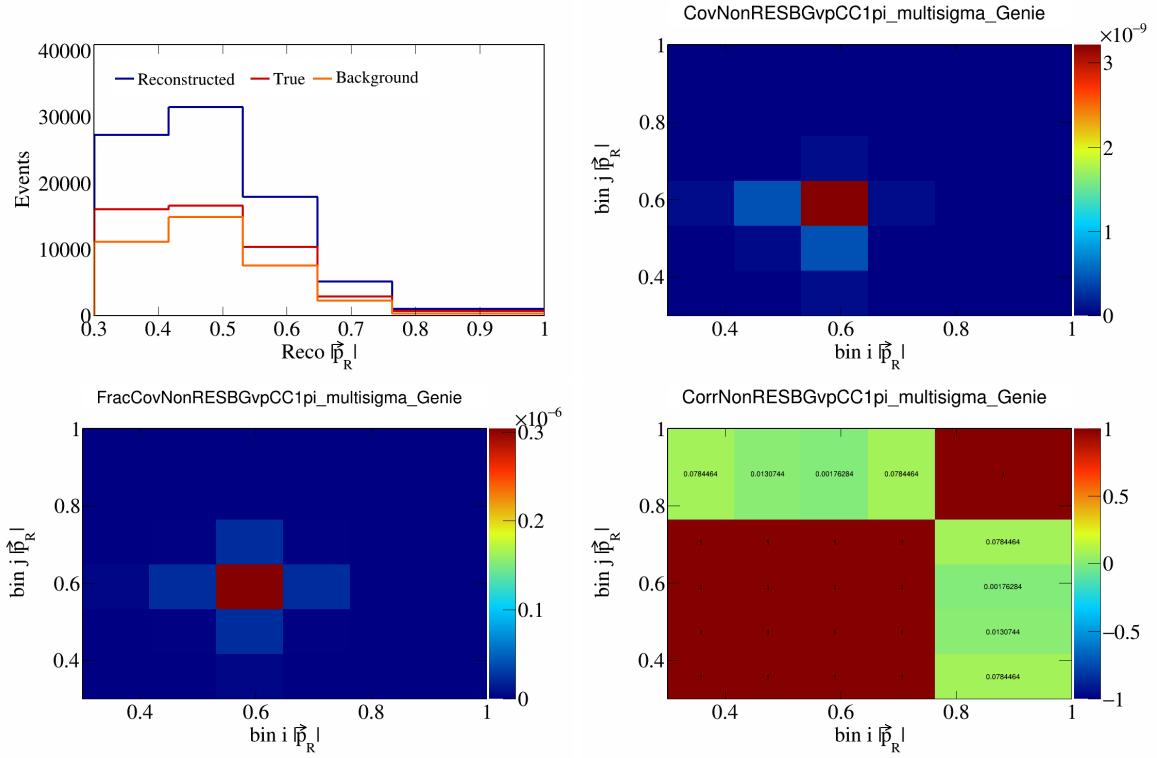


Figure 561: NonRESBGvpCC1pi variations for  $|\vec{p}_R|$ .

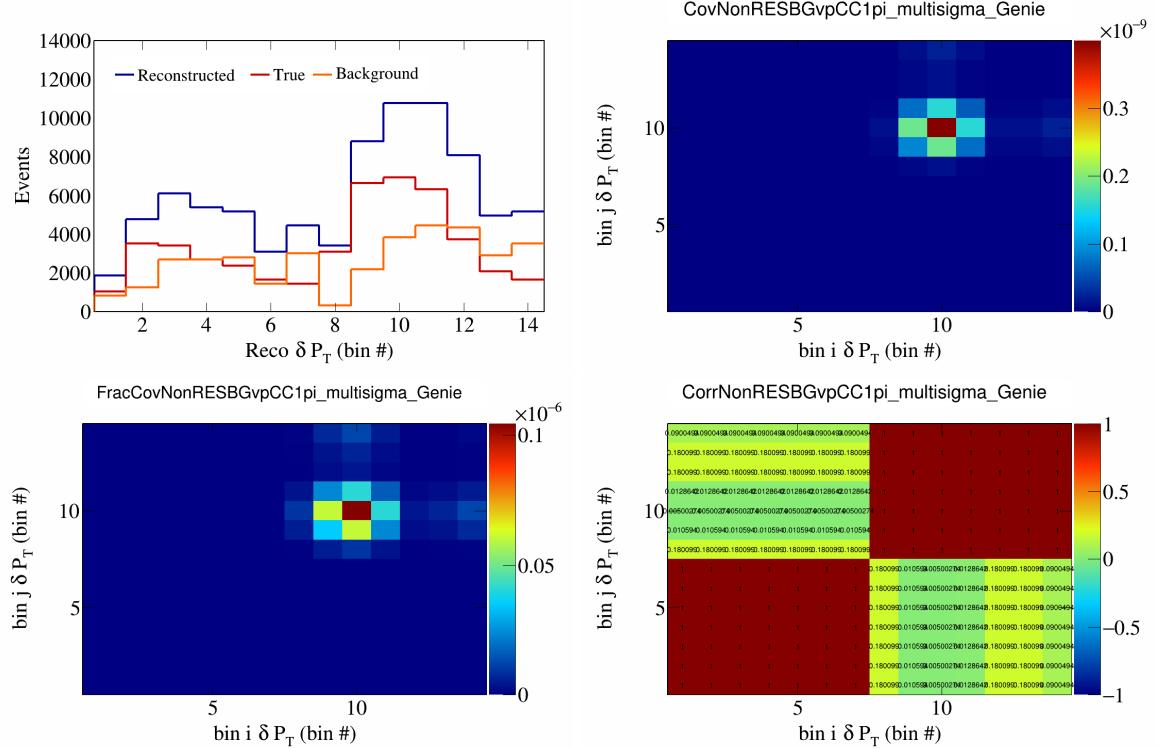


Figure 562: NonRESBGvpCC1pi variations for  $\delta P_T$  in  $\cos(\theta_{\vec{p}_\mu})$ .

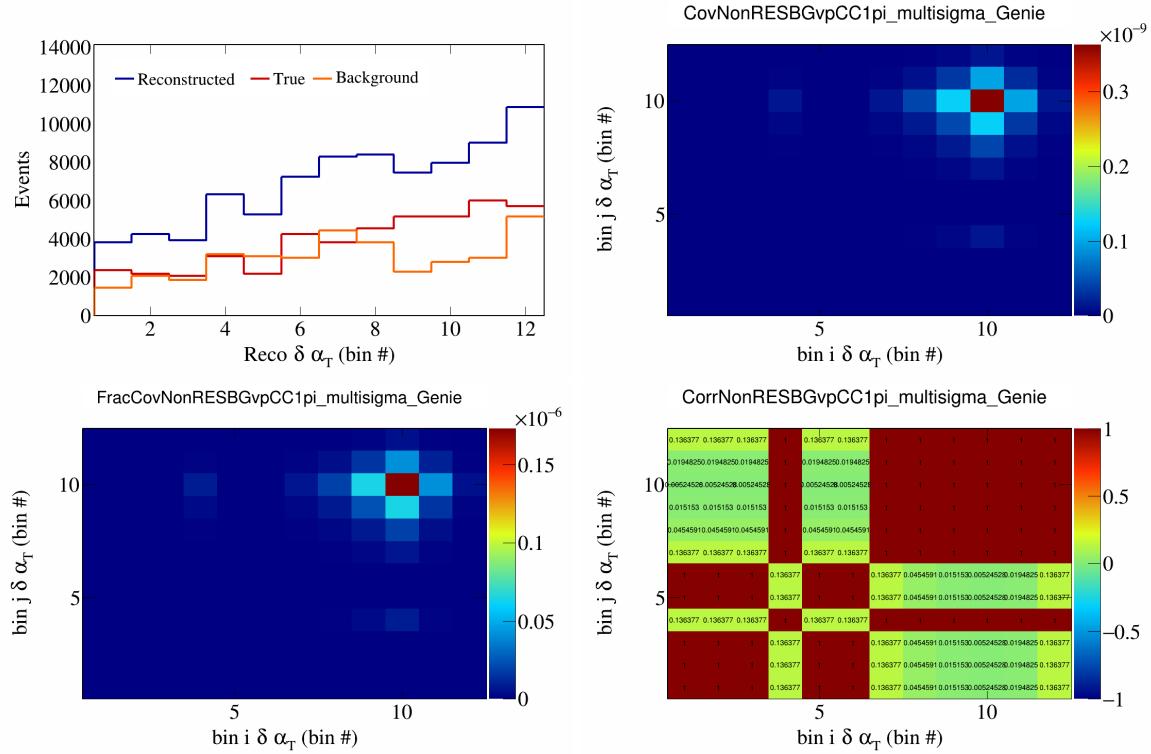


Figure 563: NonRESBGvpCC1pi variations for  $\delta\alpha_T$  in  $\cos(\theta_{\vec{p}_\mu})$ .

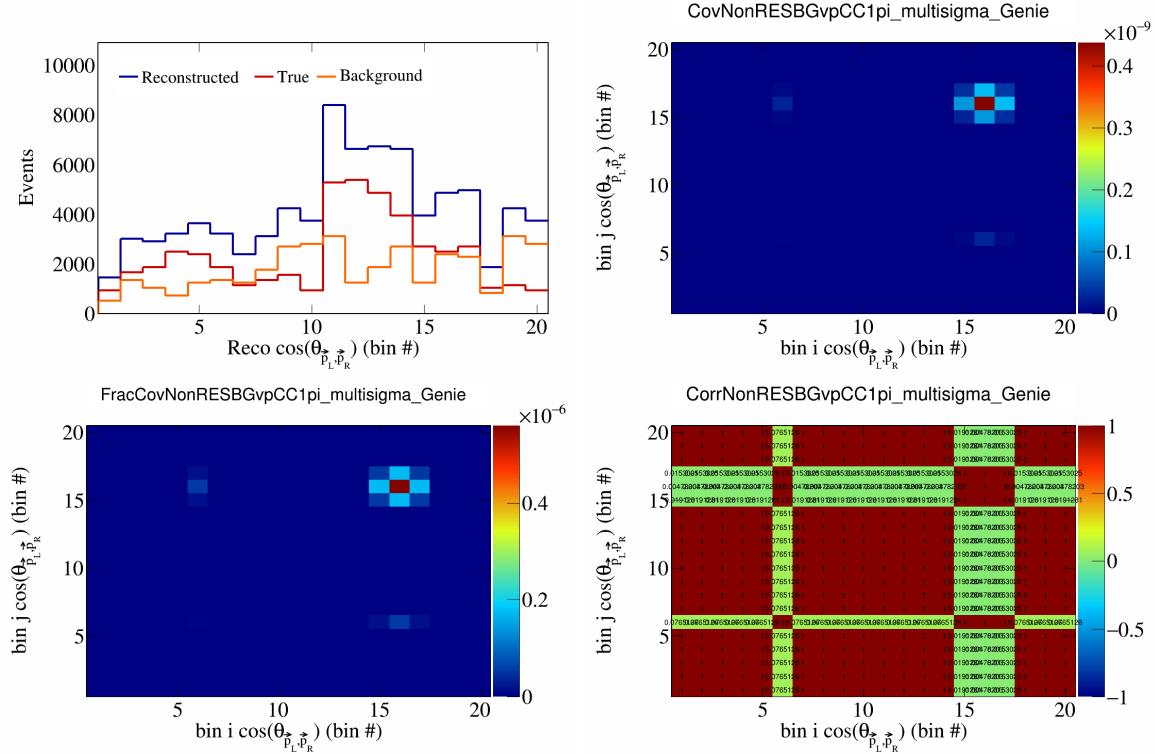


Figure 564: NonRESBGvpCC1pi variations for  $\cos(\theta_{\vec{p}_L, \vec{p}_R})$  in  $\cos(\theta_{\vec{p}_\mu})$ .

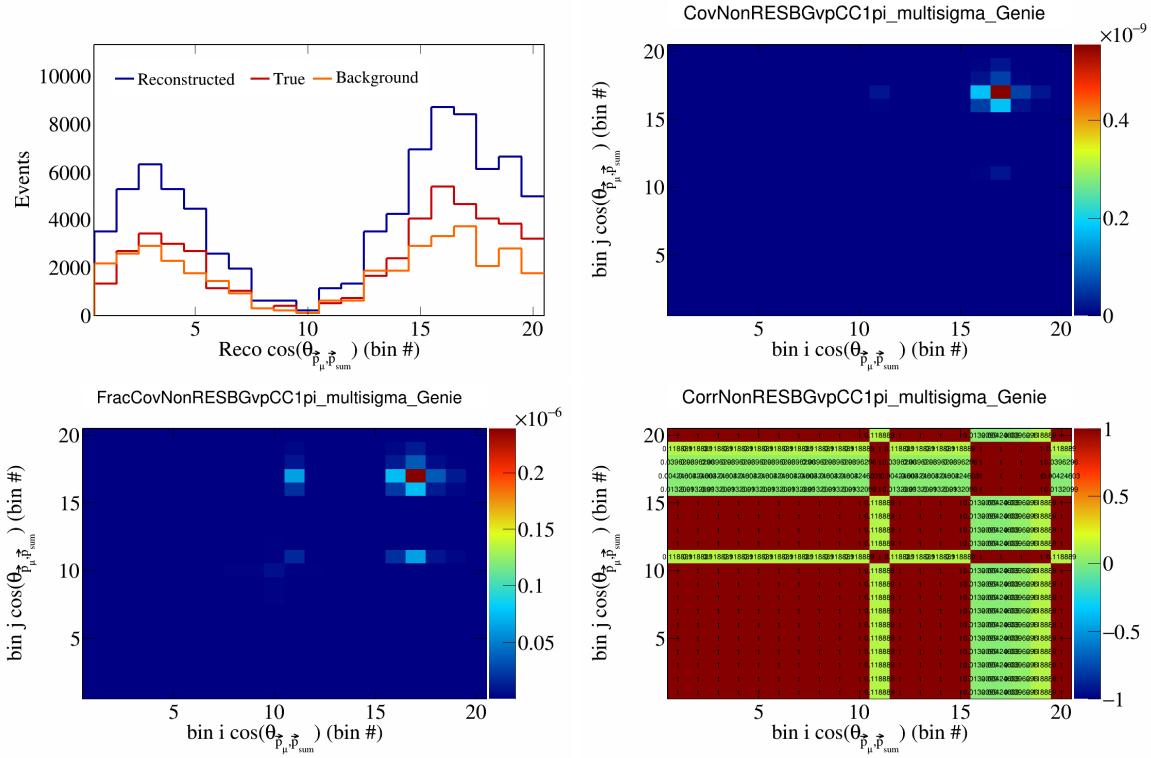


Figure 565: NonRESBGvpCC1pi variations for  $\cos(\theta_{\vec{p}_\mu})$  in  $\cos(\theta_{\vec{p}_\mu})$ .

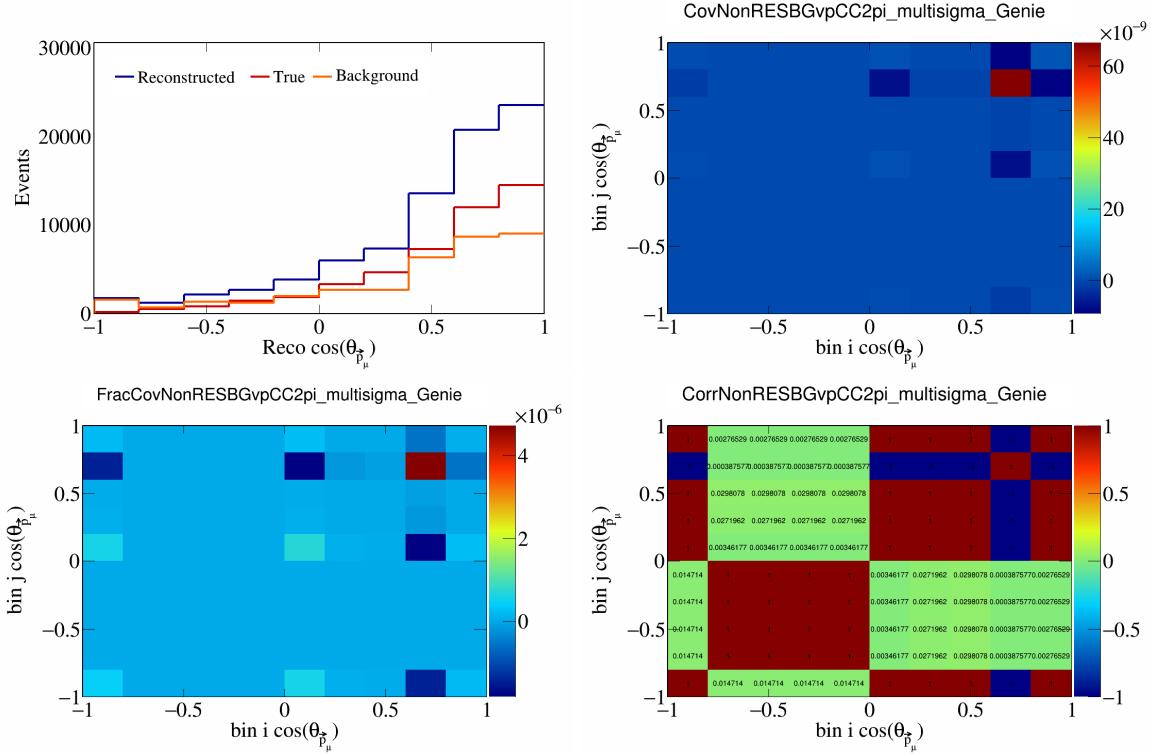


Figure 566: NonRESBGvpCC2pi variations for  $\cos(\theta_{\vec{p}_\mu})$ .

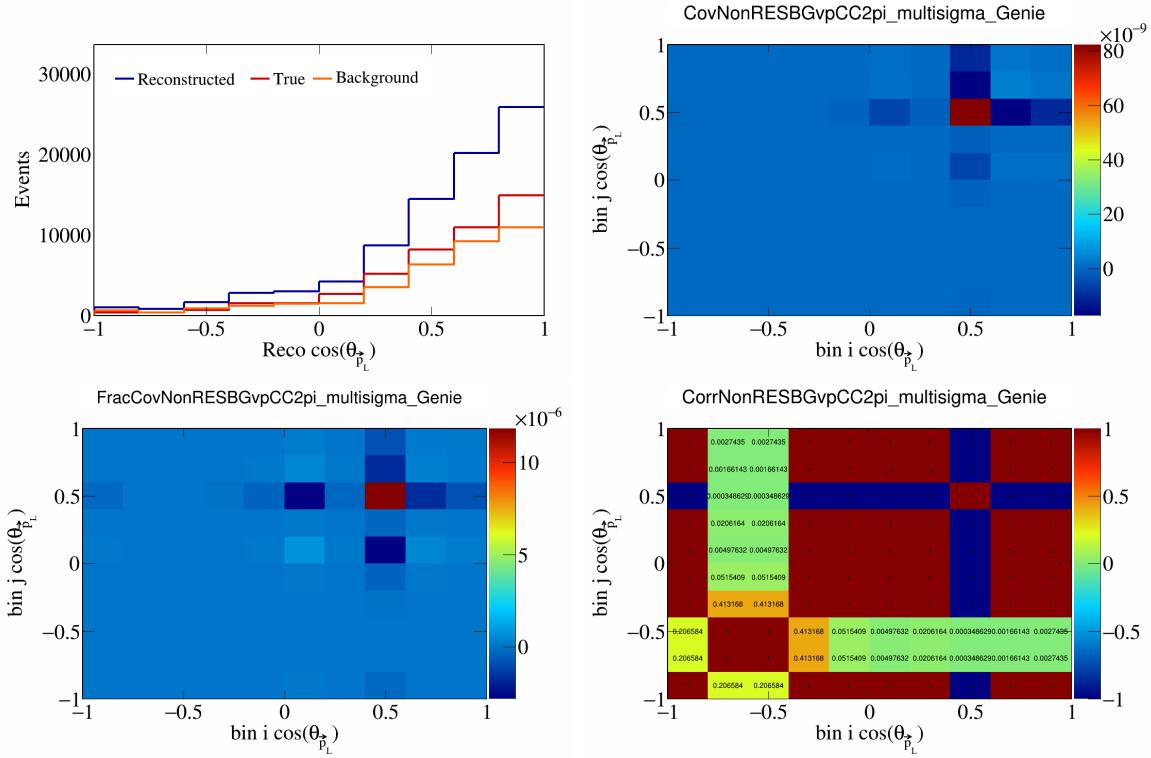


Figure 567: NonRESBGvpCC2pi variations for  $\cos(\theta_{\vec{p}_L})$ .

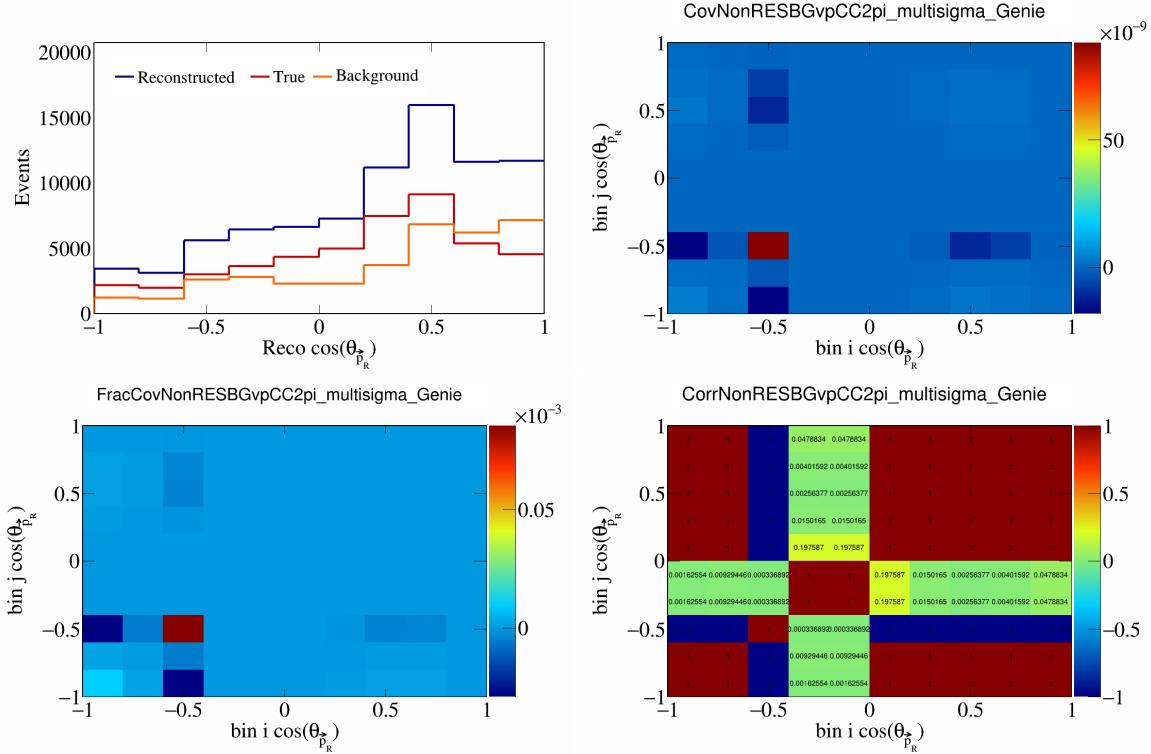


Figure 568: NonRESBGvpCC2pi variations for  $\cos(\theta_{\vec{p}_R})$ .

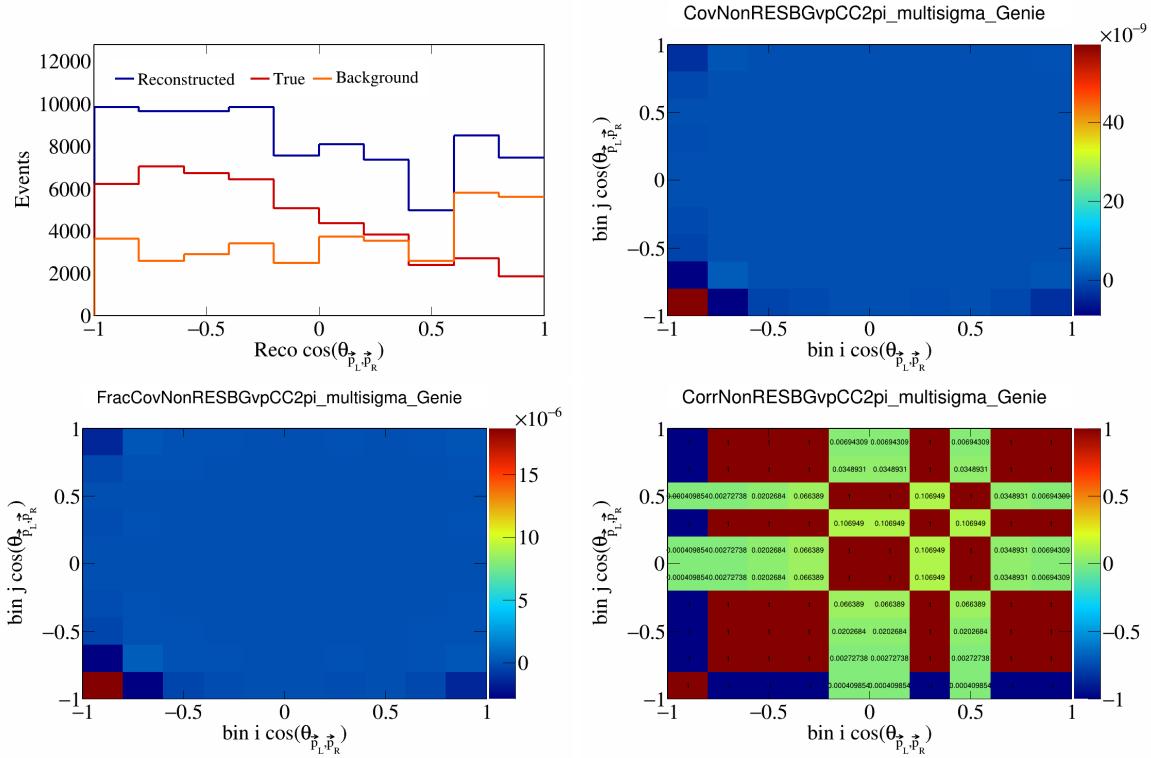


Figure 569: NonRESBGvpCC2pi variations for  $\cos(\theta_{\vec{p}_L, \vec{p}_R})$ .

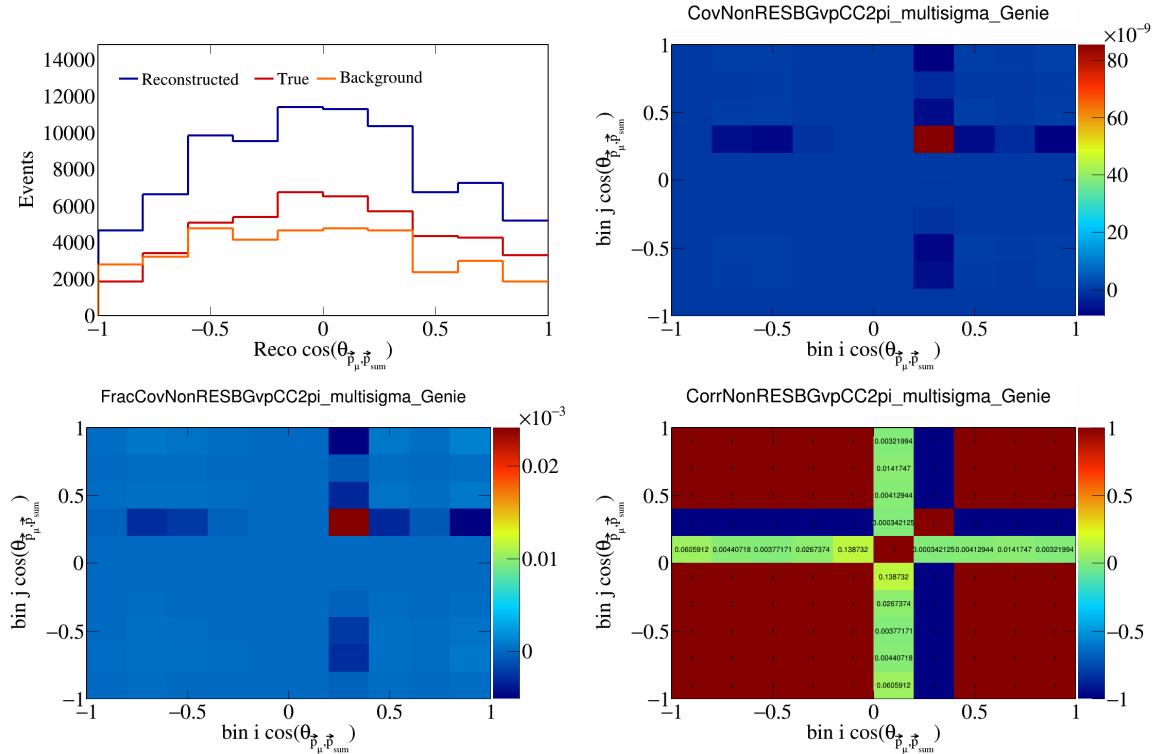


Figure 570: NonRESBGvpCC2pi variations for  $\cos(\theta_{\vec{p}_\mu, \vec{p}_{\text{sum}}})$ .

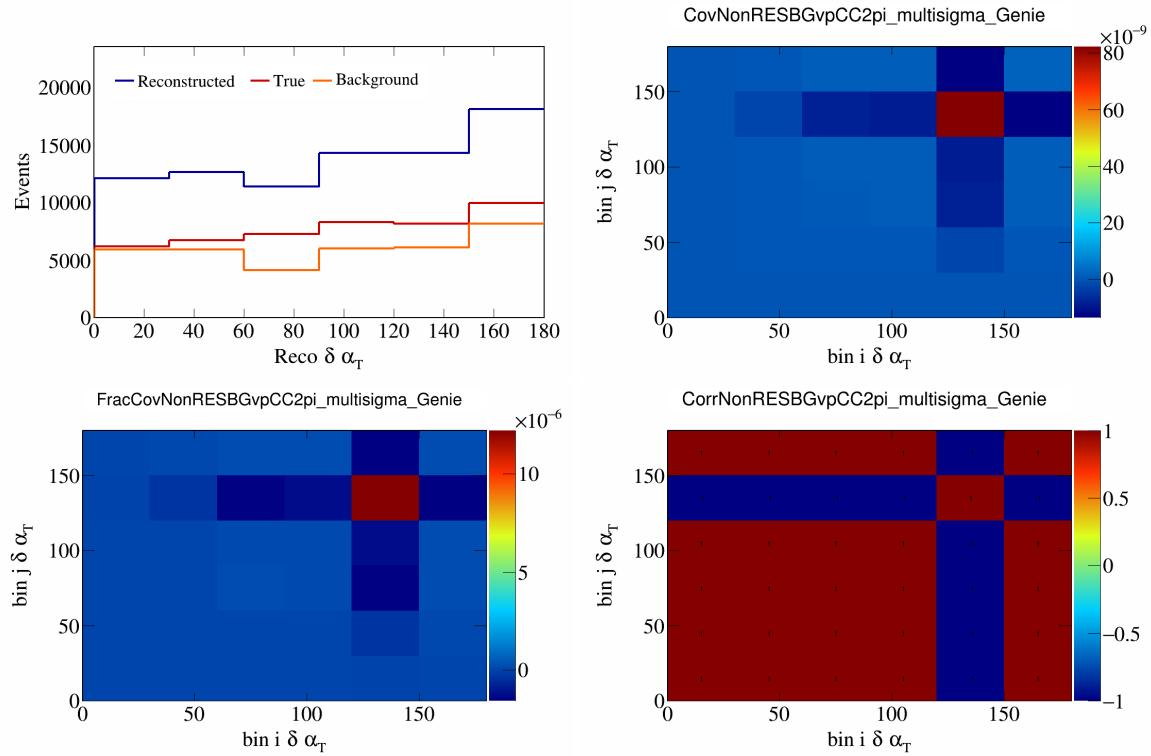


Figure 571: NonRESBGvpCC2pi variations for  $\delta\alpha_T$ .

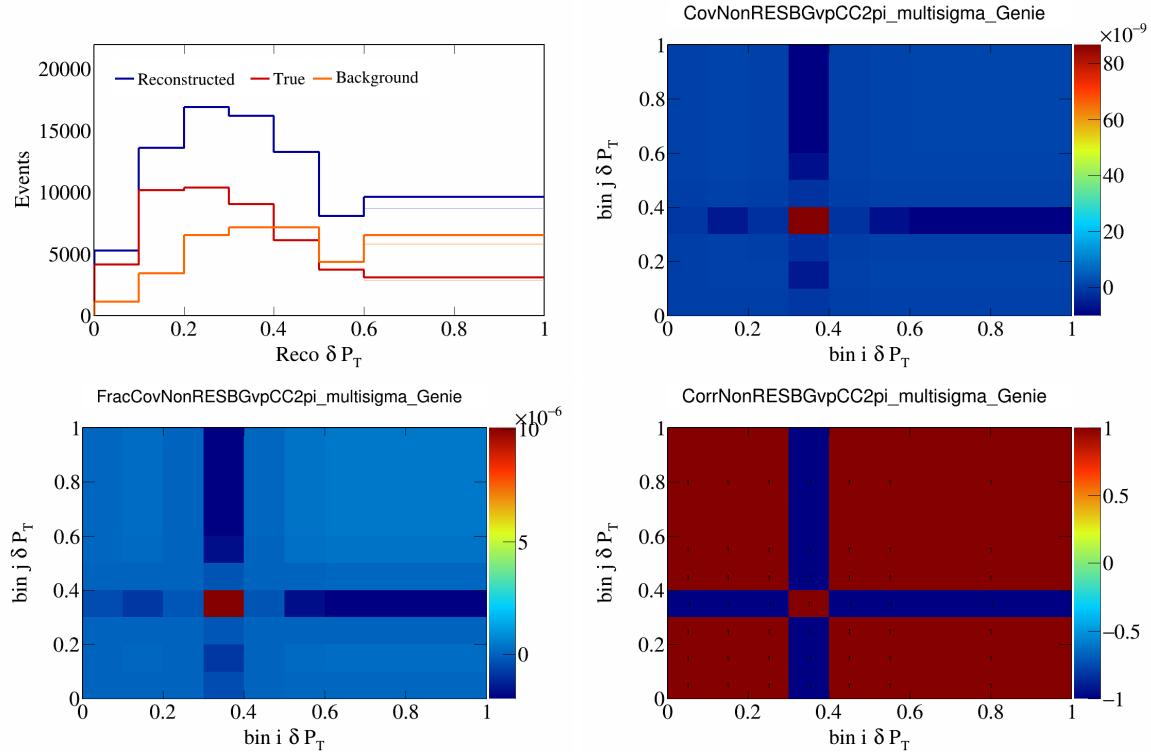
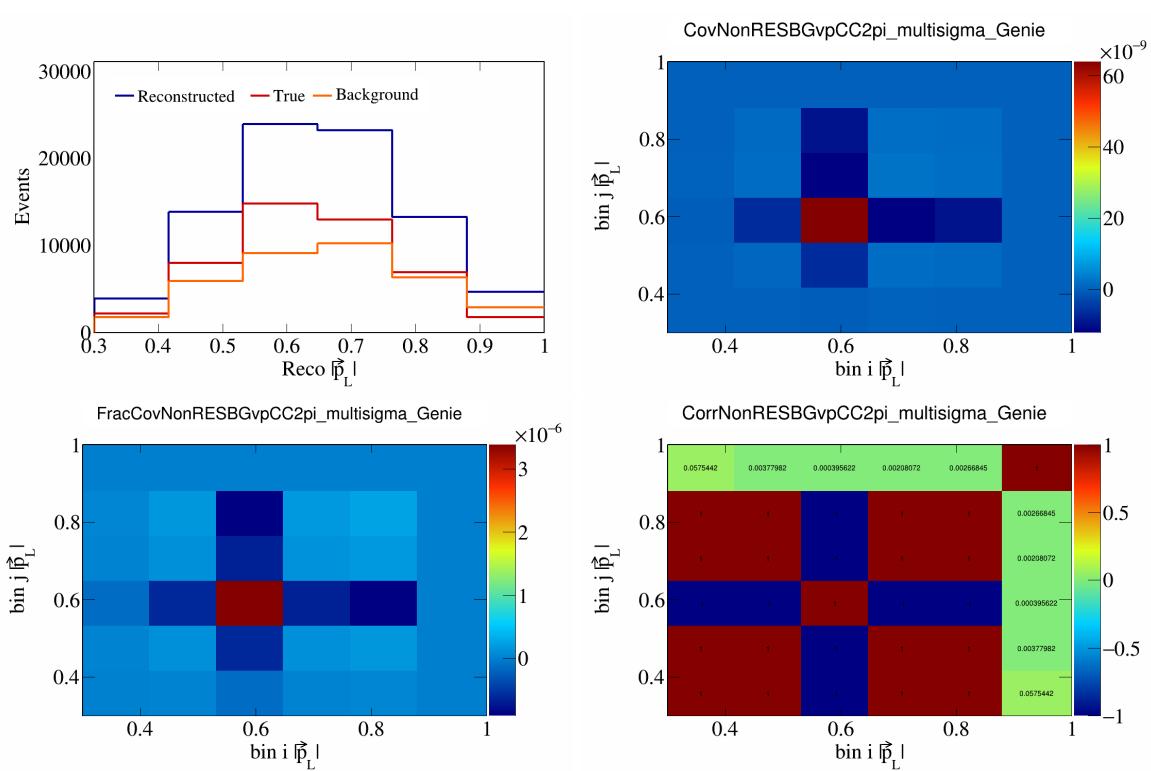
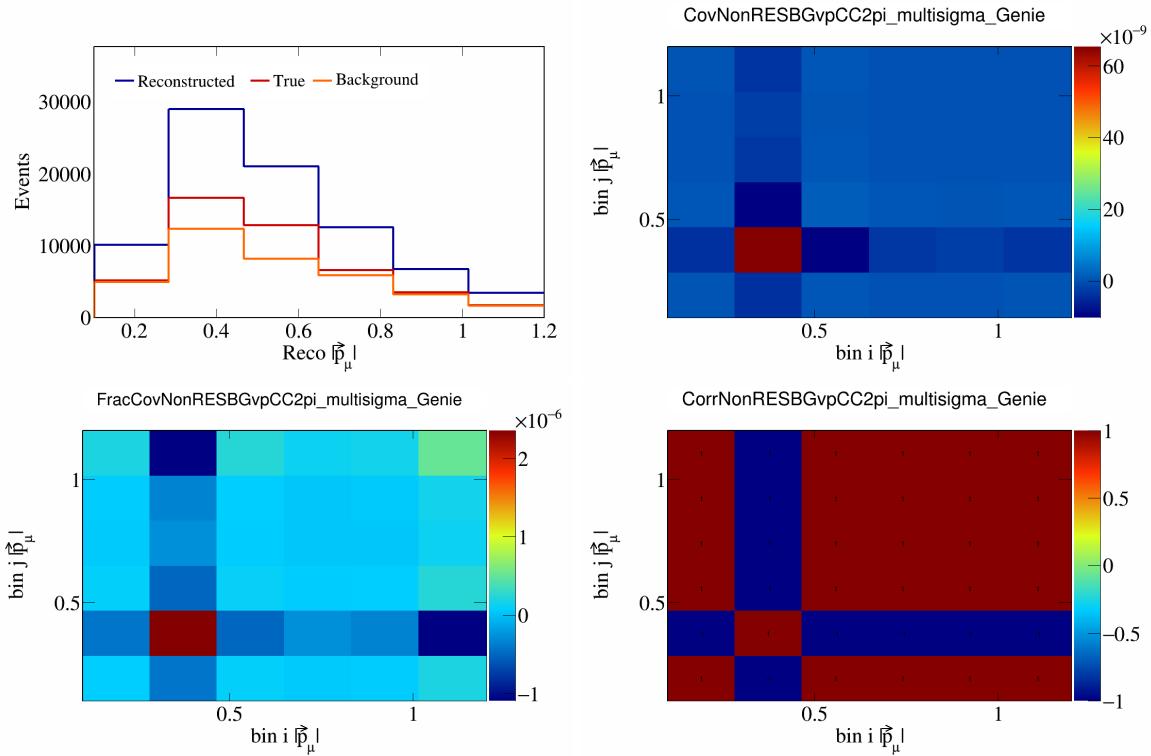


Figure 572: NonRESBGvpCC2pi variations for  $\delta P_T$ .



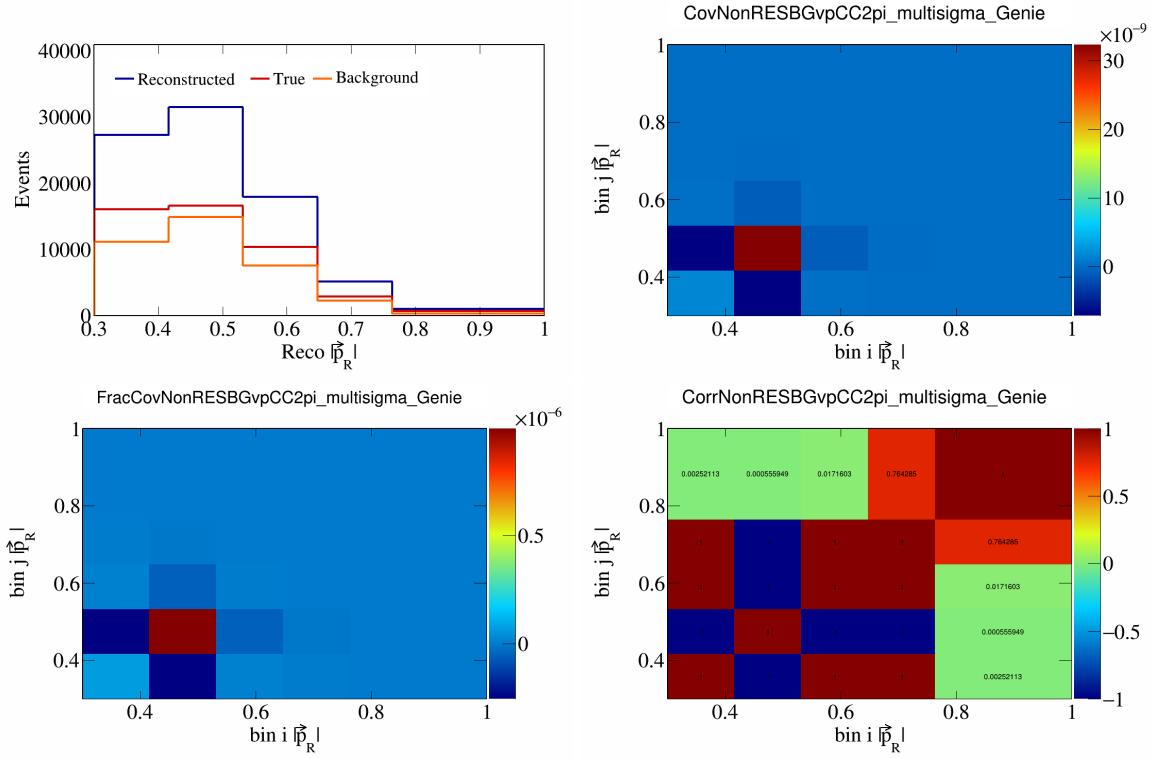


Figure 575: NonRESBGvpCC2pi variations for  $|\vec{p}_R|$ .

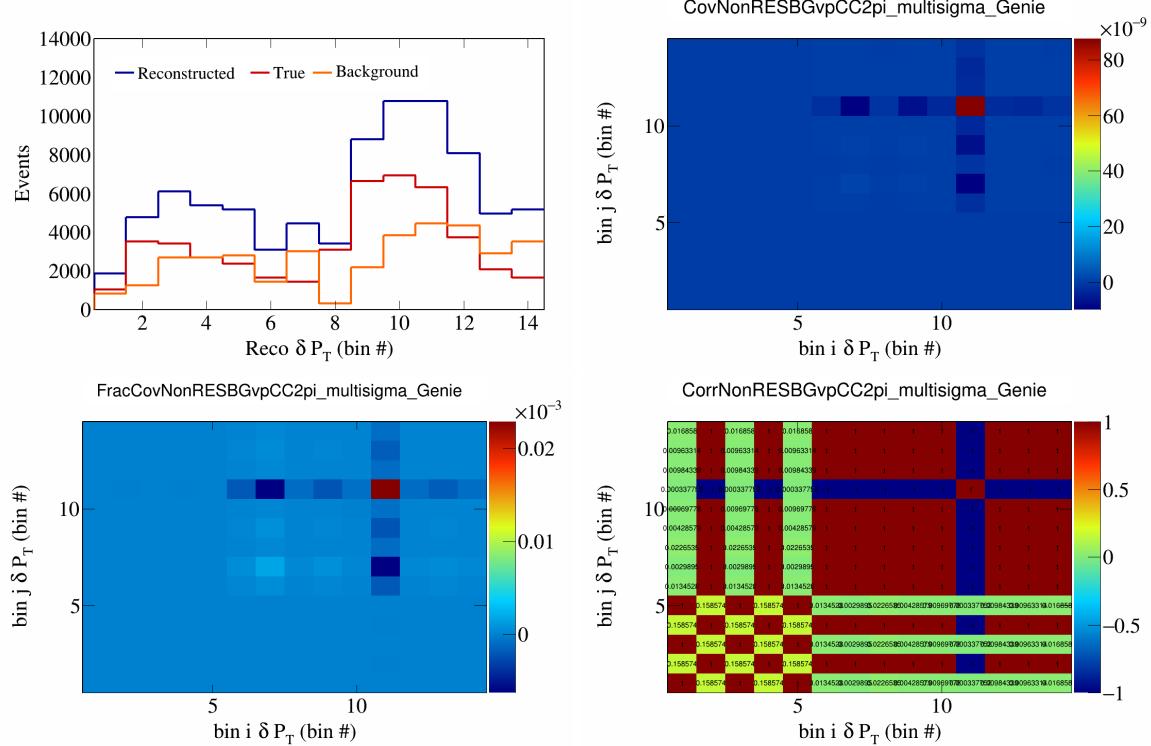


Figure 576: NonRESBGvpCC2pi variations for  $\delta P_T$  in  $\cos(\theta_{\vec{p}_\mu})$ .

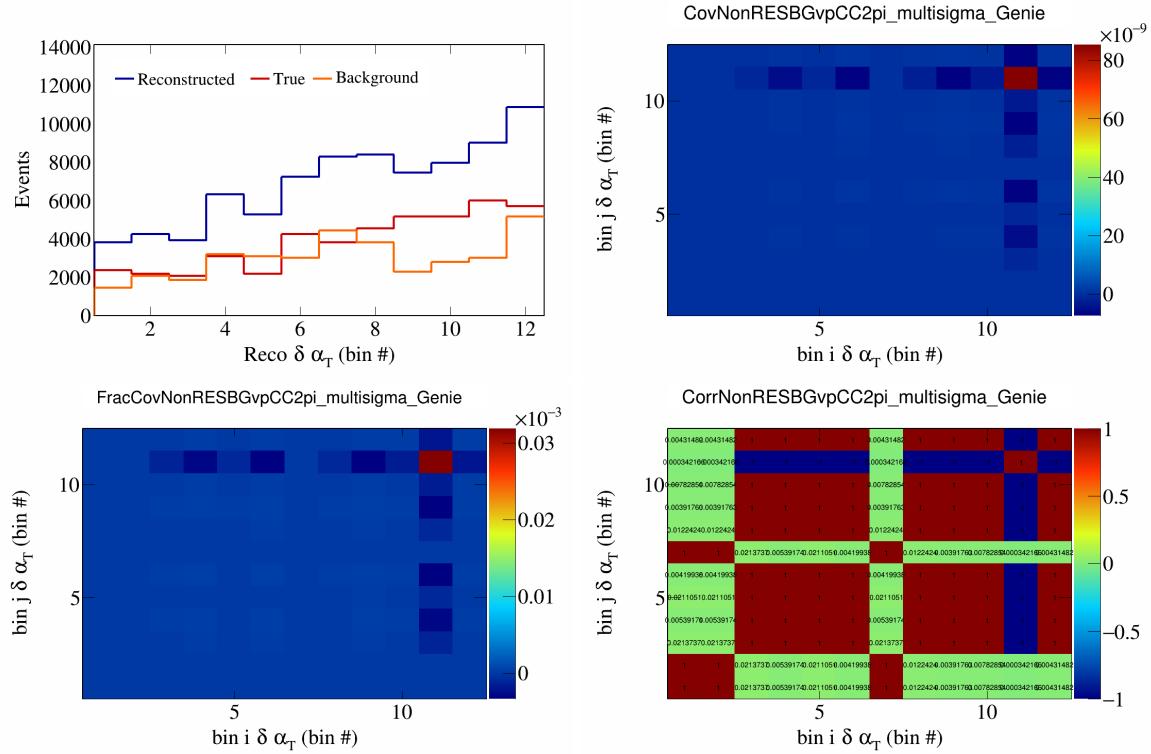


Figure 577: NonRESBGvpCC2pi variations for  $\delta\alpha_T$  in  $\cos(\theta_{\vec{p}_\mu})$ .

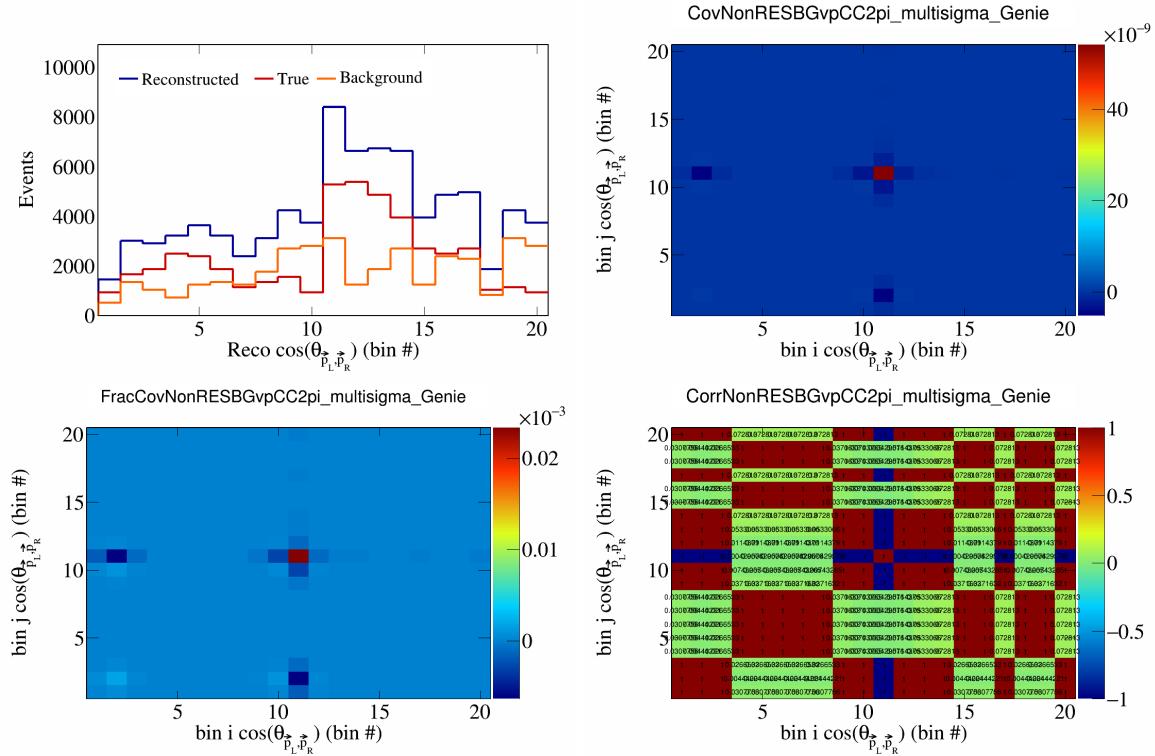


Figure 578: NonRESBGvpCC2pi variations for  $\cos(\theta_{\vec{p}_L, \vec{p}_R})$  in  $\cos(\theta_{\vec{p}_\mu})$ .

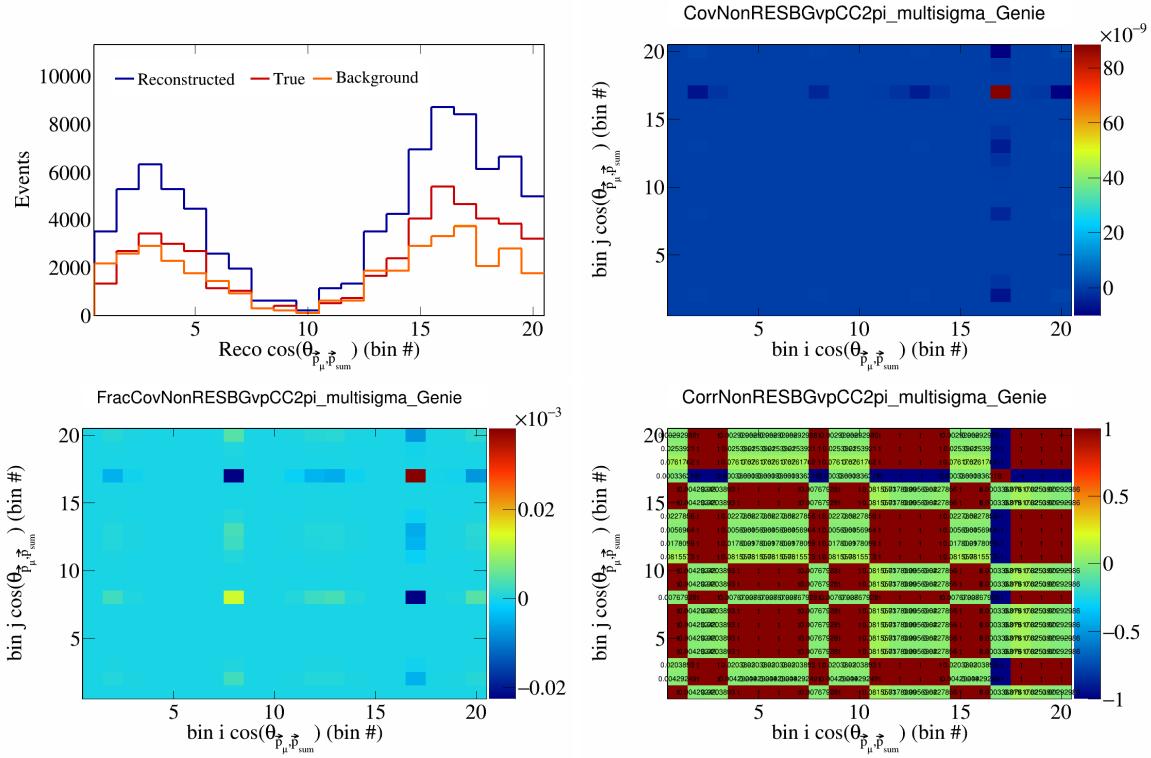


Figure 579: NonRESBGvpCC2pi variations for  $\cos(\theta_{\vec{p}_\mu, \vec{p}_{\text{sum}}})$  in  $\cos(\theta_{\vec{p}_\mu})$ .

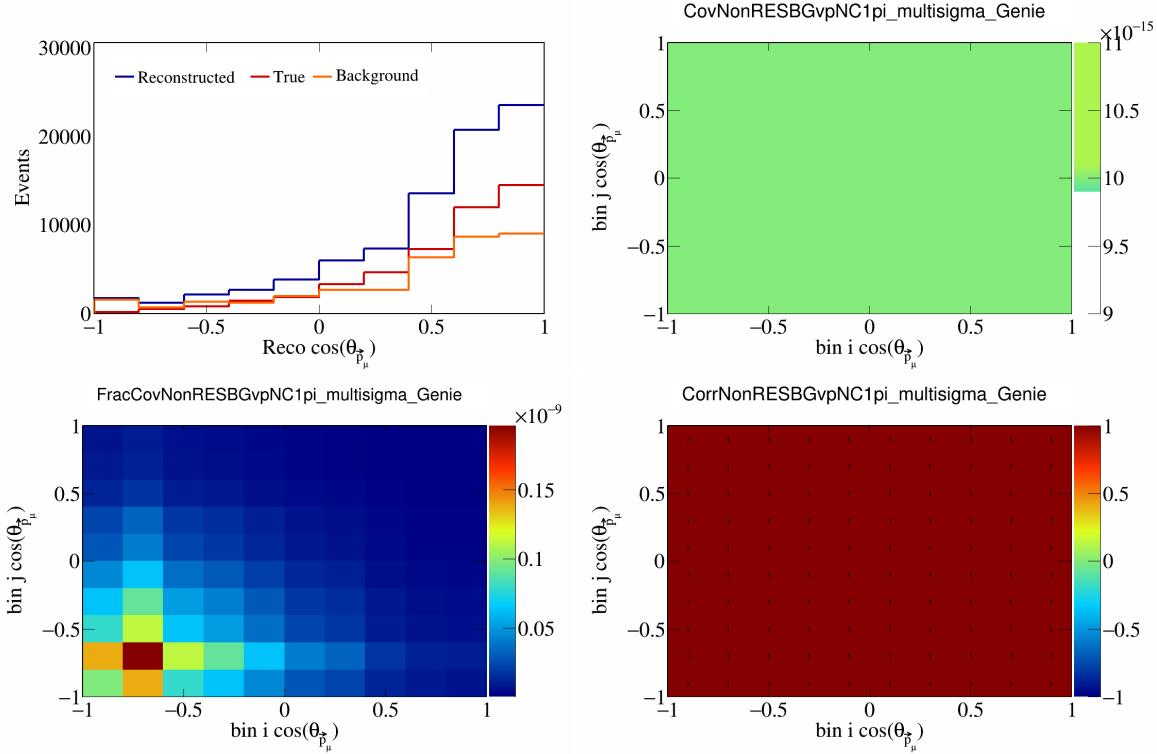


Figure 580: NonRESBGvpNC1pi variations for  $\cos(\theta_{\vec{p}_\mu})$ .

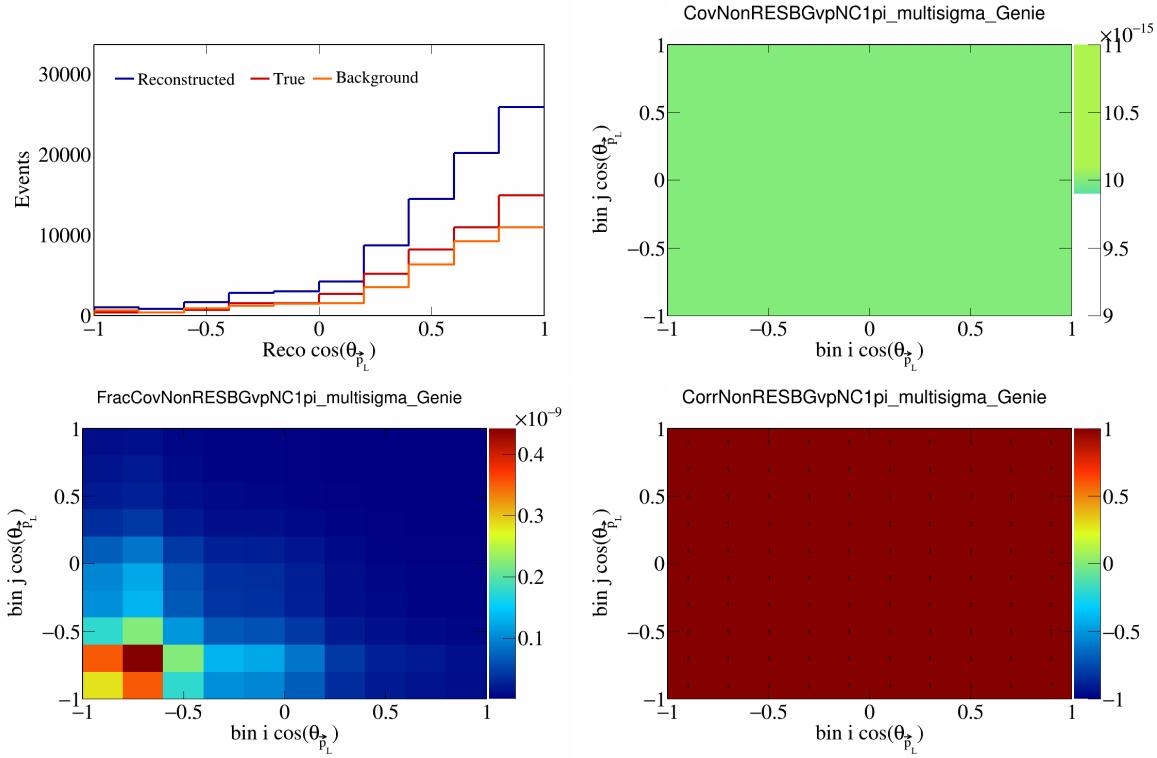


Figure 581: NonRESBGvpNC1pi variations for  $\cos(\theta_{\vec{p}_L})$ .

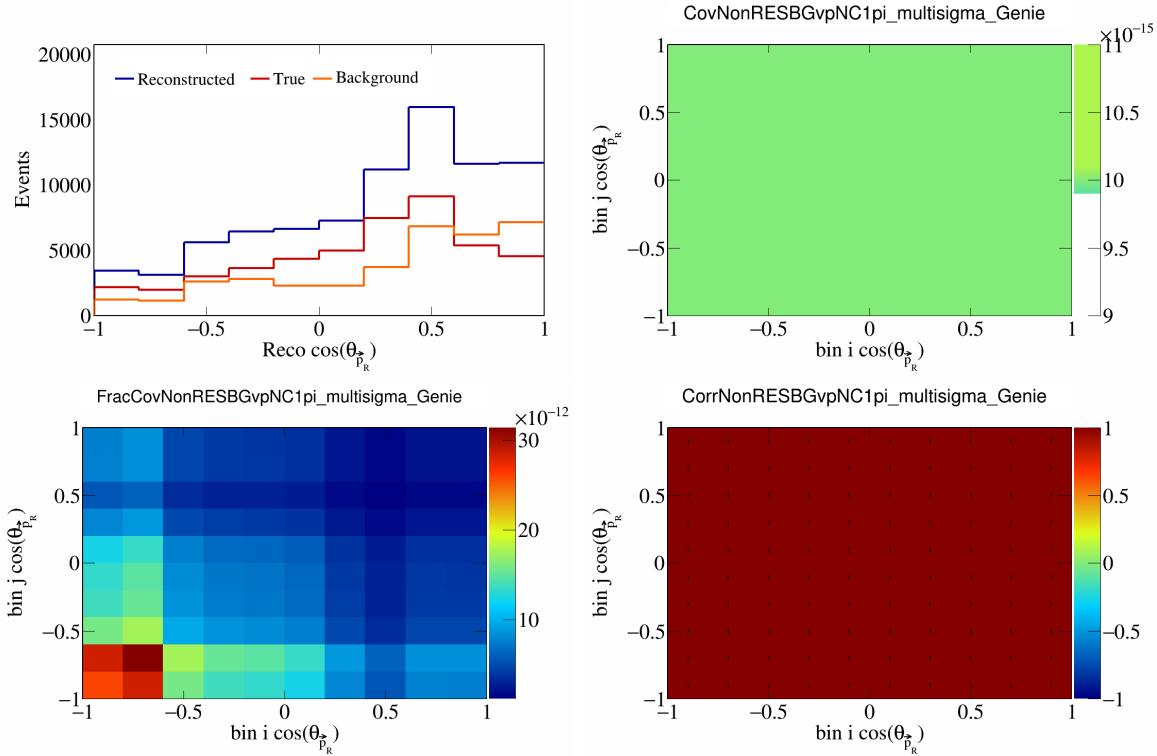


Figure 582: NonRESBGvpNC1pi variations for  $\cos(\theta_{\vec{p}_R})$ .

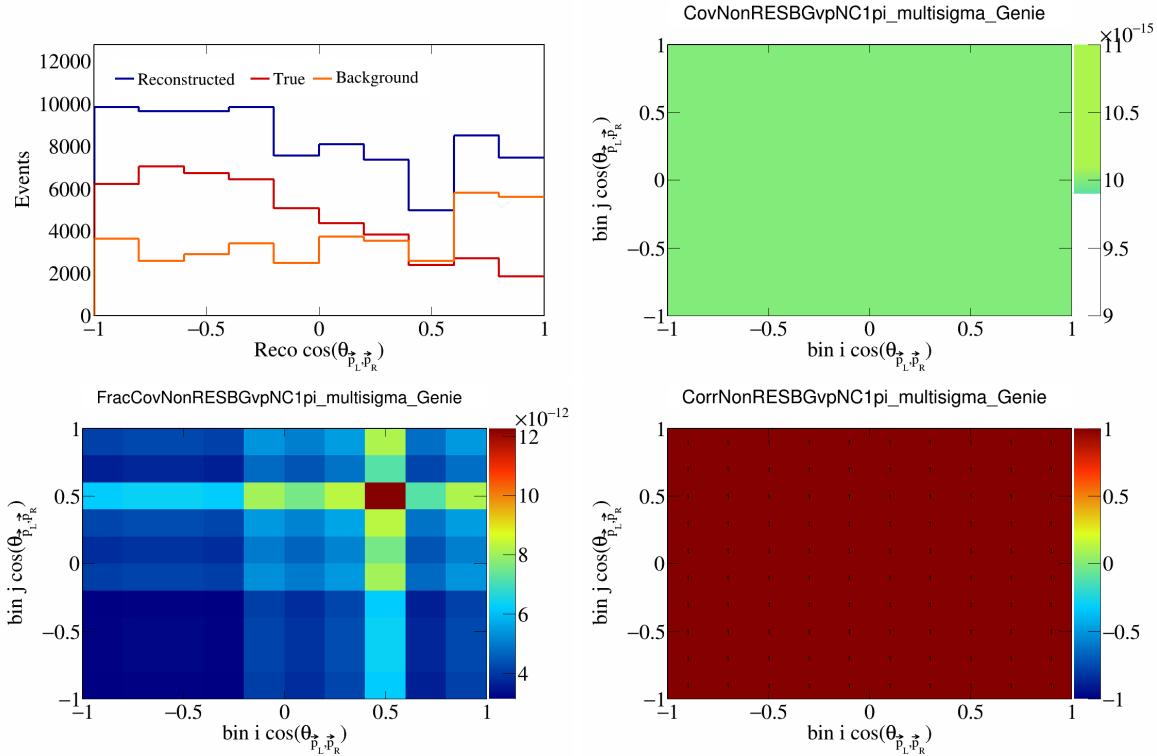


Figure 583: NonRESBGvpNC1pi variations for  $\cos(\theta_{\vec{p}_L, \vec{p}_R})$ .

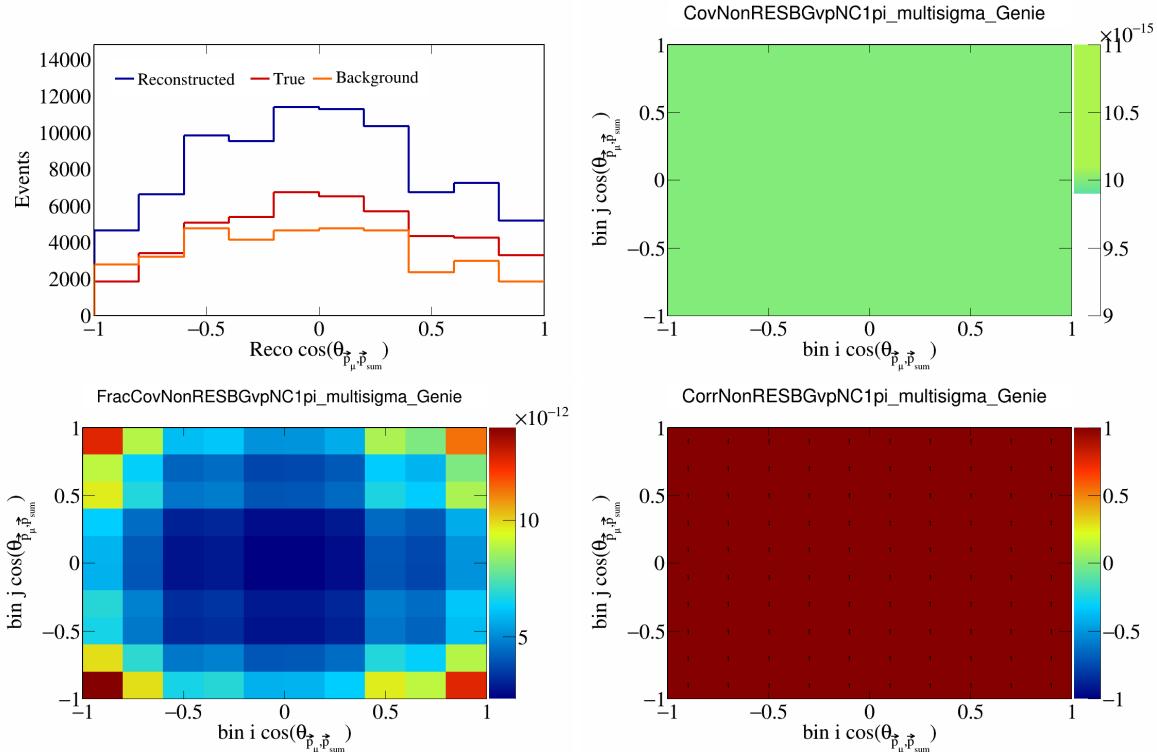


Figure 584: NonRESBGvpNC1pi variations for  $\cos(\theta_{\vec{p}_\mu, \vec{p}_{\text{sum}}})$ .

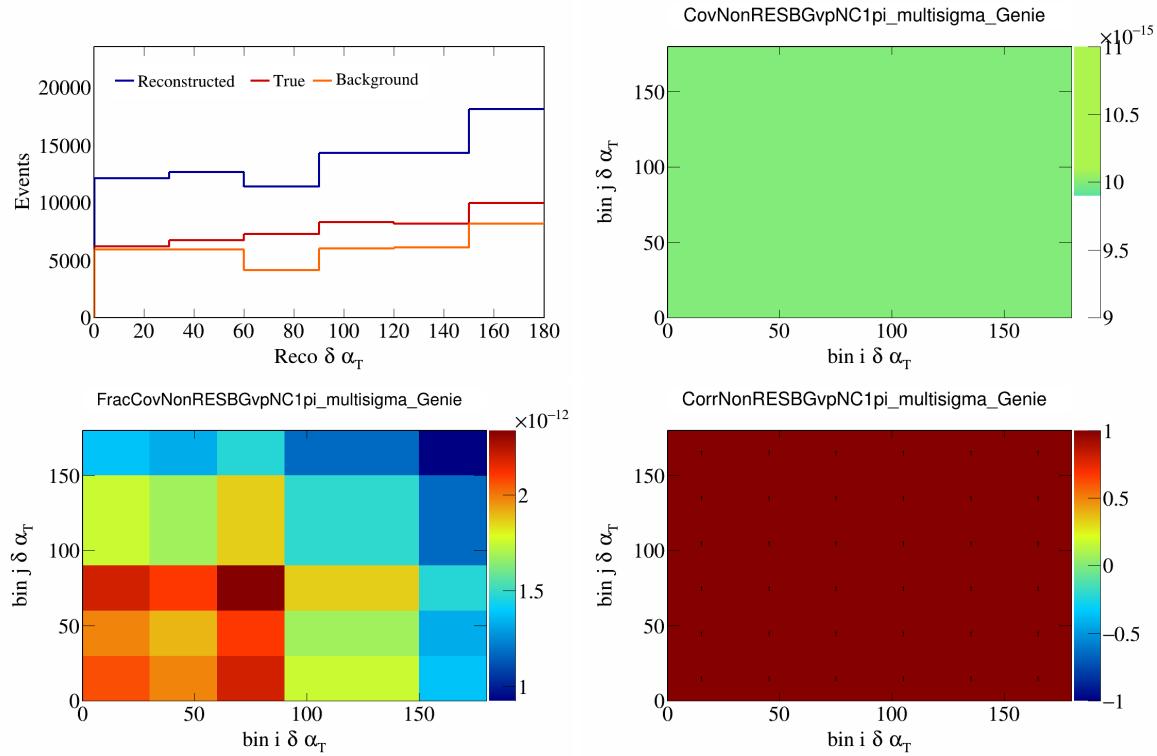


Figure 585: NonRESBGvpNC1pi variations for  $\delta\alpha_T$ .

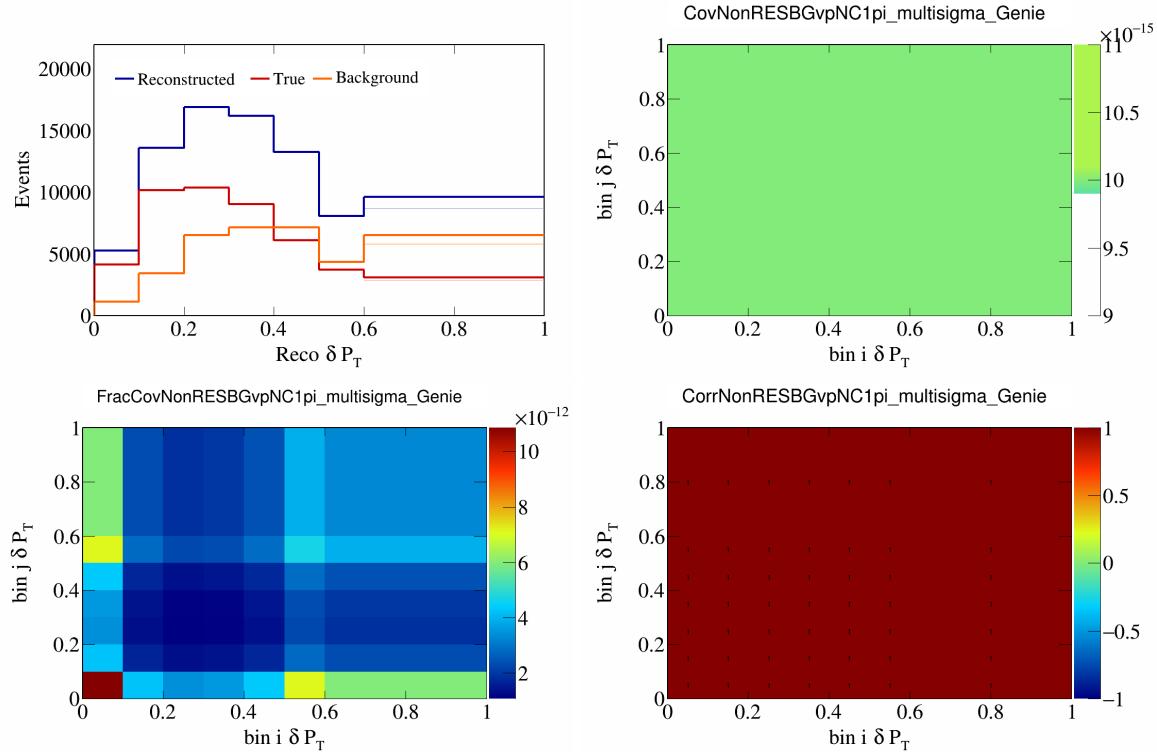


Figure 586: NonRESBGvpNC1pi variations for  $\delta P_T$ .

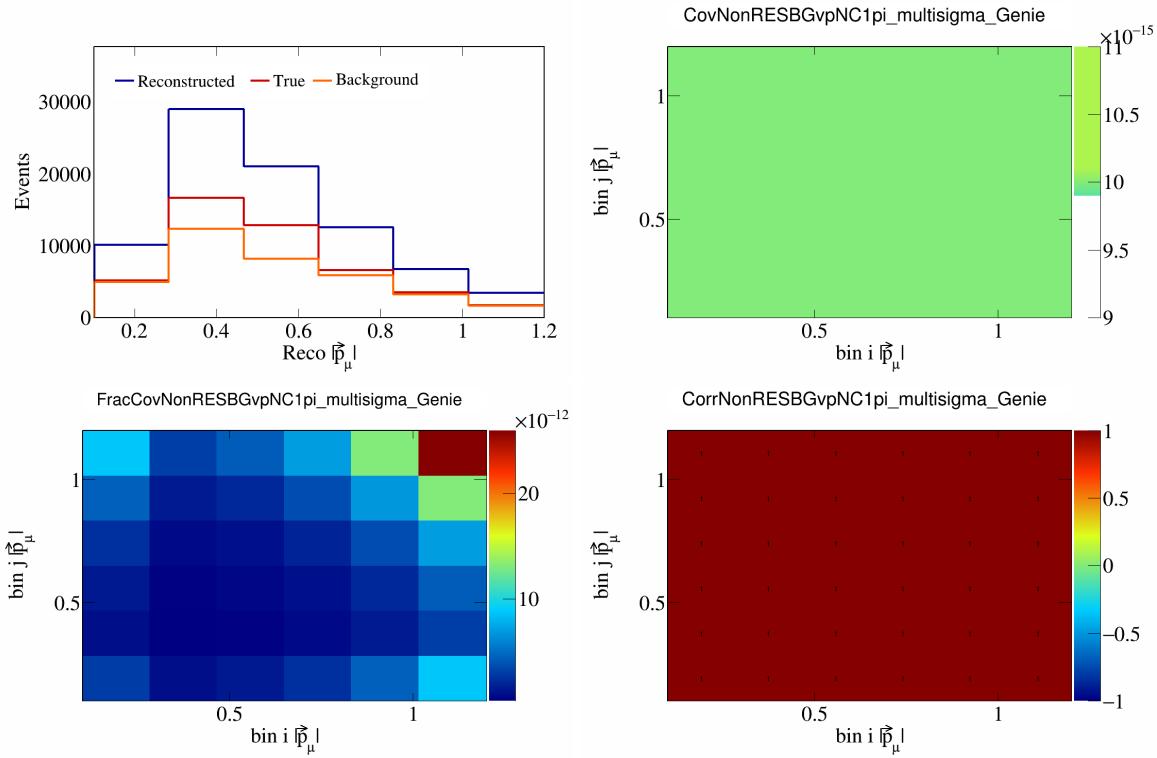


Figure 587: NonRESBGvpNC1pi variations for  $|\vec{p}_\mu|$ .

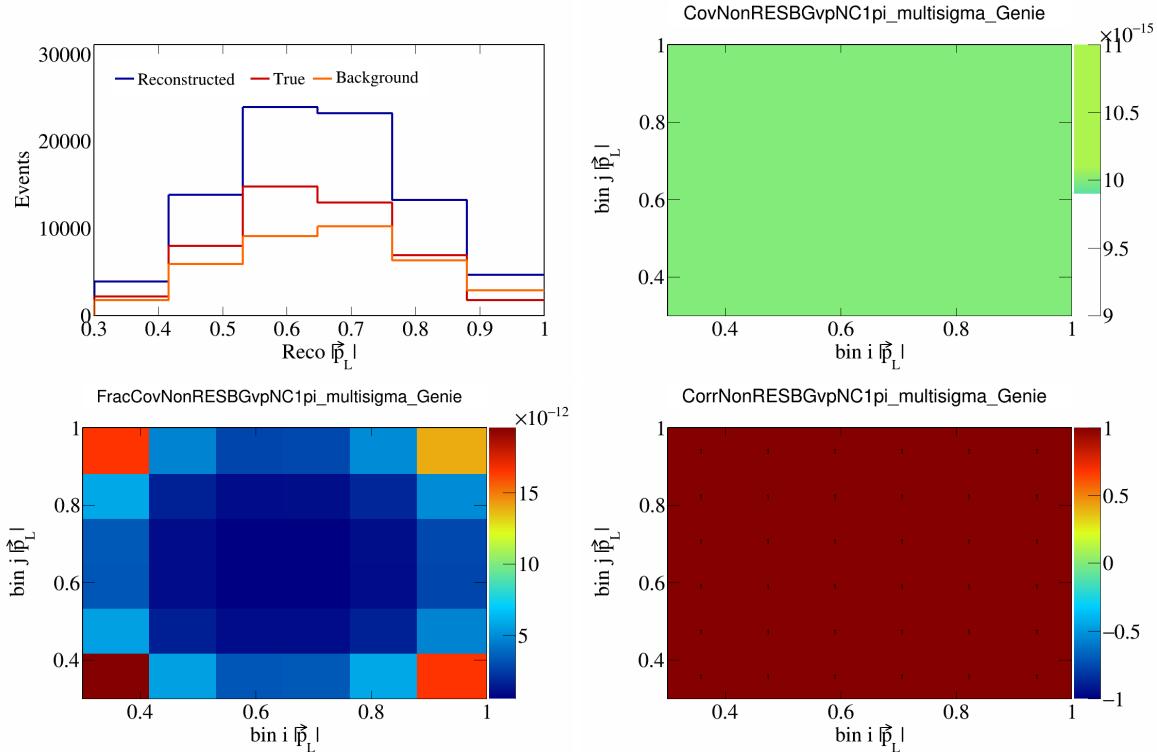


Figure 588: NonRESBGvpNC1pi variations for  $|\vec{p}_L|$ .

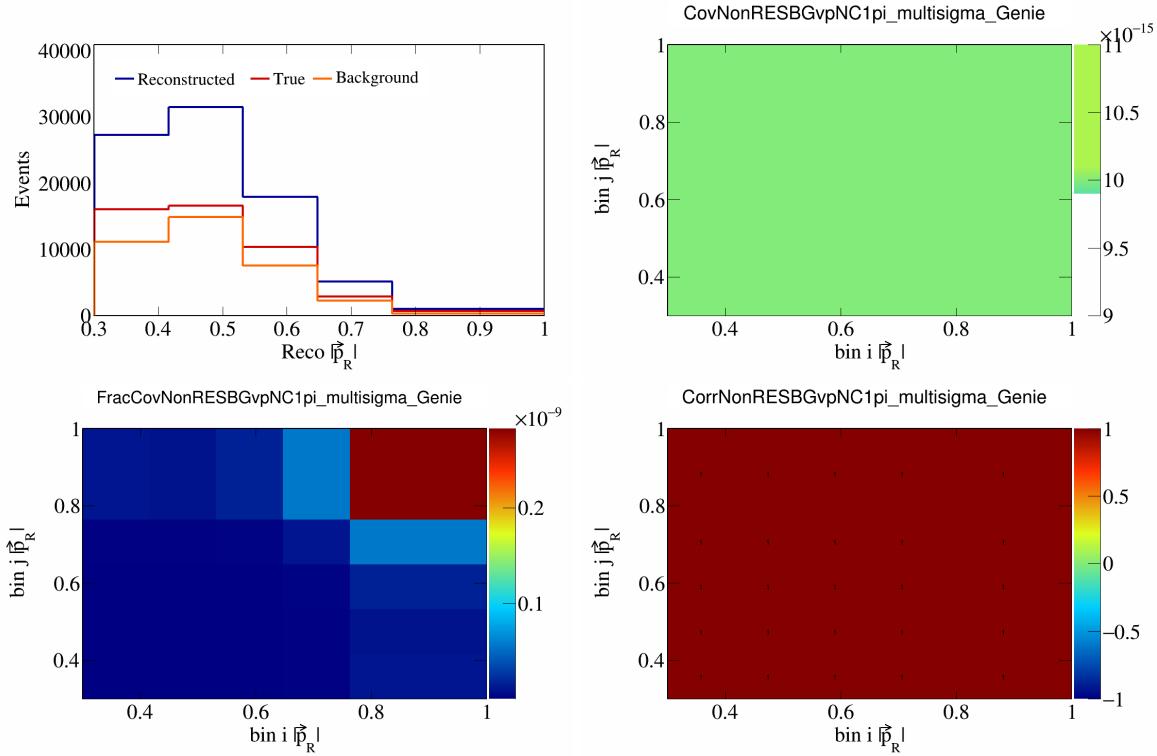


Figure 589: NonRESBGvpNC1pi variations for  $|\vec{p}_R|$ .

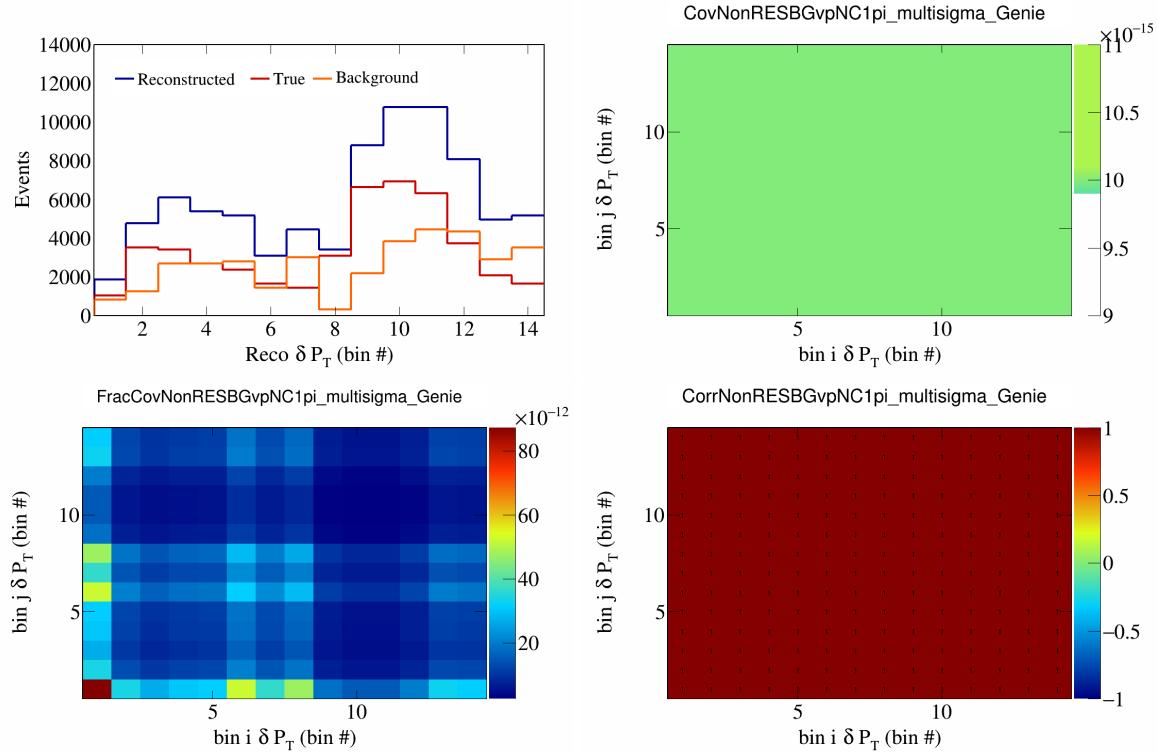


Figure 590: NonRESBGvpNC1pi variations for  $\delta P_T$  in  $\cos(\theta_{\vec{p}_\mu})$ .

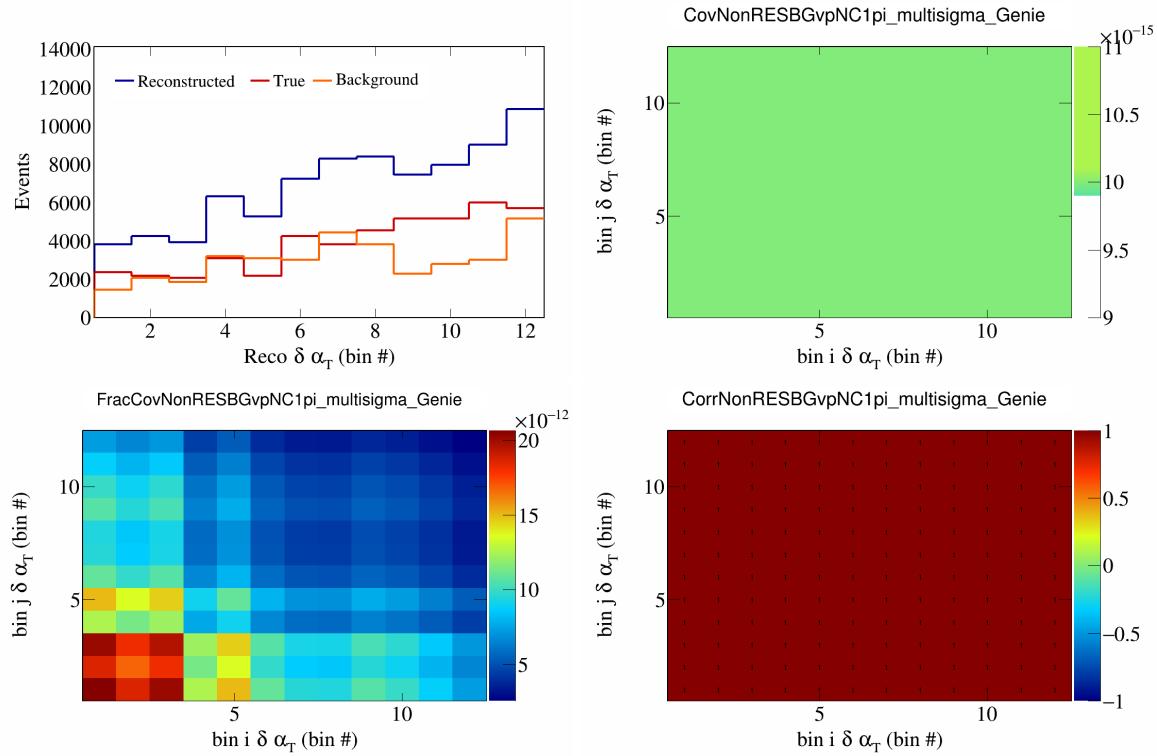


Figure 591: NonRESBGvpNC1pi variations for  $\delta\alpha_T$  in  $\cos(\theta_{\vec{p}_\mu})$ .

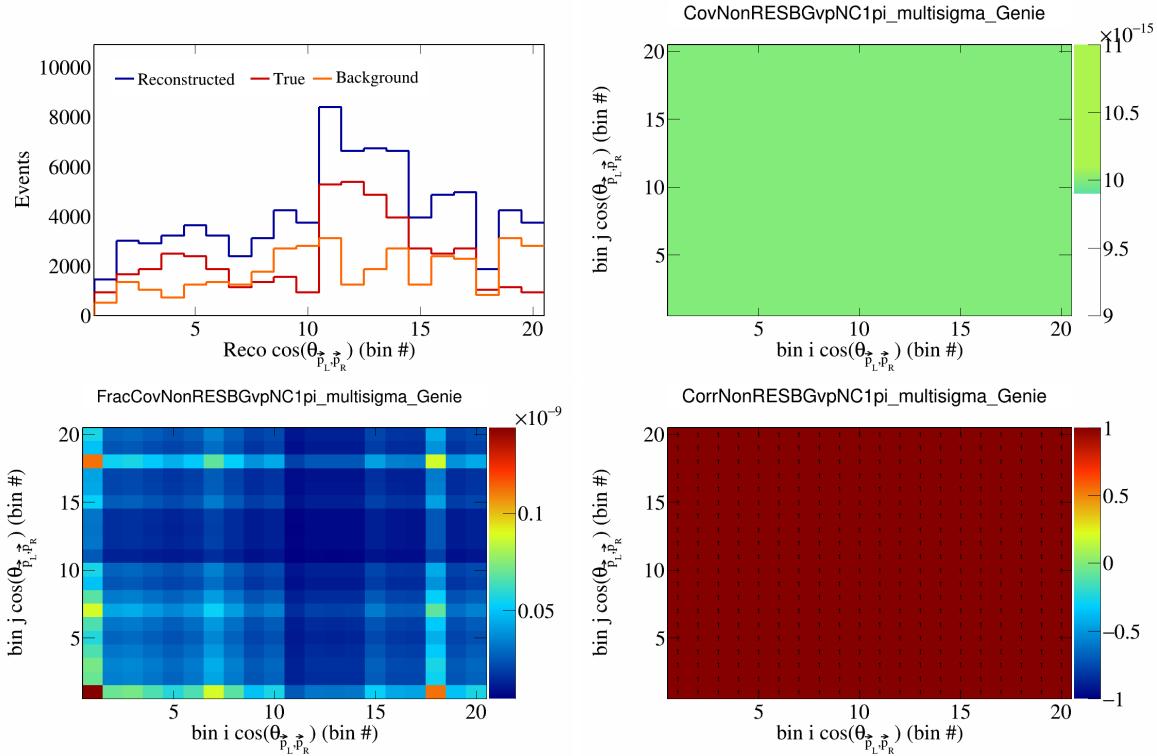


Figure 592: NonRESBGvpNC1pi variations for  $\cos(\theta_{\vec{p}_L, \vec{p}_R})$  in  $\cos(\theta_{\vec{p}_\mu})$ .

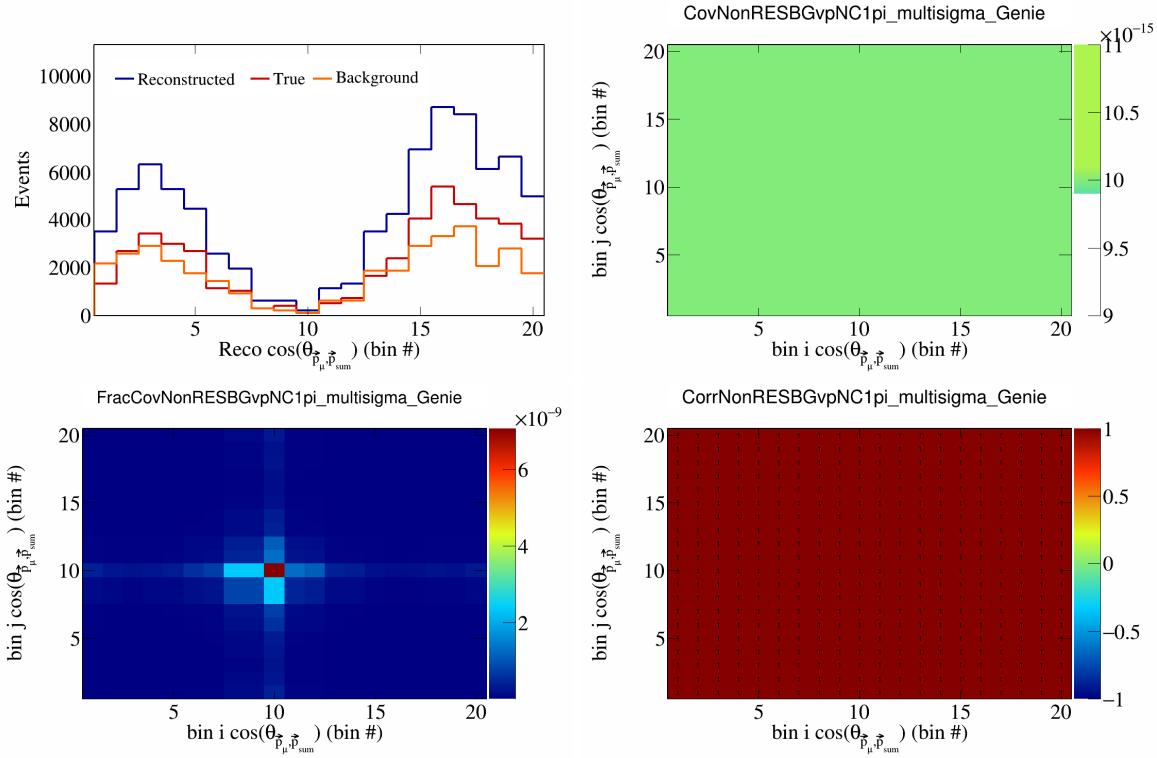


Figure 593: NonRESBGvpNC1pi variations for  $\cos(\theta_{\vec{p}_\mu, \vec{p}_{\text{sum}}})$  in  $\cos(\theta_{\vec{p}_\mu})$ .

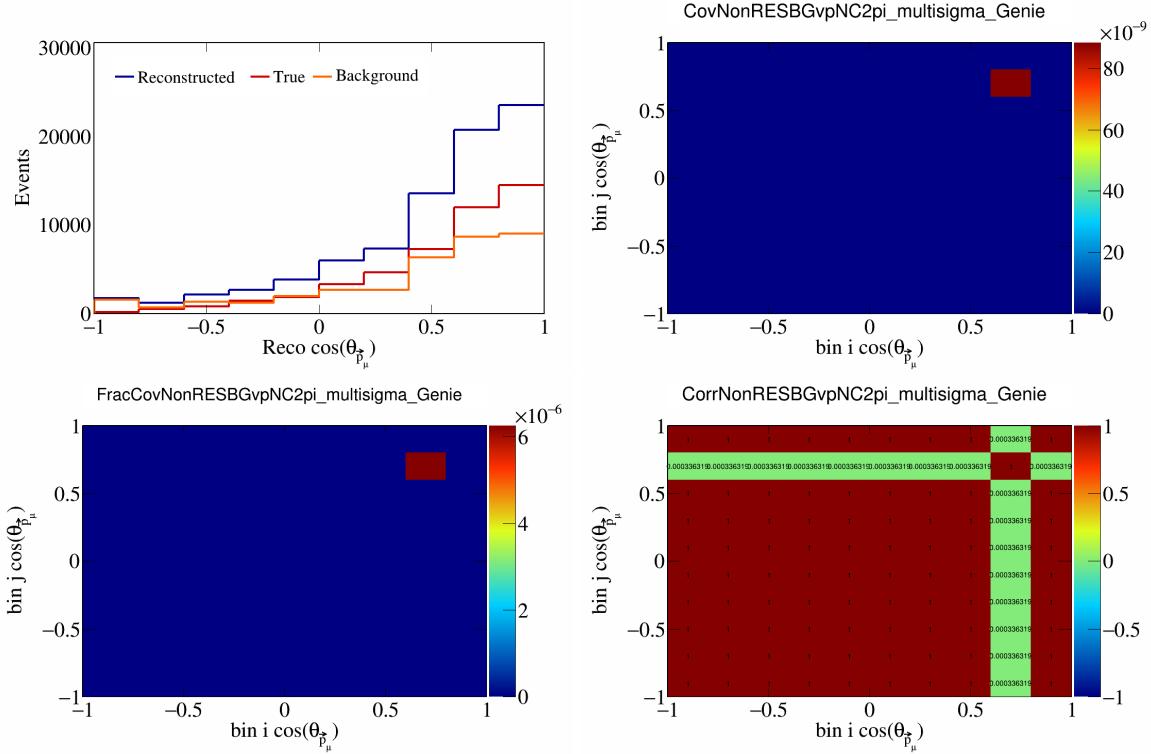


Figure 594: NonRESBGvpNC2pi variations for  $\cos(\theta_{\vec{p}_\mu})$ .

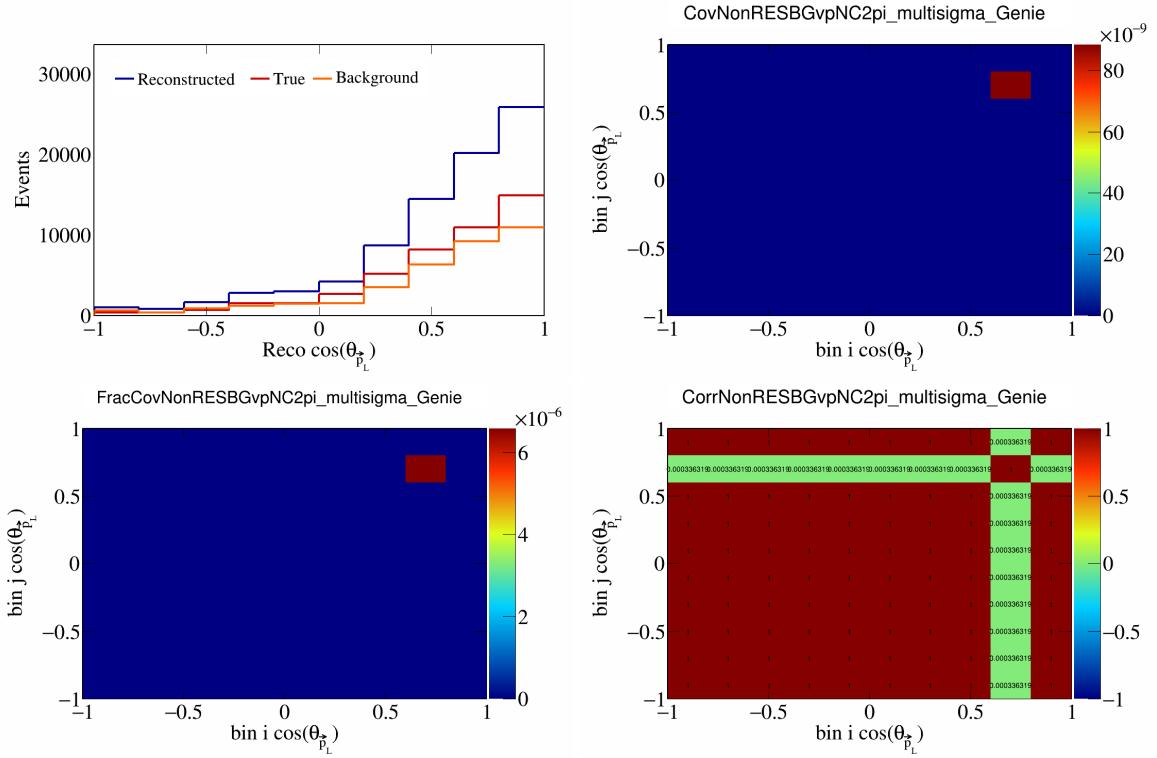


Figure 595: NonRESBGvpNC2pi variations for  $\cos(\theta_{\vec{p}_L})$ .

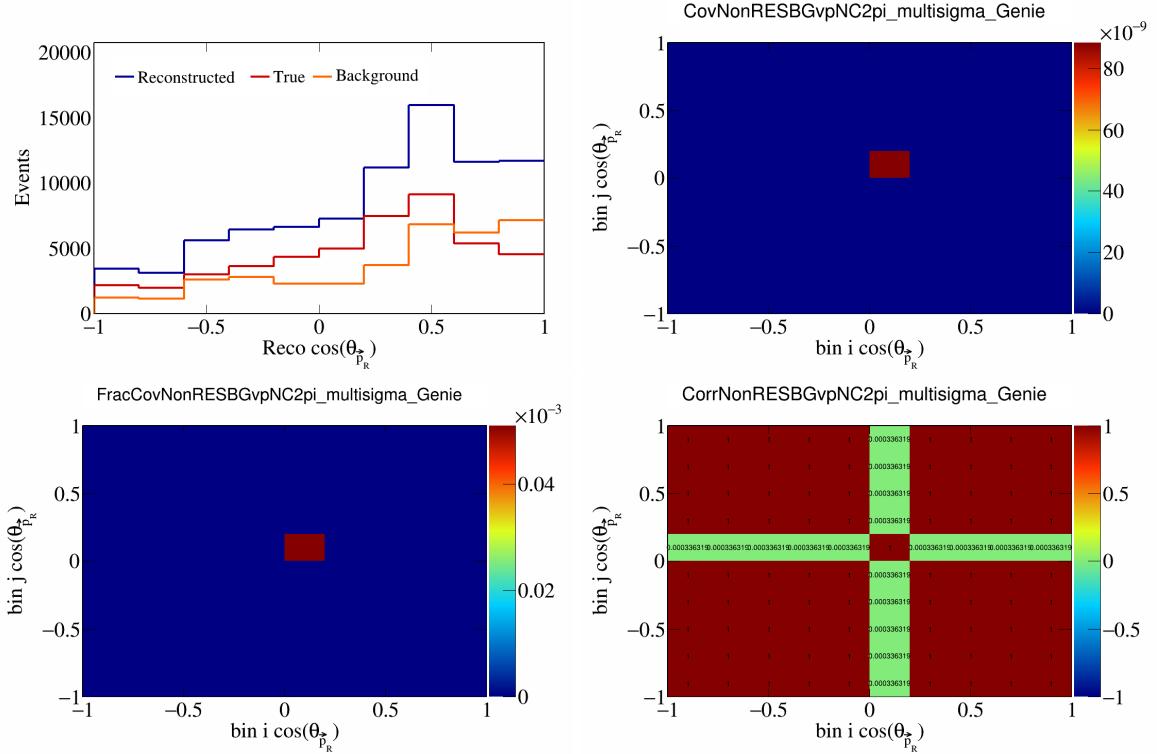


Figure 596: NonRESBGvpNC2pi variations for  $\cos(\theta_{\vec{p}_R})$ .

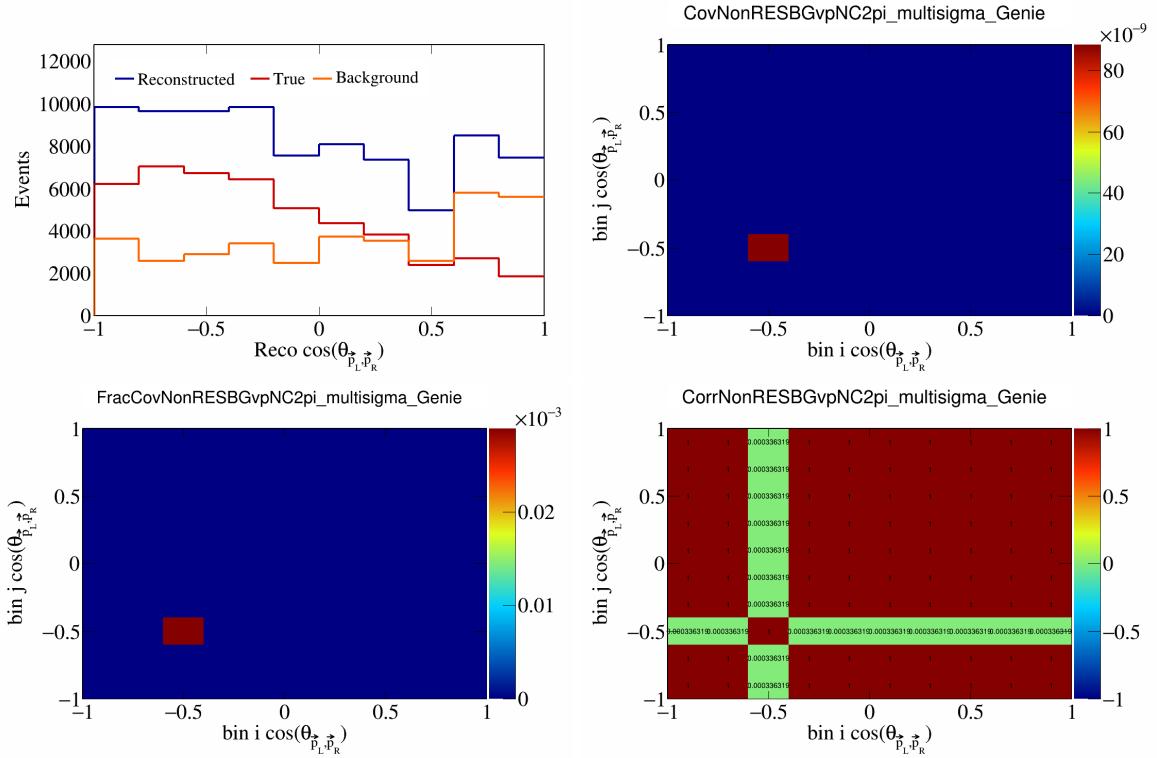


Figure 597: NonRESBGvpNC2pi variations for  $\cos(\theta_{\vec{p}_L, \vec{p}_R})$ .

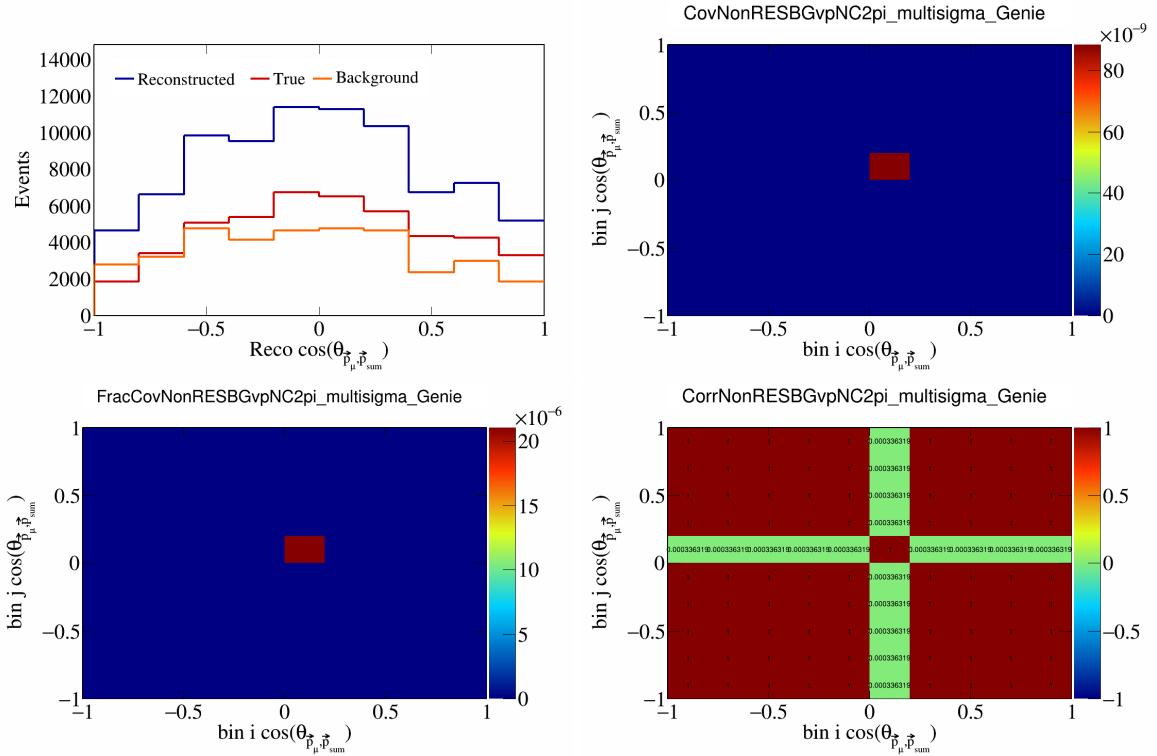


Figure 598: NonRESBGvpNC2pi variations for  $\cos(\theta_{\vec{p}_\mu, \vec{p}_{\text{sum}}})$ .

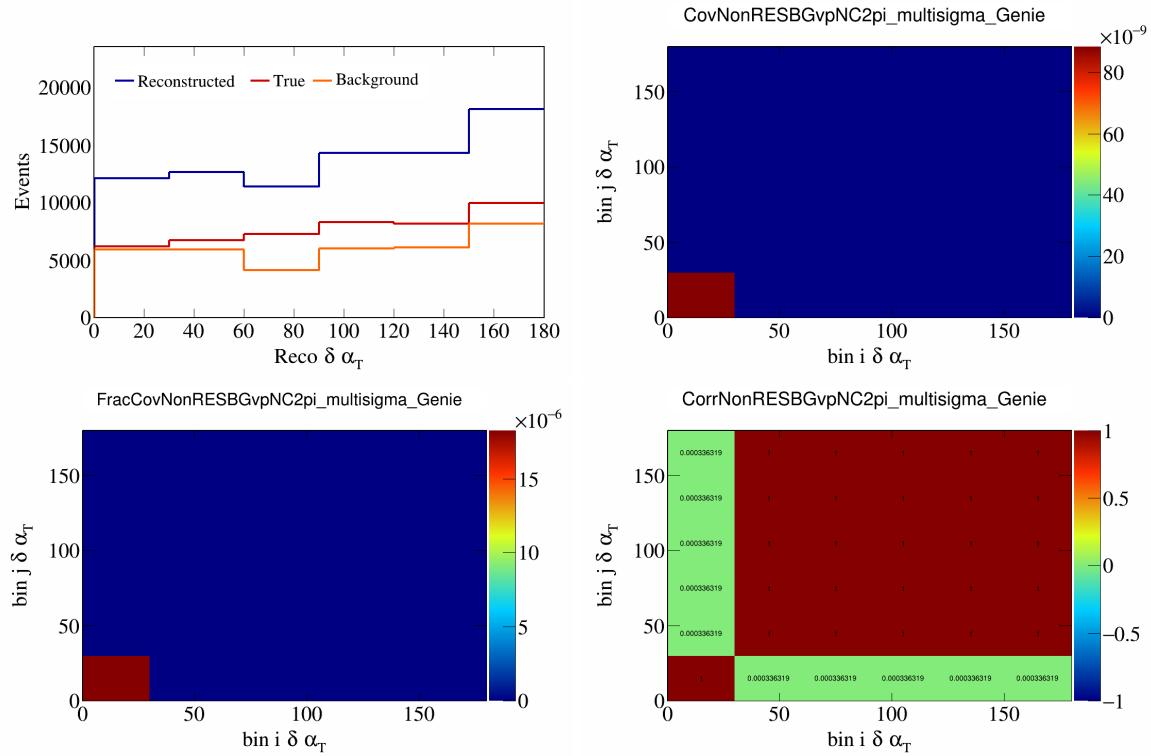


Figure 599: NonRESBGvpNC2pi variations for  $\delta\alpha_T$ .

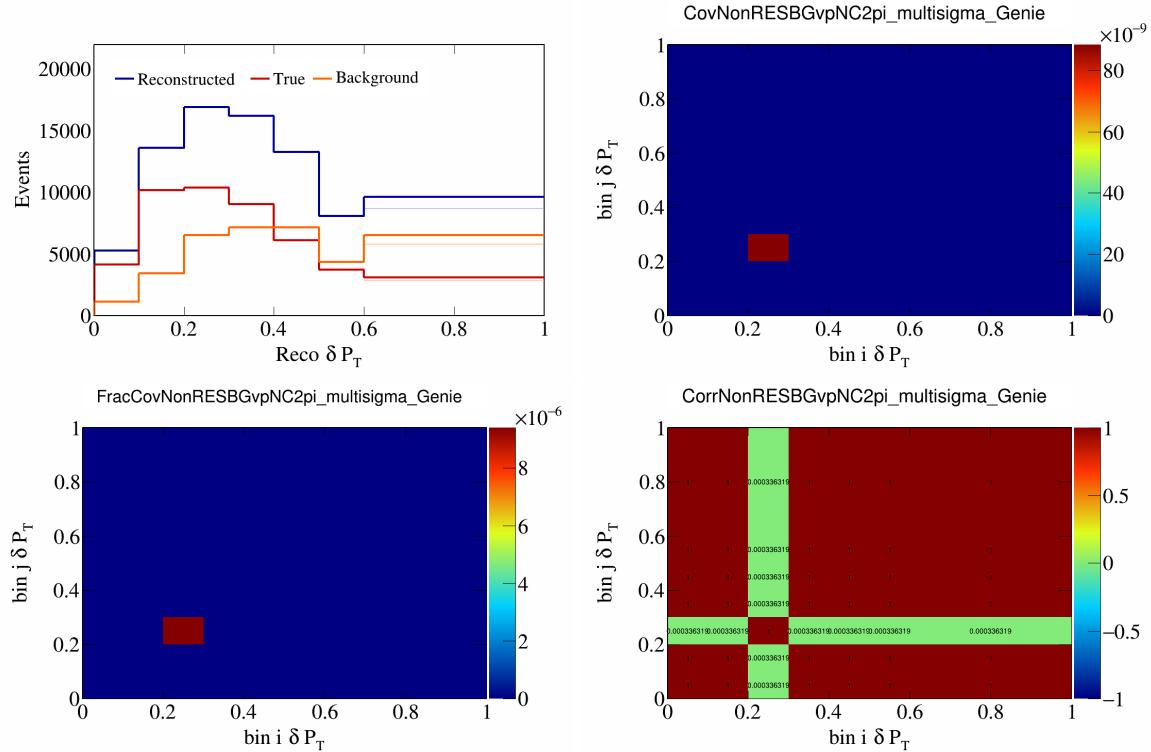


Figure 600: NonRESBGvpNC2pi variations for  $\delta P_T$ .

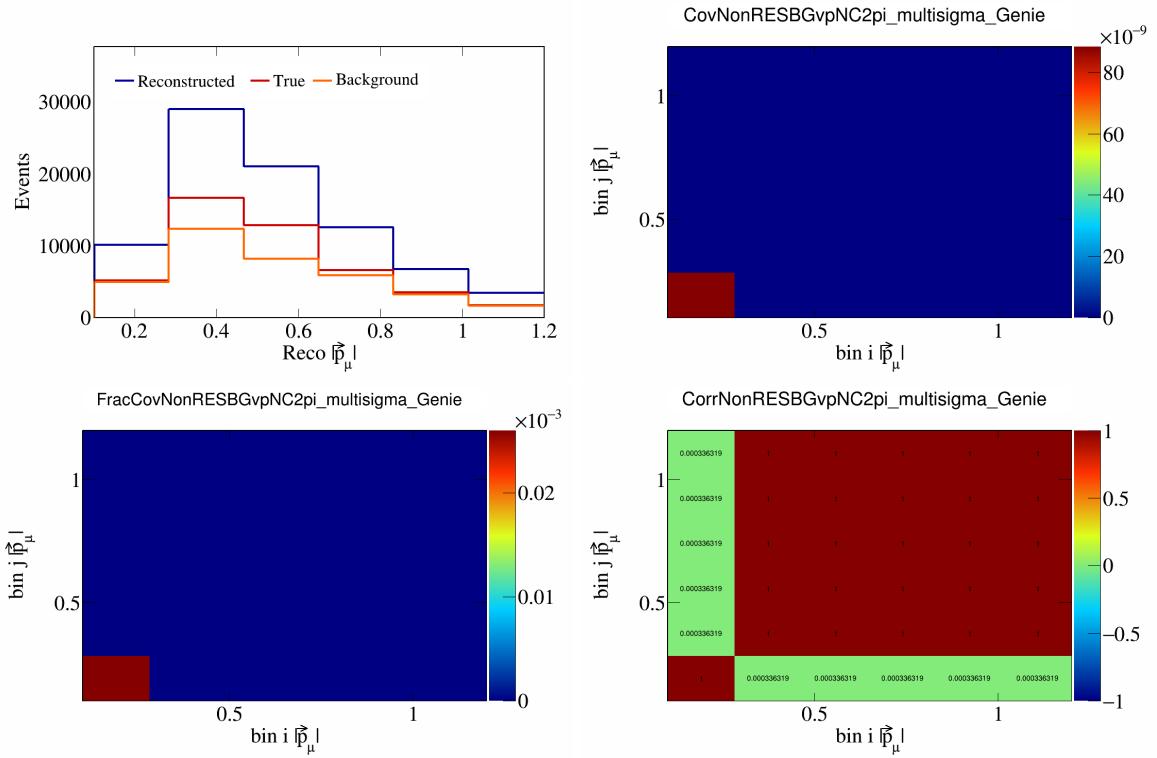


Figure 601: NonRESBGvpNC2pi variations for  $|\vec{p}_\mu|$ .

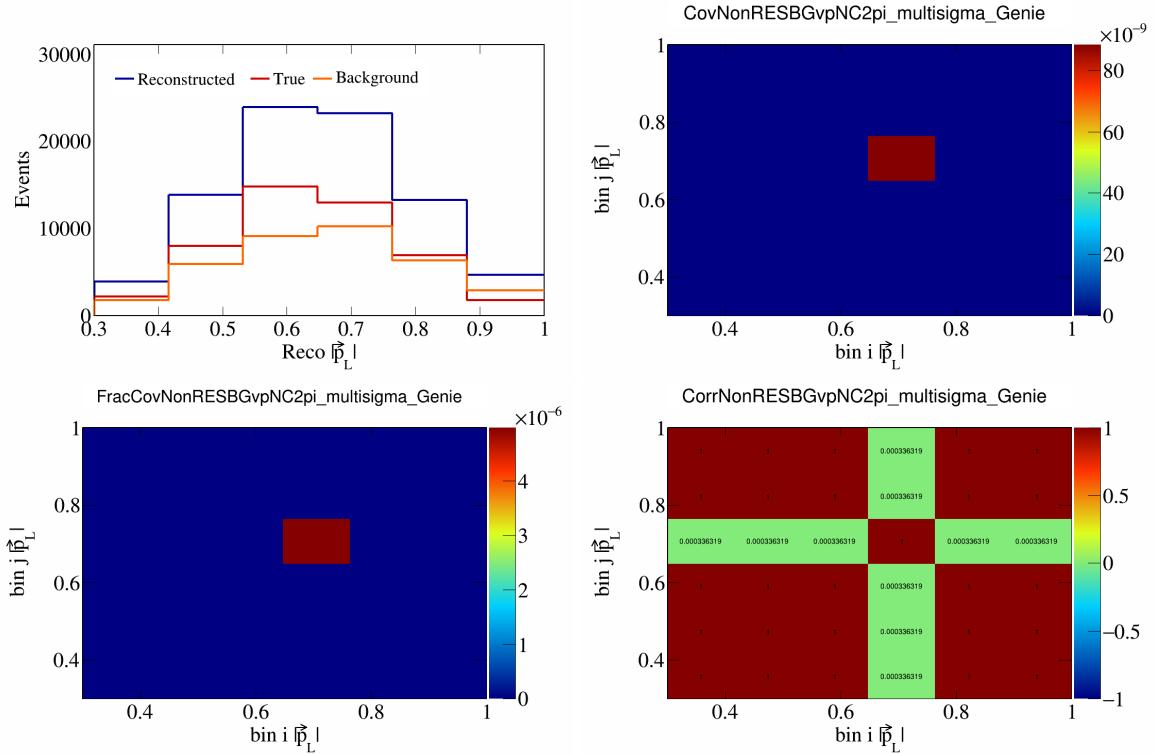


Figure 602: NonRESBGvpNC2pi variations for  $|\vec{p}_L|$ .

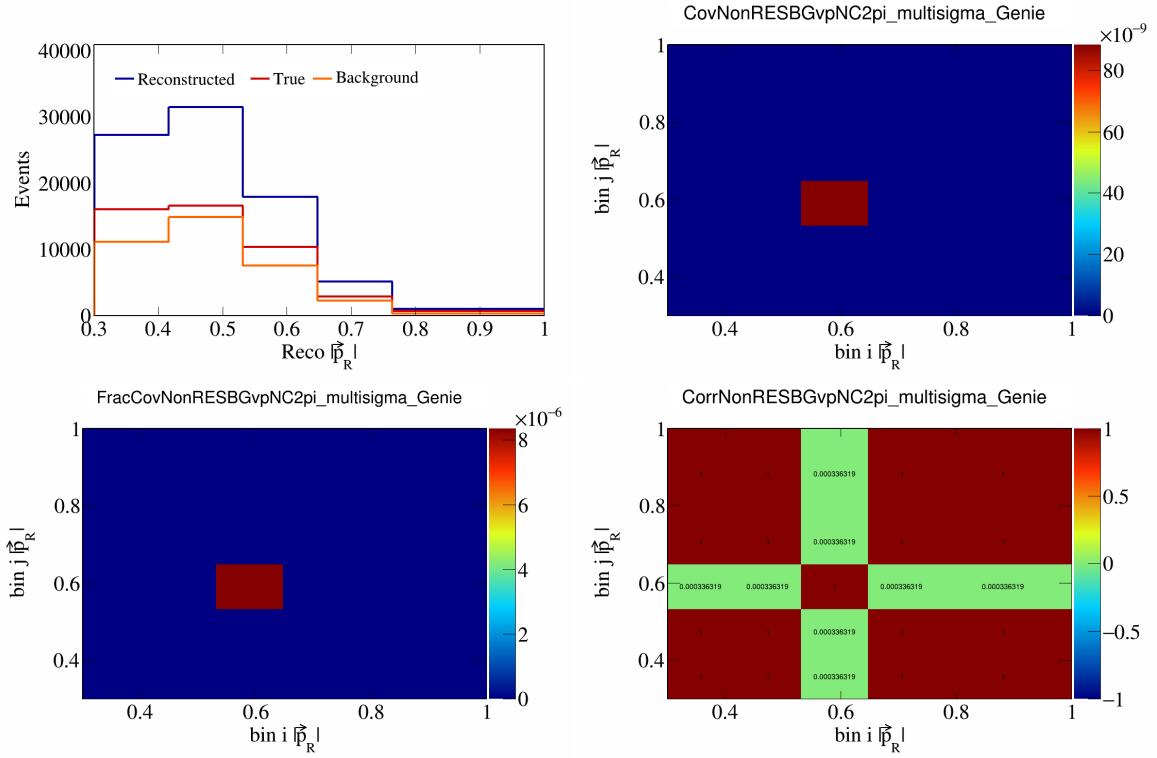


Figure 603: NonRESBGvpNC2pi variations for  $|\vec{p}_R|$ .

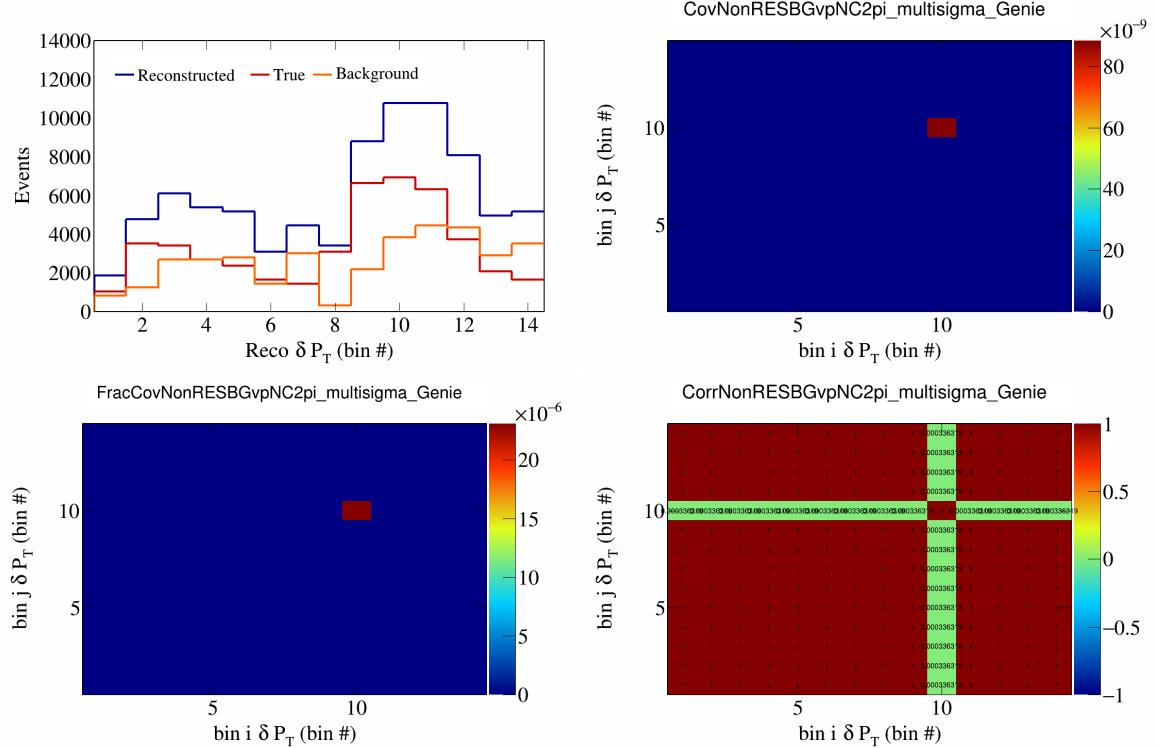


Figure 604: NonRESBGvpNC2pi variations for  $\delta P_T$  in  $\cos(\theta_{\vec{p}_\mu})$ .

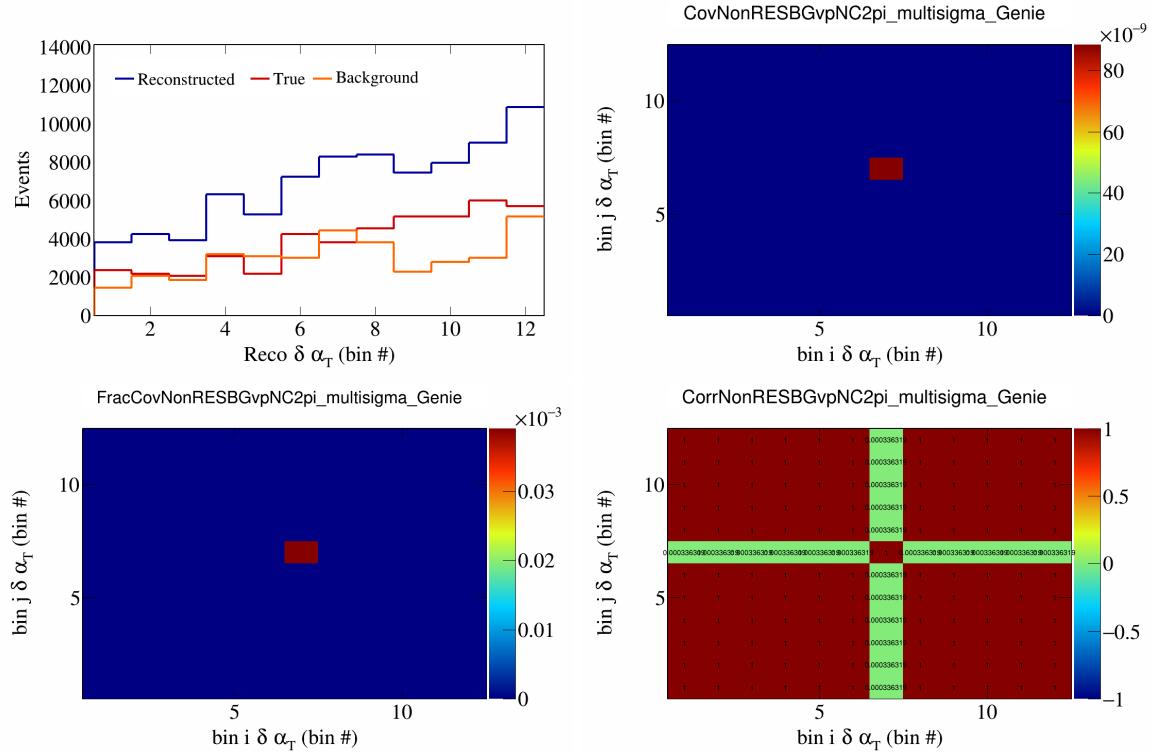


Figure 605: NonRESBGvpNC2pi variations for  $\delta\alpha_T$  in  $\cos(\theta_{\vec{p}_\mu})$ .

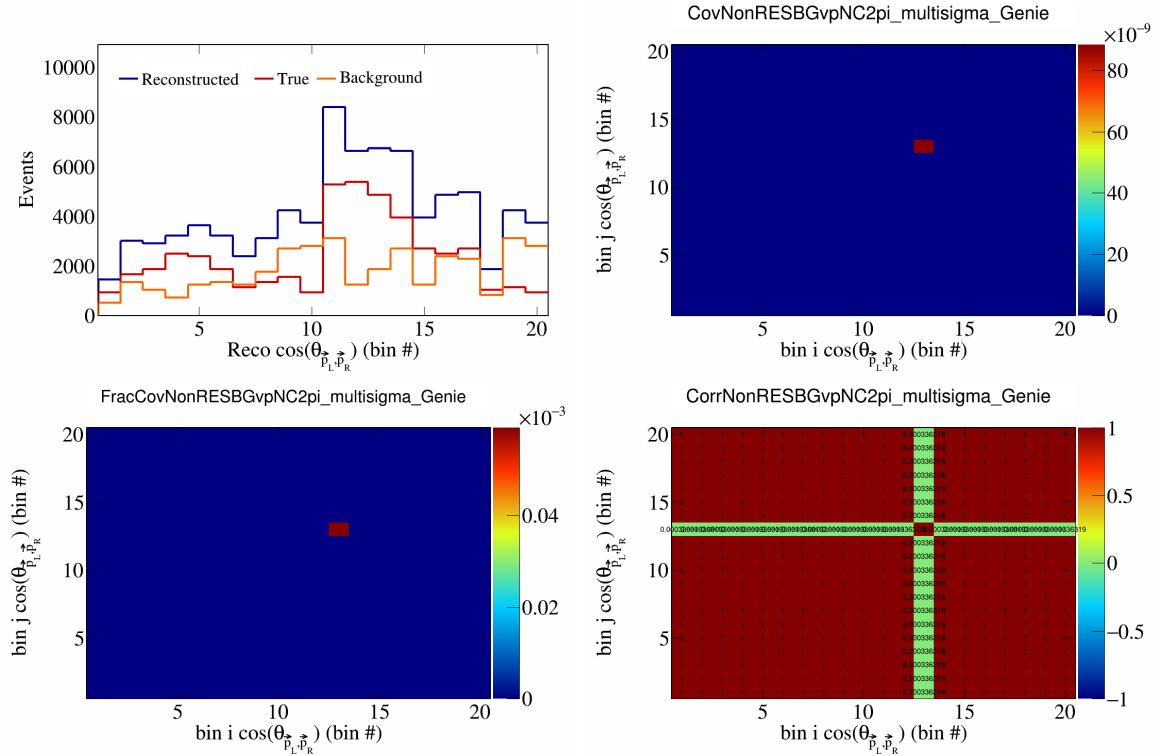


Figure 606: NonRESBGvpNC2pi variations for  $\cos(\theta_{\vec{p}_L, \vec{p}_R})$  in  $\cos(\theta_{\vec{p}_\mu})$ .

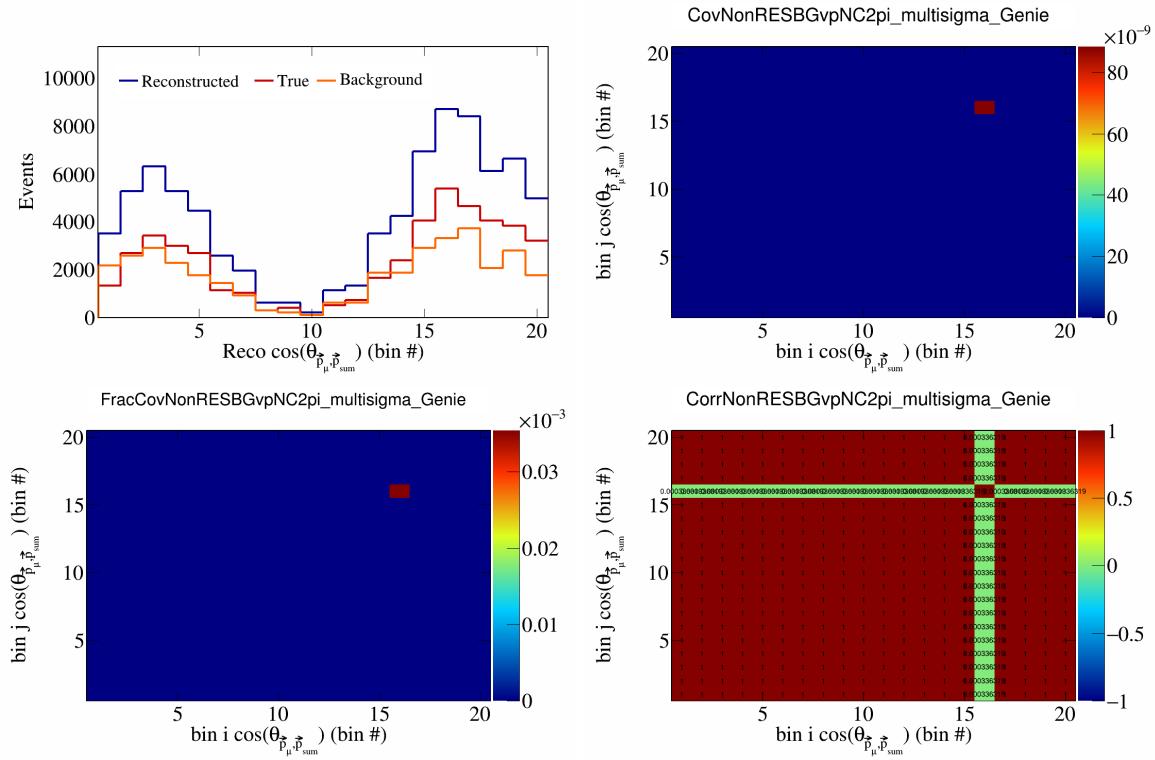


Figure 607: NonRESBGvpNC2pi variations for  $\cos(\theta_{\vec{p}_\mu, \vec{p}_{\text{sum}}})$  in  $\cos(\theta_{\vec{p}_\mu})$ .

286 **6.2 Flux systematics**

287 In this appendix, the variations, covariance matrices, fractional covariance matrices, and correlation matrices  
 288 are plotted for all of the flux systematics and variables.

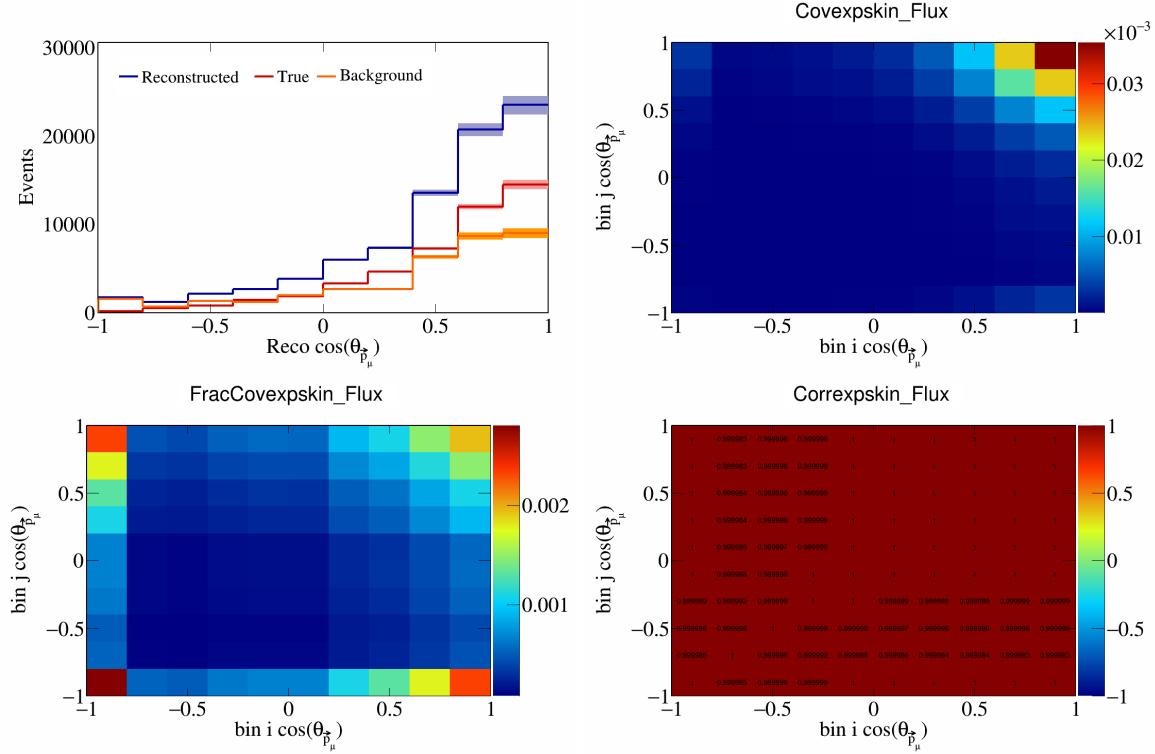


Figure 608: Epskin variations for  $\cos(\theta_{\vec{p}_\mu})$ .

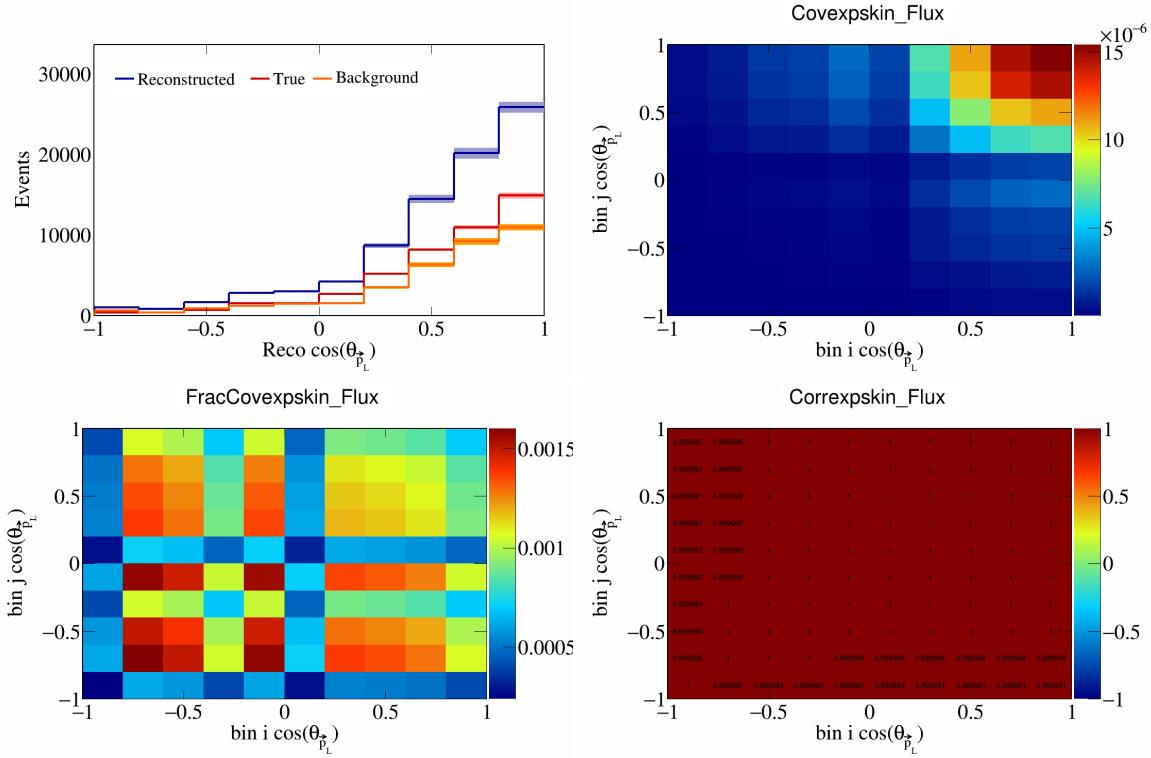


Figure 609: ExpSkin variations for  $\cos(\theta_{\vec{p}_L})$ .

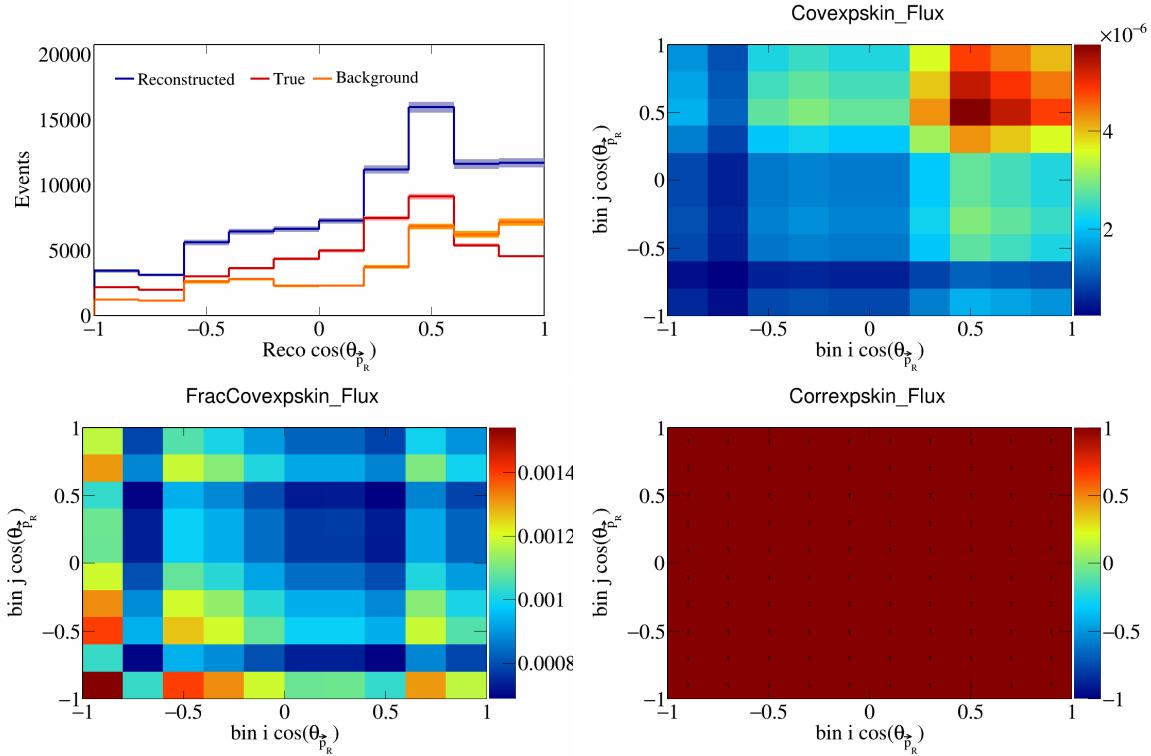


Figure 610: ExpSkin variations for  $\cos(\theta_{\vec{p}_R})$ .

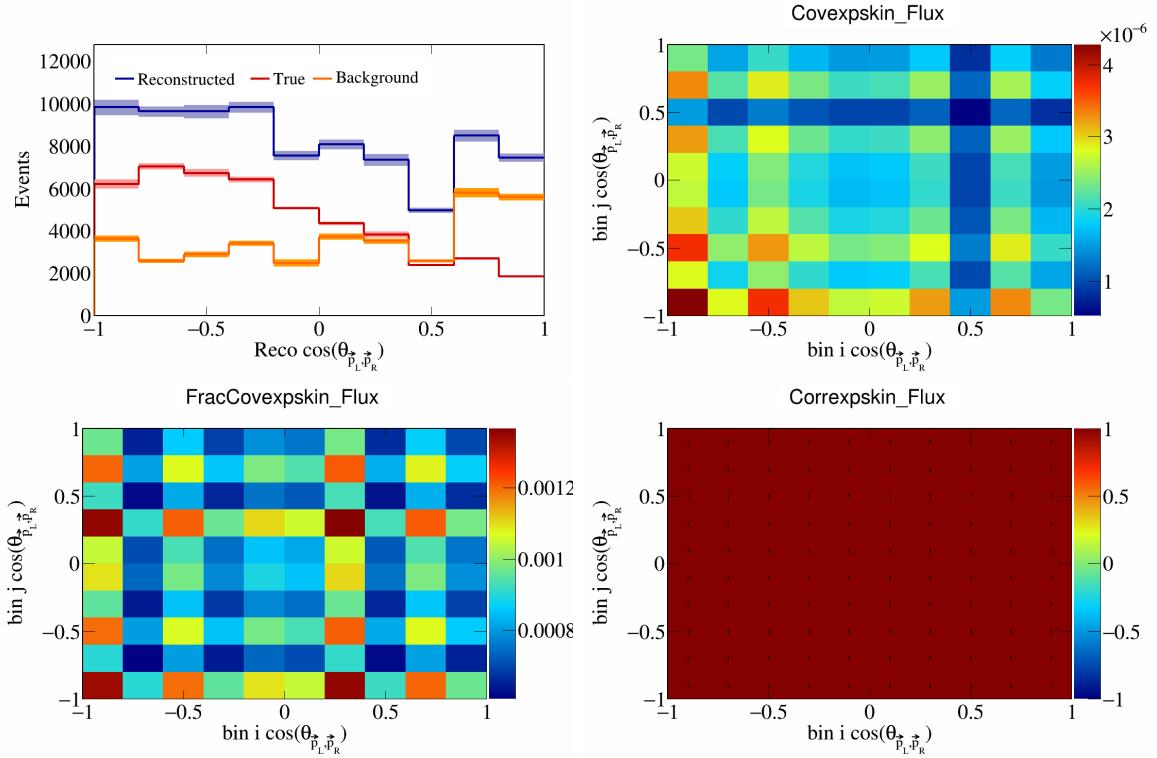


Figure 611: Exp skin variations for  $\cos(\theta_{\vec{p}_L, \vec{p}_R})$ .

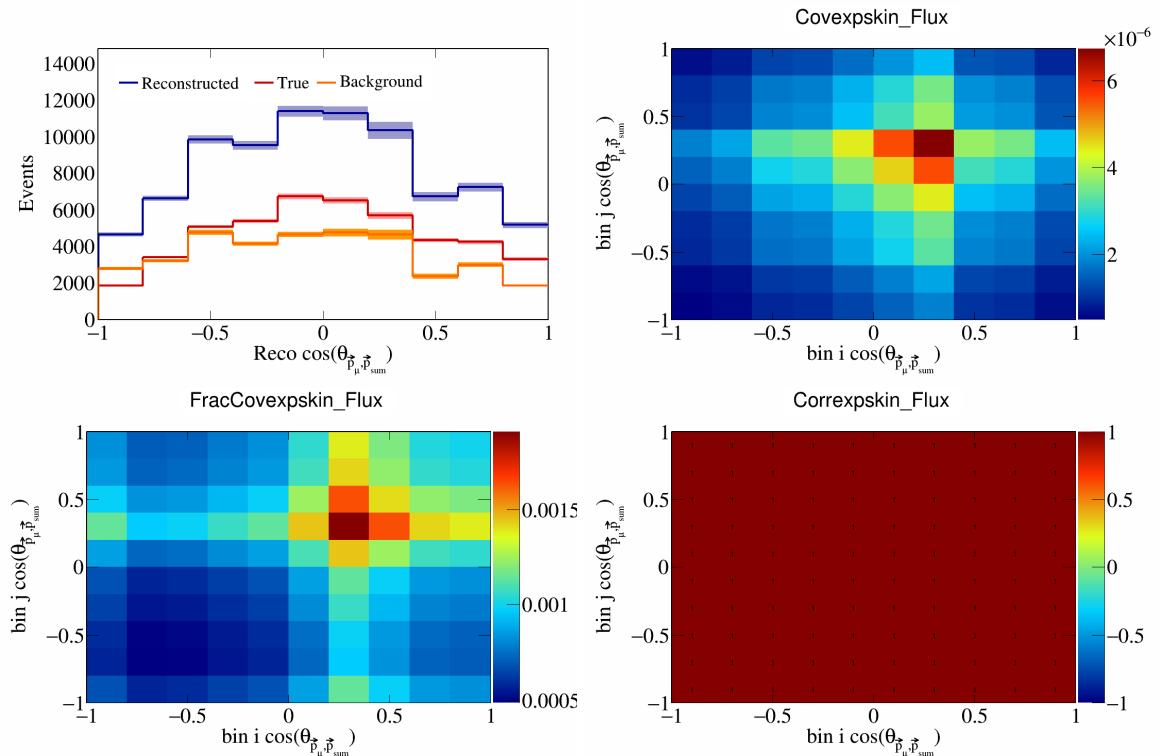


Figure 612: Exp skin variations for  $\cos(\theta_{\vec{p}_\mu, \vec{p}_{\text{sum}}})$ .

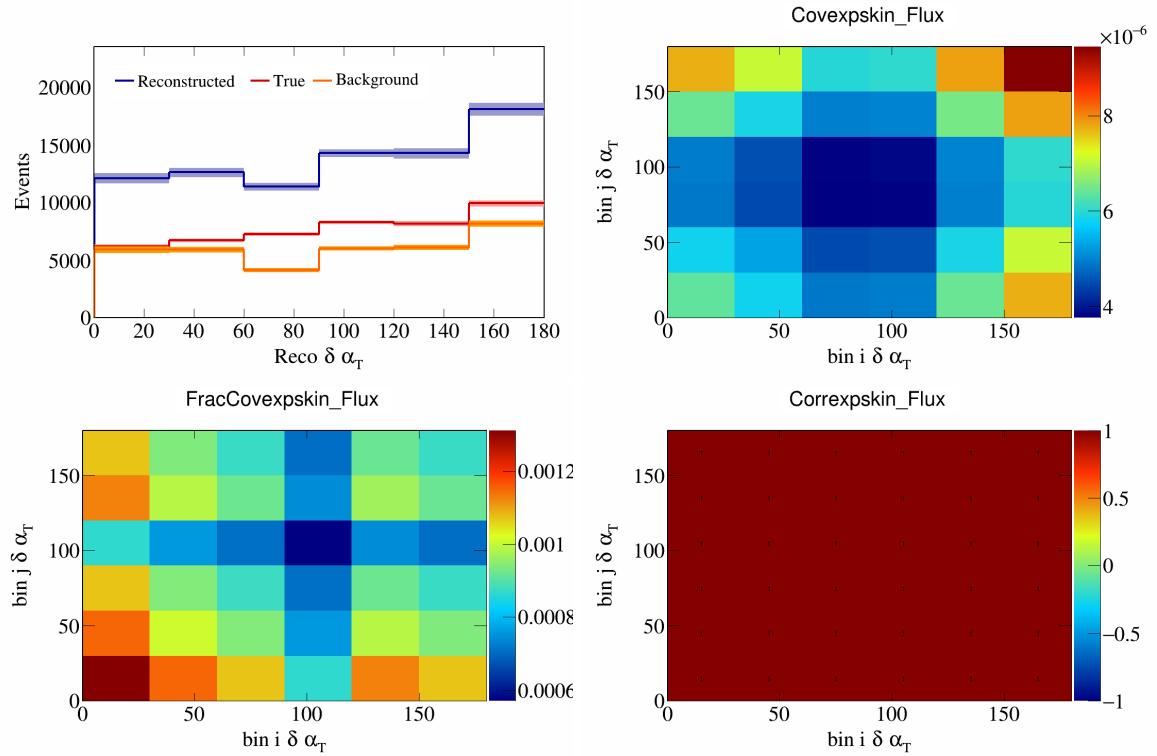


Figure 613: Expskin variations for  $\delta \alpha_T$ .

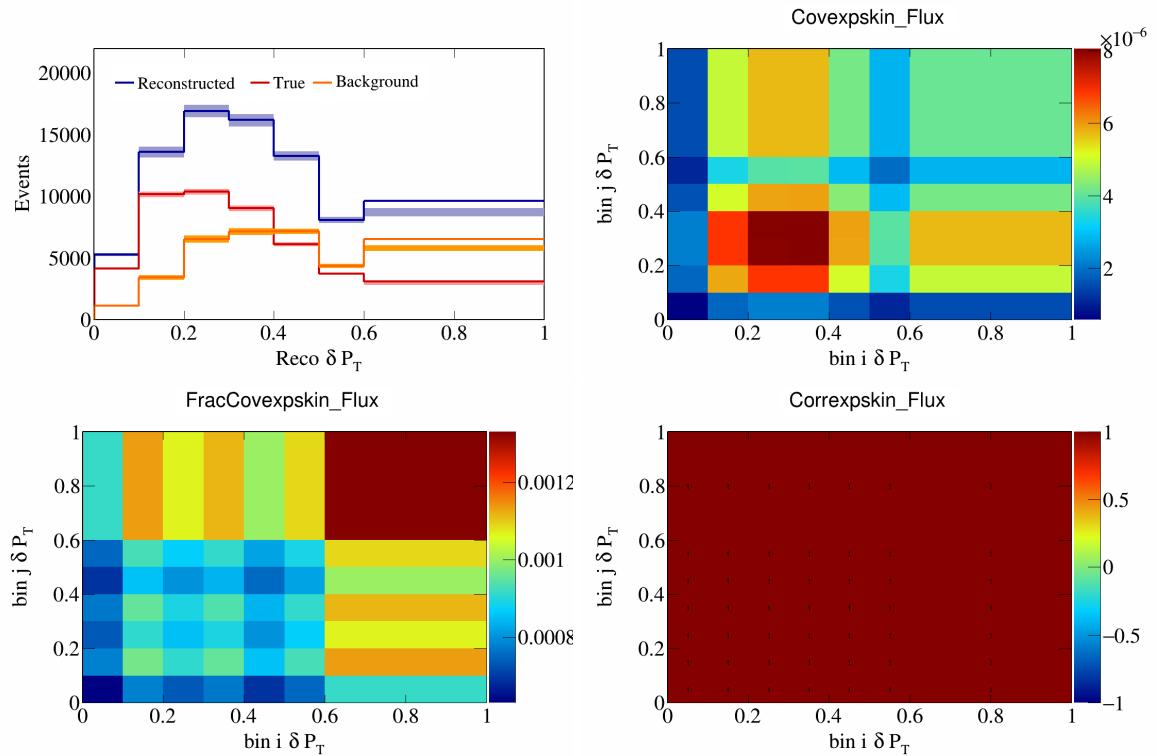


Figure 614: Expskin variations for  $\delta P_T$ .

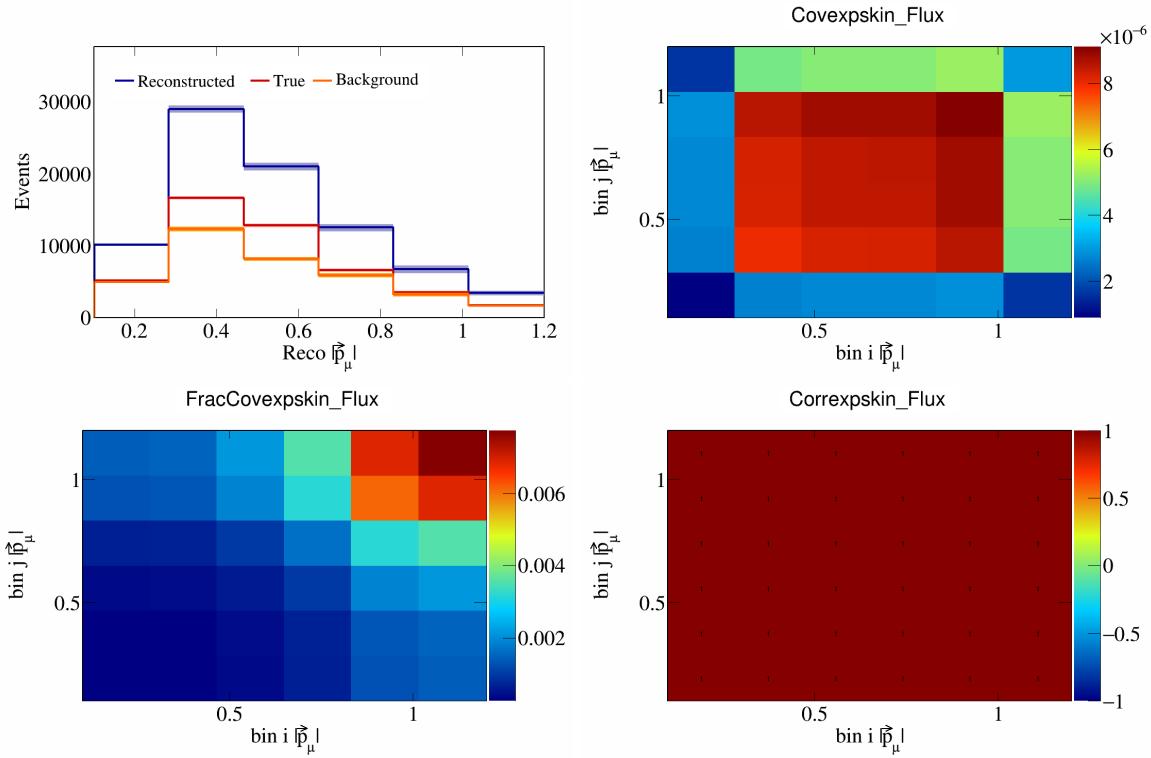


Figure 615: Epskin variations for  $|\vec{p}_\mu|$ .

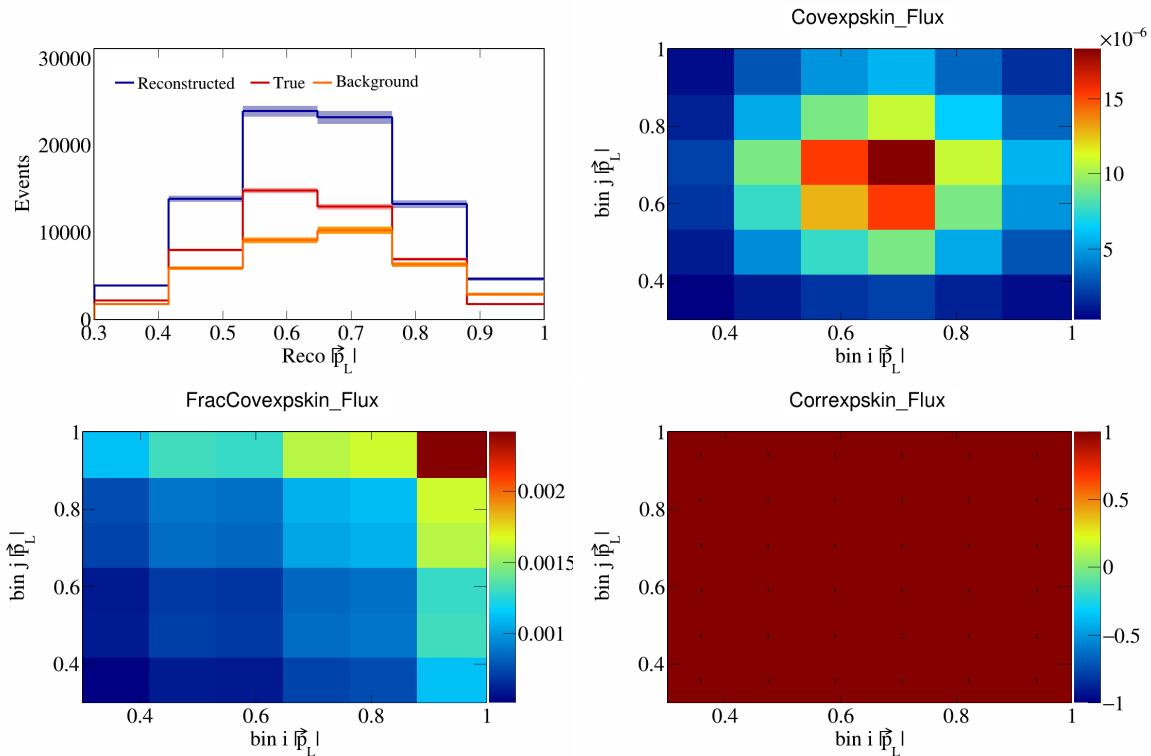


Figure 616: Epskin variations for  $|\vec{p}_L|$ .

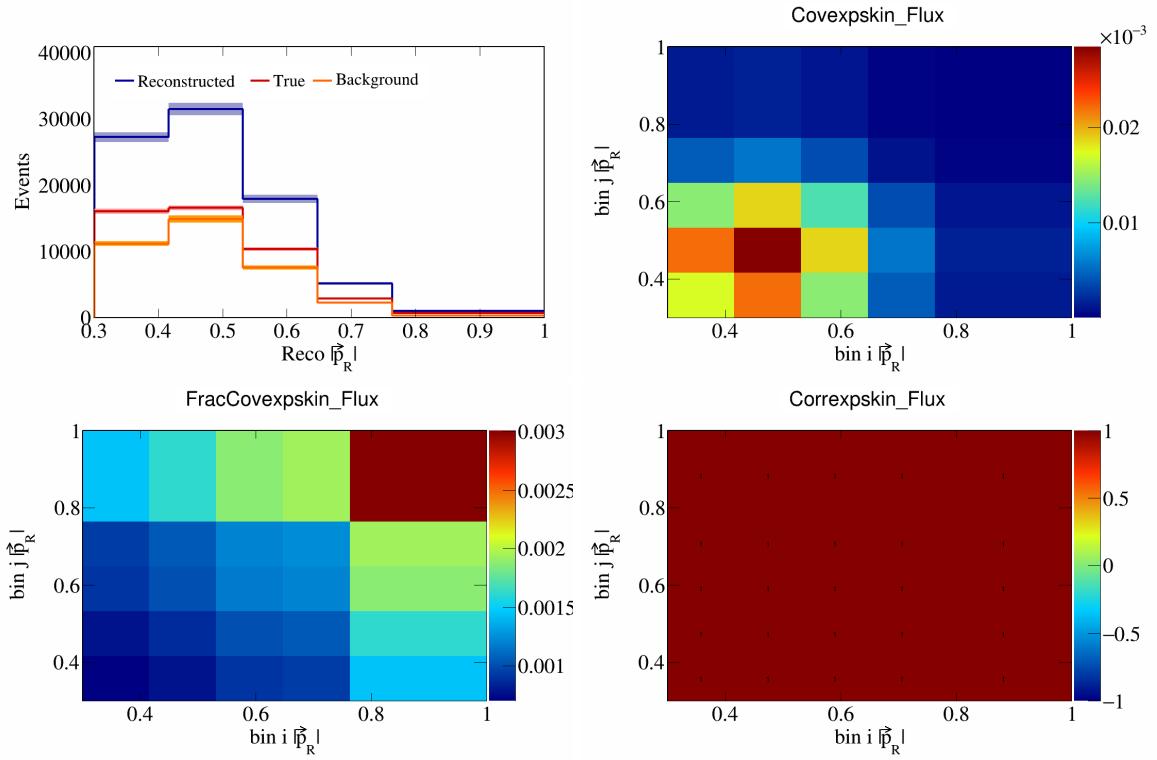


Figure 617: Expskin variations for  $|\vec{p}_R|$ .

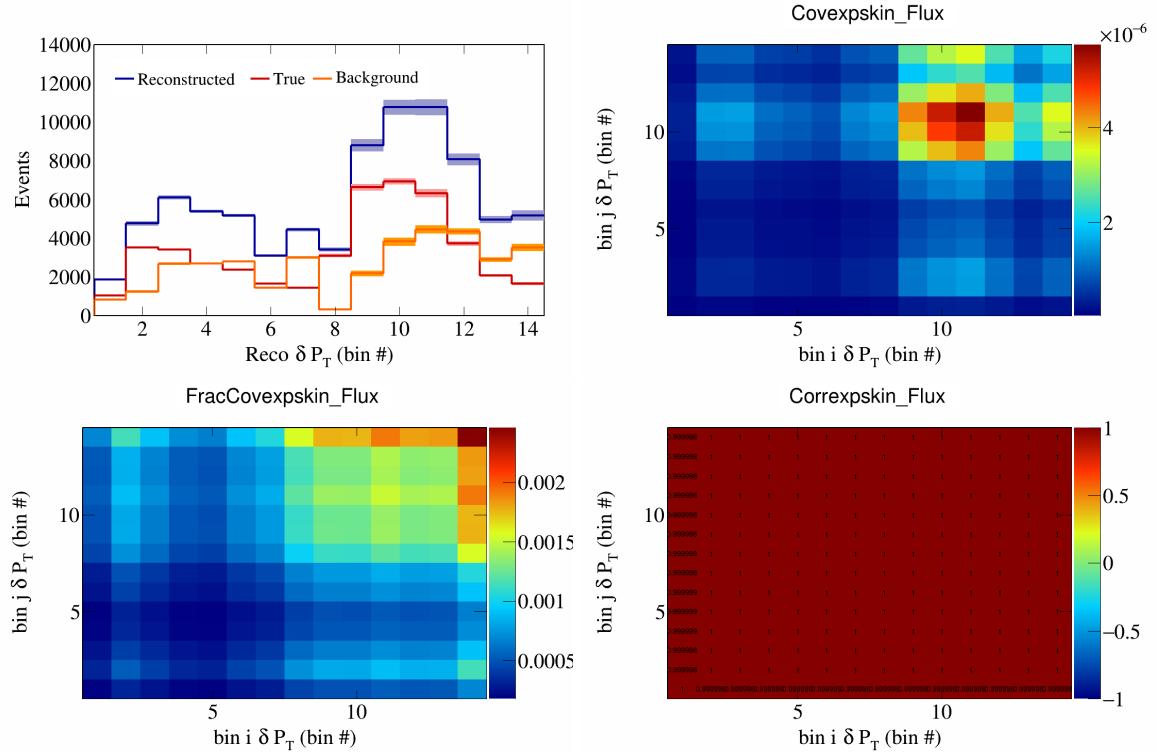


Figure 618: Expskin variations for  $\delta P_T$  in  $\cos(\theta_{\vec{p}_\mu})$ .

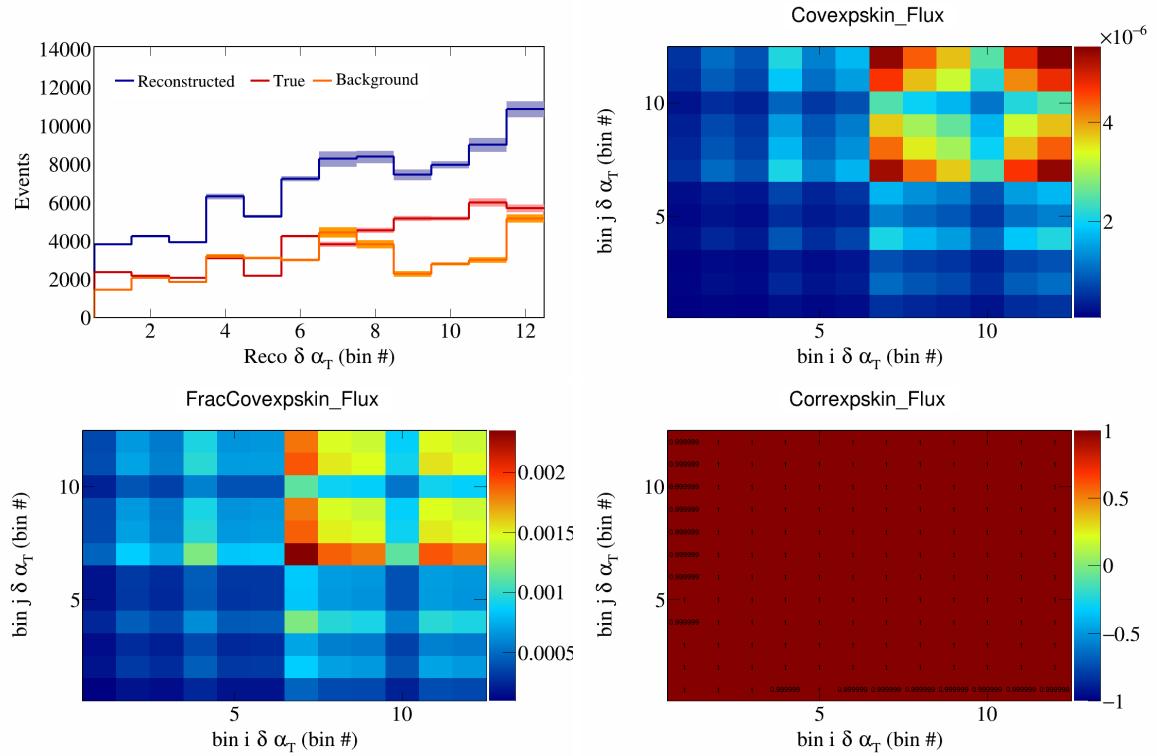


Figure 619: Expskin variations for  $\delta\alpha_T$  in  $\cos(\theta_{\vec{p}_\mu})$ .

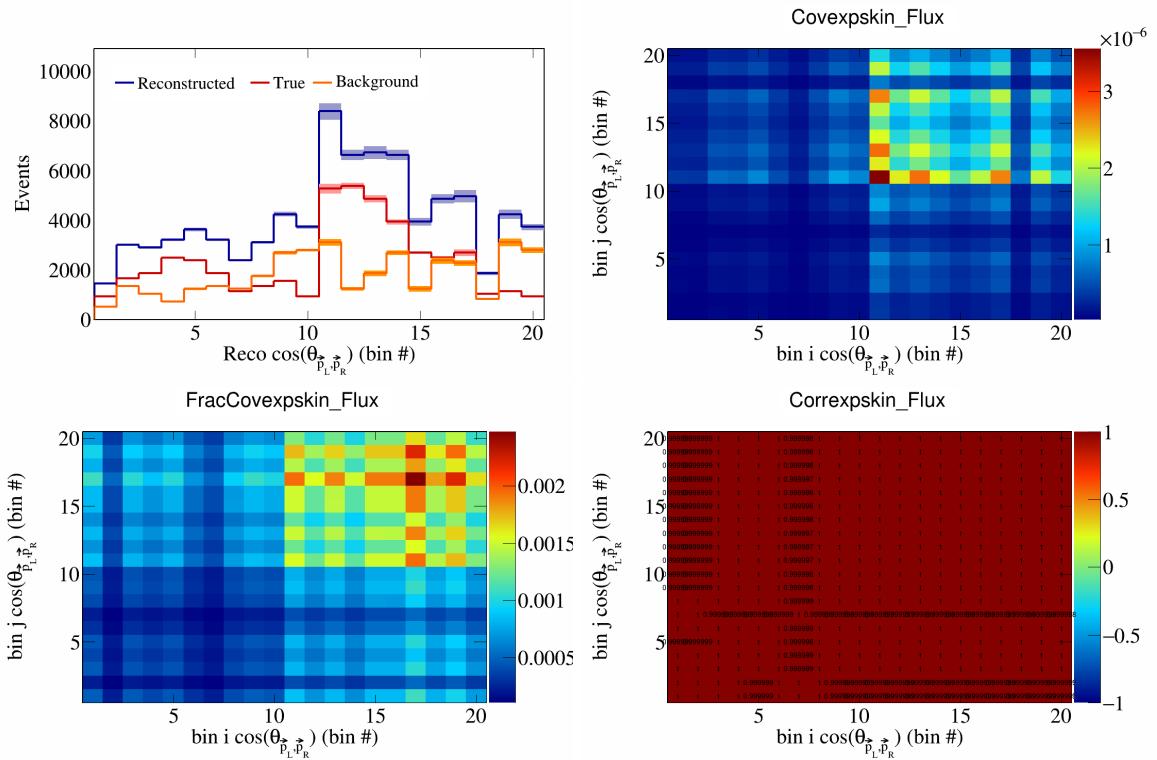


Figure 620: Expskin variations for  $\cos(\theta_{\vec{p}_L, \vec{p}_R})$  in  $\cos(\theta_{\vec{p}_\mu})$ .

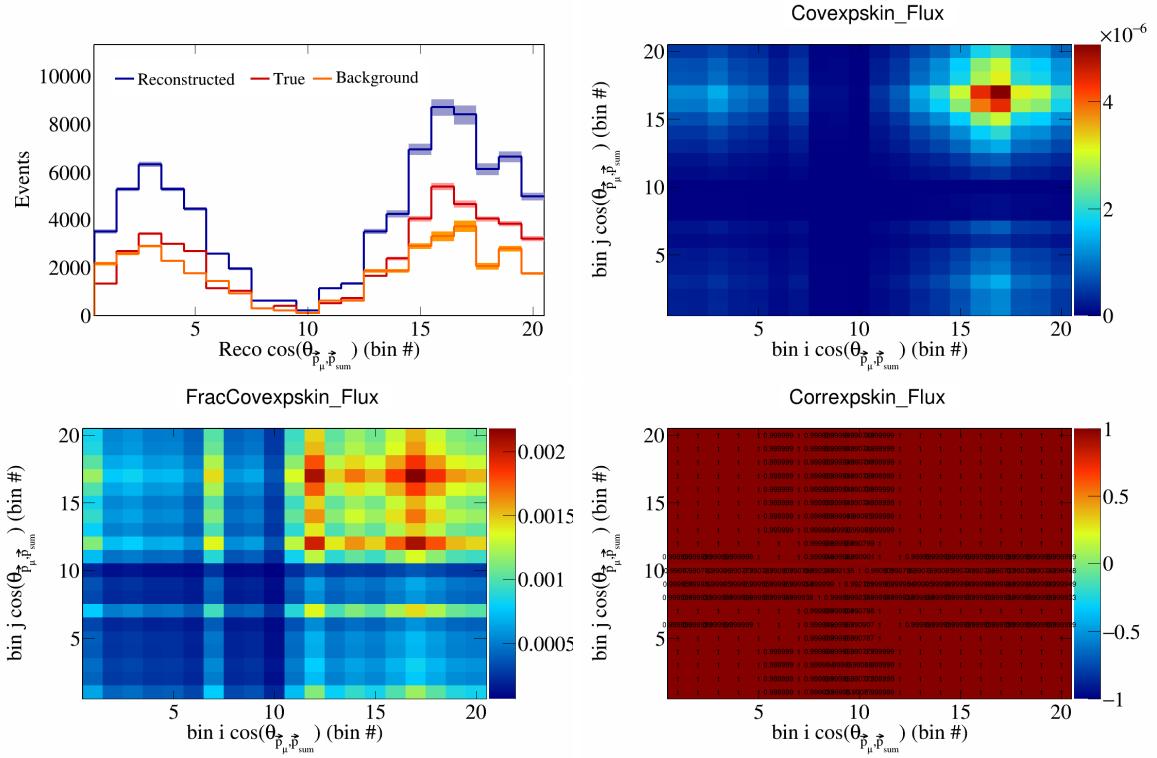


Figure 621: Expskin variations for  $\cos(\theta_{\vec{p}_\mu, \vec{p}_{\text{sum}}})$  in  $\cos(\theta_{\vec{p}_\mu})$ .

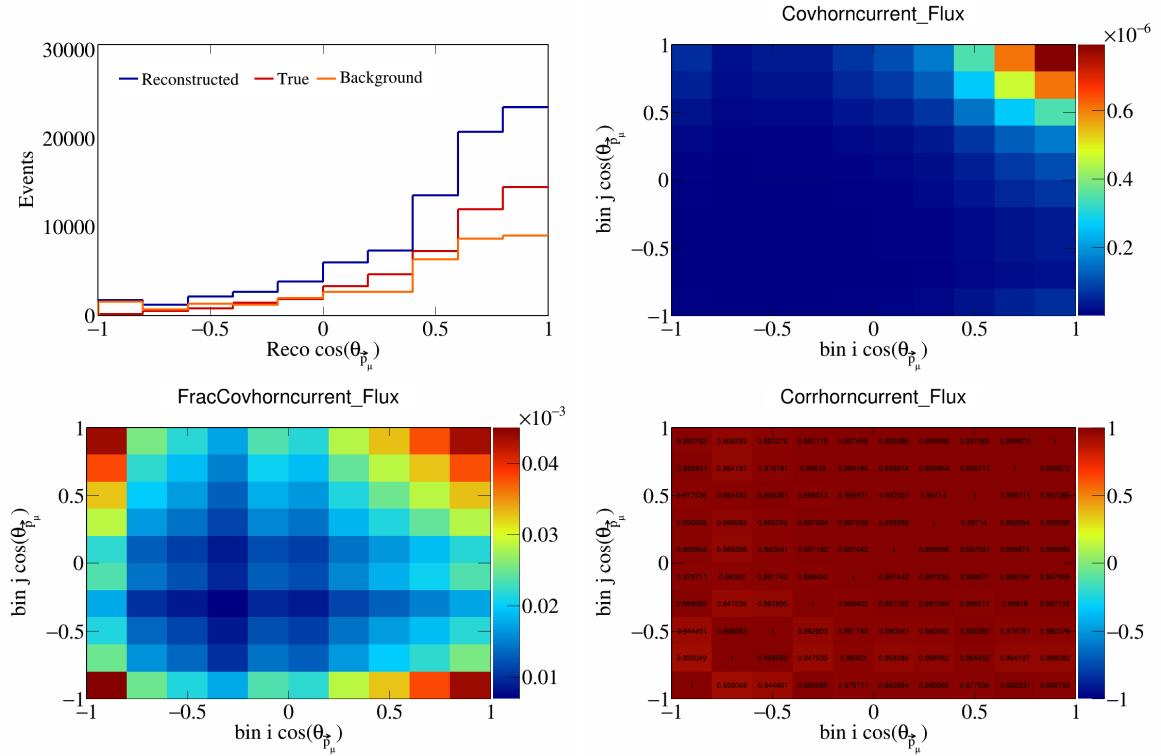


Figure 622: HornCurrent variations for  $\cos(\theta_{\vec{p}_\mu})$ .

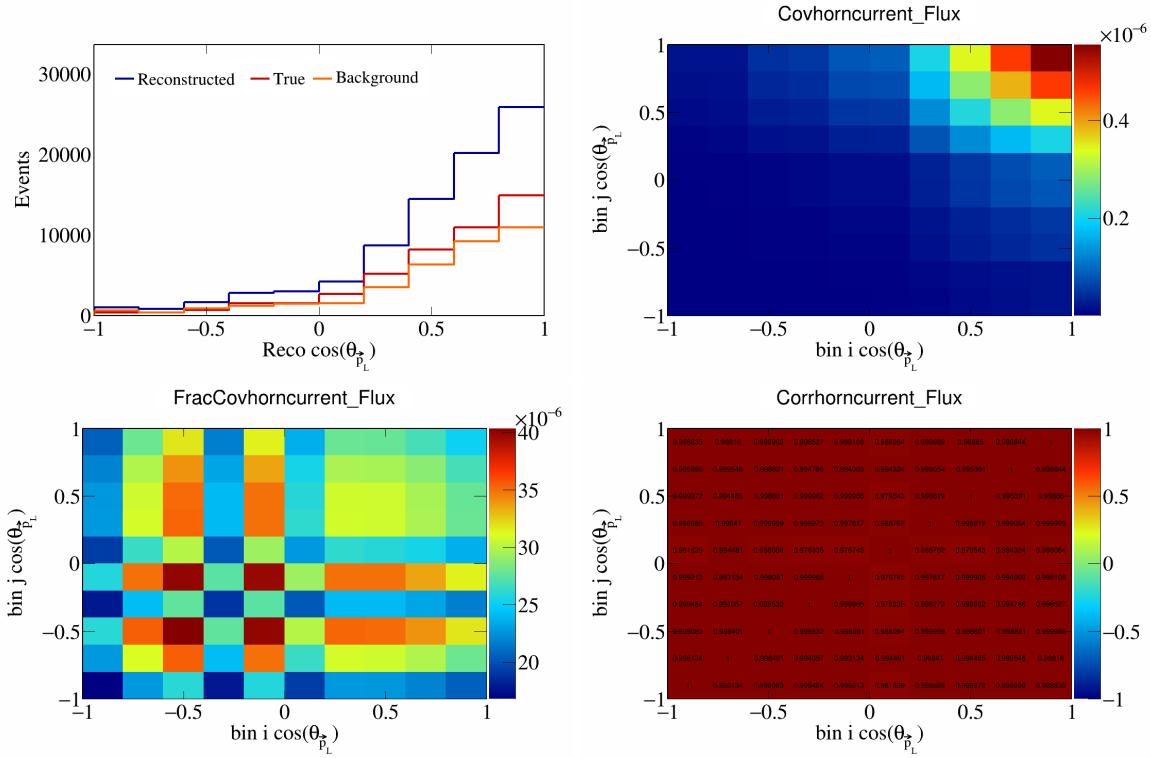


Figure 623: HornCurrent variations for  $\cos(\theta_{\vec{p}_L})$ .

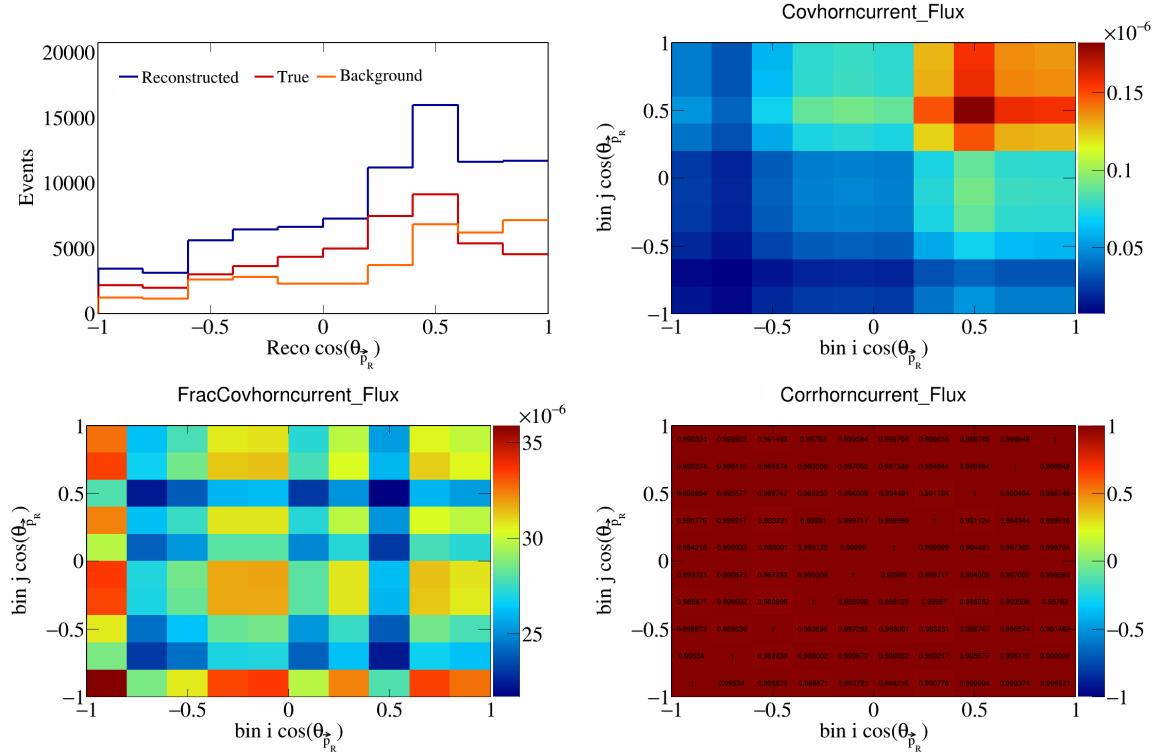


Figure 624: HornCurrent variations for  $\cos(\theta_{\vec{p}_R})$ .

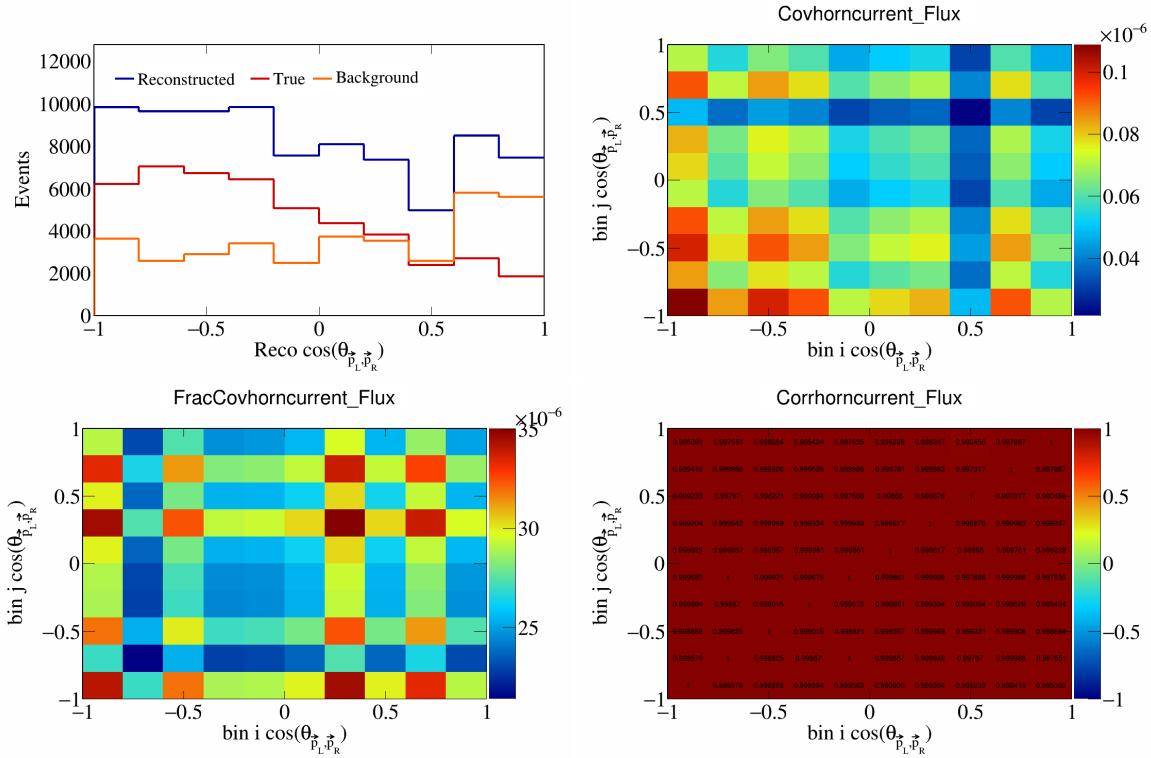


Figure 625: HornCurrent variations for  $\cos(\theta_{\vec{p}_L, \vec{p}_R})$ .

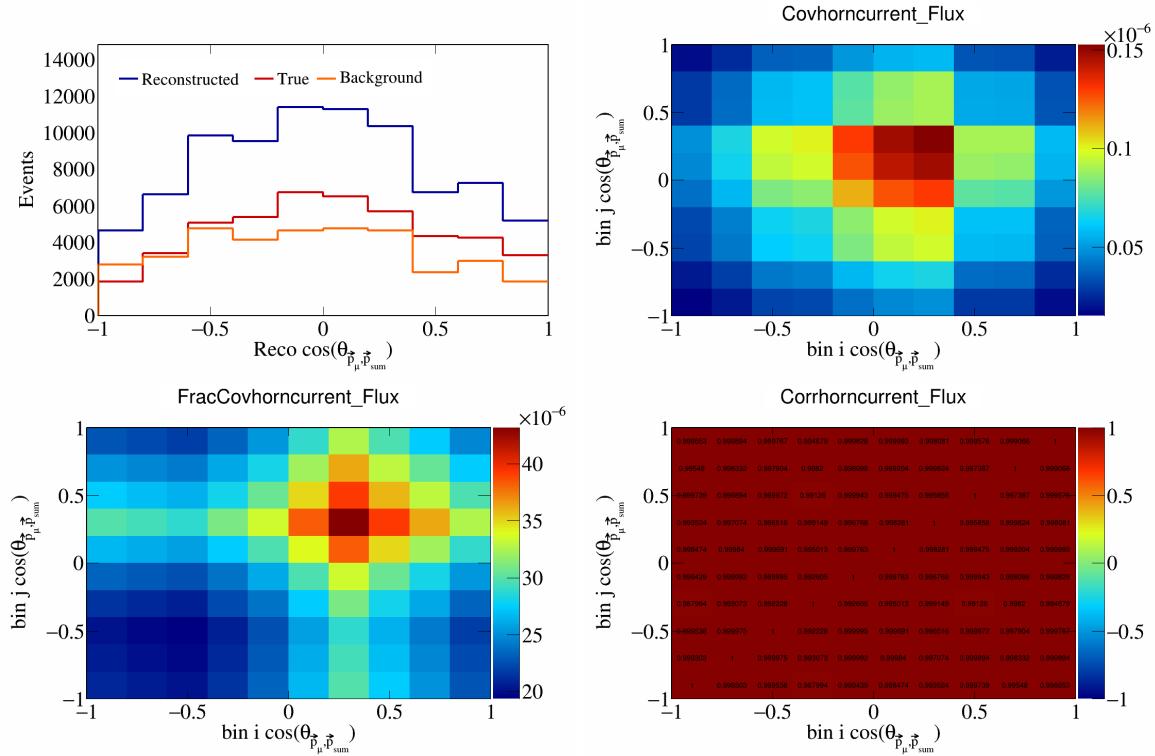


Figure 626: HornCurrent variations for  $\cos(\theta_{\vec{p}_\mu, \vec{p}_{\text{sum}}})$ .

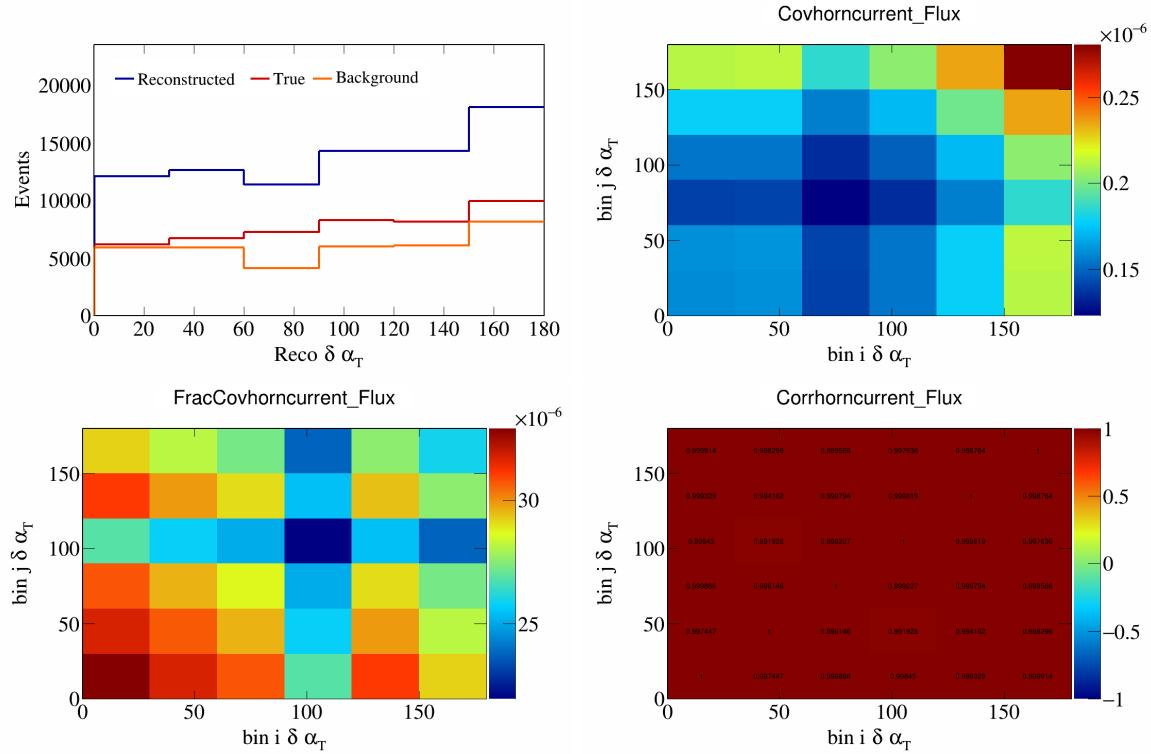


Figure 627: HornCurrent variations for  $\delta\alpha_T$ .

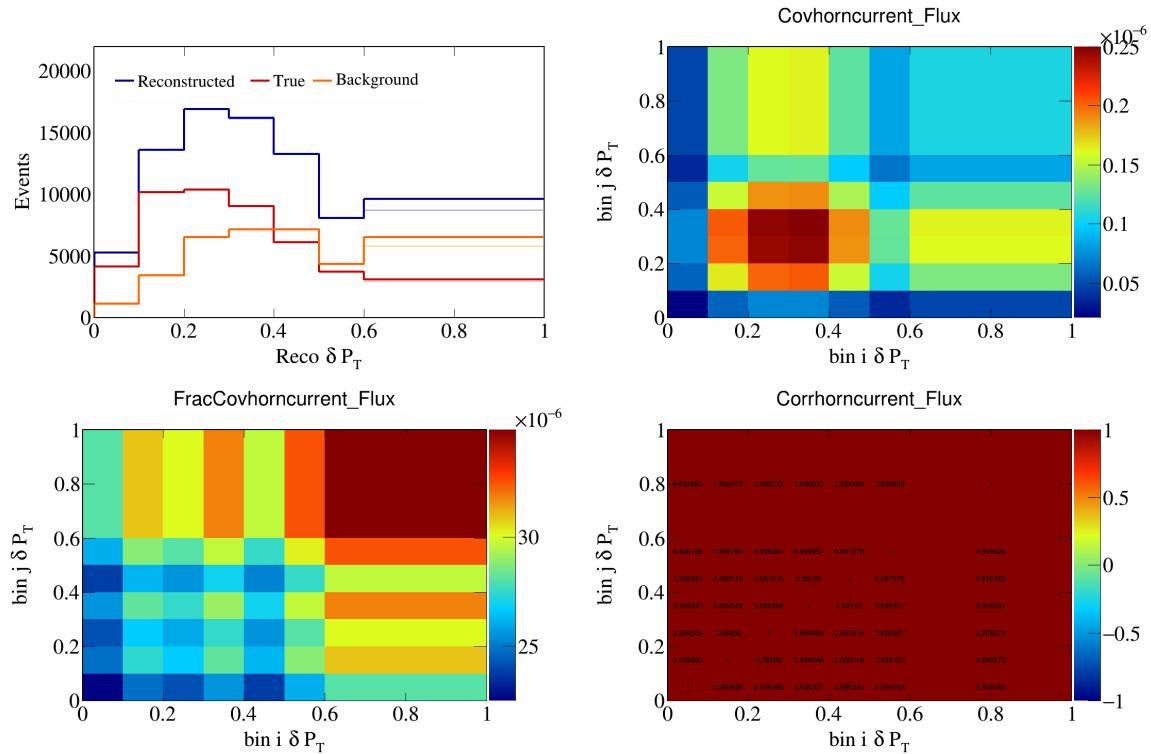


Figure 628: HornCurrent variations for  $\delta P_T$ .

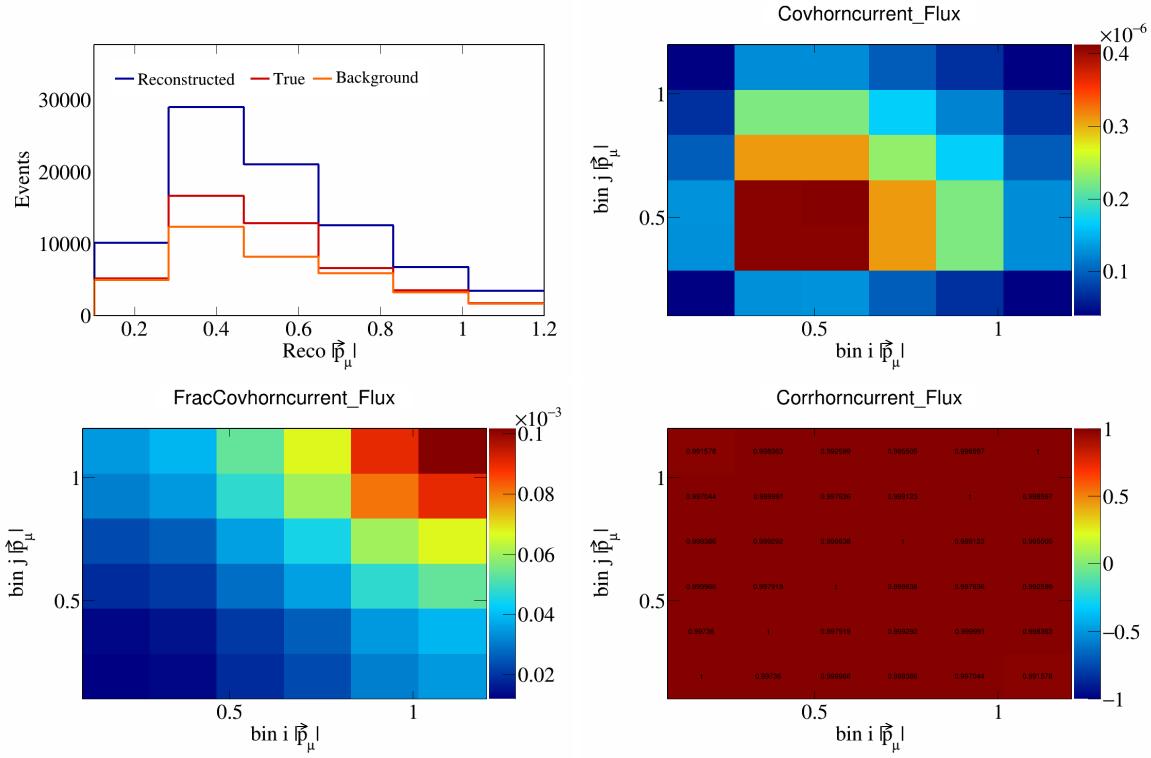


Figure 629: HornCurrent variations for  $|\vec{p}_\mu|$ .

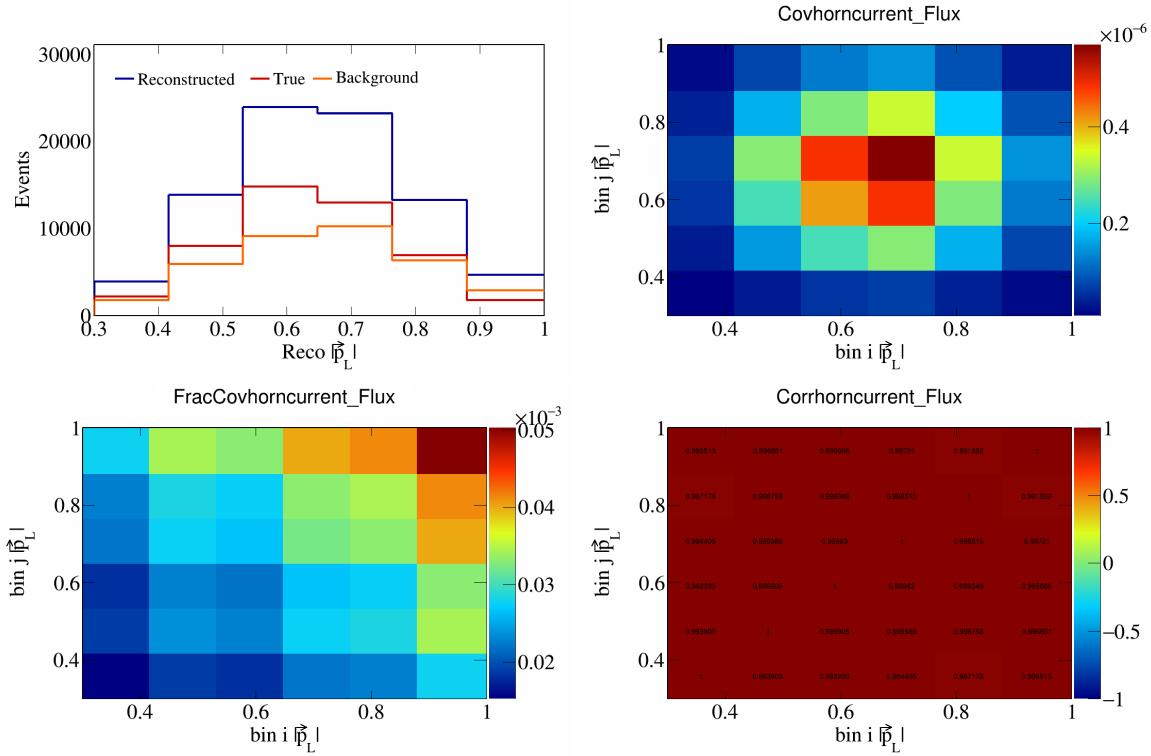


Figure 630: HornCurrent variations for  $|\vec{p}_L|$ .

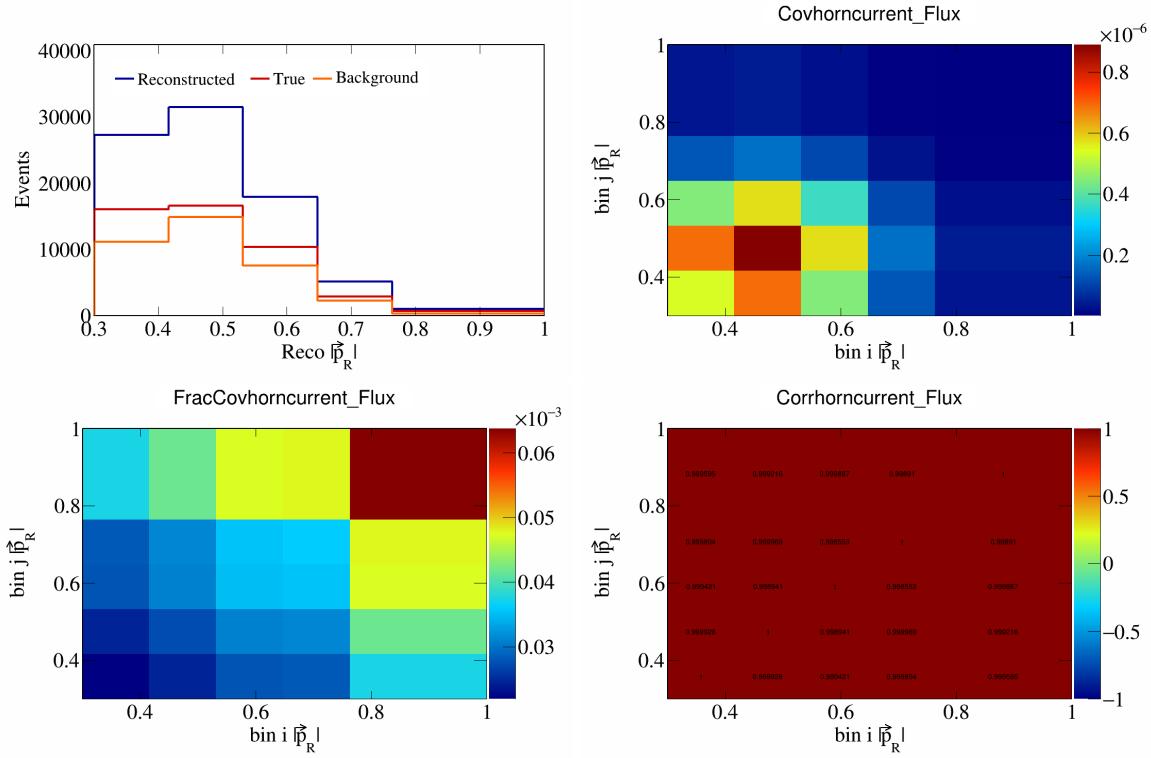


Figure 631: HornCurrent variations for  $|\vec{p}_R|$ .

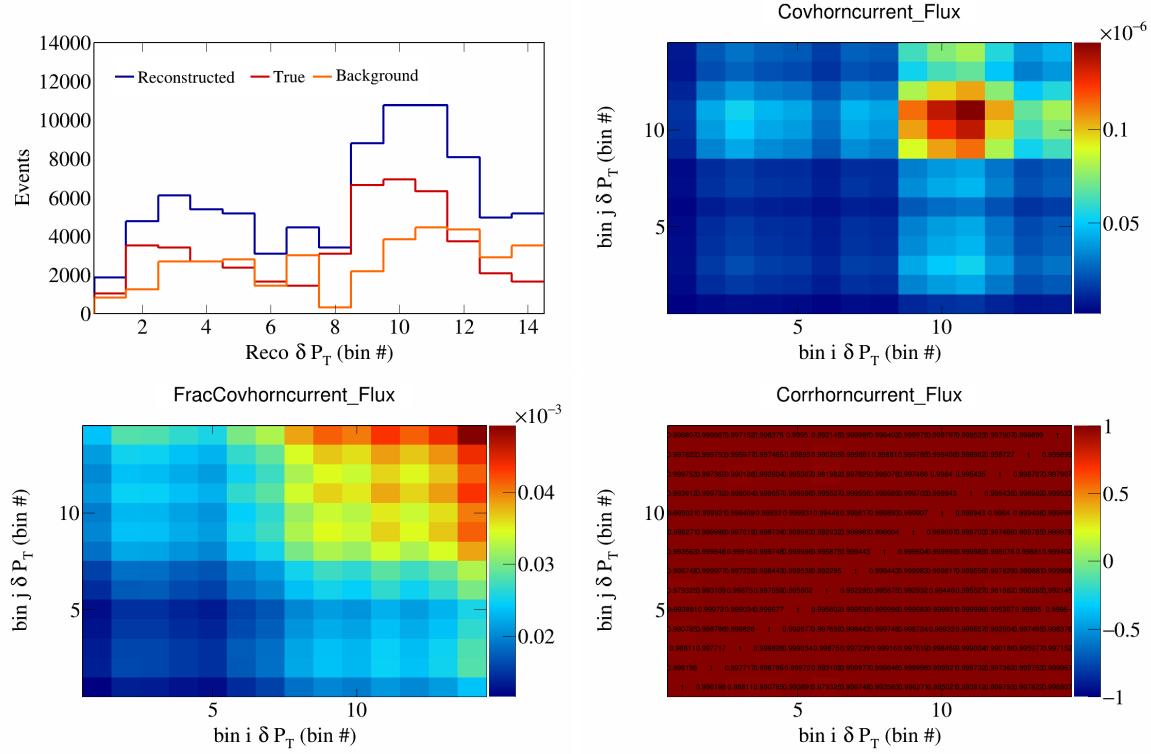


Figure 632: HornCurrent variations for  $\delta P_T$  in  $\cos(\theta_{\vec{p}_\mu})$ .

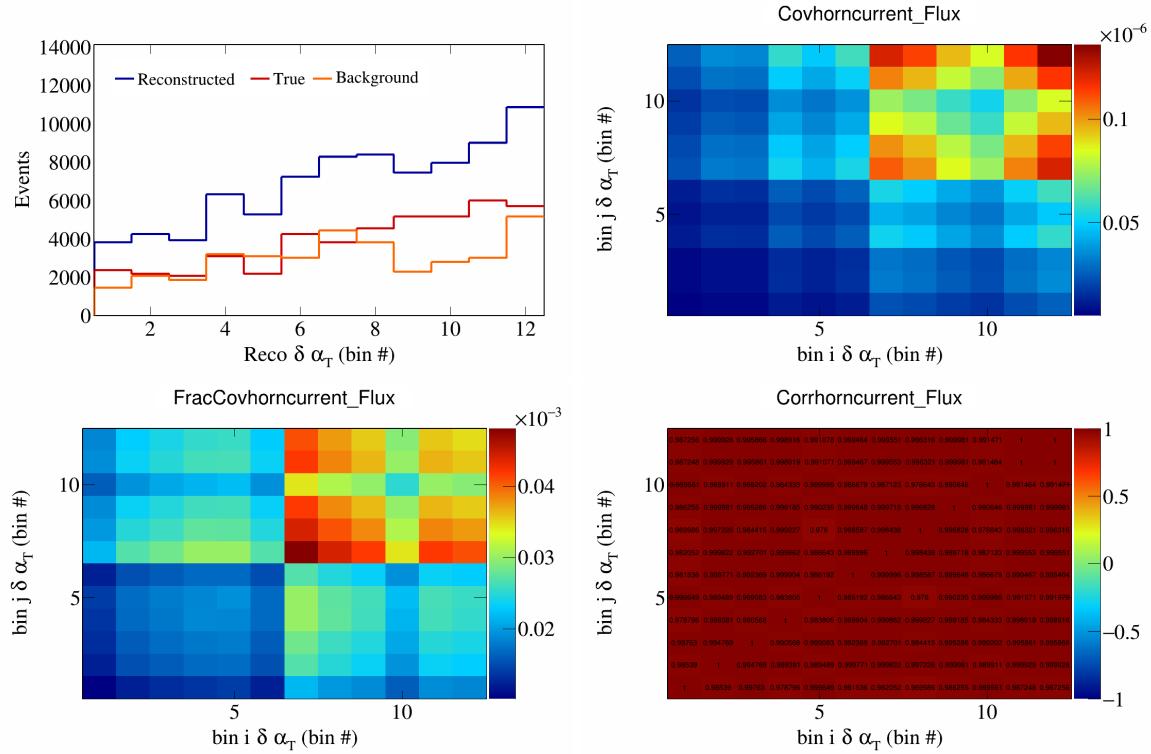


Figure 633: HornCurrent variations for  $\delta\alpha_T$  in  $\cos(\theta_{\vec{p}_\mu})$ .

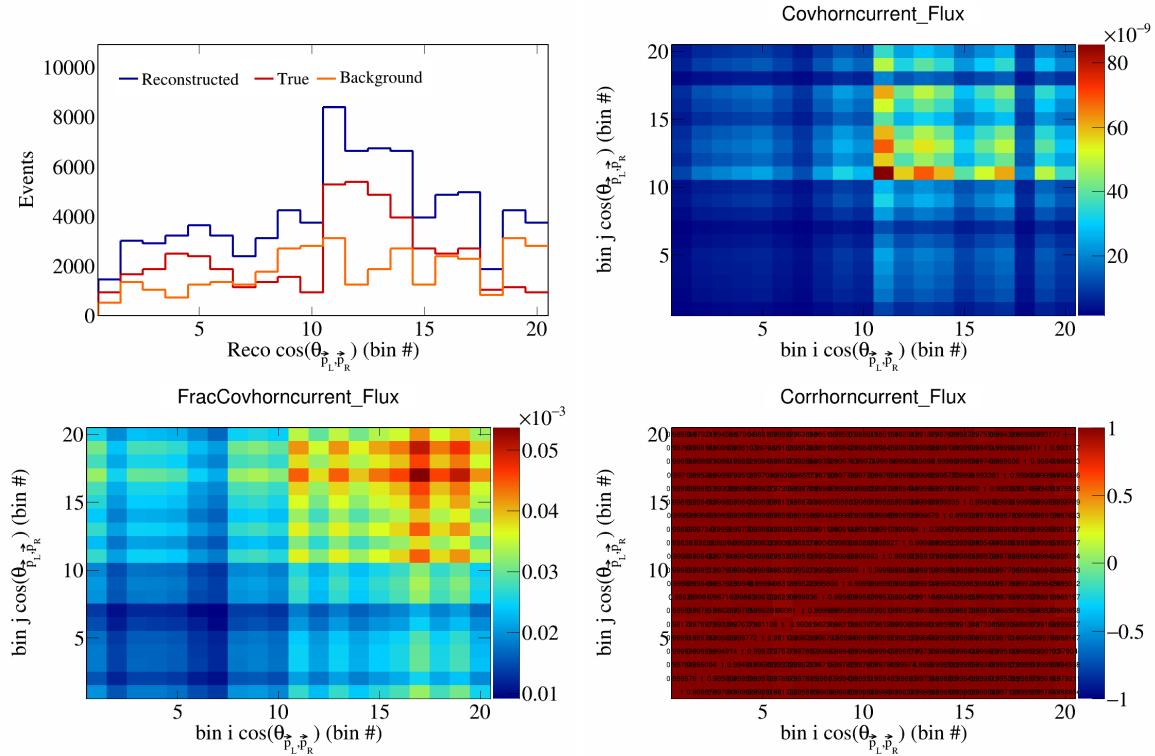


Figure 634: HornCurrent variations for  $\cos(\theta_{\vec{p}_L, \vec{p}_R})$  in  $\cos(\theta_{\vec{p}_\mu})$ .

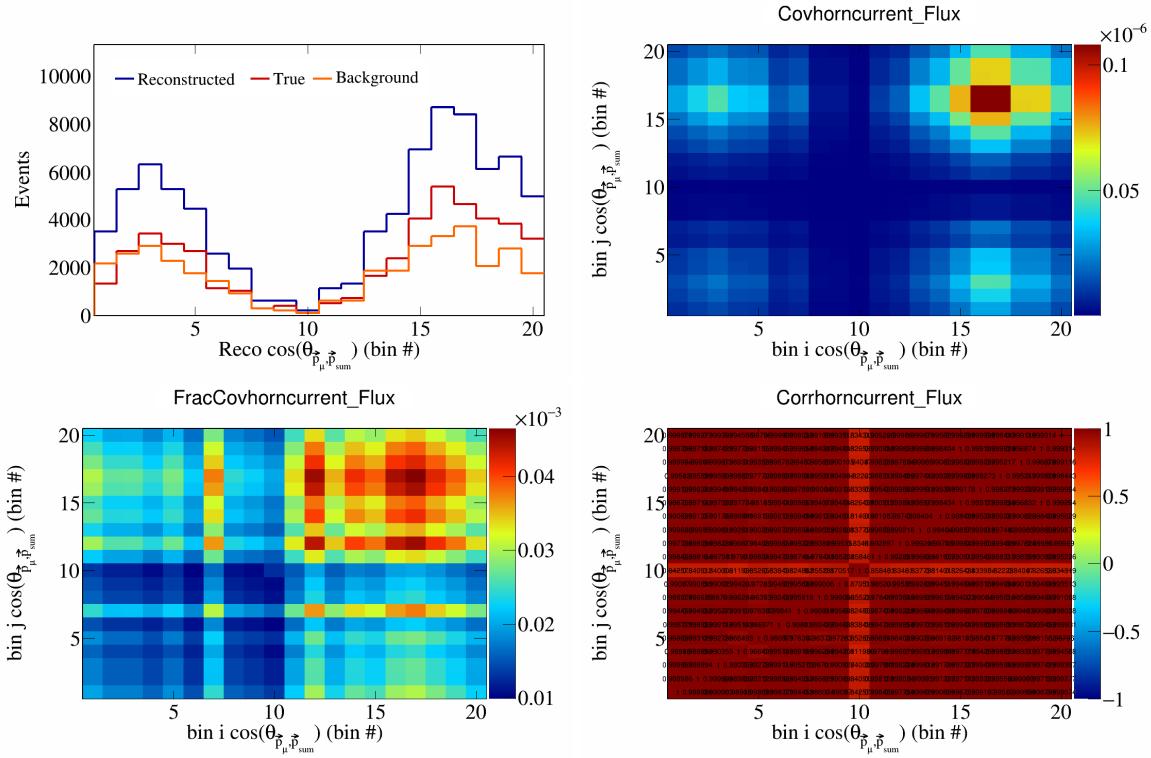


Figure 635: HornCurrent variations for  $\cos(\theta_{\vec{p}_\mu} \cdot \vec{p}_{\text{sum}})$  in  $\cos(\theta_{\vec{p}_\mu})$ .

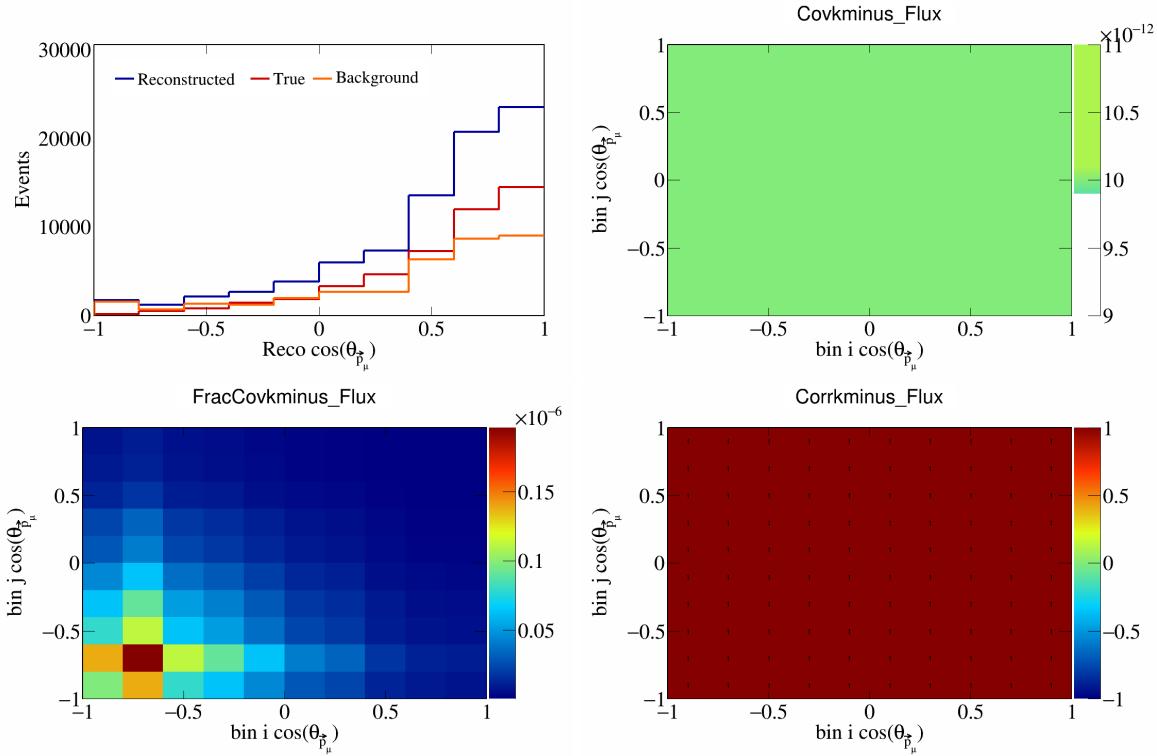


Figure 636: KMinus variations for  $\cos(\theta_{\vec{p}_\mu})$ .

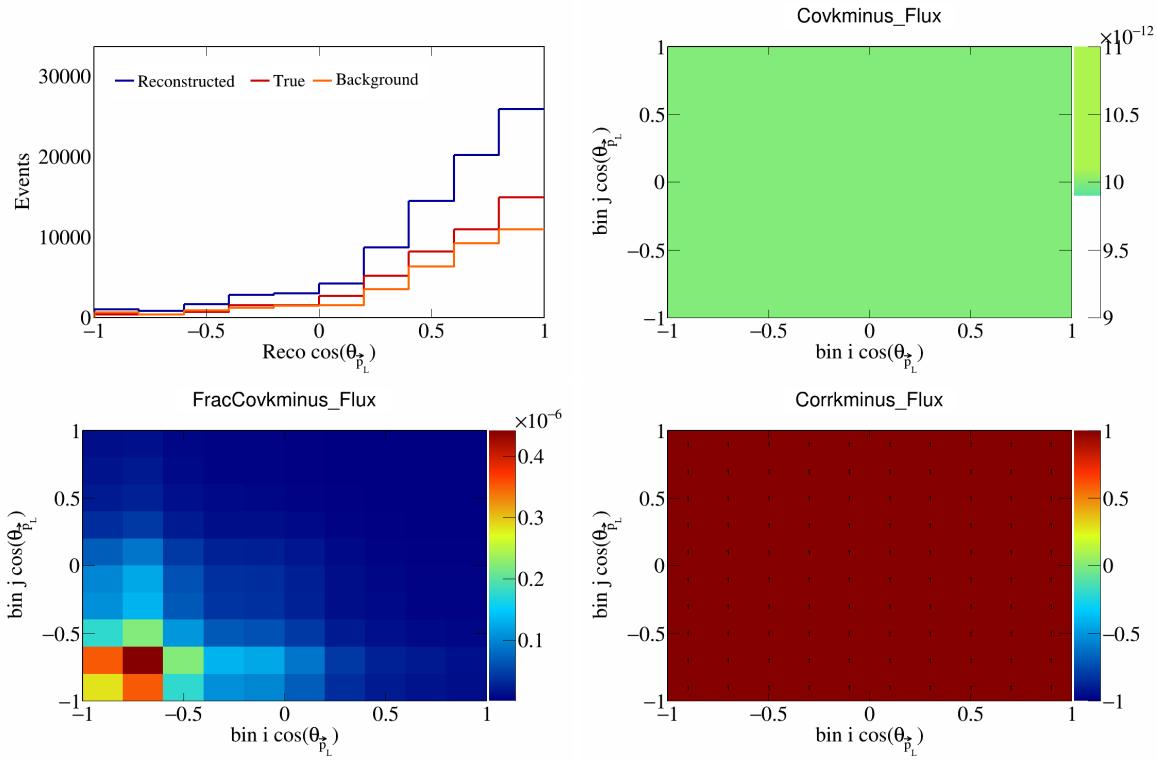


Figure 637: KMinus variations for  $\cos(\theta_{\vec{p}_L})$ .

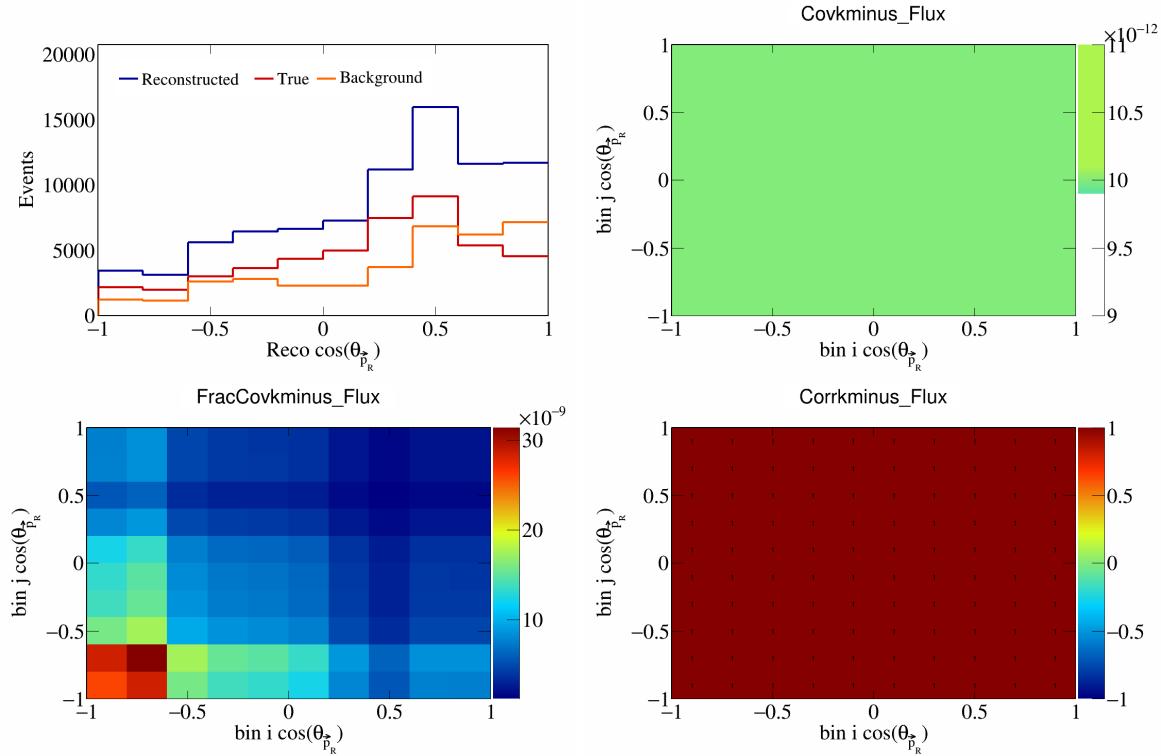


Figure 638: KMinus variations for  $\cos(\theta_{\vec{p}_R})$ .

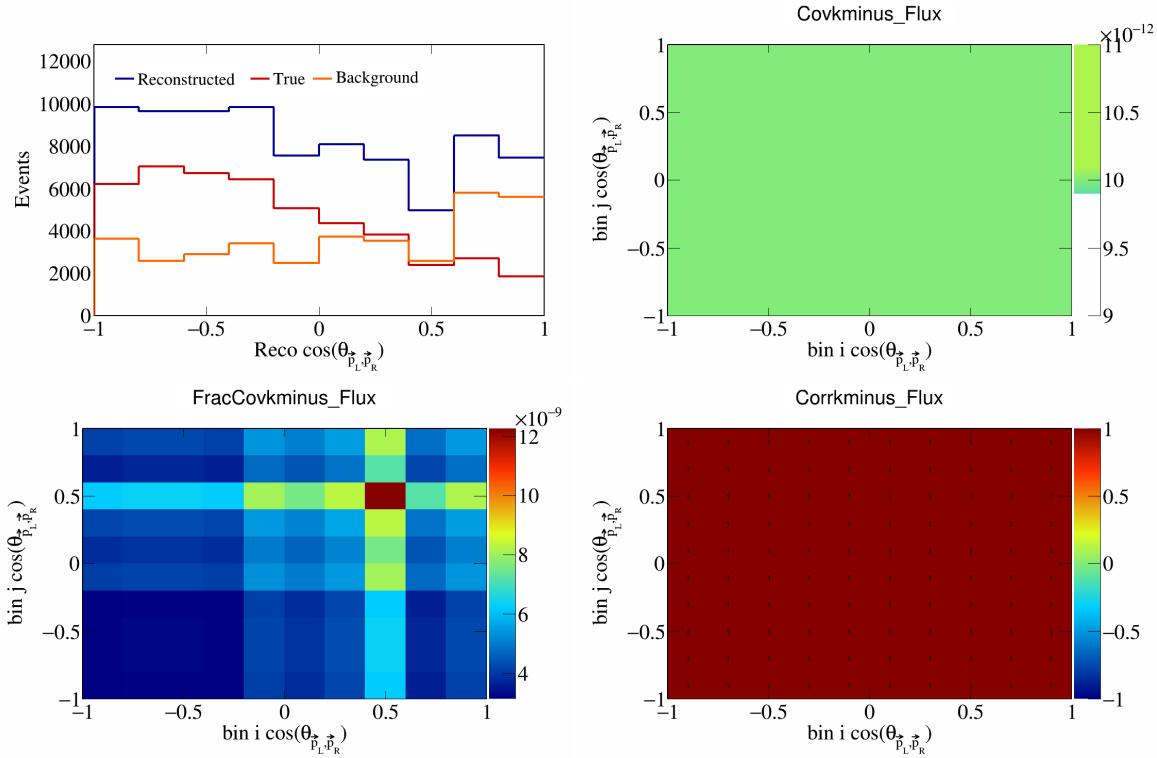


Figure 639: KMinus variations for  $\cos(\theta_{\vec{p}_L, \vec{p}_R})$ .

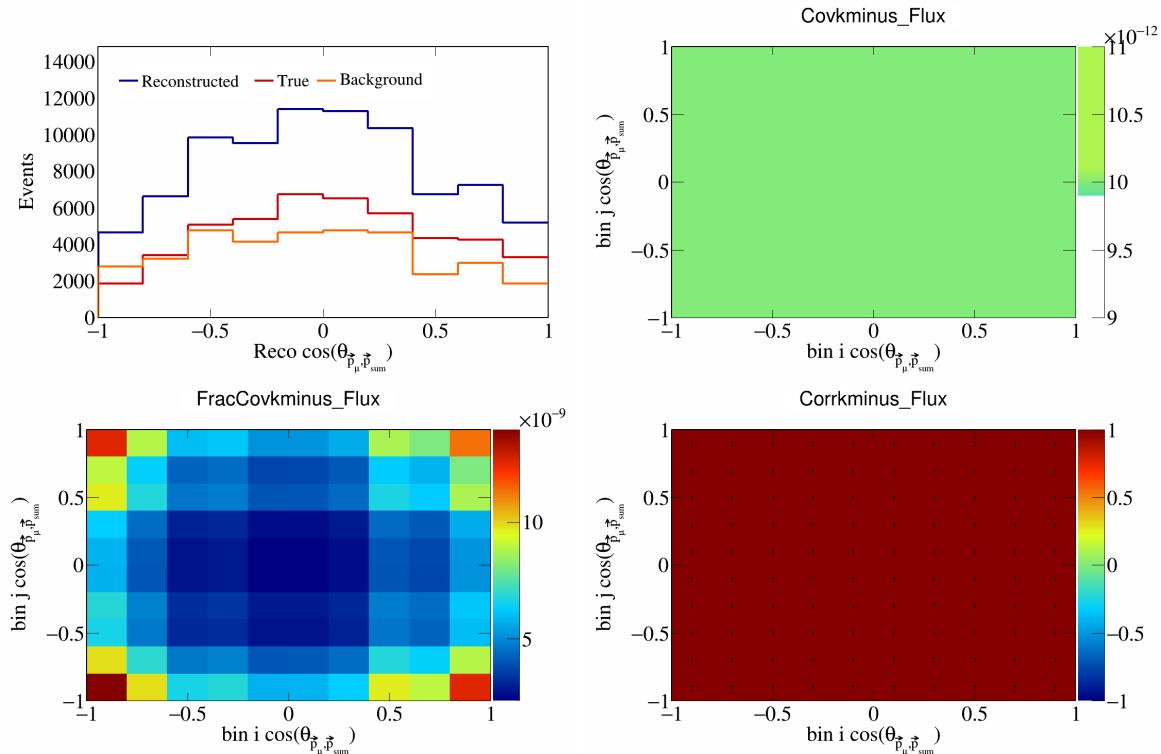


Figure 640: KMinus variations for  $\cos(\theta_{\vec{p}_\mu, \vec{p}_{\text{sum}}})$ .

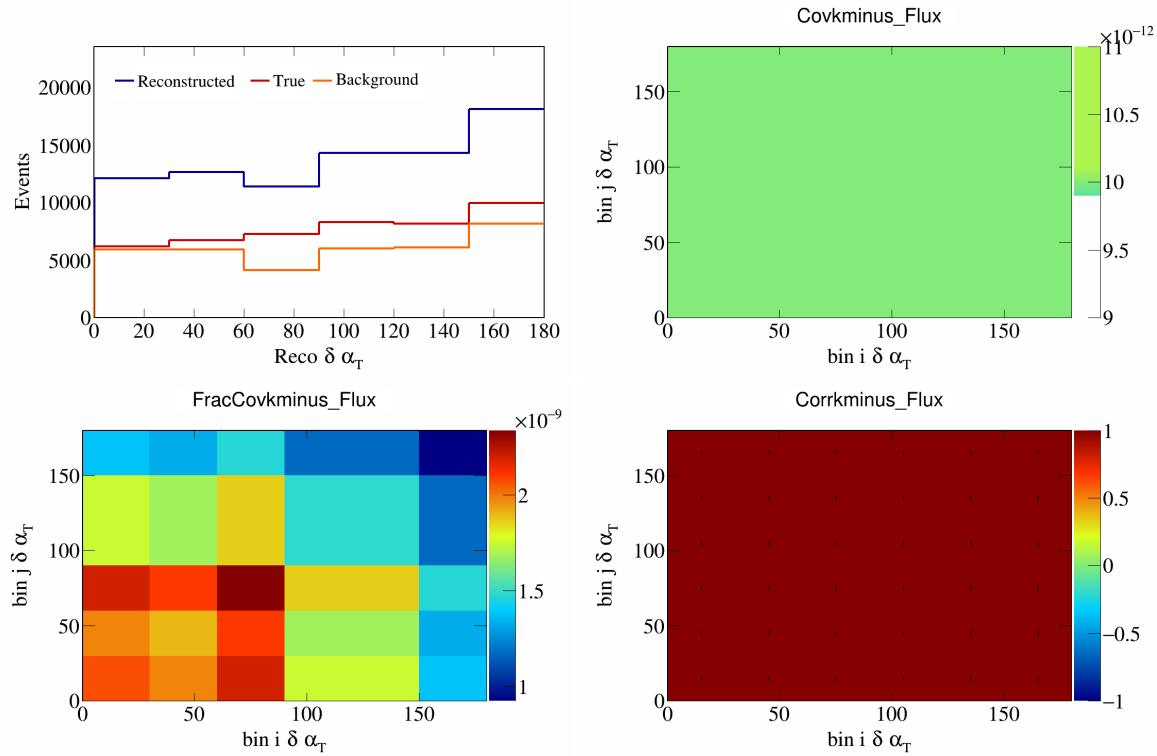


Figure 641: KMinus variations for  $\delta\alpha_T$ .

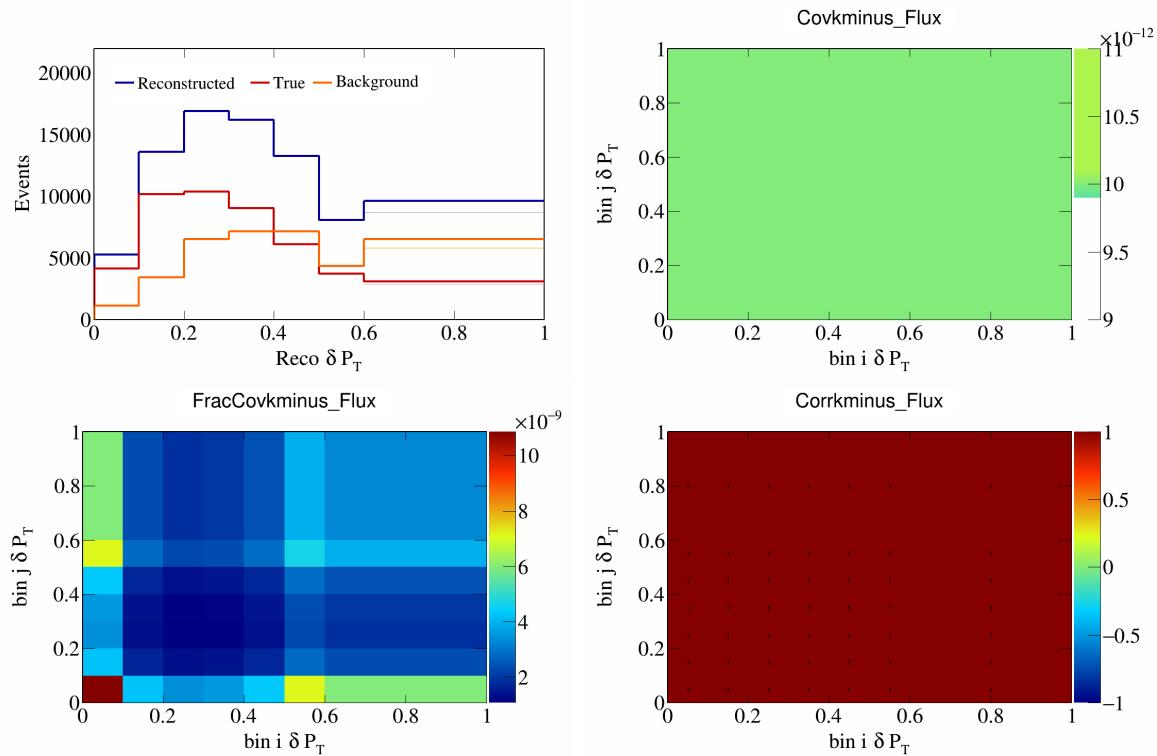


Figure 642: KMinus variations for  $\delta P_T$ .

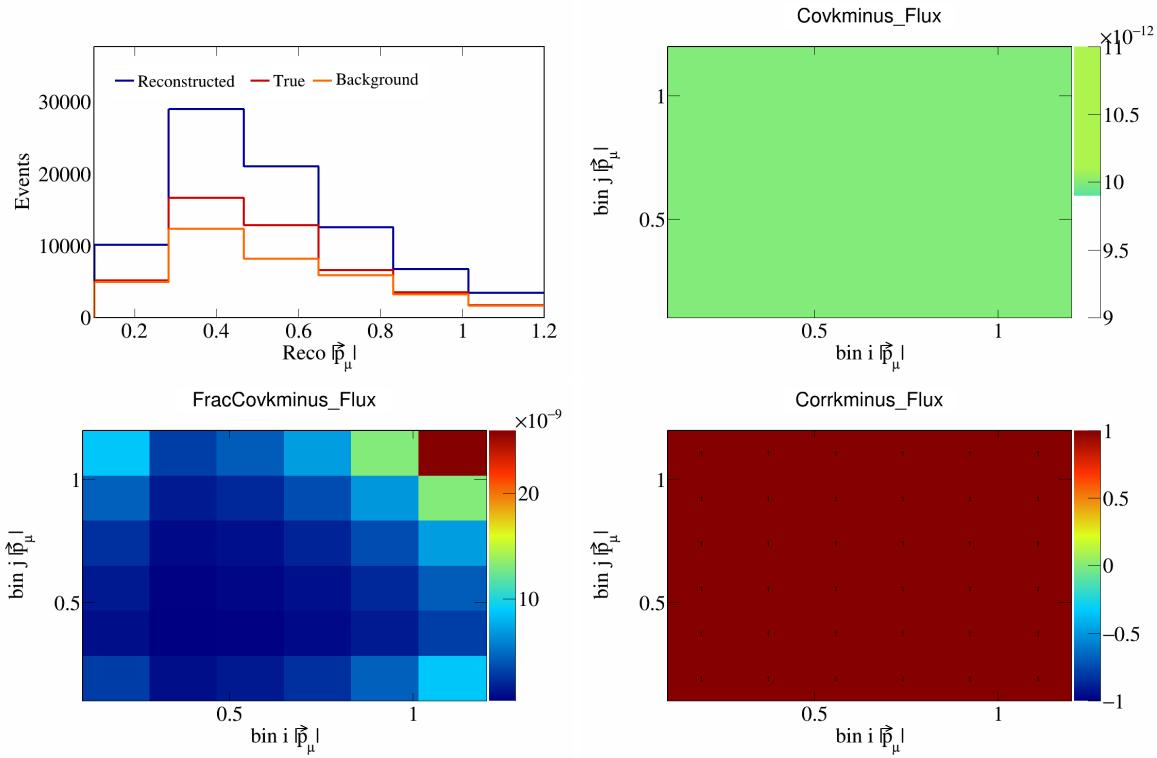


Figure 643: KMinus variations for  $|\vec{p}_\mu|$ .

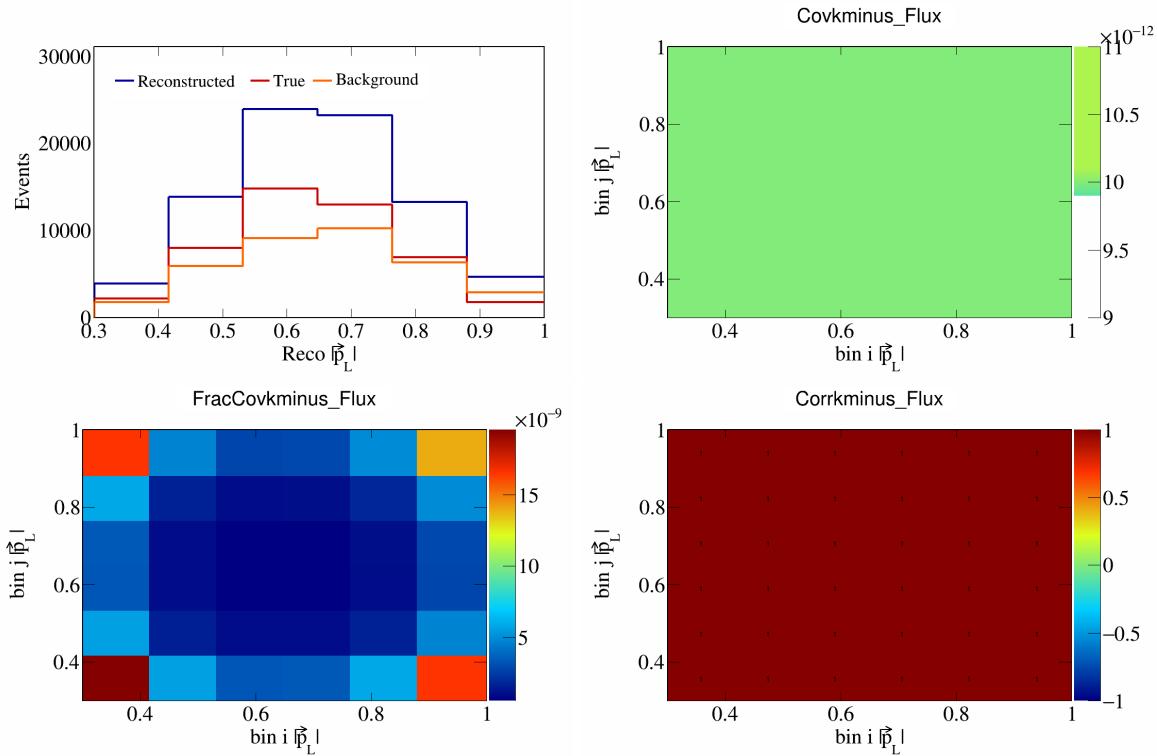


Figure 644: KMinus variations for  $|\vec{p}_L|$ .

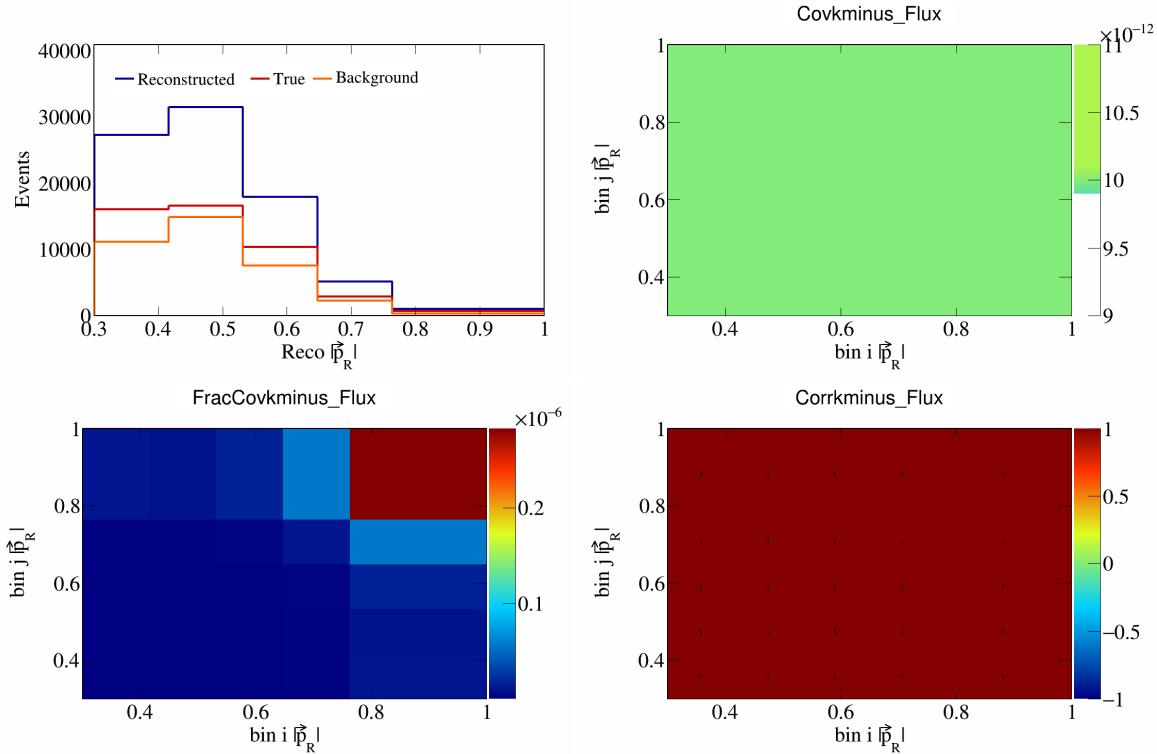


Figure 645: KMinus variations for  $|\vec{p}_R|$ .

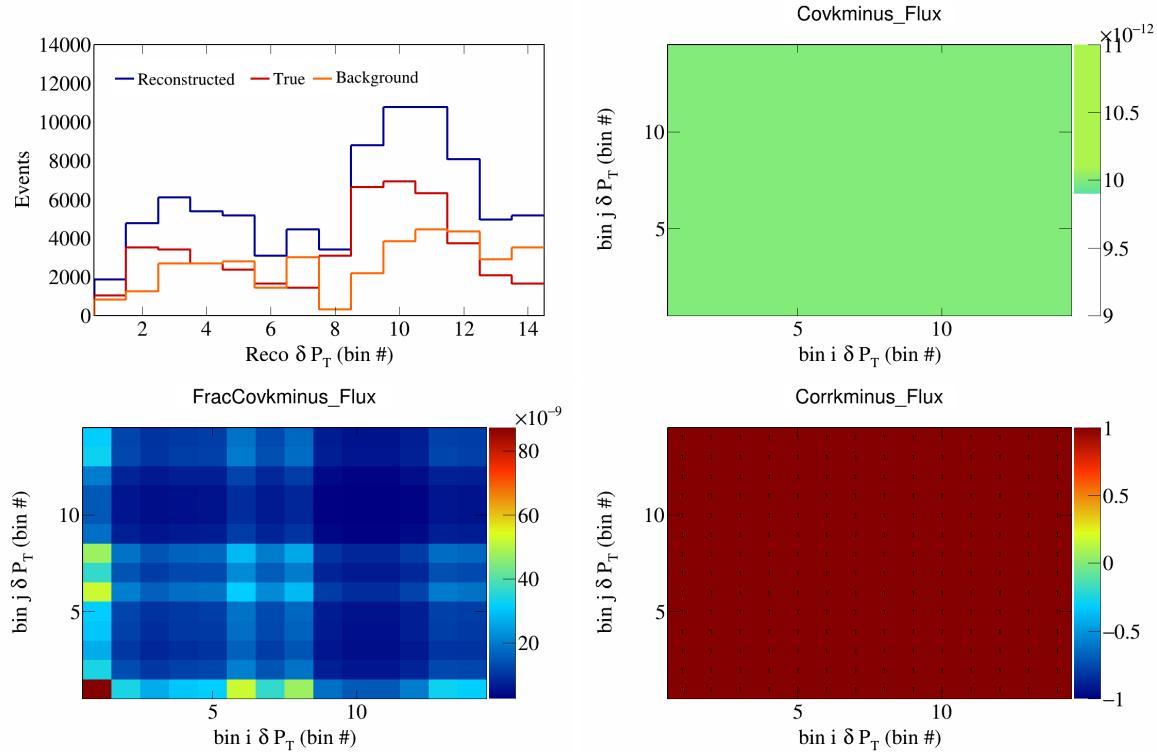


Figure 646: KMinus variations for  $\delta P_T$  in  $\cos(\theta_{\vec{p}_\mu})$ .

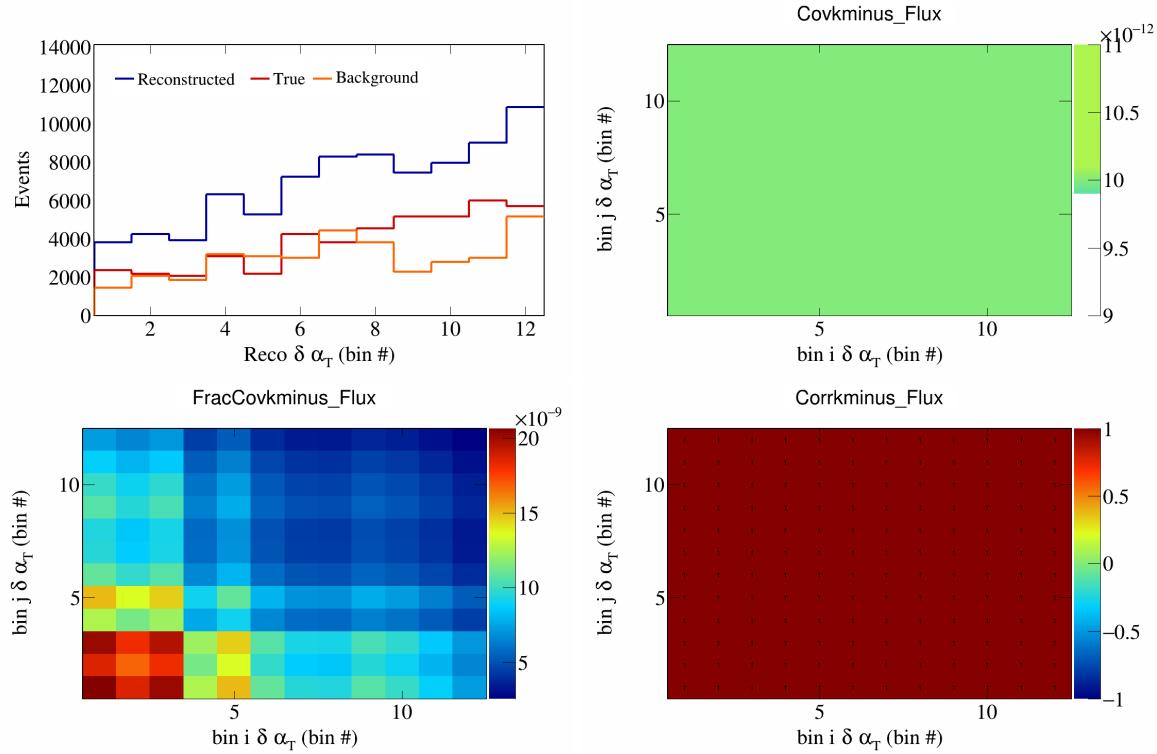


Figure 647: KMinus variations for  $\delta\alpha_T$  in  $\cos(\theta_{\vec{p}_\mu})$ .

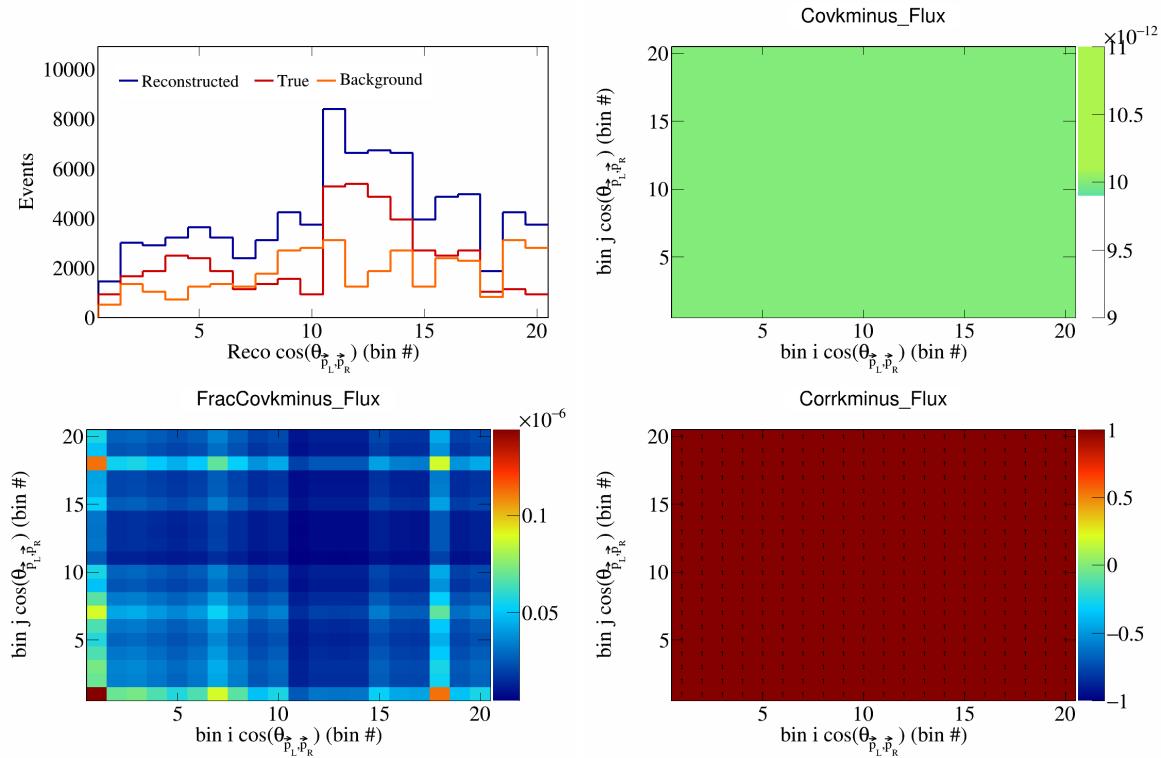


Figure 648: KMinus variations for  $\cos(\theta_{\vec{p}_L, \vec{p}_R})$  in  $\cos(\theta_{\vec{p}_\mu})$ .

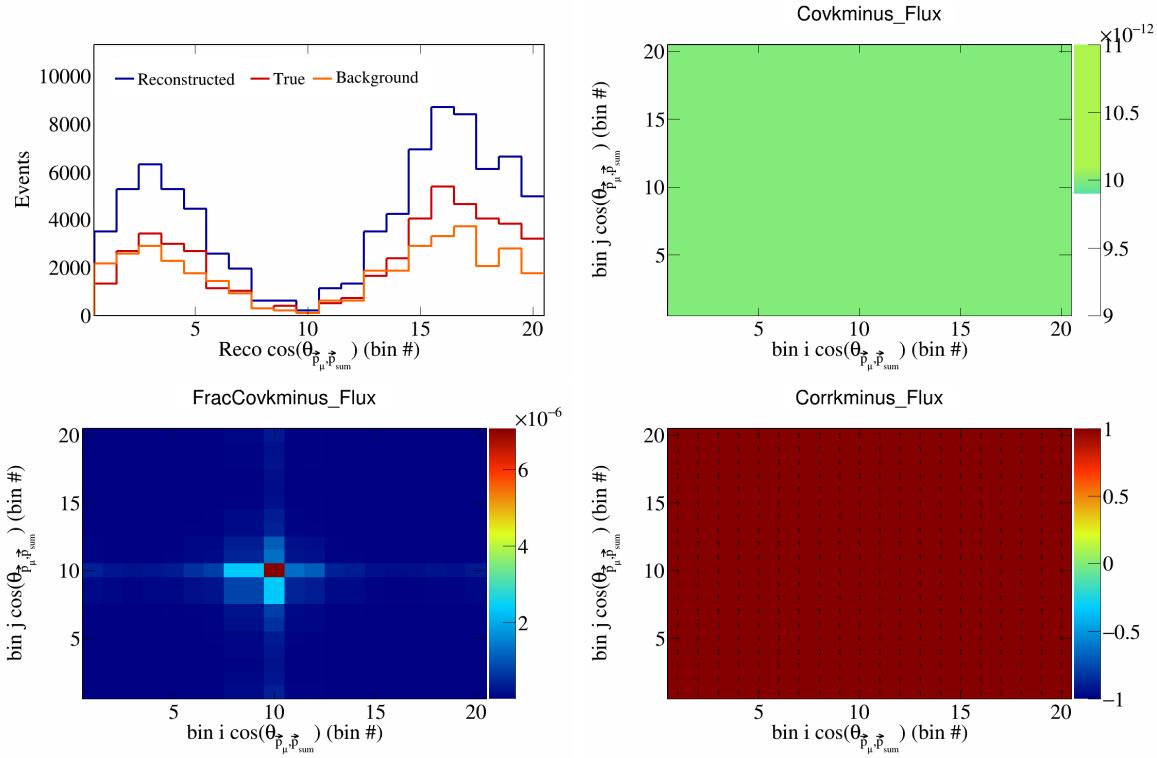


Figure 649: KMinus variations for  $\cos(\theta_{\vec{p}_\mu^*, \vec{p}_{\text{sum}}})$  in  $\cos(\theta_{\vec{p}_\mu})$ .

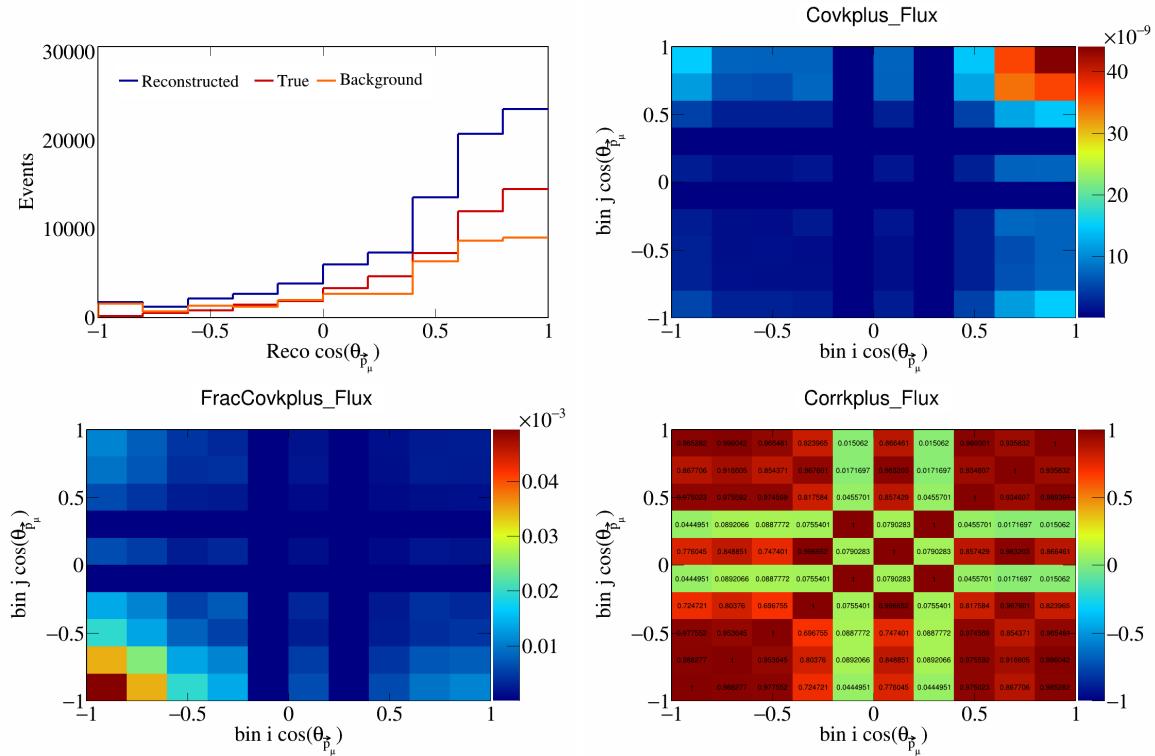


Figure 650: KPlus variations for  $\cos(\theta_{\vec{p}_\mu^*})$ .

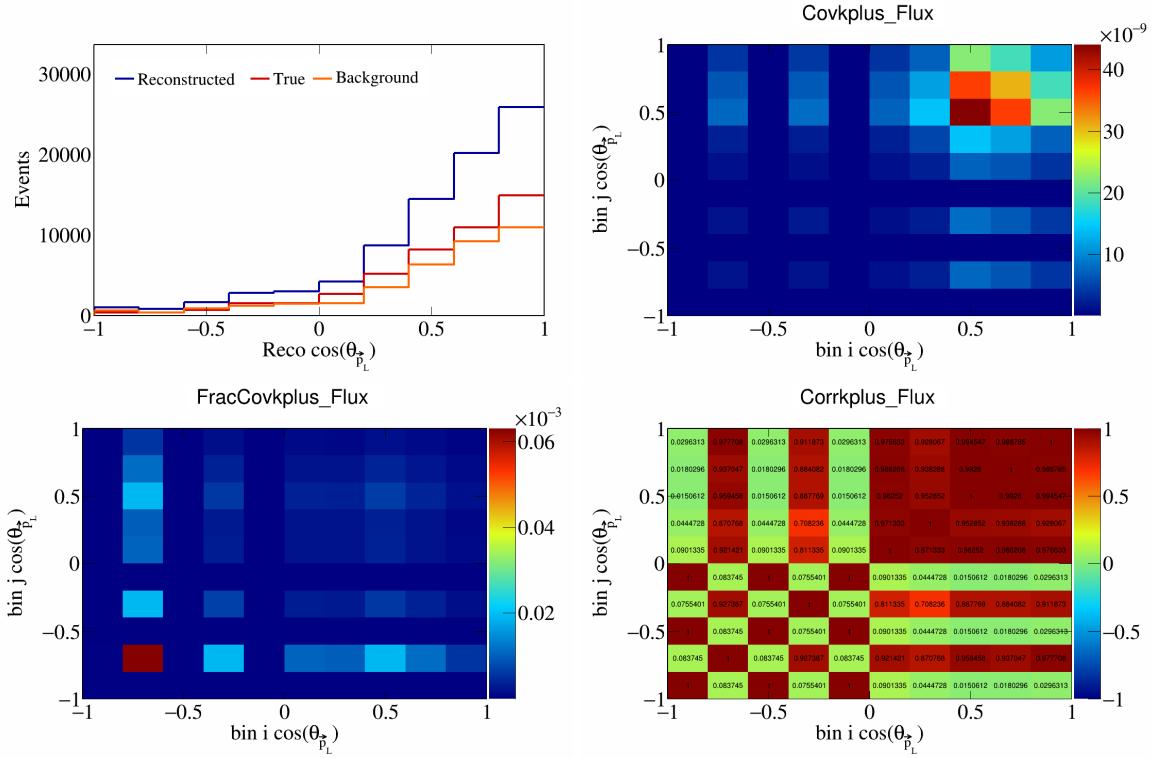


Figure 651: KPlus variations for  $\cos(\theta_{\vec{p}_L})$ .

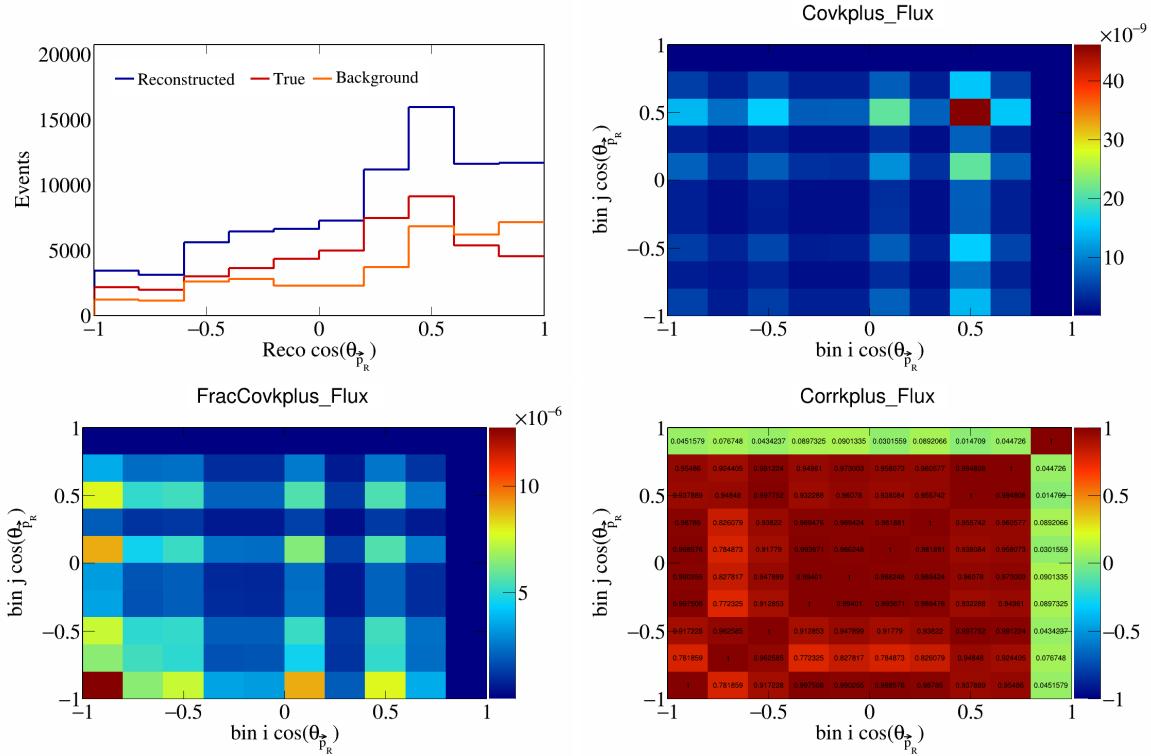


Figure 652: KPlus variations for  $\cos(\theta_{\vec{p}_R})$ .

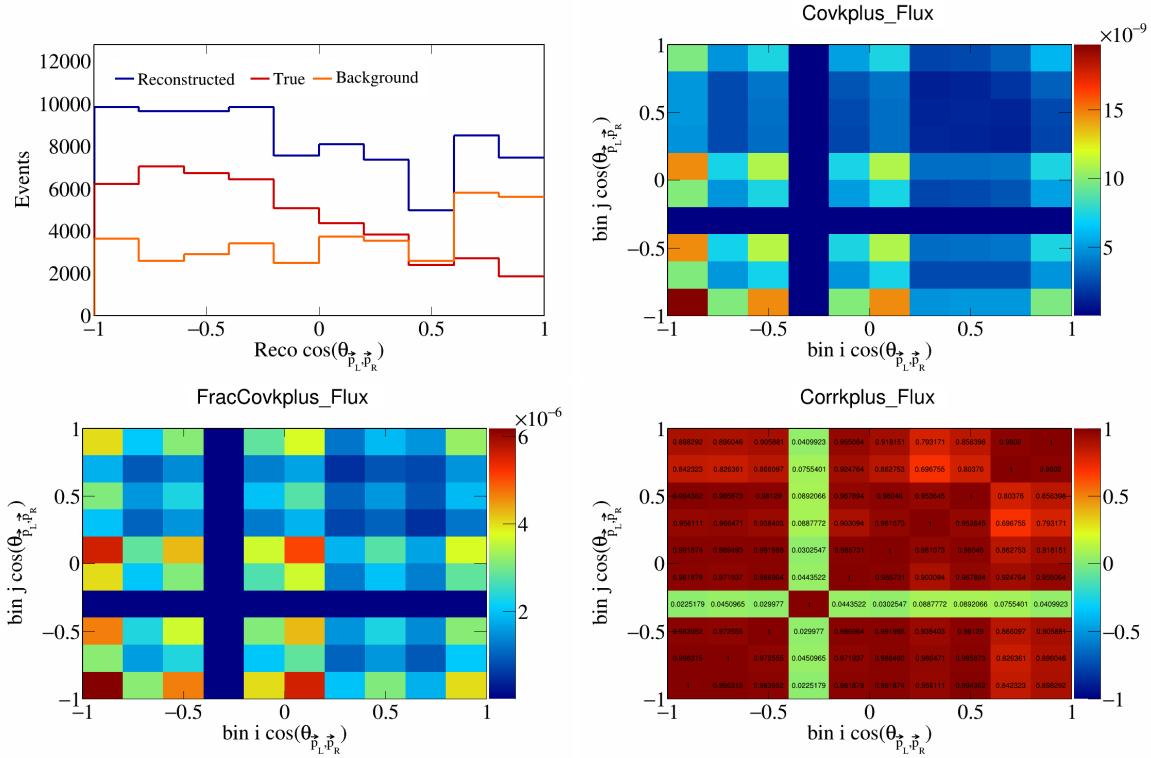


Figure 653: KPlus variations for  $\cos(\theta_{\vec{p}_L, \vec{p}_R})$ .

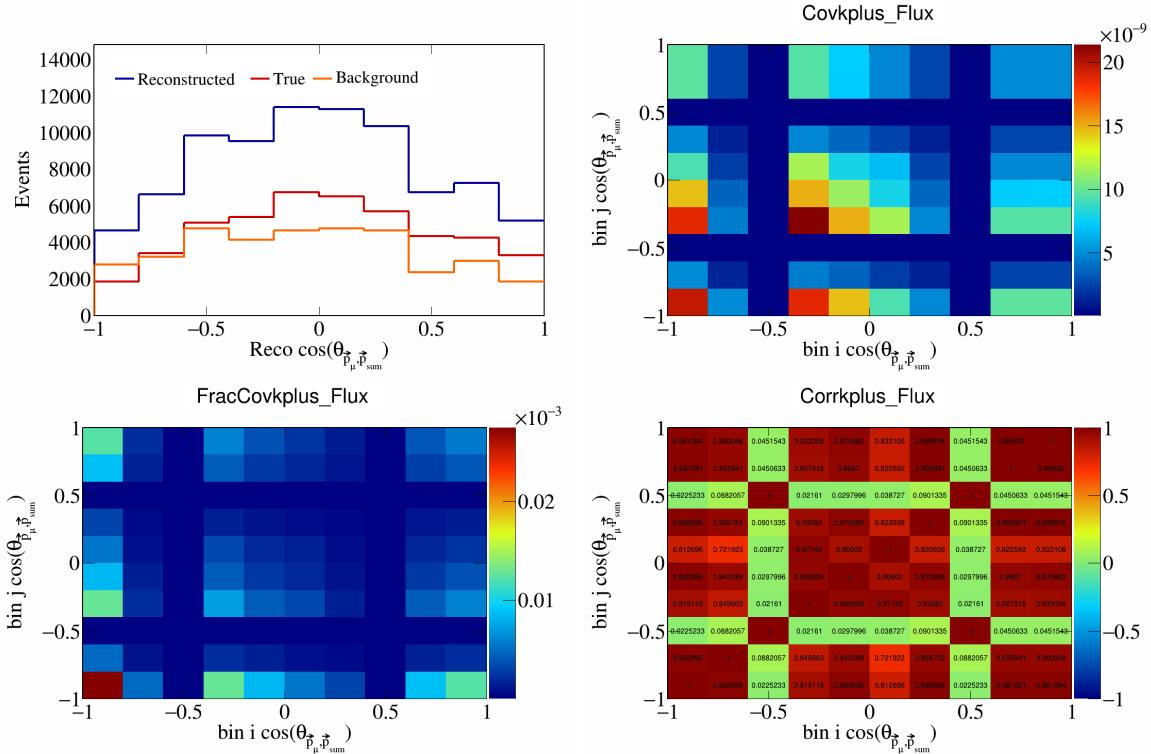


Figure 654: KPlus variations for  $\cos(\theta_{\vec{p}_\mu, \vec{p}_{\text{sum}}})$ .

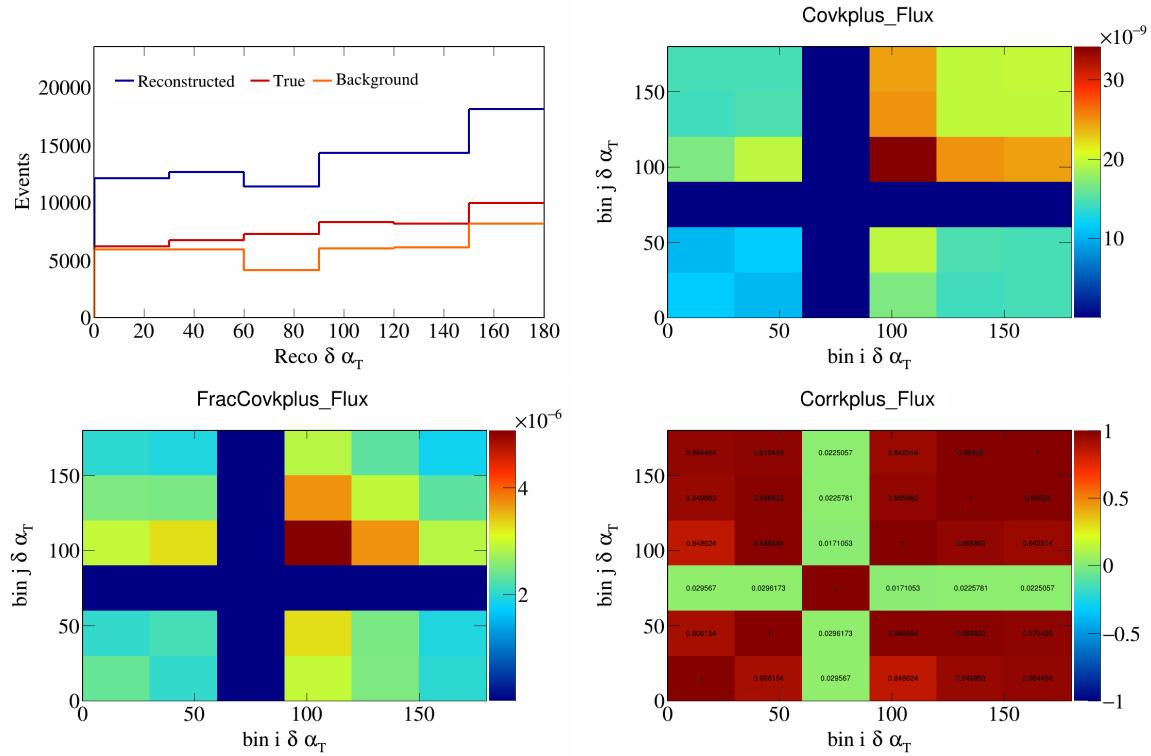


Figure 655: KPlus variations for  $\delta\alpha_T$ .

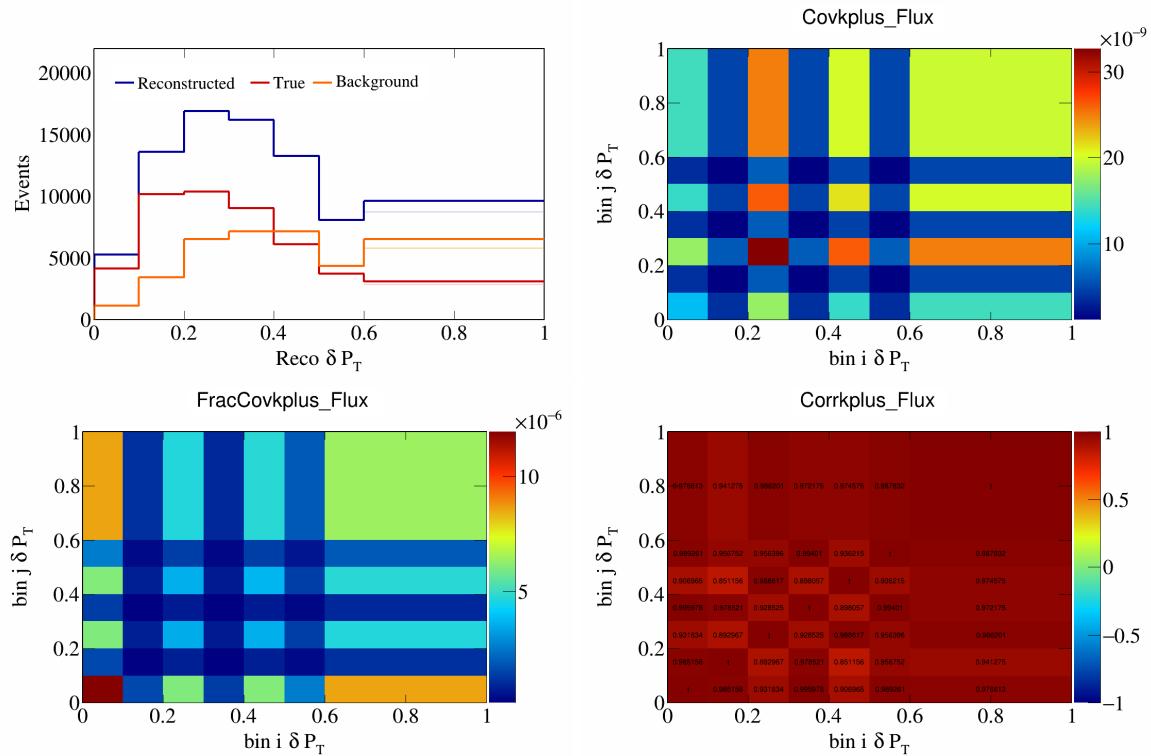


Figure 656: KPlus variations for  $\delta P_T$ .

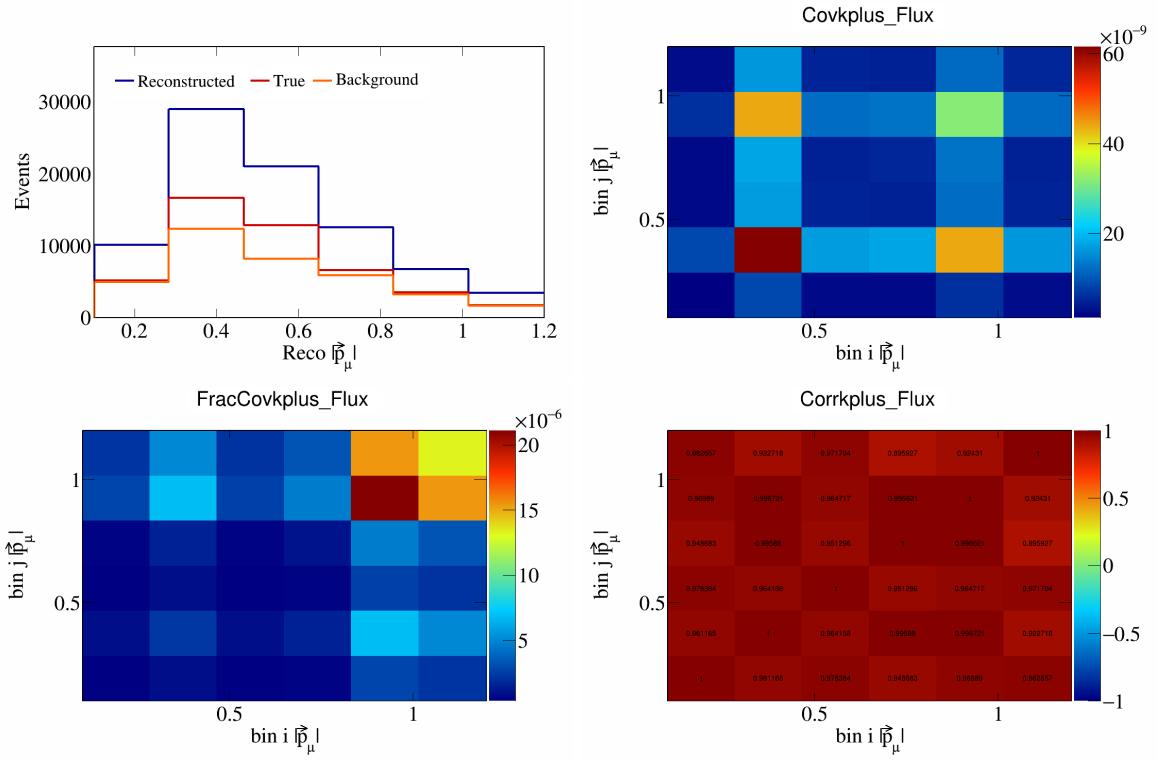


Figure 657: KPlus variations for  $|\vec{p}_\mu|$ .

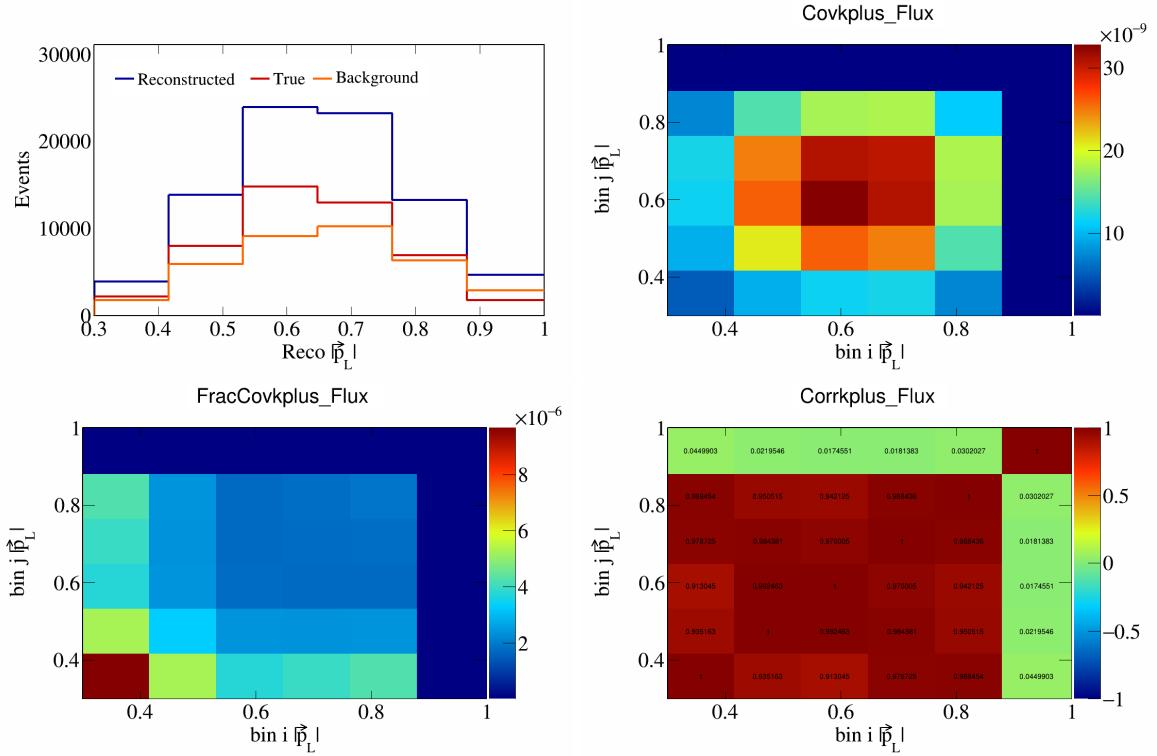


Figure 658: KPlus variations for  $|\vec{p}_L|$ .

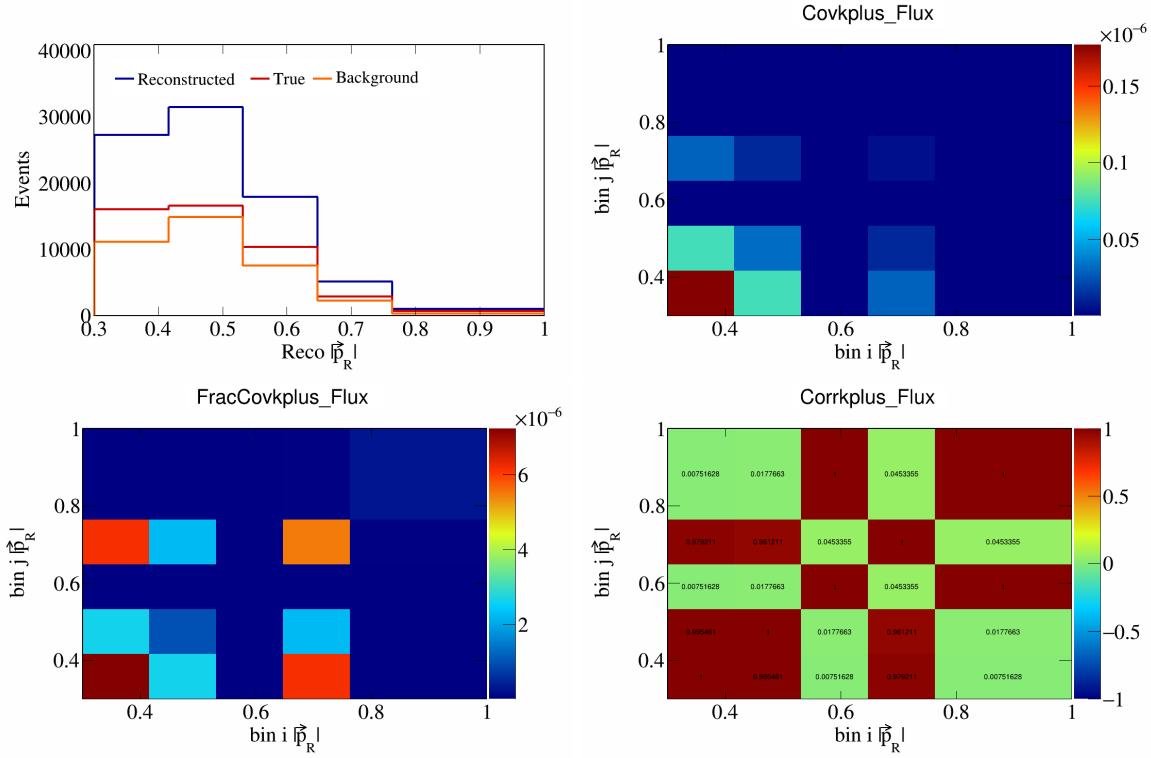


Figure 659: KPlus variations for  $|\vec{p}_R|$ .

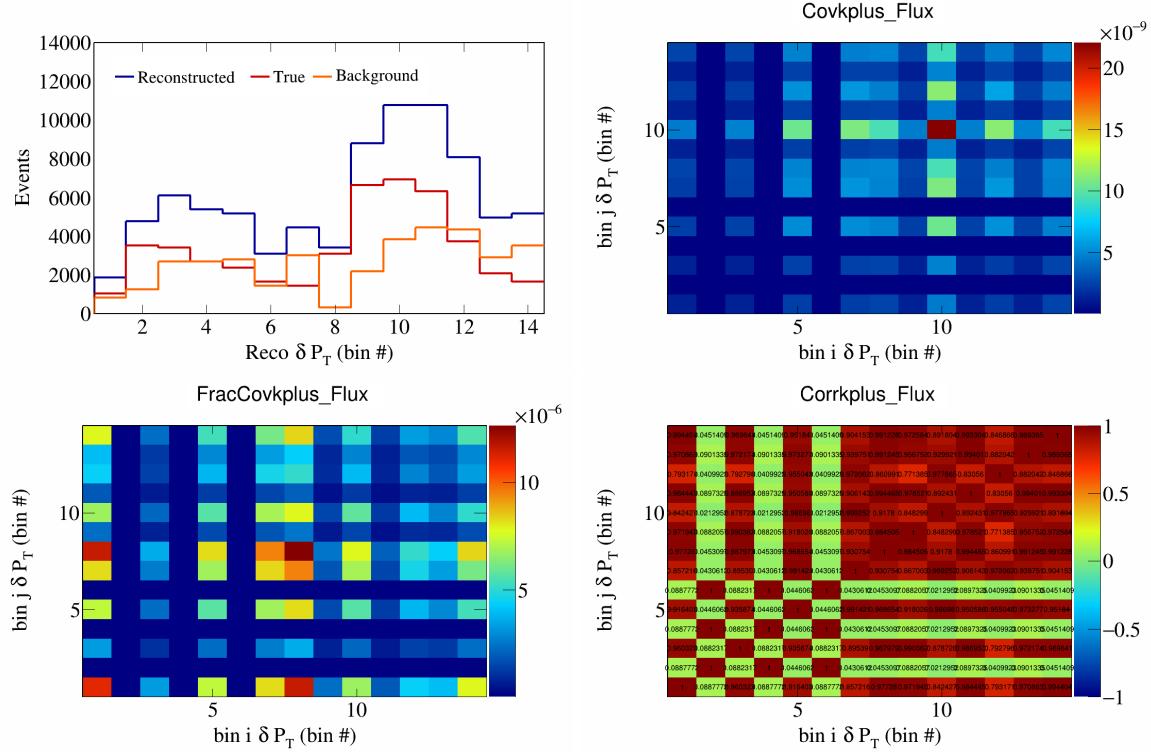


Figure 660: KPlus variations for  $\delta P_T$  in  $\cos(\theta_{\vec{p}_\mu})$ .

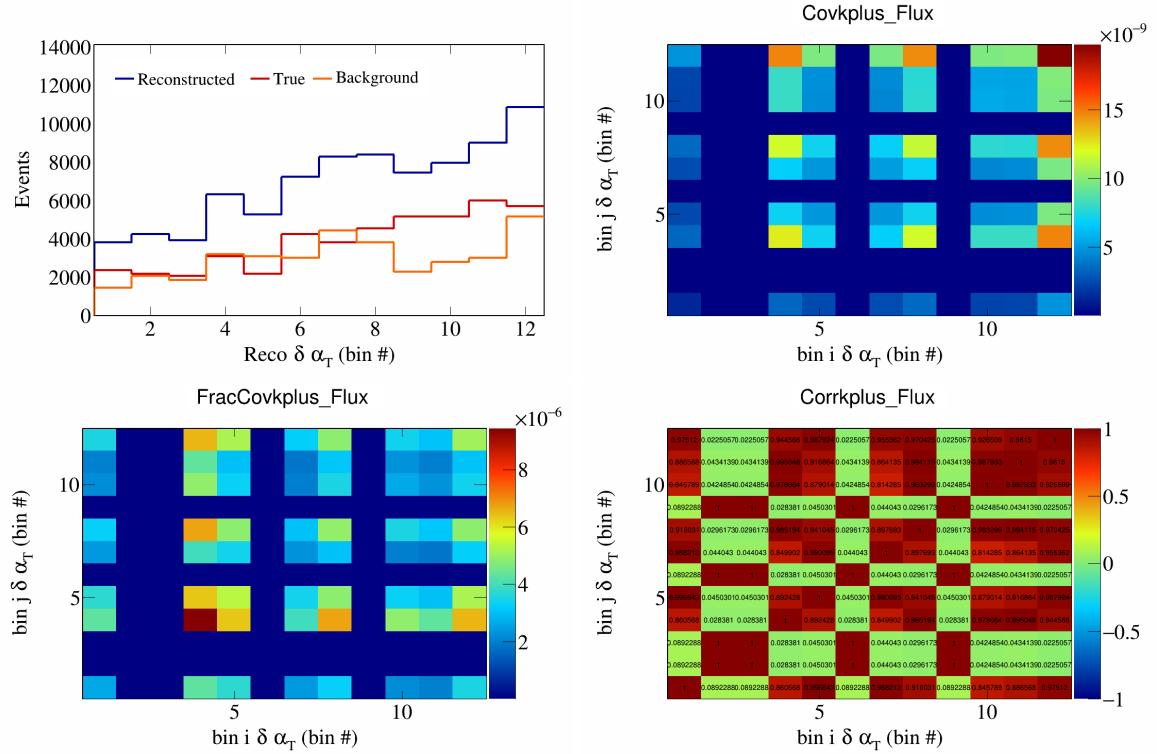


Figure 661: KPlus variations for  $\delta\alpha_T$  in  $\cos(\theta_{\vec{p}_\mu})$ .

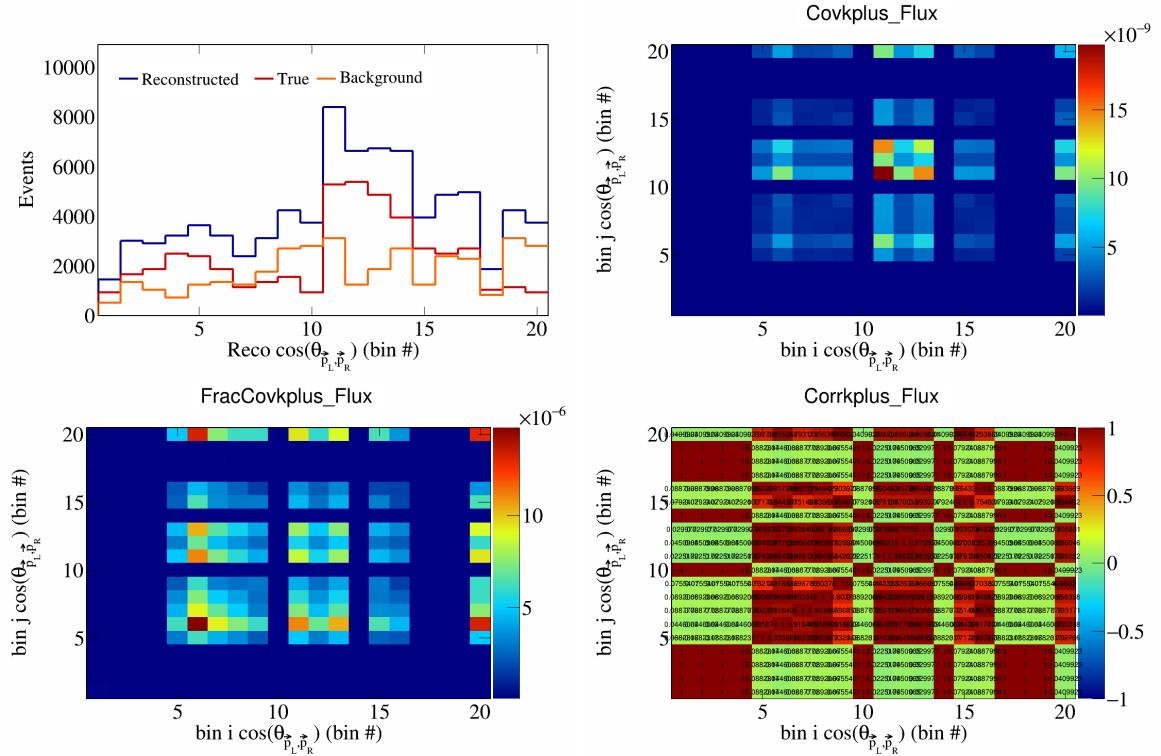


Figure 662: KPlus variations for  $\cos(\theta_{p_L, p_R})$  in  $\cos(\theta_{\vec{p}_\mu})$ .

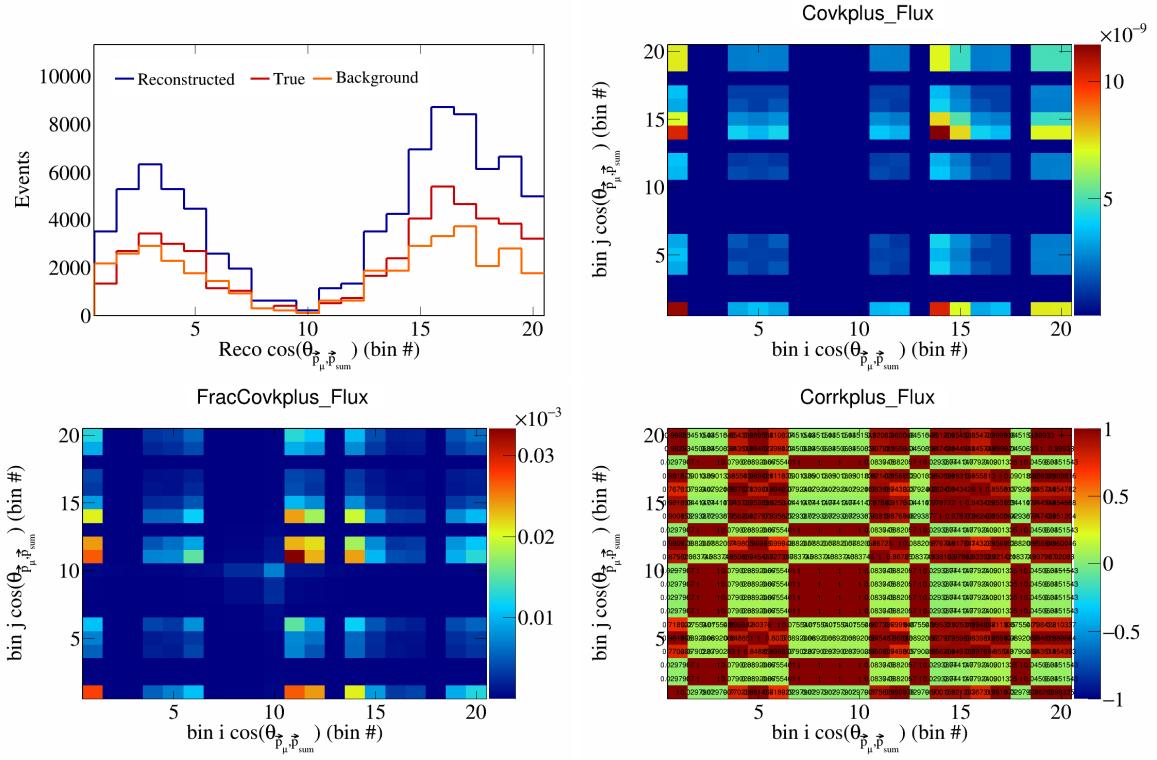


Figure 663: KPlus variations for  $\cos(\theta_{\vec{p}_\mu, \vec{p}_{\text{sum}}})$  in  $\cos(\theta_{\vec{p}_\mu})$ .

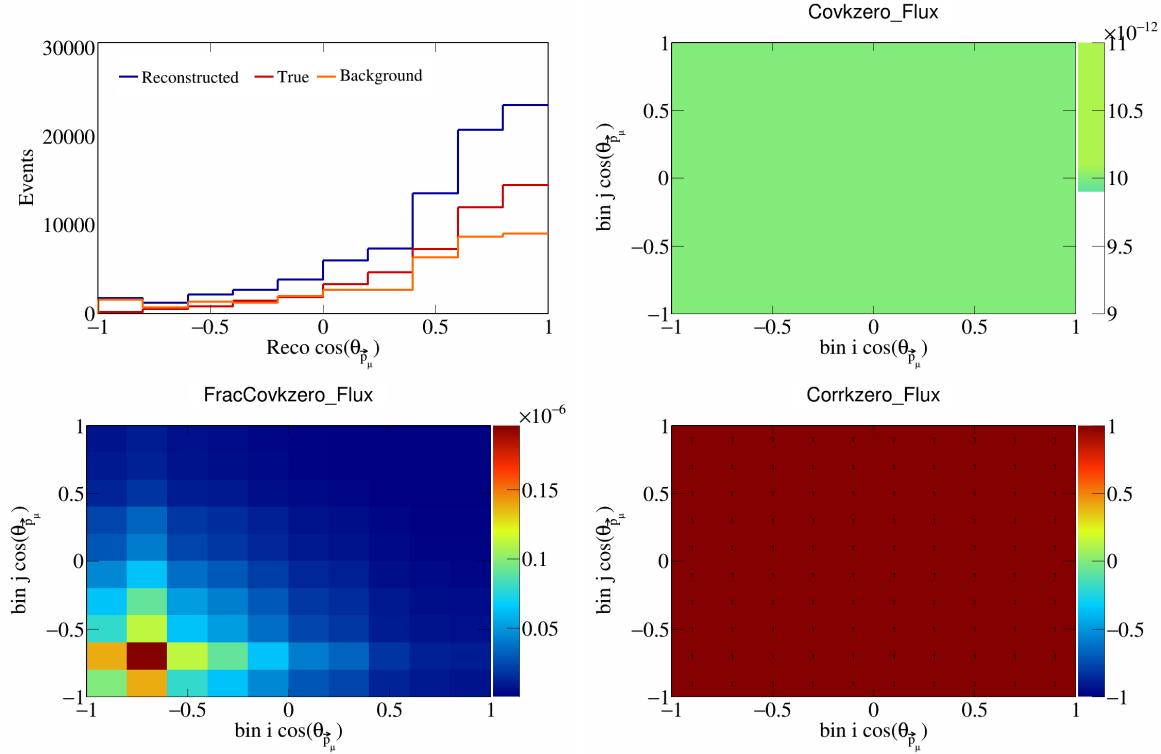


Figure 664: KZero variations for  $\cos(\theta_{\vec{p}_\mu, \vec{p}_{\text{sum}}})$  in  $\cos(\theta_{\vec{p}_\mu})$ .

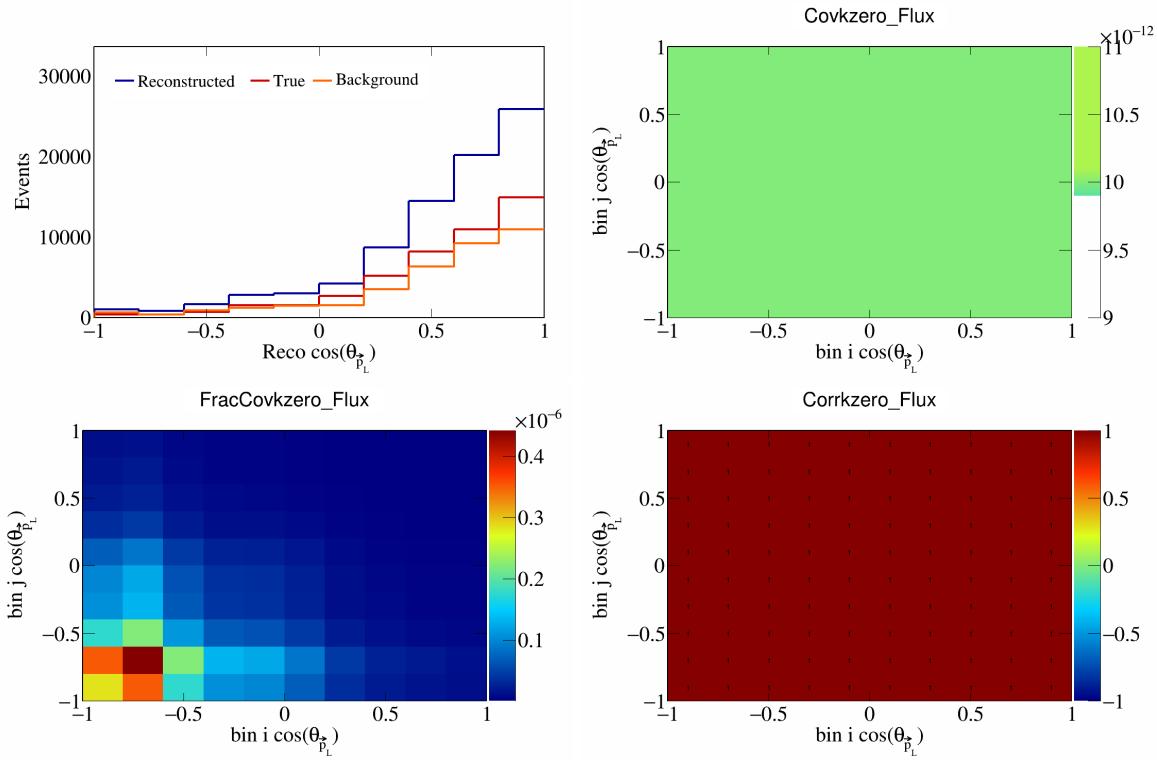


Figure 665: KZero variations for  $\cos(\theta_{\vec{p}_L})$ .

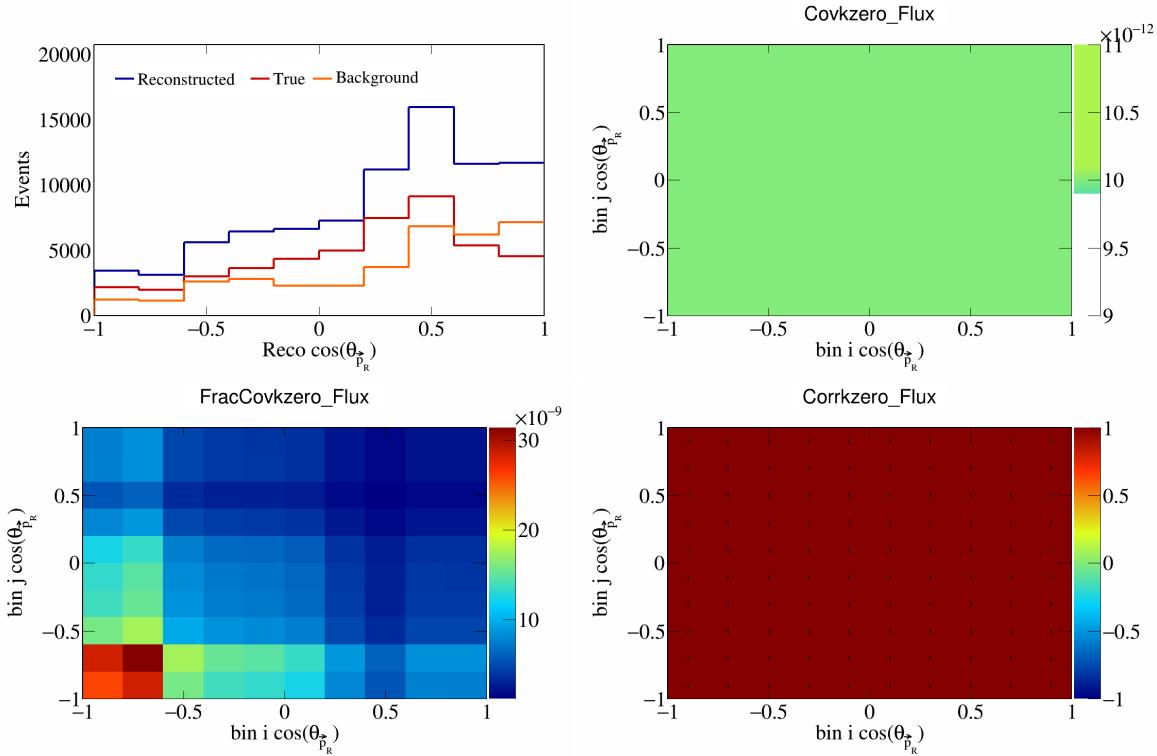


Figure 666: KZero variations for  $\cos(\theta_{\vec{p}_R})$ .

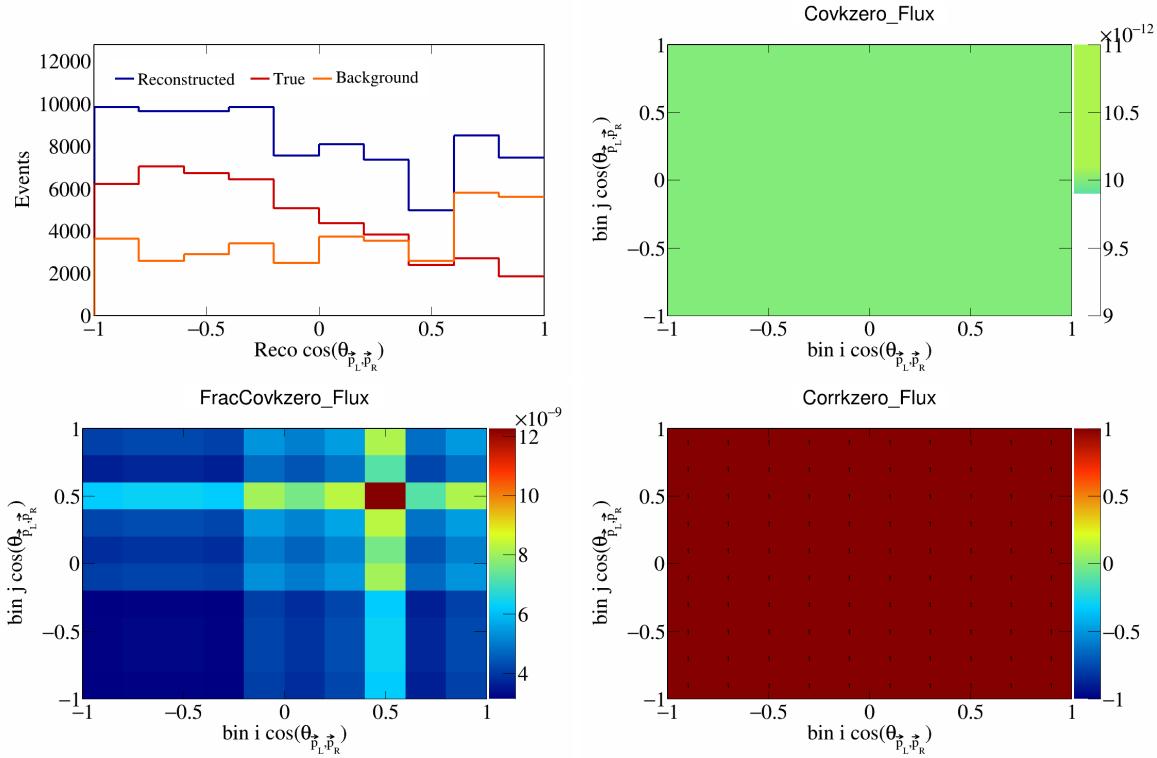


Figure 667: KZero variations for  $\cos(\theta_{\vec{p}_L, \vec{p}_R})$ .

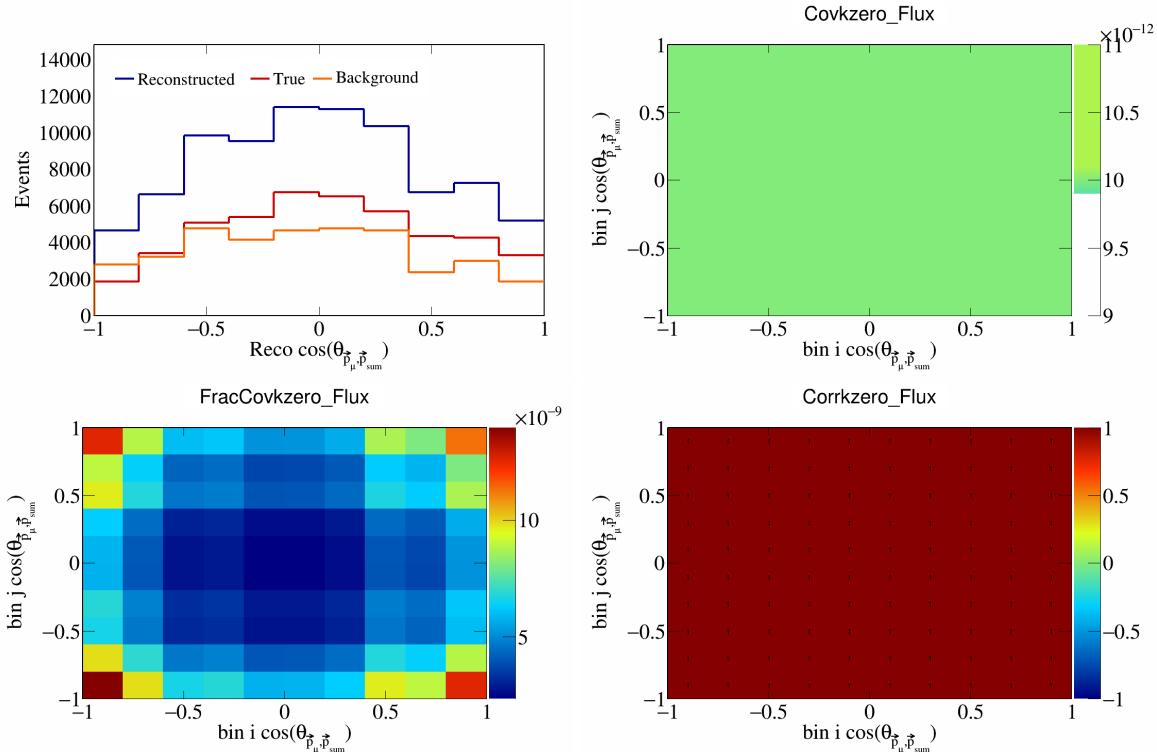


Figure 668: KZero variations for  $\cos(\theta_{\vec{p}_\mu, \vec{p}_{\text{sum}}})$ .

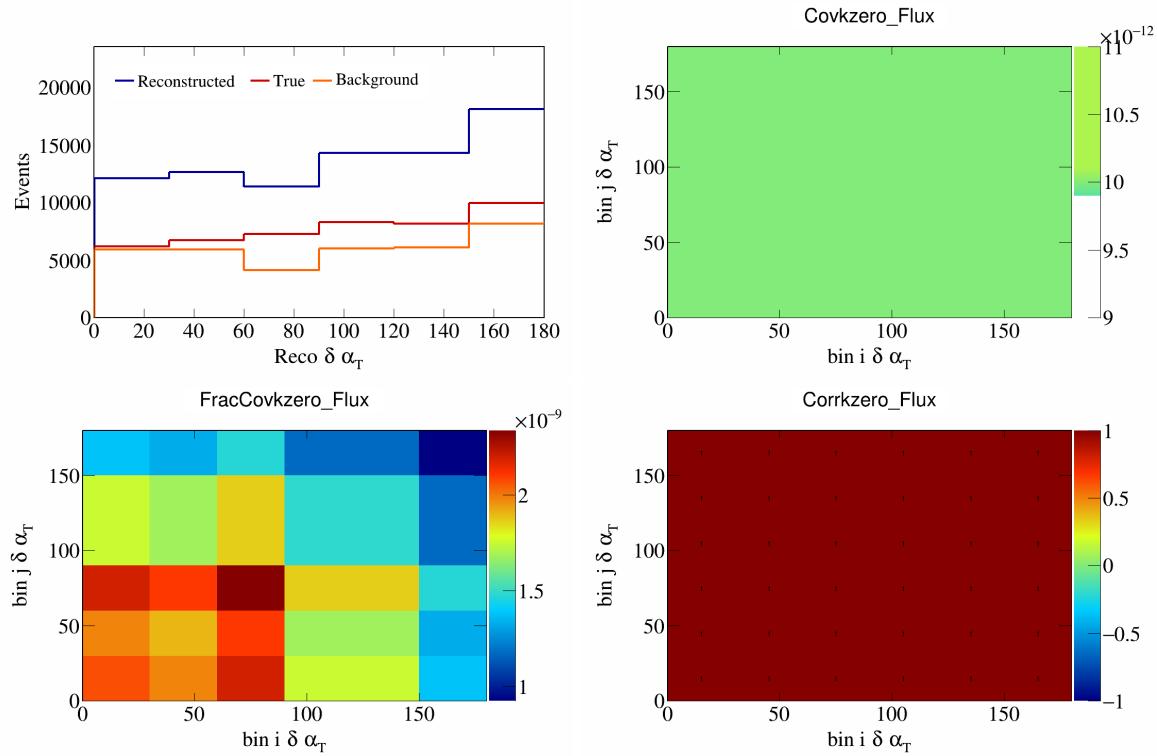


Figure 669: KZero variations for  $\delta\alpha_T$ .

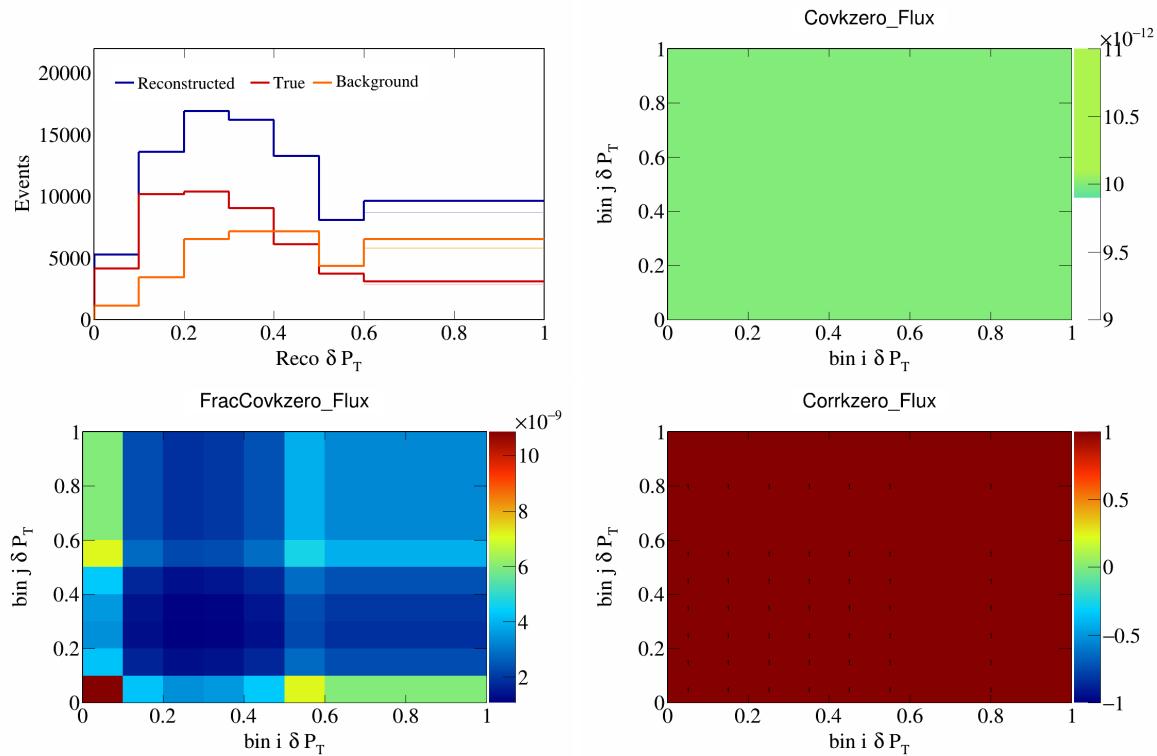


Figure 670: KZero variations for  $\delta P_T$ .

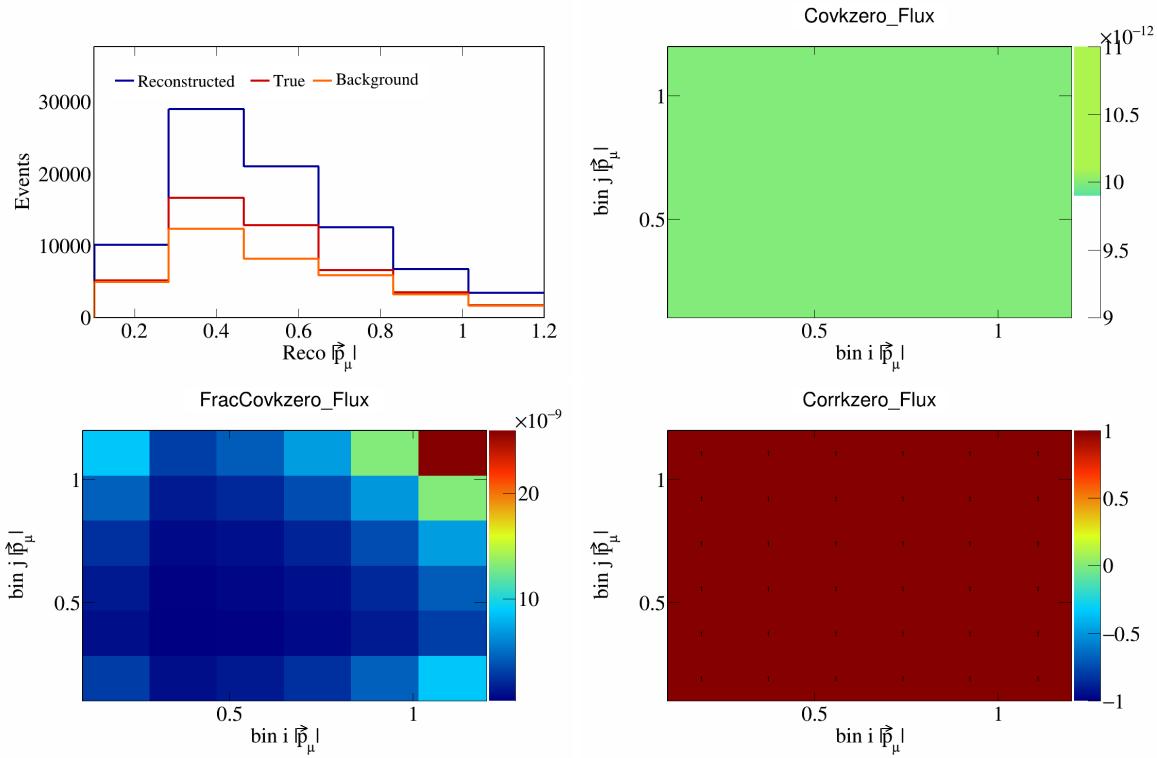


Figure 671: KZero variations for  $|\vec{p}_\mu|$ .

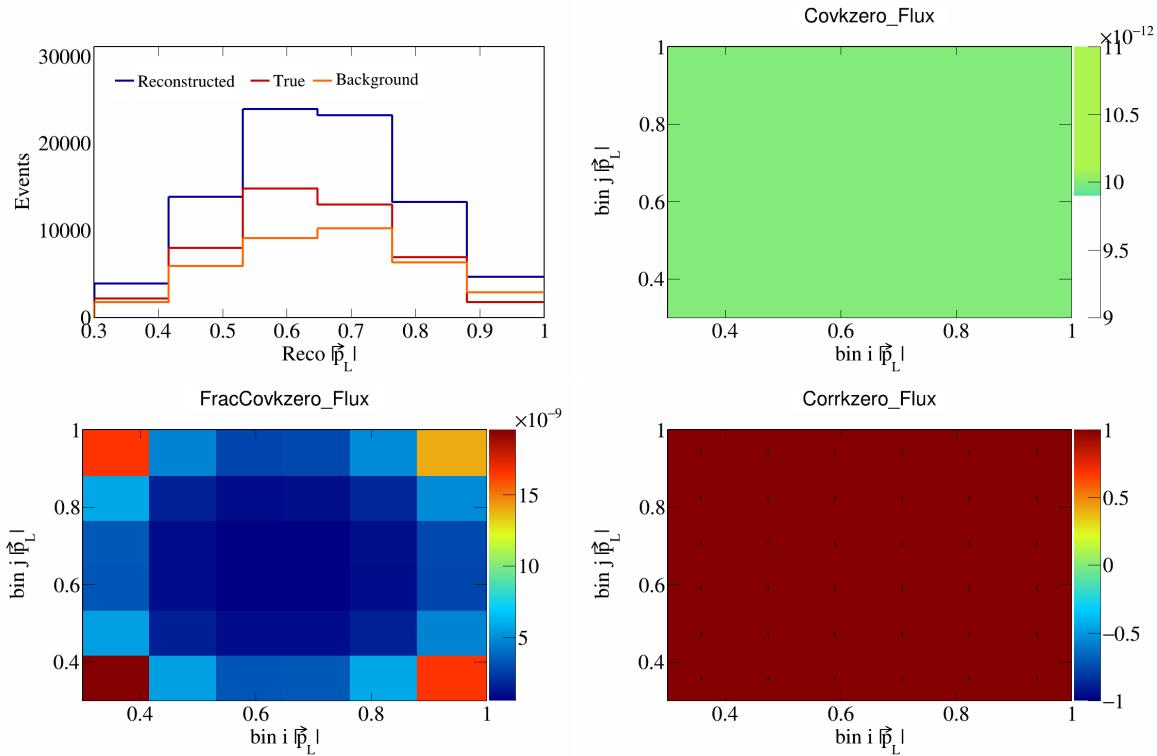


Figure 672: KZero variations for  $|\vec{p}_L|$ .

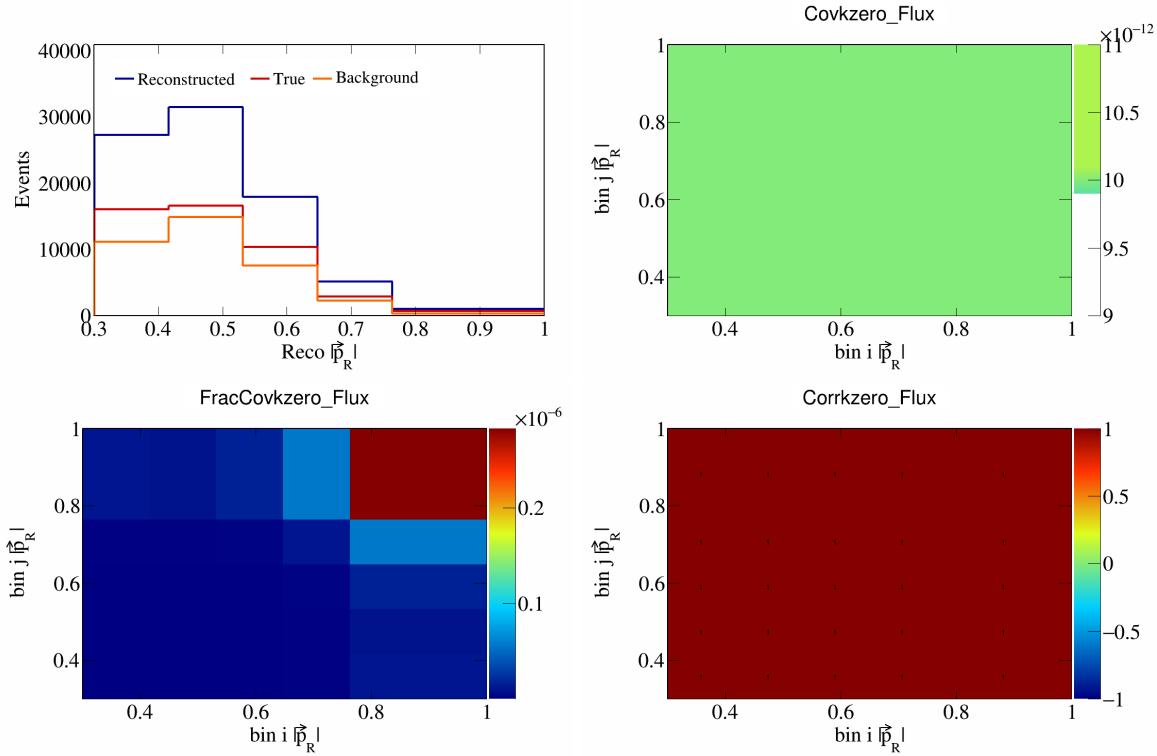


Figure 673: KZero variations for  $|\vec{p}_R|$ .

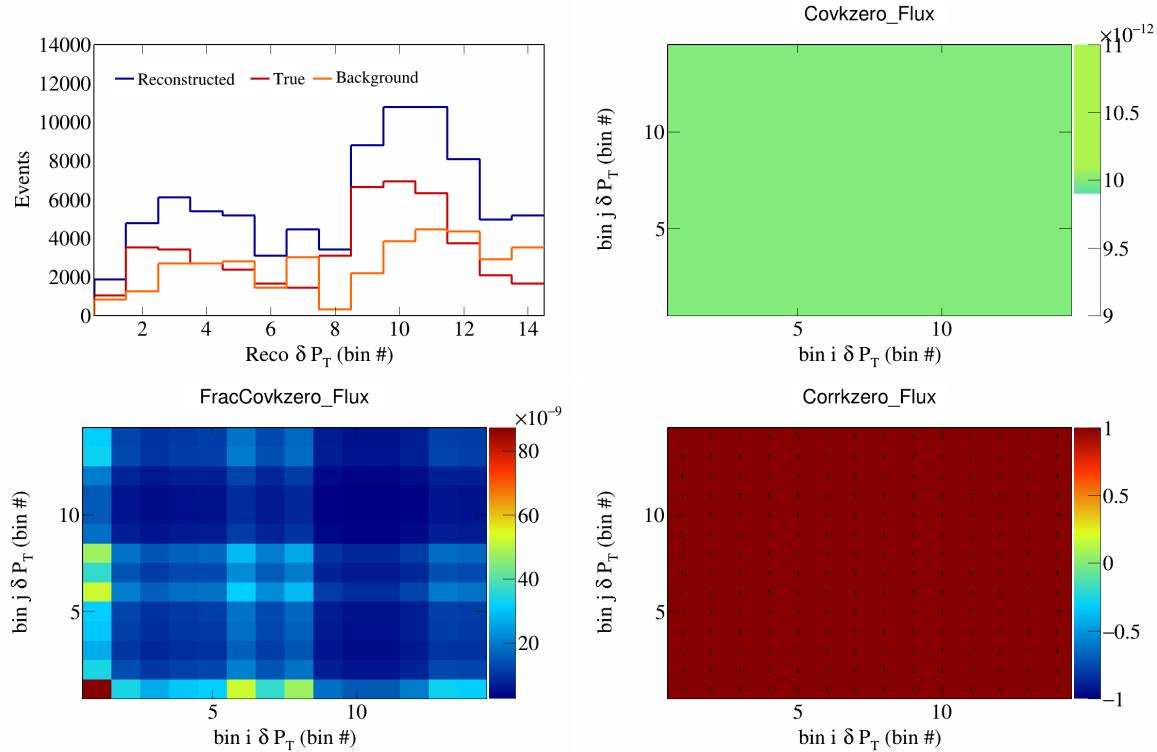


Figure 674: KZero variations for  $\delta P_T$  in  $\cos(\theta_{\vec{p}_\mu})$ .

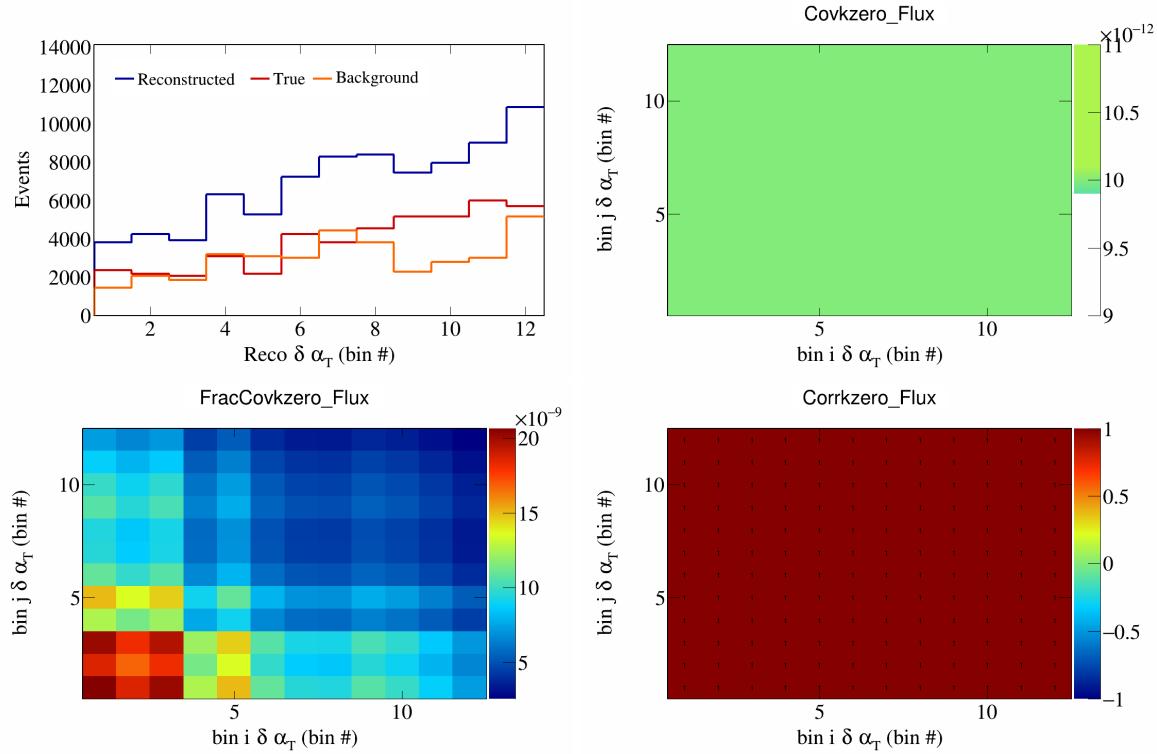


Figure 675: KZero variations for  $\delta\alpha_T$  in  $\cos(\theta_{\vec{p}_\mu})$ .

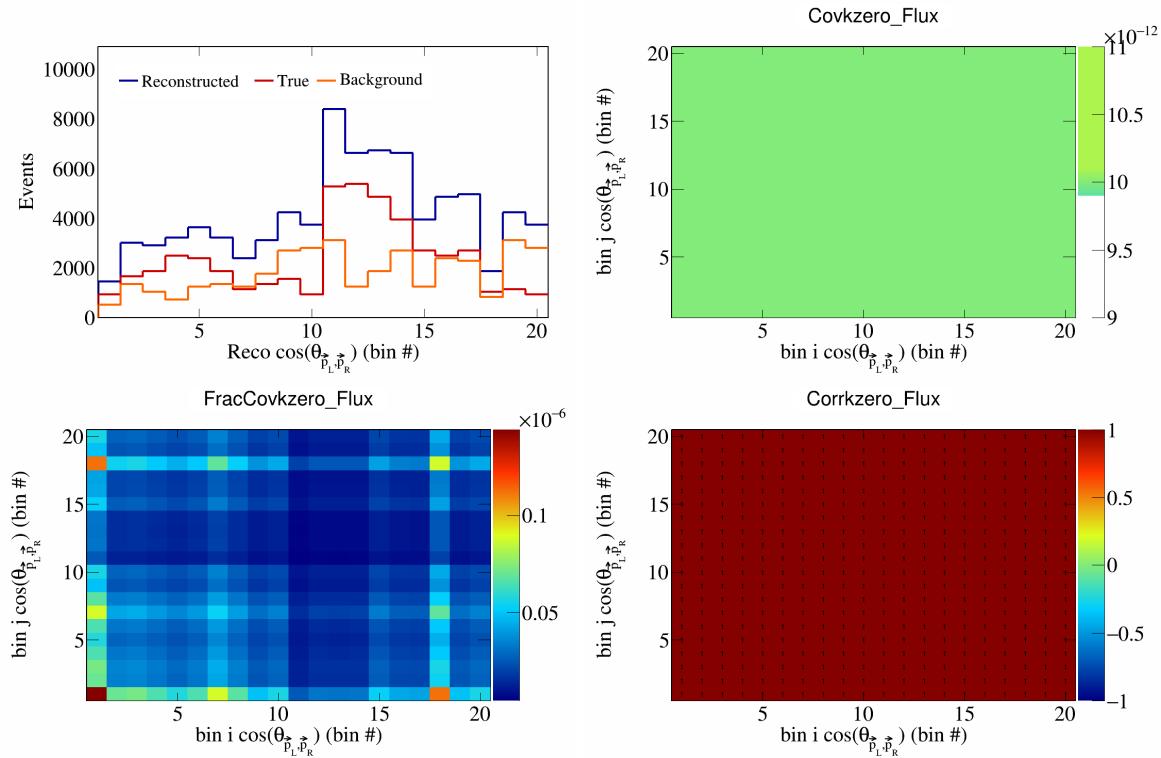


Figure 676: KZero variations for  $\cos(\theta_{\vec{p}_L, \vec{p}_R})$  in  $\cos(\theta_{\vec{p}_\mu})$ .

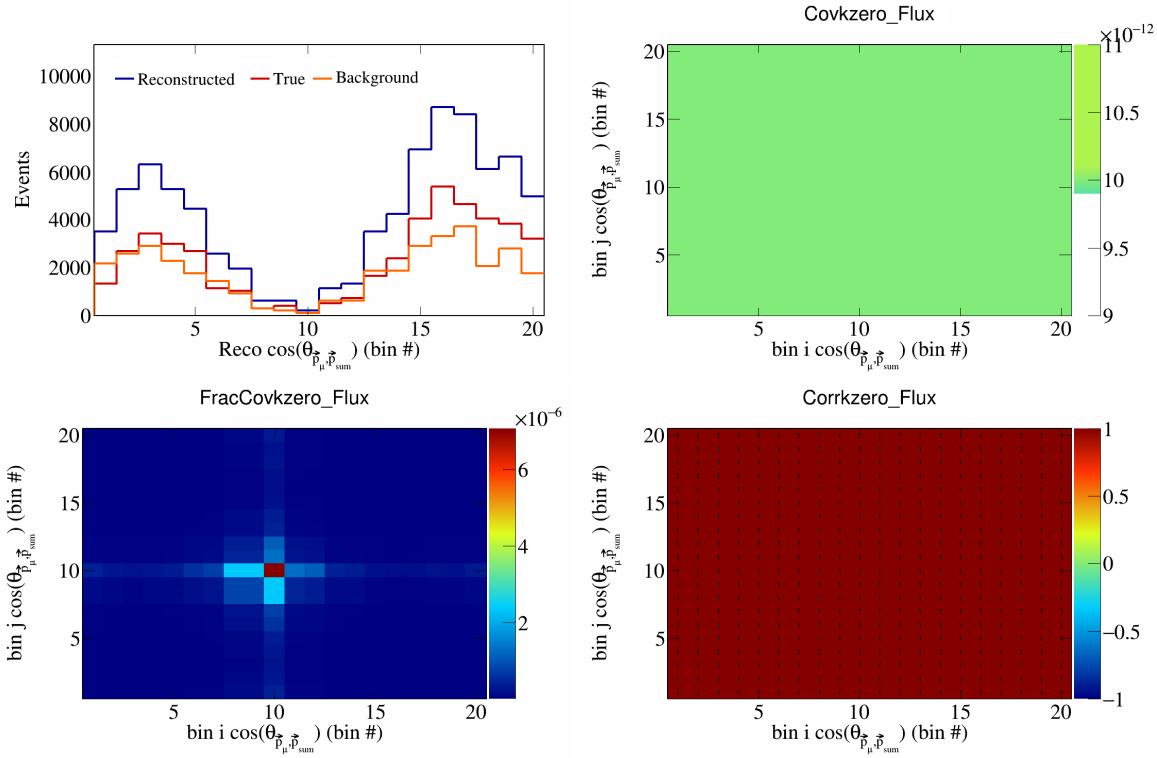


Figure 677: KZero variations for  $\cos(\theta_{\vec{p}_\mu, \vec{p}_{\text{sum}}})$  in  $\cos(\theta_{\vec{p}_\mu})$ .

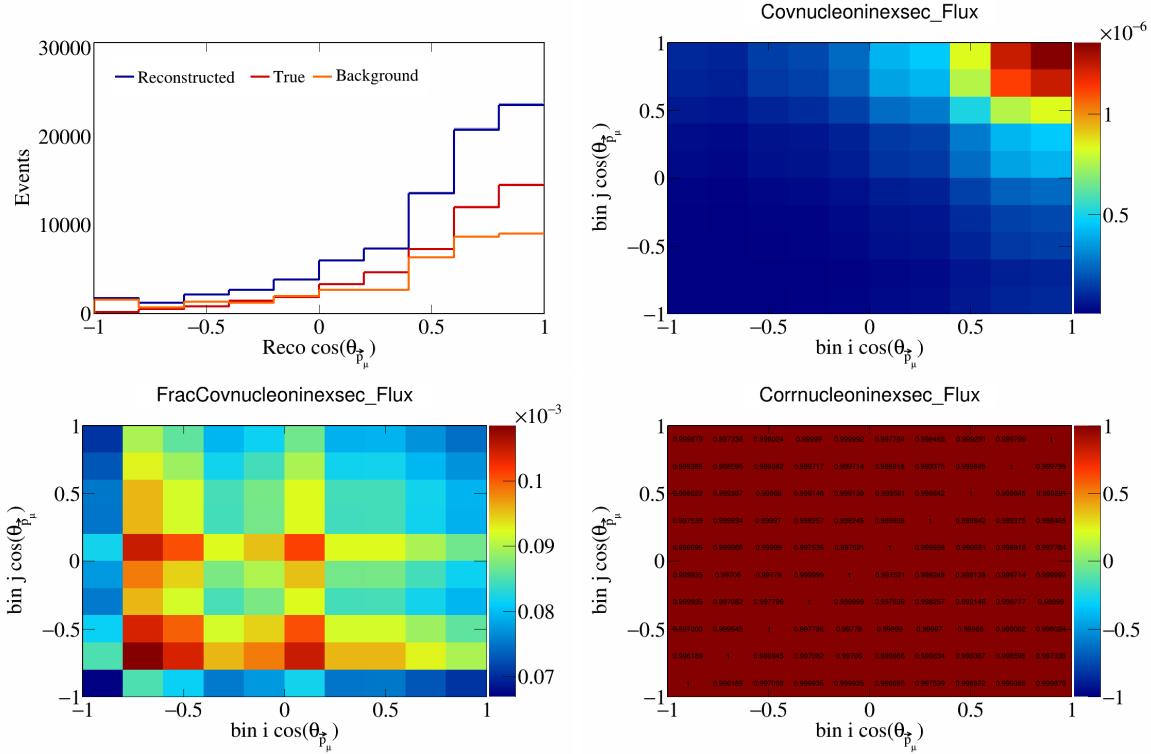


Figure 678: NucleonIneXSec variations for  $\cos(\theta_{\vec{p}_\mu})$ .

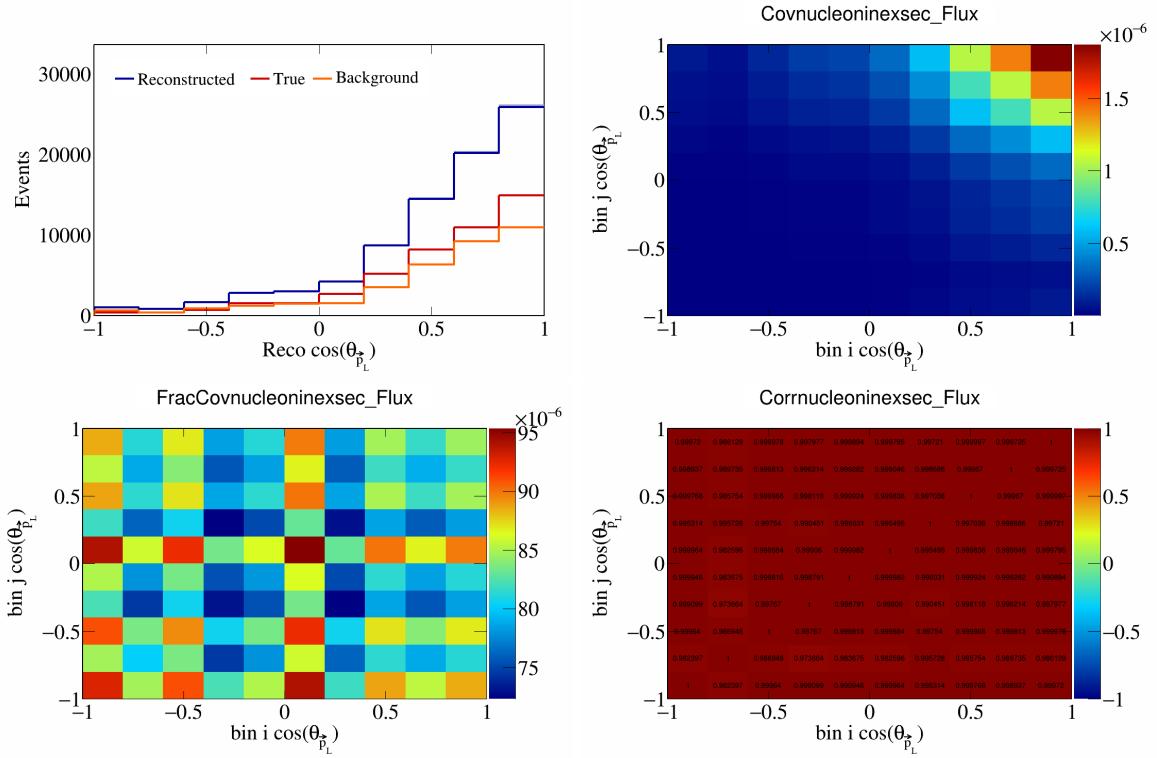


Figure 679: NucleonIneXSec variations for  $\cos(\theta_{\vec{p}_L})$ .

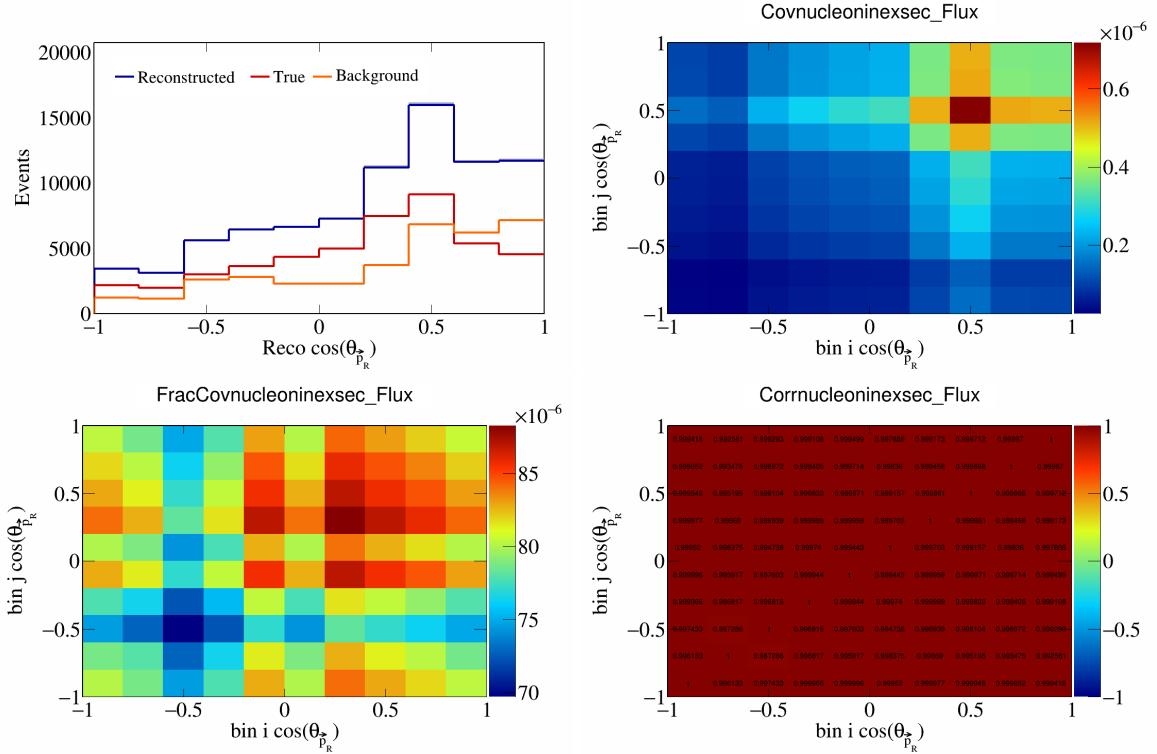


Figure 680: NucleonIneXSec variations for  $\cos(\theta_{\vec{p}_R})$ .

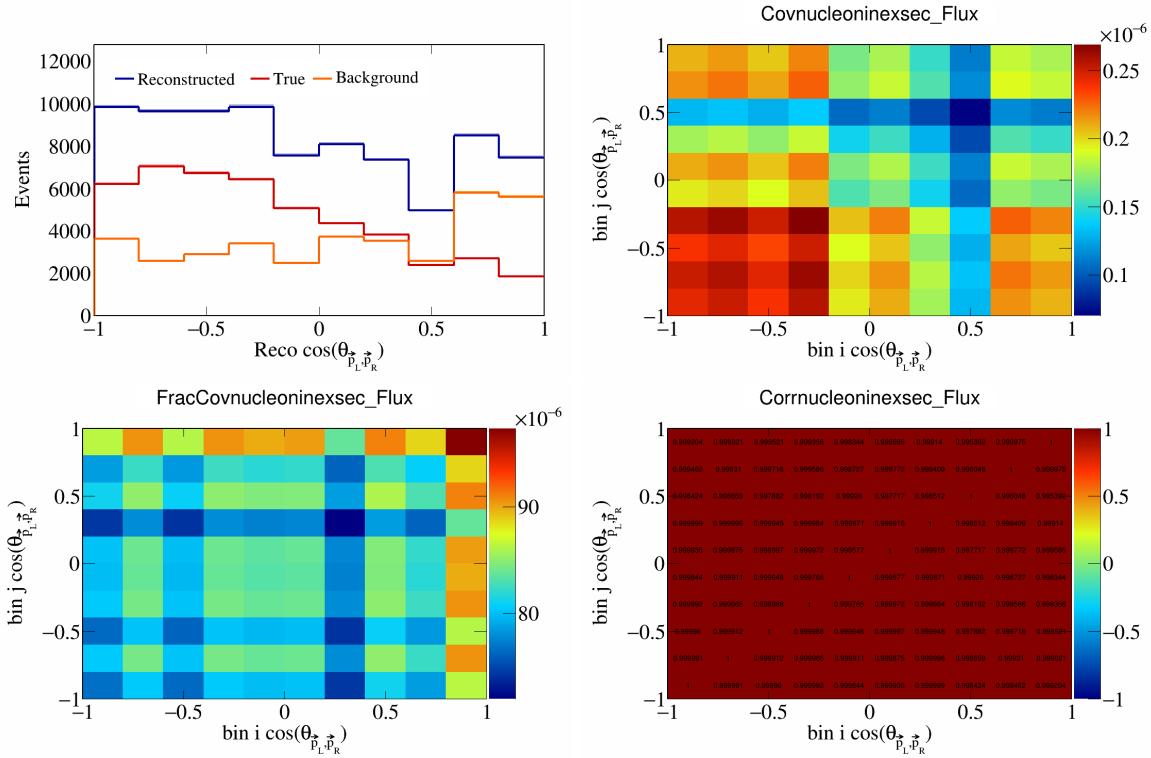


Figure 681: NucleonIneXSec variations for  $\cos(\theta_{\vec{p}_L, \vec{p}_R})$ .

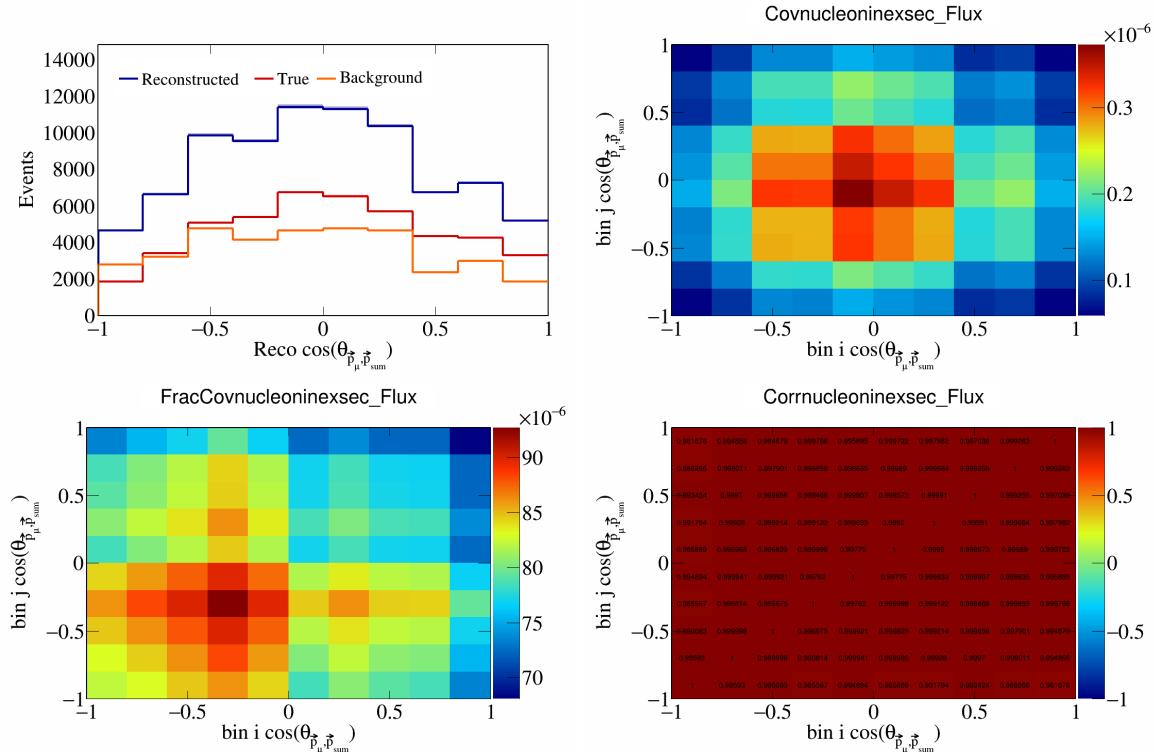


Figure 682: NucleonIneXSec variations for  $\cos(\theta_{\vec{p}_\mu, \vec{p}_{\text{sum}}})$ .

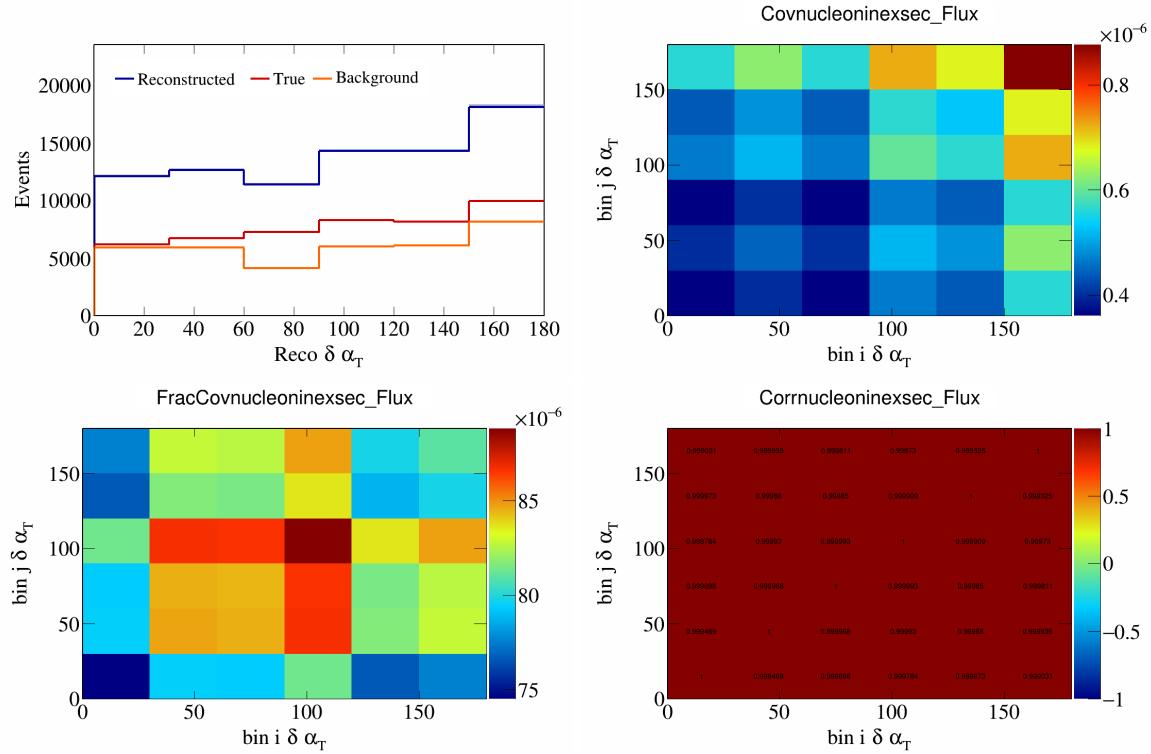


Figure 683: NucleonIneXSec variations for  $\delta\alpha_T$ .

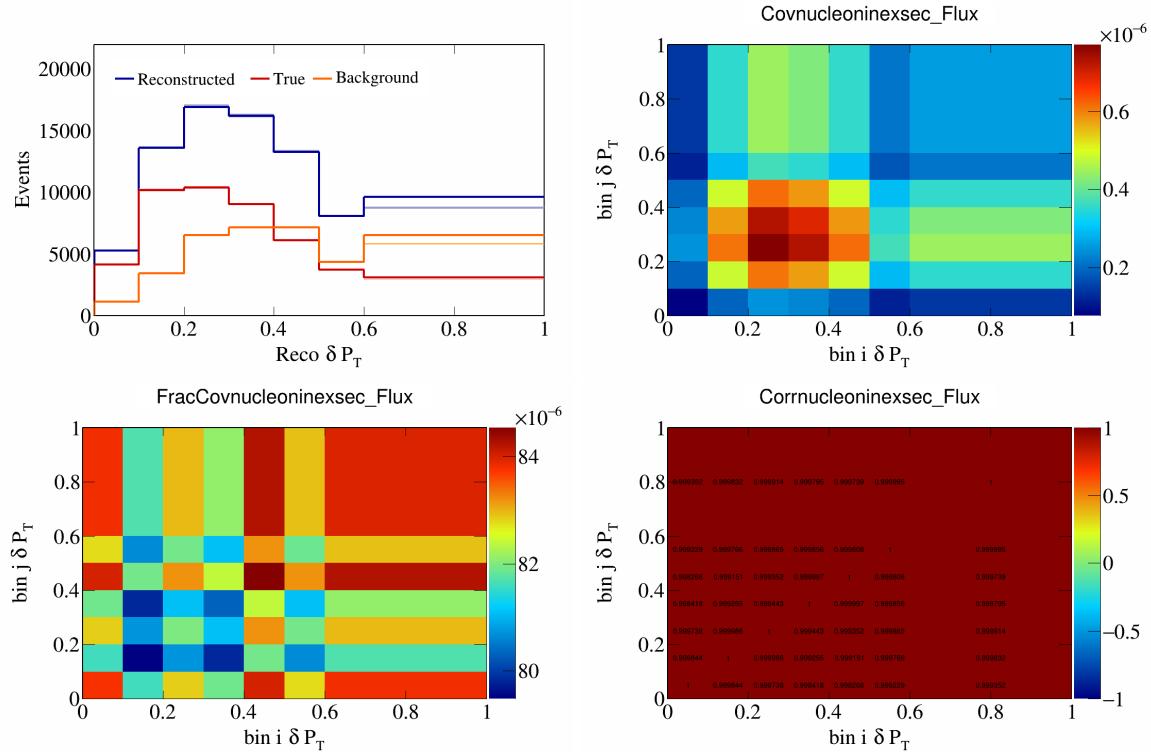


Figure 684: NucleonIneXSec variations for  $\delta P_T$ .

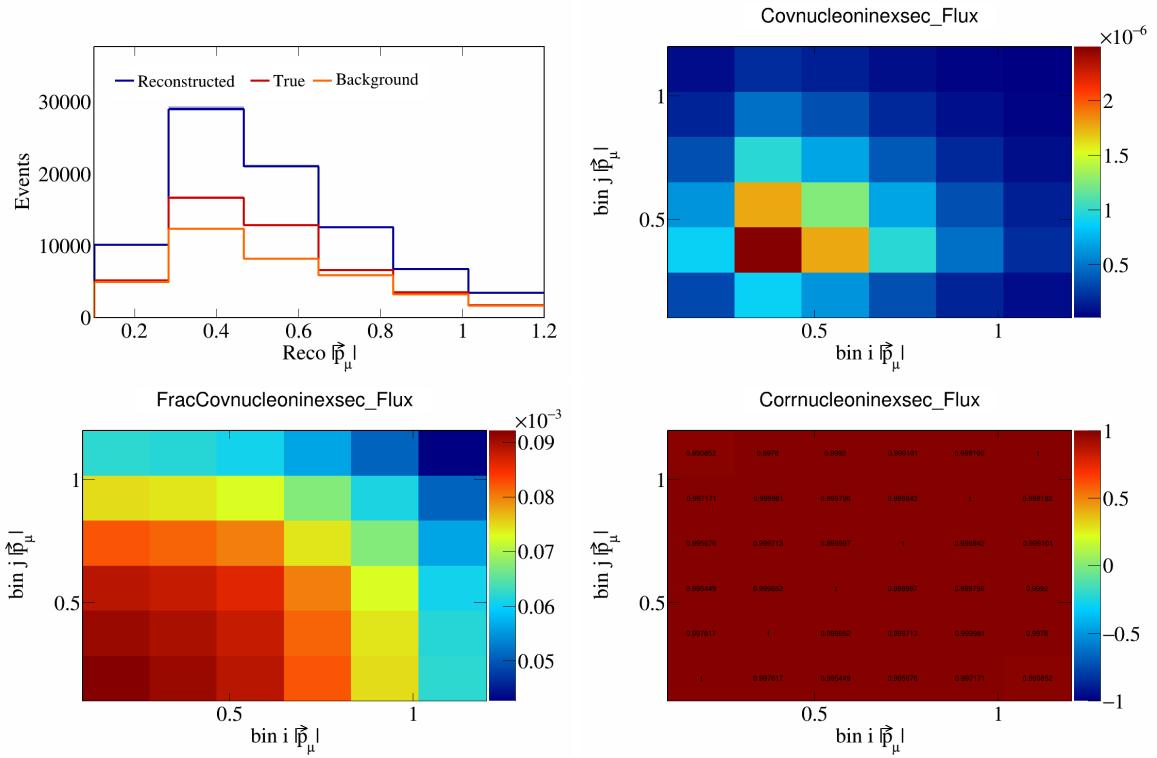


Figure 685: NucleonIneXSec variations for  $|\vec{p}_\mu|$ .

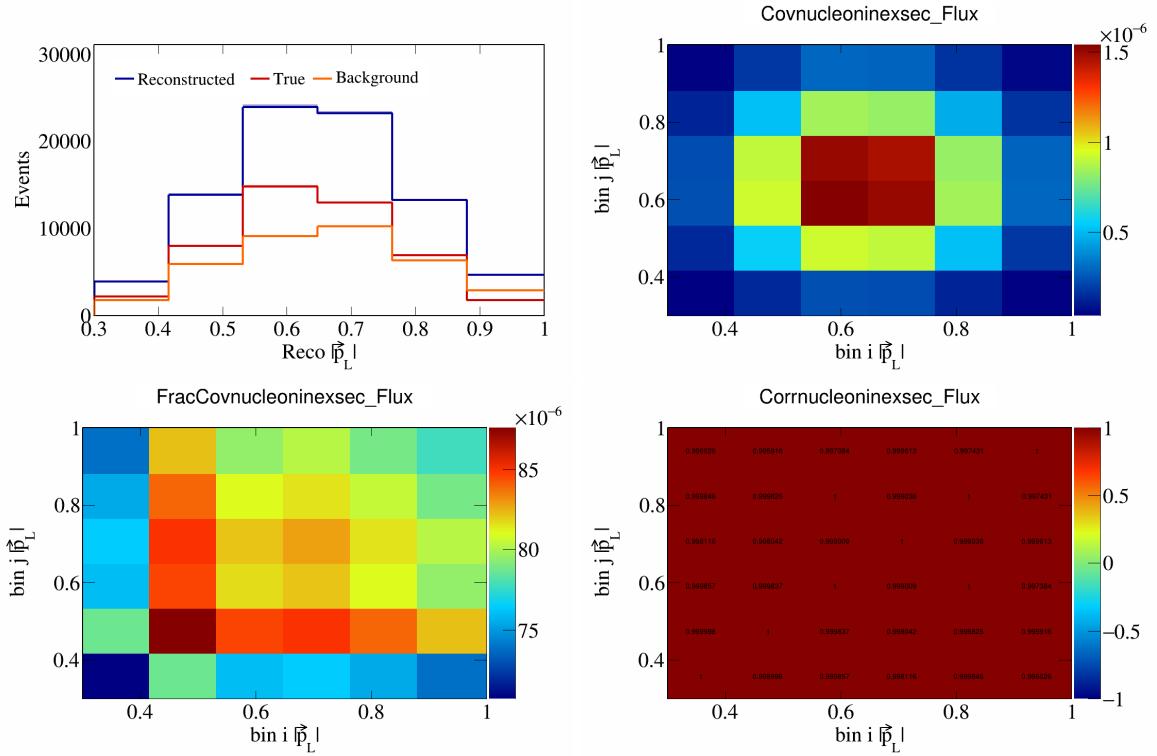


Figure 686: NucleonIneXSec variations for  $|\vec{p}_L|$ .

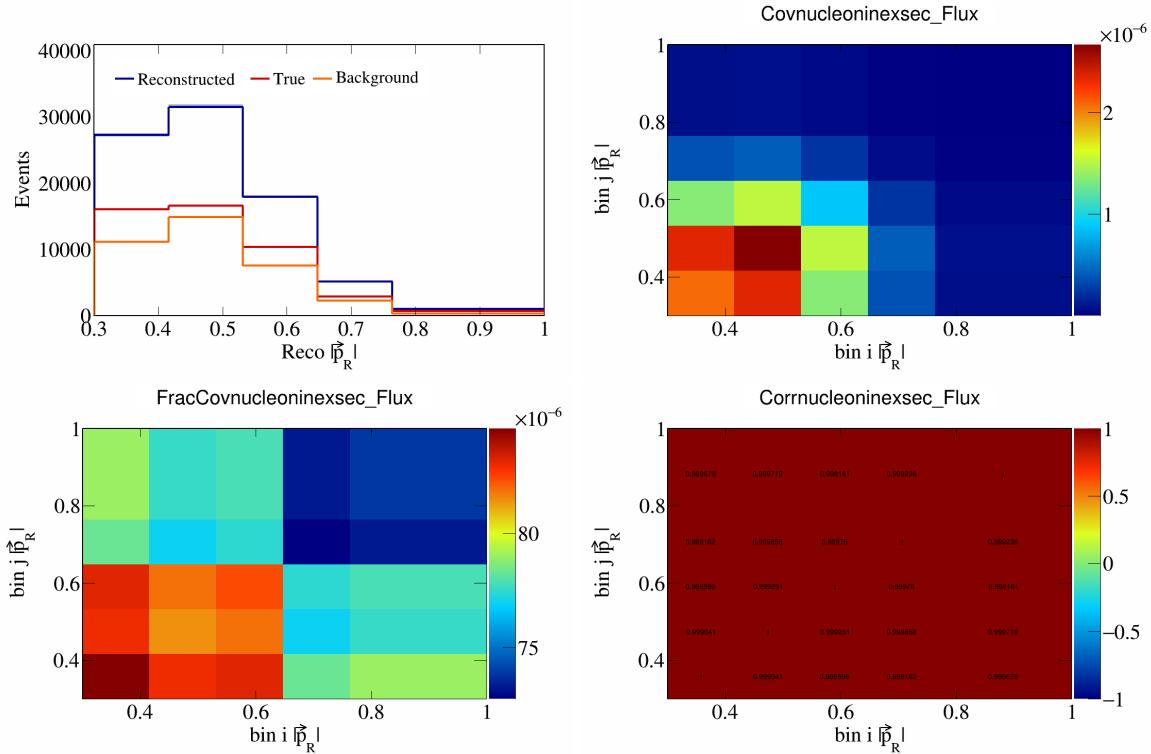


Figure 687: NucleonIneXSec variations for  $|\vec{p}_R|$ .

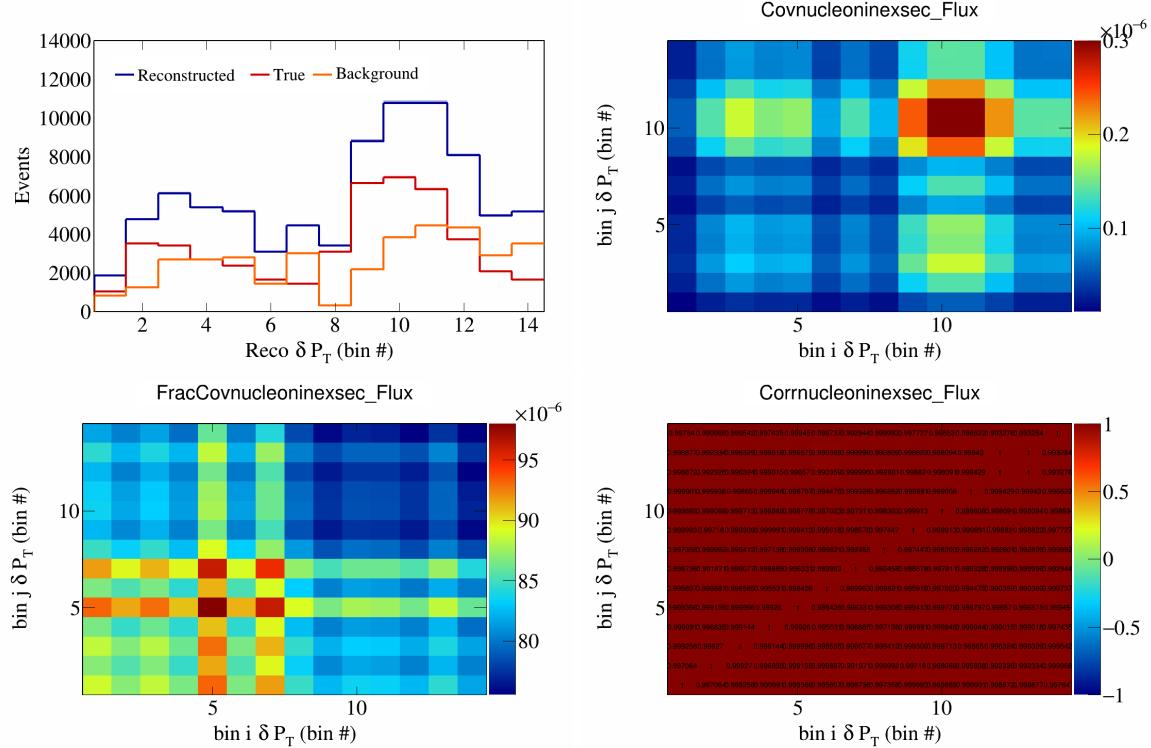


Figure 688: NucleonIneXSec variations for  $\delta P_T$  in  $\cos(\theta_{\vec{p}_\mu})$ .

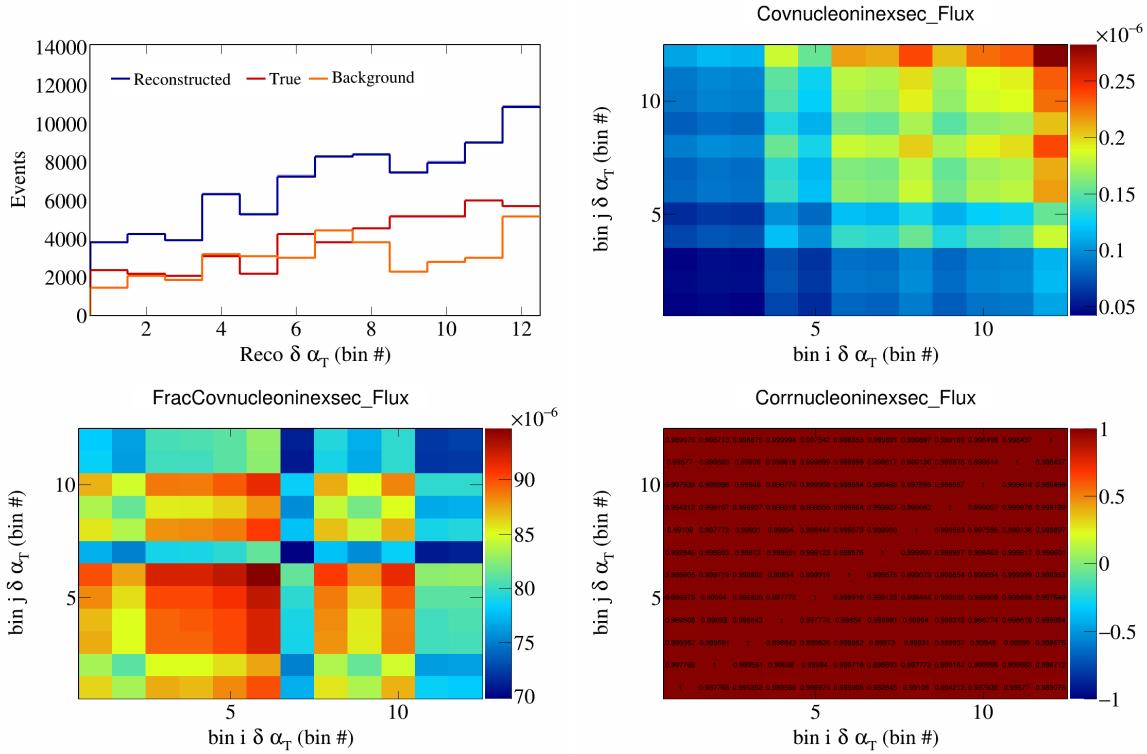


Figure 689: NucleonIneXSec variations for  $\delta\alpha_T$  in  $\cos(\theta_{\vec{p}_\mu})$ .

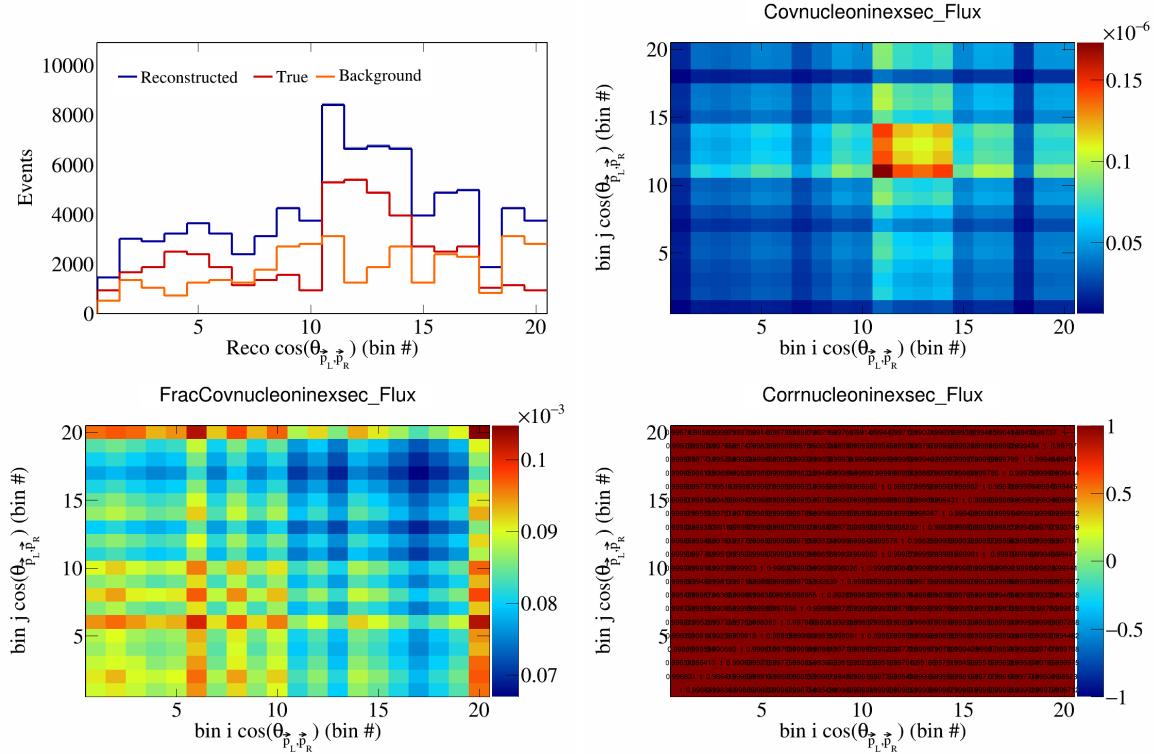


Figure 690: NucleonIneXSec variations for  $\cos(\theta_{\vec{p}_L, \vec{p}_R})$  in  $\cos(\theta_{\vec{p}_\mu})$ .

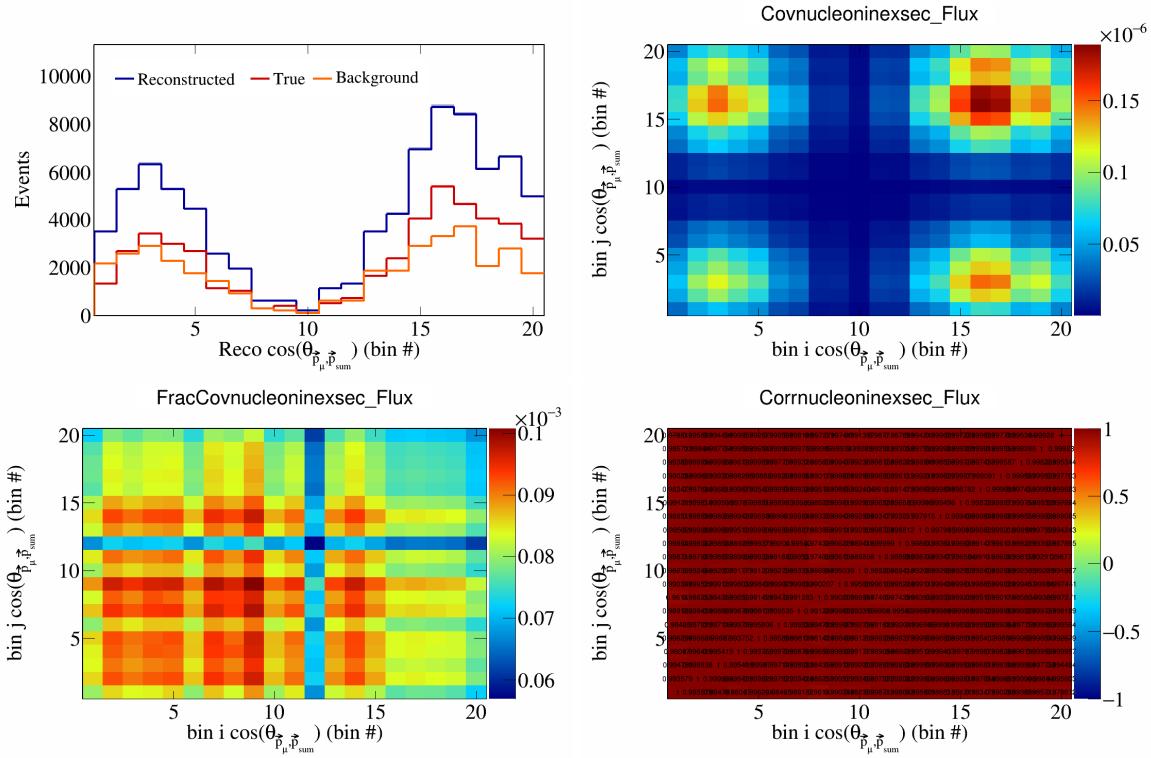


Figure 691: NucleonIneXSec variations for  $\cos(\theta_{\vec{p}_\mu, \vec{p}_{\text{sum}}})$  in  $\cos(\theta_{\vec{p}_\mu})$ .

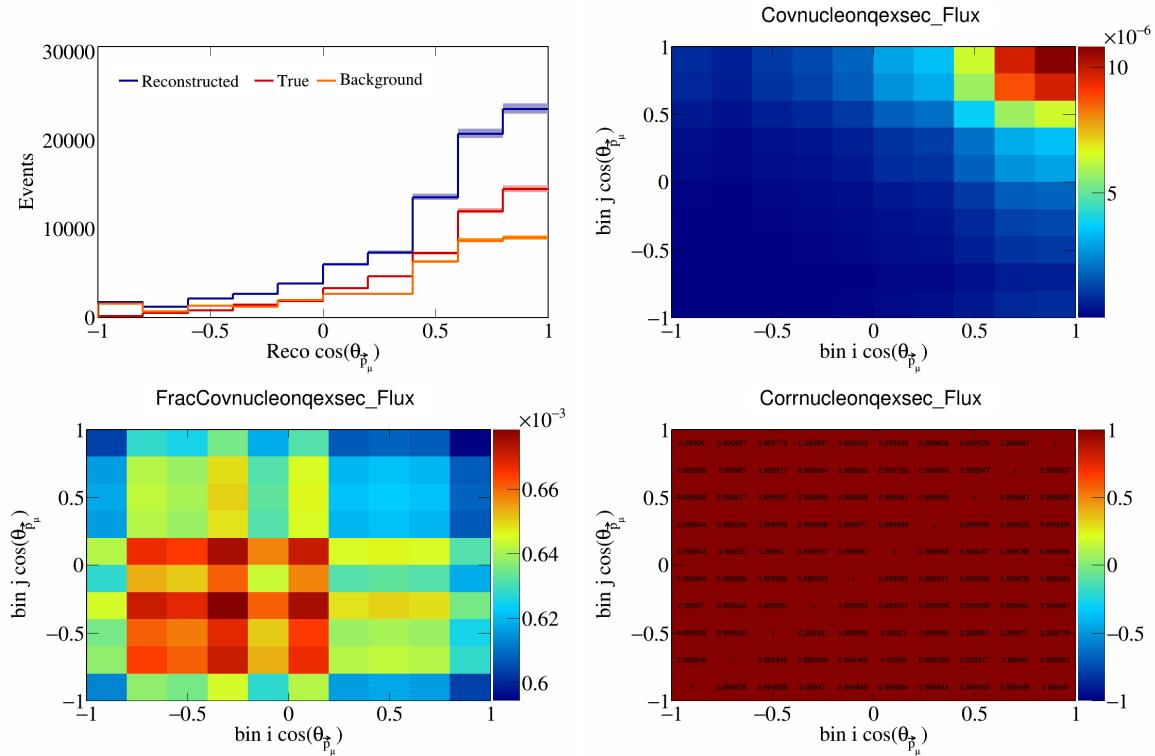


Figure 692: NucleonQeXSec variations for  $\cos(\theta_{\vec{p}_\mu})$ .

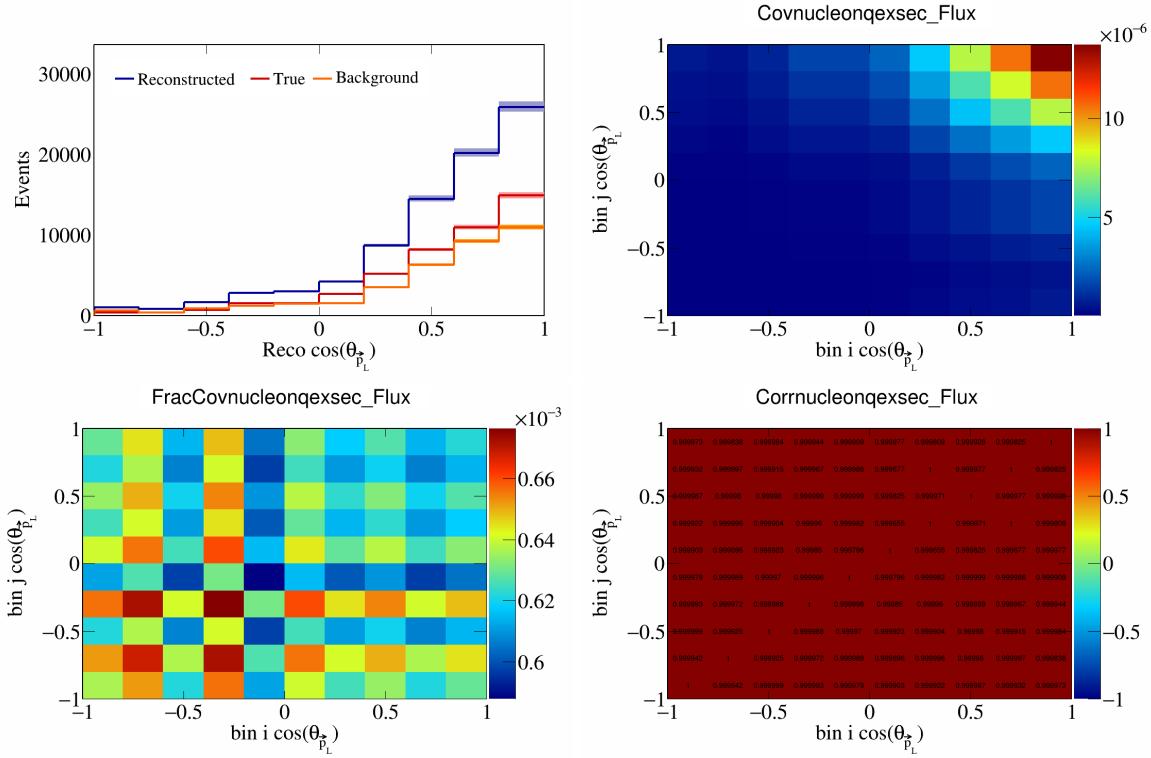


Figure 693: NucleonQeXSec variations for  $\cos(\theta_{\vec{p}_L})$ .

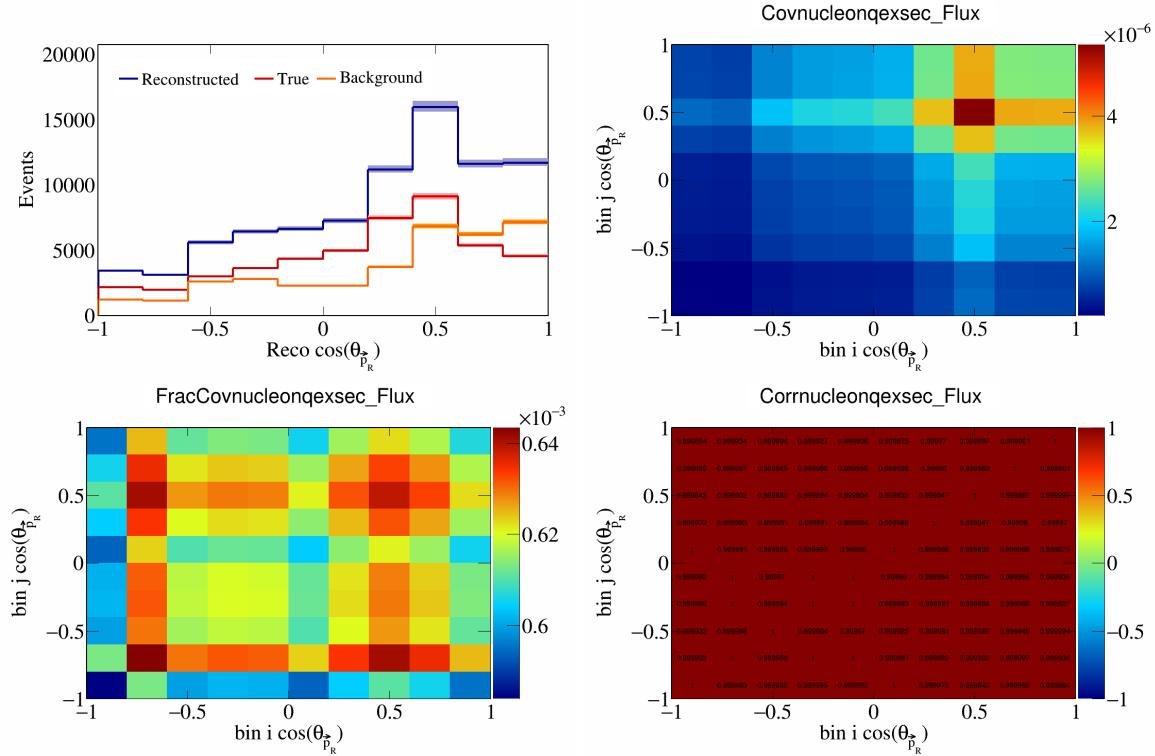


Figure 694: NucleonQeXSec variations for  $\cos(\theta_{\vec{p}_R})$ .

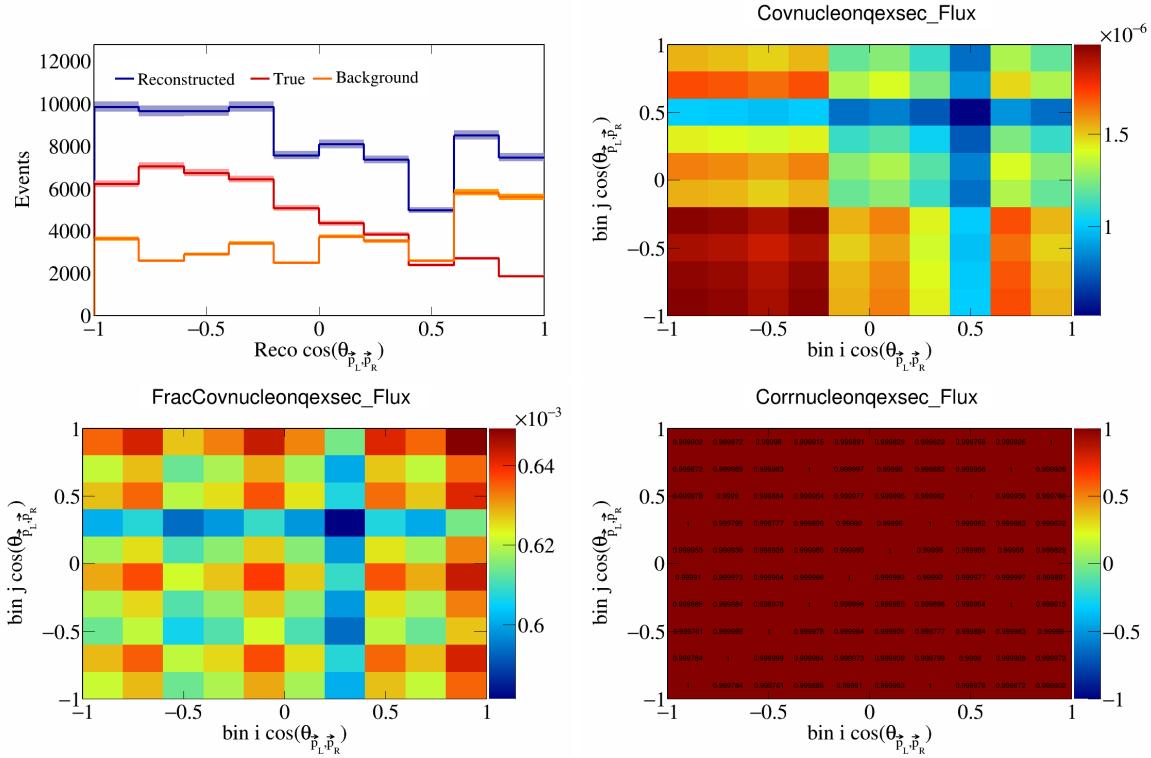


Figure 695: NucleonQeXSec variations for  $\cos(\theta_{\vec{p}_L, \vec{p}_R})$ .

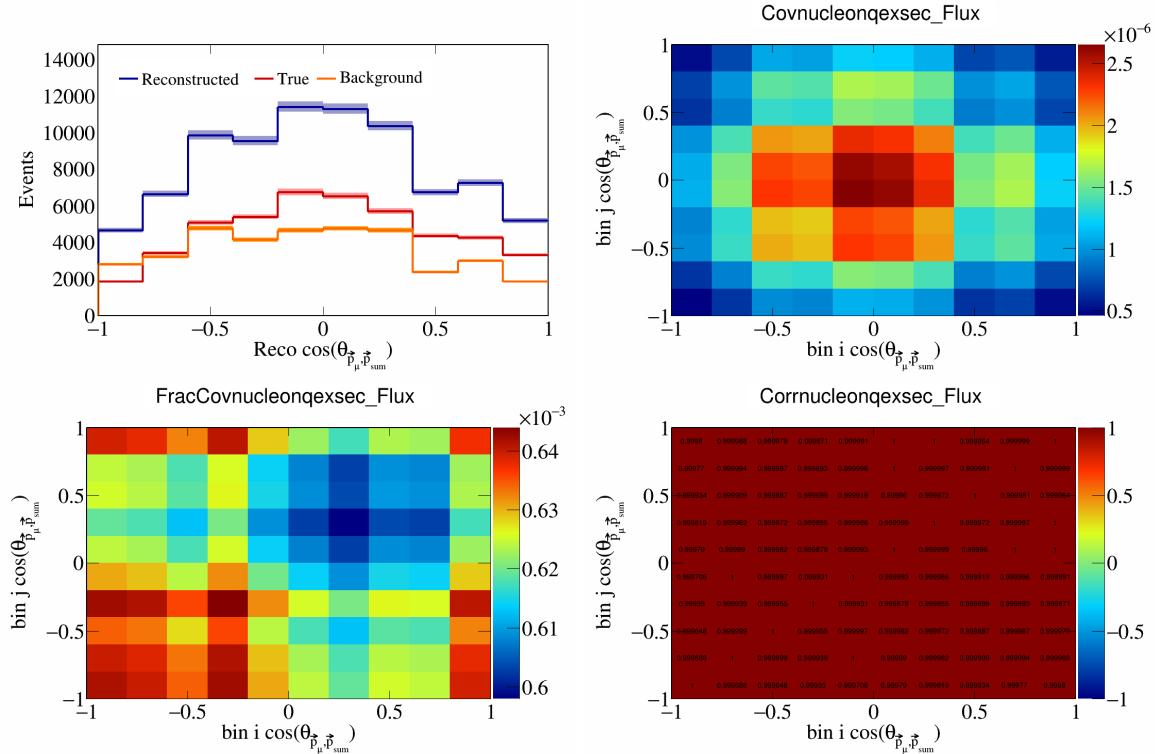


Figure 696: NucleonQeXSec variations for  $\cos(\theta_{\vec{p}_\mu, \vec{p}_{\text{sum}}})$ .

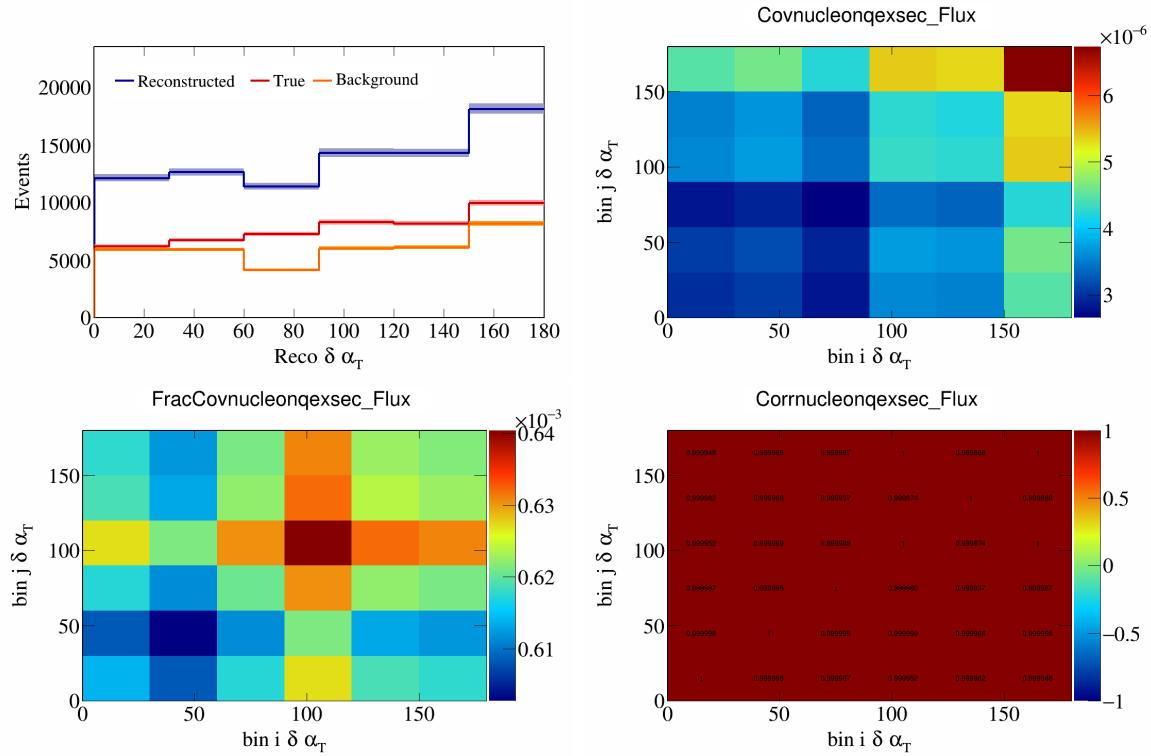


Figure 697: NucleonQeXSec variations for  $\delta\alpha_T$ .

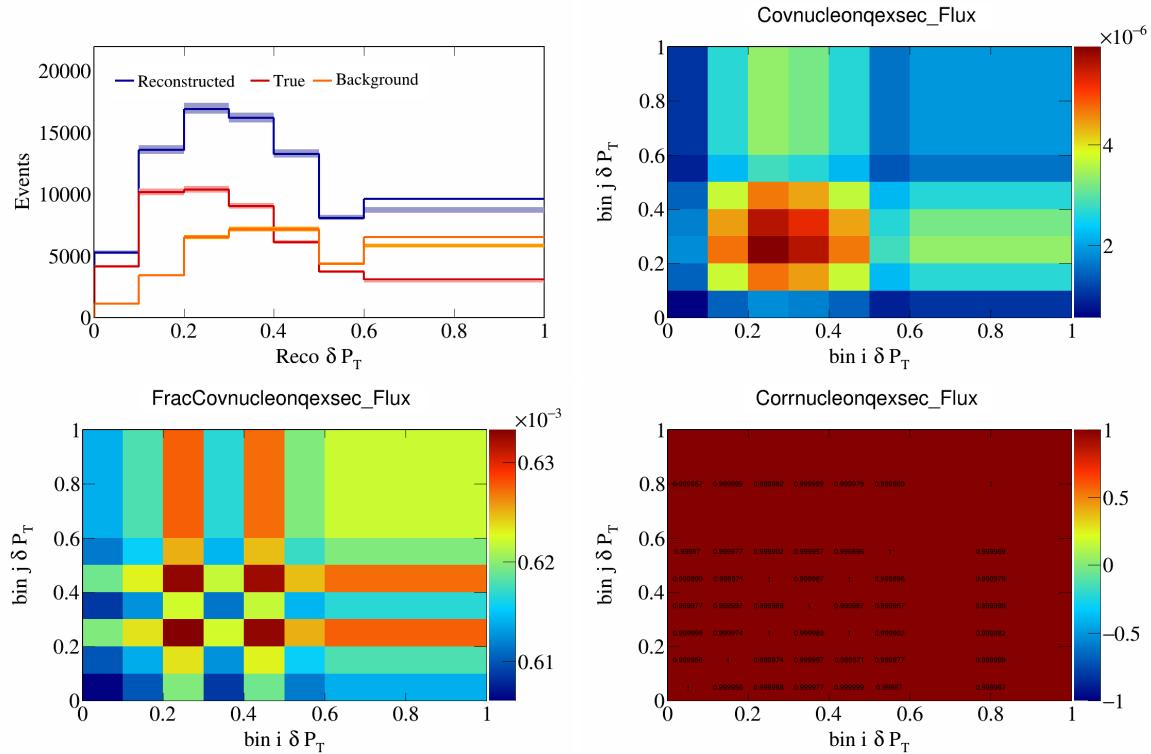


Figure 698: NucleonQeXSec variations for  $\delta P_T$ .

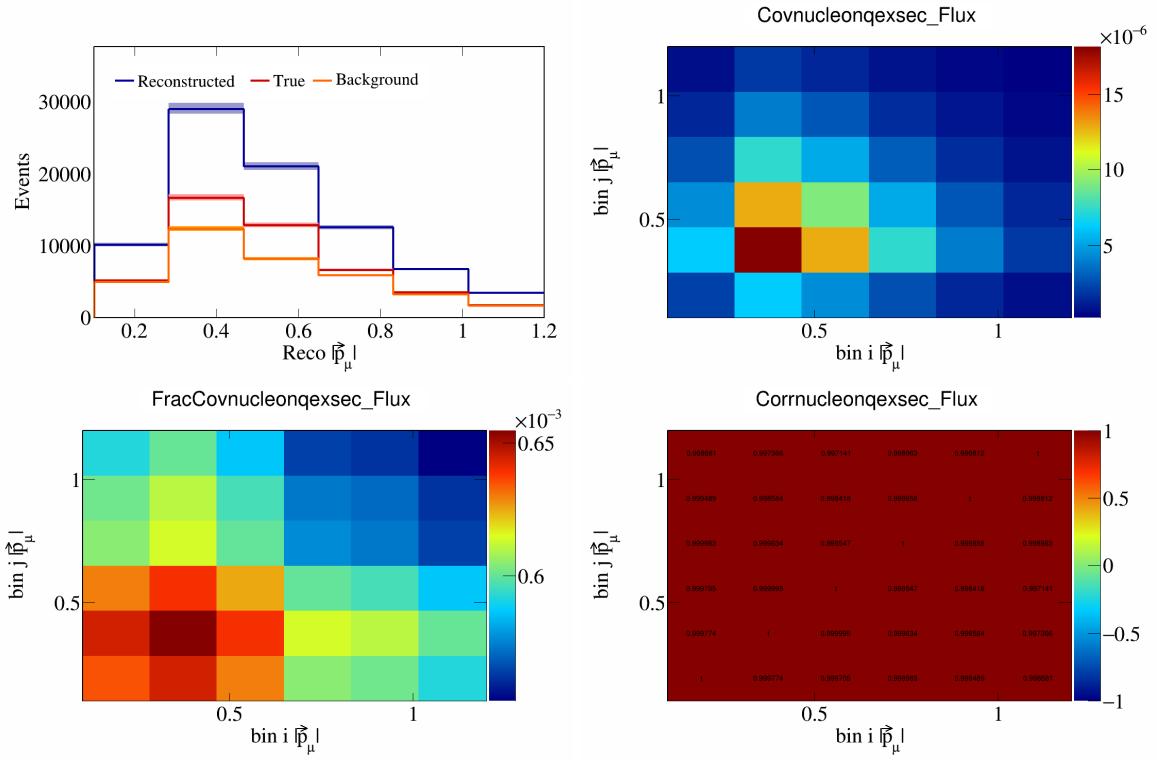


Figure 699: NucleonQeXSec variations for  $|\vec{p}_\mu|$ .

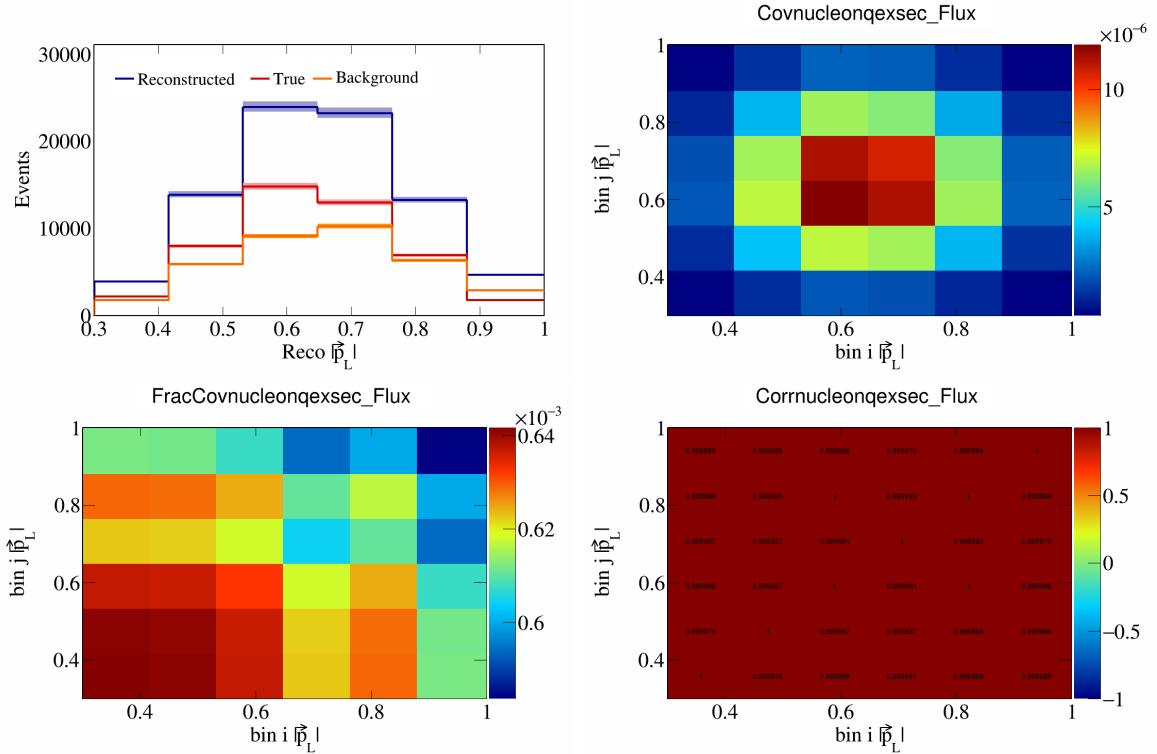


Figure 700: NucleonQeXSec variations for  $|\vec{p}_L|$ .

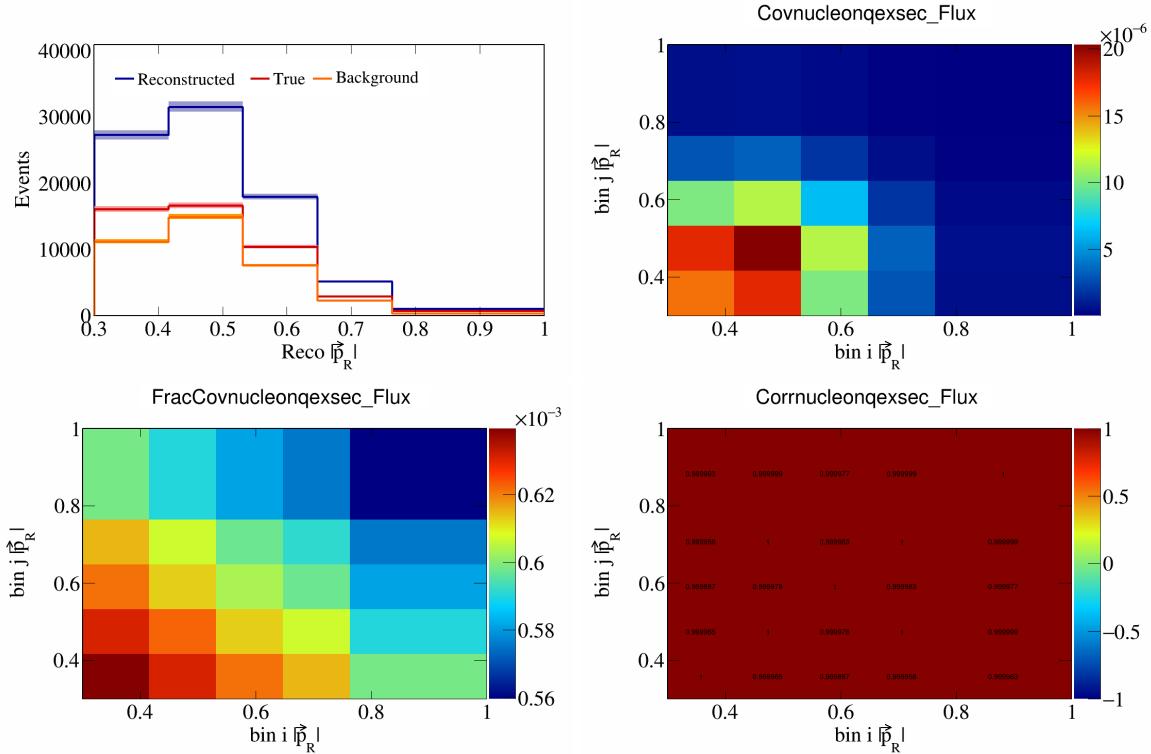


Figure 701: NucleonQeXSec variations for  $|\vec{p}_R|$ .

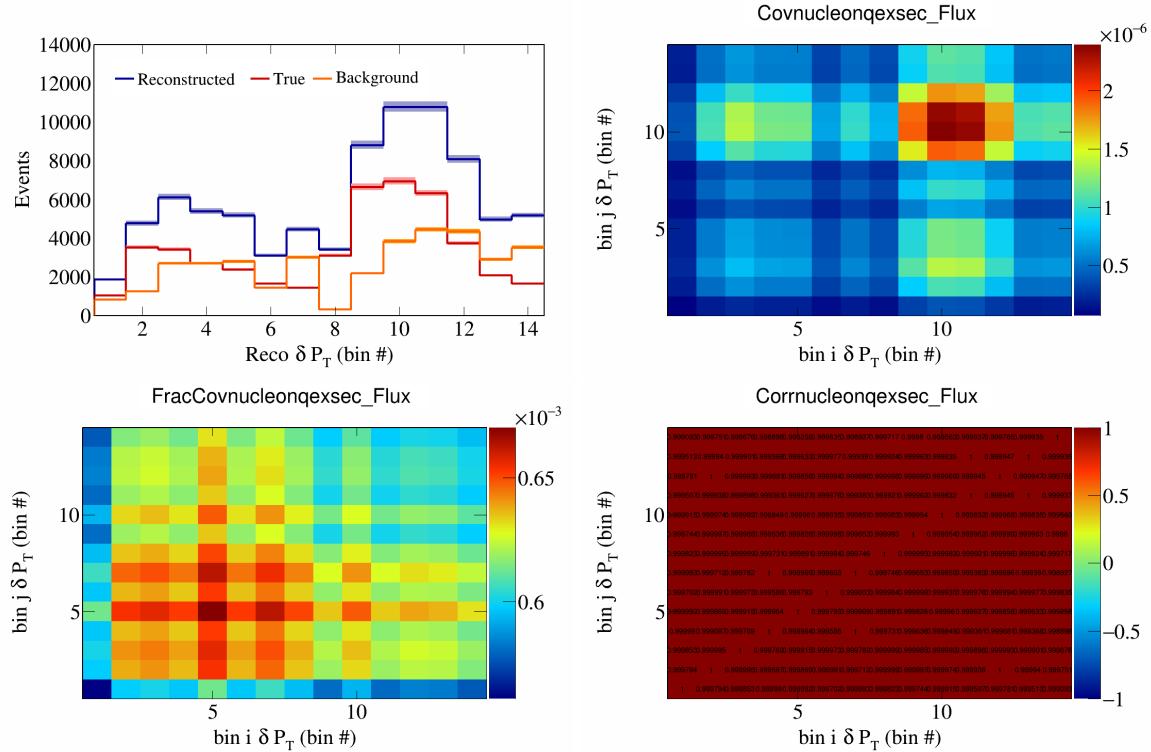


Figure 702: NucleonQeXSec variations for  $\delta P_T$  in  $\cos(\theta_{\vec{p}_R})$ .

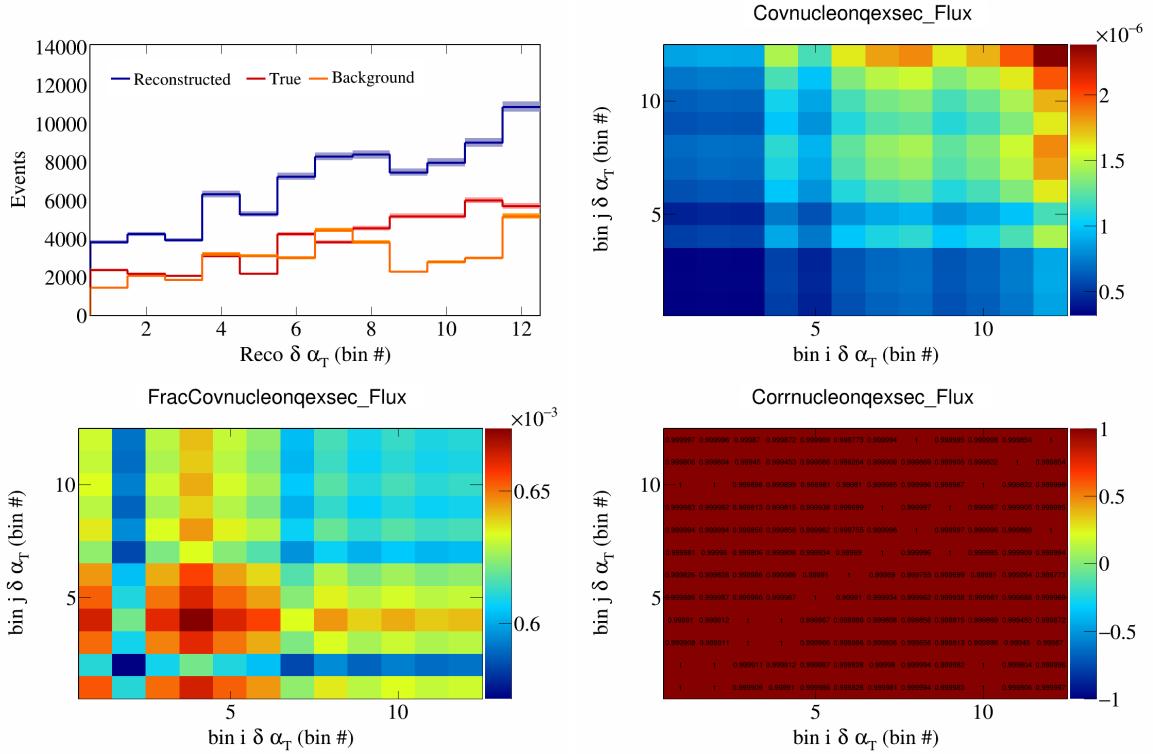


Figure 703: NucleonQeXSec variations for  $\delta\alpha_T$  in  $\cos(\theta_{\vec{p}_\mu})$ .

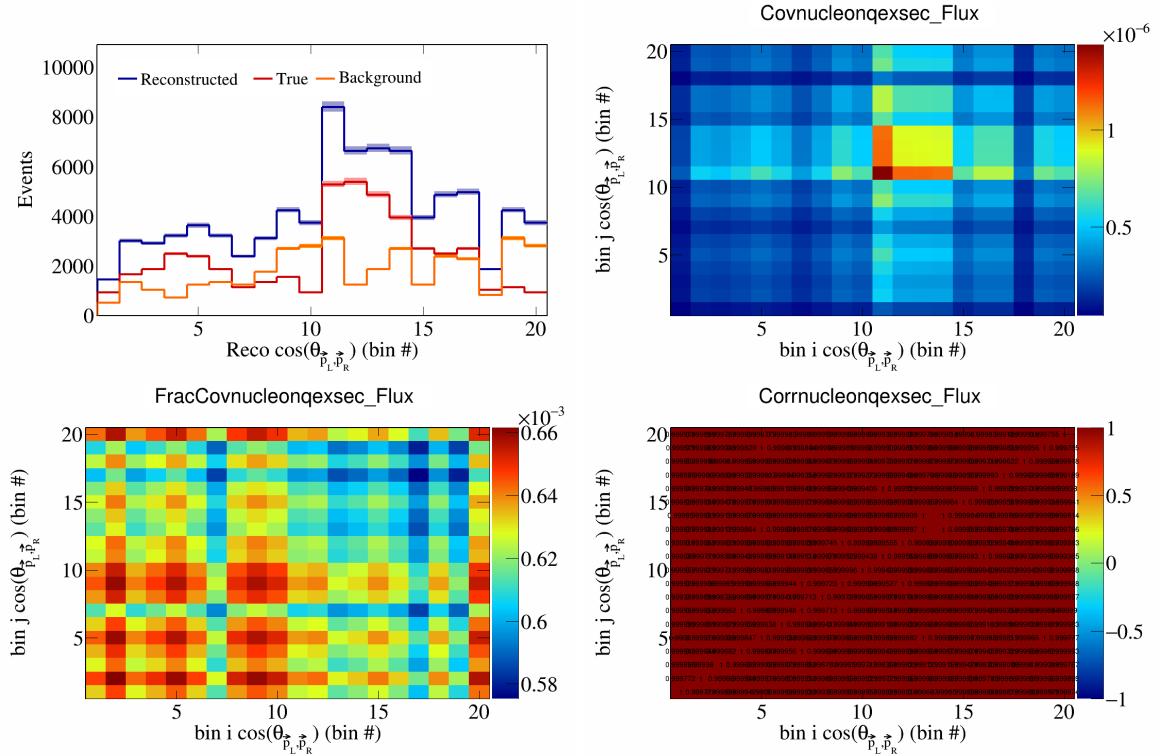


Figure 704: NucleonQeXSec variations for  $\cos(\theta_{\vec{p}_L, \vec{p}_R})$  in  $\cos(\theta_{\vec{p}_\mu})$ .

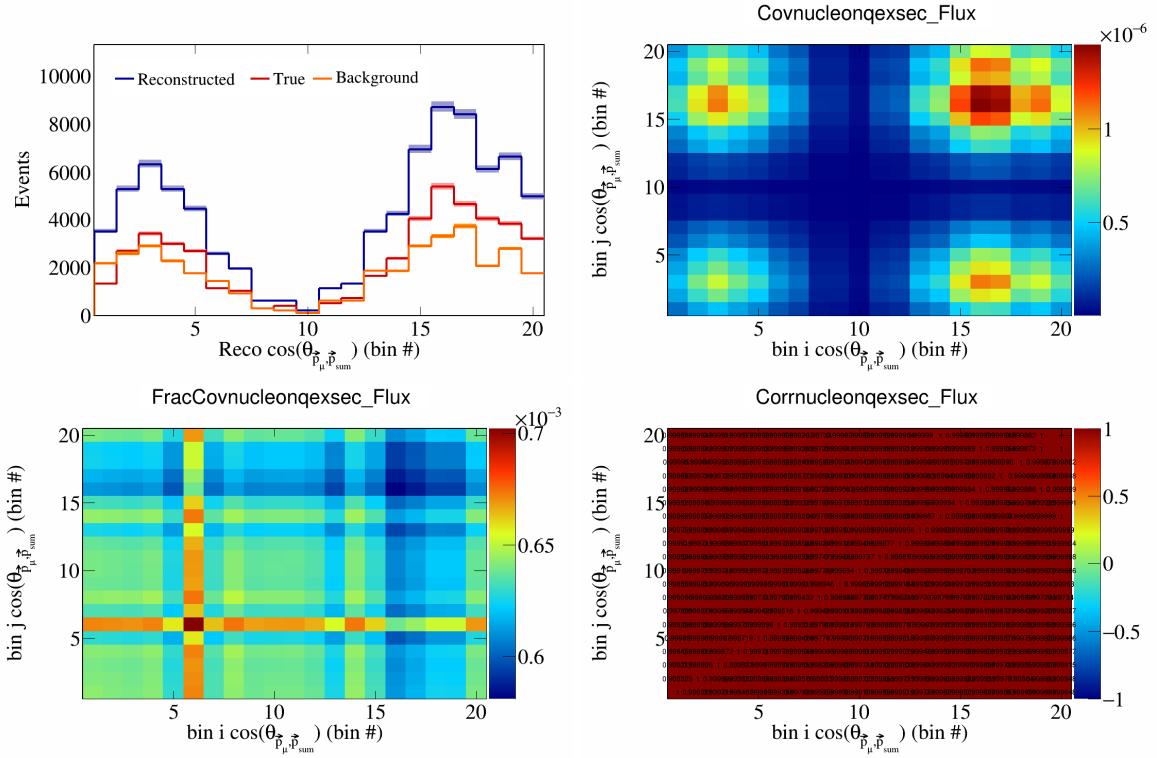


Figure 705: NucleonQeXSec variations for  $\cos(\theta_{\vec{p}_\mu, \vec{p}_{\text{sum}}})$  in  $\cos(\theta_{\vec{p}_\mu})$ .

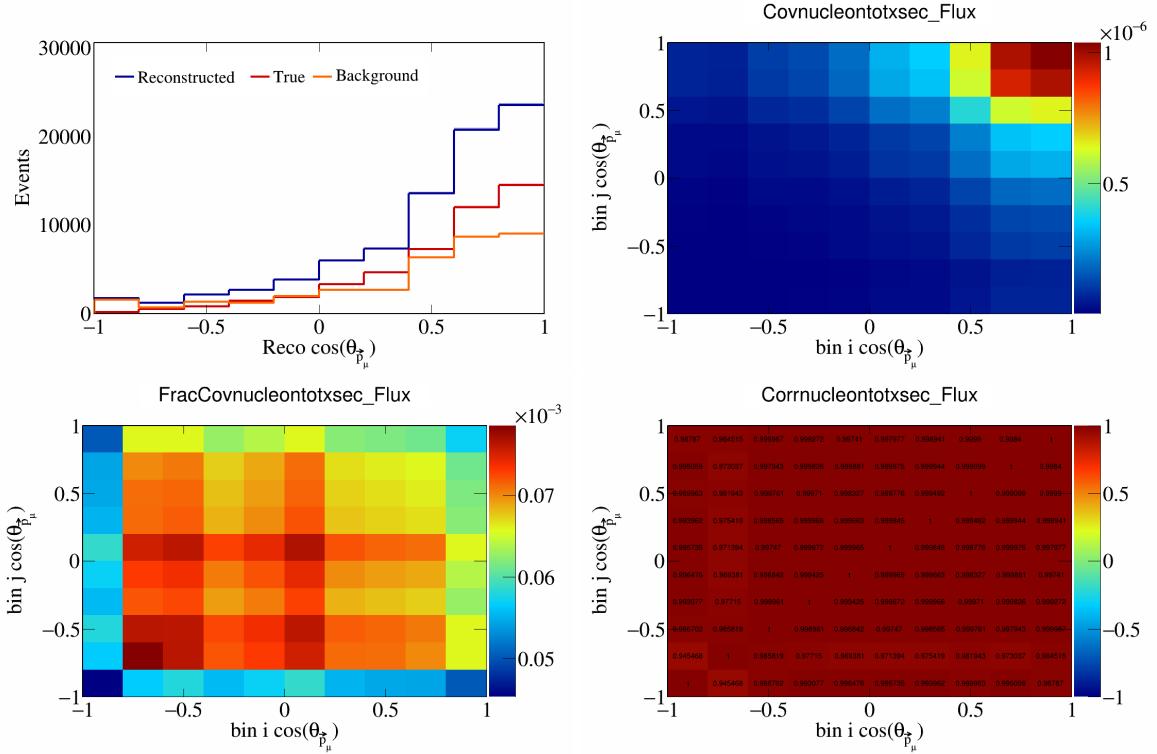


Figure 706: NucleonTotXSec variations for  $\cos(\theta_{\vec{p}_\mu})$ .

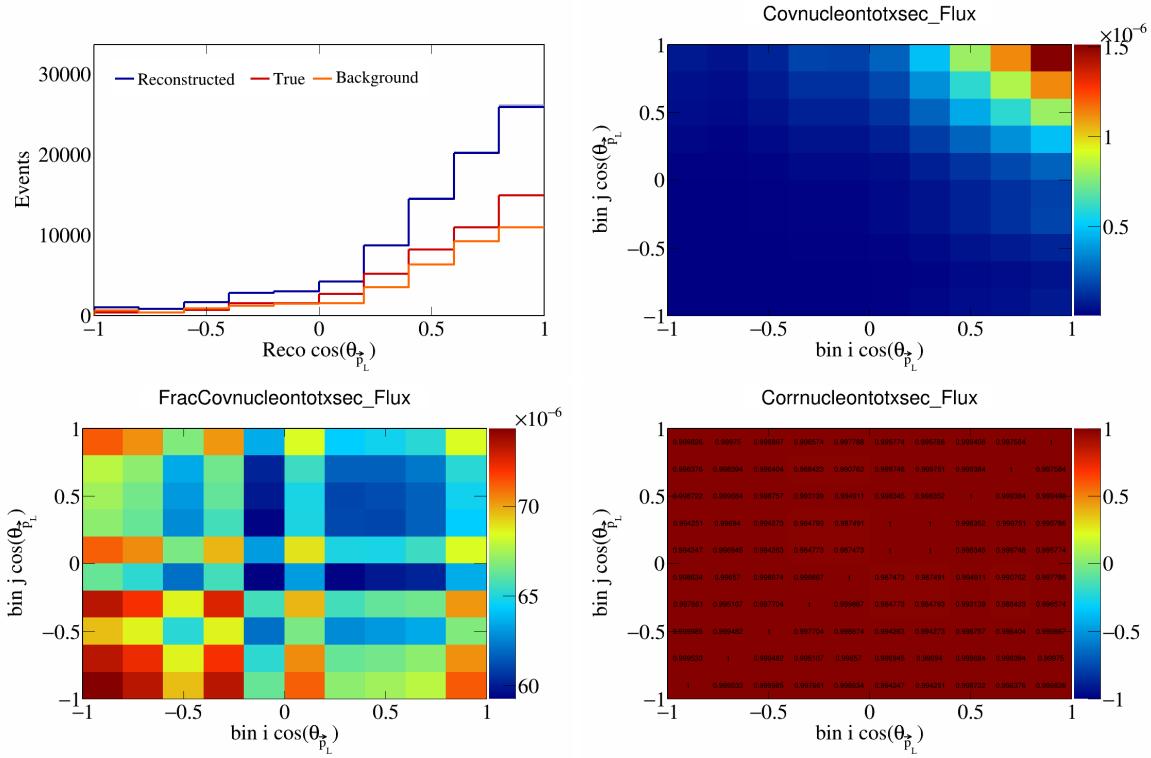


Figure 707: NucleonTotXSec variations for  $\cos(\theta_{\vec{p}_L})$ .

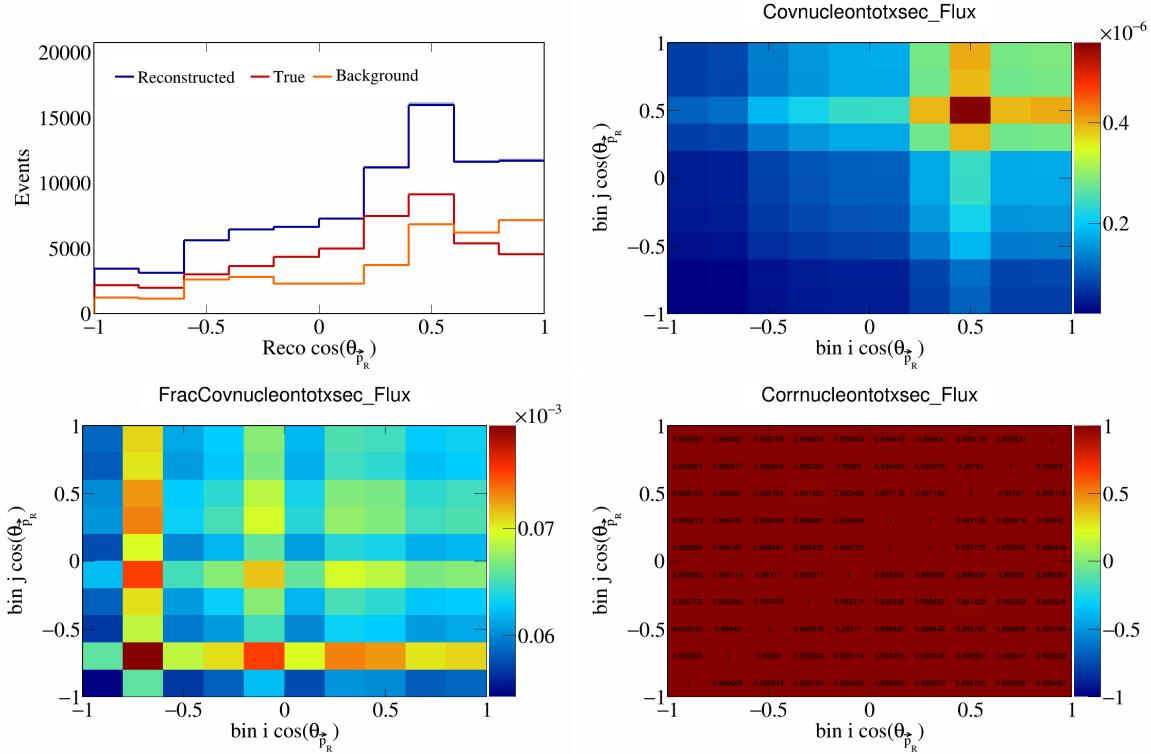


Figure 708: NucleonTotXSec variations for  $\cos(\theta_{\vec{p}_R})$ .

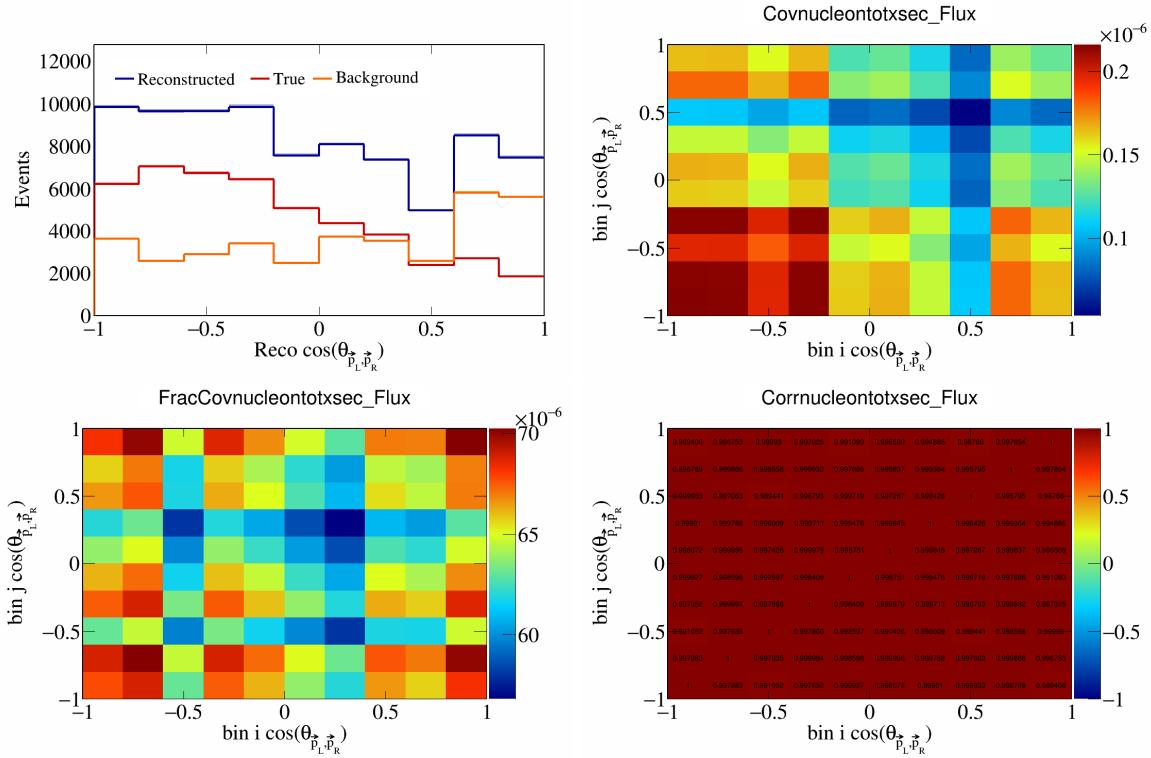


Figure 709: NucleonTotXSec variations for  $\cos(\theta_{\vec{p}_L, \vec{p}_R})$ .

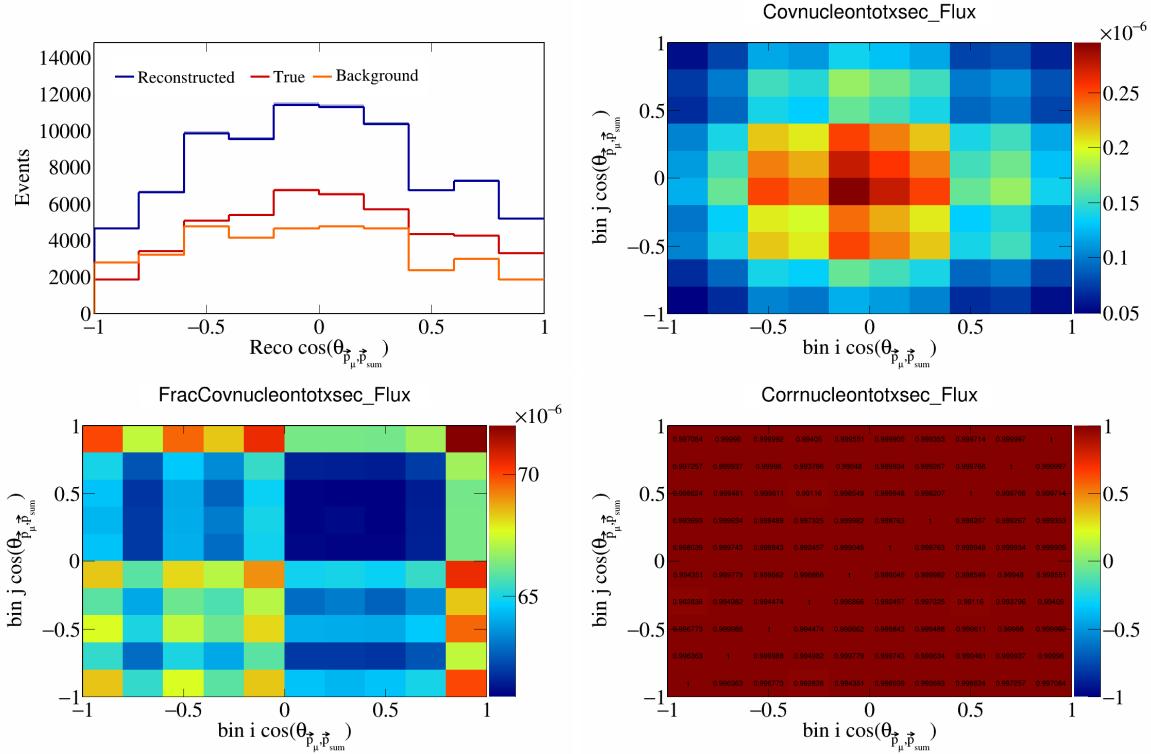


Figure 710: NucleonTotXSec variations for  $\cos(\theta_{\vec{p}_\mu, \vec{p}_{\text{sum}}})$ .

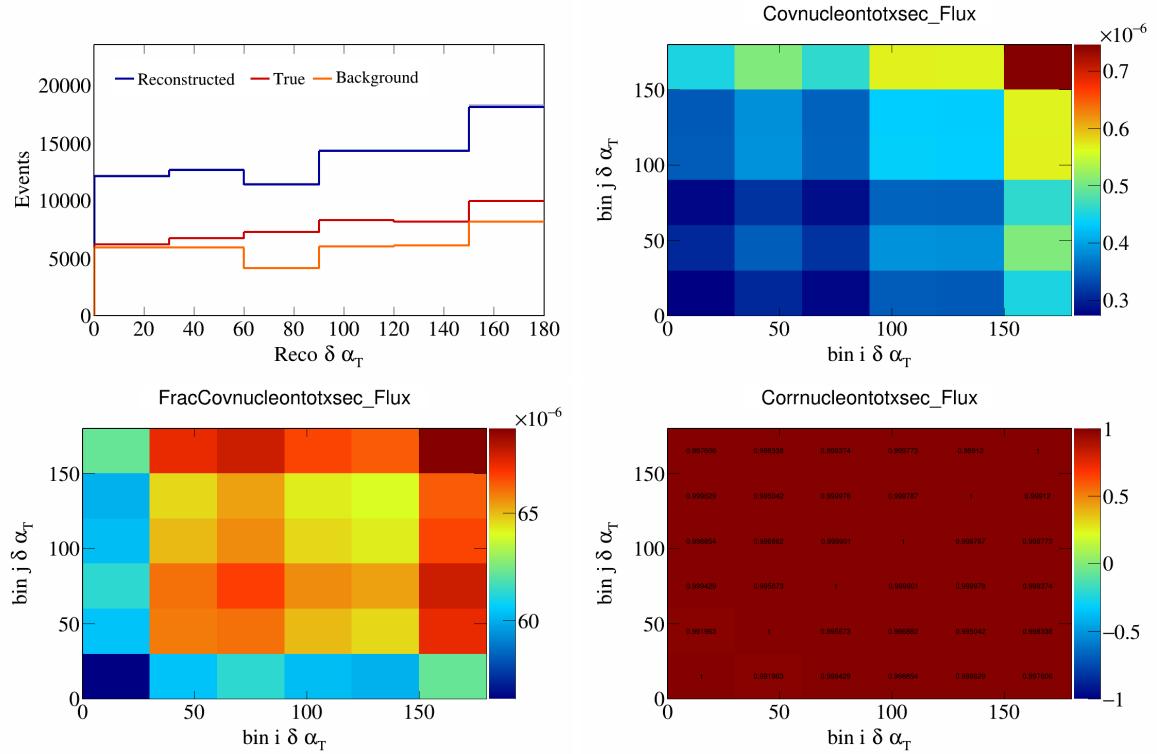


Figure 711: NucleonTotXSec variations for  $\delta \alpha_T$ .

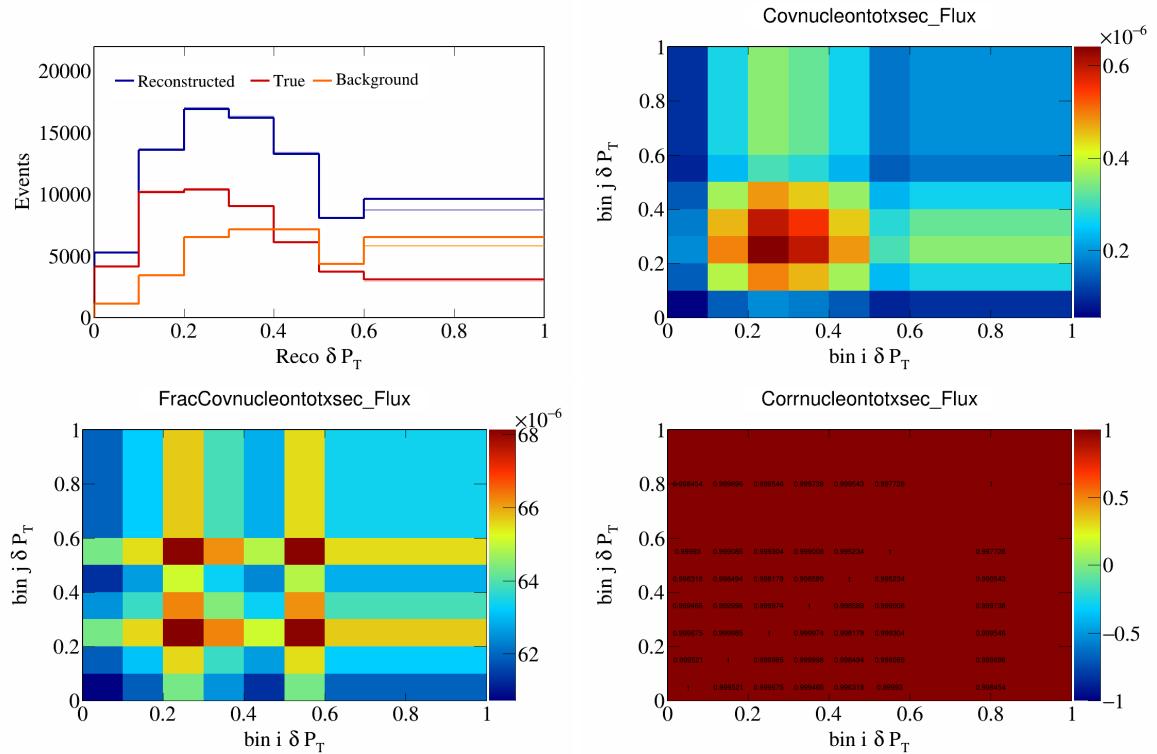


Figure 712: NucleonTotXSec variations for  $\delta P_T$ .

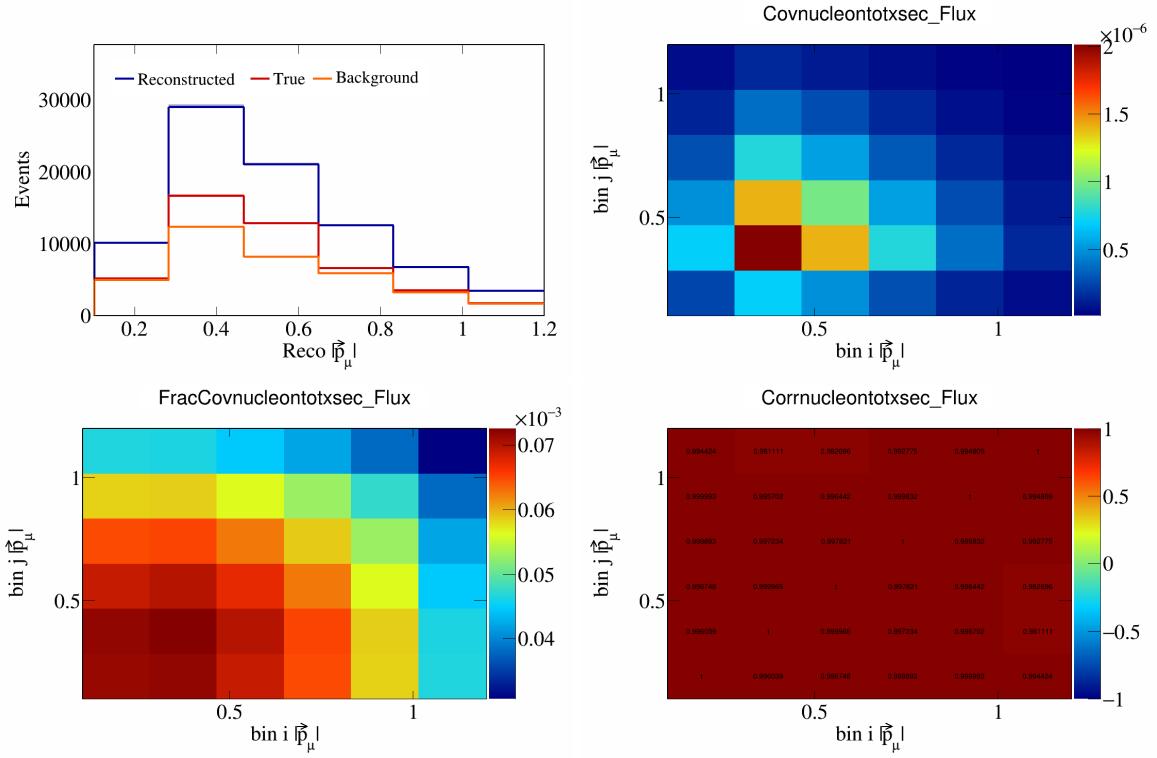


Figure 713: NucleonTotXSec variations for  $|\vec{p}_\mu|$ .

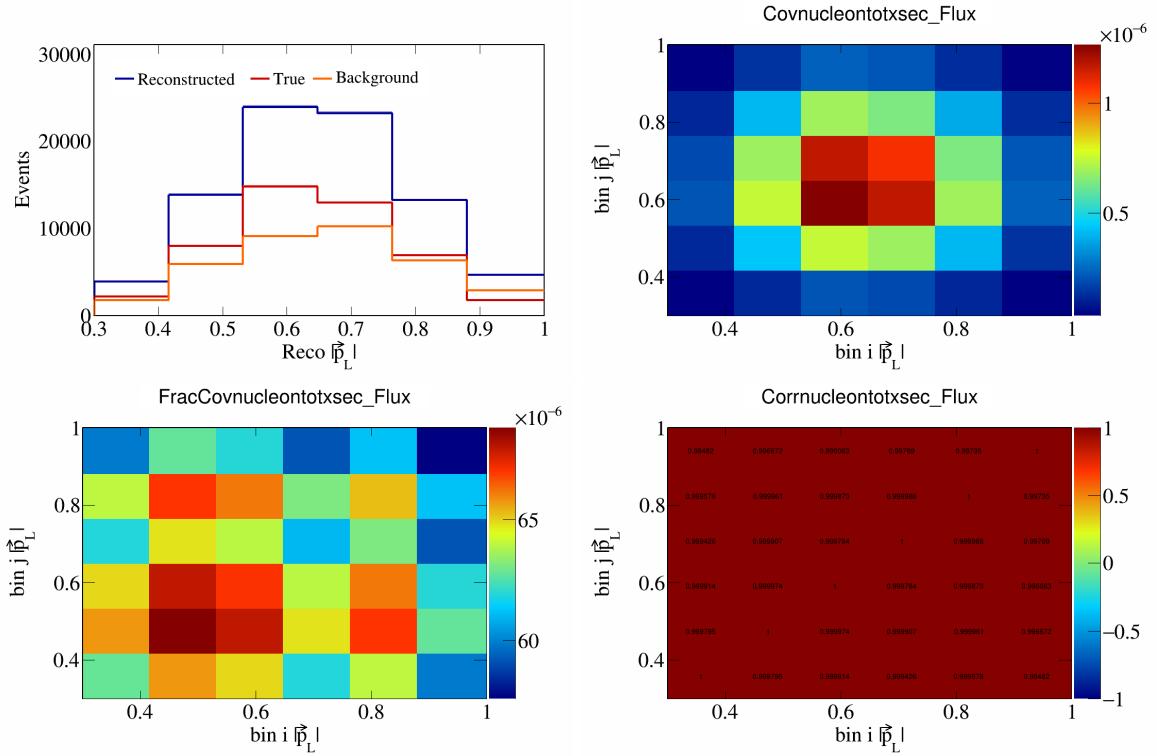


Figure 714: NucleonTotXSec variations for  $|\vec{p}_L|$ .

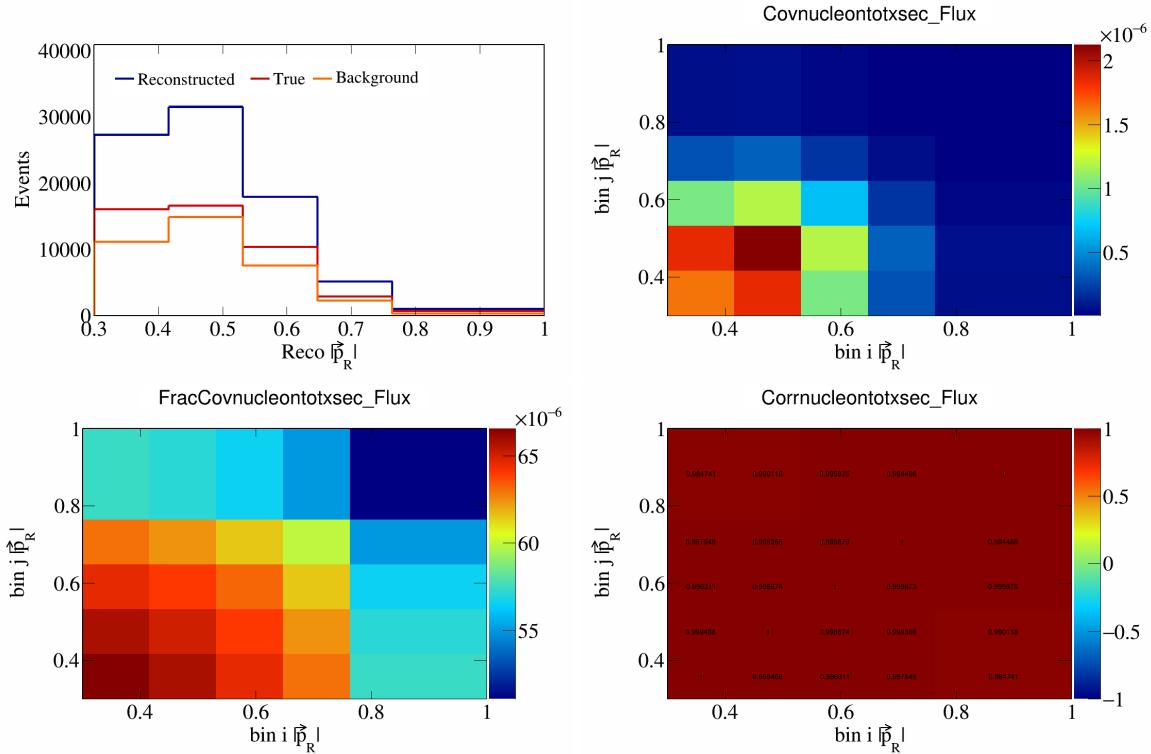


Figure 715: NucleonTotXSec variations for  $|\vec{p}_R|$ .

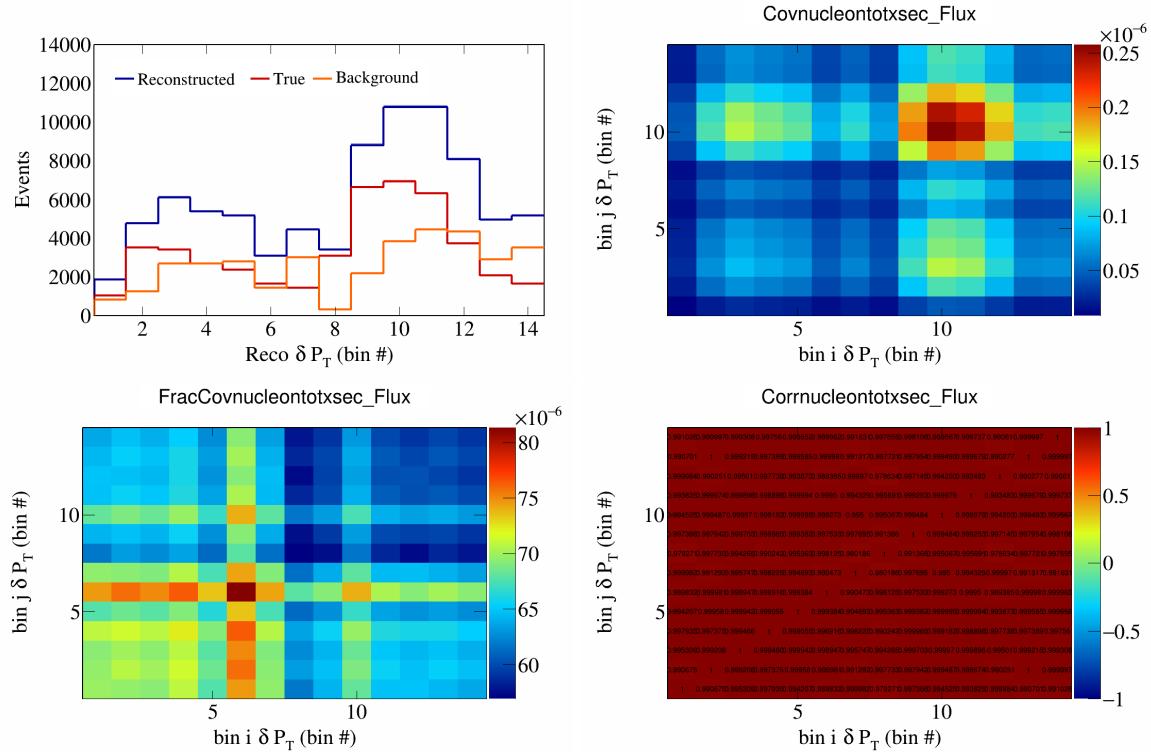


Figure 716: NucleonTotXSec variations for  $\delta P_T$  in  $\cos(\theta_{\vec{P}_\mu})$ .

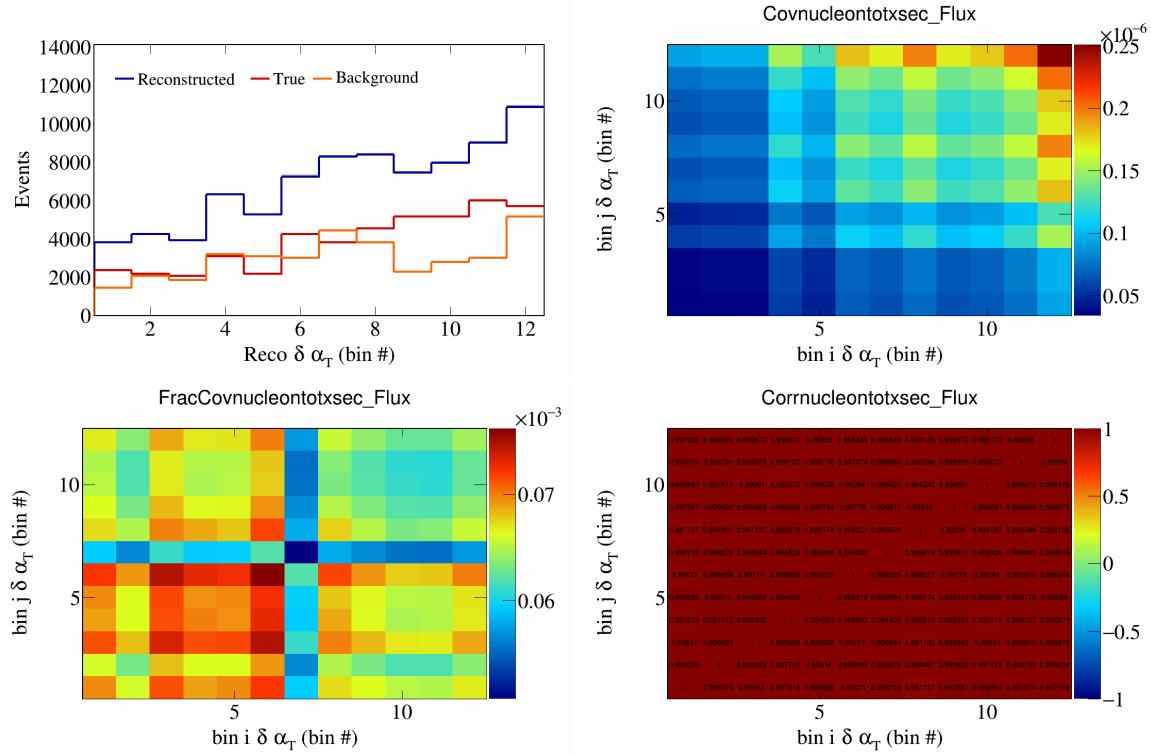


Figure 717: NucleonTotXSec variations for  $\delta\alpha_T$  in  $\cos(\theta_{\vec{p}_\mu})$ .

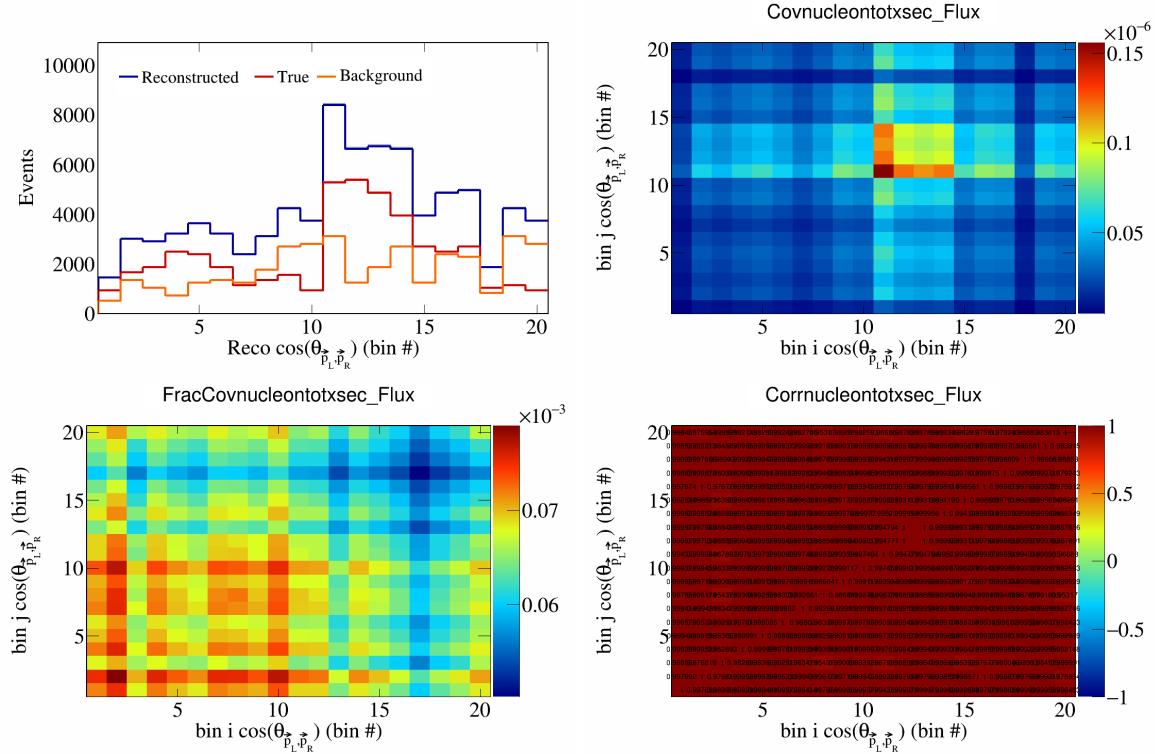


Figure 718: NucleonTotXSec variations for  $\cos(\theta_{\vec{p}_L, \vec{p}_R})$  in  $\cos(\theta_{\vec{p}_\mu})$ .

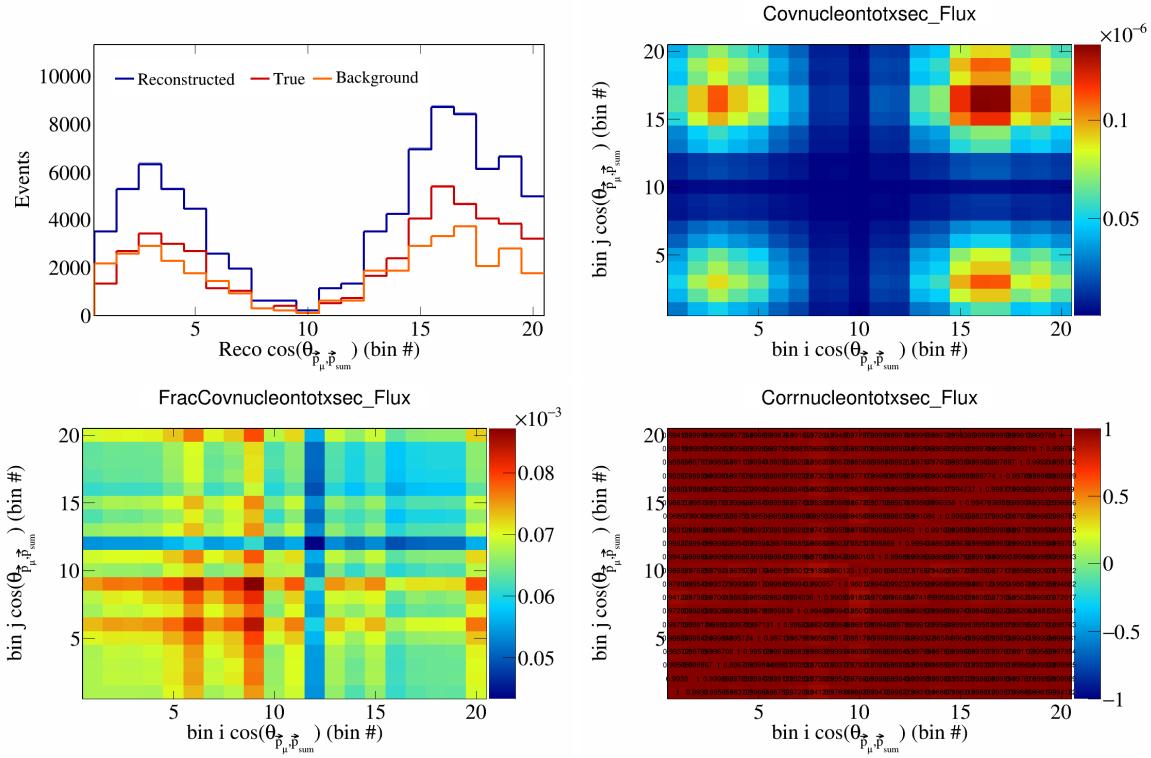


Figure 719: NucleonTotXSec variations for  $\cos(\theta_{\vec{p}_\mu, \vec{p}_{\text{sum}}})$  in  $\cos(\theta_{\vec{p}_\mu})$ .

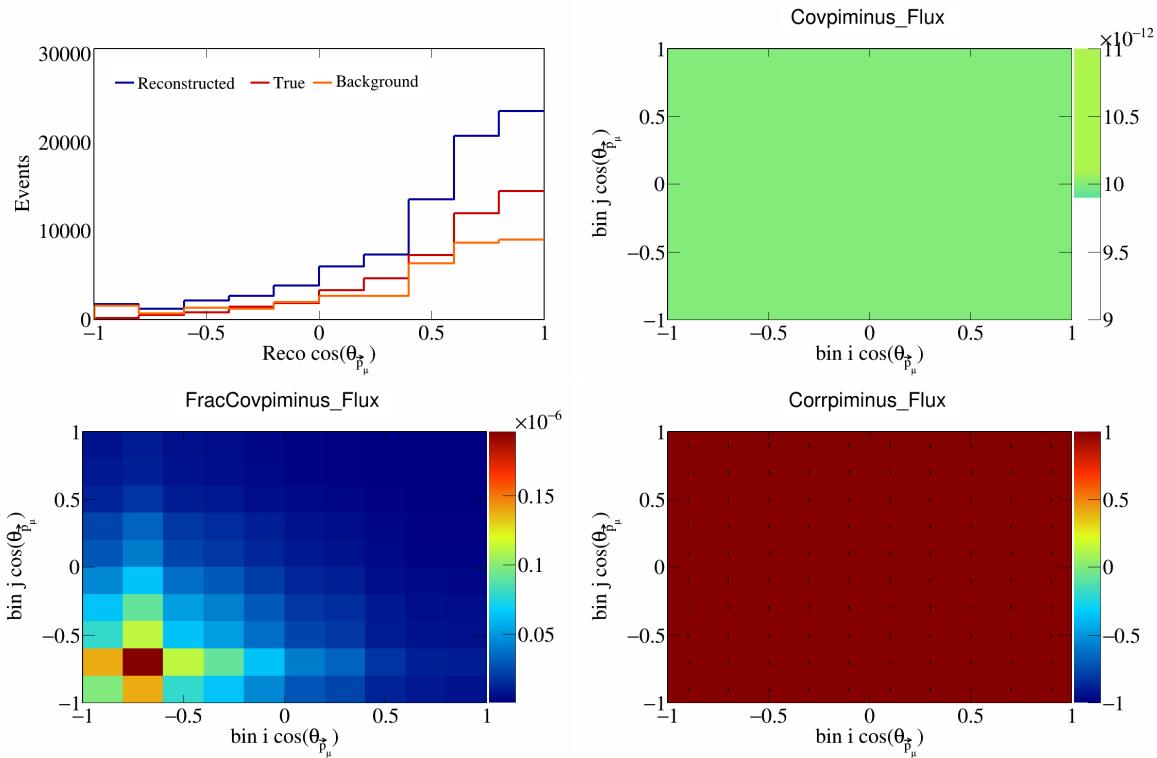


Figure 720: PiMinus variations for  $\cos(\theta_{\vec{p}_\mu})$ .

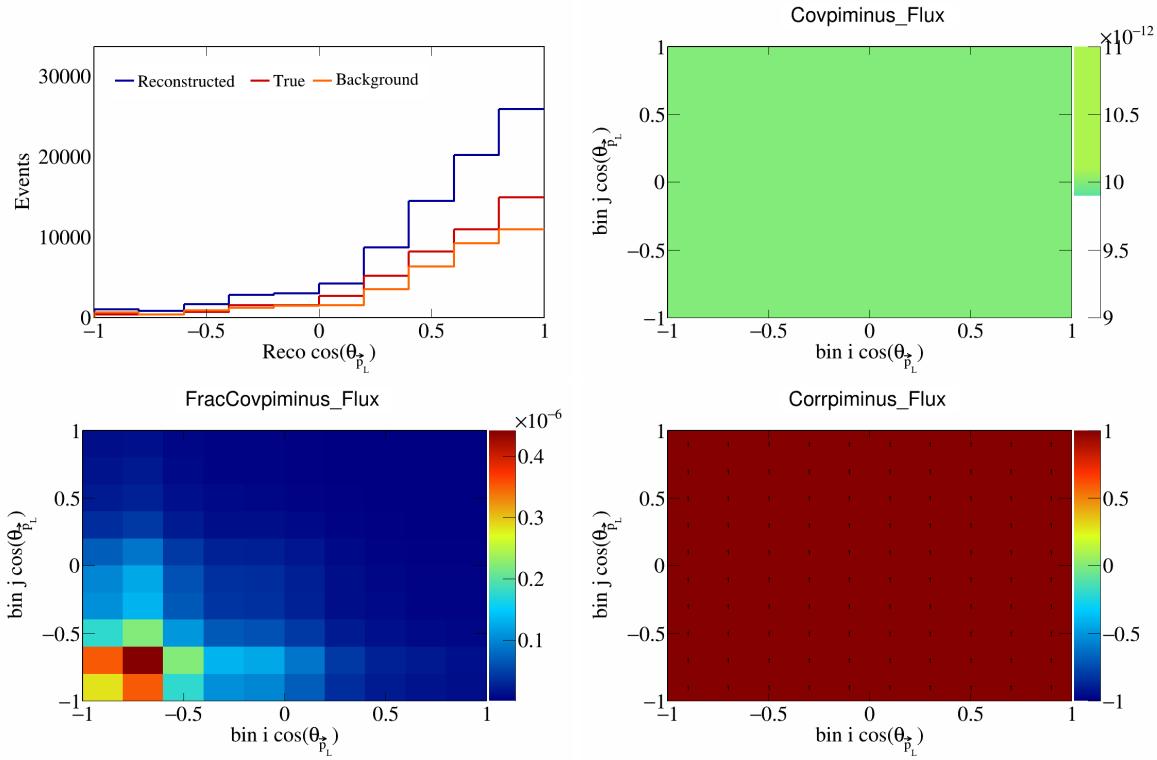


Figure 721: PiMinus variations for  $\cos(\theta_{\vec{p}_L})$ .

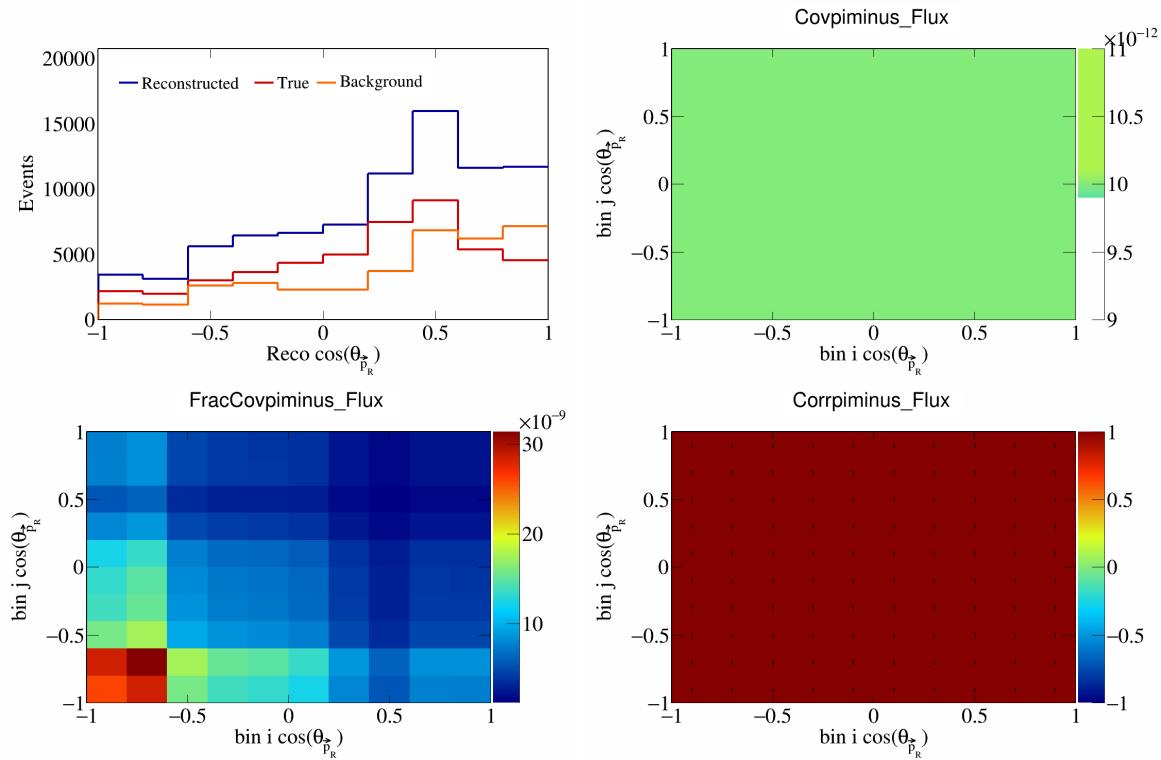


Figure 722: PiMinus variations for  $\cos(\theta_{\vec{p}_R})$ .

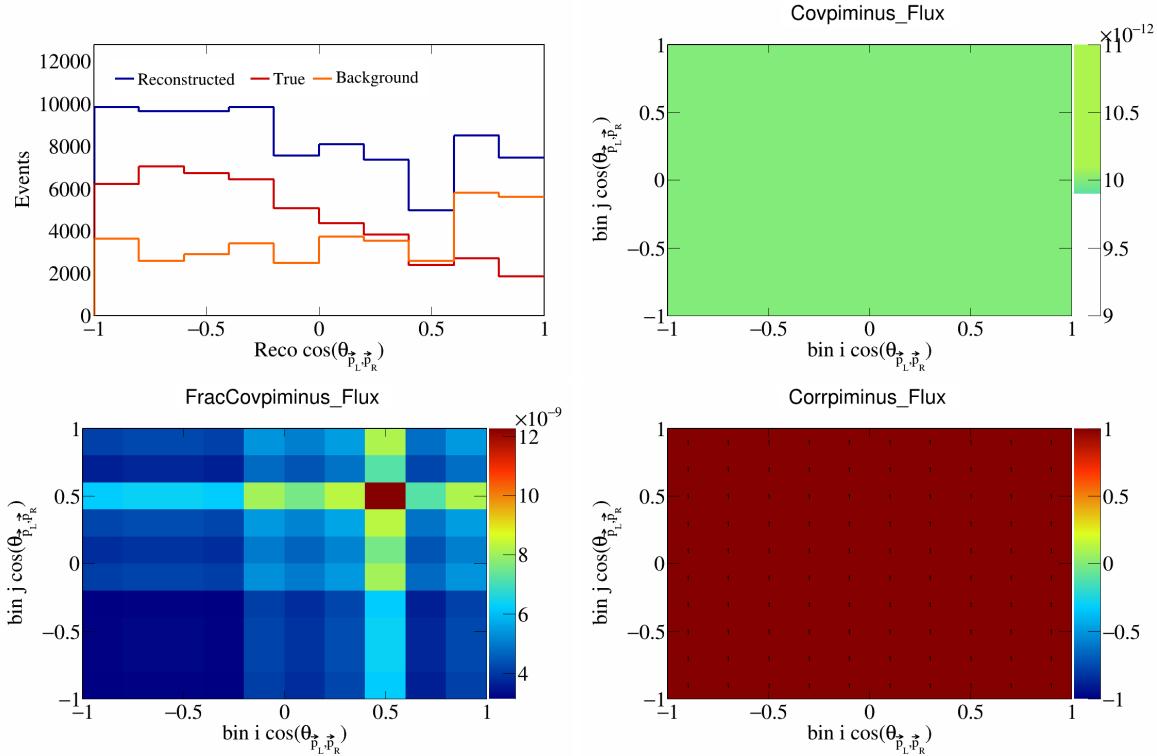


Figure 723: PiMinus variations for  $\cos(\theta_{\vec{p}_L, \vec{p}_R})$ .

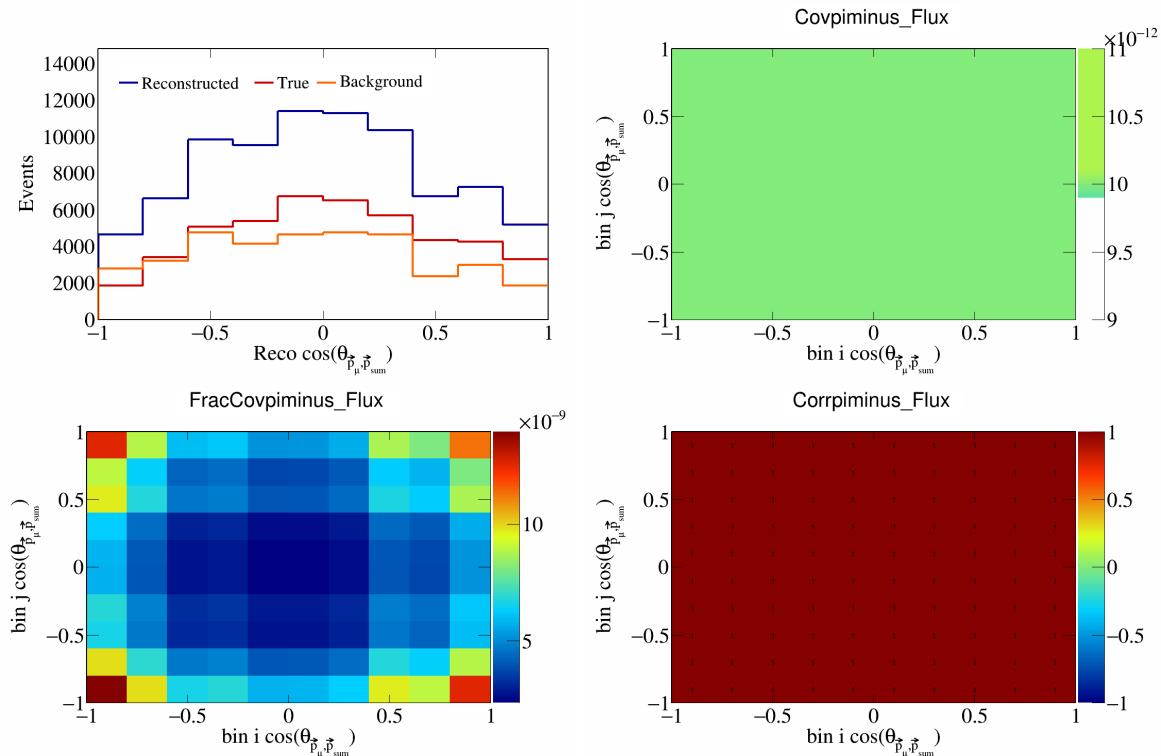


Figure 724: PiMinus variations for  $\cos(\theta_{\vec{p}_\mu, \vec{p}_{\text{sum}}})$ .

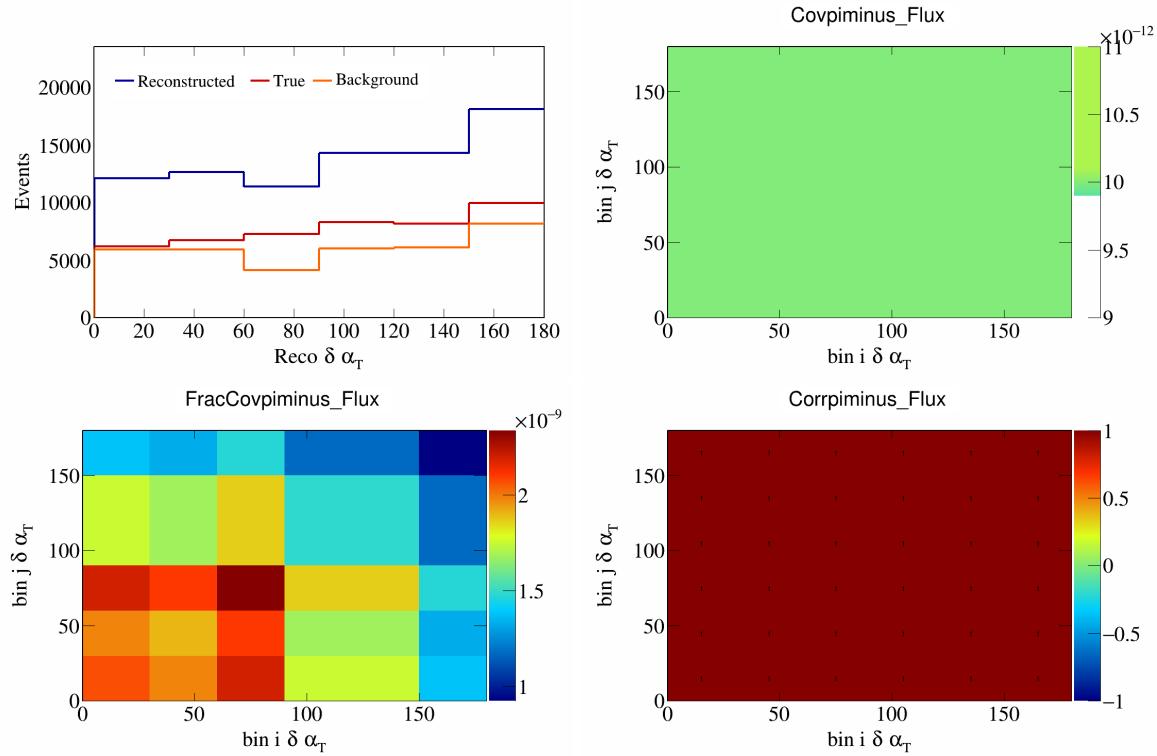


Figure 725: PiMinus variations for  $\delta\alpha_T$ .

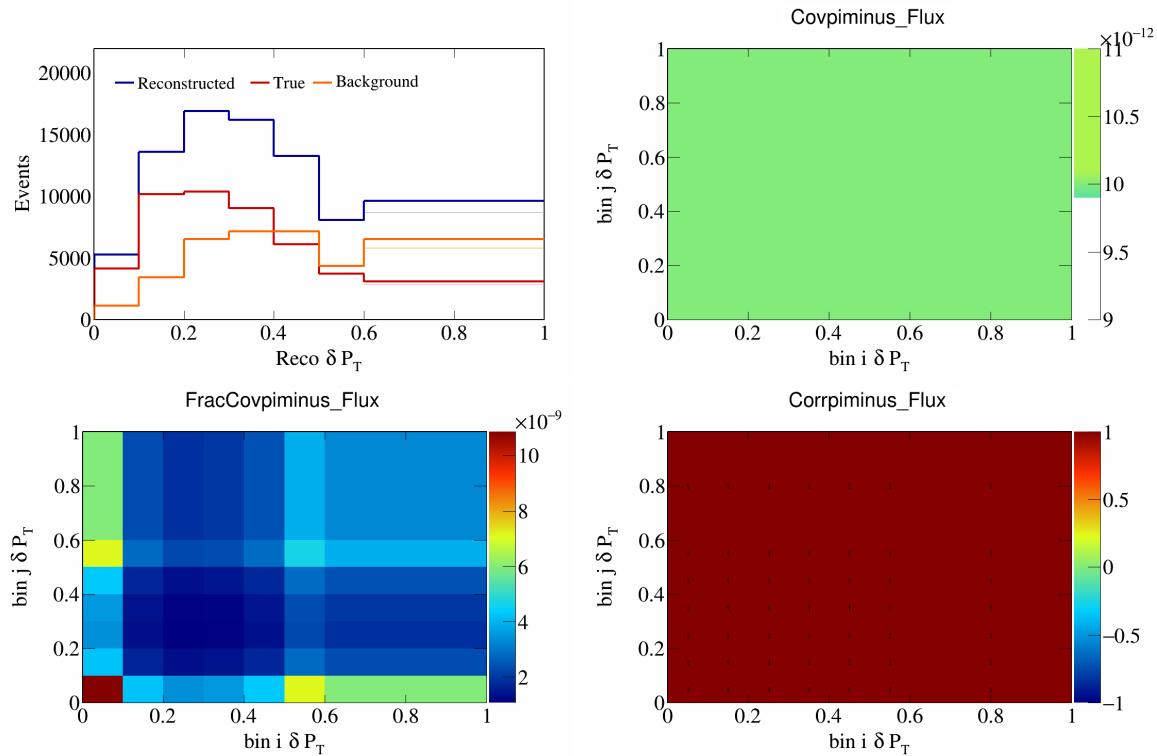


Figure 726: PiMinus variations for  $\delta P_T$ .

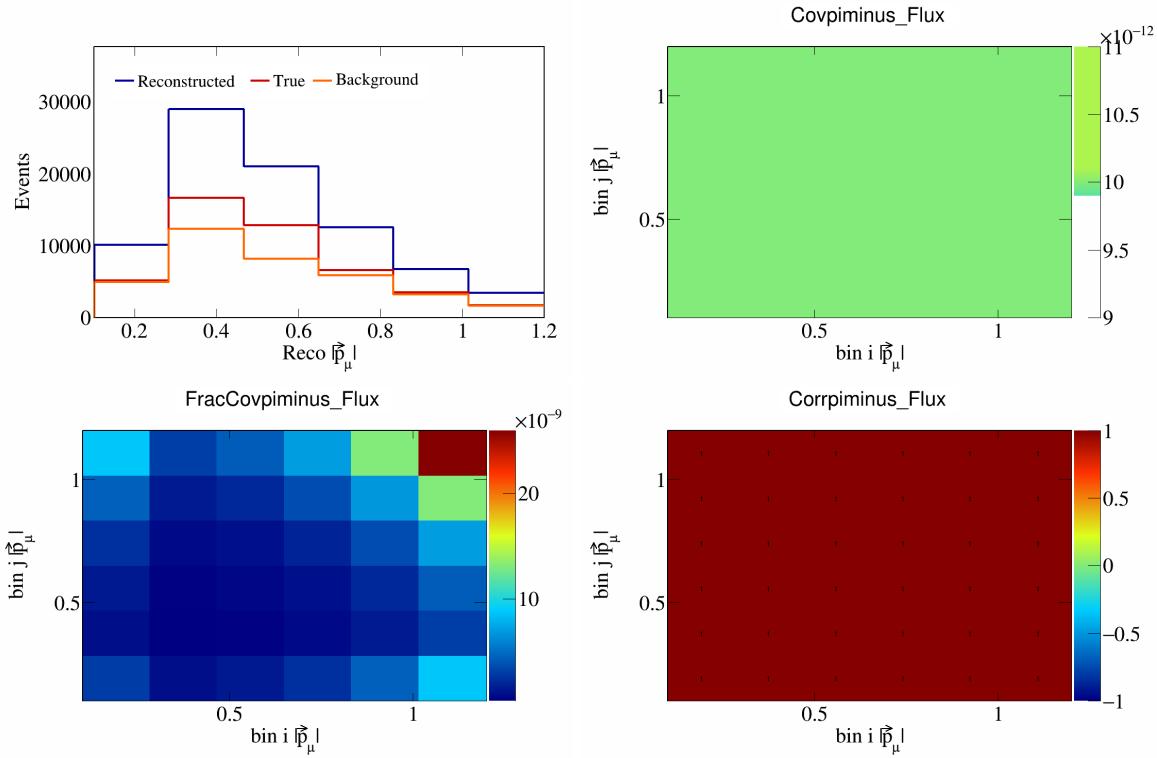


Figure 727: PiMinus variations for  $|\vec{p}_\mu|$ .

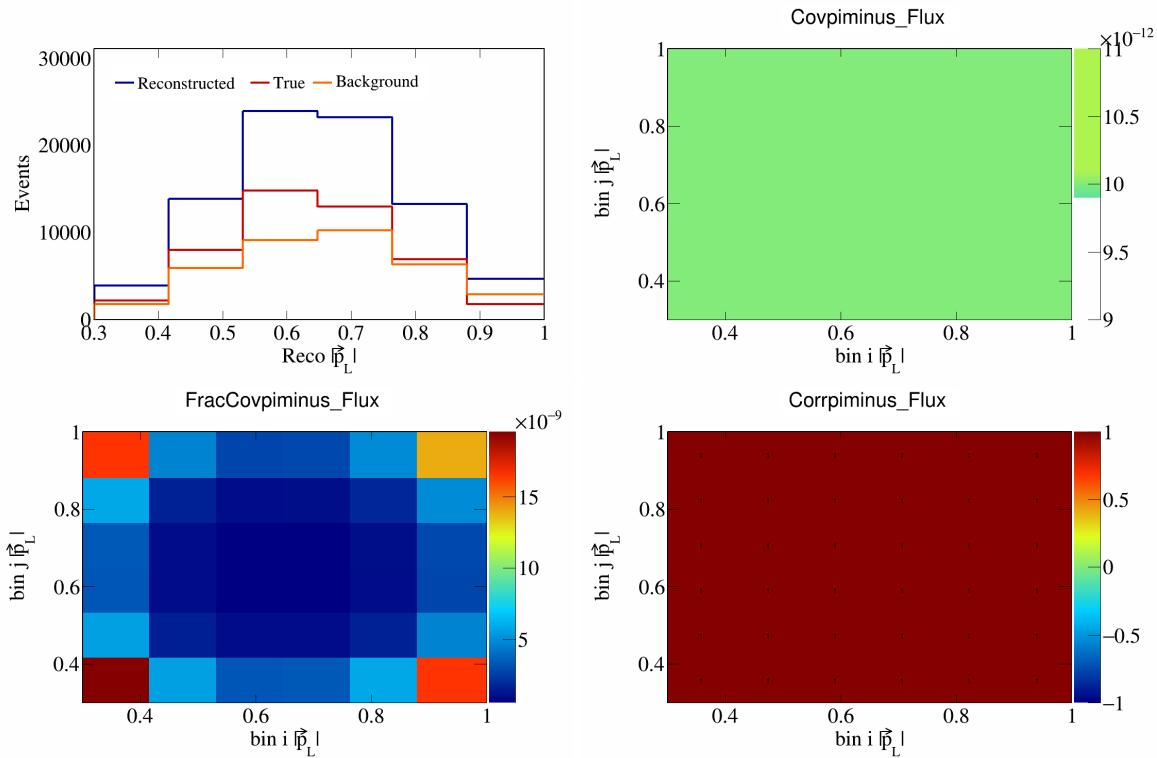


Figure 728: PiMinus variations for  $|\vec{p}_L|$ .

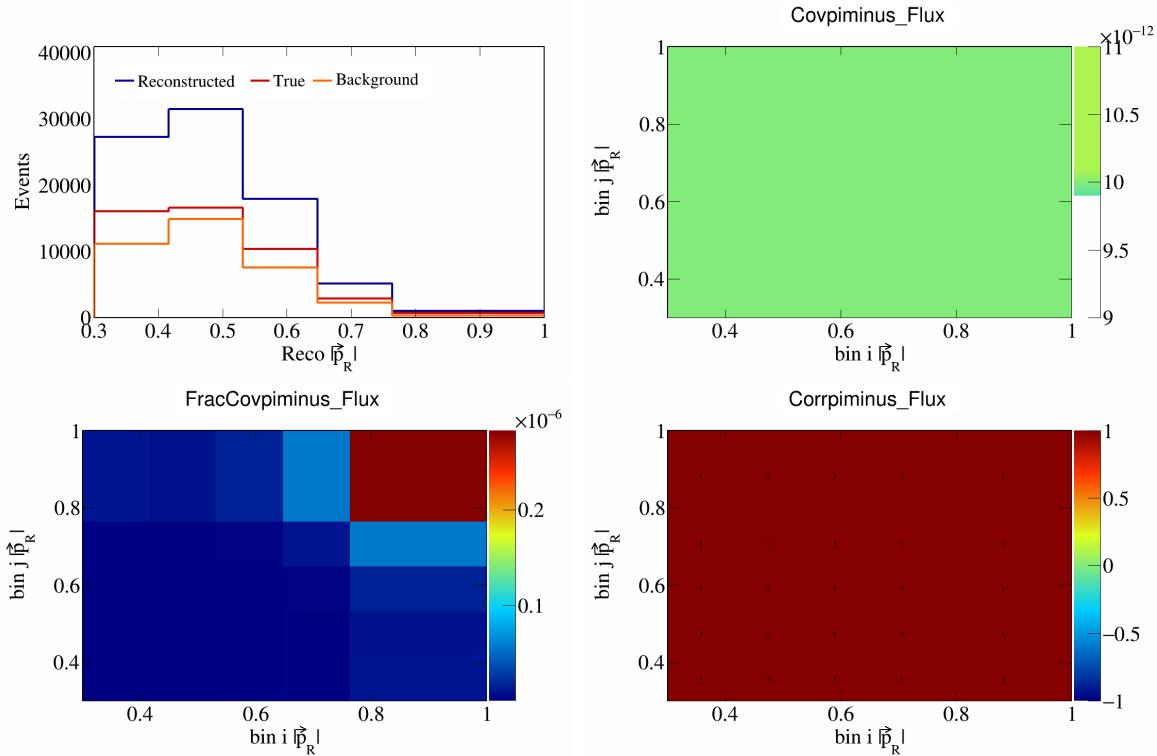


Figure 729: PiMinus variations for  $|\vec{p}_R|$ .

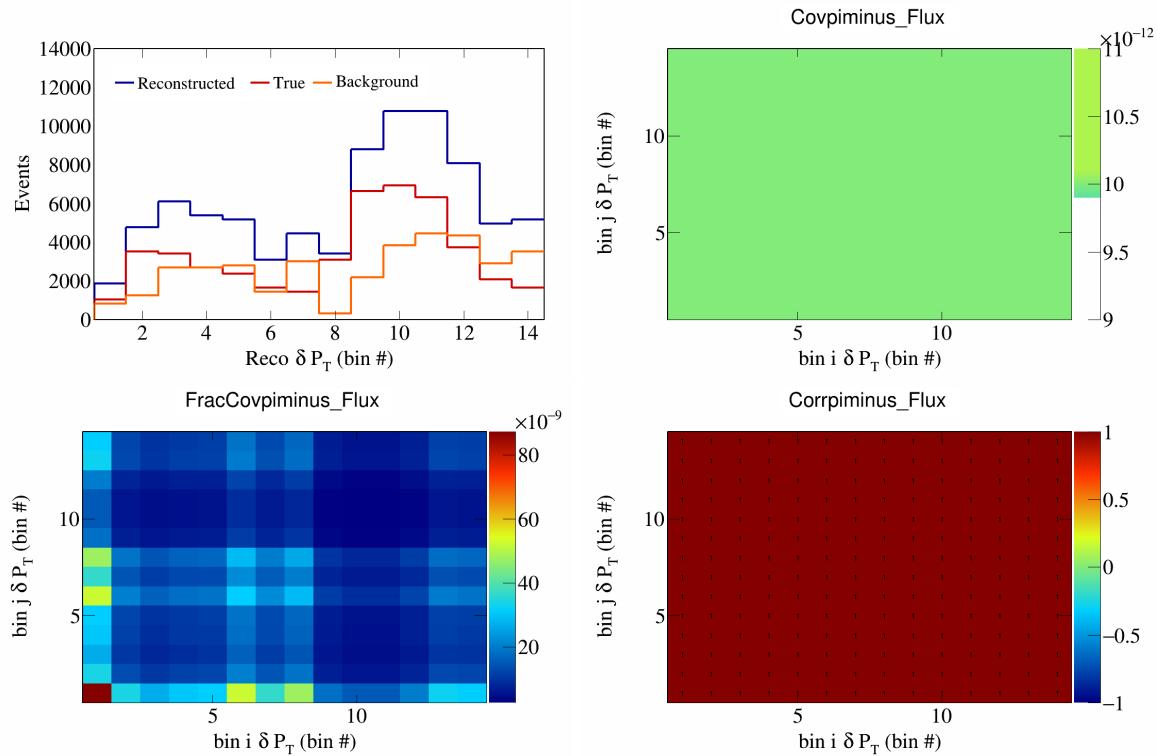


Figure 730: PiMinus variations for  $\delta P_T$  in  $\cos(\theta_{\vec{p}_\mu})$ .

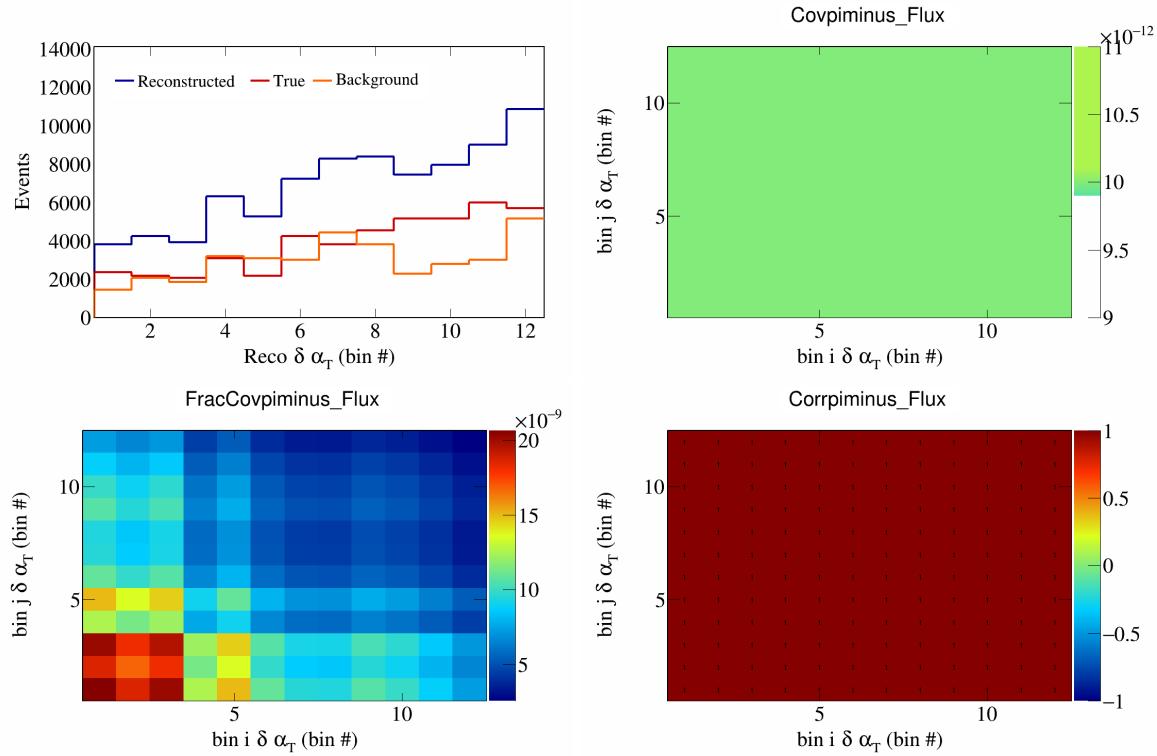


Figure 731: PiMinus variations for  $\delta \alpha_T$  in  $\cos(\theta_{\vec{p}_\mu})$ .

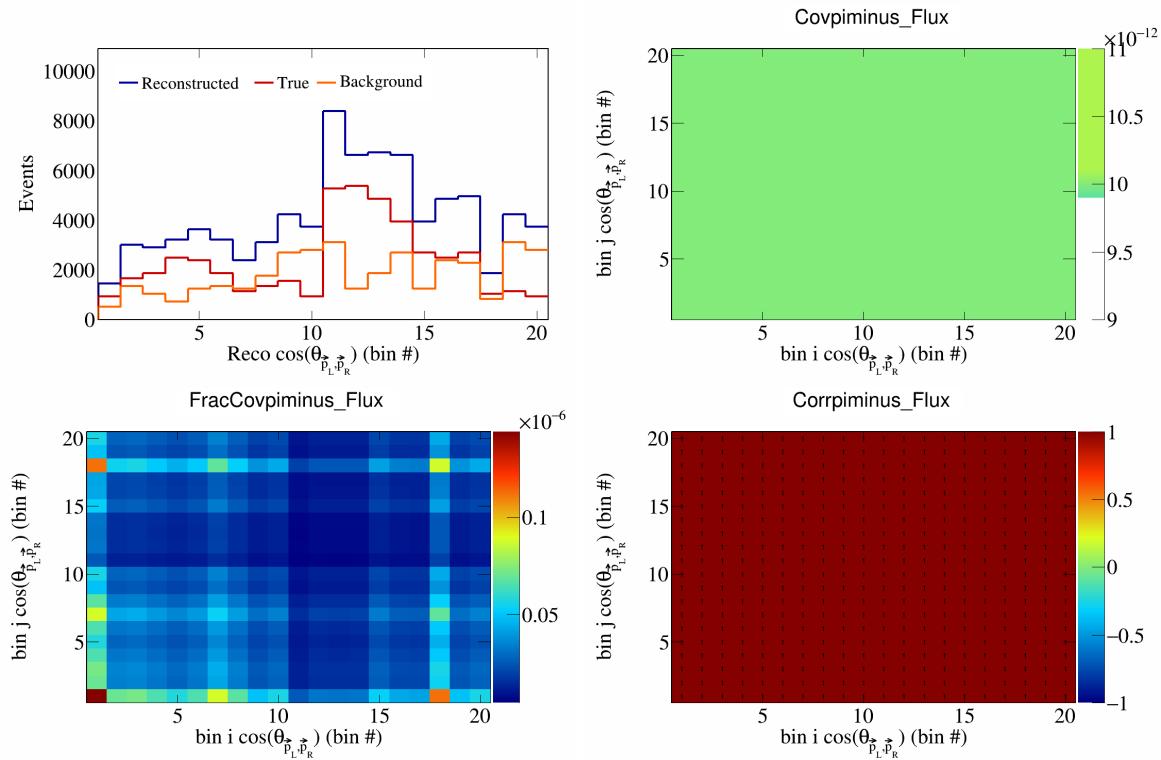


Figure 732: PiMinus variations for  $\cos(\theta_{\vec{p}_L, \vec{p}_R})$  in  $\cos(\theta_{\vec{p}_\mu})$ .

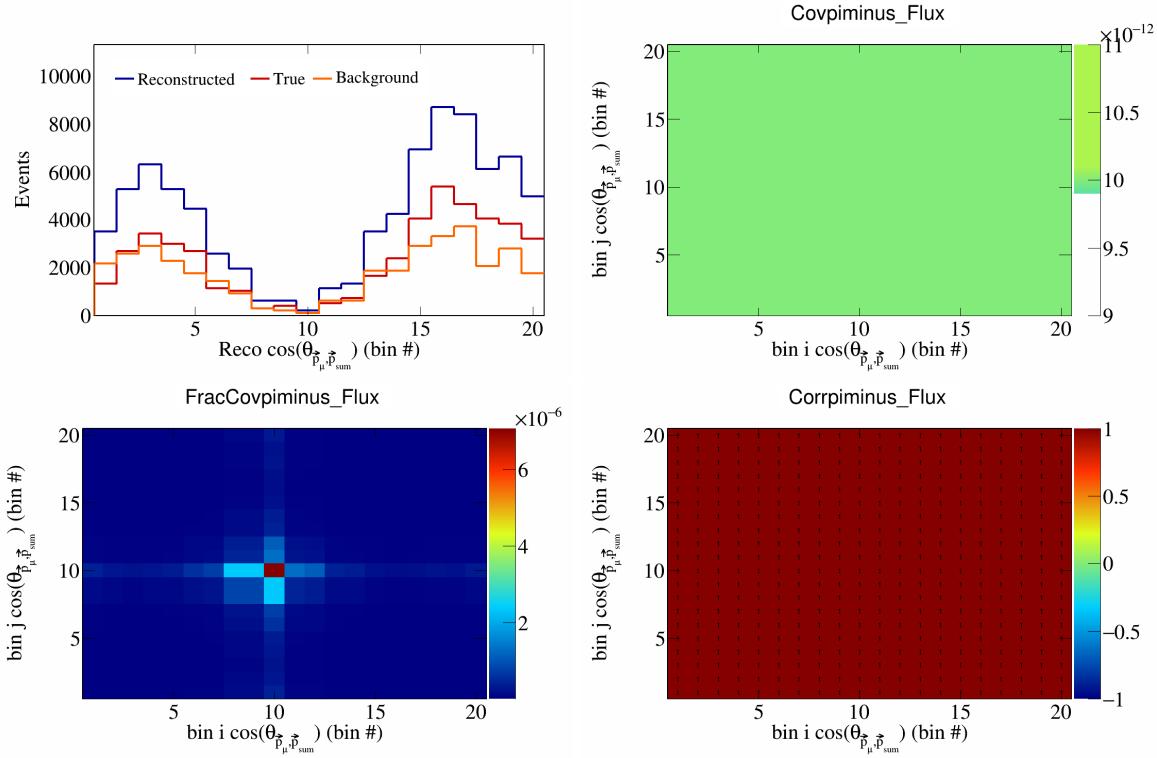


Figure 733: PiMinus variations for  $\cos(\theta_{\vec{p}_\mu, \vec{p}_{\text{sum}}})$  in  $\cos(\theta_{\vec{p}_\mu})$ .

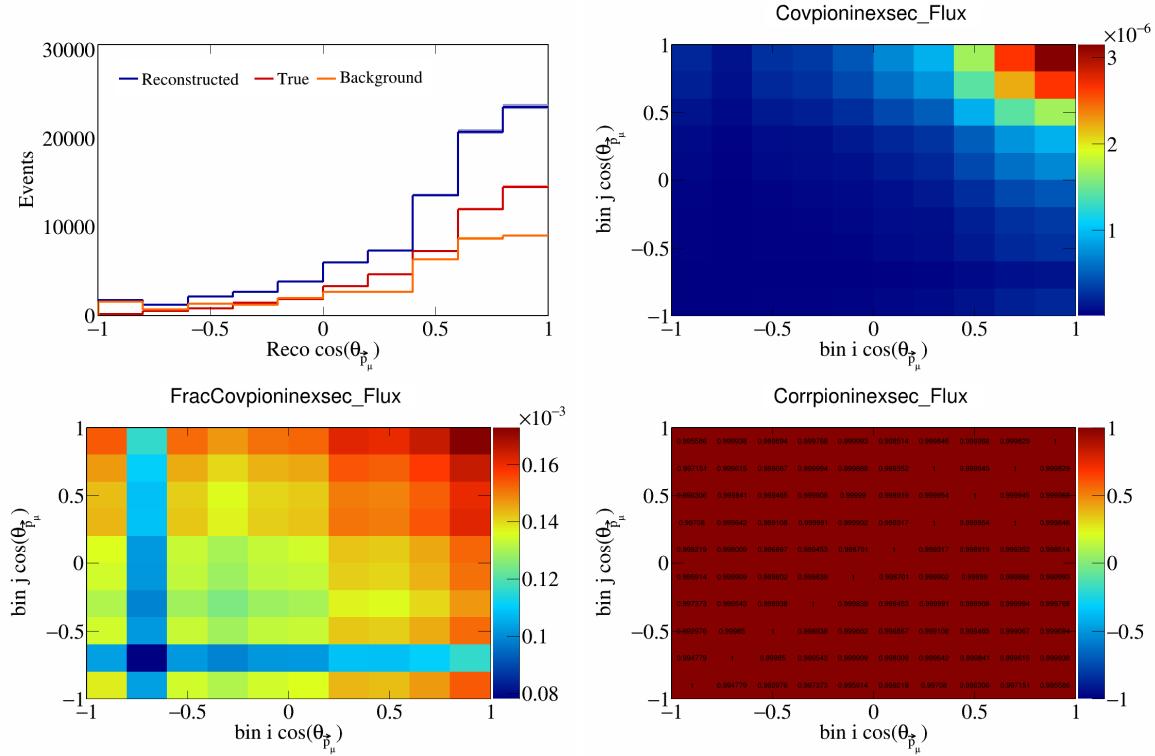


Figure 734: PionIneXSec variations for  $\cos(\theta_{\vec{p}_\mu})$ .

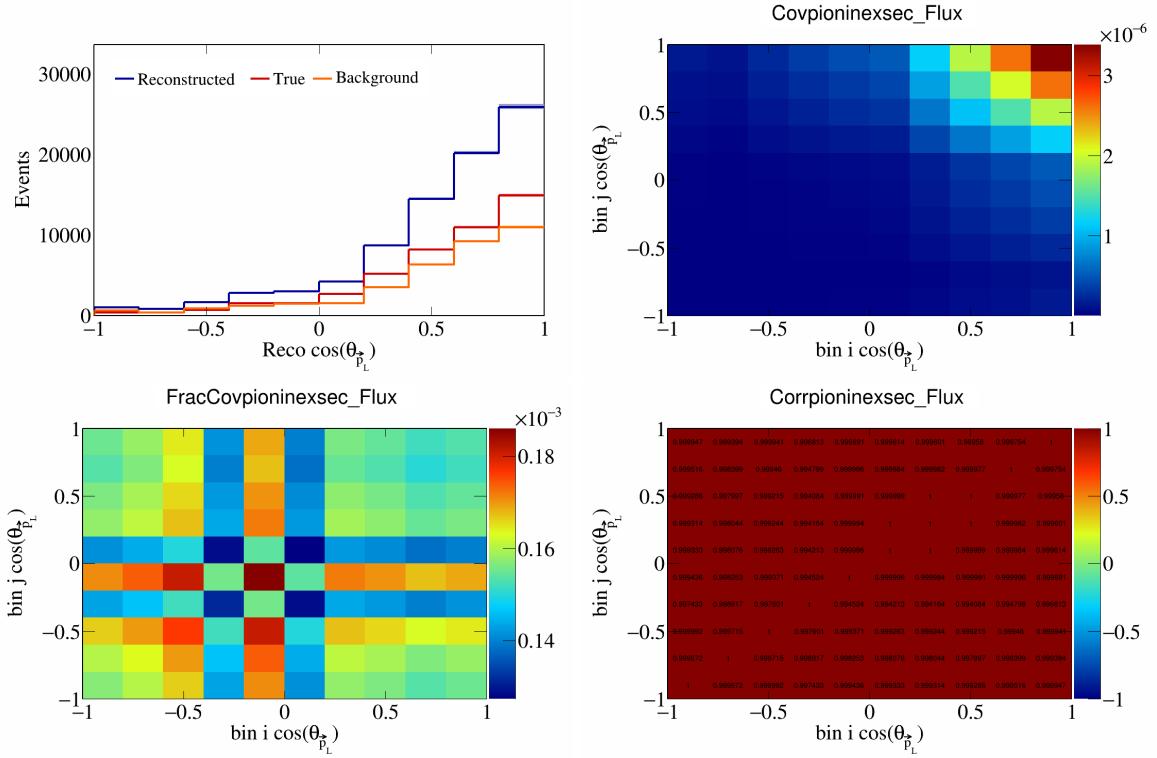


Figure 735: PionIneXSec variations for  $\cos(\theta_{\vec{p}_L})$ .

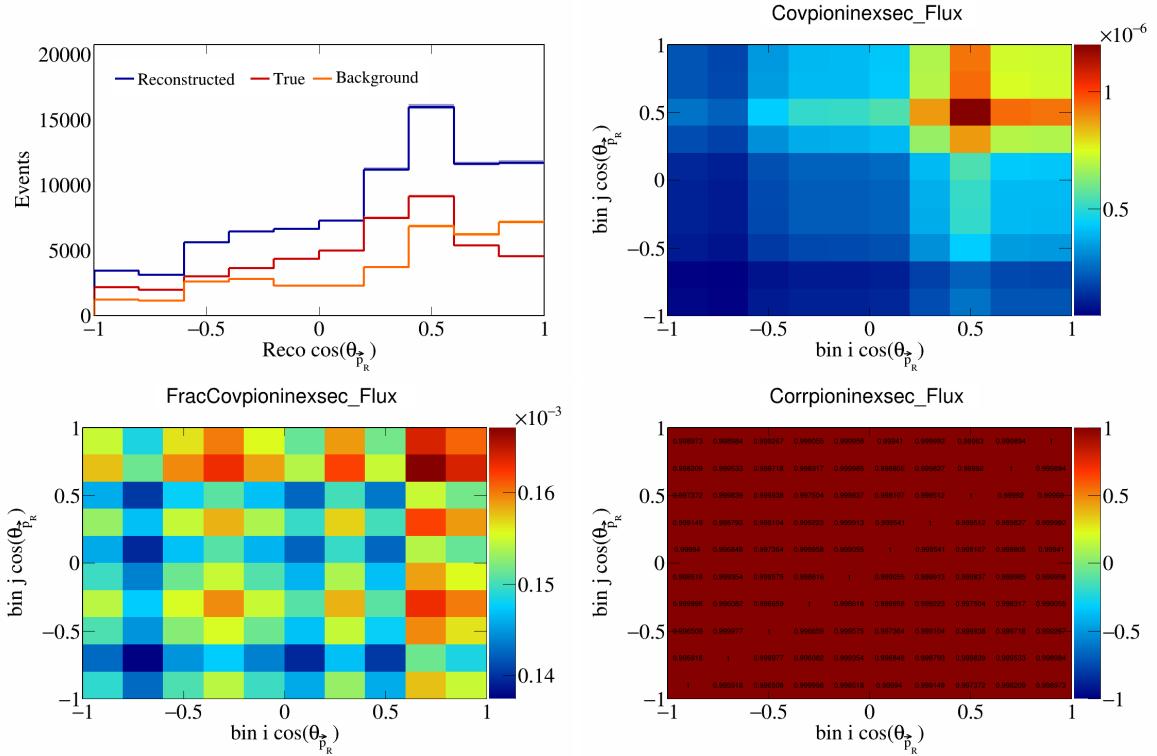


Figure 736: PionIneXSec variations for  $\cos(\theta_{\vec{p}_R})$ .

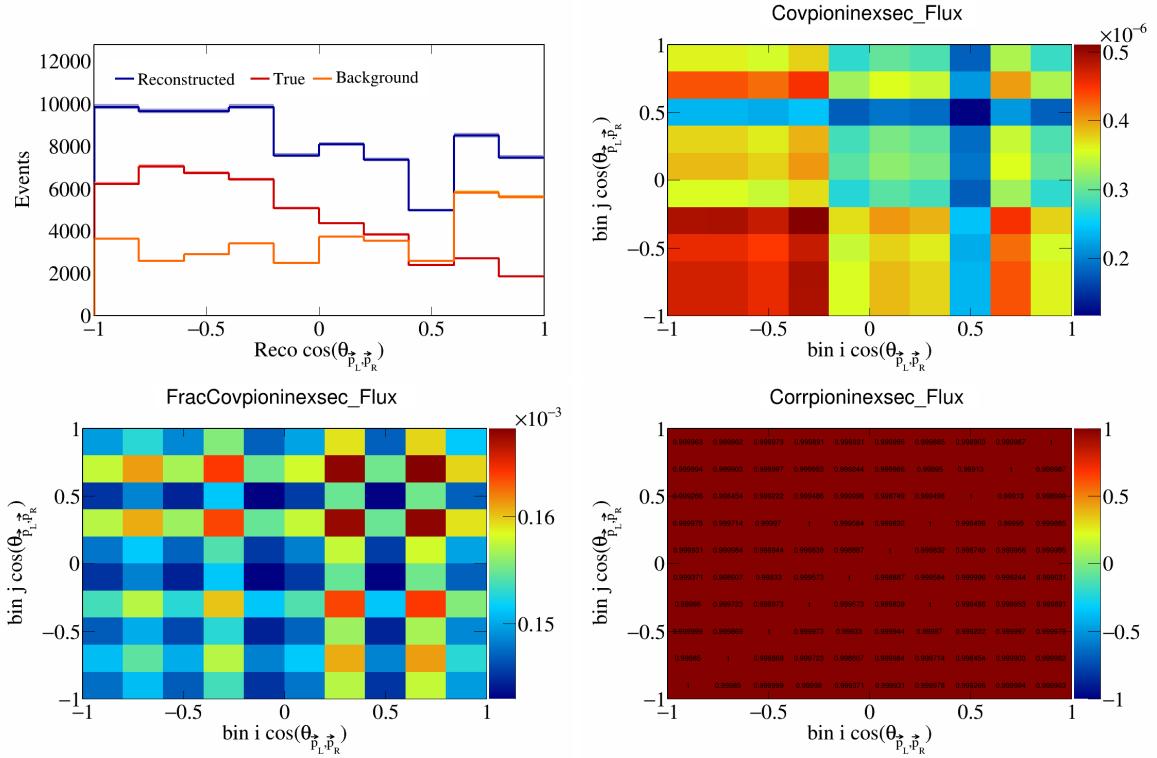


Figure 737: PionIneXSec variations for  $\cos(\theta_{\vec{p}_L, \vec{p}_R})$ .

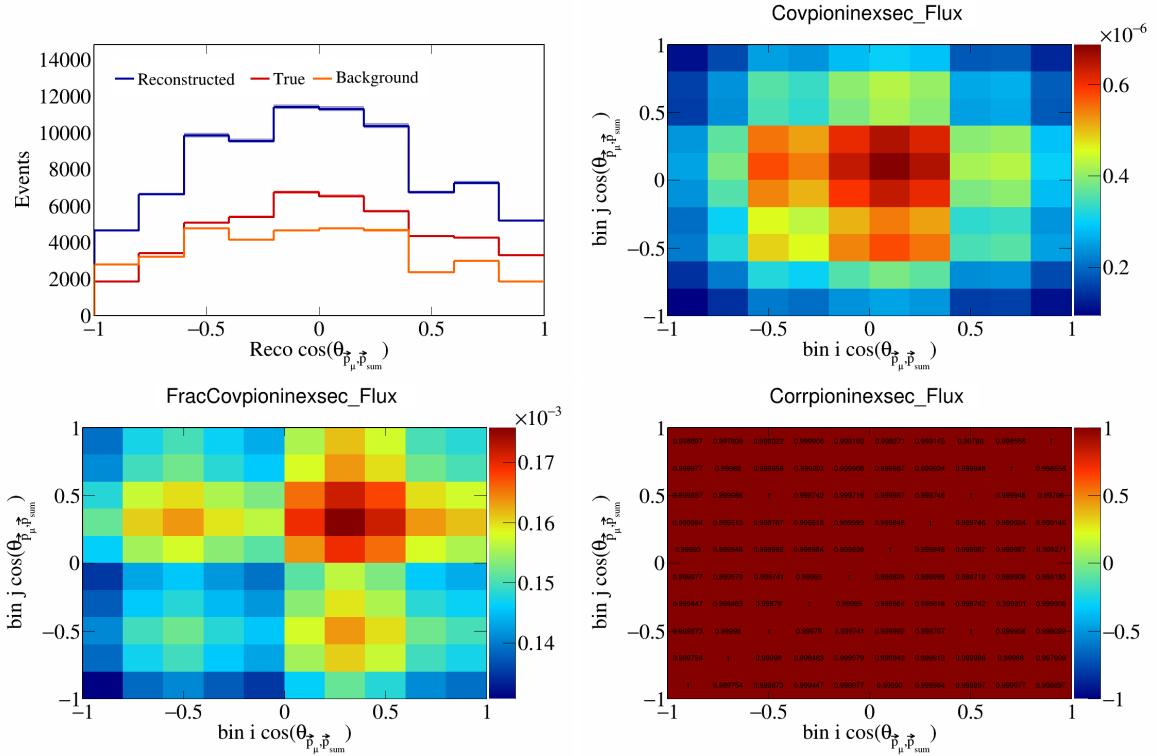


Figure 738: PionIneXSec variations for  $\cos(\theta_{\vec{p}_\mu, \vec{p}_{\text{sum}}})$ .

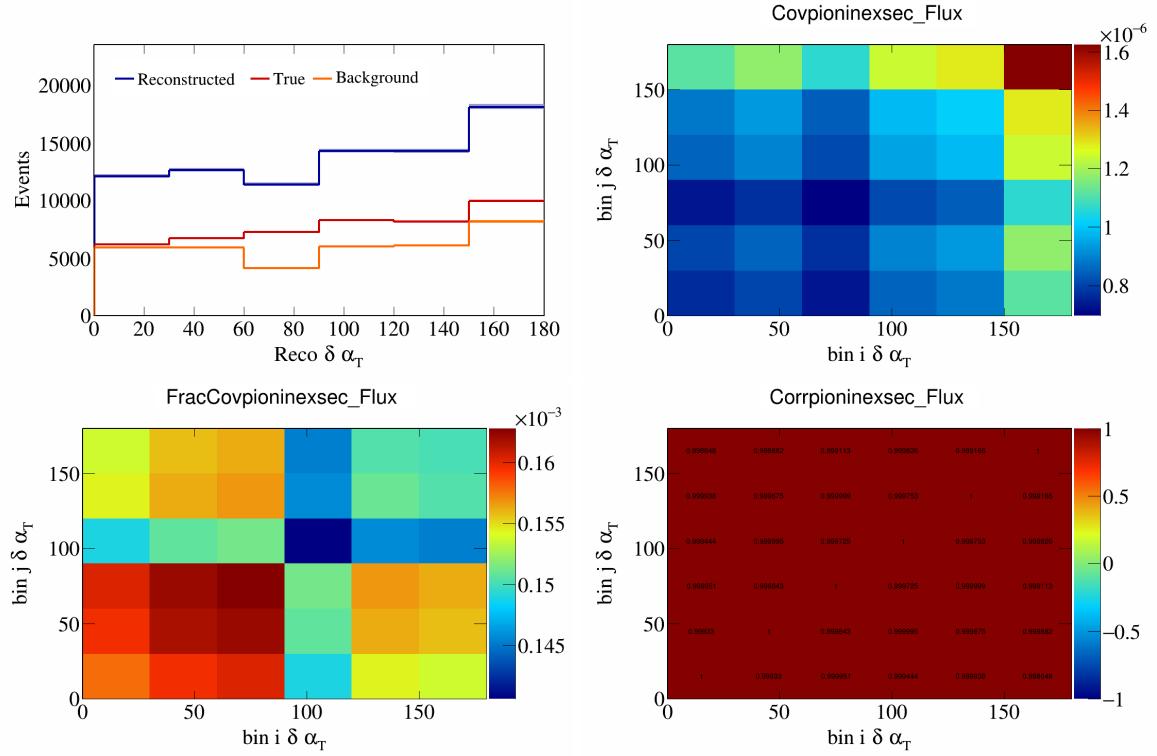


Figure 739: PionIneXSec variations for  $\delta\alpha_T$ .

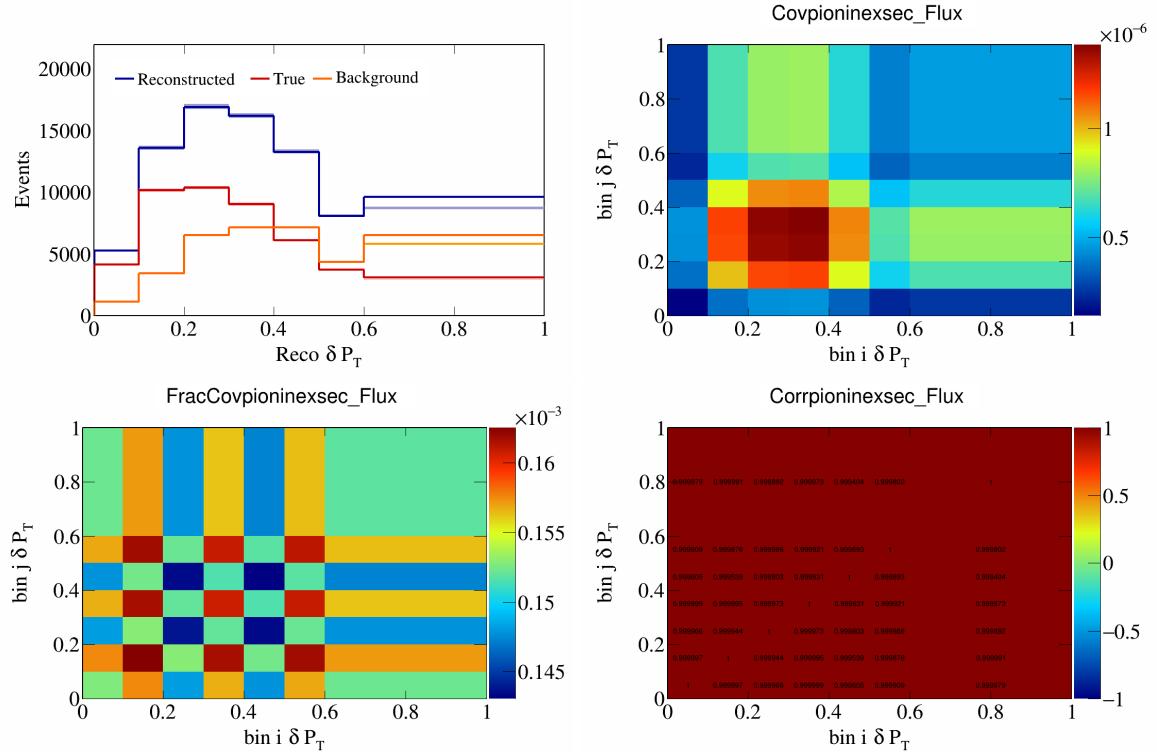


Figure 740: PionIneXSec variations for  $\delta P_T$ .

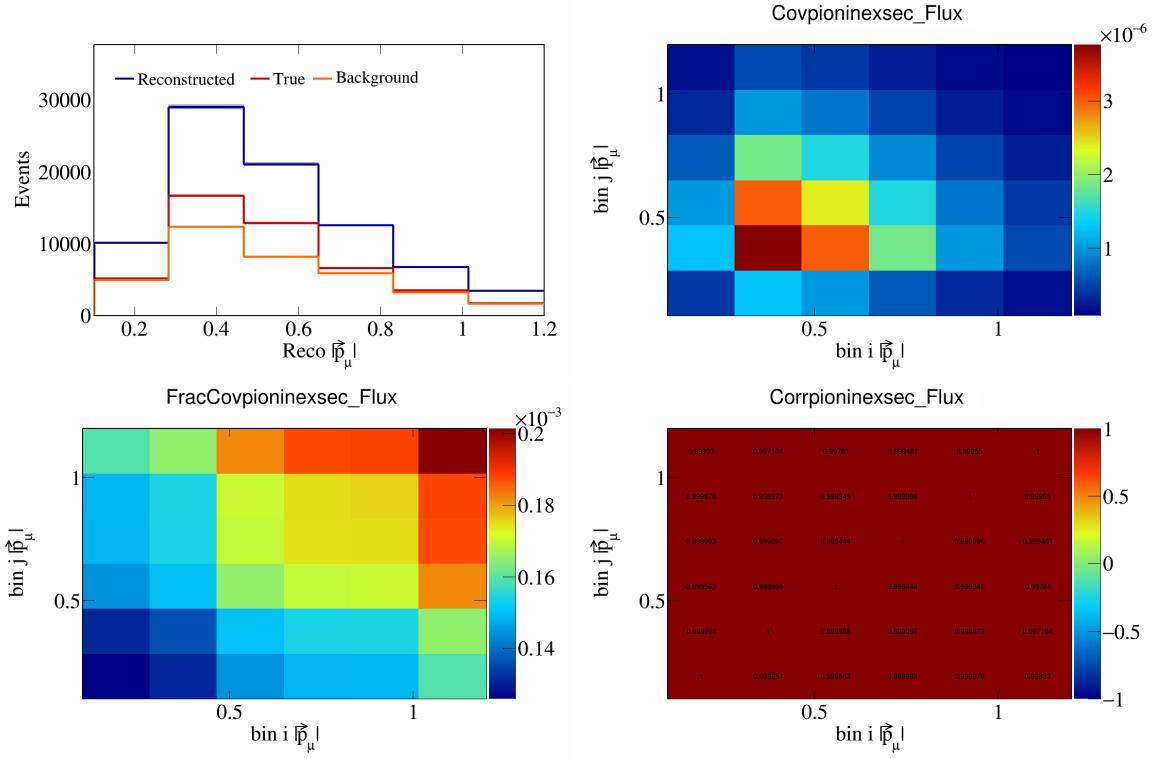


Figure 741: PionIneXSec variations for  $|\vec{p}_\mu|$ .

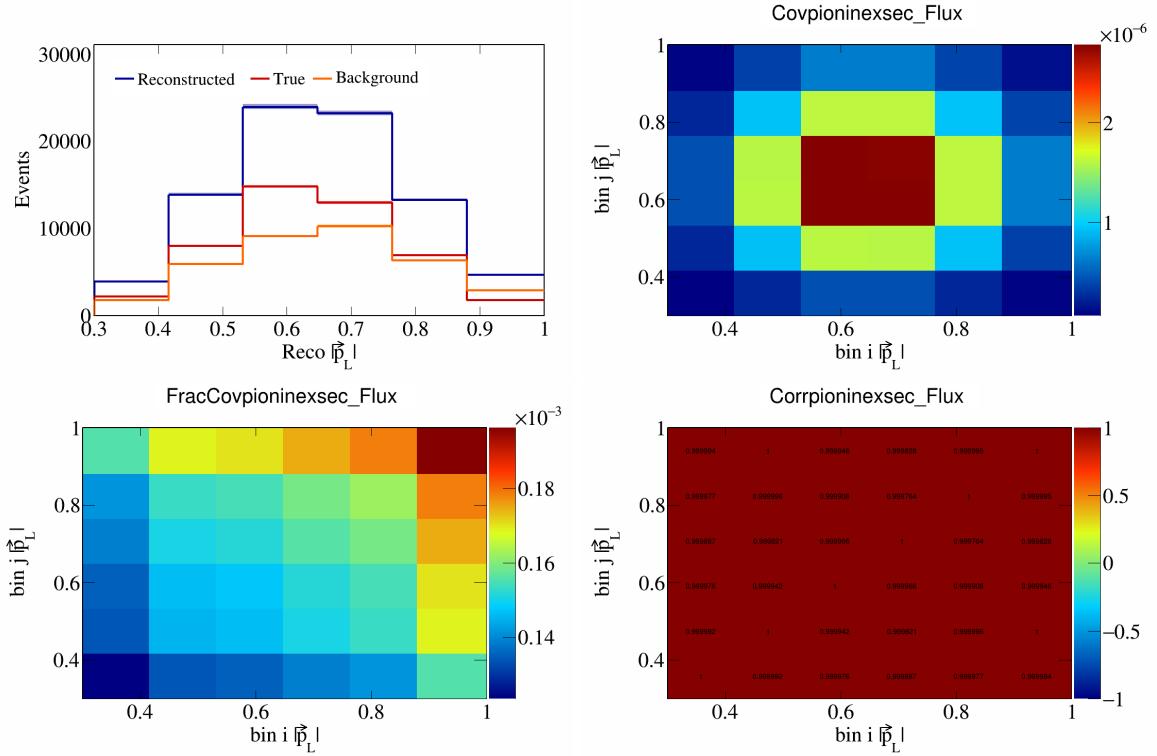


Figure 742: PionIneXSec variations for  $|\vec{p}_L|$ .

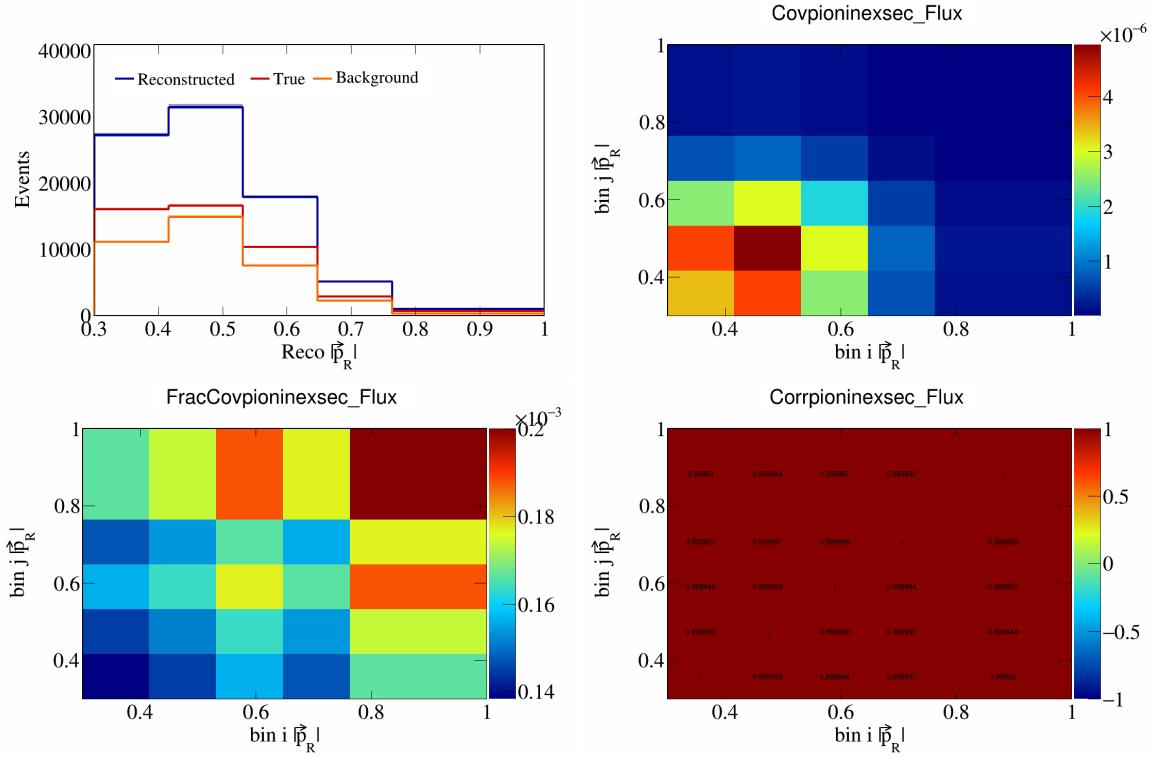


Figure 743: PionIneXSec variations for  $|\vec{p}_R|$ .

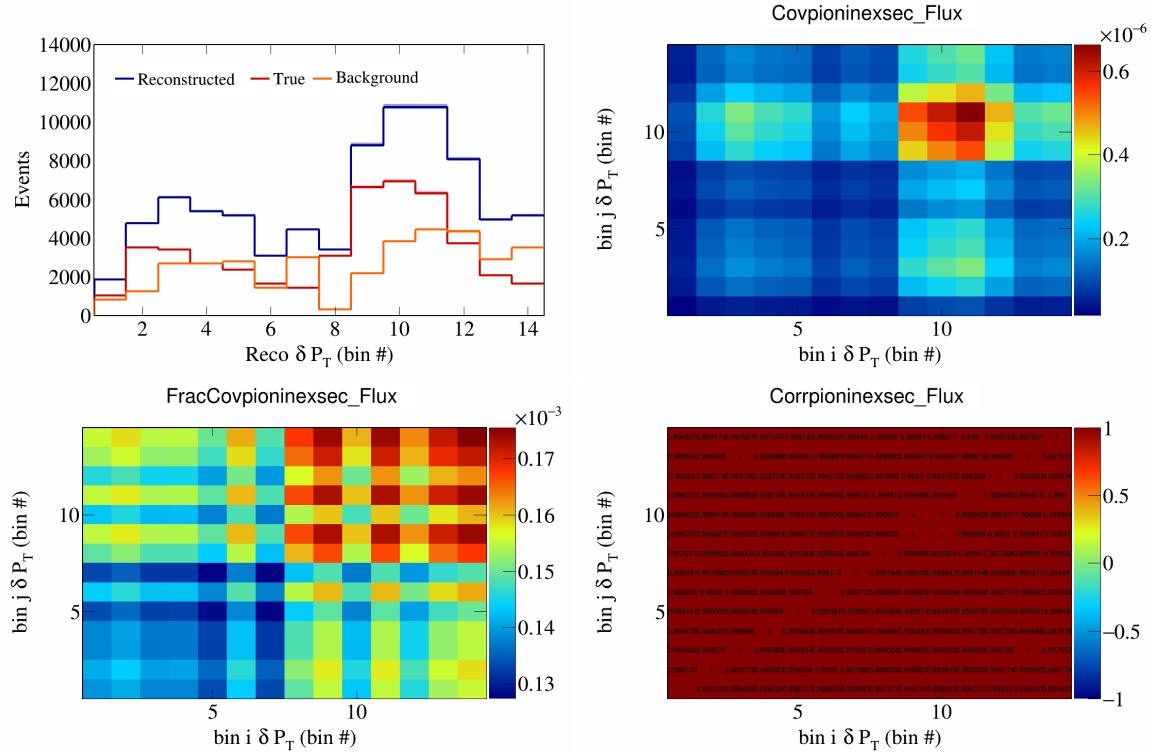


Figure 744: PionIneXSec variations for  $\delta P_T$  in  $\cos(\theta_{\vec{p}_\mu})$ .

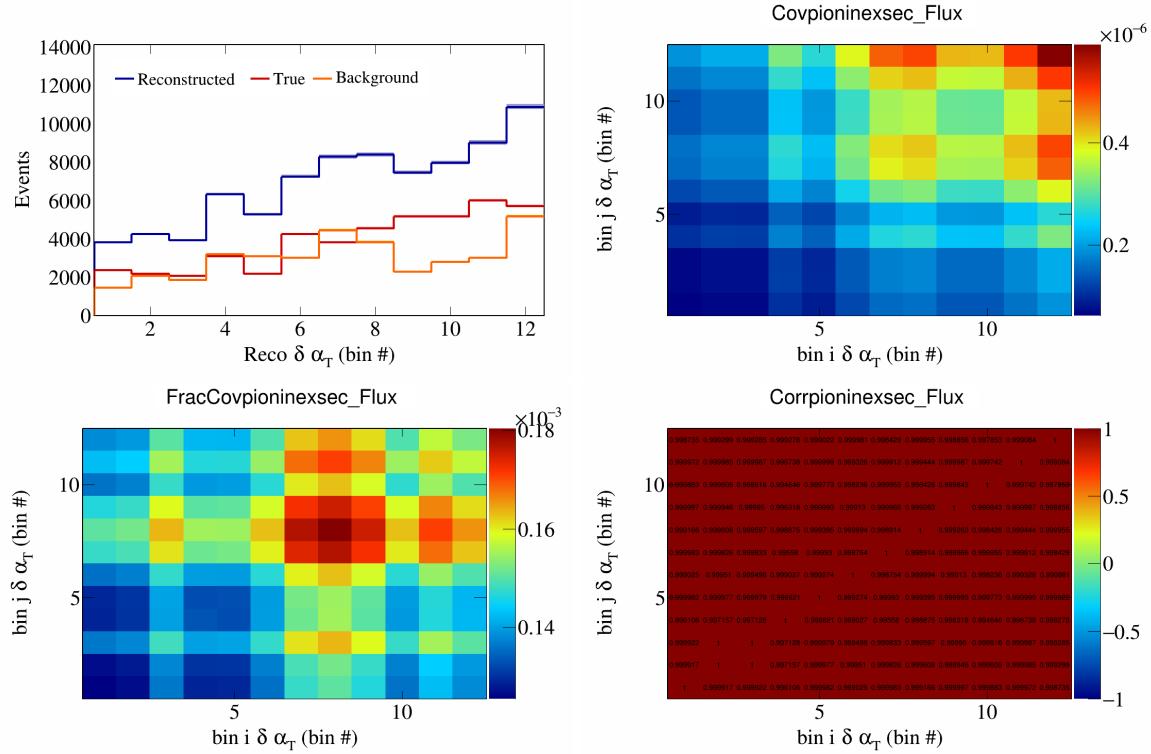


Figure 745: PionIneXSec variations for  $\delta\alpha_T$  in  $\cos(\theta_{\vec{p}_\mu})$ .

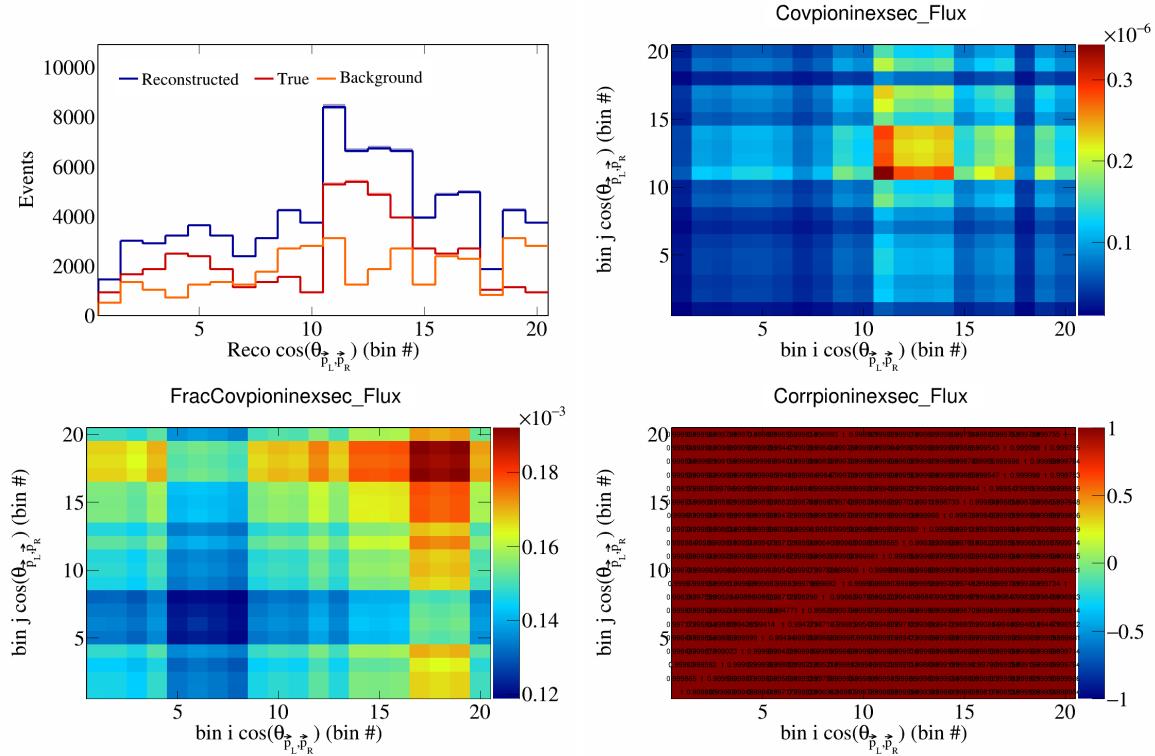


Figure 746: PionIneXSec variations for  $\cos(\theta_{\vec{p}_L, \vec{p}_R})$  in  $\cos(\theta_{\vec{p}_\mu})$ .

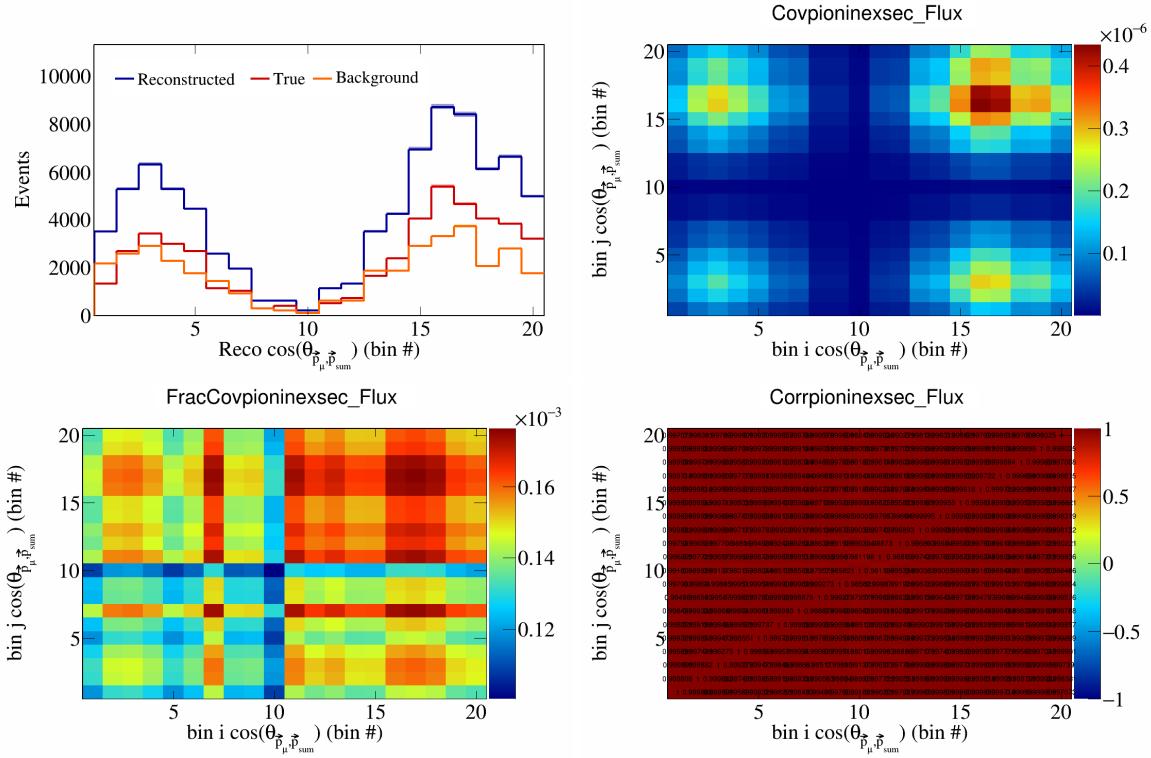


Figure 747: PionIneXSec variations for  $\cos(\theta_{\vec{p}_\mu} \cdot \vec{p}_{\text{sum}})$  in  $\cos(\theta_{\vec{p}_\mu})$ .

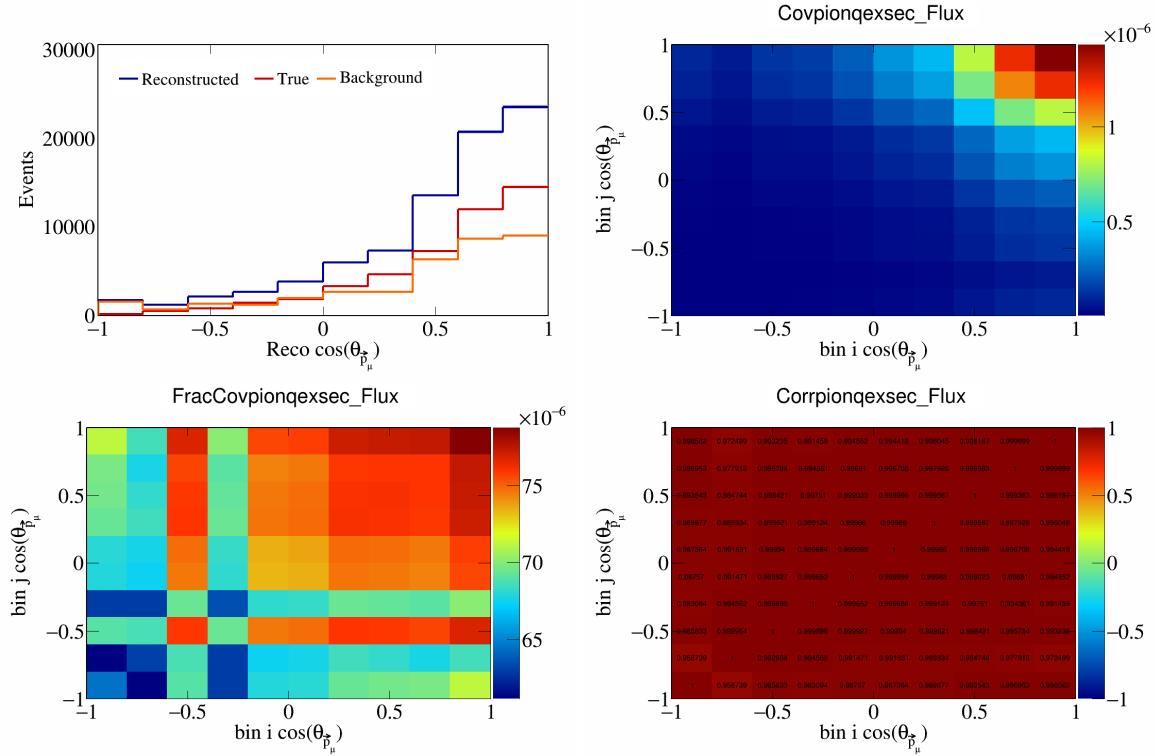


Figure 748: PionQeXSec variations for  $\cos(\theta_{\vec{p}_\mu})$ .

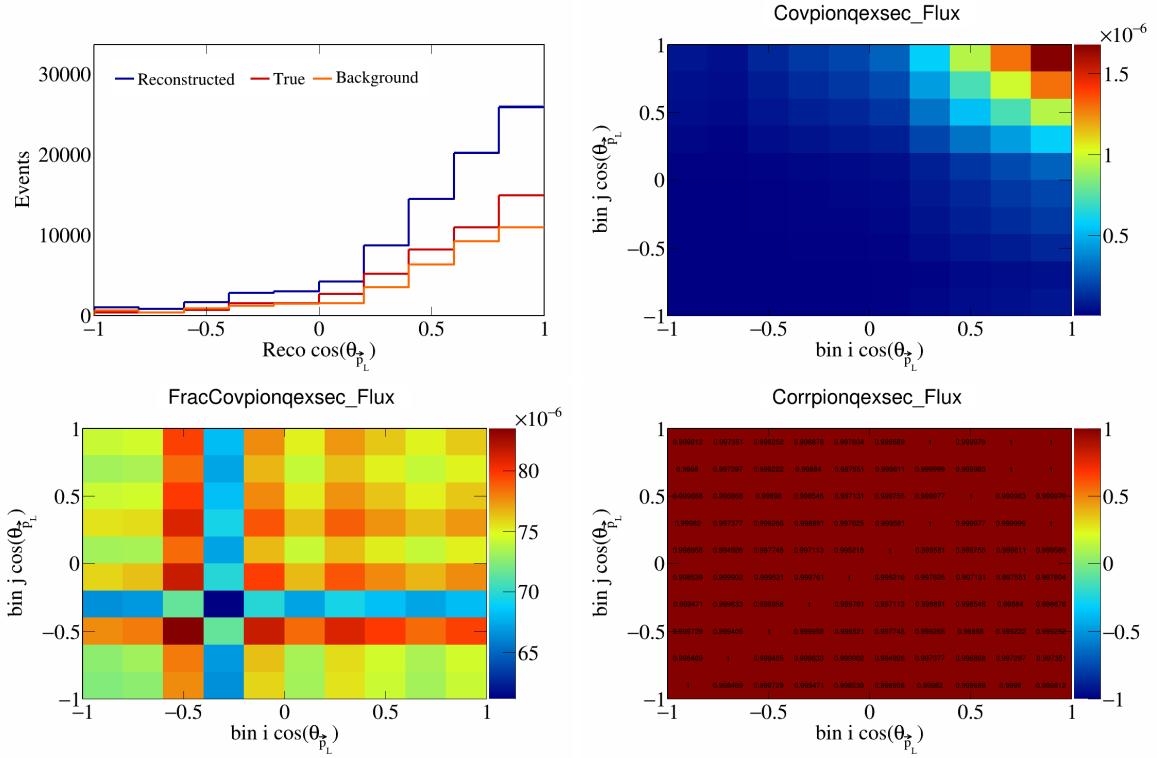


Figure 749: PionQeXSec variations for  $\cos(\theta_{\vec{p}_L})$ .

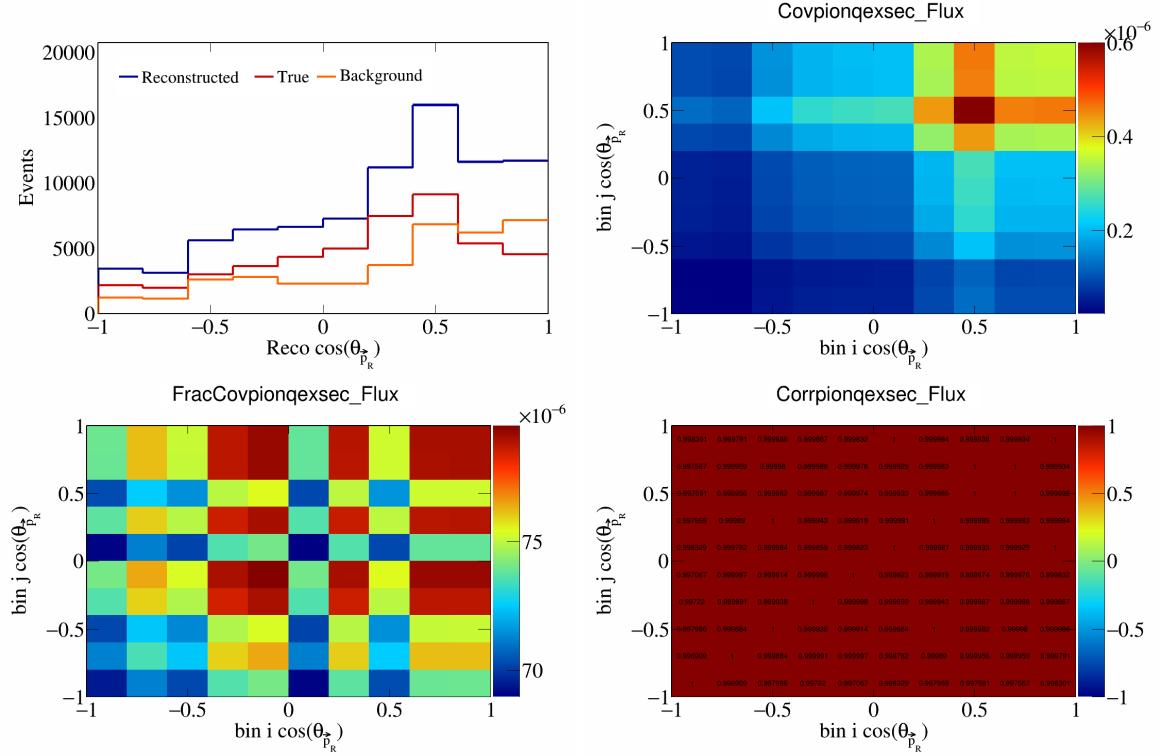


Figure 750: PionQeXSec variations for  $\cos(\theta_{\vec{p}_R})$ .

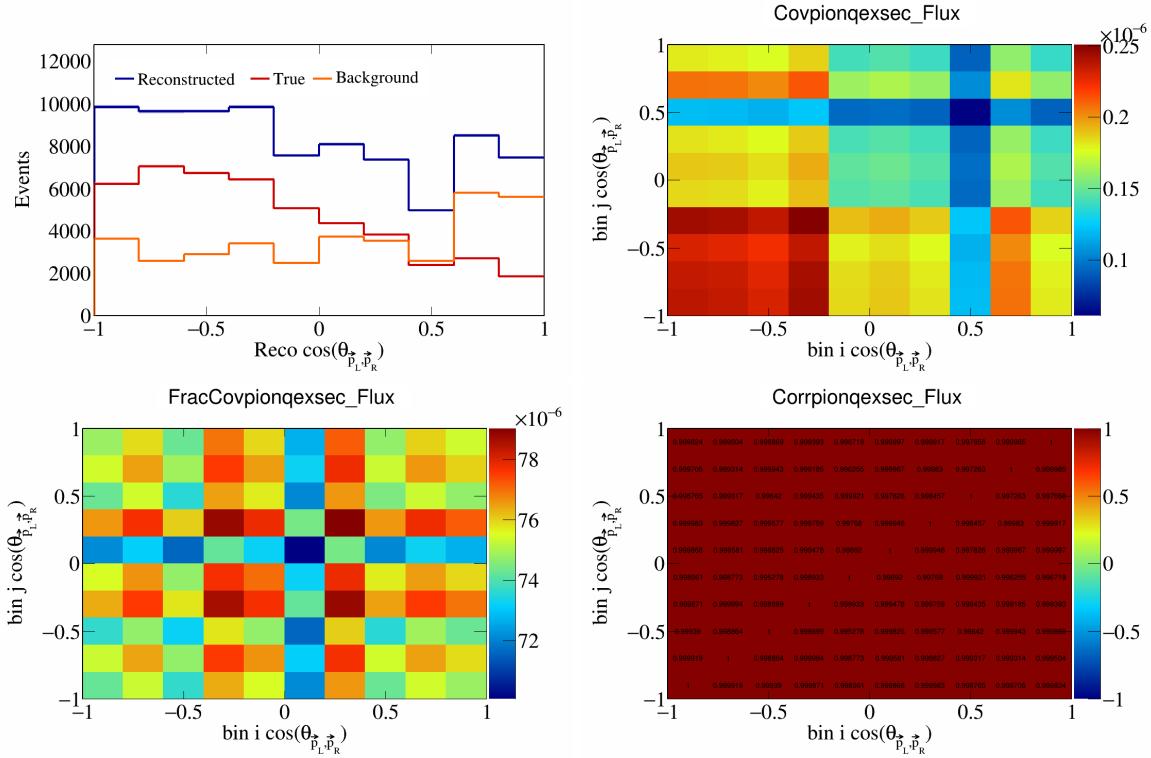


Figure 751: PionQeXSec variations for  $\cos(\theta_{\vec{p}_L, \vec{p}_R})$ .

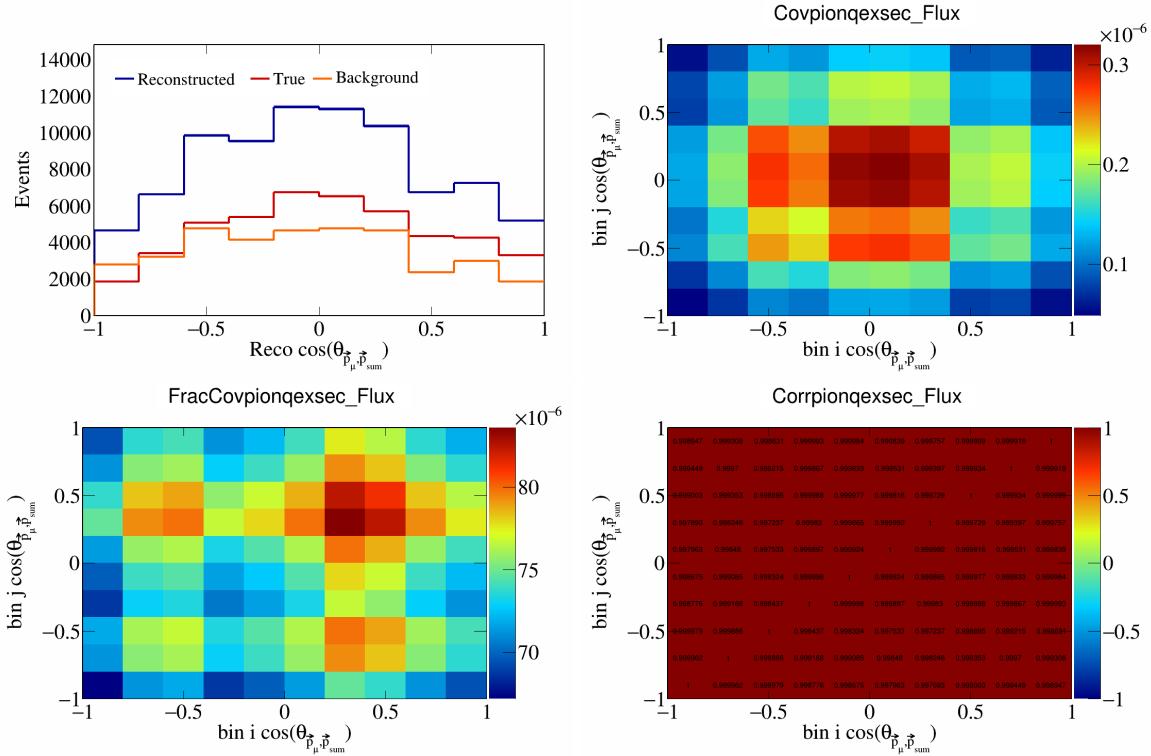


Figure 752: PionQeXSec variations for  $\cos(\theta_{\vec{p}_\mu, \vec{p}_{\text{sum}}})$ .

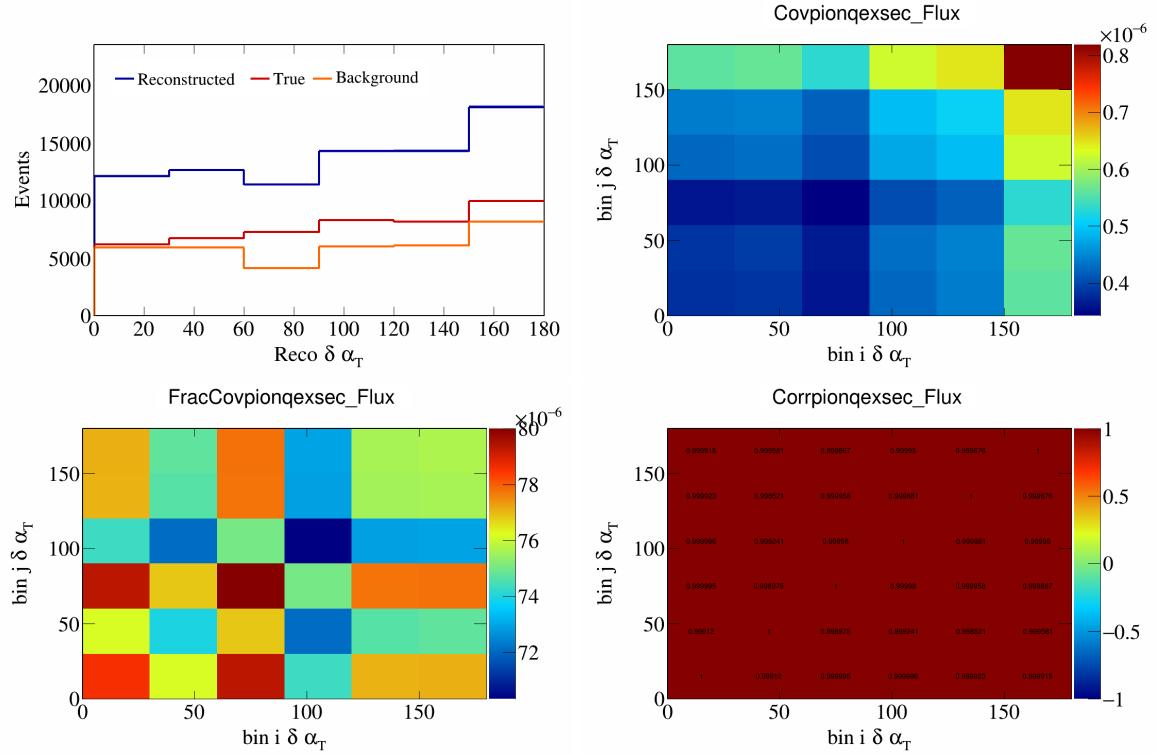


Figure 753: PionQeXSec variations for  $\delta\alpha_T$ .

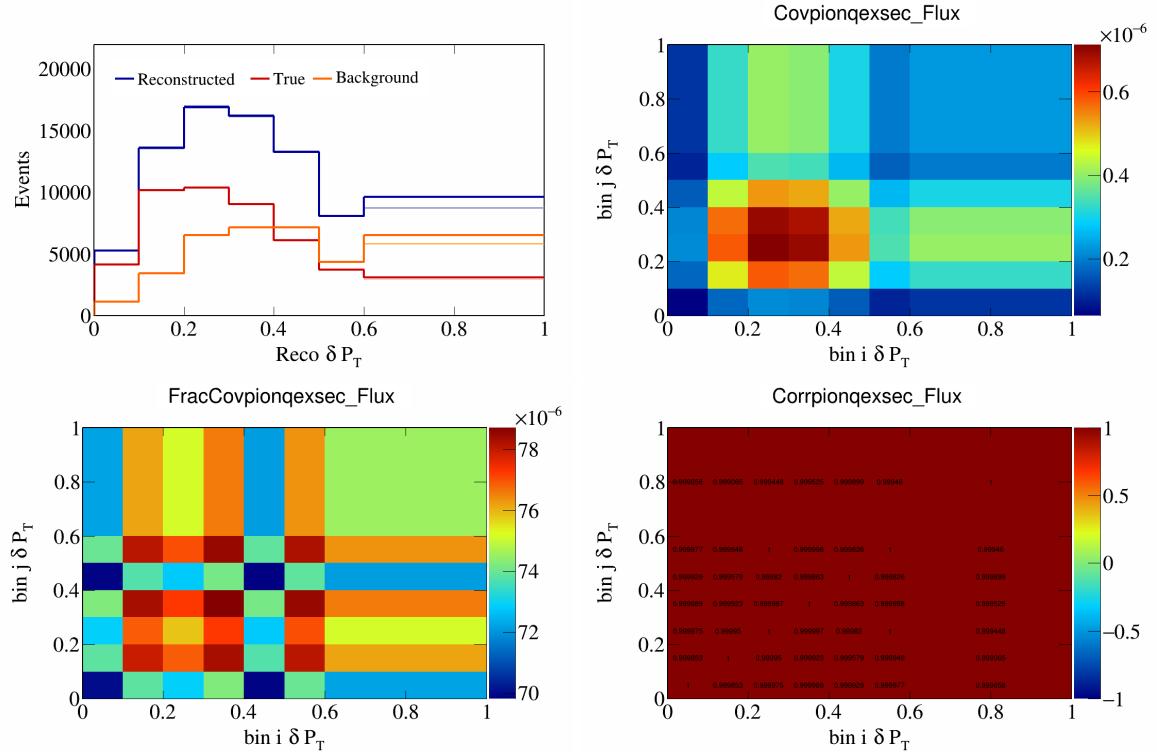


Figure 754: PionQeXSec variations for  $\delta P_T$ .

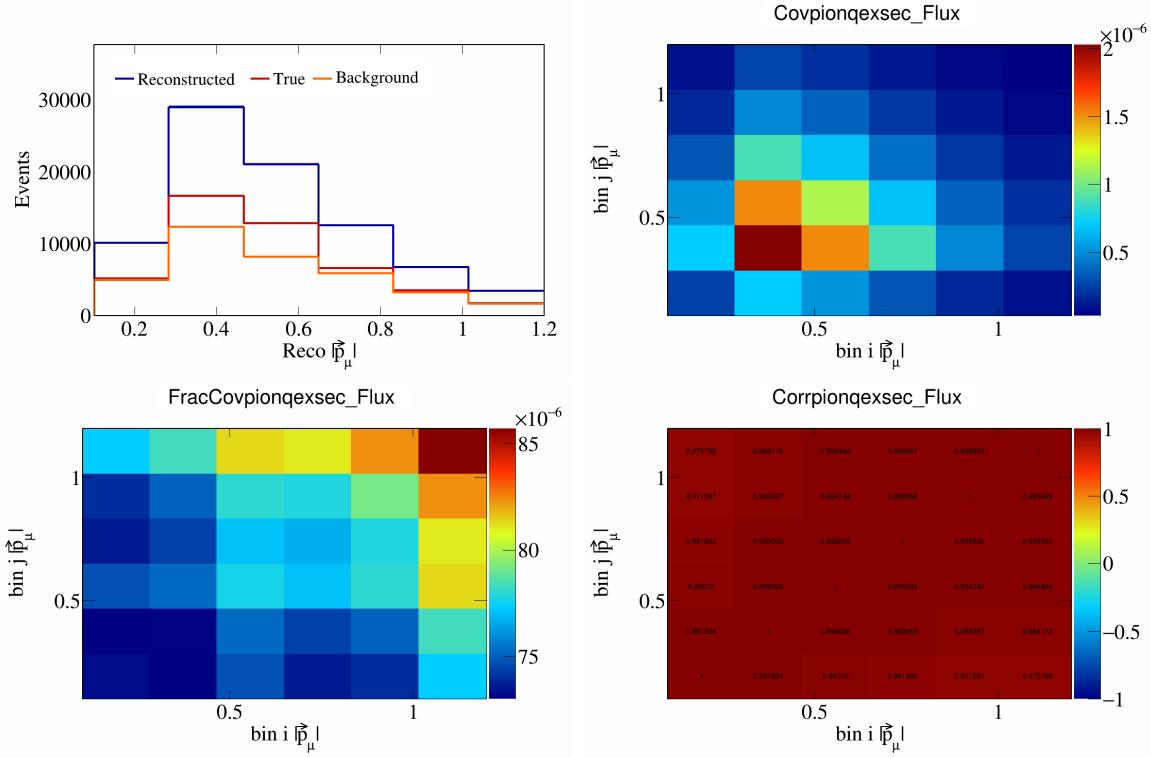


Figure 755: PionQeXSec variations for  $|\vec{p}_\mu|$ .

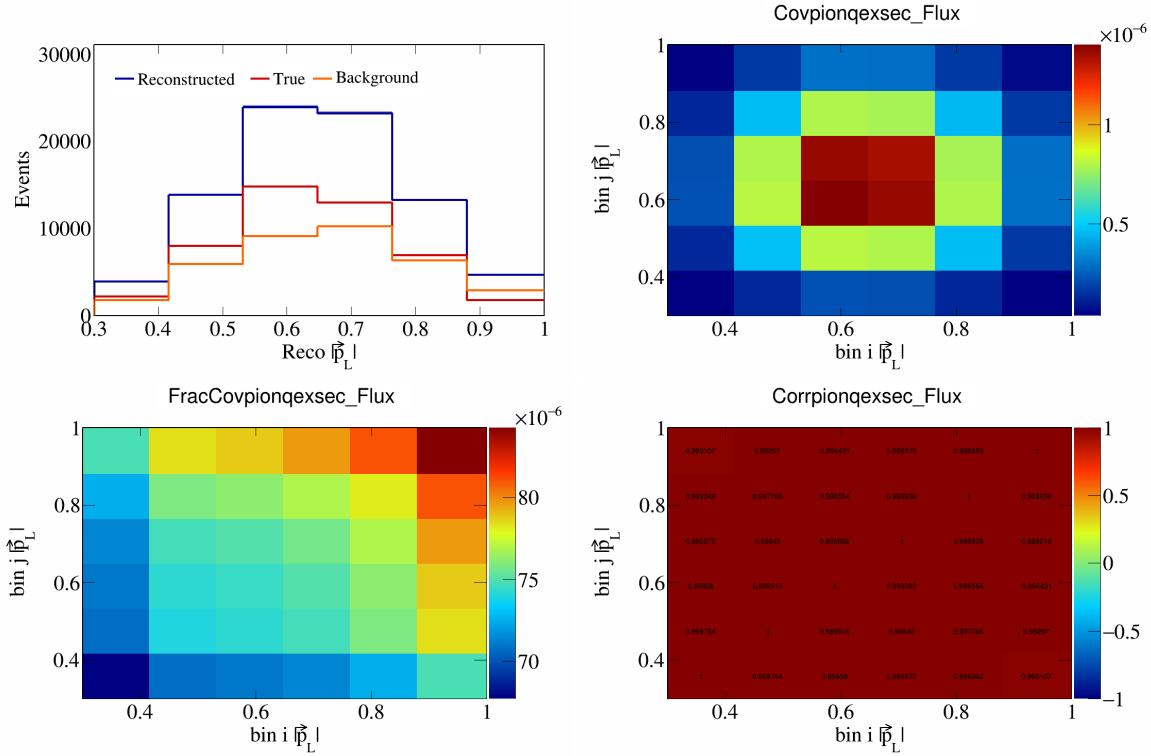


Figure 756: PionQeXSec variations for  $|\vec{p}_L|$ .

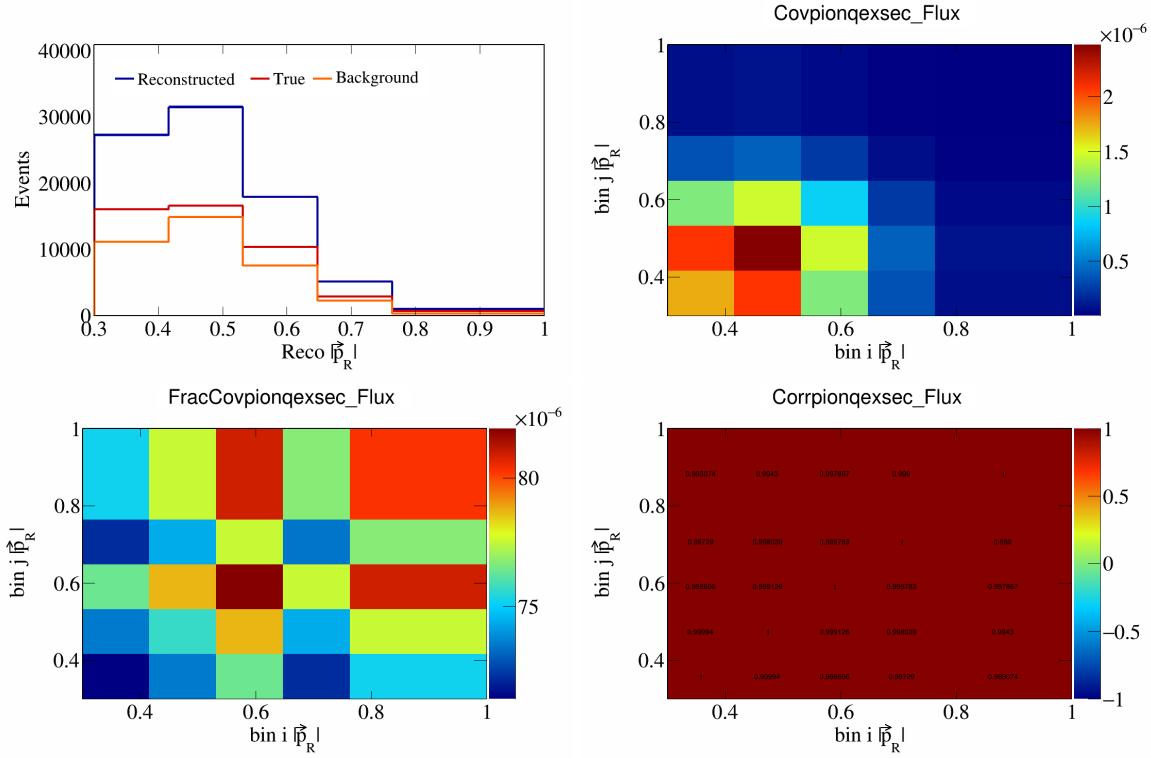


Figure 757: PionQeXSec variations for  $|\vec{p}_R|$ .

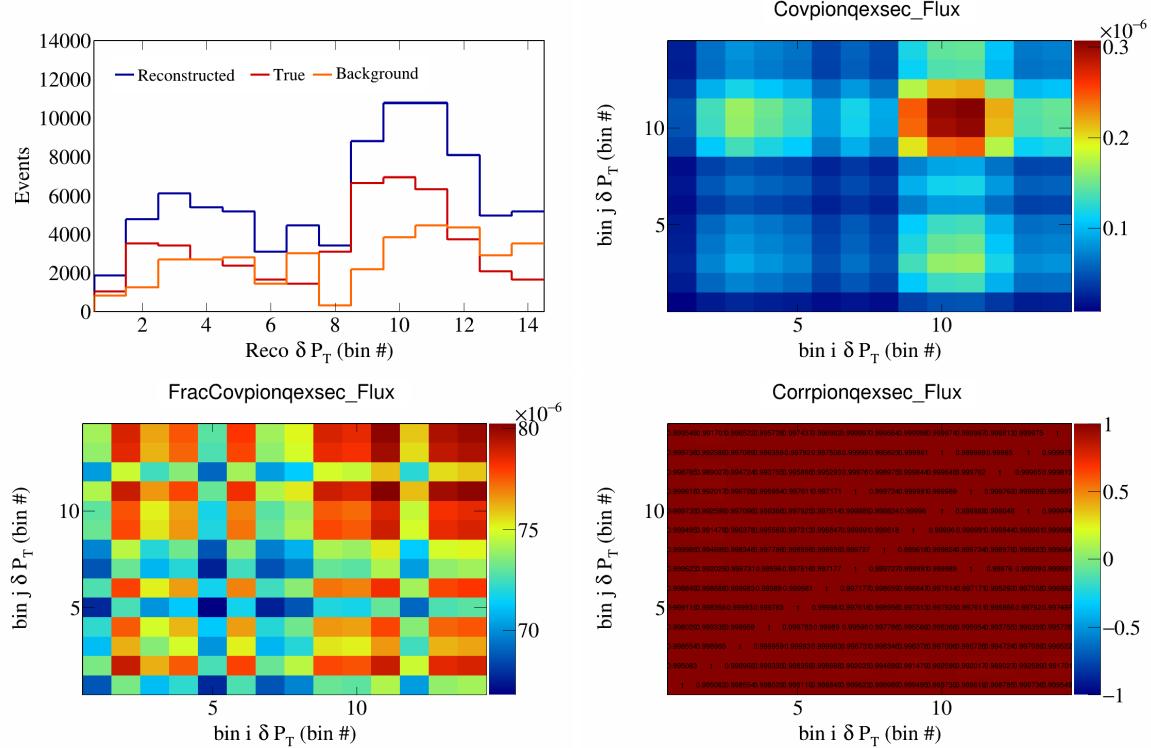


Figure 758: PionQeXSec variations for  $\delta P_T$  in  $\cos(\theta_{\vec{p}_\mu})$ .

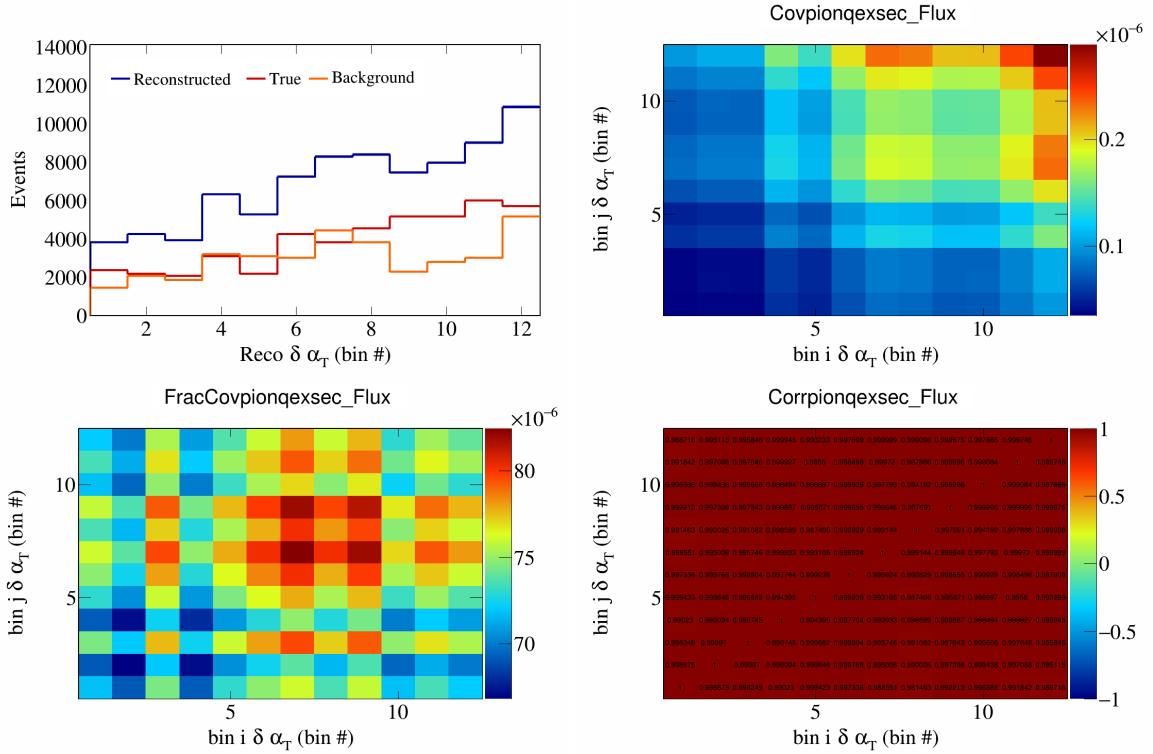


Figure 759: PionQeXSec variations for  $\delta \alpha_T$  in  $\cos(\theta_{\vec{p}_\mu})$ .

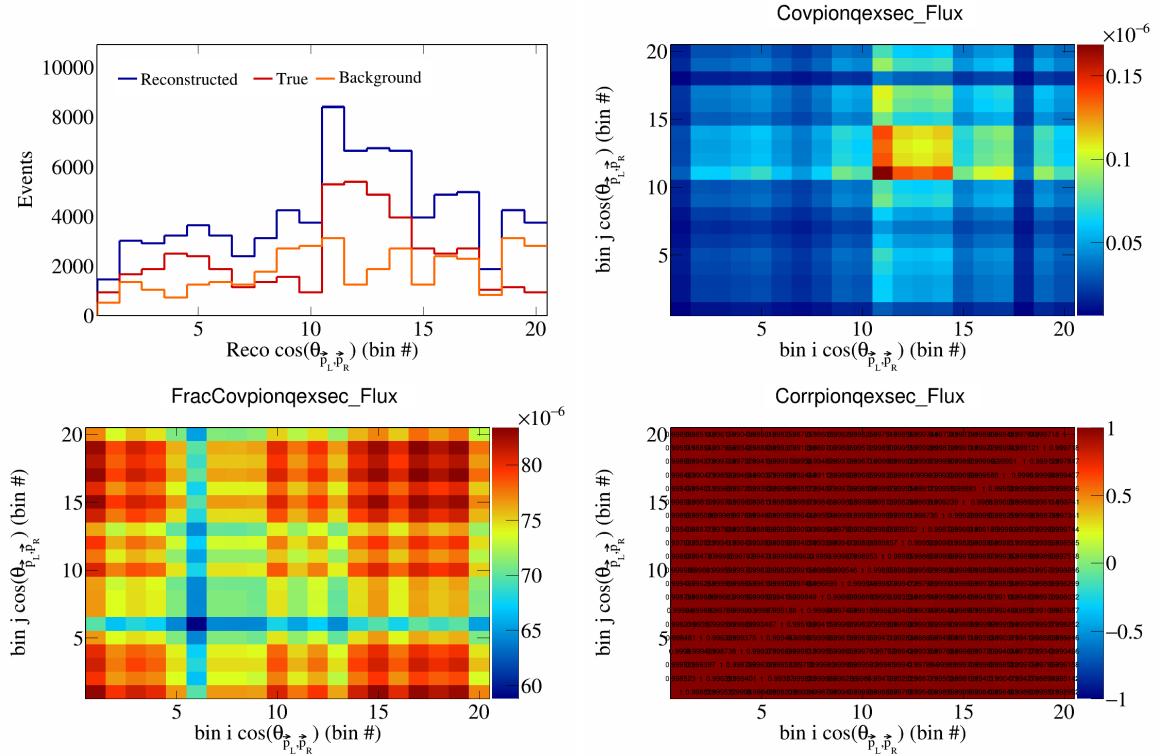


Figure 760: PionQeXSec variations for  $\cos(\theta_{\vec{p}_L, \vec{p}_R})$  in  $\cos(\theta_{\vec{p}_\mu})$ .

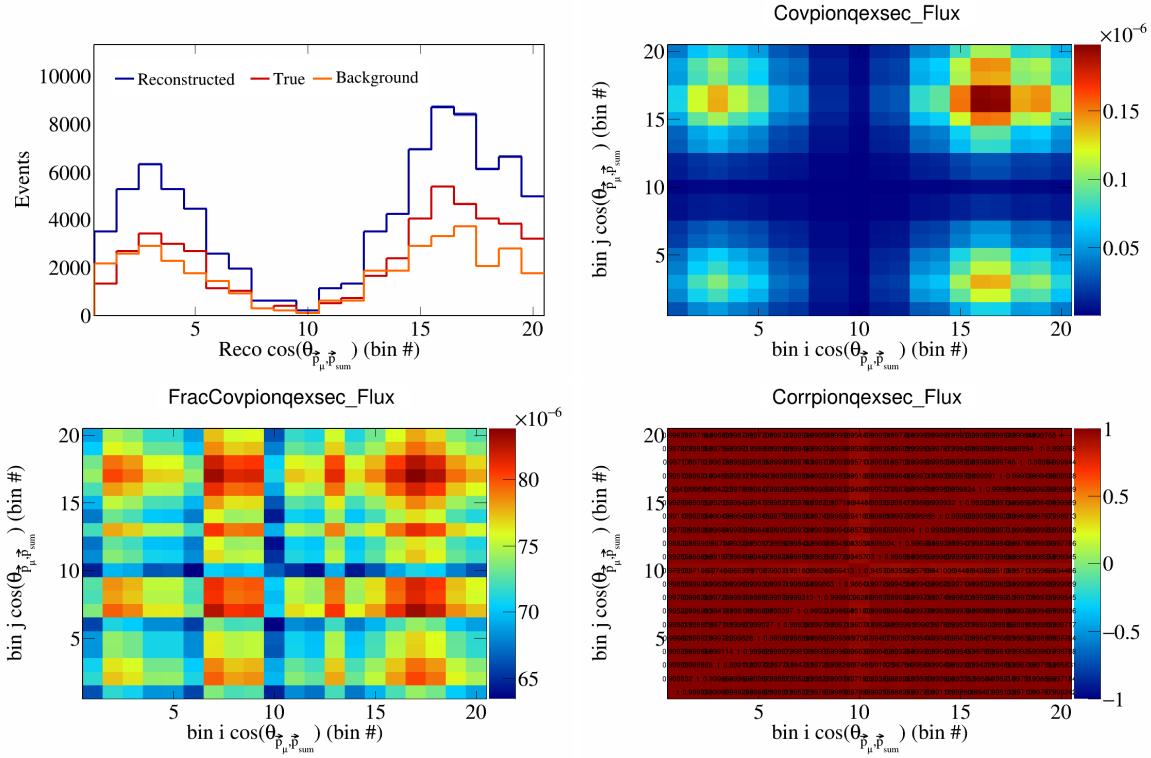


Figure 761: PionQeXSec variations for  $\cos(\theta_{\vec{p}_\mu} \cdot \vec{p}_{\text{sum}})$  in  $\cos(\theta_{\vec{p}_\mu})$ .

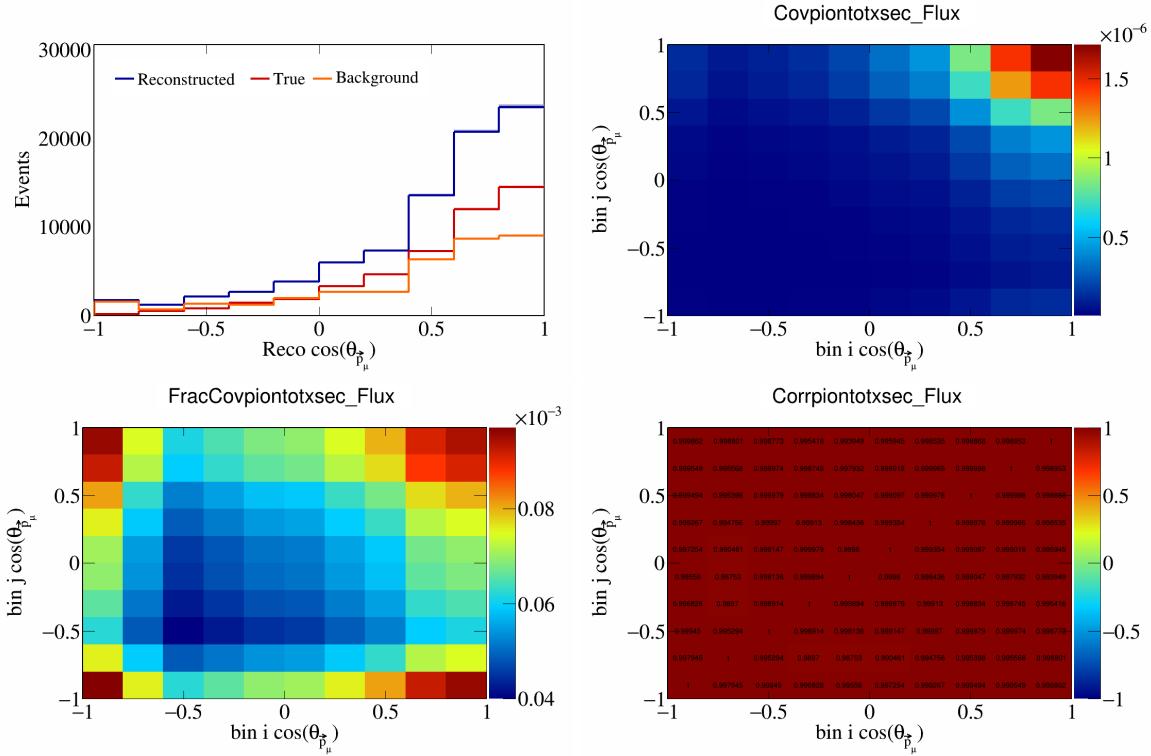


Figure 762: PionTotXSec variations for  $\cos(\theta_{\vec{p}_\mu})$ .

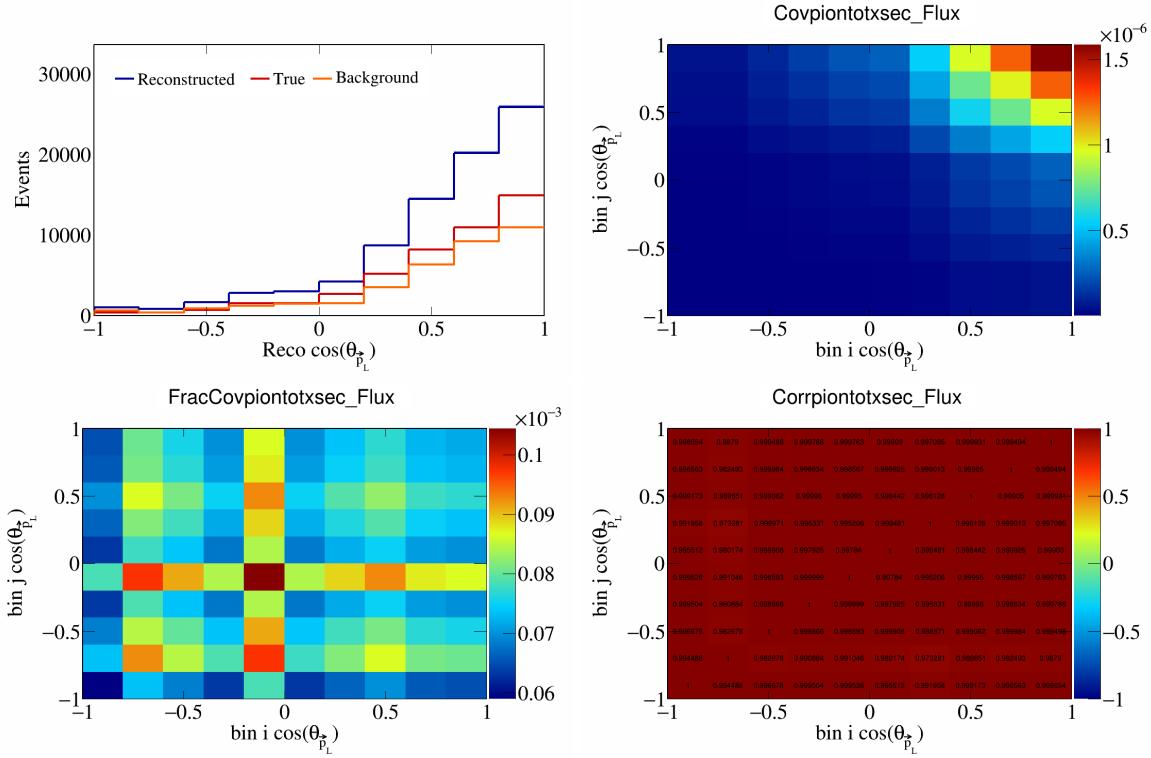


Figure 763: PionTotXSec variations for  $\cos(\theta_{\vec{p}_L})$ .

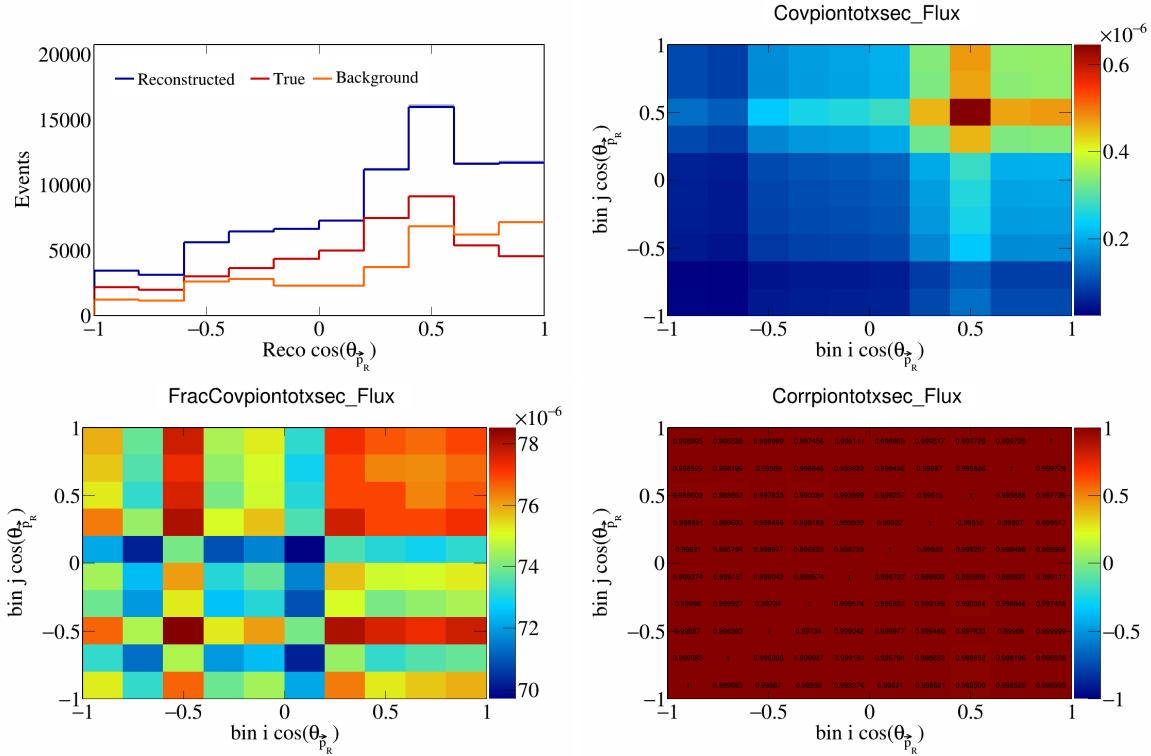


Figure 764: PionTotXSec variations for  $\cos(\theta_{\vec{p}_R})$ .

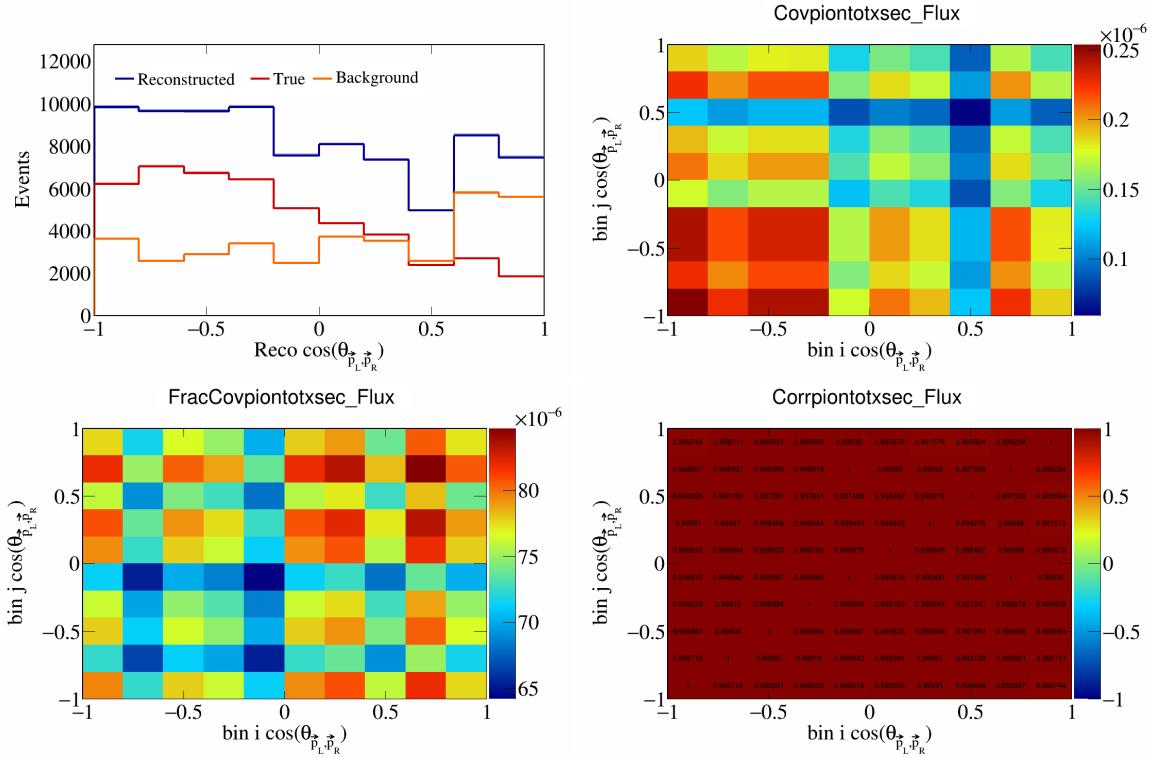


Figure 765: PionTotXSec variations for  $\cos(\theta_{\vec{p}_L, \vec{p}_R})$ .

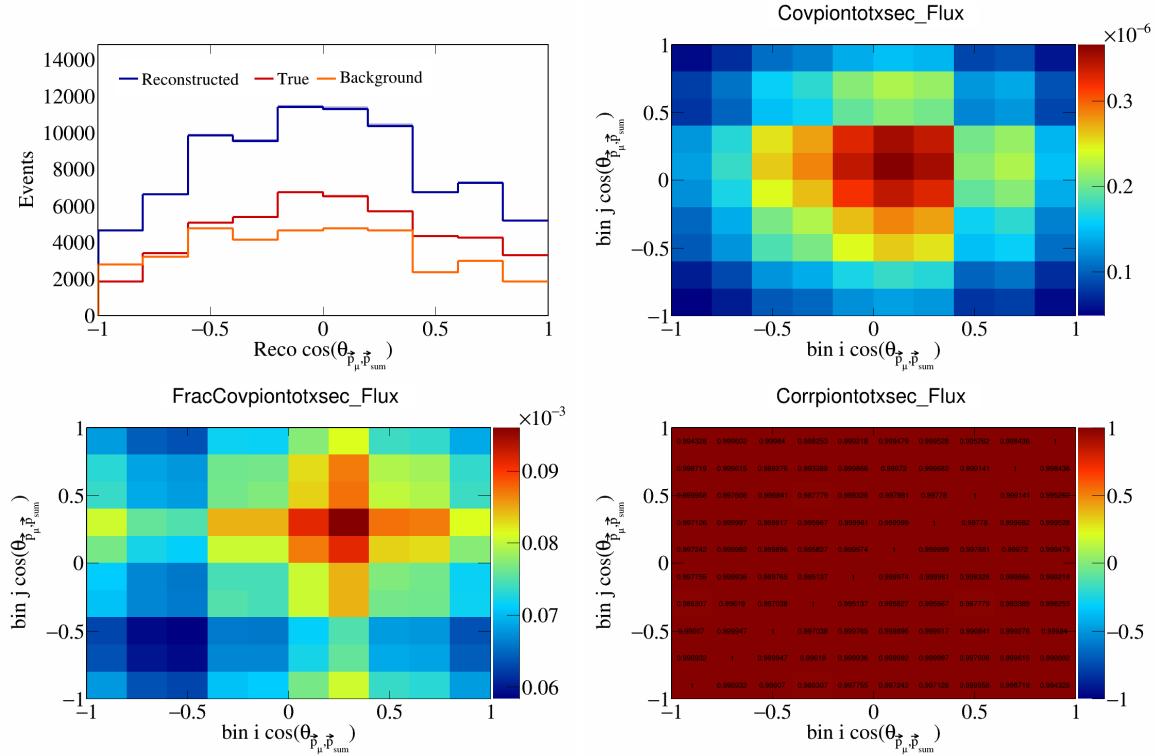


Figure 766: PionTotXSec variations for  $\cos(\theta_{\vec{p}_\mu, \vec{p}_{\text{sum}}})$ .

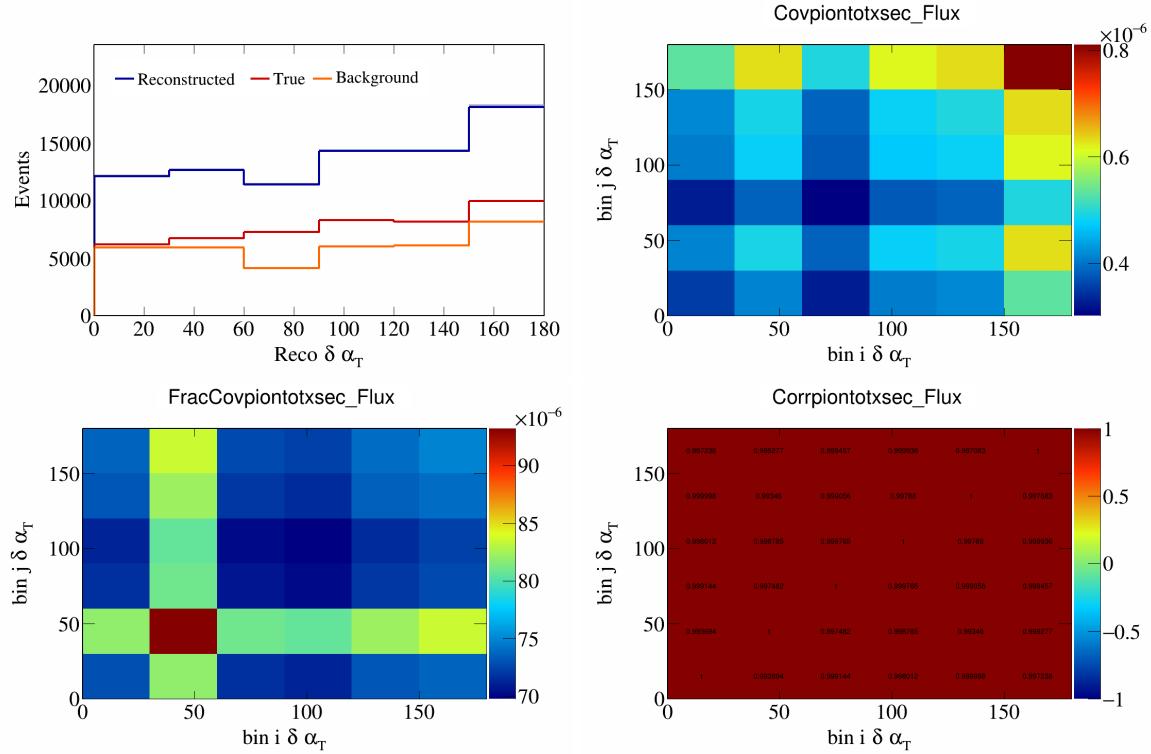


Figure 767: PionTotXSec variations for  $\delta\alpha_T$ .

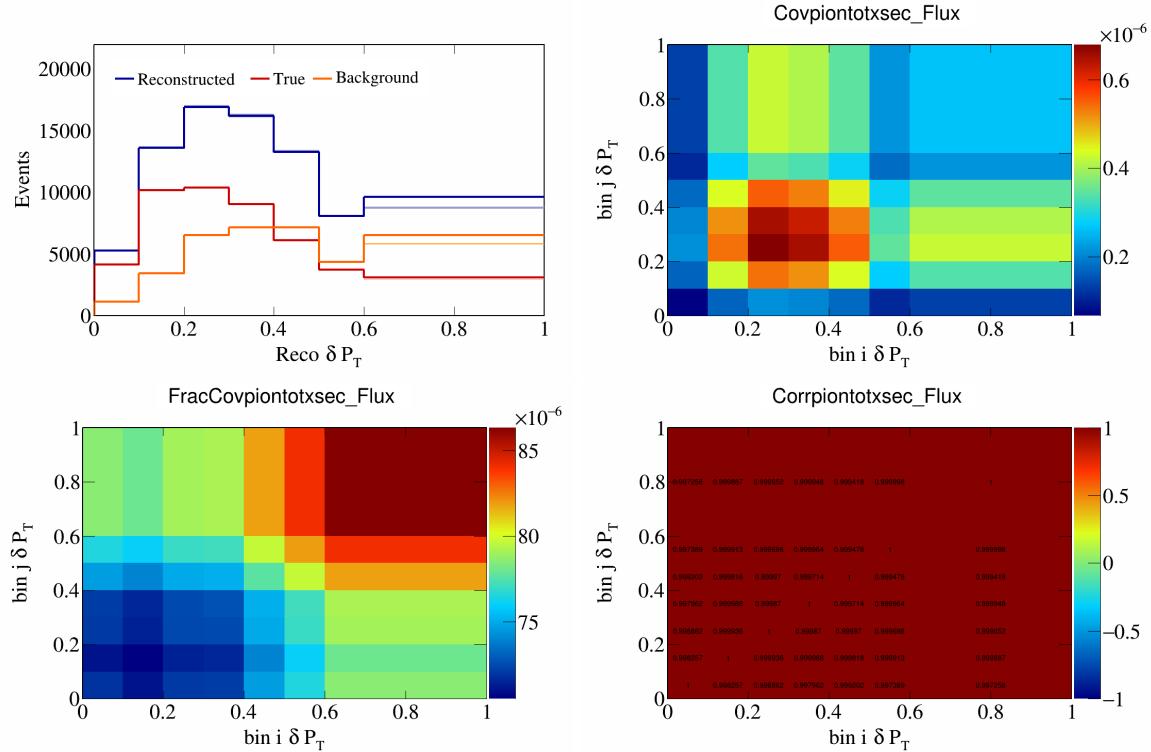


Figure 768: PionTotXSec variations for  $\delta P_T$ .

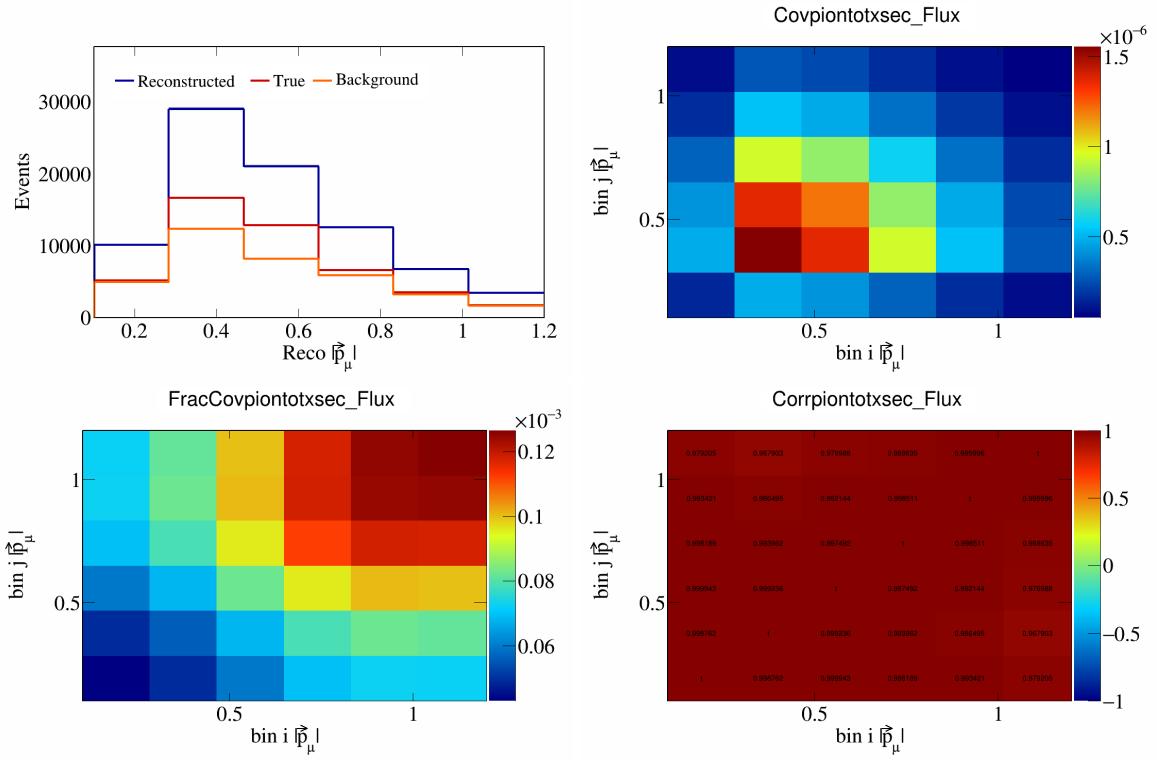


Figure 769: PionTotXSec variations for  $|\vec{p}_\mu|$ .

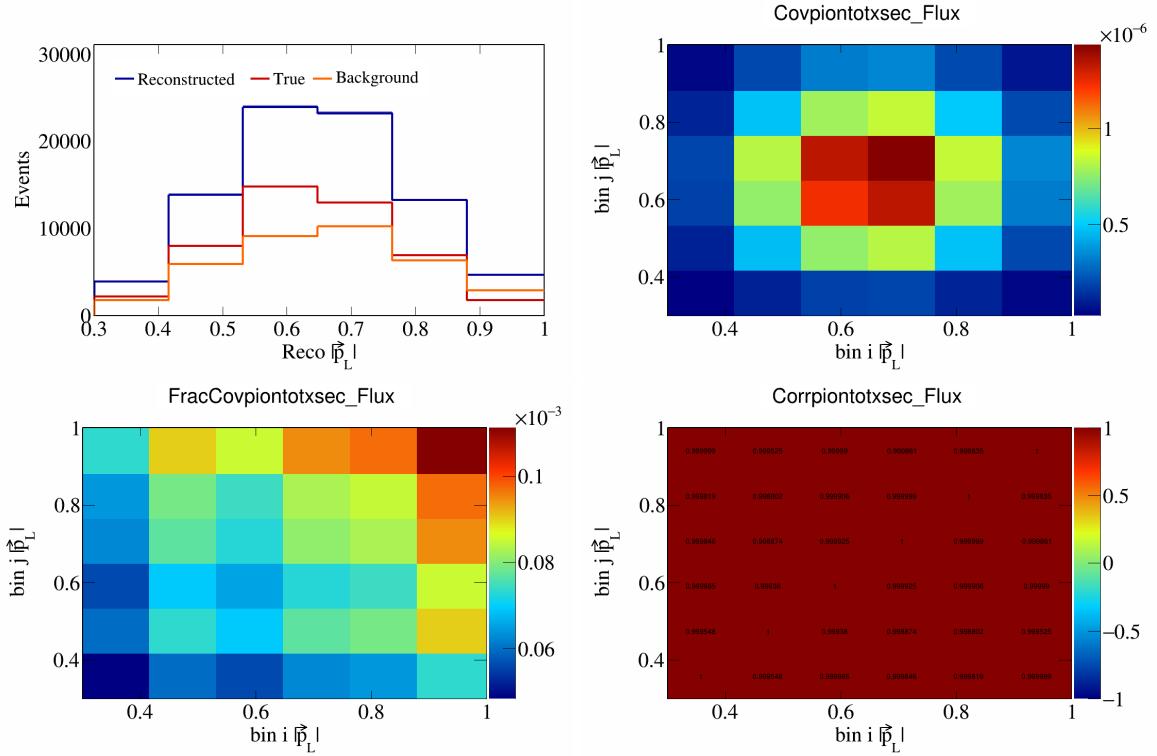


Figure 770: PionTotXSec variations for  $|\vec{p}_L|$ .

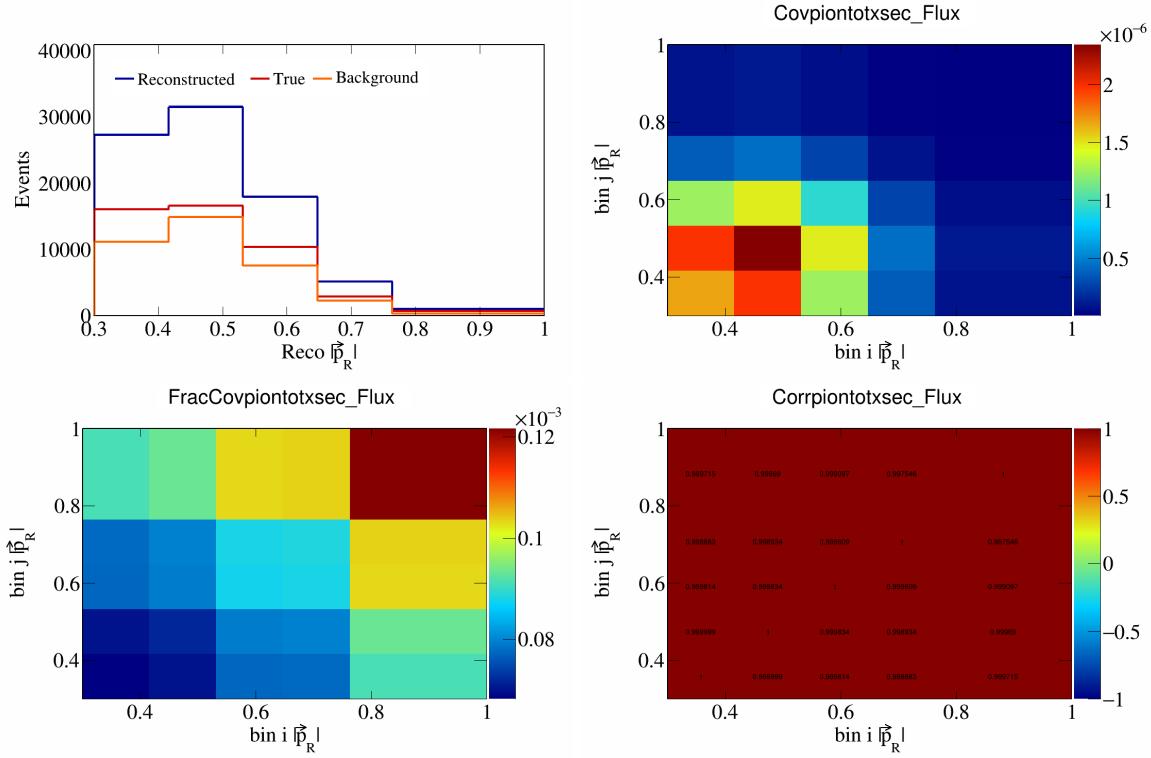


Figure 771: PionTotXSec variations for  $|\vec{p}_R|$ .

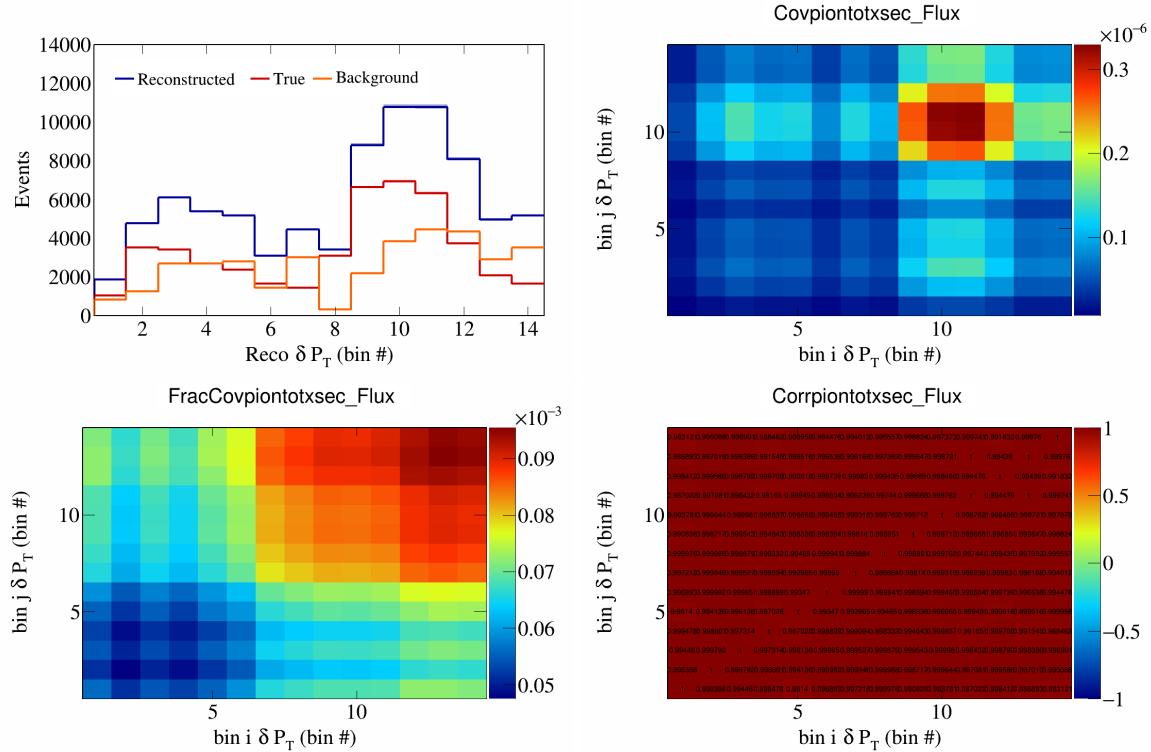


Figure 772: PionTotXSec variations for  $\delta P_T$  in  $\cos(\theta_{\vec{p}_\mu})$ .

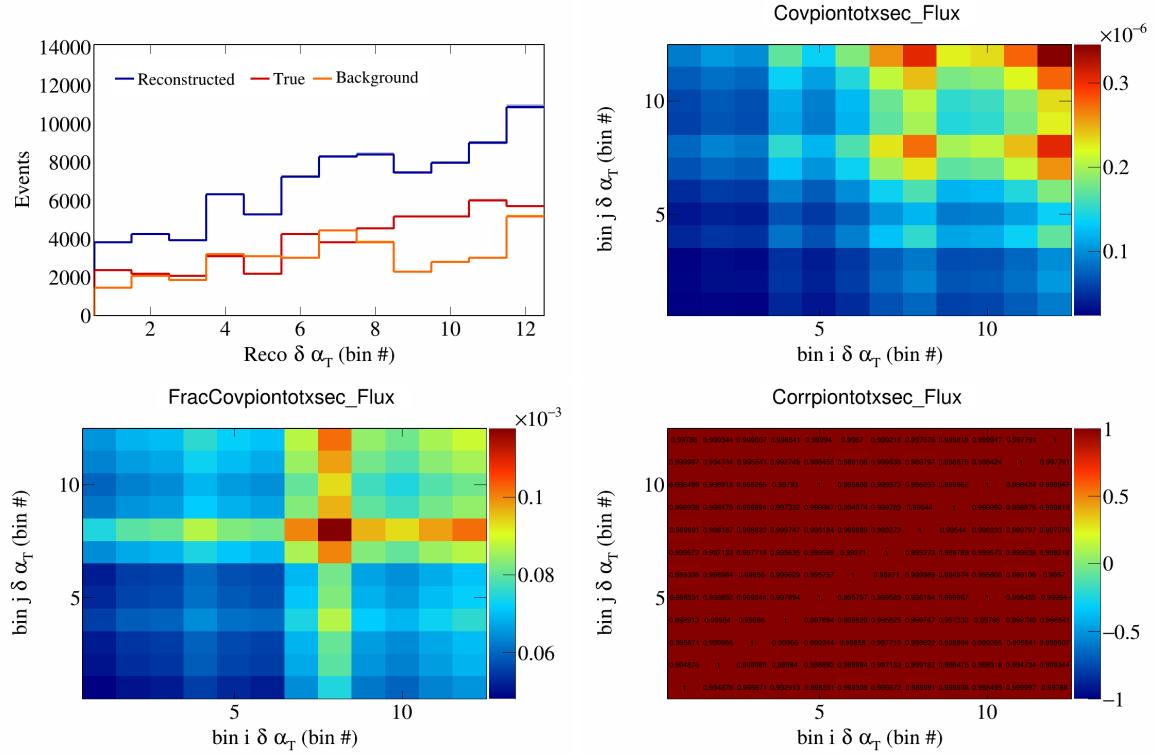


Figure 773: PionTotXSec variations for  $\delta \alpha_T$  in  $\cos(\theta_{\vec{p}_\mu})$ .

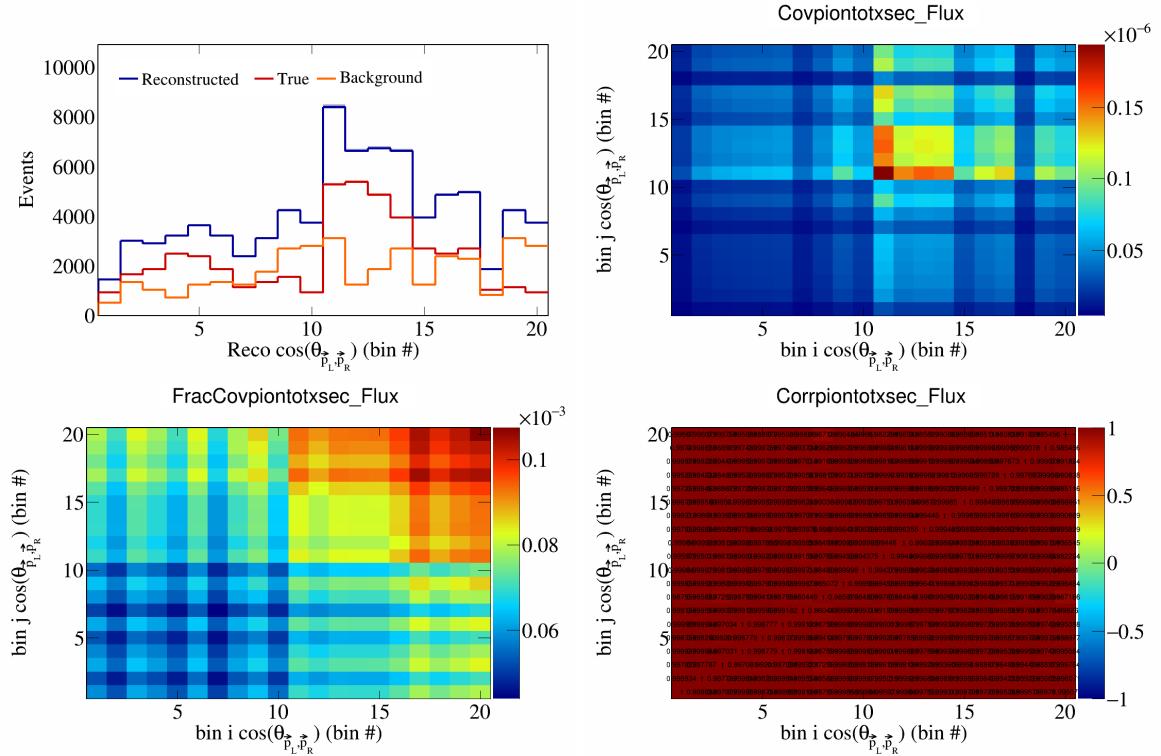


Figure 774: PionTotXSec variations for  $\cos(\theta_{\vec{p}_L, \vec{p}_R})$  in  $\cos(\theta_{\vec{p}_\mu})$ .

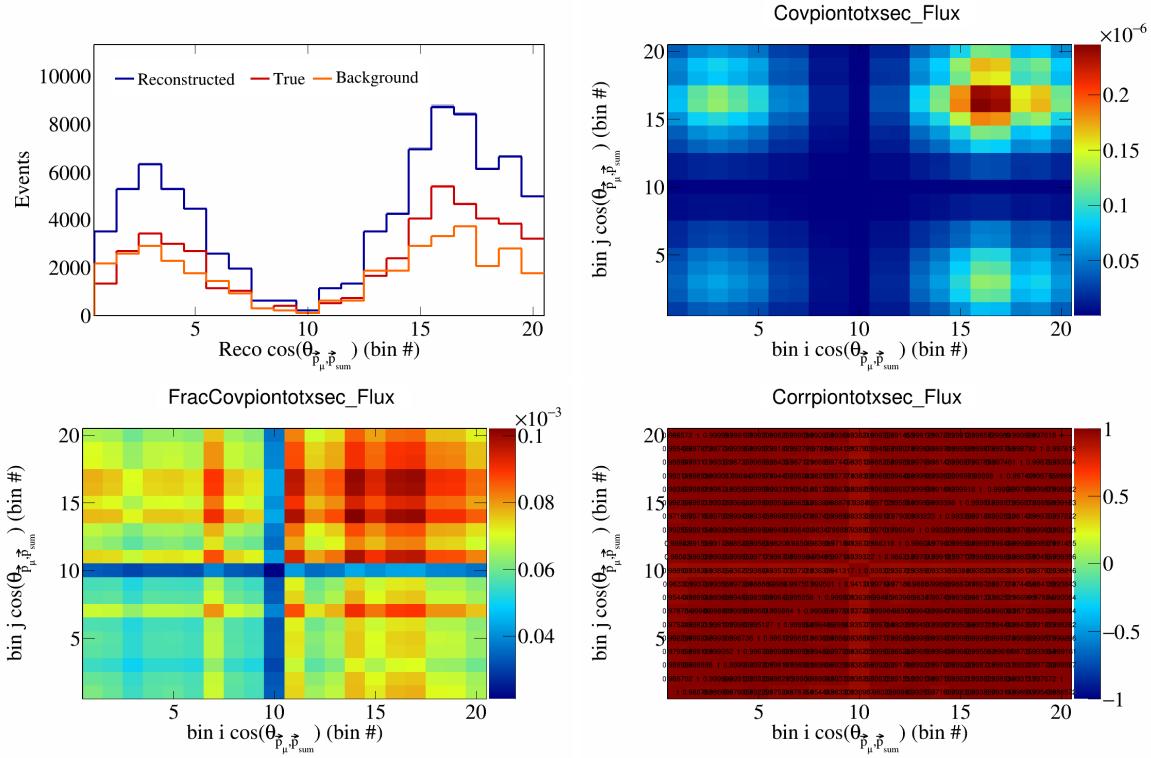


Figure 775: PionTotXSec variations for  $\cos(\theta_{\vec{p}_\mu, \vec{p}_{\text{sum}}})$  in  $\cos(\theta_{\vec{p}_\mu})$ .

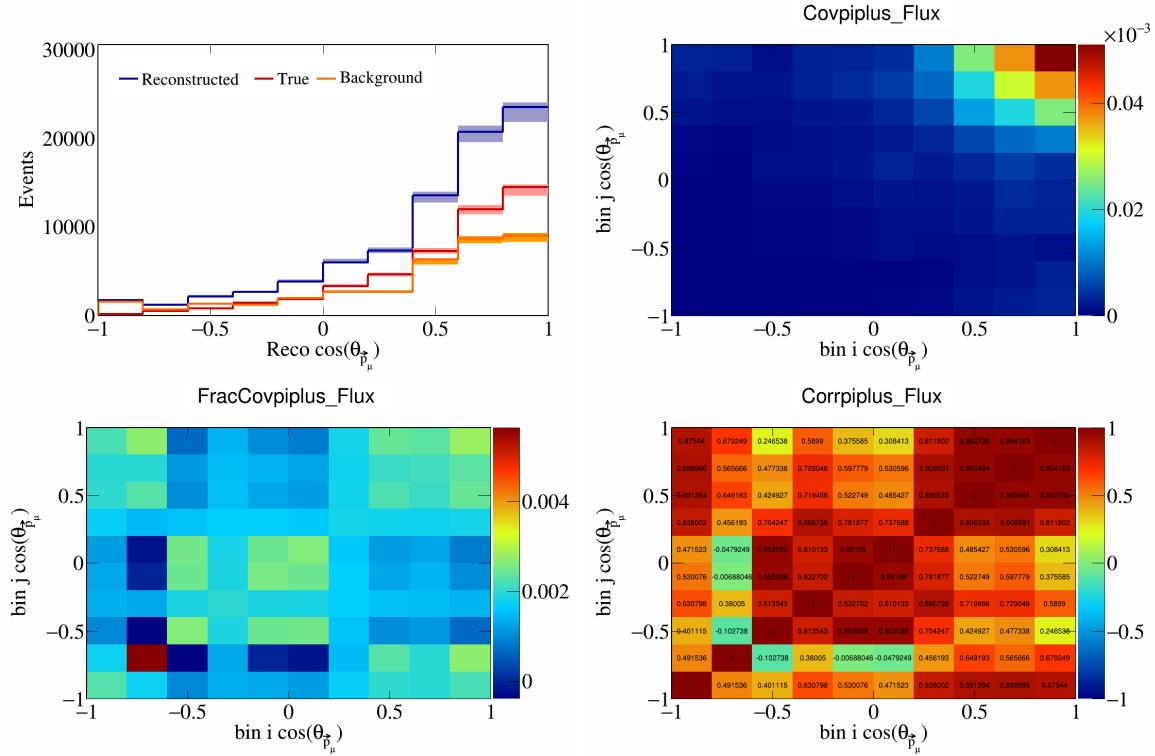


Figure 776: PiPlus variations for  $\cos(\theta_{\vec{p}_\mu})$ .

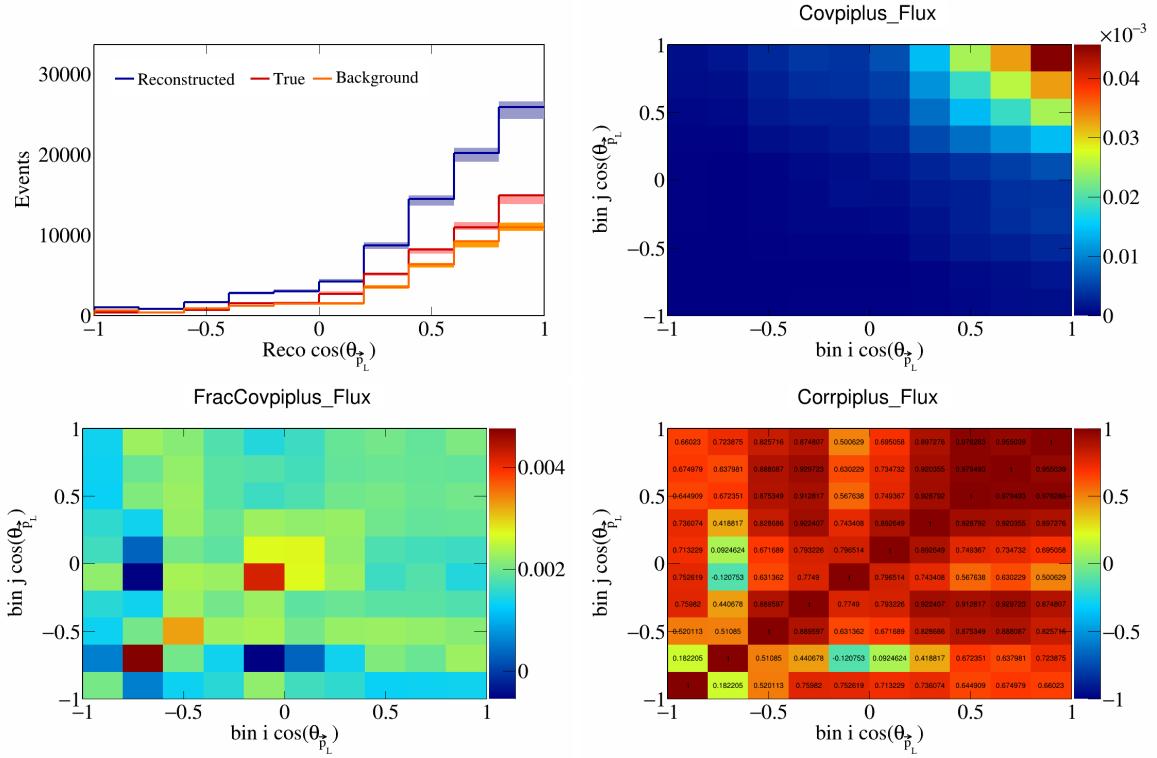


Figure 777: PiPlus variations for  $\cos(\theta_{\vec{p}_L})$ .

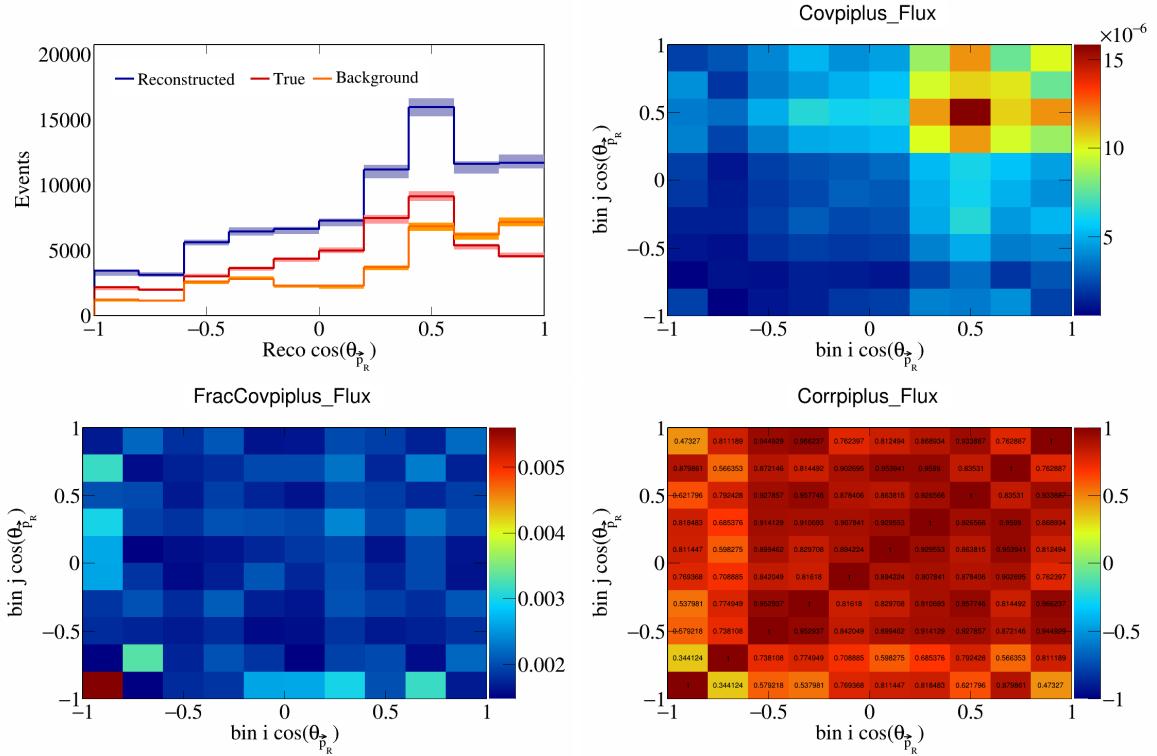


Figure 778: PiPlus variations for  $\cos(\theta_{\vec{p}_R})$ .

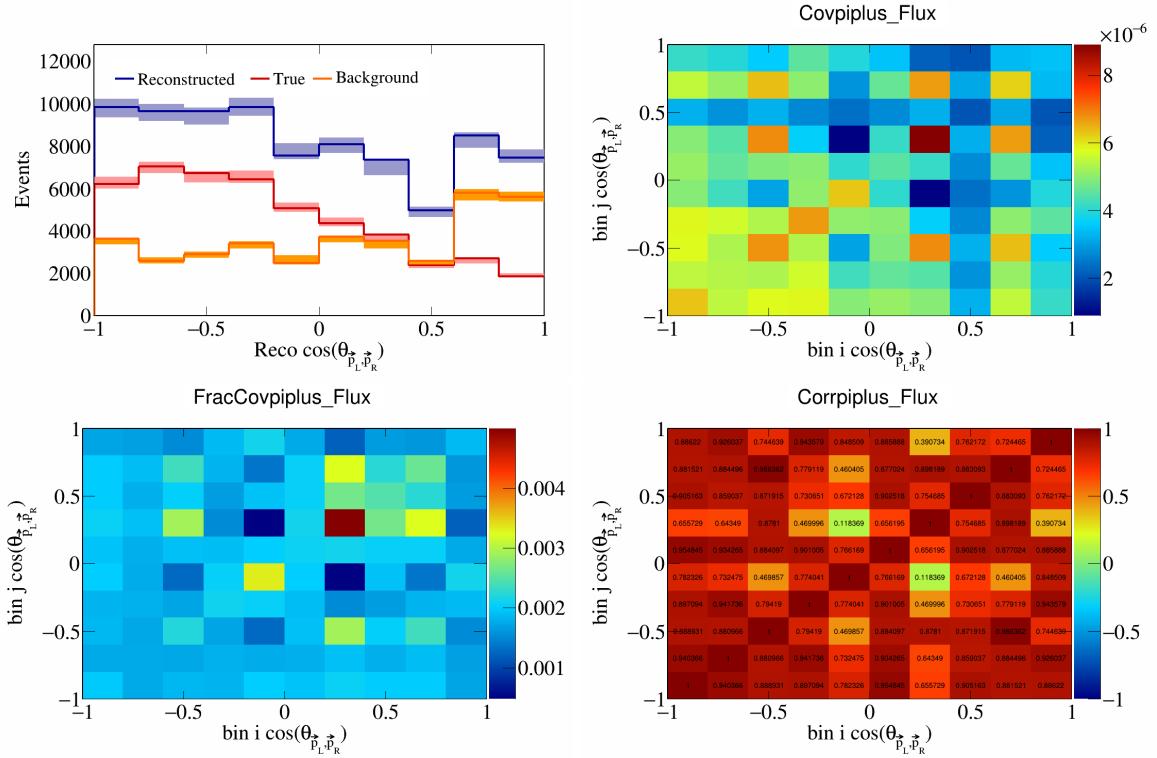


Figure 779: PiPlus variations for  $\cos(\theta_{\vec{p}_L, \vec{p}_R})$ .

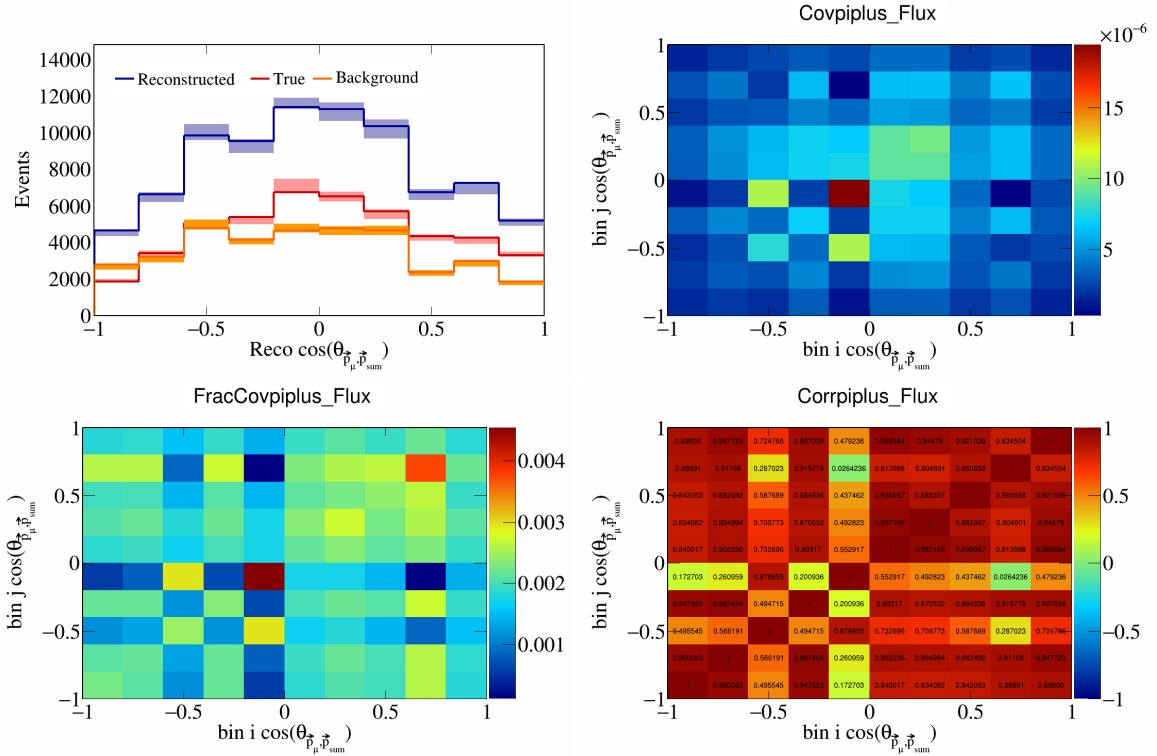


Figure 780: PiPlus variations for  $\cos(\theta_{\vec{p}_\mu, \vec{p}_{\text{sum}}})$ .

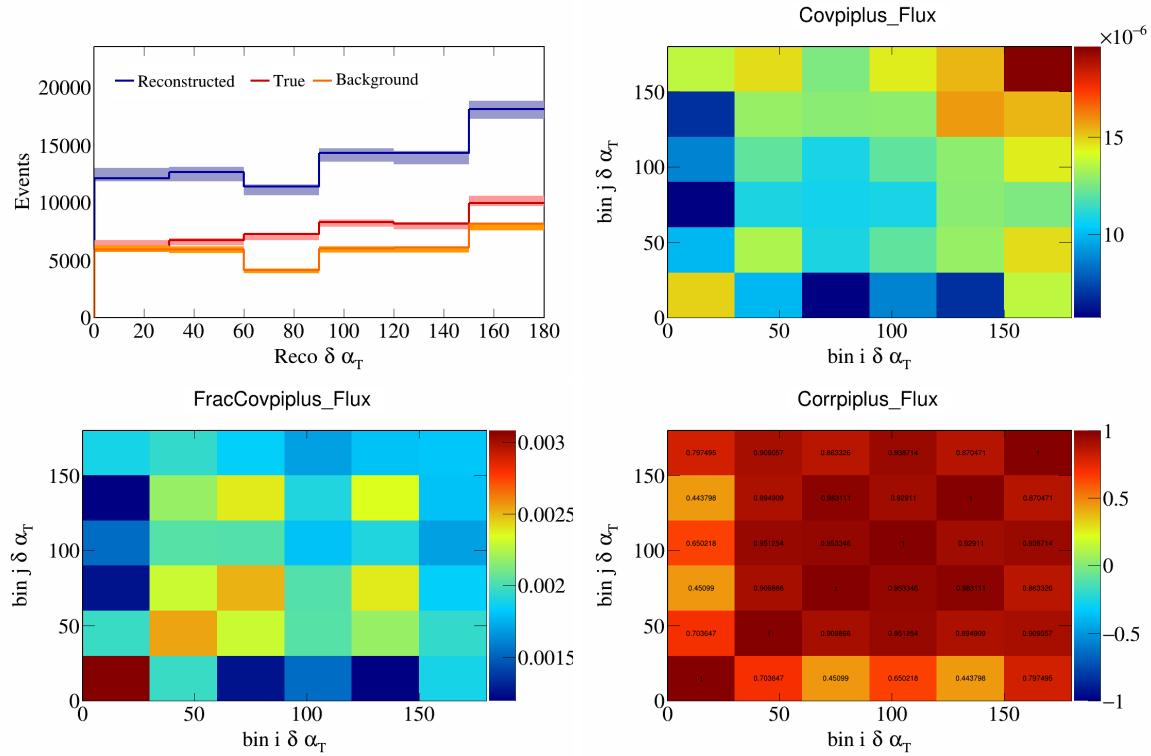


Figure 781: PiPlus variations for  $\delta\alpha_T$ .

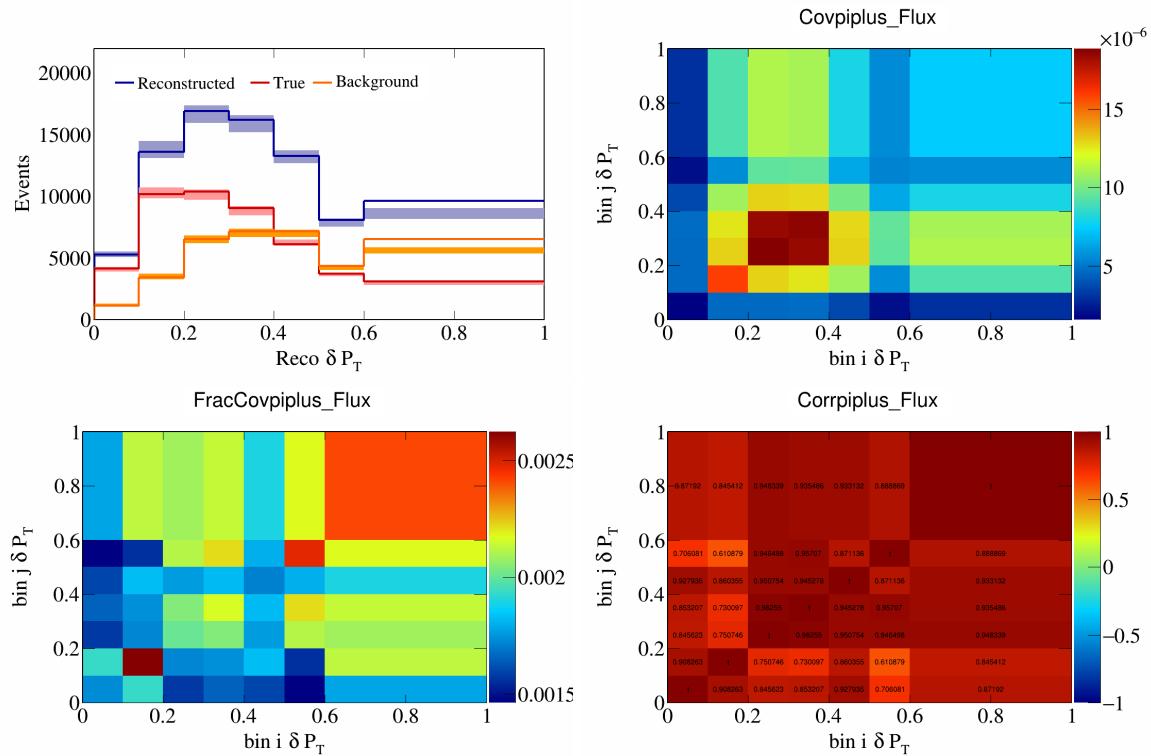


Figure 782: PiPlus variations for  $\delta P_T$ .

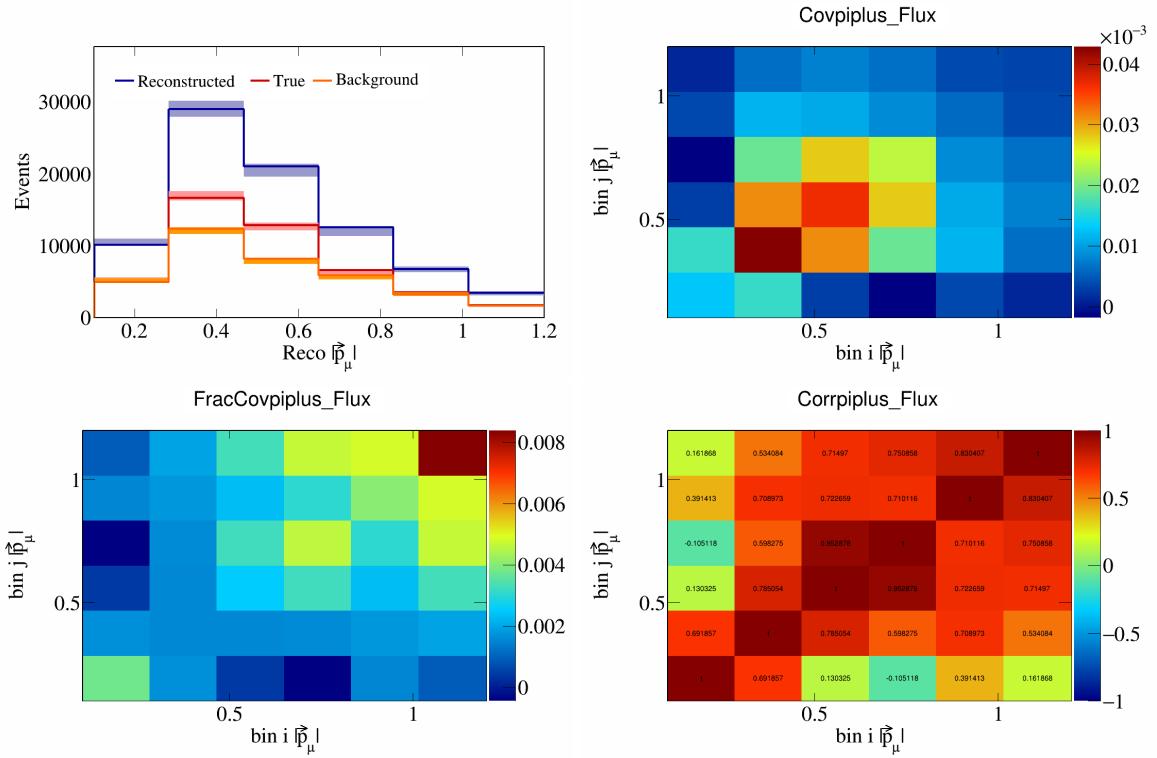


Figure 783: PiPlus variations for  $|\vec{p}_\mu|$ .

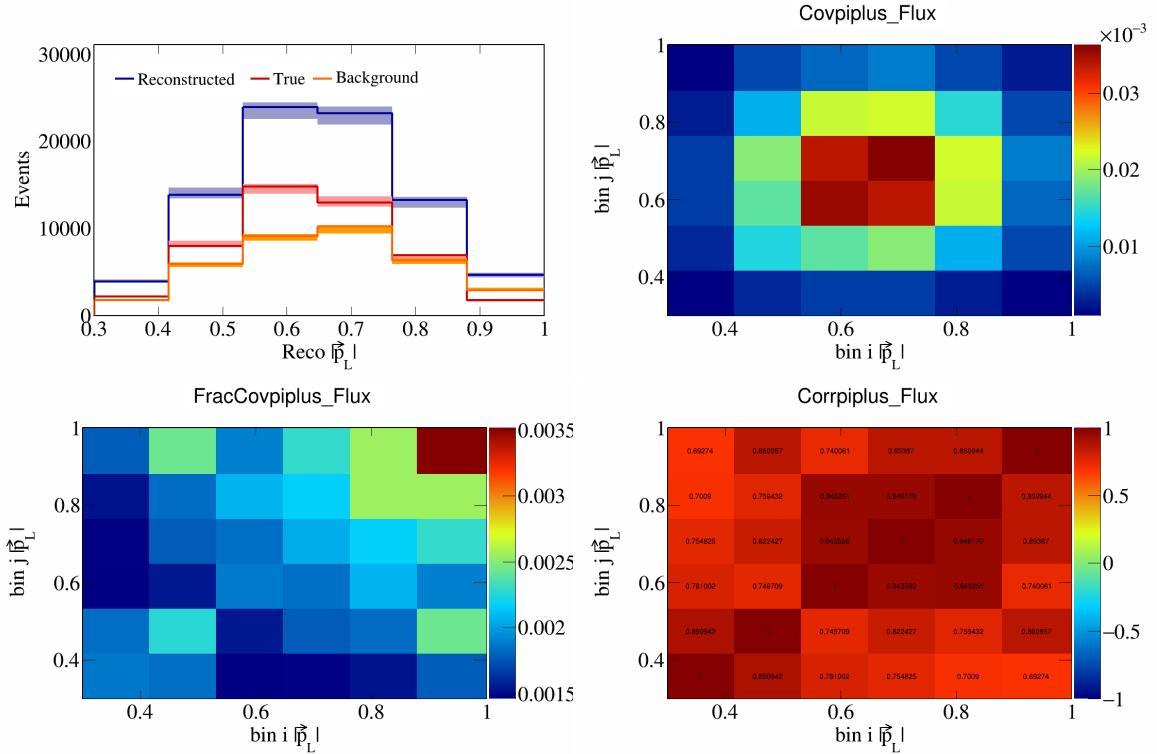


Figure 784: PiPlus variations for  $|\vec{p}_L|$ .

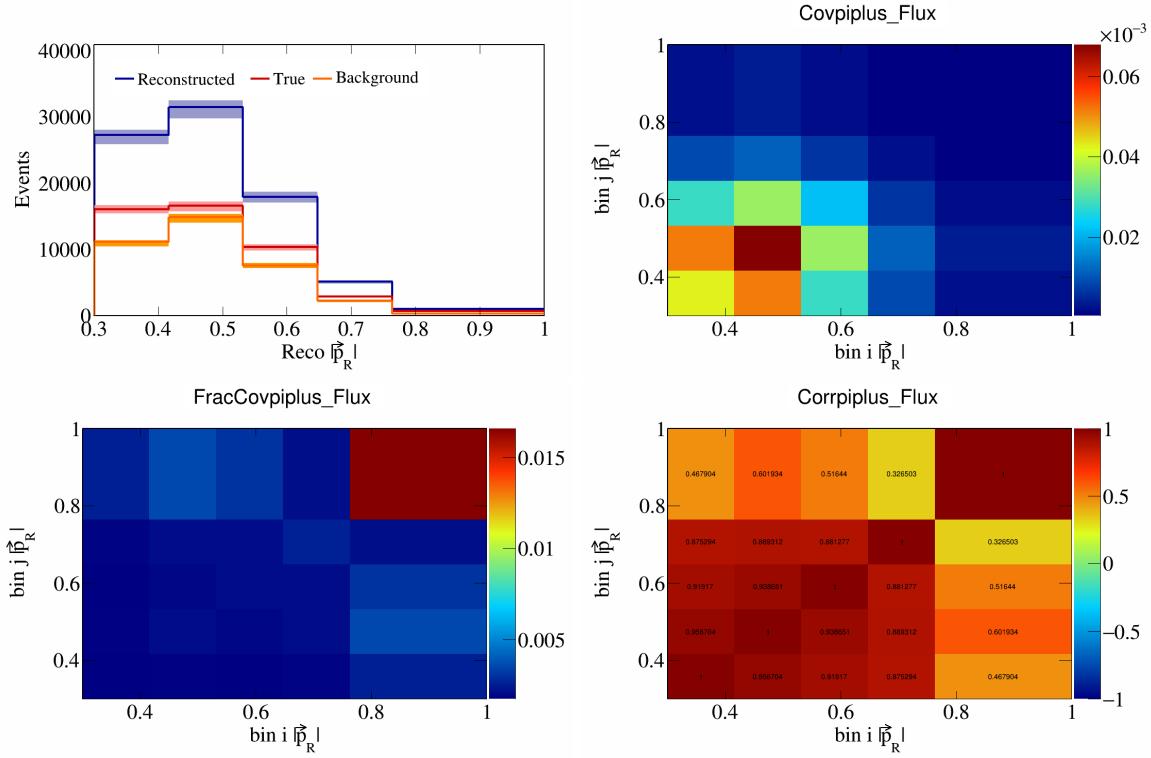


Figure 785: PiPlus variations for  $|\vec{p}_R|$ .

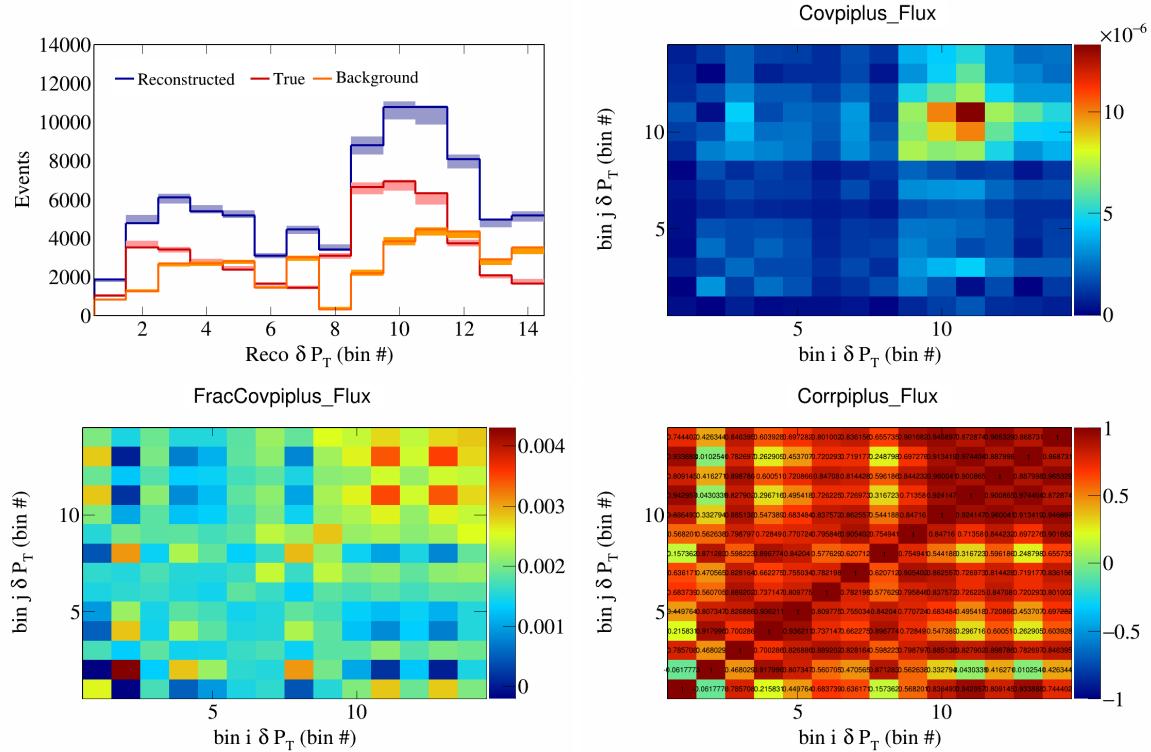


Figure 786: PiPlus variations for  $\delta P_T \cos(\theta_{\vec{p}_\mu})$ .

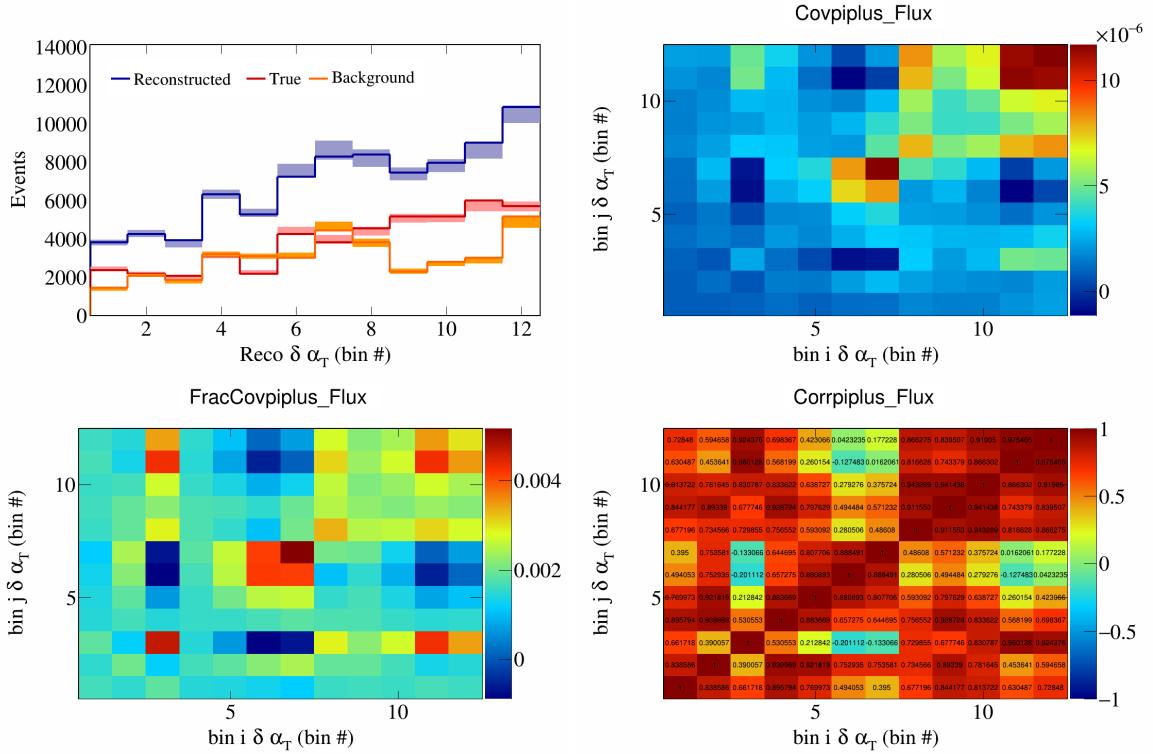


Figure 787: PiPlus variations for  $\delta\alpha_T$  in  $\cos(\theta_{\vec{p}_\mu})$ .

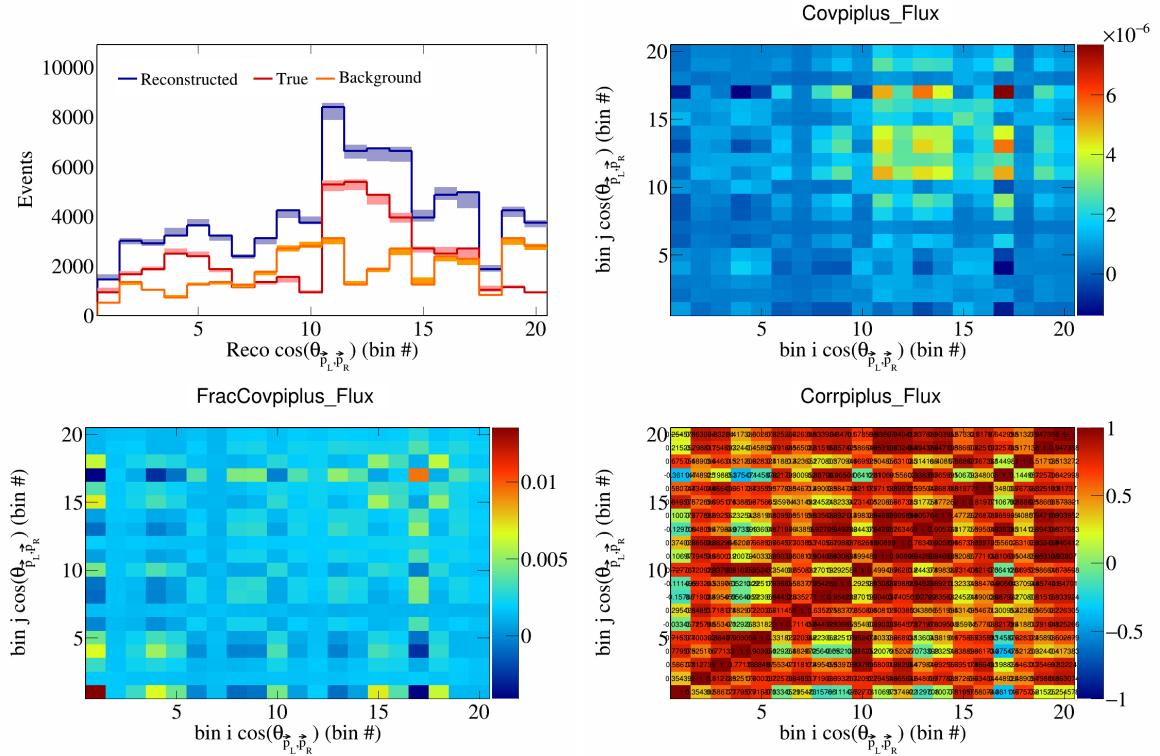


Figure 788: PiPlus variations for  $\cos(\theta_{\vec{p}_L, \vec{p}_R})$  in  $\cos(\theta_{\vec{p}_\mu})$ .

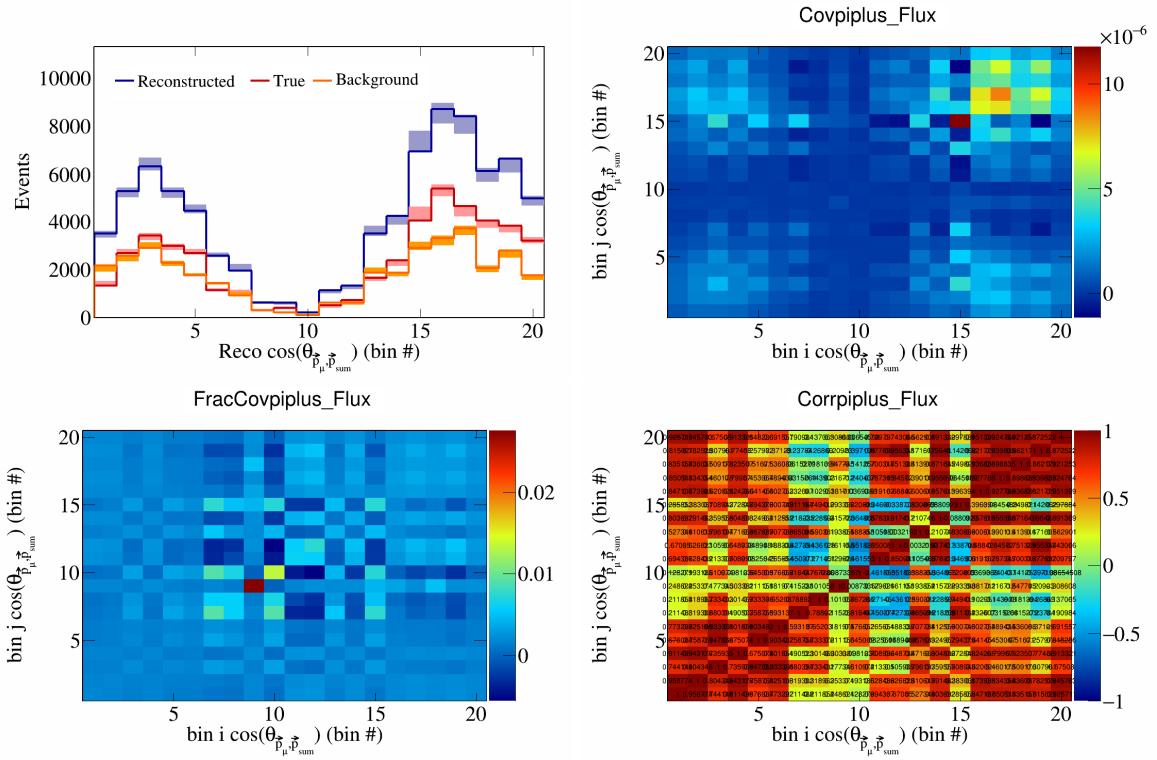


Figure 789: PiPlus variations for  $\cos(\theta_{\vec{p}_\mu})$  in  $\cos(\theta_{\vec{p}_\mu})$ .

289 **6.3 Statistical systematics**

290 In this appendix, the covariance, fractional covariance, and correlation matrices for the statistical systematics  
 291 are plotted.

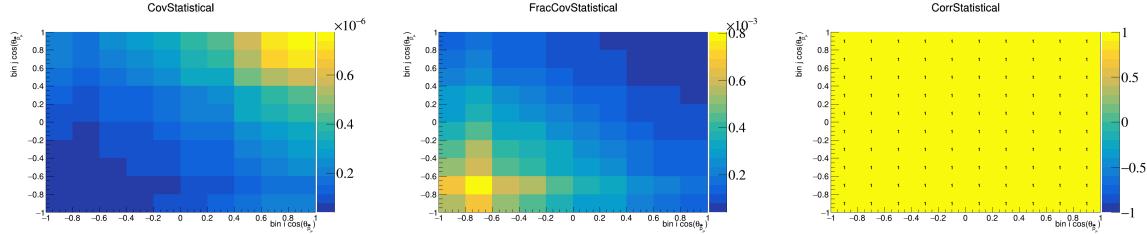


Figure 790: Statistical variations for  $\cos(\theta_{\vec{p}_\mu})$ .

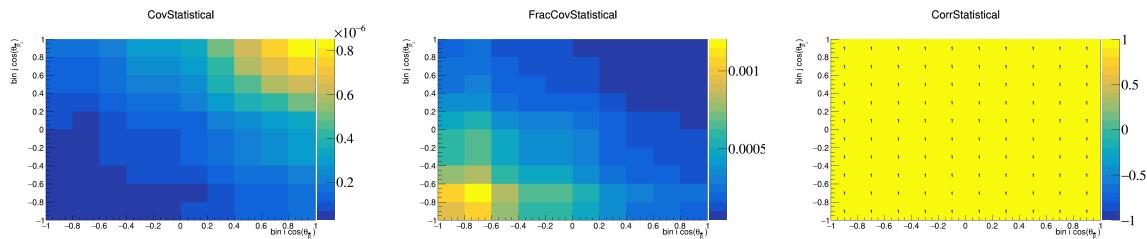


Figure 791: Statistical variations for  $\cos(\theta_{\vec{p}_L})$ .

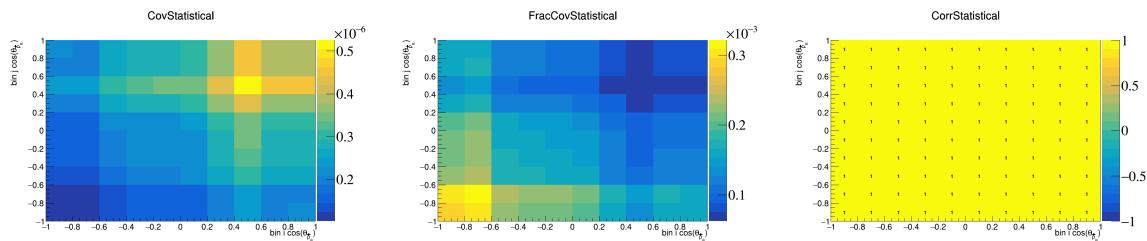


Figure 792: Statistical variations for  $\cos(\theta_{\vec{p}_R})$ .

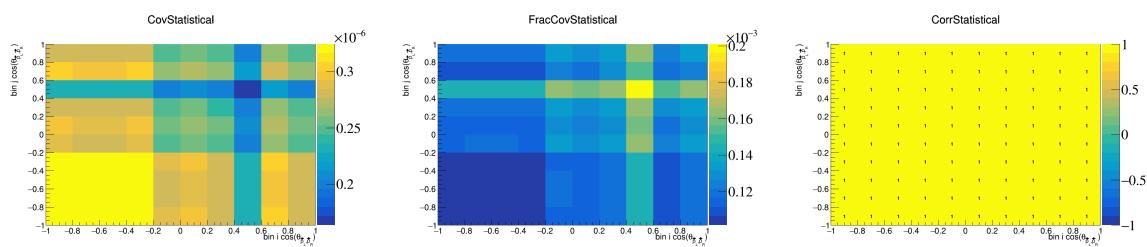


Figure 793: Statistical variations for  $\cos(\theta_{\vec{p}_L, \vec{p}_R})$ .

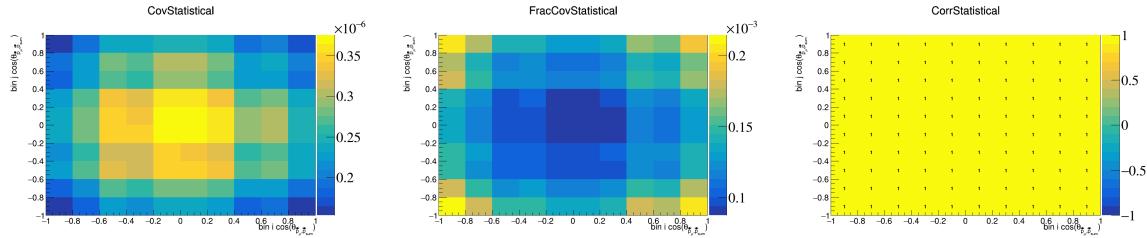


Figure 794: Statistical variations for  $\cos(\theta_{\vec{p}_\mu, \vec{p}_{\text{sum}}})$ .

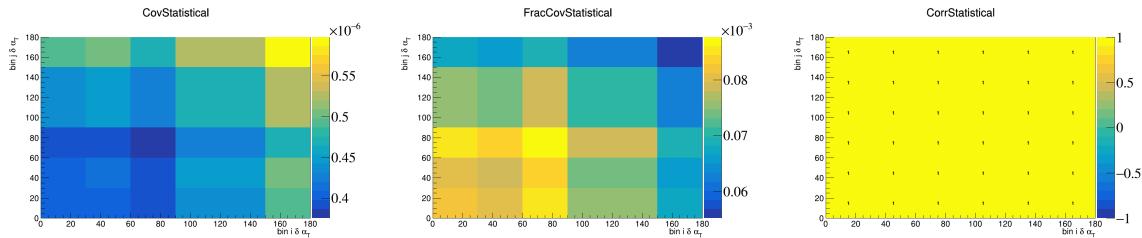


Figure 795: Statistical variations for  $\delta \alpha_T$ .

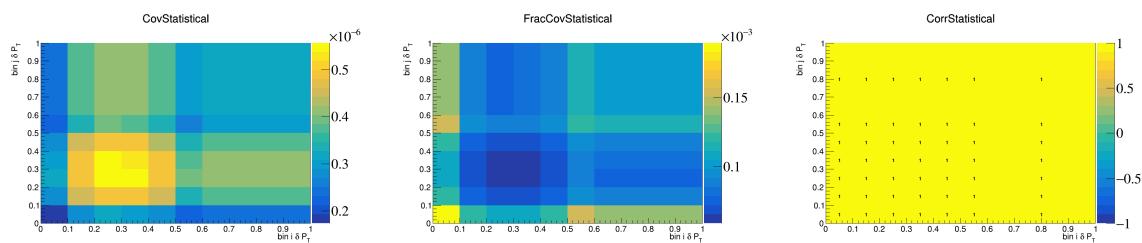


Figure 796: Statistical variations for  $\delta P_T$ .

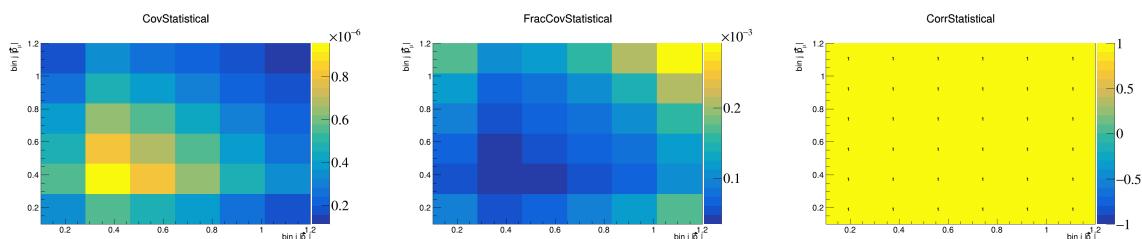


Figure 797: Statistical variations for  $|\vec{p}_\mu|$ .

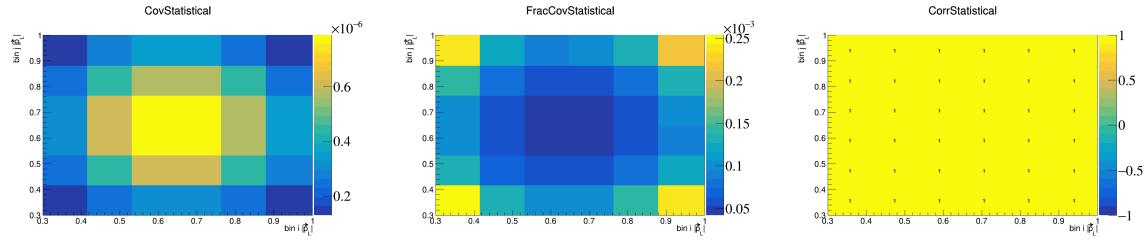


Figure 798: Statistical variations for  $|\vec{p}_L|$ .

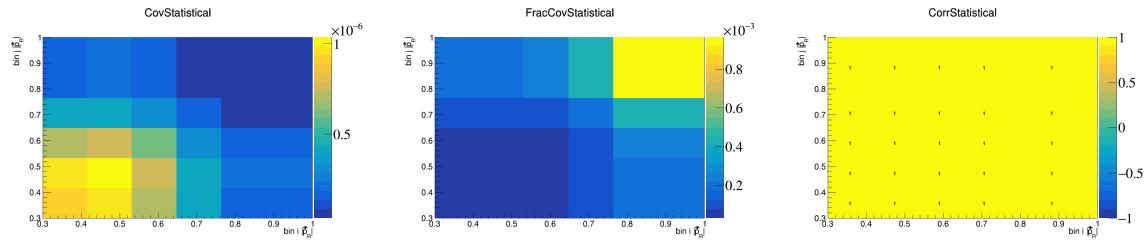


Figure 799: Statistical variations for  $|\vec{p}_R|$ .

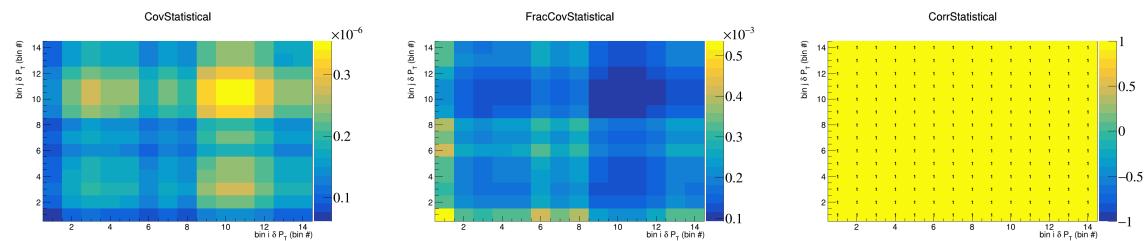


Figure 800: Statistical variations for  $\delta P_T$  in  $\cos(\theta_{\vec{p}_\mu})$ .

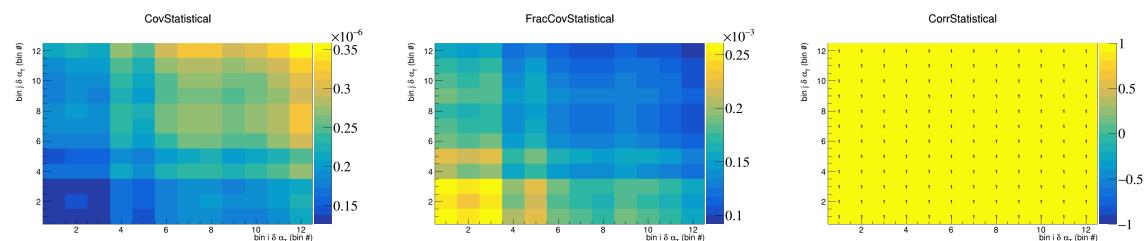


Figure 801: Statistical variations for  $\delta \alpha_T$  in  $\cos(\theta_{\vec{p}_\mu})$ .

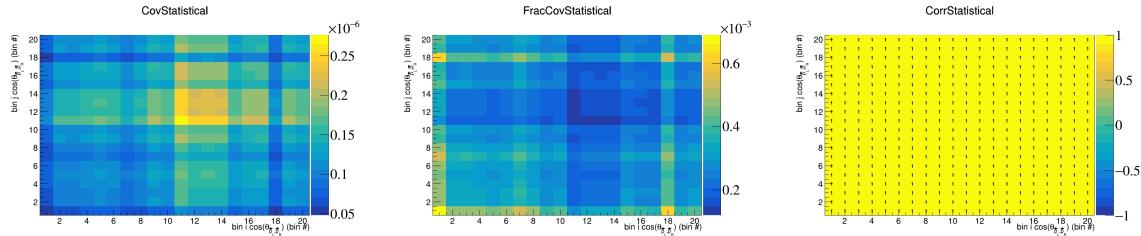


Figure 802: Statistical variations for  $\cos(\theta_{\vec{p}_L, \vec{p}_R})$  in  $\cos(\theta_{\vec{p}_\mu})$ .

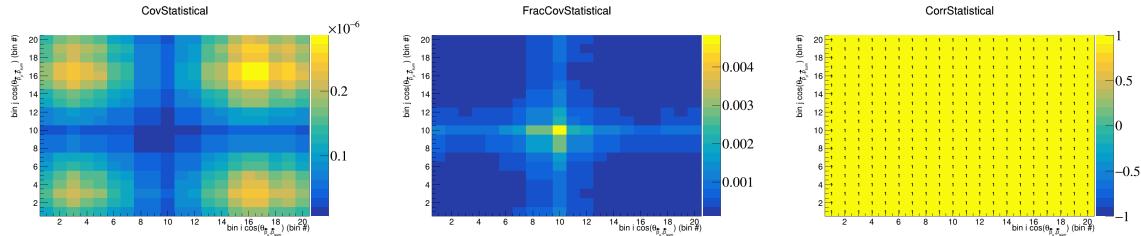


Figure 803: Statistical variations for  $\cos(\theta_{\vec{p}_\mu, \vec{p}_{\text{sum}}})$  in  $\cos(\theta_{\vec{p}_\mu})$ .

292 **6.4 POT**

293 In this appendix, the covariance, fractional covariance, and correlation matrices for the POT systematics are  
 294 plotted.

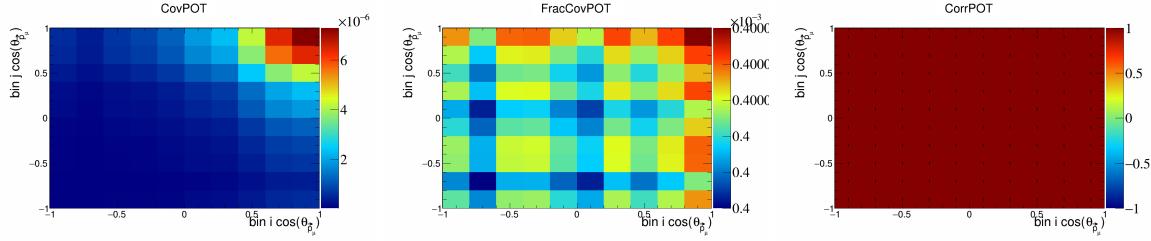


Figure 804: POT variations for  $\cos(\theta_{\vec{p}_\mu})$ .

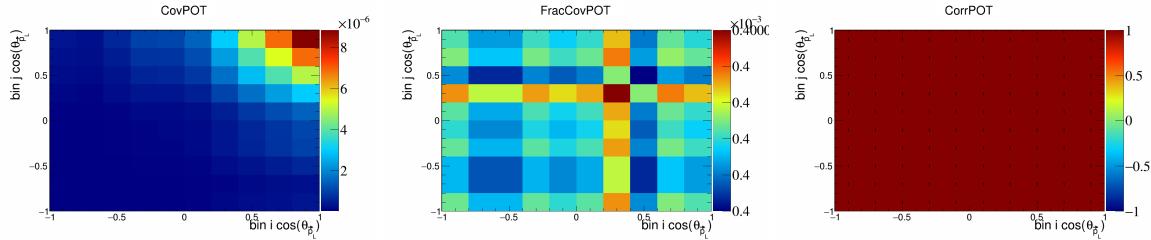


Figure 805: POT variations for  $\cos(\theta_{\vec{p}_L})$ .

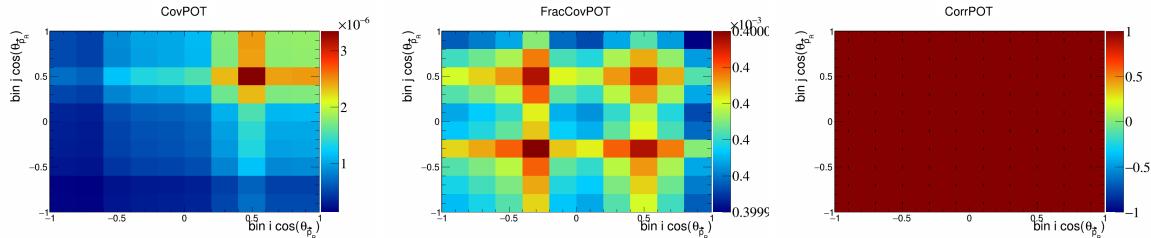


Figure 806: POT variations for  $\cos(\theta_{\vec{p}_R})$ .

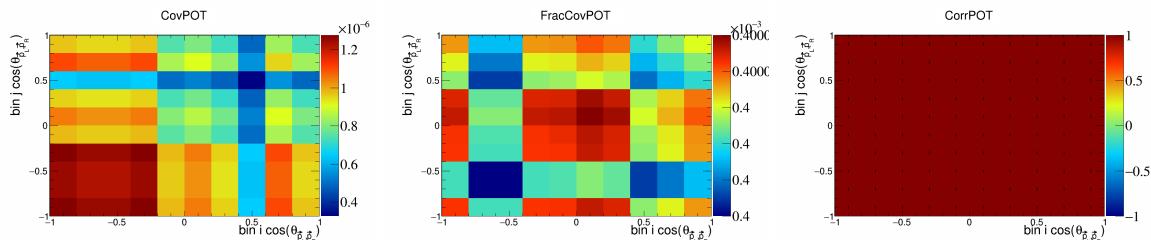


Figure 807: POT variations for  $\cos(\theta_{\vec{p}_L, \vec{p}_R})$ .

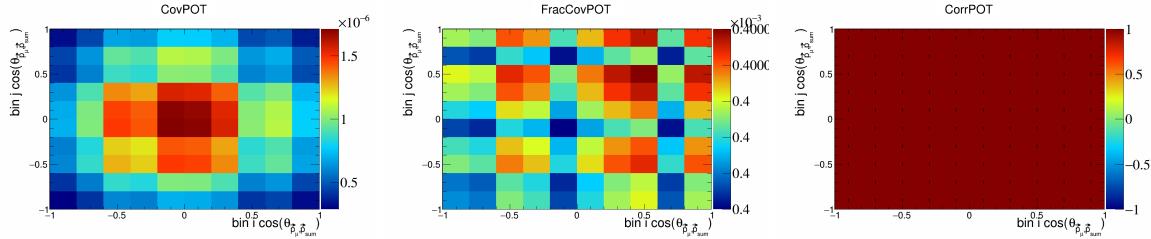


Figure 808: POT variations for  $\cos(\theta_{\vec{p}_\mu, \vec{p}_{sum}})$ .

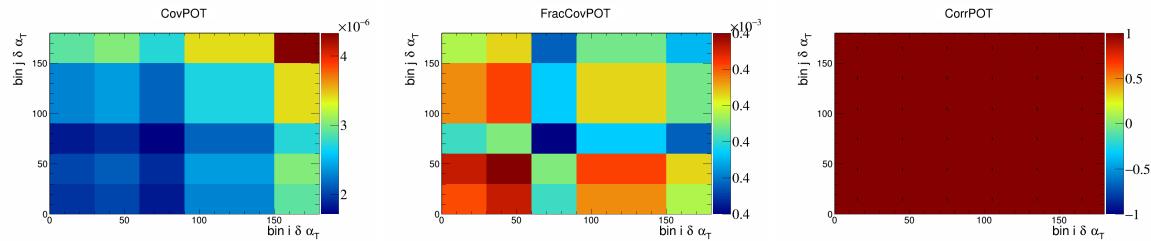


Figure 809: POT variations for  $\delta \alpha_T$ .

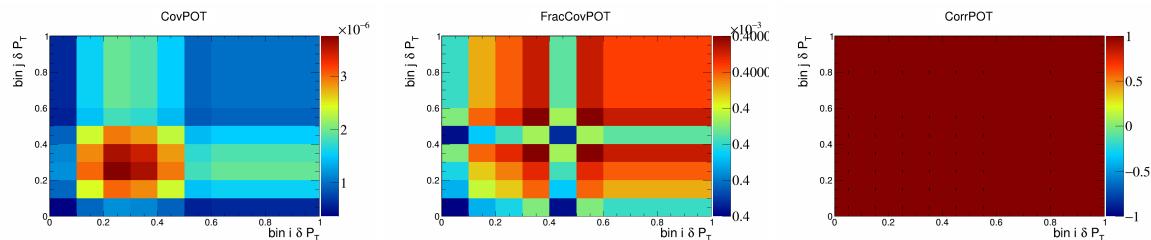


Figure 810: POT variations for  $\delta P_T$ .

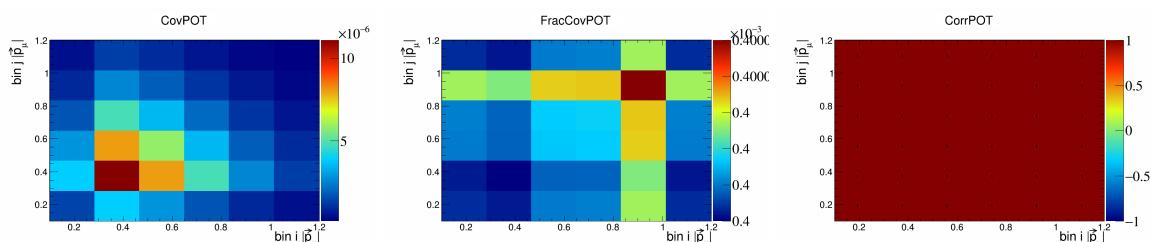


Figure 811: POT variations for  $|\vec{p}_\mu|$ .

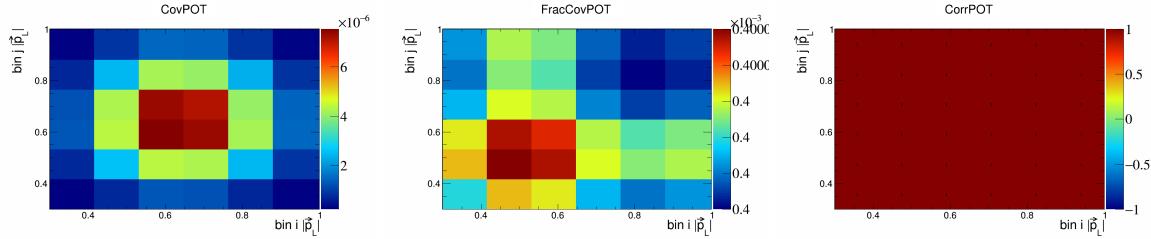


Figure 812: POT variations for  $|\vec{p}_L|$ .

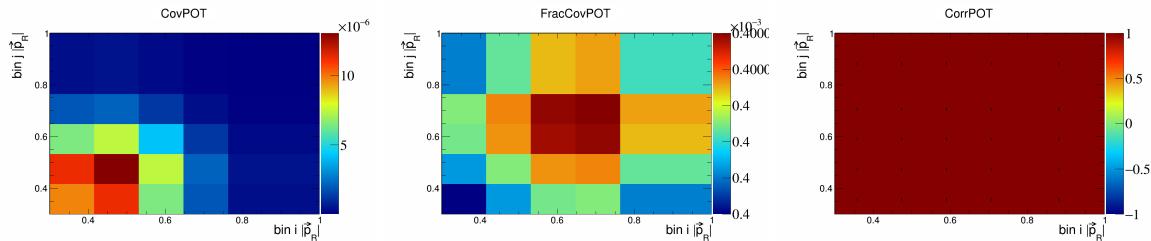


Figure 813: POT variations for  $|\vec{p}_R|$ .

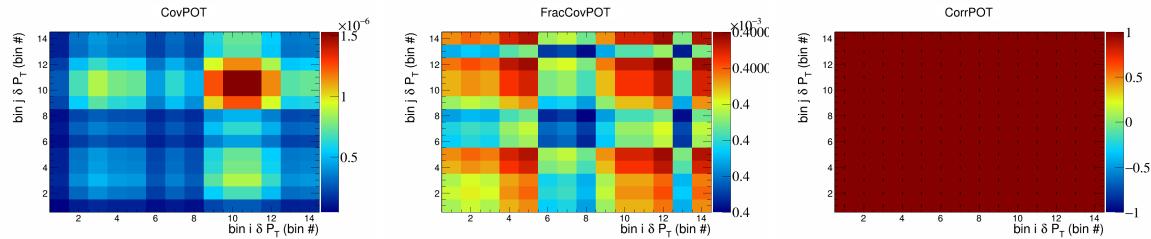


Figure 814: POT variations for  $\delta P_T$  in  $\cos(\theta_{\vec{p}_\mu})$ .

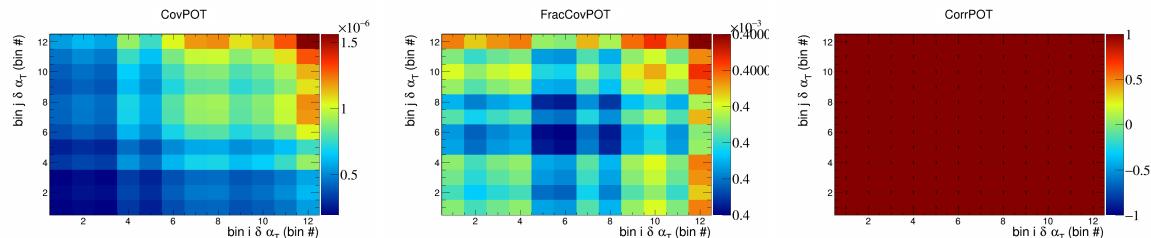


Figure 815: POT variations for  $\delta \alpha_T$  in  $\cos(\theta_{\vec{p}_\mu})$ .

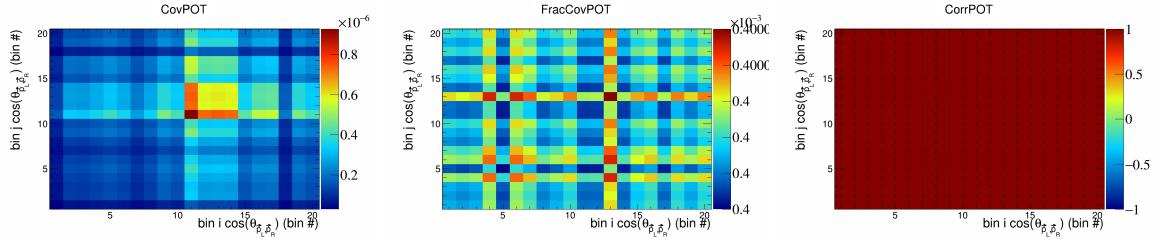


Figure 816: POT variations for  $\cos(\theta_{\vec{p}_L,\vec{p}_R})$  in  $\cos(\theta_{\vec{p}_\mu})$ .

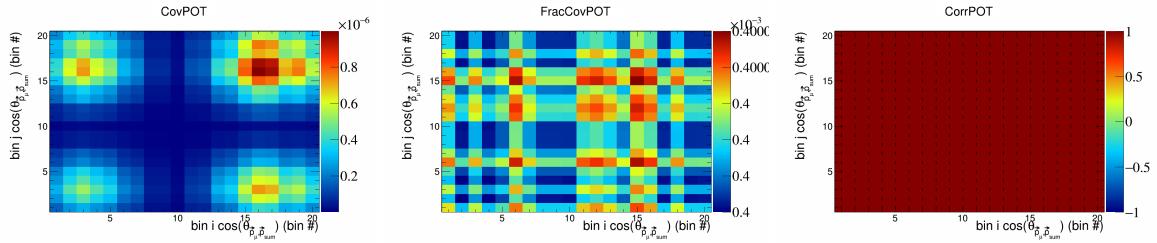


Figure 817: POT variations for  $\cos(\theta_{\vec{p}_\mu,\vec{p}_{sum}})$  in  $\cos(\theta_{\vec{p}_\mu})$ .

## 295 6.5 Number of targets

296 In this appendix, the covariance, fractional covariance, and correlation matrices for the number of targets  
 297 systematics are plotted.

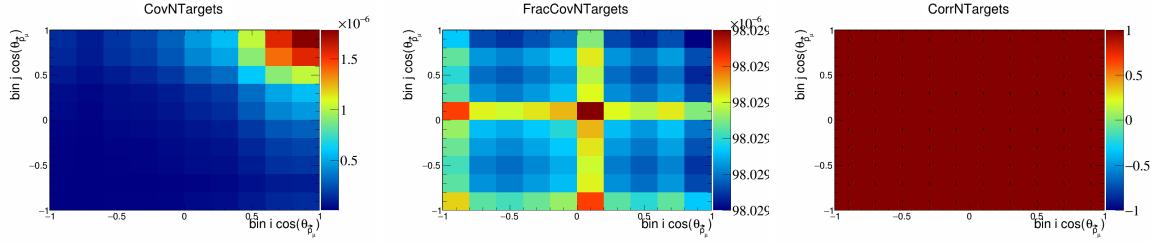


Figure 818: NTTargets variations for  $\cos(\theta_{\vec{p}_\mu})$ .

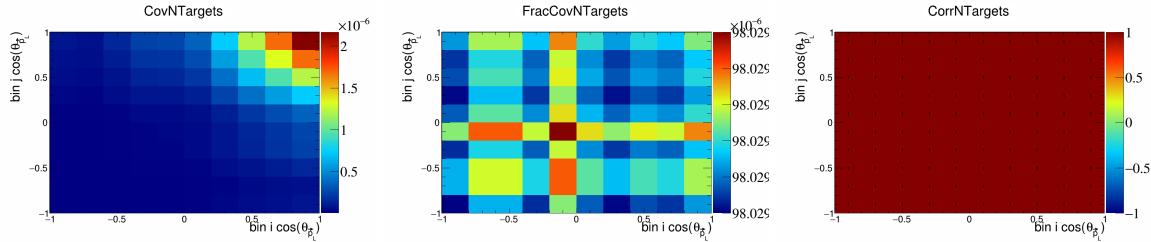


Figure 819: NTTargets variations for  $\cos(\theta_{\vec{p}_L})$ .

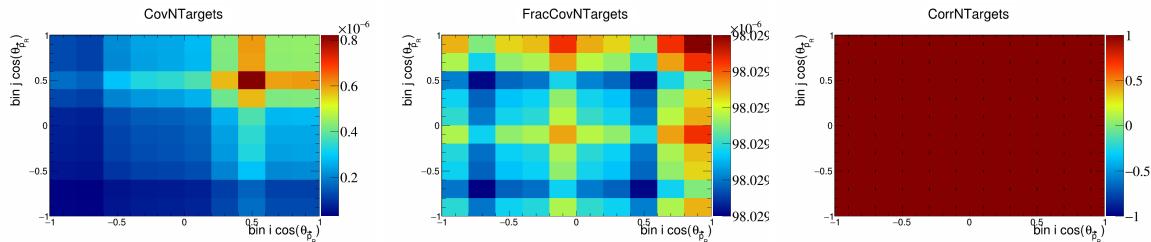


Figure 820: NTTargets variations for  $\cos(\theta_{\vec{p}_R})$ .

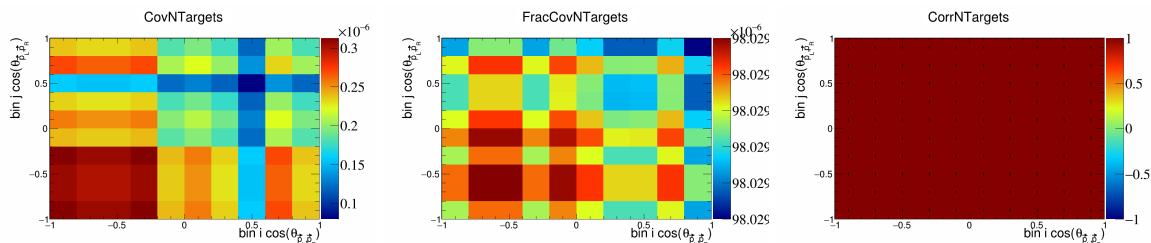


Figure 821: NTTargets variations for  $\cos(\theta_{\vec{p}_L, \vec{p}_R})$ .

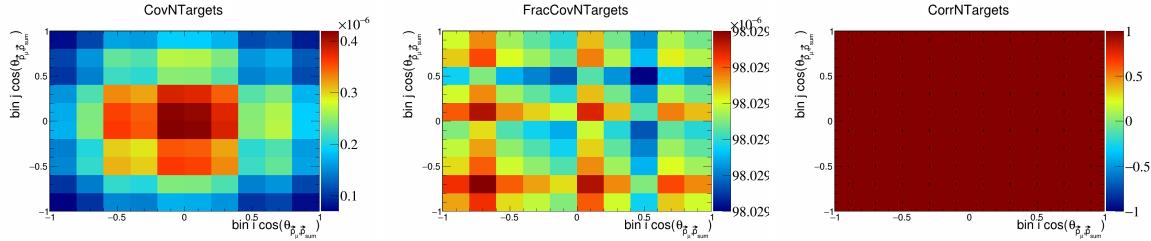


Figure 822: NTARGETS variations for  $\cos(\theta_{\vec{p}_\mu, \vec{p}_{\text{sum}}})$ .

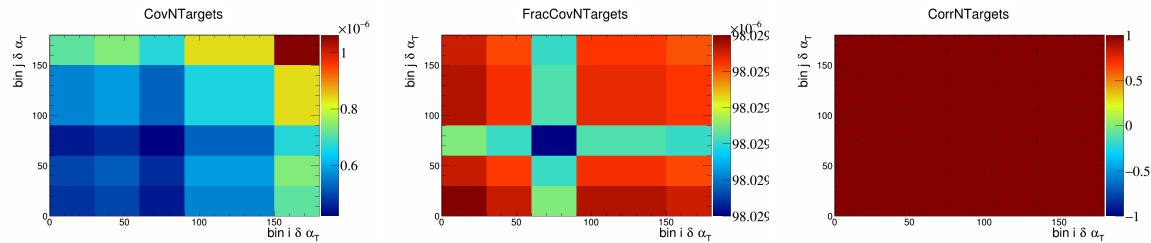


Figure 823: NTARGETS variations for  $\delta \alpha_T$ .

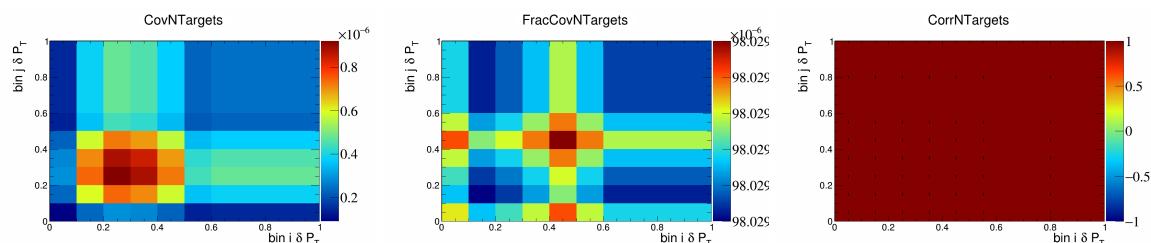


Figure 824: NTARGETS variations for  $\delta P_T$ .

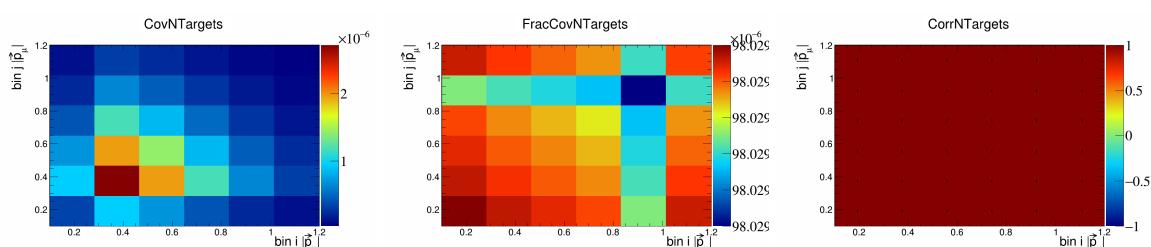


Figure 825: NTARGETS variations for  $|\vec{p}_\mu|$ .

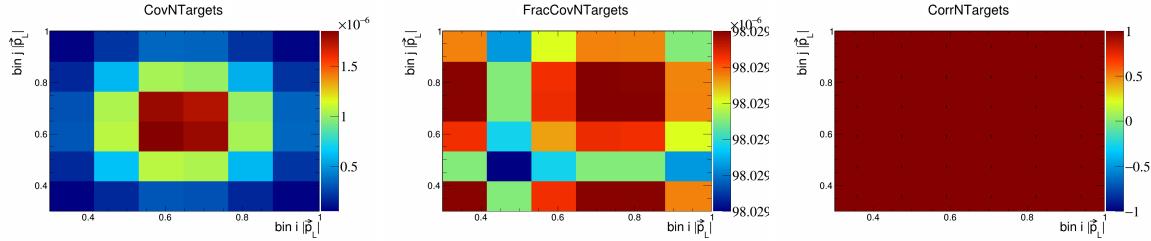


Figure 826: NTargets variations for  $|\vec{p}_L|$ .

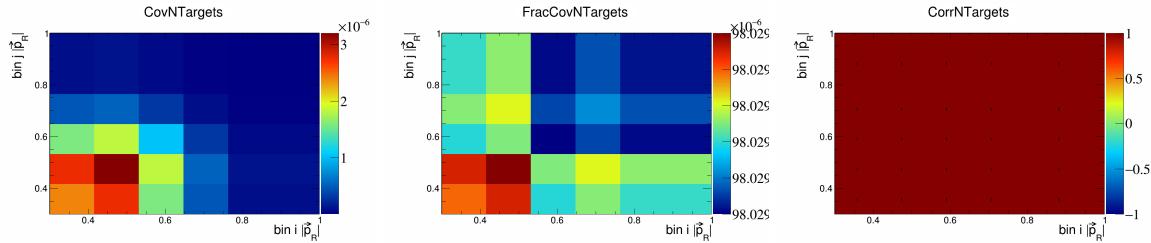


Figure 827: NTargets variations for  $|\vec{p}_R|$ .

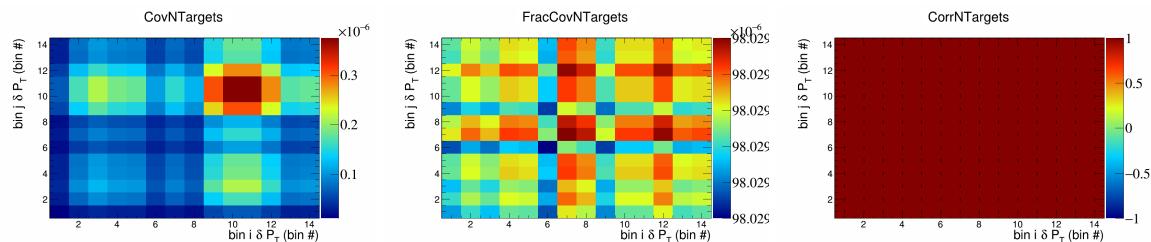


Figure 828: NTargets variations for  $\delta P_T$  in  $\cos(\theta_{\vec{p}_\mu})$ .

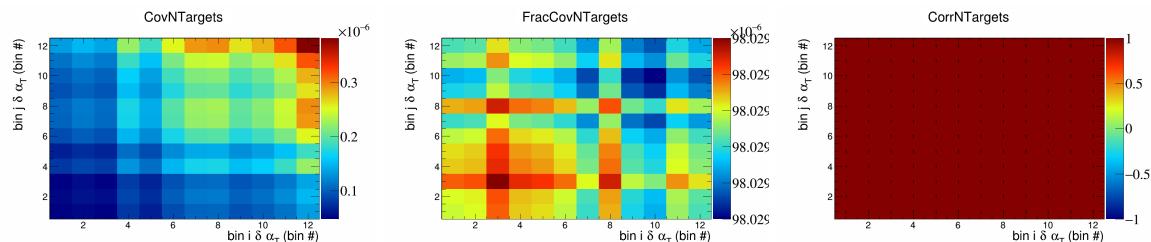


Figure 829: NTargets variations for  $\delta \alpha_T$  in  $\cos(\theta_{\vec{p}_\mu})$ .

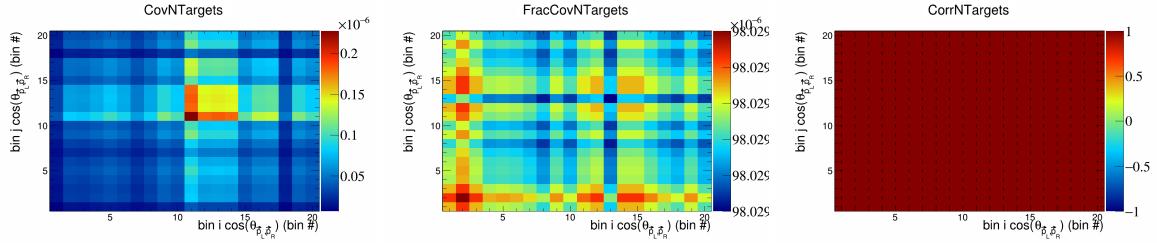


Figure 830: NTARGETS variations for  $\cos(\theta_{\vec{p}_L, \vec{p}_R})$  in  $\cos(\theta_{\vec{p}_\mu})$ .

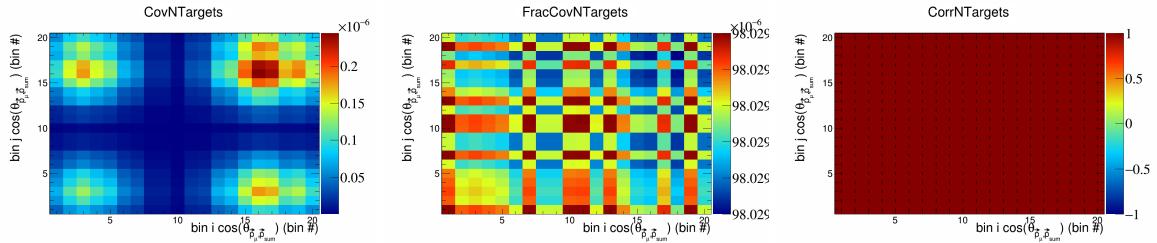


Figure 831: NTARGETS variations for  $\cos(\theta_{\vec{p}_\mu, \vec{p}_{\text{sum}}})$  in  $\cos(\theta_{\vec{p}_\mu})$ .

## 298 6.6 Detector

299 In this appendix, the covariance, fractional covariance, and correlation matrices for the detector systematics  
300 are plotted.

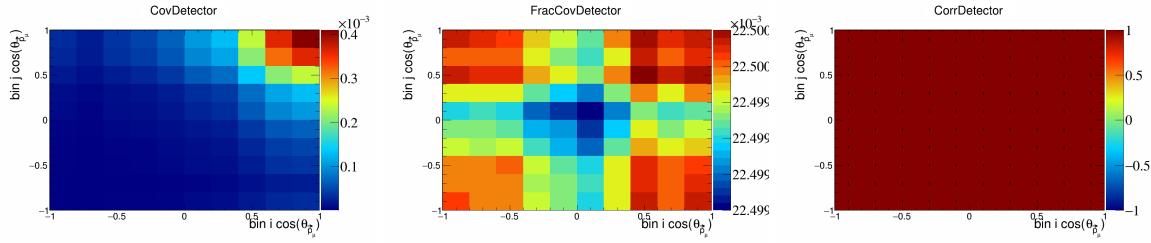


Figure 832: Detector variations for  $\cos(\theta_{\vec{p}_\mu})$ .

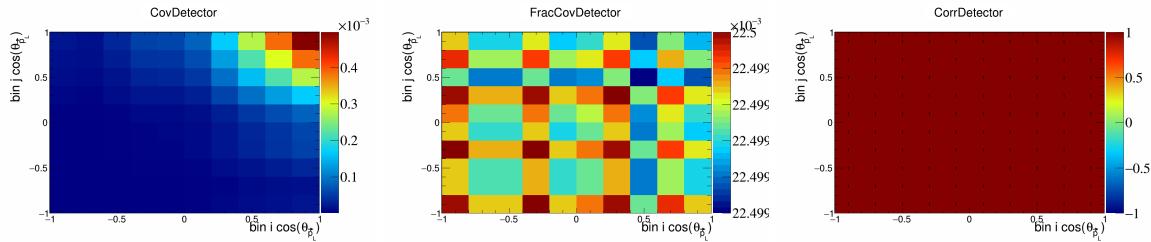


Figure 833: Detector variations for  $\cos(\theta_{\vec{p}_L})$ .

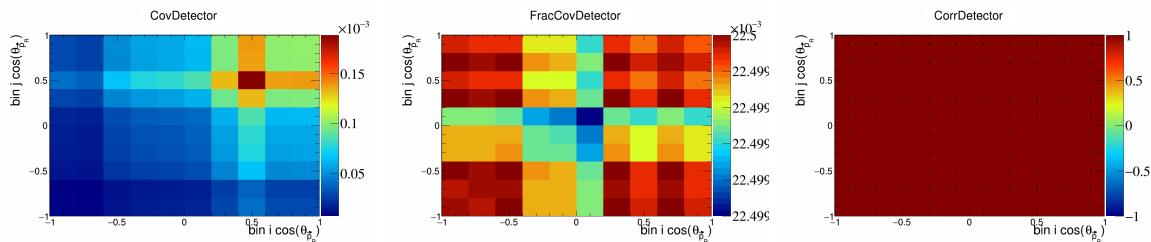


Figure 834: Detector variations for  $\cos(\theta_{\vec{p}_R})$ .

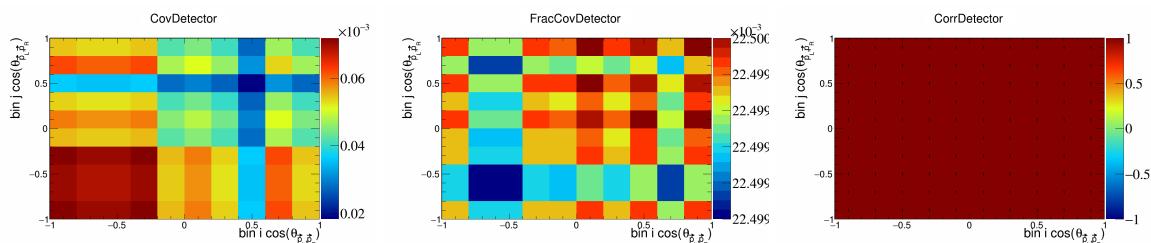


Figure 835: Detector variations for  $\cos(\theta_{\vec{p}_L, \vec{p}_R})$ .

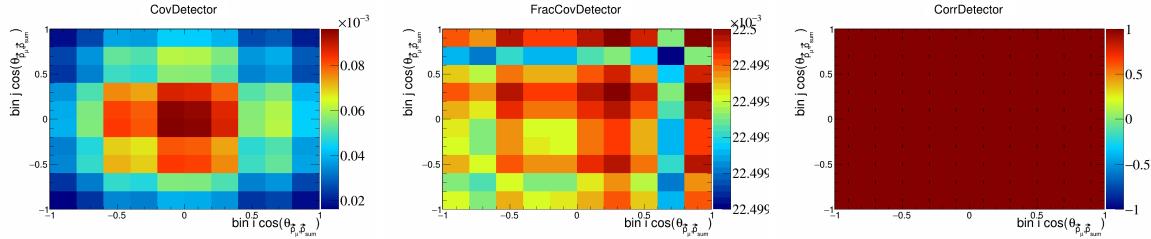


Figure 836: Detector variations for  $\cos(\theta_{\vec{p}_\mu}, \vec{p}_{\text{sum}})$ .

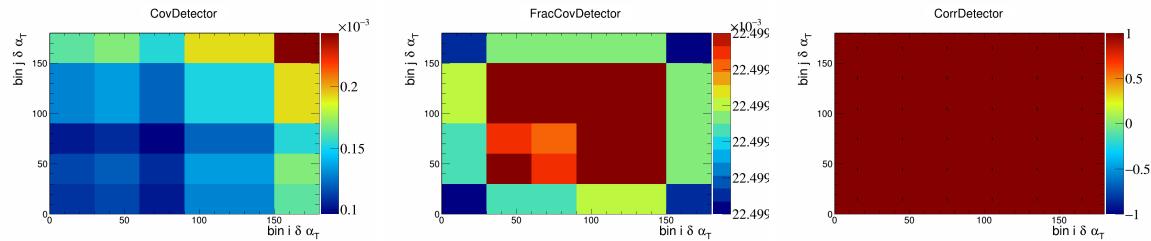


Figure 837: Detector variations for  $\delta \alpha_T$ .

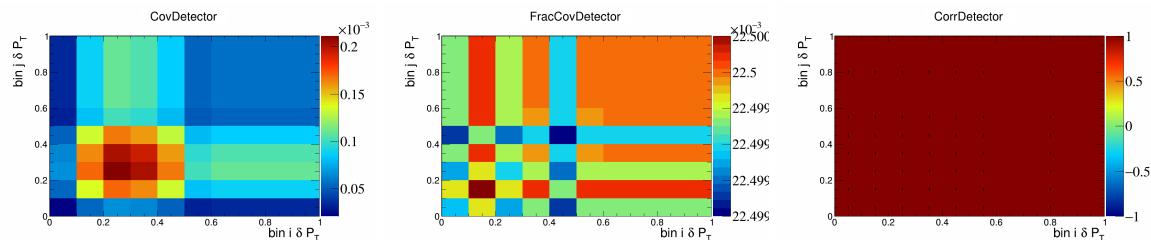


Figure 838: Detector variations for  $\delta P_T$ .

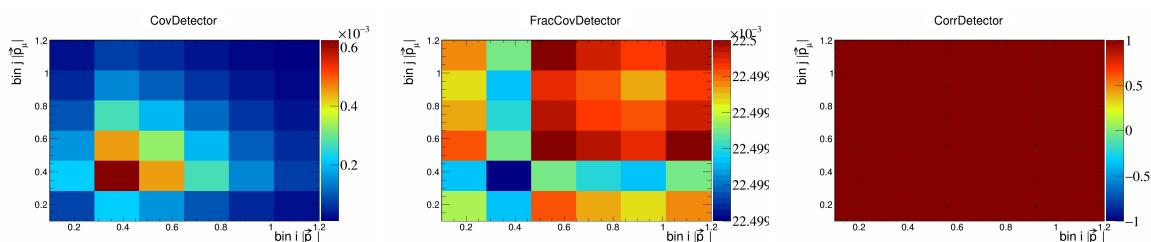


Figure 839: Detector variations for  $|\vec{p}_\mu|$ .

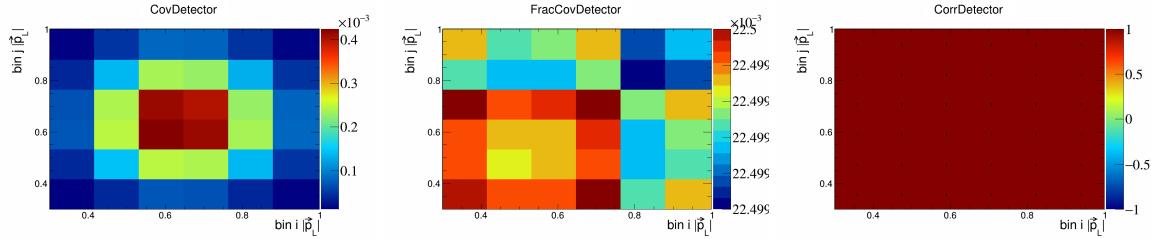


Figure 840: Detector variations for  $|\vec{p}_L|$ .

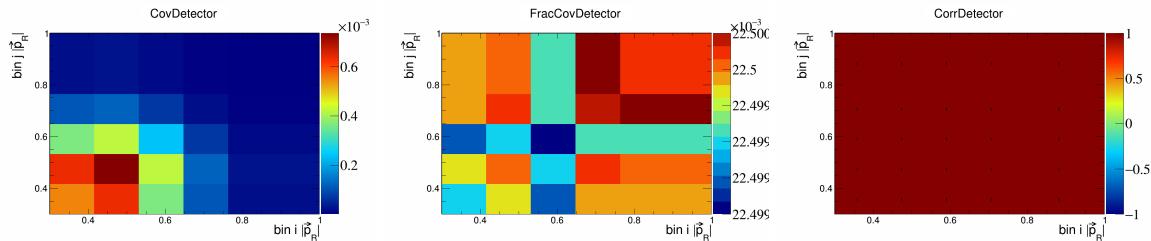


Figure 841: Detector variations for  $|\vec{p}_R|$ .

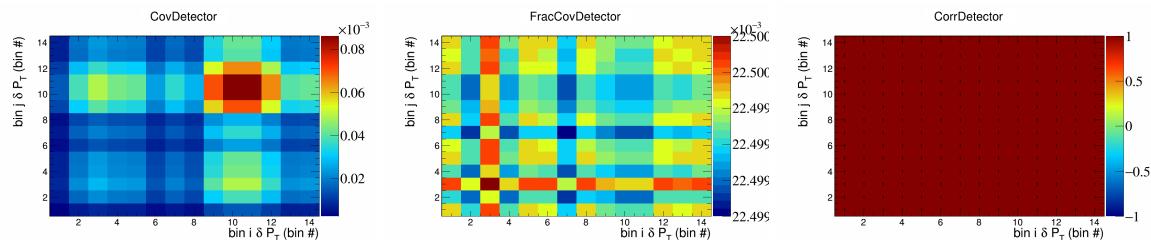


Figure 842: Detector variations for  $\delta P_T$  in  $\cos(\theta_{\vec{p}_\mu})$ .

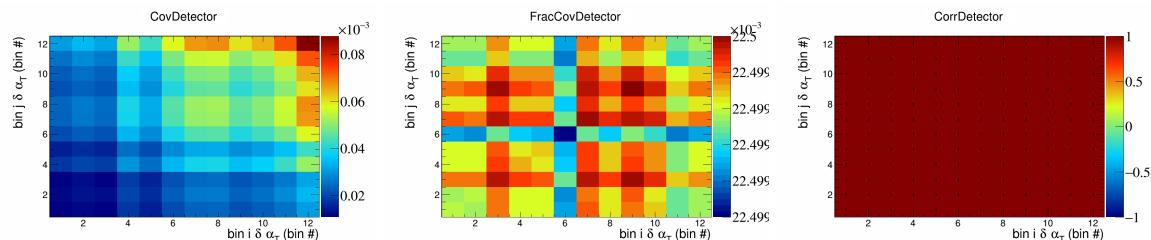


Figure 843: Detector variations for  $\delta \alpha_T$  in  $\cos(\theta_{\vec{p}_\mu})$ .

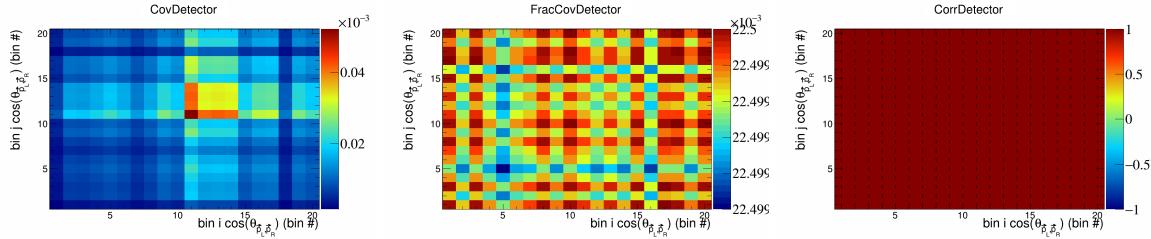


Figure 844: Detector variations for  $\cos(\theta_{\vec{p}_L, \vec{p}_R})$  in  $\cos(\theta_{\vec{p}_\mu})$ .

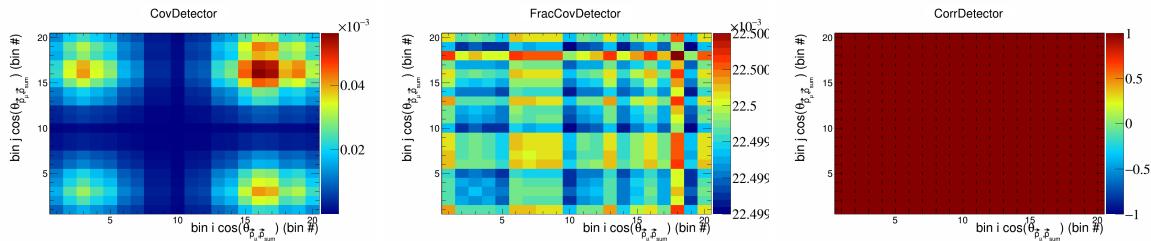


Figure 845: Detector variations for  $\cos(\theta_{\vec{p}_\mu, \vec{p}_{\text{sum}}})$  in  $\cos(\theta_{\vec{p}_\mu})$ .

## 6.7 Reinteraction

In this appendix, the covariance, fractional covariance, and correlation matrices for the reinteraction systematics are plotted.

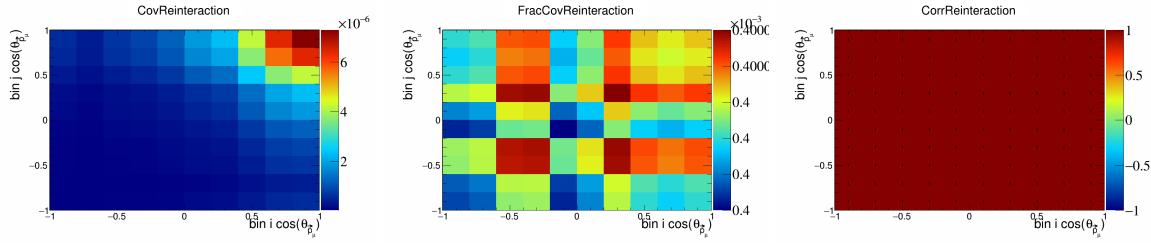


Figure 846: Reinteraction variations for  $\cos(\theta_{\vec{p}_\mu})$ .

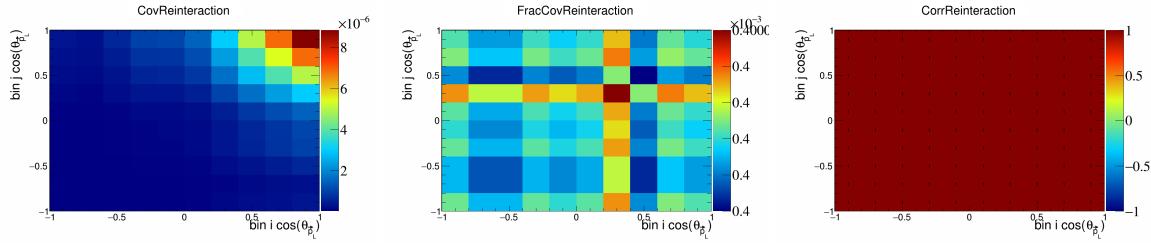


Figure 847: Reinteraction variations for  $\cos(\theta_{\vec{p}_L})$ .

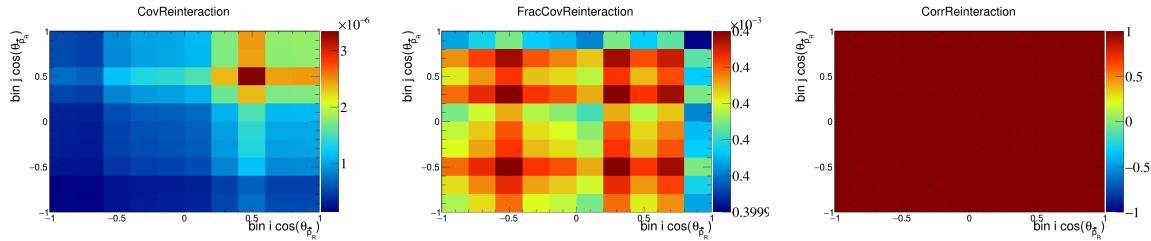


Figure 848: Reinteraction variations for  $\cos(\theta_{\vec{p}_R})$ .

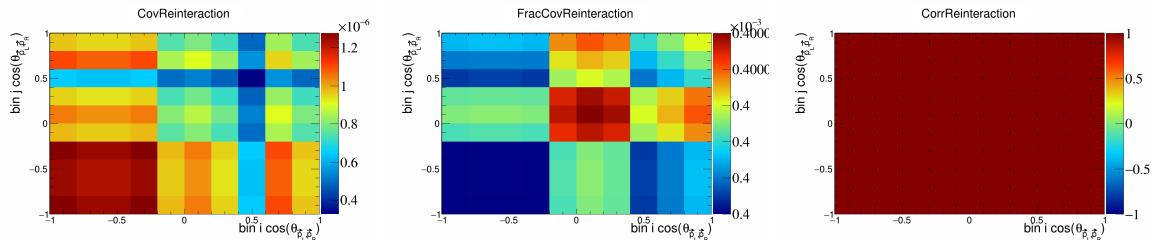


Figure 849: Reinteraction variations for  $\cos(\theta_{\vec{p}_L, \vec{p}_R})$ .

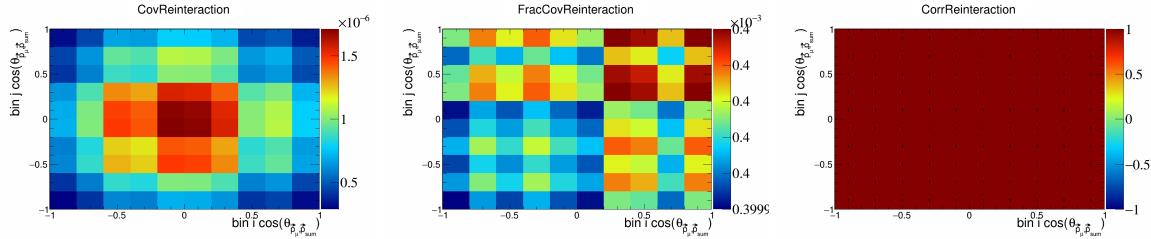


Figure 850: Reinteraction variations for  $\cos(\theta_{\vec{p}_\mu, \vec{p}_{\text{sum}}})$ .

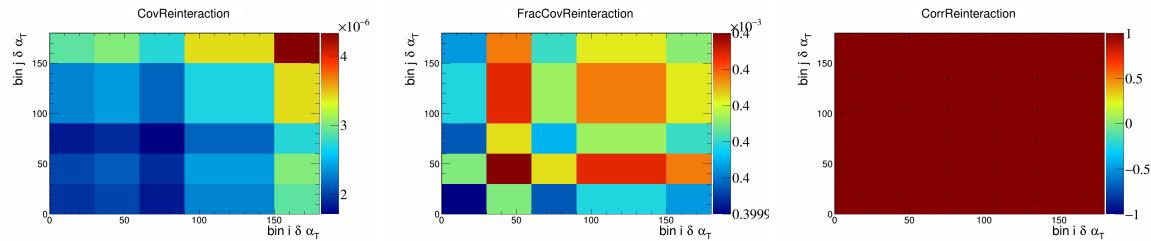


Figure 851: Reinteraction variations for  $\delta \alpha_T$ .

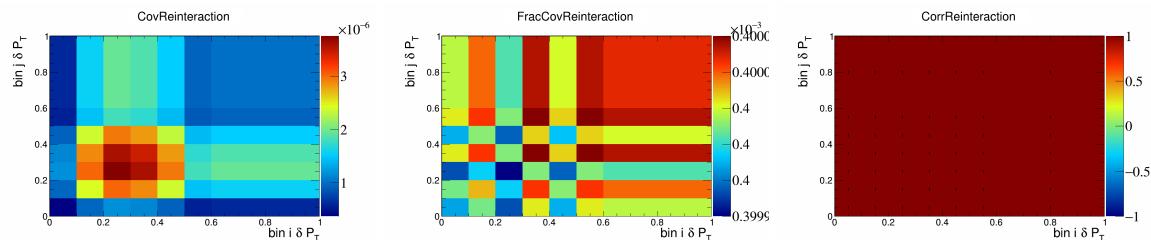


Figure 852: Reinteraction variations for  $\delta P_T$ .

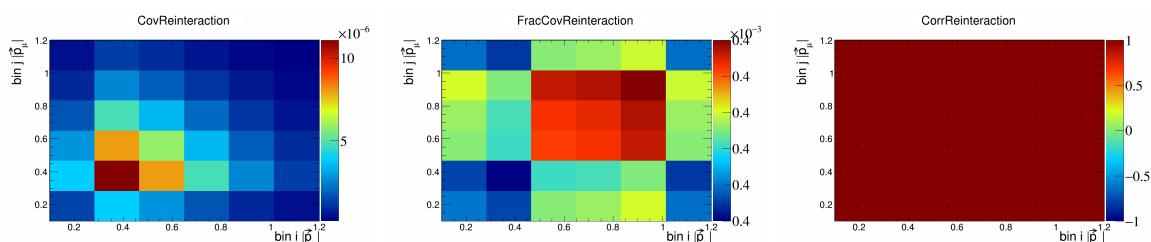


Figure 853: Reinteraction variations for  $|\vec{p}_\mu|$ .

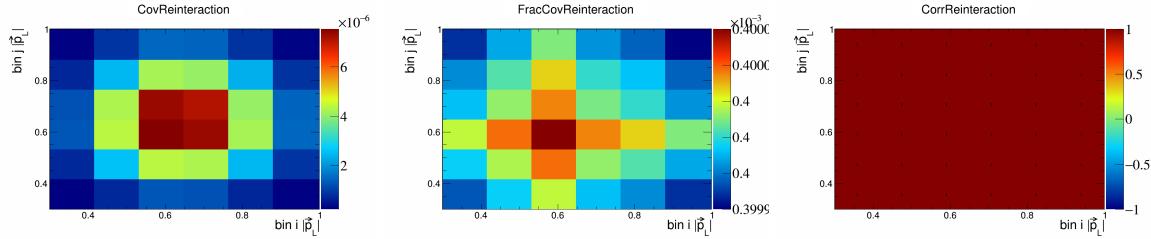


Figure 854: Reinteraction variations for  $|\vec{p}_L|$ .

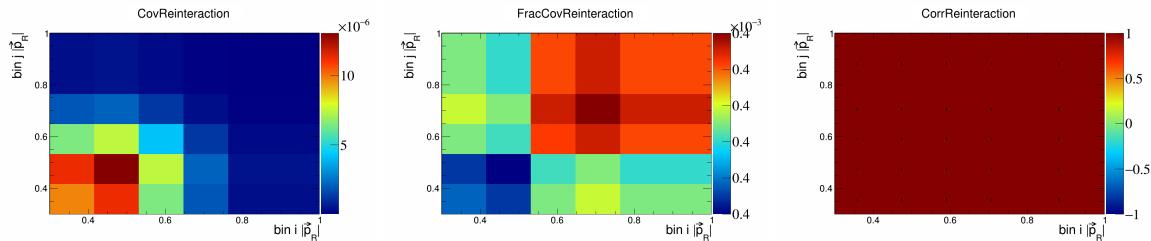


Figure 855: Reinteraction variations for  $|\vec{p}_R|$ .

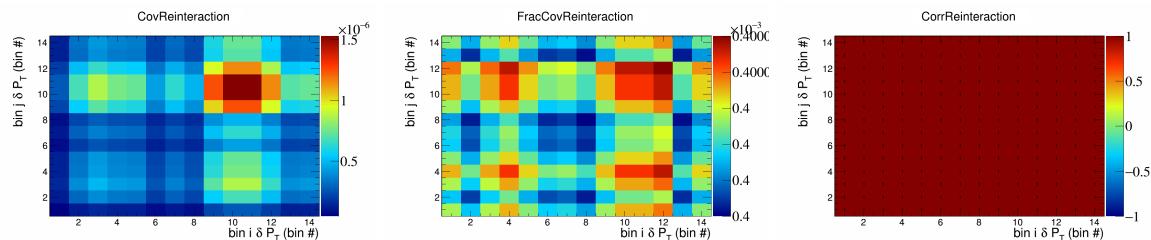


Figure 856: Reinteraction variations for  $\delta P_T$  in  $\cos(\theta_{\vec{p}_\mu})$ .

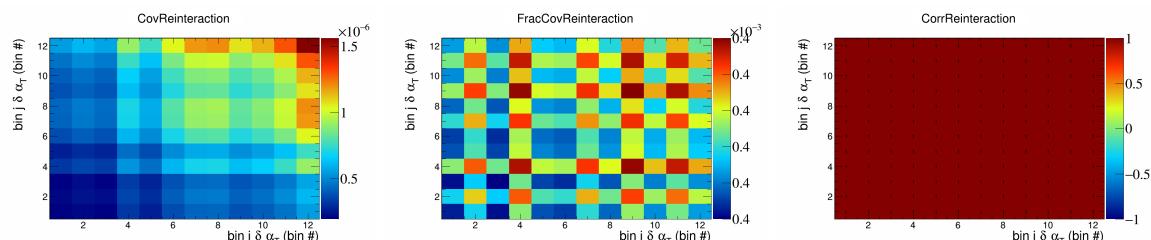


Figure 857: Reinteraction variations for  $\delta \alpha_T$  in  $\cos(\theta_{\vec{p}_\mu})$ .

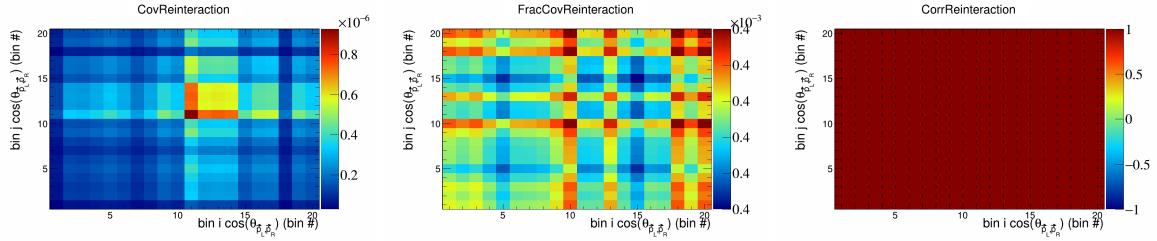


Figure 858: Reinteraction variations for  $\cos(\theta_{\vec{p}_L, \vec{p}_R})$  in  $\cos(\theta_{\vec{p}_\mu})$ .

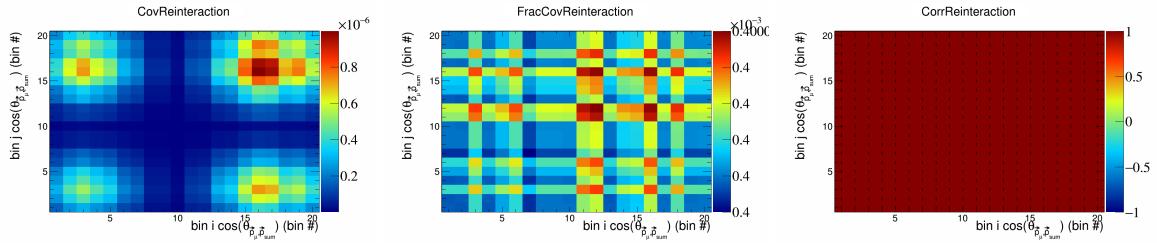


Figure 859: Reinteraction variations for  $\cos(\theta_{\vec{p}_\mu, \vec{p}_{\text{sum}}})$  in  $\cos(\theta_{\vec{p}_\mu})$ .

304    **7 References**

- 305 [1] R. Acciarri, C. Adams, J. Asaadi, B. Baller, T. Bolton, C. Bromberg, F. Cavanna, E. Church, D. Edmunds, A. Ereditato, S. Farooq, B. Fleming, H. Greenlee, G. Horton-Smith, C. James, E. Klein, K. Lang, P. Laurens, R. Mehdiyev, B. Page, O. Palamara, K. Partyka, G. Rameika, B. Rebel, M. Soderberg, J. Spitz, A. M. Szelc, M. Weber, T. Yang, and G. P. Zeller. Detection of back-to-back proton pairs in charged-current neutrino interactions with the argoneut detector in the numi low energy beam line. *Phys. Rev. D*, 90:012008, Jul 2014.
- 311 [2] C. Andreopoulos, A. Bell, D. Bhattacharya, F. Cavanna, J. Dobson, S. Dytman, H. Gallagher, P. Guzowski, R. Hatcher, P. Kehayias, A. Meregaglia, D. Naples, G. Pearce, A. Rubbia, M. Whalley, and T. Yang. The genie neutrino monte carlo generator. *Nuclear Instruments and Methods in Physics Research Section A: Accelerators, Spectrometers, Detectors and Associated Equipment*, 614(1):87–104, 2010.
- 316 [3] Costas Andreopoulos, Christopher Barry, Steve Dytman, Hugh Gallagher, Tomasz Golan, Robert Hatcher, Gabriel Perdue, and Julia Yarba. The genie neutrino monte carlo generator: Physics and user manual, 2015.
- 319 [4] D. Ashery, I. Navon, G. Azuelos, H. K. Walter, H. J. Pfeiffer, and F. W. Schlepütz. True absorption and scattering of pions on nuclei. *Phys. Rev. C*, 23:2173–2185, May 1981.
- 321 [5] P. S. Auchincloss, R. Blair, C. Haber, E. Oltman, W. C. Leung, M. Ruiz, S. R. Mishra, P. Z. Quintas, F. J. Sciulli, M. H. Shaevitz, W. H. Smith, F. S. Merritt, M. Oreglia, P. Reutens, R. Coleman, H. E. Fisk, D. Levinthal, D. D. Yovanovitch, W. Marsh, P. A. Rapidis, H. B. White, A. Bodek, F. Borcherding, N. Giokaris, K. Lang, and I. E. Stockdale. Measurement of the inclusive charged-current cross section for neutrino and antineutrino scattering on isoscalar nucleons. *Zeitschrift für Physik C Particles and Fields*, 48(3):411–431, Sep 1990.
- 327 [6] Ch. Berger and L. M. Sehgal. Lepton mass effects in single pion production by neutrinos. *Phys. Rev. D*, 76:113004, Dec 2007.
- 329 [7] Ch. Berger and L. M. Sehgal. Partially conserved axial vector current and coherent pion production by low energy neutrinos. *Phys. Rev. D*, 79:053003, Mar 2009.
- 331 [8] B. Bourguille, J. Nieves, and F. Sánchez. Inclusive and exclusive neutrino-nucleus cross sections and the reconstruction of the interaction kinematics. *Journal of High Energy Physics*, 2021(4):4, Apr 2021.
- 333 [9] R.C. Carrasco and E. Oset. Interaction of real photons with nuclei from 100 to 500 mev. *Nuclear Physics A*, 536(3):445–508, 1992.
- 335 [10] R. Cruz-Torres, D. Lonardoni, R. Weiss, N. Barnea, D. W. Higinbotham, E. Piasetzky, A. Schmidt, L. B. Weinstein, R. B. Wiringa, and O. Hen. Many-body factorization and position-momentum equivalence of nuclear short-range correlations. *Nature Phys.*, 17(3):306–310, 2021.
- 338 [11] Jonathan Engel. Approximate treatment of lepton distortion in charged-current neutrino scattering from nuclei. *Phys. Rev. C*, 57:2004–2009, Apr 1998.
- 340 [12] T. Golan, J.T. Sobczyk, and J. Źmuda. Nuwro: the wrocław monte carlo generator of neutrino interactions. *Nuclear Physics B - Proceedings Supplements*, 229-232:499, 2012. Neutrino 2010.
- 342 [13] Krzysztof M. Graczyk and Jan T. Sobczyk. Form factors in the quark resonance model. *Phys. Rev. D*, 77:053001, Mar 2008.
- 344 [14] Yoshinari Hayato and Luke Pickering. The neut neutrino interaction simulation program library. *The European Physical Journal Special Topics*, 230(24):4469–4481, Dec 2021.
- 346 [15] Teppei Katori. Meson exchange current (MEC) models in neutrino interaction generators. *AIP Conference Proceedings*, 1663(1):030001, 05 2015.

- 348 [16] Konstantin S. Kuzmin, Vladimir V. Lyubushkin, and Vadim A. Naumov. Lepton polarization in neutrino–nucleon interactions. *Modern Physics Letters A*, 19(38):2815–2829, 2004.
- 349
- 350 [17] T. Leitner, L. Alvarez-Ruso, and U. Mosel. Charged current neutrino-nucleus interactions at intermediate energies. *Phys. Rev. C*, 73:065502, Jun 2006.
- 351
- 352 [18] C.H. Llewellyn Smith. Neutrino reactions at accelerator energies. *Physics Reports*, 3(5):261–379, 1972.
- 353 [19] Selection of numu charged current induced interactions with  $N > 0$  protons and performance of events with  $N = 2$  protons in the final state in the MicroBooNE detector from the BNB, Oct 2018.
- 354
- 355 [20] First Extraction of Single Differential Cross-Sections on Argon for CC1 $\mu$ 2p0 $\pi$  Event Topologies in the MicroBooNE Detector. May 2022.
- 356
- 357 [21] Ulrich Mosel. Neutrino event generators: foundation, status and future. *Journal of Physics G: Nuclear and Particle Physics*, 46(11):113001, Sep 2019.
- 358
- 359 [22] J. Nieves, J. E. Amaro, and M. Valverde. Inclusive quasielastic charged-current neutrino-nucleus reactions. *Phys. Rev. C*, 70:055503, Nov 2004.
- 360
- 361 [23] J. Nieves, F. Sánchez, I. Ruiz Simo, and M. J. Vicente Vacas. Neutrino energy reconstruction and the shape of the charged current quasielastic-like total cross section. *Phys. Rev. D*, 85:113008, Jun 2012.
- 362
- 363 [24] J. Nieves, I. Ruiz Simo, and M. J. Vicente Vacas. Inclusive charged-current neutrino-nucleus reactions. *Phys. Rev. C*, 83:045501, Apr 2011.
- 364
- 365 [25] J. Schwehr, D. Cherdack, and R. Gran. Genie implementation of ific valencia model for qe-like 2p2h neutrino-nucleus cross section, 2017.
- 366
- 367 [26] Torbjörn Sjöstrand, Stephen Mrenna, and Peter Skands. Pythia 6.4 physics and manual. *Journal of High Energy Physics*, 2006(05):026, may 2006.
- 368
- 369 [27] W. Tang, X. Li, X. Qian, H. Wei, and C. Zhang. Data unfolding with wiener-svd method. *Journal of Instrumentation*, 12(10):P10002–P10002, October 2017.
- 370
- 371 [28] Júlia Tena-Vidal, Costas Andreopoulos, Adi Ashkenazi, Christopher Barry, Steve Dennis, Steve Dytman, Hugh Gallagher, Steven Gardiner, Walter Giele, Robert Hatcher, Or Hen, Libo Jiang, Igor D. Kakorin, Konstantin S. Kuzmin, Anselmo Meregaglia, Vadim A. Naumov, Afroditi Papadopoulou, Gabriel Perdue, Marco Roda, Vladyslav Syrotenko, and Jeremy Wolcott. Neutrino-nucleon cross-section model tuning in genie v3. *Phys. Rev. D*, 104:072009, Oct 2021.
- 372
- 373 [29] U. K. Yang and A. Bodek. Parton distributions,  $d/u$ , and higher twist effects at high  $x$ . *Phys. Rev. Lett.*, 82:2467–2470, Mar 1999.
- 374
- 375
- 376
- 377